OCS Study
MMS 98-0040

An Observational Study of the Mississippi-Atchafalaya Coastal Plume

Final Report

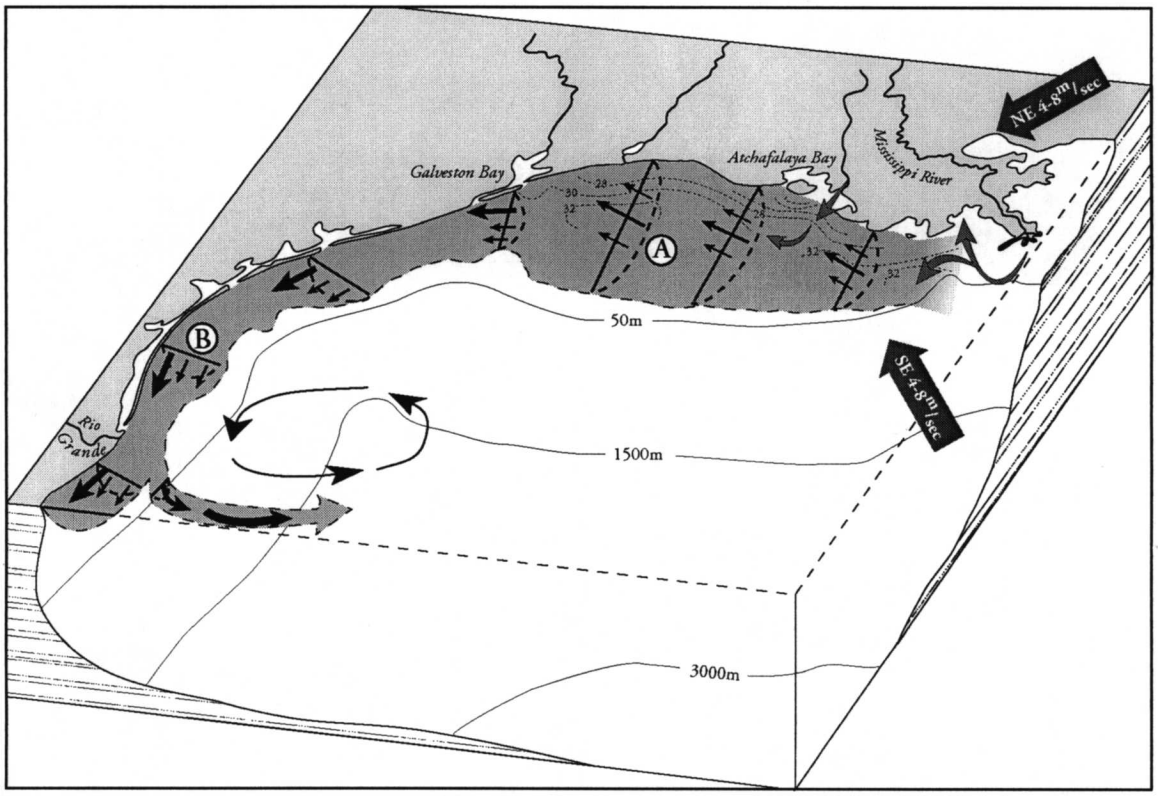

MMS U.S. Department of the Interior
Minerals Management Service
Gulf of Mexico OCS Region

OCS Study
MMS 98-0040

An Observational Study of the Mississippi-Atchafalaya Coastal Plume

Final Report

Editor

Stephen P. Murray

Prepared under MMS Contract
14-35-0001-30632
by
Coastal Studies Institute
Louisiana State University
Baton Rouge, Louisiana 70803

Published by

U.S. Department of the Interior
Minerals Management Service
Gulf of Mexico OCS Region

New Orleans
September 1998

DISCLAIMER

This report was prepared under contract between the Minerals Management Service (MMS) and Coastal Studies Institute, Louisiana State University. This report has been technically reviewed by the MMS and approved for publication. Approval does not signify that the contents necessarily reflect the views and policies of the Service, nor does mention of trade names or commercial products constitute endorsement or recommendation for use. It is, however, exempt from review and compliance with MMS editorial standards.

REPORT AVAILABILITY

Extra copies of the report may be obtained from the Public Information Office (MS 5034) at the following address:

U.S. Department of the Interior
Minerals Management Service
Gulf of Mexico OCS Region
Public Information Office (MS 5034)
1201 Elmwood Park Boulevard
New Orleans, Louisiana 70123-2394

Telephone Number: (504) 736-2519 or
1-800-200-GULF

CITATION

Suggested Citation:

Murray, S.P. 1997. An observational study of the Mississippi-Atchafalaya coastal plume: Final report. OCS Study MMS 98-0040. U.S. Dept. of the Interior, Minerals Mgmt. Service, Gulf of Mexico OCS Region, New Orleans, La. 513 pp.

Cover

The cover was drawn by Lisa Wood and Robert Paulsell, Center for Coastal Energy and Environmental Resources, Special Programs. This drawing shows an idealized steady state coastal plume and is one of five showing schematics of coastal plume dynamics. See Figures 84a-e for detailed discussion.

PRINCIPAL INVESTIGATORS AND KEY PERSONNEL

Remote Sensing and Image Processing
Nan D. Walker, Coastal Studies Institute, LSU, Baton Rouge, LA
Lawrence J. Rouse, Jr., Coastal Studies Institute, LSU, Baton Rouge, LA
Oscar K. Huh, Coastal Studies Institute, LSU, Baton Rouge, LA

Hydrographic Survey
Stephen P. Murray, Coastal Studies Institute, LSU, Baton Rouge, LA
Curtis C. Ebbesmeyer, Evans-Hamilton, Inc., Seattle, WA
Neal Pettigrew, Department of Oceanography, University of Maine, Orono, ME

Sediment Flux
Wilford D. Gardner, Department of Oceanography, Texas A&M, College Station, TX
Mary Jo Richardson, Department of Oceanography, Texas A&M, College Station, TX

Benthic Boundary Layer
L. Don Wright, School of Marine Science, VIMS, College of William & Mary, Gloucester Point, VA
R. W. Sternberg, School of Oceanography, University of Washington, Seattle, WA
C. Sherwood, Battelle Marine Sciences Laboratory, Sequim, WA

Light and Nutrients
R. Eugene Turner, Coastal Ecology Institute, LSU, Baton Rouge, LA

Hypoxia and Pigments
Nancy Rabalais, Louisiana Universities Marine Consortium, Cocodrie, LA

Phytoplankton
Quay Dortch, Louisiana Universities Marine Consortium, Cocodrie, LA

Zooplankton
Richard F. Shaw, Coastal Fisheries Institute, LSU, Baton Rouge, LA

Pollutant Chemistry
Jay C. Means, Aquatic Toxicology Laboratory, School of Veterinary Medicine, LSU, Baton Rouge, LA
Debra J. McMillin, Aquatic Toxicology Laboratory, School of Veterinary Medicine, LSU, Baton Rouge, LA

Data Management
Mary L. White, Coastal Ecology Institute, LSU, Baton Rouge, LA

Program Management
Stephen P. Murray, Coastal Studies Institute, LSU, Baton Rouge, LA

Field Logistics
Rodney Fredericks, Coastal Studies Institute, LSU, Baton Rouge, LA

TABLE OF CONTENTS

Page

LIST OF FIGURES

LIST OF TABLES

I. GENERAL INTRODUCTION

The Mississippi River Plume Hydrography study (LATEX B) is part of a larger Louisiana-Texas Physical Oceanography Program, which conducted field observations from 1992-1994. The objective of this component of the program was to characterize the hydrographic and the velocity structure, the pollutant chemistry, and biological properties of the coastal plume arising from the discharge of the Mississippi and Atchafalaya Rivers. A general geographic map of the area is presented as Figure 1.

This final report of the project presents new data from our cruises in 1994, including the one cruise designed to sample the near-field plume of the Mississippi River. More importantly, this report synthesizes the data from all six cruises over a three-year period. Considering the paucity of knowledge prior to our study, the original objectives were laid out without the benefit of extensive supporting data and reflected the physical processes identified at an MMS-sponsored workshop (Symposium on the Physical Oceanography of the Louisiana/Texas (LA/TX) Shelf, Galveston, Texas, May 24-26, 1989) as important in this area. After five years of cruises and data analyses, the complexity of detail and the extreme spatial and temporal variability in the velocity and property fields of the Mississippi-Atchafalaya coastal plume has now come to light. Prior to this project, detailed knowledge of this coastal plume was sorely lacking.

The Mississippi-Atchafalaya River system typically has a peak discharge in April in excess of 30,000 m^3/s and a low in September to October of about 10,000 m^3/s. Satellite images and scattered observations of the hydrographic and current regimes of the coastal waters from the Mississippi Delta west and south to the Texas-Mexico border indicate the presence of a brackish water, turbid plume emanating from this discharge. This plume is strongly modulated and even reversed by the annual cycle of the winds from Louisiana to south Texas. Intense northerly wind events associated with frontal passages in late fall, winter, and early spring apparently completely disrupt the Atchafalaya source of the coastal current and its dissolved and suspended sediment particulate load. We expected the inner shelf distribution of waters and sediments to result from the interaction of momentum, buoyancy forces, winds, waves, longshore currents, and pressure gradients (sea surface slope and density gradients).

Fresh water distribution has heretofore been the most valuable tracer of large-scale water motion in the LATEX region. The fresh water content in the coastal plume and on the shelf is clearly an annual cycle triggered by the spring flood of the Mississippi-Atchafalaya Rivers (Dinnel and Wiseman, 1986). The Mississippi-Atchafalaya discharge is advected westerly and southerly along the LATEX coastline even as far as Mexico by downcoast wind components from the time of spring flood until early summer. The onset of strong southerly and southeasterly winds in early summer off Mexico and south Texas then exert upcoast wind stress components on the low salinity layer near the coast, reversing the flow, causing a convergence in the coastal currents, and advecting low salinity water offshore as Ekman transport in the surface layer. The result of this activity is that nearly the entire LATEX shelf east of Galveston Bay out to the 200 m isobath is covered with low salinity water by late July. With the slackening of the strong southerly and southeasterly winds in late summer, downcoast flow returns to the LATEX region and downwelling favorable winds re-establish the low salinity coastal current (Cochrane and Kelly, 1986). Salinity in the south Texas coastal current decreases as water of northerly origin advects back into the region (Smith, 1980). Salinities

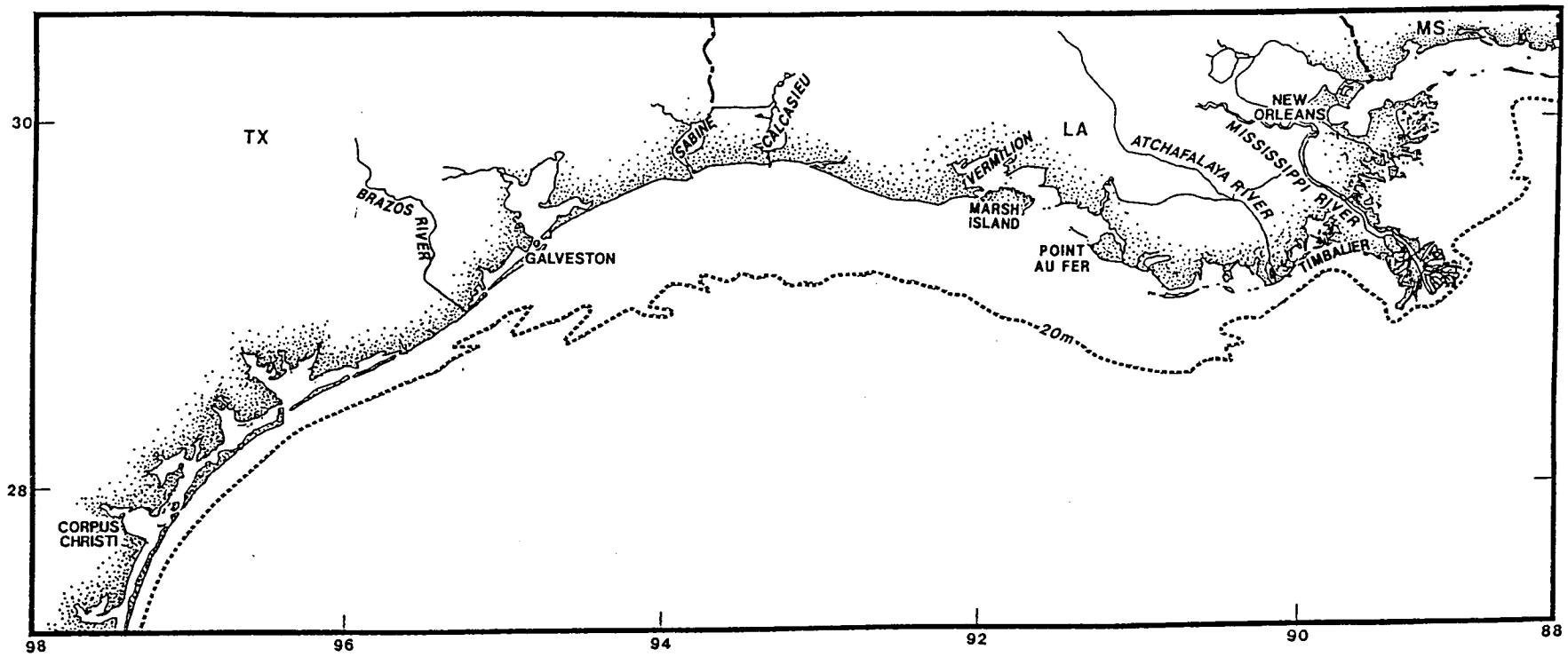

Figure 1. Location map of LATEX Program study area.

gradually increase in October all along the LATEX coastal plume region as the major rivers approach low river discharges.

The link between the dynamics of the coastal plume and its chemistry and biology is nowhere more apparent than off central Louisiana. The Mississippi and Atchafalaya Rivers (a third of the total flow of the Mississippi River system enters the Gulf of Mexico via the Atchafalaya River) are the major source of "new" nutrients to phytoplankton on the inner and mid-shelf. Since the 1950s, water quality in the Mississippi River has changed dramatically (Meade and Parker, 1985; Smith et al., 1987; Turner et al., 1987). Suspended sediments and silicate concentrations have decreased since the 1950s, whereas nitrogen and phosphorus loadings have increased. These large changes, resulting from human activities, provide a basis for concern that this loading, combined with increased water clarity, have resulted in a "eutrophication" effect on the shelf. The area impacted by, and the duration of, hypoxia on the Louisiana shelf is of considerable concern since Louisiana fisheries are 28% of the U.S. total. Fish, shrimp, and benthic annual densities are severely depressed in these hypoxic zones and critical periods of the life history of several commercially important species (Renaud, 1986) may be affected. Of more recent concern is the content of chemical pollutants as they are transported via fresh water into the open Gulf waters.

Accordingly, this project has focused on the structure and dynamics of the coastal plume, its nutrient and pollutant chemistry, its biological characteristics—phytoplankton, zooplankton and ichthyology—and the characteristics of its suspended sediment. The extensive use of satellite-acquired remotely sensed data added a unifying element to the interpretation of the physical, biological, and chemical data.

The following chapters present our first real attempt to explore these links. The impressive sum of data gathered during our project and the conclusions reached from its analysis will allow for an increasingly more detailed understanding of the coastal plume system in the future.

II. Physical Oceanographic Observations of the Coastal Plume

by Stephen P. Murray, Ewa Jarosz and E.T. Weeks, III

A. Introduction

A series of five cruises was run in 1992-1994 with the objective of characterizing the velocity and salinity-temperature-density structure of the coastal plume that emanates from the discharge of the Atchafalaya and Mississippi Rivers. Satellite images in both thermal and visible bands have long suggested the presence of a longshore coherent plume-like structure that originates often (but not always) near the Mississippi River mouths, is augmented by the outflow of the Atchafalaya River and then extends westward at least as far as Galveston, TX, and episodically as far south and west as the U.S.- Mexican border. See Figure 2 for a location map.

The observed westward extension of this plume is, of course, in general agreement with the simple notion of a geostrophic adjustment of a major river outflow: It deflects to the right upon entering the Gulf of Mexico basin and produces a buoyancy driven coastal current trapped against the coastline as modeled by Chao (1987).

Observations, however, did not readily support this simple conveyor belt model. Rather, they suggested strong seasonal and spatial variability along the coast. Prior to 1986, observations of currents in the region, occupied by this coastal plume were usually limited to a few closely spaced moorings at widely separated sites (Kelly et al., 1983; Crout et al., 1984). Crout et al. (1984), for example, report weak, disorganized currents in summer on the western Louisiana inner shelf but much stronger currents in winter, coherent with the stronger winter wind forcing. Smith (1978b, 1980) similarly reports significant current variability on the central Texas inner shelf.

The benchmark synthesis of physical data on the Louisiana-Texas shelf by Cochrane and Kelly (1986) (hereafter referred to as C/K) proposed a low frequency circulation scheme consistent with the diverse hydrographic current and wind data sets available at that time. The major feature emerging from this study is a large cyclonic gyre that occupies most of the shelf except during July and August. Figure 3a from this study shows the prevalent circulation with presumed geostrophic westward currents along the inner shelf and a counter current on the outer shelf to complete the gyre. In the late summer (Figure 3b) a high develops on the Louisiana inner shelf, and the inshore coastal current actually reverses to flow eastward along the Texas coast. It is important to note that the temporal resolution of the C/K flow schema is seasonal-monthly. Earlier drift studies, Kimsey and Temple (1964), suggested an eastward (or upcoast) flowing current in summer extending well onto the Louisiana shelf. We will frequently use the terminology downcoast and upcoast. Downcoast refers to the direction of propagation of a coastal Kelvin wave that must travel with the coast to its right in the northern hemisphere. Downcoast movement is thus westward on the Louisiana inner shelf and southwestward and southward on the Texas coast. Upcoast movement correspondingly is northward, northeastward, and eastward moving from south Texas into Louisiana.

C/K conclude that the alongshore wind stress is the major driving mechanism for the coastal currents. The westward low frequency currents that form the inner limb of the gyre are largely in phase with the downcoast alongshore wind stress component from September through June, especially west of 92.5° W. With the advent of the summer wind regime, an upcoast component of the prevailing winds migrates northward and eastward from the south Texas coast reaching almost to Cameron, Louisiana, in July. These eastward wind stresses then are associated with the proposed high pressure area over the inner and mid-shelf and eastward coastal currents in summer.

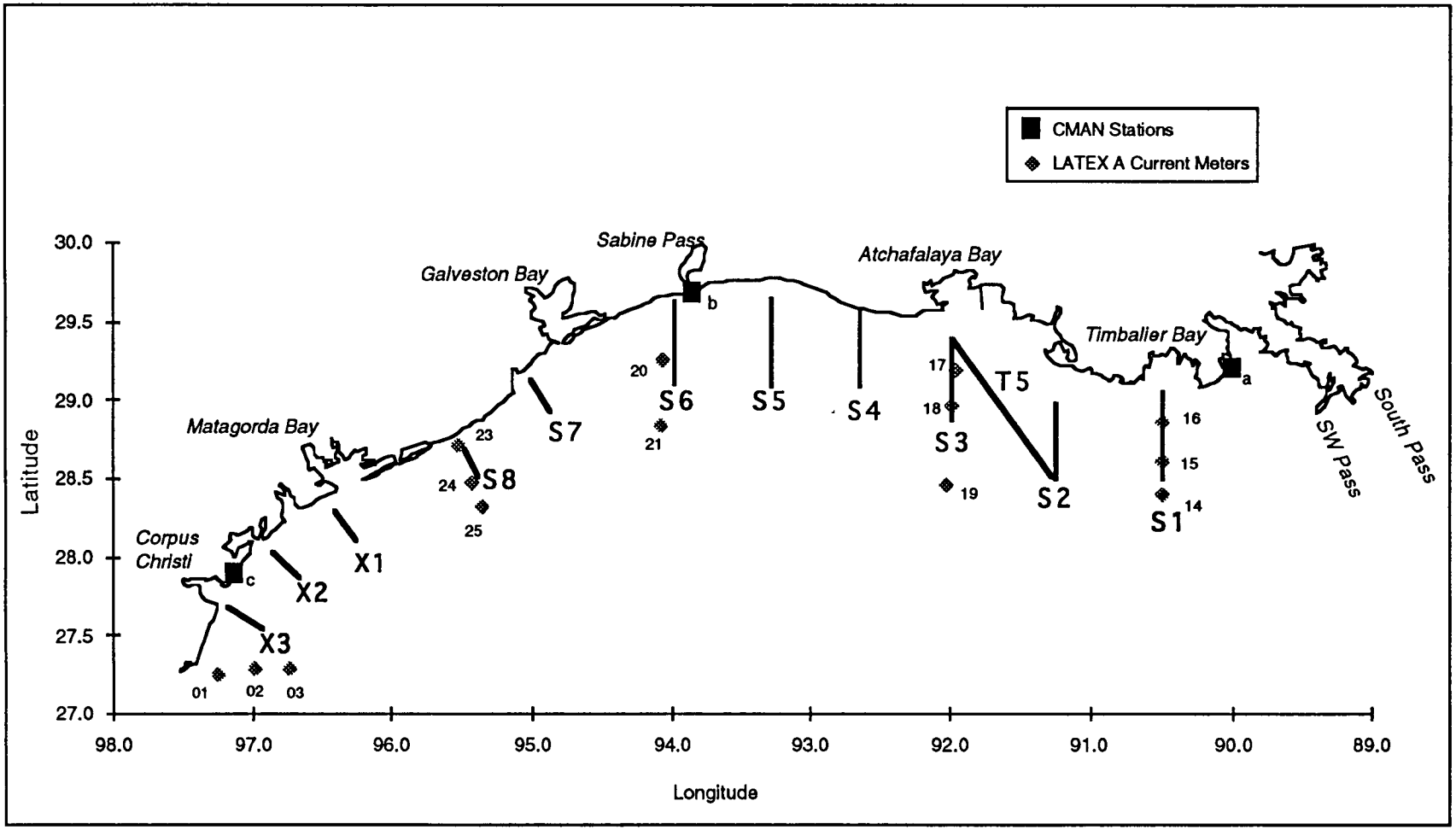

Figure 2. Location map of LATEX B study area, showing major section lines (S1 through X3). Small numbers show current meter moorings deployed by the LATEX A project; squares show the three CMAN stations mentioned in the text at (a) Grand Isle, (b) Sea Rim State Park, (c) Port Aransas, and (d) Brownsville (not shown on this map; refer to Figure 1 for location).

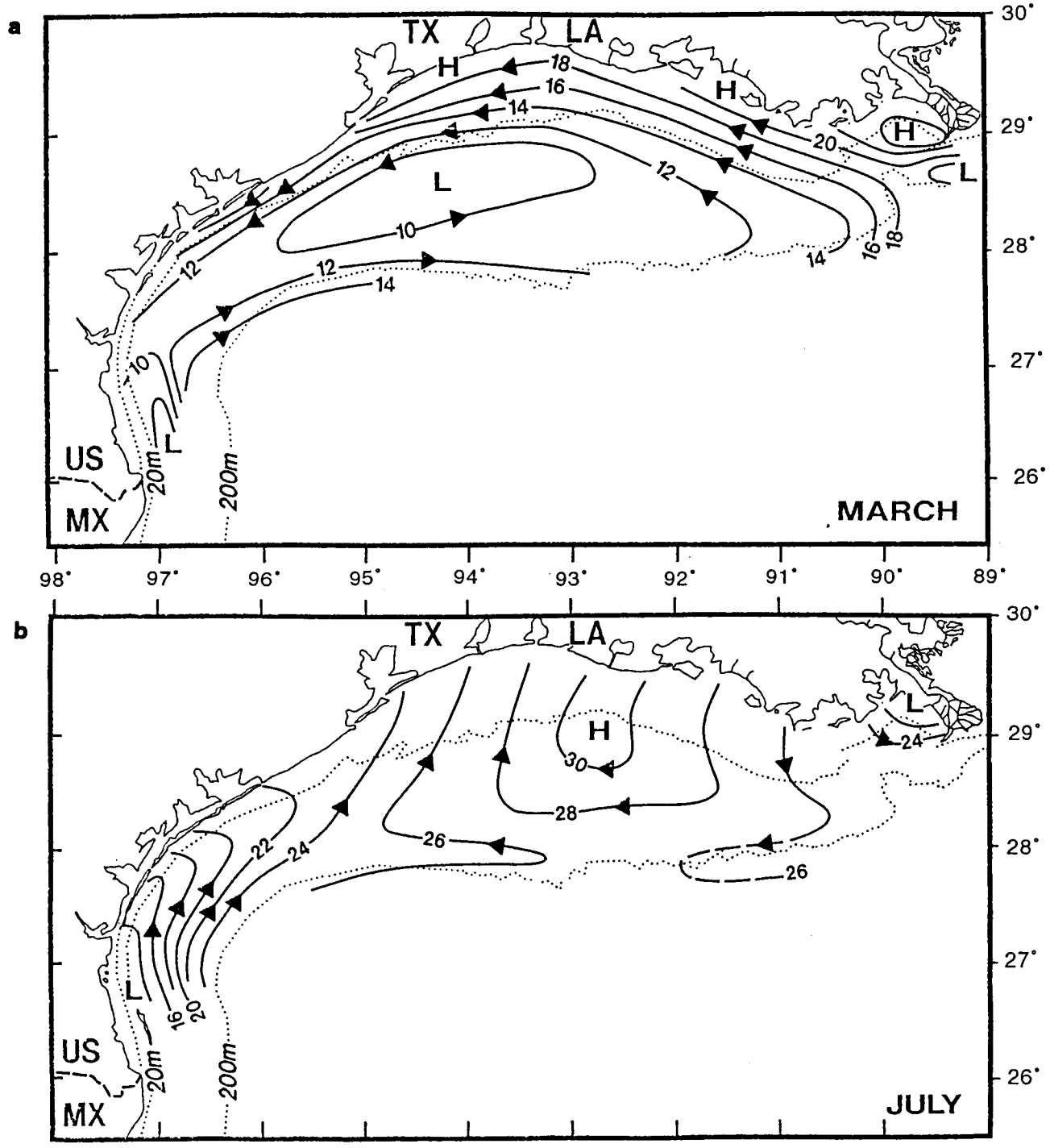

Figure 3. Winter and summer panels adapted from Cochrane and Kelly (1986) circulation schema.

The turbid plume observed along the coast in satellite images then is apparently associated with the inner or coastal limb of the C/K cyclonic gyre. The C/K synthesis leaves us with a very broad outline of the monthly variability in the location and transport direction of a wind-driven coastal current that carries the altered plume waters discharged by the Atchafalaya River and some portion of the Mississippi River. It is implied from their analysis that wind forcing is clearly dominant over buoyancy forcing in the coastal current associated with the Mississippi-Atchafalaya coastal plume.

1. Objectives

The program discussed in this report is designed with the following objectives: (1) to characterize at a much higher resolution than the C/K model the velocity and salinity- temperature (density) structure of this coastal plume and coastal current, including vertical, cross-shore and longshore variability; (2) to document the role of temporal variability produced by variation in wind forcing in the weather band (2-4 days); (3) to evaluate the role of a seasonal variability of freshwater discharge in determining the spatial structure of the coastal plume with regard to both internal velocity fields and hydrographic properties; (4) to investigate the relative importance of wind forcing buoyancy and longshore pressure gradients in the dynamics of the coastal plume; and, (5) to provide a seasonally based descriptive circulation model to the biologists, chemists, and remote sensing scientists to aid in the interpretation of their data sets.

The hydrographic featuares arising largely from the combined discharges of the Mississippi and Atchaflaya Rivers is referred to in this report as "the coastal plume" or the Mississippi-Atchafalaya coastal plume (MACP). Others, e.g., Wiseman and Garvine (1995), refer to parts of this same feature as the Louisiana Coastal Current. Additionally, Vastano et al. (1995) refer to the downcoast extension of the MACP as the Texas current.

B. Measurement Techniques

The principle observational technique was the collection of data on five cruises of the R/V Pelican, the research vessel of the Louisiana Universities Marine Consortium (LUMCON). The five cruises listed in Table 1 extended from off Terrebonne Bay, Louisiana at 90° 30′ W westward and southward along the Texas coast, in two cases as far as 28° 34′ N just south of Corpus Christi. It generally took about 6 to 7 days to complete the outbound survey grid, making from 100 to 120 CTD stations on each cruise. Another two to three days were used in various small scale sampling requirements and the return leg home.

A Sea Bird Model 911+ CTD, deployed at each station and equipped with a Rosette sampler, obtained profiles of temperature, salinity, oxygen, and other parameters discussed in the subsequent sections. Calibration was maintained with pre- and post-cruise checks against a bench salinometer and scheduled factory calibrations. For this particular study an RDI 1200 Khz acoustic Doppler current profiler (ADCP) was deployed in an "over the side" configuration. Over 90% of our ADCP data was taken in bottom-track mode.

Table 1. Statistics for each LATEX B cruise.

Cruise	Dates	# of CTD Stations	Km ADCP	Atchafalaya River Discharge (m^3/sec)	Wind Season
I	April 13-22, 1992	127	2300	12,500	late winter, energetic
II	October 5-15, 1992	118	2014	5,900	early winter, energetic
III	April 13-22, 1993	110	2156	19,000	spring, energetic
IV	July 13-22, 1993	141	1857	13,000	summer, low energy
VI	July 11-22, 1994	122	2017	7,500	summer, low energy

In addition to the inherent accuracy of the bottom track mode, we performed reciprocal (repeat section) calibration, lines at the beginning and end of each 10 day cruise. We also performed a special one-day cruise date devoted entirely to ADCP calibration. Nominally 10 ensembles of two-minute duration were collected on two orthogonal repeat lines (referred to as runs, e.g., R2 is the reciprocal of R1), which typically gave a standard deviation of 2-3 cm/sec for the bottom track data. The usual formulations of Joyce (1989) and Pollard and Read (1989) were used to compute the transducer misalignment and amplitude coefficients. Examples of calibration results are given in Table 2, after applying the average calibration coefficients determined from that entire set of runs.

Table 2. Examples of ADCP calibration data.

Cruise II W = 0.45; AMP= 1.0103		Special Calibration Cruise W = .196; AMP = 1.0170	
Run No.	Speed Error (cm/sec)	Run No.	Speed Error (cm/sec)
R1-R2	2.2	R1-R2	5.3
R3-R4	2.7	R3-R4	4.5
R5-R6	3.5	R5-R6	3.4
R9-R10	4.9	R7-R8	2.3
R11-12	3.6	R9-R10	5.5
Mean	3.4	Mean	4.2
St. Dev.	0.9	St. Dev.	1.2

Four of the five coastal cruises discussed here and the Mississippi River near-field plume cruise (Chapter III) were run with an outboard boom containing the ADCP transducer rigidly attached to the side of the ship, a configuration that consistently gave high quality data returns. Cruise I, however, was run with the ADCP fixed into a partially submerged sled towed from a boom extending off the port beam of the ship. This configuration performed adequately in low seas but data quality deteriorated markedly in moderate seas. This Cruise I ADCP data set required considerable editing and subsequent data loss. Deviations in the magnetic flux gate compass caused by the ship's magnetic field and orientation of the ship required correction as detailed in Munchow et al. (1995).

The third major instrument system was a thermosalinograph equipped with a Sea Bird conductivity cell. Water intake was one meter below the still-water surface. Navigation of Cruise I and II was by conventional GPS while on subsequent cruises differential GPS was available. Ancillary data used in the implementation of the cruise-derived data sets include current meters

deployed under the LATEX-A program, NOAA wind stations, and NOS and Corps of Engineers water level data. Drifter data from the MMS sponsored SCULP program was also utilized.

C. The Driving Forces

1. River Discharge

The Mississippi River drains over one-third of the continental watershed of the United States and produces an annual discharge of over 300 km^3 of fresh water to the Louisiana shelf west of the Mississippi Delta (Dinnel and Wiseman, 1986). The annual average discharge rate of 14,000 m^3/sec (1950-1985) is composed of a huge annual cycle with peaks exceeding 30,000 m^3/sec occurring between January and June and low discharges of ~5,000 m^3/sec occurring August through October (Walker, 1996a). Figure 4 shows the Mississippi River discharge at Tarbert Landing, about 500 km upstream of the mouth of the Mississippi River, from 1988 through 1994. About 15 km upstream of Tarbert Landing the Atchafalaya River is controlled to siphon off about 30% of the total Mississippi River discharge and funnel it directly southward to the Gulf of Mexico. The Atchafalaya River discharge at Simmesport, located about 25 km downstream of the Mississippi River-Atchafalaya bifurcation is also plotted on Figure 4 for comparison. The Atchafalaya River first discharges into the wide and shallow (1 to 2 m deep) Atchafalaya Bay where it is subject to strong tidal and wind mixing. The majority of this discharge then exits into the Gulf of Mexico through the wide (45 km) and shallow (1-2 m) passage between Marsh Island and Point Au Fer, which is 200 km west of the major mouths of the Mississippi River. The Atchafalaya Bay effluent then discharges onto a broad shallow alluvial ramp whose depths are only 10 m as far as 35 km from the coast. The Mississippi River outflow plume, in contrast, immediately encounters deep water, e.g., 40-50 m depths off Southwest Pass (Wright and Coleman, 1971).

This study was designed to focus mainly on the coastal plume that arises from the Atchafalaya River outflow. It is difficult to assess *a priori* how much of the Mississippi River outflow proper is advected westward to join the Atchafalaya River outflow and form the coastal plume. A preferential mode of Mississippi River plume kinematics involves an anticyclonic eddy that forms in the bight west of the Delta. Its presence has been documented by current meter data, satellite images, and drifters (Daddio et al., 1978; Walker, 1996a; Murray,1982). This anticyclonic eddy can be heavily charged with Mississippi River outflow water and, upon impacting shallow water at the coast to the north, it bifurcates, with the western limb of the bifurcation carrying low salinity Mississippi River outflow water westward to join the Atchafalaya River discharge and form the coastal plume. Walker (1996a) notes that 42% of images examined from a five-year period showed this anticyclonic circulation west of the Delta. Image availability, however, is heavily dependent on clear sky, windy conditions. A special cruise, devoted to the Mississippi River outflow plume including this anticyclonic eddy, is discussed in more detail in Chapter III.

The timing of the five coastal plume cruises and the Mississippi River plume cruise is noted in Figure 4. The year 1992, during which both an April and an October cruise were executed, was clearly a low flow year with the spring discharge lower than the previous three years. The October 1992 cruise occurs in a transition month; fresh water discharge is at a minimal average low, but winter wind conditions had begun. In April 1993 (Cruise III) the level of fresh water input was near a long-term average high, but the discharge continued high all through the summer and fall, associated with catastrophic floods in the upper Mississippi River Valley, described in Rabalais, et al., 1994. Cruise IV in July 1993 captured summer climatic conditions combined with an usually high river discharge condition. Cruise VI, the second of the summer cruises, in contrast, observed a representative low river discharge situation.

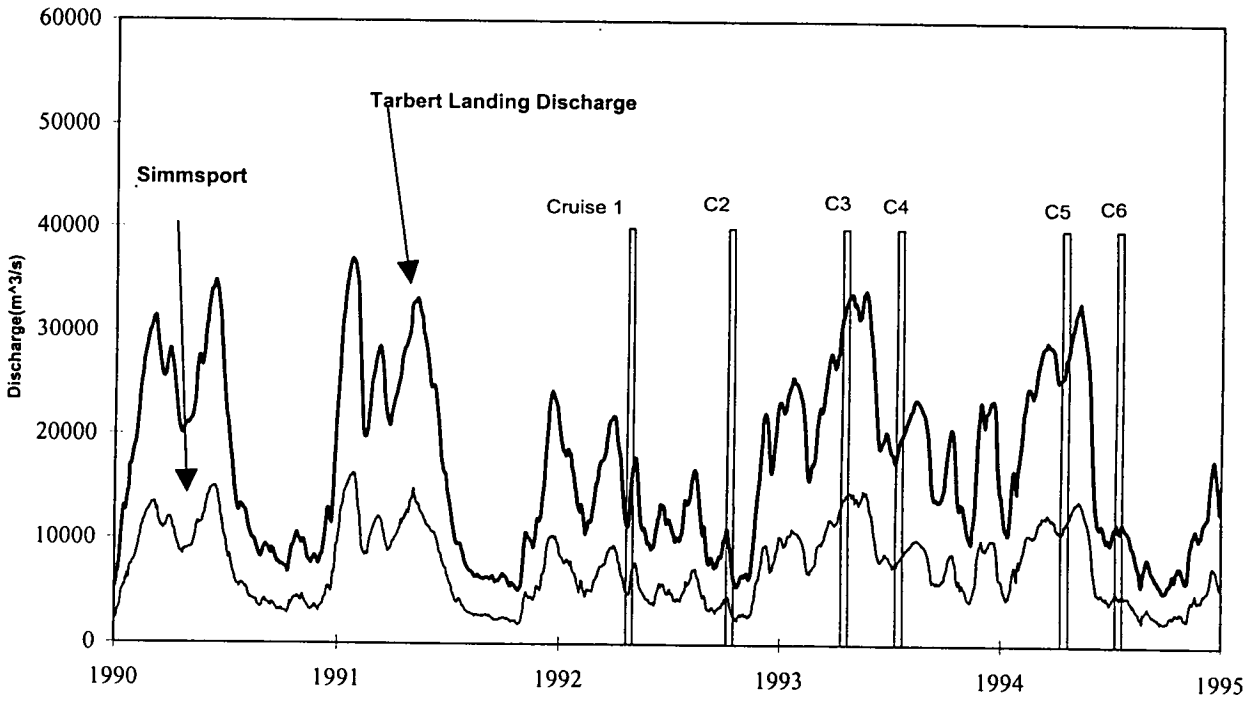

Figure 4. Mississippi River discharge at Tarbert Landing and Atchafalaya discharge at Simmesport. Atchafalaya and Mississippi River discharges 1990-1995 with 6 cruise occurrences.

2. Wind Forcing

C/K emphasizes the importance of the alongshore wind stress in driving the coastal current along the western Louisiana and Texas inner shelf. Accordingly, we show in Figure 5 the alongshore wind stress components from three CMAN stations at Grand Isle, LA, Sea Rim State Park (Sabine River Area) on the Louisiana -Texas border, Port Aransas, South Texas and the Brownsville, TX NWS station (see Figure 2) for the three years that include our cruise observations. The monthly averaged wind stresses shows that the seasonal cycle of the alongshore wind stress described in C/K is present in all 3 years of our observations.

Note that at Brownsville, the wind stress is directed northward (upcoast) all year long except for January 1993. This northward wind stress is at a maximum in summer, peaking in July each year. At Port Aransas, the alongshore wind stress is upcoast only for 2-3 months in summer, being strongly downcoast (southwestward) the rest of the year. At Sabine (SRST2), we again see the summer upcoast peak and long periods of downcoast wind stress the rest of the year. At Grand Isle (GDIL1), in central Louisiana, wind stresses are considerably weaker and less organized seasonally but a summer upcoast stress is evident at least in 1992 and 1993. Westward or downcoast wind stress is common the remainder of the time.

Thus, if wind stress is the dominant forcing mechanism, we may expect a prevailing westward or downcoast advection of the coastal plume during our April cruises in 1992 and 1993, and an upcoast or eastward flow regime during the summer cruises of 1993 and 1994. The wind stress record in Figure 5 also suggests a downcoast advection for the October 1992 cruise.

3. Hydrographic and Velocity Response Time Scales

Careful consideration of the observational data sets suggest that there is often a considerable mismatch between time scales associated with the hydrographic structure of the coastal plume and the ADCP velocity measurements. The along-shore length scale of the buoyant plume from our observational data is about 400 km. A time scale associated with an along-shore length scale requires specifying a scale velocity. We can follow Garvine (1995) using $C = \sqrt{g'h}$ the internal phase speed, where g' is reduced gravity and h is depth of the buoyant layer. The observed value then is $0.4 < C < 0.5$ m/sec, which gives an alongshore plume time scale of 9 to 12 days. If we use a longshore velocity scale from our observations of .25 m/sec then this increases to 14 days. These results indicate that the alongshore dimensions of the coastal plume are controlled by processes operating at a 1-2 week time scale.

The ADCP, in contrast, is measuring at a two-minute resolution. If wind forcing is dominant as suggested by C/K, the response of the currents is by the frictional time scale

$$Tf = \frac{H(x)}{2U_* C_d^{1/2}}$$

(Pettigrew and Murray, 1986; Csanady, 1982) where H is water depth, U* is the square root of wind stress over water density, and the drag coefficient $C_d \sim 2.5 \times 10^{-3}$. For our nominal depths of 10 m, the response time to wind driving of 5 m/sec is 3 hours; for winds of 7.5 m/sec, the response time is 2 hours. In the stratified near surface layers we can then expect currents measured by the ADCP to respond at an hourly time scale to changes in wind speed and direction.

Thus, winds and currents at the weekly time scale determine the large scale structure of the plume. Net transport of properties to be identified with the large scale coastal plume should be computed at the weekly time scale. The ADCP velocities, however, can represent high frequency

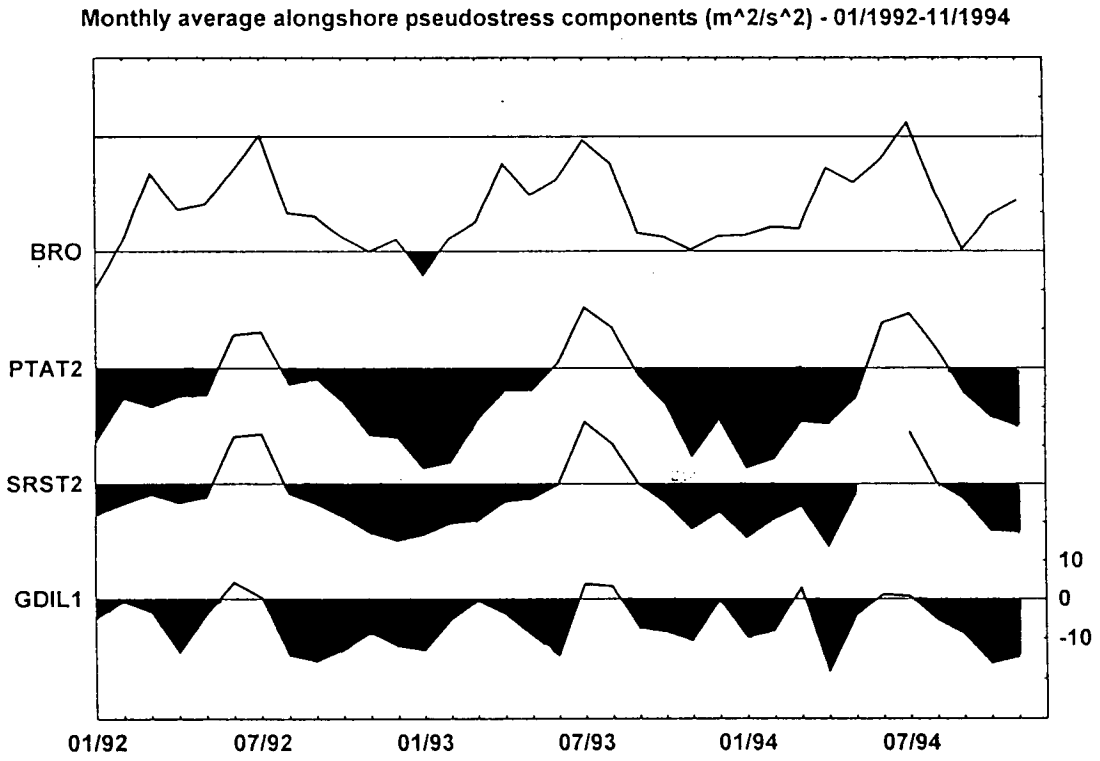

Figure 5. Alongshore wind stress components from three CMAN stations at Grand Isle, LA, Sea Rim State Park (Sabine River Area) on the Louisiana-Texas border, Port Aransas, South Texas and the Brownsville, TX National Weather Service (NWS) station . Time series of monthly average stress 1992-1994 from Brownsville (BRO), Port Aransas (PTAT2), Sabine area (SRST2), and Grand Isle (GDIL1). Downcoast winds components are shaded.

events such as a transient storm that are but perturbations on the large-scale flow field that generates and maintains the coastal plume over its several hundred kilometer extent. Clearly, great care must be taken when interpreting the instantaneous ADCP velocity fields with respect to plume characteristics because of the mismatch in time scales.

4. Tidal Currents and Inertial Oscillations

Tidal currents often mask the low frequency or mean current field that is of primary interest to this study. Techniques to "detide" the observed currents are described by Candela et al. (1992) and Munchow et al. (1995). The extensive array of LATEX A current meters shows that tidal currents exceed the resolution of our ADCP (3-5 cm/sec) in only one location on the inner shelf of Louisiana-Texas. Table 3 gives the semi-major and semi-minor ellipse axes at 10 of these locations (S. DiMarco personal communication, 1996) for the M2, 01, and K1 constituents. Only at Mooring 17, influenced by the tidal flux through the Atchafalaya Bay entrance, can we note a significant impact on the subtidal current. Thus, we do not detide our ADCP data sets but recognize the inner portion of the S3 line can be significantly affected by tidal oscillations in our interpretations. In fact, because of the short frictional adjustment time, variations in wind forcing appear far more important than tidal fluctuations in our ADCP observations.

In fact, considerable effort was expended to detide our ship track ADCP data. Neal Pettigrew, consultant to this project, concluded that the Candela scheme performed inadequately on our data sets where rather weak tidal currents were masked by a strong wind-driven component that had major aperiodic spikes caused by frontal passages.

Table 3. The semi-major and semi-minor ellipse axes at 10 mooring locations for the M2 and O1 constituents. Locations are shown on Figure 2.

Mooring	M2		O1	
	Semi-major	Semi-minor	Semi-major	Semi-minor
01 bot	0.23	0.02	0.41	0.00
01 top	0.51	0.22	0.31	0.07
02 bot	0.78	0.27	0.85	0.26
02 top	1.01	0.51	1.33	1.03
15 bot	1.57	0.06	1.52	0.57
15 top	1.49	0.03	4.21	3.25
16 bot	1.58	0.06	0.75	0.07
16 top	2.00	0.09	2.72	1.81
17 bot	6.70	2.53	4.21	1.27
17 top	9.58	4.94	8.49	3.80
18 bot	3.90	0.70	0.77	0.60
18 top	4.68	1.63	3.77	2.96
20 bot	3.22	0.48	0.95	0.03
20 top	4.23	0.13	2.72	1.47
21 bot	4.14	0.77	1.66	1.06
21 top	5.56	1.79	3.25	2.72
23 bot	1.78	0.22	1.26	0.51
23 top	2.29	0.40	1.58	0.74
24 bot	1.97	0.69	1.02	0.72
24 top	2.66	1.05	2.26	1.32

Inertial oscillations are also another major feature on the Louisiana-Texas shelf that can mask the low frequency circulations in the ADCP observations. Chen et al. (1996) have analyzed the LATEX A current meter data set and determined the spatial (along-shore, cross-shore, and vertical) distribution of energy in the inertial band. Inertial energy is at a maximum at the shelf break and decreases gradually onshore and more abruptly offshore. Both in the data (Chen et al. 1996) and in a numerical study by Chen and Xie (1996), it is shown that the inertial energy on the inner shelf has decreased to 20% of its offshore maximum. We then can expect inertial oscillation to be relatively unimportant in the shallow waters of our study area, except intermittently at the relatively deep offshore end of line S1 and the transit lines between S1 and S2 where the deepest waters (over 30 m) of our study are encountered. The ADCP profiles provide, for the first time, information on the internal velocity structure of the Mississippi-Atchafalaya coastal plume, during both upcoast and downcoast regimes.

D. Seasonal Cycles of Currents from LATEX-A Current Meters and SCULP Drifters

1. Monthly Current Meter Flow Fields

In order to understand the low frequency flow regime in which our cruise data are embedded, we have analyzed the monthly average current vectors at 12 of the LATEX-A moorings nearest the coast. Unfortunately, these instruments are generally underneath the coastal plume or just seaward of it. For 30 months (April 1992 through November 1994), the 3 annual cycles of the low frequency component of the coastal current are clearly resolved. From September through April, in all the years, a downcoast current is coherent across the near-coastal mooring array listed in Table 3. May continues a weakened downcoast regime. The summer counter-current, or upcoast flow regime, appears well-developed in June of 1992 and 1994. June 1993 current vectors, however, suggest a variable regime still in transition. July has a strongly upcoast flow regime in 1992 and 1993, and upcoast but less strongly developed in 1994. August of 1992 and 1993 continue the upcoast summer flow regime but in August of 1994, the downcoast winter regime has already begun. September re-initiates the 9 to 10 month winter-spring period of downcoast flow in 1992 and 1993. In summary, the model of a summer upcoast flow regime on the inner shelf in June through August and downcoast flow the rest of the year appears well met in the LATEX years of 1992-1994. The most notable exceptions are a late start of the summer regime in 1993 (as June 1993 still has a mean downcoast flow) and an early start to the downcoast winter regime in August 1994.

Four of our five cruises then were conducted in months representative of the seasonal cycle. Figure 6a shows the monthly averaged current meter vectors in April 1992, the month of our first observation of the spring downcoast flow regime. Downcoast currents were dominant again in October 1992 (Figure 6b) during Cruise II after the summer flow reversal. Cruise III was conducted in April 1993 when the current meter array (Figure 6c) shows that the expected monthly mean downcoast flow was reversed at 5 of the 10 reporting current meters. The current meter data for July 1993 (Figure 6d) shows Cruise IV, our first summer regime observation, was conducted in a strong upcoast flow regime. The current meter data from July 1994 (Figure 6e) suggest that our second summer observation in that month also took place in an expected upcoast flow regime but one less well developed than the previous July.

2. Seasonal Cycles from SCULP Drifters

The SCULP near-surface layer drifter program conducted by P. Niiler of Scripps Institute of Oceanography and the U.S. Minerals Management Service during October 1993 to January 1995 also provides valuable insight into the seasonal circulation on the mid- and inner shelf. Maps

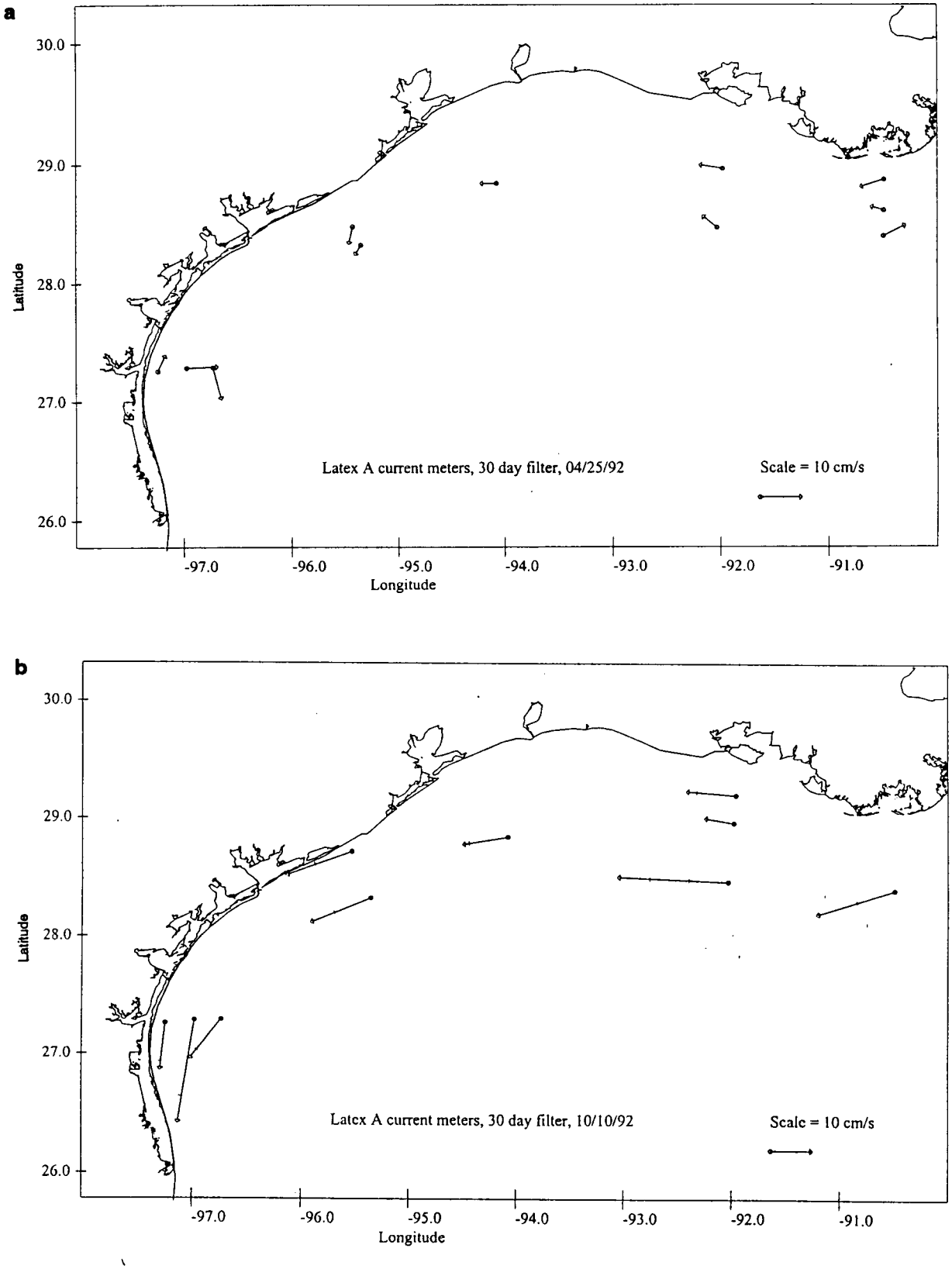

Figure 6. Monthly average current vectors for innermost LATEX A moorings during (a) April 1992; (b) October 1992; (c) April 1993; (d) July 1993; and, (e) July 1994.

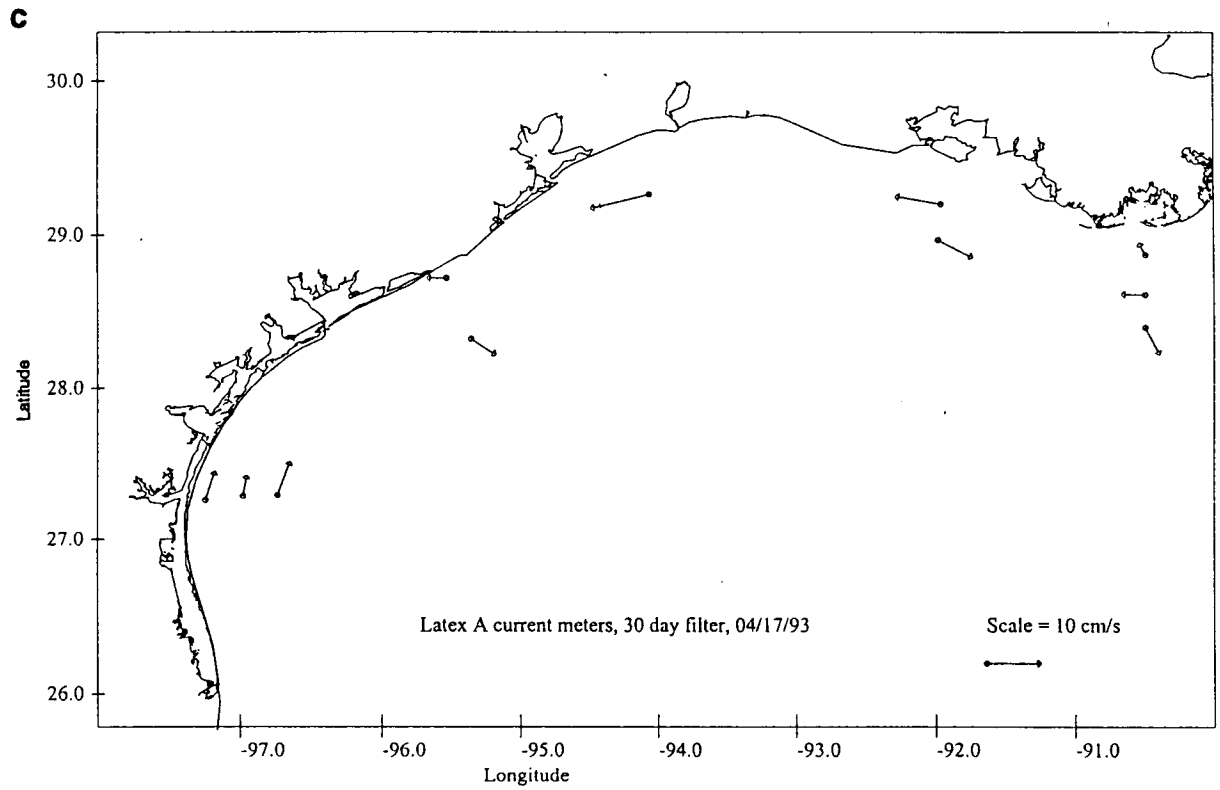

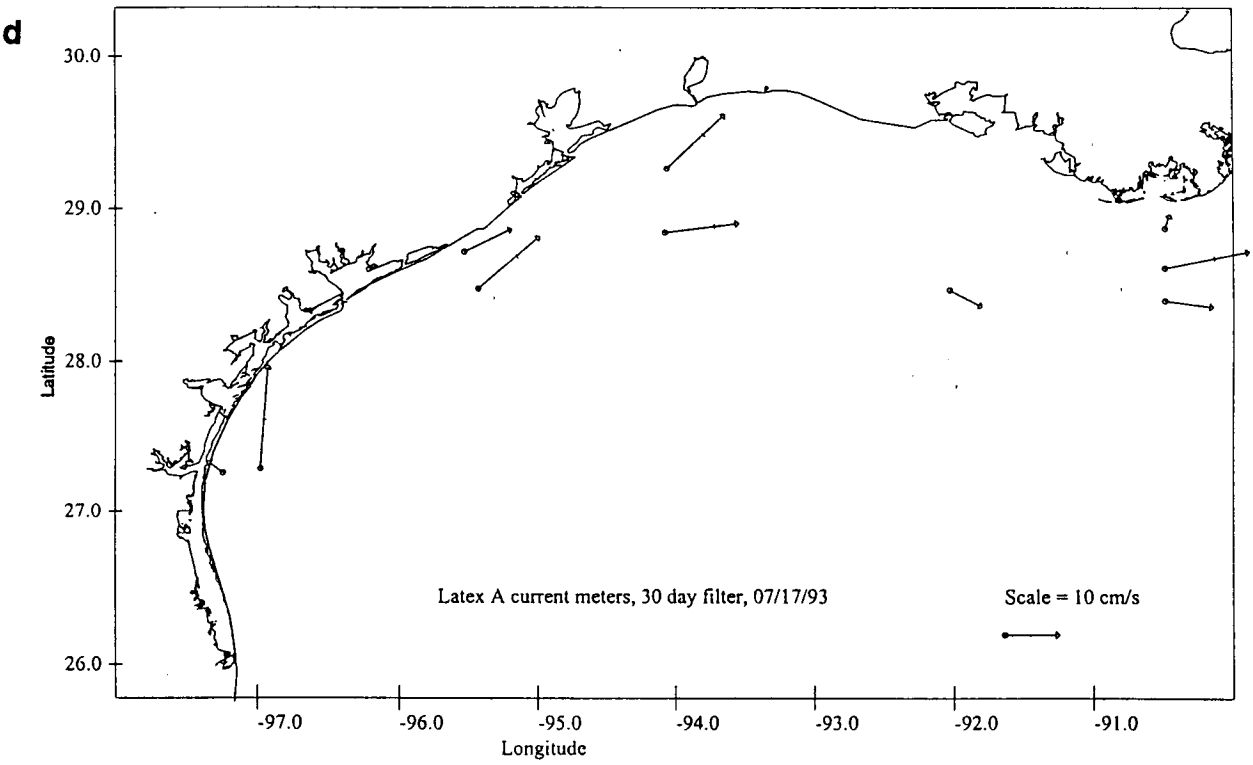

Figure 6 cont'd.

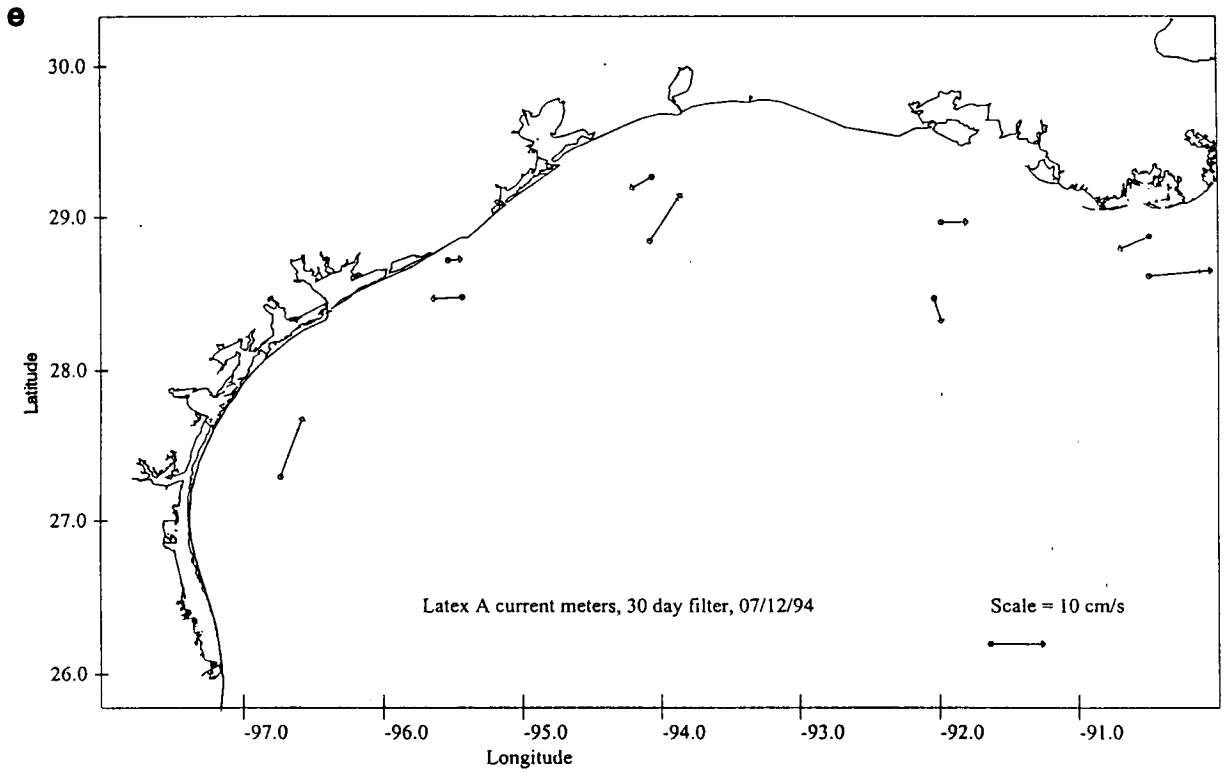

Figure 6 cont'd.

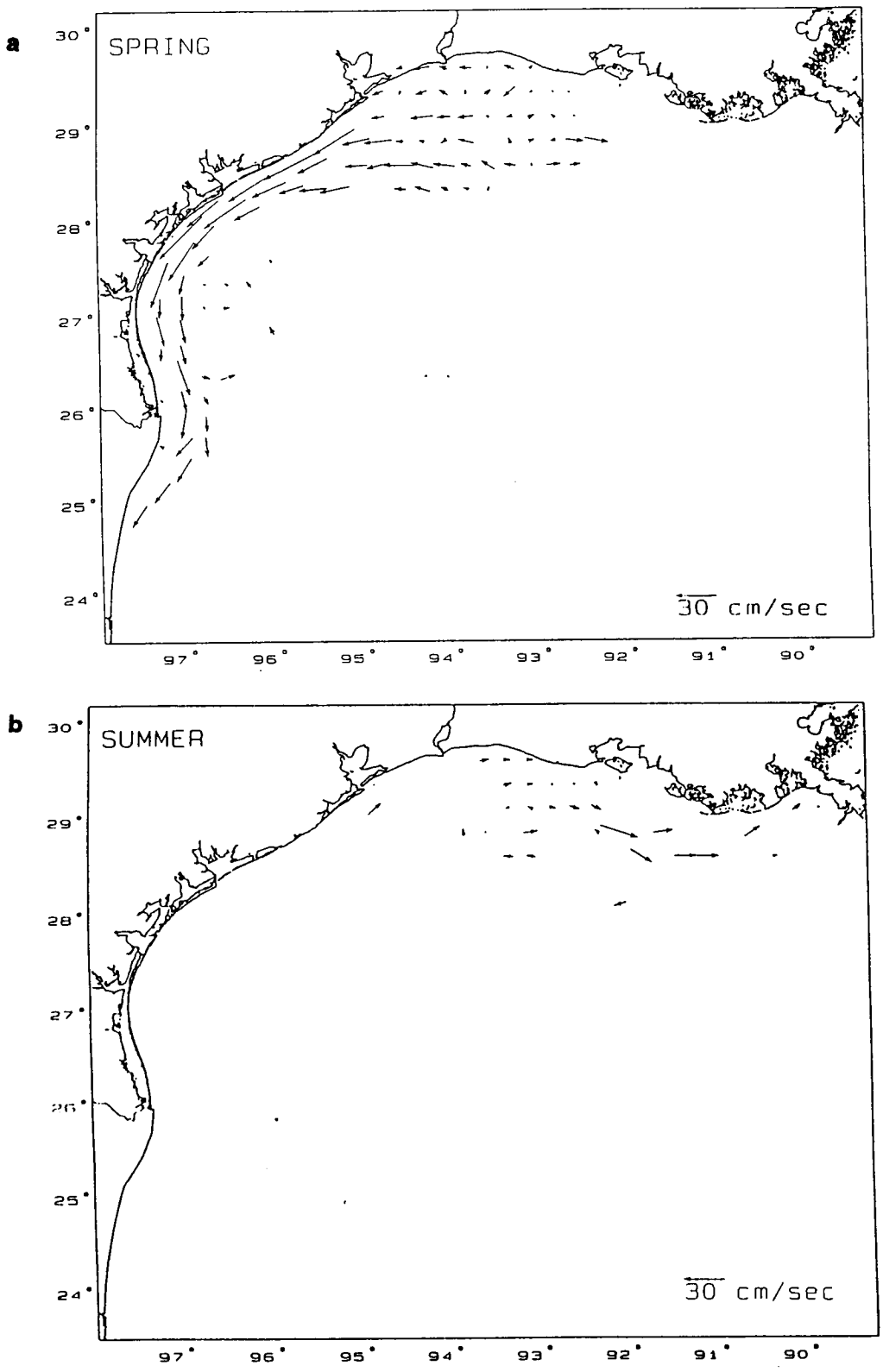

Figure 7. Seasonally averaged near-surface velocity maps from SCULP drifter data; (a) spring season; (b) summer season.

of the fall, winter, and spring seasonally averaged drifter vectors (Niiler, 1995) all demonstrate a well-developed downcoast flow regime on the mid- and inner shelf. Figure 7a, the winter season results, shows a broad relatively weak downcoast flow on the western Louisiana-east Texas shelf that coalesces south of Galveston into a narrow high spread jet that extends southward to the Mexican border and beyond. The inner shelf off western Louisiana in spring (not shown) appears disorganized, but in fall and winter the downcoast regime is well-organized and highly energetic and in Figure 7a.

Data from the summer (Figure 7b) is essentially restricted to the Louisiana shelf, as a result of their upcoast movements from the initial drogue positions. The summer flow reversal is barely resolved by the drifter data from 92° 30' W to 93° 30' W but clearly observed south of Atchafalaya Bay (91° W-92° W).

E. Coastal Plume Observations: Downcoast Regime

In the previous sections, we have described the low frequency (monthly and seasonal time scales) of wind and buoyancy forcing of the LATEX inner shelf. Results from the innermost LATEX-A current meters and the SCULP drifters indicate the large-scale and low-frequency response to be expected from the injection of Atchafalaya plume water onto the Louisiana inner shelf. Clearly, we expect downcoast advection of the buoyant coastal plume in fall, winter, and spring, and an upcoast advection in the summer months of July and August. Thus, in this section, we will first examine the results from the three downcoast regime cruise observations. The details, previously unknown, of the spatial structure of this buoyant coastal plume and the time and spatially varying velocity field internal to the plume are the main focus of this report.

1. The Coastal Plume, Spring 1992: Anomalously Low River Discharge and Typically Strong Wind Conditions

In order to characterize the hydrographic and velocity structure of the coastal plume in Spring 1992, our sampling program extending from 90° 30' W off Terrebonne Bay, LA west to 97° W, was conducted April 22-28, 1992. The six-day sampling time obviously set bounds for our resolution of the plume structure, which is by necessity temporally and spatially aliased by the immense size of the plume and the speed of the ship. Nonetheless, transiting over 2200 km and collecting data from 127 CTD stations allowed an unprecedented three-dimensional visualization of its structure.

Despite April being the month of highest average discharge, the Atchafalaya River discharge peaked 10 days prior to the cruise at only about 9500 m^3/sec (Figure 4), more than one-third less than the 1991 and 1993 spring peaks. A time of travel estimate of this peak of 3 to 5 days from Simmesport to the open Gulf indicates its contribution of fresh water is included in our observation of the plume.

The time series behavior of the wind velocities affecting the coastal waters during this cruise observation period is illustrated from the three available Coastal Marine Automated Network (CMAN) stations at Grand Isle, Sabine Pass, Port Aransas, and the Brownsville NWS station. Figure 8 shows this data from April 19-30. The velocity sticks on April 19 and 20 show the end of the long period of southeasterly winds set up by a big high pressure cell off the eastern seaboard (Wind Episode I). The eastward movement of the ensuing north-south oriented front brought northeasterly winds first to Port Aransas and, in turn, to Sabine Pass and Grand Isle. These winds lasted for only about 24 hours (Episode II). A succeeding weak high pressure system brought moderate southeasterly winds to the northern LATEX shelf on April 22-25, as seen in Figure 8 (Wind Episode III). The orientation of this front early on April 26 was quasi-parallel to the Louisiana coast as it passed and showed an almost simultaneous onset of northerly winds at all

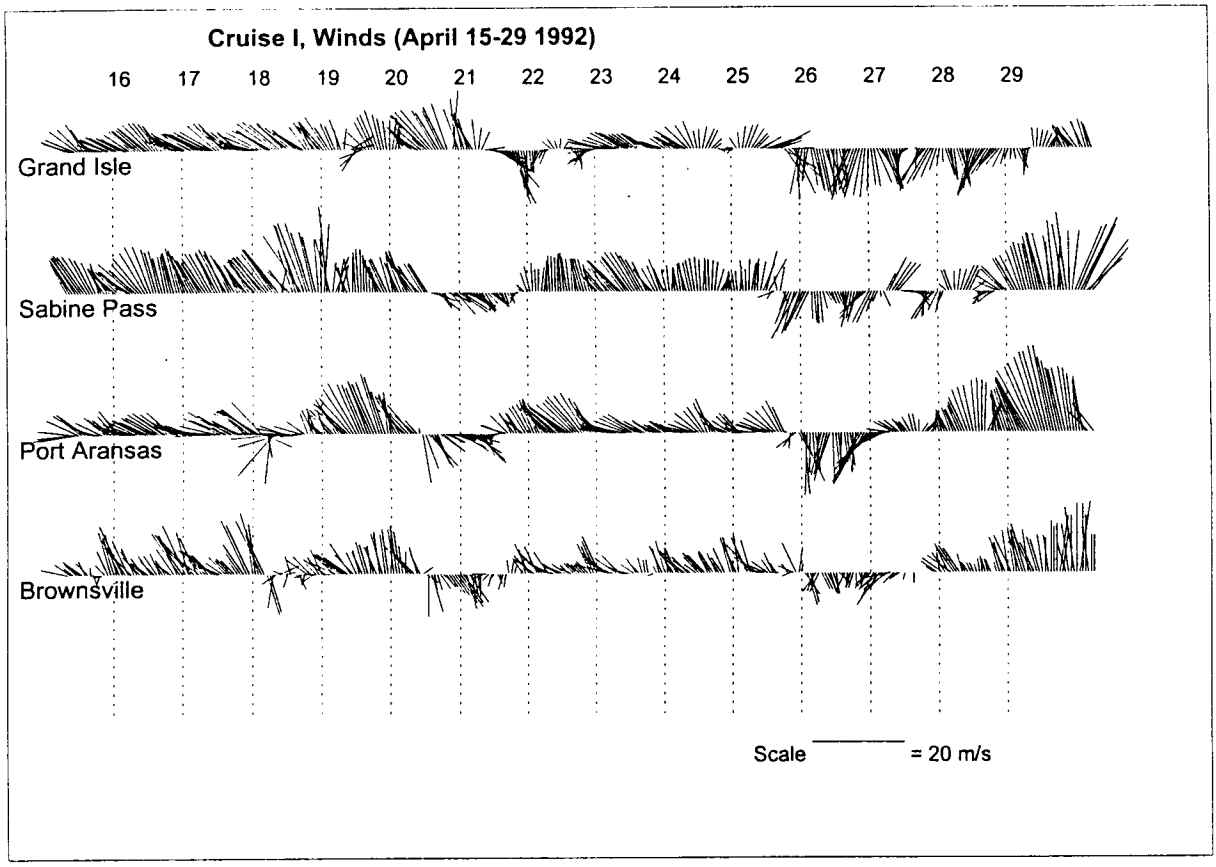

Figure 8. The time series behavior of the wind velocities affecting the coastal waters during the observation period April 15-29, 1992 is illustrated from the three available Coastal Marine Automated Network (CMAN) stations at Grand Isle, Sabine Pass, and Port Aransas, and the Brownsville NWS station. Vectors pointing to the top are winds to the North.

three stations, which lasted for 1.5 to 3 days, depending on location (Wind Episode IV). It is important to note the large phase lag from north to south in the re-establishment of southerly winds after Wind Episode IV. Southeasterly winds on the back side of this high pressure cell began mid-day on April 27 at Port Aransas, late on April 27 at Sabine Pass, and not until early on April 29 at Grand Isle.

Another instructive view of the wind forcing is that measured by the ship as it transits through the time and space varying wind field. Figure 9, the half-hour averaged wind vector sampled by the ship, shows there is good agreement with the large scale wind episodes resolved by the CMAN station. There is a significant departure, however, of the ship winds from the Sabine SRST coastal station as the ship transits westward from Sabine Pass to west of Galveston Bay. This is a result of a small cyclonic system migrating northeastward on a reciprocal to the ship's path.

The alongshore wind stress components (Figure 10) prior to the cruise observations were strongly downcoast at Grand Isle (GDIL1) and predominantly downcoast at Sabine Pass (SRST2) and Port Aransas (PTAT2), while strongly upcoast at Brownsville (BRO). During the cruise (April 22-29), wind stresses were predominantly downcoast (except, of course, at Brownsville) until a strong upcoast wind stress event impacted the inner shelf-coast plume water from April 27-29, coherent from Brownsville upcoast to Sabine Pass.

a. Surface Salinity

The underway thermosalinograph logs salinity and temperatures from 1m below the sea surface at 12 second intervals. A nominal ship speed of 3 to 4 m/sec is equivalent to a spatial sampling interval of 30 to 40m; but, we use 500 m averages of surface salinity sufficient to resolve all features of interest to this study. Figure 11, the surface salinity field observed in late April, does, in fact, show an immense low salinity coastal plume extending westward over 500 km along the coast from the source regions of the Atchafalaya and Mississippi River mouths into central and south Texas. We expect the long period of SE winds during Episode I and the general downcoast flow in April (Figures 5 and 6) to drive the low salinity Atchafalaya discharge well to the west and downcoast during the seven day period prior to Cruise 1, thus building a sizable coherent coastal plume in that direction.

Isohalines in the 26-27 psu range run quasi-parallel to the coast from the easternmost section at 90°30' W over 400 km westward to Galveston Bay where they abruptly bend seaward. The significant change in the salinity field west of Galveston suggests a major change in the physical processes there. Note that the Atchafalaya River outflow plume is clearly resolved seaward of the Atchafalaya Bay mouth with minimal salinities sampled of ~16 psu near the mouth and an alongshore length scale of ~75 km estimated from the curvature of the 25 psu isohaline. Figure 11 also shows that surface salinities below 25 psu are common in the inner shelf waters east of Galveston but are rare southwest of that location. The influence of the Brazos River outflow, historically high in Spring 1992, and the Galveston Bay outflow can be seen in the presence of waters with salinity less than 24.5 psu southwest of the Galveston entrance. The bull's eye of high salinity at 96° W is likely an intrusion from mid-shelf, often observed in this area in satellite images.

The surface temperature field from the thermosalinograph (not shown) is extremely uniform, varying only 1° C over the entire study area. The salinity at the 7m level from the CTD station data is shown in Figure 12. Note the isohalines again tend to be oriented parallel to the coast as far west as Galveston, reflecting the continuity of the coastal plume over that distance. Immediately west of the Galveston Bay entrance, a large area of low salinity water was encountered, apparently derived from the anomalously high spring outflow of the Brazos River. West of 95.5° W, salinities have returned to the background levels of 28 to 30 psu expected for

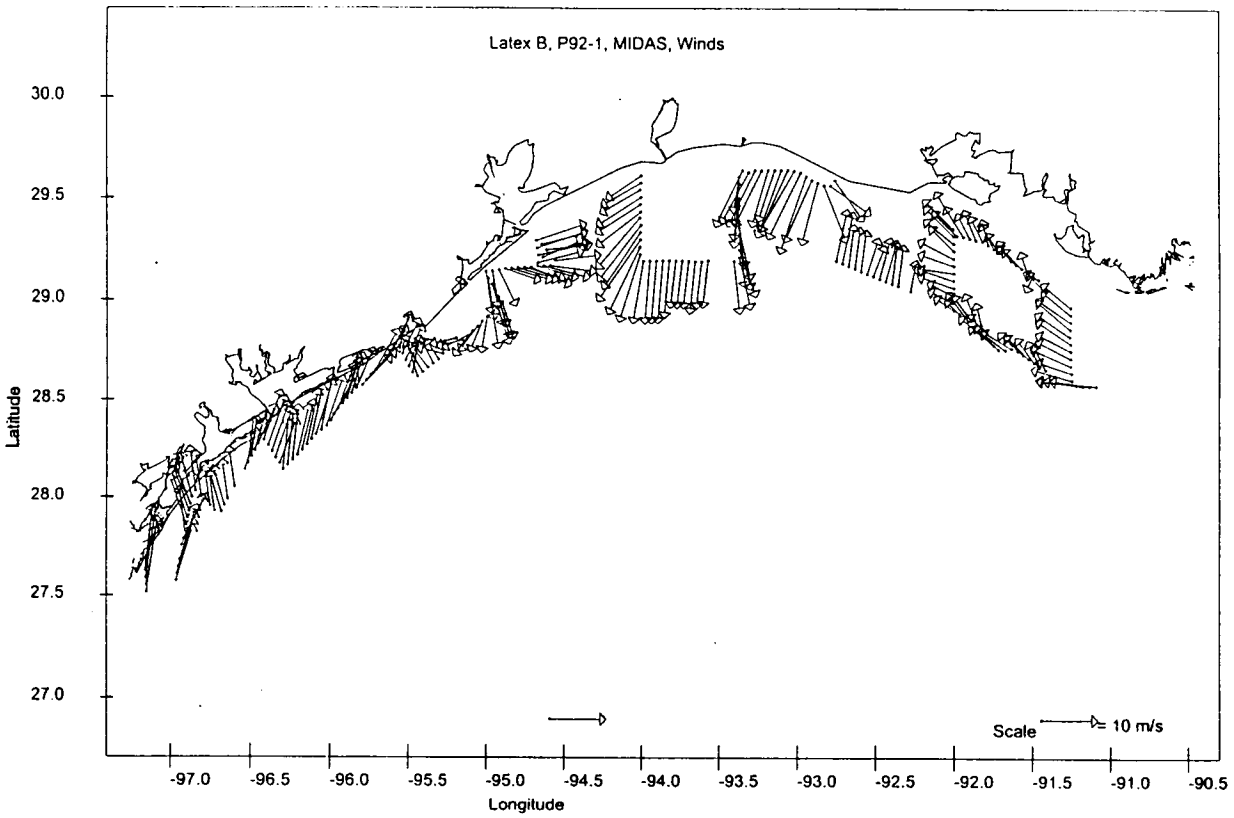

Figure 9. Corrected winds measured on the research ship, prior to and during the April 22-28, 1992 observations of the coastal plume.

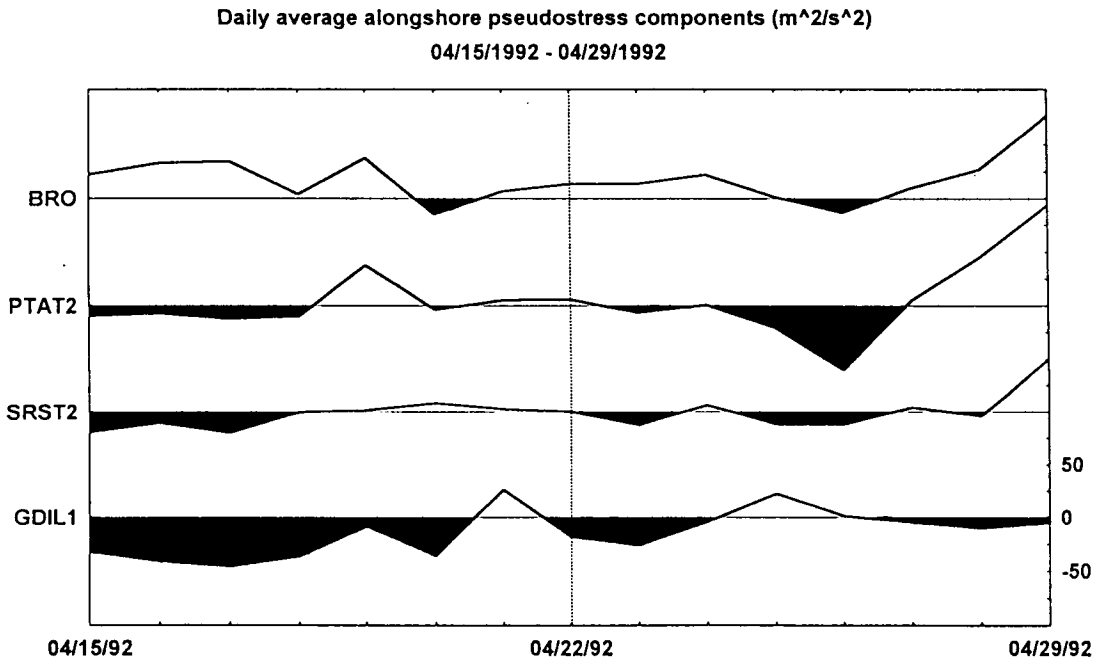

Figure 10. Daily average alongshore wind stress from four coastal stations one week prior to and during April 1992 observations. Downcoast wind stress is shaded to illustrate its importance at all stations except at Brownsville.

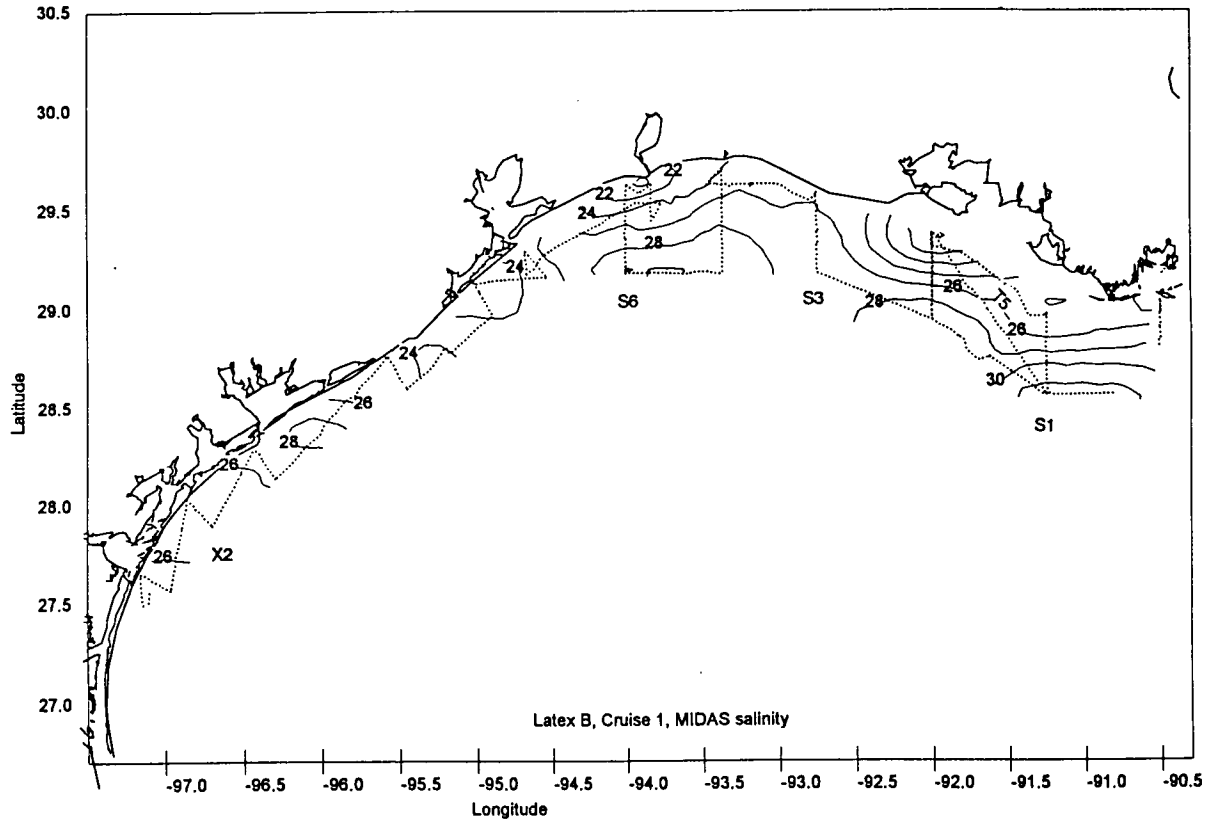

Figure 11. Near-surface salinity (~1 m) from the underway thermosalinograph during the April 1992 observations of the coastal plume. The ship track is shown as a dotted line.

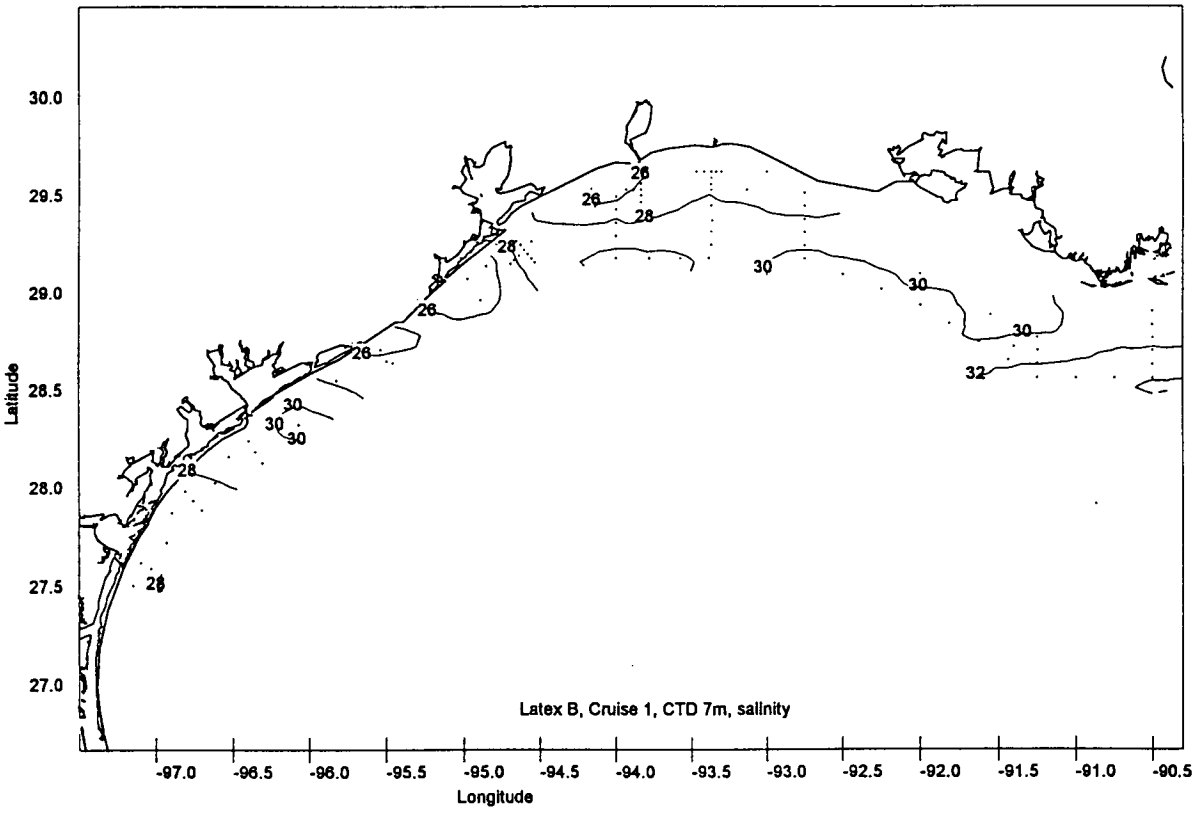

Figure 12. The salinity at the 7 m level from the CTD station data, April 1992 observations. CTD stations are located with a dot.

this depth level. Note, however, the lack of longshore continuity in the isohalines in this western region reflecting the increased importance of local processes.

At the 15 m level (not shown) the salinities are markedly higher in the eastern region south of Atchafalaya Bay where they reach 35 psu. There is a sharp decrease of salinity at this level to the west down to 32 psu at about 93.3° W. Higher salinities (34 psu) appear again south of Galveston. West of Galveston, salinities remain in the 31-32 psu range.

The picture that emerges from the constant depth salinity maps is of an immense buoyant coastal plume extending from east of the Atchafalaya River mouth over 500 km westward to Corpus Christi and beyond. West of Galveston discharges from the local bays and small scale intrusions from offshore decrease and increase, respectively, the generally low salinity background level of the plume. There is an abrupt change in the orientation of the isohaline from shore parallel east of Galveston to shore normal west of Galveston. The convergence in the surface wind field west of Galveston, readily apparent in Figure 9, suggests the presence of surface current convergence in the same area. The wind records suggest such a convergence would persist for several days until a strong northern (such as on April 26; Figure 8) would bring downcoast winds from Grand Isle to Brownsville. The overall character of the surface plume is in essential agreement with the advective field expected from the winter-spring season as observed by current meters (Figure 6a) and surface drifters (Figure 7a).

b. Vertical Salinity Sections

Here we examine the vertical salinity structure of the April, 1992 plume with selected vertical sections. We will examine 4 of the 11 coastal normal sections and 1 diagonal line that characterize various regimes along the length of the plume.

(1) East (Upstream) of the Atchafalaya Source The vertical section of salinity along our easternmost line S1 (Figure 13) shows almost a textbook picture of a coastal plume under downwelling favorable winds. A prism of low salinity (buoyant) water hugs the coast with lowest salinities of ~24 to 25 psu nearest the shoreline. The low salinity layer extends seaward about 50 km. The isohalines at the base of this layer are horizontal over most of this distance before rising abruptly to the sea surface in a fairly uniform spacing as distance increases offshore. The steeply inclined isohalines at the outer edge of the section reflect a downwelling favorable wind stress and a downcoast transport consistent with the Grand Isle wind stress shown in Figure 10. Note the presence of full salinity Gulf water below 20 m at the outer edge of this section. Near the bottom the 34, 35, and 36 psu isohalines slope down to the coast, suggesting a wedge-like intrusion of this denser high salinity water. It appears likely that the fresh water in this section is not of Atchafalaya River origin, as the section is 100 to 150 km east of the Atchafalaya River mouth. Winds blew from the northwest on April 21 (Episode II) prior to the cruise for about 36 hours, which even for a 0.5 m/sec current would displace Atchafalaya water only ~50 km to the east. Prior to Episode II, winds were unfavorable for eastward flow. Outflow from the bays and channels of the Mississippi bight, combined with some fraction of the discharge from the Mississippi River itself, is apparently the freshwater source for this section. S2 (not shown) is quite similar to S1 although the plume structure is squeezed seaward by the shoaling bathymetry as the Atchafalaya Delta is approached.

(2) The Atchafalaya Source Region Sections S3 (Figure 14) and T5 (Figure 15) are shore normal and diagonal sections, respectively, designed to sample the structure near the Atchafalaya River mouth. Note the fundamental differences between S1 and S3. S1 shows a buoyant plume with an 8-10 m vertical thickness whose base is fairly level out to 35 km from the coast. This plume is floating above an 8 to 10 m thick layer of high salinity Gulf of Mexico (GOM) water. In contrast, at S3 the surface-trapped plume is absent; the isohalines are all steeply inclined and intersect the bottom as observed in the density structure of the Delaware coastal current (Munchow

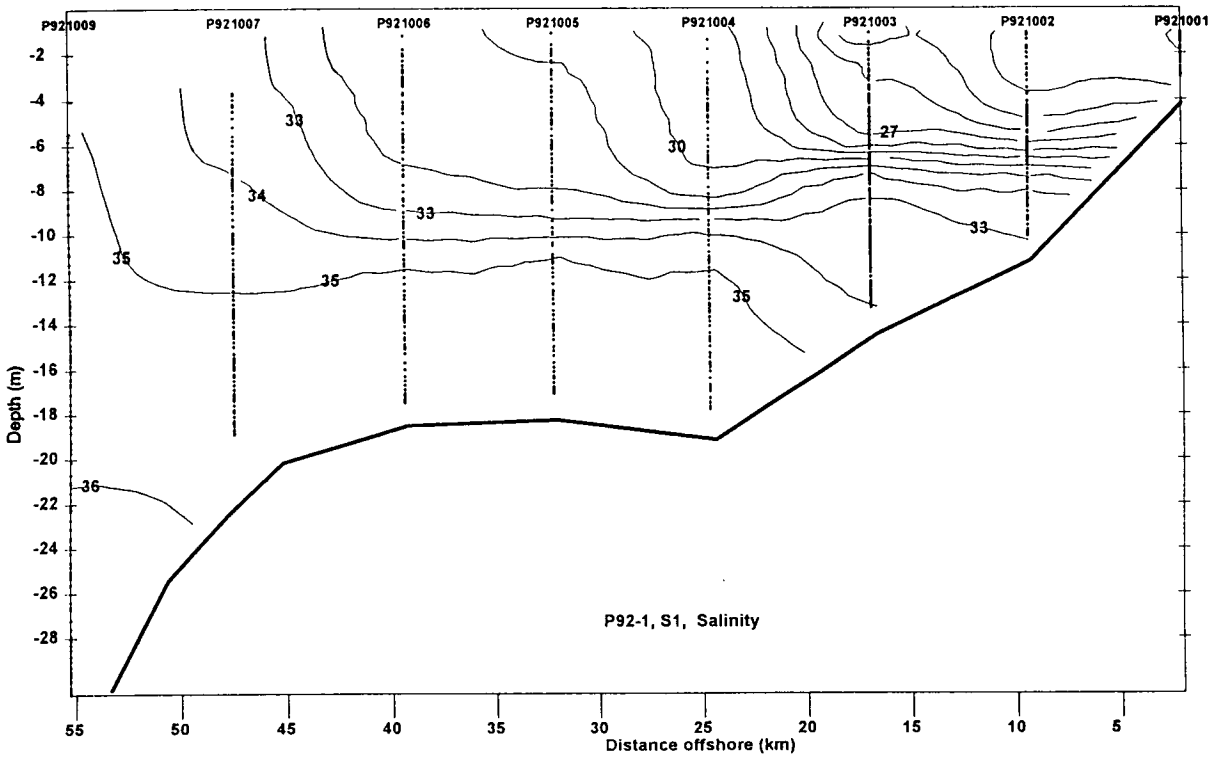

Figure 13. Vertical distribution of salinity (psu) on the S1 line during the April 1992 observations.

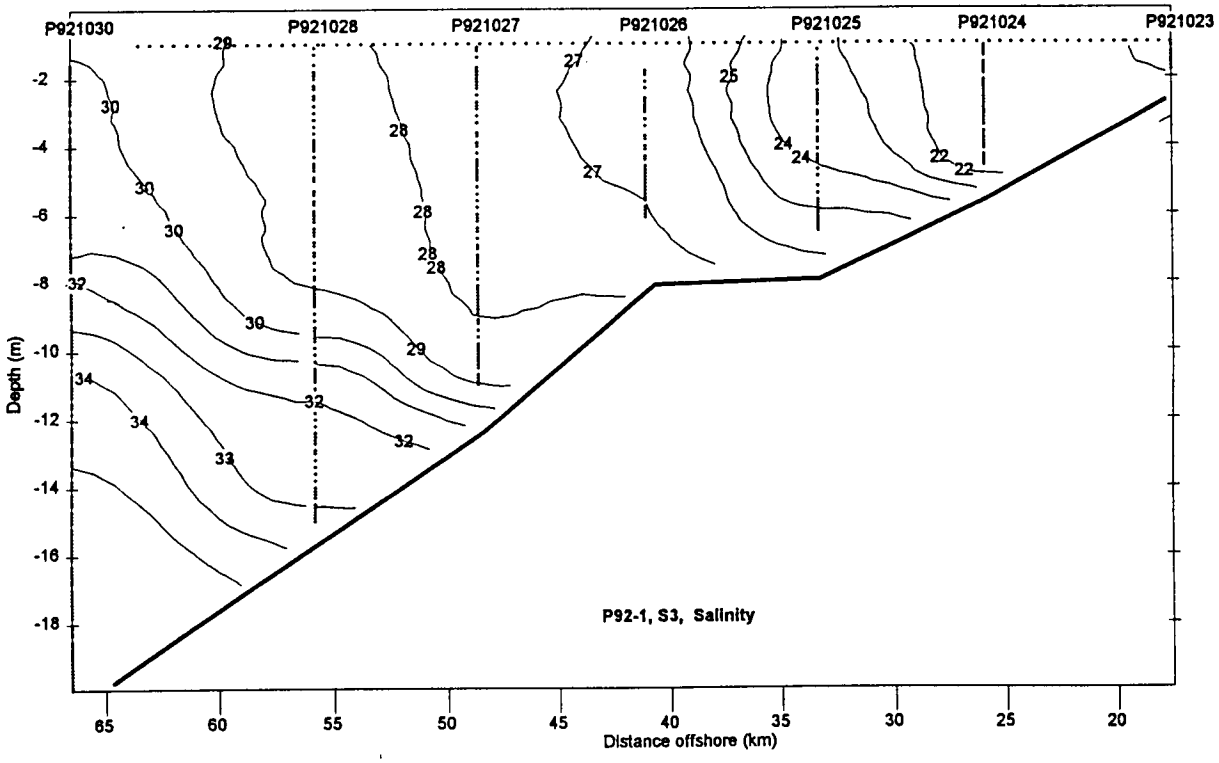

Figure 14. Vertical distribution of salinity (psu) on the S3 line during the April 1992 observations. Note the dotted line on the surface identifies data points from the thermosalinograph.

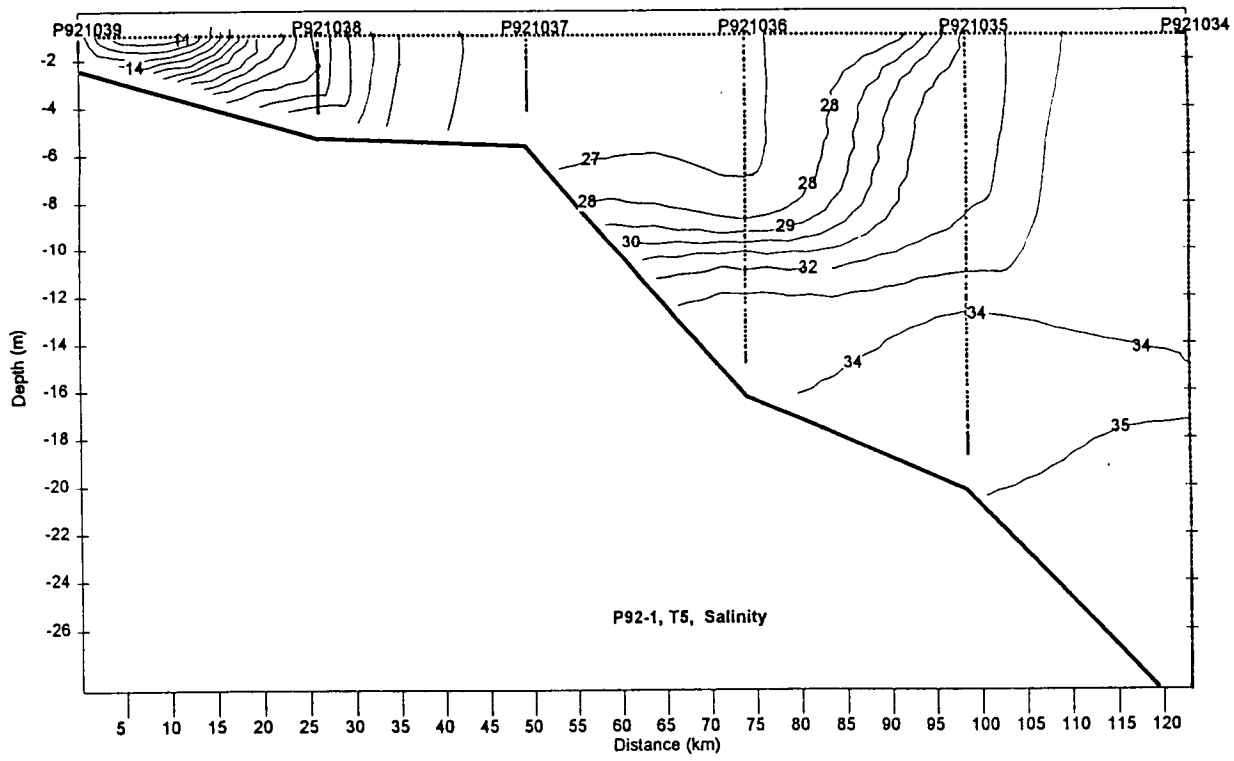

Figure 15. Vertical distribution of salinity (psu) on the T5 line during the April 1992 observations.

and Garvine, 1993b). The outer regions of these two sections are markedly different. In the upstream section S1, the 33 psu isohaline would outcrop about 40 km from the coast, but at S3 it is depressed 10 to 15 m below the surface at the same distance offshore. This could only be the effect of the outflow jet of the Atchafalaya River filling sections with its mixed discharge water and impulsively depressing the underlying density (salinity) structure. Salinities within the inner 20 km of S1 and S3, however, are quite similar, both containing water of <27 psu.

The salinity structure on the diagonal line T5 appears to uniquely capture a section along the axis of the Atchafalaya discharge jet as it enters the receiving basin. Four zones can be demarcated:

(a) a very low salinity zone (10-20 psu) of initial mixing within the first 25 km of the mouth;
(b) a well-mixed zone both vertically and longitudinally of 25 to 27 psu water from 40 to 75 km of the mouth; this could represent the well-mixed turbulent nose or tip of the outflow jet as it intrudes into and over the high salinity receiving water;
(c) the frontal region between the outflow jet and the ambient receiving water is marked by a steep halocline from 27-32 from 65-95 km from the mouth; and,
(d) the relatively unified uniform receiving waters of salinity (>34 psu) underlie and surround the nose of the outflow jet.

Thus, the salinity structure suggests the Atchafalaya outflow plume is in full contact with the bottom over the inner 50 km beyond which it separates from the bottom and becomes a detached free jet.

(3) West Louisiana Region: Downstream Sections Section 6 (Figure 16) is 220 km downcoast from Section 3, which was our source region example. After the sampling of S3, winds continued south to southeasterly for another 12 hours when they abruptly switched to the northerly winds of Episode IV (Figure 8). Thus, strong northerly winds (7.5 - 10.0 m/sec) had already impacted the coastal plume for over 20 hours when Section 6 was sampled. Surprisingly, the hydrographic structures at S5 and S6 show no indication of offshore advection of the surface layer from the strong offshore-directed wind forcing. While the cross-shore salinity gradient remains intact, it appears that strong vertical mixing has produced an almost vertically homogenous water column but with no evidence of strong cross-shore motion (e.g., the up-to-coastline tilt of isohalines characteristic of upwelling is absent). It is remarkable that the coastal plume structure remains intact under such strong offshore directed wind forcing.

The strong northerly winds that blow dominantly cross-shore (offshore) during the measurements at S4, S5 and S6 extend all the way south to Port Aransas (Figure 8). West of the great coastal bend near the Texas-Louisiana border, these same winds have a strong alongshore-downcoast component and will drive the coastal current at great speeds downcoast during the north wind episodes (Barron and Vastano, 1994).

(4) Central Texas: Far-field Coastal Plume By the time our measurement program reached the south Texas sampling sections X1, X2, and X3, the strong northerly winds had abated this far south and intense southerly winds had set in (Figure 8). (Note especially the strong upcoast wind component at Port Aransas, April 27-30 in Figure 8a.) The salinity structure at X2 (X1 and X3 are essentially identical) shown in Figure 17 clearly reflects a strong upcoast wind regime that produces a classic upwelling type response in the coastal plume structure, i.e., (a) the freshest water is a lens detached from the coastline; (b) the surface layer isohalines have flattened out seaward. Both (a) and (b) reflect an Ekman drift offshore, and the halocline and high salinity lower layers tilt up toward the coast. Considering the alongshore wind stress shown in Figure 10, we can expect this upcoast flow to extend north at least as far as the Sabine River.

These south Texas observations are important in that they have captured a recurring phenomenon of episodic upcoast flow reversals imbedded in the seasonal mean downcoast flow

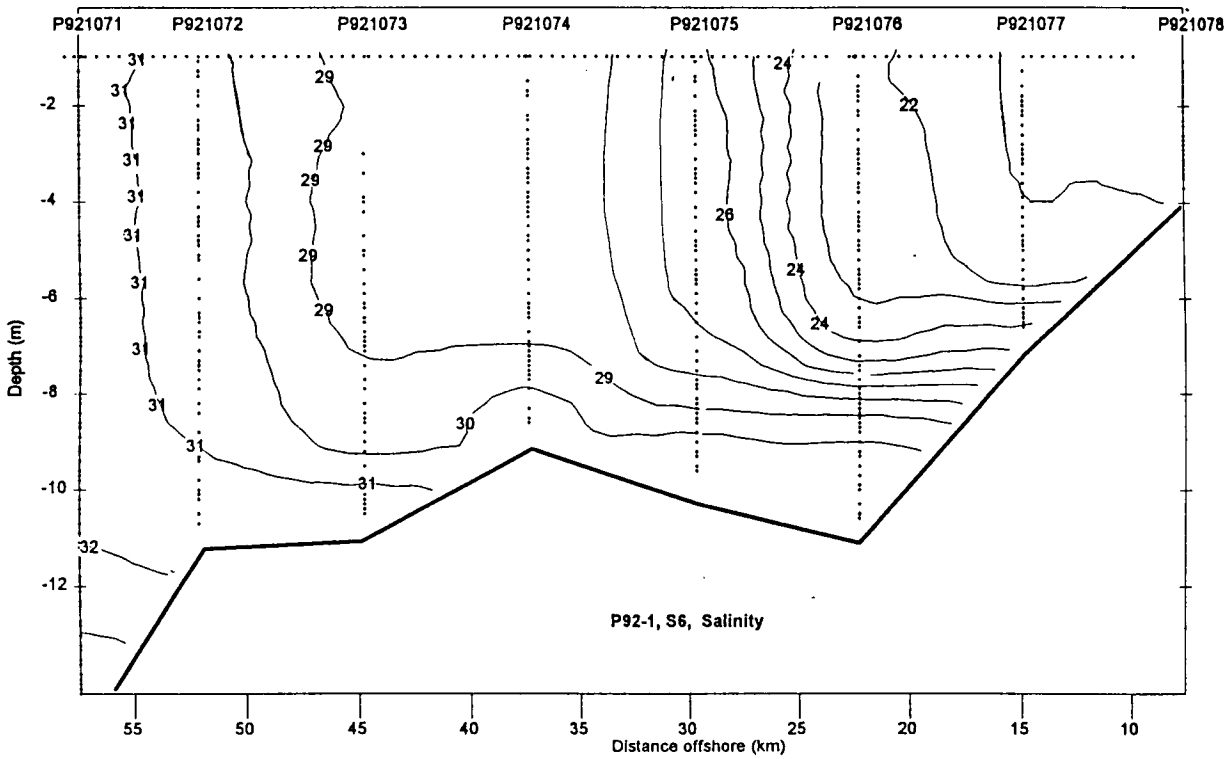

Figure 16. Vertical distribution of salinity (psu) on the S6 line during the April 1992 observations.

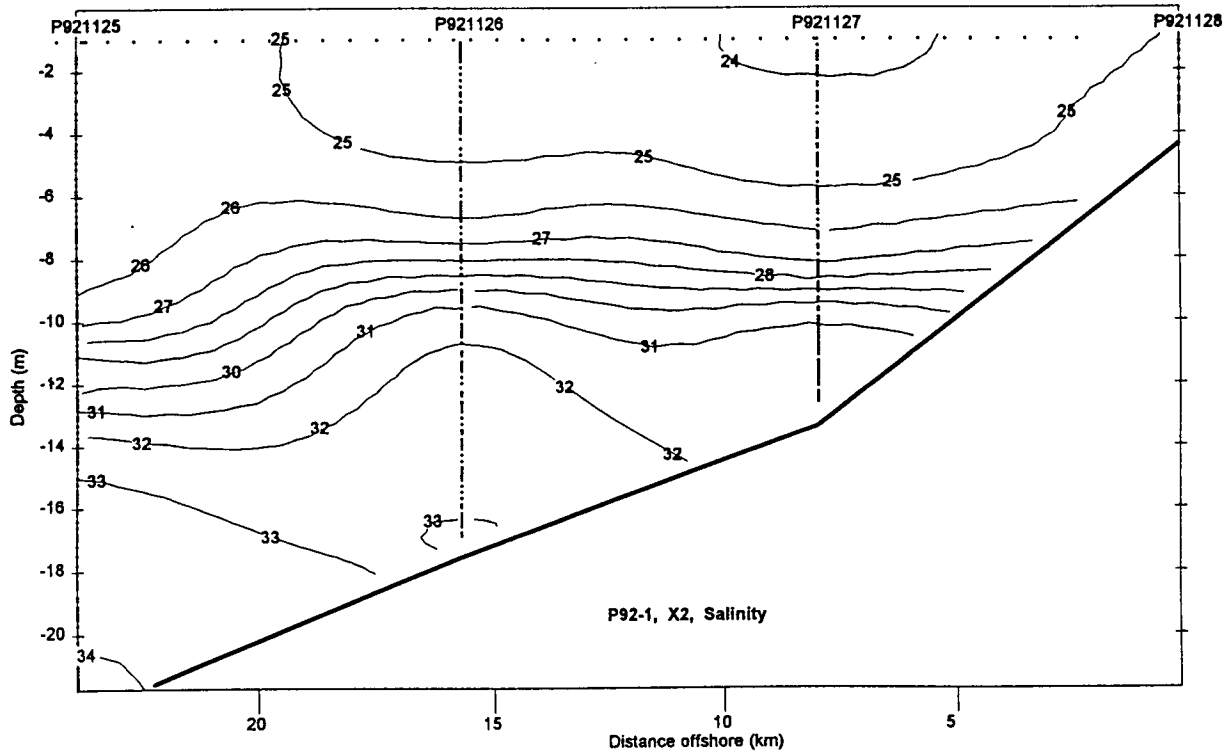

Figure 17. Vertical distribution of salinity (psu) on the X2 line during the April 1992 observations.

regime. The alongshore wind stress diagrams (Figure 10) imply a convergence of currents somewhere east of Galveston during the upcoast episodes.

c. Velocity (ADCP Observations): Spring 1992

(1) Vertical Sections: Atchafalaya Source Region Acceptable ADCP data return from the April 1992 sampling was low because of the poor performance of the towed sled configuration as discussed earlier. Particularly lacking was data east of the Atchafalaya mouth, so we first inspect the Atchafalaya source region itself in plan view (Figure 18). At S2 through S3, winds were steady out of the southeast and the water at S2 is on a convergence course with the outflow jet from the Atchafalaya River moving southeastward along T5. The westward velocities along the southern half of S3 carry (Figure 14) Atchafalaya River outflow water that has been mixed with the ambient inner shelf water and thus depicts the onset of the fully developed coastal plume. In Figure 19, a vertical section along T5, the convergence of the river outflow plume water and the upstream coastal water is seen to occur at the salinity front delineated in Figure 15. We can expect intense mixing and lateral entrainment along this front as the river outflow plume is increased in volume and salinity and evolves into the coastal plume. The vertical structure of the alongshore current at S3 (Figure 20) shows a 25-30 cm/sec jet carrying the newly modified coastal plume water westward along the coast. The eastward flow in the northern 20 km of this section may be the west limb of a small re-circulating eddy trapped along the side of the Atchafalaya outflow jet.

(2) West Louisiana Downstream Region After a period of southerly winds a cold frontal passage brought a period of fairly steady northerly winds (Figure 9) allowing an assessment of this type of recurrent forcing on the velocity structure at the western Louisiana region of the coastal plume as shown in Figure 21. These southward directed wind stresses have a minimal alongshore component and accordingly currents weaken and appear disorganized at S5. When the ship reaches S6, where the coastline has already begun its great bend to the south, the wind has shifted towards a downcoast orientation and currents are quick to respond. The vertical section through S6 (Figure 22) shows an energetic downcoast jet centered at 30 km offshore has already developed. These intense northerly winds had an even stronger downcoast component further southwest along the Texas coast. An accompanying strong downcoast current as indicated by the drifter data (Figure 7a) would create a longshore pressure gradient perhaps strong enough to pull water westward from the vicinity of S5-S6, but present data is insufficient to resolve this question.

(3) Central Texas: Far-field Coastal Plume When the observations extend into central Texas, we enter a region (from S7 to X3) dominated by strong southeasterly winds (Figures 7, 8). The upcoast components of the winds drive a strong (40-60 cm/sec) current northeastward along the coast. Four of the five sections in Figure 23 indicate a coastally trapped jet with a cross-shore length scale of ~25 km and an inshore velocity maximum. The alongshore velocity at X2 illustrates this structure in its fully developed form (Figure 24) with an upcoast speed maximum of 45 cm/sec located 10 km offshore. Further north at S7, the upcoast jet becomes weak and narrow and even reverses direction at its offshore end. Note that the wide inner shelf characteristic of Louisiana and east Texas abruptly narrows near our section S7 from 60 km to 22 km (based on distance offshore to 18.3 m isobath), suggesting a role for topographic control in this change in the upcoast jet.

2. Downcoast Regime, Spring 1993: High River Discharge and Strong Winds

Our second sampling of the spring downcoast flow regime took place April 13-19, 1993. The Atchafalaya discharge (Figure 4) at 14,000 m^3/sec is about twice the amount that generated the plume sampled in April 1992. The monthly average winds for March and April 1993 at Grand Isle, Sabine Pass, and Port Aransas were largely downcoast (Figure 5) as expected. Figure 25,

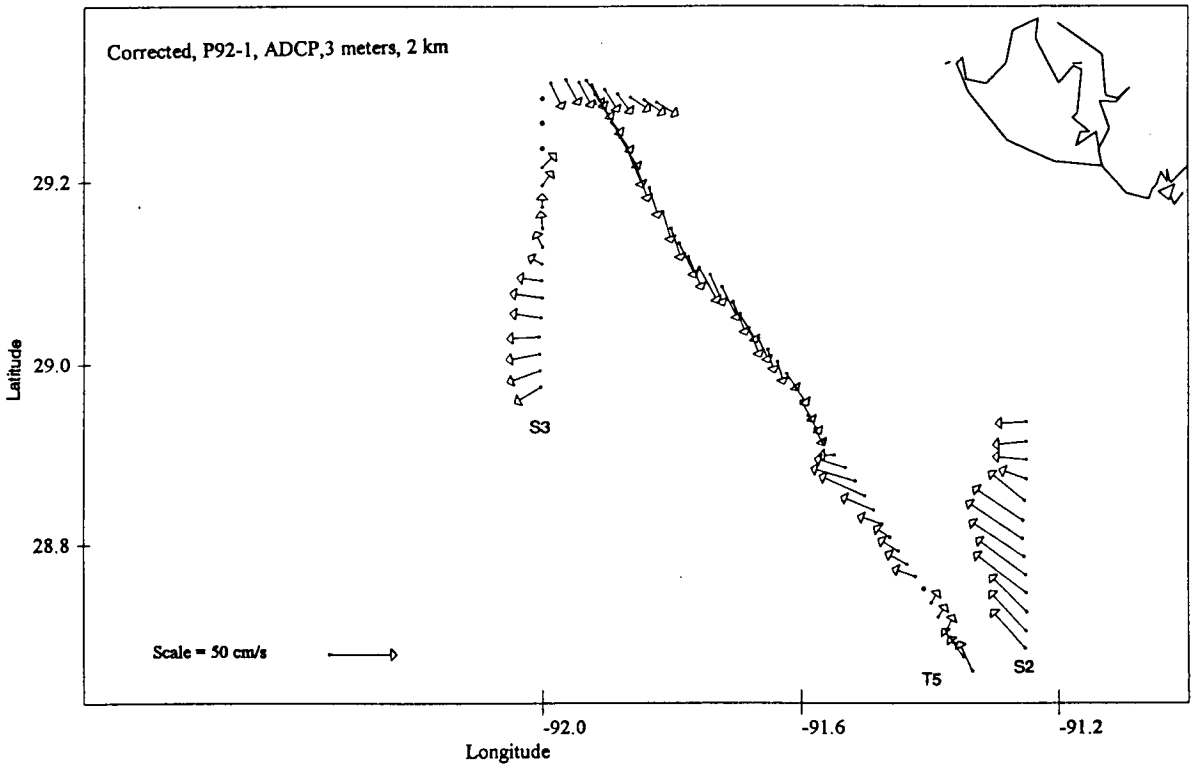

Figure 18. Near surface ADCP velocities at the 3 m level in the Atchafalaya source region.

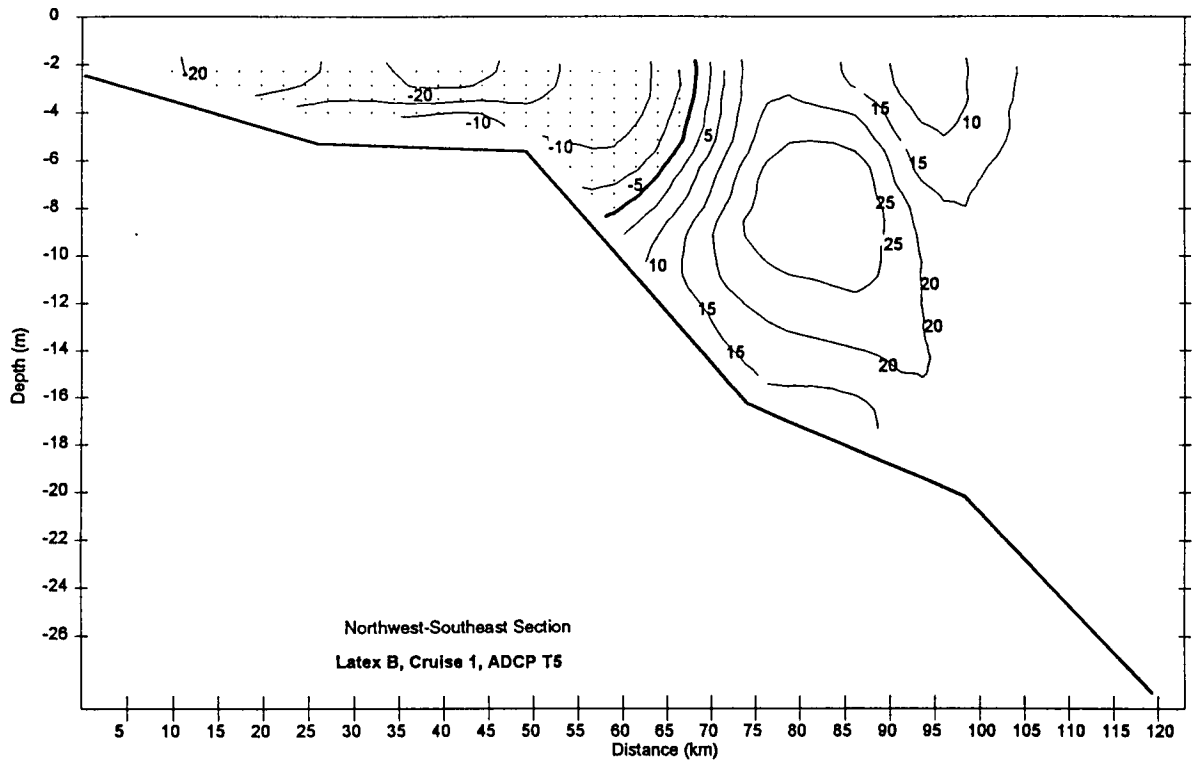

Figure 19. Vertical section of ADCP velocities along T5 (April 1992 observations) in the Atchafalaya outflow plume. Negative speeds are to the SE along the sampling line. Positive speeds are to the NW.

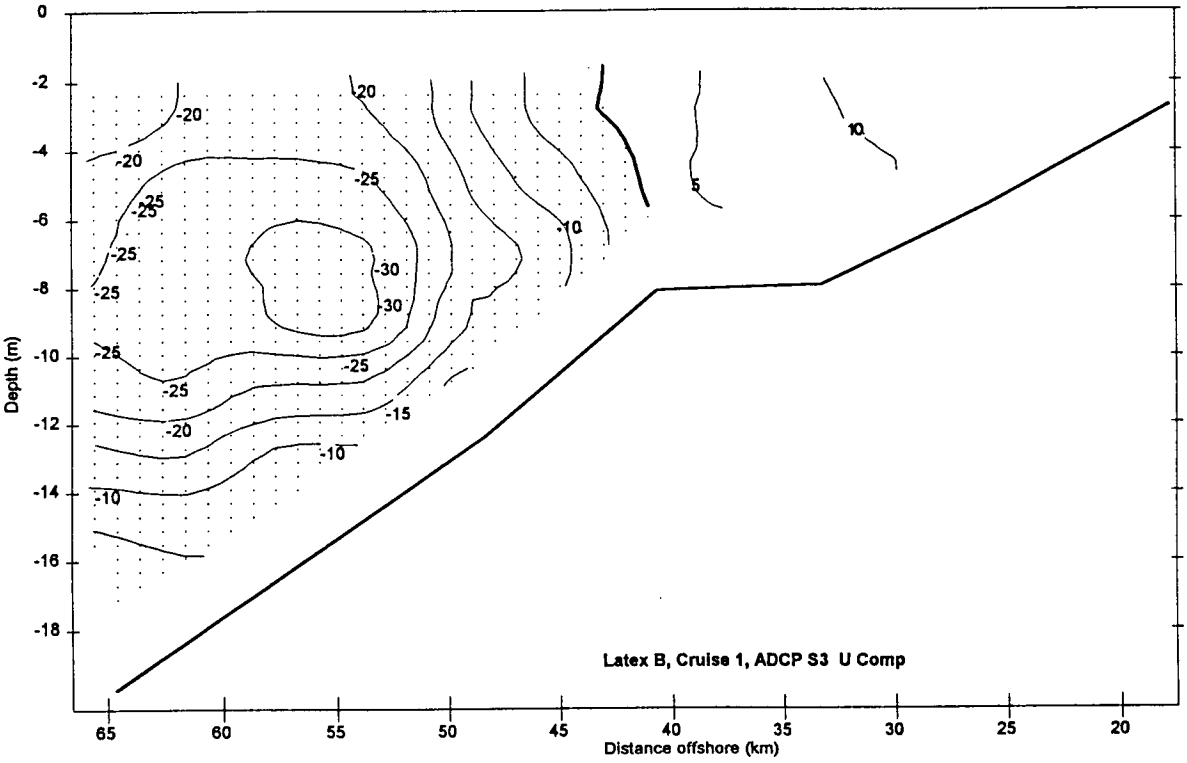

Figure 20. Alongshore speed components from the ADCP on S3 during the April 1992 observations. Negative speeds are downcoast (westward).

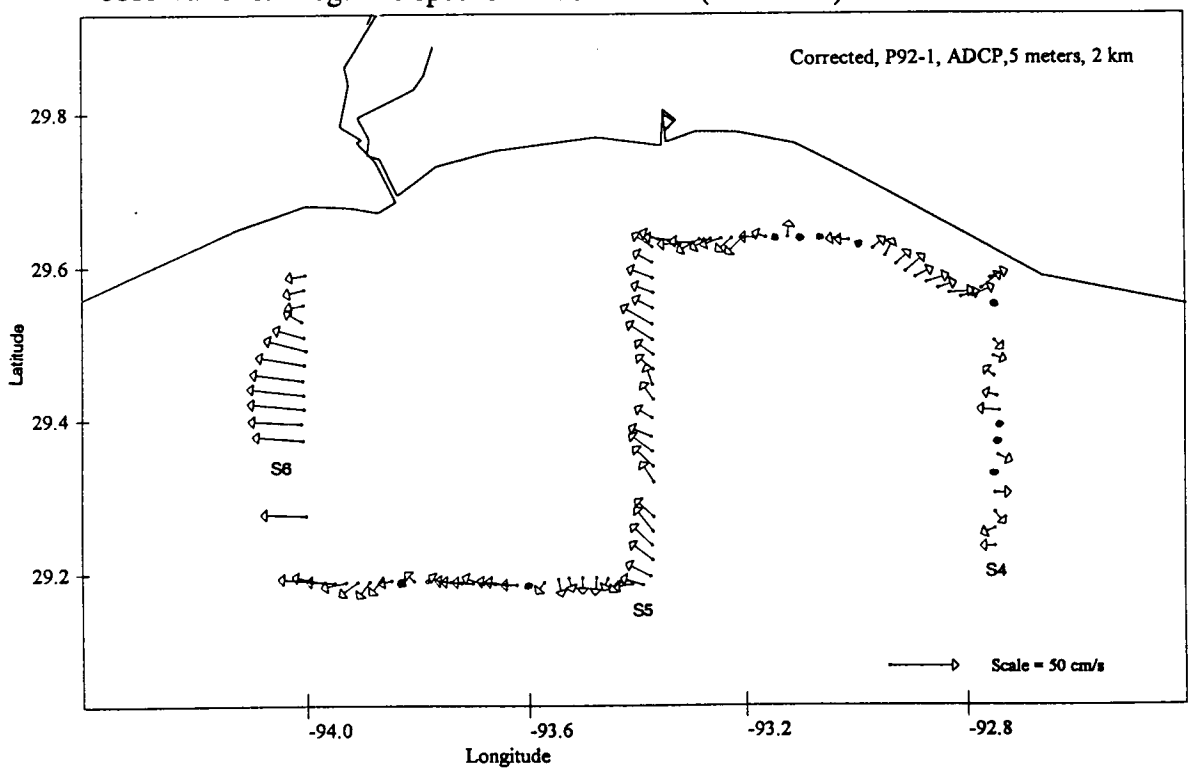

Figure 21. Velocity vectors from the ADCP at the 5 m level in the western Louisiana region. Closed circles at ensemble points indicate velocities are less than the standard error of 4 cm/sec.

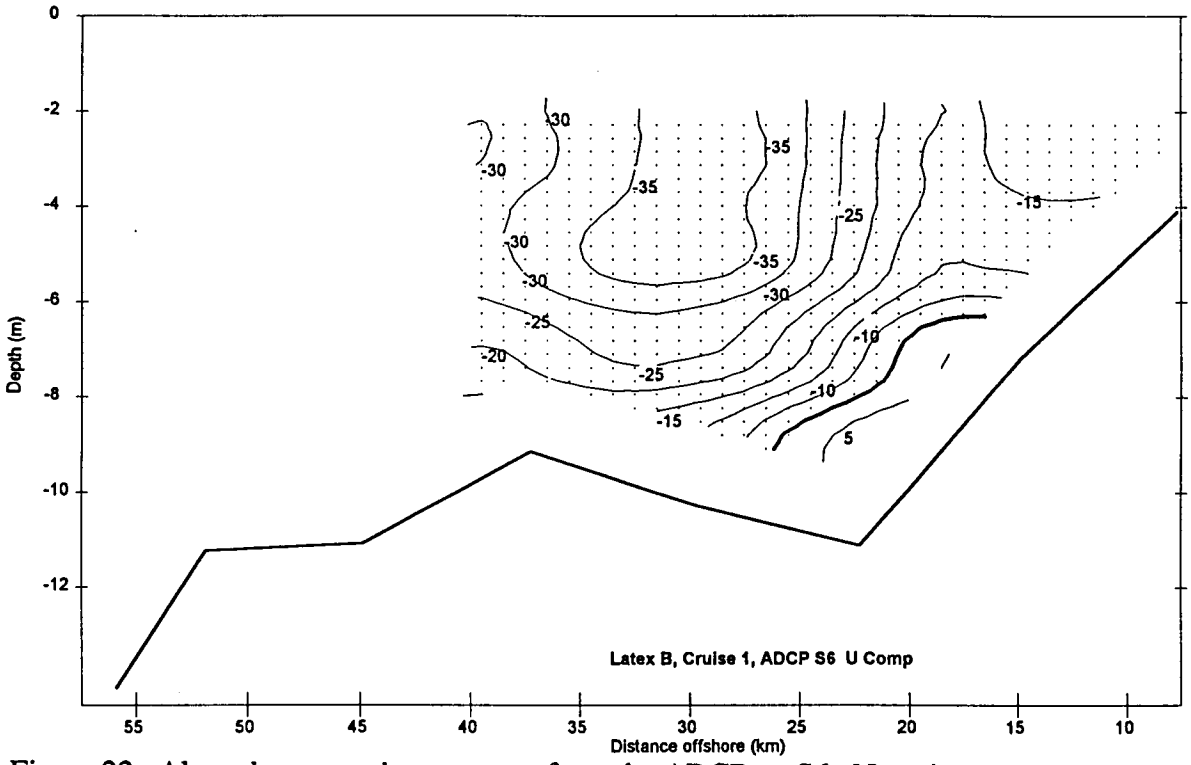

Figure 22. Alongshore speed component from the ADCP on S6. Negative speeds (dotted pattern) are directed downcoast (westerly here). Lack of data offshore of 40 km is due to instrument malfunction. Note well-developed downcoast jet located 25-35 km offshore.

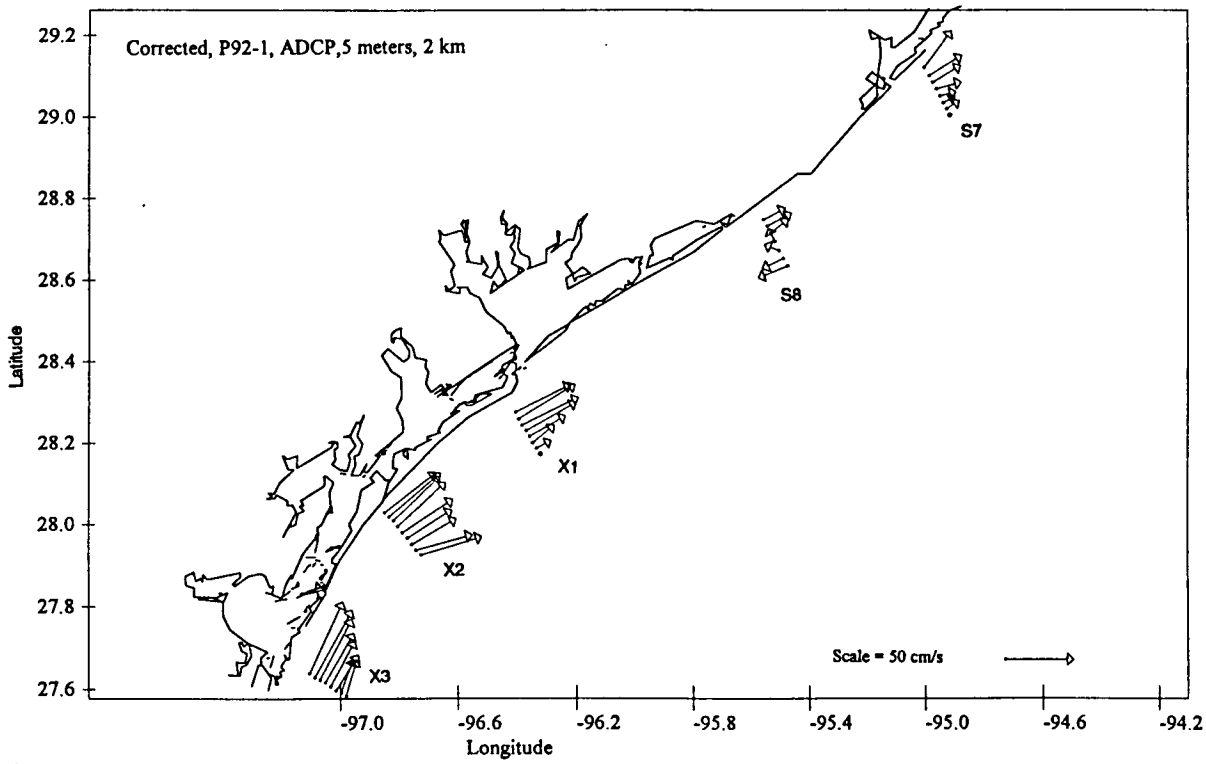

Figure 23. ADCP velocity vectors at the 5 m level in south-central Texas region of the coastal plume illustrating the episodic upcoast jet embedded in the downcoast coastal plume characteristic of this season.

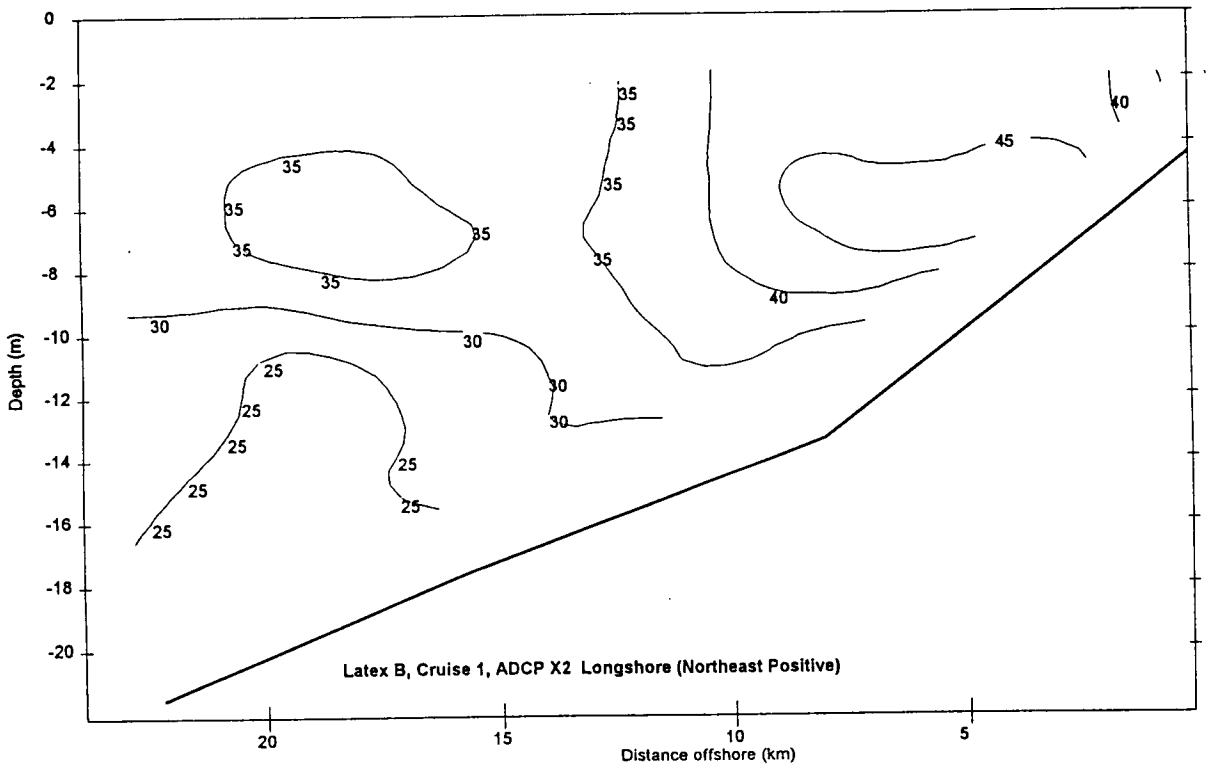

Figure 24. Alongshore speed component from the ADCP on X2. An upcoast near shore jet arises from strong southeasterly winds.

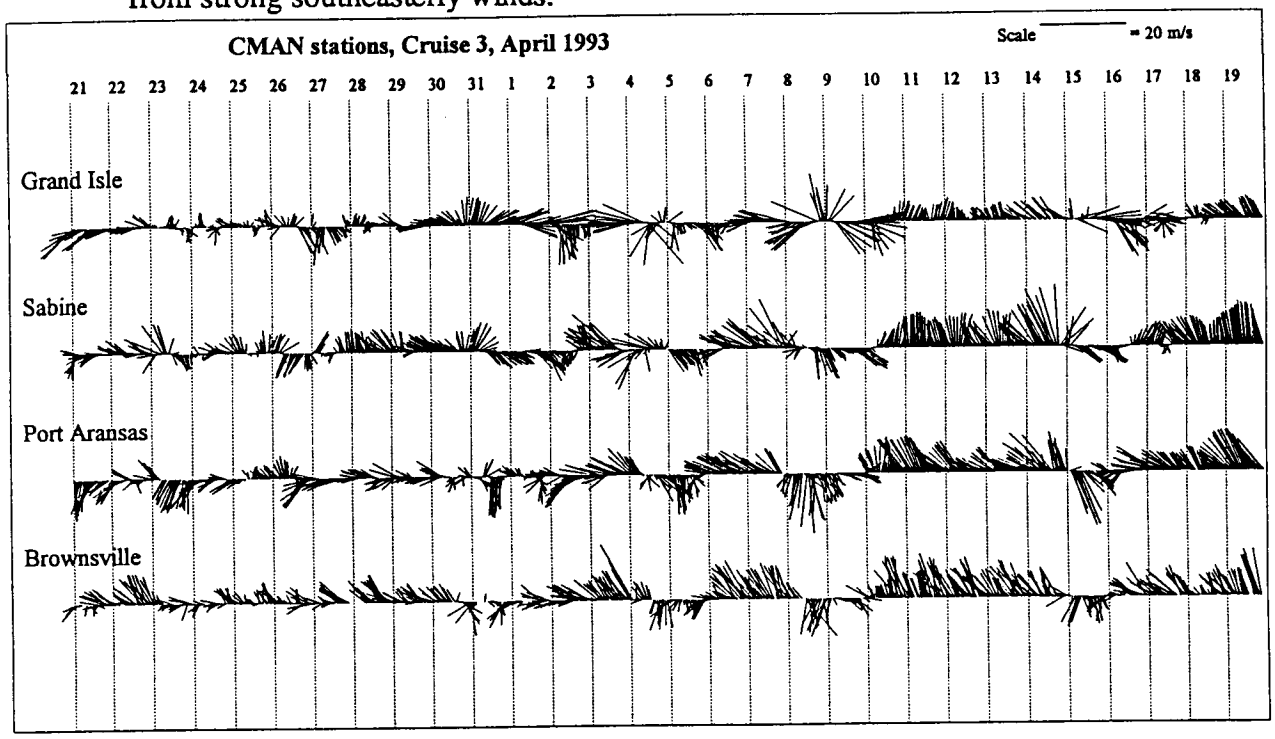

Figure 25. The time series behavior of the wind velocities affecting the coastal waters during the observation period April 6-19, 1993 is illustrated from the three available Coastal Marine Automated Network (CMAN) stations at Grand Isle, Sabine Pass, and Port Aransas, and the Brownsville NWS station. Vectors pointing to the top are winds to the North.

however, shows that the winds at the four coastal stations record only two frontal passages for the 14 days prior to and during the cruise. This leads to a dominance of upcoast wind stresses during the cruise itself as documented in Figure 26. The daily average alongshore wind stress shown in Figure 26 identifies a significant upcoast wind event of three to four day duration that impacted the coastal plume from Port Aransas to Grand Isle, just prior to the April 1993 observations. A second upcoast wind event lasting two to three days also occurred during the cruise (Figure 26). Thus, we may expect a downcoast extension of the coastal plume but upcoast ADCP currents during these particular wind events.

a. Near Surface Salinity

The basic pattern of the coastal plume (Figure 27) during this second of our two spring observations is markedly similar to the previous year. The 26 psu isohaline, for example, outlines a continuous plume of low salinity water that extends along the coast from east of the Atchafalaya mouth at S1 over 350 km westward to where it pinches out into the coast near Galveston Bay. Waters east of the Atchafalaya are a few psu fresher in the spring 1993 sample than the previous year, as expected from the increased discharges. The Atchafalaya Bay outflow plume also appears more intense, with steeper gradients that more resemble a semi-circular jet than the previous year. The 27 and 28 psu isohalines are pushed further seaward (outside our sampling range) in 1993 because of the increased strength of the Atchafalaya discharge jet.

Intensification of the cross-shore salinity gradients south of Cameron and the Sabine is present in both spring 1992 and spring 1993 observations (Figures 11 and 27, respectively). Such a pattern would be compatible with intensification of the along-shore flow in that region as observed by SCULP surface drifters (Figures 7b).

Southeast of Galveston the surface salinity pattern again in 1993 changes markedly from quasi-parallel to coastal normal. In April 1993, however, the low salinity anomalies from east Texas river discharges are absent, and the salinity increases gradually down plume from 27 psu at S7 to 30 psu at X3 as entrainment and mixing diminish the salinity anomaly of the plume.

b. Vertical Salinity Sections

(1) East of the Atchafalaya Source The regime upcurrent or east of the Atchafalaya mouth is illustrated (Figure 28) again with section S1. Note this section extends an additional 15 km seaward compared to the previous spring observation. The 30 psu isohaline outcrops 53 km offshore during this high flood year, compared to only 23 km offshore in April 1992, reflecting the increased amount of fresh water entering the plume. The two sections are geometrically similar with length scales of most features being larger in 1993. Both sections show isopycnals outcropping at their offshore ends, indicative of downwelling favorable winds; both show a halocline zone ascending toward the coast, and high salinity Gulf of Mexico waters underlying the plume and encroaching up the slope.

(2) Source Region: Atchafalaya Outflow Section S3 (Figure 29) presents an extremely revealing section through the Atchafalaya River outflow jet as it intrudes onto the inner shelf. In contrast to S1 in which waters of less than 25 psu were absent, the inner half of this section 45 km out from the coast is filled with mixed Atchafalaya River outflow water of less than 25 psu. Intense turbulent mixing is indicated by the extreme vertical and horizontal salinity gradients in the outflow jet. Seaward of the outflow jet, high salinity contours (e.g., 29 to 33 psu) rise strongly up the slope, consistent with entrainment into the base of the outflow jet.

Inspection of Figures 14 and 29 allows comparison of sections through the Atchafalaya outflow plume for two successive years. The outer edge of the jet (defined by the end of the steep horizontal salinity gradient (about at the 26.5 psu isohaline in both years) is only 10 km further

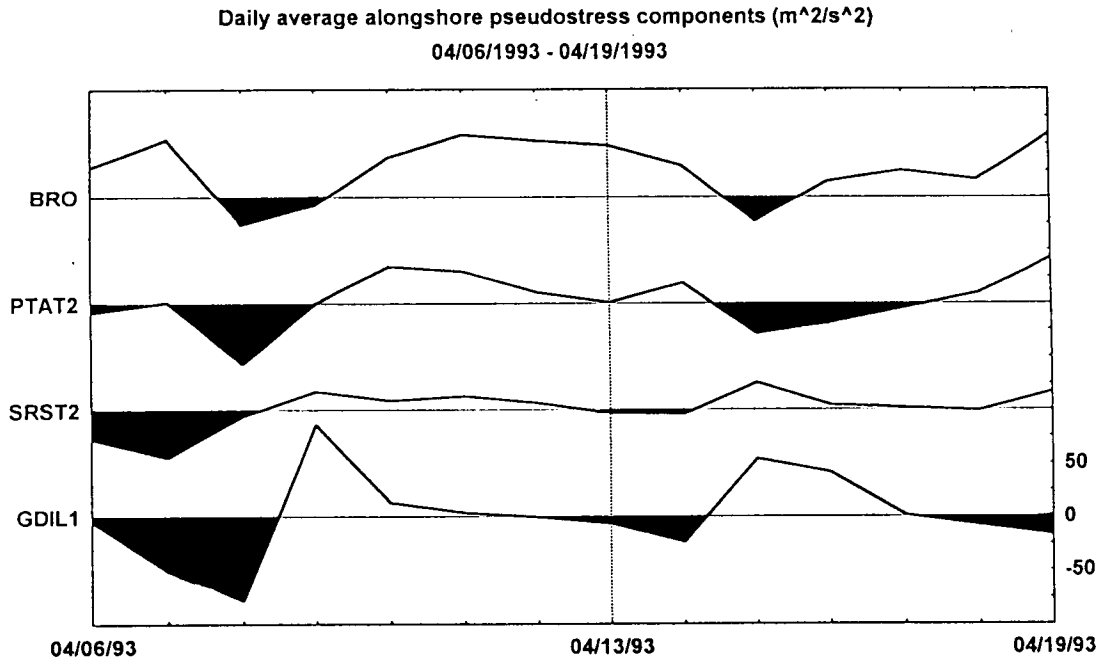

Figure 26. Daily average alongshore wind stress from four coastal stations one week prior to and during the April 1993 observations. Note the dominance of upcoast wind stresses (unshaded) prior to and during the cruise observations.

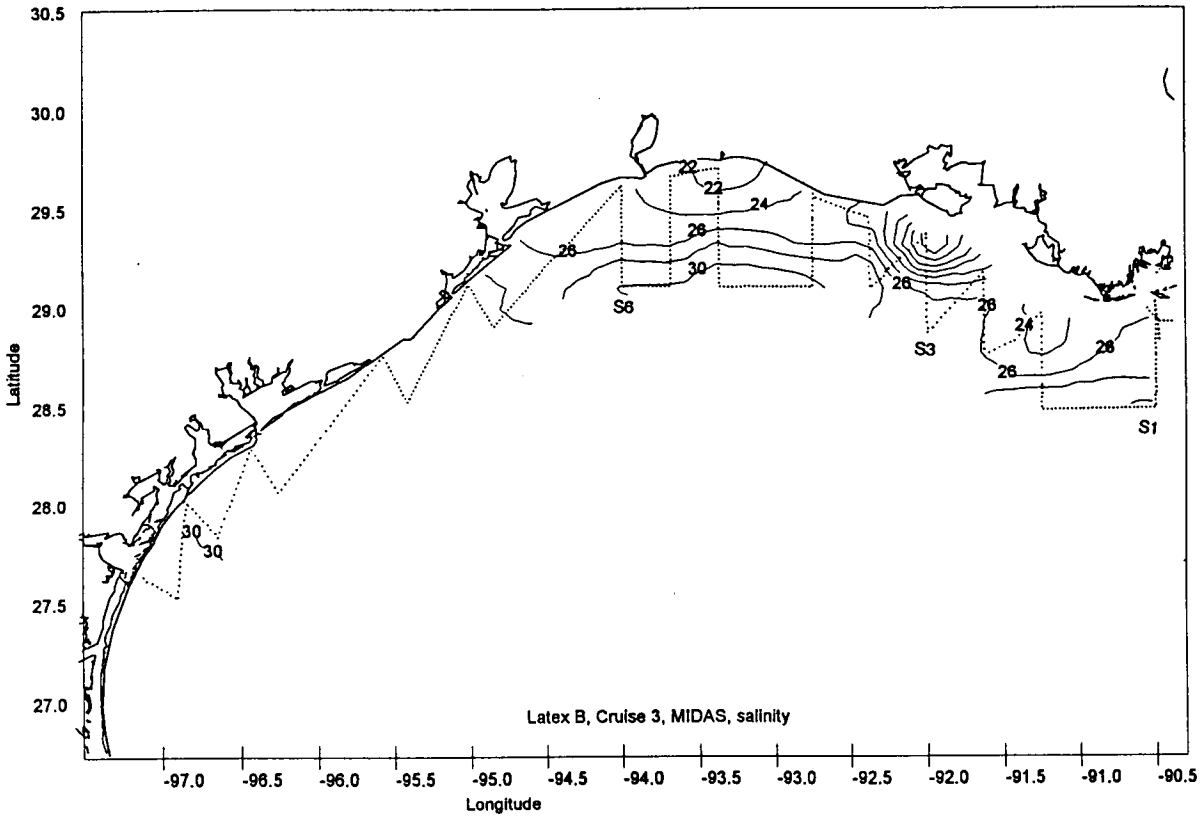

Figure 27. Near-surface salinity field (psu) observed during April 13-19, 1993 coastal plume cruise observations.

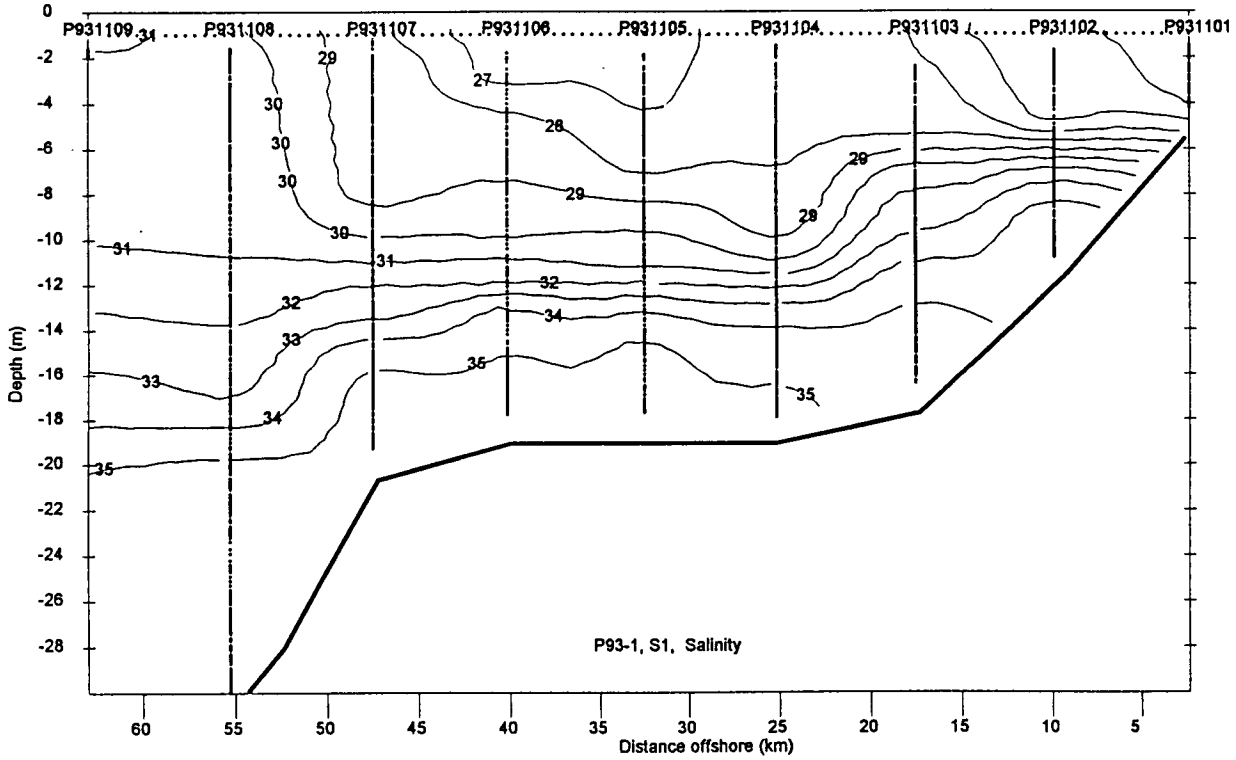

Figure 28. Vertical distribution of salinity on the S1 line during the April 1993 observations.

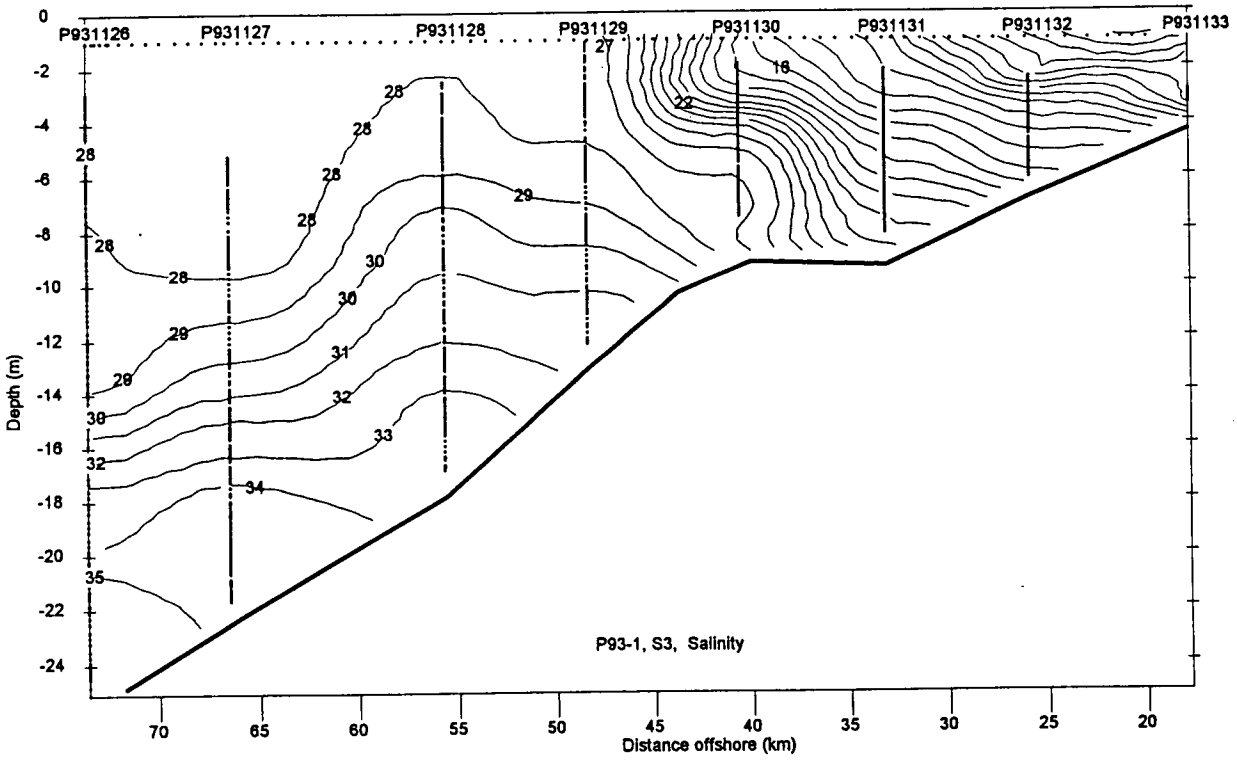

Figure 29. Vertical distribution of salinity (psu) on the S3 line during the April 1993 observations of the coastal plume. Note the presence of the Atchafalaya River outflow plume extending 45 km out from the coast.

seaward in 1993 but the salinities (and salinity gradients) inside the jet are much lower (stronger) during the higher 1993 flood year. Salinities near the mouth are only 5 to 6 psu during the 1993 observation (Figure 29) but are dramatically higher (21 psu) during the 1992 sampling when the Atchafalaya discharge was half of that in 1993 (Figure 4). As discussed above, tidal currents are at a maximum for the region off Atchafalaya Bay, and such comparison could be seriously aliased by tidal displacements. An estimate of the maximum tidal trajectory $L_t \equiv UT$; however, where U is maximum tidal current (20 cm/sec)and T is taken as 10 hours, gives an upper bound of 7 km for L_t, much lower than the 35-45 km cross-shore length scale of the outflow plume proper.

(3) West Louisiana Region Section S6 just west of Sabine Lake is similar to the previous spring observation in that the coastal plume is strongly in evidence (Figure 30). The seaward upturning of isopycnals suggest a downwelling regime. The first 30 km from the coast shows a well-mixed zone (~24.5 psu) down to the 9 m level which is underlain by a steep halocline zone, a feature that was absent in 1992. The 31.0 isohaline outcrops 65 km offshore during this observation, compared to only 48 km offshore the previous year, i.e., the cross-shore length scale γ is larger in accord with the larger fresh water influx this year.

(4) Central Texas: Far-field Coastal Plume As the ship transits into central Texas, we enter again by chance in April 1993 an upcoast (south-southeasterly) wind regime nearly identical to that encountered in April 1992. Such strong southerly winds events often follow the northerly winds after a frontal passage in this region. The salinity structure in this far field region is much like that observed the previous April (Figure 17) under similar wind driving conditions and described above in 1.b.(4).

c. Velocity Observations: Spring 1993

The velocity field measured by the ADCP again has high spatial variability as a result of the rapid changes in the wind forcing resulting from migrating pressure cells and associated frontal passages.

(1) Atchafalaya Source Region During collection of data from S1 through T4 winds were steady out of the southeast (Figure 25) so we may investigate the quasi-steady flow field (Figure 31) that develops in this region upstream of the coastal plume. The flow directions at S1 and S2 are in agreement with the downcoast wind driving. Likewise, the salinity structure seen at S1 (Figure 28) is consistent with the downwelling favorable nature of the wind. The offshore component in the surface flow at T2 is difficult to explain. This water along T2 is our only section deep enough for inertial oscillation to begin to become important. The 7.5 hour transit along T2 should see a ~100° rotation in current direction for an inertial motion but the observations along this line do not support this possibility.

Note that halfway up S2B, the ship, moving northward, enters a zone of intense current shear (Figure 31); currents turn 90° from northwestward to northeastward. The coastal wind station (Figure 25) and the ship winds (not shown), however, both indicate steady southeasterly winds all along T4. All the currents along T4 are against the wind and carrying low salinity Atchafalaya outflow water. The surface salinity data (Figure 27) indicate that the ambient coastal water coming from the east is converging here with the Atchafalaya River outflow plume, which is moving northeastward at this particular time apparently under inertial or tidal forcing. These figures provide some limited insight into the complex, strongly non-linear flow field that develops when the ambient coastal current from the east converges with a well-developed Atchafalaya outflow plume.

A vertical section at S2 (Figure 32) shows the well developed down coast flow extends to 15 m below the surface with two distinct downcoast jets in excess of 25 cm/sec. Note the presence

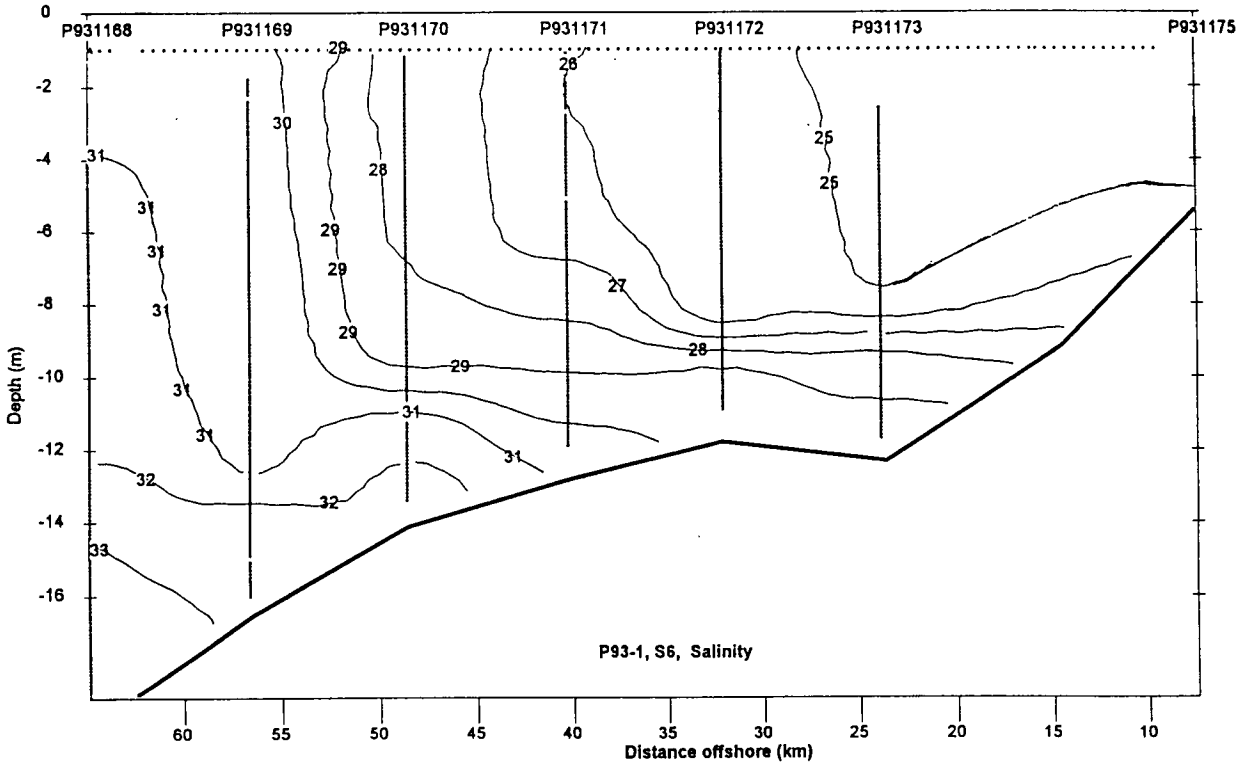

Figure 30. Vertical distribution of salinity (psu) on the S6 line west of Sabine Pass during the April 1993 observation of the coastal plume.

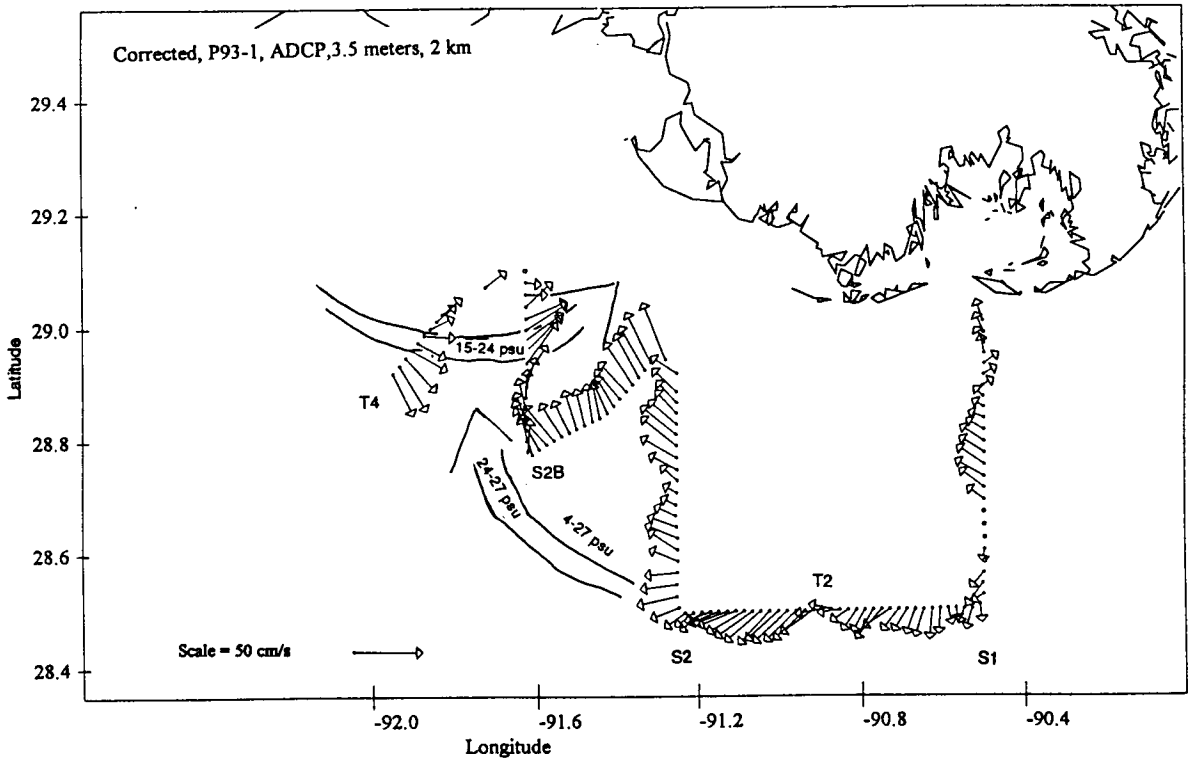

Figure 31. ADCP velocity vectors at the 3.5 m level in the source region east of the Atchafalaya outflow plume during the April 1993 observations.

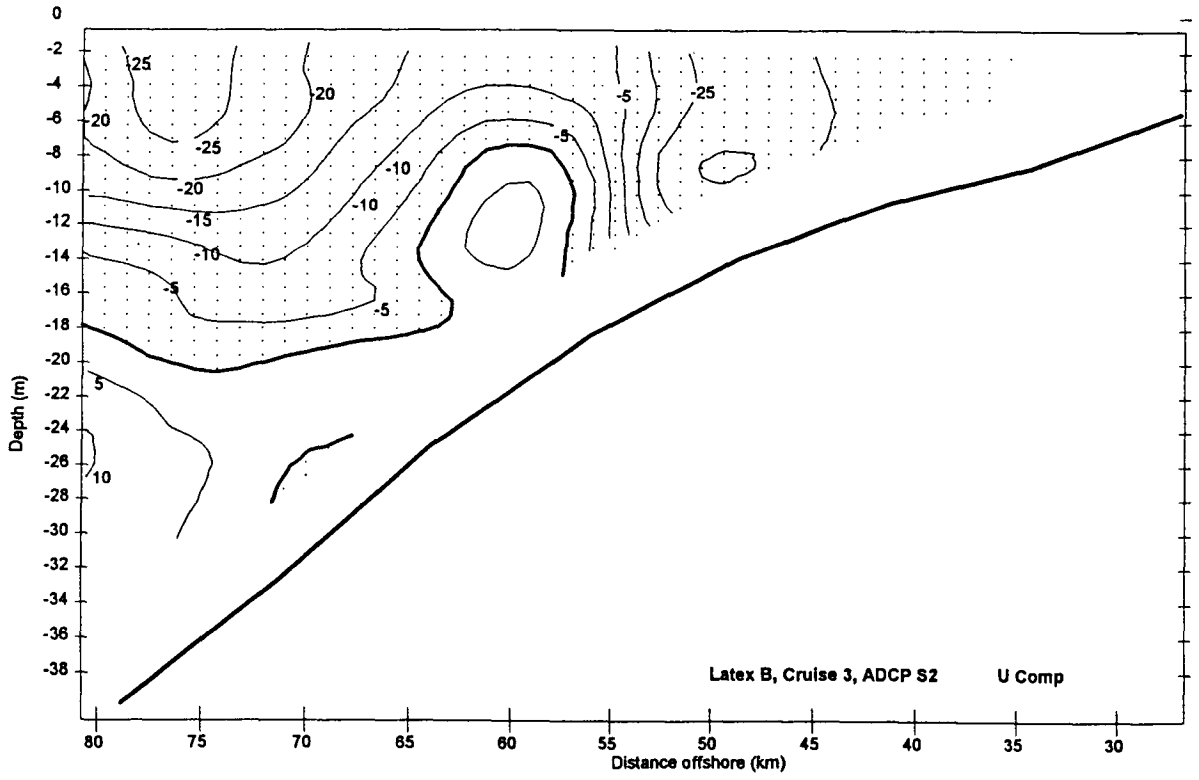

Figure 32. Alongshore speed components from the ADCP on S2 (negative speeds are downcoast) during the April 1993 observations of the coastal plume.

of a weak counter current at depth which is associated with the high salinity (>33 psu) bottom water.

(2) Western Louisiana: Downcoast Region In the downcoast region off western Louisiana, the wind varies slowly enough to provide a reasonably clear picture of its impact on the flowfield there as shown in Figure 33. From section S3B westward to S5, winds rotate clockwise from upcoast (eastward) stress to offshore to downcoast wind stress in a 28-hour interval (Figure 26). A dominantly upcoast wind stress began 5 hours prior to the start of line S3b, and continued until the ship was midway southward through line S4 when wind stress weakened and clockwise rotation began. Currents in Figure 33 clearly closely follow the wind to the extent of developing a strong upcoast transport, somewhat anomalous for this season. At S4 the upcoast flow extends fully to the bottom (Figure 34) with a robust upcoast jet in excess of 35 cm/sec located 15-25 km offshore. Of considerable interest, the cross-shore flow component (Figure 35) shows a well-developed upwelling circulation with an Ekman offshore transport in the upper 8-10 m and a shoreward "adjustment" drift in the lower half of the section extending all the way into the coast. With a speed of 25 cm/sec and a duration time scale of 20 hours, the length scale or along-coast excursion of the upcoast event is only 18 km, a slight perturbation in the 300 km alongshore length scale of the coastal plume. Similarly, the cross-shore excursion is only 10 km compared to a cross-shore of the coastal plume of 50 km. Nonetheless, despite its transient nature, this is a fascinating event. The cross-shore flow component through the ensuing east-west section T7 (Figure 36, shows that the offshore winds can sustain the strong upwelling circulation pattern for at least the additional seven hours that it took to observe this line.

(3) Central Texas: Far-field Coastal Plume The sections S7 through X3 were all observed during the intense south-southeasterly wind episode of April 17-19. Figure 37 shows the coastal plume waters near the coast responded within five hours of the onset of this wind system with a well-defined coastal jet with a velocity maximum near the coast. Note the offshore flow at S8. It appears that this is a favorable location for short wave length motions to intrude onto the inner shelf as the upcoast jet was narrowest at this same location in the April 1992 observations. This major upcoast flow regime is coherent over at least 250 km, and it appears driven, in large part, by the southeasterly winds that follow the frontal passage. Pressure gradients along the coast set up by the wind systems are also probably important and are investigated in a later section.

A vertical section through this current at Section X2 (Figure 38) shows a high speed jet (35-40 cm) trapped up against the coast with speeds decreasing nearly to zero 30 km offshore. A weak remnant of the previous downcoast flow regime remains below 18 m. The wind stress record, e.g., Figure 26, shows there were only two previous such upcoast events at Port Aransas in April 1993, with duration time scales of two days and five days.

3. Transition to Winter: Downcoast Regime, October 1992 Observations

We next investigate the development and characteristics of the coastal plume during a period of low river discharge and early winter downcoast wind forcing. In October 1992, the Atchafalaya River discharge has fallen to near a low-term average low of 4400 m^3/sec (Figure 4) and the winter downcoast wind stress regime is clearly reestablished (Figure 5) after its summer hiatus.

Winds were not only downcoast in October 1992 (Figure 5), but they far more persistently downcoast during our 7-day observation interval (October 6-13) than during the two April observations discussed above. Figure 39, the ship winds, shows strong downcoast winds except for brief intervals of northeasterly winds during frontal passages while observing at lines S3 and S5. The alongshore daily wind stress history (Figure 40) also shows that since September 26, wind stresses were persistently downcoast at all four stations.

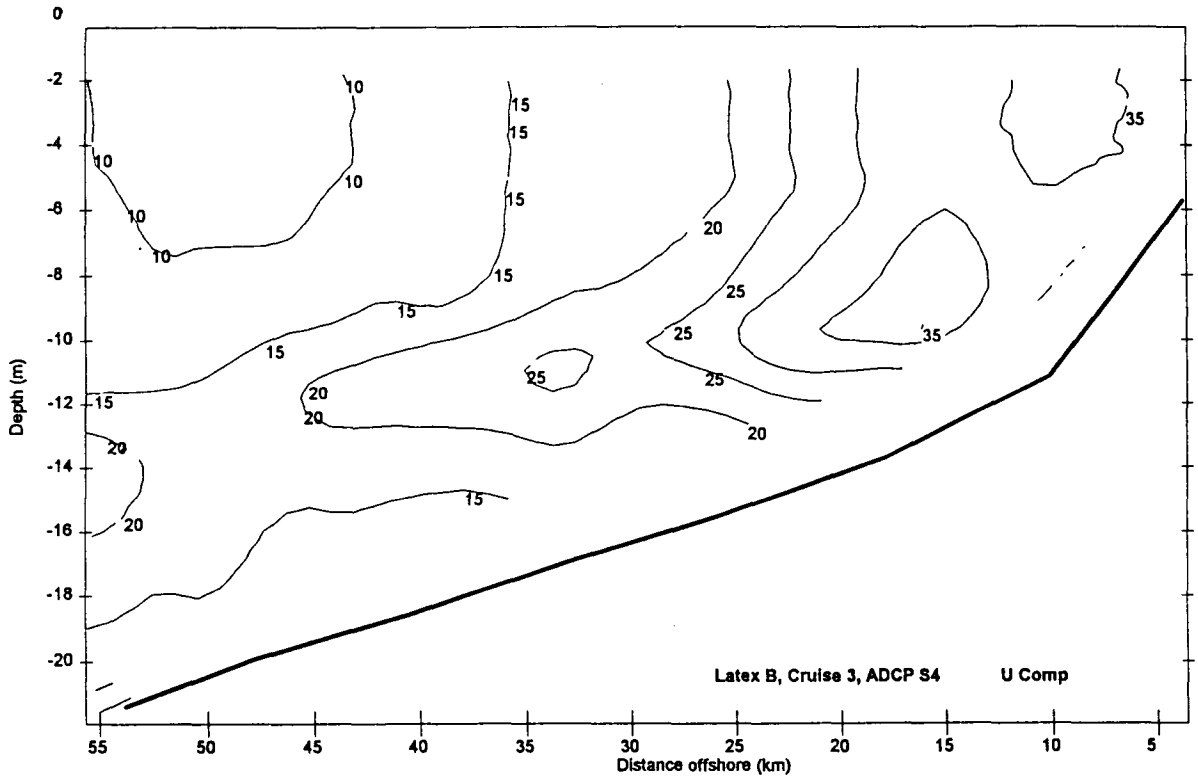

Figure 33. ADCP velocity vectors at the 3.5 m level in the region off western Louisiana during the April 1993 observations. The dark arrows reppresent the evolution of the wind velocity (m/sec) as measured along the ship track.

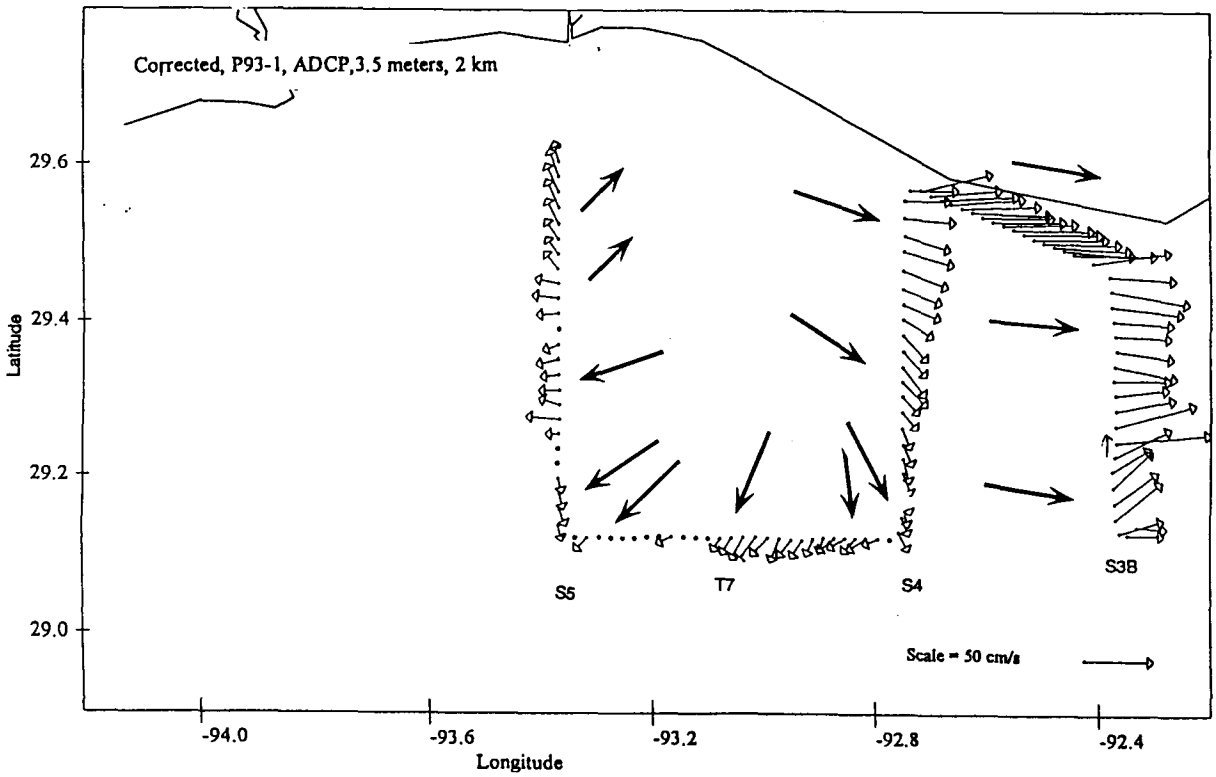

Figure 34. Alongshore speed components from the ADCP on S4 (positive speeds are upcoast) during the April 1993 observations of the coastal plume.

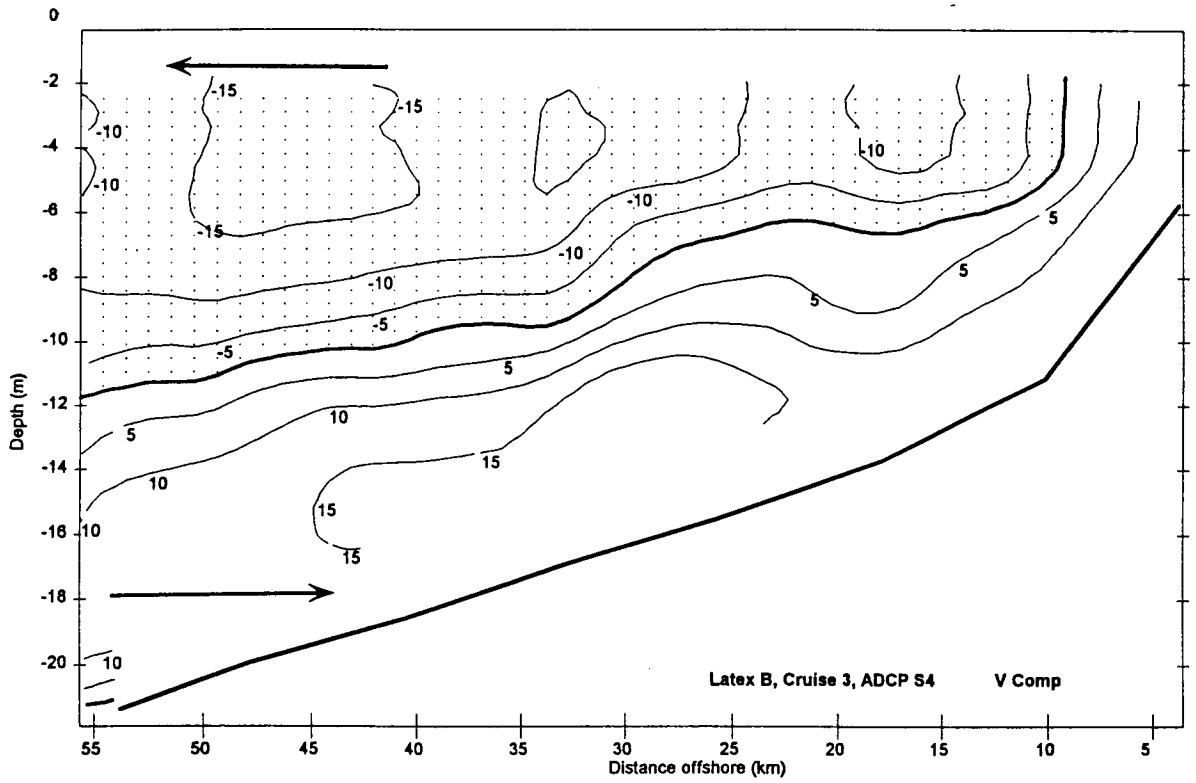

Figure 35. Cross-shore speed components from the ADCP on S4 (negative speeds are offshore) during the April 1993 observations. Note the well-developed upwelling circulation system. Arrows show the direction of currents.

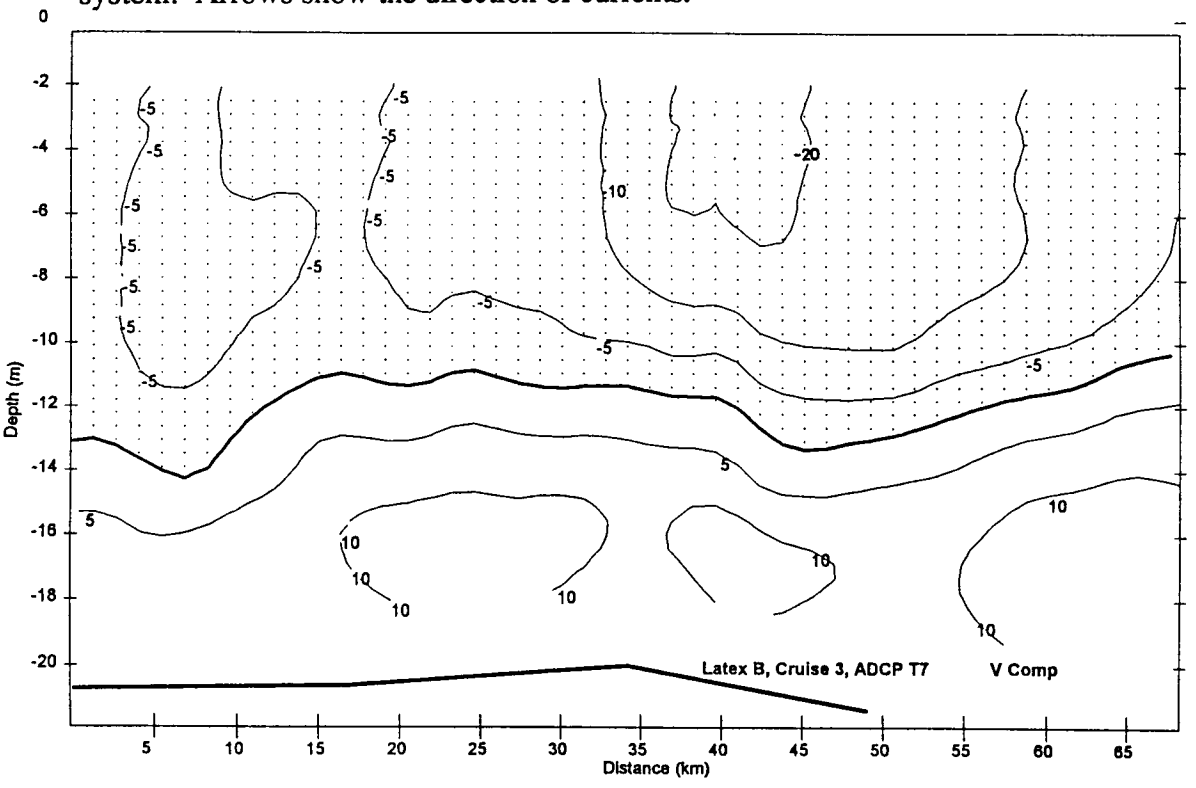

Figure 36. Cross-shore velocity components from the ADCP on section T7, which runs parallel to the coast. Note the two-layer flow indicative of the upwelling event in progress during the observations in April 1993.

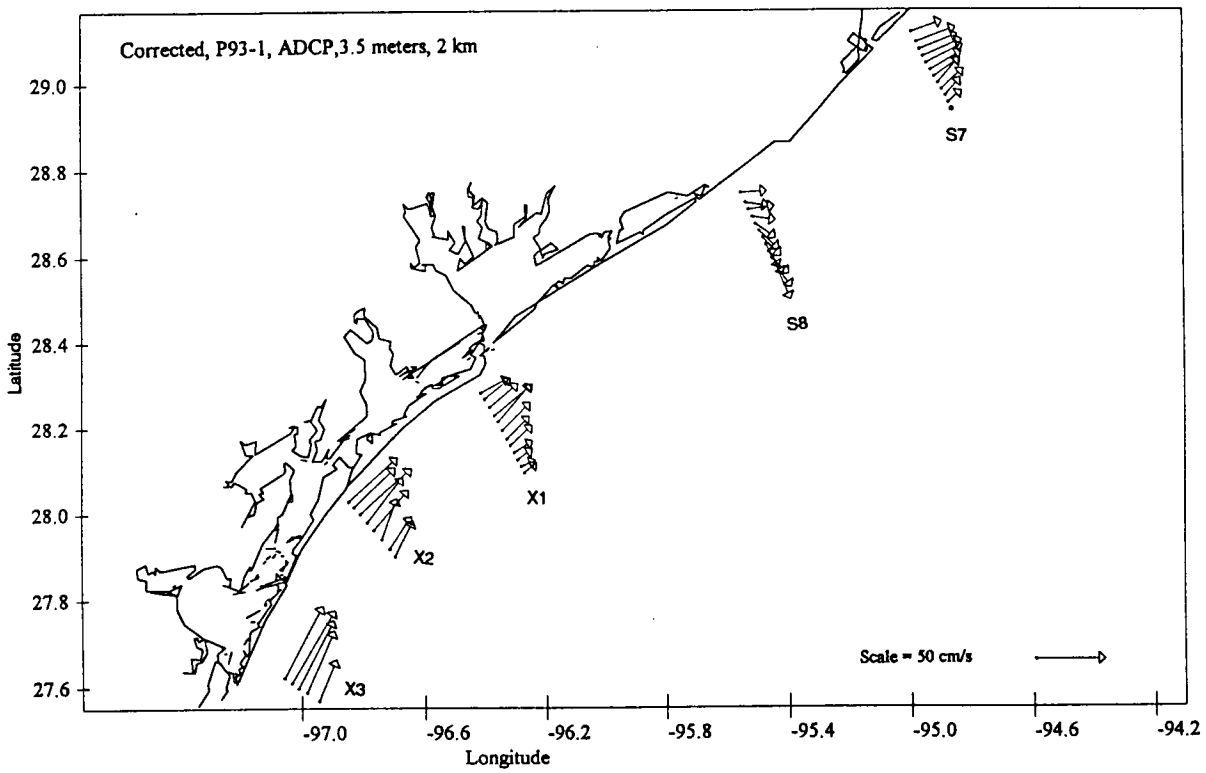

Figure 37. ADCP velocity vectors at the 3.5 m level in the region off south central Texas during the April 1993 observations.

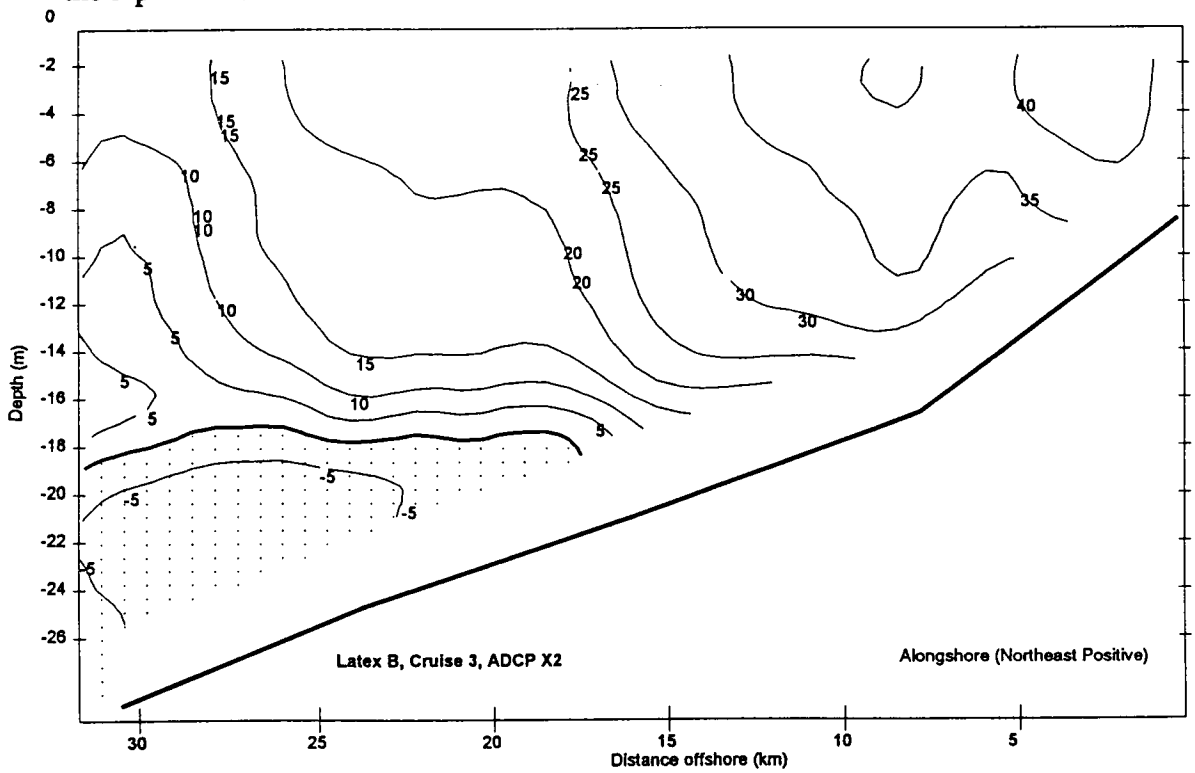

Figure 38. Alongshore speed components (upcoast positive) on section X2 during a strong upcoast wind event during the April 1993 observations. Note the high speed jet within 10 km of the coastline and the deep counter current further offshore.

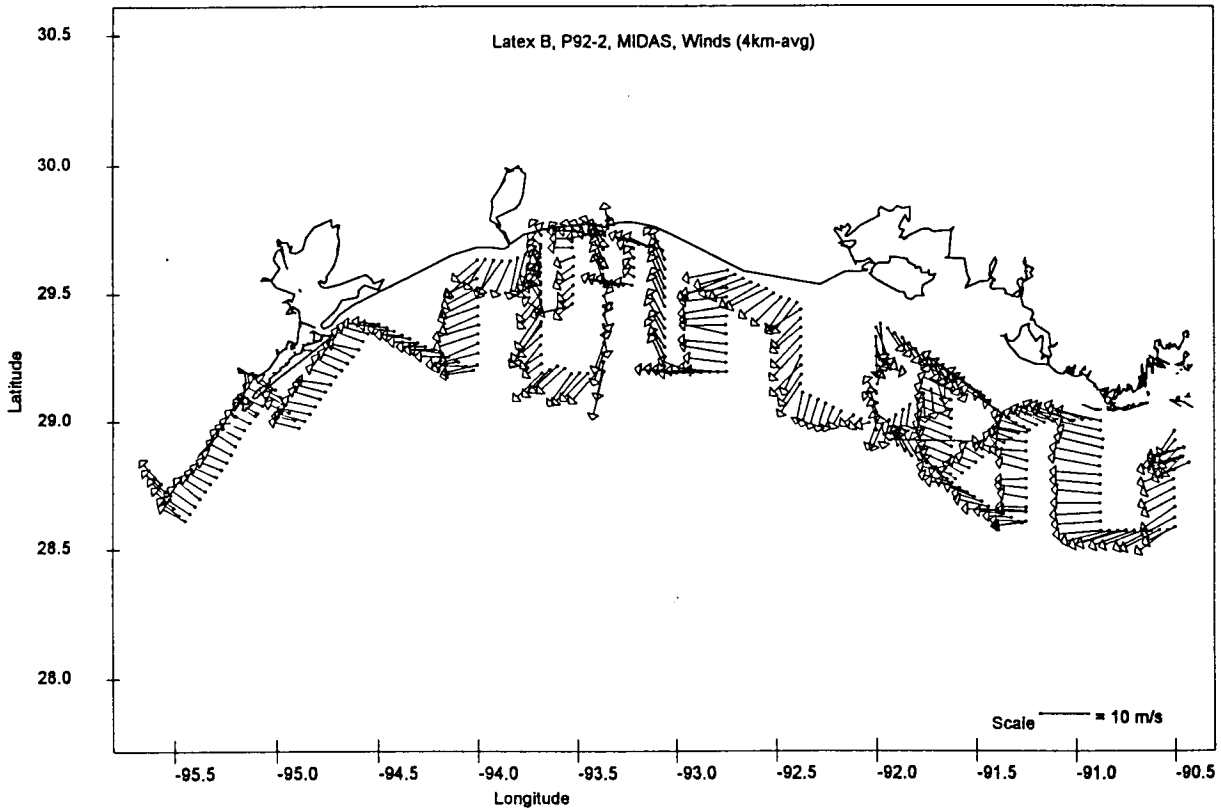

Figure 39. Corrected ship winds during the fall 1992 observations of the coastal plume. Note the dominance of downcoast wind stress except for brief events off Atchafalaya Bay and Cameron, Louisiana.

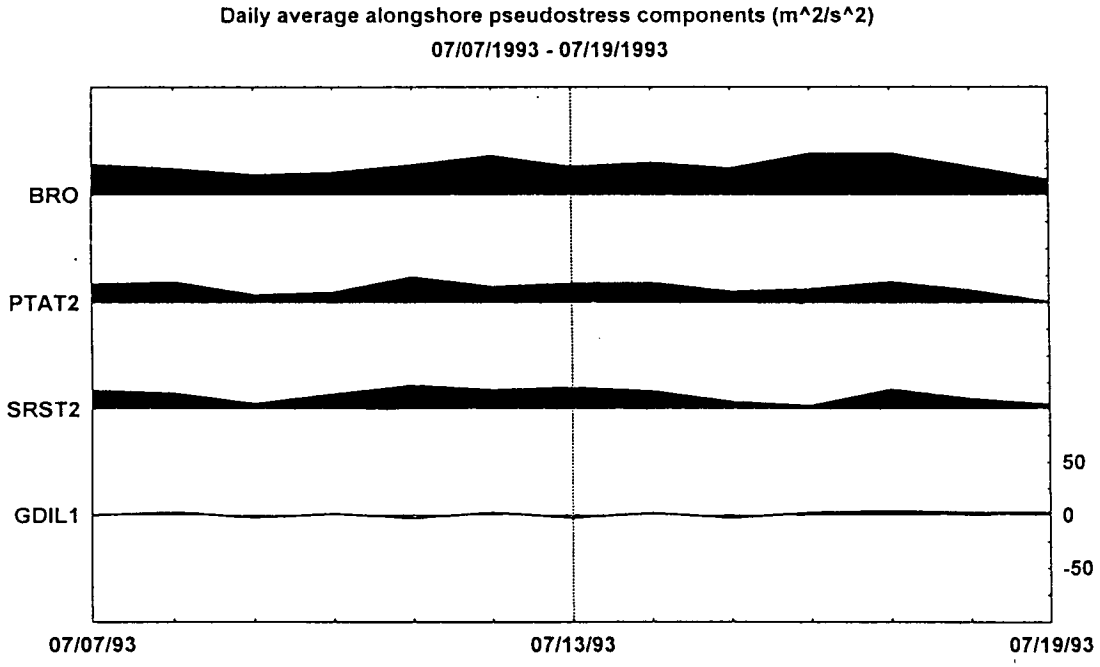

Figure 40. Daily average alongshore wind stress from four coastal stations one week prior to and during the October 1992 observations. Upcoast wind components are shaded.

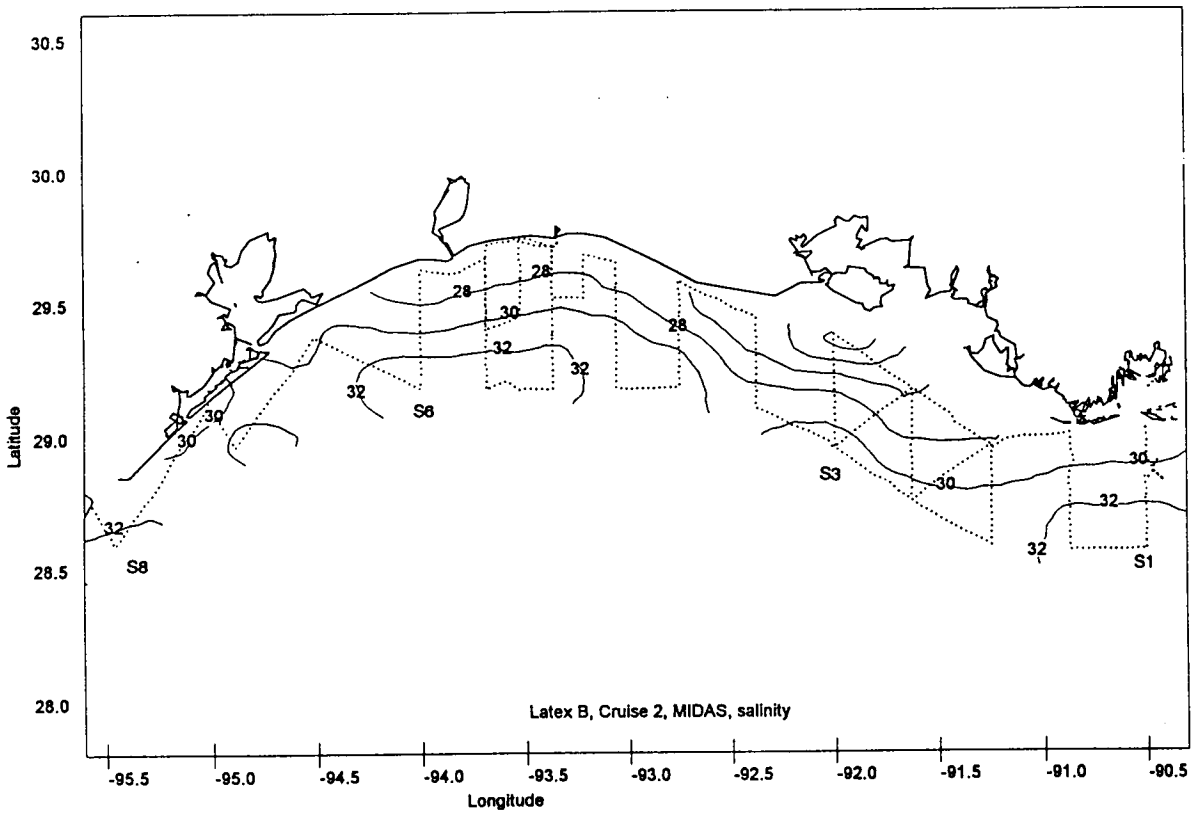

Figure 41. Near-surface salinity (psu) field observed by underway thermosalinograph during October 6-13, 1992 coastal plume observations.

a. Surface Salinity

As anticipated from the steady wind forcing, our observations delineate a beautifully developed coastal plume (Figure 41). Relatively high salinities of 29 to 33 psu characterize the ambient coastal water converging on the Atchafalaya River outflow plume from the east. The lowest salinities observed at the inshore end of S3 is 20.5 psu indicating extensive mixing of river water and coastal water inside Atchafalaya Bay during this low discharge season. The 29 psu isohaline provides a continuous outline of the resultant coastal plume from Terrebonne Bay 330 km westward to Galveston Bay. Note the persistent downwelling favorable wind acts to drive the surface Ekman layer toward the coast intensifying and maintaining the integrity of the salinity gradients. The coastal plume again narrows south of Sabine in the S5-S6 area as indicated by the intrusion of the 32 psu isohaline into that region. The abrupt contraction of the coastal plume to the west of Galveston is clearly manifested by the 31.0 psu isohaline which outcrops 33 km offshore south of Sabine Lake on line S6 but converges toward the coast outcropping only 15 km offshore on S8. In this observation we appear to have captured a quasi-steady state snapshot over the entire length of the coastal plume. With no obvious indication of cross-shore flow it appears that the near coastal low salinity waters (21-28 psu) are laterally and vertically mixed along the length of the plume, having essentially disappeared by the time of their arrival at S8, 410 km downstream of the Atchafalaya source.

b. Vertical Salinity Sections

Vertical sections through this coastal plume show its downstream evolution from its initial condition at S1 to its widest section at S3 in the Atchafalaya source region to its virtual disappearance at S8. At the easternmost (upstream) section S1 the 29 psu isohaline outcrops only 8 km offshore (Figure 42). Note the peculiar structure of the seaward end of S1. The high salinity water (34 psu) normally underlying the buoyant surface water is present only on the inshore end of the section. In fact, the entire outer edge of the coastal plume here has been truncated by a high speed jet streaming southwestward after accelerating around the tip of the Mississippi Delta. This transient phenomenon is described in detail in Walker et al. (1996).

In the Atchafalaya source region, the influx of Atchafalaya River water pushes the 29 psu outcrop seaward along S3 (Figure 43) out to 37 km offshore. The gradual downstream mixing of the plume with ambient shelf water moves the 29 psu outcropping back to within 25 km of the coast at S6 (Figure 44). Mixing appears to accelerate in the far-field region as by its arrival at S7, the 29 psu outcrops is back to within 8 km of the coast and by S8 water of 29.0 psu or less has been removed by mixing (Figure 45). It is notable that vertical stratification is relatively weak in all three of these sections that extend along the entire coastal plume. The energetic wind conditions (Figures 39 and 40) and the low river discharge in this season (Figure 4) both act to enhance vertical mixing and reduce stratification.

c. Velocity Observations

The near-surface velocity field (Figure 46) echoes the salinity distribution (Figure 41) in showing the longshore coherence of the downcoast flow transporting the coastal plume water from the Atchafalaya mouth westward to and beyond Galveston. The intensification of the coastal flow as the plume abruptly narrows south of Galveston is evident in the velocity data. A vertical section at S1 (Figure 47) shows a surface intensified high speed jet moving toward the Atchafalaya source region carrying ambient coastal water largely of 30-33 psu water. Note the high salinity water (15 to 25 km offshore of Figure 42) underlying the downcoast surface flow appears as an upcoast counter-current. In the source region at S3 (not shown), the Atchafalaya outflow jet (clearly seen in the salinity section (Figure 43) is barely discernible probably because of the episode of northerly winds which disrupted this section during our observation.

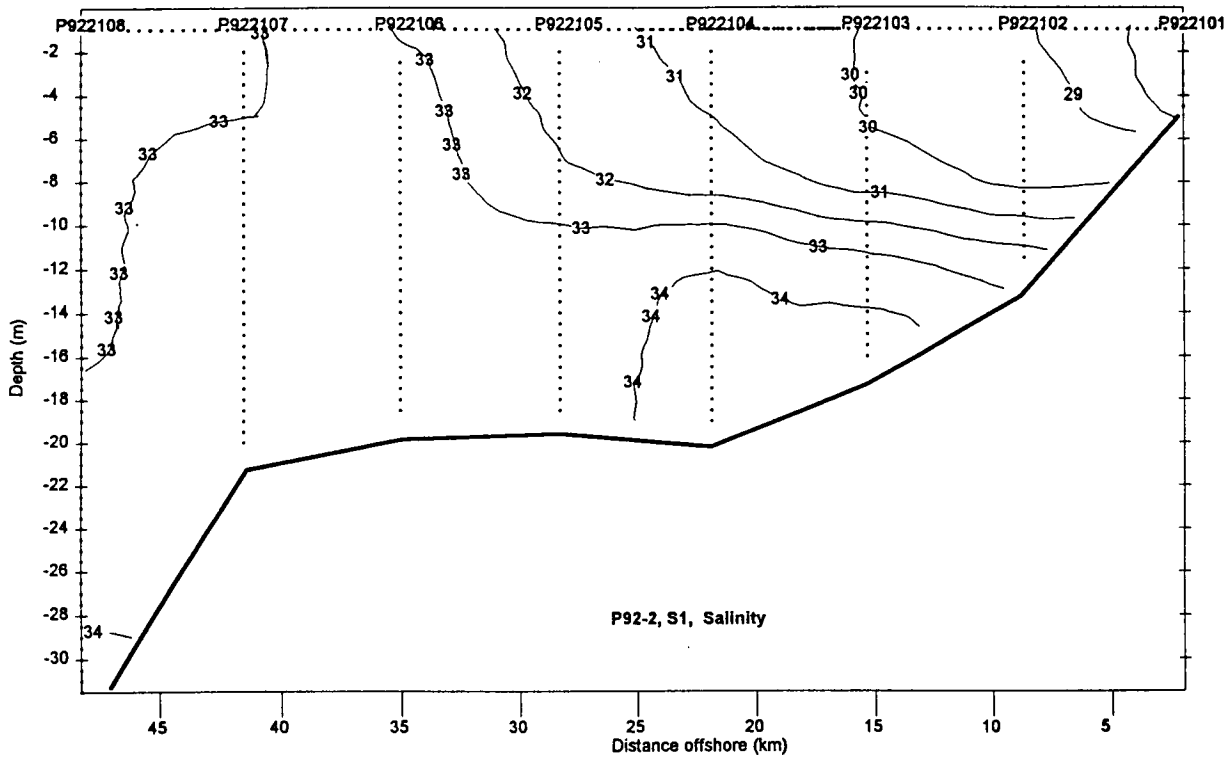

Figure 42. Vertical distribution of salinity (psu) in the S1 line during the October 1993 observations. Note the relative absence of low salinity water near the coast at this section upward of the Atchafalaya River outflow in a period of low river discharge.

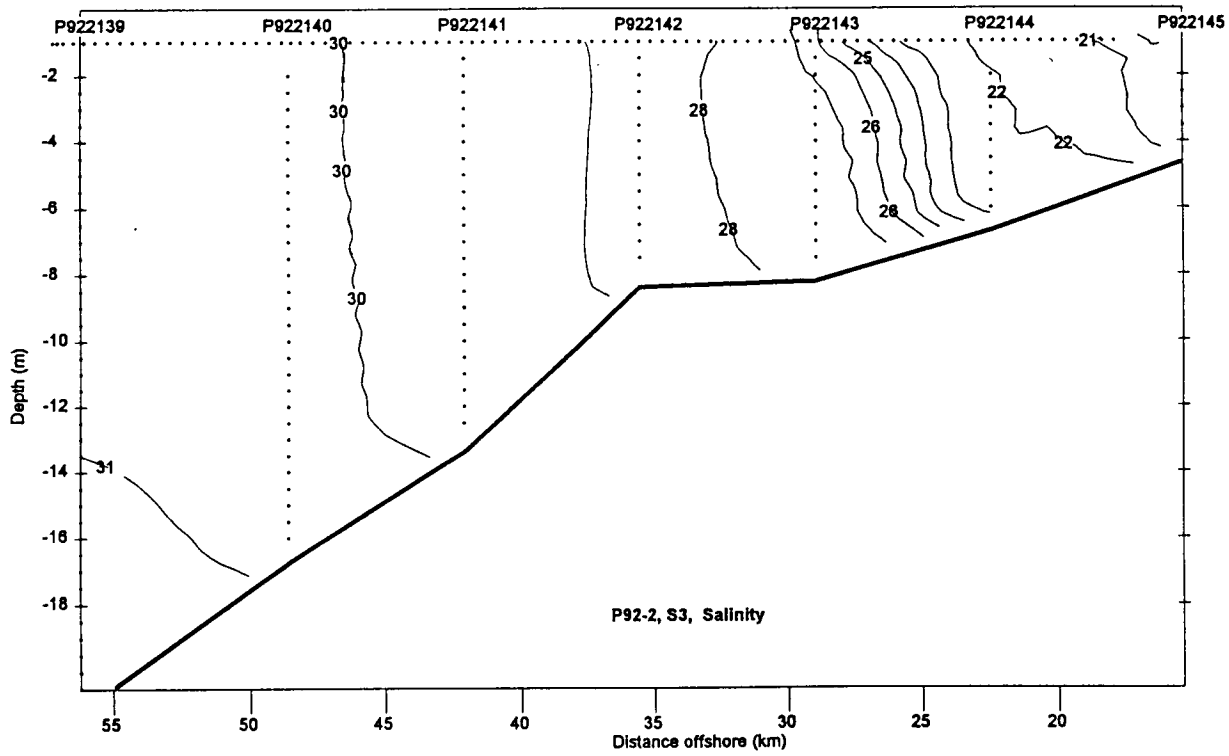

Figure 43. Vertical distribution of salinity (psu) on the S3 line during the October 1993 observations.

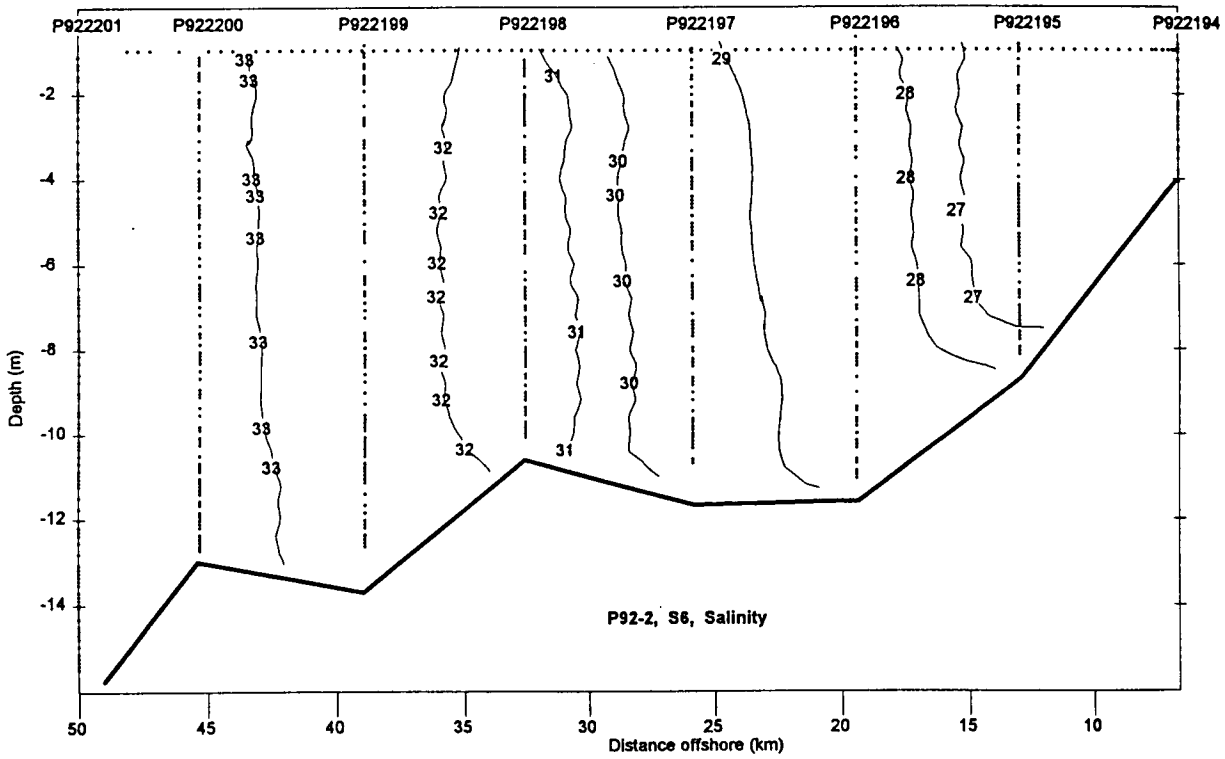

Figure 44. Vertical distribution of salinity (psu) on the S6 line during the October 1993 observations. Note intense vertical mixing producing vertically homogeneous conditions but a strong cross-shore salinity gradient is maintained.

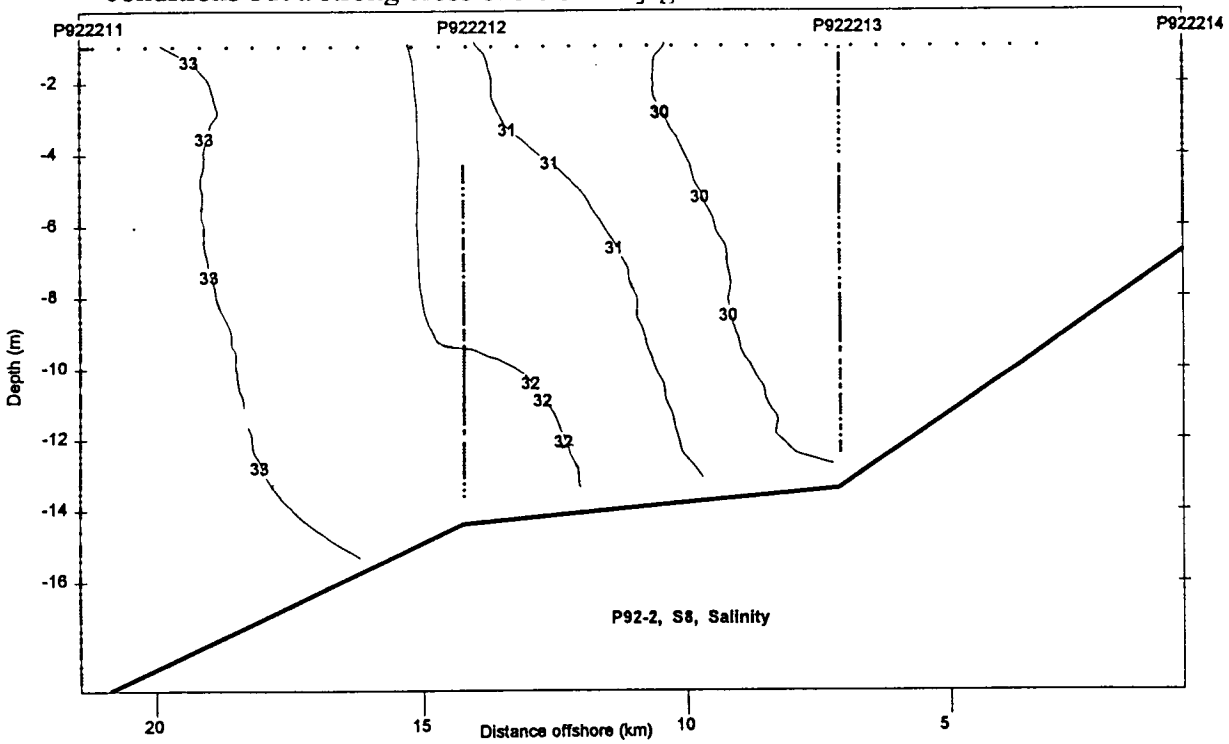

Figure 45. Vertical distribution of salinity (psu) on the S8 line during the October 1993 observations.

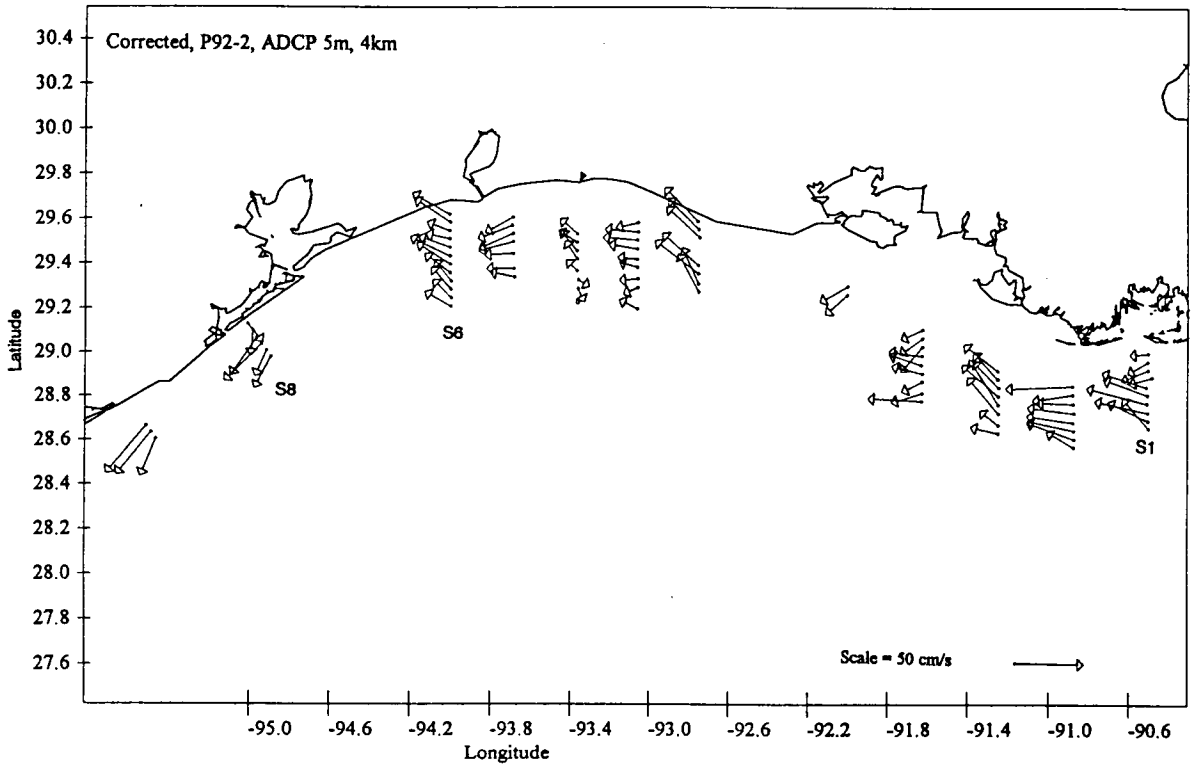

Figure 46. ADCP velocity field at the 5 m level over the entire cruise observation domain during the October 1992 observations. ADCP data points are 4 km averages.

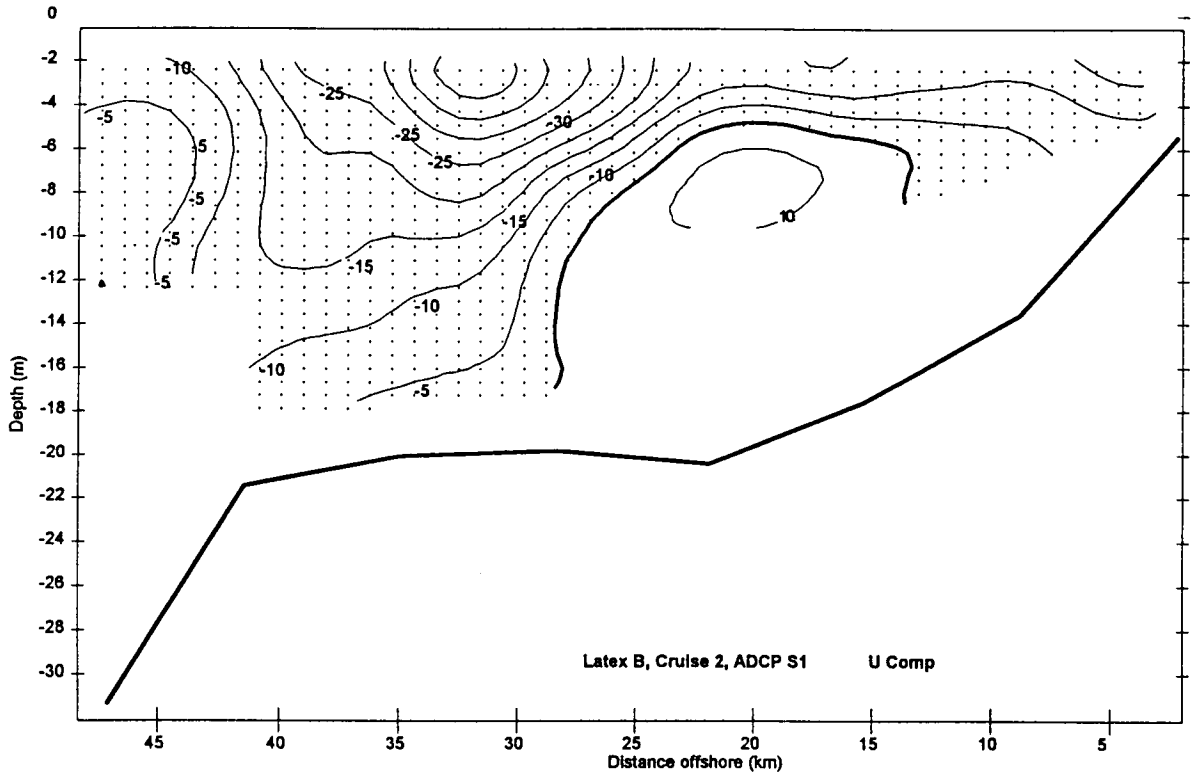

Figure 47. Alongshore speed components from the ADCP on S1 during the October 1992 observations. Note the premier downcoast jet and the upcoast flow in the high salinity bottom layer, 15-25 km offshore.

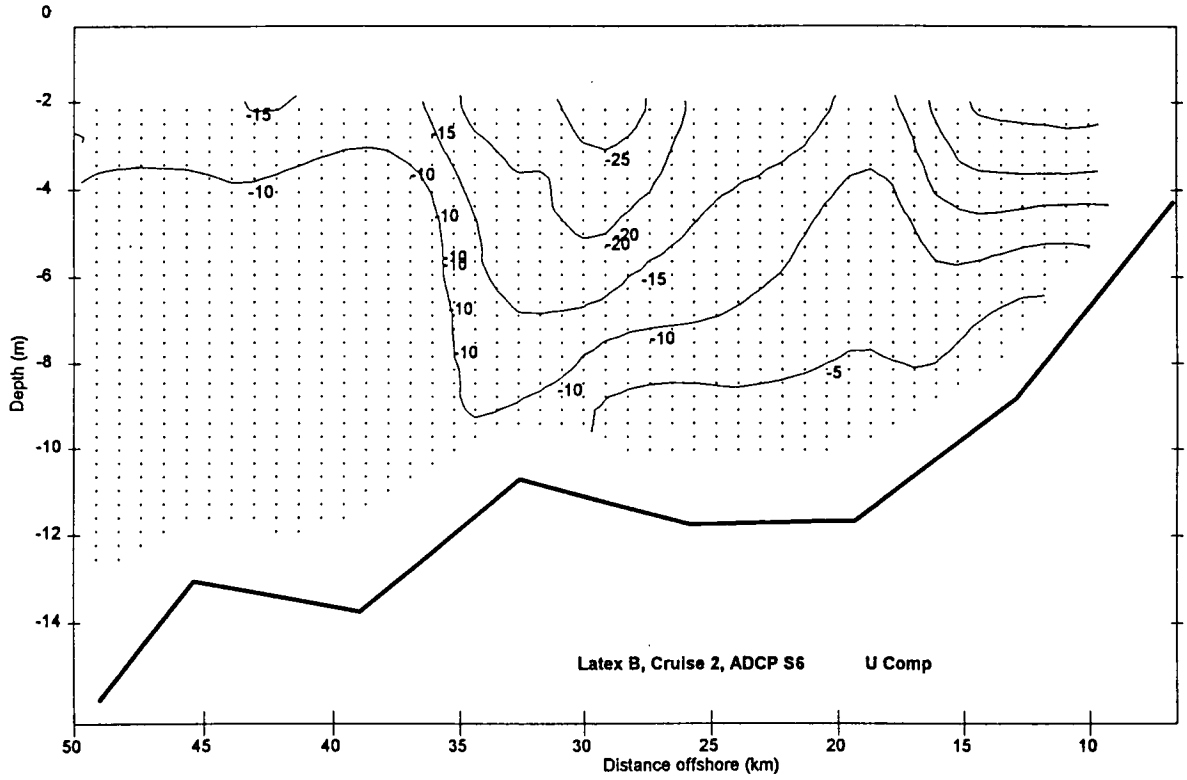

Figure 48. Alongshore speed components from the ADCP just west of Sabine Pass on S6 during the October 1992 observations.

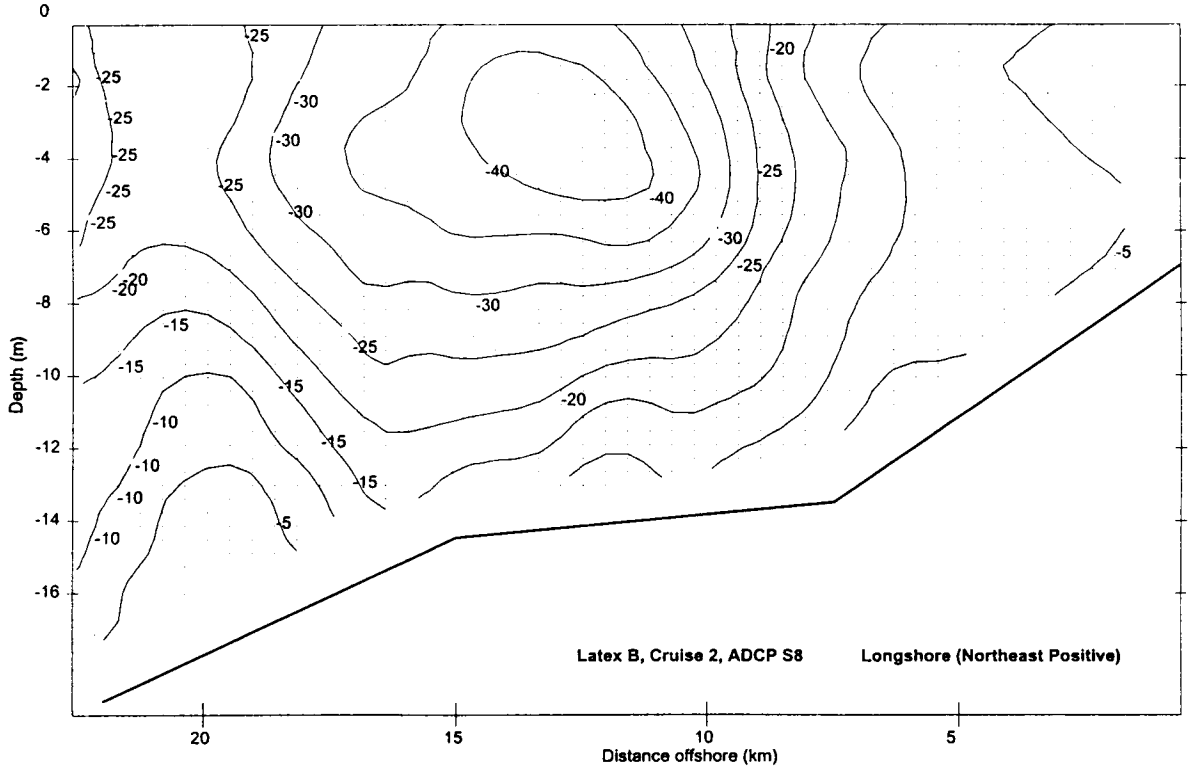

Figure 49. Alongshore speed components from the ADCP off central Texas on S8 during the October 1992 observations. Note the axis of the downcoast jet has moved onshore to within 12 km of the coast in this region.

Down-current in the western Louisiana region the velocity section at S6 (Figure 48), however, clearly shows the downcoast flow is dominated by a jet with a cross-shore length scale of 25 km. The jet is confined to the coastal plume water of salinity less than 32 psu and its outer edge appears to be controlled by the collapse of the intense lateral salinity gradient (Figure 44) as expected from thermal wind dynamics.

As pointed out above in the far field region of central Texas, the plume has contracted after narrowing abruptly between Sabine and Galveston. At Section S8 (Figure 49), we document the downcoast flow in the far field coastal plume for the first time; upcoast wind events have dominated in the region in the two spring observations discussed earlier. Our observations extend out only 20 km from the coast, but they clearly resolve a high speed (40 to 50 cm/sec) surface intensified jet. This jet occupies the entire water column over most of the section but is centered only 10 to 15 km offshore coincident with the maximum lateral salinity gradient (Figure 45). At the seaward limit of our observation speeds remain substantial downcoast.

d. Circulation Pattern from SCULP Drifters

Our two spring observations of the downcoast plume regime occurred in April 1993 and 1994, as discussed above. The intensive sampling of the spring downcoast regime by the SCULP surface drifter program did not occur until 1994. Accordingly, in Figure 50 we present for comparison the drifter velocity vectors from all drifters in the domain of the coastal plume in April 1994. The basic flow pattern that emerges is in substantial agreement with our hydrographic and ADCP observations. A wide comparatively slow downcoast flow that characterizes the coastal plume off western Louisiana contracts into a high speed jet tightly trapped to the coast as it transits southwestward and south along the Texas coast to the Mexican border. Intermittent wind events in opposition to the downcoast flow that appears as a major disruption in the ADCP data are suppressed in the drifter data as their velocities are calculated from daily average positions only.

F. Observations of the Coastal Plume during the Summer Upcoast Flow Regime

Observations of the regime that develops in the coastal plume region under summer wind forcing were conducted in July 1993 and July 1994. The July 1994 observations discussed first were especially insightful as the SCULP drifter program deployed a suite of drifters along our standard cruise track. The spatial variability of their trajectories proved a key in unlocking our understanding of the summer flow regime on the inner shelf.

1. Summer Upcoast Regime, 1994

a. Winds

Wind conditions prior to and during the July 12-17, 1994 observation interval were the usual summer pattern of weak and variable southeasterlies off Louisiana and strong south-southeasterlies off central and south Texas. The daily averaged wind stress diagram (Figure 51) shows a strong convergence in the along-coast wind field. Upcoast forcing from south Texas converged toward a zone of negligible stress along the Louisiana coast. The Atchafalaya River discharge was down to ~2500 m^3/sec, the lowest value for our 5 observations of the coastal plume (Figure 4). It is clear from the C/K synthesis, the wind stresses, the monthly current vector maps (Figure 6), and the summer drifter velocity maps (Figure 7b), that we can expect a general upcoast flow across the shelf in July. Details of the temporal and spatial variability of this upcoast flow across the inner shelf, the region occupied by the coastal plume for the 8- to 9 month-long winter downcoast regime, however, remain unknown. We will discuss the summer regime velocity and salinity fields from west to east since the movement of the coastal plume waters are expected to be in that direction.

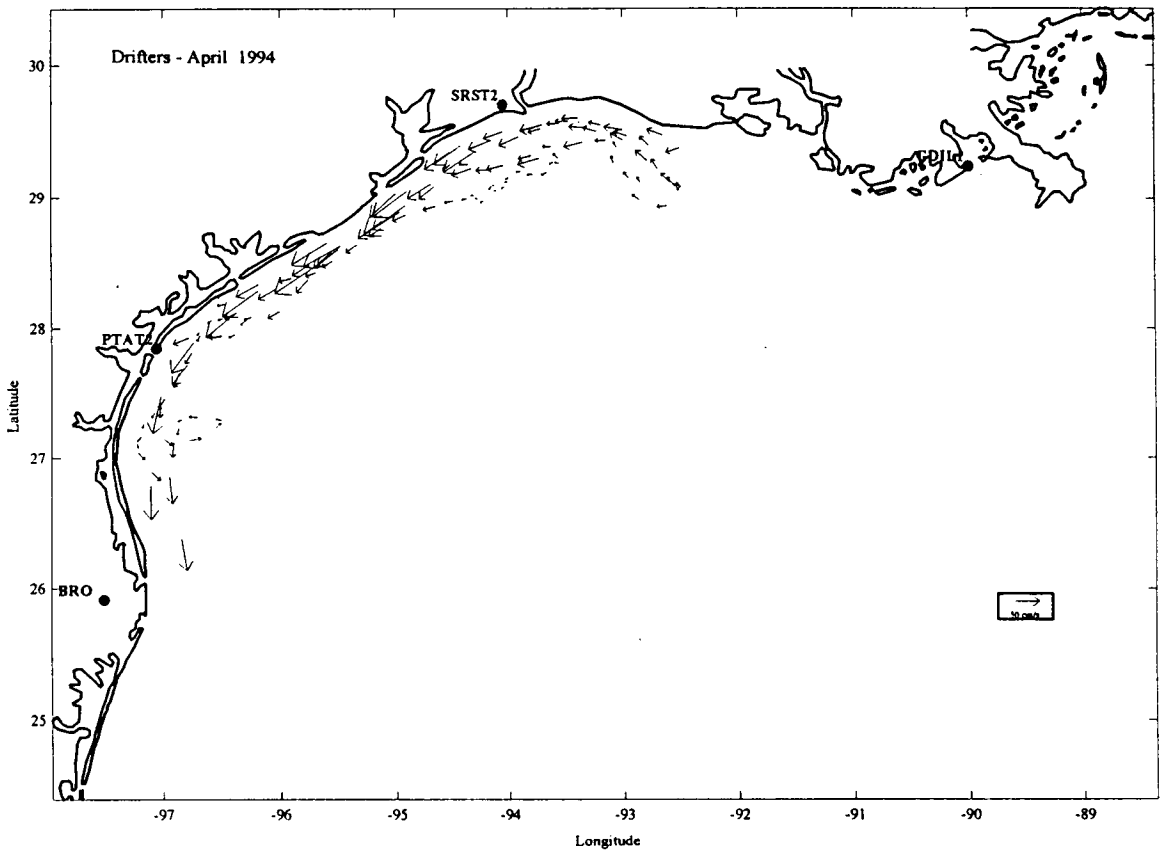

Figure 50. Daily averaged velocity vectors from SCULP drifters during the 1994 downcoast flow regime in April 1994. Three CMAN stations and the Brownsville NWS are identified with solid dots.

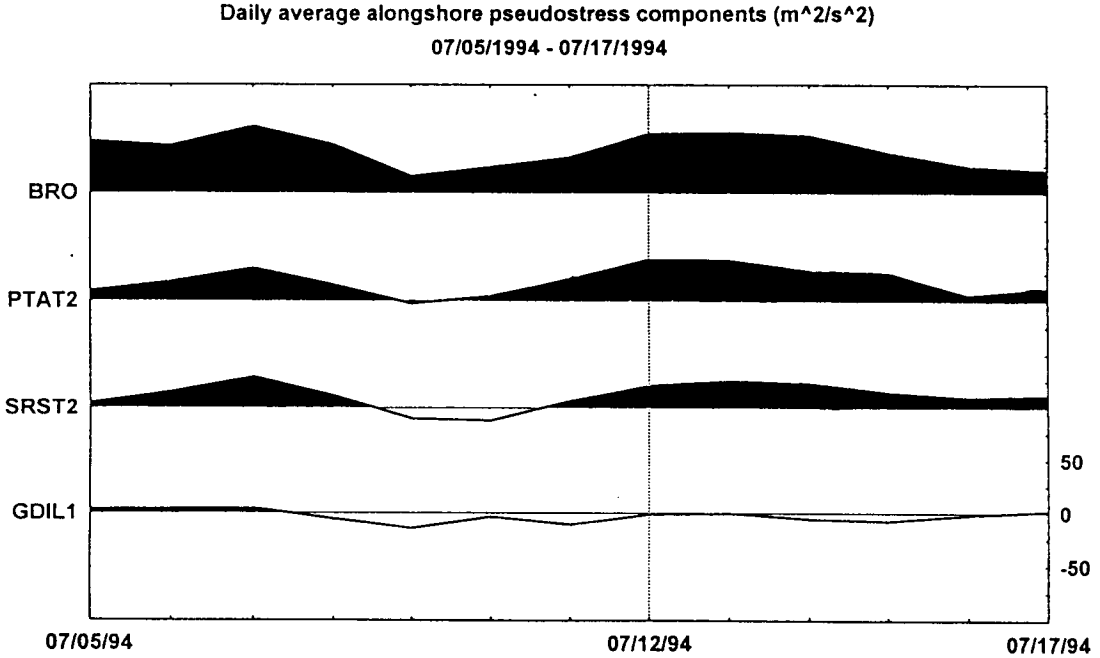

Figure 51. Daily averaged alongshore wind stress from four coastal stations prior to and during the cruise observations of July 1994. Upcoast wind stresses are shaded, illustrating their dominance from Brownsville north to Sabine Pass (SRST2). Wind stress off central Louisiana appears downcoast but relatively very weak.

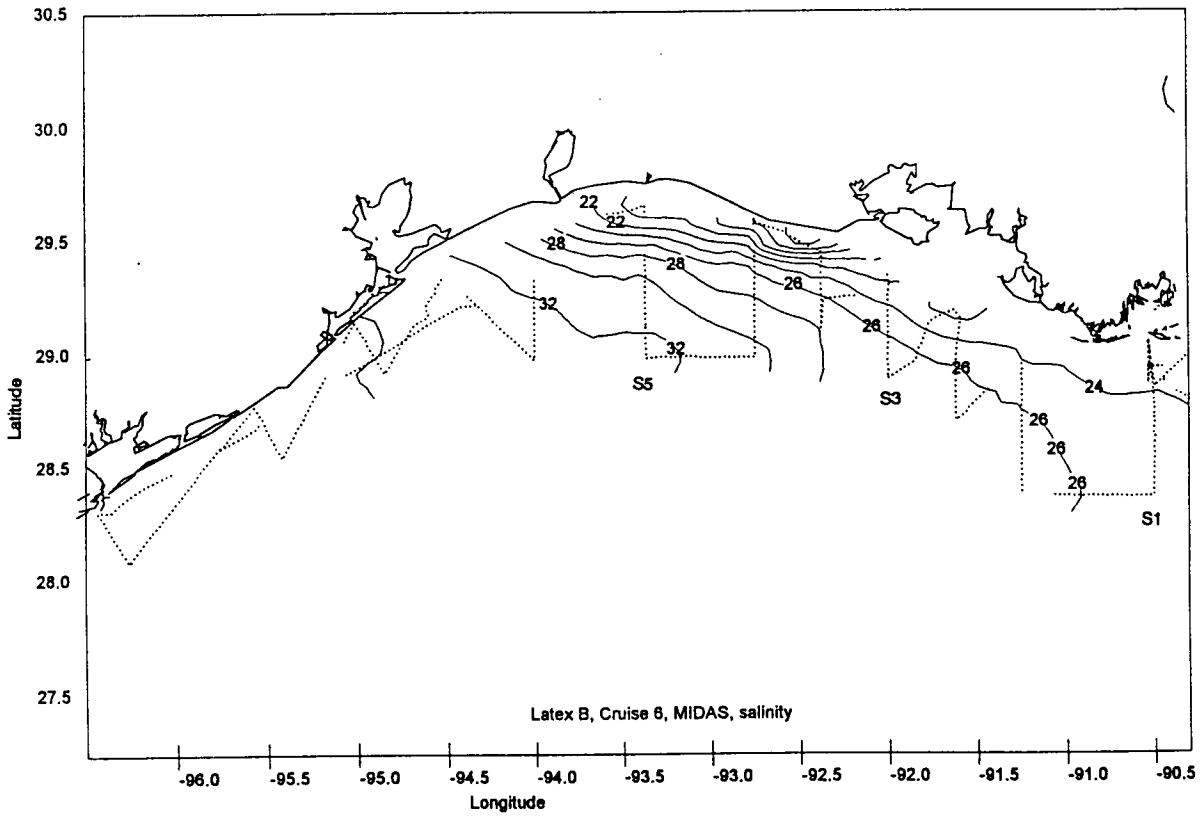

Figure 52. Near-surface salinity field (psu) observed during coastal plume cruise of July 12-17, 1994.

b. Salinity Fields

Our observations, which extended west to line X1, showed the near-surface salinity field (Figure 52) to be markedly different than observed during the winter regime. High salinities of 33 psu appear along the coast as far north as Galveston and 35 psu north of Corpus Christi, indicating northward advection of relatively unmixed Gulf of Mexico water from the Mexican border region. The 28 and 30 psu contours leave the coast between Galveston and Sabine Lake and trend southeastward, suggesting the possibility of a flow of the high salinity waters in that direction. An inshore band of low salinity (12-20 psu) outflow from the Atchafalaya River extends westward along the coast from the Atchafalaya Bay mouth to a point 40 km west of Sabine Pass, suggesting the Atchafalaya River outflow plume water is, to the contrary, advected westerly in a narrow layer tightly confined to the coast. An intermediate zone, referred to here as the mixing zone, about 40 km in width of 20 to 30 psu water, extends eastward between these two high and low salinity end members. The vertical sections at X1 and S8, for example, (not shown) are occupied by a quasi-homogeneous high salinity water mass with salinities between 35-36 psu. The section at S7 (not shown) is also lacking in vertical or horizontal structure but salinities have reduced to 34 psu as the Atchafalaya source region is approached. Only at S6 does the observation section finally cut into the intermediate 20 to 30 psu zone at about 30 km from the coast.

Section S5 further eastward along the path of the eastward moving high salinity water depicts (Figure 53) the internal structure of the high salinity outer zone of 30 to 33 psu and the intense lateral salinity gradients characteristic of the mixing zone. Section S5 is especially valuable as it cuts through all three zones. The low salinity zone <20 psu, confined to within 20 km of the coast, is seen to be a shallow (5 m thick) buoyant plume. The intermediate or mixing zone (20-30 psu) is about 20 km wide and grades seaward to the broad high salinity, weakly stratified zone of presumed upcoast flow.

Section S3 (Figure 54), 300 km further eastward of S5 and at the western of the Atchafalaya Bay freshwater source, shows the mixing zone of 20 to 30 psu water that occupies most of the section from 25-75 km offshore down to a depth of 13 m. Here, the mixing zone water is underlain by the high salinity water 30-35 psu that filled almost the entire inner shelf of Texas. Only within 25 km of the coast do we encounter the intense lateral salinity gradients of the low salinity Atchafalaya River outflow water.

Our farthest eastward section during this summer upcoast flow season is at S1 (Figure 55). This entire section down to the 14 m level is filled with water from 23 psu to 34 psu. Isohalines in this upper layer are relatively level (except at the seaward limit of the section) reflecting the expected offshore Ekman transport in an upcoast moving upper layer. The upper buoyant layer overlays a quasi-homogeneous high salinity (34 to 36 psu) lower layer that encroaches landward to within 10 km of the shoreline. The section at S1 appears markedly different than the more westerly sections. It shows a wide flat layer of buoyant water about 15 m in thickness that apparently extends well over 80 km from the coast. This upper buoyant layer has steep vertical salinity gradients resulting from weak mixing by the light summer winds. It is floating above another thick layer essentially of undiluted (35 to 36 psu) Gulf of Mexico water, which can be traced back westward underneath all our sections until the 35 psu surface outcrops at S8.

We interpret this zone of intermediate salinity water to be composed of "old" coastal plume water that had been previously advected downcoast prior to the onset of the summer regime current reversal. It is squeezed between the upcoast-moving high salinity Gulf of Mexico water and the bubble of recent low salinity Atchafalaya River outflow itself trapped against the coast. We next investigate the velocity structure of this strikingly different summer hydrographic regime on the inner shelf.

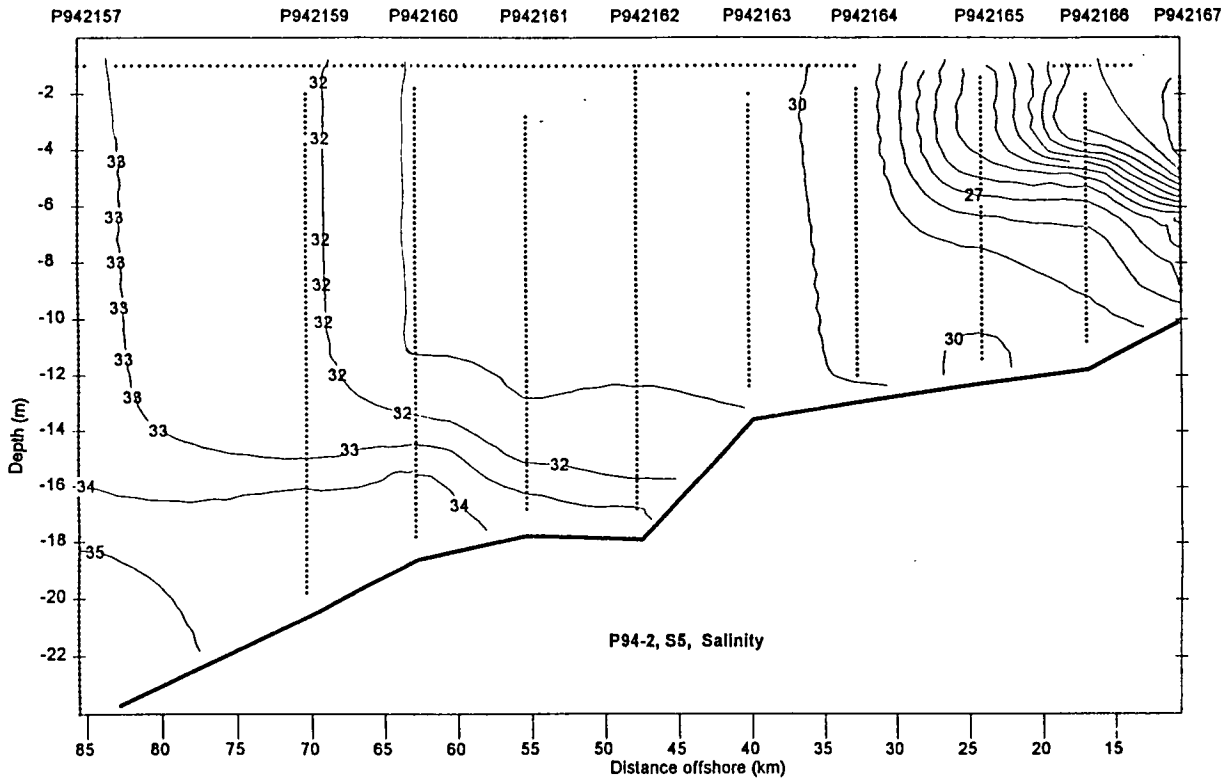

Figure 53. Vertical section of salinity (psu) along line S5 (July 1994 observations). This section cuts through three zones: (a) the band of high salinity water returning upcoast in the summer; (b) the intermediate or mixing zone of salinities 20-30 psu; and, (c) the low salinity (<20 psu) Atchafalaya outflow being advected westward along the coast.

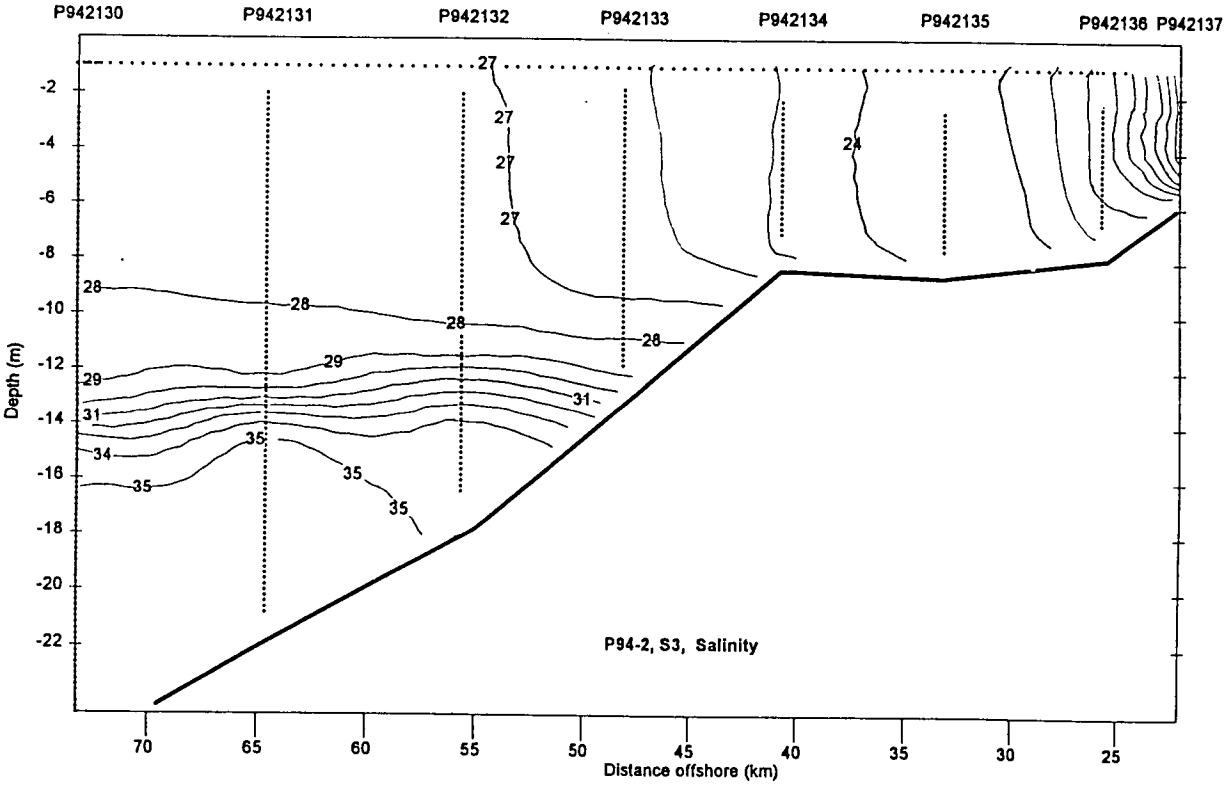

Figure 54. Vertical section of salinity (psu) along line S3 (from July 1994 observations) showing the mixing zone water and the inshore zone of low salinity Atchafalaya outflow water. Note the mixing zone water (20-30 psu) is underlain by relatively undiluted Gulf of Mexico water.

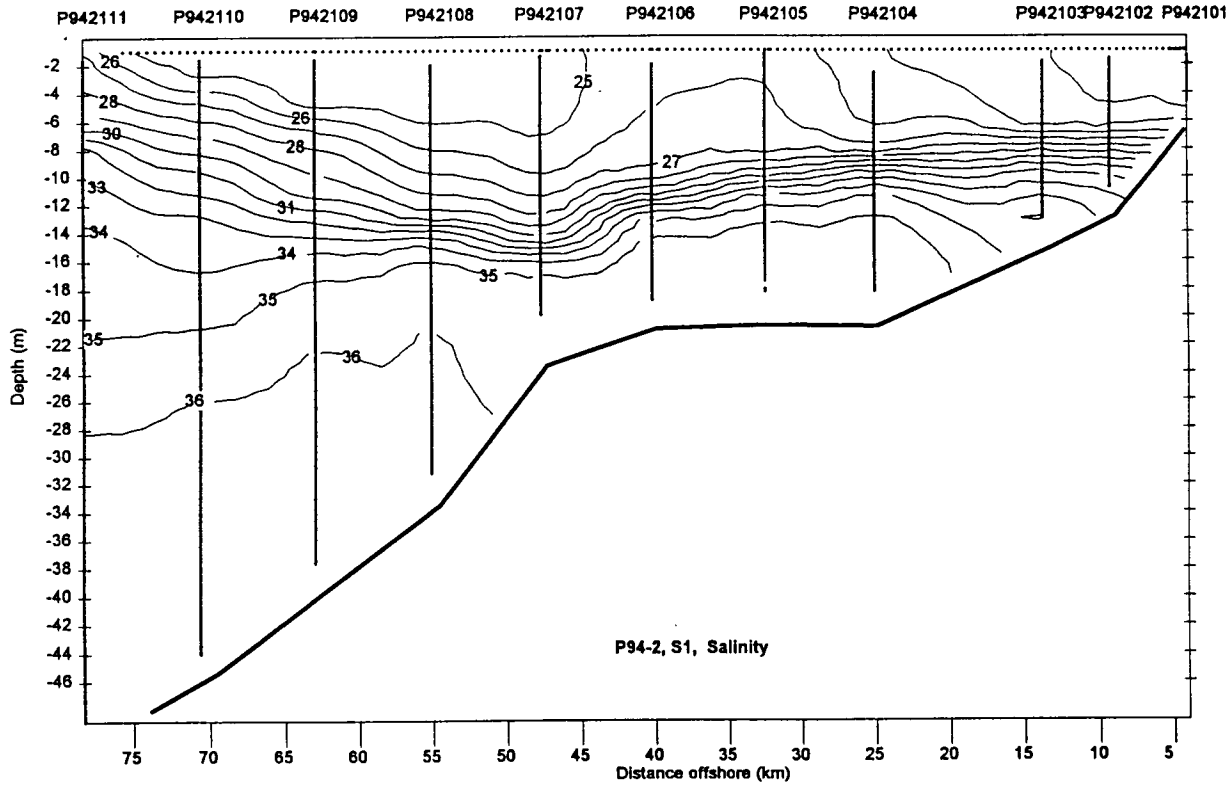

Figure 55. Vertical section of salinity (psu) along line S1 (July 1994 observations) showing a strongly stratified low salinity upper layer overlaying undiluted Gulf of Mexico waters of 36 psu.

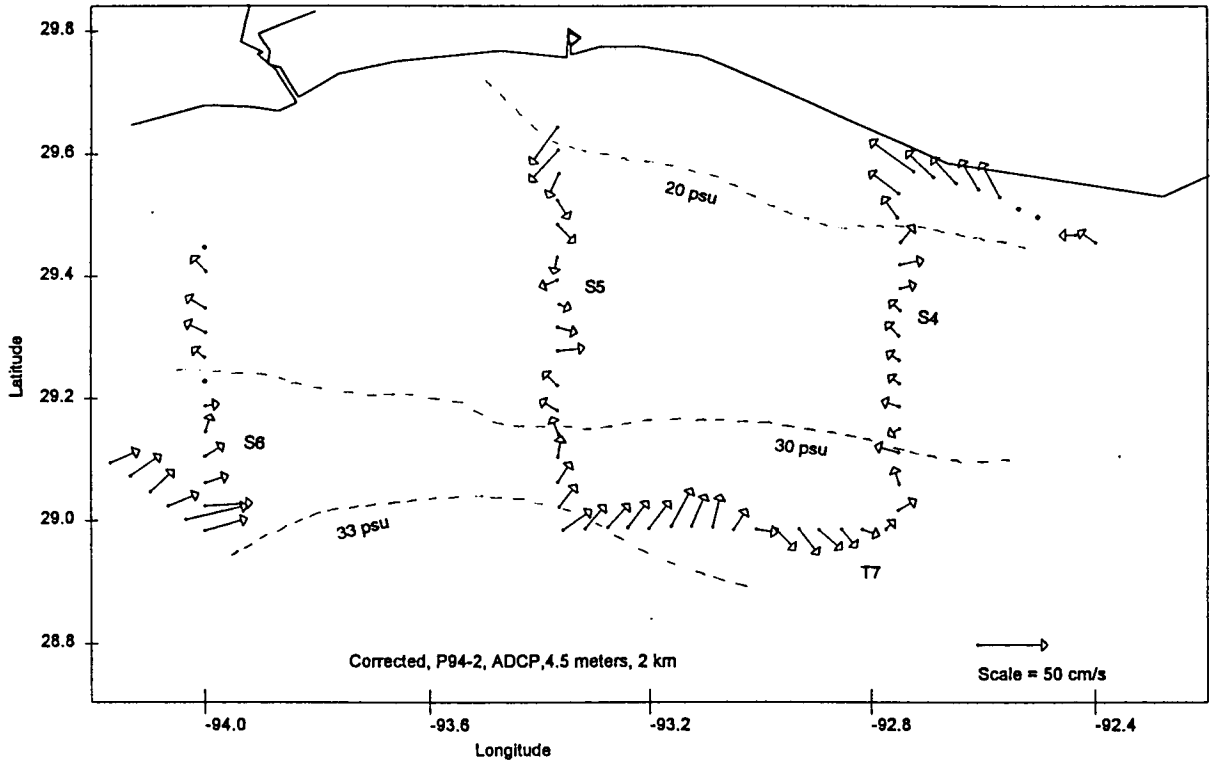

Figure 56. ADCP velocity field at the 4.5 m level in the western Louisiana region of the coastal plume during the July 1994 observations. Data points are 4 km averages.

c. Summer Regime Velocity Structure

Because of the steadiness of the summer wind field we might expect a correspondingly steady and highly coherent current field. Instead, we observe considerable variability in the upcoast current regime, especially in the western and central sectors. Figure 56 shows the ADCP velocities at the 4.5 m depth level in the region covering S4 through S6. The approximate locations of the 20 and 30 psu isohalines that delineate the three salinity zones discussed above are added for reference. Seaward of the 30 psu contour a general upcoast (eastward) flow, albeit with a significant meander along T7, is evident. The limited data, in the shallow water shoreward of the 20 psu isohaline shows a 20 to 40 cm/sec downcoast flow in this westward extension of the Atchafalaya River outflow plume. In the broad intermediate zone between these two end members (see especially along S5) a series of flow reversals suggestive of a cellular structure with no clear mean flow direction is evident. A vertical section along S5 (Figure 57) confirms that this is not merely surface structure but three dimensional mixing elements that have vertical scales on the order of the water depth (10-20 m) and cross-shore scales of 10 to 15 km. Similar features are present in the vertical sections along S4 (not shown) 85 km to the east. Thus, the intermediate salinity zone of at least ~100 km alongshore extent, sampled by sections S4 to S5, appears to be a region of weak net circulation but populated with numerous small scale mixing structures of 15 cm/sec amplitude that extend over the entire water column.

In the eastern region the flow field appears fundamentally different. From S1 to S3 (Figure 58), the flow is far more coherent, especially east of line S2B. Even though containing intermediate salinity water (Figure 52), a distinct upcoast jet extends from S2B to S1. The vertical section through S1 (Figure 59) shows this well-defined jet has a vertical scale of 12 m and extends about 75 km offshore in close accord with the low salinity stratified upper layer seen in Figure 56. This upcoast, strongly baroclinic flow appears highly unstable and prone to meanders. Note the strong onshore flow at S3 in Figure 58, which is carrying this same intermediate salinity water. A vertical section through S3 (Figure 60) shows the cross-shore component of the speed has the same characteristics as seen at S1: a 12 m vertical extent and a maximum speed near 30 cm/sec. It appears likely based on the velocity vectors, interpolated stream lines, and water properties that this onshore baroclinic jet is executing, a dramatic clockwise turn to continue eastward in continuity with the jets observed in the four sections from S2B to S1 as sketched in Figure 58.

d. Insights from a Special Drifter Experiment

On July 13, on the second day of our observations of the 1994 summer plume regime, the SCULP program deployed Argos surface layer drifters along our cruise track. The trajectories from the four to six times per day fixes (de-spiked but not daily averaged) are presented in Figure 61. The 20 and 30 psu isohalines demarcating the three salinity zones discussed above are shown for comparison. Note the three distinct flow regimes within each salinity zone described by the drifters. (1) The outer high salinity zone is a strong upcoast flow along the central Texas coast, which turns offshore to flow eastward along the outer edge of the intermediate salinity zone near 28° 30' N and then turns northeastward toward the Louisiana coast east of 91° 5' W. (2) In the intermediate salinity zone where the ADCP sections (Figure 57), show the small scale cellular structure in the velocity field the drifter describes an unorganized "turbulent" mixing pattern with no obvious net flow direction. (3) Drifters deployed in the low salinity zone near the coast move rapidly westward in agreement with both the displacement of low salinity from the Atchafalaya River outflow and the near-coastal ADCP vectors in Figure 56.

Additionally, we plot in Figure 62 the daily averaged drifter velocity vectors for July 14 when the ship was observing along S2 to S4. July 15 gives an essentially identical plot. These two independent realizations of the flow field compare quite favorably with the flow pattern deduced from the salinity field and the ADCP velocity field, namely (a) coherent eastward flow of

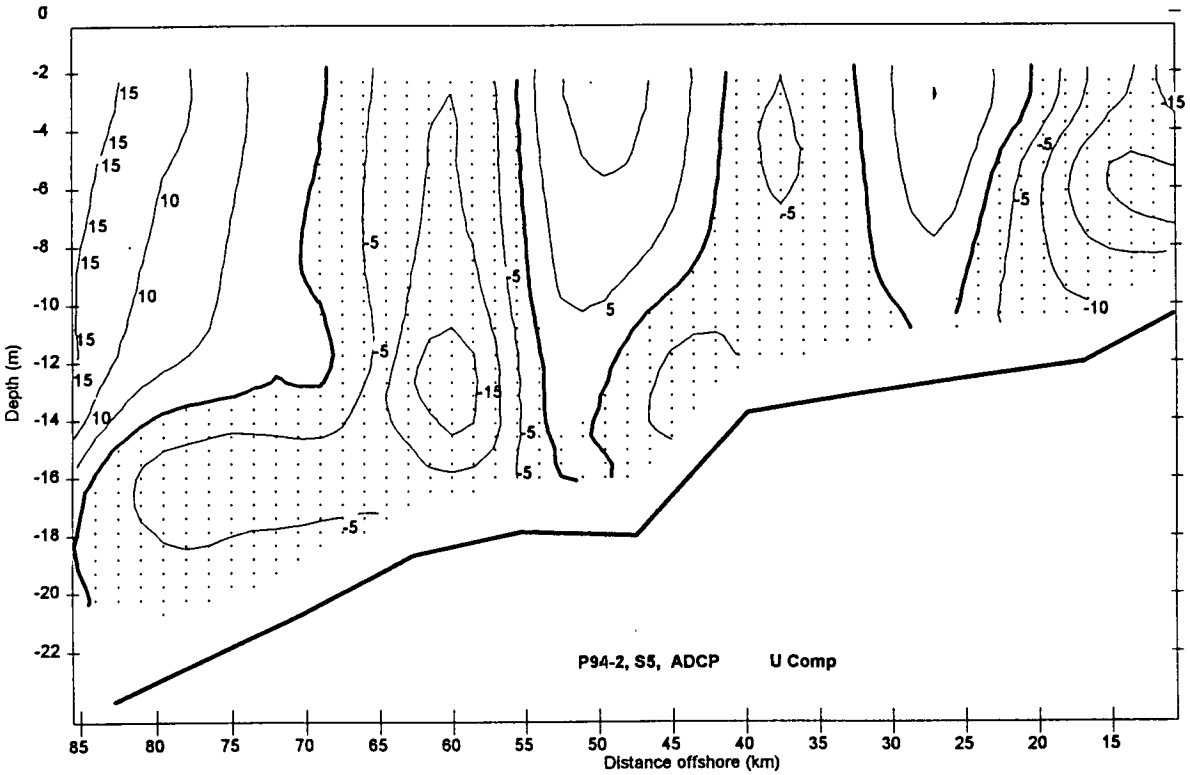

Figure 57. Vertical section along S5 of the longshore component of the ADCP velocities. Note the pronounced cellular structure in the velocity field internal to the mixing zone of salinities of 20-30 psu.

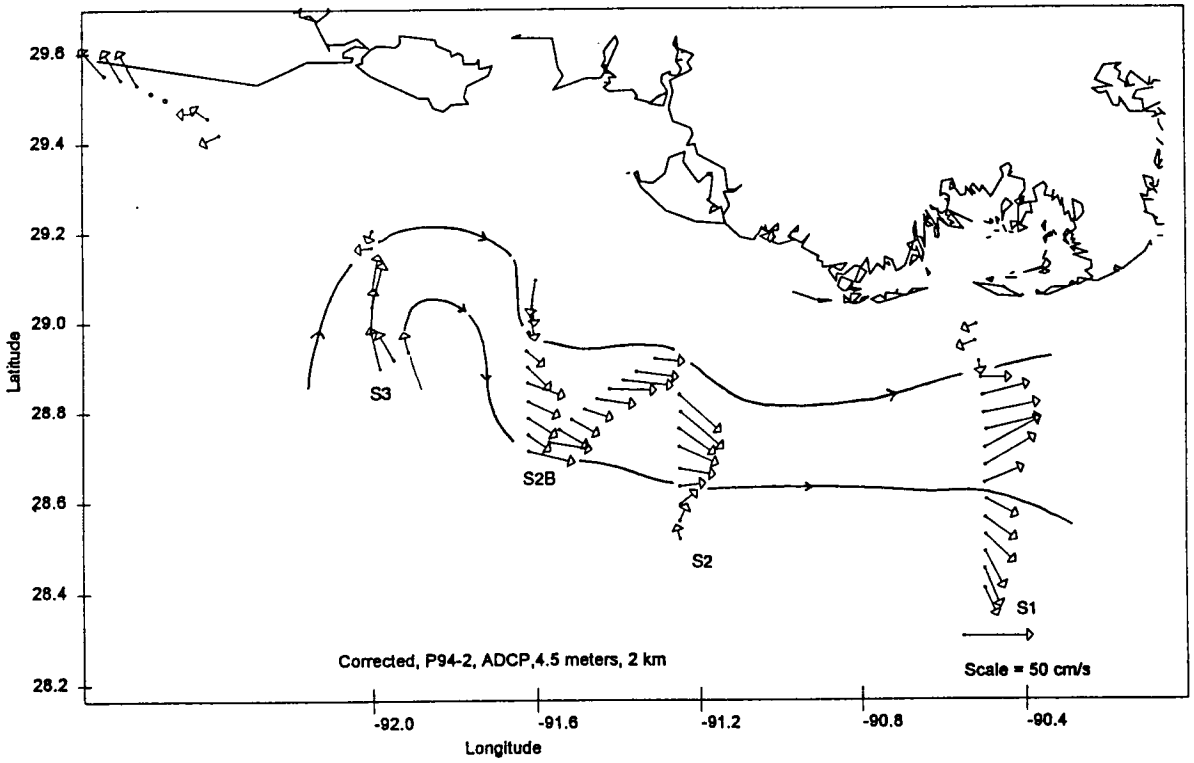

Figure 58. ADCP velocity field at the 4.5 m level in the central Louisiana region east of the Atchafalaya River source region during the July 1994 observations. Streamlines are sketched in based on salinity values and velocity vectors.

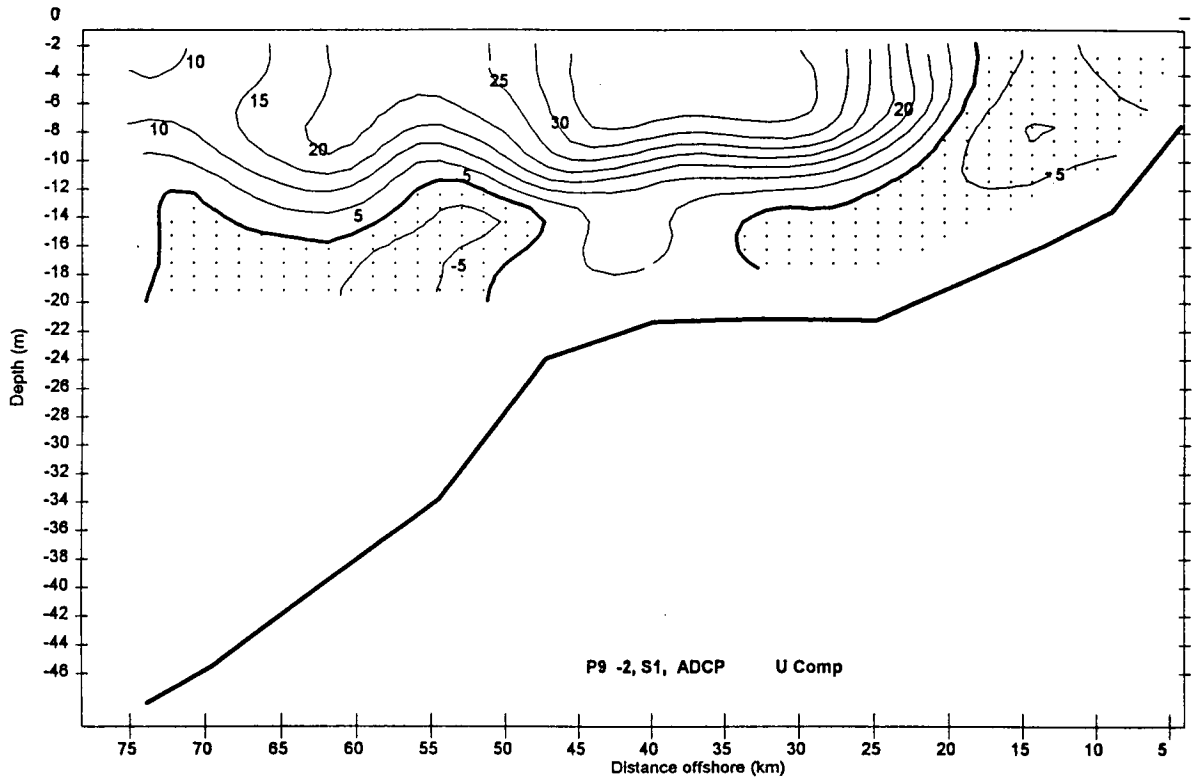

Figure 59. Alongshore speed components (positive eastward) on line S1 from the ADCP during the July 1994 observations of the coastal plume. Note the high speed jet in the highly stratified upper layer overlaying a quasi-stagnant high salinity lower layer.

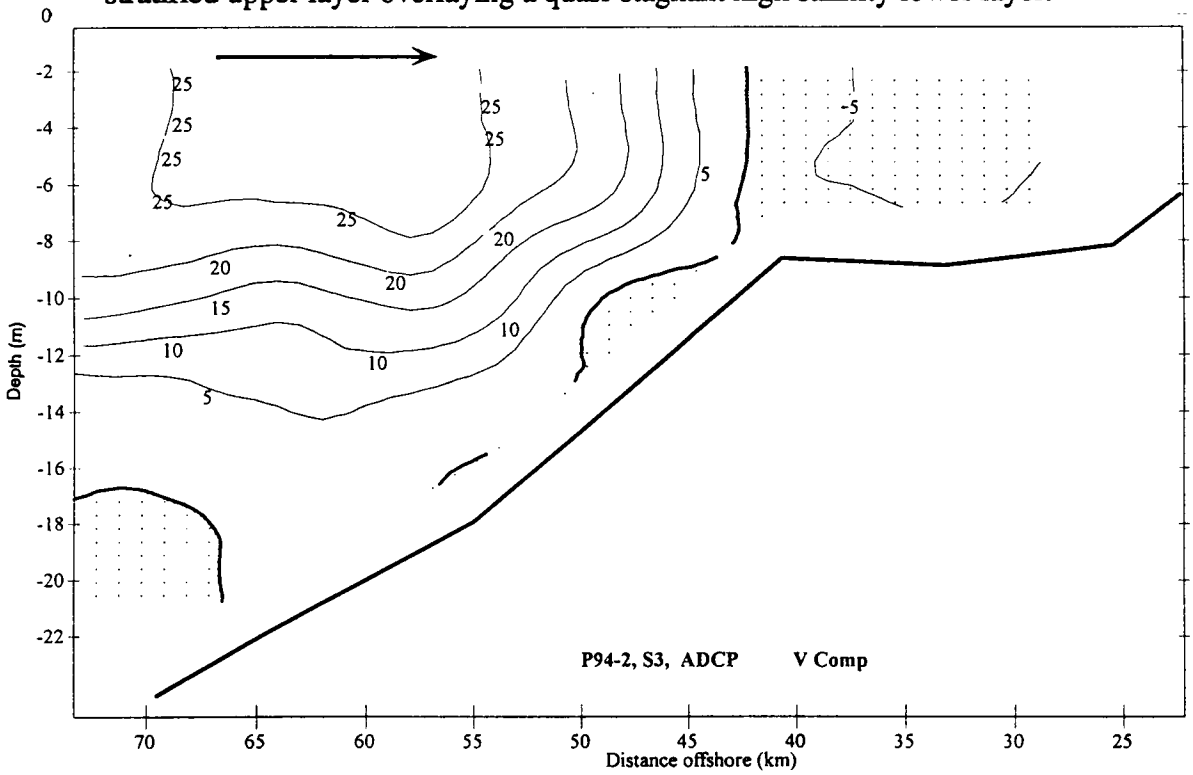

Figure 60. Cross-shore speed components on line S3 during the July 1994 observation of the coastal plume. Note the strong onshore flow in the buoyant upper layer.

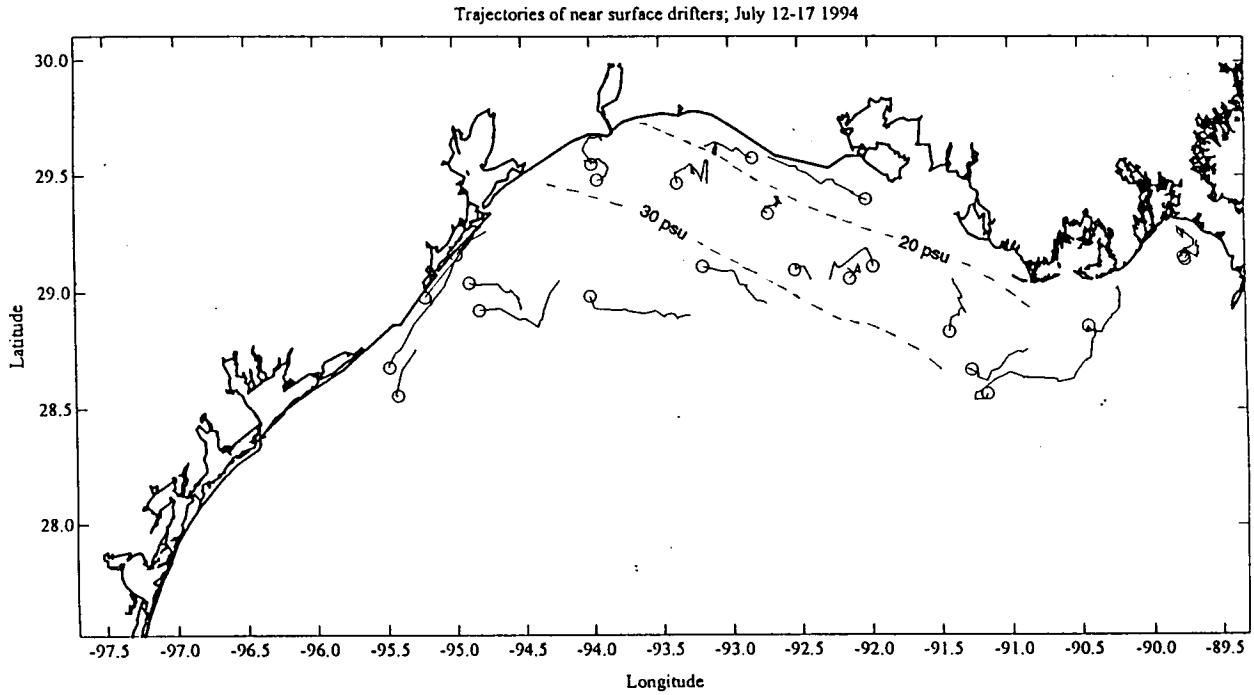

Figure 61. SCULP drifter tracks July 12-17 during the shipboard observations of the coastal plume in July 1994. Note the three distinct flow zones discussed in the text. The open circle indicates the initial position of the drifter.

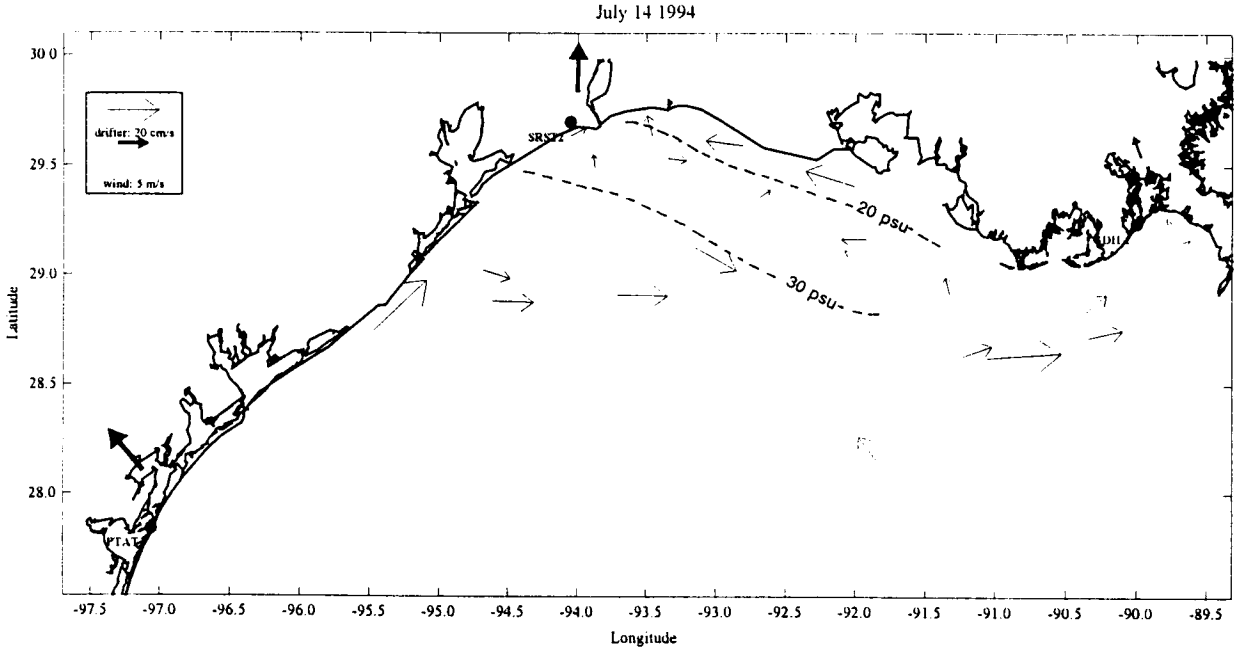

Figure 62. Velocity vectors from SCULP drifters on July 14 during the summer July 1994 coastal plume observations.

high salinity water in the outer zone; (b) an interior zone of slow disorganized flow intermediate salinity water; and, (c) a near-coastal energetic westward flow of Atchafalaya outflow water.

Our interpretation is in general agreement with C/K in that in summer the high salinity water pushing upcoast from the south Texas-Mexico border region plows the relict coastal plume water before it resulting in a layer of brackish water spreading out over the shelf. Our more detailed observations, however, show that there is a zone of intermediate salinity (a mixed zone), of relict coastal plume water that had been pushed back upcoast and is now being squeezed between the piston-like upcoast movement of the high salinity water on the one side (the hammer) and the coast and the new Atchafalaya outflow plume water that moves westward hugging the coast on the other side (the anvil).

2. A Second Look at the Summer Flow Regime: July 1993

In mid-July 1993, the coastal wind field from Brownsville to the Mississippi Delta shows the expected pattern of strong-south-southeasterlies along the Texas coast and weak variable winds off Louisiana. similar to the July 1994 winds shown in Figure 50. This wind pattern results in a persistent net upcoast wind stress on the coastal waters since mid-June. The alongshore wind stresses prior to and during our July 13-19, 1993 observations are shown in Figure 63.

a. Salinity

During this summer of the record high flood year of 1993, our observations of the salinity distribution of the coastal plume on the inner shelf are qualitatively similar to that of July 1994. Figure 64 shows that 32 to 34 psu water outcrops on the surface just southwest of Galveston and the curvature of the contours (see e.g., the 26 psu isohaline along S5) again indicate an upcoast intrusion of these high salinity waters onto the Louisiana shelf. These waters again converge with the low salinity outflow from the Atchafalaya River in a massive frontal zone that extends alongshore for over 175 km from near Sabine Pass to the east end of Atchafalaya Bay. The salinity increases rapidly east of Atchafalaya Bay as the Atchafalaya plume water is mixed with ambient shelf water.

b. Vertical Sections

Vertical sections at S7 and S8 (not shown) in the high salinity return flow zone are essentially homogeneous in salinity. Vertical sections at S5 and S6, however, cut through the large volume of intermediate salinity water that has been driven northward up the coast by the advance of the high salinity water mass from south Texas as documented by the current meter data (Figure 6). Figure 65, for example, shows the vertical homogeneous high salinity water mass occupying the outer 15 km of section S6. A broad interior region from 25-60 km offshore is vertically and laterally homogeneous, filled with water of 28 psu salinity. A thin band of lower salinity water of 24-28 psu hugs the coast. These zones are consistent with those observed in S5 in the July 1994 (Figure 53) albeit the absolute values of salinity are higher in 1994, as expected.

At section S3 (Figure 66), at the western end of the Atchafalaya Bay mouth, the salinity structure is markedly different than S6. A surface layer of low salinity water extends across the entire section down to a depth of 10m. Salinities of only 4 to 15 psu at the inshore end mark the input of the Atchafalaya River outflow. A distinct and intense halocline zone 4 to 5 m thick slopes upward toward the coast. This feature is underlain by a wedge of homogeneous high salinity water encroaching up the slope under the halocline zone. At the eastern limit of our sampling domain at S1 (Figure 67), 150 km to the east, the surface layer appears consistent with S3 but thinned to about 6 m. The halocline zone and the deep high salinity bottom layer also persist. In fact, the five sections from S3 to S1 exhibit the coherent salinity structure illustrated at S3 and S1.

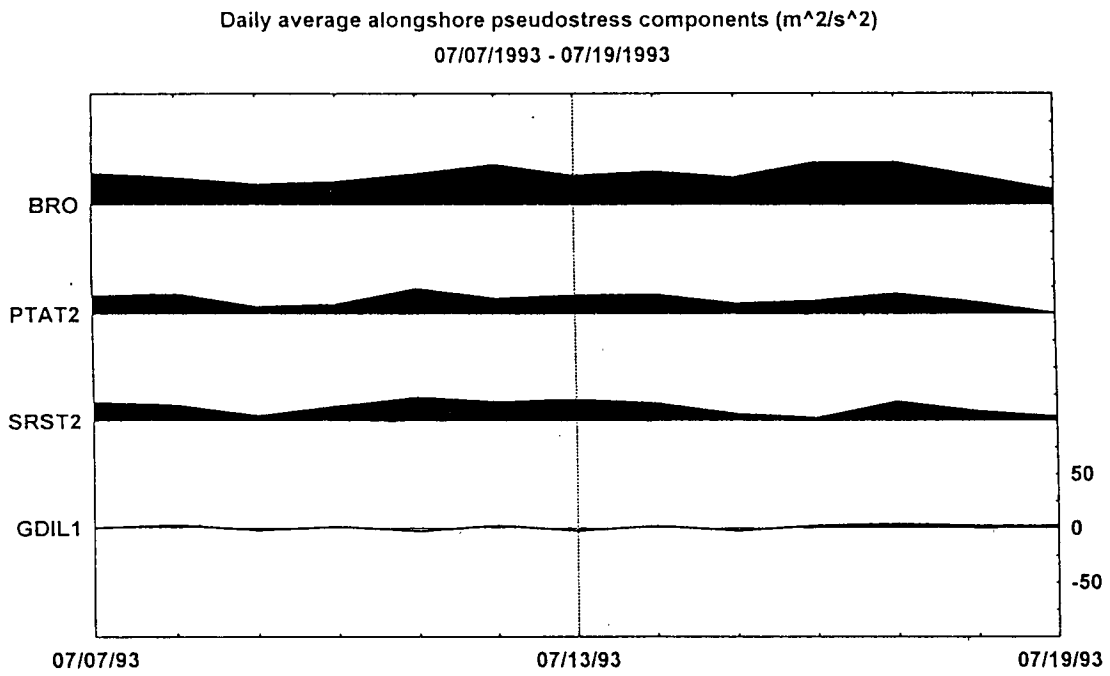

Figure 63. Daily averaged alongshore wind stresses from four coastal stations prior to and during the cruise observations of July 1993. Upcoast wind stresses are shaded.

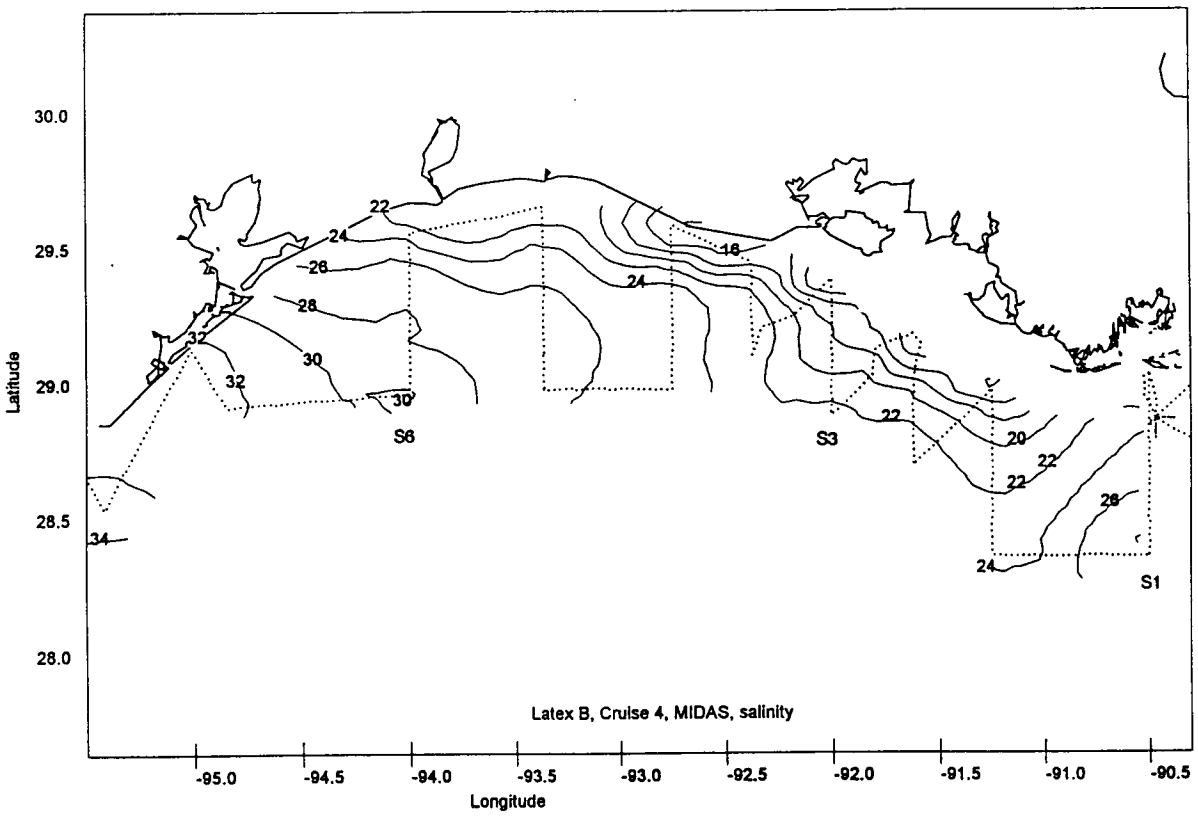

Figure 64. Near-surface salinity field (psu) observed during coastal plume cruise of July 13-19, 1993. Note the upcoast intrusion of high salinity water from south Texas onto the Louisiana shelf.

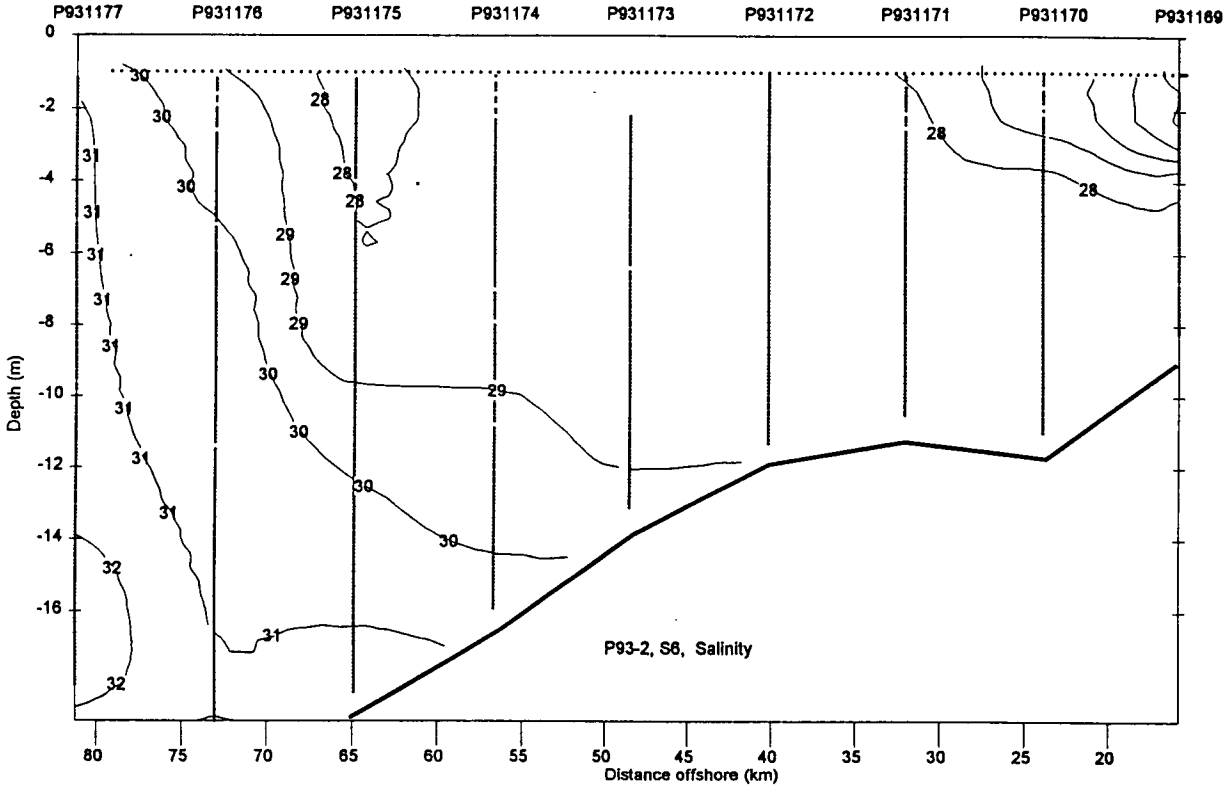

Figure 65. Vertical distribution of salinity (psu) on the S6 line during the July 1993 observations.

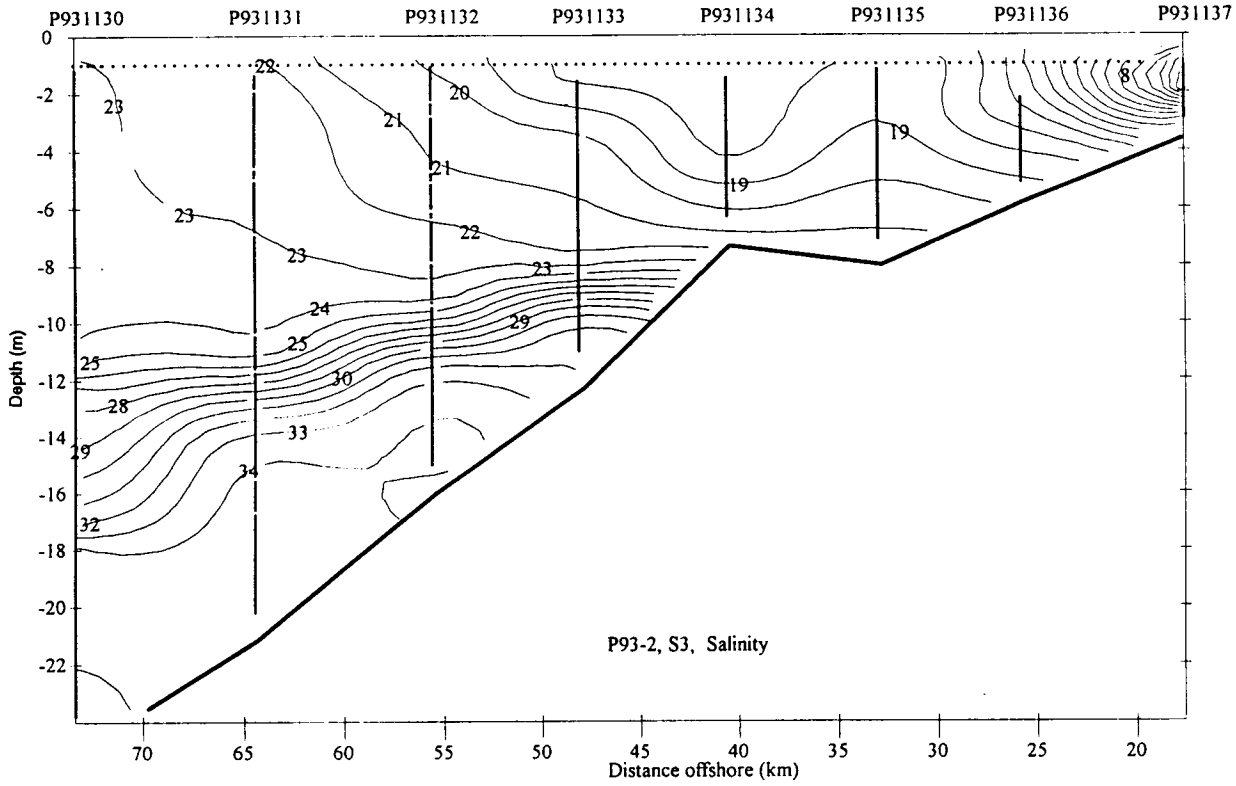

Figure 66. Vertical distributions of salinity on the S3 line during the July 1993 observations.

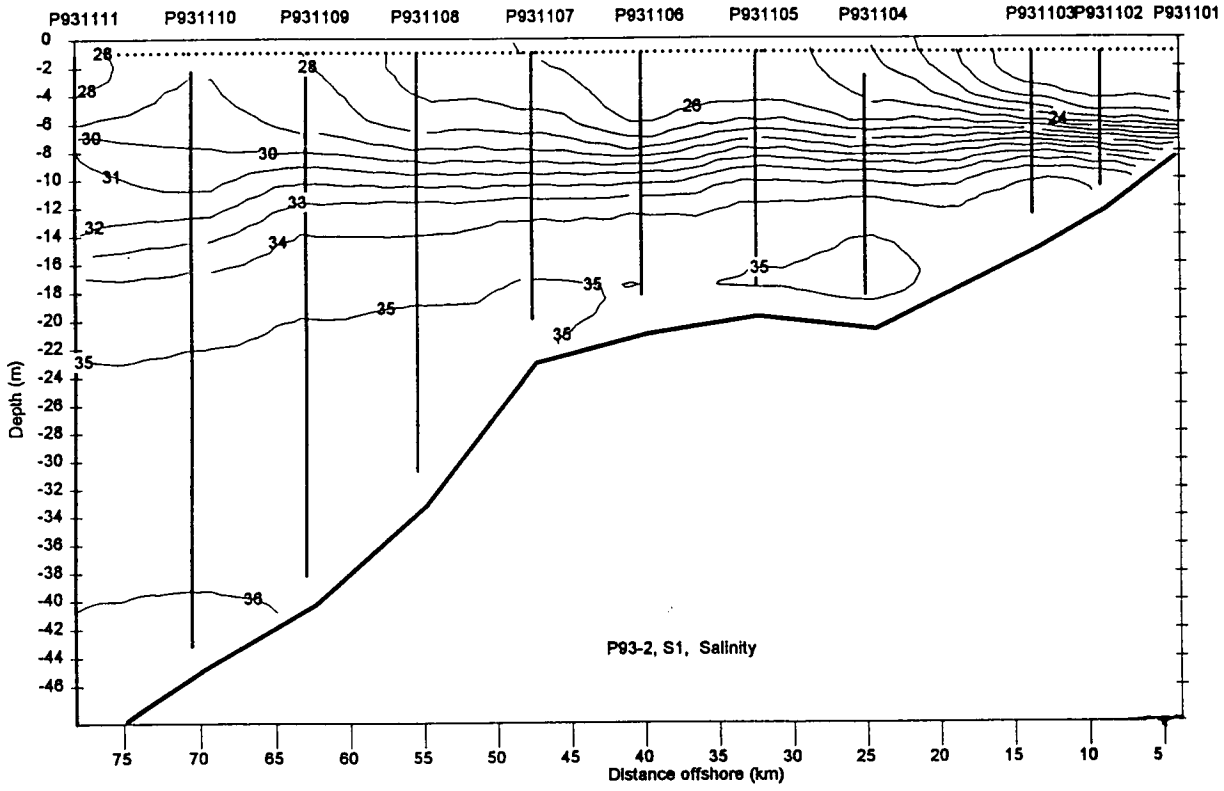

Figure 67. Vertical distribution of salinity (psu) on the S1 line during the July 1993 observations.

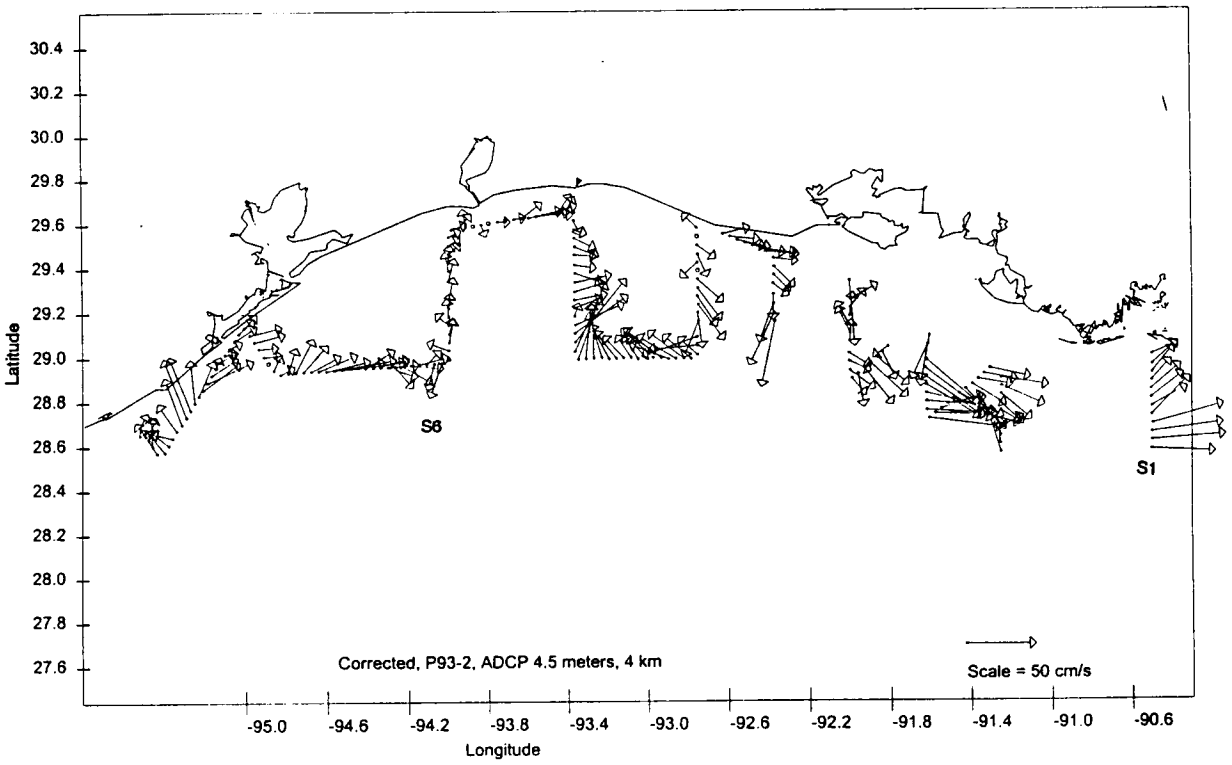

Figure 68. Velocity field at the 4.5 m level over the entire sampling domain during the July 1993 cruise observations.

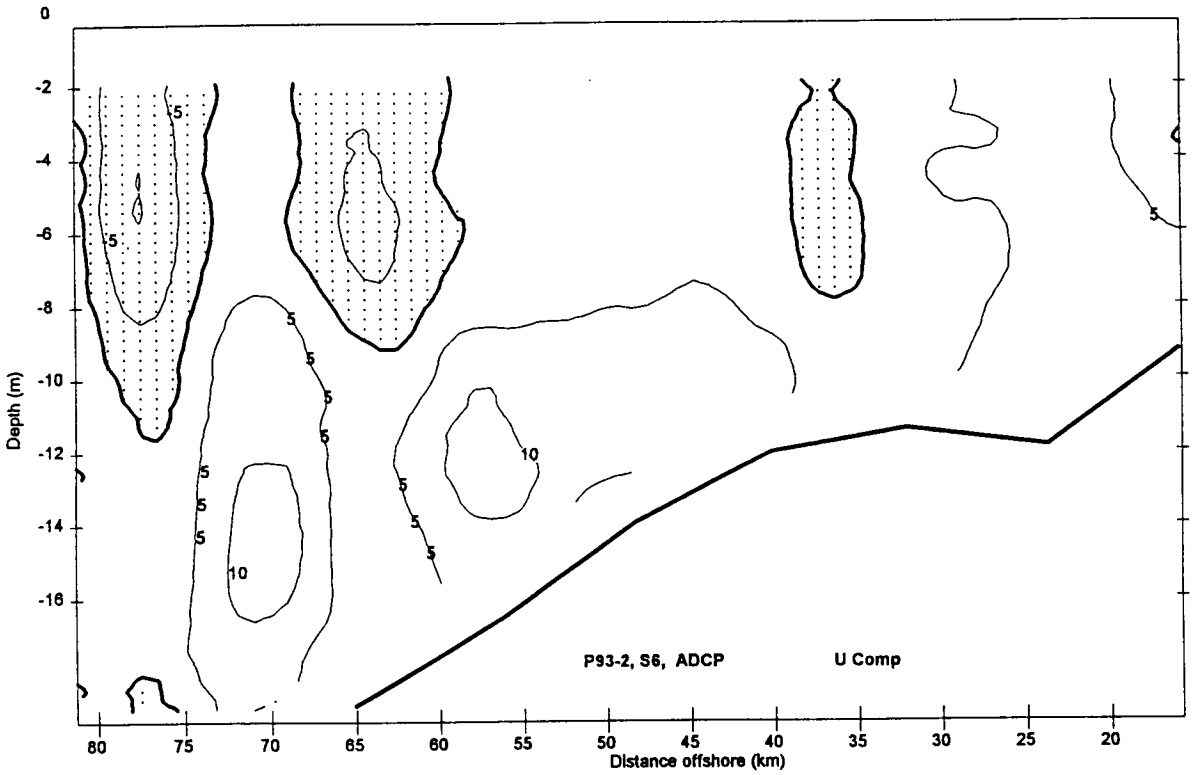

Figure 69. Alongshore speed components from the ADCP on S6 during the July 1993 cruise observations.

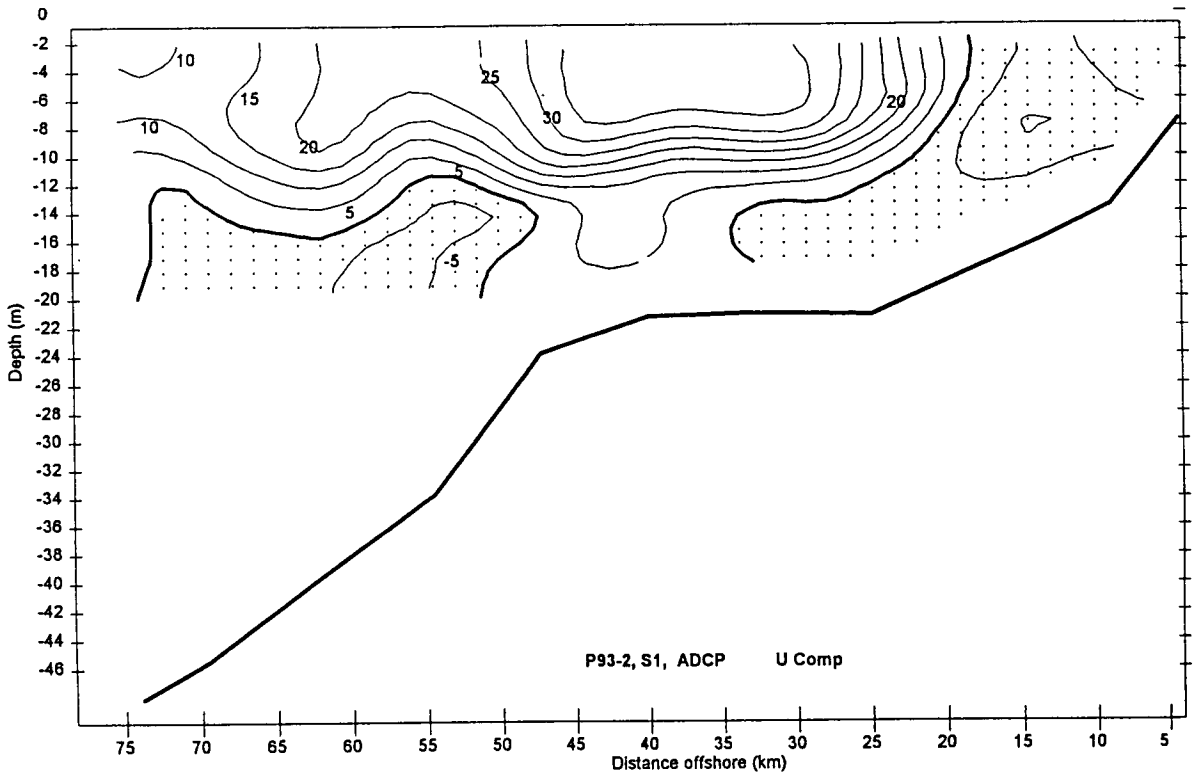

Figure 70. Alongshore speed component from the ADCP on S1 during the July 1993 cruise observations.

c. Velocity Field from ADCP Observations

Despite its extreme complexity we present the entire seven days of ADCP observations in one overview (Figure 68). Winds are extremely steady before and during the cruise and unlike the winter regime cruises, are not the cause of the alongshore and cross-shore variability observed in the current field. The observational domain is covered with a huge volume of buoyant water from the historic flood of the Mississippi river system in 1993. As a result erratic motions at a variety of scales appear to dominate nearly the entire domain. Even in the homogeneous high salinity upcoast flow at the west end of the domain, a short wavelength feature exhibits clockwise rotation and strong onshore flow between S7 and S8. Continuing east a vertical section through S6 (Figure 69) shows the banded structure associated with the intermediate salinity mixing zone and erratic drifter movements during the summer 1994 observations (Figure 57).

Sections S5, T7, and S4 (Figure 68) appear to be involved in a circular circulation feature with a current speed scale of 40 cm/sec and a cross-show and along-shore length scales of at least 50 km. While supporting data is limited, we suspect this is the result of an inertial oscillation set up by the impact of a major thunderstorm system.

At the eastern end of the domain a zone of coherent eastward flow emerges, as it did in the July 1994 observations, from the chaotic flows characteristic of the central region. From the south half of S3 eastward through S1, a dominant eastward flow extends throughout most of the surface layer. At S1 (Figure 70) the surface layer exits the domain carrying water of 26 to 30 psu eastward. Note this patch of organized flow at the east end of our domain is consistent with the summer season drifter velocity map (Figure 7b). Study of the vertical sections indicate, however, that this seemingly coherent pattern is composed of a complex maze of subsurface and surface jets whose continuity and evolution remains quite unclear.

d. Pre-SCULP Drifter Data

The full array SCULP drifter deployments did not begin until after our July 1993 observations of the summer upcoast regime. However, a pilot deployment of six to eight drifters was deployed off western Louisiana centered at about 29° N, 93° W, in early June of that year. After two weeks of sluggish movements in this transition season, the strong northeasterly winds of tropical storm Arlene (June 20-22) drove these drifters rapidly down the Texas coast as far south as 27° N. After an additional week of lying essentially stagnant, the summer regime wind field became fully established and these drifters began their upcoast trajectory from south and central Texas into Louisiana. Figure 71 shows the daily average velocity of six pre-SCULP drifters as they move upcoast from June 29 to July 19, two days after the end of our cruise observations. Evident in this figure are (1) the continuity of the general upcoast flow in the near-coastal region from south Texas to central Louisiana; (2) a zone of high current speeds (50 to 60 cm/sec) nearest the coast extending from south of Galveston Bay to Sabine Pass; and, (3) weak variable currents along the Louisiana coast. The inset in Figure 71 shows the daily drifter velocities, captured only the interval of our July cruise (cf. Figure 66). The (a) eddy-like motion at 30-km length scale southeast of Galveston and (b) the weak incoherent motion (stagnation zone) in the shallow water south of Marsh Island are consistent with the highly variable ADCP flow field of Figure 68.

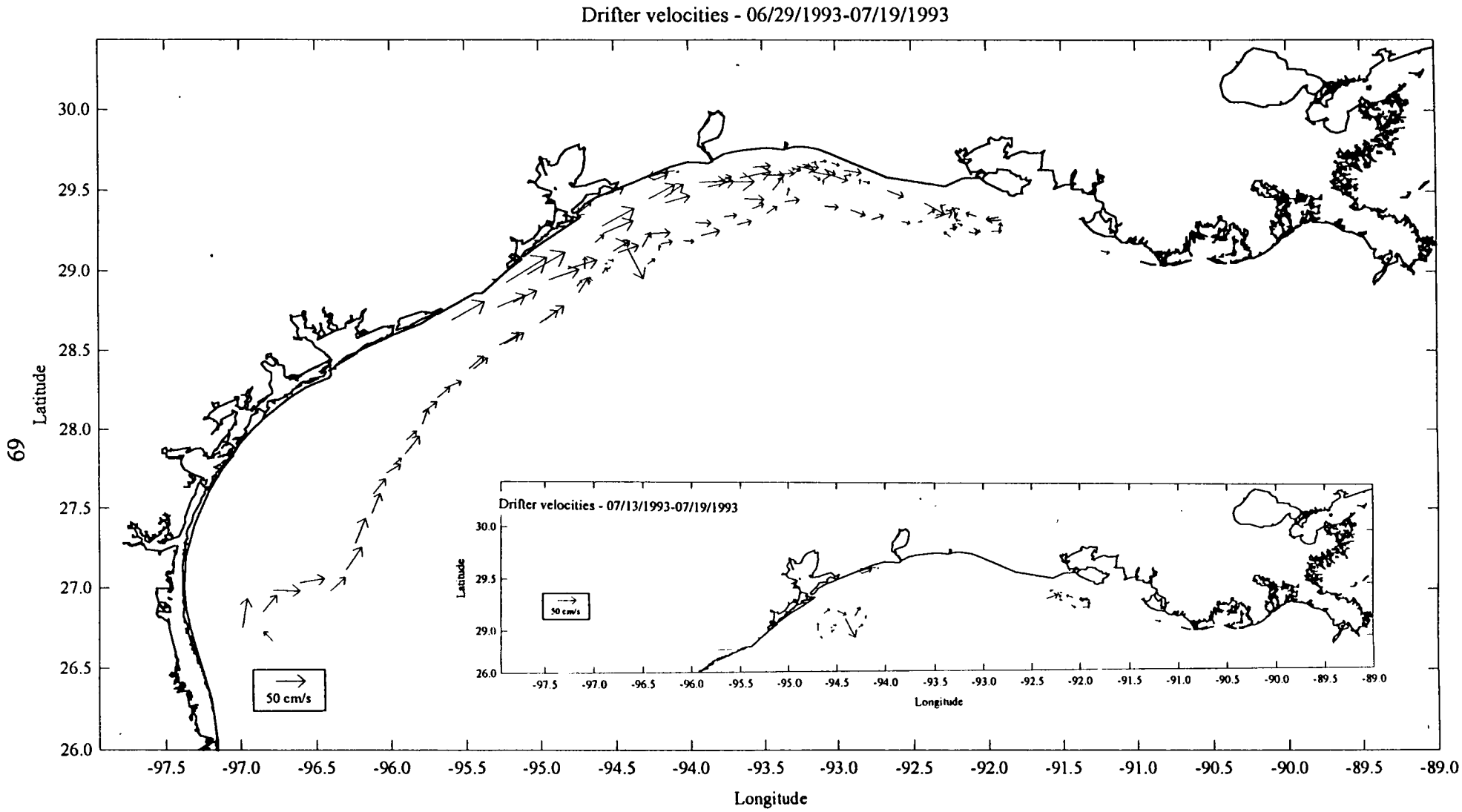

Figure 71. Daily average drifter velocities from a pre-SCULP pilot deployment June-July 1993. Inset show drifter trajectories during the plume observations.

G. Freshwater Content

The most significant identifying feature of the coastal plume is, of course, the reduced salinity caused by the injection of fresh water from the Mississippi and Atchafalaya Rivers. The freshwater fraction of any volume of sea water is defined as F = (Sb-S)/Sb, where Sb is a baseline salinity and S is the temporal and spatially dependent salinity measured at each CTD station. Thus, the measured salinity profile can be turned into an equivalent height of fresh water (the reduced freshwater volume V_f) at each CTD station allowing the absolute freshwater distribution to be mapped.

Dinnel and Wiseman (1986), using a relatively coarse shelf-wide data set, identified an annual cycle to the freshwater volume stored on the west Louisiana-Texas shelf. In their data, an annual maximum occurred about a month after peak spring river discharge and a minimum shelf-wide volume occurred just prior to the spring flood. Additionally, they found in the spring discharge season that the highest concentration was contained in a narrow band along the inner shelf, i.e., the coastal plume. In winter, when freshwater content is lowest there is also a maximum in a band along the coast. In summer they found that the freshwater maximum moved offshore to mid-shelf in accord with the upcoast summer flow regime with its surface Ekman layer directed offshore as discussed in C/K.

Etter (1996) also presents freshwater distribution maps from the ten shelf-wide LATEX A hydrographic cruises. While of far greater detail than the data set available to Wiseman and Dinnel (1988), the general pattern of the freshwater distribution remains consistent. In May 1993 and May 1994, the highest freshwater content on the shelf occurs in a narrow band along the inner shelf especially along the Texas shelf west of Sabine Pass where values of V_f exceeds 5 m. In the summer observation of August 1993 and August 1994 values of V_f are less than 1 m along the central Texas coast, and the highest values are on the mid-outer shelf of Louisiana. These results are, of course, consistent with the spring downcoast flow regime where the broad downcoast flow on the Louisiana inner shelf collapses into a much narrower coastal jet (Figure 7a) along the central Texas coast. The summer upcoast flow regime reduces the fresh water concentration along the Texas coast and deflects the accumulation of fresh water out onto the mid-shelf. Etter (1996) shows that in November of 1993 and 1994 the downcoast flow regime has re-established the high fresh water band (V_f ~ 3-4 m) along the central Texas coast.

The freshwater distribution from our five observations of the inner shelf are shown in Figures 72a through 72e. Our two April observations of the coastal plume (Figure 72 a, b) at the end of the long downcoast flow regime season show the expected high values of 2 to 3 m of fresh water along the Louisiana shelf and even higher valued of 3 to 4 m along the central Texas coast. Near the onset of the 1992-1993 downcoast coastal flow season, our October 1992 observation (Figure 72c) during a low freshwater discharge year shows the Louisiana inner shelf covered with 2 to 3 m of water with the mound exceeding 3 m just west of the Atchafalaya Bay mouth. Values decrease to 2 m along the upper Texas coast. Unfortunately the LATEX A cruise of November 1992 only sampled as far west as our S6 line, just west of Sabine Pass. The patterns, however, are similar and provide some evidence that the 3 m mound of fresh water we observed west of Atchafalaya Bay had translated to the region off Sabine Pass in the 30 days between cruises, a translation speed of 5 km/day, consistent with our section averaged speeds of 5 cm/sec at section S5 and 12 cm/sec at S6. Transports and cross-sectionally averaged speeds are discussed in the next section.

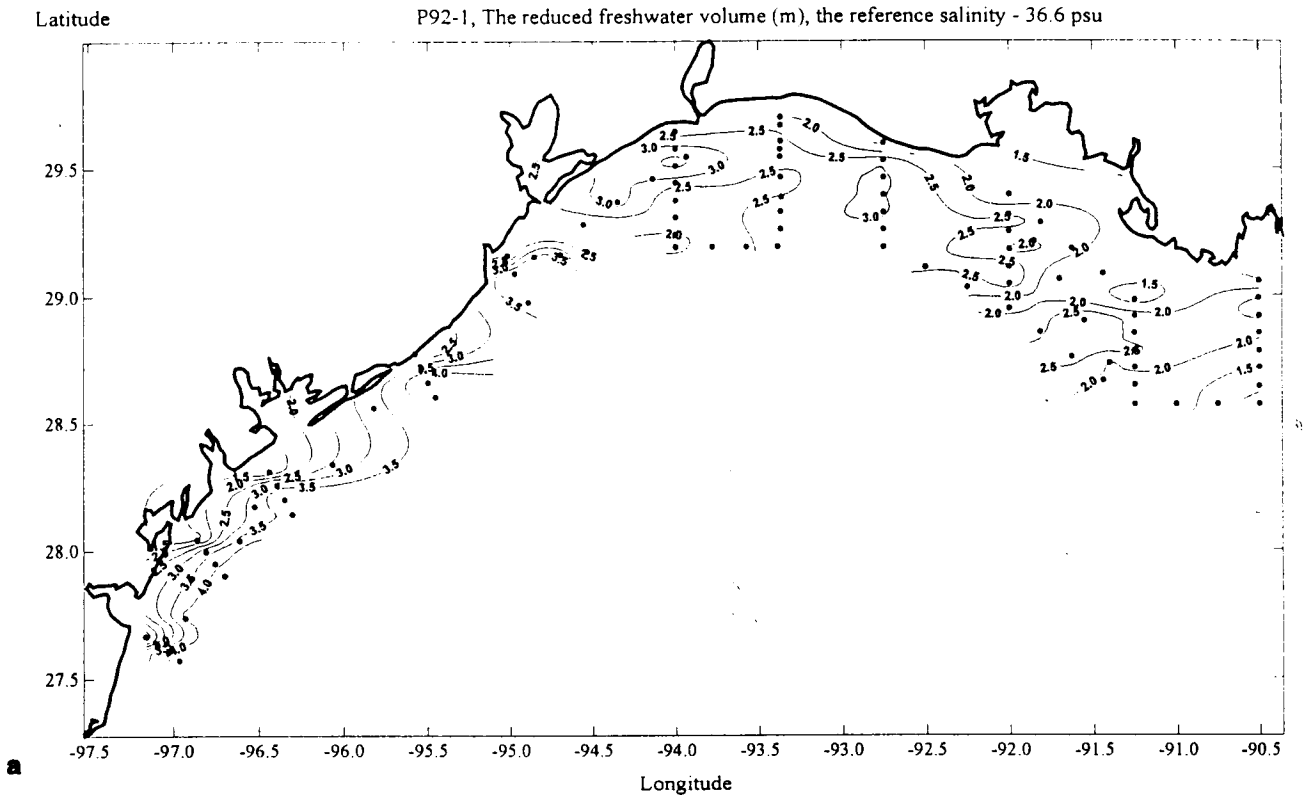

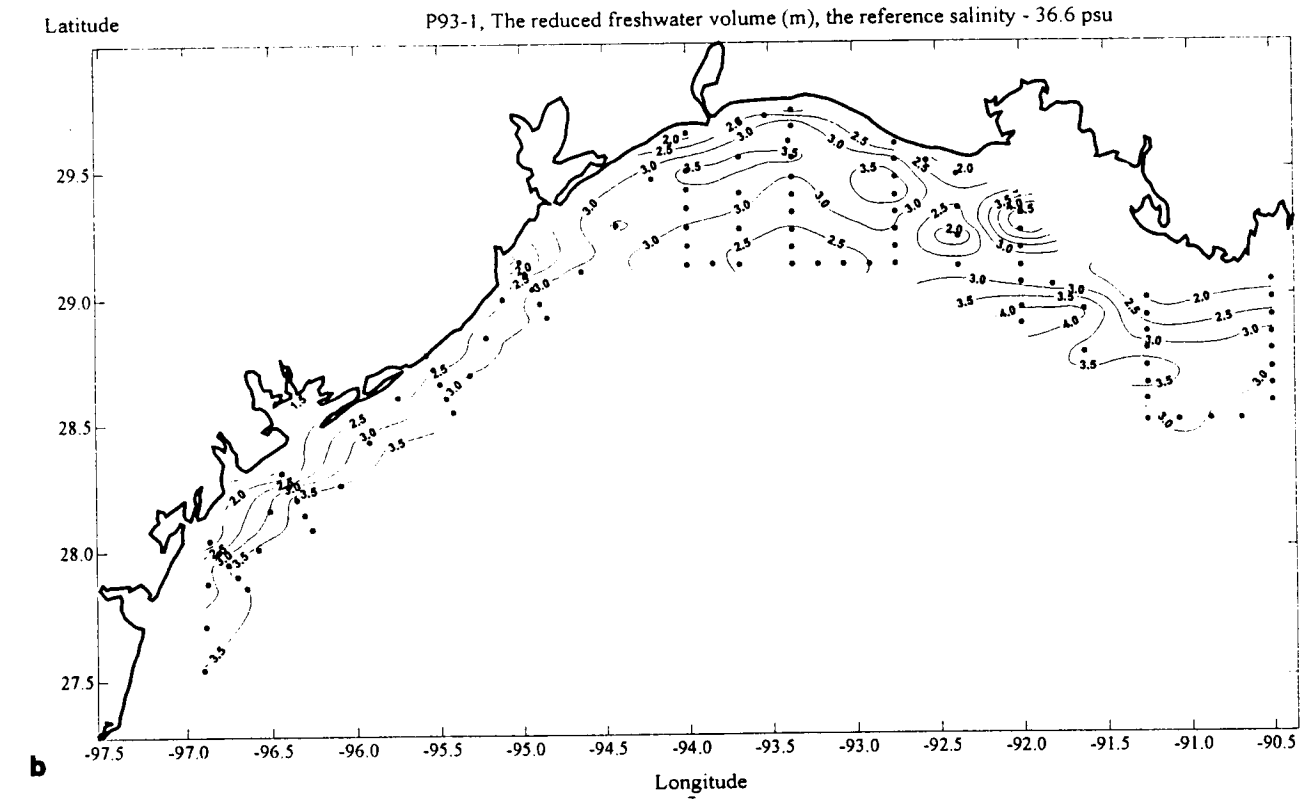

Figure 72. Freshwater distribution (m) for the cruise observations of (a) April 1992; (b) April 1993; (c) October 1992; (d) July 1993, and (e) July 1994.

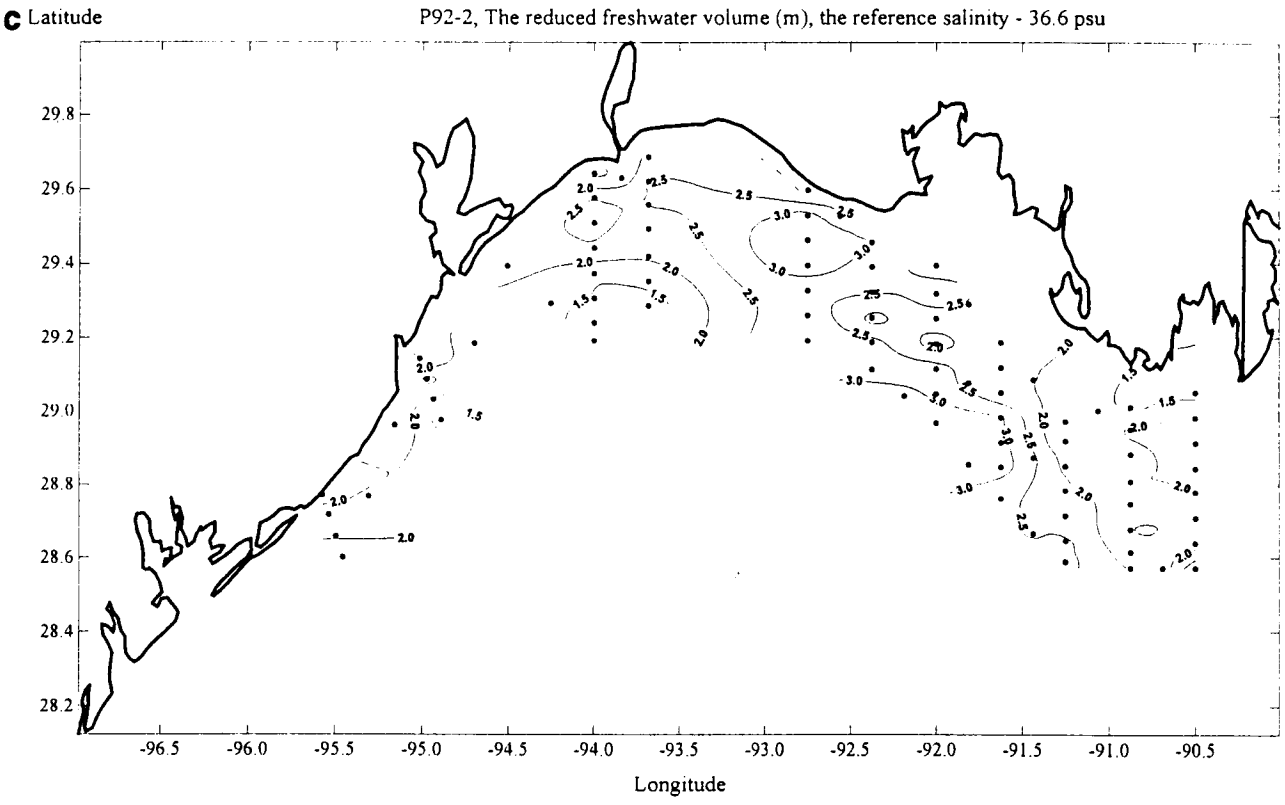

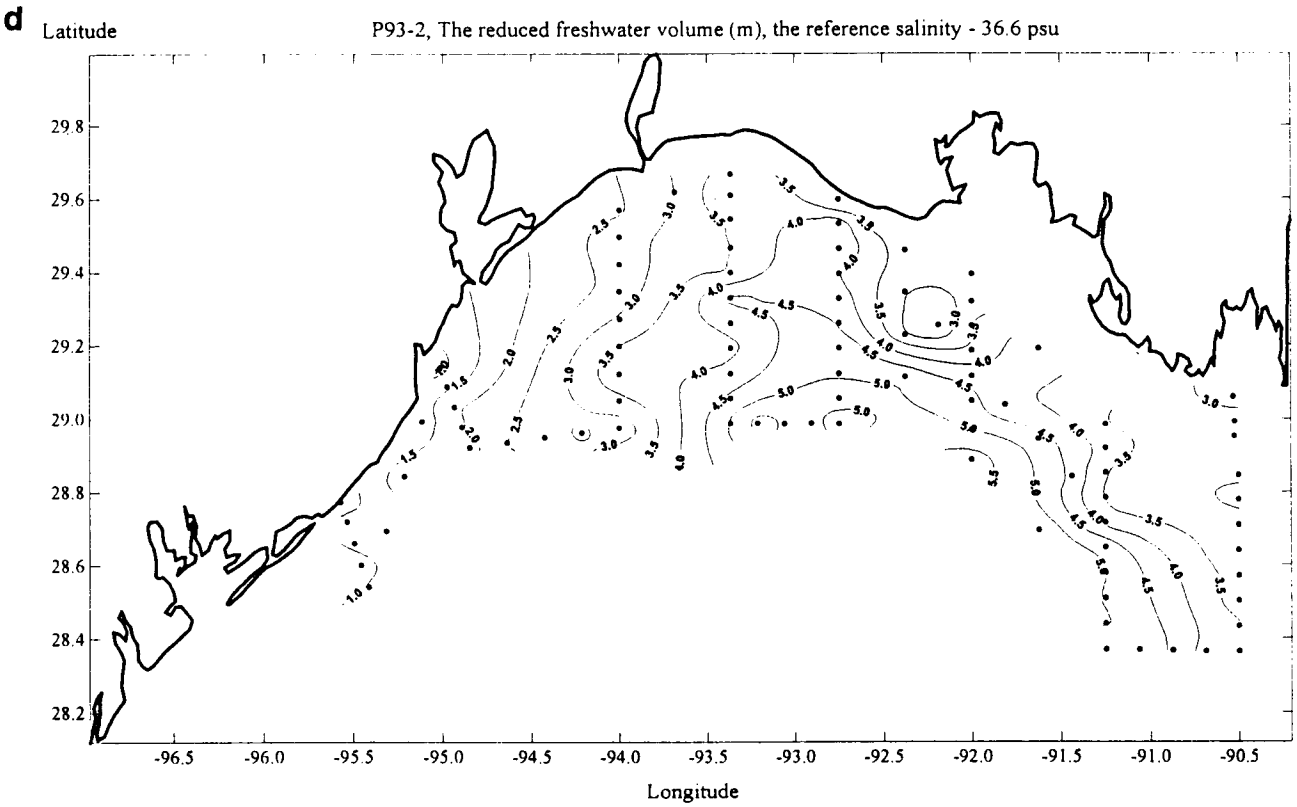

Figure 72 cont'd.

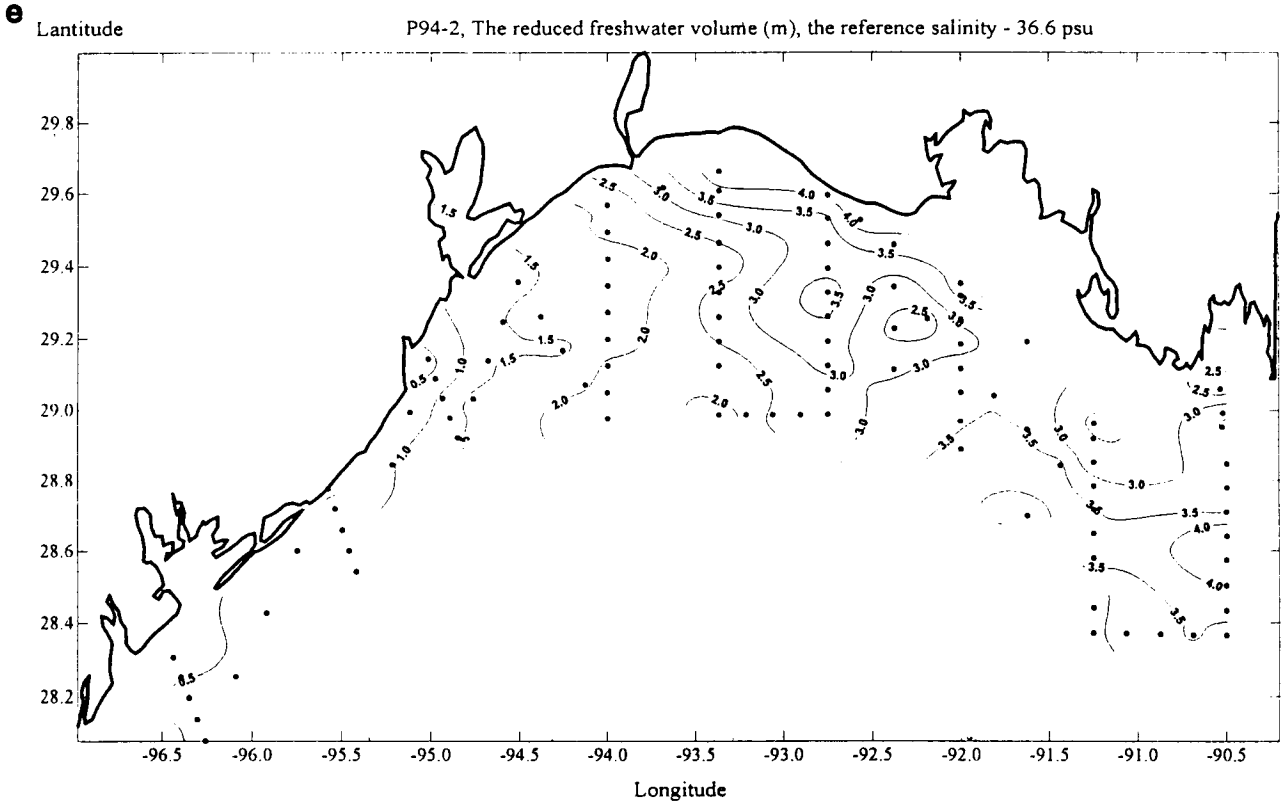

Figure 72 cont'd.

The freshwater distribution mapped during our two mid-summer observations of July 1993 and July 1994 are shown in Figures 72d and 72e. During the great flood year of 1993 we observed (Figure 72d) as much as 5 m of fresh water along the offshore boundary of our observations south of Atchafalaya Bay with the contours indicating an extension of this high freshwater concentration to the east. The piston-like advance of the low freshwater content from south Texas is clearly reflected in the presence and orientation of the 1 m and 2 m contours south of Galveston.

In the summer of 1994 (July), with much less fresh water on the shelf, the highest freshwater content (3.5-4 m) is again on the outer edge of our observational domain and extending eastward (Figure 72e). There is a secondary high of 3.5-4 m of fresh water accumulated in front of the Atchafalaya Bay and displaced westward in the shallow waters along the coast. The upcoast intrusion of south Texas water of very low fresh water content is again present southwest of Galveston. These distributions of fresh water accumulations are all consistent with (a) the models of the downcoast flow regime in fall, winter, and spring, where the freshest water tends to concentrate in a narrow band along the coast and (b) the model of the upcoast flow regime in summer where the flow reversal deflects the relict coastal plume water offshore to form a concentration of fresh water at mid-shelf and a secondary high where the recent Atchafalaya River outflow plume is trapped against the coast west of outflow mouth.

In addition to the distribution of fresh water another important environmental parameter in the region occupied by the coastal plume is the flushing time, the time necessary to replace the amount of fresh water present in the volume of sea water under consideration. We will estimate flushing time T(t) for the inner shelf-coastal plume region using the standard relation

$$V(t) = \int_{t-T(t)}^{t} R\, dt$$

where V(t) is the volume of fresh water in our standard inner shelf grid, and R is river discharge . Dinnel and Wiseman (1986) studied the water balance on the entire Louisiana-Texas shelf, a surface area six times larger than our standard grid, which necessitated including precipitation and evaporation effects. The total amount of fresh water stored in the domain of each cruise is given in Table 4. Freshwater content is given in this table both for the entire domain for each cruise and for a standard domain i.e., that of Cruise II, October 1992. Using these standard volumes we determined an upper bound for the flushing time T(t) by using the Atchafalaya River discharge alone, and then estimated a mid-range value by integrating Atchafalaya River plus 25% of the Mississippi River at Tarbert Landing for the freshwater input rate R. The 25% value is a rough estimate based on Dinnel and Wiseman's (1986) convention that 50% of the Mississippi River discharge to the delta ends up on the western shelf combined with Walker's (1996a) estimate that the anticyclonic eddy that brings Mississippi River outflow into the coast in the Louisiana Bight occurs about half the time.

We can deduce several important conclusions from these statistics. (1) Except for the anomalously high values of July 1993, caused by the extreme flood of that year, the freshwater content of the (standard area) coastal plume falls in a relatively narrow band of 52-66 km^3 of fresh water with little relation to the annual flood cycle. (2) As the volume of the standard grid is 323 km^3, we note that the coastal plume is typically composed of 20% fresh water, which corresponds to a nominal average salinity of 29 psu. (3) The interannual variability in the Mississippi-Atchafalaya River flood cycle appears to exert far more control on the freshwater content of the coastal plume than the seasonal cycle of river discharge.

Table 4. Freshwater volume and flushing time.

	Total Observed Surface Area		Standard Surface Area (10^3 km^2)		Flushing Time
	FW Content km^3	Area 10^3 km^2	FW Content km^3	Standard Grid 10^3 km^2	Days
Cruise I, April 1992	73.7	28.7	56.5	23.2	75-120
Cruise II, October 1992	52.0	23.2	52.0	23.2	79-128
Cruise III, April 1993	100.5	35.2	66.4	23.2	50-87
Cruise IV, July 1993	116.1	33.6	83.0	23.2	59-83
Cruise V, July 1994	86.7	35.4	61.3	23.2	62-87

The resulting range of flushing times for our inner shelf standard volume are plotted against the average combined discharge for the 30 days prior to each cruise in Figure 73. This plot indicates that flushing time for the coastal plume water on the inner self appears to be in the range of 2-3 months regardless of the strength of river discharge. The seasonal dominance of either upcoast or downcoast wind forcing likewise shows little control on the flushing time. This value for the inner shelf-coastal plume region is in contrast to the 8 to 12 months noted by Dinnel and Wiseman (1986) for the entire west Louisiana-Texas shelf. It appears that the high rate of advection in the coastal plume in both spring and summer regimes act to flush the inner shelf waters much more effectively than the entire shelf is flushed by larger scale processes.

H. Transport along the Coastal Plume

One of our objectives was to determine the volume flux in the current that advects the coastal plume along the shore. In Figures 74a-e, the volume flux determined from the ADCP measurements is presented section by section from east to west for each cruise. Because of the strong temporal and spatial variability in the transport resolved by the ADCP our purpose is not to seek closure in a volume balance but to establish a range of transport under different seasonal forcing. Our observations show that the coastal plume water of lowered salinity generally does not extend below the 15 m depth level so we determine the transport by integrating the alongshore current speed over the ADCP field in each section down to the 15 m level. As section are of slightly variable length, we list the cross-sectional area A and the sectionally averaged speed T/A in Table 5. No attempt has been made to weight the transport with cross-sectional area. The average fresh water content in each section f (also listed in Table 5) is used to calculate the instantaneous fresh water flux (Tf) at each section as shown in Figure 74.

We may obtain a coarse but useful estimate of the transport in the coastal plume by averaging over all (or several) coastal normal transport sections. The spatial and temporal distribution of the samples (sections) yield a nominal average over a six to seven day-long weather window and source, downstream and far-field conditions.

1. Downcoast Flow Regime (Spring)

The observation of the transport in April 1992 (Figure 74) naturally breaks into the two regimes: (1) the downcoast flows observed at S2-S6 interrupted intermittently by the northwesterly wind events associated with frontal passage winds , and (2) the upcoast flows observed at S7-X3 driven by the five-day long southeasterly wind event in central and south Texas. Averaging all the downcoast flow sections together gives a transport estimate of 70 x 10^3 m^3/sec while the upcoast flow sections averaged 68 x 10^3 m^3/sec. Table 5 and Figure 74 indicate

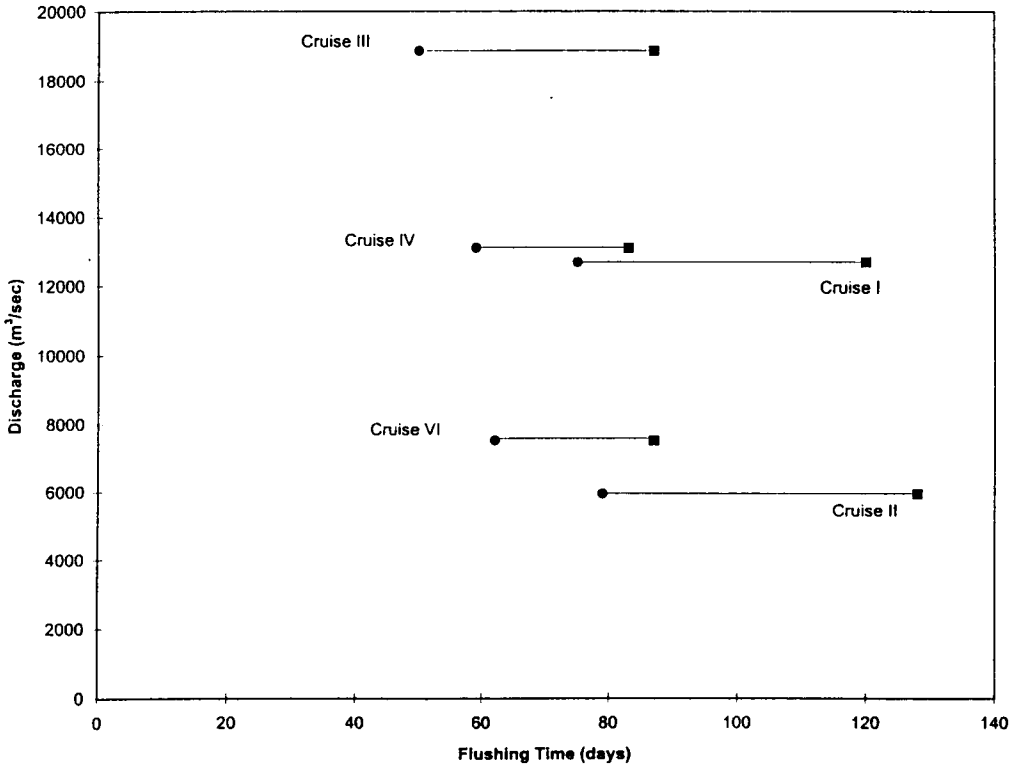

Figure 73. Range of flushing times of standard volume sample of coastal plume plotted against 30-day average discharge prior to each cruise composed of the Atchafalaya River plus 25% of the Mississippi discharge at Tarbert Landing.

Table 5. Sectionally averaged speed for each cruise.

	Transect	Transport m^3/sec	Area m^2	f	T/A Tran/Area cm/sec	Tf $10^3 m^3/sec$
Cruise I, April 199	S1			0.15		
	S2	-152,660	540,000	0.23	-28	-35.1
	S3	-40,819	476,000	0.28	-9	-11.2
	S4	-1,709	552,000	0.24	0	-0.4
	S5	-46,463	712,000	0.23	-7	-10.7
	S6	-109,960	524,000	0.26	-21	-28.6
	S7	56,565	268,000	0.31	21	-17.5
	S8	9,037	272,000	0.29	3	2.6
	X1	67,113	328,000	0.20	20	13.4
	X2	96,095	288,000	0.24	33	23.1
	X3	110,068	348,000	0.22	32	24.2
Cruise II, October 1992	s1	-64,778	632,000	0.13	-10	-8.4
	s1b	-108,703	560,000	0.14	-19	-15.2
	s2	-78,710	488,000	0.16	-16	-12.6
	s2b	-49,862	488,000	0.21	-10	-10.4
	s3	-17,241	452,000	0.26	-4	-4.5
	s3b	10,829	388,000	0.25	3	2.7
	s4	-71,182	568,000	0.21	-13	-14.9
	s4b	-51,790	576,000	-	-9	-
	s5	-36,301	668,000	-	-5	-
	s5b	-63,343	460,000	0.18	-14	-11.4
	s6	-63,811	520,000	0.17	-12	-10.9
	s7	-27,508	268,000	0.15	-10	-4.1
	s8	-32,001	292,000	0.15	-11	-4.8
Cruise III, April 1993	s1	-113,200	924,000	0.18	-12	-20.3
	s2	-21,226	744,000	0.22	-3	-4.6
	s3	91,209	664,000	0.39	14	35.6
	s4	37,995	696,000	0.21	5	8.4
	s5	71,218	824,000	0.23	9	16.4
	s6	130,431	724,000	0.22	18	28.6
	s7	29,972	468,000	0.18	6	5.4
	s8	12,873	460,000	0.17	3	2.1
	x1	51,409	476,000	0.17	11	8.7
	x2	115,828	488,000	0.16	24	18.4
Cruise IV, July 1993	S1	150,183	1,048,000	.18	14	27.0
	S2	119,327	872,000	.28	14	33.4
	S2b	309,582	776,000	.36	40	111.4
	S3	87,993	576,000	.43	15	37.8
	S3b	25,491	364,000	.33	7	8.4
	S4	-70,169	888,000	.29	-8	-20.3
	S5	230,820	1,088,000	.26	21	60.0
	S6	64,137	856,000	.21	7	13.5
	S7	29,690	460,000	.11	6	3.3
	S8	10,301	412,000	.07	3	0.7
Cruise VI, July 1994	S1	57,607	1,032,000	.19	6	1.1
	S2	170,718	856,000	.19	20	32.4
	S2b	190,388	728,000	.27	26	51.4
	S3	21,565	640,000	.32	3	6.9
	S3b	75,114	440,000	.21	17	15.8
	S4	-142,153	1,000,000	.23	-14	-32.7
	S5	78,111	1,116,000	.20	7	15.6
	S6	45,937	848,000	.13	5	6.0
	S7	15,559	452,000	.06	3	0.9
	S8	-28,873	460,000	.05	-6	1.4

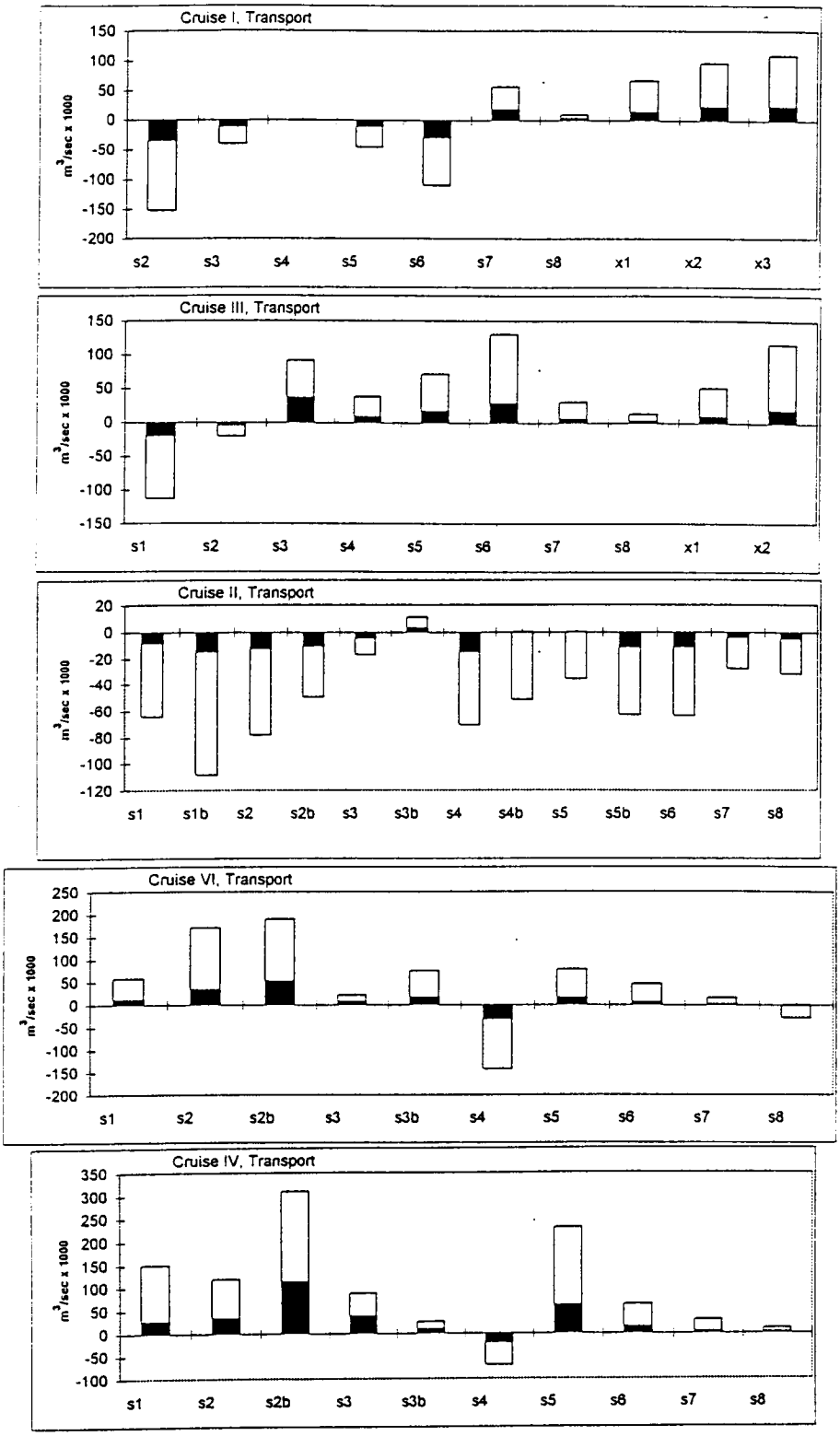

Figure 74. Bar graphs of total transport and freshwater transport along the coastal plume. Observation dates are (a) April 1992; (b) April 1993; (c) October 1992; (d) July 1994; (e) July 1993. The shaded portion of each bar represents the component of fresh water transport at that section

that close to 25% of these transports are fresh water. This freshwater flux in the coastal plume of about 17 x 10^3 m^3/sec is reasonably close to the 30-day average combined river discharge (12.7 x 10^3 m^3/sec) used in Figure 73.

The six days of the April 1993 observation period were paradoxically dominated by upcoast winds despite occurring in the downcoast flow season. Eight out of the ten sections showed upcoast transports (Figure 74b) as a result of persistent westerly winds arising from the pattern of the synoptic scale atmospheric pressure cells transiting the area. The average of the upcoast transport sections is 68 x 10^3 m^3/sec of which 22% is fresh water. This 15.2 x 10^3 m^3/sec of fresh water in flux in the coastal plume is only 20% less than the 30-day average combined river discharge preceding the cruise observations.

The seven-day long October 1992 observation occurs during a period of extremely persistent downcoast winds. Twelve of the thirteen sections (Figure 74c) accordingly display downcoast transport with all sections averaging 52 x 10^3 m^3/sec total transport with 16.5% of this total or 8.6 x 10^3 m^3/sec of fresh water in flux along the coast. The 30-day average combined river discharge is 6 x 10^3 m^3/sec (Figure 73), about a third smaller than the coastal fresh water transport.

2. Upcoast Flow Regime (Summer)

The July 1994 cruise shows eight of ten sections with an upcoast transport (Figure 74d). Averaging across all sections indicates a nominal upcoast transport of 48.4 x 10^3 m^3/sec. The freshwater component of this flux is 10.6 x 10^3 m^3/sec, about 30% higher than the 30-day average combined river discharge.

The July 1993 observations of the coastal plume took place during a record high flood year. All but one of our ten sections (Figure 74e) show an upcoast transport. The average of all sections of 95.7 x 10^3 m^3/sec is the highest of our five seasonal observations and the corresponding flux of 27.6 x 10^3 m^3/sec of fresh water in the coastal plume regime is likewise by far the highest of our five seasonal observations. It is nearly three times the coastal fresh water flux we observed the following summer discussed above and nearly twice the 30-day average combined river discharge prior to these cruise observations.

Despite our rather small sample of five integrated observations of the coastal plume, it is notable that the "windy" months of April 1992 and 1993 have transports ~70 x 10^3 m^3/sec in the coastal plume, which decreases to 52 x 10^3 m^3/sec during a "normal" summer, i.e., July 1994. During the summer of the 1993 great flood, the wind stresses are slightly smaller than in the summer of 1994, yet the volume flux in the coastal plume doubles in magnitude. As of yet, we have no dynamical explanation for this major difference in summer transport, but the role of large-scale pressure gradients associated with the massive volume of fresh water on the shelf deserves close scrutiny in this regard.

I. Transport, Wind Stress, and Dynamical Relations

1. Transport and Wind Stress

We will next address in more detail the relationship between the observed transport at each section and the local wind stress. Consider a conventional coordinate system with positive y-directed onshore and positive x-directed to the right of an observer looking onshore with u, v the speed components in the x, y directions, respectively. The alongshore (or x direction) momentum

balance can be written in terms of the Coriolis trm, the longshore surface slope and vertical eddy friction in terms of the Coriolis term, the longshore surface slope and vertical eddy friction

$$0 = fv - g\frac{\partial \eta}{\partial x} - \frac{1}{\rho}\frac{\partial \tau_x}{\partial x} \tag{1}$$

neglecting the alongshore baroclinic pressure gradient and assuming $\partial u/\partial t$ and the field accelerations are relatively small. The terms η, τ, ρ, and f are sea surface elevation (positive up), frictional stress, water density, and the Coriolis parameter, respectively. Integrating (1) over the water depth h and taking

$$\int_0^h v\, dz \approx 0$$

caused by the coastal constraint (1) becomes

$$0 = -g\rho h \frac{\partial \eta}{\partial x} - (\tau_{bx} - \tau_{sx}) \tag{2}$$

where τ_{bx} and τ_{xs} are bottom stress and surface stress, respectively. Putting aside the alongshore sea surface slope term for the moment, (2) becomes the so-called frictional balance

$$\tau_{bx} = \tau_{sx} \tag{3}$$

where τ_s is the local wind stress and τ_b can be parameterized with a depth mean speed u_m and a linear friction coefficient with dimensions of velocity

$$\tau_b \approx \rho\, r\, u_m \tag{4}$$

as in Cochrane and Kelly (1986); Scott and Csanady (1976). Multiplying both sides of (4) by h(y), the water depth, and integrating across the coastal current between the nearshore and the offshore ends of the section, a distance L

$$\int_{y=o}^{L} \tau_{sx}(y)\, h(y)\, dy = \rho\, r \int_{y=o}^{L} u_m(y)\, h(y)\, dy = \rho r T \tag{5}$$

as the quantity in the integral on the right side of (5) is the transport T observed by the ADCP and given in Table 5. Note that if τ_{sx}, the local wind stress, is approximately constant along the cross-section, then the left side of (5) becomes

$$\bar{\tau}_{sx} \int_{y=o}^{L} h(y)\, dy = \bar{\tau}_{sx} A \tag{6}$$

where A is the cross-sectional area and $\bar{\tau}_{sx}$ is the average alongshore wind stress across the section. We can then rewrite (5) as

$$\frac{T}{A} = \frac{1}{\rho r}\bar{\tau}_{sx} \tag{7}$$

to show the transport is linearly dependent on the alongshore wind stress in the frictional balance model.

Now consider the surface slope term in (2), which, with an alongshore slope constant across the section, becomes

$$g\rho \frac{\partial \eta}{\partial x} \int_{y=o}^{L} h^2(y) dy \sim g\rho \frac{\partial \eta}{\partial x} \bar{h}^2 L \tag{8}$$

where $\bar{h}$ is the average depth across a section.

So a linear relationship between transport and wind stress will yield an estimate of the frictional coefficient r, and any non-zero value of transport at $\tau_{sx} = o$ would be related to the longshore surface slope.

In Figure 75, we plot the transport/area against the alongshore component of the average wind stress for each section for the three downcoast plume regime cruises, the "windy" months of April and October 1993, and April 1994. The longshore component of the wind stress is calculated from the ship board wind data as shown in Figures 9 and 39, taking the appropriate component of $\tau = K\rho_a W^2$, where $K = 2.5 \times 10^{-3}$, ρ_a is air density and W is wind velocity. Considering the nature of the data, the relation of τ_{xs} to transport is reasonably linear (correlation coefficient = .67), which supports the linear friction law (4) as in Scott and Csanady (1976). The slope of the best fit line indicates a linear resistance coefficient of 0.11 cm/sec similar to the 0.16 cm/sec of Scott and Csanady (1976), deduced from current meter data in the Long Island coastal current and in the same range (0.1 to 0.01 cm/sec) as deduced from water level studies by Chuang and Wiseman (1983).

The regression intercept value for a zero wind stress is 1.9 cm/sec, which, although potentially related to the longshore surface slope by (8), is not significantly different from zero at the 95% level. This suggests that other mechanisms, such as buoyancy forcing and longshore surface slopes, are relatively unimportant compared to wind stress in the longshore dynamical balance for the spring-winter downcoast regime.

Performing the same analysis on the section transports for the two summer upcoast regime cruises yields an entirely different result (Figure 76). The sectional transports appear quite unrelated to local wind stress, even though 85% of the transport values are upcoast. Clearly some other forcing mechanisms, such as the longshore pressure gradient or buoyancy forcing, become important during the summer upcoast regime.

2. Multiple Coherence Analysis from Current Meter Data

To seek further insight into the dynamical relationships controlling currents in the domain of the coastal plume, we studied multiple and partial coherence at three locations between longshore currents and forcing functions: (a) longshore wind stress; (b) cross-shore wind stress; (c) longshore pressure gradient (sea level slope); and, (d) buoyancy forcing proxied by river discharge as in Münchow and Garvine (1993). Wind stresses are computed from CMAN station data (as explained in the figure captions), sea level slopes from coastal water level gauge differences, and buoyancy forcing is represented by Atchafalaya River discharges. Hourly data were used in all analyses. Data gaps of several hours were filled by linear interpolation, and linear trends were removed from all signals prior to analysis.

Specifications of the current meters closest to shore in the LATEX A current meter array (whose data are employed in this analysis) are given in Table 6.

Table 6. Details of current meters.

Location	Mooring No.	Latitude N	Longitude W	Water Depth	Instrument Depth	Distance Offshore
South Texas	1	27.26	97.25W	23 m	11 m	10 km
Central Texas	23	28.713	95.536	15 m	9 m	12 km
Central Louisiana	18	28.963	91.983	23 m	10 m	63 km

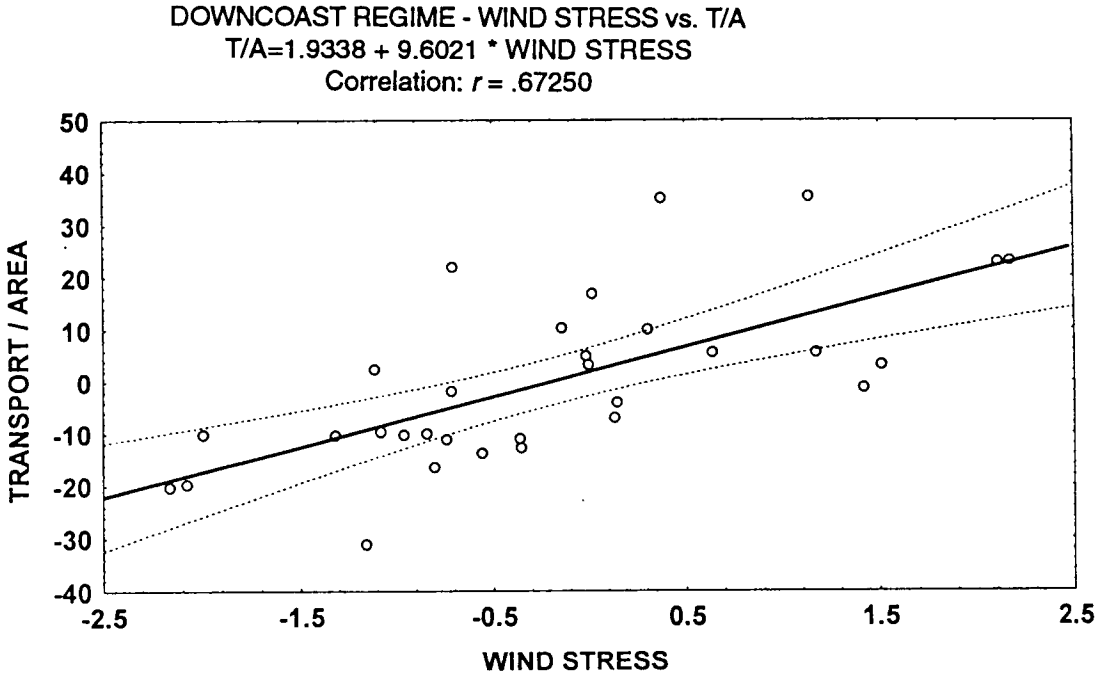

Figure 75. The average alongshore wind stress at each section plotted against the alongshore transport through each section normalized by cross sectional area for the downcoast (windy) regime cruises of April 1992, April 1993, and October 1992.

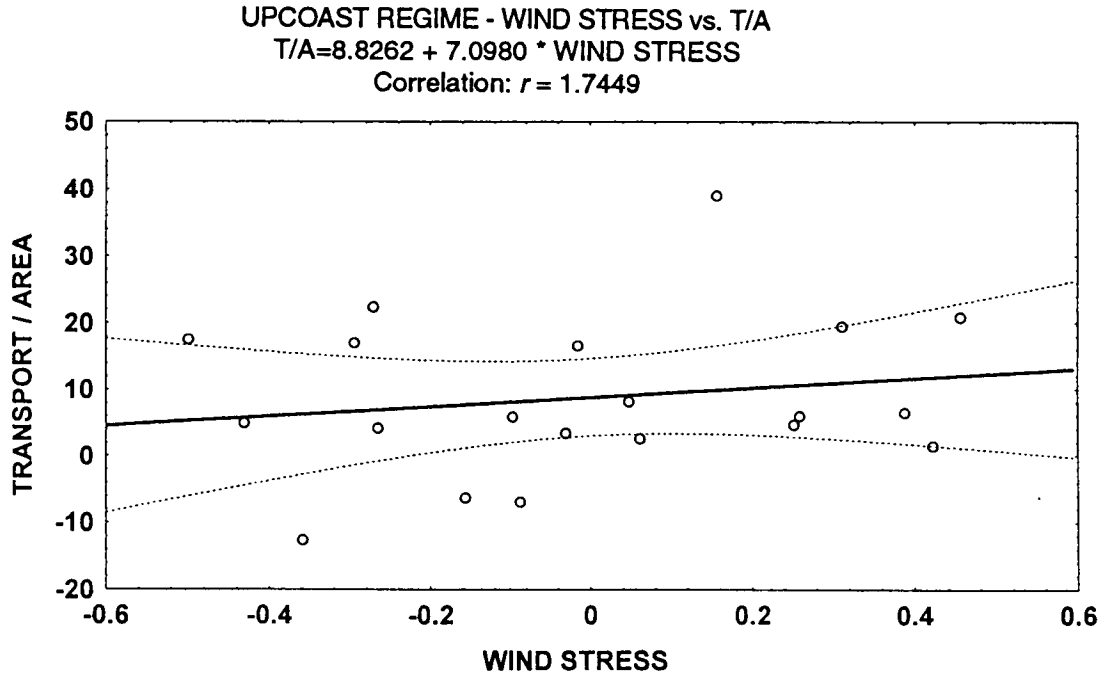

Figure 76. The average alongshore wind stress at each section plotted against the alongshore transport normalized by cross sectional area for the two summer regime cruises of July 1993 and July 1994.

Data from inner shelf moorings 17 and 20 were also inspected but judged unsuitable because of shortness of reliable record length for this type of analysis.

a. Downcoast Regime

(1) South Texas In Figure 77 we show partial and multiple coherence over the .05 to 0.5 cpd frequency band (2- to 20-day period band) between CM1 and longshore and cross-shore wind stress, sea level slope and buoyancy forcing. For the winter-spring period of 1992-1993, 70 to 80% of the variance in the alongshore current speed is explained by the four forcing variables considered. Note that maximum multiple coherence of 90% occurs in the middle of the weather band at 0.2 cpd. Looking at individual partial coherences, we see that longshore wind stress clearly accounts for the majority of the current variance. The cross-shore wind stress, the longshore pressure gradient (S. Padre Island less Galveston water levels), and the buoyancy forcing represented by the Atchafalaya River discharge all appear statistically unimportant in accounting for variance in the longshore current.

(2) Central Texas Two hundred and thirty km further north at CM23, the coastal orientation has rotated 45°. At this location, 70 to 80 % of the variance in the alongshore current is explained by multiple coherence with the four forcing variables across the 0.05 to 0.5 cpd frequency band (Figure 78). The pressure gradient parameterized by the Galveston-S. Padre Island sea level differences clearly has the dominant partial coherence with the longshore current at CM 23, accounting for 50 to 60% of the current variance. Longshore and cross-shore wind stress appears equally important as secondary sources of fluctuations in the alongshore current here. The importance of the buoyancy forcing remains insignificant at all frequencies.

(3) Central Louisiana At the CM18 site an eight-month long record covering the entire period of the downcoast 1992-1993 regime from fall to winter to spring is examined. Despite the long record, results (Figure 79) appear less organized than at the central and south Texas sites. The multiple coherence of the four variables explain only about 50 to 70% of variance in the longshore currents. There are only two frequency bands where partial correlations are clearly significant. In the 4- to 6-day period band the partial coherencies of the longshore wind explains about 40% of the variance in the current. In the intraseasonal band of 10- to 40-day periods, the partial coherence of the cross-shore wind at 33% appears to account for most of the fluctuations in the longshore current. Alongshore pressure gradient and, more surprisingly, buoyancy forcing appear to play no significant role in the current fluctuations at CM18, despite being located south of the Atchafalaya River mouth.

b. Upcoast Regime

(1) South Texas Two periods of three-month duration, June through August, 1992 and 1993, were analyzed for multiple and partial coherence from CM1. While 70 to 80% of the current fluctuations were accounted for by the multiple coherence with the four forcing variables, significant partial coherence was shown only with the longshore sea surface slope in the 1993 summer in the period band 4- to 15-days (Figure 80). In contrast, during the winter downcoast regime discussed above, the longshore wind stress showed stronger partial coherence with the current over wider frequency bands. Note that at first we parameterized the sea surface slope affecting CM1 with the sea level difference (Port Aransas-South Padre Island), which indicated no influence at all of sea surface slope on the current. Extending the station separation, however, to (Galveston-South Padre Island) identified a significant influence of sea surface slope on currents in the 4- to 15-day band.

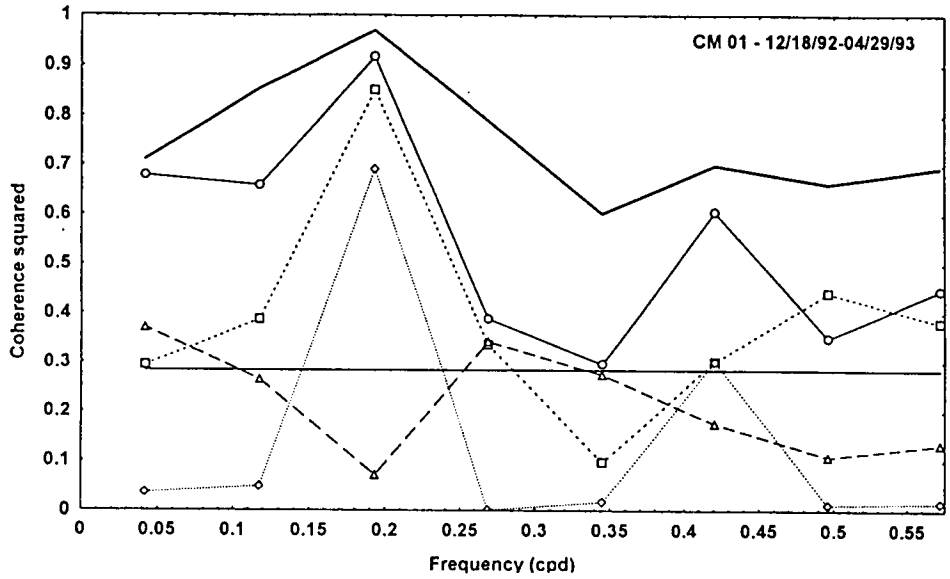

Figure 77. Multiple coherence (dark line) and partial conference (symboled lined) for the period December 1992 through April 1993 between longshore current at CM1 (south Texas) and (a) longshore wind stress (open circle); (b) cross-shore wind stress (open square); (c) longshore pressure gradient (diamond); and (d) buoyancy forcing, i.e., at Atchafalaya River discharge (open triangle). For CM1 Port Aransas wind is used and rotated 10° clockwise from the north. Alongshore pressure gradient (diamond) is taken as demeaned Port Aransas (PA) sea level less demeaned South Padre Island (SPI) sea level in Brazos-Santiago Pass. Daily Atchafalaya River discharges were linearly interpolated. The lower straight solid line is the 95% confidence level.

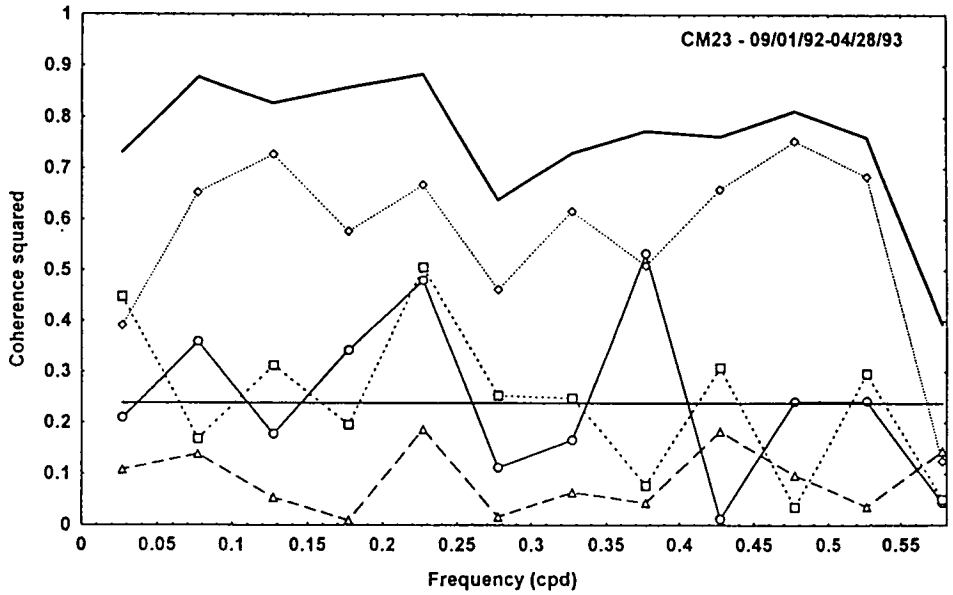

Figure 78. Multiple coherence and partial coherence as in Figure 77 for longshore current at CM23 (central Texas) for the period September 1992 through April 1993. Wind stress components are calculated from Port Aransas wind rotated 45° from true north. Alongshore pressure gradient is demeaned Galveston (GAL) sea level less demeaned SPI sea level.

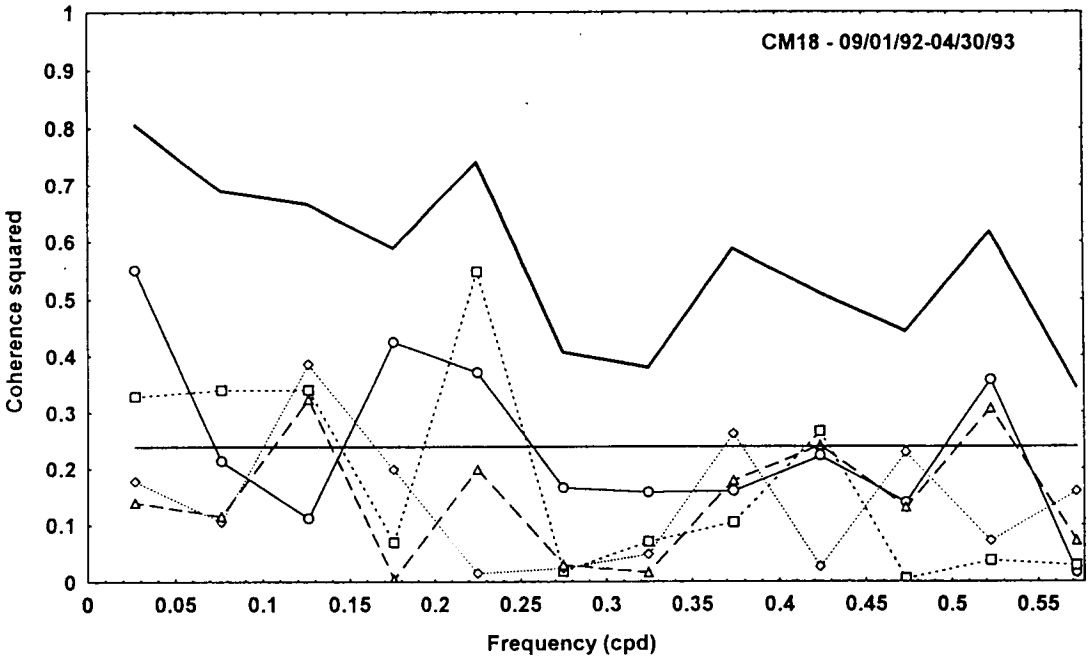

Figure 79. Multiple coherence and partial coherence as in Figure 77 for longshore current at CM 18 (central Louisiana) for the period September 1992 through April 1993. Wind stresses were computed from weighted average of Sabine Pass winds (2/3) and Grand Isle winds (1/3). Alongshore pressure gradient is computed from water level differences between Atchafalaya Bay (AB) and Sabine Pass (SP).

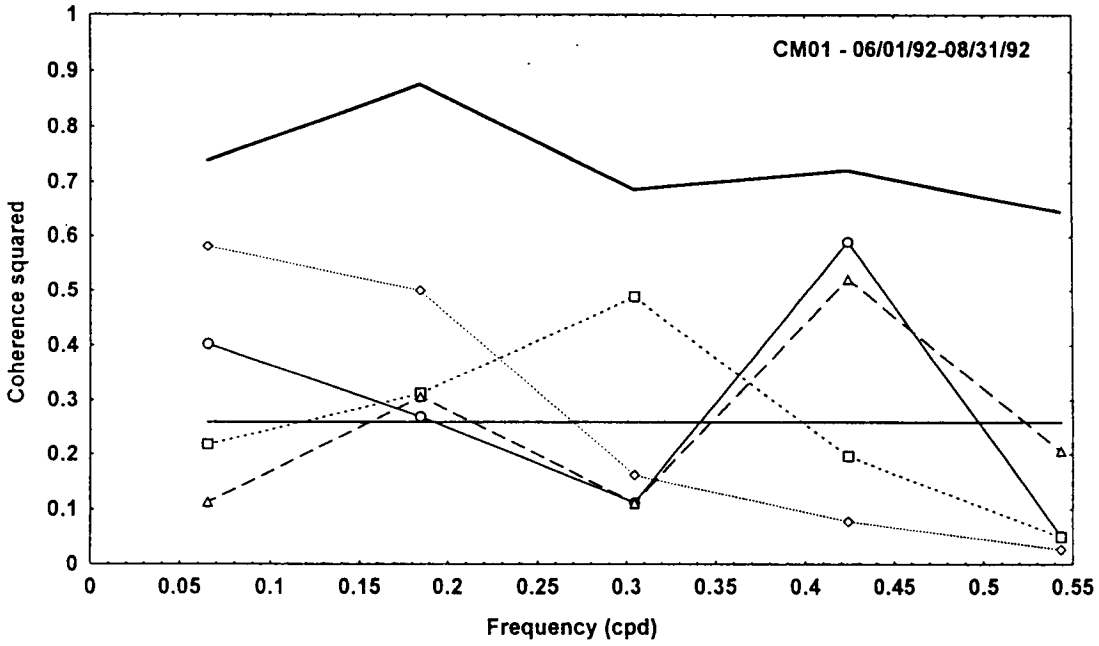

Figure 80. Multiple and partial coherence for south Texas CM1 in upcoast flow season, June through August 1992. Winds are the same as Figure 77 but pressure gradient is computed from (GAL - SPI).

(2) Central Texas At CM23, a very significant result for the summer upcoast regime emerges. In Figure 81, we see that multiple coherence with the four variables accounts for 70 to 80% of current variance over the entire frequency band examined. However, the partial coherence of the longshore sea level slope is clearly the dominant factor controlling current fluctuations in the 2- to 5-day period band. We know from Figure 76 (summer transport regression) that direct wind-driving appeared relatively unimportant in summer in forcing the coastal current. Figure 81 now suggests the longshore barotropic pressure gradient is a principal force in driving fluctuations of 2- to 10-day periods in the longshore current off central Texas.

(3) Central Louisiana At site CM18 in the summer of 1992, the results of the multiple and partial coherence analyses (Figure 82) are strikingly similar to the central Texas result. Seventy to eighty percent of the energy in the currently fluctuations are accounted for by multiple coherence with the four forcing variables. Inspection of the partial coherence of each of the four variables, however, clearly identifies the longshore sea surface slope between the Atchafalaya coast and Galveston as the dominant and highly significant driving force controlling these fluctuations in the 2- to 6-day period band.

In summary, multiple and partial coherence analyses of three inshore current meters in the domain of the coastal plume have shown (a) that during the fall-winter-spring downcoast regime, current fluctuations are controlled largely by the alongshore wind stress and secondarily off central Texas by the longshore surface slope. During the summer upcoast flow regime the forcing of the fluctuations observed in the current in south Texas is less clear but significantly associated with the longshore surface slope and the wind stress components at various frequencies. However, variance in the currents in central Texas and central Louisiana in summer is highly coherent with sea level gradients. We may surmise that the strong southeasterly winds characteristic of south Texas in summer are elevating the water level in the Texas coastal bend (i.e., between Port Aransas and Galveston), which provides an eastward pressure gradient to drive fluctuations in the upcoast flow off central and east Texas and the Louisiana coast.

3. A Wind-driven Model

We continue in more detail our examinations of the importance of the local wind stress on controlling variability in the alongshore current using coincident current meters and wind measurements at two locations. There is only one period at each of these locations of about 5 weeks duration when an S4 current meter located 3 m below the surface operated simultaneously with a buoy-mounted anemometer at the top of the same mooring. One is on mooring 20, the innermost LATEX A mooring, south of Sabine Lake (94° W) in March and April 1993, and the other is at mooring 17, the innermost LATEX A mooring south of Atchafalaya Bay (92° W). Lentz (1995) showed that, in the Amazon River plume, the variability in the along-plume current at the days-to weeks time scale was clearly caused by wind forcing. We will use the same model Lentz (1995) used to simulate the along-plume current fluctuation, i.e., the input of energy from the wind into the surface layer plume is balanced by a linear drag force and the temporal acceleration of the alongshore flow

$$\frac{\partial u_w}{\partial t} + \frac{r u_w}{h} = \frac{\tau_{sx}}{\rho_o h} \qquad (9)$$

where u_w is the wind driven current within the plume, r is a drag coefficient, h is plume thickness, ρ_o is a reference density for the plume, and τ_{sx} is the surface wind stress. Taking a plume thickness from our observations at these sections in the same month and calculating the wind stress adjusted to a 10 m height (wind instrument height is 3.3 m) and using an air-sea drag coefficient of 2.5×10^{-3} we solve (9) for u_w using Laplace transforms similar to Lentz (1995).

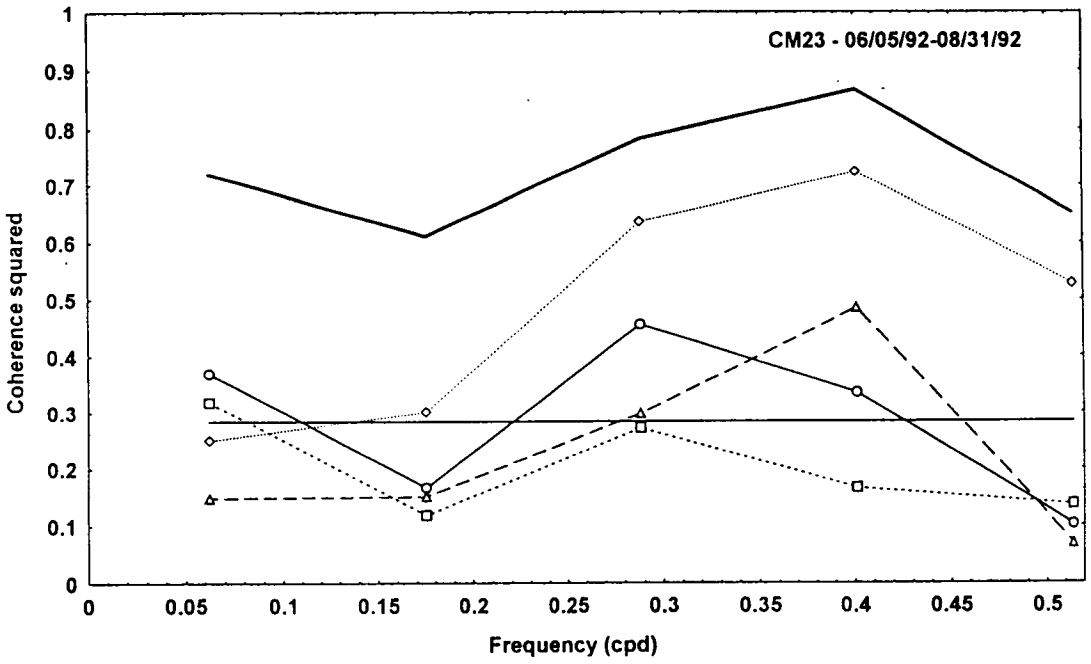

Figure 81. Multiple and partial coherence for central Texas CM23 in upcoast flow season July through August 1992. Wind stresses are computed the same as in Figure 78 but pressure gradient is computed from (GAL - PA).

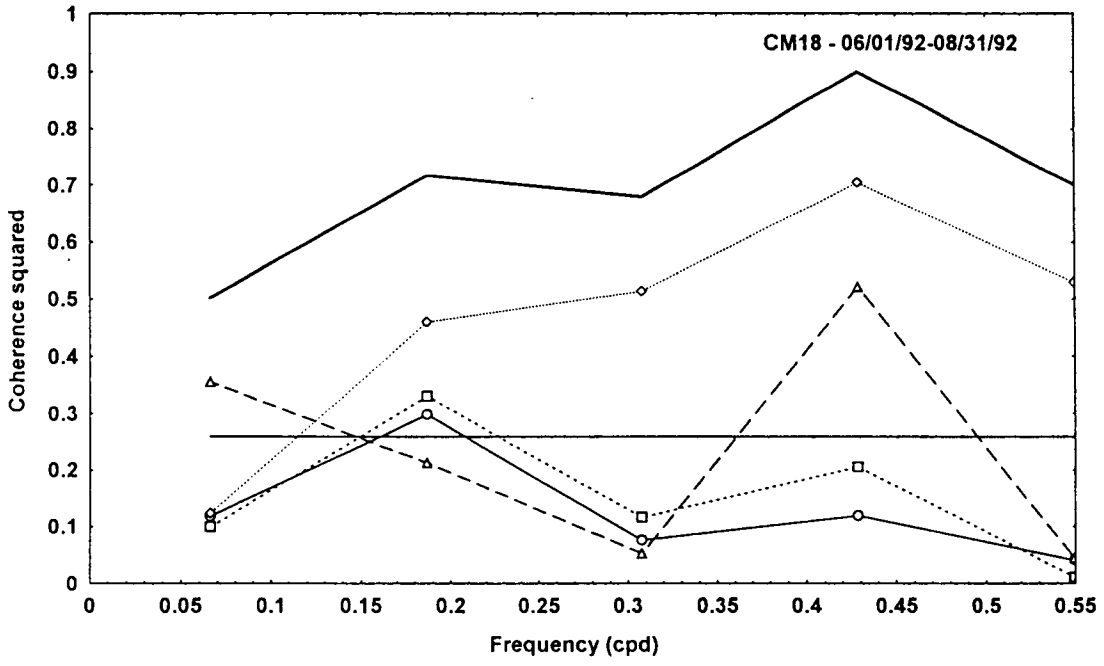

Figure 82. Multiple and partial coherence for central Louisiana CM18. Wind stresses and water levels are computed the same as in Figure 79.

Figure 83a,b compares the current predicted by (9) for both the M17 and M20 moorings to the 40-hour low pass currents from the S4 current meters. Both results provide convincing evidence that major fluctuations of 2- to 7-day time scales, and 20 to 60 cm/sec range are directly wind driven. Both correlation coefficients between the observed and predicted time series of the along-plume currents ($r = 0.82$ at M17 and $r = .77$ at M20) are significant at the 95% level. The simulation at M20 (Figure 83b) is the less impressive of the two; note the under-prediction of the first major peak on March 26 and the over-prediction of the second major peak on April 2. M17 is near the buoyancy source of the Atchafalaya River outflow and wind forcing of a buoyant surface layer should be more effective there in March and April than at M20, 150 km downplume. The longshore pressure gradient, absent from the successful balance of (9) in the 2-7 day period band, is perhaps important for longer time scales.

These results reinforce our earlier conclusion about the dominance of wind forcing on the coastal plume during the spring season of the downcoast flow regime.

4. Comparison to Model Results

At this point, it is instructive to briefly compare our observations of the downcoast regime of the MACP to results from several numerical models prominent in the literature. Chao's (1987) model of a river outflow plume and the coastal plume and current that arises downcoast from it employed an idealized rectangular model basin with dimensions of 200 km alongshore and 111 km cross-shore. The model basin was 30 m deep with a flat bottom. Although not clearly enumerated in the paper, the light water input through the 20 km opening into the basin appears to be 6000 m^3/sec, not unlike our low river discharge of the October 1992 observation. Despite its simplification, especially its 30-m deep flat bottom, a number of general features reported in the wind- driven buoyant plume model of Chao (1987) can be seen in our downcoast plume observations. In the model results, the application to the buoyant plume of a 1 dyne/cm^2 downwelling favorable wind stress narrows the coastal plume and accelerates the nearshore jet from a few cm/sec up to 20 to 50 cm/sec as the plume narrows and deepens, which we observed in many of our downcoast plume sections. The instabilities along the Chao coastal jet are not observed (or resolved) in our data but are likely suppressed by our shallower bottoms. Our jet is wider and shallower and further offshore than the Chao coastal jet (his Figure 10), but we do observe the undercurrent seen in his Figure 10b in many of our sections.

For upwelling favorable winds, the model surface layer of lighter water does surface and expand offshore. However, the well-developed upwelling event we observed at Section S4 and T7 (Figures 35 and 36) in April 1993 with an upcoast wind-driven flow counter to the buoyancy-driven current does not appear likely to reproduce in the Chao model (cf. his Figure 9c).

More recently, Kourafalou et al. (1996a,b) produced a considerably more sophisticated model of the coastal plume that arises along the coast of the South Atlantic Bight from multiple river discharges. Using a Blumberg-Mellor type model, experiments were first conducted using a box model basin with dimensions 500 km alongshore and 200 km cross-shore and with a flat bottom of $h \leq 20$ m and sloping bottoms where the outer depth could reach 100 m. One principal result notes that the plume is "supercritical" if the initial offshore bulge (L) by the river mouth is greater than the width of the coast current (Lc). A major characteristic of a supercritical plume is a meandering coastal current, which was present in the box model results with river discharges ranging from 800 to 3200 m^3/sec. Reduction of depth to 10 m and then to 5 m produced a subcritical plume, which more closely resembled our observational results on the shallow inner shelf of Louisiana. In general, the offshore and alongshore extent of the Kourafalou model plumes appear consistent with our observational results, suggesting the application of this modeling approach to the MACP would be a highly desirable follow-up study.

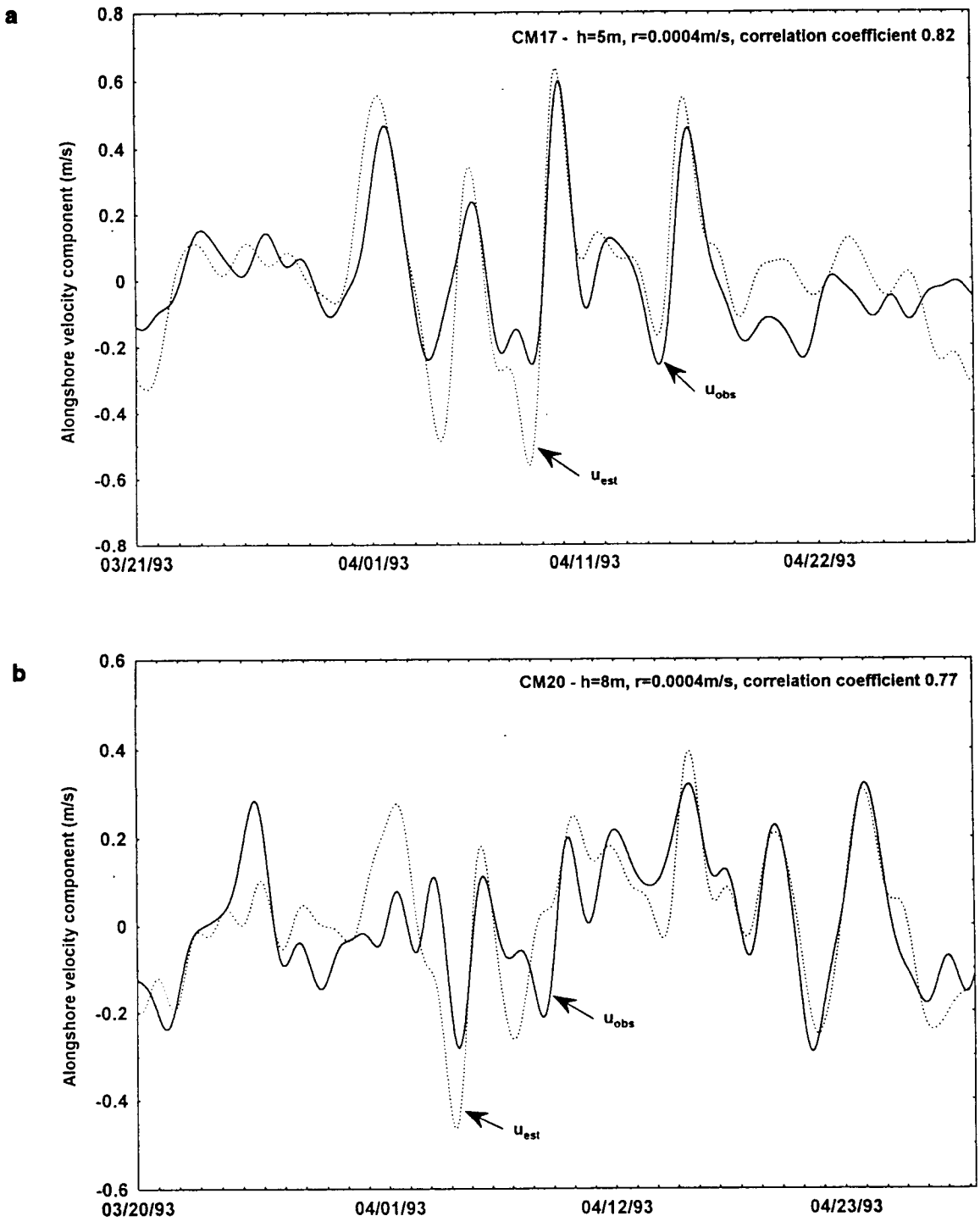

Figure 83. (a) Longshore currents observed at mooring 17, south of Atchafalaya Bay, in March-April 1993 compared to prediction from equation (9); (b) currents are mooring 20 south of Sabine Pass compared to prediction from equation (9).

Other results from this model consistent with our observations are that even a moderate bottom slope produces an elongate and narrow plume. The evolution of the MACP from a wide, sluggish plume off Louisiana to the narrow elongate plume we obsered along the realtively steep Texas shelf appears quite consistent with this result. Additionally, the action of an opposing wind stress in reversing the strictly buoyancy-driven plume (their Figure 12) is more consistent with our observations.

In Kourafalou et al. (1996b), the model is applied with realistic topography, tides and winds to the U.S. South Atlantic Bight. Their results indicate the dominant mode of current variability over the shelf is the large-scale wind-forced barotropic response. The local stratification, however, determines the response of the inner shelf plume water to the wind forcing. These results again appear consistent with our observation of the MACP.

J. Dynamical Scaling

It is appropriate in this concluding section to present our observations of the Mississippi-Atchafalaya coastal plume (MACP) in terms of the dynamical scaling recently put forward by Garvine (1995). Garvine (1995) formulated dimensionless expressions for the terms in the cross-shore (y) and longshore (x) momentum equations applicable to a buoyant coastal plume in terms of the horizontal advection terms (A_x, A_y), the Coriolis acceleration (C_x, C_y), the wind stress (W_x, W_y), the basal stress (B_x, B_y), and the baroclinic pressure gradient (P_x, P_y). As his objective was a dynamical classification of coastal discharges where buoyancy was by definition the dominant driving force, Garvine ignored barotropic pressure gradients terms $g\frac{\partial \eta}{\partial x}$, $g\frac{\partial \eta}{\partial y}$. As our regression analyses indicate the importance of sea level slopes in the dynamics we include scaled terms for $g\frac{\partial \eta}{\partial x}$, $g\frac{\partial \eta}{\partial y}$ consistent with Garvine's (1995) scaling notation.

Defining the usual external Froude number $F' \equiv \frac{U}{c'}$ where U is the nominal alongshore current speed scale and where $c' = \sqrt{gh}$ allows the alongshore barotropic pressure gradient term $g\frac{\partial \eta}{\partial x}$ to be expressed non-dimensionally as

$$P(bt)_x \simeq \frac{F^2}{F'^2}\frac{L}{H}\frac{\partial \eta}{\partial x} \qquad (10a)$$

where the internal Froude number is $F = \frac{U}{c}$ and where c is the internal phase speed defined below and the cross-shore barotropic pressure gradient as

$$P(bt)_y \simeq \frac{F^2}{F'^2}\frac{\gamma L}{H}\frac{\partial \eta}{\partial y} \qquad (10b)$$

Garvine's (1995) equations 5a,b are then restated for the longshore component as

$$\frac{A_x + C_x = P(bc)_x + P(bt)_x + W_x + B_x}{F^2\,KF\;1\;\frac{F^2}{F'^2}\frac{L}{H}\left(\frac{\partial \eta}{\partial x}\right)\frac{KF}{\gamma}\left(\frac{V_E}{HU}\right)\frac{KF}{\gamma}\left(\frac{r}{fH}\right)} \qquad (11a)$$

and for the cross-shore component as

$$\frac{A_y + C_y = P(bc)_y + P(bt)_y + W_y + B_y}{\gamma^2 F^2 \; KF \; 1 \; \frac{F^2 \gamma L}{F'^2 H}\left(\frac{\partial \eta}{\partial x}\right) KF \left(\frac{V_E}{HU}\right) \; \gamma KF \left(\frac{r}{fH}\right)} \qquad (11b)$$

where the baroclinic pressure gradient term in normalized to unity by dividing through by (a) $\frac{c^2}{L}$ in the x momentum equation and (b) by $\frac{c^2}{\gamma L}$ in the y momentum equation. The term c is the internal phase speed = $\left(g\frac{\Delta\rho}{\rho o} H\right)^{\frac{1}{2}}$; $\Delta\rho$ is the mean density difference between the plume and the ambient coastal water, ρ_o the ambient coastal water density, H the mean plume depth, L the alongshore length scale of the plume, γL is the cross-shore length scale of the plume, K is the Kelvin number $\left(K \equiv \frac{\gamma L}{c/f}\right)$ the ratio of the cross-shore length scale to the local internal Rossby radius, V_E is the Ekman volume transport $V_E = \tau_w / \rho_o f$ where τ_w is the wind stress at the 7 to 10 day time scale, f is the coriolis parameter, and r is the basal friction coefficient.

From these scaled equations Garvine (1995) shows that for buoyancy to provide the dominant forcing in the alongshore momentum balance then

$$V_E/HU < O(\gamma/KF) \qquad (12)$$

In other words, if $\gamma/KF \leq V_E/HU$ then the plume structure is dominated by wind forcing . Similarly for the buoyancy forcing to be dominant over the basal friction term in the alongshore balance then

$$\frac{r}{fH} \leq O\left(\frac{\gamma}{KF}\right) \qquad (13)$$

Our observations in the MACP give the nominal values shown in Table 7 for these parameters at a weekly time scale for the two seasonal flow regimes.

Table 7. Values for scaling analysis.

Regime	U	γ	L	K	F	r	H
Downcoast	.3 m/sec	.16	300 km	7	0.6	4 x 10-4 m/sec	5-8 m
Upcoast	.2 m/sec	.50	200 km	14	0.4	2 x 10-4	5 m

We calculate V_E using a 5 m/sec wind in the downcoast regime and a 2 m/sec wind in the upcoast regime. Testing the relative importance of buoyancy forcing for the MACP equation (12) shows that $\frac{\gamma}{KF} \simeq .04$, and $\frac{V_E}{HU} \simeq .36$ so that wind is clearly dominant over buoyancy forcing as our data analysis indicated. Similarly, with the basal friction term $\frac{r}{fH} \simeq 0.05$ the buoyancy term in (13) is clearly secondary again.

Our observations in the MACP provide the values shown in Table 8 for (11a), the longshore balance.

Table 8. Scaling of longshore balance.

Regime	A_x	+	C_x	=	$P(bc)_x$	+	$P(bt)_x$	+	W_x	+	B_x
Downcoast	0.4		4.2		1		5.3, 3.6		13.3		20.5
Upcoast	0.4		8.4		1		2.7		1.9		9.3

where P(bt)x is obtained from inspection of time series of sea level differences between Galveston-South Padre Island, Galveston-Port Aransas, and Atchafalaya Bay coast-Sabine Pass. Differences between time series demeaned over the record lengths of 3 months and 9 months all indicate relative alongshore slopes of ~ 2 to 3 x 10^{-7}. Thus, wind stress, basal stress and the barotropic pressure gradient are expected to be the dominant forces in the longshore balance in agreement with our multiple-partial coherence studies above. In the summer upcoast regime the coastal plume is clearly wider (~ 100 km) and shorter (~200 km) and the wind stress is weaker (~2 m/sec). Taking r = 2 x 10^{-4} m/sec the longshore balance changes slightly with the greatly decreased importance of wind stress and the enhanced importance of the barotropic pressure gradient and Coriolis term.

In the cross-shore momentum balance during the downcoast regime, using a 10-cm change in sea level over the cross-shore plume width γL, we estimate values of the terms in (11b) as in Table 9.

Table 9. Scaling of cross-shore balance.

Regime	A_y	+	C_y	=	$P(bc)_y$	+	$P(bt)_y$	+	W_y	+	B_y
Downcoast	0.01		4.2		1		4		3.0		0.8
Upcoast	.04		5.6		1		2		0.2		1.6

This result suggest the cross-shore flow is not a strictly geostrophic balance between the pressure gradient terms and the coriolis force but that wind driving can also be significant. The horizontal advection terms are again negligible. In the summer upcoast regime, we estimate only a 5-cm sea level difference over the cross-shore length scale γ L (100km). The results in Table 9 suggest the cross-shore balance in the summer up coast regime is again not strictly geostrophic but between the Coriolis term, the pressure gradient terms, and the basal frictional stress, which are of 0(1). The wind stress appears to be of $0(10^{-1})$ and the horizontal advection term $0(10^{-2})$.

We note that these dynamical scaling arguments are only expected to produce estimates reasonable to within an order of magnitude. Nonetheless, it is quite encouraging that there is general agreement between the dynamical approach and the statistical analyses discussed earlier.

K. Summary

Observations from our five cruises, each of six-to-seven-day duration, have provided an unprecedented visualization of the three-dimensional nature of the Mississippi-Atchafalaya coastal plume (from the Mississippi River delta westward to south Texas) with regard to its large-scale hydrographic and velocity structure. CTD observations (over 100 on each cruise) and underway thermosalinography and ADCP data allow us to evaluate the temporal variability (e.g., the effect of frontal passages) at the synoptic time scale, and the seasonal variability between the long fall-winter-spring downcoast regime and short summer upcoast regime.

1. Downcoast (Fall-Winter-Spring) Regime

Three of these five observations of the coastal plume occurred during April 1992, 1993, and October 1993 when prevailing downcoast wind stresses are expected to generate a coastally trapped elongated plume of low salinity water extending from the source region of the Atchafalaya and Mississippi Rivers westward and southward into south Texas and the Mexican border region. Our observations of the near surface salinity field (see e.g., Figures 11, 27, and 41) bore out these expectations. Westward along the Louisiana coast from the source region we observed in all three cases a low salinity plume with a cross-shore length scale of 50-70 km and vertical depth scales of 10-12 m. We observed that the plume contracted abruptly to a width of 30-40 km in the Sabine-Galveston region, where the depth contours converge toward the coast as the coast begins its great bend toward a southwest and southern orientation. SCULP drifter velocities show that a wide sluggish flow off western Louisiana collapses in the same location into a narrow high speed coastal jet that continues all the way south to the Mexican border.

While all observations showed the elongated downcoast low salinity plume, these three observations during the nine months of downcoast wind regime were all subject to different short-term (three-to-seven day) wind forcing. The April 1992 observation was characterized by the intense wind shifts of three frontal passages (Figure 8) along the Louisiana coast and a period of intense southerly winds off the central and south Texas coast. The April 1993 observation was characterized by an unusual period of westerly, upcoast winds on the Louisiana coast and another period of strong southerly winds off central and south Texas (Figure 26). The wind forcing during the October 1992 observation, interrupted by only a brief frontal passage while sampling off the Atchafalaya delta, was closest to a scenario of steady easterly winds (Figures 39, 40) that would produce a steady state plume. The major perturbations to this conceptual steady state plume are caused by wind shifts associated with migrating synoptic scale weather systems, often involving frontal passages. As documented in Figure 8, such systems involve an abrupt shift from southeasterly to northwesterly winds, which then rotate clockwise to northerly, northeasterly, and eventually returning to southeasterly as the atmospheric system passes to the east. Because we were sampling different segments of the plume during the various stages of wind forcing, we illustrate plume response with schematic diagrams of a composite of our three separate observations of the downcoast plume (Figure 84a-d). Figure 84e is a schematic composite of the upcoast plume.

The prototypical downcoast plume is shown schematically in Figure 84a. In the source region, the combination of the fresh water from the Mississippi delta area and the Atchafalaya outflow produces a transport of 50-70 x 10^3 m^3/sec of plume water along the coast, which has a fresh water component of 8-14 x 10^3 m^3/sec. The merger of the plume water coming from east of the Atchafalaya with the Atchafalaya outflow plume itself appears, from our few sections, to be a complex non-linear process highly variable in space and time (see e.g., Figures 19 and 20). It will require a more detailed and focused study to determine its spatial structure and temporal variability. Off western Louisiana, persistent easterly winds maintain a coastal plume structure with a width of ~50 km and a vertical scale of 10 m. As it moves downcoast, dilution of the plume by mixing

appears rather weak as nominal salinity increases only 2 psu—from 27 psu off Atchafalaya to 29 psu off Cameron. Currents are 10-20 cm/sec in this segment of the plume.

Figure 84a shows that near Galveston the steady state plume contracts into a narrow, high speed jet that can continue all the way to the Mexican border and beyond. While the jet maximum is observed within 12 km of the coast (Figure 49), its cross-shore length and depth are 30 km and 14 m, respectively. Another mode frequently observed in both thermal satellite and drifter data shows the plume water drawn offshore in south Texas in an offshore jet caused by the interaction of a cyclone-anticyclone pair. These cyclone-anticyclone pairs (or modons) are apparently associated with the decay of Loop Current eddies after they impact the western wall of the Gulf basin.

In the early stages of a frontal passage, illustrated in Figure 84b, winds are northwesterly shifting to northerly for 6-12 hours. The northwesterly winds and perhaps adjusting pressure gradients initially decelerate the central-south Texas coastal current and reverse the flow in the plume along the Louisiana coast. The Atchafalaya and Mississippi River outflow plume are temporarily driven southeasterly, disrupting the injection of freshwater into the downcoast plume. When the wind rotation eventually reaches a northerly orientation, the alongshore component of the wind stress in south and central Texas increases markedly and the downcoast jet reappears. This strong offshore wind is along the western Louisiana coast and produces a quasi-stagnant plume (Figure 21), which is, however, mixed nearly to vertical homogeneity (Figure 16) by the intense wind action.

As the wind rotates further to northeasterly there are downcoast wind stress components all along the coastal plume (as illustrated in Figure 84c). The coastal plume water on the shallow Louisiana shelf returns to a broad, moderately energetic downcoast state. The Texas extension of the coastal plume intensifies to speeds of 50-75 cm/sec. In a special case of this wind phase observed by Barron and Vastano (1994), a lingering high pressure system centered northeast of Louisiana brought five days of northeasterly winds to the northwestern Gulf Coast. Four ARGOS drifters initially located (it appears) in coastal plume waters along a line stretching between 90° W (west of the Mississippi delta) and 95° W (southwest of Galveston) all moved coherently downcoast for the five days of northeasterly wind forcing at a mean speed of 53 cm/sec.

In the waning stages of the frontal passage cycle, illustrated in Figure 84d, northeasterly winds weaken to 2-4 m/sec and gradually shift to southeasterly winds of 3-5 m/sec. Off south Texas, however, a period of strong southeasterly winds (10-15 m) often occur in this phase bringing severe wave conditions and a strong upcoast current regime that we (unfortunately) sampled on both the April 1992 and April 1993 cruises. These strong southeasterly wind episodes propagate northward at least as far as Galveston, reversing and driving the coastal current upcoast with it. Examples of this flow regime from our observations are seen in Figures 23 and 24 (ADCP) and Figure 17 (salinity). During this phase, a convergence develops between the strong upcoast current on the Texas coast and the more sluggish westward drift of the coastal plume water on the Louisiana shelf illustrated in Figure 84d. We, in fact, by chance observed this stage directly on the return leg from south Texas on the April 1992 cruise (see Figure 85). The ship transited along the 15 m depth contour and observed the strong upcoast current off Texas, the offshore flow in the convergence zone south of Galveston and westward flow on the Louisiana shelf. After this stage winds with persistent easterly components may set in for several days, the south Texas winds weaken, the steady state downcoast plume re-establishes itself as illustrated in Figure 84a.

A

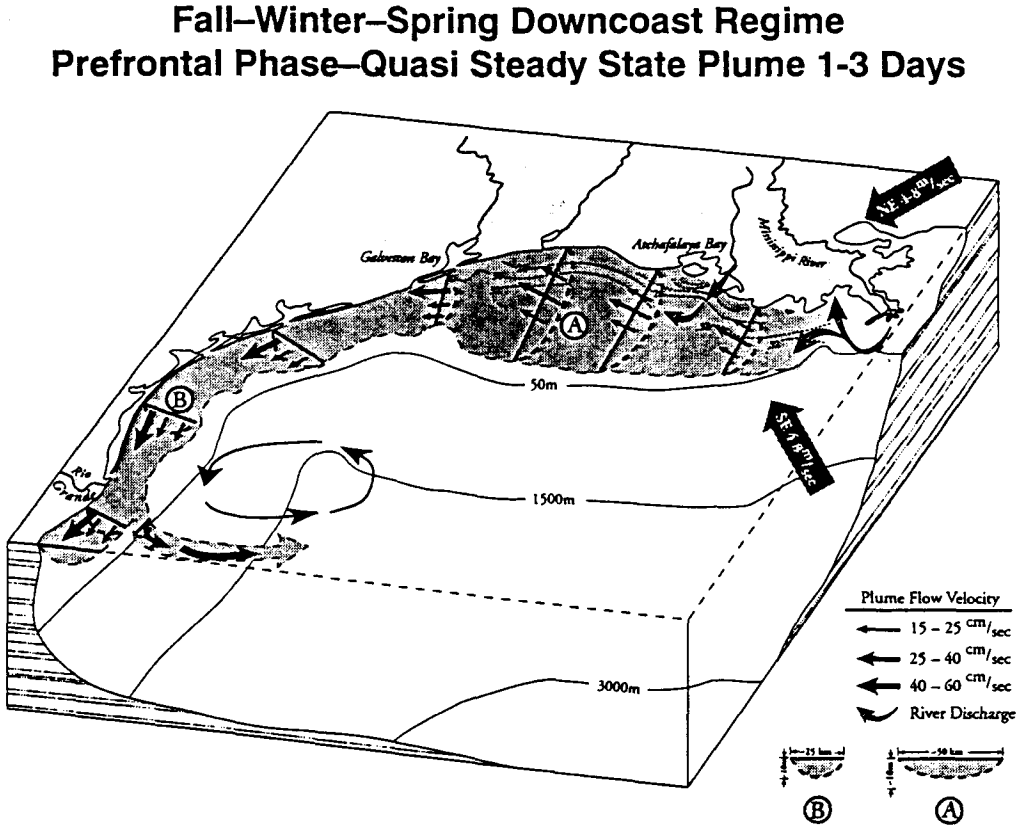

Figure 84. (a) Schematic diagram of a quasi-steady state coastal plume under persistent easterly wind forcing. Note the narrowing and acceleration of the coastal plume near Galveston and the frequently observed offshore jets near the Mexican border. Salinities are from the October 1992 observations. (b) Schematic diagram of the downcoast coastal plume in the early phase of a frontal passage with northwesterly-northerly wind forcing. (c) Schematic diagram of the downcoast coastal plume during the late phase of a frontal passage when winds are shifting from northerly to northeasterly. (d) Schematic diagram of the downcoast coastal plume during the waning stage of a frontal passage when weak easterly component winds are present off Louisiana, and strong southeasterly winds range north along the Texas coast, causing a convergence in the coastal plume currents. (e) Schematic diagram of the coastal plume during the upcoast (summer) flow regime.

B

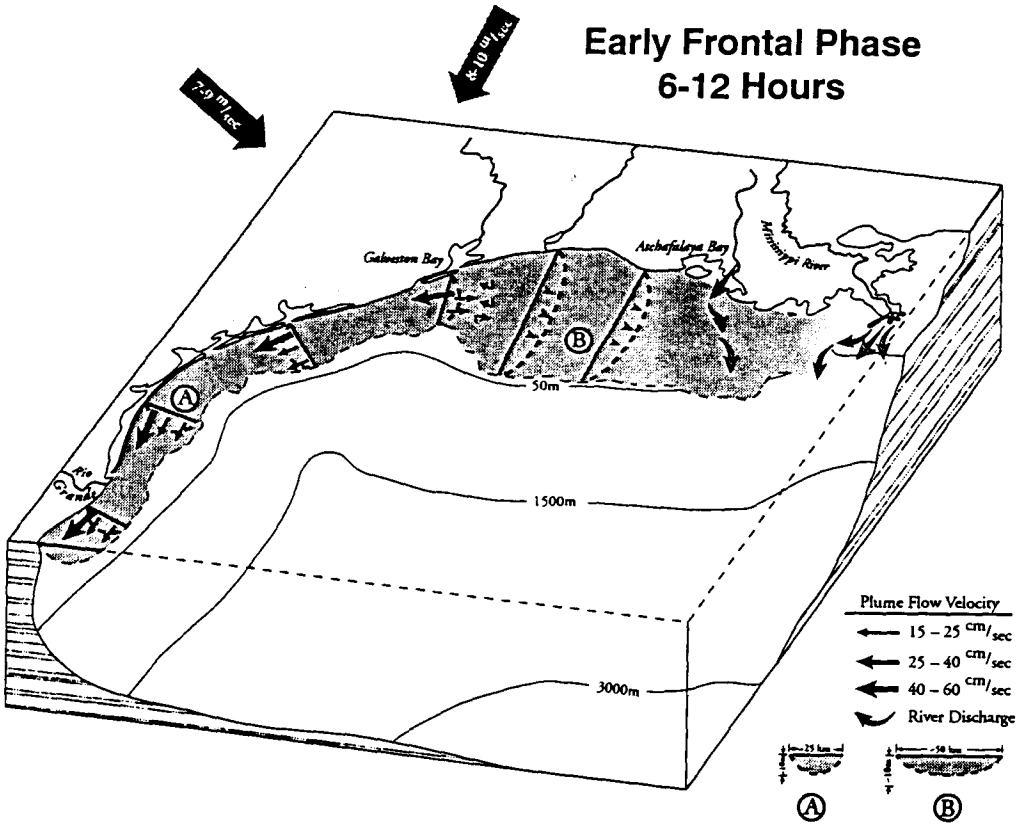

Figure 84 cont'd.

C

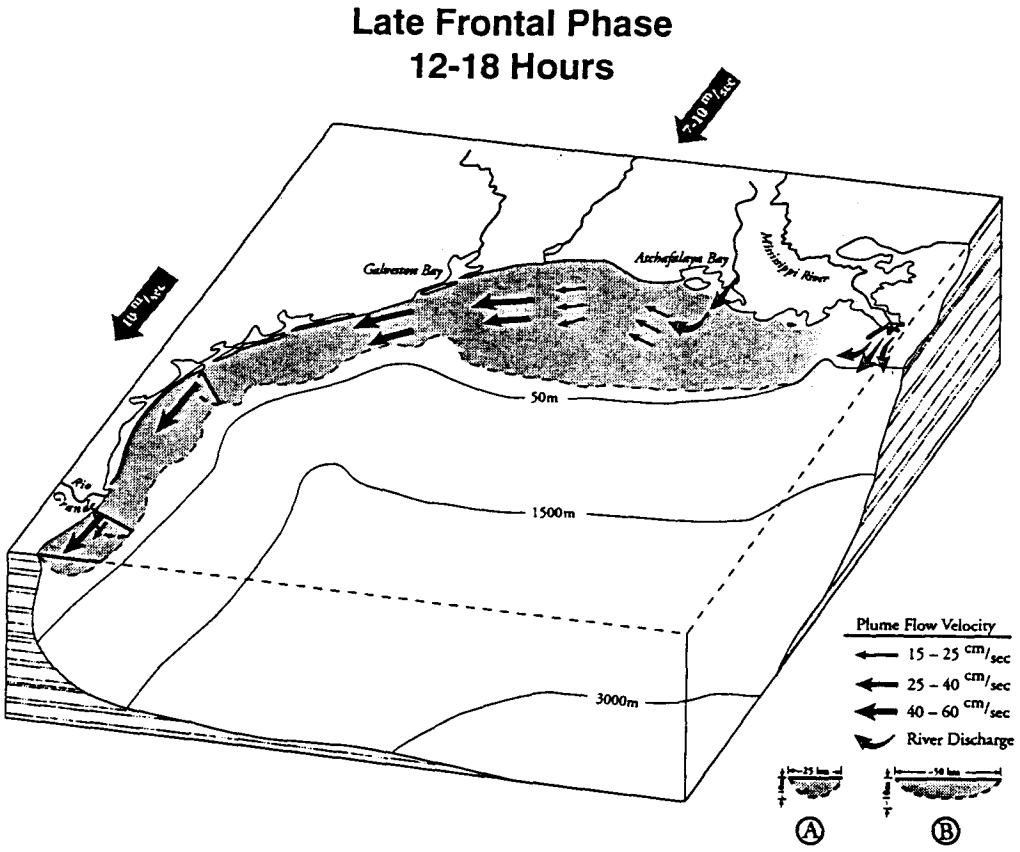

Figure 84 cont'd.

D

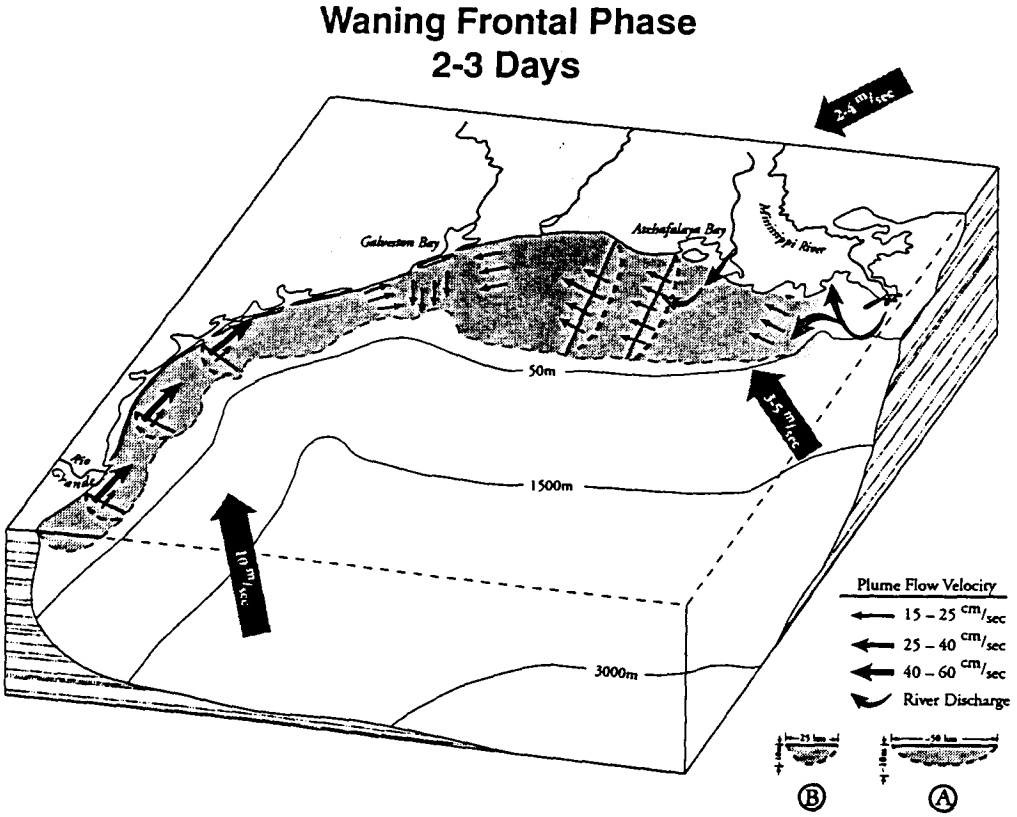

Figure 84 cont'd.

E

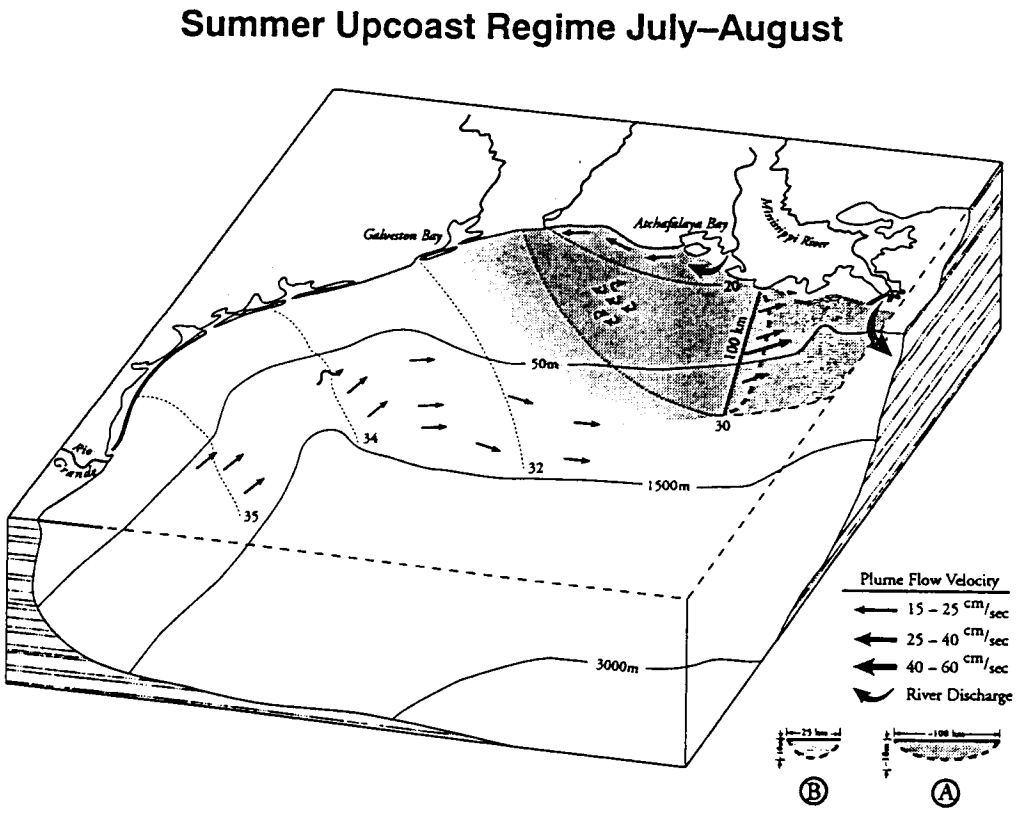

Figure 84 cont'd.

2. Upcoast (Summer) Regime

Our two observations of the coastal plume in the summers of July 1993 and 1994 give a consistent picture, illustrated in Figure 84e, except, of course, that the volume of plume water is larger in 1993, the great flood year. With net upcoast wind stresses probably assisted by longshore pressure gradients, high salinity Gulf of Mexico water pushes upcoast driving the relict plume back up eastward. The relict plume water of ~ 20-30 psu salinity appears to display a chaotic motion characterized by small scale 10-15 km mixing elements, imparting a cellular structure to the flow field. Based on our July 1994 cruise data and the August 1994 LATEX A cruise, it appears the eastward drift of this zone is ~4-6 km/day. Salinity patterns and drifter data suggest the Atchafalaya outflow advects westward in a narrow band trapped near the coast. Lateral mixing processes apparently incorporate the new plume water into the body of relict plume water, which is itself drifting slowly albeit chaotically eastward.

The schematic (Figure 84e shows that at the eastward end of our observation domain (S2-S1) the highly buoyant summer plume appears to organize into a coherent jet (Figure 68) as it is forced to round the bathymetric promontory south of Isle Dernier. With this general understanding of the scales and variability of the MACP in hand, we next investigate important hydrographic properties in more detail and examine forcing and response in different seasons and different regions.

3. Results of Analyses

Our detailed observations of the salinity field within the coastal plume are readily converted to an absolute freshwater distribution, mapped as an equivalent height of fresh water. As observed previously (Dinnel and Wiseman, 1986; Etter, 1996) the major freshwater concentration is in a narrow band along the coast. During the downcoast flow regime we observed 2 to 3 m of fresh water in the coastal plume off Louisiana and 3 to 4 m along the central Texas coast where the coastal plume has narrowed.

During the summer upcoast regime, the offshore Ekman flow of the surface leads to a maximum accumulation of 5 m of freshwater at mid-shelf with an apparent eastward extension. A secondary high of 3.5 to 4 m of fresh water accumulates in front of Atchafalaya Bay that appears to displace westward in the shallow waters along the coast. Except for the anomalously high values of July 1993, caused by the extreme flood of that year, the freshwater content of the (standard area) coastal plume falls in a relatively narrow band of 53 to 66 km^3 of fresh water with little relation to the annual flood cycle. As the volume of the standard grid is 323 km^3, we note that the coastal plume is typically composed of 20% fresh water, which corresponds to a nominal of average salinity of 29 psu. The interannual variability in the Mississippi-Atchafalaya River flood cycle appears to exert far more control on the freshwater content of the coastal plume than the seasonal cycle of river discharge.

Estimates of flushing time for the coastal plume are based on observed river discharges for the Atchafalaya and Mississippi Rivers. Regardless of the strength of river discharge or the seasonal dominance of upcoast or downcoast wind forcing, we find flushing times fall in the range of 2 to 3 months, considerably less than the 8 to 12 months noted by Dinnel and Wiseman (1986) for the entire western Louisiana-Texas shelf.

The high variability of wind forcing on a day-to-day basis likewise produces a high variability in our observation of transport within the coastal plume. Nonetheless, we obtain a coarse but useful estimate of such transport by averaging over blocks of coastal normal sections. Despite our rather small sample of five observations of the coastal plume, it is notable that the "windy" months of April 1992 and 1993 have transports ~70 x 10^3 m^3/sec in the coastal plume,

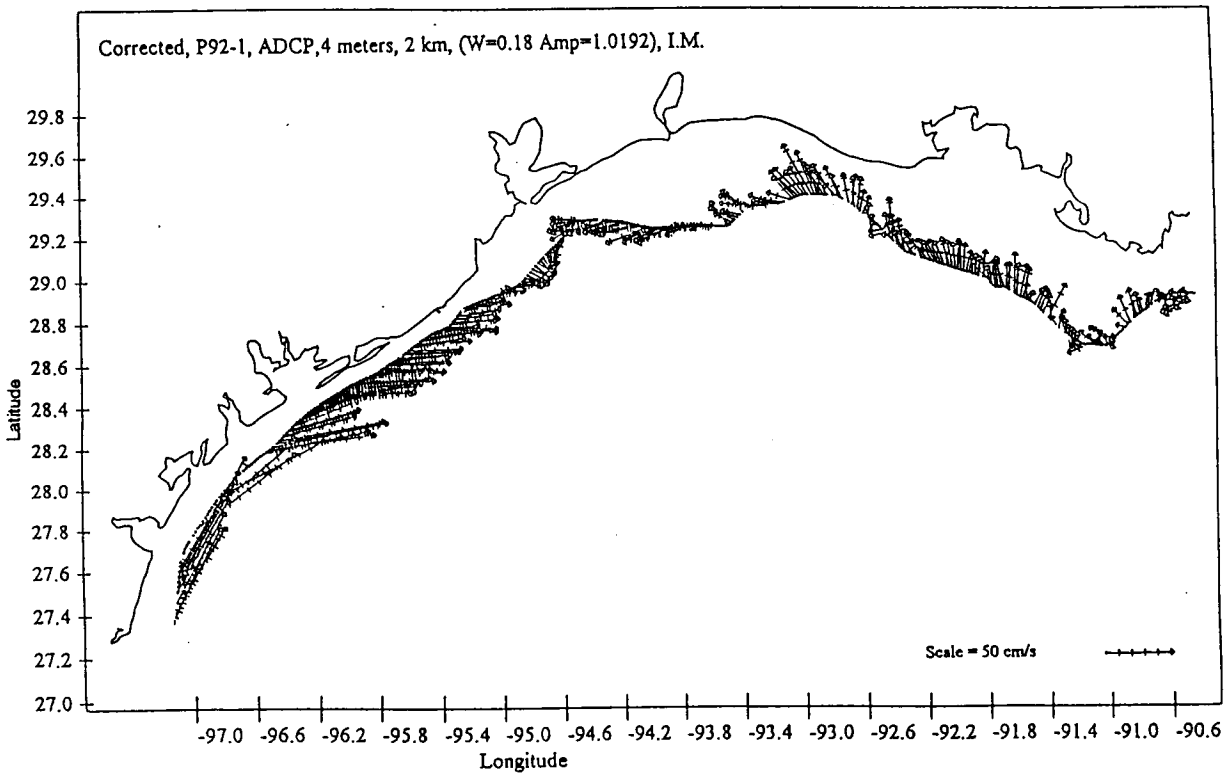

Figure 85. ADCP data from the return leg of the April 1992 cruise. Note the ship transited through a strong wind-driven upcoast current regime off central Texas, a convergence zone south of Galveston, and westward flow off western Louisiana.

which decreases to 52 x 10^3 m^3/sec during a "normal summer, i.e., July 1994. During the summer of the 1993 great flood, the wind stresses are slightly smaller than in the summer of 1994, yet the 1993 volume flux in the coastal plume doubles in magnitude over the summer of 1994. We suspect the role of large scale pressure gradients associated with the massive volume of fresh water on the shelf is important in this regard.

Using an integral form of the longshore momentum balance, we show that a reasonably linear relationship exists between transport (per unit area) of the coastal plume at each section and the local wind stress (Figure 75). This supports the operation of a simple frictional balance of wind stress and linear frictional resistance over time scales of several days-to-a-week in the longshore momentum balance. At zero wind stress the transport per unit area is not significantly different from zero, suggesting the lack of importance of buoyancy forcing in the MACP. Similar analysis for the two summer upcoast observations (Figure 76) indicates an entirely different result, i.e, the sectional transports are quite unrelated to local wind stress.

To investigate further the roles of wind forcing, pressure gradient forcing, and buoyancy forcing within the coastal plume domain, we employed multiple and partial coherence analyses. We selected three inshore current meters from the LATEX A array to represent the plume response in western Louisiana (No. 18), central Texas (No. 23), and south Texas (No. 1). These analyses showed that during the fall-winter-spring downcoast regime current fluctuations are, in all three regions, controlled by the alongshore wind stress and, secondarily, off central Texas by the longshore surface slope. During the summer upcoast flow regime the forcing of the fluctuations observed in the current in south Texas is less clear but significantly associated with the longshore surface slope and the wind stress components at various frequencies. However, variance in the currents in central Texas and central Louisiana in summer is highly coherent with sea level gradients. It appears likely that the strong southeasterly winds characteristic of south Texas in summer are elevating the water level in the Texas coastal bend (i.e., between Port Aransas and Galveston), which provides an eastward pressure gradient to drive fluctuations in the upcoast flow off central and east Texas and the Louisiana coast.

Because these analyses identify wind forcing as a primary driving force of the MACP, we next successfully simulate the observed variability in the current with a simple model of the along plume momentum balance, as employed by Lentz (1995) in the Amazon plume. Appropriate data for such an analysis were extremely limited, i.e., very near-surface currents and an adjacent moored anemometer, but two data sets, of 5 weeks duration, one off east Texas and one off central Louisiana, were identified. Both results provide convincing evidence that major fluctuations of 2- to 7-day time scales, and 20 to 60 cm/sec range are directly wind driven. Both correlation coefficients between the observed and predicted time series of the along-plume currents ($r = 0.82$ at M17 and $r = 0.77$ at M20) are significant at the 95% level. These results, combined with the transport and multiple-partial coherence analyses, document the dominance of wind forcing on the coastal plume during the spring season of the downcoast flow regime.

In the final section we employ the scaling arguments of Garvine (1995) to determine if these dynamical based approximations are consistent with our statistical analyses of the observations of the MACP. The scaling analysis of the alongshore momentum balance shows that wind stress, basal stress and the barotropic pressure gradient are expected to be the dominant forces in agreement with our multiple-partial coherence studies. In the summer upcoast regime the longshore balance changes somewhat with the greatly decreased importance of wind stress and the enhanced importance of the barotropic pressure gradient and Coriolis term. Comparison of the scaled terms for buoyancy forcing, wind driving, and basal resistance specifically show that buoyancy forcing is a relatively minor driving force in the MACP.

In the cross-shore momentum balance during the downcoast regime, the results suggest the cross-shore flow is not a strictly geostrophic balance between the pressure gradient terms and the Coriolis force but that wind driving can also be significant. The horizontal advection terms are also negligible. In the summer upcoast regime, the results suggest the cross-shore balance is again not strictly geostrophic but between the Coriolis term, the pressure gradient terms, and the basal frictional stress, which are of 0(1). The wind stress appears to be of $0(10^{-1})$ and the horizontal advection term $0(10^{-2})$.

We note that these dynamical scaling arguments are only expected to produce estimates reasonable to within an order of magnitude. Nonetheless, it is quite encouraging that there is general agreement between the dynamical approach and our statistical analyses of observations of the coastal plume.

III. Circulation and Hydrographic Structure in the Vicinity of the Mississippi River Delta

by Lawrence J. Rouse, Jr.

A. Introduction

The Mississippi River and the adjacent Louisiana Bight (Figure 86) constitute an estuarine system of considerable size and importance. Because of the large size of the adjacent brackish water bays that serve as nursery grounds, the Louisiana Bight is one of the most important and productive fishing grounds in the United States. It is also the site of large-scale oil and natural gas production and the location of a major offshore oil terminal. An understanding of the circulation in the region is of considerable importance for the wise management of fisheries resources and for prediction of the movement of accidental oil spills.

The interaction of the discharge plume of the Mississippi River with the Gulf of Mexico is complex. The discharge of the Mississippi River enters the coastal waters of Louisiana through a few major passes and a large number of smaller passes and crevasses. The discharges from these various sources mix quickly within a few kilometers. At the sampling scale of this survey (5 to 10 km), the discharge of the river can be viewed as a diffuse, curved line source. The strong vertical stratification of the water column near the river mouths effectively isolates surface waters from the deeper waters and inhibits mixing. These surface waters are also moved about very readily by changes in the wind stress (Rouse and Coleman, 1976). Further away from the mouths the stratification weakens, cross interface mixing is increased, and the response to shifts in the winds is not as dramatic.

In spite of its importance, the waters in the vicinity of the Mississippi River delta have been the focus of only a few studies. The oldest known observations, with a broad spatial extent, of the physical oceanography of this region are from a study commissioned by the Louisiana Offshore Oil Port, Inc. during the early 1970's (Wiseman et al., 1976). Salinity and temperature fields of the bight west of the delta were mapped on eight occasions between July 1973 and April 1974, at a station spacing of approximately 9 km. Not all stations were occupied on each cruise since bad weather occasionally reduced the length of a cruise. Using the low salinity water discharged from Southwest Pass as a tracer, Wiseman et al. (1976) often found a plume of water extending westward from the pass and recurving anticyclonically into the bight. The same pattern has been observed in satellite images (Rouse and Coleman, 1976; Walker, 1996a) and in drifter data (Hitchcock et al., 1997). A second set of five cruises was undertaken by the Southeastern Biology Laboratory, National Marine Fisheries Service, between March 1975 and May 1977 as part of the Ground Fish Survey Project. These cruises acquired CTD casts, compiled by Allen and Turner (1977), in conjunction with the ground fish trawls and covered a wide area on both sides of the Mississippi River Delta. Stations were not repeated from cruise to cruise and station locations were semi-randomly placed in keeping with the ground fish sampling strategy.

A third series of cruises, sponsored by the Louisiana Board of Regents focused on the near-field biological responses to inputs from the Mississippi River (Dagg et al., 1988). These cruises also had no synoptic sampling plan. Samples were taken opportunistically at fronts associated with the Southwest Pass plume and in waters of varying salinities out to the high salinity waters of the open gulf. Most of the stations were within 35 km, of the mouth of Southwest Pass, though some stations were as far

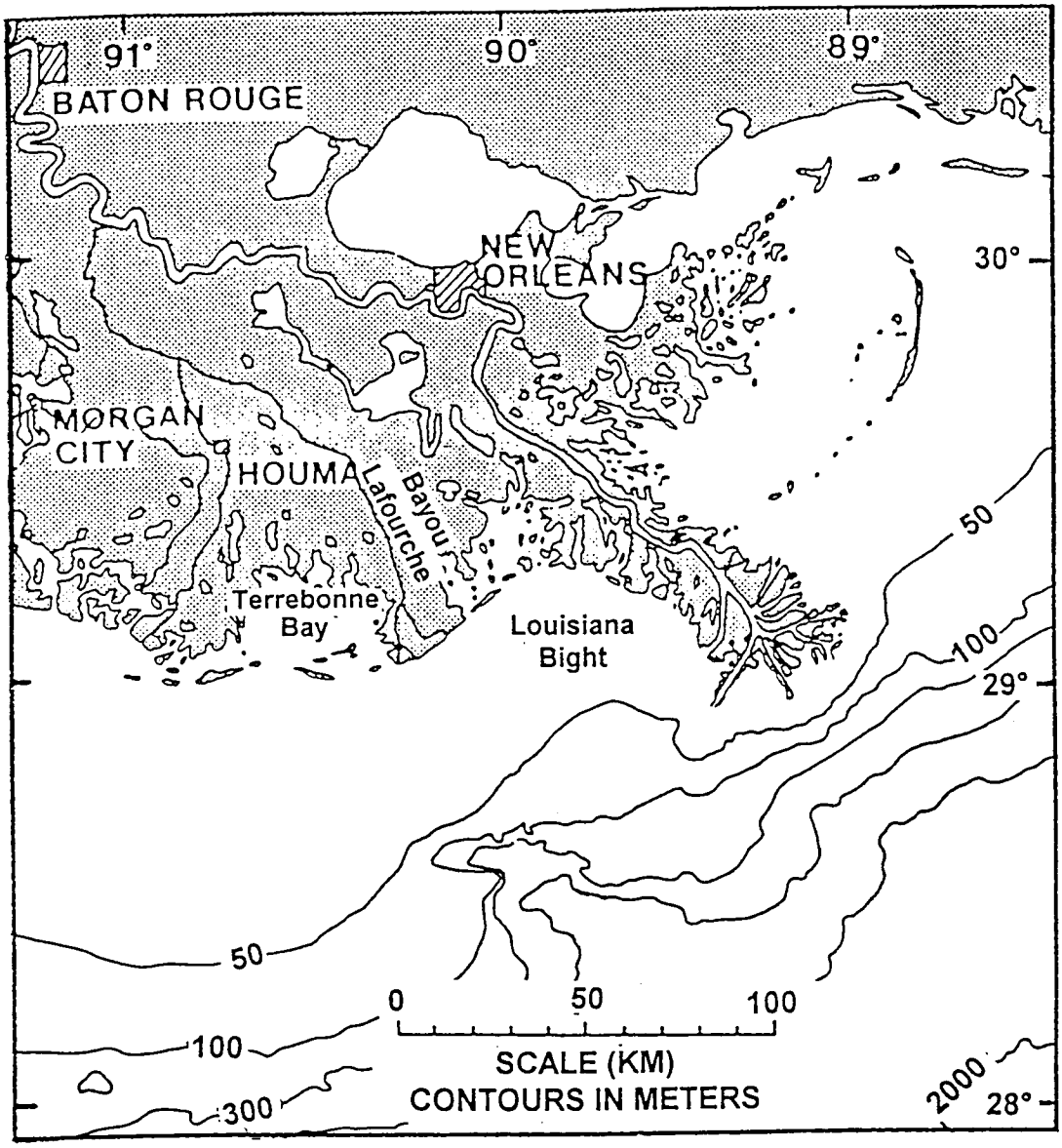

Figure 86. Site map of near-field plume cruise.

away as 70 km. A fourth data set has been acquired on a series of cruises, begun in 1985, undertaken by Rabalais and her co-workers (Rabalais et al., 1994) as part of the investigation of the extent and causes of hypoxic conditions on the Louisiana shelf. Each of these cruises, which sometimes extended to the upper Texas shelf, had several transects in the region examined by this task.

A fifth data set was acquired by a series of cruises associated with the Nutrient Enhanced Coastal Ocean Program (NECOP) effort in the vicinity of the Mississippi River. Most of the cruises in the NECOP effort were driven by a biological sampling scheme aimed at biological and chemical interactions. Four of the cruises, however, were classical CTD surveys. These cruises in March-April, 1992, May, 1992, April, 1993, and July, 1993 occupied a grid from the Mississippi Delta to west of the Atchafalaya River. The grid spacing for those cruises was about twice as great as this LATEX-B task though many of the same stations were occupied on successive cruises. The analysis of the data is not complete and no results have yet been published (Scott Dinnel, personal communication).

B. Objectives

The rationale for this task is that it is important to characterize the discharge and mixing dynamics, at scales of 10's of kilometers, of the Mississippi River, a major contributor to the Louisiana-Texas inner shelf waters. The objective of the cruise was to characterize the region of the Louisiana shelf in the immediate vicinity of the Mississippi River delta in terms of its physical and hydrologic properties. Specific questions that have been addressed are:

- What is the dynamic hydrographic structure of the region produced by the distribution of freshwater delivered to the shelf by the Mississippi River?
- What is the variability of this hydrographic structure at short time scales (five to ten days)?
- What is the structure of the velocity field?
- How is this variability related to changes in the wind stress?
- Does the discharge of the Mississippi River contribute directly to the coastal plume or only to a general freshening of the shelf?

C. Description of Data Collection

As part of the LATEX-B portion of the Louisiana-Texas Shelf Physical Oceanography Program, single cruise on the RV Pelican was undertaken in April, 1994 to investigate the transport and dispersion properties of the region immediately adjacent to the Mississippi River Delta (Figure 86). The cruise had two phases that surveyed this region. The first phase covered the shelf from the coast to the shelf edge and from Timbalier Bay to just east of the Mississippi River Delta. The second phase was a resurvey of most of the area covered in the first phase (the area to the east of South Pass was not included in this resurvey). This paper will describe the hydrographic and ADCP observations acquired during these two phases of the cruise (hereafter called Phase 1 and Phase 2).

The discharge of the Mississippi River, in April of 1994, was rising to the 1994 peak discharge of slightly more than 32,500 m^3/s in early May (Figure 87). During the cruise, the discharge averaged about 26,500 m^3/s. For several days prior to this cruise, the winds were generally from the southeast increasing from 5 to 10 m/sec on 11 April

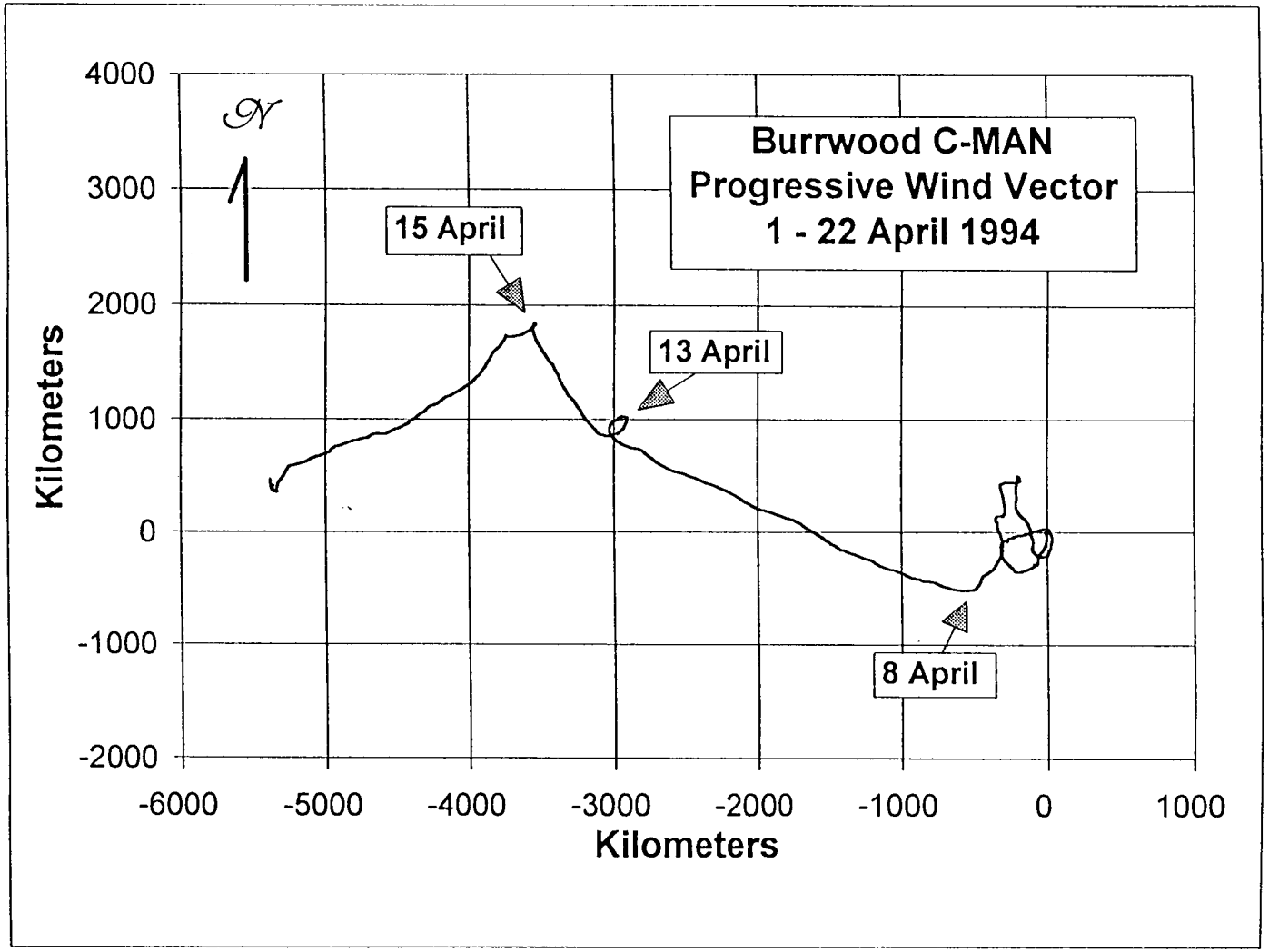

Figure 87. Progressive vector plot of the wind measured by the NOAA C-MAN station at Burrwood, LA (BURL1) for the period 1-22 April 1994.

(Figure 2). These southeast winds decreased to 5 to 7 m/sec for most of the first phase of the cruise, which began on 12 April. On 13 April a weak front passed through the region producing a complete rotation of the wind. By 14 April the wind had returned to the southeast. Near the end of the first phase a wind shift occurred with the movement of a stronger cold front through the region. Winds shifted to the northeast and had settled down to 3 to 7 m/sec by the beginning of the final phase of the cruise on the afternoon of 17 April. These two distinct wind regimes provided an opportunity to observe the variability of the synoptic distribution of freshwater and other properties of the discharge under distinctly different wind forcing conditions.

Approximately 2200 kilometers of sea surface properties were observed with the flow-through system on-board the Pelican. ADCP observations were also made along the entire track. The ADCP observations were obtained by a 1200 Hz unit in both the bottom tracking and the differential GPS modes. The ADCP profiles were obtained as 2 minute time averages using 1 meter vertical averages (depth bins). At the cruise speed of 3 to 3.5 m/sec, the resolution of the current measurements was approximately 400 meters. Observations by the flow-through system and the ADCP were obtained continuously during the cruise with down time only for cleaning the flow-through system and saving the data (because of processing problems, approximately 22 km. of ADCP data along the Phase 2 transect at 90° W are not available). Meteorological parameters (wind speed and direction, air temperature, barometric pressure, and solar irradiance) were included in the flow-through data set sampled at 5-9 second intervals.

A total of 170 stations were occupied during survey portions of the ten day cruise. Of the 170 stations, 90 were occupied in the first survey of the cruise and 80 in the second (Figure 88). CTD profiles, including dissolved oxygen, light transmission, and fluorometer measurements were made at all stations. Water samples were taken at 75 stations for determination of chlorophyll and nutrient concentrations, 54 stations for phytoplankton distribution, 27 stations for zooplankton distribution, and 16 stations for pollutant chemistry.

D. Discussion

The composite temperature-salinity (T-S) diagrams (Figure 89) for the two survey phases of the cruise illustrate the existence of three sources of water in the Louisiana Bight. The first source is the fresh water debouching from the mouth of Southwest Pass of the Mississippi River. Other contributions of fresh water come from the adjacent estuaries, river crevasses, and the Mississippi River passes to the east of Southwest Pass. The densest waters in the study area are cold and saline and are found near the bottom on the offshore ends of the transects. These waters have been observed to intrude to the inner shelf during the summer months (Wiseman et al., 1982). A third source is the warmer and slightly more saline surface waters of the open gulf. These waters are also found at the southern ends of the transects. This third source was observed to have a somewhat broad range in temperature, as would be expected of surface waters in the northern Gulf of Mexico at the end of the winter season.

The high salinity deep waters occupy a tight linear grouping, varying mainly in temperature. The waters that result from the mixing of the fresh water with the surface and near surface saline waters form a broad column on the T-S diagrams. Temperatures for this mixed water range from approximately 19° C to about 24° C. Water discharged from Southwest Pass was colder (15° C to 16° C). This fresh water quickly warmed up to 19° C within approximately 10 km. of the mouth of the pass. Through mixing, the

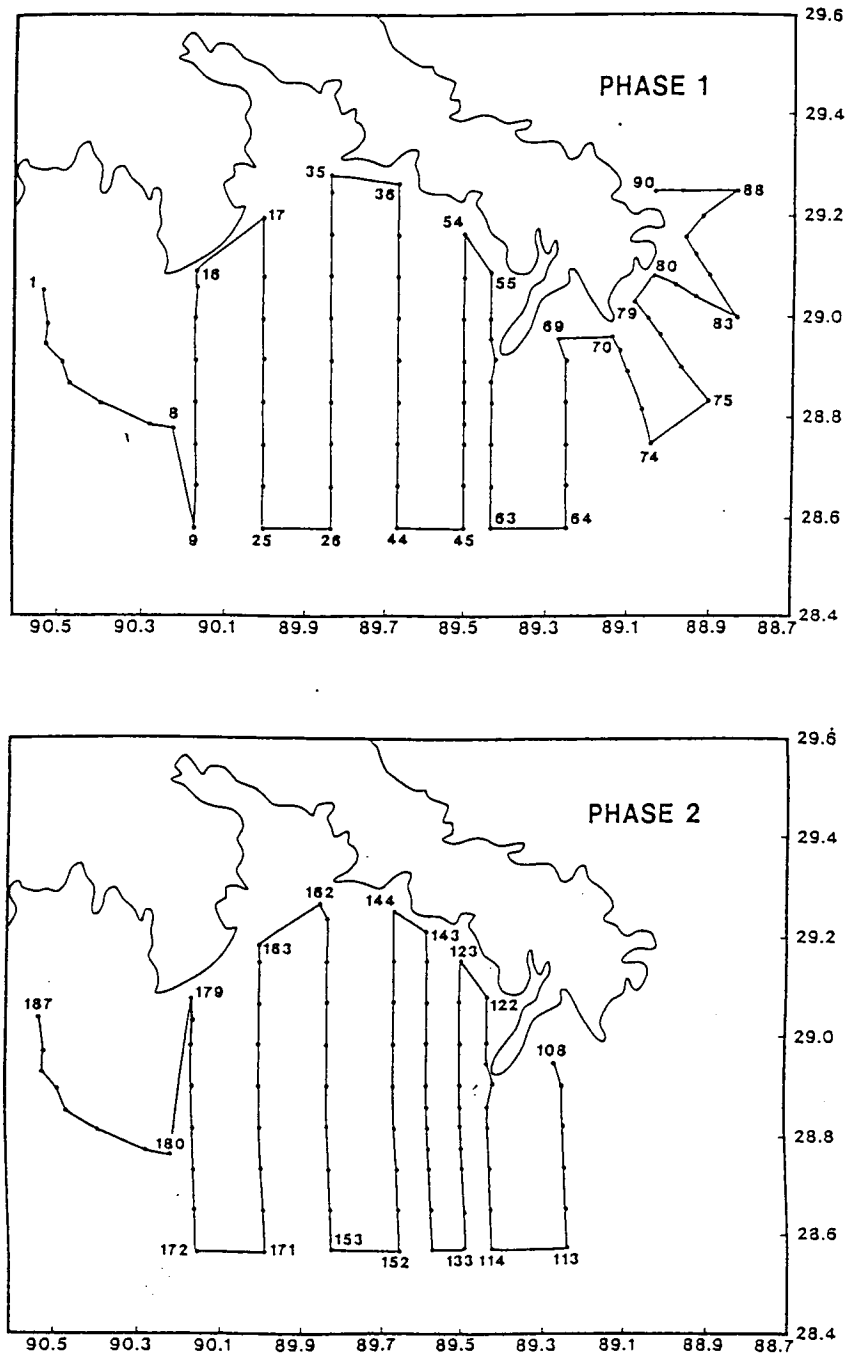

Figure 88. Cruise track and station locations: (a) Phase 1 and (b) Phase 2.

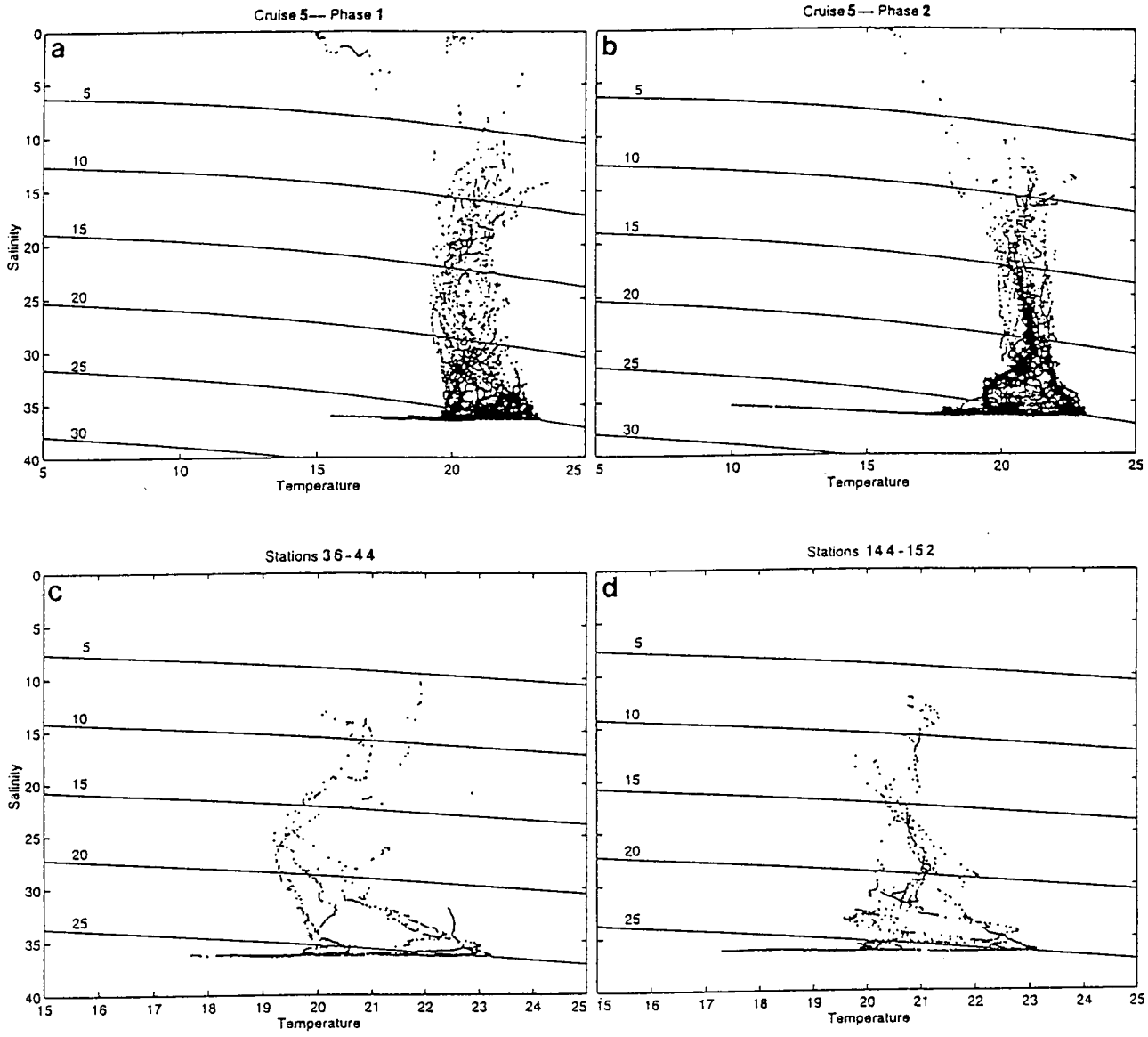

Figure 89. T-S diagrams (a) all Phase 1 stations, (b) all Phase 2 stations, (c) stations 36-44, and (d) stations 144-152.

salinity also increased to at least 15 psu within the same distance all salinities in this paper are stated according to the Practical Salinity Scale.

A comparison of the T-S diagrams for the two phases reveals only a few differences. The high salinity feature representing the deeper waters at the offshore end of the transects extends to lower temperatures in Phase 2 because the CTD cast on station 153 was down to 420 m. whereas the cast at the corresponding location in Phase 1 (station 26) was only down to 100 m. Another difference is the slight tendency of the Phase 2 temperatures to be slightly higher than the Phase 1 values. This difference is most obvious at stations on the inner portion of the study area and at salinities between 20 and 30 (Figures 89c and 89d).

The study area can be divided into two regions based on the structure of the CTD profiles. Stations on the transect at 89° 40' W can be used to illustrate these regions. The inner region is characterized by a relatively fresh surface layer with a thickness of about 5 m. and a relatively uniform temperature from surface to bottom (Figure 90, Stations 37, 39, 145, and 147). This inner region can be further divided into two subregions based on the absence or presence of the high salinity water. Those stations nearer the shore tend to have salinity profiles that either have no bottom layer of uniform salinity (Station 37) or the salinity layer at the bottom is fresher than the 35 to 36 values found in the open gulf waters (Station 145). In the middle region of the shelf, the salinity of the bottom layer is in the same range as the waters of the deep gulf (Stations 39 and 147). This inner region is where the primary area to which the freshwater discharged by the river is confined. The outer region, composed of the southernmost one to three stations on each line, is characterized by high salinity from surface to bottom. At these deeper stations the temperature is warmer at the surface than inshore but decreases with depth (Figure 90, Stations 44 and 152).

Salinity contour maps constructed with data from the surface and 10 m. illustrate the difference between the circulation patterns in Phase 1 and Phase 2. Surface and 10 m. isohalines in Phase 1 (Figure 91) tend to run east-west with a slight onshore tendency toward the western edge of the study area. This is obvious in the trend of the 20 to 32 isohalines in the surface waters. At the western edge of the study area, an offshore bend to the isohalines is observed. The surface isohalines for Phase 2 (Figure 92a) display a different pattern. The isohalines above 18 tend to be a little further offshore in the center of the study area but tend to curve toward the shore in the western portion. The isohalines that bend offshore at the western edge are for the higher salinities. Note also that the surface horizontal salinity gradient at the western edge is greater in Phase 1 than in Phase 2. The isohalines at 10 m. (Figures 91b and 92b) show a structure similar to the respective surface maps. Both 10 m. maps indicate a local salinity minimum in the center of the bight. The entire bight at 10 m. is much fresher in Phase 2. In fact the minimum 10 m. salinity of Phase 1 (30) is not within the bight at 10 m. in Phase 2.

That more fresh water is in the bight under the northeast wind conditions of Phase 2 is evident in the transect cross sections. The salinity cross-section along 89° 40' W (Figure 93) illustrates the differences in conditions. The southeast winds of Phase 1 have pushed the fresher water closer to the coast as evidenced by the differences exhibited by the 20 isohaline. In Phase 1 this isohaline is at about 6 m. until it rises steeply to the surface just inshore of station 40 (28° 55' N). In Phase 2 the same isohaline is up to two meters deeper and it rises less steeply to the surface slightly more than 20 km further offshore. Except in water less than 12 m. the 30 isohaline is 2 to 7 m. deeper in Phase 2 than in Phase 1. Like the 20 isohaline, the 30 isohaline surfaces much further offshore in Phase 2. Another difference in the structure of the isohalines is the local maximum in depth at 29° N and the rise toward the shore in Phase 1. The isohalines in Phase 2 do not

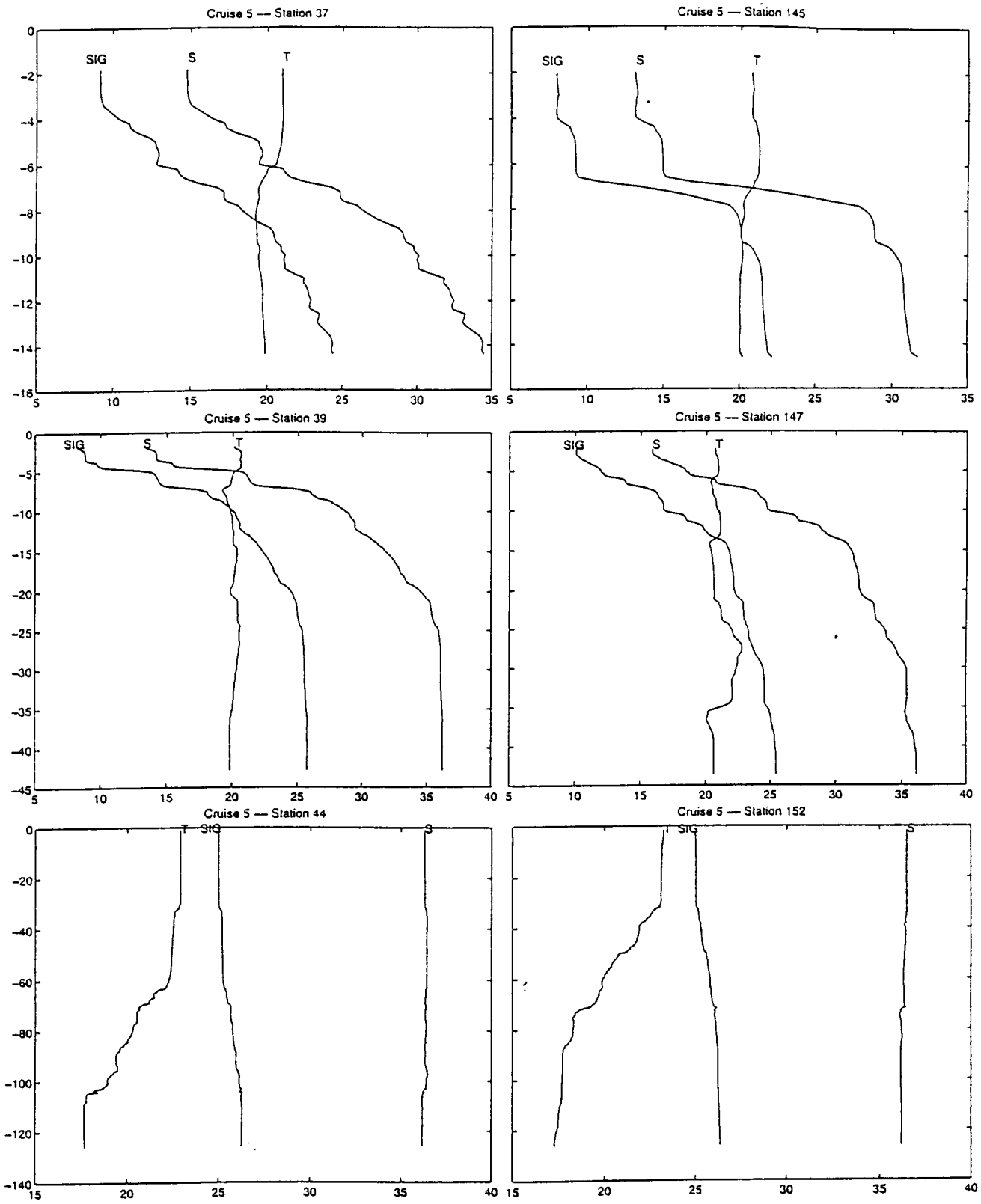

Figure 90. Profiles of salinity (S), temperature (T) and sigma-t (SIG) at selected stations along 89° 40' W. The profiles on the left were acquired during Phase 1 and are side-by-side with profiles acquired at the same location during Phase 2.

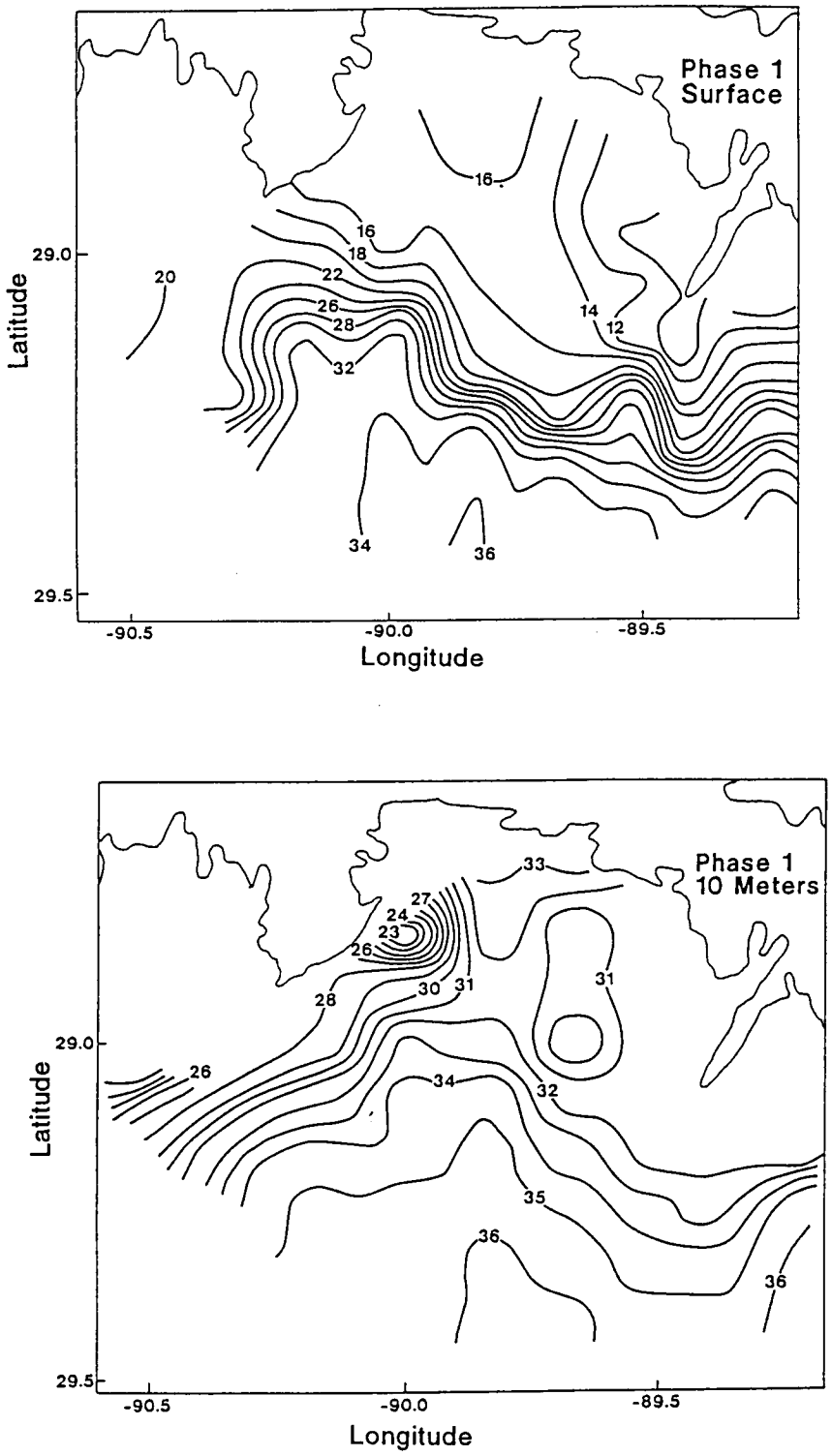

Figure 91. Phase 1 isohalines for the (a) surface and (b) 10 meters.

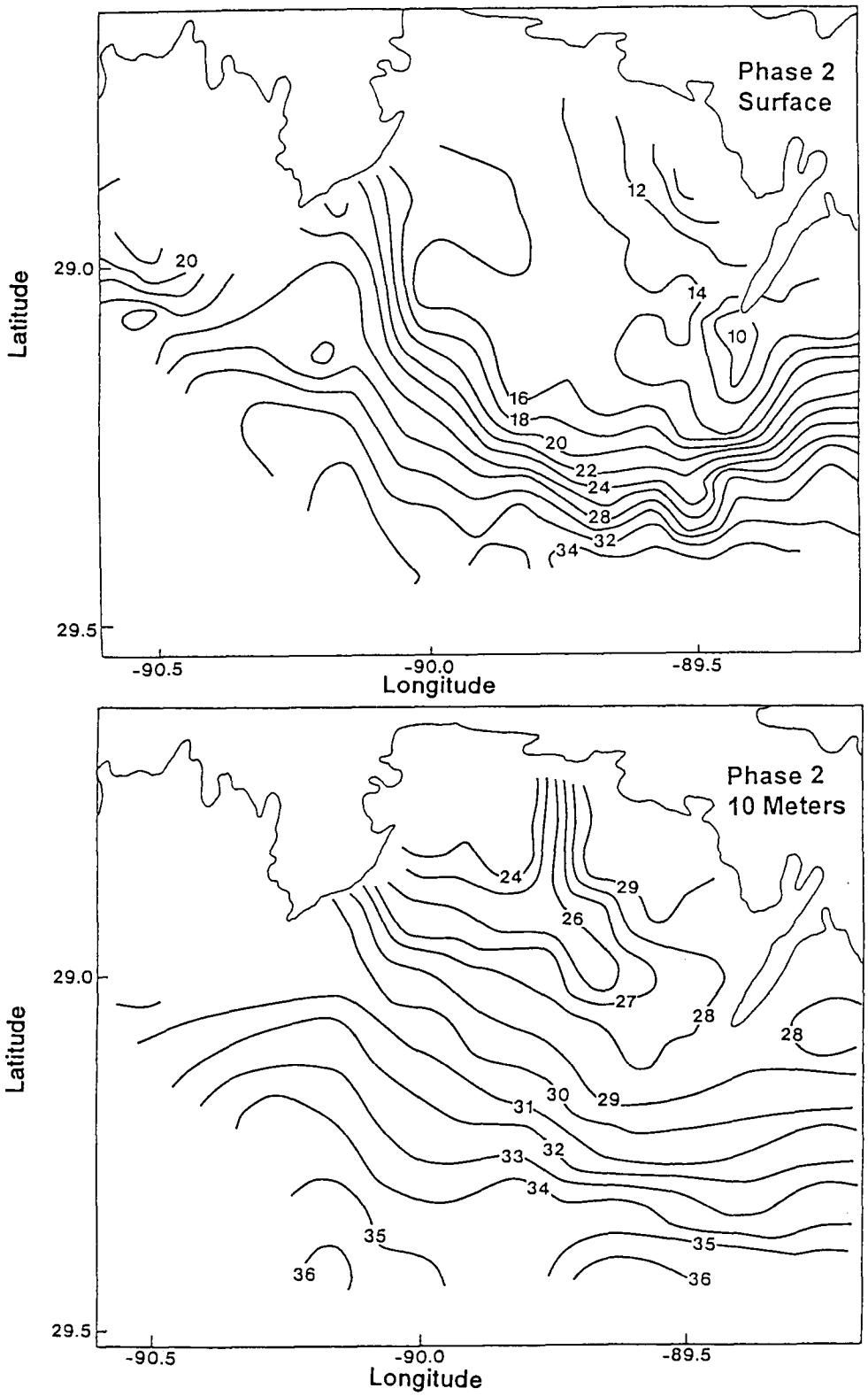

Figure 92. Phase 2 isohalines for (a) the surface and (b) 10 meters.

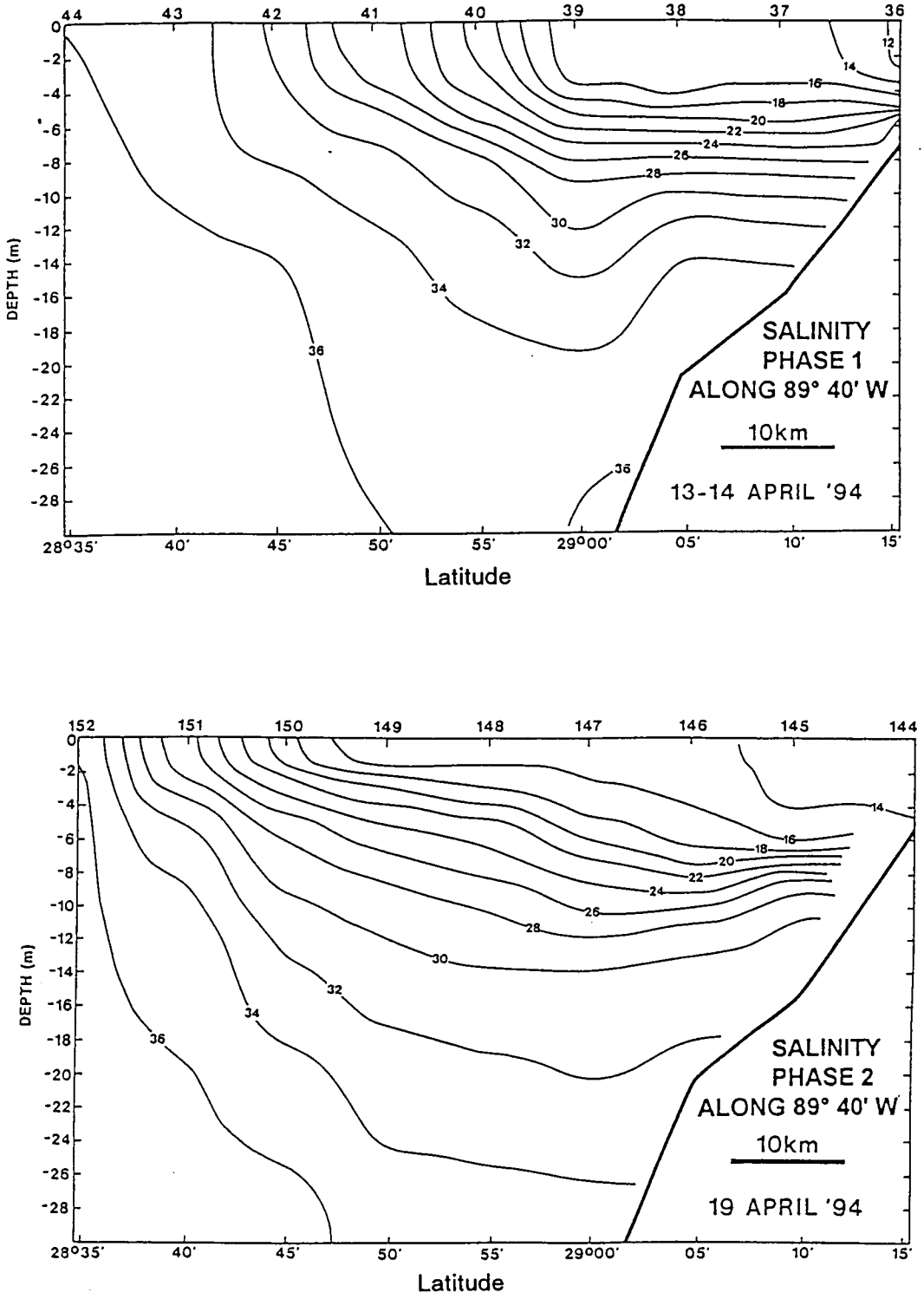

Figure 93. Salinity cross-sections along 89° 40' W: (a) Phase 1 and (b) Phase 2.

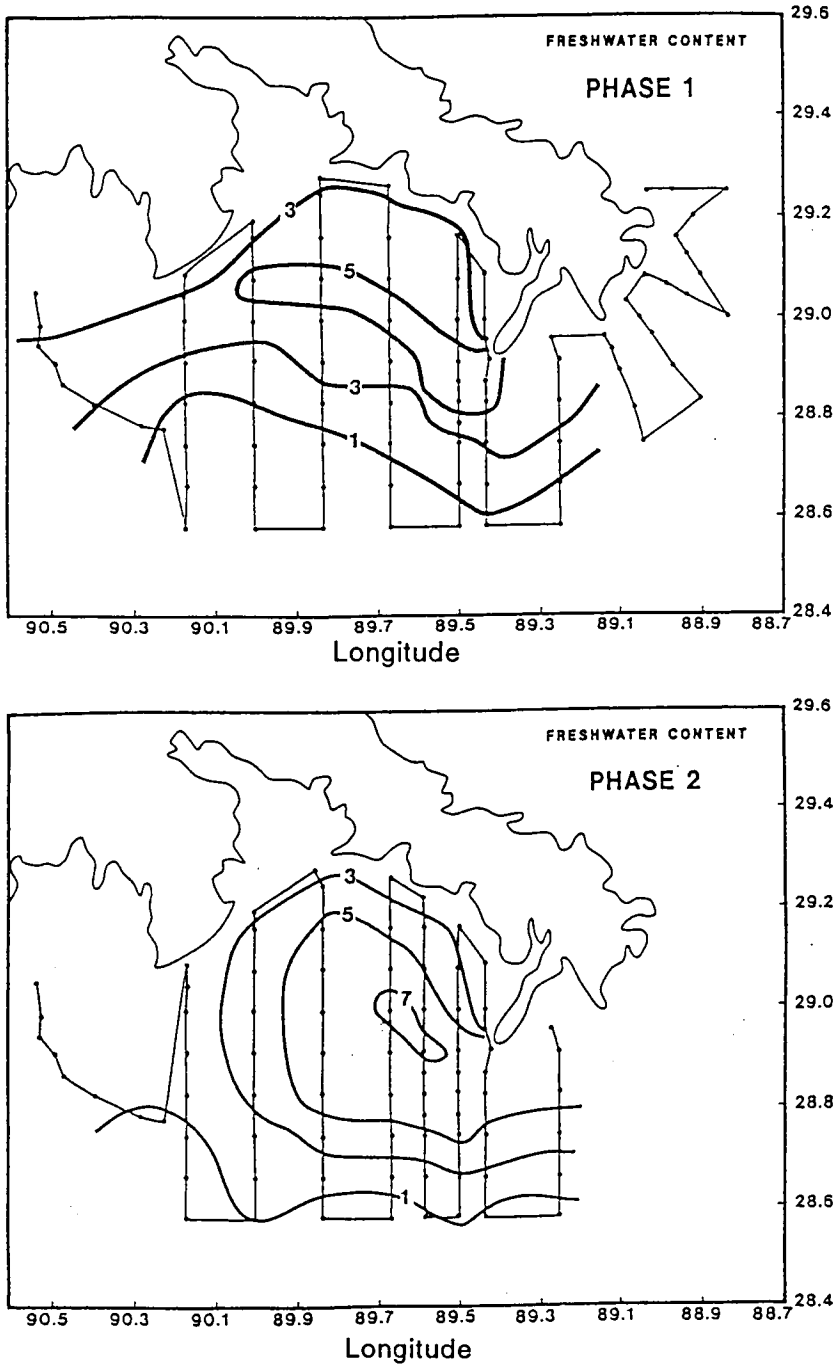

Figure 94. Fresh water content: (a) Phase 1 and (b) Phase 2. The contours are in meters and are calculated relative to a salinity of 36.6.

have a distinct maximum in depth but there is a hint of a rise toward the surface at the inshore stations.

For each of the stations in Phase 1 and Phase 2 of the survey, the fresh water content of the water column was calculated (Ketchum and Keen, 1944; Dinnel and Wiseman, 1986). The maximum salinity found in the study area (36.6) was used as the reference salinity. The values calculated for each station were contoured to display the distribution in the bight of the fresh water discharged by the Mississippi River (Figure 94). That the two phases sampled different situations is obvious from the figure. In the first phase the 3 m. contour does not close within the bight and the 5 m. contour is elongated toward the west. In the third phase, the thickness of the fresh water is in excess of 7 m. in the vicinity of the mouth of Southwest Pass. The 5 m. and 3 m. contours close within the bight and are not elongated. Within the bight the 1 m., 3 m., and 5 m. contours are further offshore in Phase 2 (cf. the transects between 89.7° W and 90.1° W).

An estimate of the total fresh water content of the study area was also made. For this estimate, the area considered was bounded by the curved transect out of Terrebonne Bay on the west, the easternmost survey line common to both phases, the coast, and the offshore 1 m. fresh water contour. Within this area, the total volume of fresh water in Phase 1 was estimated to be 16.8×10^9 m^3. Using the average discharge of the Mississippi River during the cruise (26,500 m^3/s), this volume is equivalent to approximately the amount of water discharged in 7.3 days. In Phase 2, the area covered by water inside of the 1 m. contour was approximately 25% greater than in Phase 1 and the volume was estimated to be 23.1×10^9 m^3, equivalent to 10.1 days of river discharge.

Perhaps the most exciting data set acquired on the cruise was from the ADCP. The 1200 Hz ADCP was operated in bottom tracking mode in water depths less than 30 m. and in a differential GPS mode in water depths greater than 30 m. The error in the measurements is approximately 4 cm/sec in the bottom tracking mode and 10 cm/sec in differential GPS mode. The ADCP data for the uppermost bin centered at 4.5 m. (Figure 95) show the existence of an anticyclonic gyre within the bight in both phases. The gyre was centered close to the coast under the southeast winds of Phase 1 and the speeds around the gyre were 20 to 40 cm/sec. Flow around the delta from the east was at speeds of 40 to 70 cm/sec. This flow from the east is seen to bend around the Southwest Pass Plume, which seems to be the major (if not sole) contributor to the fresh water in the gyre, and merge with the Southwest Pass discharge in the vicinity of Bayou Lafourche. The combined flow continues to the west along the coast. Peak speeds in the bight are 60 to 70 cm/sec and are found in the offshore portion of the flow that continues to the west.

The picture presented by the ADCP data for Phase 2 also shows the existence of the anticyclonic gyre under the influence of the northeast winds. The center of the gyre appears to be further offshore than in Phase 1 and the gyre occupies a greater area of the bight. Speeds around the gyre are 40 to 60 cm/sec. The flow around the delta from the east is stronger than in the first phase with speeds in excess of 80 cm/s. As in Phase 1, this flow from the east is along the offshore edge of the gyre and approaches the shore near the mouth of Bayou Lafourche. Because of the missing ADCP data along the transect at 90° W, it is not possible to describe the merging of the Southwest Pass plume with the water that came from the east. It does appear that the flow of water to the west is at higher speeds. A cross-section of the east-west component of ADCP data along the 89° 40' W transect (Figure 96) shows that the offshore portion of the gyre extended to approximately 20 m, and east-west speeds of up to 30 cm/sec were found at 10 m. Just as at the near-surface level (4.5 m), speeds to the east at 10 m were slightly weaker nearer the shore than the westerly speeds offshore.

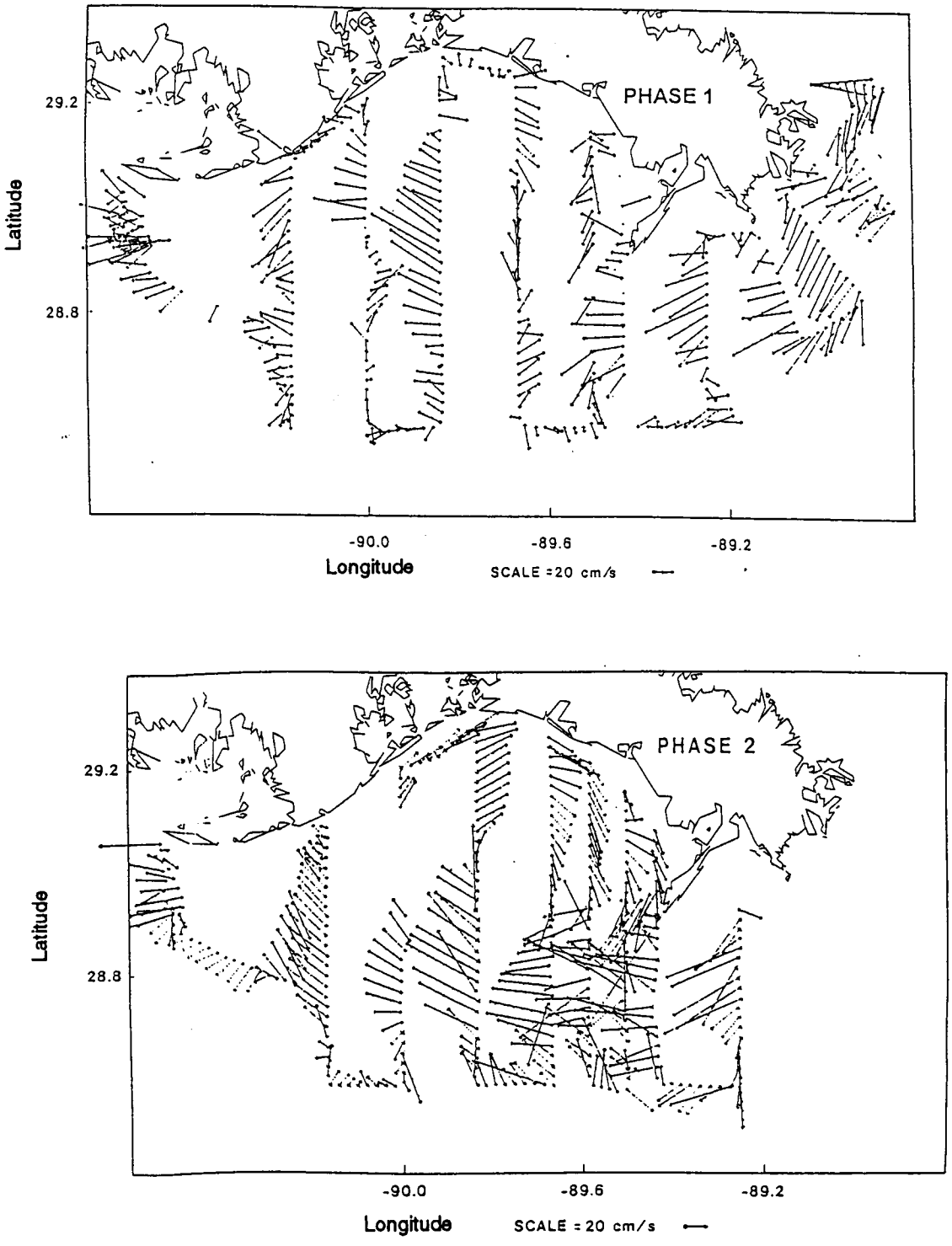

Figure 95. ADCP current vectors for the 4.5 m bin: (a) Phase I, and (b) Phase 2.

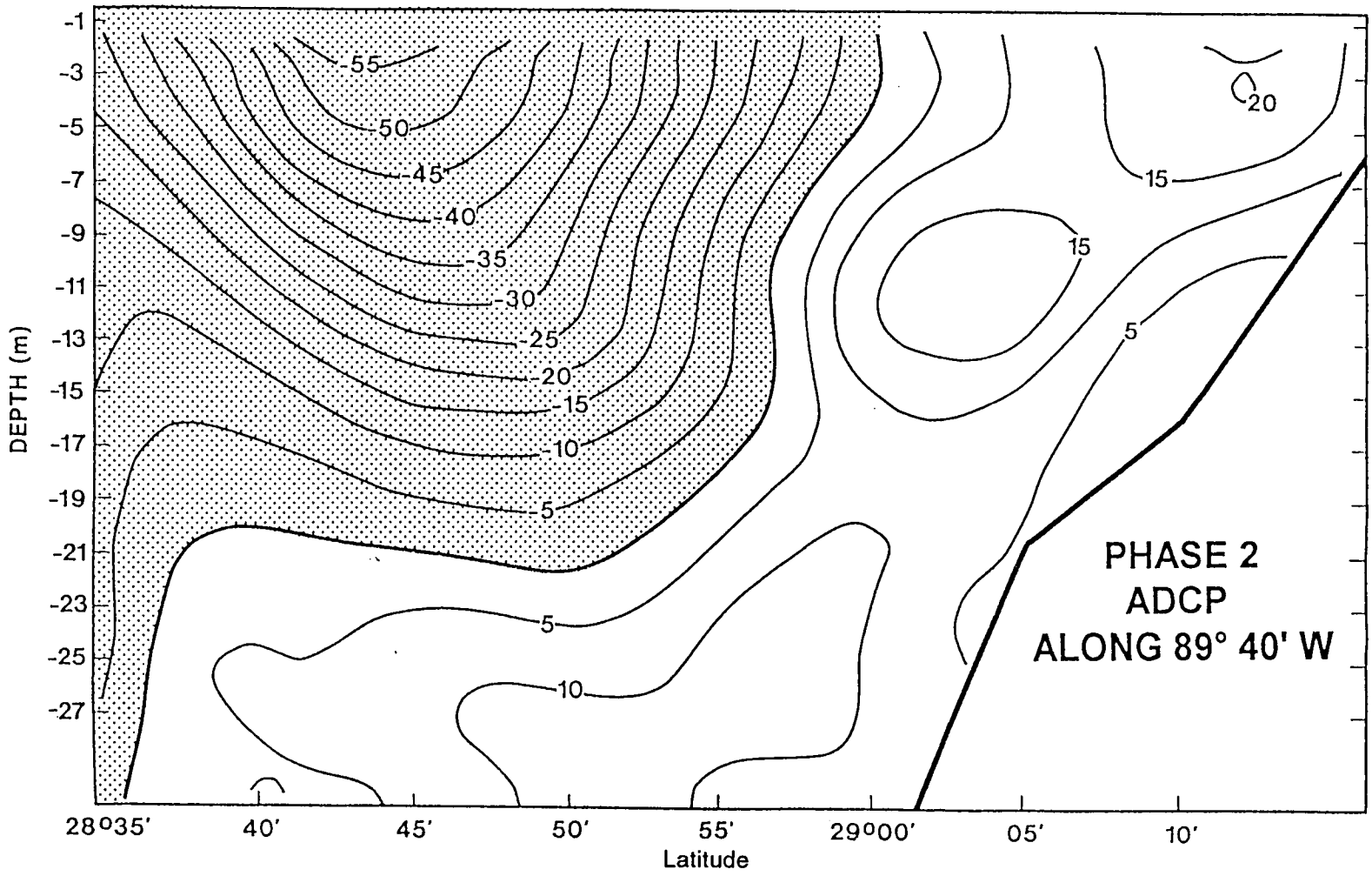

Figure 96. Cross-section along 89° 40' W of the Phase 3 east-west component fo the ADCP measured current velocities. Positive values are to the east.

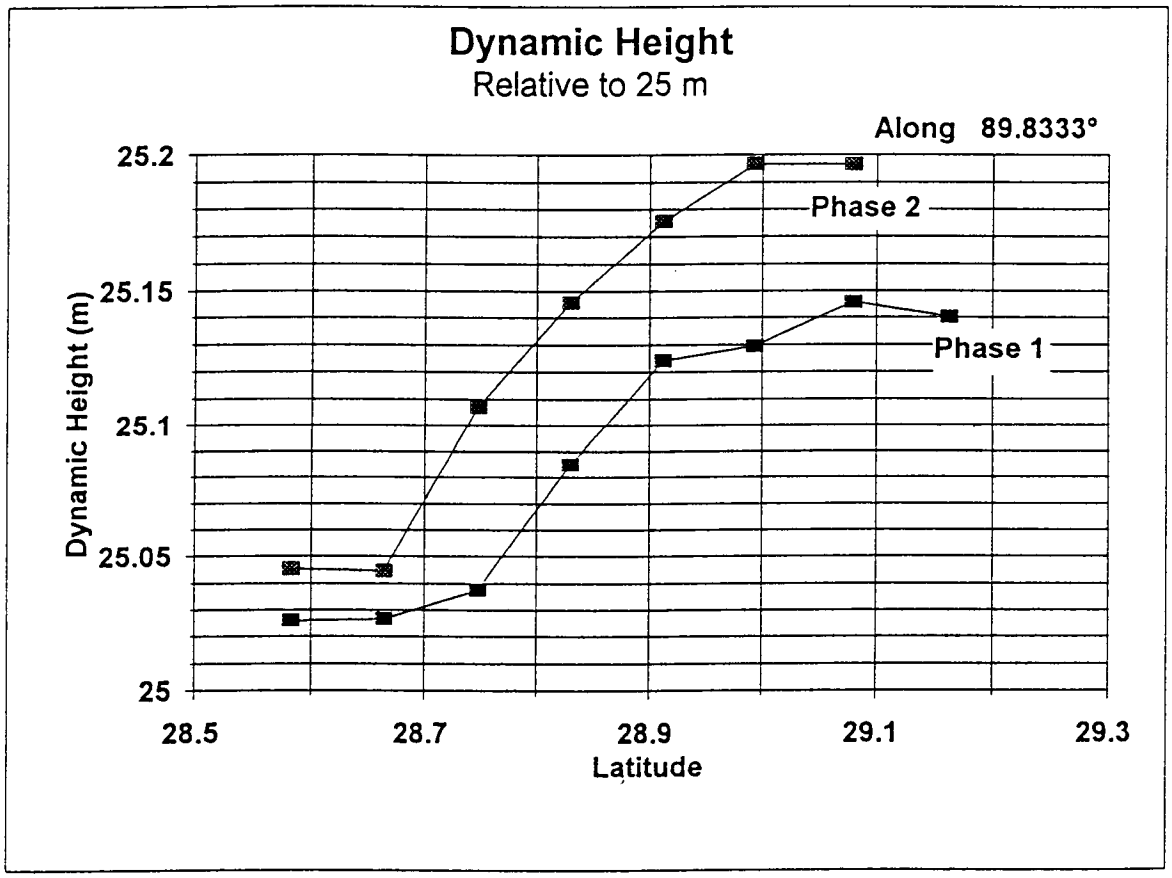

Figure 97. Dynamic height profiles along 89° 50' W relative to 25 m.

The elevation of the sea surface relative to 25 m was calculated to provide an estimate of the geostrophic component of the observed velocities. The 25 m level was chosen because the salinity at this depth was above 33 and often above 35. Choice of a depth much deeper than 25 m would have omitted too much of the region. Extending the calculation to shallower stations was not done. The lines of constant surface elevations exhibit patterns similar to the fresh water content. In the center of the bight, calculated elevations were 4 to 5 cm higher in Phase 2 than in Phase 1 (Figure 97). Surface slopes were also steeper in Phase 2. These sea surface slopes are consistent with surface current speeds between 50 and 100 cm/sec. In both phases, calculated surface current speeds are somewhat greater than the currents observed at 4.5 m with the ADCP but the spatial and temporal variations are similar to those observed in the ADCP data.

E. Conclusions

The distribution of the fresh water delivered to the shelf by the Mississippi River was observed under two different wind conditions, both of which has an easterly component. In both of these situations the flow of the fresh water was to the west with a well formed anticyclonic gyre in the bight to the west of the delta. To the west of the bight, the freshened water plume appears to flow along the inner portion of the shelf as the higher salinity surface waters of the open gulf approach the shore along the 90° 10' W transects (Figures 91, 92, and 95). The water in the study region was found to be derived from the same three sources as described by Wiseman et al. (1982). The Southeast winds of the first phase of the cruise pushed the fresher waters closer to the coast and the vertical salinity gradient appeared to be slightly greater than in the third phase. In Phase 2, surface isohalines greater than 20 were up to 20 km. further offshore. The fresh water content calculations (Figure 94) indicate that the amount of the discharge of the river trapped in the bight under the northeast winds of Phase 2 is much greater than under the southeast wind conditions. As a result the fresher waters occupied a greater volume of the shelf in the study area in this third phase. The difference between the two wind regimes suggests that a pulse of fresh water will be released to the west when winds from the southeast return, as happened within three days after the end of the cruise.

The gyre in the Louisiana Bight, present under both wind conditions, was centered closer to shore in Phase 1 and the speeds of the circulation around the center were slower than in Phase 2. ADCP data from the both phases indicate that, under both southeast and northeast wind conditions, a significant amount of water is flowing to the west around the delta. Estimates made by integrating the east-west component of the ADCP data down to the 20 m bin and to the southern end of the transect at 89° 15' indicate that the net transport to the west was in excess of 140,000 m^3/s^{-1} during Phase 1 and in excess of 165,000 m^3/s^{-1} in Phase 2. During Phase 2, the velocities around the delta were as much as 20 cm/sec greater than in Phase 1. To the west end of the study area, the salinity and ADCP data suggest that the water coming around the delta from the east merges with a portion of the Southwest Pass plume and flows toward the west as a distinct nearshore plume. Based on the data from the two wind regimes, it appears that a significant portion of the discharge of the Mississippi River does contribute directly to the coastal plume.

IV. Satellite Observations of Circulation Features in the Northern Gulf of Mexico

by Nan D. Walker

A. Objectives

Satellite image analyses and interpretation were charged by MMS as a separate and distinct task with the following objectives:

- to assess the spatial and temporal variabilities of the Atchafalaya and Mississippi plumes in relation to river discharge and wind forcing;
- to investigate spatial relationships between the river discharge plumes and the distribution of phytoplankton and key pollutants along the Louisiana/Texas shelf;
- identify areas of squirt formation and assess squirt longevities, surface velocities with drifter data, and probable forcing mechanisms; and,
- to document selected circulation events associated with river discharge, the LATEX coastal current, squirts, and eddies.

B. Introduction

Circulation in the northwesten Gulf of Mexico (GOM) is complex, as it is influenced by several time-varying environmental factors, including wind forcing, river discharges, and the location and intensity of detached Loop Current warm-core eddies. The Loop Current and the large warm-core eddies that separate from it dominate the circulation in the Gulf of Mexico (Elliot, 1982; Forristall et al., 1992). These warm core eddies typically have diameters of 200 to 400 km, extend 800 to 1000 meters vertically, and exhibit maximum surface currents of 100 to 200 cm/sec (Huh and Schaudt, 1990; Cooper et al., 1990; Forristall et al., 1992). The frequency of eddy shedding varies between 6 and 15 months (Maul and Vukovich, 1993; Sturges, 1994). After an eddy is shed from the Loop Current, it usually moves slowly westward at about 4 km/day until it reaches the western Gulf of Mexico shelf where it is constrained by shoaling topography. Thus, warm-core eddies often dominate circulation patterns in the western Gulf of Mexico (Elliot, 1982; Lewis and Kirwan, 1985). Eddy-related circulation in the western and northwestern Gulf of Mexico is thought to drive much of the surface current variability on the outer continental shelf (Oey, 1995). These warm-core eddies have longevities of several months to a year and, therefore, several Loop Current eddies may be found in the western Gulf of Mexico simultaneously (Biggs, 1992). Although less well studied, cold-core eddies (50 to 150 km in diameter) are often found in association with the warm-core eddies (Merrell and Morrison, 1981; Brooks and Legeckis, 1982; Hamilton, 1992).

On the inner shelf west of the Atchafalaya Bay, surface circulation is primarily wind-driven and strong coherence has been found between alongshore wind-stress and alongshore currents for coastal locations (Smith, 1978b; Cochrane and Kelly, 1986). This relationship results in primarily downcoast (westward) flow for much of the year with a coastal-type jet on the inner shelf (Cochrane and Kelly, 1986). The predominant east to west flow on the inner shelf is enhanced by discharge from the Atchafalaya and Mississippi Rivers, discharges that exhibit annual cycles with strongest flow onto the shelf in spring and weakest flow in late summer and autumn. The river effluents produce relatively cool, turbid, low-salinity water masses, which are identifiable along the coast for much of the year using the visible and thermal infrared channels of the NOAA satellites (Rouse and Coleman, 1976; Walker et al., 1996; Walker, 1996a).

Cochrane and Kelly (1986) suggest that a cyclonic gyre is the dominant feature of the prevailing shelf circulation. The inshore limb of the gyre is the wind-driven coastal jet.

Their data also indicate that an eastward-flowing current occurs along the shelf edge as the seaward flank of the shelf-wide cyclonic gyre. Oey (1995) uses a numerical model to show that the convergence zone on the western flank of the gyre and the shelf- break current are driven by collision and stalling of westward propagating Loop Current eddies in the northwest Gulf of Mexico, rather than by wind forcing.

C. Surface Fronts, Squirts, and Eddies

In this section of the report an attempt is made to improve knowledge of the circulation in the northwestern Gulf of Mexico by investigating the evolution and structure of thermal fronts on the shelf and their relationship to circulation features as revealed by thermal infrared satellite data, satellite altimetry and the tracks of SCULP drifters. Thereafter, a climatology of events in the northwestern Gulf of Mexico is presented for the time period 1992 through 1994.

1. Methodology

a. Satellite Image Data

Sea-surface temperature imagery obtained by the NOAA POES (Polar Orbiting Environmental Satellites) were used to detect shelf and ocean circulation features of interest in this study. The 1 x 1 km spatial resolution and the multi-daily coverage provide a powerful source of information when cloud-cover is sufficiently low. These data are downlinked from the NOAA satellites four to eight times a day by equipment at the Earth Scan Laboratory, Coastal Studies Institute, LSU. Image processing and analyses were performed using the Terascan™ software provided by SeaSpace, San Diego, California, which is currently running on an SGI Challenge. Sea surface temperatures are computed using a modification of the MCSST technique described in McClain et al (1985).

b. Satellite Altimetry Data

TOPEX and ERS-1 sea surface height data were used to create 10-day anomaly maps, which are referenced to the OSUMMS95, a mean sea surface calculated at the Ohio State University by Dick Rapp and Yuchan Yi (Leben et al., 1993). This mean sea surface is based on TOPEX, ERS-1 and Geosat data. Standard corrections were applied to the data and the "orbit" error was removed from both the TOPEX and ERS-1 data using a tilt and bias adjustment. The TOPEX and coincident ERS-1 data were mapped every 10 days using a spatial/temporal Cressman weighting scheme.

c. Drifter Data

From October 1993 through October 1994, approximately 300 ARGOS drifting buoys were released on the Louisiana shelf during the MMS-sponsored SCULP drifter program (Johnson and Niiler, 1994). The 31 drifters released in October 1993 are discsussed in this report. Daily drifter positions (at 1115 UTC) were reformatted and superimposed on SST to aid in the interpretation of circulation processes and to further our understanding of the influence of prominent oceanographic features on surface circulation.

2. Results

a. Thermal Fronts on the Louisiana/Texas Shelf

Continental shelf waters in the northern Gulf of Mexico cool substantially during autumn and winter as a result primarily of latent (evaporative) and sensible heat losses to the atmosphere and a reduction in incoming solar radiation (Nowlin and Parker, 1974; Huh et al., 1978). The annual temperature cycle is largest in coastal waters where the heat storage capacity is less because of the shallow water depths. The annual cycle in coastal water and air temperatures along the Louisiana and Texas coasts is demonstrated in the 10-year climatological data from Grand Isle, Louisiana, and Port Aransas, Texas (Figure 98; for station locations, see Figure 99). Monthly-averaged water temperatures range from 30° C in summer to 14° C in January at both sites. Throughout the year, monthly-averaged water temperatures are 1 to 2° higher than air temperatures. In Table 10, these climatological values and their standard deviations are listed.

Table 10. Monthly averaged water temperatures and their standard deviations as determined from 1985-1994 data recorded at Grand Isle, Louisiana and Port Aransas, Texas.

	GRAND ISLE		PORT ARANSAS	
	SST	SD	SST	SD
JAN	14.1	2.65	13.8	1.44
FEB	15.6	2.51	15.5	1.48
MAR	18.3	2.70	18.4	1.63
APR	21.9	2.62	21.9	1.89
MAY	26.2	1.84	25.5	1.65
JUN	28.9	1.42	28.5	1.24
JUL	29.9	1.24	28.9	1.16
AUG	30.0	1.31	29.8	0.86
SEP	28.4	1.95	28.7	1.17
OCT	23.7	2.39	25.2	1.97
NOV	19.8	2.89	20.3	2.50
DEC	15.3	2.94	16.0	3.18

As a result of the depth-controlled cooling across the continental shelf, water masses are trackable on the shelf by their temperature. In addition, thermal fronts of various intensities are evolved, separating water masses of different origins. In Figure 99, satellite-derived sea-surface temperatures (SSTs) are depicted on November 28, 1993, where cool waters are representated by darker shades of grey. The image data has been filtered with a Sobel filter, and thermal fronts are shown in Figure 99 as white lines where the intensity of white is related to the strength of the front. At the end of November 1993, surface temperatures ranged from 15 to 16° C along the coast in the coastal current to 25 to 26° C in the warm-core eddies seaward of the continental shelf. Lowest water temperatures were measured in Atchafalaya Bay and in the Atchafalaya plume on the inner shelf where temperatures reached 10° C. The autumn to winter cooling of coastal and shelf waters was further investigated by extracting surface temperatures from satellite imagery along five lines across the Louisiana/Texas shelf (locations, Figure 99). Surface temperatures were extracted from three clear sky NOAA AVHRR images (Figure 100): September 29, 1993;

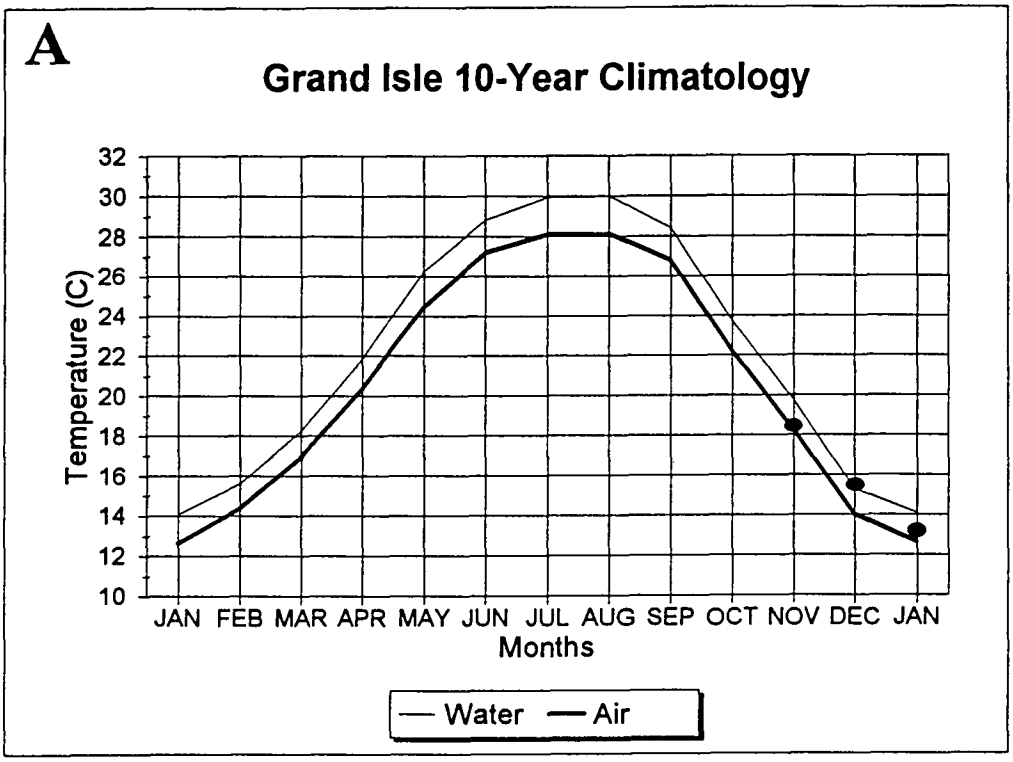

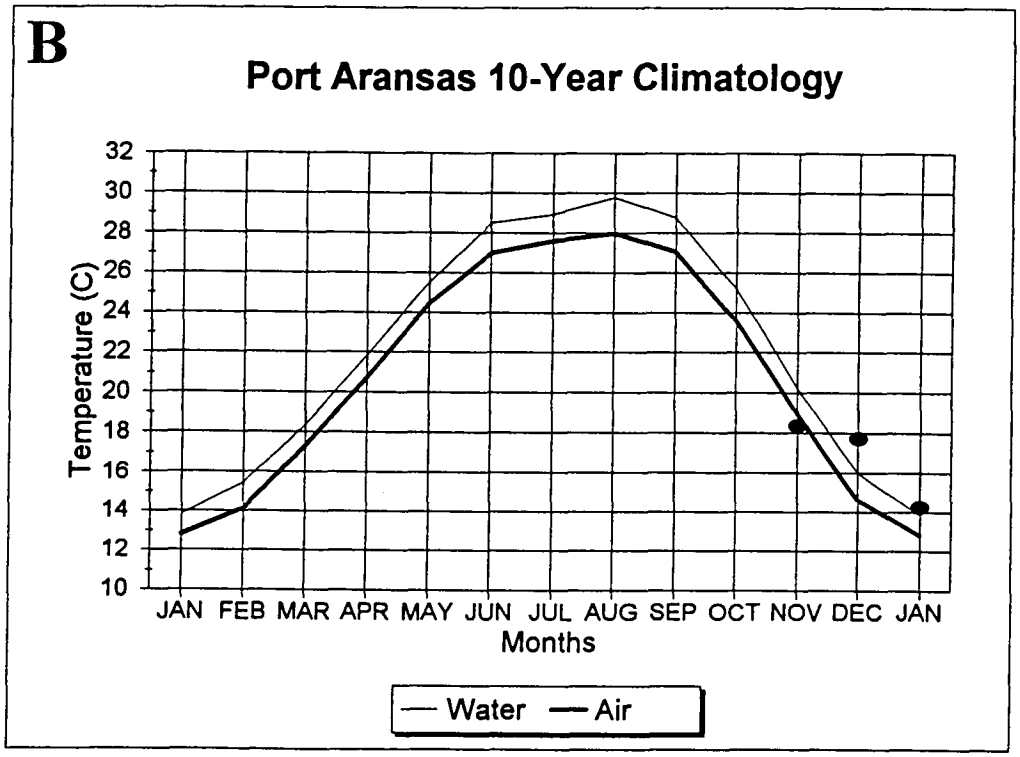

Figure 98. A 10-year climatology (1985-1994) of air and water temperatures at (a) Grand Isle, LA, and (b) Port Aransas, TX. The water temperature is shown with a solid line and the air temperature with a bold solid line. The monthly-averaged water temperatures for November 1993, December 1993 and January 1994 are shown with filled circles.

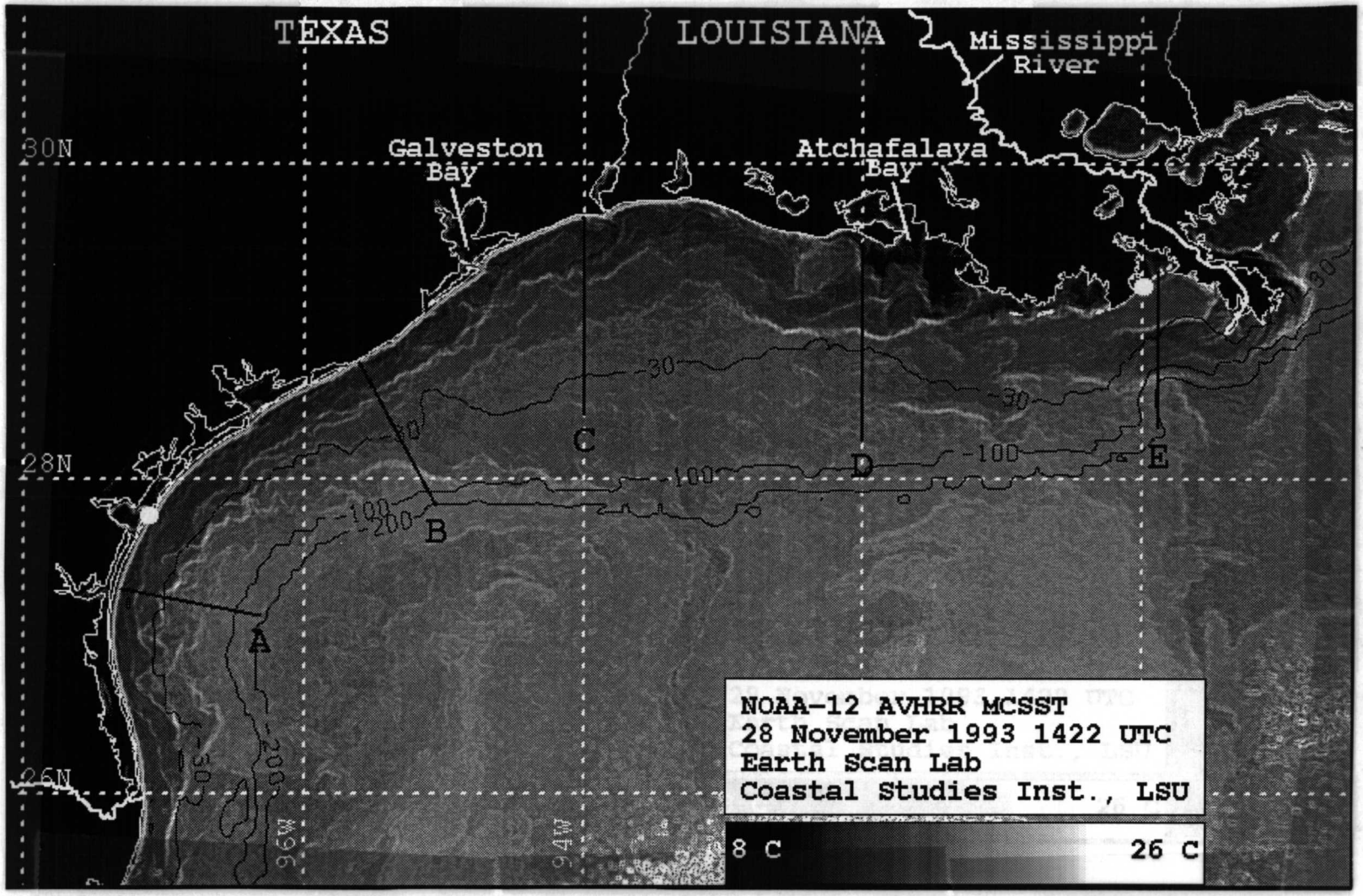

Figure 99. NOAA AVHRR sea surface temperature (SST) image of November 28, 1993 (1422 UT). Cooler waters are depicted with darker shades of grey. Sea surface temperature fronts, as determined by a sobel filter, are depicted with white lines. The profile lines from which SSTs were extracted (see Figure 100) are shown with solid black lines.

November 28, 1993; and, January 14, 1994 (February 8, 1994 for Line A). These data reveal the absence of thermal structure over much of the Texas shelf in early autumn when temperatures ranged from 29 to 30° C. However, along lines D and E (Figures 100d,e), lower temperatures along the coast were attributable to the discharge of cooler river waters. Over the next two months, dramatic cooling of shelf waters occurred. Between September 29 and November 28, 1993, the inner shelf of Texas and Louisiana cooled 12 to15 ° C, whereas, the outer portions of the shelf cooled 5 to 8° C. Comparison of the November 1993 coastal temperature data with the 10-year climatology reveals that November water temperatures were 1 to 2° C cooler than average (Figure 98).

The temperature profiles revealed the existence of distinct surface fronts particularly in inner and mid-shelf regions. The satellite image of November 28, 1993 (Figure 99) showed that these fronts were associated with the Mississippi and Atchafalaya River effluent plumes, the coastal current, off-shelf flows and detached warm-core eddies of the Loop Current and eddy filaments. Coldest shelf waters were associated with the Mississippi and Atchafalaya River discharge plumes, with an area of warmer water separating the plume regions. The term "plume" is used here to refer to the satellite observed effluent from the rivers, although in reality the region is probably an active mixing zone of river and shelf water. Downstream from the Atchafalaya plume, a continuous band of cold inner shelf water was observed with temperatures of 14 to 16° C. Distinct surface fronts separated the cool inner shelf water from deeper waters of the shelf. Frontal intensities exceeded 3° C per 10 km on lines A,B,D, and E. One of the most intense fronts (5° C per 13 km) was observed along line E (Figure 100e, see "PF1"), where cold Mississippi River water was discharged onto the shelf. This thermal front west of the Mississippi delta measured 5° C in 10 km (0.5° C/km) and was located between the 100 and 150 m isobath. A distinct front was also observed on the landward side of the Southwest pass effluent in about 30 meters of water (Figure 100e, see "PF2", because the river water was several degrees cooler than the inner shelf water within the Louisiana Bight. Another inner shelf front (Figure 100e, see "ISF") was measured close to the coast at the mouth of Barataria Bay.

Two distinct fronts were associated with the Atchafalaya plume, 20 and 60 km from the coast (Figure 100d). The inner front measured 3.8° C per 9 km (0.42° C/km) and the outer front measured 3° C/4.4 km (0.68° C/km). The outer plume front extended seaward to the 30 m isobath and marked the seaward extent of recent flushing from the bay caused by strong northerly winds, accompanying passage of an atmospheric cold-front. This outer front extended downcoast to the west; however, its intensity diminished in the downcoast direction. The inner plume front was centered about 18 km from the coast and appeared to mark the seaward extent of very cold bay water (Figure 99). A less intense plume front was measured about 40 km from the coast along line D (Figure 100d, see "PF"). West of the bay, it curved towards the coast near 92° 30' and then was fairly continuous in the downcoast direction past the U.S.-Mexico border (at 26° N). This inner shelf front was about 35 km from the coast along line C (Figure 100c) and about 28 km from the coast along lines B and A (Figure 100b, a) and exhibited a wavy character south of Matagorda Bay as the shelf narrowed (Figure 99). This front will be discussed again later in relation to the SCULP drifter tracks. Along line B, an additional front of about 2° C was measured 85 km from the coast near the 60 m isobath (Figure 100b, see "SF" for squirt front). This front was associated with the northern margin of a cyclonic eddy and marked the location of offshelf flow to the east, to be discussed in more detail later. Information on the intensity of fronts along lines A through E can be found in Table 11.

Table 11. Magnitude and locations of the main thermal fronts along profile lines A-E on November 28, 1993, January 14, 1994 and February 8, 1994.

	A		B		C		D		E	
	C°	km	C°	km	C°	km	C°	km	C°	km
11/28/93	1.5	12	3.3	25	3.8	40	3.8	20	3.3	7
	4.0	28	2.3	85	1.3	70	3.0	62	-3.0	35
					1.5	135			5.0	70
1/14/94			3.0	55	2.0	42	5.5	5	2.6	2
			3.0	97	1.3	84	2.2	110	-2.6	65
					2.0	135			6.8	80
2/8/94	3.3	25								

A comparison of the temperature profiles for November 28, 1993 and January 14, 1994 reveals that shelf temperatures continued to fall over the six-week period. Cooling of 2 to 5° C occurred across the entire shelf rather than preferentially in shallower regions. This may indicate an increase in offshelf flow and mixing during the more intense north-wind events of winter. The thermal fronts seaward of the Mississippi and Atchafalaya were of equal or greater magnitude in January 1994 as compared with November 1993 (Figure 100d, e). The filtered satellite image of January 14, 1994 (Figure 101) again demonstrates distinct thermal fronts associated with the discharge of the Mississippi and Atchafalaya Rivers. The Mississippi River plume front was located in close proximity to the 100 and 200 m isobaths and curved back northwards upon encountering the Mississippi River canyon (Figure 99). The Atchafalaya plume front was located 50 to 60 km from the coast (Figure 100d). An additional front was located 100 km from the coast along line D near the 50 m isobath. This front was observed to be fairly continuous with the Mississippi River plume front (Figure 99), suggesting that it may be partially attributable to downcoast flow of river water. Along line C (Figure 100c), the inner shelf front had moved seaward about 10 km to a position 42 km from the coast. There was also an indication that the fronts along line B had moved seaward as they were now situated 30, 56 and 95 km from the coast (Figure 100b). On January 14, the most pronounced shelf fronts along line B were at the 30 m isobath and just inside the 100 m isobath (Figure 101). The intensity and length of the front south of Matagorda Bay was noteworthy. It marks the confluence of westward flowing inner shelf waters with waters associated with a cyclonic feature resident on the slope and spilling onto the shelf near 28° N. Circulation in this area is discussed in more detail in the next section of this report. Clouds obscured the sea surface along line A, and, therefore, an image obtained on February 18 was used as a replacement. Temperatures extracted along line A (Figure 100a) demonstrated that the inner shelf front was similar in magnitude and in location to that of November 28, 1993.

Comparison of the monthly-averaged coastal temperatures for November 1993, and January 1994, with climatological values suggests that the November 1993, coastal temperatures were 1 to 2° C lower than normal, whereas the January temperatures were 1° C cooler than normal along the Louisiana coast but near normal along the south Texas coast (Figure 98). A comparison of frontal magnitude with average values (Table 12),

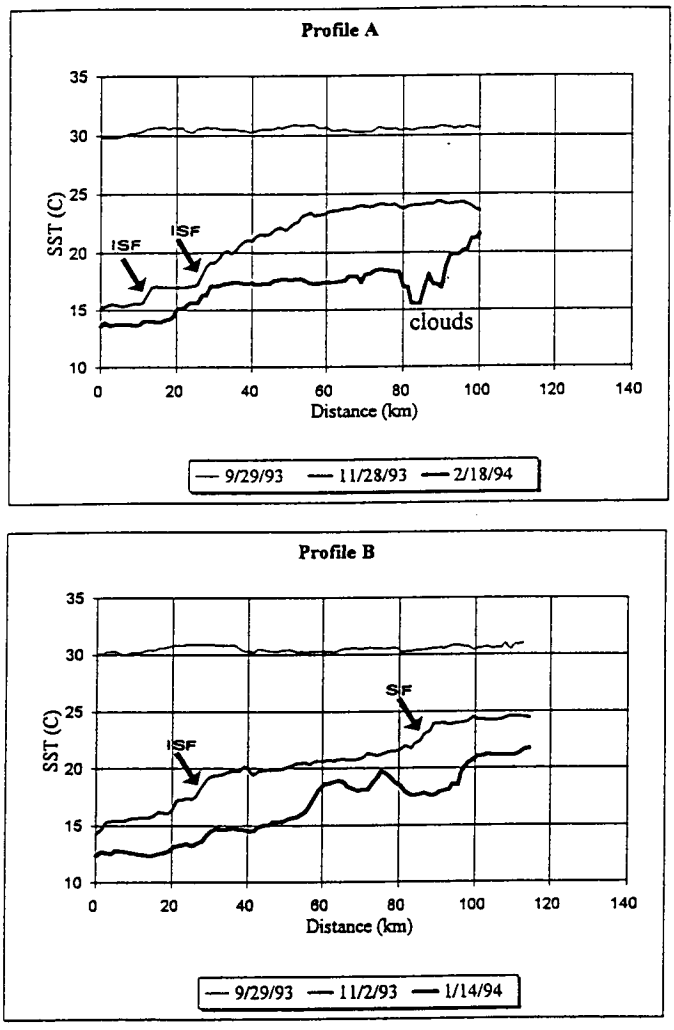

Figure 100. Sea surface temperatures extracted from profile lines A through E (a-e) on September 29, 1993, November 28, 1993 and January 14, 1994. Along line A, SSTs were extracted on February 18, 1994 rather than on January 14, 1994. Inner shelf fronts are identified with ISF, squirt fronts with SF, and plume fronts with PF.

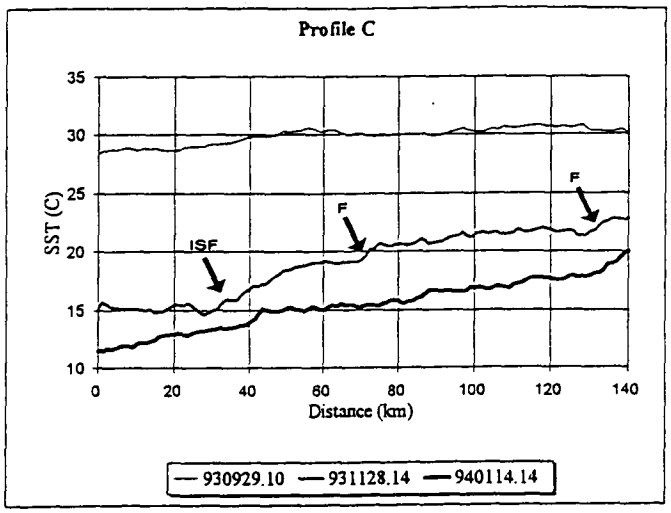

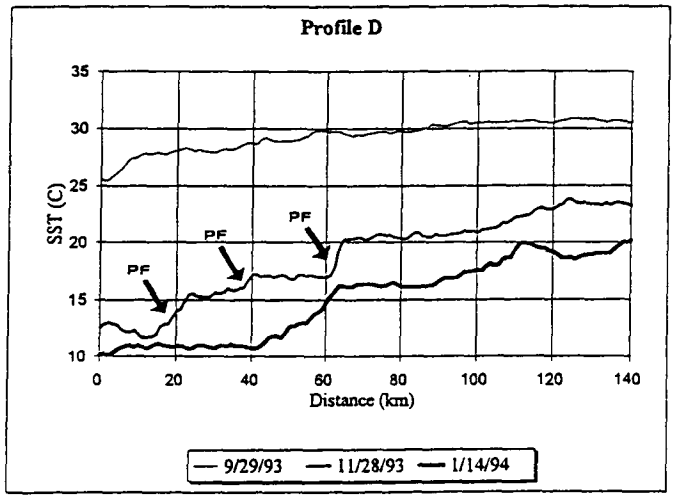

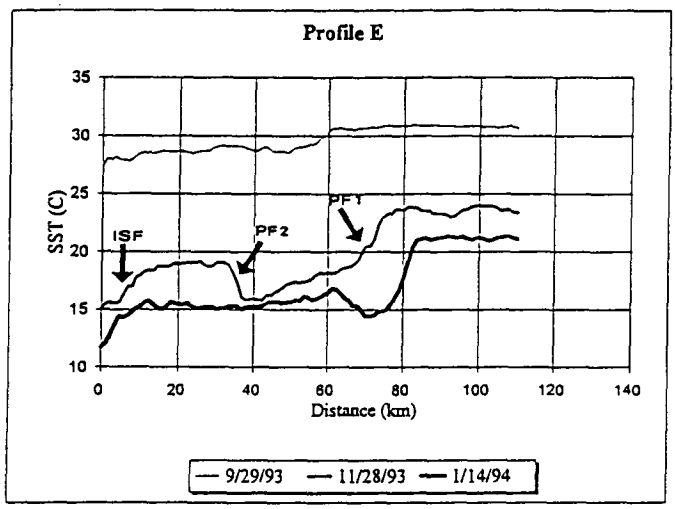

Figure 100 cont'd.

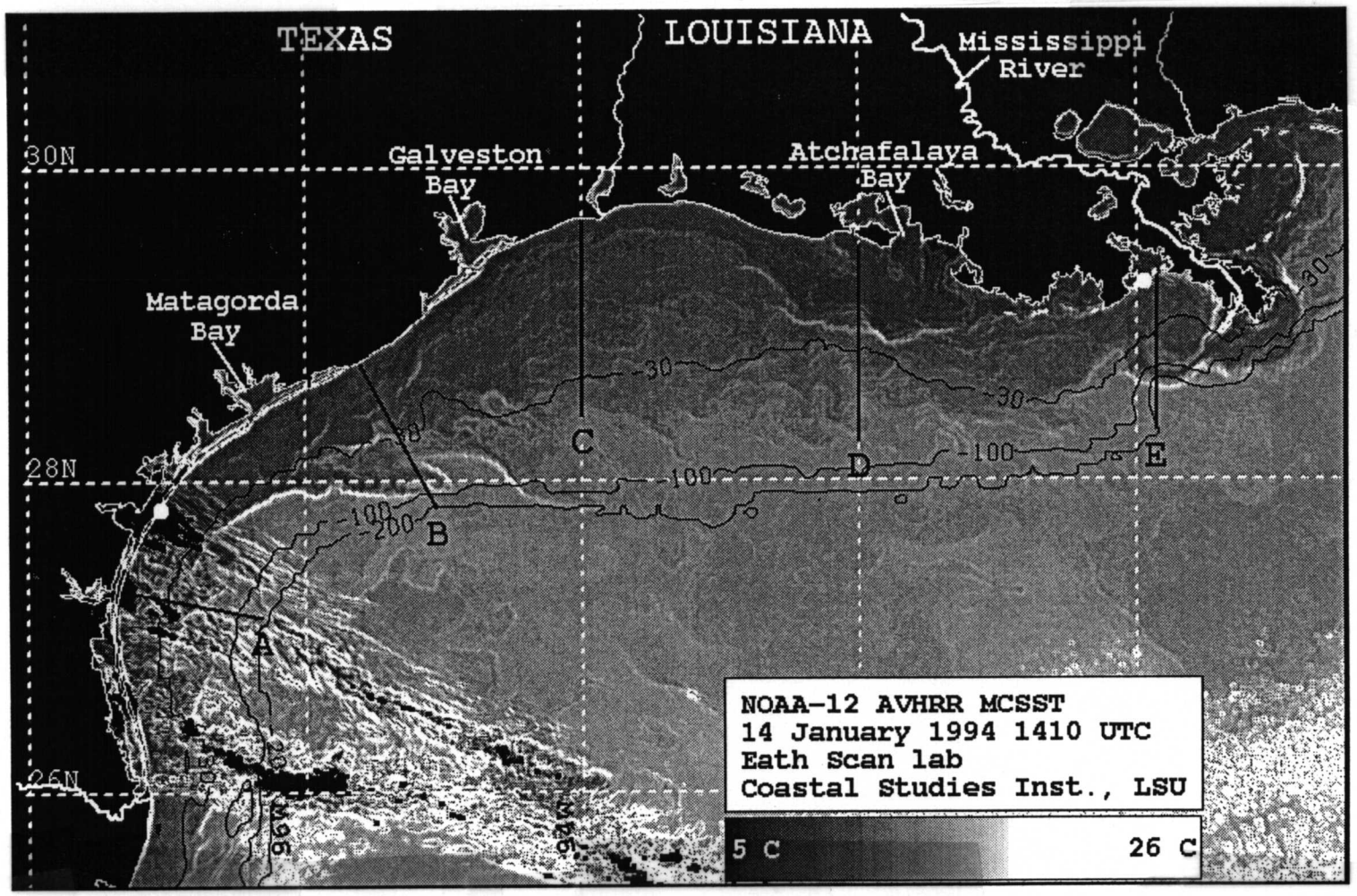

Figure 101. NOAA AVHRR sea surface temperature (SST) image of January 14, 1993 (1410 UT) where cooler waters are depicted with darker shades of grey. Sea surface temperature fronts, as determined by a sobel filter, are depicted with white lines. The profile lines from which SSTs were extracted (see Figure 3) are shown with solid black lines.

reveals that the fronts observed in the November 28, 1993, and January 14, 1994, images were more intense than average.

Table 12. Average and maximum frontal intensities for Lines A-E as determined from an analysis of satellite data during the 1989/90, 1992/93 and 1993/94 winters (Walker, 1996b).

			Average Frontal Intensity (°C)			
Year	A	B	C	D	E	*Mean*
89-90	2.5	2.1	1.4	2.2	1.7	*2.0*
92-93	2.4	2.0	1.6	2.2	2.0	*2.0*
93-94	2.1	1.9	1.7	2.0	1.8	*1.9*
Mean	*2.3*	*2.0*	*1.6*	*2.1*	*1.8*	
			Maximum Frontal Intensity (°C)			
Year	A	B	C	D	E	*Mean*
89-90	8.3	5.8	2.5	4.0	3.3	*4.8*
92-93	5.1	4.8	2.8	4.5	4.0	*4.2*
93-94	4.3	5.9	3.5	5.3	3.5	*4.5*
Mean	*5.9*	*5.5*	*2.9*	*4.6*	*3.6*	

b. Circulation Associated with Squirts, Fronts, and Eddies

The NOAA sea surface temperature (SST) image of November 28, 1993, and the concurrent 10-day sea-surface height (SSH) anomaly overlay reveal the presence of three large warm-core eddies (WCEs) in the western Gulf of Mexico (Figure 102). There is excellent agreement between the thermal patterns and the eddy locations as revealed by the SSH anomalies for the period November 23 through December 3. All three eddies displayed surface temperatures in excess of 25° C and height anomalies of 15 to 20 cm. A cold-core eddy (CCE) with a height anomaly of -15 cm was identifiable on the western margin of the eddy in the far northwestern GOM. Another CCE was detected between the two northernmost WCEs.

Deployment of the SCULP surface drifters began on October 15, 1993, west of the Atchafalaya Bay near 92° W. In Figure 103, the trajectories of a few representative drifters released in October 1993, have been superimposed on the NOAA SST image of November 28, 1993 (Figure 103). Initially, drifter movement was westward along the shelf. The wind histories at two sites within the study area (Burrwood, Louisiana and Port Aransas, Texas) (Locations, Figure 99) are illustrated in Figure 104. The progressive vector diagrams from October 15 through January 14, 1993, exhibit net wind trajectories to the southwest at both sites. Burrwood winds blew primarily towards the southwest and northwest, explaining the predominantly westward circulation on the inner shelf. At Port Aransas, northwestward winds were stronger and southwestward winds were weaker than those at Burrwood. Cold-front passages are revealed as short-lived rotational features in the diagram. The wind history during this 3-month period is typical of fall and winter, when northeast winds predominate (Rhodes et al., 1985). The drifters released in shallower water moved parallel to the coastal SST front (Figure 103). Those released in deeper waters moved westward with a slight onshore component towards the front, indicating convergence of surface flow along the Texas shelf. The coming together of the drifter tracks was also noticeable south of 29° N where the shelf narrows rapidly. Most of the drifters remained seaward of the coastal front or at least 10 km from the coast in close

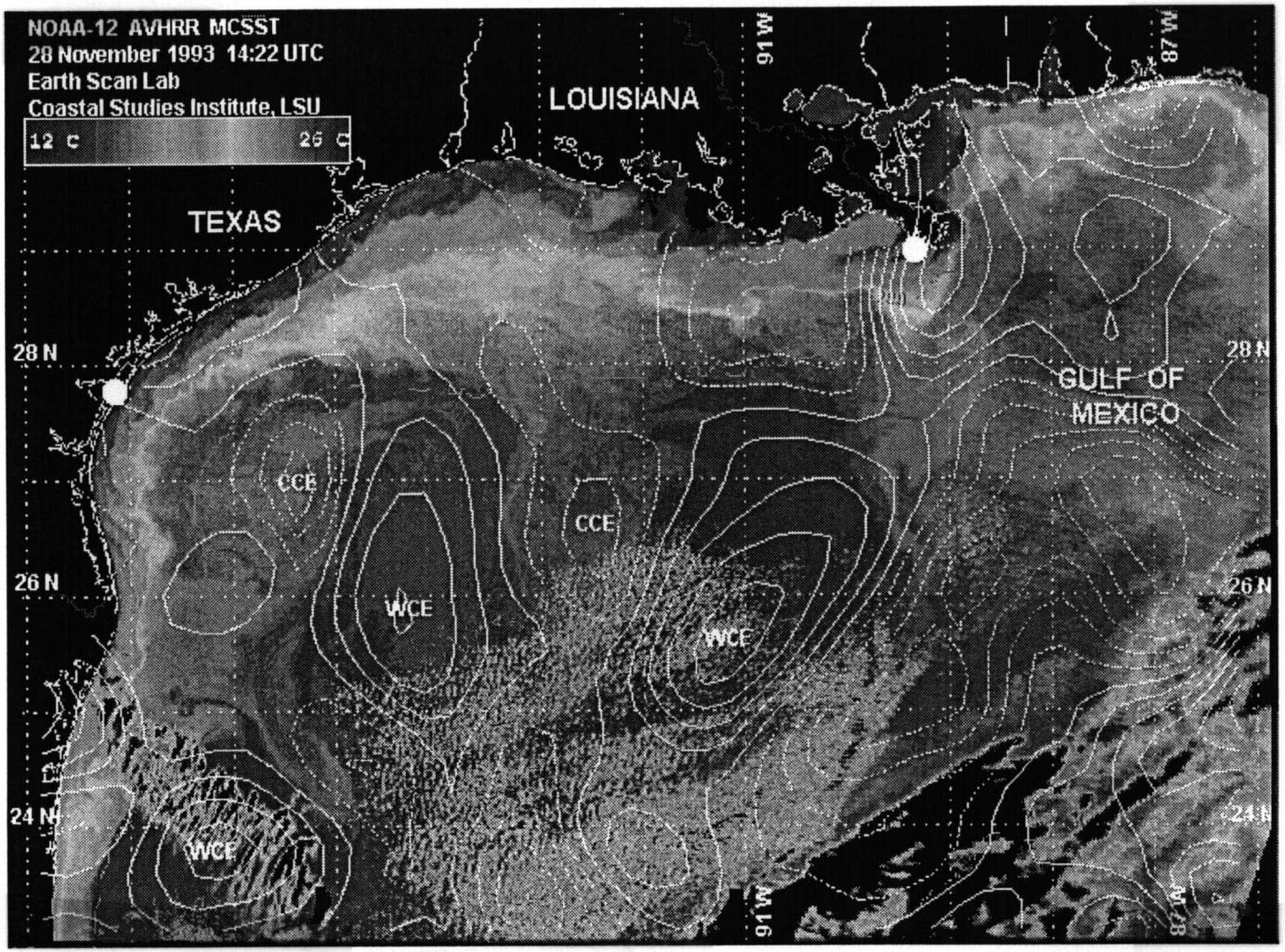

Figure 102. NOAA-12 sea surface temperature image of November 1993 with November 23-December 3, 1993 sea surface height anomalies superimposed. Positive contours are solid, negative contours are dashed, and the contour increment is 5 cm. The three warm-core eddies (WCEs) and the cold-core eddies (CCEs) are identified. The Burrwood (LA) and the Port Aransas (TX) wind stations are shown with white dots.

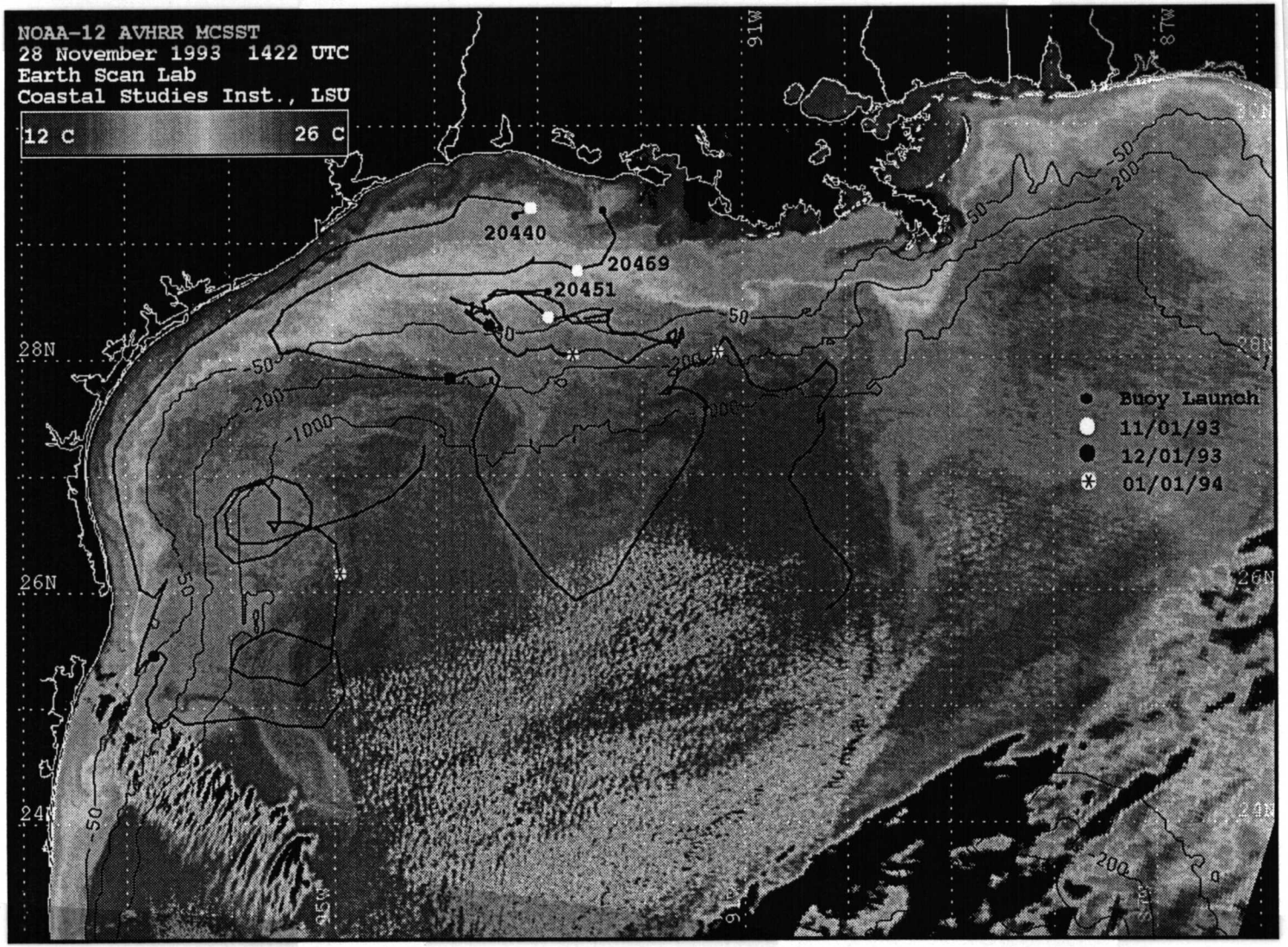

Figure 103. NOAA-12 sea surface temperature image of November 28, 1993 with selected SCULP drifters overlain. Drifters 20440 and 20469 were launched on October 29. Drifter 20451 was deployed on October 23, 1993. Launch sites are indicated with small black dots. Drifter locations on 11/1/93, 12/1/93 and 1/1/94 are shown with symbols as shown in figure legend.

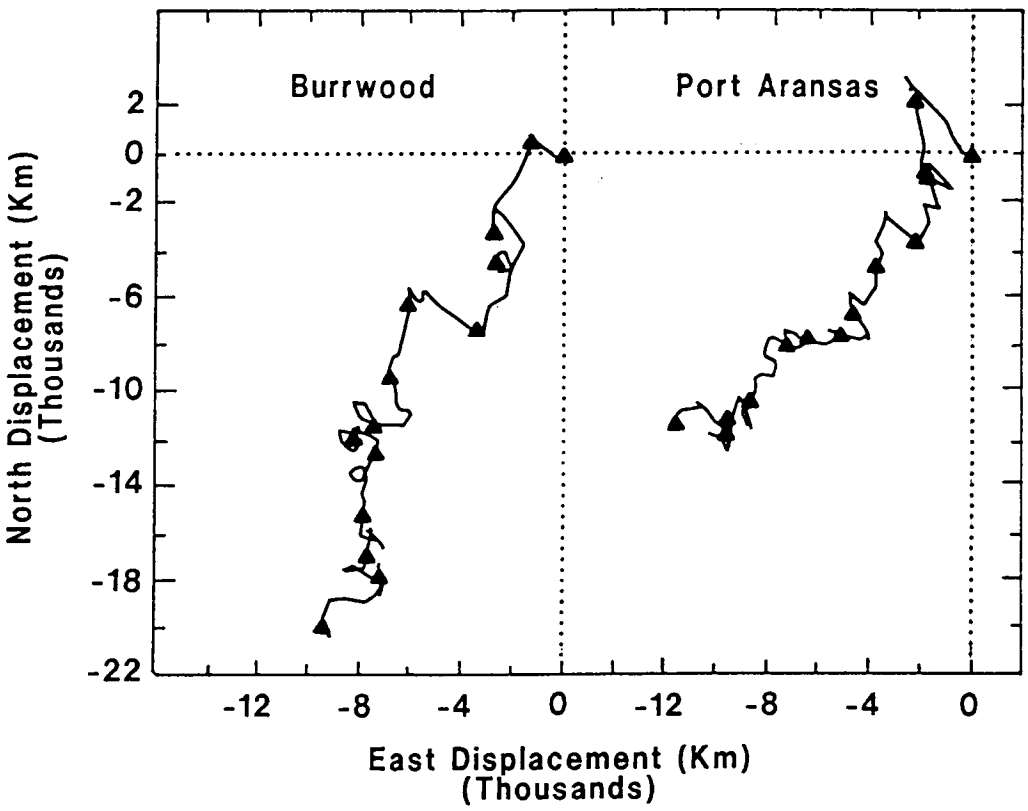

Figure 104. Progressive vector diagrams of wind displacement from October 15, 1993 through January 14, 1994 at (a) Burrwood, LA, and (b) Port Aransas, TX. Triangles are used as 7-day markers, beginning on October 15.

proximity to the coastal SST front, indicating that the Texas coast in winter is not likely to be threatened by oil spills, which occur seaward of this SST front. This is particularly true when winds are predominantly from an easterly direction.

The drifters exhibited three main modes of circulation. Thirty-five percent of the drifters traveled downcoast within the coastal current beyond the U.S.-Mexican border at 26° N. The drifters in this category reached the border after 38.5 days on average, equating to a net downcoast speed of 20.2 cm/s. The fastest drifter took 16 days (37.8 cm/sec) and the slowest took 89 days (6.8 cm/sec). The track of the fastest drifter (20440) within the coastal current group is displayed in Figure 103. Eight of the eleven in this group moved offshelf towards the east or northeast between 24° and 25° N along the northern flank of the southernmost WCE off the Mexican coast. Drifter 20440 was entrained eastward near 24° 30' N with daily averaged speeds of 32 to 45 cm/s within the seaward-directed "jet" flow. It subsequently moved northwards and displayed two series of cyclonic rotations, the last of which was in the CCE so well revealed in the altimetric data (Figure 102). Speeds averaged 28 cm/sec within the cyclonic flow regimes. A relatively strong (45 cm/sec) northward flow was observed between these two regions. The other drifters were also entrained by eddy circulations in the northwest GOM. Only one drifter remained on the shelf, traveling in close proximity to the coastal front to the Bay of Campeche (20° N).

Another thirty-five percent of the drifters were caught up in a narrow offshelf flow off the Texas coast. This group of drifters moved southeastward and eastward along the northern flank of the distinct cold-core/warm core eddy pair (Figure 102). Drifter 20469 was chosen to illustrate this pattern (Figure 103). This drifter averaged 39 cm/sec while in the south Texas "jet" and 48 cm/sec while effected by eddy motion off the shelf. This persistent offshelf "jet" was formed where the wind-driven inner and mid-shelf waters converged with the CCE/WCE pair. The origin of this offshelf flow was observed near 28° N, 96° W, where the shelf narrows rapidly causing convergence of surface flow. Distinct fronts were observed extending west to east and intersecting profile line B (Figure 100b, see "SF" for squirt front).

The third mode of circulation was a weak cyclonic flow between the 30 and 70 meter isobaths at 92 to 95° W. Drifter 20451 in Figure 103 illustrates this circulation pattern. A similar gyre was described by Cochrane and Kelly (1986). It is obvious from this analysis that the Texas jet lies on the west side of the cyclonic gyre.

c. A Climatology of Squirt Events, Northwestern Gulf of Mexico 1992-1994

Squirts and jets are well-known features of the California Current system, particularly during the summer upwelling season (Ikeda and Emery, 1984; Kosro and Huyer, 1986; Strub et al., 1991). California squirts have been defined as "one-way jets, transporting coastal upwelled water to the deep ocean, perhaps terminating in a counter-rotating vortex pair and referred to as a mushroom, hammerhead or "T" (Strub et al., 1991, pp. 14,743). In this report, any offshelf-directed flow of relatively cool water is referred to as a squirt, although the offshelf flows in the northwestern Gulf of Mexico do not always consist of upwelled waters and are not always morphologically similar to those of the California Current system (Walker et al., 1996).

During the 3-year field component of LATEX, a daily surveillance was maintained for squirt events in the northwestern Gulf of Mexico. When such a feature was identified in the satellite imagery, the feature was computer-enhanced and the thermal fronts were digitized. Line drawings and squirt alerts were provided via an OMNET bulletin board to

LATEX researchers and the community at large. The 15 main events that were identified between April 1992 through December 1994 and pertinent characteristics of each squirt, including location, length, width, surface area, surface currents (where available), longevity, and association with eddies are summarized in Table 13. Schematic diagrams of these flow features are presented for each year in Figures 105 through 107.

In July 1992, two cool tongues of inner shelf water extended offshelf along the coasts of Mexico and Texas between 24° and 27° N. This cool water is most likely attributable to wind-forced coastal upwelling. Later in October 1992, a large offshelf flow was observed extending southwestward from the Mississippi delta region. This event was described in detail by Walker et al. (1996). Analysis of in-situ measurements within the October 1992 squirt revealed that it extended about 18 m vertically into the water column. In contrast, the California squirts penetrate vertically beyond the pycnocline. Later in December 1992, another large-scale cool feature was observed off the Mexican shelf.

Table 13. Characteristicis of squirts in the northwest Gulf of Mexico as derived from NOAA POES satellite data during 1992, 1993 and 1994.

Date	Location Eddy	Length (km)	Width (km)	Surface Area (km^2)	Speed (cm/sec)	Longevity (weeks)	
1992							
July 2	Texas	170	20-40	1,858		2	T
	Mexico	250	10-20	2,555		2	U/V
October 13	Miss. Delta	250	10-50	6,550	50-100	2	V
December 20	Mexico	150	20-30	7,728		3-8	T
1993							
January 9	Mexico	200	25-30	6,553		4	T
January 26	Texas	150	20	312		1	V
March 14	Texas	170	20-60	2,826		1	V
May 3	Louisiana	260	70	9,097	30-50	1-2	V
August 1	Texas	250	20	1,230		3	V/W
November 17	Louisiana	100	5-10	1,663	50	1	V/W
November 28	Miss. Delta	200	100	15,794	34	2	X
December 15	Mexico	200	20	8,448	34	4	W
1994							
April 27	Texas/Mexico	325	10-15	4,508	45-60	2-3	W
July 8	Texas/Mexico	200	20-40	2,960		2	X/W
November 21	Texas/Mexico	350	60	39,114			Y

In 1993, the frequency of squirt events appeared to increase substantially. Eight major events were documented from the Mississippi delta to the Mexican shelf near 24° N. Each event could be linked with circulation of a large warm-core eddy and, in some cases, to warm-core/cold-core eddy pairs. The flows directed south from the Louisiana shelf in 1993 occurred on the east sides of detached warm-core eddies of the Loop Current. The May 3 flow (Figure 106) occurred along the east side of Eddy V and the November 28 flow at the Mississippi delta (Figure 106) occurred along the east side of Eddy X. Much of the squirt activity in 1993 (six squirts) can be attributed to Eddy V, which remained active

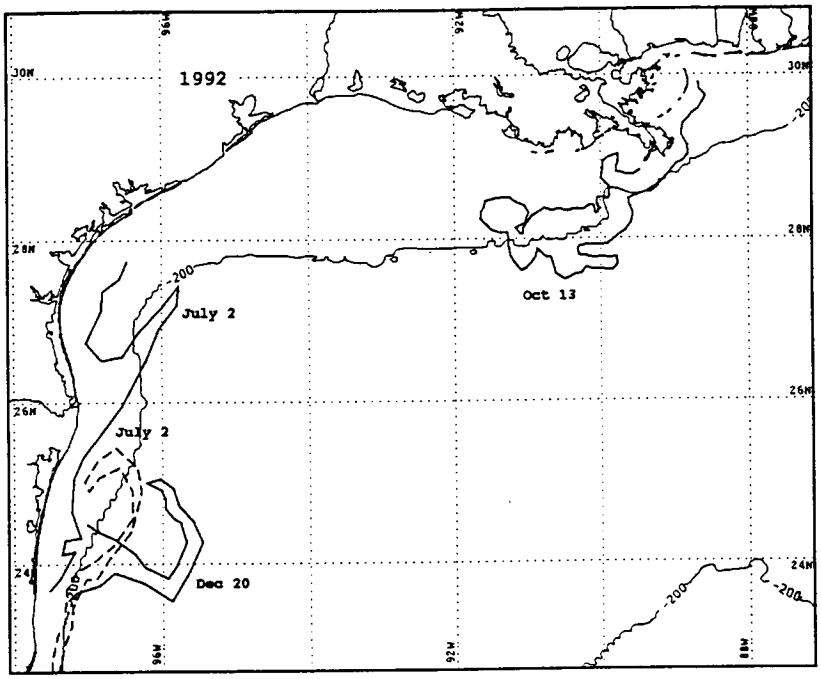

Figure 105. Schematic diagram of the surface expression of prominent squirts in the northwestern Gulf of Mexico as observed in NOAA AVHRR thermal infrared satellite data during 1992.

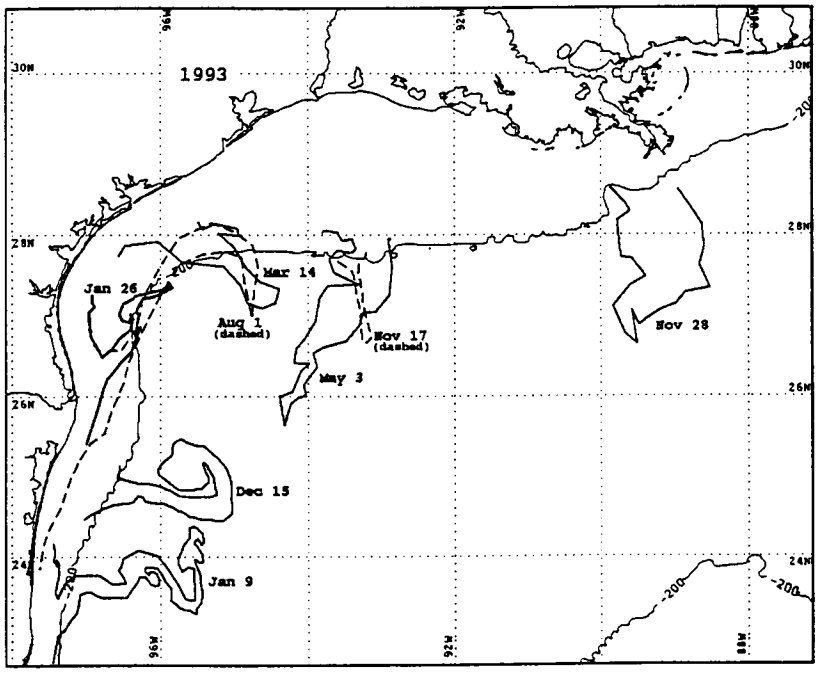

Figure 106. Schematic diagram of the surface expression of prominent squirts in the northwestern Gulf of Mexico as observed in NOAA AVHRR thermal infrared satellite data during 1993.

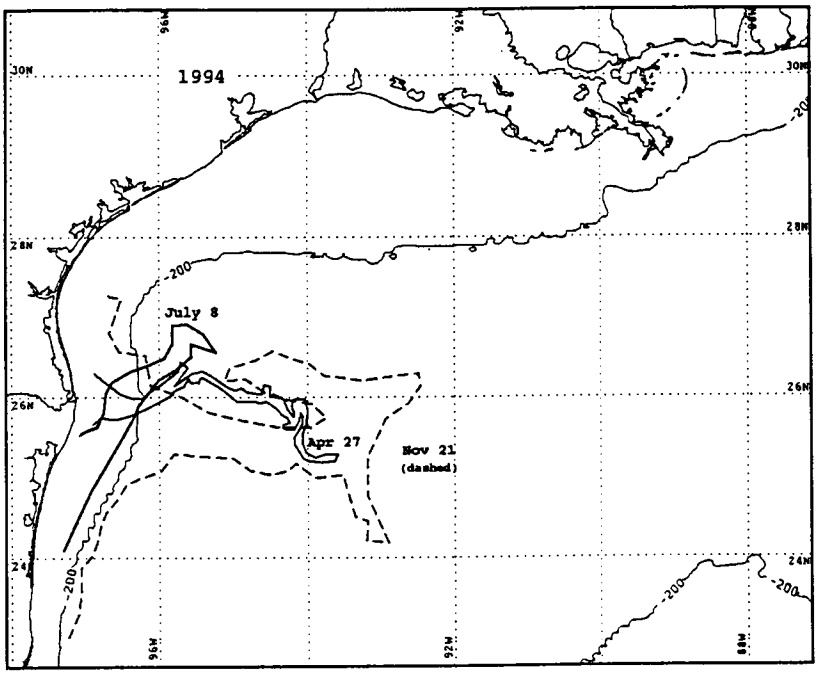

Figure 107. Schematic diagram of the surface expression of prominent squirts in the northwestern Gulf of Mexico as observed in NOAA AVHRR thermal infrared satellite data during 1994.

and in close proximity to the LATEX shelf. In summer 1993, a portion of Eddy W merged with Eddy V in the northwest 60 m. Squirt activity off the Mexican shelf was probably associated with Eddy T in January and Eddy W in December 1993.

The offshelf flow activity in 1994 was mainly along the Mexican shelf in association with Eddy W, X, and Y (Figure 100). The offshelf flow in November 21 was particularly noteworthy as it extended 350 km seaward and covered 39,114 km^2.

Figures 105 through 107 reveal that the squirts were most frequently observed along the continental shelf of the western Gulf of Mexico between 23° and 28° N. A few squirts were observed to extend south and west from the Mississippi delta region and a few in 1993 extended south from the broadest part of the LATEX shelf. A tremendous amount of variability was observed in the physical characteristics of the squirts. Length scales varied from 150 km to 350 km with an average of 215 km. Width scales varied from 5 to 100 km. Surface areas ranged from 312 km^2 to 39,114 km^2. The average surface area of all 15 squirts was 7413 km^2; however, removal of the November 21, 1994, squirt reduced this average to 5149 km^2. Surface velocities within the squirts, as determined from drifter data, ranged from 30 cm/sec to 100 cm/sec. Squirt longevity ranged from 7 to 30 days. Each squirt was found to be closely associated with circulation of a detached warm core eddy of the Loop. Eddies T through Y effected the LATEX region during the field measurement period. Squirt activity varied considerably from year to year during the LATEX field program. This analysis indicates that much of this variability can be explained by the higher frequency of offshelf flows associated with Eddy V.

Most squirts were observed between October and May, which corresponds to the occurrence of increased frequency in offshore winds along the LATEX shelf. This observation does not hold true for the south Texas and north Mexico coast where cool upwelled waters were often observed extending northeastward in summer. Squirt morphology in summer was more along-shelf than off-shelf, indicating that the prevailing flow was upcoast. The uniformity of surface temperatures over most of the Gulf of Mexico away from the Texas upwelling region in summer would preclude the observation of offshelf flows.

3. Summary and Conclusions

During September and October, the uniform sea-surface temperature distribution (characteristic of much of the Gulf of Mexico) disappears, and water masses become differentiated by temperature as a result of depth-controlled chilling associated with the passage of winter storms. Surface thermal fronts are evolved in preferential sights on the Louisiana/Texas continental shelf from autumn through early spring. Some of the most intense and persistent thermal fronts are formed where the Mississippi and Atchafalaya Rivers encounter warmer shelf waters. A fairly continuous inner shelf front is often observed 20 to 40 km from the coast and has been observed to extend westward from the Atchafalaya delta region to the border between the U.S. and Mexico at 26° N. Multiple fronts are not uncommon on the inner and mid-shelf regions, and they are thought to result from consecutive winter storms that cause heat loss and chilling of shelf waters and also force cold bay and river waters seaward. These fronts may become elongated downcoast in the extended plumes as the prevailing flow direction is westward along the Louisiana shelf and southward along the Texas shelf. In addition, distinct thermal fronts are formed where warm-core eddies encounter cooler waters on the shelf and slope or where they encounter cold-core eddies. In some instances, the eddy-induced circulations result in offshelf flows or squirts. The intensity of shelf fronts averages about 2° C with maximum fronts of 4 to 8° C.

The integration of satellite-derived sea surface temperature measurements, TOPEX and ERS-1 sea surface height anomaly data, and surface drifter data has enabled a more thorough interpretation of surface circulation in the northwestern Gulf of Mexico. The 31 drifters exhibited three main modes of circulation. One-third of the drifters demonstrated downcoast flow typical of the wind-driven coastal current along the Louisiana-Texas coast. Another one-third of the drifters exhibited offshelf flow south of Matagorda Bay near 28° N, probably as a result of the convergence of water masses on the westwern side of the quasi-shelfwide cyclonic gyre. Fifteen percent of the drifters were trapped within a slow-moving cyclonic gyre between the 30 and 70 meter isobaths on the Louisiana/Texas shelves between 92° and 94° W longitudes. Approximately 70% of the drifters were advected seaward by warm-core and cold-core eddy circulations into the deep Gulf. These results clearly demonstrate the over-riding effects that eddy motions can have on surface circulation in particular regions of the continental shelf seaward of the coastal SST front.

The presence of offshelf-directed squirts and jets delineate the location of warm-core eddies and warm-core/cold-core eddy pairs. From 1992 through 1994, squirt formation was prevalent near 28° N, 96° W along the 200 m isobath. The squirts were being advected northeastward and then offshelf around warm-core eddies resident close to the continental shelf/slope in the northwestern GOM. Another preferential area for squirt formation was between 24° N and 26° N, along the Mexican shelf. These squirts were also associated with the presence of warm-core eddies and warm-core/cold-core eddy pairs. In addition to these two regions of preferential development, a few squirts were observed extending offshelf from the Mississippi delta region and from the widest portion of the Louisiana/Texas shelf. The squirt events observed in these areas occurred during non-summer months and were probably initiated by north wind events with subsequent offshelf advection enhancement by warm-core eddy circulations.

D. Surface Structure and Variability of the Atchafalaya and Mississippi River Plumes

1. Data and Methods

Satellite data obtained by the NOAA POES (Polar Orbiting Environmental Satellites) were used in this study. The visible (0.58 to 0.68 μm), the near-infrared (0.7 to 1.1 μm), and the thermal infrared (10.5 to 11.5 μm, 11.5 to 12.5 μm) channels were used in the investigations to be presented. Sea surface temperatures were computed using the multi-channel algorithm technique of McClain et al. (1985). Surface suspended sediment concentrations were estimated using the bias correction technique of Stumpf (1992) and a reflectance-suspended sediment algorithm developed for the Mississippi River plume (Walker and Rouse, 1993; Walker, 1996a).

The historic archive of NOAA POES data (1988-1992) was used to investigate variability of the river plumes and temperature structure on the LATEX shelf. Satellite data collected during the LATEX field measurement program were used in the above-mentioned analyses and also for the investigation of squirts and for selected circulation events. Various other datasets are incorporated as supporting information in this report. Several datasets obtained during the LATEX-B cruises were re-formatted and super-imposed on clear-sky image data. These included salinity, total pigments (Rabalais, Section VI), cyanobacteria abundances (Dortch, Section VII), and key pollutants (Means and McMillan, Section X). The SCULP drifter dataset (Walter Johnson, personal communication, 1996) was used extensively to study circulation associated with the coastal current, squirts, and eddies (Walker et al., 1996). Current meter data obtained by LATEX-A was used for selected time periods overlapping with interesting circulation events.

2. Results

a. Plume Variability and Forcing Mechanisms

The Mississippi River is the major source of fresh water, sediments, nutrients and pollutants for the Gulf of Mexico. Draining 41% of the continental U.S., it discharges freshwater into the northern Gulf of Mexico at an average rate of 18,400 m^3/s and transports about 210 million tons of sediment annually onto the continental shelf and slope (Milliman and Meade, 1983). Approximately 70% of the flow enters the Gulf of Mexico through the bird's foot delta, and the remaining 30% is carried down the Atchafalaya River. The Atchafalaya averages about 50% of the water discharge and 60% of the suspended load of the Mississippi (Mossa and Roberts, 1990).

The riverine waters can often be identified along the coast of the northern Gulf of Mexico in the visible and thermal infrared satellite image data obtained daily by the NOAA series of environmental satellites. The spatial resolution, of 1.1 km at nadir, and the twice-daily coverage offered by each satellite enable tracking of the river plume in the absence of heavy cloud cover.

The visible and thermal infrared satellite data can yield different "pictures" of plume morphology. The reflectance information, revealed by the visible channel, provides a quantitative means of defining plume morphology and variability. In addition, the visible data is usable throughout the year. The main drawback to its use is that once the suspended sediment has dropped out of suspension, the plume is no longer detectable. The surface temperature patterns, revealed by the thermal infrared data, are useful when the temperature of the river discharge contrasts sufficiently with ambient shelf temperatures. The river waters are usually trackable in the thermal imagery from the first cold-air outbreak event in September through March. Beginning in April and throughout the summer, the buoyant river water warms very quickly because of increased levels of solar radiation, and it becomes more difficult to track with any certainty. In this report, both the visible and thermal infrared satellite data have been used. The visible data were more useful during the LATEX-B cruises since they were held during spring and summer. The thermal infrared data have been used to study plume and coastal circulation during selected time periods when supporting in-situ measurements were available.

Satellite observations of plume variability have revealed that the geometry and areal extent of the Mississippi and Atchafalaya plumes are determined primarily by two forcing factors: river discharge and wind speed/direction. River discharge exhibits an annual cycle with highest discharges between March and May and lowest discharge from August to October (Figure 108). The influence of river discharge on plume size is well-illustrated by the results of an analysis of the seasonal and interannual variabilities of the Atchafalaya and Mississippi River surface sediment plumes (Figures 109 and 110; Table 14). For these analyses, the surface areas of the river plumes were determined by obtaining a mean value for each pixel using all available clear-sky imagery during that period. Six to eleven images were available for the time periods to be discussed. The plumes were defined as regions where suspended sediment concentrations exceeded 10 mg/l using the algorithm developed for the Mississippi River plume (Walker, 1996a). The optical characteristics of the Atchafalaya plume should be similar (except during local flooding of the Red River)

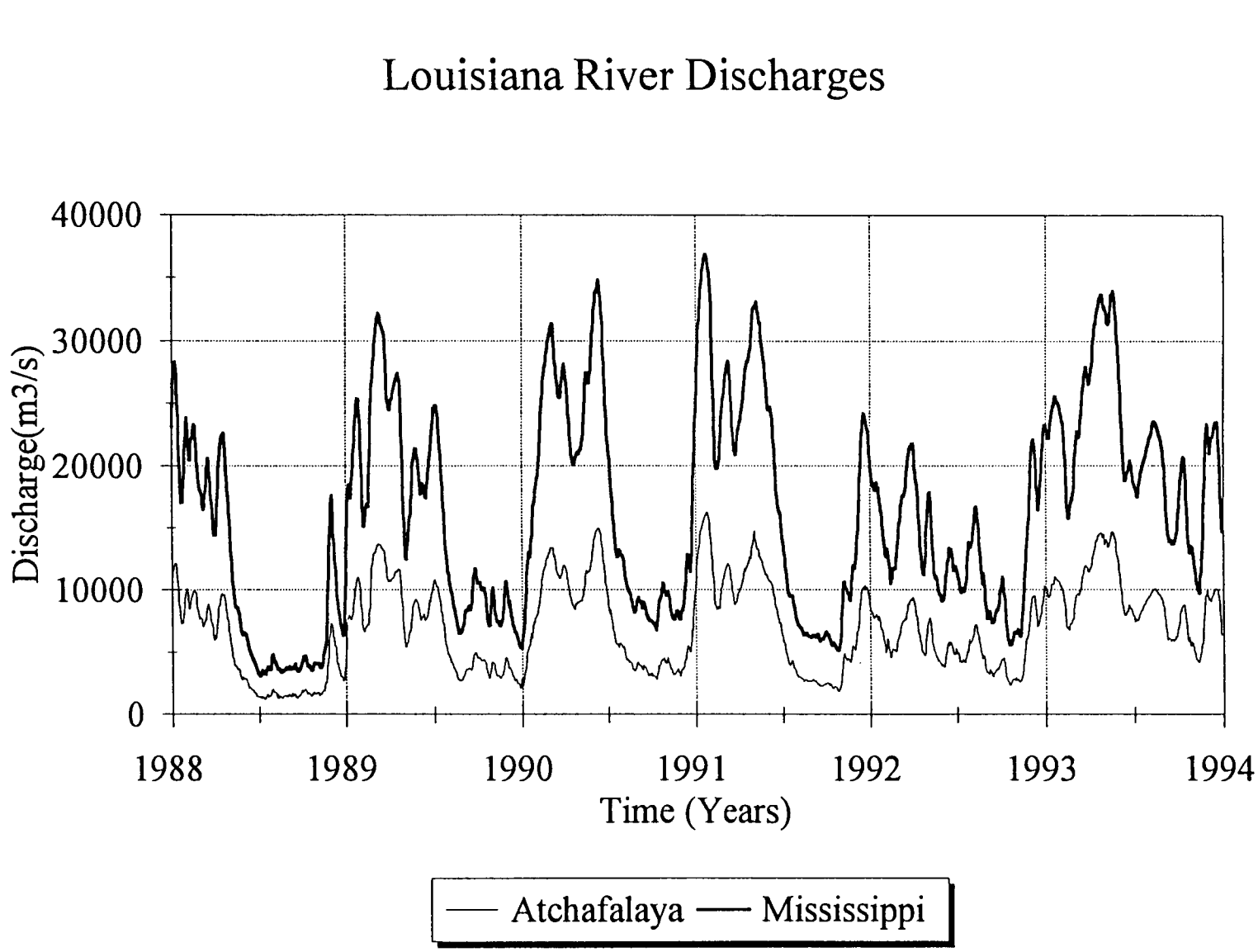

Figure 108. River discharge of the Mississippi River (at Tarbert Landing) and Atchafalaya River (at Simmesport) from January 1988 through December 1993.

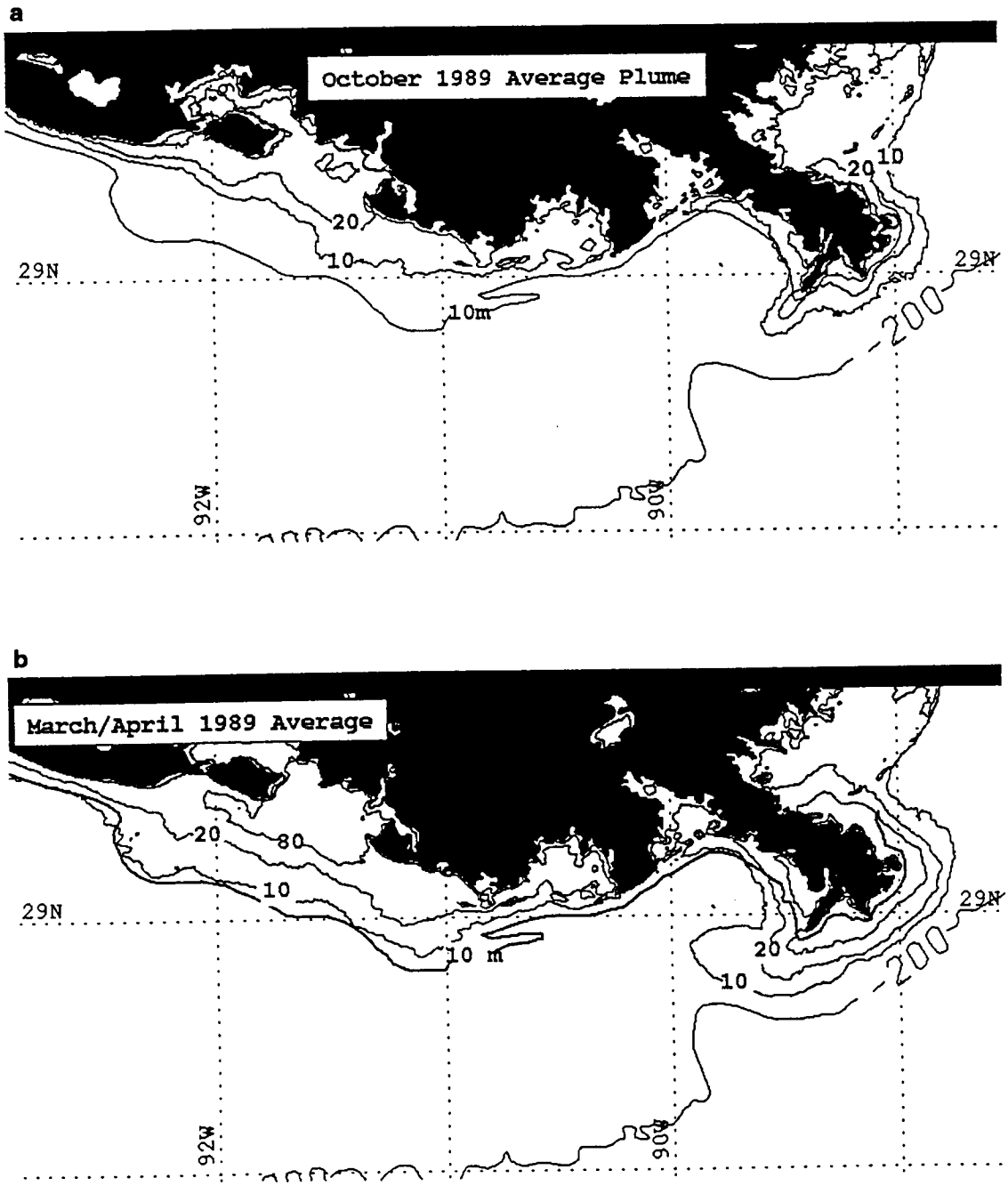

Figure 109. Suspended sediment distribution (mg/l) associated with the Mississippi and Atchafalaya River plumes along the Louisiana coast (a) in October 1989 and (b) in March/April 1989. The 10 m and 200 m depth contours are also shown.

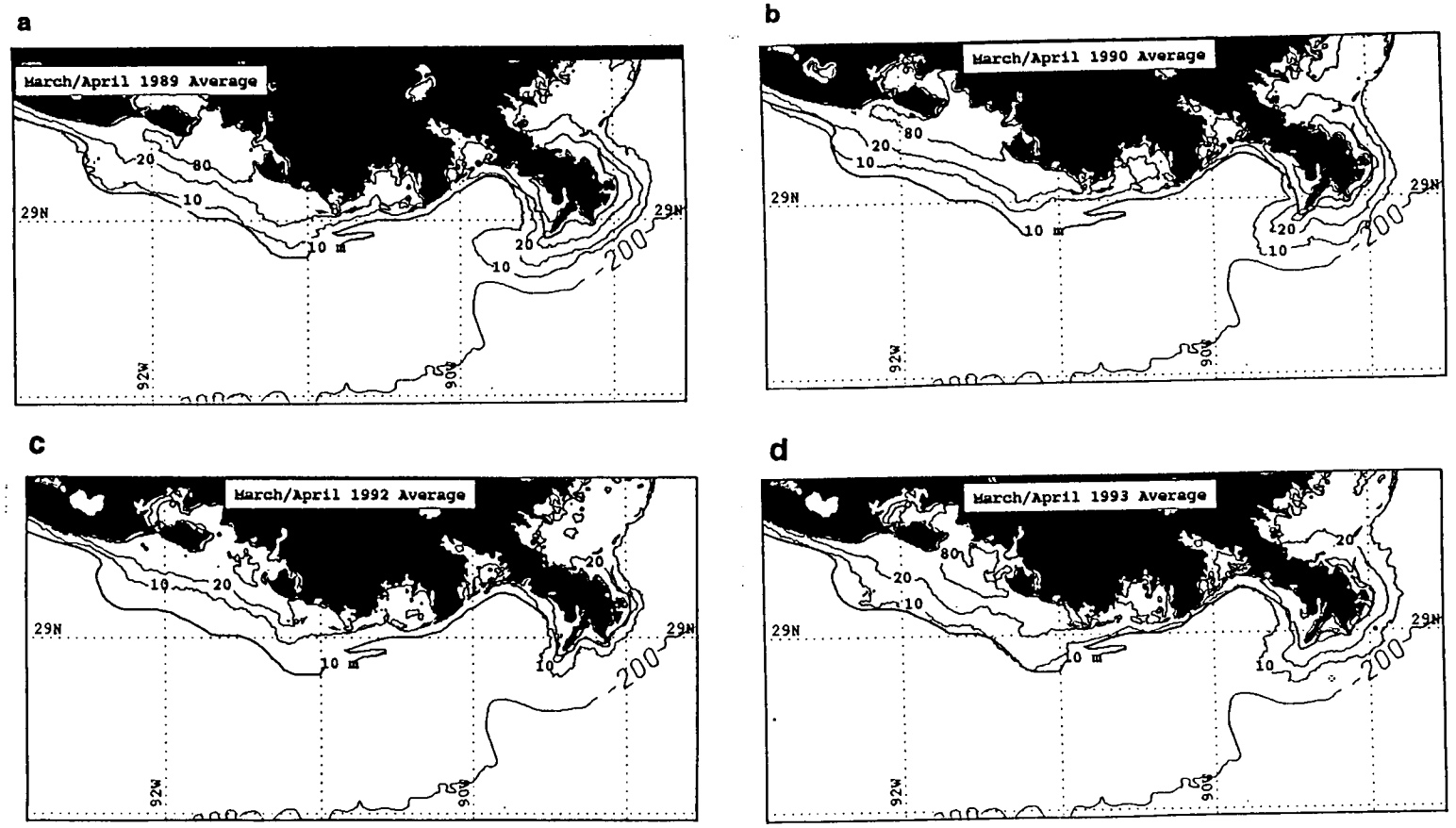

Figure 110. Suspended sediment distribution (mg/l) associated with the Mississippi and Atchafalaya River plumes along the Louisiana coast in (a) March/April 1989; (b) March/April 1990; (c) March/April 1992; and, (d) March/April 1993.

since the Mississippi River is the major source for both plumes. Only areas seaward of Atchafalaya Bay were included in the plume area measurements. A line drawn between the western tip of Point Au Fer and the eastern tip of Marsh Island defined the seaward limit of the bay. It is also important to point out that the reflectance/suspended sediment algorithm was developed using the visible and near infrared channels of the NOAA-11 satellite and fortuitously these channels exhibited little degradation from 1989 through 1993 (Y.J. Kaufman, personal communication).

Table 14. Annual and interannual variabilities in plume sizes.

Averaging Period	Atchafalaya Discharge (m^3/s)	Atchafalaya Plume Area (km^2)	Mississippi Discharge (m^3/s)	Mississippi Plume Area (km^2)
Oct 1989	4,045	2593	9314	2058
Mar/Apr 1989	11,904	5079	27,721	4595
Mar/Apr 1990	10,978	4348	25,586	3997
Mar/Apr 1992	7325	3171	17,259	1836
Mar/Apr 1993	11,892	4981	27,692	3855

As an example of the seasonal variability of the sediment plumes, the mean Atchafalaya and Mississippi River plumes for October 1989 and March/April 1989 are depicted (Figure 109). River discharge in March/April 1989 was three times greater than that in October 1989. The river plumes were approximately twice as large during March/April 1989 as they were during October 1989 (Table 14). It is interesting to note that the Atchafalaya and Mississippi plumes were similar in size in October 1989 (2593 km^2 and 2058 km^2, respectively) and in March/April 1989 (5079 km^2 and 4595 km^2), even though the Mississippi River carries twice as much water. A portion of the Atchafalaya plume results from wind-wave resuspension as the inner shelf seaward of Atchafalaya Bay is extremely shallow. In October 1989, the average concentration within the Atchafalaya plume did not exceed 80 mg/l, whereas in the 1989 spring concentrations in excess of 80 mg/l covered over 800 km^2 of the inner shelf seaward of the Bay (Figure 109) in addition to large areas within the bay that were not included in the measurements of plume area. The Mississippi plume also exhibited large seasonal changes in plume area and suspended sediment distributions (Figure 109). The information on the Mississippi River plume is included for comparison with the Atchafalaya plume; a more comprehensive study of the Mississippi plume region can be found in Walker and Rouse (1993), Walker (1994) and Walker (1996a).

Interannual variability was investigated by comparing average plume areas for the spring of four years: 1989, 1990, 1992, and 1993 (Figure 110). The 1991 spring was too cloudy to warrant investigation. Average Mississippi River discharges (at Tarbert Landing) in March/April of 1989, 1990, and 1993 were all above the 63-year long-term mean of 21,000 m^3/s, whereas, discharge in March/April 1992 was below the long-term mean. The 1989, 1990 and 1993 river discharges in spring were relatively similar (within 10%) whereas the spring discharge in 1992 was considerably lower (63% of the average of the other 3 springs). Plume areas and morphologies were similar during the high discharge springs, whereas smaller plumes with lower concentrations of suspended sediments were observed in the 1992 spring. The 1992 Atchafalaya plume was 34% smaller than the

plume average for the high discharge springs. The 1992 Mississippi River plume was 56% smaller than the high discharge plume average. This analysis clearly reveals the effect of river discharge on average plume size and suspended sediment concentration and distribution on the shelf adjacent to the river outflows. As river discharge increases, the average surface plumes of both delta regions increase in size and in surface suspended sediment concentration.

The Atchafalaya plume (10 mg/l isoline) exhibited a two-lobed morphology on the inner shelf which corresponded well with the bathymetry as depicted by the 10 m isobath. The average plume for March/April 1989 and 1993 followed the bottom topography most closely. It is hypothesized that the close correspondence between plume morphology and bottom topography is because of the process of wind-wave resuspension of bottom sediments. It is interesting to note that the suspended sediment concentrations in Terrebonne Bay—the large bay to the east of the Atchafalaya complex—show trends similar to those in the Atchafalaya Bay complex. In the 3 high discharge springs, average sediment concentration exceeded 20 mg/l over much of Terrebonne bay (Figure 110a,b,d) and along the coast between the bays, whereas, during the low discharge spring of 1992, suspended sediment concentrations were much lower (Figure 110). It appears as though suspended sediment concentrations within Terrebonne Bay and along the coast are measurably increased when Atchafalaya River discharge increases.

The average Atchafalaya plume for the low discharge spring of 1992 is compared to the plume of the high discharge spring of 1993 in Figure 111. The average spring condition would lie between these two examples. During the relatively low discharge spring, the plume ranged between 24 and 33 km from the coast or bay entrance. In contrast, during the relatively high discharge spring the seaward extent of the plume was located 39 to 45 km from the coast.

The effect of wind speed and direction on plume morphology and plume area is presented by analyzing average plumes for the four main wind directions affecting the Louisiana coastline: southeasterly, southwesterly, northwesterly, and northeasterly. In addition, individual satellite images are displayed for these wind scenarios. Most of the data used to compile these "average" plumes were obtained in the winter and spring of 1992 and 1993 when higher quality wind data were available in the Atchafalaya plume region because of automation of the Patterson airport weather station and the addition of LATEX-A Mooring 17 seaward of Atchafalaya Bay.

The first wind scenario to be investigated is the southeasterly wind, that is, the wind blowing from southeast to northwest. Winds from this direction occur more frequently than any other single direction along the Louisiana coast and are most prevalent in spring and early summer. On April 21, 1990, under conditions of moderate southeasterly wind forcing (Figure 112a), the main body of the Atchafalaya sediment plume was observed to extend out of the bay towards the west in a mud-stream type morphology, as reported by Roberts et al. (1987). An "average" plume for southeasterly wind forcing was constructed using seven clear-sky images (Figure 112b). The suspended sediment distributions again show increased concentrations towards the west with a tongue of very turbid water (> 80 mg/l) extending westward from Atchafalaya Bay. The Mississippi River plume exhibited a morphology that suggested the existence of a clockwise gyre within the Louisiana Bight, west of the Mississippi delta (Figure 112a), a circulation pattern that has been reported previously (Wiseman et al., 1976; Rouse and Coleman, 1976). The imagery suggests substantial east to west transport of water emanating from South Pass and Southwest Pass; however, turbid waters discharged on the northeast side of the delta extended northwards and northwestwards into

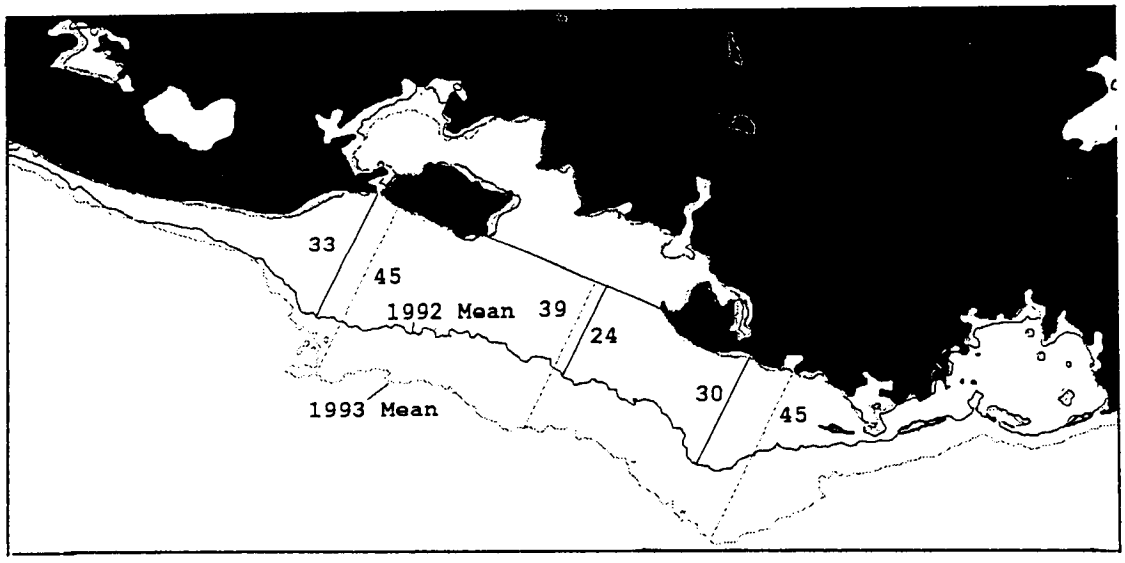

Figure 111. The seaward limit of the average composite Atchafalaya sediment plume (outlined by the 10 mg/l contour) for the relatively low discharge spring of 1992 and the relatively high discharge spring of 1993. The 10 mg/l contour was used to define the seaward extent of the plumes.

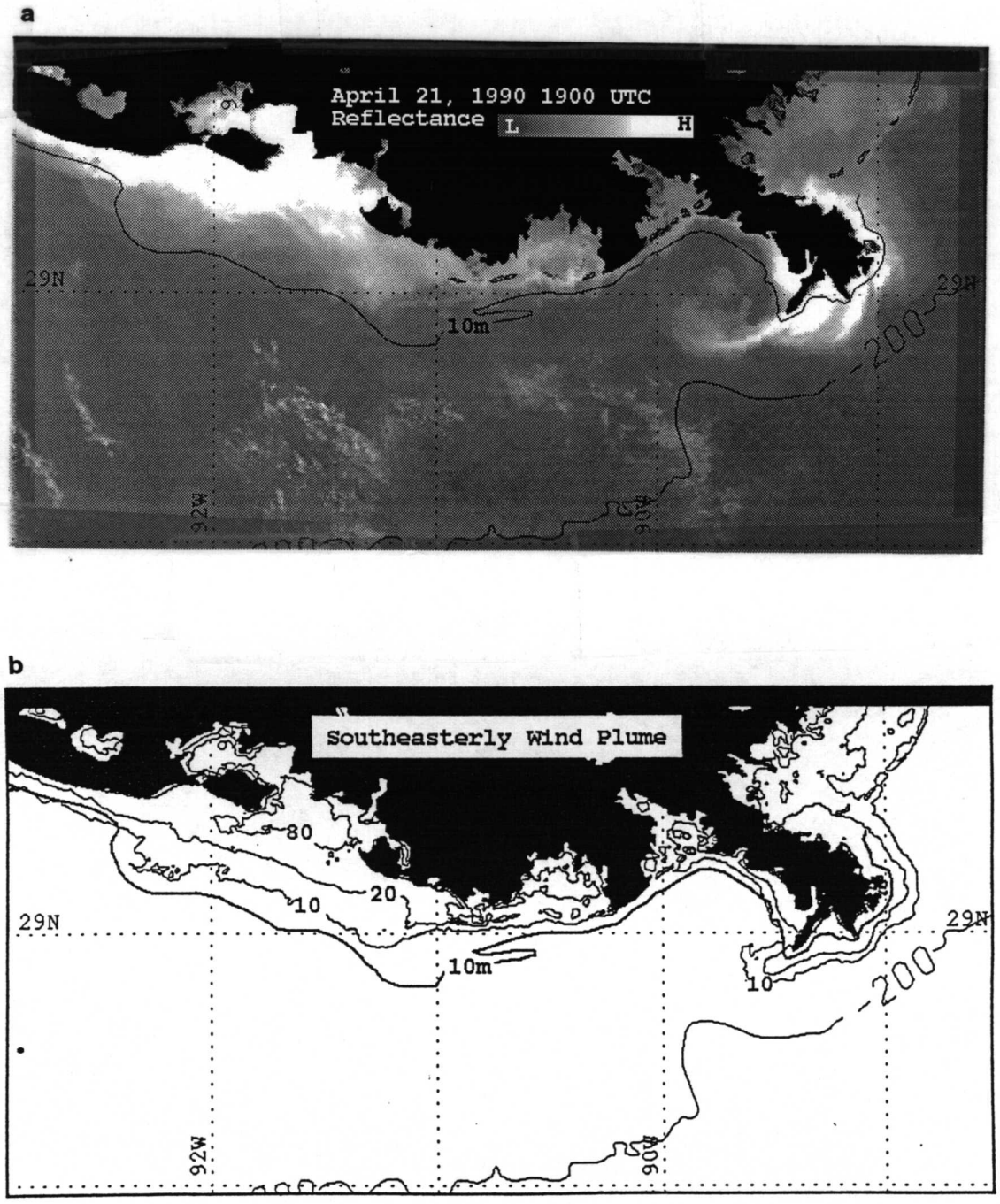

Figure 112. (a) Satellite reflectance data on April 21, 1990 under conditions of moderate southeasterly wind forcing; and (b) average suspended sediment concentrations (mg/l) for southeasterly winds derived from seven clear-sky images.

Chandeleur-Breton Sound. The average plume of 3742 km^2 (Figure 112b) shows that under southeasterly wind conditions the most turbid water is found in close proximity to the delta or extending northwards or southwestwards from Southwest Pass. The maximum surface sediment concentrations in the Mississippi plume were found to be substantially lower than those within the Atchafalaya plume. The reduction in wind-wave resuspension in the Mississippi plume case may explain this difference in sediment concentration.

The northeasterly wind case (blowing from the northeast to the southwest) is the next most frequent wind direction, mainly in autumn and spring, in the wake of cold-front passages. The January 20, 1992 image (Figure 113a) was preceded by 40 hours of strong (10 to 18 m/s) north-northeasterly winds during a period of average spring river discharge (19,000-20,000 m^3/s). Both of the turbid river plumes were observed to cover an expansive area of the shelf (Figure 113a), in both the along-shelf and across-shelf directions. Although the plumes are longer and broader than the plumes under southeasterly wind conditions (Figure 112a), plume orientation again suggests a predominant surface flow towards the west, with an additional off-shelf component. The turbid water of the Mississippi plume was observed as a broad water mass just west of Southwest Pass where it measured 40 km in width. It curved northwestward and then to the west upon encountering the coast between Barrataria and Terrebonne Bays. It was trackable in the imagery until it encountered the turbid waters associated with the extensive Atchafalaya plume. There was no clear indication of a clockwise gyre west of the Mississippi delta. Perhaps under very strong northeasterly winds the primary flow is westward and in an off-shelf direction. However, ADCP measurements collected in the Mississippi River plume region during the LATEX-B Cruise 5 (Rouse, personal communication, 1995) showed the existence of a well-defined clockwise gyre west of the delta under moderate (5 to 10 m/s) northeasterly wind conditions in addition to a strong westward flow along the coast. On January 20, after the sustained strong northeasterly wind forcing, the Atchafalaya plume was observed to cover 9060 km^2 of the continental shelf and extended as much as 72 km from the coast! It is hypothesized that the sediment plume had three main sources. One source was the discharge from the Atchafalaya River, which was about average for spring during time of image acquisition. The second source would have been sediments resuspended in the bay and flushed onto the shelf. The third source would have been unconsolidated sediments on the inner shelf that were resuspended over a large area by the wind-generated waves.

The average plume for northeasterly wind conditions was compiled using seven clear-sky images (Figure 113b). The plume morphologies during northeasterly wind conditions were quite similar to those during southeasterly wind conditions. The Atchafalaya plume during northeasterly winds was larger than under southeasterly winds (4507 km^2 compared with 3742 km^2) and extended somewhat farther offshore. However, the suspended sediment concentrations in the bay and in close proximity to the coast were higher with winds from the southeast, perhaps as a result of concentration of the sediment near the coast or the larger waves at the coast that would result from the longer fetch onshore winds. The Mississippi plume exhibited a similar morphology during southeasterly and northeasterly wind conditions. Detailed analyses of satellite imagery during northeasterly wind conditions has shown that the predominant circulation is a north-to-south flow of water on the east side of the Mississippi Delta, including southward flow out of Chandeleur-Breton Sound (Walker et al., 1996).

During autumn and winter, the frequency of west winds increases because of the passage of winter storms. Before frontal passage, the winds usually veer from southeast to southwest for a relatively short time. The image of March 14, 1989 (Figure 114a)

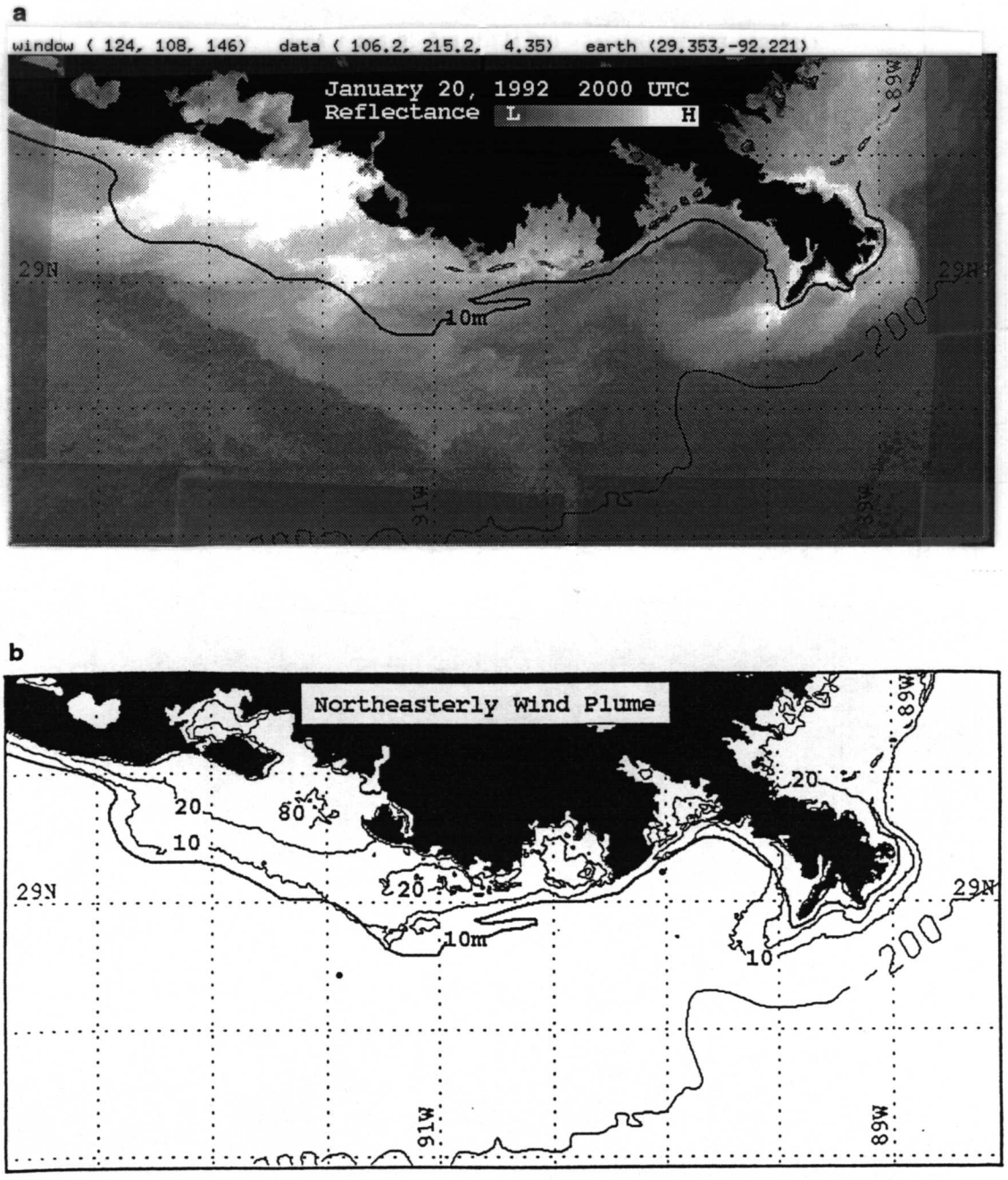

Figure 113. (a) Satellite reflectance data on January 20, 1992 under conditions of strong and sustained northeasterly wind forcing; and (b) average suspended sediment concentration (mg/l) for northeasterly winds derived from nine clear-sky images.

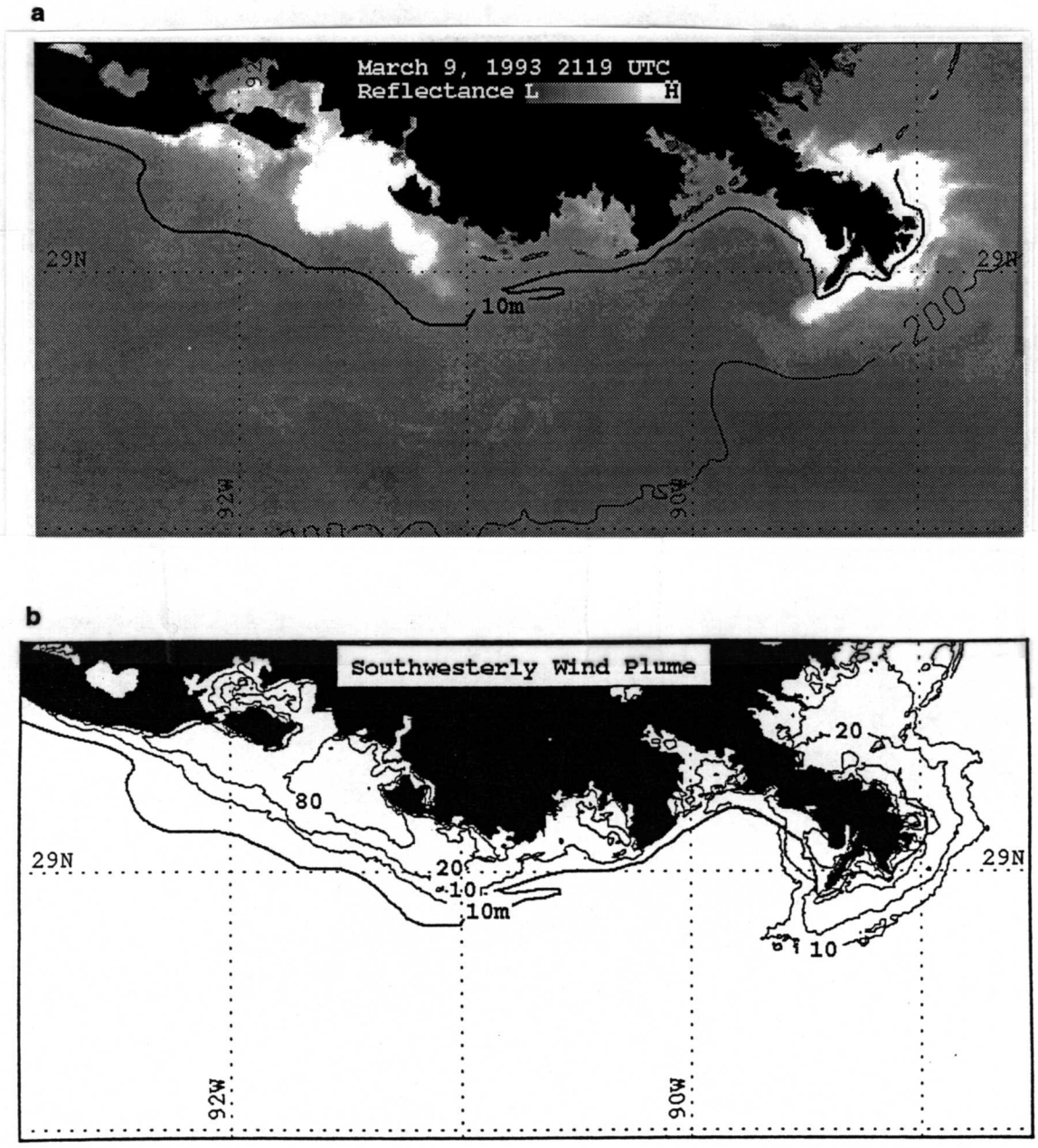

Figure 114. (a) Satellite reflectance data on March 14, 1989 under conditions of moderate to strong southwesterly wind forcing; and (b) average suspended sediment concentrations (mg/l) for southwesterly winds derived from seven clear-sky images.

depicts the Louisiana sediment plumes under conditions of moderate to strong south-southwesterly winds and high river discharge. This image reveals that the Atchafalaya plume was pushed landward on the southwest side where a region of high suspended sediments (> 100 mg/l) was confined to the bay and to the inner shelf just seaward and southeast of the bay. As a result of the strong onshore winds, sharp gradients in suspended sediment concentrations were detected on the south and southwest margins of the Atchafalaya sediment plume. The southwest winds efficiently reversed the westward flowing mud-stream often observed in the Atchafalaya region and forced the plume southeastward. The morphology of the Mississippi plume on March 14 suggests that a major reversal in surface flow accompanied the switch to southwesterly winds. The Southwest Pass plume was deflected southwards in comparison to its southwestward extension under southeasterly wind conditions (Figure 112a). It is obvious from the imagery that the surface waters east of the Mississippi delta had moved northeastward and even northward into Chandeleur-Breton Sound. Average plumes for southwesterly winds were compiled using eight clear-sky images (Figure 114b). This analysis revealed that the Atchafalaya plume covered the smallest area (3583 km^2) under southwesterly winds. This compilation demonstrates an obvious reversal in flow within both river plumes. The highest concentrations of suspended sediments within Atchafalaya Bay were observed to extend eastward under these wind conditions. The Mississippi plume was confined close to the coast on the west side and extended farther from the coast on the east side.

The last major wind direction to be investigated is the northwesterly wind case. Winds from this direction accompany the passage of cold fronts. The image of February 7, 1992 (Figure 115a) was obtained after 48 hours of strong (10 to 15 m/s) northwesterly wind forcing. The sediment plume (> 10 mg/l) measured 9630 km^2 and extended a maximum of 85 km towards the southeast. As was discussed previously, much of this plume probably resulted from resuspension of sediments in the bay and on the inner shelf. These resuspended sediments were then transported seaward by the wind-generated currents. This northwesterly wind event was preceded by strong southerly winds. Tide gauge measurements at Luke's Landing (Corps of Engineers, personal communication, 1996) revealed a one-foot setup before the frontal passage and a four-foot set-down after the frontal passage. Thus, a considerable volume of water was flushed onto the shelf prior to image acquisition. Results of Chuang and Wiseman (1983) showed that water level fluctuations within Atchafalaya Bay respond most strongly to onshore-offshore winds rather than alongshore winds. The Mississippi River plume's surface morphology was substantially altered by the strong northwesterly winds as the turbid river water extended southward on all sides of the delta. There was no indication of the existence of a clockwise gyre in the Louisiana Bight under these strong northwesterly wind conditions. The average plume for northwesterly wind conditions was constructed using seven clear-sky images. Although this average Atchafalaya plume did not extend as far seaward as that of February 7, 1992 (Figure 115b), it showed the same general morphology and distribution of sediments. The average plume exhibited a two-lobed structure that conforms to the bottom topography. The Atchafalaya plume extended further offshore and reached a maximum size (of 6337 km^2) under these wind conditions. The Mississippi River plume did not show such pronounced changes in morphology, except that the turbid waters did extend farther south than usual.

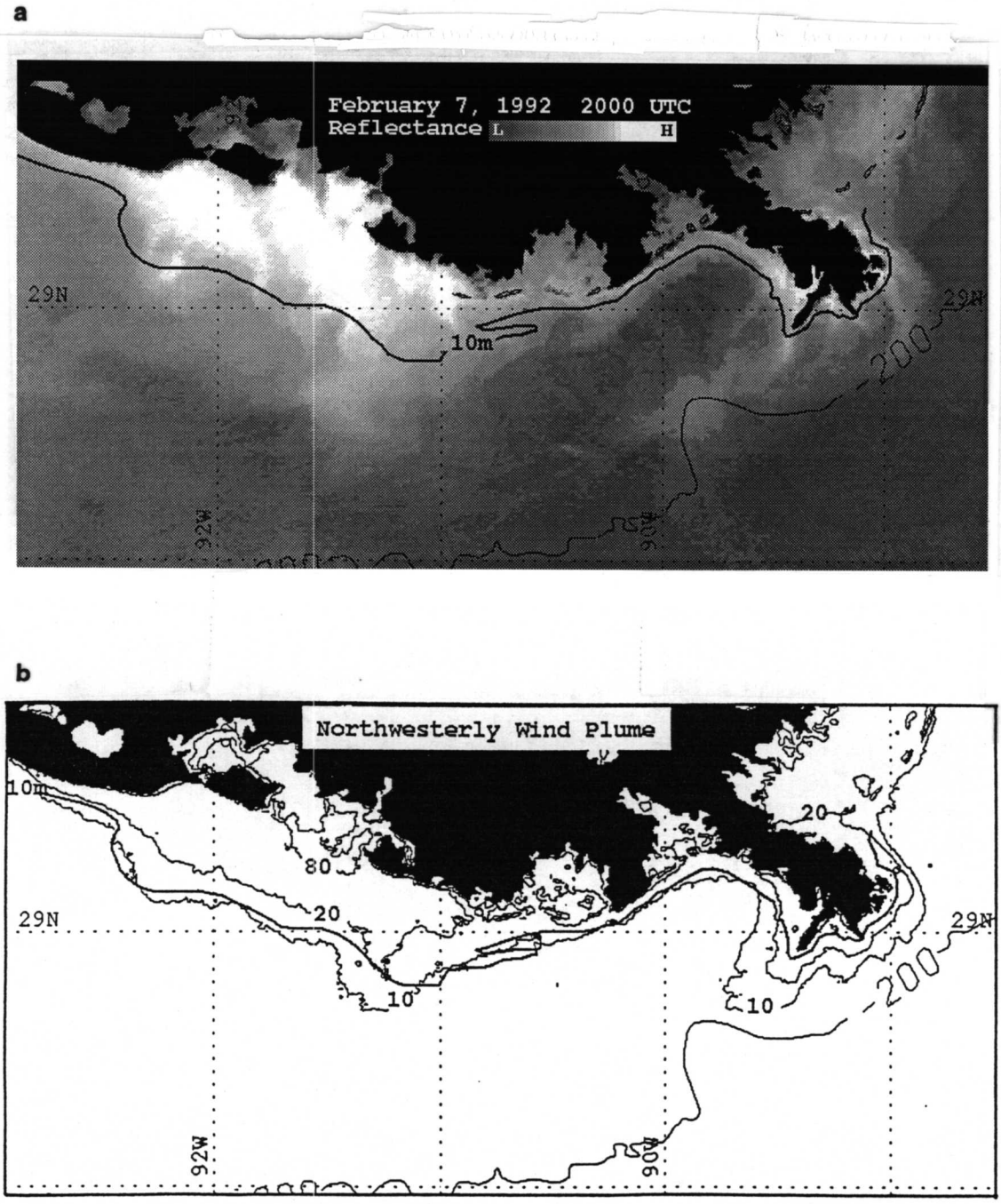

Figure 115. (a) Satellite reflectance data on February 7, 1992 under conditions of strong and sustained northwesterly wind forcing; and (b) average suspended sediment concentrations (mg/l) for northwesterly winds derived from six clear-sky images.

b. LATEX-B Plume Structure and Relationships with Other Measurements

(1) Cruise I: April 22-29, 1992 Imagery obtained at the outset of Cruise I, April 1992, demonstrates how rapidly plume morphology can change with major wind direction changes. The suspended sediment information obtained from the afternoon passes (2000 UT) of April 21 and April 22 are displayed in Figure 116. The wind was strong northwesterly for the 24 hours before the cruise, and substantial flushing of Atchafalaya Bay occurred with a set-down of 3.7 feet (measured at Luke's Landing). The Atchafalaya suspended sediment plume covered an expansive area of the inner shelf on April 21 (Figure 116). Its surface area was 5493 km^2, larger than any of the spring plume averages discussed previously. The Atchafalaya plume again exhibited a two-lobed morphology, which corresponded with the bathymetry, and the sediment plume lay roughly along the 10 m isobath. Resuspension of sediment on the inner shelf and offshore transport resulted in the extensive Atchafalaya plume. Early on the 22nd (first day of the cruise) the wind switched to east-southeast and moderated in strength. Comparison of the plume outlines from the two images reveals that over the 24 hours between images, the plume retreated 20 to 25 km shoreward. The largest changes occurred seaward and east of the bay entrance. The plume of April 22 measured 2930 km^2, which was a 2563 km^2 reduction in area over 24 hours.

Cruise I occupied the inshore side of line S1 during acquisition of the April 22 image (Figure 116a). Note that on April 21 there was a conspicuous discharge plume extending seaward from Terrebonne Bay; however, by the afternoon of April 22 it was no longer detectable. At the inshore station along S1 (on April 22) a minimum light transmission of 76% was measured (Figure 117a), which equated to about 10 mg/l according to the satellite image data. The light transmission section confirms that the surface plume did not extend onto the inner shelf past the first station. However, below the surface (from mid-depth to the bottom) a region of lowered transmission (higher concentration of sediment and biological material) was encountered at the inner three stations. This sub-surface region of high turbidity corresponded closely with the offshore extent of the surface plume 24 hours earlier. It is hypothesized that at least part of the reduced transmission resulted from the sinking of sediments from the Terrebonne Bay discharge plume after it was discharged onto the inner shelf. Another large region of low transmission was identified starting 35 km offshore in a water depth of 18 m. The imagery does not indicate any direct relationship between this region and past surface plumes. The data on light transmission was obtained with a SeaTech, Inc. 5-cm transmissometer (LED 670 nm).

The S2 line occupation started at the offshore station six hours after acquisition of the April 22 image. By this time, only the innermost station was in the Atchafalaya plume. The minimum light transmission value measured at the nearshore station was 80% (Figure 117b). Notice that the S2 line transected the region where the eastern lobe of the Atchafalaya plume was observed on April 21 (Figure 116). Although the surface plume had retreated substantially landward over the 30 hours, a region of low transmission was encountered below the surface six stations from the coast (Figure 117b). The surface plume on April 21 extended to the fifth station. As along S1, the occurrence of relatively high turbidity water subsurface was found to correspond closely with the region occupied previously by the surface plume. The lowest transmission value (36%) of the three lines was detected at the inshore station on S3 (not shown), a region often affected by Atchafalaya plume water in its westward movement along the coast. In contrast to the other two lines, the waters at the four innermost stations were well-mixed from surface to bottom. This vertical homogeneity may have resulted from an increase in southeastern wind

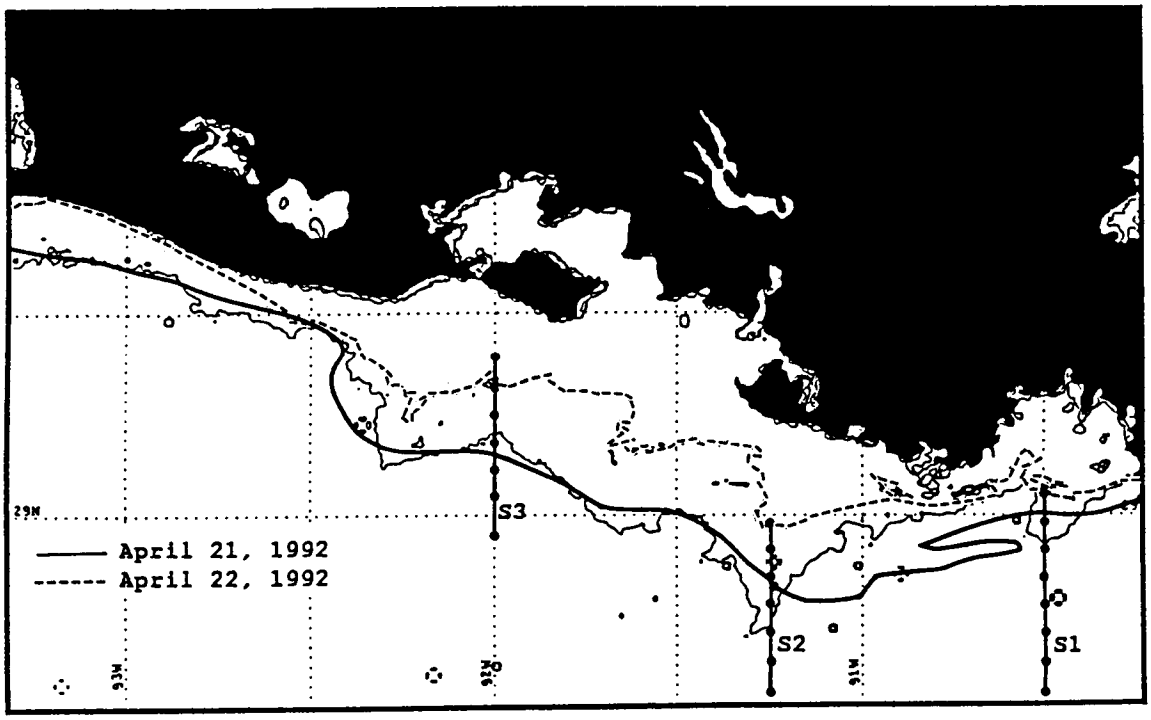

Figure 116. Spatial plots of the estimated 10 mg/l suspended sediment contours derived from satellite image analyses of April 21 (2000 UT; outer contour) and April 22 (2000 UT; inner contour). The S1, S2, and S3 lines of the LATEX-B cruise are overlain. The 10 m isobath is plotted as a bolder solid black line.

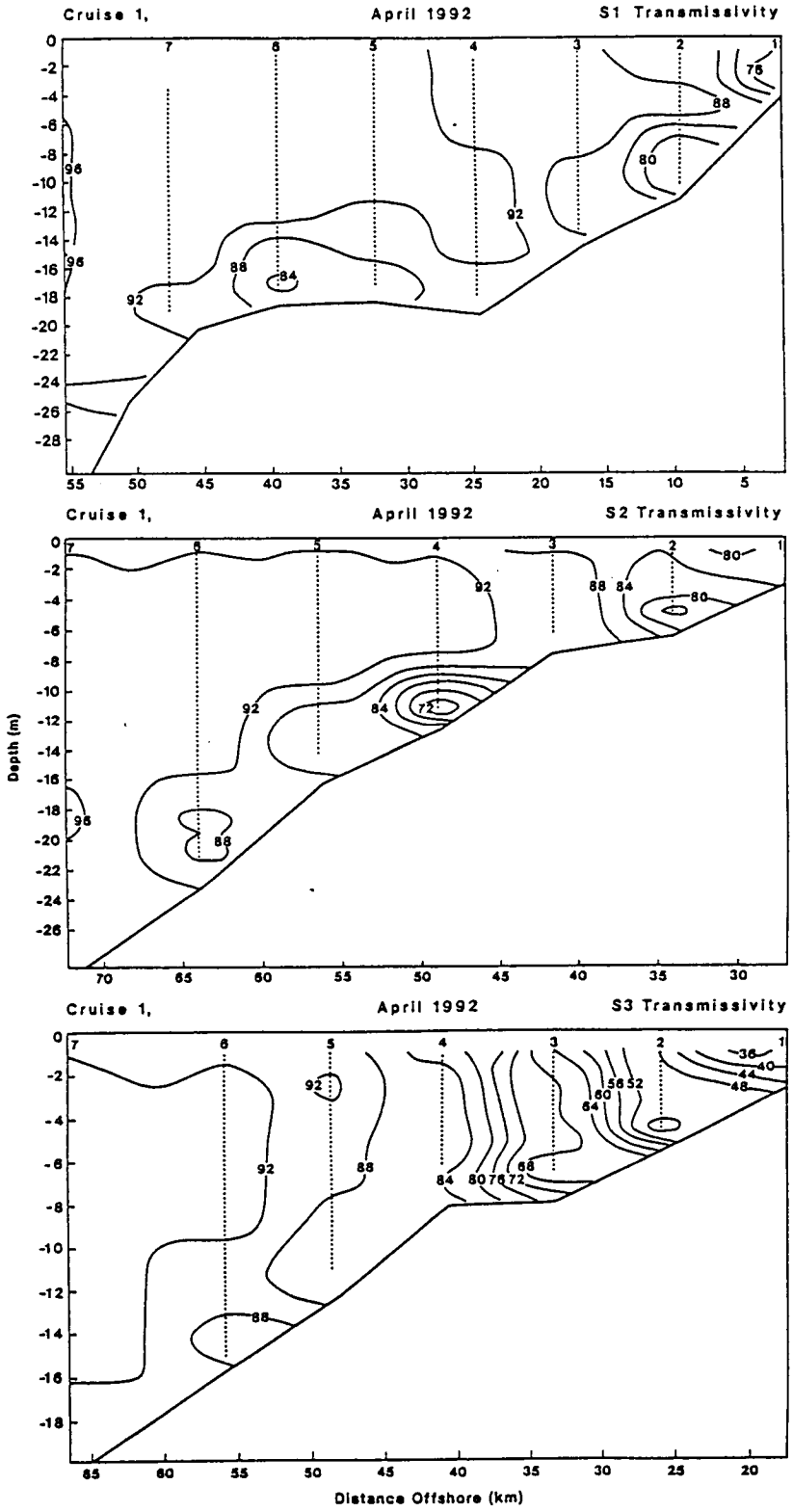

Figure 117. Light transmission during LATEX-B cruise 1 along (a) S1; (b) S2; and (c) S3. Stations have been renumbered starting with "1" at the coast. Values are in percent.

speed early on April 23, which may have increased vertical mixing and resuspension of bottom sediments.

In Figure 118, the surface salinity contours are overlain on the April 22, 1992 map of suspended sediment concentrations. A bulge of low salinity water (22-25 psu) was encountered on the inner shelf that corresponded spatially to the surface suspended sediment plume (Figure 118a). Downstream from the Atchafalaya plume a shoreward intrusion of higher salinity water was indicated (Figure 118a, See "A"), separating the Atchafalaya River discharge region from relatively freshwater (< 25 psu) west of Calcasieu. This cruise was preceded by a period of anomalously high rainfall along much of the northern Texas coast, possibly explaining the relatively low salinities. An interesting region of higher suspended sediments was observed in the imagery extending southwestward from the Calcasieu area (Figure 118a, See "B"). This feature may depict a convergence zone between freshwater runoff along the Texas coast and the intrusion of Gulf water from the south.

Surface concentrations of total chlorophyll (personal communication, N. Rabalais, 1996) are overlain on the image data in Figure 118b. A large region of elevated chlorophyll values was observed on the inner shelf seaward of the Atchafalaya delta as a result of the enhancement of nutrients from the river discharge. This region of elevated chlorophyll extended towards the southeast, conforming better to the plume of April 21 than that of April 22. This chlorophyll "plume" indicates how effective northwesterly wind events are in flushing nutrients out of the bay onto the shelf where they fuel phytoplankton blooms. Chlorophyll values showed a secondary maximum south and west of Sabine and a distinct minimum in the high salinity intrusion of Gulf water.

The distribution of cyanobacteria abundance (personal communication, Q. Dortch, 1996) in surface waters is shown in Figure 118c. The surface contours corresponded in a general way to those of total pigments (Figure 118b) as they showed elevated values southwest of the Atchafalaya plume and in the nearshore region between Calcasieu and Galveston Bay. Strong gradients in cyanobacteria abundance were associated with the southwestward-extending turbid water mass (Figure 118c, "B"). Almost no cyanobacteria was found in the low reflectance, high salinity Gulf water intruding northwards between Atchafalaya Bay and Sabine (Figure 118c, "A").

The surface contours of the herbicides metolachlor and atrazine are shown in Figure 119 superimposed on the satellite image data of April 22. These plots indicate two main source regions for these herbicides, namely the Atchafalaya Bay region and the bays and lakes from Calcasieu to Galveston. The patterns revealed in the two contour plots are very similar; however, they differ more than would be expected from the contour plots of salinity, chlorophyll, and cyanobacteria. The herbacide data exhibited large ranges in values over small areas, which made contouring difficult. It is noteworthy that the maximum values off Sabine Lake were an order of magnitude higher than those within the Atchafalaya plume region.

(2) Cruise III: April 13-19, 1993 River discharge was fairly constant during the April 1993 cruise at about 34,000 m^3/s, the highest of any of the LATEX-B cruises. A clear-sky satellite image was obtained on April 12, 1993 (2106 UT, 1606 CDT) approximately eight hours before the cruise started (Figure 120). The next good image was obtained on April 16 (1300 UT, 0800 CDT), after sampling of the Atchafalaya outflow region was completed. The April 12 image shows that the Atchafalaya plume covered a relatively small area, considering how high the river discharge was at this time. The surface waters of the plume had been pushed shoreward (particularly on the west side) by

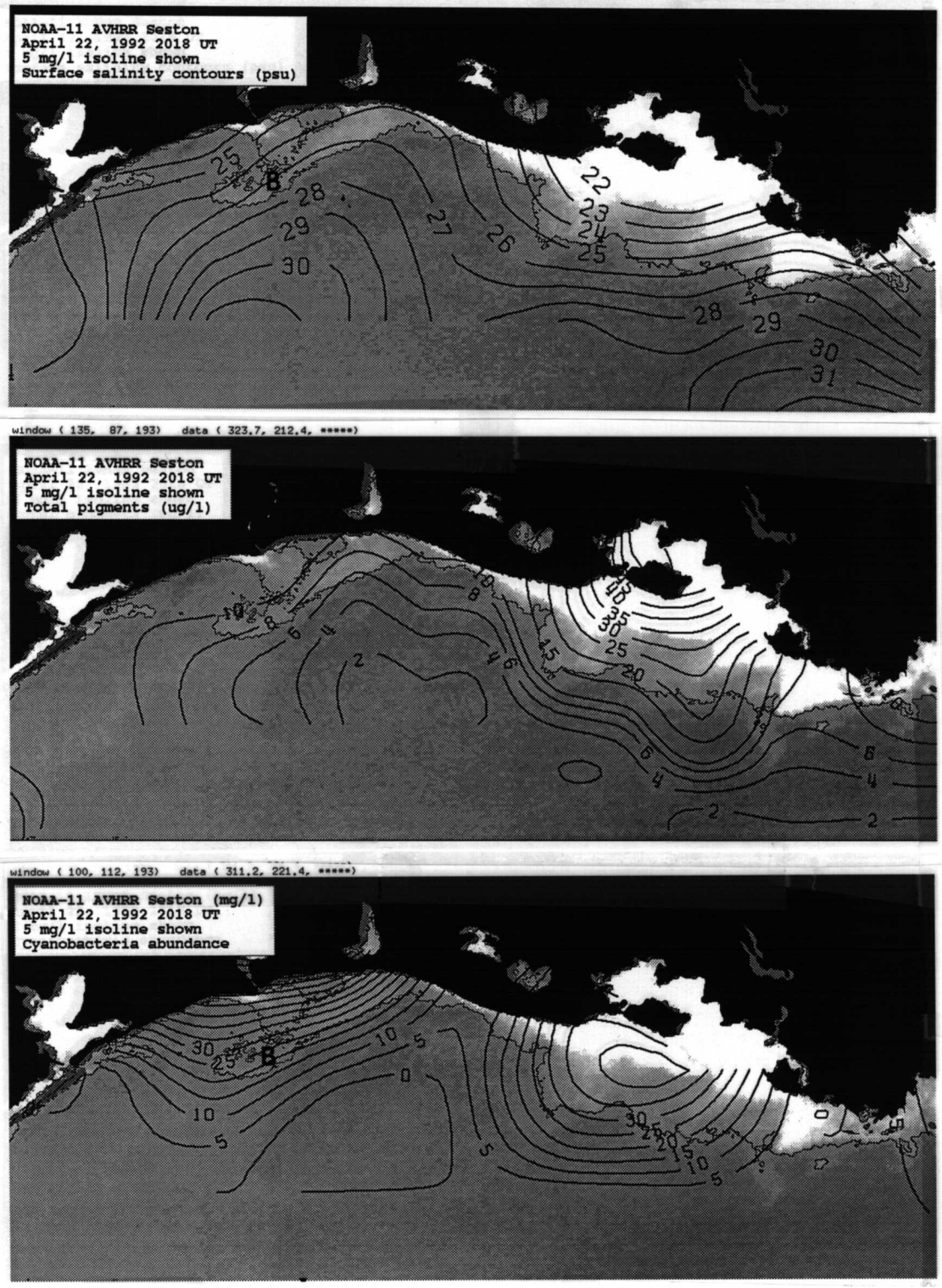

Figure 118. (a) Satellite image of reflectance on April 22, 1992 with the estimated seston contour of 5 mg/l (solid line) shown. Lightest shades of grey are indicative of highest concentration of sediments. The LATEX-B salinity contours (heavy solid lines) are superimposed on the image data. (b) Same as (a) with pigment values (in µg/l) superimposed. (c) Same as (a) with cyanobacteria abundance (in cells/liter * 10^6) superimposed.

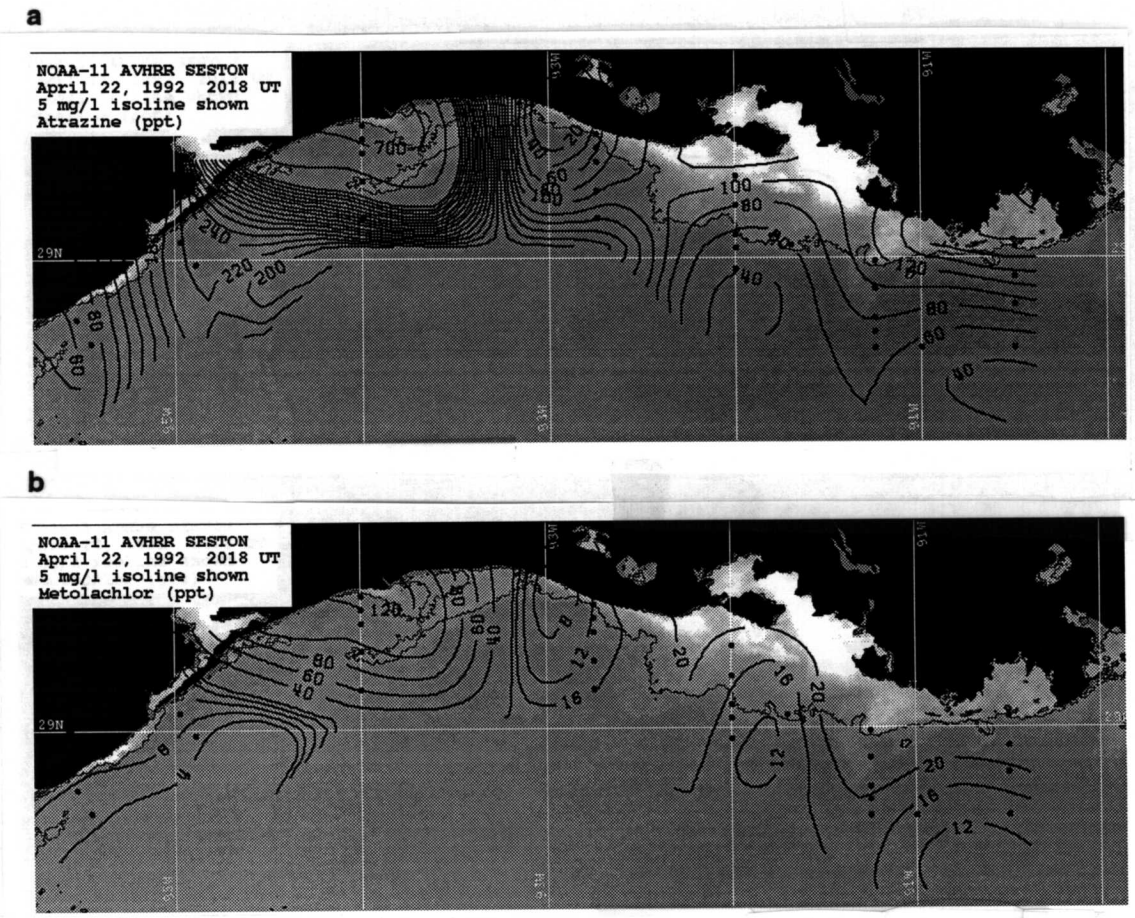

Figure 119. Satellite image of reflectance on April 22, 1992 with the estimated seston contour of 5 mg/l (solid line) shown. The surface contours of the herbicides (a) metolachlor and (b) atrazine (in parts per trillion) are superimposed on the image data.

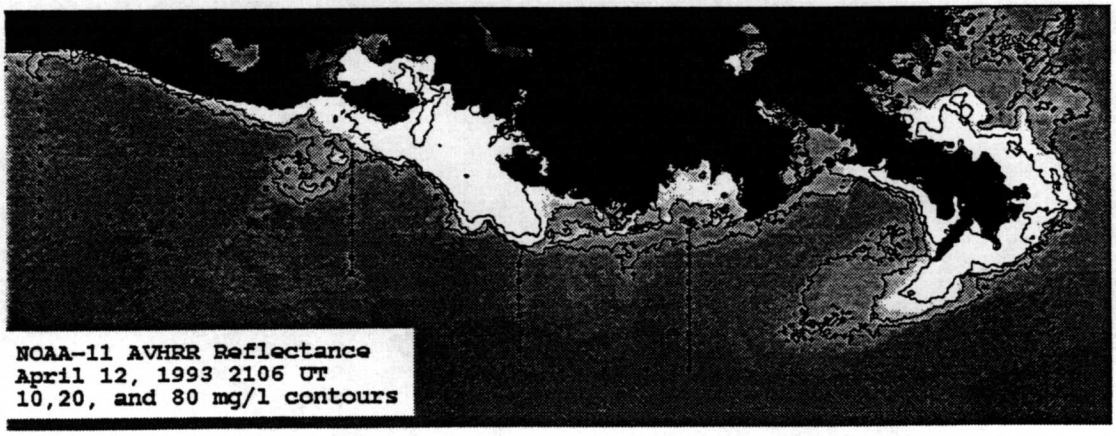

Figure 120. Satellite image of reflectance on April 12, 1993 (2106 UT) with the estimated 10, 20, and 80 mg/l seston contours shown. The LATEX-B cruise track and stations are superimposed on the image.

the moderate southerly and south-southwesterly winds of the previous two days. The suspended sediment distributions suggested a flow of water along the coast and out of the bay towards the southeast (Figure 120). The plume morphology on April 12 closely resembled the average composite plume for southwesterly winds, discussed earlier (Figure 114b). Although the surface plume was compressed against the coast, the suspended sediment concentrations within and just outside Atchafalaya Bay were relatively high (> 80 mg/l) as a result of the strong river outflow.

The winds shifted from south-southwest to south-southeast after image acquisition and remained fairly consistent until April 15 when they switched to northwest. Thus, lines S1 and S2 were occupied under similar wind conditions to that of April 12, and, as a result, the plume probably did not change dramatically over this time period. As during Cruise I, only the inshore stations intersected the high turbidity region of the Terrebonne and Atchafalaya plumes. The transmission sections along S1, S2, and S3 are shown in Figure 121. The patterns shown are similar to the Cruise I patterns (compare Figures 121 and 117) except that the transmission values were much lower in April 1993, particularly below the surface (low values=high concentrations of sediment and biological material). The lowest transmission values along each line were found close to the coast at the surface or along the bottom. Along S1, inshore transmission values near the bottom were about 50% compared with Cruise I (Figure 121a) when minimum bottom values of 80% were measured. The volume of low transmission water was much greater than during Cruise I (compare Figures 117a and 121a). Moving west towards the Atchafalaya Bay entrance, the transmission values decreased further and the area of low transmission water increased tremendously. Along S2 in April 1993, the zone of reduced transmission was much more continuous and extended about 68 km seaward. Transmissions below 50% were observed near the bottom 62 km from shore in April 1993, whereas the lowest transmissions in April 1992 were 72% up to 50 km from shore. The transmission values were lower along S3 than any of the other lines. Transmission values as low as 20% were measured in the surface plume at the nearshore station and 32 km from the coast (Figure 121c). The lower transmission values in April 1993 along the bottom may be attributable to the greater discharge of freshwater and sediments in 1993 as compared with 1992.

In Figure 122, surface salinities, surface pigments and surface cyanobacteria distributions are shown superimposed on the April 12 satellite image of suspended sediment distributions (a,b,c, respectively). Comparison of the salinity contours for Cruise I and Cruise III reveal that the freshwater plume was larger and fresher in 1993 (compare Figures 122a and 118a). The surface waters between Galveston and Sabine, however, were actually fresher in 1992, caused by local flooding. In both years, higher salinity shelf water intruded landward between Atchafalaya and Galveston Bays. The intrusion was further west in 1992. The surface pigment data (N. Rabalais, personal communication, 1996) exhibited maximum concentrations southeast of the entrance to Atchafalaya Bay (Figure 15b), confirming a previous southeastward discharge of river water onto the inner shelf. The maximum surface values were not quite as high as those observed during Cruise I. This is somewhat surprising in light of the high 1993 river discharge. However, the onshore winds had recently confined the nutrient-rich river waters to the nearshore area, particularly on the west side of the Atchafalaya plume where the high concentrations of suspended sediment may have inhibited rather than enhanced phytoplankton growth. It is interesting to note that during Cruise III, the near-bottom pigment concentrations were actually higher than the surface values (Rabalais in Murray and Donley, 1995). The cyanobacteria abundances at the surface off the Atchafalaya delta were also much lower during Cruise III than during Cruise I (Ccompare Figures 122c and 118c). Order of magnitude changes were noted in this comparison. These observations suggest that wind direction may play an important role in controlling productivity on the LATEX shelf. Northwesterly winds that flush the bay (Cruise I) appear to enhance surface phytoplankton

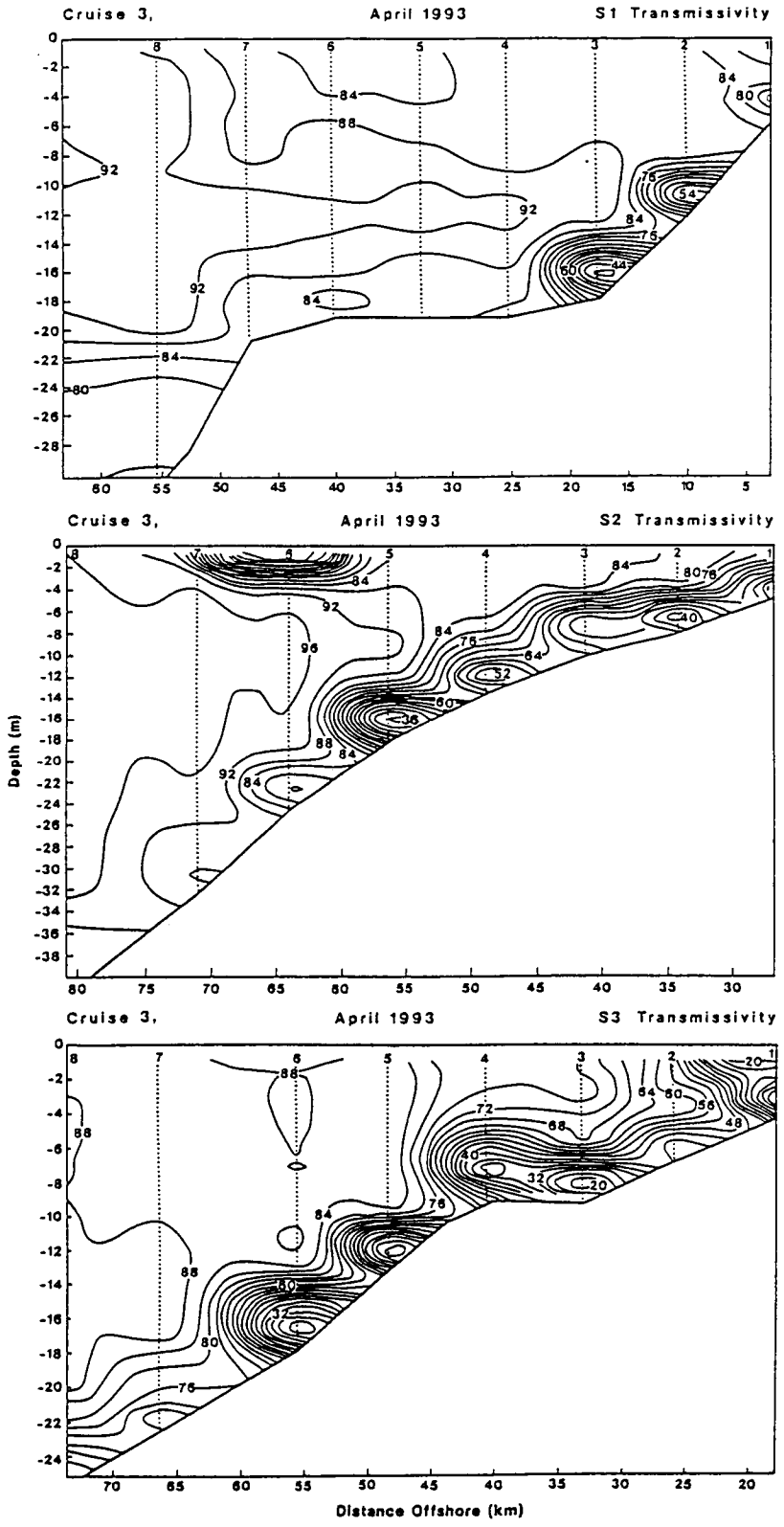

Figure 121. Light transmission during LATEX-B Cruise III along (a) S1, (b) S2, and (c) S3. Stations have been renumbered starting with "1" at the coast. Values are in percent.

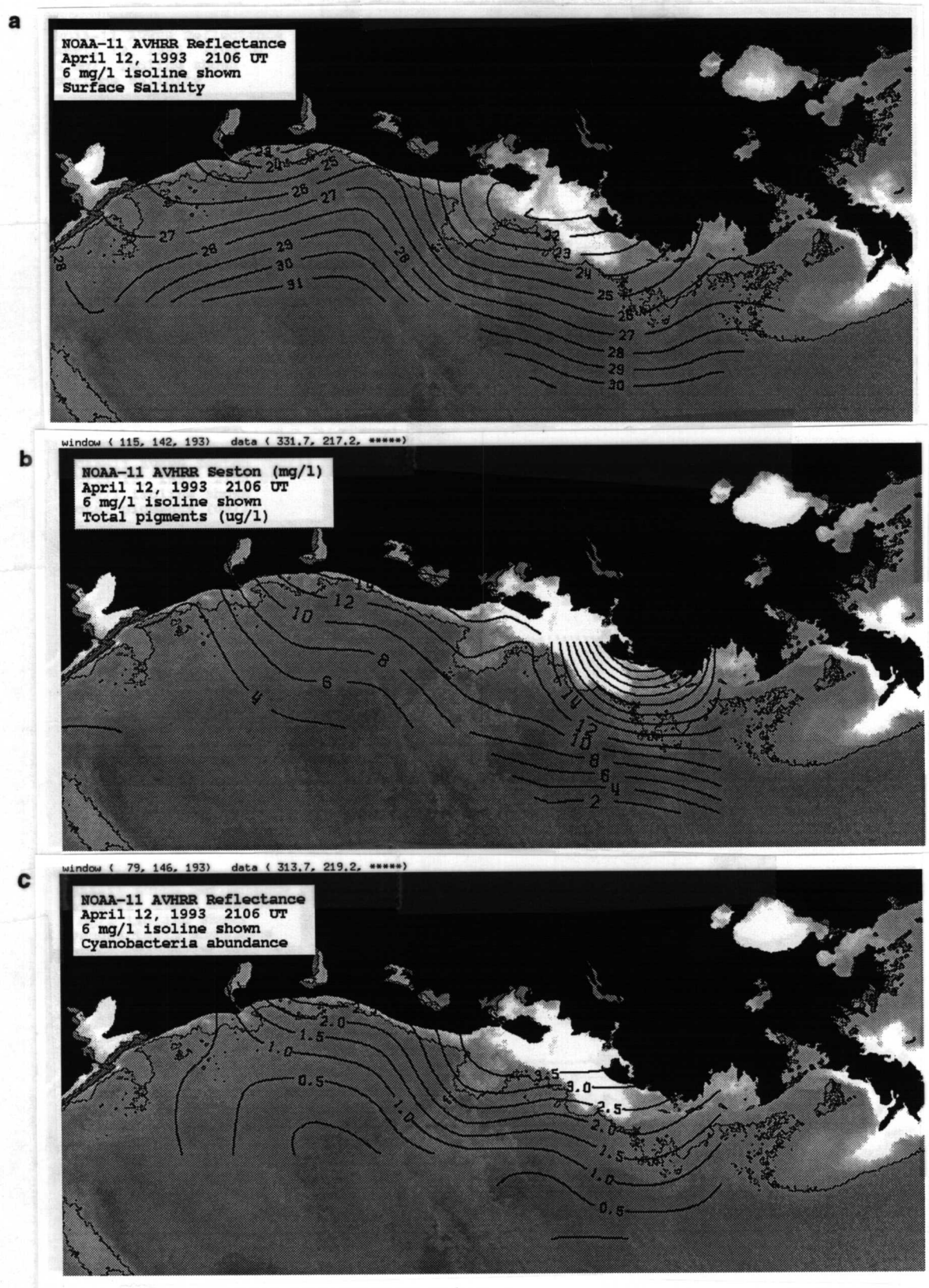

Figure 122. (a) Satellite image of reflectance on April 12, 1993 with the estimated seston contour of 6 mg/l (solid line) shown. The LATEX-B salinity contours (heavy solid lines) are superimposed on the image data. (b) Same as a) with pigment values (in μg/l) superimposed. (c) Same as (a) with cyanobacteria abundance (in cells/liter * 10^6) superimposed.

concentrations on the inner shelf, whereas southwest onshore winds (Cruise III) appear to inhibit near-surface phytoplankton concentrations.

The surface distributions of atrazine and metolachlor are shown in Figure 123 superimposed on the April 12 satellite image. Each herbicide shows elevated values near the Atchafalaya outflow and also along the Texas coast between Galveston and Port Aransas. Maximum values were observed off the Atchafalaya delta in 1993, but off the Texas coast in 1992 (compare Figures 123 and 119). This observation is explained by the volume of water discharged into the coastal ocean at these sites in the different time periods. It is interesting to note that the area of highest concentration along the Texas coast was further south in 1993.

(3) Cruise II: October 6-13, 1992 Circulation along the inner shelf during the October cruise was primarily westward and fairly typical of autumn/winter circulation on the LATEX shelf, except that the cruise was preceded by an abnormally strong northeasterly wind event. The exceptionally strong winds from the northeast were caused by a tropical depresssion that moved north from the Yucatan region. The intense and long-lived wind forcing event generated a Mississippi River squirt and dipole eddy, which extended 200 km towards the southwest from the Mississippi delta on October 4, 36 hours prior to the cruise. Its surface morphology was revealed in the SST image of October 4, 1992 (Figure 124a). The LATEX-B Cruise II crossed the northern margin of the dipole eddy that had formed on the leading edge of the squirt on October 6, revealing the squirt to be a cool, low-salinity, low-density feature well-mixed to about 16 m water depth (Figure 124a). Detailed analysis of LATEX-A time-series data of temperature, salinity, and current components enabled further investigation of the sub-surface characteristics of the squirt and associated dipole eddy. For a complete description of the evolution and structure of this squirt and its impacts, the reader is referred to Walker et al. (1996). A preliminary analysis of the satellite and in-situ datasets was described in Walker et al. in Murray (1996).

During this cruise, the satellite information on SST was useful in identifying water mass types. Because of the passage of a few winter storms prior to the cruise, differential cooling of shelf and coastal water masses had occurred. In Figure 124a, the 26.5° C SST contour is used to delineate waters emanating from coastal embayments and river discharge. The cool low-salinity water of the Atchafalaya plume extended a considerable distance offshore at the time of image acquisition and, in fact, in some places extended beyond the cruise track. The distribution of suspended sediments is shown in Figure 124b. The 10, 20, and 80 mg/l contours are displayed in relationship to the ship track. The sediment plume was observed to be rather disorganized although suspended sediment concentrations were relatively high for a great distance seaward of the Atchafalaya Bay. Without having a sequence of clear-sky imagery, it is difficult to know how much of the surface suspended sediment was transported offshore and how much was resuspended from the bottom. It is hypothesized that the very high turbidities southeast of the Atchafalaya resulted primarily from resuspension rather than from sediment advection since the north-northeasterly winds would have driven a westward flow out of Atchafalaya Bay. The transmission measurements on lines S1, S2, and S3 (Figure 125 a,b,c) were even lower (thus, more suspended material) than those obtained during the high discharge spring of April 1993. In contrast to the April 1993 cruise, the transmission data revealed the water column to be more well-mixed in the vertical, which is attributed to the extremely strong winds before the outset of the cruise. The lowest light transmission was observed along line S2 (Figure 125b), southeast of Atchafalaya Bay, an observation which agrees with the satellite imagery (Figure 124b), even though the imagery was obtained about 2 days earlier.

a

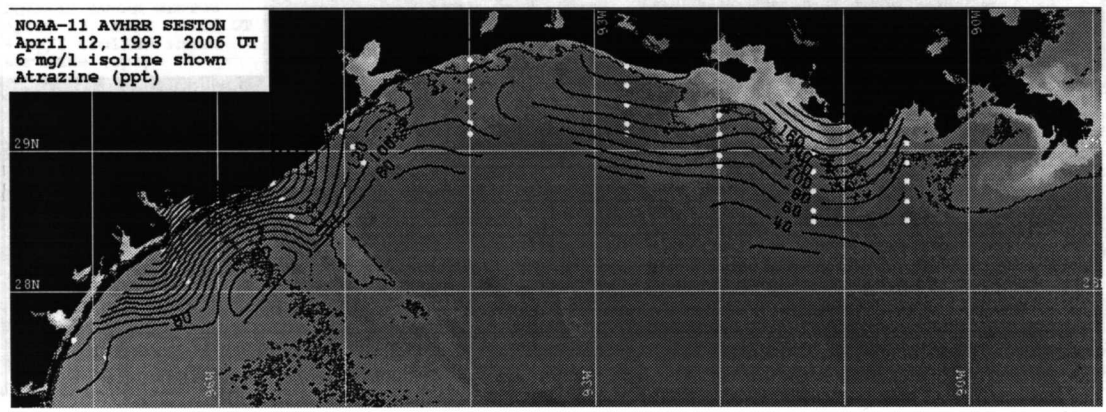

b

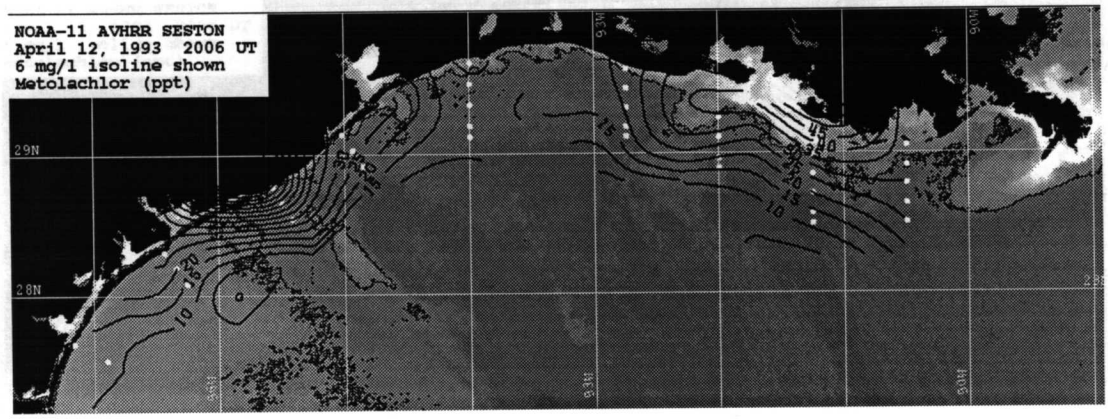

Figure 123. Satellite image of reflectance on April 12, 1993 with the estimated seston contour of 6 mg/l (solid line) shown. The surface contours of the herbicides (a) metolachlor and (b) atrazine (both in parts per trillion) are superimposed on the image data.

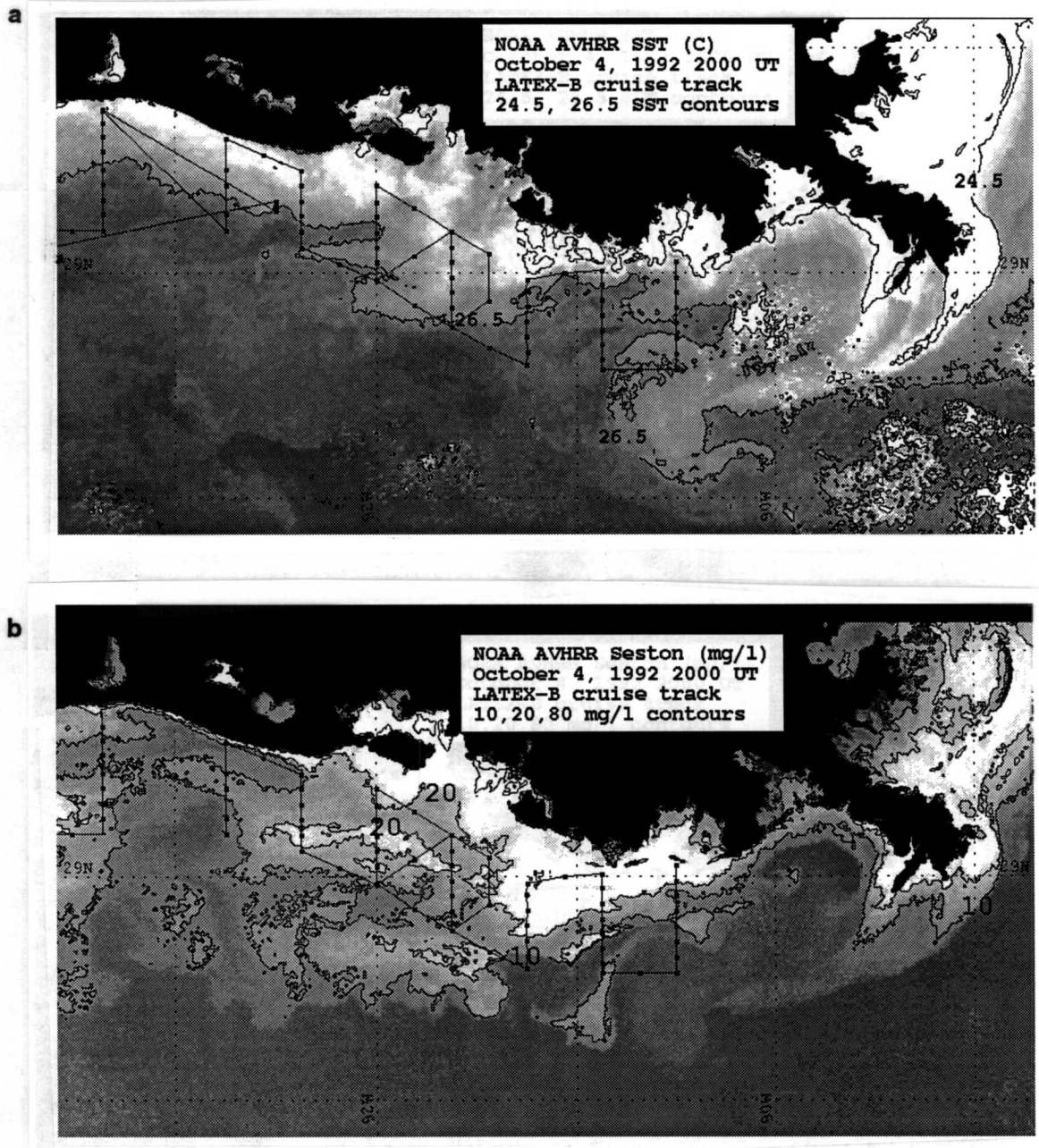

Figure 124. (a) NOAA AVHRR SST image on October 4, 1992 with 24.5 and 26.5° C contours drawn. The 26.5° C contour delineates the Mississippi squirt and dipole eddy, crossed by S1 of the cruise track. The 26.5° contour also delineates cool waters of the Atchafalaya outflow and the coastal current extending westward along the coast. The 24.5° C contour delineates the coolest waters which are within the Mississippi plume and northof the Mississippi delta. b) NOAA AVHRR image showing the distribution of suspended sediment on October 1992. The 10, 20, and 80 mg/l contours are shown.

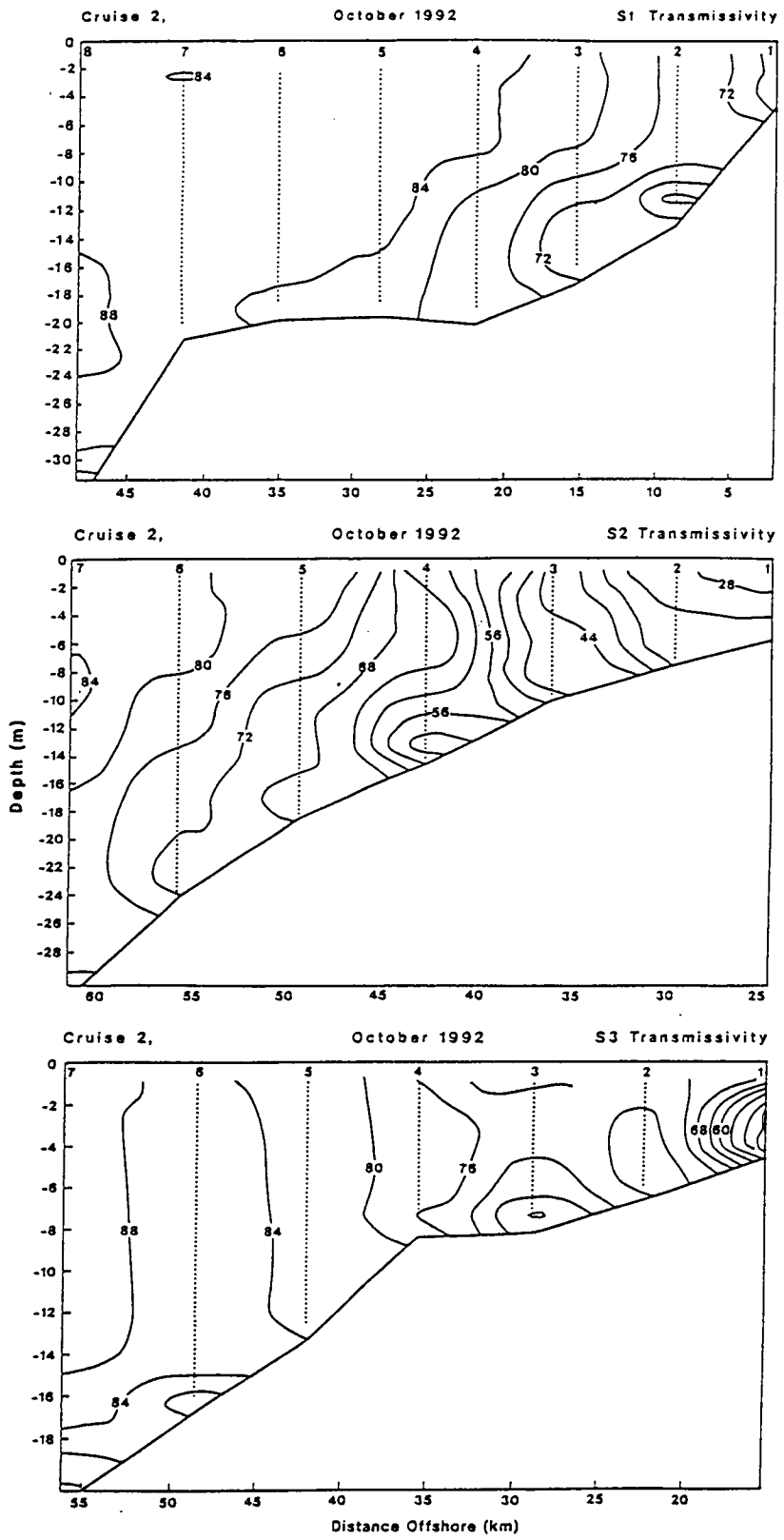

Figure 125. Sections of percent light transmission obtained during LATEX-B cruise 2 along (a) S1; (b) S2; and (c) S3. Stations have been renumbered starting with "1" at the coast.

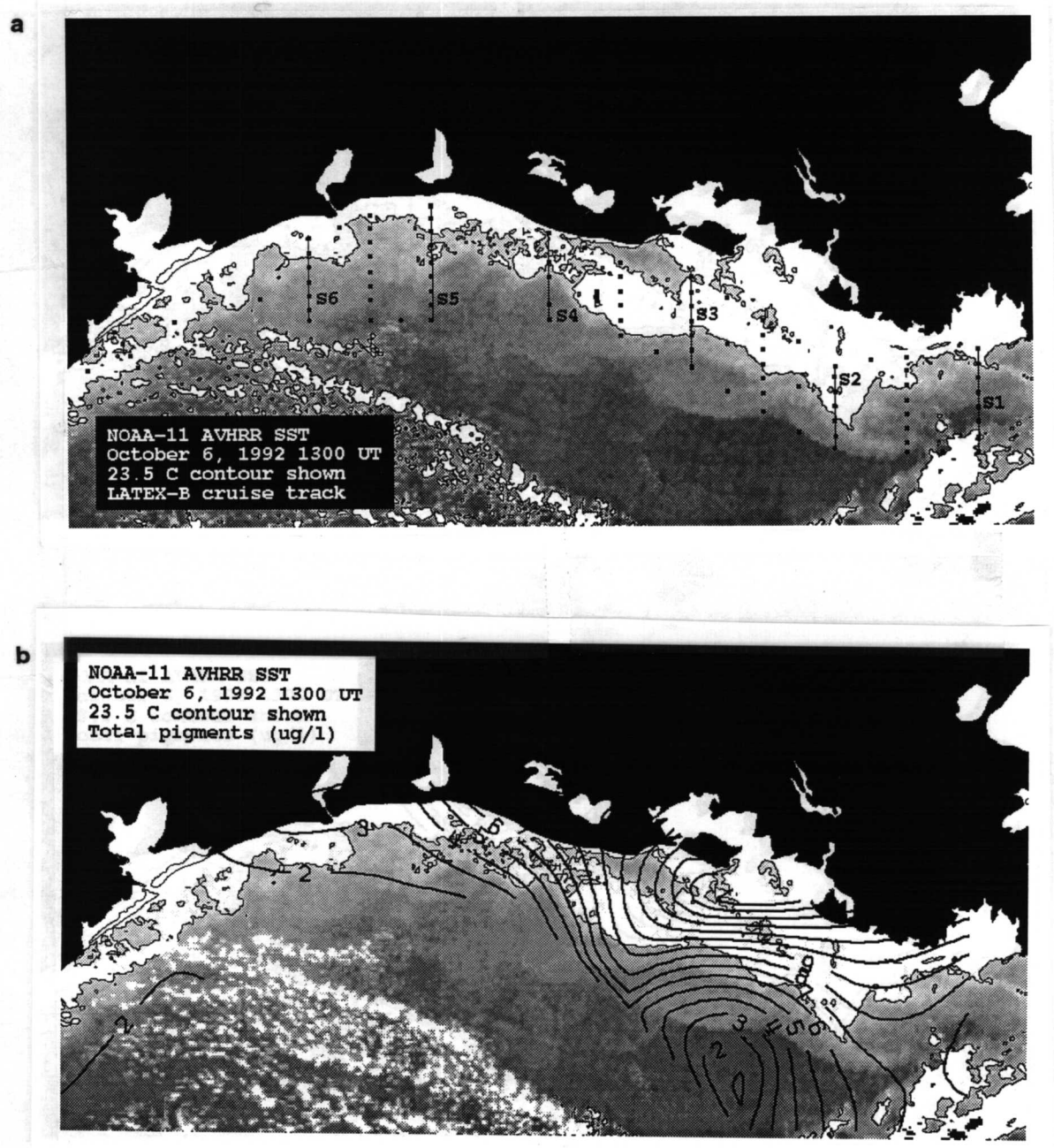

Figure 126. (a) NOAA-11 SST image of October 6, 1992 depicting cool water with lightest shades of grey. The 23.5 C contour is used to delineate the major SST front of the Atchafalaya outflow and the coastal current region to the west. Note the second Atchafalaya SST front seaward of the 23.5 contour, which is only reached on line S2. (b) Same background image as in (a) with total pigments in micrograms/liter superimposed. (c) Same background image as in (a) with contours of atrazine concentration (in parts per trillion) superimposed. (d) Same background image as in (a) with metolachlor concentrations (in parts per trillion) superimposed.

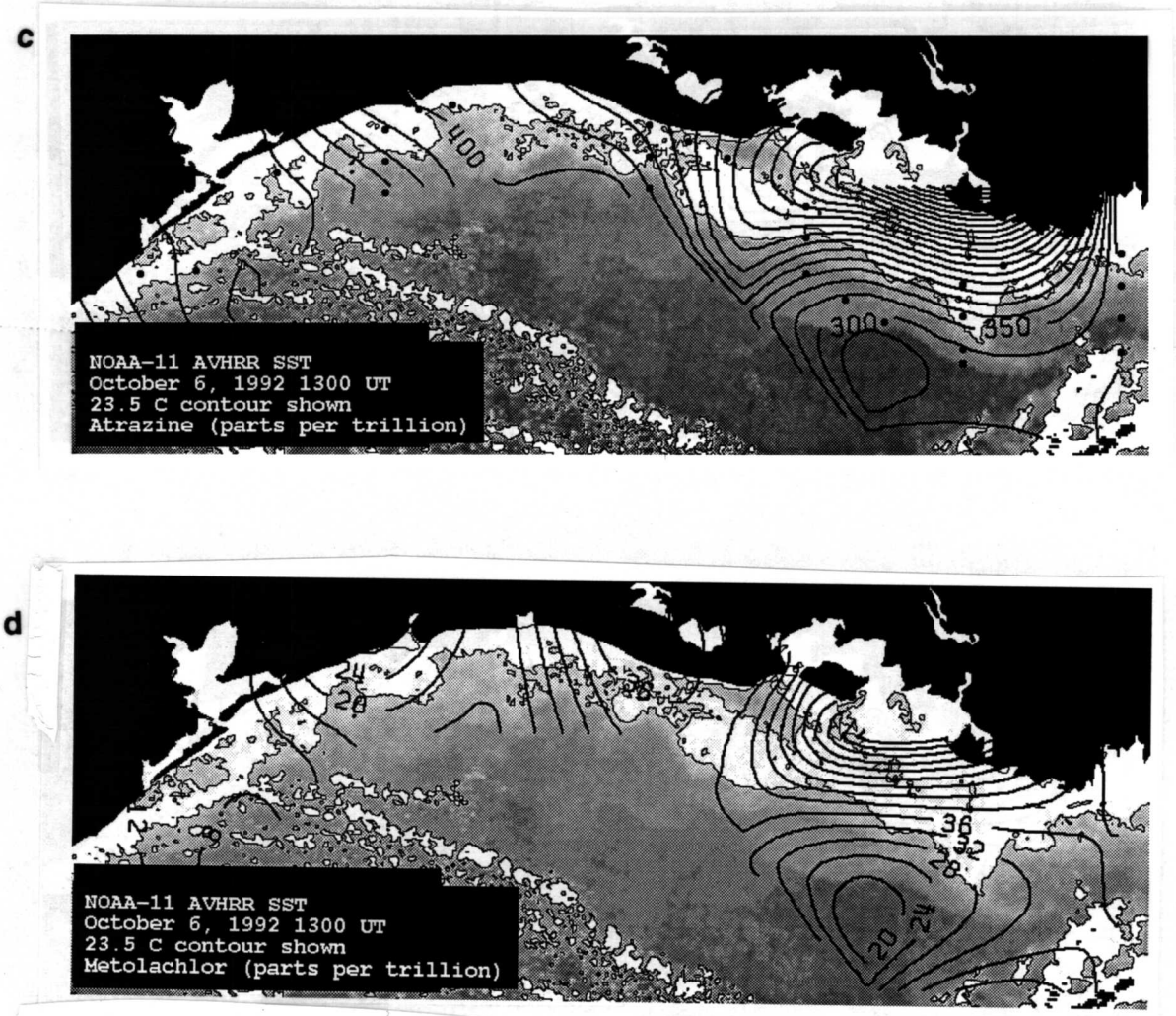

Figure 126 cont'd.

A clear-sky SST image was obtained on October 6, 1992 at 1300 UT, during occupation of the S1 line (Figure 126). The 23.5 SST contour is depicted on the imagery as it delineated the major offshore surface front of the Atchafalaya plume, as well as the extended plume towards the west. As is often observed in satellite imagery, the main coastal SST front was closer to the coast downstream from the Atchafalaya region (Figure 126a). A comparison of the near-surface ADCP with the location of SST fronts reveals that there is a close correlation between the strongest surface currents and the position of the main surface thermal front.

In Figure 126b, the total pigment values have been superimposed on the SST image of October 6, 1992. Again, the highest values were associated with the Atchafalaya plume, and the elevated values extended primarily southwest from the bay (Figure 126b). The values were relatively low compared with those of the two spring cruises, discussed previously. The cyanobacteria abundance plots resemble those of total pigments and, thus, are not shown.

The herbicides atrazine and metolachlor are superimposed on the October 6, 1992 satellite image in Figure 126c and 126d. These contour plots indicate a strong relationship between the outflow of the Atchafalaya River and the highest concentrations of these herbicides. It is interesting to note that the herbicide concentrations associated with the Atchafalaya River discharge were highest during the October 1992 cruise.

(4) Cruises IV and VI: July 13-20, 1993 and July 12-17, 1994 The circulation during these two summer cruises was primarily eastward (upcoast), a situation that contrasted markedly with the October 1992 cruise, when autumn/winter conditions of downcoast flow were observed. In July 1993 and July 1994 the prevailing direction of surface flow was eastward as a result of the strong southerly winds along the south Texas shelf and southwest winds along the Louisiana coast. Before each of the summer cruises, the process of coastal upwelling was in evidence along the southern Texas shelf (Figure 127). The July 1993 cruise stopped before Matagorda Bay and, thus, may not have encountered coastally upwelled water. However, in July 1994, coastal upwelling extended unusually far north as is shown in the image of June 28, 1994 (Figure 127b) and Cruise VI did encounter previously upwelled water.

During the July 1993 cruise, the best image of the LATEX region was obtained towards the end of the cruise on July 20, 1993 at 2109 UT. The reflectance measurements revealed that the discharge plumes along the Texas and Louisiana shelf extended eastward. The surface salinity is superimposed on this image in Figure 128a and shows a relatively high salinity tongue intruding eastward toward the Atchafalaya plume region. The low salinity waters of the Atchafalaya plume bulged towards the east although there was also an indication of a narrow coastal band of lower salinity water as far west as Sabine. The cyanobacteria abundances confirm the net eastward transport of high nutrient river water as very high concentrations of the low salinity cyanobacteria species were detected in the eastern portion of the Atchafalaya sediment plume (Figure 128b). The maximum cyanobacteria counts in the Atchafalaya plume were 100 times greater in July 1993 than during the spring cruises.

The SST information obtained on July 17, 1993 at 2142 UT (Figure 129a) was particularly interesting as the ship crossed a coastal temperature/salinity/density front twice within nine hours of image acquisition. The image data revealed a thermal front ranging from 0.4 to 0.7° C running approximately east-west, becoming narrower towards the west. Lines S5 and S6 crossed this coastal front and showed that the SST image data identified a water mass with distinctly different temperature, salinity and density characteristics (Murray and Donley, 1996). Cyanobacteria information presented by Quay

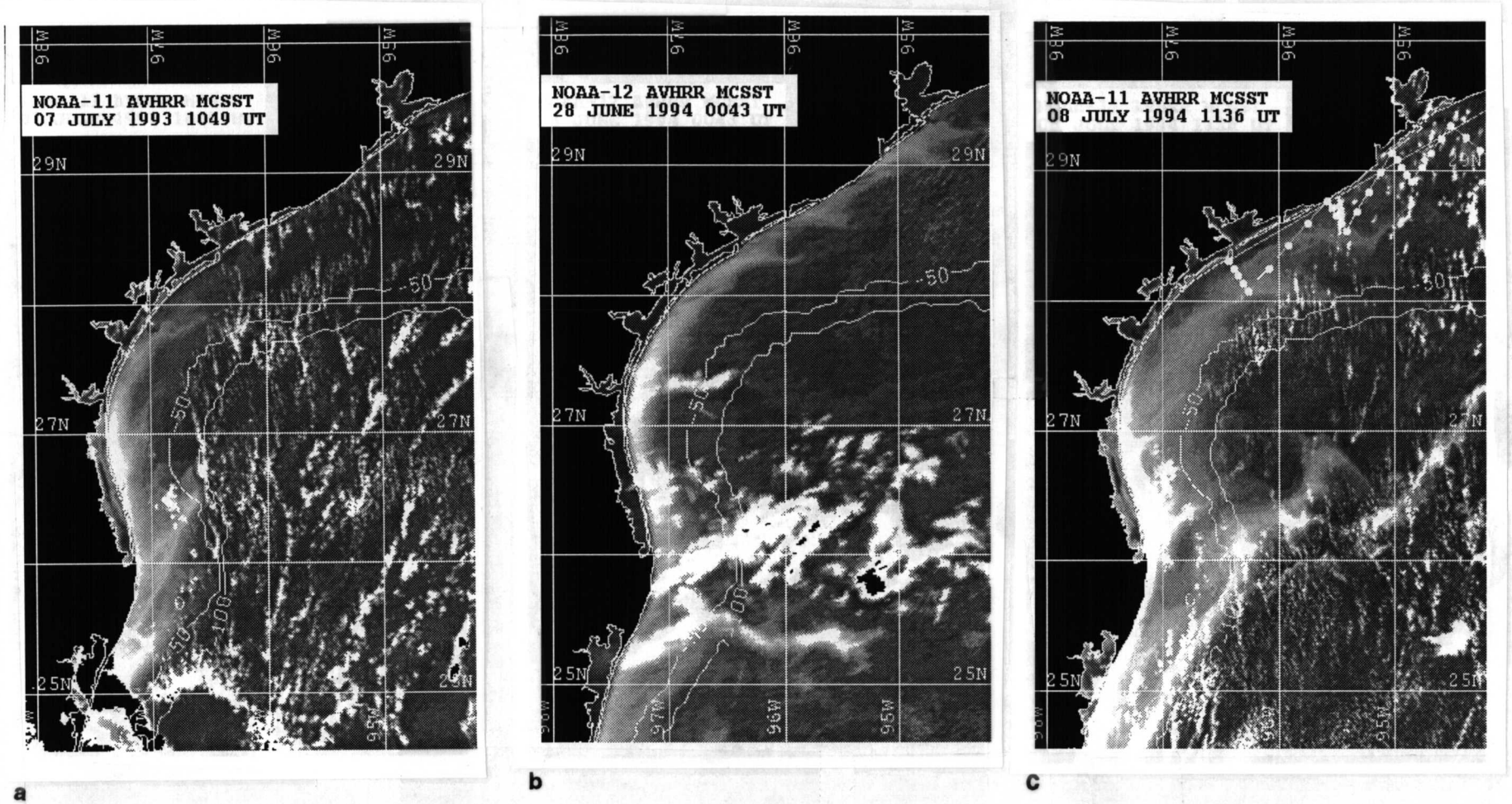

Figure 127. (a) NOAA-11 SST image obtained on July 7, 1993 showing the cool upwelled waters along the south Texas coast (light shades of grey) a few days prior to Cruise IV. (b) NOAA-12 SST image obtained on June 28, 1994 showing active upwelling along the entire Texas coastline as far north as Galveston prior to Cruise VI. (c) NOAA-11 SST image of July 8, 1994, 11 days after the active upwelling event of June 28, 1994 and 4 days before the start of Cruise VI. The region of active upwelling has moved south of Port Aransas Bay, however a wide region of relatively cool water is observed out to the 50 m contour extending northeastward. The LATEX-B cruise track is overlain.

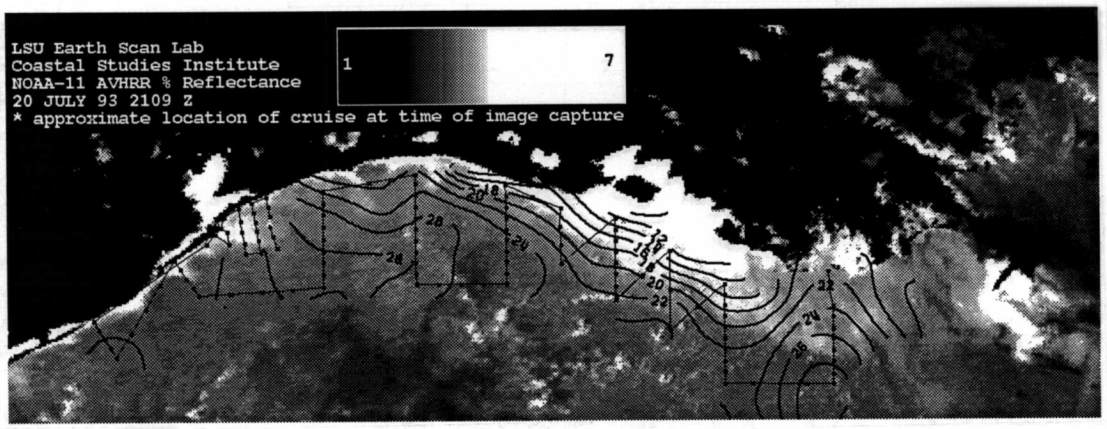

a

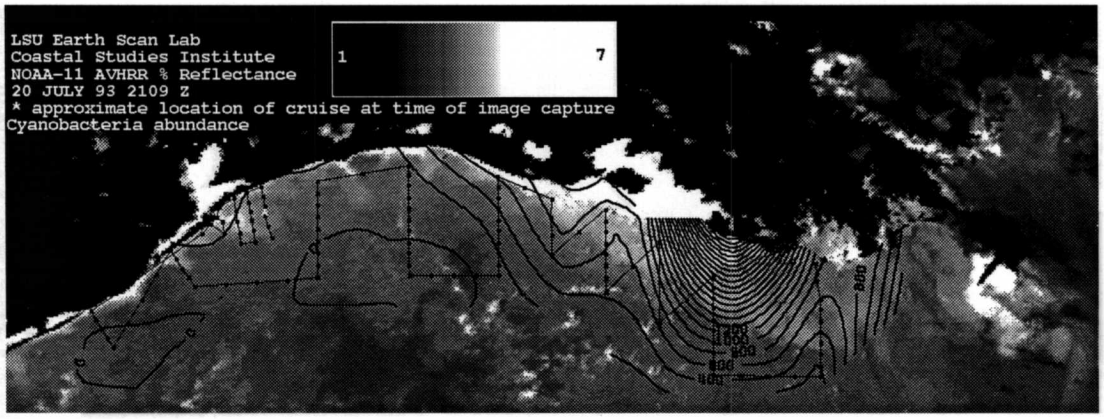

b

Figure 128. (a) NOAA reflectance image (in %) of July 20, 1993 depicting the distribution of suspended sediments with the LATEX-B cruise track and the surface salinity contours superimposed. (b) same as (a) with the contours of cyanobacteria abundance (cells/liter * 10^6) superimposed.

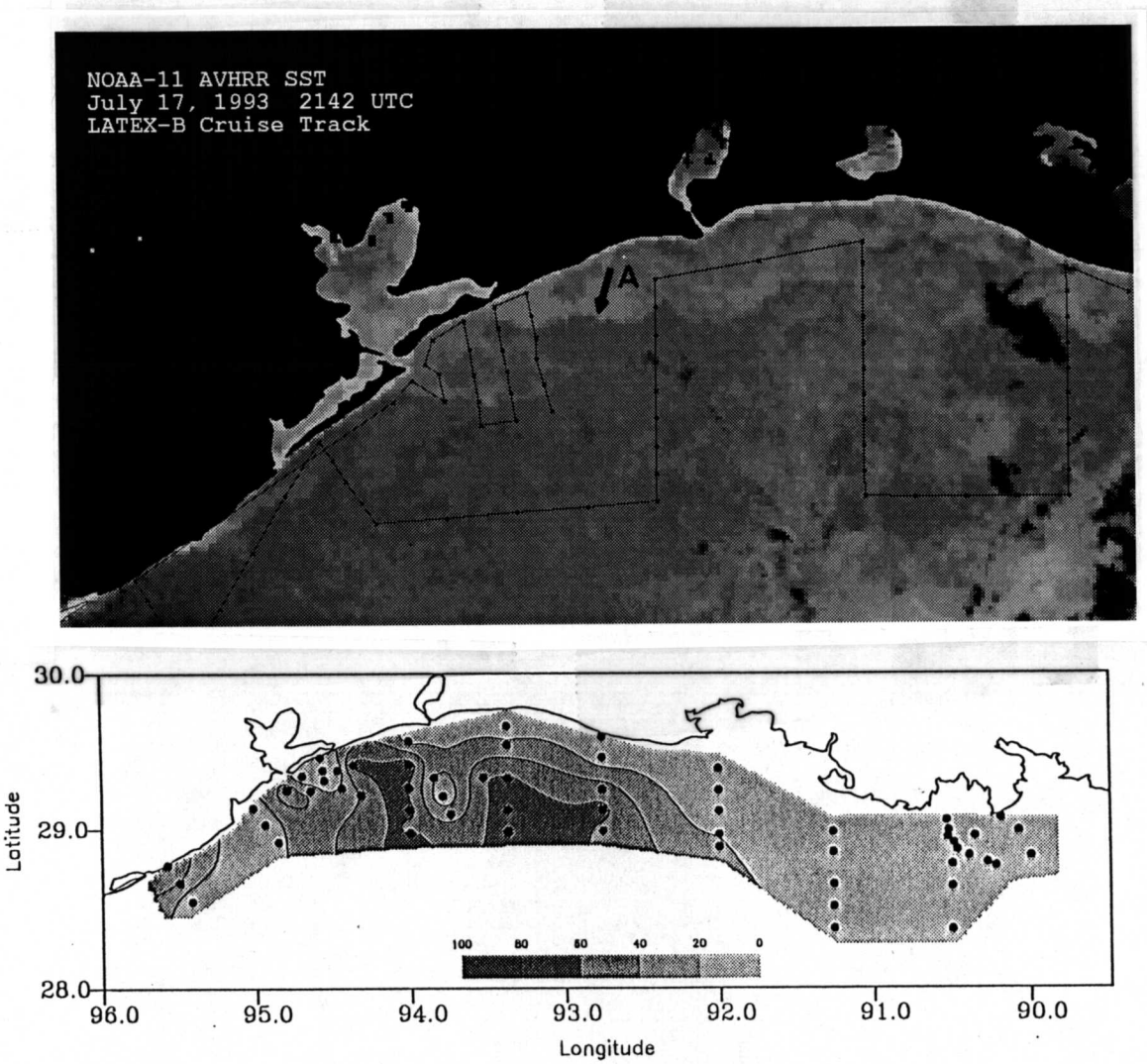

Figure 129. (a) NOAA-11 SST image of July 17, 1993 depicting the SST front east of Galveston Bay (See "A"). (b) Contours of Percent High PU/PE cyanobacteria/total cyanobacteria during the July 1993 cruise (From Dortch in Murray and Donley, 1996).

Dortch in the 2nd Annual Report is shown here in Figure 129b (Dortch in Murray and Donley, 1996). The contour plot of % high PU/PE cyanobacteria to total cyanobacteria suggests that a very different water mass intruded shoreward on the south side of this coastal front, and it contained a distinct cyanobacteria assemblage (Figure 129b).

During Cruise VI, most of the LATEX shelf was cloudy. The best imagery was obtained (before the cruise started) of the upwelling area that extended from northern Mexico to Galveston in late June (Figure 127 b,c). A 20-km band of cool waters (25-26° C) was observed to extend northwards from south Texas to Galveston Bay on June 28. Cool filaments extended offshore 20 km to the northeast from the zone of coastal upwelling. Seaward of the upwelling zone, water temperatures climbed to 29° C. During the previous two summers, active upwelling was not observed northwards of Matagorda Bay. Thus, during the 1994 summer, coastal temperatures were distinctly colder between Matagorda Bay and Galveston Bay as a result of coastal upwelling. Abnormally low temperatures were recorded in Galveston Bay between June 25 and July 4 (Melinda Bailey, National Weather Service Forecast Office, personal communication, 1994). A minimum temperature of 23° C was recorded on June 30, two days after image acquisition. There is no doubt that the source of the cold water in Galveston Bay was wind-induced upwelling along the coast to the south. However, by July 8, active upwelling was only observed south of Port Aransas Bay (Figure 127c). The S8 and X1 lines of the July 1994 LATEX-B cruise crossed a portion of the shelf previously influenced by the northward advection of cool coastally upwelled waters (Figure 127c). The temperature measurements obtained along the most southern line, X1, revealed slightly lower temperatures 20 to 30 km from shore as a result of the previous active upwelling activity in the region. No obvious changes in salinity were noted.

3. Summary and Conclusions on Plumes

The size and morphology of the Atchafalaya and Mississippi River sediment plumes are controlled primarily by river discharge and wind direction and speed. Both plumes can change rapidly with major wind direction shifts. The surface sediment plumes of the Atchafalaya and Mississippi Rivers are similar in size, even though the Mississippi River carries twice as much water on average. This observation can be attributable to the shallow receiving basin in the Atchafalaya region. When winds exceed about 5 m/s, resuspension of sediment is initiated in shallow bay areas and on the inner shelf and the satellite-observed sediment plume is increased accordingly. Monthly- averaged surface sediment plumes were found to range from 2000-3000 km^2 when discharge is low (Mississippi River < 10,000 m^3/s) and from 4000-5000 km^2 when discharge is high (Mississippi River > 20,000 m^3/s). The Atchafalaya plume increases dramatically in areal extent when winds are strong and blowing offshore. Plumes in excess of 9000 km^2 have been observed when northwesterly or northeasterly winds exceeded 15 m/s for 24 hours or more. Under these conditions, plume waters were detected over 70 km seaward of the Atchafalaya Bay mouth. Southerly and southwesterly winds confine Atchafalaya River waters close to the coast and, therefore, minimize plume areas. Plume morphology and direction of water movement is fairly easily predicted from a knowledge of the wind history preceding image acquisition. River waters flow predominantly westward along the coast when winds blow towards the west and eastward when winds blow towards the east. Circulation in the Mississippi plume region is complicated by the clockwise gyre which is a semi-permanent feature in the Louisiana Bight under conditions of westward winds. The gyre appears to break down when winds switch from the prevailing westward direction to eastward and the Southwest Pass plume reverses direction.

Comparisons of LATEX-B cruise measurements with the available satellite datasets reveal that the surface concentrations of chlorophyll *a*, phytoplankton, and herbicides are increased where Atchafalaya River waters flow onto the inner shelf. Offshore northwesterly winds efficiently flush freshwater, sediments, herbicides and nutrients out of the bays where the nutrients were used by phytoplankton for growth on the inner shelf. In contrast, southerly and southwesterly winds confine river waters close to the coast and plankton growth is inhibited as the nutrient-rich waters contain sediment loads which are too high for phytoplanton growth.

V. Sediment Flux

by Wilford D. Gardner, Youcheng Zhang and Mary Jo Richardson

A. Introduction

In an attempt to measure particle settling and resuspension fluxes, sediment traps were attached to current-meter moorings at six sites across the Louisiana shelf along two transects (90.5° W and 92° W) which straddled a region of known summer hypoxia (Rabalais et al., 1991, 1994b). Trap fluxes were compared with bed shear stresses determined from currents as a predictor of resuspension. These samples also provided material for compositional and particle size analysis to assess pollutant transport and the impact on the biological community.

Trap collections are integrations of the material collected at one point over the time of deployment. This adds a temporal dimension to point sampling of particulate matter in the water column during hydrographic cruises, providing the opportunity to assess conditions and variations between cruises. It is important to remember, however, that traps primarily collect the large, settling particles such as fecal pellets and aggregates, which are the greatest contributors to the vertical settling of particles, rather than the total concentration of particles, which is heavily dominated by the small, slowly settling particles. The resulting profiles of sediment fluxes are likely to differ significantly from the instantaneous profiles of particle concentrations determined optically or by water bottle filtration.

B. Methodology

Sediment traps were attached to LATEX A current meter Moorings 14, 15 and 16 along 92° W and 17, 18, and 19 along 90.5° W during the 2.5 years of deployment (Figure 130). Our contract was for just one year of sampling, but the results were so interesting we continued to the end of the mooring program. Traps were located 1 m above bottom (mab) at each site. Additional traps were attached at depths indicated in Table 15 to be above the bottom boundary layer or as close to the surface plume as possible. Mooring and safety requirements usually necessitated that the uppermost traps were at least 6 m below the surface. Moorings were generally serviced every 45 days to minimize biofouling, but occasionally traps were out for 90 days.

The traps were 76 cm tall butyrate cylinders with a 7.3 cm inside diameter, resulting in an aspect ratio (height/diameter) of 10. The upper 5 cm of the trap contained a honeycomb baffle made of epoxy-impregnated nylon. The purpose of the baffle was to exclude large swimmers from the trap (those > 1 cm) and to stabilize the turbulent flow within the trap. No poisons or preservatives were used in the traps. Traps were exchanged using divers except on Moorings 14 and 19 where the moorings were recovered using acoustic releases and redeployed. Some trap samples were lost during the latter procedure because of the difficulty of keeping the traps upright during recovery.

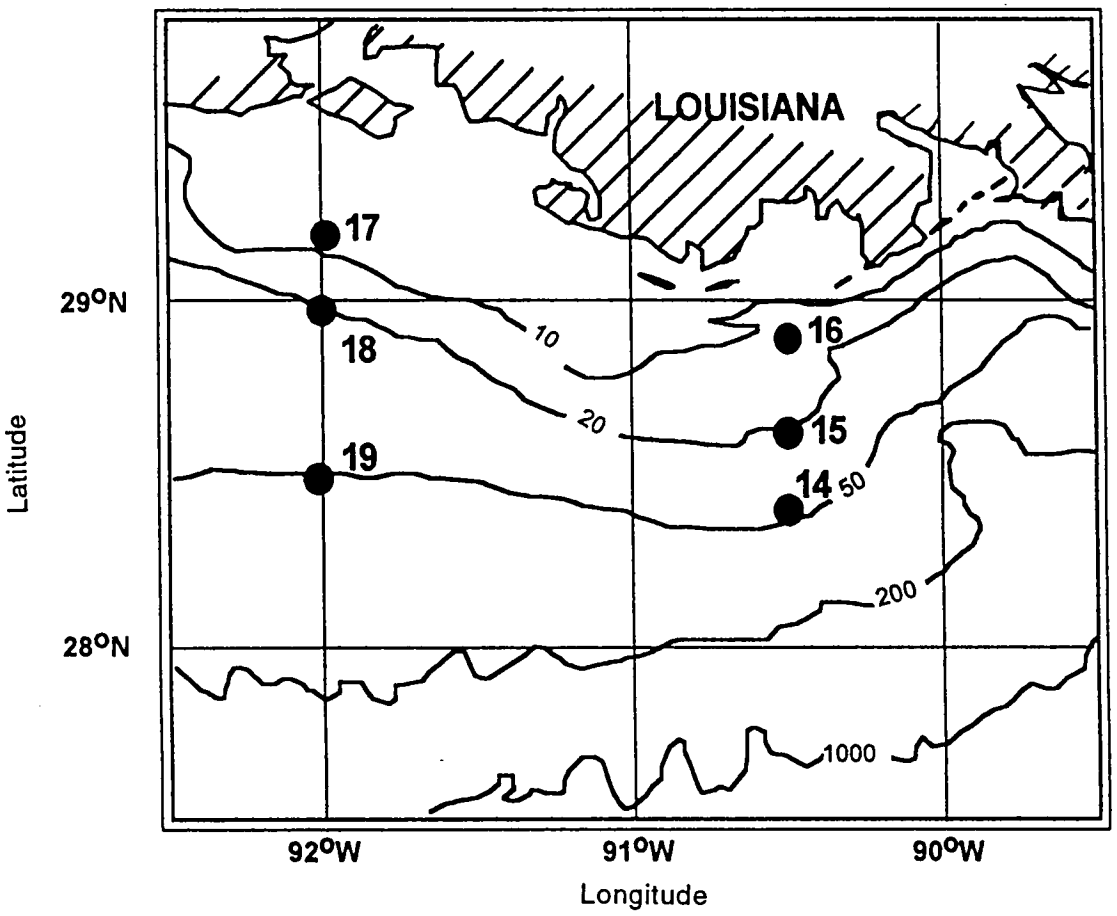

Figure 130. Location of moorings on which sediment traps were located. The three VIMS tetrapod deployments were near Mooring 16.

Table 15. Mooring data for sediment traps

Mooring	Water Depth (m)	Trap Depth (m)	M above Bottom (mab)	Attachment Point
17	7.6	6	1	Base of Minispec
18	22	13	9	Mooring wire
		17	5	Mooring wire
		21	1	Base of Minispec
19	50	13	37	Mooring wire
		41	9	Mooring wire
		45	5	Mooring wire
		49	1	Anchor
16	20	13	7	Mooring wire
		19	1	Base of Minispec
15	27	21	6	Mooring wire
		23	4	Mooring wire
		26	1	Anchor
14	48	13	35	Mooring wire
		39	9	Mooring wire
		43	5	Mooring wire
		47	1	Anchor

In addition to the traps on current meter moorings, an independent mooring with 5 or 6 traps was deployed near the VIMS tetrapod during the boundary layer studies in May 1992, April 1993 and June 1993. Another trap was attached to the base of one leg of the tetrapod with the trap top at 0.76 mab.

Sample analysis was contracted to include only total mass, particle size distribution and percent organic carbon. In addition we have measured the percent carbonate in trap samples. Portions of selected samples were shipped to LSU for analysis of a suite of chemical pollutants. These results are reported in the pollutant chemistry section (see Section X). Trap samples were carefully wet-sieved through a 1 mm mesh, and swimmers were removed from the sample. The sample portion <1 mm was split using a fast, high-precision splitter that used air pressure to discharge a continuously-mixed particle suspension into six subsamples (Tennant and Baker, 1992). Compositional and size analyses were made only on the portion <1mm in size, which generally included >90% of the total sample, except the near-sea-surface samples on the outer shelf where the >1 mm fraction was as much as 25% because of high biogenic input. Grain size distributions were obtained by wet-sieving samples into fractions <63 μm, 63-125 μm, 125-250 μm, 250-500 μm and 500-1000 μm. Size fraction samples were vacuum filtered onto pre-weighed 0.4 μm Poretics filters, dried and reweighed.

Carbonate content was determined for one sample split from each trap by freeze-drying, weighing, acidification by dilute HCl, drying and reweighing for calculation of weight loss. Corrections were made for salt content based on water content and salinity. A portion of this sample was then analyzed for organic carbon and nitrogen content with a Carlo Erba NA 1500 Analyzer.

It is important to note some caveats in the use of sediment traps in shelf environments. Studies suggest that traps are unbiased collectors in currents where Reynolds' numbers ($R = \rho * u * D/\upsilon$, where ρ is water density, u is the velocity past the trap

opening with diameter D, and υ is viscosity) are less than 30,000 with a cylindrical trap aspect ratio (A = trap height to diameter ratio-H/D) of 8 (Baker et al., 1988). This would allow unbiased collections of particles in flows up to 40 cm/sec for the 7.3 cm diameter cylinders we used. At higher velocities the traps undercollect the particle flux. Data from current meters at these sites indicated that currents 1 m above bottom exceeded 30 cm/sec for only a few percent of the deployment time.

Another caveat in using traps in shelf environments is the trajectory and flux of particles within boundary layers. Surface and bottom boundary layers have turbulent diffusion and secondary flows that can circulate particles through a boundary layer more than once before they settle out from the surface boundary layer or to the seafloor from the bottom boundary layer. On the shelf the surface and bottom boundary layers may overlap, depending on stratification and current velocities, so the entire water column may be part of a boundary layer. Therefore, trap measurements may yield overestimates of vertical flux in boundary layers which are actively overturning (Gardner and Richardson, 1992), so we refer to fluxes in this report as "apparent" fluxes as a reminder of the above caveats.

The boundary-layer dynamics make it difficult to distinguish between the primary flux of particles (particles settling through the water column for the first time) and the resuspended flux of particles from the seafloor. It is also challenging to distinguish between resuspension of bottom sediments and deposition from a turbid plume advected from the Mississippi or Atchafalaya Rivers or a nearby erosional event. At the very least the trap samples yield (1) relative fluxes over the same time at different locations; (2) measurements of annual variations at the same location; and, (3) provide samples for compositional and size analyses in different segments of the boundary layer.

C. Results

1. Moorings

The flux data considered reliable from Moorings 14-19 during Deployments 1-15 (April 1992 to July 1994) are graphed versus time (Figure 131). The fluxes were averaged at each depth over the entire deployment period and plotted versus height above bottom (Figure 132). Fluxes increased exponentially with depth by 1-2 orders of magnitude during individual deployments. Fluxes varied spatially by nearly three orders of magnitude among the sites over the same time period and temporally by more than two orders of magnitude at the same site (site 14), though the temporal variability is usually closer to one order of magnitude at a given site. Temporal variability was substantially smaller on the outer shelf (Moorings 14 and 19).

The largest fluxes at most sites coincided with the passage of Hurricane Andrew. The eye of Andrew passed between Moorings 14 and 15 on August 26 during deployment 3 (July 21 to September 1, 1992). A few days after passage of the hurricane, the moorings were serviced. A total of four traps, including all those on Mooring 15, were missing from the mooring lines and one mooring could not be found. One of the traps was on a current meter frame rigidly attached to a railroad wheel resting on the seafloor. The divers found the frame on its side, half buried in the mud. After attaching a cable and bringing the frame to the surface, the trap contained 15-20 cm of sediment, but the integrity of the sample was too suspect to be used.

The percentage of organic carbon in trap samples decreased from 2 to 5% at 6 to 9 mab to about 1% at 1 mab (Figure 133), although the total calculated flux of organic carbon increased with depth. The percentage of organic carbon varied seasonally with highest

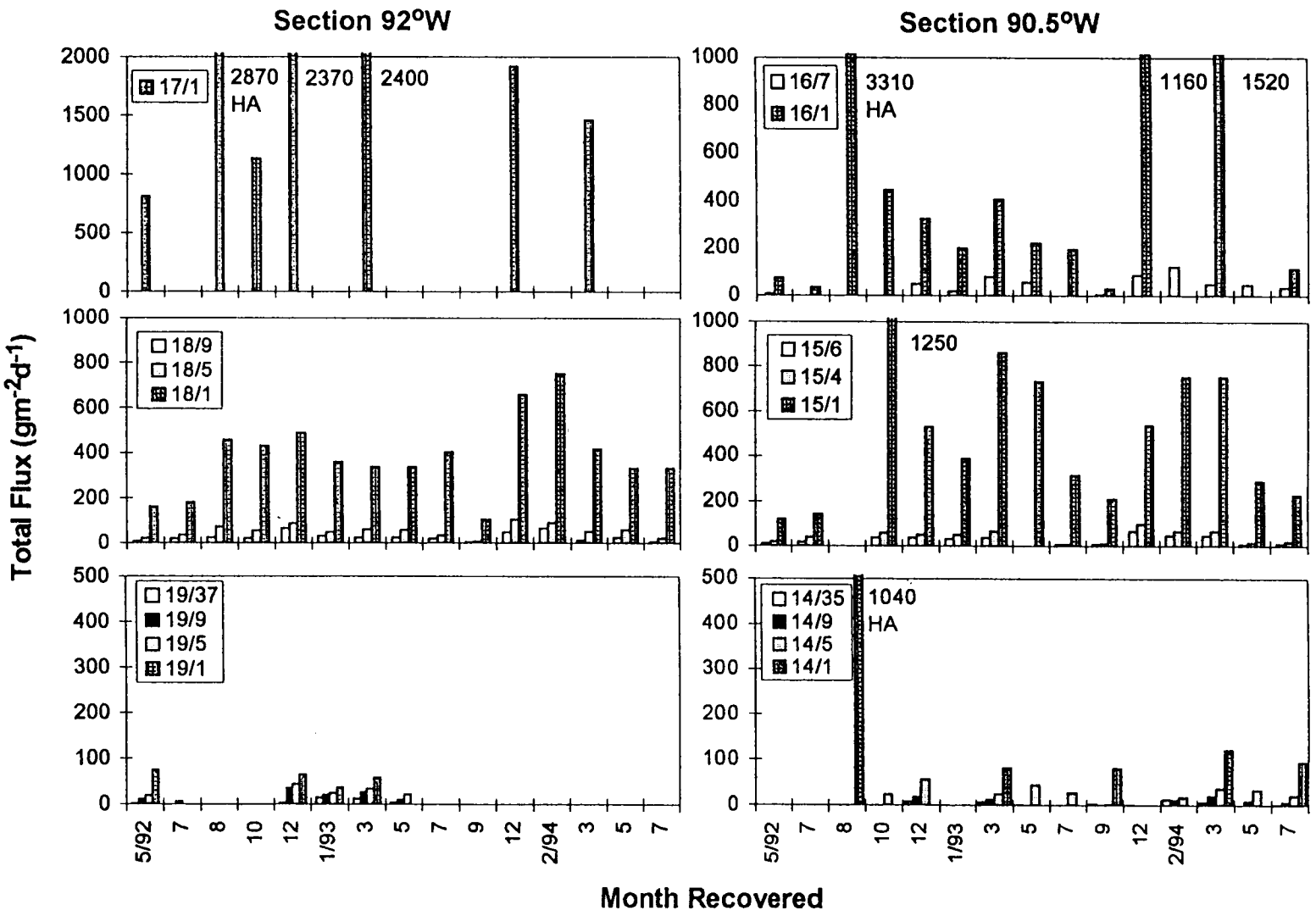

Figure 131. Fluxes calculated for sediment traps on LATEX A Moorings 14-19 during Deployments 1-15 (April 1992-July 1994). Legends in each box (e.g. 17/1) refer to mooring number (17) and trap position in meters above bottom (1). Numbers in the box give the value for data that are off scale. HA denotes the time when Hurricane Andrew passed. Note different scales for flux.

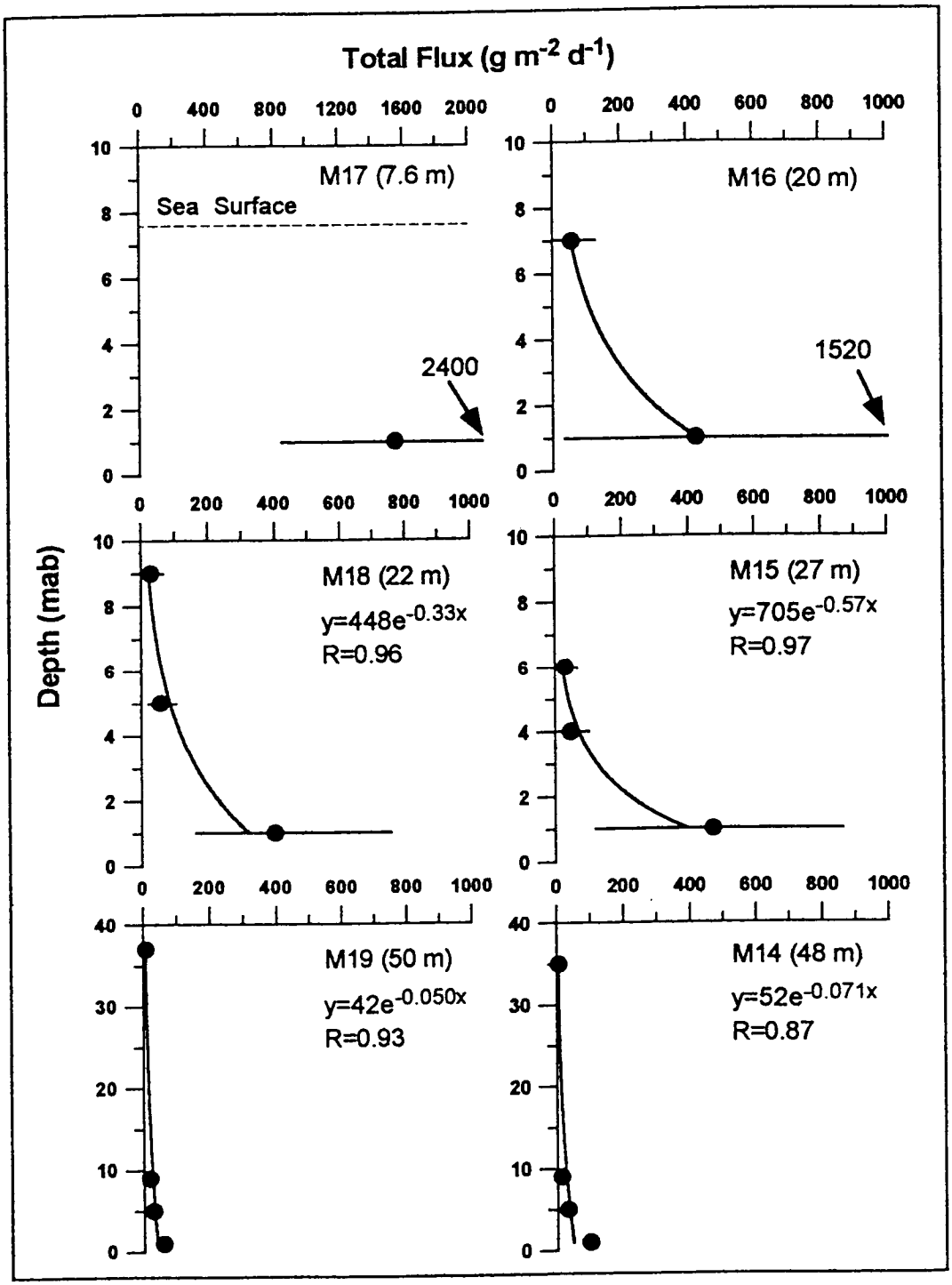

Figure 132. The mean total flux and one standard deviation are plotted for the entire 28 months of deployments at each mooring. Depth scale is in meters above bottom. Total water depth is noted next to the mooring number in each box. For moorings with three or more trap depths, an exponential equation was fit to the data and the quality of fit is given as R. Note the wide range of temporal variability in the near-bottom traps of the 4 shallower moorings. Note also the different flux scale for Mooring 17 and the large depth scale for Moorings 14 and 19.

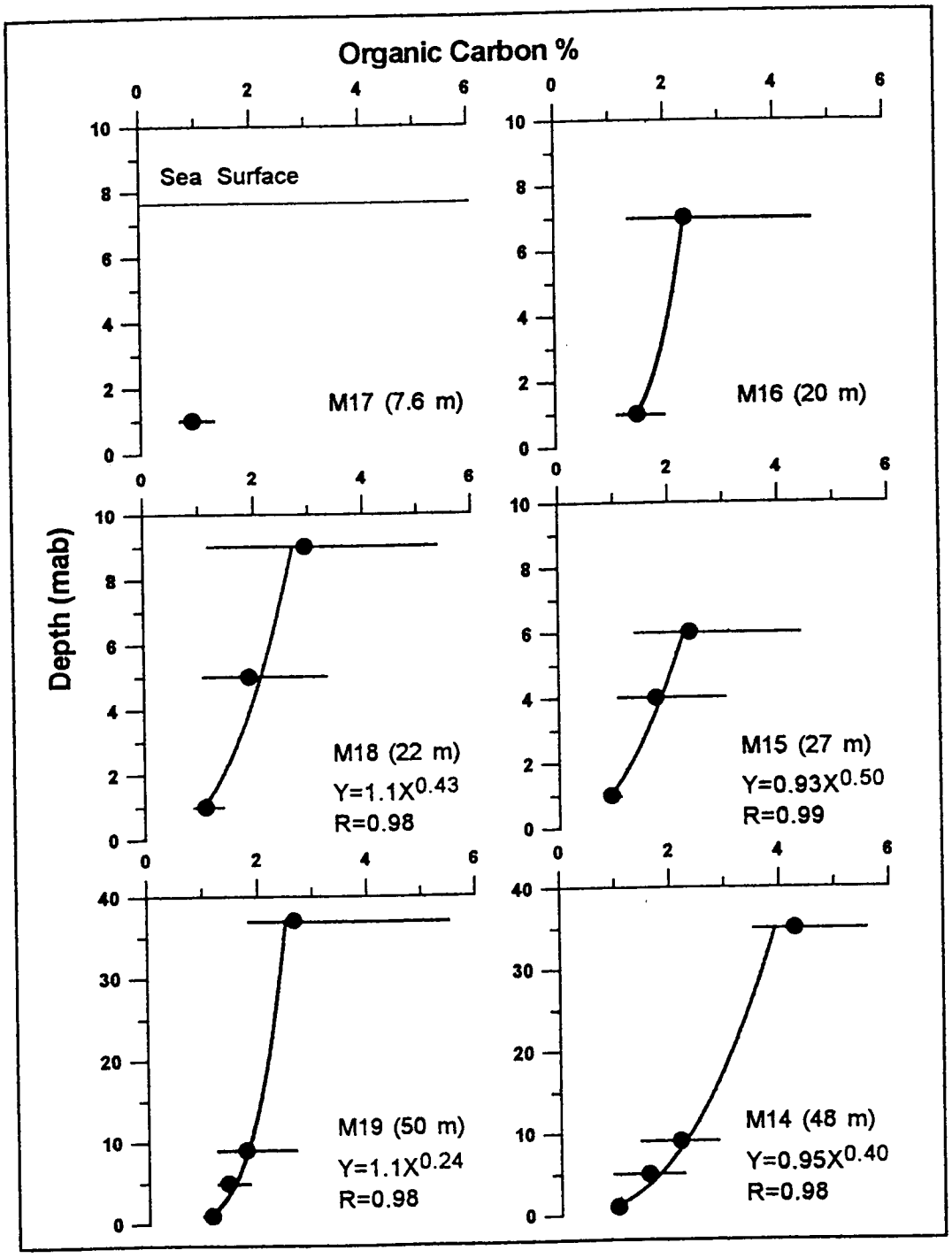

Figure 133. The mean percentage and standard deviation of organic carbon in the trap fraction <1 mm as a function of mooring site and depth as in Figure 132.

percentages occurring in early to late summer (Figure 134). There were also interannual variations in the timing of the maximum. The C/N ratio (by atomic weight) increased with depth from about 9 at 6 to 10 mab to as much as 15 at 1 mab (Figure 135). Temporal variations in C/N showed no clear seasonal pattern, but there appeared to be an overall decrease in C/N over the 28 months of study (Figure 136).

During each deployment the carbonate percentage of trap samples decreased substantially with depth from as much as 40% at 6 to 9 mab to only 10% at 1 mab (Figure 137). As with organic carbon, even though the percentage of carbonate decreased with depth, the apparent total flux of carbonate increased with depth.

2. Tetrapod

During the deployments of the VIMS tetrapod and our simultaneously deployed trap mooring (Table 16), total fluxes increased with depth. The percentage of organic carbon and carbonate decreased with depth and the C/N ratio increased with depth (Figure 138). The apparent flux measured with the trap attached to the leg of the tetrapod (0.75 mab) always exhibited a larger flux than the bottom trap of the adjacent mooring at 1 mab. The surface sediment at the site had a lower percentage of organic carbon and carbonate than the material collected in the bottom traps. The wet-sieved size distribution of material collected in the traps for each deployment is compared with the size distribution of bottom sediments (Figure 139).

Table 16. Tetrapod and associated trap mooring deployment data.

Time	Dates	Latitide ° N	Longitude ° W
Spring 1992	April 22-30, 1992	28° 56.29'	90° 28.81'
Spring 1993	May 16-June 15, 1993 ?	28° 56.22'	90° 27.72'
Summer 1993	July 12-22, 1993	28° 52.20'	90° 27.72'

D. Discussion and Interpretation

Trap samples are integrations of conditions over the time of deployment, with the mooring samples integrating over six weeks and the tetrapod samples integrating over one to four weeks. The mooring samples provide spatial coverage over different shelf regimes and water depths relative to the coastal plume and fronts. As noted earlier, trap fluxes measured in boundary layers are maximum fluxes because particles may cycle several times in the boundary layer before they are deposited. Analysis of the LATEX A current meter data at the trap sites indicates mean speeds were between 10 and 20 cm/sec and exceeded 30 cm/sec for only a few percent of the deployment time. This is much lower than the maximum of 40 cm/sec for which these traps should collect an unbiased sample, though we suspect that the 40 cm/sec value for unbiased trap samples is a bit high. Although the traps occasionally were exposed to currents >40 cm/sec, generally it was only for short periods of time. The high aspect ratio of the traps (A=10) significantly inhibited loss of collected samples because of wave action (U.S. GOFS Report No. 10, 1989).

In the LATEX A Final Synthesis Report, Dr. Robert Reid (Nowlin, 1998) suggested that based on the mean wind stress and bottom currents over the Texas-Louisiana shelf, the upper and lower Ekman layers are likely to merge in water less than 50

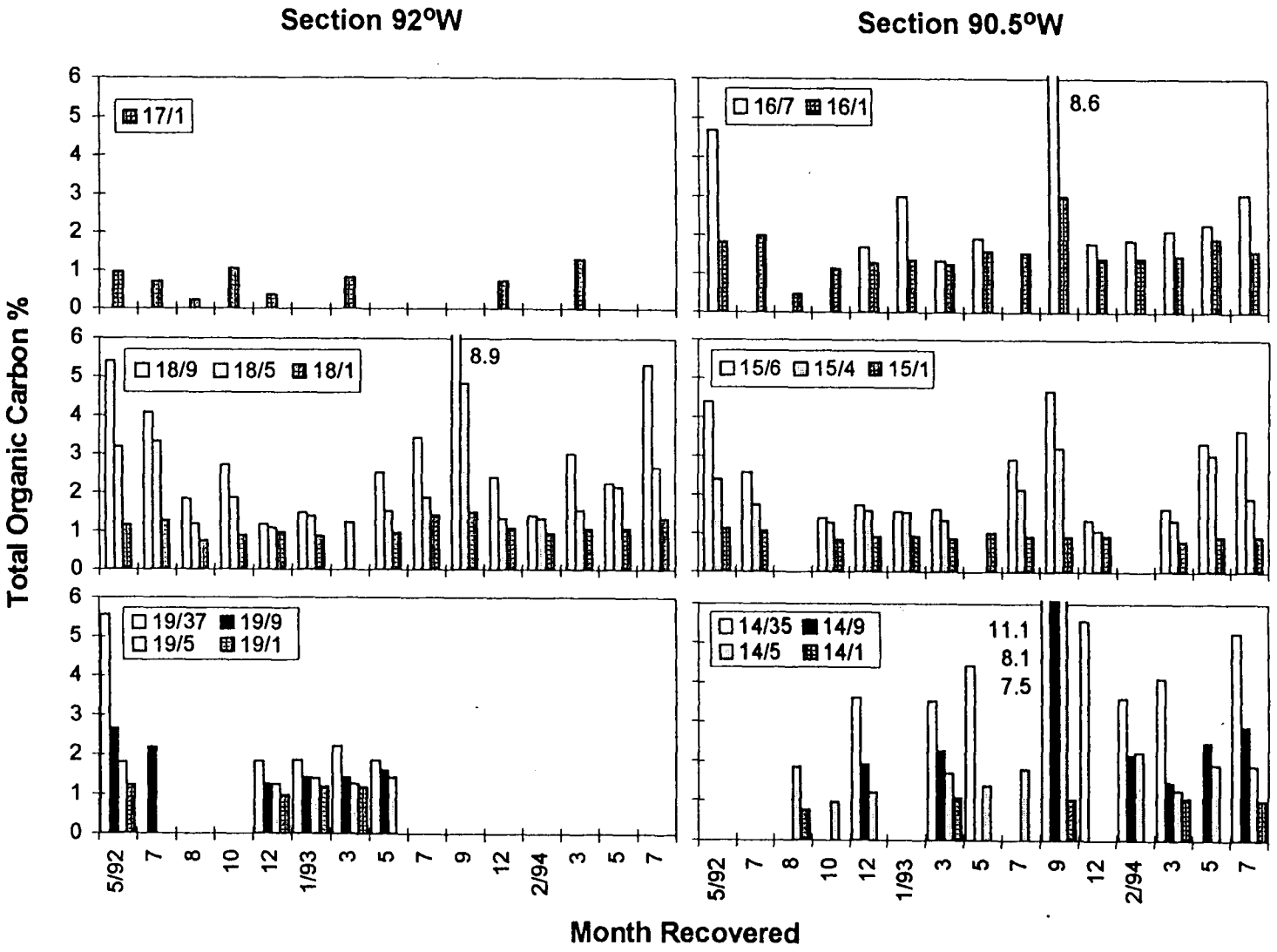

Figure 134. Percent organic carbon for trap samples on LATEX A Moorings 14-19. Legends in each box (e.g. 17/1) refer to mooring number (17) and trap position in meters above bottom (1). Numbers in the box give the value for data that are off scale.

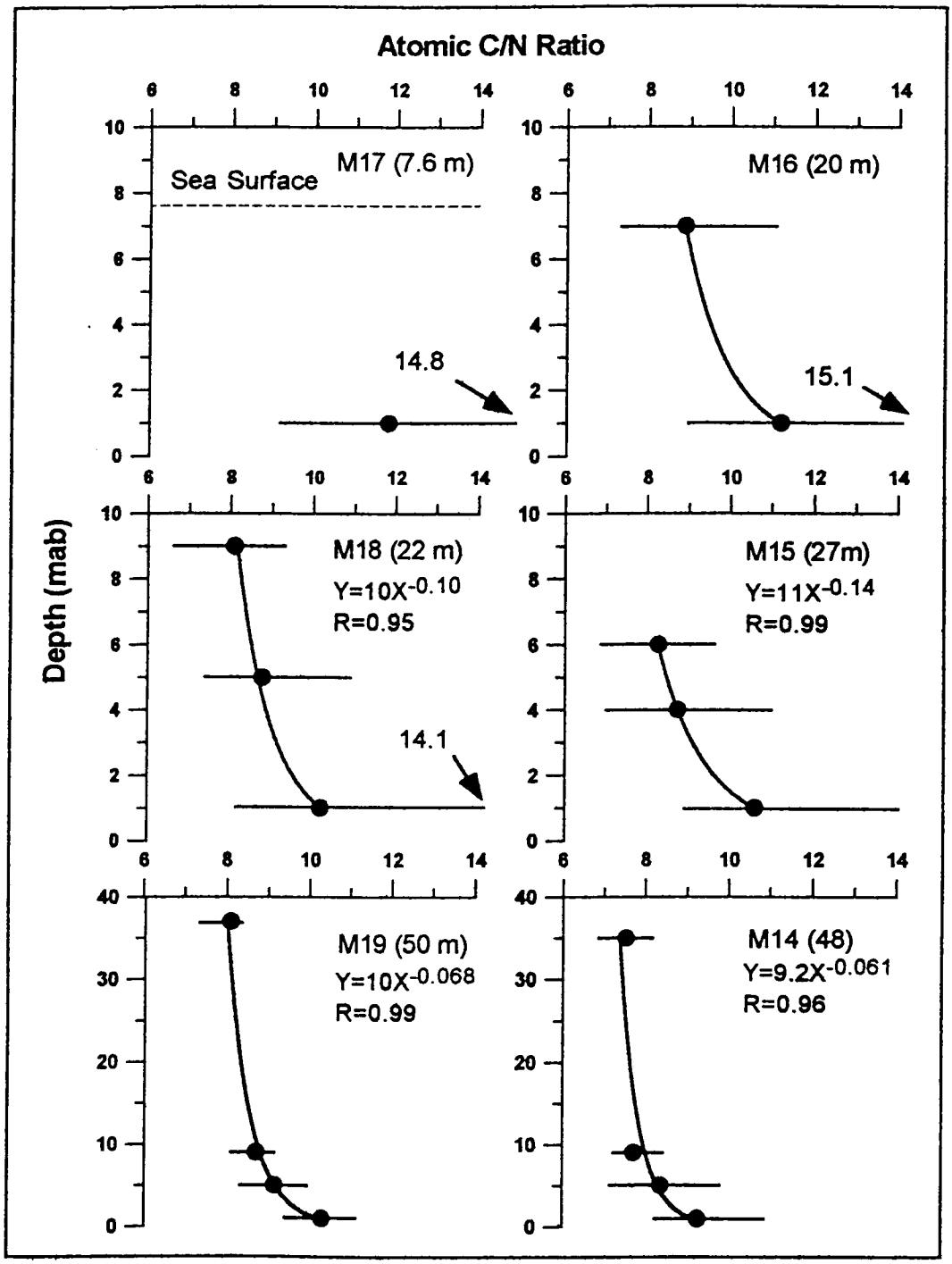

Figure 135. The C/N ratio and standard deviation of organic matter in the trap fraction <1 mm as a function of mooring site and depth as in Figure 132.

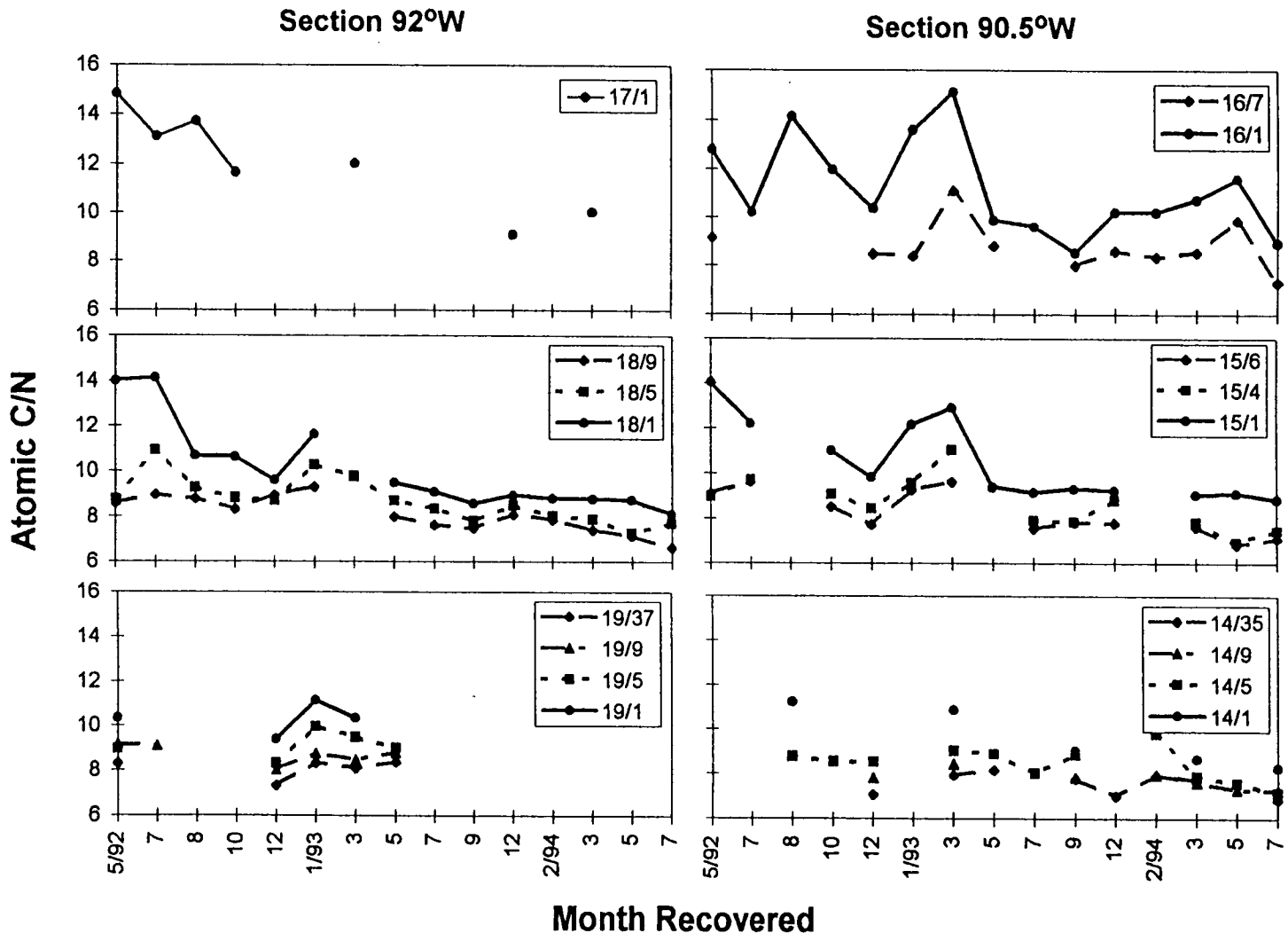

Figure 136. The C/N ratio for trap samples on LATEX A Moorings 14-19. Legends in each box (e.g. 17/1) refer to mooring number (17) and trap position in meters above bottom (1).

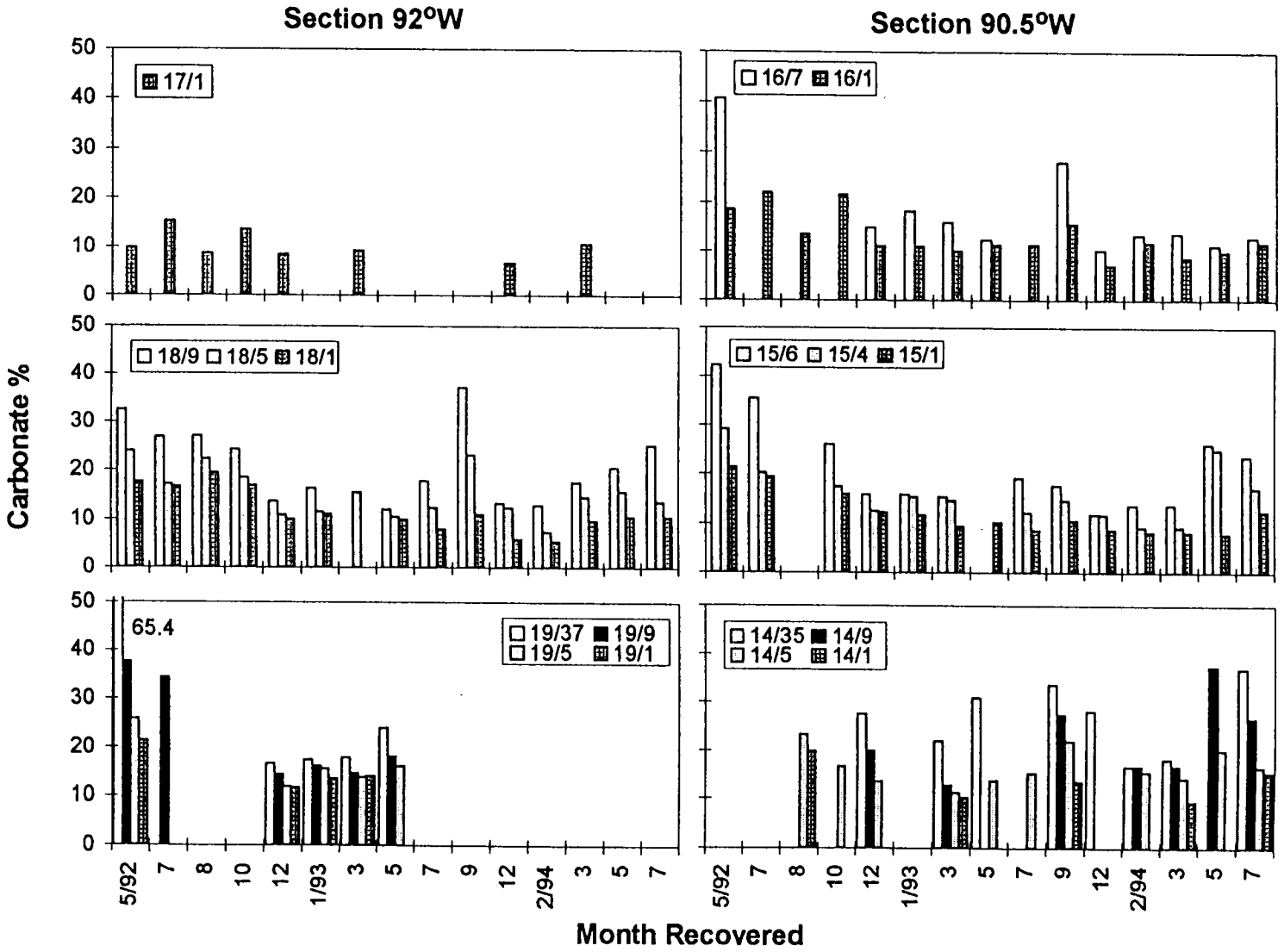

Figure 137. The percentage of carbonate in the fraction <1 mm.

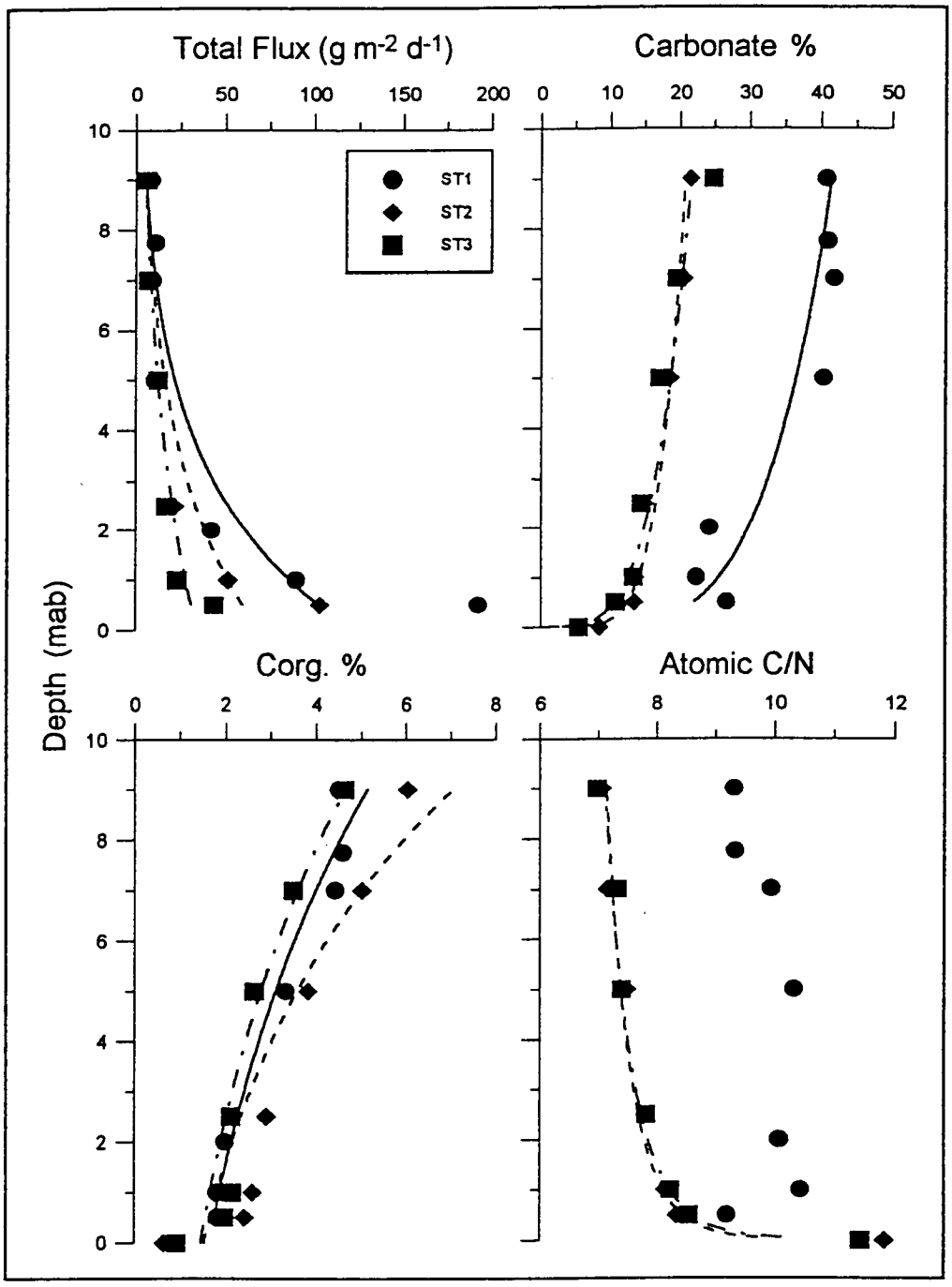

Figure 138. Four parameters for trap samples from the traps moored near the three VIMS tetrapod deployments (ST1-ST3), the trap attached to the foot of the tetrapod (at 0.75 mab), and the surface sediment. ST1 was deployed in 15.5 m of water and ST2 and ST3 were in 20.5 m of water.

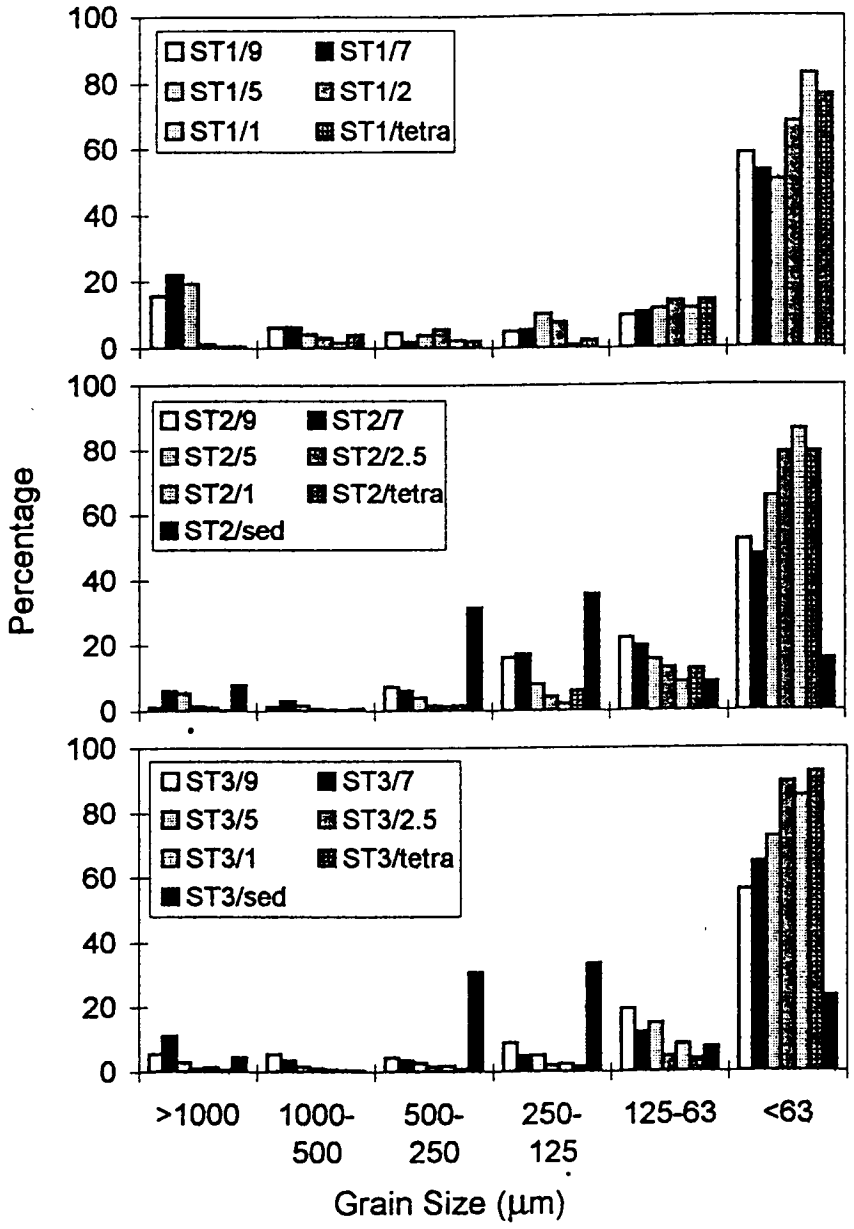

Figure 139. Wet-sieve size analysis of trap samples near the three VIMS tetrapod deployments. The percentage of small particles in trap samples generally increases near the seafloor. The percentage of fines contained in trap samples is about four times the percentage of fines that are contained in the surface sediments. Surface sediments are dominated (~75%) by the 125-500 µm size fraction.

m in depth. He further stated that the maximum filtered wind speed during the deployment time would suggest a maximum surface logarithmic layer of 7 m, with a similar thickness for the bottom logarithmic layer if the current shear stress were similar. However, the bottom shear was usually much less than that. Thus, it is likely that our traps were always within an Ekman boundary layer, but the traps five to nine mab were usually outside the logarithmic layer. Stratification of the water column can also affect the boundary layer dynamics. Detailed analysis of the times when the traps were in and out of various portions of boundary layers is beyond the scope of this analysis, especially when the trap samples are averages of six weeks of sampling during which time boundary layers can vary significantly.

The exponential decrease in flux with distance above the seafloor reflects the resuspension and recycling that occur near the seafloor in this region. Unfortunately, we cannot ignore, nor can we differentiate between resuspension and redeposition of bottom sediments and graded deposition of particles from a turbid plume advected into the region from the Mississippi or Atchafalaya Rivers or another portion of the shelf. The VIMS tetrapod recorded no time during its three deployments when critical bed shear stresses were exceeded locally, yet during the first deployment their turbidity sensors recorded a time of increased particle load, with the particle maximum occurring at the time of minimum bed shear stress. The currents, bed shear stresses and fluxes near the tetrapod site matched well the currents and fluxes measured around those times at the nearby LATEX A Mooring 16 (Figures 131, 138, 140). The other LATEX A moorings on which our sediment traps were deployed spanned a much larger region and time. The current meter data clearly recorded times when the critical bed shear stress was exceeded. We can examine the composition of the trapped particles for insight into the processes that occurred.

The decrease in the percentage of organic carbon with depth in trap samples (Figures 133 and 138) suggests that the increase in flux with depth results from resuspension of bottom sediments, which contain <1% organic carbon. The increase with depth in the C/N ratio was further evidence that the material collected in the bottom traps contained older material that had time to decompose, probably at the seafloor, thus increasing the C/N ratio. The percentage of carbonate also decreased with depth (Figures 137 and 138), and could result from bottom sediments being resuspended and diluting the primary flux particles with low-carbonate (<5%) bottom sediments (Figure 138). The wet-sieved size analysis of trapped particles (Figure 140) revealed that most of the near-bottom material was very fine-grained or was composed of aggregates that were easily broken up in the sample handling. Bottom sediments contained one fourth the percentage of material <63 μm than the trap material and much more material in the fine sand range (125-500 μm). This is still consistent with the resuspension of bottom sediments as it requires a greater bed shear stress to resuspend larger grains. It is well known and accepted that shelf sediments may be resuspended and deposited many times before they are finally buried.

Bottom fluxes decrease sharply with distance offshore (Figures 131 and 132). The high fluxes at Mooring 17 were caused by the close proximity to the Atchafalaya River, the shallow water depth, fast currents, large bed shear stress, and the large resulting resuspension fluxes. We were able to deploy only one trap on that shallow mooring, so we have no information about vertical variations in the flux. During the passage of Hurricane Andrew the total settling flux in near-bottom traps increased by up to an order of magnitude near the hurricane path (Figures 131 and 132). The currents were so great at Mooring 15 that all the traps were torn from the mooring line and lost. Mooring 18 was 150 km west of the eye of the hurricane, yet the bottom trap registered no abnormal increase during that time, suggesting an intense, but rather localized effect of the hurricane on resuspension. Indeed, the bed shear stress at Mooring 18 was much lower than those

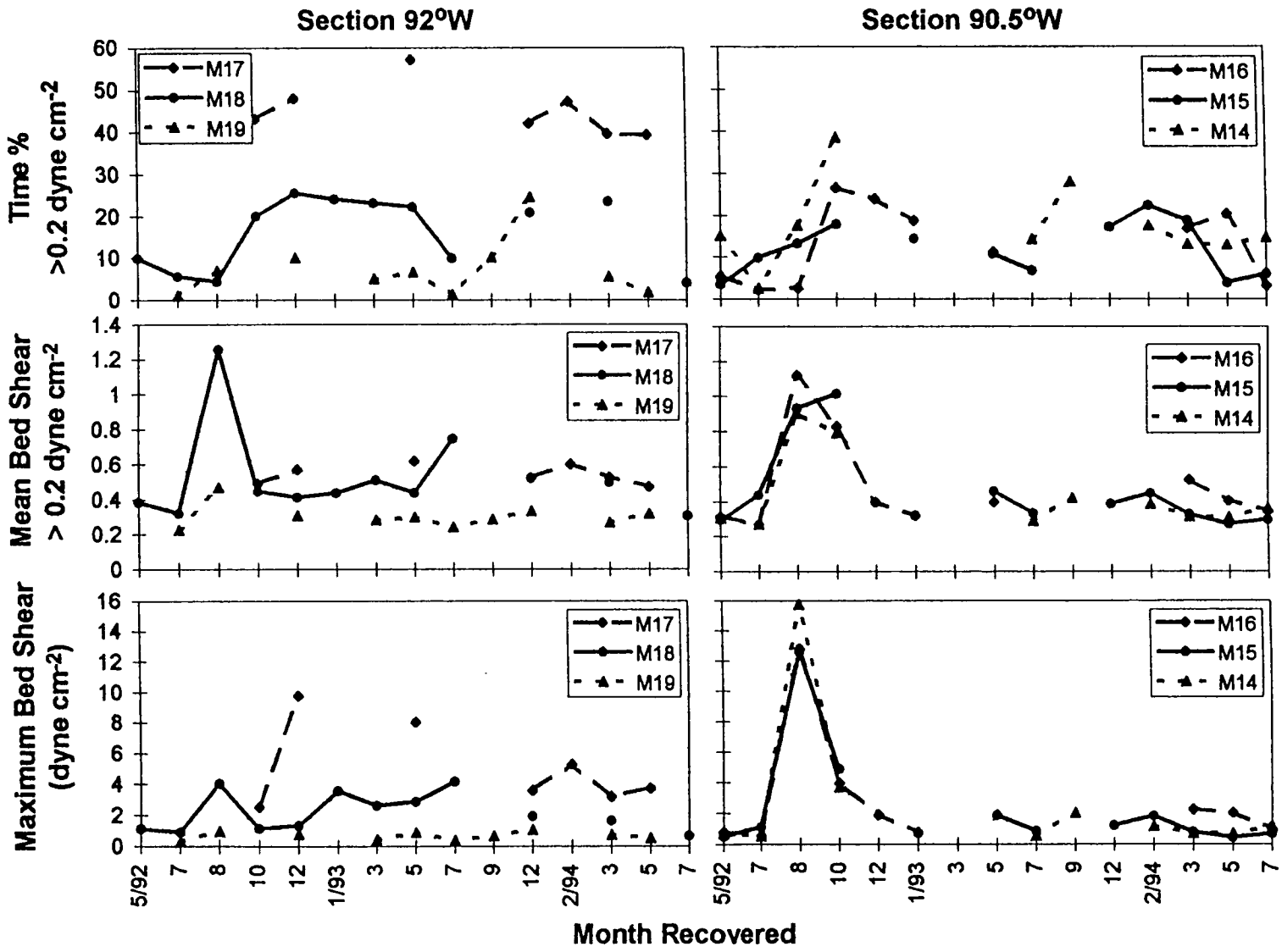

Figure 140. Summary information from LATEX A current meter data. Top; percent of time when the bed shear stress exceeded 0.2 dynes cm^{-2}; Middle: mean bed shear stress for the data points that exceeded 0.2 dynes cm^{-2} during each trap deployment; Bottom: maximum bed shear stress during each deployment. Values at Mooring 14 were similar to those of Moorings 15 and 18. Values at Mooring 19 were lowest of all sites.

along 90.5° W, and it was lower still at Mooring 19, but we failed to retrieve a good trap sample during that time.

The two outer moorings near the 50 m isobath (14 and 19) should be expected to have lower total and resuspension fluxes for several reasons. First, they were much further from the sources of river sediments. Second, the plume of the rivers entering into the Gulf of Mexico is dynamically steered to the west along the coast. Hydrographic fronts are formed as a result of plume waters. The mean position of the front was between Moorings 15 and 16 at 90.5° W and at about Mooring 18 at 92° W (see Section IV in this report). Moorings 14 and 19 were well to the south of the fronts. Bed shear stresses at Mooring 14 were similar to those at Moorings 15 and 18 (Figure 140) but bed shear stresses at Mooring 19 were lowest of the six sites. Being in deeper water, Moorings 14 and 19 were also less affected by wave action, which can increase the rate of resuspension.

1. Seasonal Trends

A seasonal signal in the percentage of organic carbon collected in sediment traps is evident but has considerable interannual variability (Figure 134). The trap samples away from the seafloor are least likely to be contaminated by resuspended sediment and should best represent the composition of material settling from surface waters. Primary production in surface waters would be expected to be highest in the spring and decrease during the year. Thus the percentage of organic carbon in the traps away from the seafloor should be highest in the spring and decrease during the year. During 1992 the highest percentage of organic carbon occurred in April and May, but the maximum shifted to August in 1993 and perhaps in 1994 (Figure 134). This shift is consistent with the differences in river runoff for those years. Runoff in 1992 was lower than the 65-year mean and was abnormally low by mid-April, greatly decreasing the supply of new river nutrients to the shelf. River discharge was well above the mean in 1993 and 1994 and didn't decrease to normal values until mid-June, thus fueling higher primary production later into the year.

While we observe large temporal variations in the total flux of near-bottom traps, we can discern no seasonal trend in the total fluxes (Figure 131). This is consistent with the lack of a seasonal signal in the mean or maximum bed shear stress at the mooring sites (Figure 140). There are obvious effects from the passage of a hurricane, but the six-week averages from trap samples was too long to pick out the effects of individual storms at other times of the year.

2. Spatial Trends in Organic Carbon

There are also regional differences in the percentage of organic carbon collected in the traps. The most obvious is the increase in percent organic carbon with distance from shore (Figure 133). The percentage of organic carbon in the off-shore surface traps (~4%) was twice the value of in-shore traps, although there was not a lot of difference between the traps at 9 mab at the various trap sites.

It appears that the percentage of organic carbon in traps (Figure 134) from the area of hypoxia (Moorings 14, 15, 16, and 18) is greater than from outside the hypoxic area based on the distribution mapped by Dr. Nancy Rabalais (Section IX) and from the LATEX A hydrographic cruises. This mid-shelf region may be an area of higher primary production caused by increased water clarity and high nutrients. The particulate carbon could then quickly settle to the seafloor and utilize oxygen during degradation.

3. Flux versus Bed Shear Stress

Resuspension of bottom sediments occurs when the bed shear stress exceeds a critical value. The VIMS tetrapod data were used to calculate the bed shear stress by making several measurements of velocity in the logarithmic velocity layer near the seafloor. We can make estimates of the bed shear stress from the LATEX A near-bottom current measurements using the quadratic stress equation, $T = \rho C_D * u^2$, where T is the bed shear stress, ρ is the density of the fluid, C_D is a drag coefficient, and u is the current speed. For comparison with the trap fluxes, we have calculated the mean shear stress at each site for that portion of the record when the shear stress exceeded 0.2 dynes cm^{-2} for each trap deployment (Figure 140). We have also calculated the maximum bed shear stress during each deployment period and the percent of time the bed shear stress exceeded 0.2 dynes cm^{-2}, which we take as an approximate critical bed shear stress. The drag coefficient used was 1.4×10^{-3}, which was derived from data at a site about 20 km east of Mooring 17 by Adams et al. (1982). When the total flux at 1 mab is plotted against the above parameters the correlations range from very good to poor (Figure 141). However, if we do a three-dimensional fit of the flux data to both the mean bed shear stress (for the time when $T > 0.2$ dynes cm^{-2}) and the percent of time greater than the critical bed shear stress, we achieve an excellent fit between our calculated flux and the measured flux. This suggests that there is a strong correlation between the total flux and bed shear stress not only in the bottom traps, but also in traps 6 mab (Figure 142). By 9 mab the correlation is greatly diminished. Thus, it appears that for this region of the Louisiana shelf we can estimate the average amount of resuspension that is likely to occur based on the bed shear stress measured.

E. Conclusions

The marked vertical variations in total and organic carbon fluxes, percent organic carbon and C/N ratio are consistent with extensive resuspension of bottom sediments into the bottom boundary layer. In the vicinity of the VIMS tetrapod the near bottom increases were more likely a result of deposition from a turbid plume advected into the area. Bottom fluxes decreased with distance off shore as a result of decreased bottom stresses as the water deepens, and increased distance from sources of river sediment. Overall, the total bottom fluxes are well-correlated with the combined parameters of mean bed shear stress (mean of the data >0.2 dynes cm^{-2}) and the percent of time when the critical bed shear stress is exceeded at the site.

The mid-shelf area of summer hypoxia is well-correlated with an increase in the percentage of organic carbon collected in the traps in that region.

The passage of Hurricane Andrew increased the near-bottom fluxes (resuspension fluxes) by up to an order of magnitude near the path of the hurricane, but not at all 100 km west of the hurricane, suggesting a rather localized effect on resuspension.

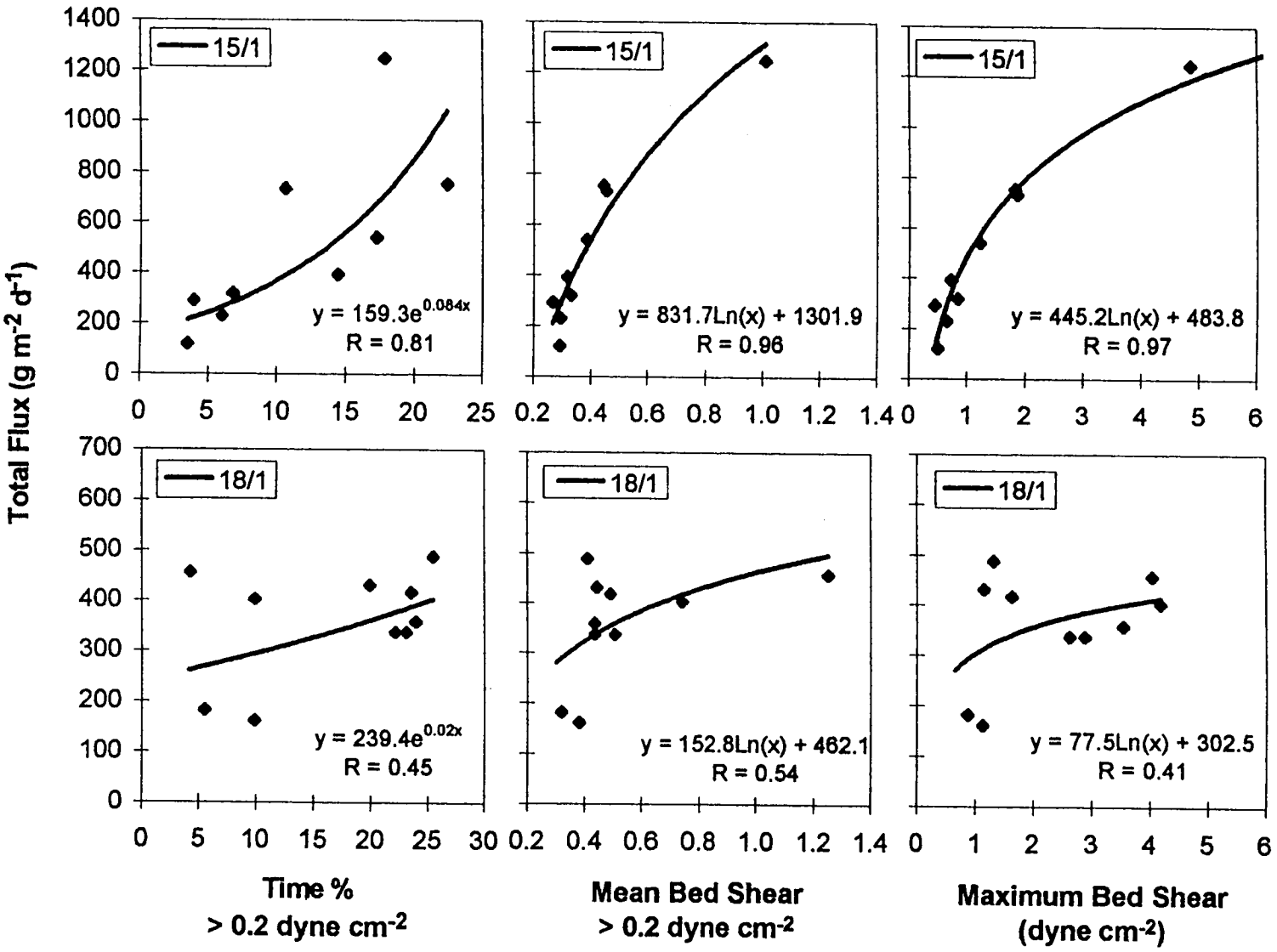

Figure 141. Total flux of sediment during individual deployments on Moorings 15 (upper) and 18 (lower) versus (1) the percentage of time the bed shear stress was greater than 0.2 dyne cm^{-2}, (2) mean bed shear stress for the data points that exceeded 0.2 dynes cm^{-2} during each trap deployment, and (3) maximum bed shear stress (Zhang, Ph.D. dissertation, in preparation)

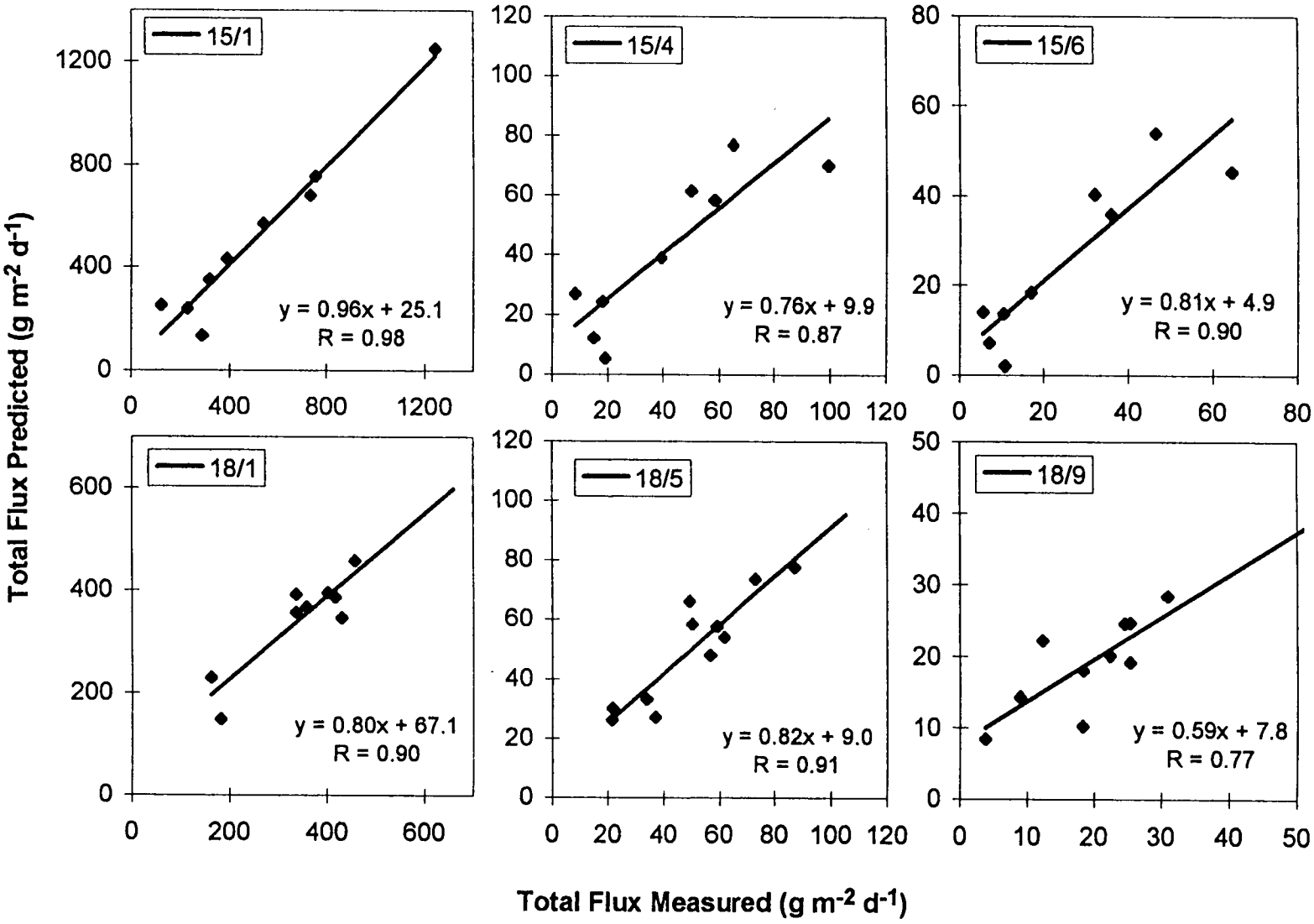

Figure 142. Total predicted flux versus total measured flux with traps at three depths on two moorings. The predicted flux was based on a 3D fit of measured fluxes, mean bed shear stress for data >0.2 dynes cm^{-2} and the percent of time when the critical bed shear stress was exceeded.

VI. Light, Nutrient, and Phytoplankton Pigment Charateristics

A. Light Conditions Within and Near the Louisiana Coastal Current

by R. Eugene Turner and Nancy N. Rabalais

1. Introduction

The coastal plume associated with the Louisiana Coastal Current (LCC) is characterized by strong turbidity gradients and a well-defined density structure responsive to local winds, freshwater supplies, and weather fronts. The LCC, therefore, has a relatively unstable structure over periods of days to weeks, as shown by remotely sensed images of turbidity in the surface layer. Visual observation of only the surface layers gives a substantially inadequate description of the LCC, for the physical structure is not homogeneous with depth. Light conditions within the LCC vary temporally along the three spatial axes and, when characterized, can be used to both define its location and to quantify its variability. One of the tasks of LATEX B was to define the light field of the LCC and to establish relationships between the physical and biological components. The light field within the LCC, regardless of cause, has important biological consequences. Microbes, zooplankton and fish are dependent on the phytoplankton whose production and accumulation is responsive to light conditions as well as the same forces delimiting the physical structure of the LCC.

We completed this investigation using traditional methodology, e.g., data from transmissometers, Secchi disks, and photosynthetically-active radiation (PAR) sensors. Data were also obtained from other programs and historical records. The Secchi disk has been around longer and used routinely, compared to the newer instrumentation. Its simplicity, low cost and frequent use has provided many measurements of turbidity over the last two decades. Measurements from Secchi disk depths and optical measurements (i.e., from an in situ light meter) are well correlated. Secchi disk measurements are therefore potentially valuable sources of information on the light field within the LCC. We used these data to construct historical trends in the light for the region.

2. Methods

The cruise tracks, general instrumentation, logistics and hydrographic data are contained in other portions of this report.

The light meter used was a hand-held BioSpherical Instruments, Inc. PNF profiler. This light meter is equipped with a deck reference PAR sensor and a submersible PAR sensor within a wired instrument package that includes sensors for depth, natural fluorescence, and temperature. The lowering cable is wired to a portable computer that displays results while on station. The computer software computes the estimated extinction coefficient, with depth, the percent irradiance at depth, and a relative estimate of phytoplankton production. The latter estimate was made using an empirical conversion factor to convert the natural fluorescence values and PAR to instantaneous phytoplankton production rates. Secchi disk measurements and light meter readings were made on the lighted side of the vessel, within three hours of local apparent noon. Shipboard measurements of phytoplankton pigments and salinity are described later.

Historical data were acquired from the personal data files of the investigators, including results from the NMFS R/V Oregon II and SEAMAP cruises (unpublished data), as well as from the hypoxia monitoring studies conducted by Louisiana scientists

during the last 20 years (e.g., Turner and Allen 1984a, b; Rabalais et al. 1991, 1994a,b, 1996 a, b).

3. Results

Figures 143 through 146 illustrate spatial and temporal scales of variability in the light regime on the Louisiana shelf. Figure 143 shows changes in the extinction coefficient (k) and primary production rates along a transect south of Grande Isle, in April 1992. The LCC is shown in the right side, looking westward and the data profile extends to 30 m. The extinction coefficient (k) ranges from less than 0.2 to greater than 1.5 on this transect. There was a mid-shelf area of slightly higher turbidity, a beginning of higher extinction coefficient at the oceanic end of the transect in bottom waters (nepheloid layer?), and a surface high with what is probably the LCC. Phytoplankton production rates (relative scale) are highest at the shoreward end of the transect and at the surface.

Figure 144 illustrates the percent surface irradiance with depth along the 20 m isobath from west of the Mississippi River bight to the south Texas coastline. The 20 m isobath was chosen as an example of changes along the edge of the LCC. At no place is light impinging on the bottom. In fact, light did not penetrate below 10 m anywhere along the transect on this cruise. The bottom light conditions are important to understand because the extensive hypoxic zones that form during the spring (and last throughout the summer) may be limited on their seaward edge by the oxygen produced in situ on the seafloor (by benthic microalgae, for example).

Figure 145 shows the relationship between the log10 transformation of Secchi disk depth (SDD; m) and surface salinity at all of the LATEX B sampling stations where SDD was measured. The total depth at these stations is between 10 and 100 m. The SDD ranges from less than 1 m to greater than 25 m on these LATEX B cruises but is restricted to a range up to about 12 meters within the 10 to 100 m depth contours. There is a general tendency for the SDD to increase with salinity (note: this is a logarithmic scale). The relationship between SDD and salinity is much more noticeable if the data for each cruise are used separately, rather than as one data set, and are shown in Figure 146. We made several estimations of the percentage of the surface light at the SDD and found it to be about 10-12% for any one particular cruise.

The light regime has an effect on phytoplankton populations and vice versa. Phytoplankton production requires light, of course, and the relationship of photosynthesis to light is typically a rising curvilinear relationship showing saturation at some level and sometimes light inhibition. The biomass produced absorbs light. Figures 147 (April 1992) and 148 (October 1992) show examples of a contour plot of phytoplankton pigments as a function of salinity and turbidity. April 1992 had very high chlorophyll *a* concentrations (up to 150 μg/L) and the October 1992 data set relatively low values (less than 20 μg/l). For both cruises, the highest concentration of phytoplankton is located in the region of intermediate salinity where the light conditions are beginning to improve. Plots of data from other cruises and from fixed sampling locations over seasons and among years show similar patterns. Just seaward of the LCC is where nutrients are relatively high, phytoplankton are basically light limited, and where intense phytoplankton activity is developing.

Phytoplankton biomass is generally considered to be proportional to phytoplankton pigments, i.e., total chlorophyll *a* (μg/L). The amounts of pigments are high enough to absorb light in significant amounts. Figure 149 shows the relationship between the log10 transformed Secchi disk depth (m) and the total phytoplankton

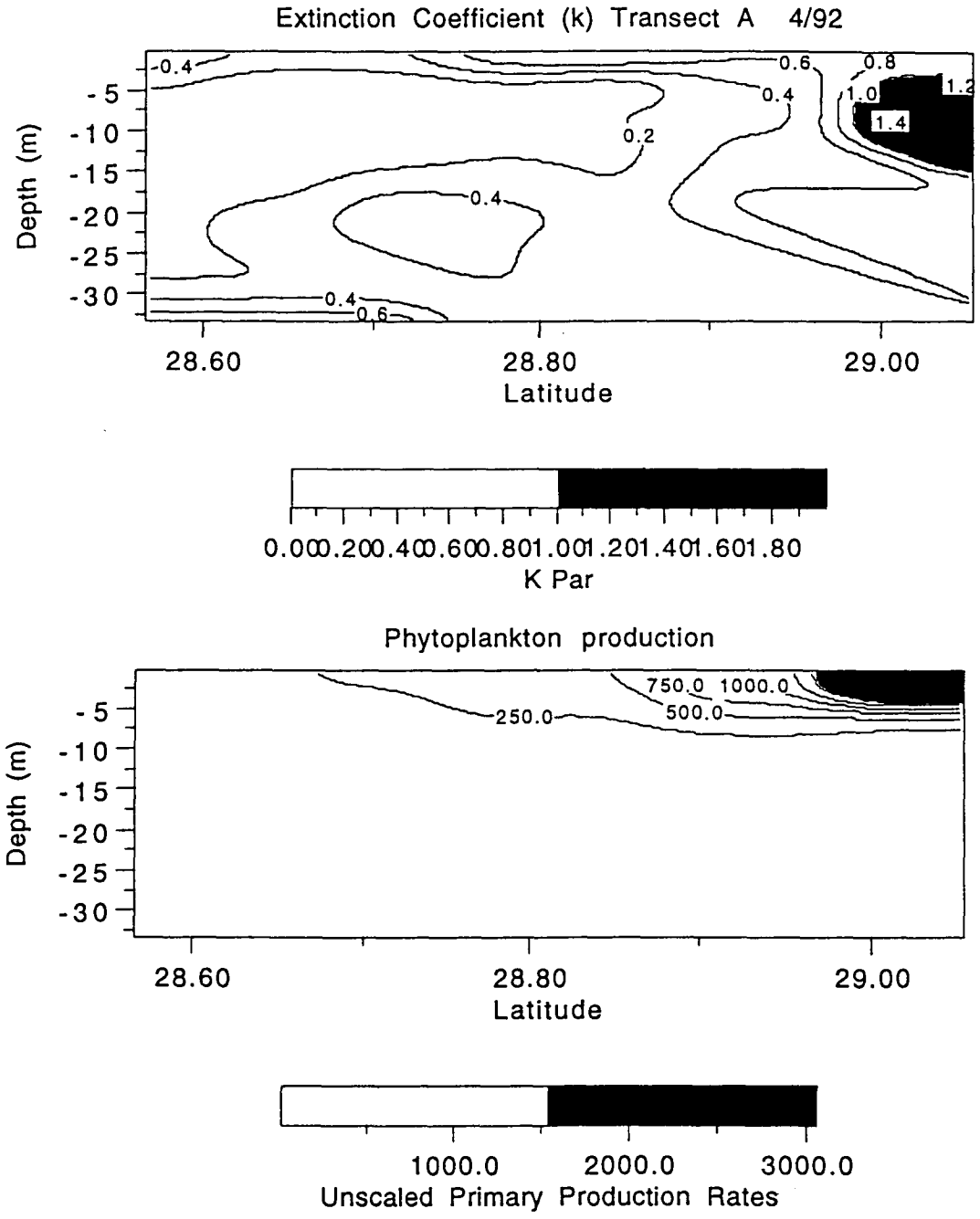

Figure 143. Changes in the extinction coefficient (k) and primary production rates along a transect south of Grande Isle in April 1992.

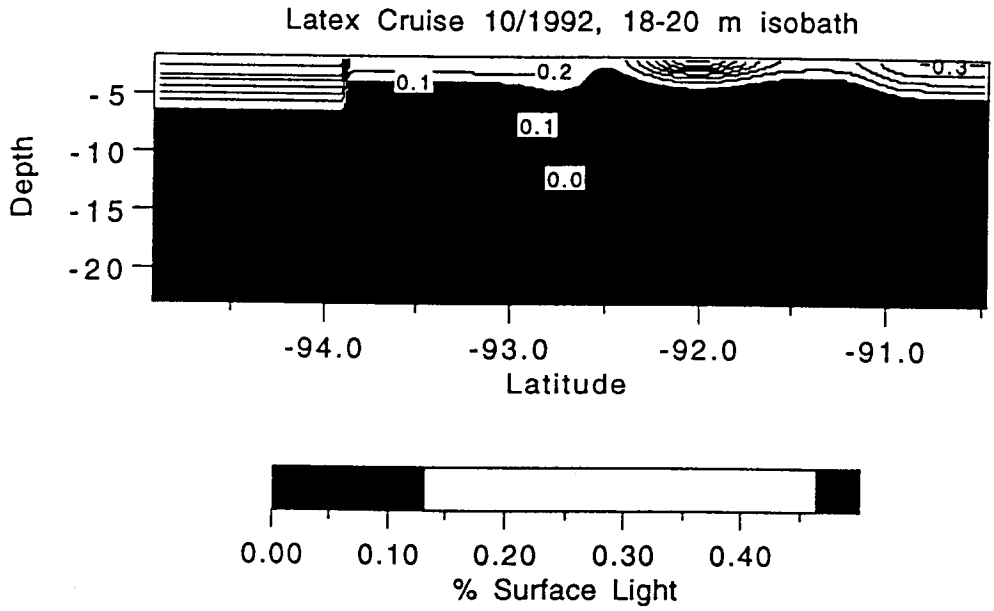

Figure 144. The percent surface irradiance with depth along the 20 m isobath from south of Terrebonne Bay to the south Texas coastline. The Mississippi River is approximately one inch from the right hand border, and the Atchafalaya River inputs arrive at about 91.5° W.

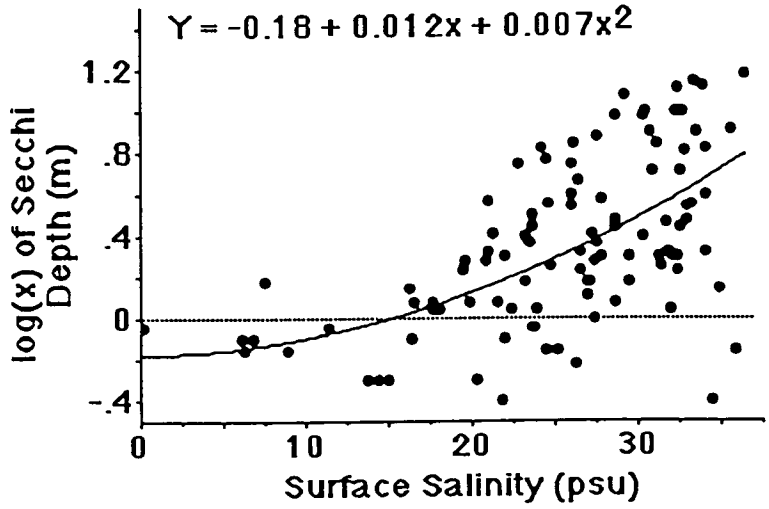

Figure 145. The relationship between the $\log_{10}$ transformation of Secchi disk depth (m) and surface salinity for the LATEX B sampling stations. The total depth at these stations is between 10 and 100 m.

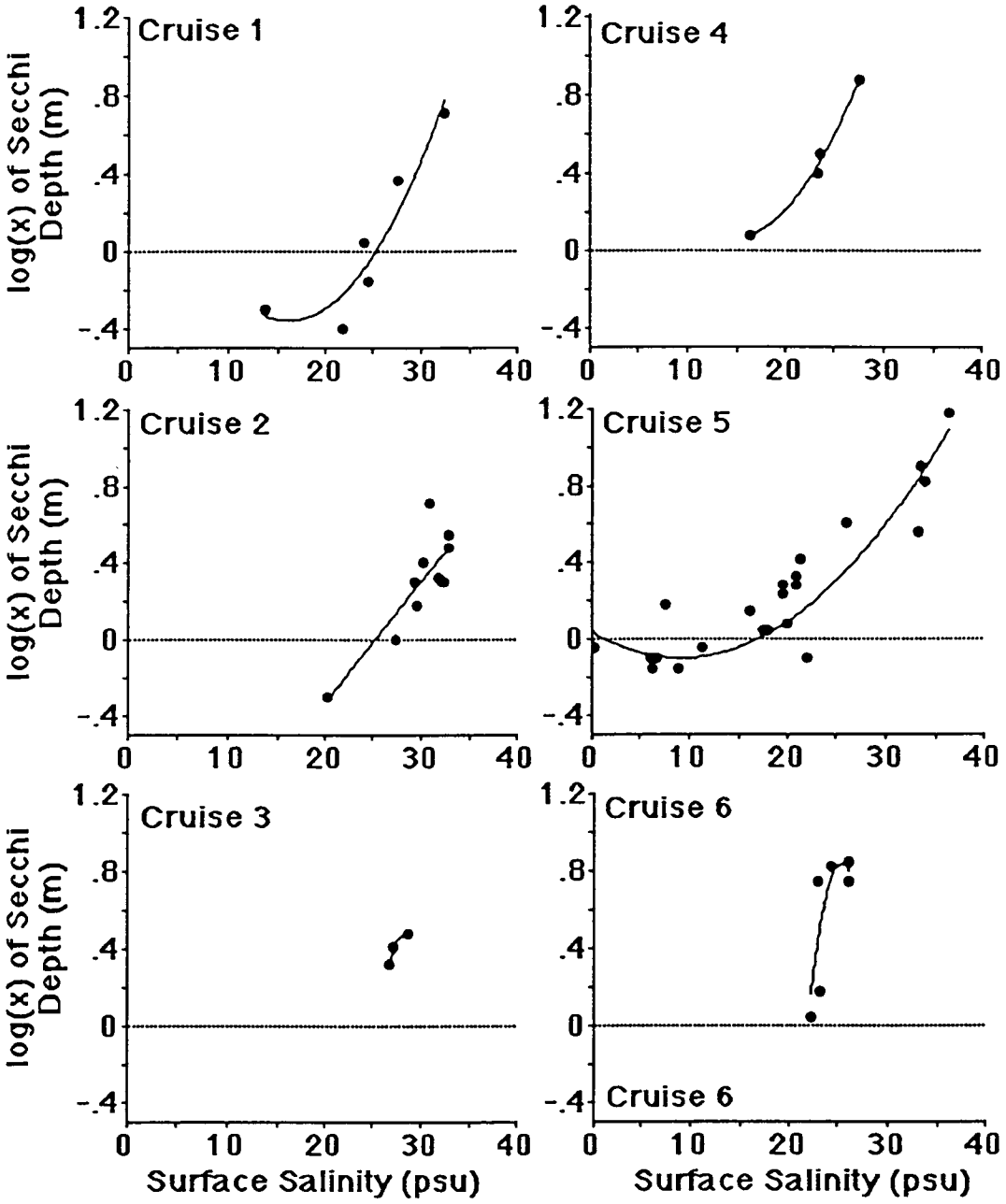

Figure 146. The relationship between the $\log_{10}$ transformation of Secchi disk depth (m) and surface salinity for the LATEX B sampling stations by cruise. The total depth at these stations is between 10 and 100 m.

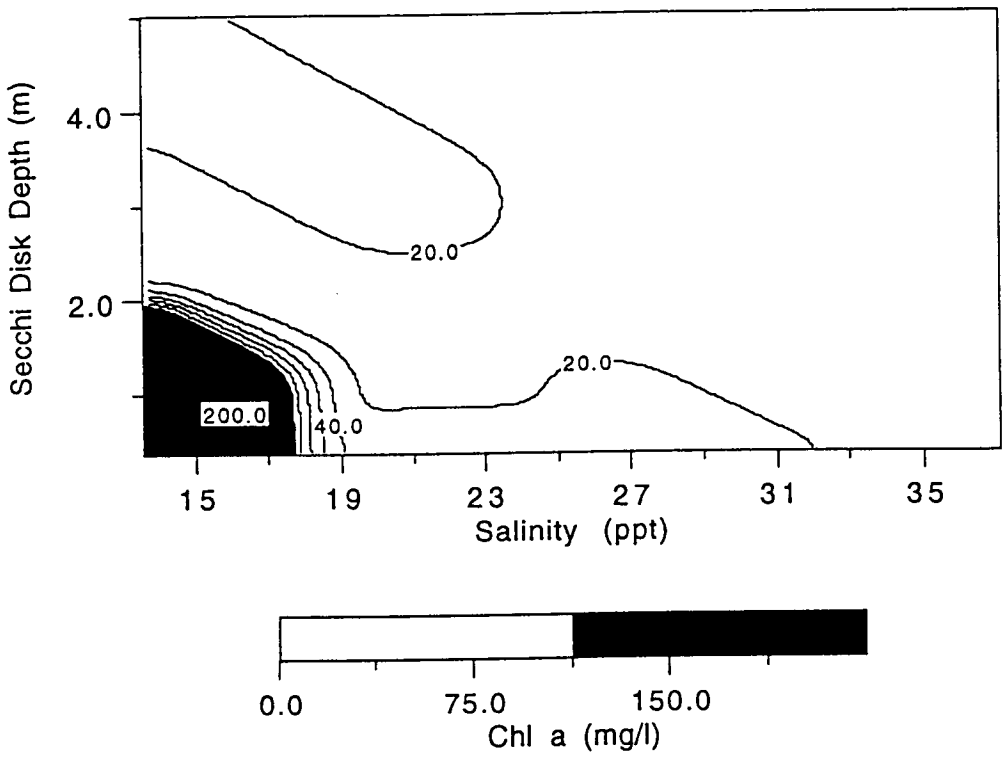

Figure 147. Contour plot of chlorophyll *a* versus the Secchi disk depth and salinity for surface samples taken in April 1992.

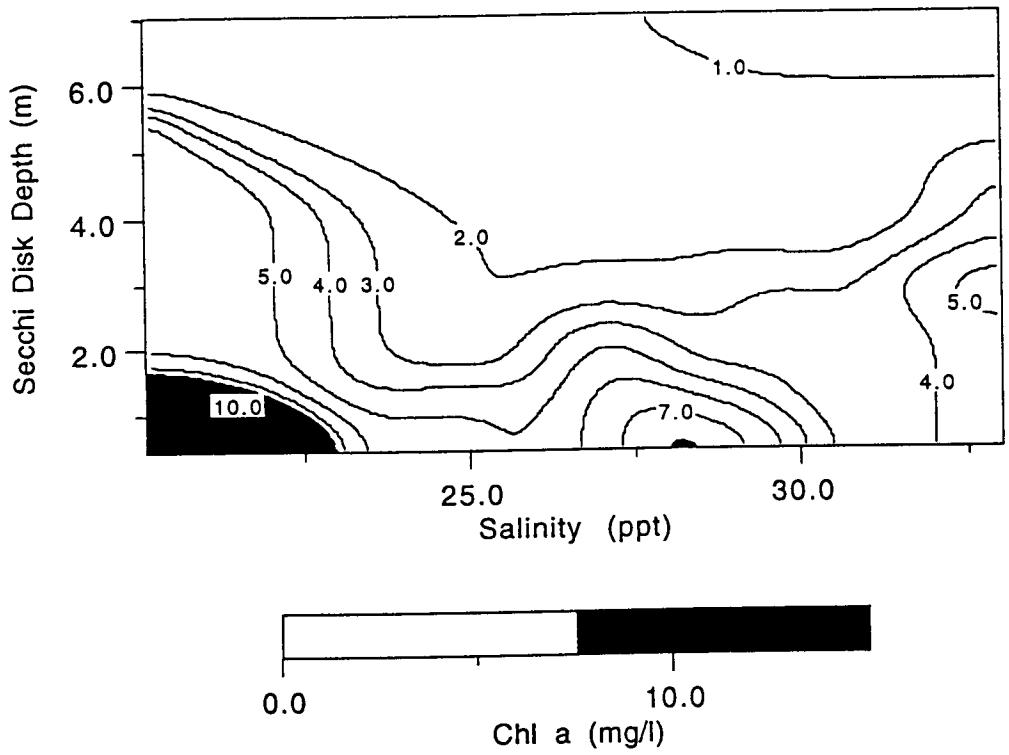

Figure 148. Contour plot of chlorophyll *a* versus the Secchi disk depth and salinity for surface samples taken in October 1992.

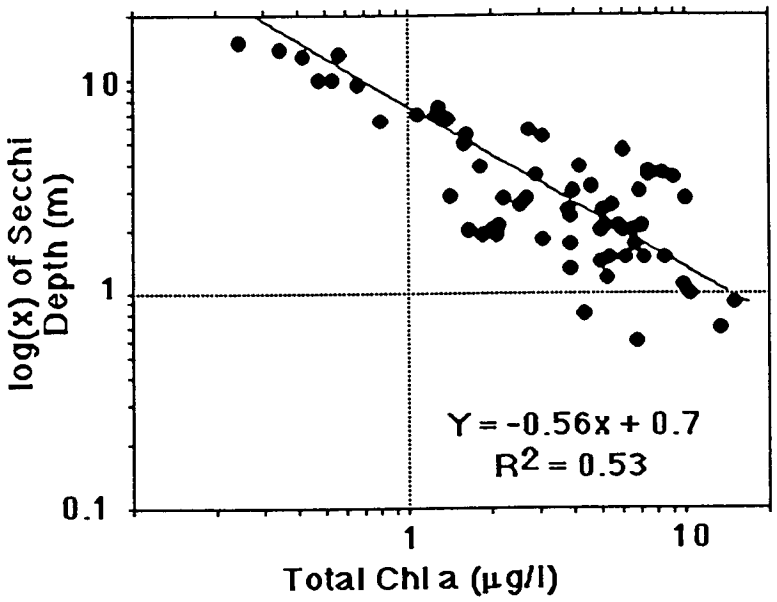

Figure 149. The relationship between the $\log_{10}$ transformed Secchi disk depth (m) and the total phytoplankton pigment concentration (µg/l) for the LATEX B sampling stations. Total depth at these stations is between 10 and 100 m and the salinity is > 20 psu.

pigment concentration (μg/L) for the LATEX B sampling stations. The total depth at these stations is between 10 and 100 m and the salinity is > 20 psu. The >20 psu salinity range was chosen because of the relatively low amounts of inorganic suspended matter present at higher salinities (<10 mg/l). The concentration of chlorophyll *a* present on this shelf obviously has a very significant impact on light absorbance.

A preliminary analysis of the average Secchi disk measurements on the Louisiana shelf west of the Mississippi River delta is shown in Figure 150. The data are restricted to samples between 20 and 25 psu and depths between 10 and 100 m. The slope of the regression line is significant at the 8% level of significance. The error bars are ± 1 Standard Error. The data are from cruises over most of the Louisiana shelf, rather than for fixed station locations over seasons and are therefore comparable and only from spring and summer. The decline in SDD is about 4% annually.

4. Discussion

Turbidity, quantified as light transmittance, attenuation, extinction coefficients, has both physical and biological components. Suspended sediments and phytoplankton pigments are the main contributors to the extinction coefficient (k) in coastal systems, although dissolved materials, such as humics, may be significant inhibitors to light transmitance at some wavelengths. Some geophysicists may view the biology as a regrettable complication to elegant mathematical modeling of the LCC, but the data analysis herein reveals that the light attenuation by phytoplankton may be significant, even within and near the Mississippi River delta and the LCC.

The light regime in the LATEX B study area shows substantial variability across the shelf in three directions, over days (not shown but documented elsewhere), weeks and seasonally. A decade-long change in the light regime is possible for two basic reasons. First, the suspended load of the Mississippi River has changed with land use, water control structures and water delivery patterns. Land use changes began in the 1800s with European settlement, and soon led to flood protection measures, including dam construction. Water diversions from the Mississippi River to the Atchafalaya River began in the 1920s. Thus the seasonal timing, the quantity and the allocation of water supplies, and therefore sediment supplies, changed in the last 200 years. These changes would have been limited to waters <20 psu because of the sedimentation of suspended inorganic materials. The second basic influence on decadenal light regime changes involve the nutrients necessary for phytoplankton growth, largely released as a consequence of more intensive fertilizer applications. The concentration of nitrogen in the Mississippi River doubled since the 1950s, whereas the concentration of silicate declined by 50%. These nutrient changes affected the quantities and qualities of phytoplankton in the LCC and therefore the pigments. It is noteworthy that the decline in SDD was about 3 to 4 % annually (Figure 149), which is about the same rate of increase in nitrate concentration in the Mississippi River (2.5% annually) during the same period (Turner and Rabalais, 1991). The argument has been made and substantiated that these nutrient concentration increases caused more diatom production. This argument is supported by the accumulations of biogenic silica, a residual diatom remnant found in sediments, that temporally track these riverine changes in nitrogen loading (Turner and Rabalais, 1994). Other analyses have shown that foraminiferal species assemblages have been altered in the same time period to favor hypoxia tolerant species and select against hypoxia-intolerant foraminiferans (Sen Gupta et al., 1996). The clear implication is that riverine nutrient loading controls the phytoplankton production in surface waters that eventually sinks to the bottom, is respired and removes oxygen at sufficient amounts to cause the extensive hypoxic zones covering the Louisiana shelf (recently summarized by

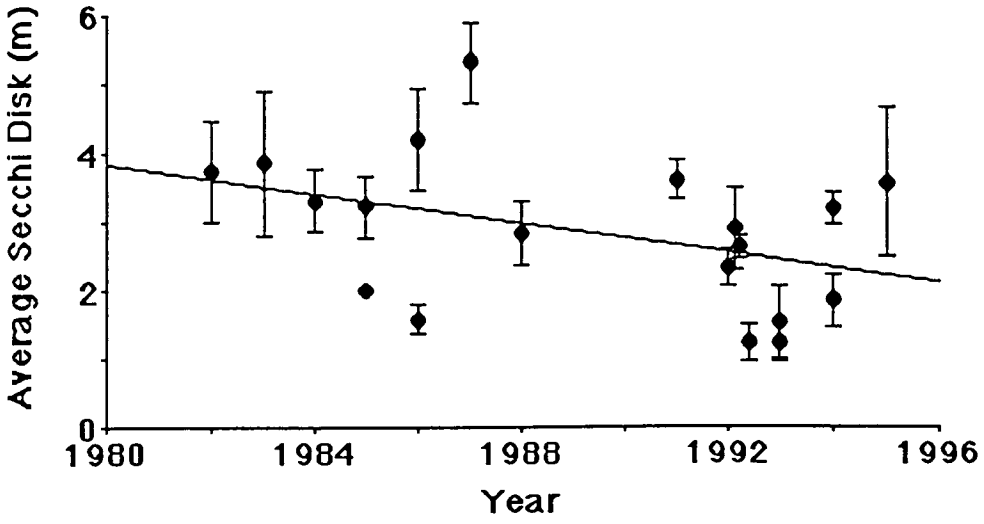

Figure 150. A preliminary analysis of the average Secchi disk measurements on the Louisiana shelf west of the Mississippi River delta. The data are restricted to samples between 20 and 25 psu and depths between 10 and 100 m. The slope of the regression line is significant at the 8% level of significance. The error bars are ± 1 Standard Error.

Rabalais et al., 1996a). The historical changes in SDD support those conclusions quite nicely.

B. Pigment and Nutrient Distributions

by Nancy N. Rabalais and R. Eugene Turner

1. Introduction

Turbidity, as shown on satellite imagery, reflects contributions of suspended sediments and phytoplankton biomass. Phytoplankton biomass is generally considered to be proportional to phytoplankton pigments, i.e., total chlorophyll *a*. As part of the physical and biological characterization of the coastal plumes of the Mississippi and Atchafalaya Rivers, the amount of chlorophyll *a* was used as a method of estimating phytoplankton biomass. A standard fluorometric method was used to determine the amount of chlorophyll *a* and phaeopigments (Parsons et al., 1984).

Fluorometric measurements do not provide the detailed pigment speciation available from high performance liquid chromatography. Nor is fluorometry an indicator of biomass of phycocyanin-, phycourobilin- or phycoerythrin-containing organisms, unless the cyanobacteria are so abundant as to account for most of the phytoplankton biomass. Most of the larger-sized phytoplankton, which often contribute proportionally more to phytoplankton biomass, do contain chlorophyll *a*. Dortch (see Section VII) reported that the biomass as carbon of the two major groups of phytoplankton in the northern Gulf of Mexico, diatoms and cyanobacteria, were positively correlated with chlorophyll *a* concentration when one or the other dominated the phytoplankton biomass. That is, for three cruises when diatoms dominated the biomass, there was a strong, positive relationship of diatom biomass with chlorophyll *a* and not with cyanobacteria; and when cyanobacteria dominated the phytoplankton biomass, as was the case in July 1993, their biomass was strongly and positively correlated with chlorophyll *a*, and diatom biomass was not. In addition, diatom abundance was positively correlated with chlorophyll *a* concentration, but cyanobacteria abundance was not Thus, chlorophyll *a* is a good indicator of phytoplankton biomass but not necessarily the relative abundance of specific groups.

The influence of the Mississippi and Atchafalaya outflows is evident in plots of surface salinity and Secchi disk values accumulated from numerous hydrographic cruises between 85° W (just east of Cape San Blas, Florida) to 95° W (just west of Galveston Bay, Texas) (Figure 1652 in Rabalais et al., 1996a, b). The influence of the freshwater input is more obvious west of the Mississippi delta (approximately 89° 30' W), with additional inputs near the Atchafalaya delta (approximately 91° 30' W). Plots of nutrient values show a more pronounced decrease in concentration over an equal distance from the deltas when compared to salinity. This indicates a nonconservative mixing caused by biological uptake. Examination of the nutrient concentrations in the biologically productive coastal plumes is relevant to issues of changing water quality in the riverine sources and ecosystem changes on the continental shelf. Shifts in nutrient concentrations and ratios in the riverine end-member have resulted in biological responses indicative of increased eutrophication and oxygen stress.

2. Objectives

As part of the biological characterization of the coastal plume, pigment and nutrient concentrations were determined to:

- define the longshore, seasonal, and interannual variability of the coastal plume;

• define the relationship of these variables with plume geometry and other physical variables;

• provide information to determine potential nutrient limitations on phytoplankton growth;

• provide information concerning the relationship of pigments with the light field, plume geometry, bottom water respiration rates, and the occurrence of hypoxia (see Section A above, Chapter IV, Chapter IX, and Chapter IX, respectively);

• provide ancillary data for phytoplankton and zooplankton characterizations (see Chapters VII and VIII, respectively).

The first two objectives will be addressed here.

3. Data Collection

The station locations sampled for phytoplankton pigments and nutrients are shown in Figure 151 and are approximately every other station of the CTD grid. Five cruises were conducted along the Louisiana/Texas continental shelf from 90° 31' W westward (April 1992 and 1993, July 1993 and 1994, October 1992), and one cruise (April 1994) was conducted in the plume of the Mississippi River. During the July cruises additional stations were occupied to the east of 90° 31' W to 90° W. The arrows in Figure 151 represent the approximate longitude of the Mississippi and Atchafalaya River deltas (large arrows) and estuarine entrances (small arrows). Only data from stations between 10 and 100 m are included in the longitudinal comparison analysis.

Water samples for chlorophyll *a* and phaeopigments, nutrients and salinity were collected from the surface by bucket, and from mid-water and near-bottom in 5-l Niskin bottles on a CTD /rosette system. Salinity determinations were made on an AutoSal. Water for chlorophyll *a* and phaeopigments (30-100 ml) was filtered on board ship through GF/F filters. The filters were fixed in 5 ml of DMSO/90% acetone (40/50) solution and allowed to extract for at least 1 hour in the dark. The extracts were measured pre- and post-acidification with 10% HCl on a Turner Model 10 fluorometer (Parsons et al., 1984). The fluorometer was calibrated for chlorophyll *a* against a chemical supply house chlorophyll *a* standard measured on a spectrophotometer. Water samples for nutrients, unfiltered, were frozen on board ship for later analysis in the laboratory. Nitrogen and phosphorus were analyzed according to methods in USEPA (1979) method 350.1 for ammonia-N, method 353.2 for nitrate/nitrite-N, and method 365.1 for phosphate-P. Silicate was analyzed according to method 186-72W/B (Technicon, 1977).

4. Results and Discussion

a. Pigment Distributions

The average conditions for the six LATEX B cruises are provided in Table 17. Distribution of surface water salinity and chlorophyll *a* and bottom water total pigments are provided in Figures 152 through 157. In general, the highest concentrations of phytoplankton pigments were found in surface waters near the Mississippi and Atchafalaya deltas and in the spring. Similar results were found for phytoplankton abundance (see Section VII). Comparisons of surface salinity and chlorophyll *a* plots showed peaks of chlorophyll displaced somewhat from lowest salinity water (where

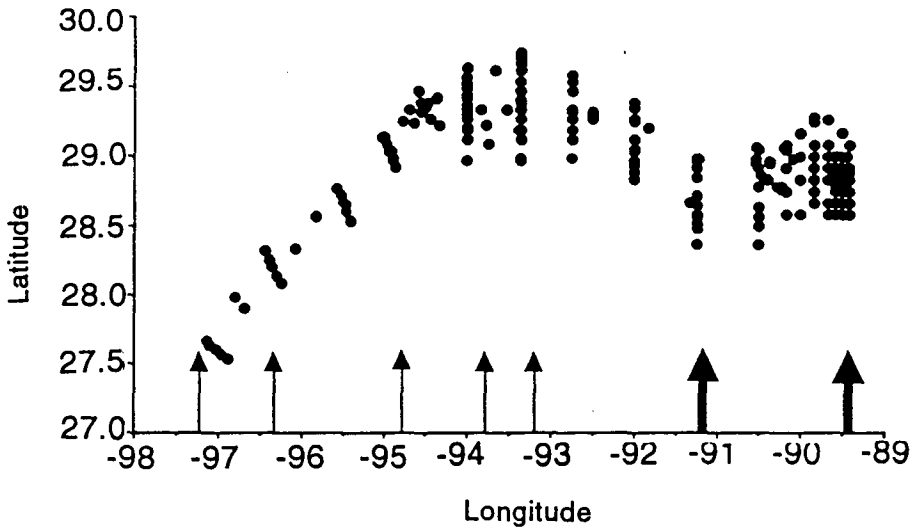

Figure 151. LATEX B stations sampled for nutrients and phytoplankton pigments. The arrows indicate the source and relative contribution of freshwater inputs.

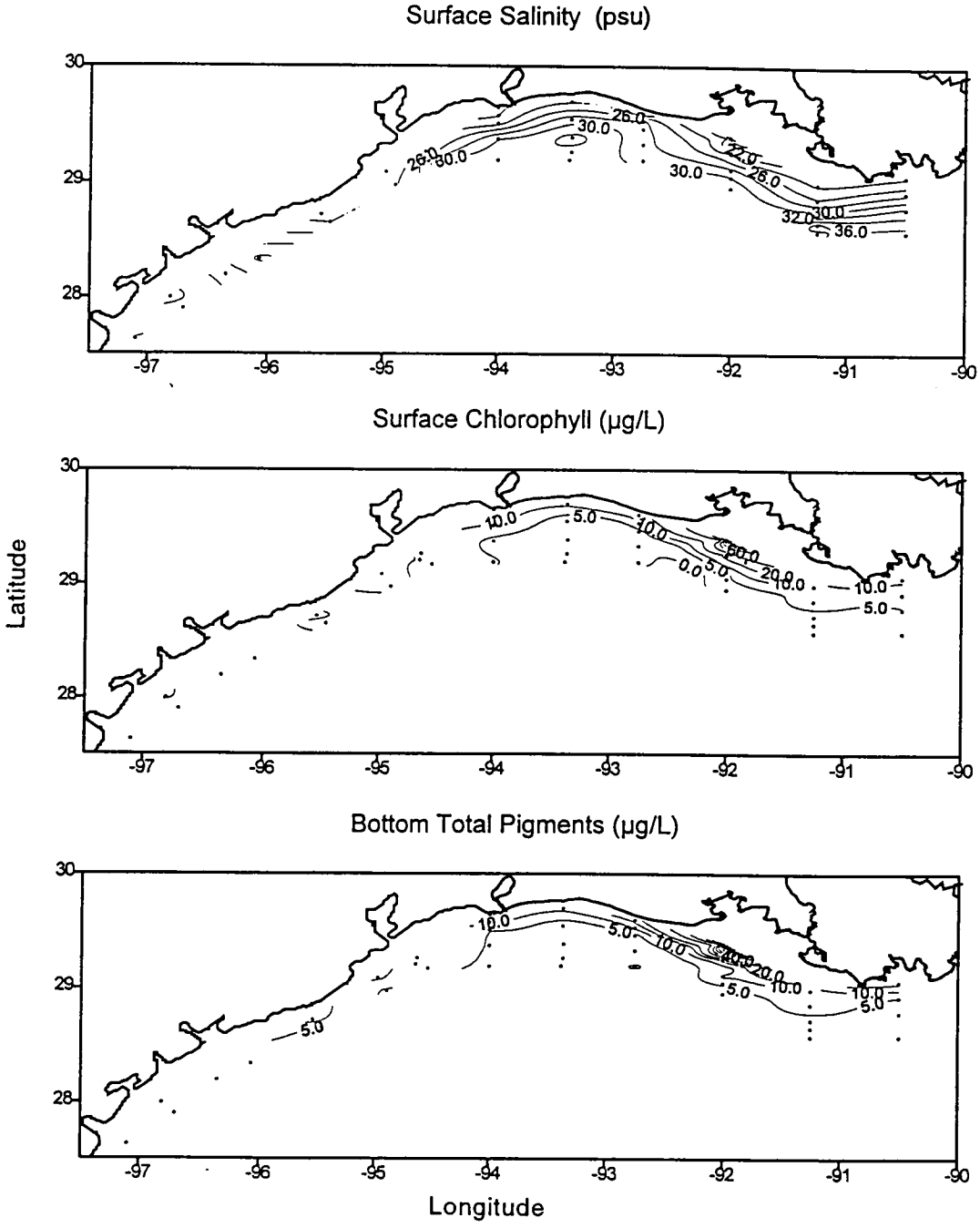

Figure 152. Contours of surface water salinity and chlorophyll *a* and bottom water total pigments for April 1992.

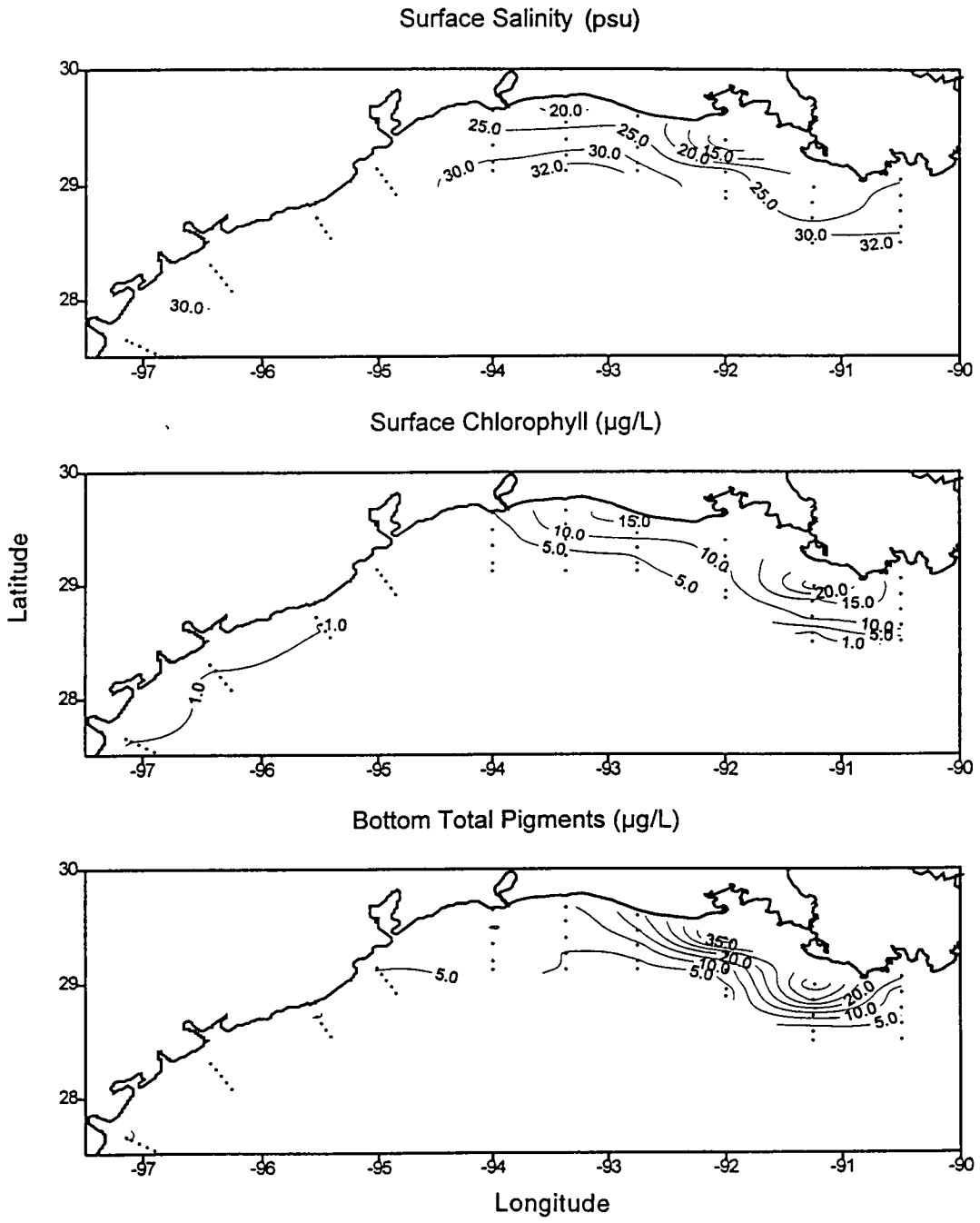

Figure 153. Contours of surface water salinity and chlorophyll *a* and bottom water total pigments, April 1993.

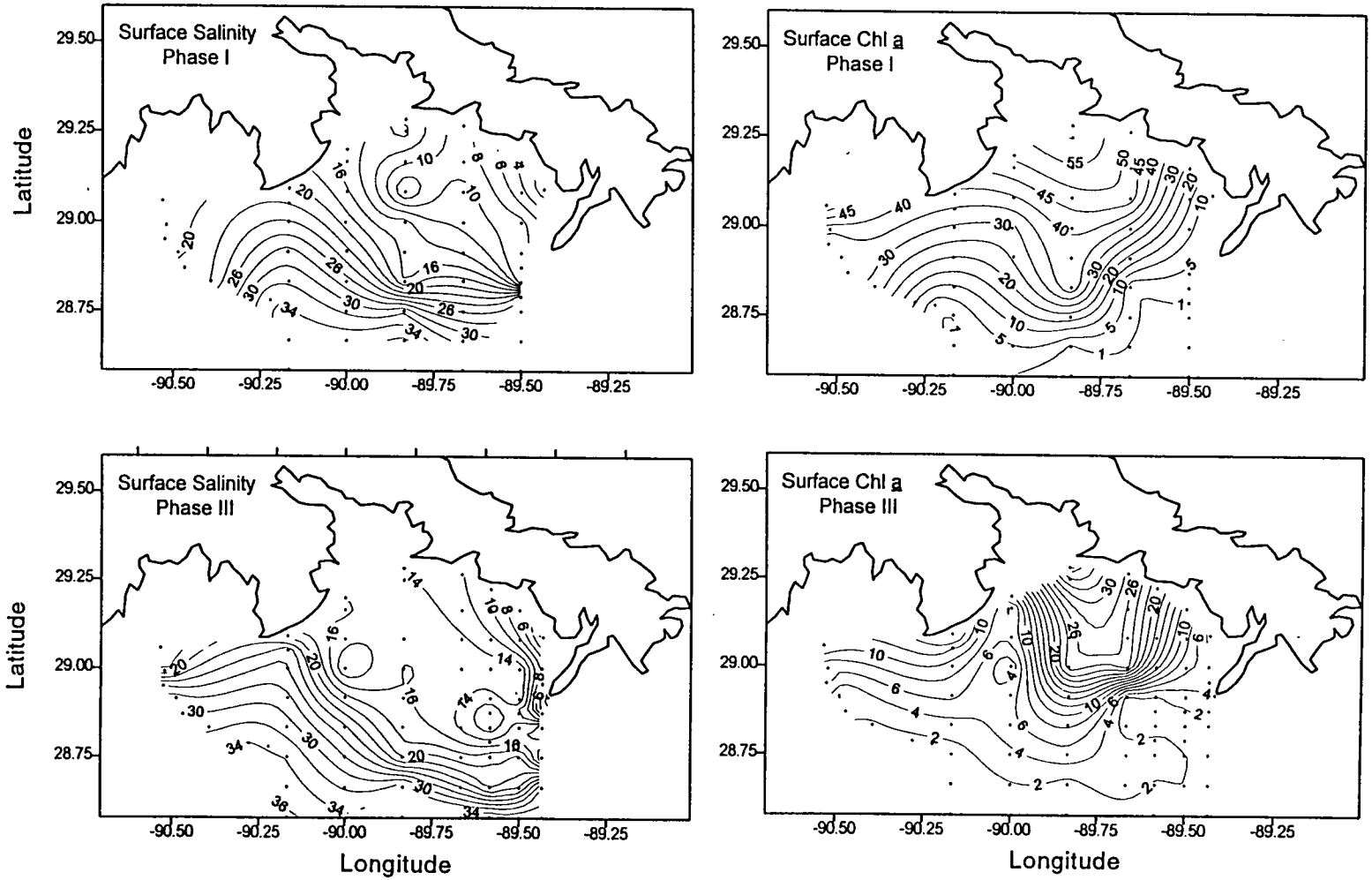

Figure 154. Contours of surface water salinity and chlorophyll *a* for Phases I and II of the Mississippi Delta near field plume observation, April 1993.

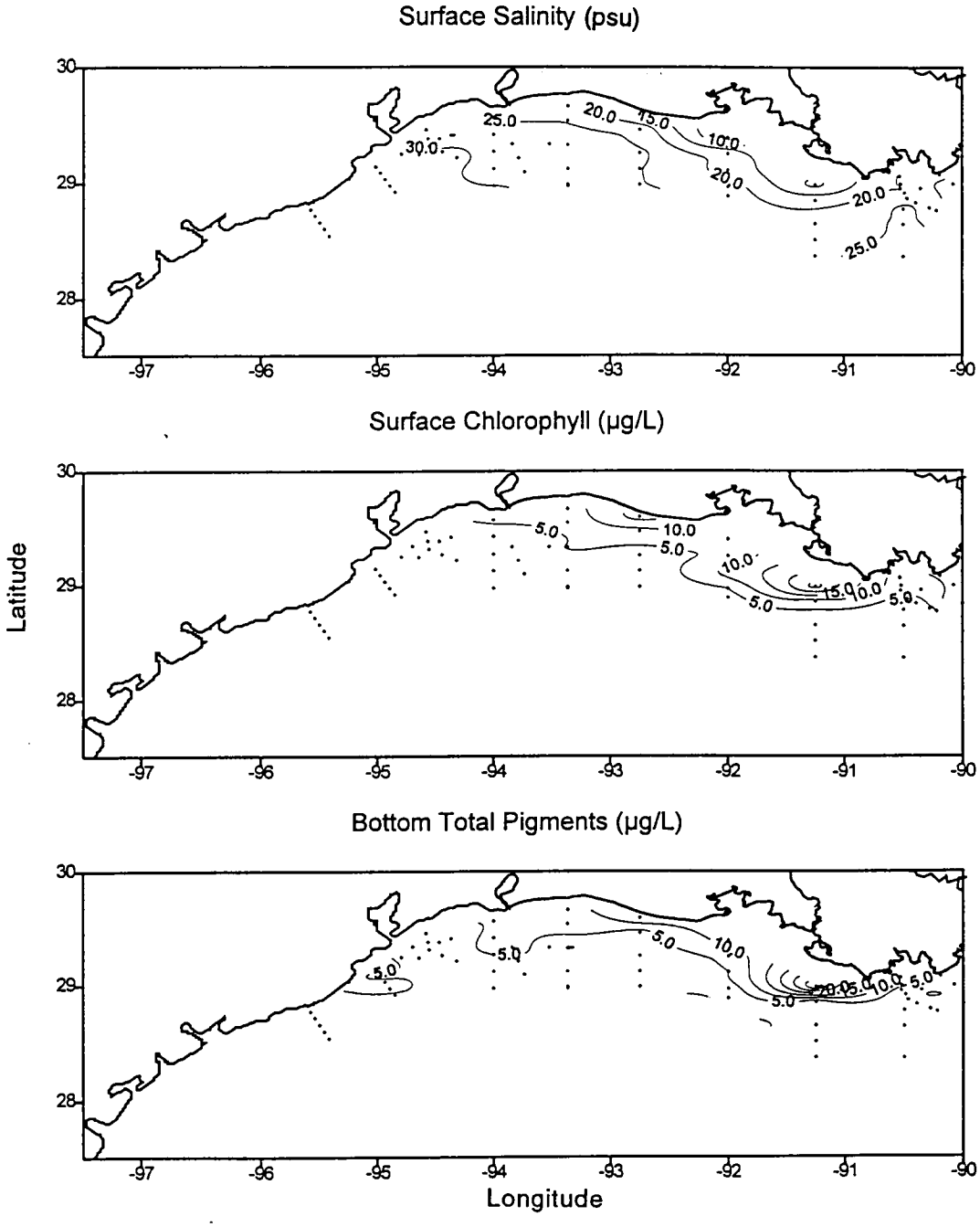

Figure 155. Contours of surface water salinity and chlorophyll *a* and bottom water total pigments for coastal plume observations, July 1993.

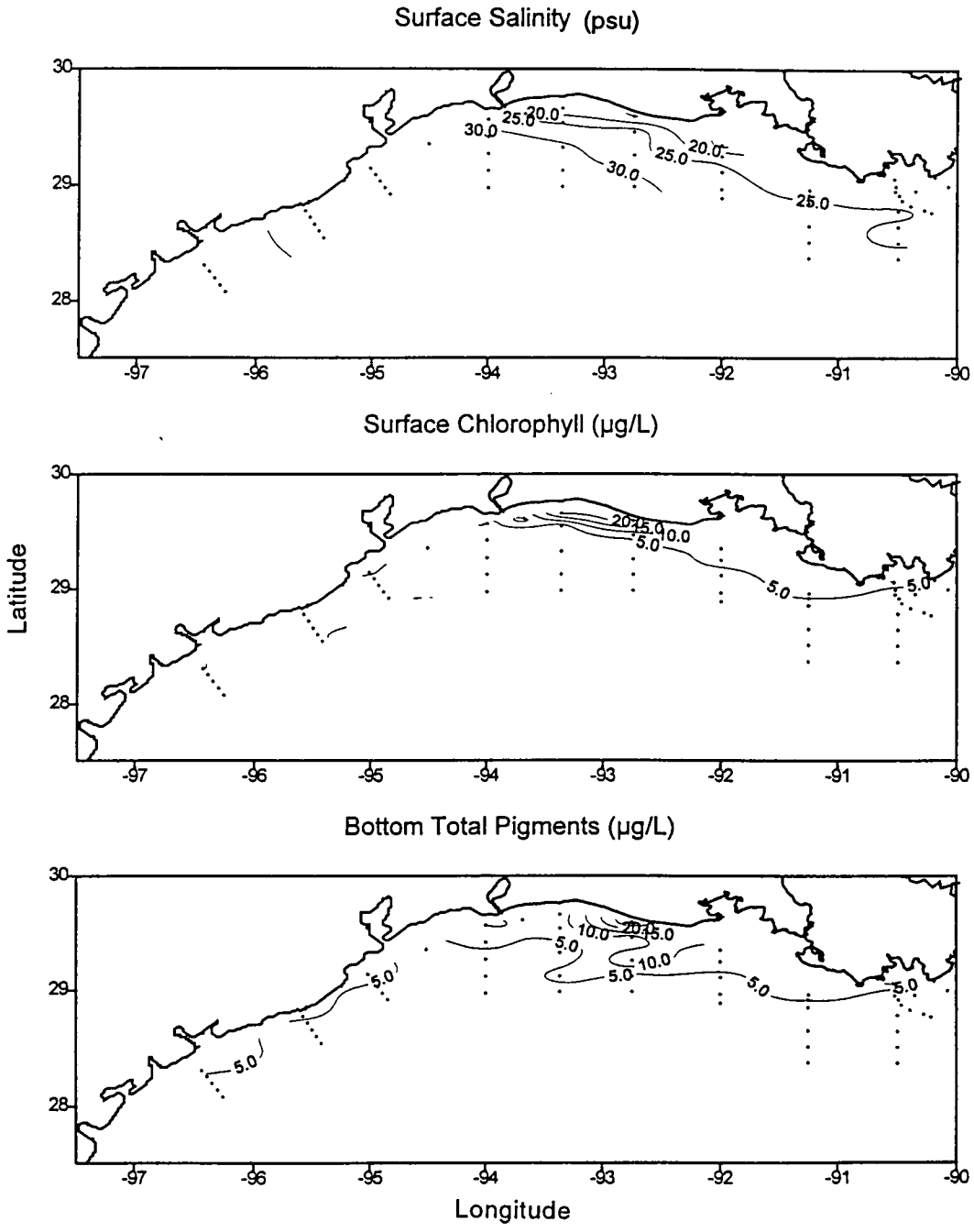

Figure 156. Contours of surface water salinity and chlorophyll *a* and bottom water total pigments for the coastal plume observations, July 1994.

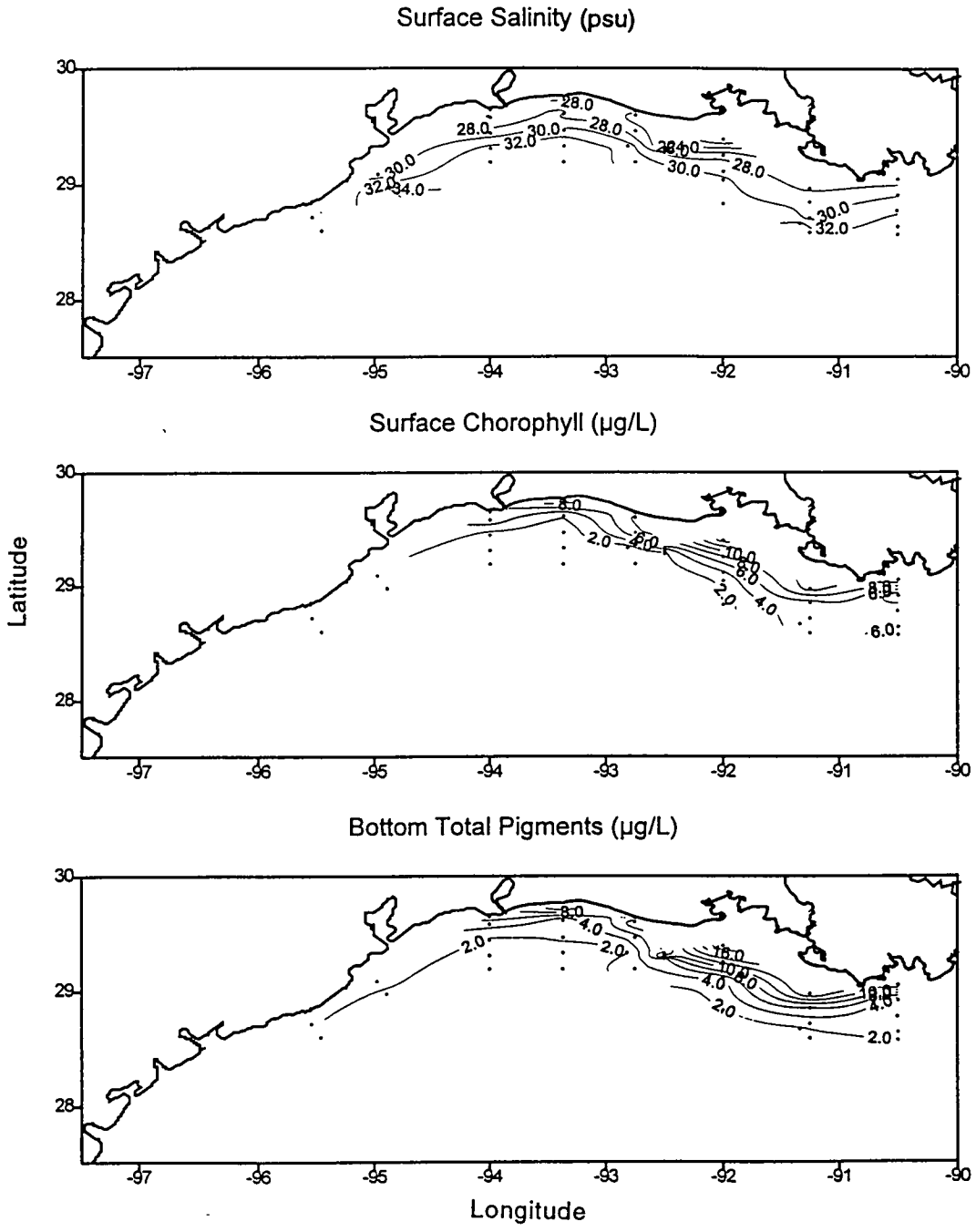

Figure 157. Contours of surface water salinity and chlorophyll *a* and bottom water total pigments for October 1992.

turbidity may be limiting phytoplankton growth), but in general the pigment contours were similar to the salinity contours.

Table 17. Average surface water values for chlorophyll *a*, salinity, Secchi depth, and selected nutrient parameters for six LATEX B cruises (X ± se, *n*).

Cruise	Date	Chl *a* (µg/L)	Salinity (psu)	Secchi (m)	Nitrate (µg at/L)	DIN (µg at/L)	Silicate (µg at/L)	Si:N ratio	Phosphate (µg at/L)
P921	Apr	9.09	27.67	1.69	6.18	8.68	3.08	0.33	0.33
	92*	±1.62	±0.79	±0.44	±1.14	±1.28	±0.40	±0.06	±0.07
		33	*28*	*11*	*33*	*33*	*33*	*33*	*33*
P922	Oct	4.32	29.30	2.28	1.08	2.91	6.89	3.98	0.40
	92	±0.55	±0.48	±0.30	±0.23	±0.42	±0.52	±0.43	±0.04
		42	*42*	*24*	*42*	*42*	*42*	*42*	*42*
P931	Apr	5.65	27.27	5.12	2.54	3.88	10.04	3.69	0.20
	93	±0.85	±0.70	±0.92	±1.09	±1.22	±2.15	±0.50	±0.02
		50	*49*	*20*	*48*	*48*	*48*	*48*	*48*
P932	Jul	4.21	25.68	4.96	3.17	5.68	14.14	3.63	0.32
	93	±0.58	±0.75	±0.69	±1.57	±1.62	±2.33	±0.47	±0.04
		66	*66*	*17*	*66*	*66*	*66*	*66*	*66*
P941	Apr	7.98	18.13	2.92	32.08	36.38	30.38	1.05	0.71
	94	±1.29	±1.21	±0.78	±2.83	±2.97	±2.36	±0.13	±0.06
		78	*78*	*26*	*78*	*78*	*78*	*78*	*78*
P942	Jul	3.12	27.67	4.16	1.29	4.88	12.58	2.61	0.62
	94	±0.59	±0.72	±0.90	±0.52	±0.85	±1.71	±0.30	±0.11
		61	*61*	*20*	*39*	*38*	*54*	*37*	*52*

* station with high value of 209 µg/L Chl *a* omitted.

Cruises in April 1993 and April 1994 represented typical high flow conditions (34,000 $m^3 s^{-1}$ and 26,000 $m^3 s^{-1}$, respectively) while low spring runoff characterized April 1992 (15,000 $m^3 s^{-1}$). Surface chlorophyll *a* values were much higher associated with the Atchafalaya River plume in April 1992 (Figure 152) than in April 1993 (Figure 153). Extremely high concentrations of chlorophyll *a* were obtained from surface waters at the second sampling of the nearshore station (P921039) on the S3 line (Atchafalaya Bay). Values exceeded 200 µg/L and were associated with a dinoflagellate bloom. When this station was sampled 1 day earlier (P921023), chlorophyll *a* concentrations were high (44 µg/L) but not extraordinarily so. For this report, discussions and figures of pigment concentrations mostly exclude P921039. In both years, there were strong cross-shelf gradients as far west as the Galveston estuary in 1992 and the Calcasieu estuary in 1993, and the surface chlorophyll *a* distributions mirrored the plume surface salinity signature but displaced somewhat to either the east or west. Additional peaks in surface water chlorophyll *a* in April 1992 in fresher waters off Galveston and Sabine were related to the flooding in east Texas following heavy spring rains.

Comparisons of surface chlorophyll *a* to satellite imagery of the turbidity plume were made by Walker for April 1992 (Figure 118b, Section IV). The surface chlorophyll *a* contours demonstrated the typical two-lobed morphology of the plume. There were high chlorophyll *a* concentrations nearshore despite extremely high turbidity values. Walker suggested that a shift to east southeasterly winds following a day of northwesterly winds may have pushed the surface chlorophyll peaks inshore. The values of surface chlorophyll *a* for the period immediately preceding the cruise, however, are not available.

The April 1993 turbidity plume (Figure 122b, Section IV) covered a small area despite the high Atchafalaya River flow. The maximum surface water chlorophyll *a* values were southeast of the Atchafalaya Bay entrance, which confirmed a previous southeastward discharge of river water onto the inner shelf. Maximum surface chlorophyll *a* values were not as high in April 1993 as in April 1992, although there was higher river discharge in 1993 (see above) and probably higher nutrient loading. Prior to the LATEX B April 1993 cruise, recent onshore winds confined the fresher waters closer to shore in high turbidity zones that would not be optimal to phytoplankton growth (light limitations).

Higher surface chlorophyll *a* concentrations were associated with lower salinity plume waters in the gyre circulation in the Louisiana bight in April 1994, but not the lower salinity nearshore waters between Southwest Pass and Barataria Bay (Figure 154).

Surface water pigment distributions in July 1993 (Figure 155) were very similar to those of April 1993 (Figure 153). Mississippi River discharge in July 1993 was also high for the summer period (17,000 $m^3 s^{-1}$). Again there were strong cross-shelf gradients from offshore of Terrebonne Bay to offshore of the Sabine estuary, and the geometry followed that of the surface salinity field but displaced to the east. During typical summertime low discharge (6,000 $m^3 s^{-1}$) in July 1994 (Figure 156), pigment concentrations were lower, and the highest values were restricted in nearshore samples between Atchafalaya Bay and the Calcasieu estuary.

In July 1993 and 1994 large-scale surface water circulation was primarily eastward. In July 1993, the discharge plume of the Atchafalaya extended eastward (Figure 128a, Section IV), although there was also an indication of a narrow coastal band of lower salinity water as far west as Sabine. The highest surface chlorophyll *a* concentrations were concentrated just offshore and eastward of the highest turbidity water (less light limitation and sufficient nitrate and silicate levels for phytoplankton growth). Satellite imagery from July 1994 was mostly cloudy.

Pigment levels were low in October 1992 during normal low fall river discharge (7,000 $m^3 s^{-1}$). The highest values were restricted to nearshore samples off Atchafalaya Bay. The suspended sediment plume of the Atchafalaya was rather disorganized, although high suspended sediment levels were found a great distance seaward of Atchafalaya Bay (Figure 124b, Section IV). Because the surface chlorophyll *a* levels were so low and the plume was so disorganized, there was not much correlation of the two. The higher chlorophyll *a* concentrations, however, appeared to be in an area of lower turbidity.

April 1992, July 1993, and October 1994 bottom total pigment contours were very similar to surface chlorophyll values. Differences between the concentrations of surface and near-bottom waters were minimal. Near-bottom total pigments for April 1993 were higher than surface chlorophyll *a* and composed primarily of phaeopigments, indicating flux of materials to the lower water column. Although July 1993 surface contours were similar to April 1993, bottom concentrations were not higher than the surface as in April, but more similar to the surface values. In fact, bottom water phaeopigment concentrations were surprisingly low, since they are often elevated during mid-summer, especially during hypoxic conditions as documented on this cruise. Bottom water total pigments in July 1994 were somewhat higher than surface chlorophyll *a* values, and hypoxia was documented in the study area.

Chlorophyll *a* concentrations in the plumes of the Mississippi and Atchafalaya Rivers typically peak at intermediate salinities (approximately 15-25 psu) where light conditions improve and sufficient nutrients remain to support phytoplankton productivity (Figure 158 for all LATEX B cruises combined). A similar pattern was seen for most of the individual LATEX B cruises (Figure 159), where an adequate salinity range was obtained. Surface salinities for most cruises, however, were typically higher than 20-25 psu (see also Table 17). There were also low chlorophyll *a* concentrations at the intermediate salinities. These chlorophyll/salinity patterns follow the same trend as diatom abundance (see Section VII).

b. Longitudinal Comparisons

The surface salinity for the LATEX B study area is shown in Figure 160. The effect of the Mississippi and Atchafalaya rivers is evident westward and downstream of the point of their effluents.

The concentration of dissolved nitrogen (DIN = NO3 + NO2 + NH4; µg/L) in surface waters is in Figure 161 and of phosphate and silicate in Figure 162. The highest nitrate and silicate concentrations are on the eastward boundary of the LATEX B study area where they are clustered relatively densely. The concentration of nitrate is consistently much higher than nitrite and ammonia. On the average, 95 and 87% of the surface and bottom DIN pool, respectively, occurs as nitrate (Figure 163).

The relationship between the concentration of phytoplankton pigments (phaeopigments, chlorophyll *a* and total; µg/L) and longitude in surface and bottom waters at the LATEX B sampling stations is shown in Figures 164 and 165, respectively. Phaeopigments are a rather minor component of the total pigment pool in surface waters (Figure 164). The general trend is for the higher pigment concentrations to be in the east and to decrease gradually westward. In contrast to the pattern in surface waters, the bottom water pigment concentrations (phaeopigments and chlorophyll *a*) are lowest in the eastern portion of the study area, rise in the middle section, and then decline heading westward. The bottom water pigments have a more equal concentration of phaeopigments and chlorophyll *a*.

A comparison of the pigment concentrations in surface and bottom waters at the same station are shown in Figure 166. There is a general tendency for similar values at the same location, with the greatest percent differences at the lowest concentrations. The surface waters have an average 18% more phaeopigments, 36% more chlorophyll *a*, and 20% more total pigments compared to bottom waters.

Figure 167 shows the relationship between the ratio of the concentration of the total phytoplankton pigments (µg/L) and longitude in surface and bottom waters in the LATEX B study area. There is relatively more chlorophyll *a* on the eastern end of the study region and less on the western region. This pattern is consistent with our knowledge of the sources and sinks in in situ organic production and the prevailing currents. Phytoplankton production is near riverine nutrient sources and drifts westward, while losing material from the surface waters to the bottom layers. The transit downward enriches the bottom waters in a westerly direction with degraded pigments. These phaeopigments accumulate downstream of the surface accumulations because the surface water flow westward is relatively greater than the flow in bottom waters. A peak in phaeopigment concentration therefore appears near 93° W.

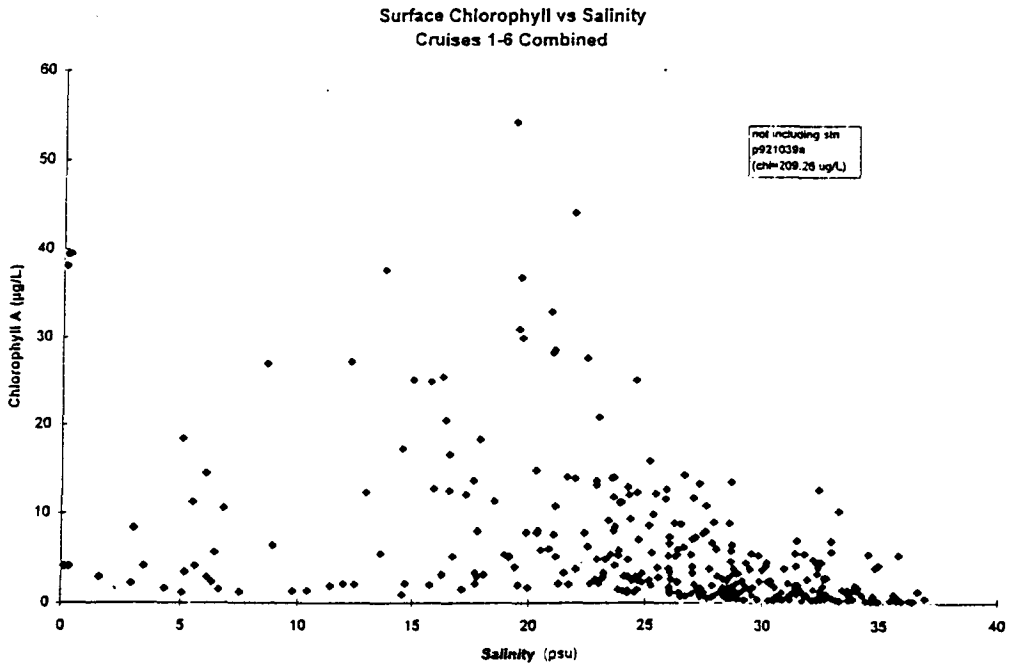

Figure 158. Relationship of surface chlorophyll *a* and salinity for all LATEX B cruises combined.

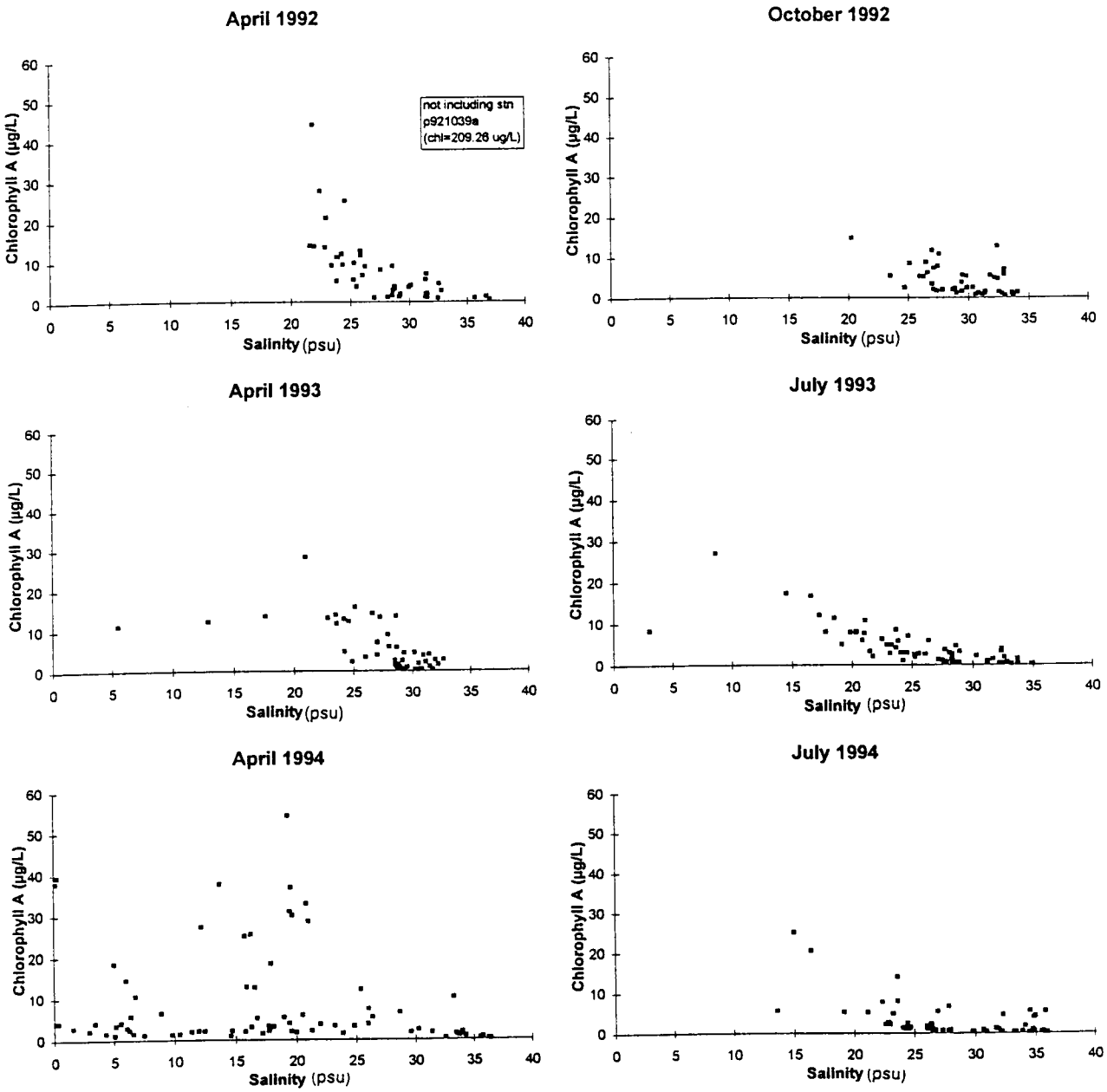

Figure 159. Relationship of surface chlorophyll a and salinity for each LATEX B cruise.

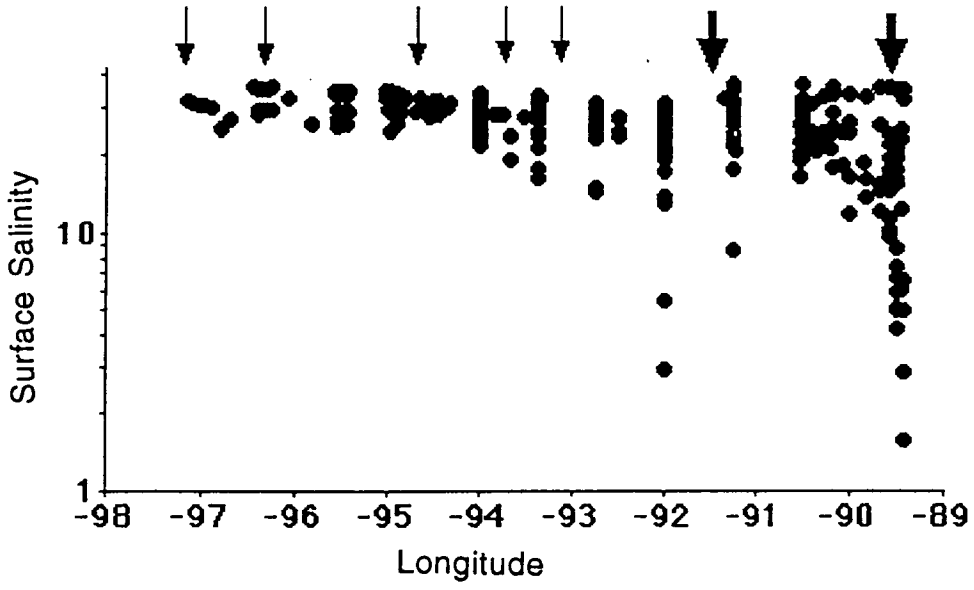

Figure 160. Surface salinity (psu) at the LATEX B sampling locations. The arrows indicate the source and relative contribution of freshwater inputs.

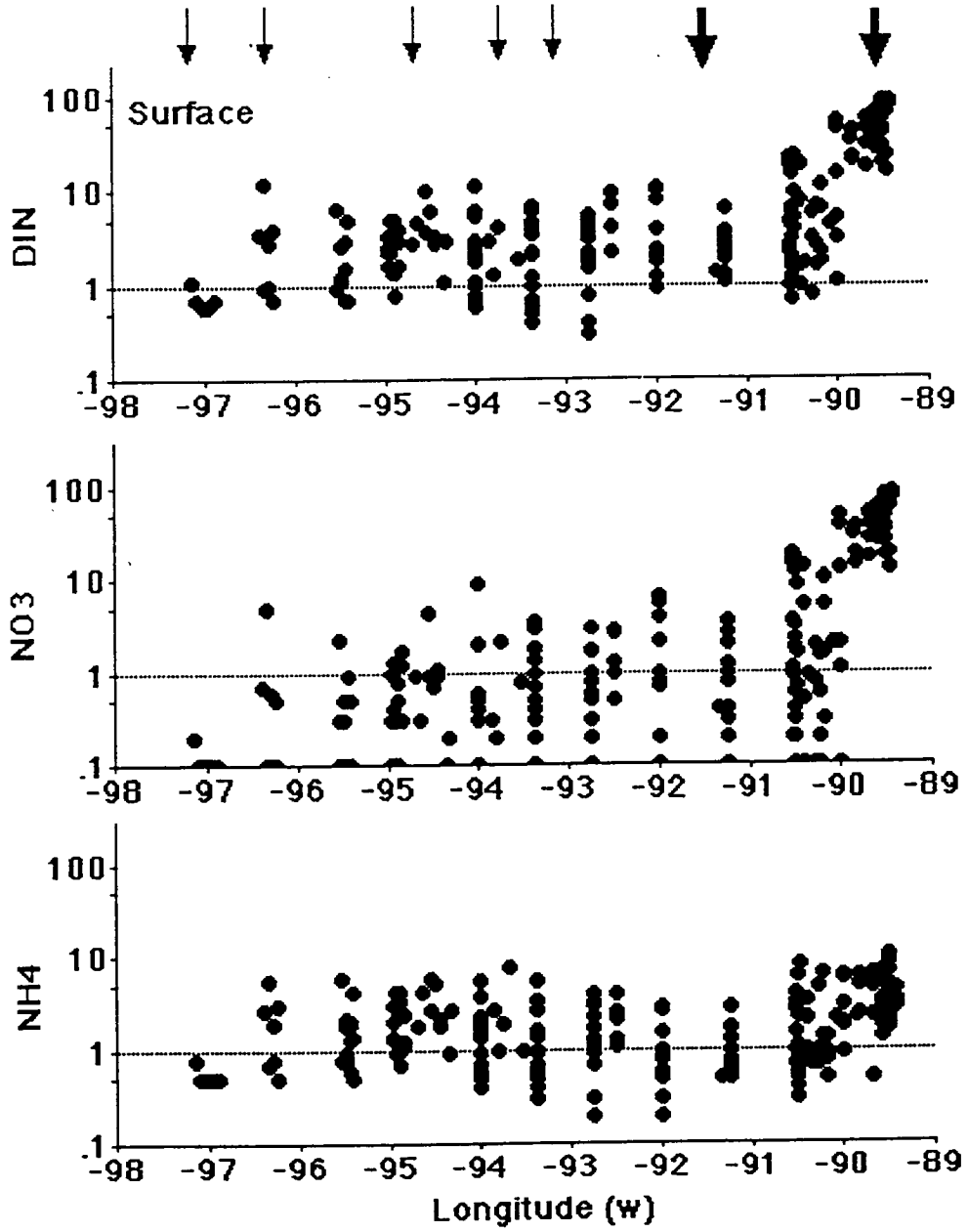

Figure 161. Concentration of dissolved nitrogen (DIN = NO_3 + NO_2 + NH_4; µg/L) in surface waters at the LATEX B sampling locations shown in Figure 151. Total depth at these stations is between 10 and 100 m. The arrows indicate the source and relative contribution of freshwater inputs.

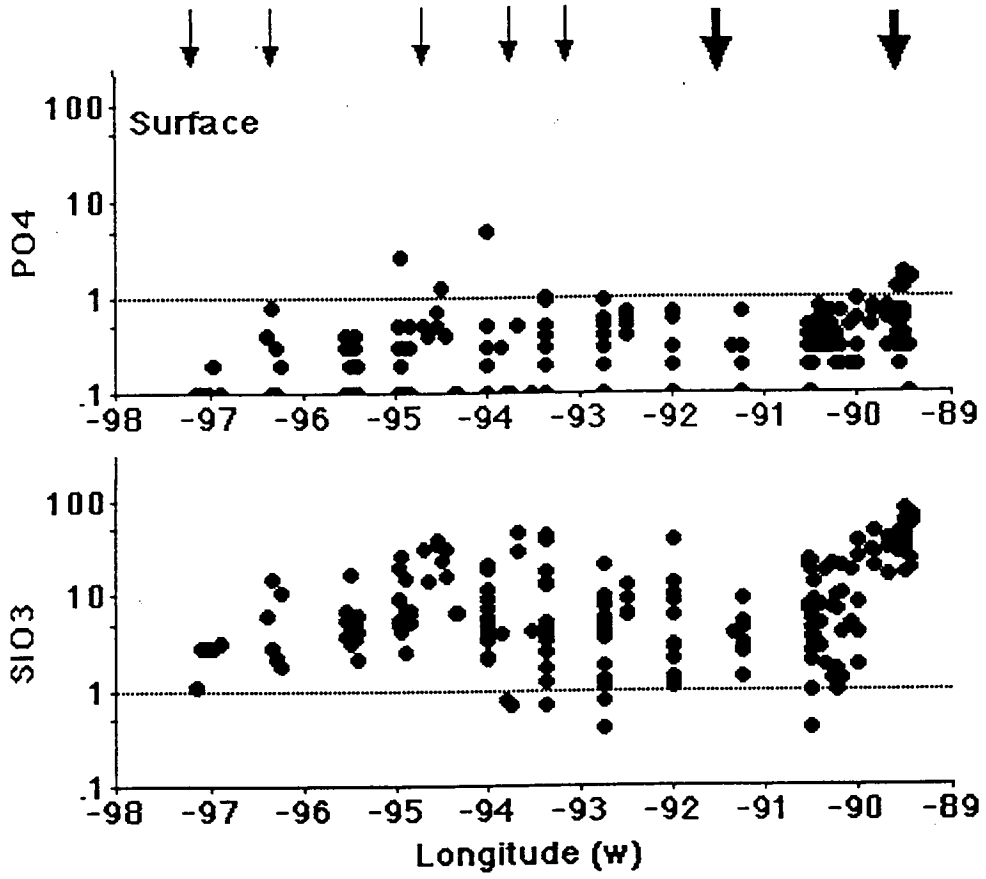

Figure 162. Concentration of dissolved phosphate and silicate ($\mu g\ l^{-1}$) in surface waters at the LATEX B sampling stations shown in Figure 151. Total depth at these stations is between 10 and 100 m. The arrows indicate the source and relative contribution of freshwater inputs.

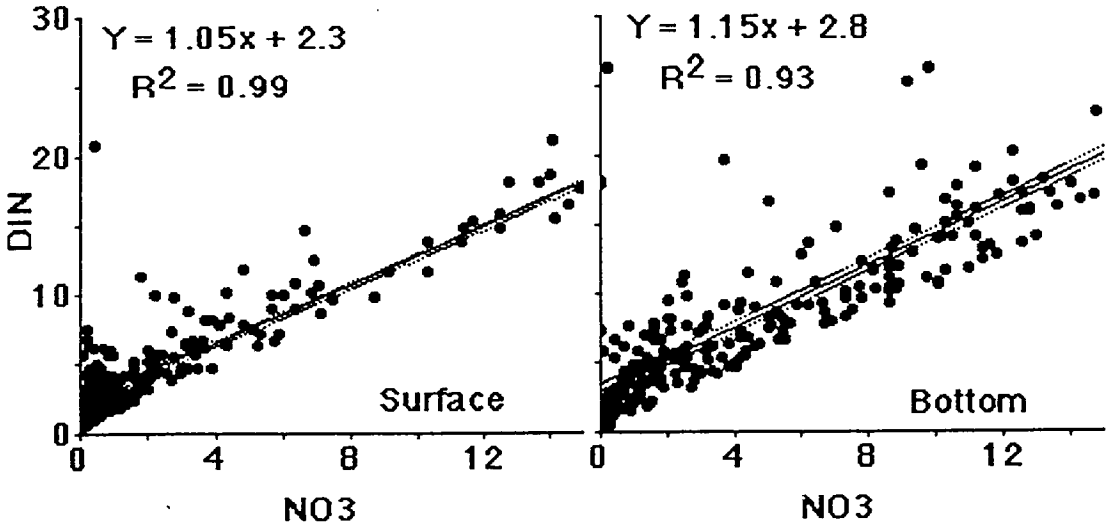

Figure 163. Relationship between the concentration of dissolved nitrogen (DIN = $NO_3 + NO_2 + NH_4$; $\mu g\ l^{-1}$) and nitrate in surface waters at the LATEX B sampling locations shown in Figure 151. Total depth at these stations is between 10 and 100 m.

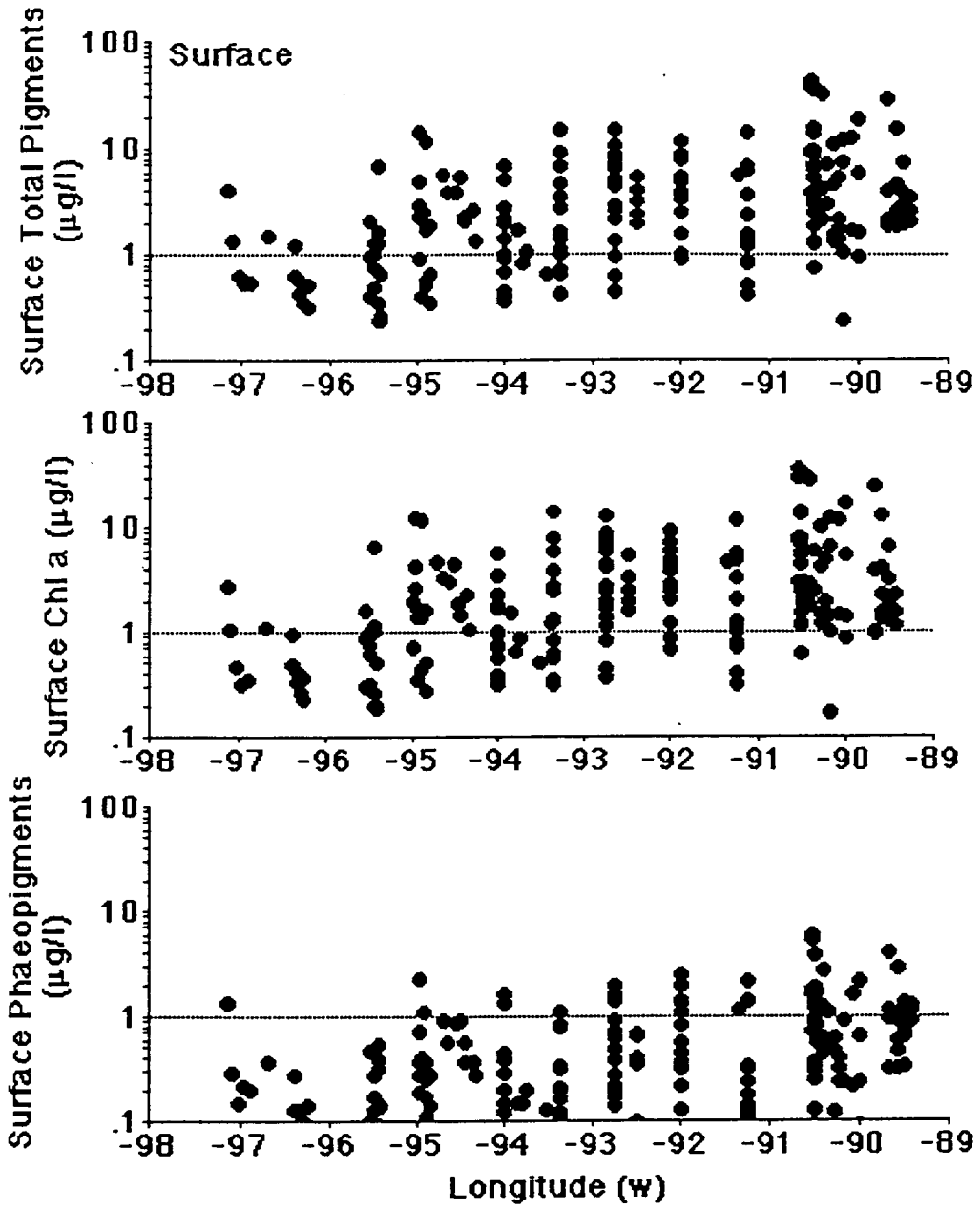

Figure 164. Relationship between the concentration of phytoplankton pigments (total, chlorophyll *a* and phaeopigments; µg l^{-1}) and longitude in surface waters at the LATEX B sampling locations shown in Figure 151. Total depth at these stations is between 10 and 100 m.

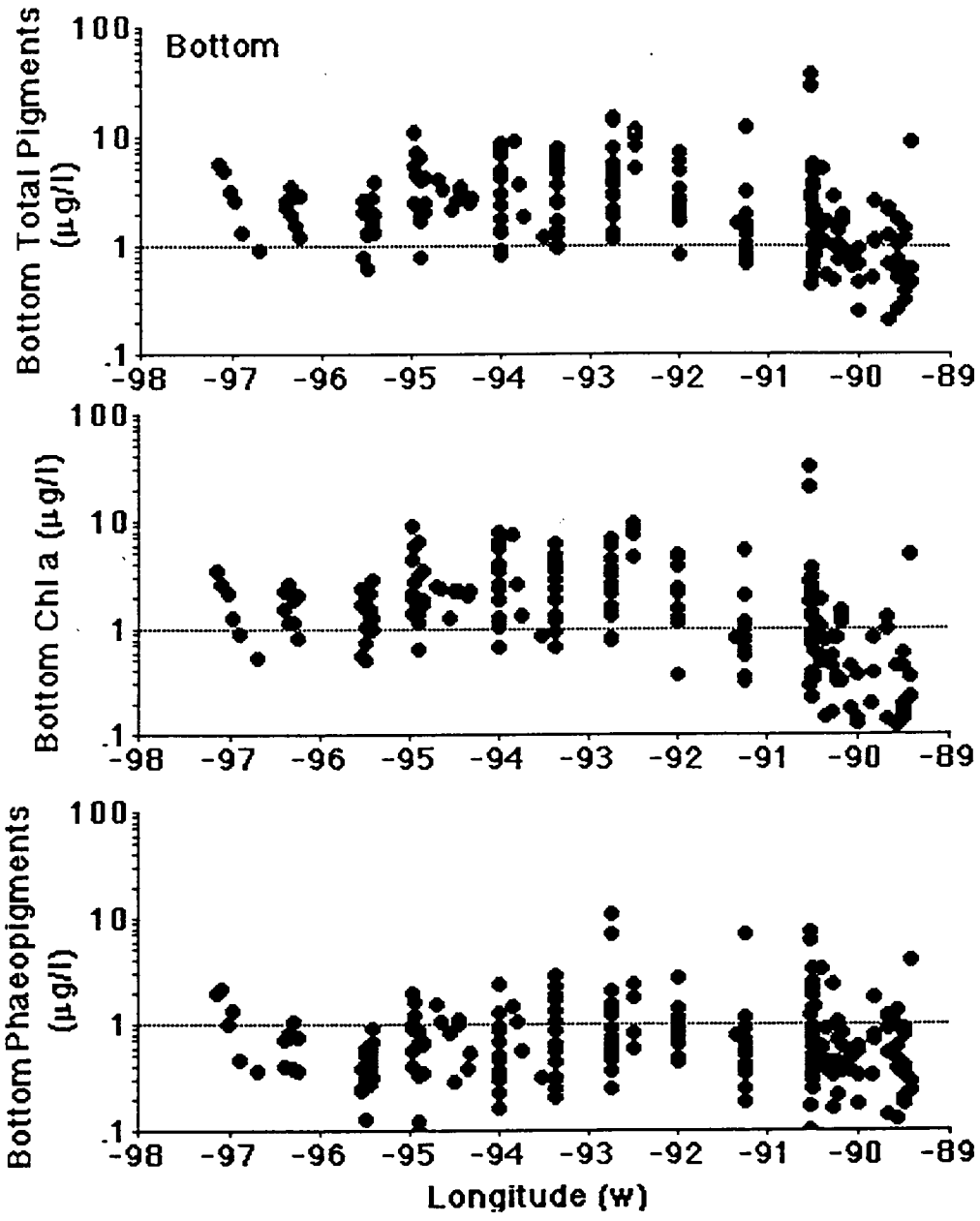

Figure 165. Relationship between the concentration of phytoplankton pigments (total, chlorophyll *a* and phaeopigments; µg l^{-1}) and longitude in bottom waters at the LATEX B sampling locations shown in Figure 151. Total depth at these stations is between 10 and 100 m.

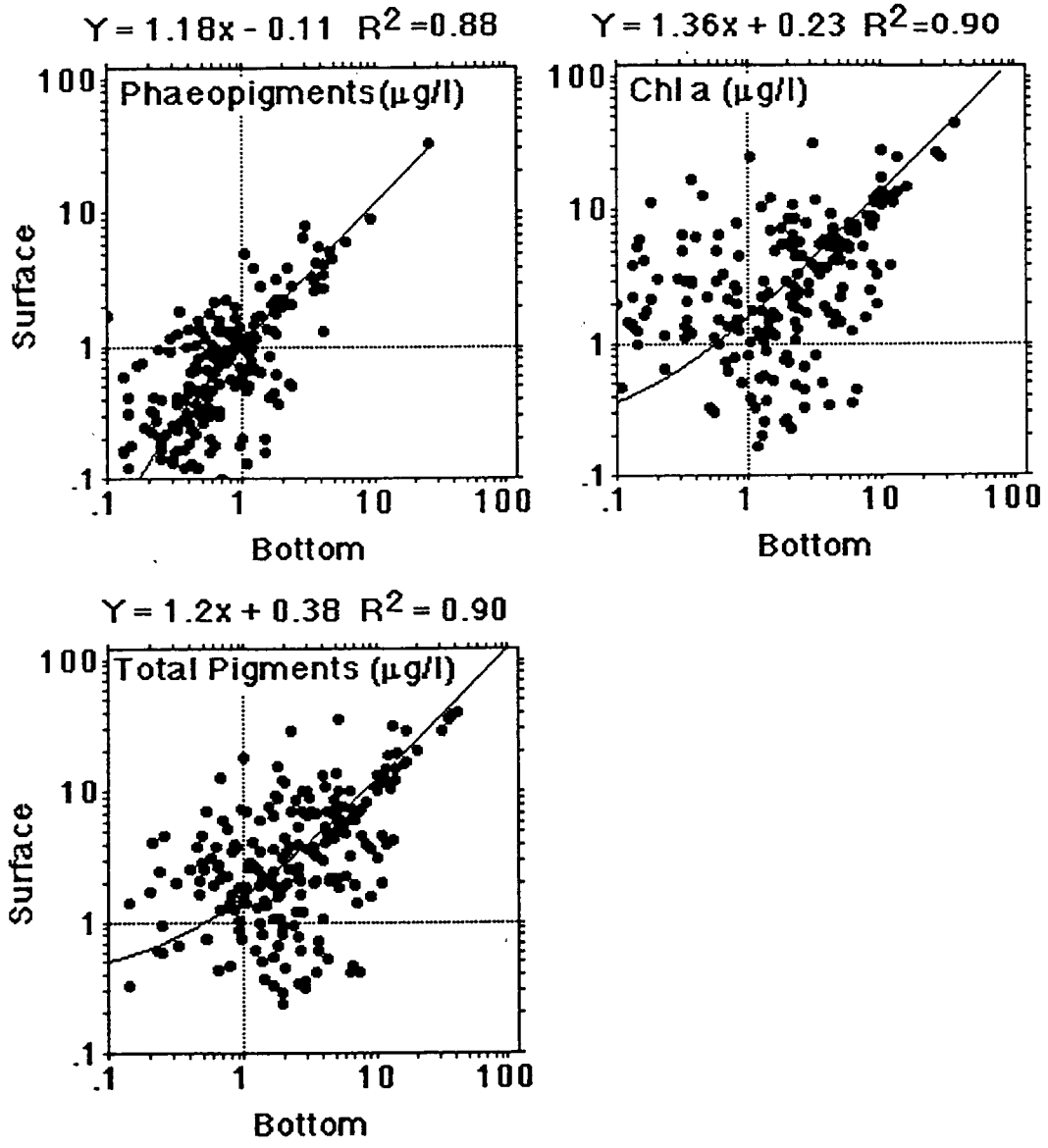

Figure 166. Relationship between the concentration of phytoplankton pigments (phaeopigments, chlorophyll *a* and total; µg l^{-1}) in bottom and surface waters at the LATEX B sampling locations shown in Figure 151. Total depth at these stations is between 10 and 100 m.

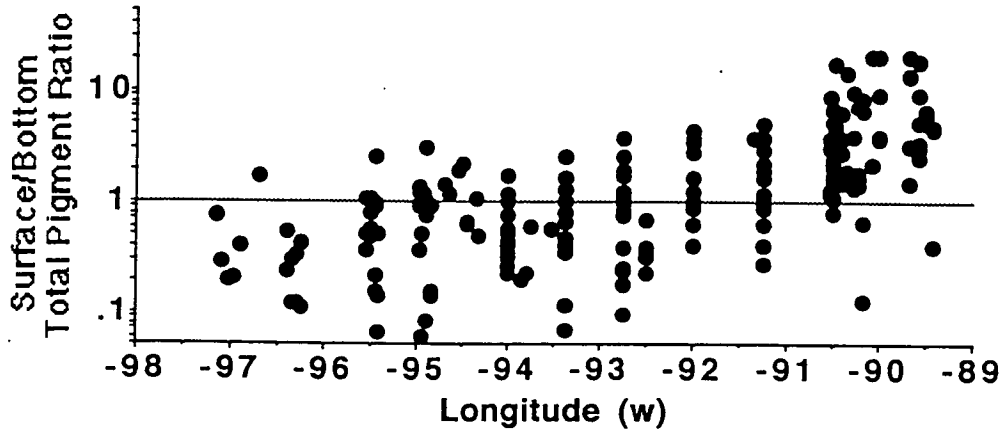

Figure 167. Relationship between the ratio of the concentration of total phytoplankton pigments ($\mu g\ l^{-1}$) and longitude in surface and bottom waters at the LATEX B sampling locations shown in Figure 151. Total depth at these stations is between 10 and 100 m.

The surface-to-bottom relationships in pigments indicate that what is being generated in the surface waters is getting to the bottom with a spatial and temporal lag. Respiration rates are higher in shallower waters and related to chlorophyll *a* concentration (see Chapter IX). Therefore, there is a consistent transition away from the river discharges along the coastal plume of higher to lower nutrients, chlorophyll *a* concentrations, flux of organic material, respiration rates, and incidence of bottom water hypoxia.

3. Summary and Conclusions

1. The highest concentrations of surface water chlorophyll *a* were found in surface waters near the Mississippi and Atchafalaya deltas and in the spring. Chlorophyll levels in April 1993 were lower than in April 1992, although spring river discharge was much higher in 1993 than in 1992. July 1993 surface chlorophyll levels were similar to April 1993; this is consistent with higher than average summertime river discharge in July 1993.

2. There were usually strong cross-shelf gradients in surface and bottom water pigment concentrations, that extended as far westward as the Calcasieu and Sabine estuaries. Higher surface pigment concentrations near the outflows of the Sabine, Galveston or Matagorda estuaries were related to localized freshwater runoff. Elevated values in the western end of the LATEX B study area in April 1992 were related to runoff following heavy spring rainfall in east Texas.

3. Surface chlorophyll *a* concentrations paralleled suspended sediment plume geometry in April 1992. Peaks in surface water chlorophyll *a* in April 1993 and July 1993 were displaced from the highest suspended sediment concentrations, in areas of better light conditions for phytoplankton growth. Correlations between surface chlorophyll *a* concentrations and plume geometry for October 1992 were not feasible, but the highest chlorophyll levels were in an area of less turbidity.

4. Surface chlorophyll *a* concentrations peaked at intermediate salinities where light conditions improved because of decreased suspended sediment concentrations and where nutrient concentrations were sufficient for phytoplankton growth.

5. The highest nitrate and silicate concentrations in surface waters were on the eastward boundary of the LATEX B study area. Most of the dissolved inorganic nitrogen pool was composed of nitrate.

6. There was a general tendency for surface waters and bottom waters at the same location to have similar pigment concentrations with the surface waters being approximately 20% higher. Higher values in bottom waters were often related to higher phaeopigment concentrations, i.e., fluxed surface organic material.

7. There is a consistent westward and downstream transition away from the discharges of the Mississippi and Atchafalaya Rivers along the coastal plume in lower to higher salinities, higher to lower nutrients, and higher to lower surface chlorophyll concentrations. These gradients are further reflected in the flux of organic material as seen in surface-to-bottom pigment ratios and accumulation of phaeopigments in the lower water column. The gradient is further exemplified by bottom water respiration rates and incidence of bottom water hypoxia.

C. Potential Nutrient Limitations on Phytoplankton Growth Within and Near the Louisiana Coastal Current

by R. Eugene Turner

1. Introduction

Water quality problems in continental shelves are widespread (Rosenberg, 1985; Wulff and Rahm, 1988) and often related to eutrophication from the freshwater sources. The nutrients causing these problems are not the same everywhere, nor always constant. When one nutrient is limiting, then increased phytoplankton production is the likely result. Nitrogen is thought to be limiting for many oceanic and coastal food webs (Harris, 1986; Valiela, 1984). Many coastal systems are not nitrogen limited, however. Phytoplankton in the Huanghe delta region (China), for example, are phosphorus limited (Turner et al., 1990). Coastal diatom communities are certainly influenced by silicon supplies and the Si:N atomic ratio of 1:1 is the average for diatoms (i.e., the Redfield ratio; Redfield, 1958). Diatom abundance will decline with a decrease in silicate availability, if all other factors remain constant. The result of a combination of decreased siliate loading and increased nitrogen and phosphorus loading is that phytoflagellates have a growth advantage over diatoms (Officer and Ryther, 1980)

Examination of the atomic ratios and concentrations of essential dissolved nutrients (silicate, dissolved inorganic nitrogen and phosphate) is useful to understand how phytoplankton growth is limited within the LCC. In situations where the nutrient ratios are in balance, or when no one nutrient is limiting to plant growth, the N:Si:P atomic ratio is around 16:16:1. Significant deviations from the "optimal growth ratios" reveal how ecosystem processes are different. We examined these nutrients to determine the spatial and temporal variability in the likely nutrients that limit phytoplankton growth.

2. Methods

The cruise tracks, general instrumentation, logistics and hydrographic data are contained in other portions of this report. The nutrient ratios that were considered limiting are summarized in Table 18, and are gleaned from the literature (e.g., Nelson and Dortch, 1996; Harris, 1986; Justic et al., 1995 a, b; and Valiela, 1984) for this region and elsewhere.

Table 18. Summary of characteristics that limit nutrients (Nelson and Dortch, 1996; Harris, 1986; Justic et al., 1995 a, b; and Valiela, 1984).

Nutrient	is limiting when:
N	where DIN is the sum of the dissolved inorganic nitrogen pools (nitrate+nitrite+ammonia) concentration (µg/L); and the concentration of DIN < 10 µg/L; DIN:DIP < 7; DIN:Si>1
P	where DIP is the dissolved inorganic phosphate concentration (µg/L); and the concentration of DIP < 0.2 µg/lL DIN/DIP > 30;
Si	where Si is the dissolved silicate concentration (µg/L); and the concentration of Si ≤ 1 µg/L; Si:DIN < 1

3. Results and Discussion

Figure 168 shows the relationship between the ratio of the concentration of DIN:DIP and DIN:Si (μg/L) and longitude in surface waters at the LATEX B sampling stations. The total depth at these stations is between 10 and 100 m. The DIN:DIP atomic ratio varied from 2 to 100 and DIN:Si atomic ratio from 0.2 to over 20 in surface waters between the 89° and 98° W on the continental shelf. The nutrient concentrations for DIN, DIP and Si ranged from 0 to 100, 1.8 and 120 μg/L respectively, for all data. Both the DIN:DIP atomic ratio and the DIN:Si atomic ratios were clustered more tightly together near the eastern end of the study area compared to the rest of the study area. The DIN:DIP atomic ratio was much above 16:1 in the same area, but then declined to around 10 within 1.5° Long. The Si:DIP atomic ratio was clustered around the 1:1 atomic ratio near the Mississippi River delta, but then spread mostly above a 1:1 ratio away from the region of the rivermouth.

The relationship between the atomic ratio of the concentration of DIN:DIP (μg/L) for each cruise at the LATEX B sampling stations is in Figure 169. There was considerable variation in the cluster of points. Cruise V covered stations near the Mississippi River almost exclusively and these values are much higher, on the average, than data from the other five cruises. Data from Cruise I were mostly at or above the 16:1::N:P atomic ratio (shown with a dotted line). Data from cruises II, IV and VI were mostly located near or below the same line.

Figure 170 shows the relationship between the atomic ratio of the concentration of DIN:DIP for the different longitudinal ranges of LATEX B sampling stations. The DIN:P ratio is seen to decrease from above the Redfield ratio to below it going across the shelf from east to west. The average concentration decreases in the same direction.

Figure 171 shows the relationship between the atomic ratio of the concentration of DIN:Si for the different longitudinal ranges of LATEX B sampling stations. The DIN:Si ratio is seen to decrease from near the Redfield ratio to a lower value going across the shelf from east to west. The average concentration decreases in the same direction.

There were 281 stations with data for all nutrients on their concentration and nutrient ratios. Figure 172 illustrates the geographical location of the inferred nutrient limitation (N, P or Si) at the LATEX B sampling stations. At the time of sampling these stations, 64 (69%) appeared to be N-limited stations, and these were scattered across the coast from east to west and offshore to inshore. Only 19 (7%) appeared to have a potential for P-limitation. These stations were more narrowly positioned seaward across the shelf, but also spread longitudinally like the N-limited stations. Only 5 (1.8%) stations appeared to be Si-limited stations. There was an apparent balance of potentially limiting nutrients at the remaining 193 stations.

The analysis of nutrient ratios provides a mechanism to quickly survey potential nutrients limiting phytoplankton growth. The results support the hypothesis that this shelf is primarily N-limited when phytoplankton growth potential is limited by a single nutrient. The three nutrients are, however, more often closer, than further, from a situation when one nutrient is not limiting. The nutrients appear to be close enough to the Redfield ratio and in high enough concentration at most of these stations so that no one nutrient dominates phytoplankton growth at the majority of stations. This is consistent with the arguments of Justic et al. (1995 a, b) who argued that the nutrients in the Mississippi River had moved closer to the Redfield ratio this century. The consequence of this development is that the environment for phytoplankton growth on the continental shelf changed from an N-limited to a nutrient-balanced situation. These changes

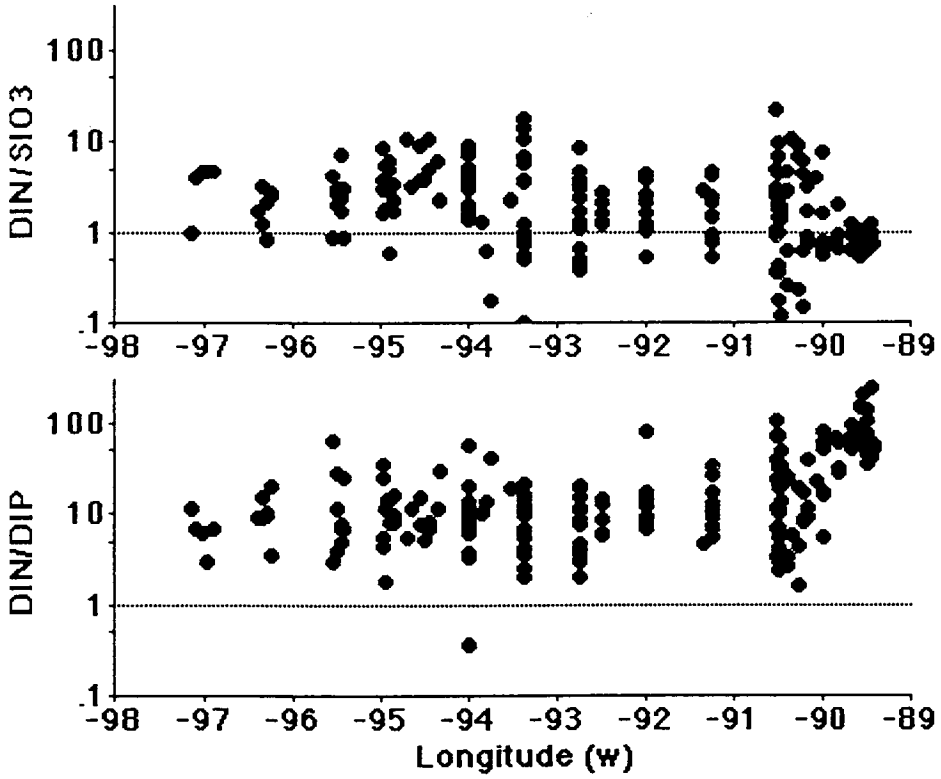

Figure 168. The relationship between the ratio of the concentration of DIN:DIP and DIN:Si (µg/l) and longitude in surface waters at the LATEX B sampling stations. The total depth at these stations is between 10 and 100 m.

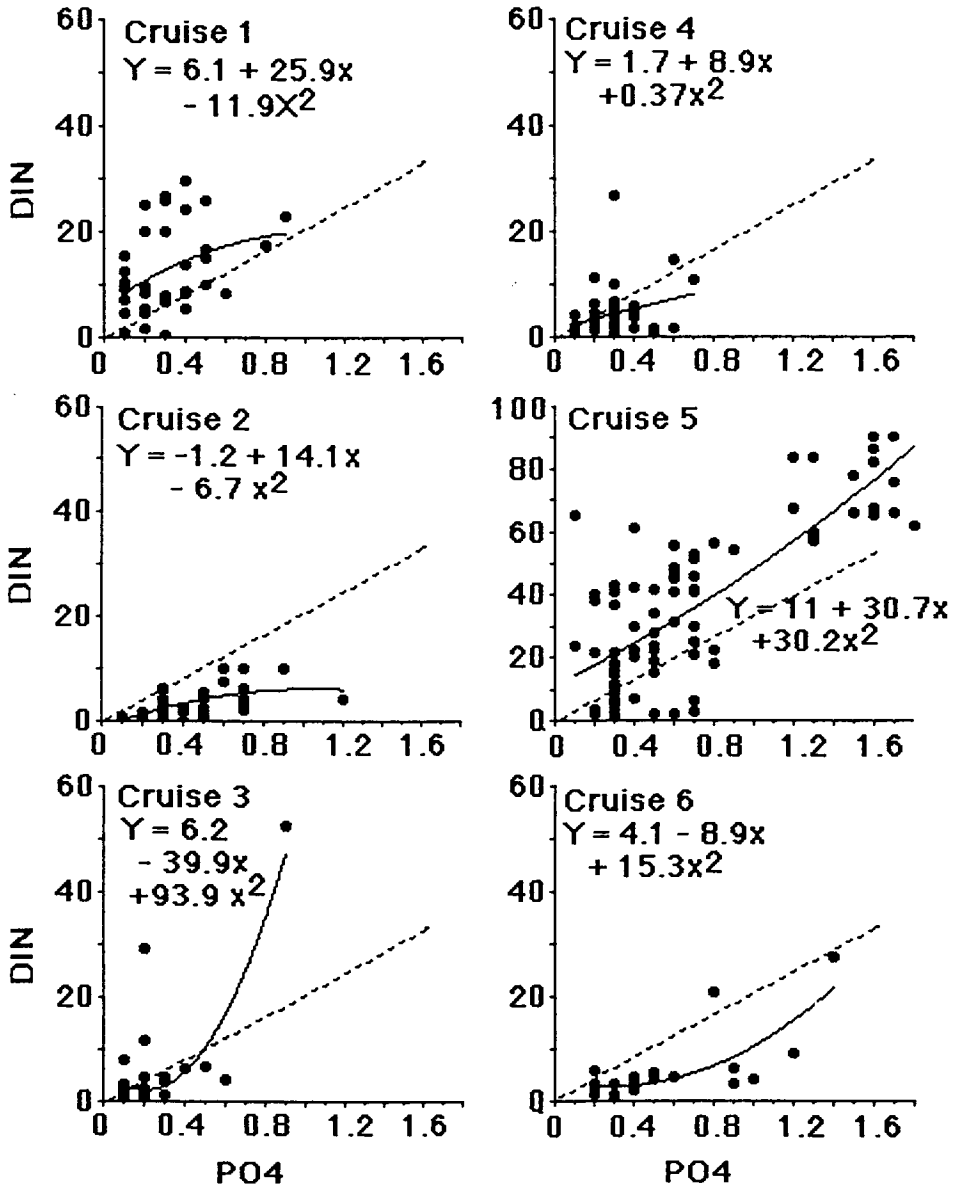

Figure 169. The relationship between the ratio of the concentration of DIN:DIP (µg/l) for each cruise at the LATEX B sampling stations. The total depth at these stations is between 10 and 100 m. The dotted line is a 16:1::DIN:Si atomic ratio.

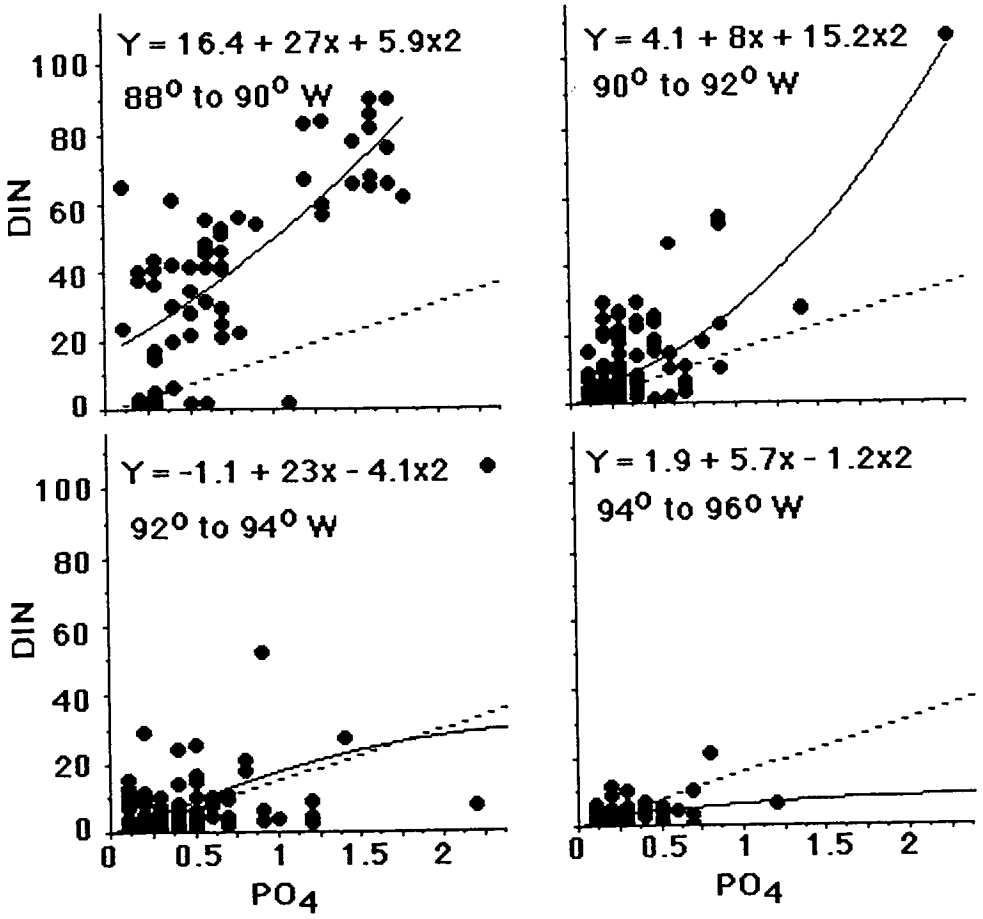

Figure 170. The relationship between the ratio of the concentration of DIN:DIP (µg/l) for the different longitudinal ranges of LATEX B sampling stations. The total depth at these stations is between 10 and 100 m. The dotted line is a 16:1::DIN:Si atomic ratio.

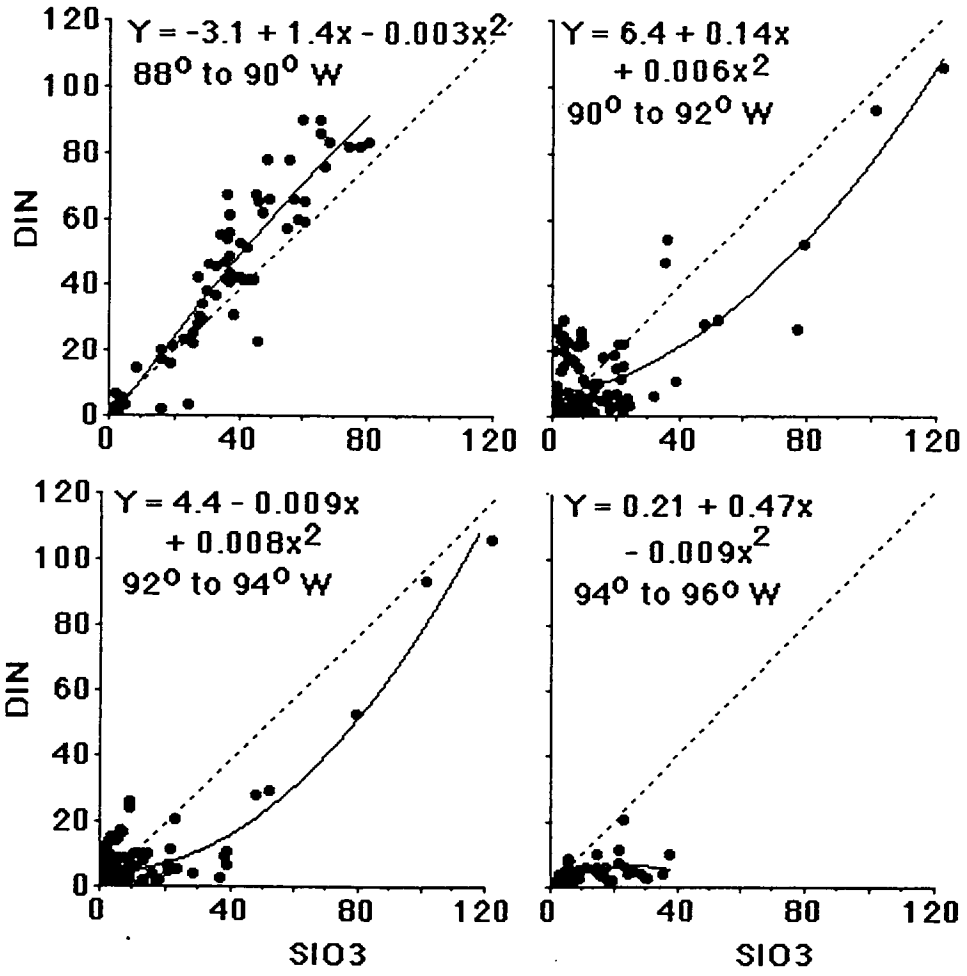

Figure 171. The relationship between the ratio of the concentration of DIN:Si (µg/l) for the different longitudinal ranges of LATEX B sampling stations. The total depth at these stations is between 10 and 100 m. The dotted line is a 1:1::DIN:Si atomic ratio.

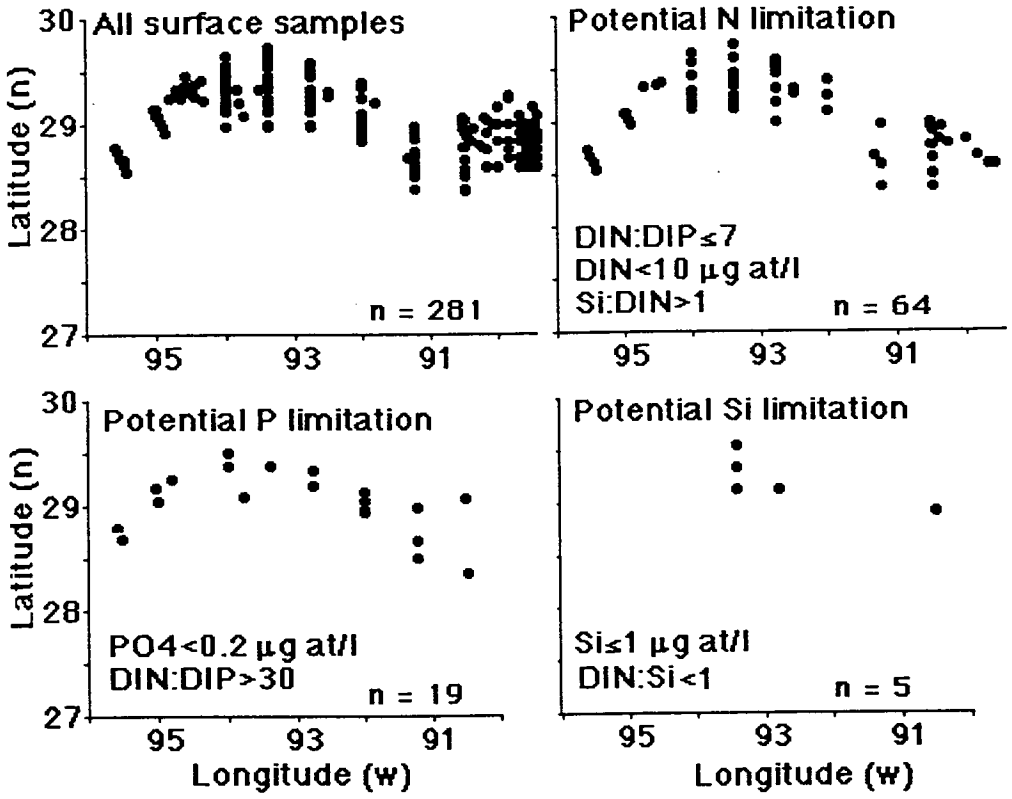

Figure 172. The inferred nutrient limitation (N, P or Si) at the LATEX B sampling stations. The total depth at these stations is between 5 and 100 m. The assumptions for each potential nutrient limitation are shown in the panel.

contributed to the eutrophication of the coast by increasing the likelihood of optimal, rather than minimal conditions for increased phytoplankton production.

These results are consistent with field studies showing an increase in phytoplankton from nitrogen concentration increases within the freshwater end member (Turner and Rabalais, 1994). The changed nutrient ratios in the riverine end member occurred as nitrogen loading was increasing (Turner and Rabalais, 1991) and was proportional to the diatom accumulations in sediments (Turner and Rabalais, 1994; Rabalais et al., 1996a, b).

VII. Phytoplankton Characteristics
by Quay Dortch

A. Introduction

Little is known about the temporal and spatial variation of phytoplankton species abundance and composition in the northern Gulf of Mexico. Most studies have focused on a small area (Simmons and Thomas, 1962; Fucik and El-Sayed, 1973), examined only the larger phytoplankton readily counted and identified with traditional bright-field light microscopy (Simmons and Thomas, 1962; Fucik and El-Sayed, 1973; Bontempi, 1995, Bontempi and Lyons 1996), or investigated species composition in relation to specific processes or problems (Dortch et al., 1992; Fahnestiel et al., 1995; Nelson and Dortch, 1996; Robichaux et al., 1996; Bode and Dortch, 1996, Dortch et al., submitted). Primary production in some parts of this region is extremely high (Sklar and Turner, 1981; Lohrenz et al., 1990, 1994), primarily caused by high nutrient inputs (Turner and Rabalais, 1992; Rabalais et al., 1996a). The phytoplankton species that are present determine how nutrients are used and how carbon is transferred to higher trophic levels, as well as providing some indication of the health of the system. Thus, it is necessary to evaluate the phytoplankton community composition as part of the process of understanding the productivity of the northern Gulf of Mexico.

In the northern Gulf of Mexico highly eutrophic, low salinity, coastal waters occur in close proximity to extremely oligotrophic, highly saline waters offshore. Some phytoplankton are found in certain types of water masses and can be used to trace the spatial extent and movement of these water masses. In particular, it was hypothesized that the coastal current, which flows along the Louisiana/Texas shelf, usually from east to west, would separate distinctly different phytoplankton populations with very strong gradients in the region of the coastal current. In addition to these cross-shelf gradients, it was also hypothesized that there would be much more gradual along-shelf gradients in the abundance and composition of phytoplankton, related to the location of the large riverine nutrient sources.

A series of phytoplankton indicators of specific types of water have been proposed for the northern Gulf of Mexico (Table 19; Dortch 1994, 1996). The small (1-2 μm), coccoid cyanobacteria, probably from the genus *Synechococcus*, have a variety of photosynthetic pigments, besides chlorophyll *a*, that give them distinctive colors under epifluorescence microscopy (Table 20). One group, containing the pigment phycocyanin (PC) (Waterbury et al., 1986; Vaulot and Xiuren, 1988), is usually the only cyanobacteria at low salinities in this area (Table 19). Phytoplankton in offshore waters are generally dominated by another group of small cyanobacteria, containing primarily phycoerythrin with a high phycourobilin content (PE/High PU) (Table 19) (Wood et al., 1985; Olson et al., 1988, 1990). Another group of cyanobacteria, those with low or no phycourobilin (Wood et al., 1985; Olson et al., 1988, 1990) (PE/LowPU), are intermediate in color and habitat (Tables 19 and 20; Dortch, 1994, 1996). The pigment differences between these groups are hypothesized to be related to either salinity or light quality (Wood et al., 1985; Waterbury et al., 1986; Vaulot and Xiuren, 1988; Pick, 1991), but regardless of the cause, they are specific indicators of water sources in this area (Dortch, 1994). Thus, the degree to which the PE/High PU or PC cyanobacteria dominate can delineate water masses and indicate mixing. The time scale of survival of particular types of cyanobacteria after changes in environmental conditions, is unknown at present.

Table 19. Proposed phytoplankton groups or species which can be used to trace water masses and mixing in the LATEX B area.

Group/Species	Indicator
Phycocyanin-containing *Synechococcus* (PC)	Direct river input
Skeletonema costatum	High productivity core of plume
% Diatoms/Total Autotrophs	River plume
Phycoerythrin/ High Phycourobilin-containing *Synechococcus* (PE/HiPUB)	High salinity water offshore

Table 20. Appearance of different pigment groups of cyanobacteria (0.2-3 μm size fraction) under epifluorescence microscopy with blue and green excitation light (see Methods for filter combinations).

Pigment Group	Blue Light	Green Light
Phycocyanin	Dull Red	Bright Red
Phycoerythrin/Low Phycourobilin[1]	Orange	Orange
Phycoerythrin/High Phycourobilin[1]	Yellow	Orange

[1]Difficult to distinguish because the amounts of phycourobilin are quite variable and represent a continuum rather than distinctly different types. The PE/LoPUB includes a range of hues, but the PE/HiPUB contains only cells which are distinctly yellow under blue light. Futher, phycoerythrin with a high phycourobilin may fluoresce green (Olson et al., 1988) and may not be counted because they cannot be distinguished from green fluorescing, heterotrophic bacteria (stained slightly by glutaraldehyde). This problem is particularly serious for surface water samples in the summer because pigments fade quickly during counting.

Because of the very low nutrient concentrations, there are few diatoms in offshore waters. In coastal waters generally, diatom abundance tends to be much higher. In river plumes, phytoplankton, especially diatom, biomass and growth, is usually maximal at some distance from the river mouth because it is necessary for the sediment to settle out so there is enough light to stimulate photosynthesis. In the northern Gulf of Mexico the first species to respond is often *Skeletonema costatum*, an opportunistic, fast-growing diatom. Growth of this species is then followed by that of other diatoms. Further down the axis of the plume the nutrients become depleted, and, although there is plenty of light, there are insufficient nutrients to support high phytoplankton biomass. Thus, it can be hypothesized that high numbers of *S. costatum* will indicate the high productivity areas most strongly influenced by riverine inputs and that high diatom numbers will indicate the more extended plume area.

A negative consequence of high nutrient inputs to a region can be the occurrence of toxic and noxious algal blooms. Nutrient inputs to the northern Gulf of Mexico have resulted in other negative impacts of eutrophication, such as bottom water hypoxia

(Rabalais et al., 1992, 1996a). The occurrence of toxic and noxious algae has also been documented (Rabalais et al., 1995, 1996a; Robichaux et al., 1996; Dortch et al., submitted). Two species have received particular attention because of the serious consequences of large blooms. *Gymnodinium sanguineum* is a dinoflagellate which is often associated with fish kills, although the mechanism is unknown. It is sporadically present along the entire Louisiana and Texas shelf (Robichaux et al., 1996). *Pseudo-nitzschia* spp. are a group of diatoms, some of which produce a toxin, domoic acid. This toxin, which can accumulate in higher trophic levels, causes Amnesic Shellfish Poisoning (ASP) in humans and other consumers. *Pseudo-nitzschia* spp. are present in extremely high numbers on the Louisiana/Texas continental shelf, especially in the spring (Dortch et al., submitted), although there have been no known outbreaks of ASP. Other potentially toxic and noxious species are also present in the northern Gulf of Mexico, although less is known about their occurrence (Rabalais et al., 1995). It is believed that the coastal current could be an important mechanism for spreading these organisms throughout the region to any environment with suitable conditions for their growth.

During this project five cruises were conducted which covered variable portions of the Louisiana/Texas continental shelf (Section II), and one cruise (April, 1994) (Section III) was conducted in the plume of the Mississippi River. On all cruises, surface and bottom water samples were collected at approximately every other station for phytoplankton identification and enumeration. Samples were size fractionated and examined with epifluorescence microscopy in order to count the full range of phytoplankton sizes. These data are the first quantitative description of the temporal and spatial variation in abundance and composition of the entire phytoplankton community in the northern Gulf of Mexico. The utility of specific phytoplankton groups as indicators of specific water masses will be tested and used to examine the effect of the coastal current on phytoplankton populations on the Louisiana/Texas shelf. Finally, the frequency and magnitude of occurrence of potentially toxic and noxious phytoplankton will be examined for the northern Gulf of Mexico and the temporal and spatial variability of abundant species will be identified and related to water movements and hydrography in the region.

B. Methods

Phytoplankton samples were collected at the surface using a bucket and at the bottom using 10-liter Niskin bottles on a CTD Rosette. The method for preserving and counting phytoplankton was adapted from Murphy and Haugen (1985), Shapiro and Haugen (1988), and Shapiro et al. (1989). One hundred milliliters of seawater was preserved with 50% glutaraldehyde to a final concentration of 0.5% (by volume) and refrigerated for at least 1 hour and not more than 24 hours prior to size fractionated filtration. One aliquot of sample was filtered through a 3-μm polycarbonate filter and onto a 0.2-μm poloycarbonate filter without prior staining. The 3-μm filter was discarded and the 0.2-μm filter was retained (0.2 to 3 μm size fraction). Another aliquot of sample was filtered through an 8-μm polycarbonate filter and then a 3-μm filter; both filters were retained (3 to 8 and >8 μm size fractions). Before filtration this aliquot was made up to 25 ml with filtered seawater of approximately the same salinity and stained with 0.05 ml proflavine monohydrochloride (Sigma P-4646, 1.5 g/liter in distilled, deionized water). If possible, all samples were filtered without vacuum, but if necessary, <100 mm vacuum was applied. All filters were transferred to slides and mounted with low fluorescence, low viscosity immersion oil.

Phytoplankton were counted using an Olympus BH2-RFA epifluorescence microscope with blue and green excitation (excitation filters BP-490 and BP-545, barrier

filters O-515 and O-590, and dichroic mirrors DM500 and DM580, respectively). The 0.2 and 3 μm pore size filters were counted immediately at 1000x. The 8 μm pore size filters were stored frozen and counted as soon as possible. Three different counts were made on the 8 μm filters, using different magnification and counting different areas of the filter, in order to adequately count small, abundant organisms, as well as large, rarer organisms. To avoid counting an organism more than once they were separated according to length. Phytoplankton were identified to the nearest possible taxon, and Table 21 describes the types of organisms usually observed in each size fraction. It is possible for some groupings of taxa and even individual species, to be present in more than one size fraction, if the size of colonies or individuals varied considerably or if they occurred both singly and in aggregates of sediment, organic matter and cells. The 0.2 and 3 μm filters were discarded after counting, because they quickly become uncountable; 8 μm filters are archived frozen at Louisiana Universities Marine Consortium.

Table 21. Common phytoplankton groups counted in each size fraction.

Size	Phytoplankton Groups
0.2-3 μm (count immediately on ship)	Coccoid cyanobacteria--mostly *Synechococcus* Autotrophic eukaryotes Heterotrophic eukaryotes
3-8 μm (count on ship within several days)	Photosynthetic flagellates and non-flagellates Heterotrophic flagellates and non-flagellates Cryptomonads Athecate dinoflagellates Diatoms Coccoid cyanobacteria
≥8 μm (freeze and count in lab, detailed taxonomy to species, where possible)	Diatoms Dinoflagellates Ciliates Cryptomonads Colonial cyanobacteria Colonial, freshwater chlorophytes Coccoid cyanobacteria[1]

[1]Many coccoid cyanobacteria occur in aggregates, especially when suspended particulate matter concentrations are high, which do not break up during size fractionation.

C. Results And Discussion

1. Phytoplankton Abundance, Estimated Biomass, and Overall Composition

Mean total phytoplankton abundances ranged from 3.4×10^7 cells/liter to 7.21×10^8 cells/liter (Table 22). Abundance was approximately an order of magnitude greater in the summer and fall than it was in the spring, primarily because of increases in the numbers of small phytoplankton, in the 0.2 to 3 and 3 to 8 μm size ranges, during the summer/fall. In contrast, except in 1993, when Mississippi River flooding occurred in the late spring (Dowgiallo, 1994), phytoplankton abundance in the largest size fraction

(>8 μm) decreased in the summer/fall. Numerically, the phytoplankton were dominated by the picoplankton at all times of the year.

The two major groups of phytoplankton in the northern Gulf of Mexico were diatoms and cyanobacteria (Table 22). The cyanobacteria dominated numerically, especially in the summer/fall. Although *Trichodesmium* spp. and a few other, large, colonial, estuarine cyanobacteria are occasionally present in low numbers, most of the cyanobacteria are approximately 1 to 2 μm in size. They comprised the majority of the picoplankton but were also found in other size fractions (see below). The remainder of the phytoplankton included a wide variety of types, as described in Table 21, with no other major groups clearly dominating.

Table 22. Comparison of phytoplankton abundance, size, composition, and biomass between cruises for all samples and all depths.

	April 1992	October 1992	April 1993	July 1993	April 1994	July 1994
Phytoplankton Abundance (#cells/liter x 10^6)						
0.2-3 μm	75.0	214.00	30.60	691.00	47.80	289.00
3-8 μm	5.36	11.20	1.31	26.20	3.43	22.70
>8 μm	4.32	1.41	2.04	4.20	9.38	6.25
Total	84.6	226.00	34.00	721.00	59.30	318.00
% Phytoplankton[1]						
Diatoms	6.97	0.38	9.75	0.12	10.26	1.00
Cyanobacteria	82.90	95.33	74.52	97.12	72.87	95.94
Estimated Biomass[2] (μg C/liter)						
Diatoms	200.00	33.0	127.00	14.90	600.00	36.00
Cyanobacteria	7.11	21.0	2.80	69.00	4.74	30.00

[1]Abundance Diatoms or Cyanobacteria/Abundance Total Phytoplankton x 100
[2]Calculated from cell volume, assuming Carbon/Cell Volume = 0.185 pg/μm^3 (Dortch, unpublished). Cell volume for cyanobacteria calculated assuming cells are spherical with a diameter of 1 μm. Cell volume for diatoms in 3-8 μm size fraction calculated assuming cells are spherical with a diameter of 5 μm. Cell volume for diatoms > 8 μm calculated using average volume of *Skeletonema costatum*, determined from sediment trap samples for one year (442 ± 226 μm^3/cell), since it is the dominant diatom and is a typical size.

By making assumptions concerning the sizes, shapes, and carbon content of the phytoplankton present (Table 22), it is possible to estimate the relative biomass of diatoms and cyanobacteria in terms of carbon. In general, the biomass of a single diatom is many times greater than that of a cyanobacteria. For example, *Skeletonema costatum*, a dominant diatom in the northern Gulf of Mexico, has a volume of 442 μm^3 whereas a cyanobacteria with a diameter of 1 μm has a volume of 0.5 μm^3. Despite these orders of magnitude differences in size, the cyanobacteria are so abundant in the summer/fall that their estimated carbon biomass approached, or in 1993 exceeded, that of the diatoms (Table 22).

When chlorophyll *a* concentration, which is another measure of phytoplankton biomass, was compared with total phytoplankton numbers for surface samples from all cruises, there was no correlation (Table 23). Further, there was no correlation between chlorophyll concentration and cyanobacteria abundance, while there was a strong, positive, highly significant correlation between chlorophyll and diatom numbers (Table 23; Figure 173a). This result is somewhat misleading because diatoms overwhelmingly dominated the biomass during three cruises and cyanobacterial only showed similar dominance during one cruise (Table 22). When numbers are converted to carbon biomass, as described in Table 22, and plotted against chlorophyll, for the cruise during which cyanobacterial dominated the biomass (Figure 174b; Cruise IV, July 1993), there was a strong, positive correlation between chlorophyll and cyanobacterial biomass and none with diatom biomass. Conversely, for a cruise dominated by diatom biomass (Figure 174c; Cruise V, April, 1994), there was a strong, positive correlation between diatom biomass and chlorophyll and none with cyanobacteria. Given the approximations of the biomass estimate, the slope of the lines in Figure 174b and 174c, are remarkably similar. Consequently, cyanobacteria and diatoms have the same C/Chlorophyll *a* ratios, 22-25 μg/μg, indicating similar chlorophyll *a* contents. This C/Chl ratio is relatively low and suggests that the phytoplankton are light limited and nutrient sufficient (Chloern et al., 1995).

Table 23. Regression (Model II, Laws and Archie, 1981) between chlorophyll *a* (μg/liter) concentrations and phytoplankton abundance (#cells/liter) for all surface samples from all cruises (n = 314).

Regression	Slope	Intercept	r^2	F
Chlorophyll *a* vs Abundance Total Phytoplankton	1.18×10^{-8}	1.61	0.0144	4.58*
Chlorophyll *a* vs Abundance Cyanobacteria	1.18×10^{-8}	1.68	0.0132	4.19*
Chlorophyll *a* vs Abundance Diatoms	2.52×10^{-6}	1.46	0.4798	287.73*

*Significant $p<0.05$

As expected, diatom abundance reached maximum values at intermediate salinities (Figure 175a), although low abundances also occurred at intermediate salinities as well. In contrast, cyanobacterial abundance increased exponentially with increasing salinity in the spring but decreased exponentially with increasing salinity in the summer and fall (Figure175b). Thus, abundances of cyanobacteria in all seasons converged on similar values at high salinities.

Although most of the cyanobacteria were 1 to 2 μm in size, a significant fraction (0-60%; Table 24) were counted in the 3 to 8 μm and > 8 μm , rather than in the 0.2 to 3 μm size fractions. These were not just a few organisms that happened to land on the wrong filter during size fractionation since, visually, they were often incorporated into sediment/cell aggregates. To test the hypothesis that they might be associated with sediments in the water, the abundance of cyanobacteria > 3 μm was compared with the turbidity of the water, and measured with a transmissometer for 4 cruises for which the data are available (Table 24). For 3 out of the 4 cruises, there was a significant, negative relationship between the abundance of cyanobacteria > 3 μm and percent light

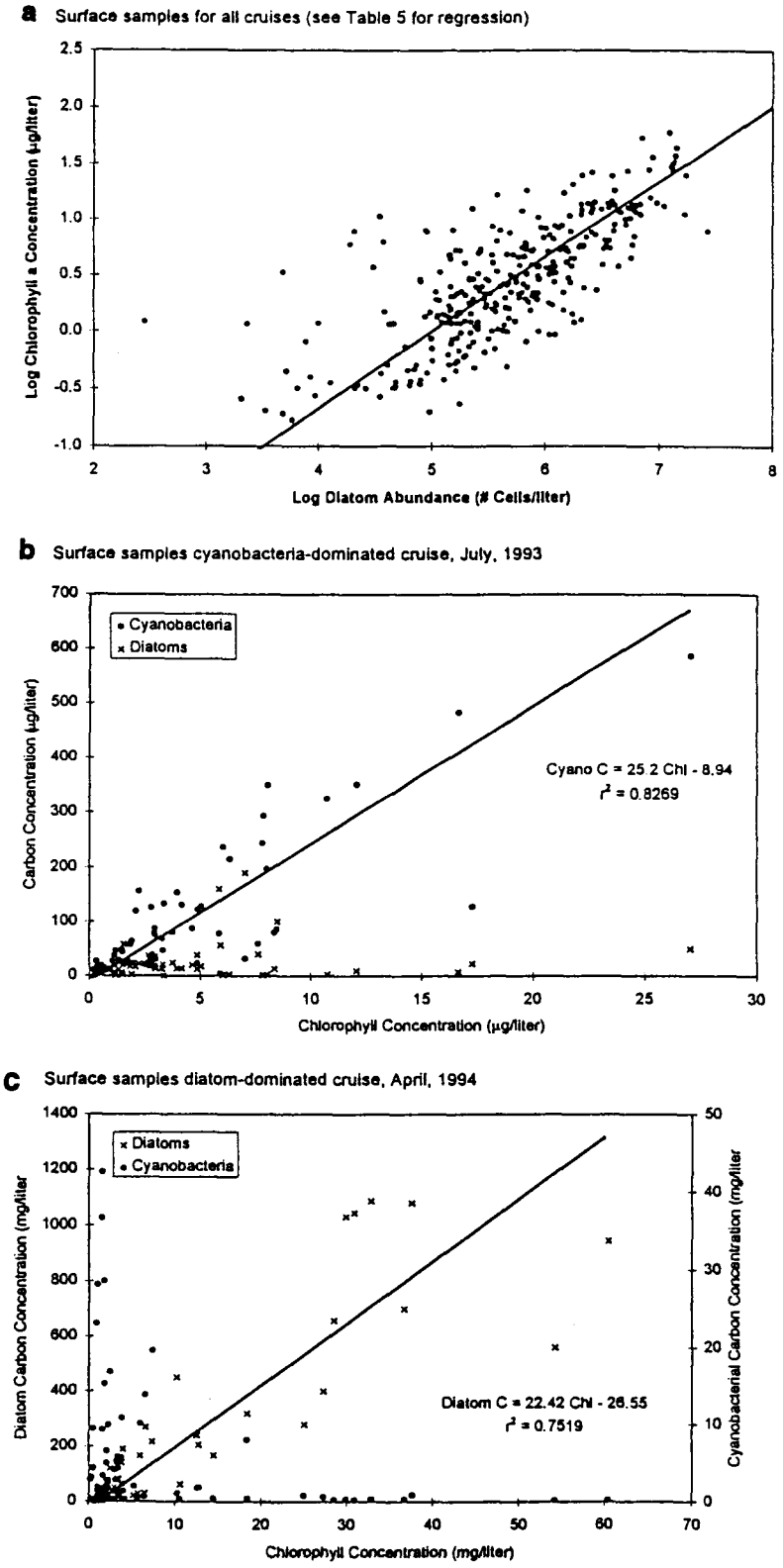

Figure 173. Relationship between chlorophyll *a* and cell numbers for (a) all cruises or (b and c) carbon for selected cruises dominated by one taxon. Regressions are Model II (Laws and Archie, 1981).

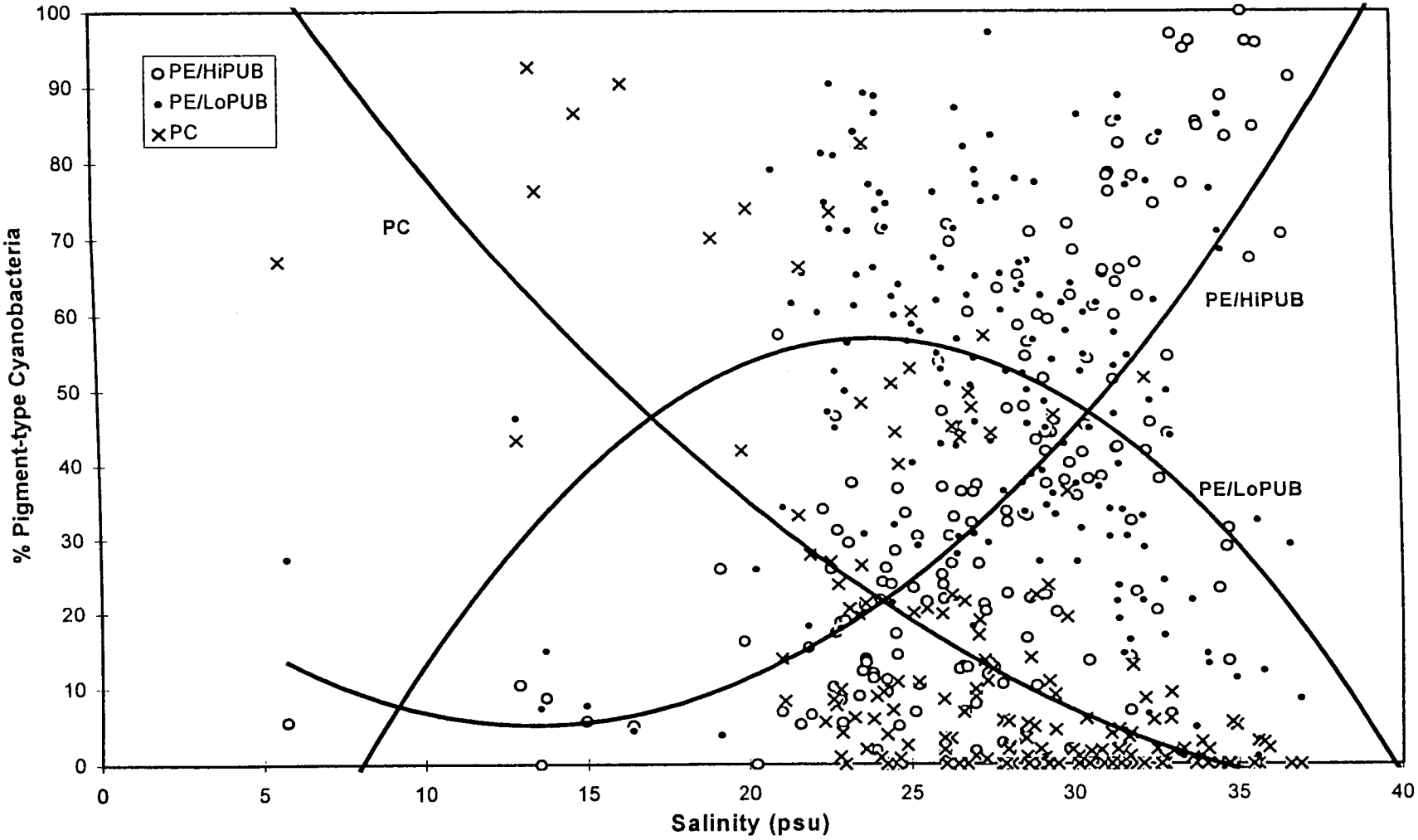

Figure 174. Variation of different cyanobacterial pigment types with salinity in surface waters for all cruises except July 1993 and April 1994. %PC = 0.0842 S^2 - 7.0184 S + 141.79, r^2 = 0.4043; %PE/LoPUB = -0.2262 S^2 + 10.819 S - 72.401, r^2 = 0.1828; %PE/HiPUB = 0.1421 S^2 - 3.8006 S + 30.609, r^2 = 0.4511; n= 174.

transmission, confirming that it is likely that cyanobacteria are associated with particulates. There was considerable variation from cruise to cruise in the percentage of cyanobacteria associated with particles (Table 6). In part, these differences parallel the relationship between total cyanobacteria and salinity (Figure 175c).

Table 24. Comparison of % Cyanobacteria >3 μm/Total Cyanobacteria between cruises for surface samples. % T indicates cruises for which there was a significant (S), negative, linear relationship between Abundance of Cyanobacteria > 3 μm and % Light Transmittance of the water; NS = not significant; NA = data not available for analysis.

Cruise		% > 3μm	% T
April, 1992	Mean	1.5	NS
	Range	0 to 14.5	
	SD	2.72	
	n	39	
October, 1992	Mean	3.2	S
	Range	0.1 to 21.4	
	SD	4.26	
	n	42	
April, 1993	Mean	0.4	S
	Range	0 to 8.0	
	SD	1.32	
	n	46	
July, 1993	Mean	2.6	S
	Range	0.2 to 30.8	
	SD	4.54	
	n	63	
April, 1994	Mean	7.40	NA
	Range	0 to 33.3	
	SD	7.02	
	n	69	
July, 1994	Mean	7.02	NA
	Range	0.1 to 59.4	
	SD	11.18	
	n	61	

On all six cruises the total abundance of phytoplankton was greater at the surface than in bottom water, as would be expected (Table 25). The differences were significant only for three cruises, probably because of the high spatial variability in abundance on each cruise. There were few differences in overall composition, percent diatoms and percent cyanobacteria, of the phytoplankton between surface and bottom (Table 25).

Phytoplankton in the northern Gulf of Mexico are numerically dominated by small phytoplankton, with the dominance increasing in the summer/fall. Small (1 to 2 μm), coccoid cyanobacteria are the dominant small phytoplankton and diatoms are the dominant large phytoplankton, although there are also small diatoms (3 to 8 μm size

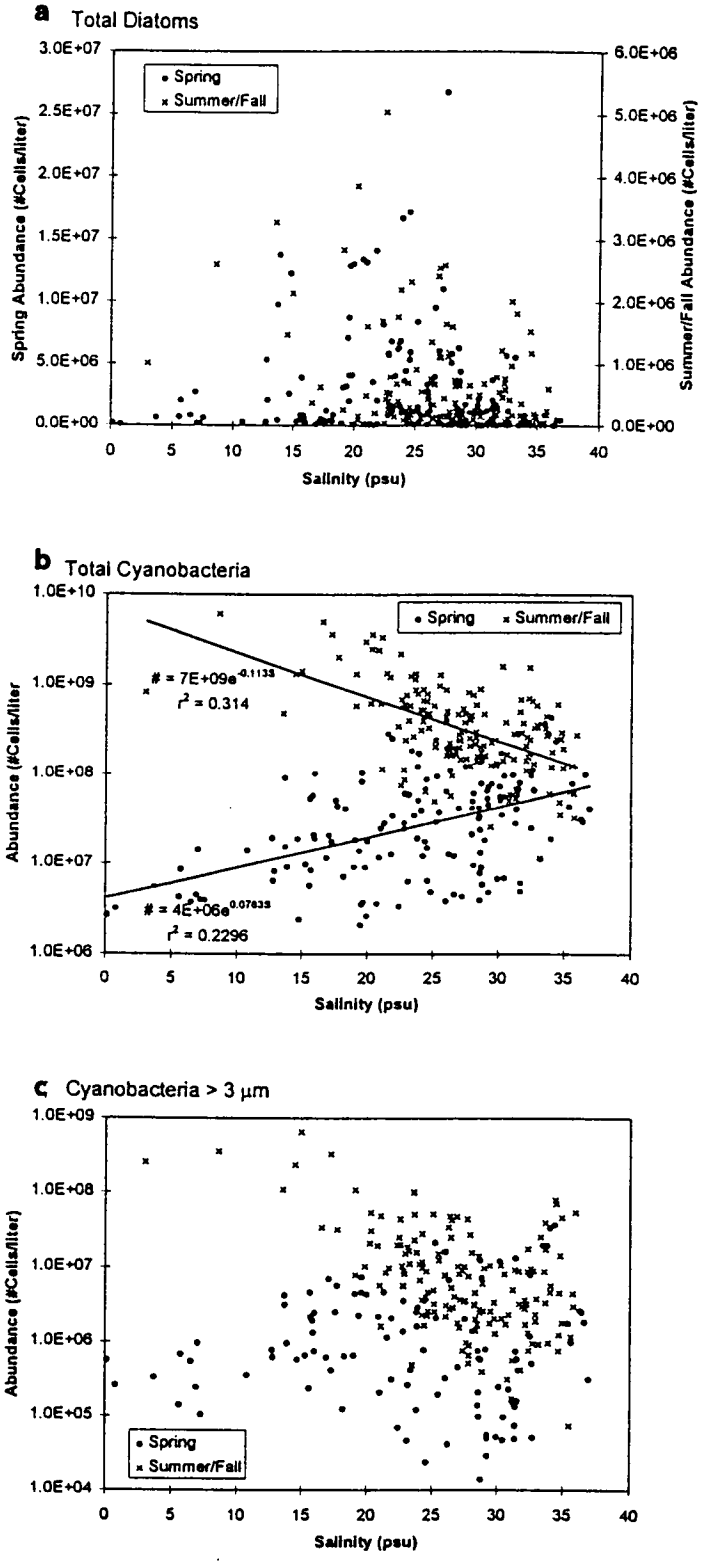

Figure 175. Abundance of total diatoms, total cyanobacteria, and cyanobacteria counted in 3-8 µm and > 8 µm size frations as a function of salinity in surface water during spring and summer/fall cruises. In 175b, F for both lines significant at $p<1x10^{-10}$.

Table 25. Comparison of mean surface and bottom water phytoplankton (Phyto) total abundance (cells/liter x 10^6) and diatom and cyanobacterial (Cyano) abundance, as a % of total phytoplankton. *** indicates surface and bottom means are significantly different, two-tailed Student's t-test; **indicates that surface mean is significantly larger than bottom mean and * indicates that bottom mean is significantly larger than surface mean, one-tailed, Student's t-test, $p<0.05$. SD = standard deviation, n = number of samples.

			Total Phyto Abundance	Diatoms % Total Phyto	Cyano % Total Phyto	n
April, 1992	Surface	Mean	92.7	8.4	82.3	
		SD	78.7	10.0	16.4	39
	Bottom	Mean	76.8	5.6	83.5	
		SD	76.2	6.7	15.4	40
Oct., 1992	Surface	Mean	262	0.3	96.0	
		SD	153 ***	0.3 ***	3.2 *	42
	Bottom	Mean	186	0.5	94.6	
		SD	166	0.6	3.3	37
April, 1993	Surface	Mean	42.6	10.9	75.3	
		SD	29.3 ***	17.0	21.1	46
	Bottom	Mean	25.3	8.6	73.7	
		SD	24.4	11.6	20.4	46
July, 1993	Surface	Mean	1080	0.1	98.5	
		SD	1240 ***	0.1	1.4 ***	63
	Bottom	Mean	388	0.1	95.8	
		SD	827	0.1	5.9	67
April, 1994	Surface	Mean	64.4	10.6	70.7	
		SD	89.9	20.2	25.8	69
	Bottom	Mean	53.4	9.7	75.9	
		SD	121	22.2	23.9	50
July, 1994	Surface	Mean	380	1.8	96.2	
		SD	313	11.6	12.0	61
	Bottom	Mean	258	0.2	95.7	
		SD	236	0.4	6.1	63

fraction) and small cyanobacteria that are part of larger aggregates. In terms of biomass, diatoms clearly dominate in the spring, but in the summer, the biomass of cyanobacteria equals or exceeds that of diatoms.

The dominance by small phytoplankton, especially in warmer months, is not unexpected. Studies of size-fractionated chlorophyll or productivity have yielded similar results (for example, Malone et al., 1991; Tamigneaux et al., 1995; Bode and Dortch, 1996). However, there are very few studies anywhere in the world which have enumerated the entire size range of phytoplankton, so that different taxa rather than size groups can be compared. The few studies with this type of data are summarized in Table 26, but the data are too limited for a thorough geographic analysis. It is clear that cyanobacteria are numerically dominant in all areas. In two out of three areas for which there is biomass data (Eastern Subarctic Pacific and northern Gulf of Mexico), cyanobacteria at times can also be a major fraction of the biomass. The abundance of cyanobacteria in the northern Gulf of Mexico in summer is at the very high extreme of abundances observed worldwide. Highest abundances are usually observed in eutrophic areas when temperatures are at their seasonal maximum (Glover, 1985; Waterbury et al., 1986; Vaulot and Xuiren, 1988; Ray et al., 1989; Kuparinen and Kuosa, 1993).

Table 26. Total cell numbers (#Cells/liter), % Abundance (% Abund = #Cells in Taxa/Total # Cells) of diatoms (Diat) and cyanobacteria (Cyanos) relative to total phytoplankton, and diatom and cyanobacterial carbon (μgC/liter) in other areas. Most data represent means of many analyses.

Location Date	Depth (m)	Total #	% Abund Diat	 Cyanos	Carbon Diat	 Cyanos
Eastern Subarctic Pacific (Booth et al., 1993)						
May-Sept	0-80	1.34×10^7	2.3	81.3	2.7	2.8
North Atlantic Open Ocean (Murphy & Haugen, 1985)						
May	1-100	1.34×10^7	-	43.2	-	-
North Atlantic Slope (Murphy & Haugen, 1985)						
Aug./Sept.	1-100	1.58×10^7	-	86.2	-	-
North Atlantic Neritic (Murphy & Haugen, 1985)						
Aug	1-100	4.50×10^7	-	81.7	-	-
Lower York River (Ray et al., 1989)						
July-Sept.	1-5	2.94×10^8	4.15	93.78	226.7	31.8
Equatorial Pacific 5°N-5°S (Chavez et al., 1990)						
Nov.	0-60	1.59×10^7	0.3	80.8	-	-
Equatorial Pacific N of 5°N (Chavez et al., 1990)						
Nov.	0-60	4.89×10^6	0.2	69.6	-	-

The pattern of phytoplankton abundance and biomass, with a spring peak in diatoms and a summer peak in cyanobacteria may be typical of highly eutrophied, river-dominated estuaries like the Chesapeake Bay (Ray et al., 1989; Malone et al., 1996) and the northern Gulf of Mexico (this study). These types of estuaries also experience peaks

in ammonium uptake and regeneration during the summer (Carpenter and Dunham, 1985; Pennock, 1987; Fisher et al., 1992; Malone et al., 1996, Dortch and Bode, 1996). Thus, despite high inputs of new N from riverine sources, they are also ecosystems in which small phytoplankton and regenerative processes dominate for a significant part of the year.

2. Phytoplankton Indicators and the Coastal Current

a. Cyanobacteria as an Indicator

Three groups of cyanobacteria were seen on all cruise (Table 27; Figures 174, 176, and 177). At low salinities, the PC cyanobacteria predominated and at high salinities the PE/High PUB cyanobacteria predominated. At intermediated salinities, the PE/Low PUB cyanobacteria reached maximum abundance, although their distribution with salinity tended not be as clearly defined as for the other two groups. Although these groups have been distinguished with a flow cytometer (Wood et al., 1985; Olson et al., 1988; 1990), this is the first time that they have been distinguished routinely using microscopic analysis.

There was variation between cruises in both the overall dominance of a pigment group (Table 27) and the variation with salinity (Table 28; Figures 174, 176, 177). The differences were not clearly seasonal in that spring cruises were not similar and different from summer/fall cruises. Four cruises were similar (Table 28): the lines describing the relationship between % PC and salinity and %PE/High PUB and salinity intersected at the same salinity and the maximum % PE/Low PUB occurred at approximately the same salinity. Two cruises were distinctly different: the July 1993 cruise (Cruise IV), during which spring-like river flow continued into the summer and the April 1994 cruise (Cruise V), which had a cruise track much closer to the mouth of the Mississippi River (Table 28). Consequently, the data for the four similar cruises were combined (Figure 174) to show the relationship between the three pigment groups and salinity. Because of the large differences in total abundance of cyanobacteria between spring and summer/fall cruises, only relative abundance data could be combined in this way.

The surface water data suggests a clear relationship between salinity and cyanobacterial pigment type and culture studies support the contention that PC-containing cyanobacteria are halotolerant, whereas PE-containing cyanobacteria are marine (Waterbury et al., 1986). However, previous studies have also suggested that light quality may be the controlling factor (Pick, 1991; Wood, 1985; Hauschild et al., 1991). From studies in many lakes, PC-containing cyanobacteria are predicted to dominate in eutrophic, turbid, or discolored water, whereas PE-containing cyanobacteria are predicted to dominate in clear, oligotrophic water (Pick, 1991). In oligotrophic marine systems, where the water is clear, a high PUB content in the PE may increase light harvesting capability, especially at depth (Wood, 1985). The Louisiana/Texas coastal zone is an ideal environment to distinguish between these two competing hypotheses. If salinity is the controlling factor, then, when the water column is stratified with lower salinity water at the surface, which is often the case on the Louisiana shelf, the distribution of cyanobacterial pigment types should vary with depth. If light quality is the determining factor, then the pigment composition at depth will be determined by the surface water characteristics, which are usually turbid and discolored, and there will not be significant differences with depth in relative abundance of different pigment types.

On five of six cruises the relative abundance of PE/HiPUB cyanobacteria was significantly greater on the bottom, whereas the relative abundance of PE/LoPUB cyanobacteria was greater at the surface (Table 27). This supports the hypothesis that

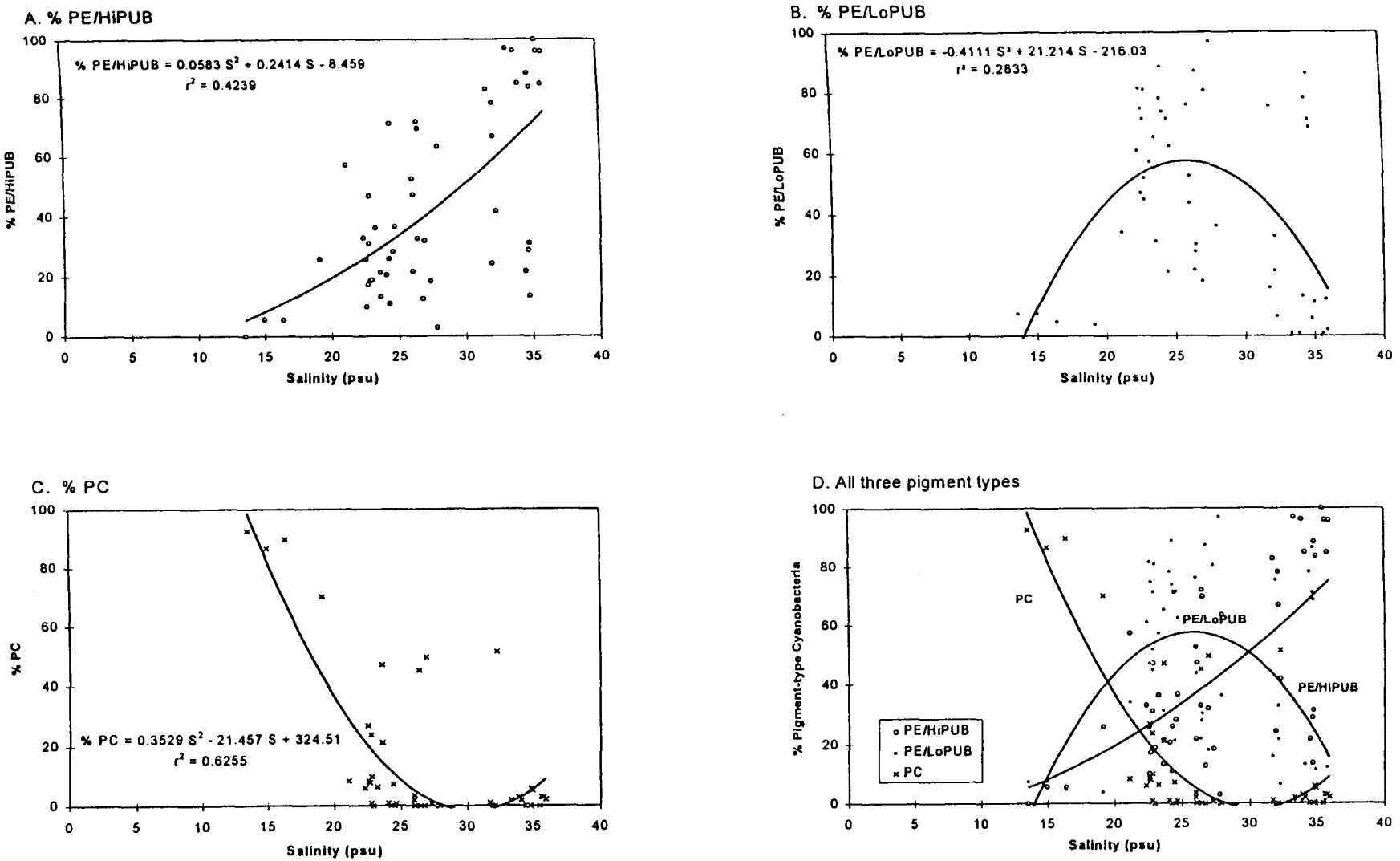

Figure 176. Variation of different cyanobacterial pigment types in the 0.2 to 3 μm size fraction with salinity for all surface samples, July 12-18, 1994, n = 51.

Table 27. Comparison of mean surface and bottom water abundance of cyanobacteterial pigment types, as a % of abundance of all cyanobacteria (0.2 to 3 μm). See text for abbreviations of cyanobacterial pigment types. Delta sigma t is the mean difference between surface and bottom water sigma t values, calculated from SeaBird CTD data. *** indicates means are significantly different, two-tailed Student's t-test; **indicates that surface mean is significantly larger than bottom mean and * indicates that bottom mean is significantly larger than surface mean, one-tailed, Student's t-test, $p<0.05$. SD = standard deviation, n = number of samples.

			% Cyano PE/ HiPUB	% Cyano PE/ LoPUB	% Cyano PC	Delta Sigma t
April, 1992	Surface	Mean	8.4	37.5	43.4	2.52
		SD (n)	10.0 (39)	27.9 (39)	23.5 (39)	2.67 (30)
	Bottom	Mean	5.6	47.4	38.9	
		SD (n)	6.7 (40)	28.8 (40)	22.0 (40)	
Oct., 1992	Surface	Mean	35.7	45.8	18.5	0.84
		SD (n)	27.2 (42) **	18.4 (42) *	19.0 (42)	1.03 (38)
	Bottom	Mean	46.4	38.0	15.6	
		SD (n)	25.2 (37)	17.0 (37)	18.0 (37)	
April, 1993	Surface	Mean	33.1	59.3	7.5	3.54
		SD (n)	17.9 (46) ***	16.2 (46) ***	14.4 (46)	2.03 (42)
	Bottom	Mean	51.8	42.5	5.7	
		SD (n)	25.5 (46)	21.7 (46)	13.1 (46)	
July, 1993	Surface	Mean	22.4	51.4	26.3	5.54
		SD (n)	25.9 (63) ***	21.8 (63) ***	27.3 (63)	4.51 (63)
	Bottom	Mean	49.9	30.3	19.8	
		SD (n)	31.2 (67)	17.7 (67)	23.8 (67)	
April, 1994	Surface	Mean	51.4	36.2	12.4	8.55
		SD (n)	26.2 (69) ***	20.0 (69) *	21.00 (69) ***	5.19 (68)
	Bottom	Mean	69.5	28.7	1.8	
		SD (n)	24.3 (51)	22.0 (51)	4.7 (51)	
July, 1994	Surface	Mean	44.7	43.0	12.3	4.14
		SD (n)	31.2 (61) ***	32.1 (61) ***	23.4 (61)	4.12 (61)
	Bottom	Mean	69.7	22.3	8.0	
		SD (n)	28.4 (63)	22.2 (63)	17.4 (63)	

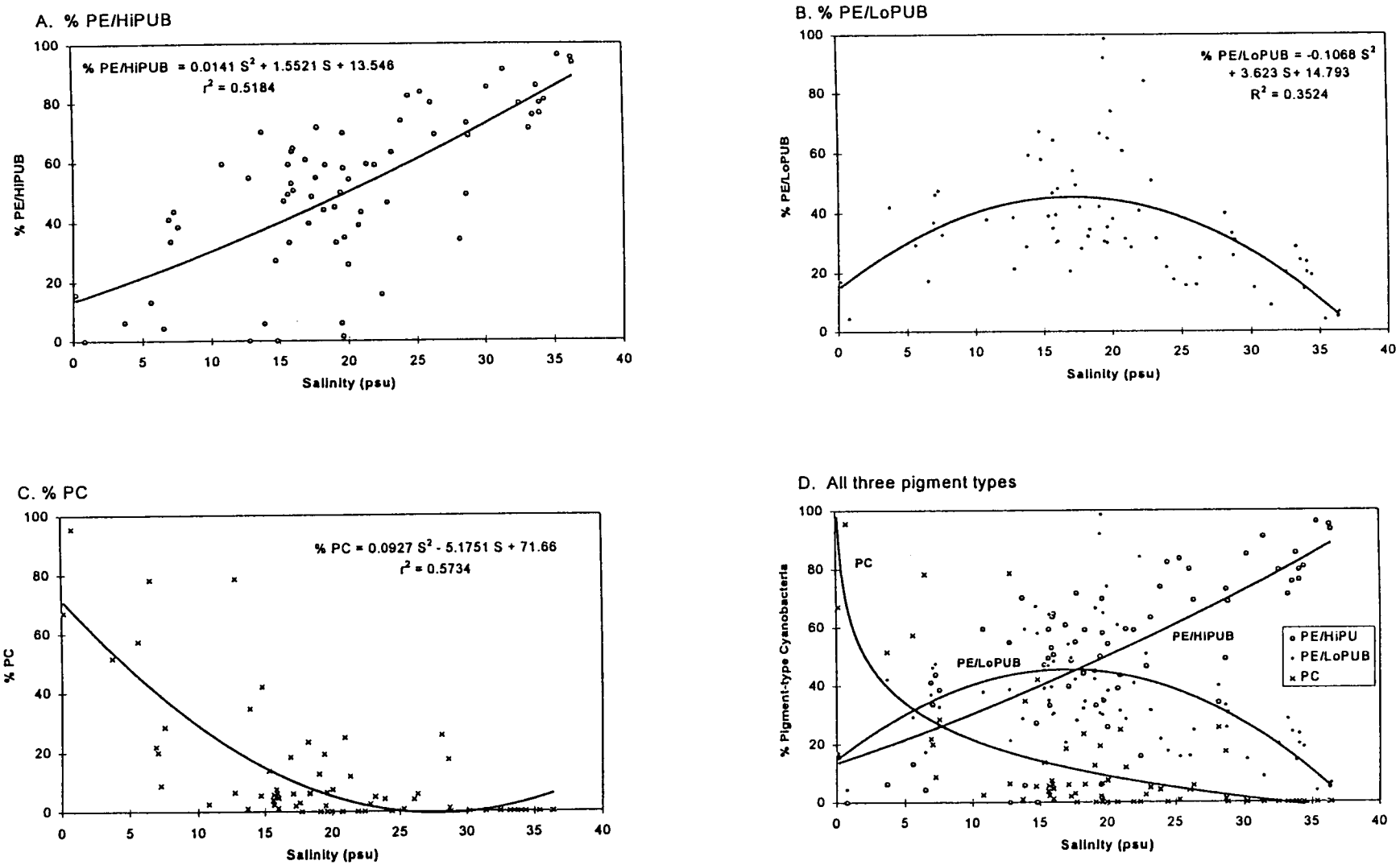

Figure 177. Variation of different cyanobacterial pigment types in the 0.2 to 3 μm size fraction with salinity for all surface samples, April 12-22, 1994, n = 69.

Table 28. Polynomial fit and r^2 of % abundance of each cyanobacterial pigment group/total cyanobacteria (0.2-3 μm) vs. salinity (S). The %PE/HiPUB=%PC is the salinity at which the curves for each group intersect. The Max %PE/LoPUB is the salinity at which the maximum % of that pigment group is observed. n = number of samples.

Cruise	% PC	% PE/LoPUB	% PE/HiPUB	Salinity		n
			%PC	%PE/HiPUB=PUB	Max %PE/Lo	
April 1992	0.1412S2-11.234S+2.1624 0.5204	-0.2605S2+12.843S-106.06 0.2008	0.1193S2-1.6097S-10.174 0.6830	25	24.6	36
Oct 1992	0.1521S2-13.082S+2.69.01 0.5422	-0.5479S2+29.304S-337.48 0.2339	0.3958S2-16.221S+168.46 0.5561	27.8	26.7	41
April 1993	0.0524S2-4.6836S+94.889 0.7229	-0.127S2+5.903S-4.2997 0.1422	0.0746S2-1.2196S+9.4124 0.3264	21.7	23.2	46
July1 1993	0.0217S2-4.7058+130.46 0.6459	-0.0579S2+4.265S-17.652 0.2424	0.0361S2+0.4407S=12.809 0.2146	26.1	none	51
April2 1994	0.0927S2-5.1751+71.66 0.5734	-0.1068S2+3.623S+14.793 0.3524	0.0141S2+1.5521S+13.546 0.5184	7.8	17.0	69
July 1994	0.3529S2-21.457S+324.51 0.6255	-0.4111S2+21.21S-216.03 0.2833	0.0583S2+0.2414S-8.459 0.4239	21.7	26.1	54
Four[1,2] Cruises	0.0842S2-7.0184S+141.79 0.4043	-0.2263S2+10.819S-72.401 0.1828	0.1421S2-3.8006S+30.609 0.4511	24	23.5	174
All Cruises	0.0197S2-2.6942S+70.944 0.2982	-0.1203S2+5.3922S-7.3928 0.1332	0.1005S2-2.6981S+36.449 0.2427	21	22.5	297

[1]High flow in July, excluded in "Four cruises"
[2]Cruise track concentrated in Mississippi River plume, excluded in "Four cruises"

salinity and not light quality is the controlling factor. The high relative abundance of PE/HiPUB cyanobacteria in the bottom water (water depths not greater than 30 m) in the summer is particularly indicative that light quality is not playing a major role. These bottom waters are often hypoxic for extended periods of time (Rabalais et al., 1992, 1996a) and, thus, the cyanobacteria are exposed for long periods to water filtered through the turbid, discolored surface layer. Despite exposures of what is likely to be months, these PE/HiPUB cyanobacteria are the brightest yellow and the easiest to distinguish from the PE/LoPUB because of their overall high pigment content at such low light levels. There was no clear relationship with stratification since the stratification was greater on the cruise that was the exception than one of the other cruises. The difficulty may be in combining data from a geographically diverse area in order to compare cruises.

In contrast, the % PC was significantly greater at the surface than at depth on only one cruise (Table 27). There are two alternate explanations for this result. One is that salinity is not the controlling factor. The other is that the distribution of PC-containing cyanobacteria is geographically limited to shallow areas near freshwater sources (see below), where stratification tends not to be as great and salinities are low throughout the water column. The cruise which showed the significant difference was conducted in the plume of the Mississippi River where the river flows out into deep water and stratification is present at all stations.

The data from the northern Gulf of Mexico support the hypothesis that the pigment-types of cyanobacteria can be used as an indicator of different salinities. Whether these differences are genotypic or phenotypic is a matter of some argument (Glover, 1985; Waterbury et al., 1986; Hauschild et al., 1991), but has some bearing on their usefulness as indicators. If these cyanobacteria can adapt chromatically to changes in light quality by changing the ratios of pigment types, then it is necessary to know the time scales on which they adapt. Similarly, if it is genetically determined, it is necessary to know the extremes of conditions that a particular cyanobacterial pigment group can tolerate. Thus, their utility as an indicator of mixing of different types of water is limited by lack of information about time scales. However, for use as an indicator of salinity, in conjunction with satellite remote sensing, they would be extremely useful (see below).

b. Diatoms and *Skeletonema costatum* as Indicators

As mentioned in a preceding section the highest diatom abundances are observed at intermediate salinities (Figure 175a), although low abundances can also occur at intermediate salinities The peak often corresponds to salinities where the water is less turbid and nutrients are almost, but not completely removed. An example for the April 1993 cruise (Cruise IV; Figure 178a) shows the increase in light transmittance with salinity, the decrease in silicate, and a peak in diatom abundance between 20 and 30 psu. This represents the region of optimal conditions for diatom growth during that cruise. At lower salinities light is limiting and at higher salinities one or more nutrients is limiting. The salinity at which the maximal abundances occur varies from cruise to cruise, for reasons that are not entirely clear. Further, the number of samples at intermediate salinities that do not have high abundances is also variable. The reason for this is unclear, but may it be related to the history of individual water parcels and whether sufficient time was available for diatoms to grow before the nutrients became diluted by mixing. Thus, it is likely that high diatom relative abundance indicates regions of high productivity.

Skeletonema costatum is the single most abundant diatom species on the Louisiana/Texas shelf. Maximum abundances approached 1 x 10^8 cells/liter and

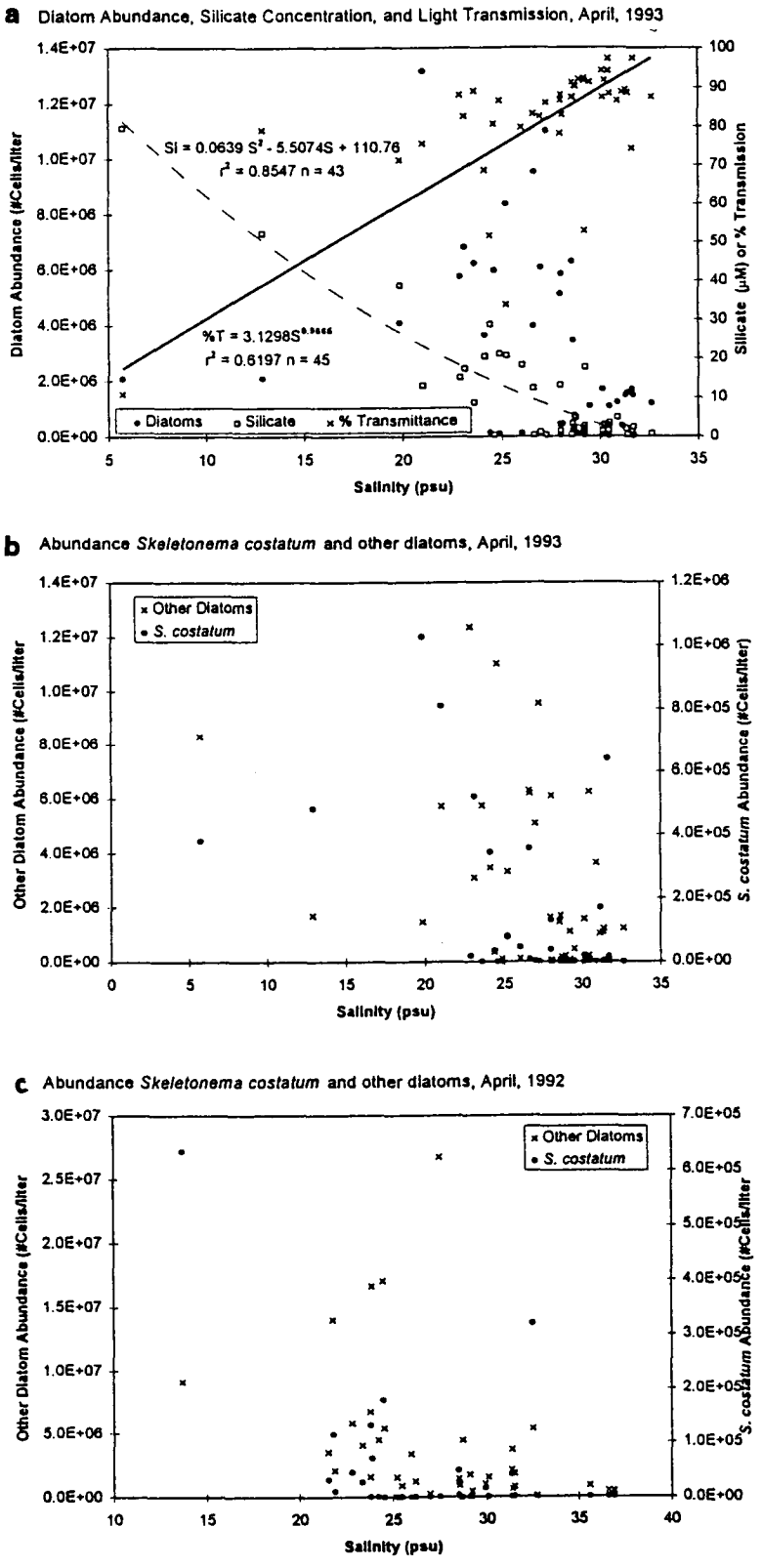

Figure 178. Diatom abundance, silicate concentration, and light transmission vs. salinity at the surface in (a) April 1993, and *Skeletonema costatum* and other diatom abundance vs. salinity at the surface in (b) April 1993 and (c) April 1992.

comprised up to 85% of the total diatoms on the April 1994 (Cruise V) cruise in the plume of the Mississippi River (Table 29). Total numbers and abundance relative to diatoms varies between cruises, but the variation is not obviously seasonal. Often the maximum abundances are observed in the bottom water (Table 29) because this species has very high sedimentation rates after blooms (Dortch et al., 1992). If the conditions which prevail when *S. costatum* is present in the surface water are compared with condtions when *S. costatum* is absent (Table 30), it is apparent that *S. costatum* grows at lower salinities in the eastern part of the study area where and when silicate, DIN, chlorophyll concentrations, and diatom abundances are higher; i.e., it has a preference for areas with riverine influence. From casual observations, it appears to be one of the diatoms that increases first when low salinity water mixes with higher salinity water. To test this observation more rigorously, the abundance of *S. costatum* and, separately, the abundance of all other diatoms was plotted as a function of salinity for a cruise in which *S. costatum* was a large fraction of the diatom population (Figure 178b); April 1993, Cruise IV) and one in which it was a smaller proportion (Figure 178c, April 1992, Cruise II). There is some tendency for the higher concentrations of *S. costatum* to occur at low salinities, although the pattern is not clear cut. Thus, the evidence is equivocal for showing that *S. costatum* indicates conditions substantially different from the total diatom abundance.

Table 29. Abundance (#cells/liter) and relative abundance (% relative to diatom abundance) of *Skeletonema costatum.*

Date	Depth	Abundance			Relative Abundance		n
		Mean	SD	Max	Mean	Max	
April 1992	Surf	5.32×10^4	1.27×10^5	6.34×10^5	0.7	6.5	39
	Bot	9.26×10^4	2.27×10^5	1.21×10^6			40
Oct. 1992	Surf	7.56×10^4	1.9×10^5	9.18×10^5	7.3	58.5	42
	Bot	1.19×10^5	3.66×10^5	1.73×10^6			37
April 1993	Surf	1.15×10^5	2.35×10^5	1.03×10^6	7.0	44.1	46
	Bot	1.25×10^5	2.36×10^5	1.06×10^6			47
July 1993	Surf	3.91×10^4	1.72×10^5	1.06×10^6	2.2	45.5	63
	Bot	1.58×10^4	5.92×10^4	3.84×10^5			67
April 1994	Surf	3.29×10^5	4.97×10^5	2.19×10^6	22.5	85.0	69
	Bot	1.67×10^6	1.14×10^7	8.13×10^7			51
July 1994	Surf	1.16×10^5	2.58×10^5	1.22×10^6	9.6	64.8	61
	Bot	1.31×10^5	3.63×10^5	1.68×10^6			64

Table 30. Comparison of mean (± one standard deviation) conditions that are significantly different (two-tailed, Student's t-test, $p<0.05$) when *Skeletonema costatum* is present and absent in surface water.

	Present			Absent		
	Mean	SD	n	Mean	SD	n
Longitude (°W)	91.6850	2.0844	152	92.7710	1.9789	155
Salinity (psu)	23.42	7.70	152	27.61	5.30	155
Silicate (µM)	21.63	19.30	148	8.38	13.85	148
DIN (µM)	20.24	23.86	141	2.65	2.94	127
Total Diatoms (#Cells/liter)	2.56×10^6	3.56×10^6	152	8.67×10^5	2.59×10^6	155
Chlorophyll *a* (µg/liter)	8.32	9.95	152	3.12	4.09	155
Month	5.42	4.17	152	6.42	4.34	155

c. Indicators and the Coastal Current

It was hypothesized that phytoplankton would indicate specific types of water or areas where specific processes were occurring.

1. High relative abundance of PC-containing cyanobacteria would outline river plumes.
2. High relative abundance of PE/HiPUB-containing cyanobacteria would indicate that off-shore water was intruding on the shelf.
3. There would be strong cross-shelf gradients in relative abundance of cyanobacterial pigment types in the region of the coastal current and more gradual gradients along-shelf to the west as riverine influences decreased.
4. Relative abundance of diatoms would be maximal "downstream" from the highest relative PC-cyanobacterial abundance and indicate the high productivity areas influenced by riverine input.
5. For reasons analagous to the cyanobacteria, there would be strong, cross-shelf gradients in diatoms and more gradual along-shelf gradients.
6. Originally it was proposed that high abundances of *Skeletonema costatum* would indicate the areas where there was an initial response to riverine inputs, but the preceding analysis of the data casts some doubt on its usefulness as an indicator.

The use of these indicators is demonstrated in a series of surface contour plots from a cruise during a period of normal high flow in the spring (Figures 179 and 180; April 1993, Cruise IV) and of normal low flow in the fall (Figures 181 and 182; October, 1992). In all cases except plots of *S. costatum*, relative abundance is used to minimize seasonal differences, so that comparisons between seasons are more meaningful.

In both spring and summer the % PC are highest in the areas adjacent to major freshwater sources (Figure 179). Despite the much higher riverine freshwater input in the spring, the area of high % PC is much larger in summer than in fall; a similar result was obtained for the other cruises (data not shown). The % PE/HiPUB are highest offshore and in the west of the study area (Figure 180), indicating the decreased riverine influence in those areas. Higher % PE/HiPUB are observed over a wider area in the fall compared with spring, consistent with the decreased freshwater input during low flow periods. Neither Figures 179 or 180, nor any of the other cyanobacteria contour plots, show strong cross-shelf gradients, although gradual along-shore gradients consistent with gradual dilution of the riverine influence are observed.

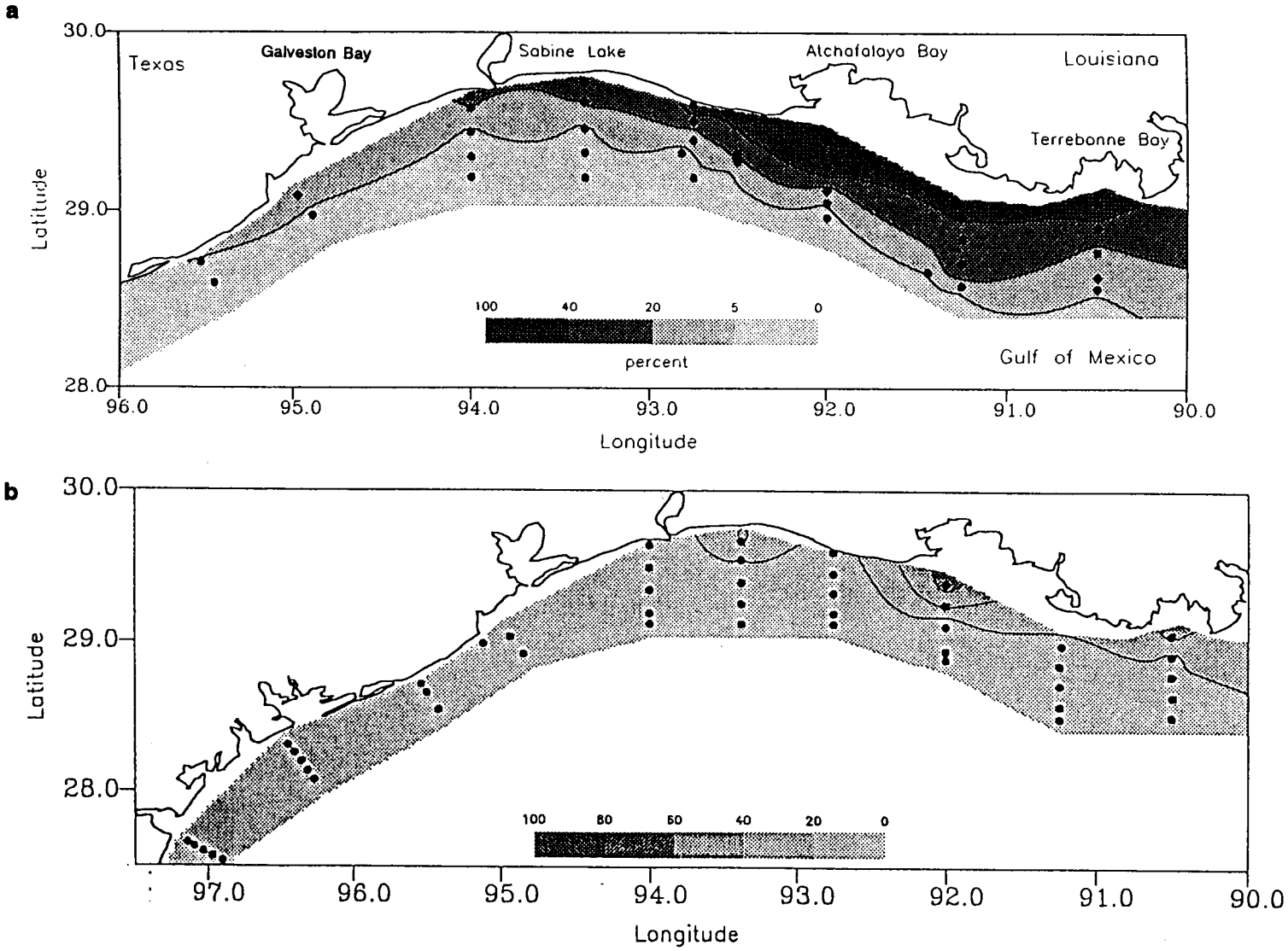

Figure 179. Surface contours of % PC cyanobacteria/Total cyanobacteria (0.2-3 μm size fraction) in (a) October 1992 and (b) April 1993.

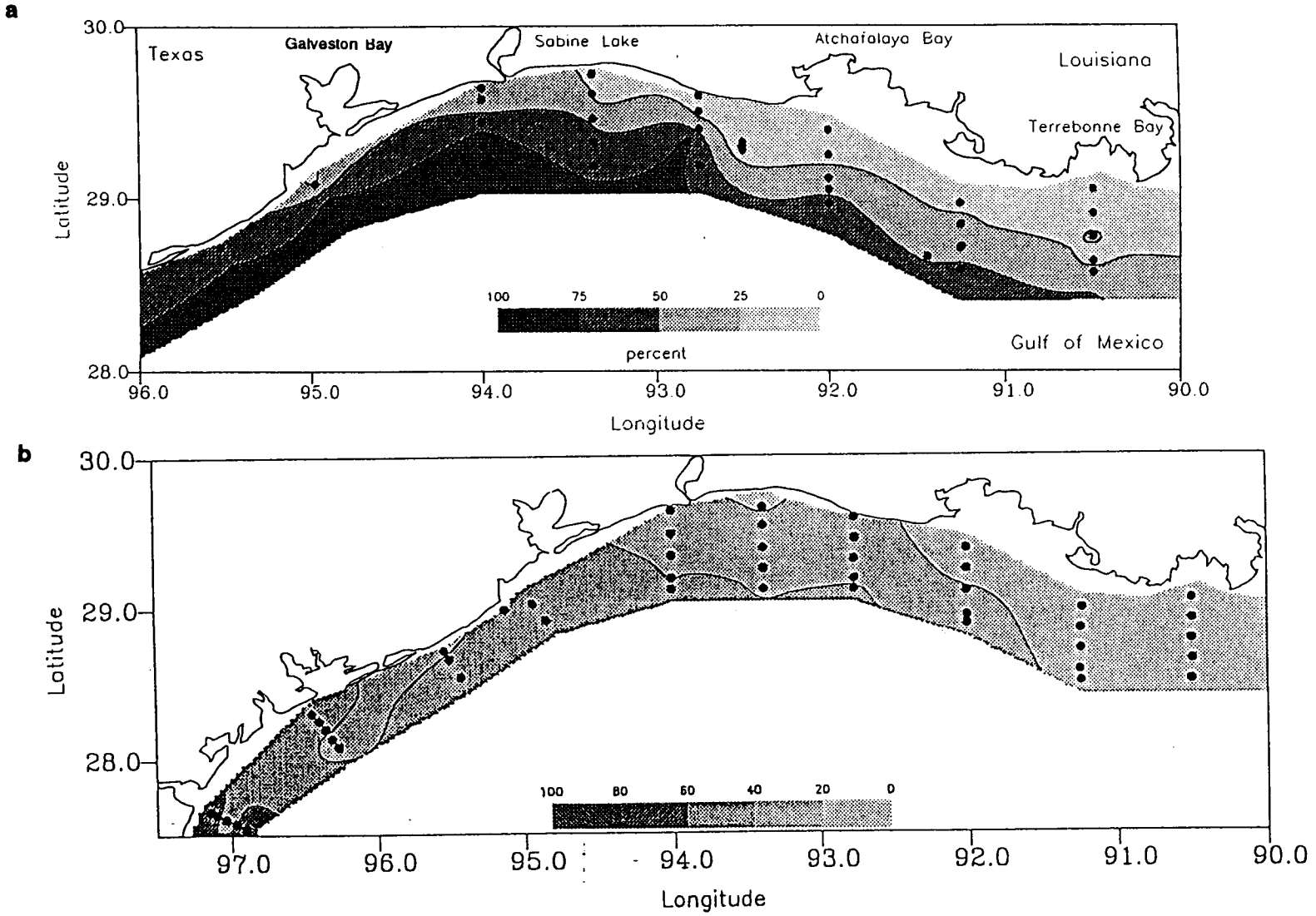

Figure 180. Surface contours of % PE/HiPUB cyanobacteria/Total cyanobacteria (0.2-3 μm size fraction) in (a) October 1992 and (b) April 1993.

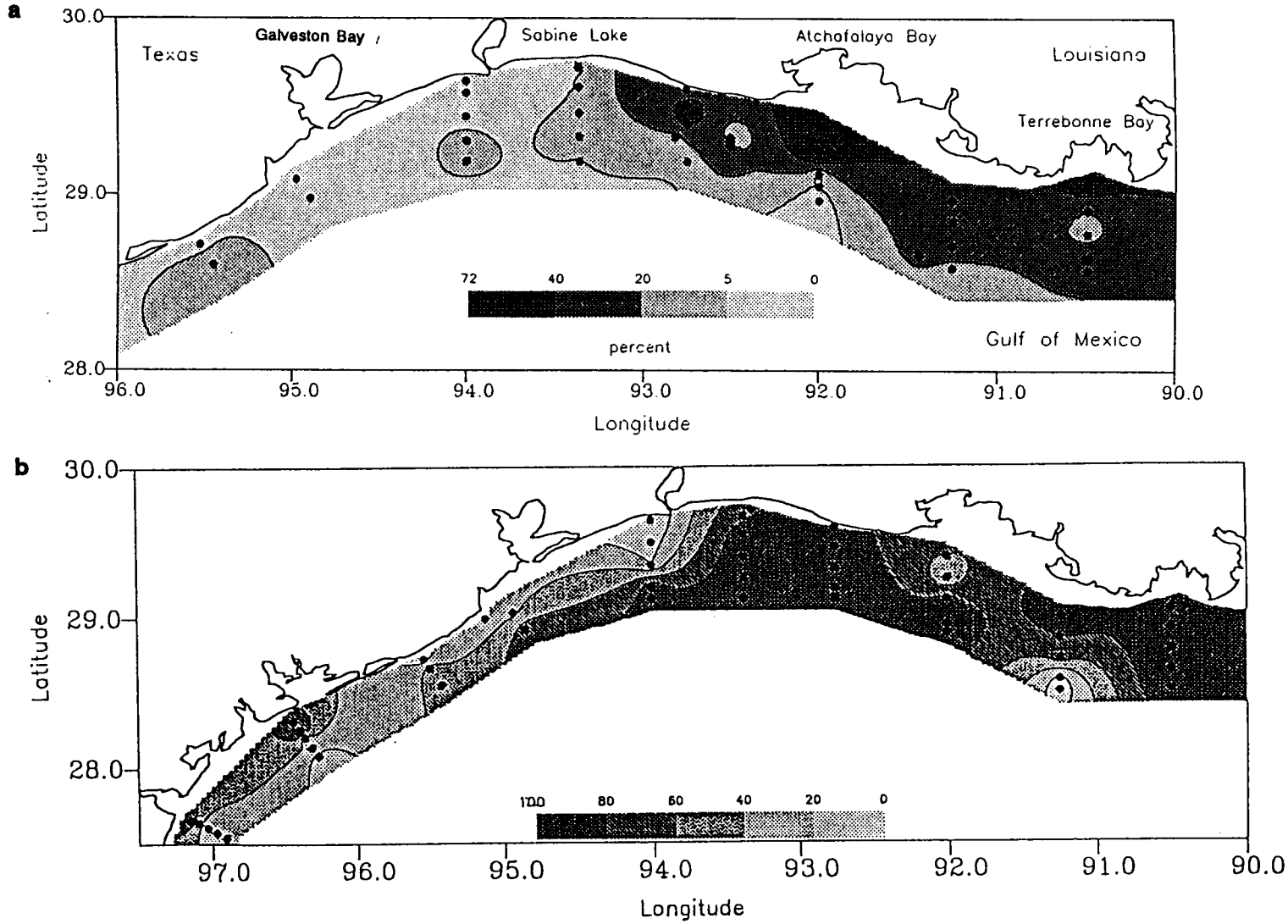

Figure 181. Surface contours of % Abundance Diatoms/Total Phytoplankton (> 8μm) in (a) October 1992 and (b) April 1993.

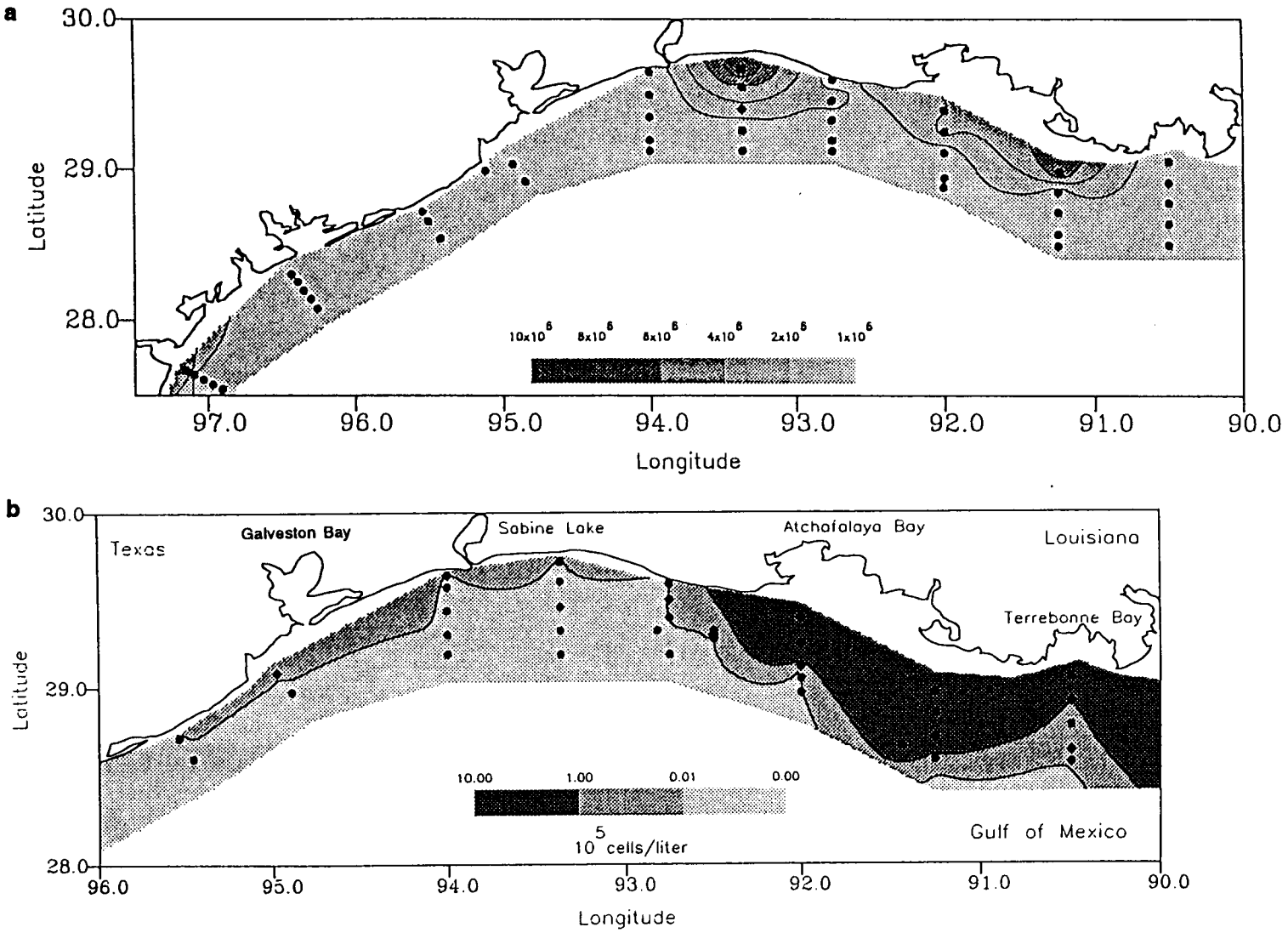

Figure 182. Surface contours of *Skeletonema costatum* in (a) October 1992 and (b) April 1993.

The relative abundance of diatoms is higher in the spring and covers a much larger area than in the fall (Figure 181). In both cases, the areas with highest relative abundances are in areas which are strongly influenced by the Mississippi and Atchafalaya Rivers. In spring, the maximum diatom abundance occurs some distance from the mouth of the Atchafalaya Rivers, reflecting the time required for the turbidity to decrease and nutrient uptake to be initiated during high flow periods. In the spring the lowest abundance of *Skeletonema costatum* exceeded the highest abundance in the fall (Figure 182). High abundances are not necessarily observed in the same places as high relative abundances of diatoms and are generally closer to the freshwater sources. As observed for the cyanobacterial pigment groups, there are no strong cross-shelf gradients in either relative abundance of diatoms or abundance of *S. costatum*, although there are along-shelf gradients which reflect decreasing riverine influence.

The phytoplankton distributions fit the expected patterns in terms of influence by freshwater inputs and seasonality. However, there are no clear cross-shelf gradients which can be attributed to a coastal current that clearly delineates coastal from off-shore water. There are several reasons for this. (1) The coastal current was not a well-defined feature that would be expected to influence plankton populations, as hypothesized. (2) The length of transects often was inadequate, especially in the eastern part of the study area, to cross into truly oligotrophic, oceanic water. (3) The spacing of stations was insufficient to capture really sharp gradients. (4) Many other processes were acting upon the phytoplankton simultaneously, complicating interpretation in terms of the coastal current. For example, wind reversals during some cruises pushed the low salinity plume of the Atchafalaya River south and east, instead of west in the usual way (see below).

d. Cyanobacterial Pigment Groups and Remote Sensing

The relationship between cyanobacterial pigment groups and salinity prompted a comparison between satellite images of AVHRR Seston and surface contours of abundance or relative abundance of cyanobacterial pigment types. Several types of features stood out. The plume of the Atchafalaya River, and to a lesser extent, plumes from the Calcasieu, Sabine, and Galveston estuaries were apparent in both the satellite images and the contours of abundance or relative abundance of PC-containing cyanobacteria. For example, during the July, 1993 cruise, the plume of the Atchafalaya River was pushed offshore and to the east by shifting winds, which is clearly evident in the satellite image and the cyanobacterial contour plots . Another feature that is apparent for many cruises is an area somewhere between Galveston and the Atchafalaya River where less turbid (remote sensing image), higher salinity (% PE/HiPUB) comes very far up onto the shelf. The size and position of the area varied between cruises.

The correspondence between the images and contours is not perfect, for several reasons. (1) Turbidity and salinity would not necessarily be expected to be influenced by the same factors and always covary. (2) The phytoplankton sampling lacks the spatial resolution of the satellite image and was collected over a 7 to 10 period.

What may be more important is the potential use of cyanobacterial pigment types as a remotely sensed indicator of salinity changes in coastal areas with wide variations in salinity, such as the Louisiana/Texas shelf. The SeaWiFS sensors include wavelengths for detecting the PE/HiPUB (490 to 510 nm) and PE/LoPUB (555 to 575 nm) cyanobacteria (Richardson, 1996). If the signals can be detected in the presence of high suspended load and other pigments, their abundance may provide a means of remote sensing salinity, with appropriate ground-truthing. SeaWiFS does not have the capability for detecting PC-cyanobacteria, although other sensors can (Richardson, 1996).

e. Toxic and Noxious Phytoplankton on the LATEX Shelf

A variety of potentialy harmful phytoplankton occur on the Louisiana/Texas shelf (Table 31). The most frequent and most abundant are *Pseudo-nitzschia* spp. Only some species of *Pseudo-nitzschia* produce toxins, and then only under some conditions, but it is impossible to determine if toxin-producing species are present with standard microscopic techniques. Two toxic species have been identified in the area (Fryxell et al., 1990; Dortch et al., submitted; M. Parsons, perssonal communication, 1996). Dortch et al. (submitted) prepared composite seasonal maps, summarizing data from 19 cruises, including the 6 reported here. These showed that the highest concentrations occurred near the Mississippi and Atchafalaya Rivers and in the spring. Surface contour plots of individual cruises show much wider variation in the area where maximum abundance is observed (Figure 183), although the high spring abundance still prevails (Figure 183, Table 31). The maximum abundance in April, 1994 (Cruise V; Table 31) is the highest ever observed, and the abundances overall are a cause for concern if these are the toxin producing species. The high abundances observed on average in the Mississippi and Atchafalaya River plumes is thought to result because of the high riverine nutrient inputs (Rabalais et al., 1996a; Dortch et al., submitted). Because of the usually westward flowing coastal current, any blooms that start near the Mississippi and Atchafalya Rivers can be transported along the entire Louisiana/Texas coast.

Another group which occurs frequently are the *Prorocentrum* and *Dinophysis* spp. (Table 31). None of these species has been directly shown to produce the toxins leading to Diarrhetic Shellfish Poisoning (DSP) but have been present when DSP occurred elsewhere (Rabalais et al., 1995). *P. minimum* has been linked with venerupin poisoning (VP; a type of shellfish poisoning that occurred briefly in Japan from consuming short-necked clams and oysters) elsewhere (Rabalais et al., 1995) and blooms in this area have caused water discoloration (Maples et al., 1981).

Gymnodinium sanguineum occurs sporadically in this area (Robichaux et al., 1996) and was observed on three out of six cruises. On several occasions in the past, it has caused red tides on the Louisiana/Texas shelf that were associated with fish kills, and it is the suspected cause of other mortality events elsewhere (Robichaux et al., 1996). Considerable indirect evidence suggests that *G. sanguineum* forms cysts, and it is suspected that there are cyst beds in estuaries, such as Calcasieu and Sabine, that initiate blooms (Robichaux et al., 1996). Further, when it blooms in one location, it is often present in lower numbers over a wide area. The coastal current may play a major role in transporting blooms derived from cyst beds to new locations.

D. Conclusions

1. The entire size range of phytoplankton was identified and enumerated for the first time in the northern Gulf of Mexico. Such complete identification and enumeration has only been accomplished in a few other studies. Small phytoplankton, primarily cyanobacteria in the 1 to 2 μm size range, dominate numerically. In the spring large diatoms dominate the biomass, but in the summer/fall the biomass of cyanobacteria can equal or exceed that of diatoms. This suggests that this ecosystem, with very high nutrient inputs and high production, is also highly dependent on regenerative processes typical when small phytoplankton dominate.

2. Three pigment-types of cyanobacteria were distinguished for the first time, using routine epifluorescence microscopy. Their distributions were related to variations in salinity, so they serve as indicators of the spatial extent of riverine or estuarine plumes

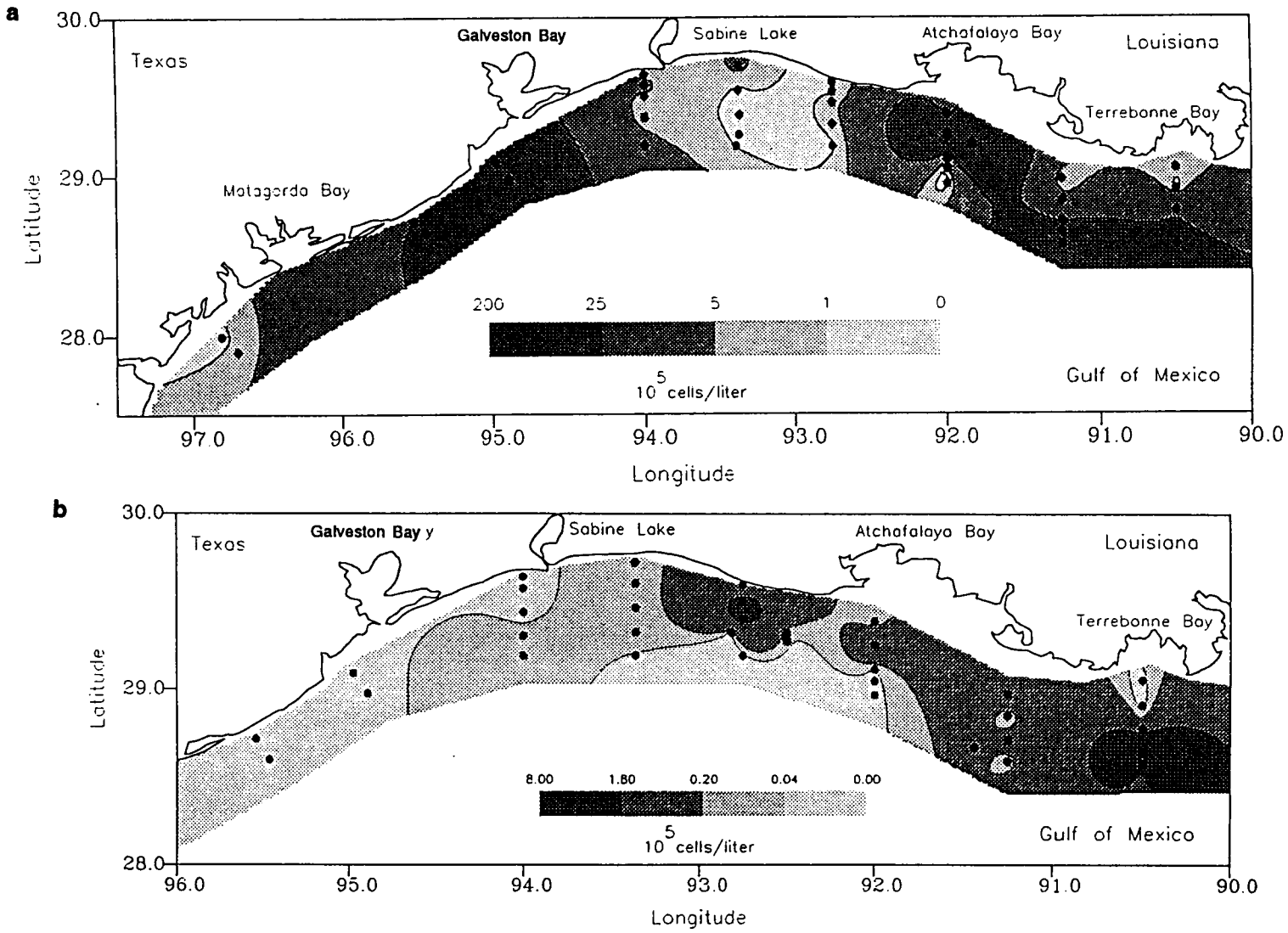

Figure 183. Surface contours of *Pseudo-nitzchia* spp. in (a) April 1992 and (b) October 1992.

or intrusion of off-shore water onto the shelf. It is hypothesized that their unique spectral signatures may be useful for remote sensing of salinity by SeaWiFS in areas with large salinity variations like the northern Gulf of Mexico, if high sediment and other pigment concentrations do not interfere.

3. It was hypothesized that the coastal current would separate coastal and oceanic phytoplankton populations, so that there would be sharp cross-shelf gradients in various indicator groups of phytoplankton in the region of the coastal current. Instead, only gradual cross-shelf gradients were observed in the four phytoplankton indicators used for this analysis: relative abundance of two cyanobacterial pigment groups, relative abundance of diatoms, and abundance of *Skeletonema costatum.*

4. Along-shelf gradients and seasonal differences in phytoplankton indicators showed the changing influence of riverine inputs.

5. These six cruises provided an opportunity for large scale surveys for potentially toxic and noxious phytoplankton. Phytoplankton associated with Amnesic Shellfish Poisoning (ASP), Diarrhetic Shellfish Poisoning (DSP), and fish kills were observed. Details for *Pseudo-nitzschia* spp. (ASP) and *Gymnodinium sanguineum* (fish kills) have been reported elsewhere (Robichaux et al., 1996; Dortch et al., submitted). It is hypothesized that the coastal current could transport blooms or cysts of toxic and noxious species long distances on the Louisiana/Texas shelf, magnifying their potential impact.

Table 31. Maximum abundance (#Cells/liter) and % frequency of occurrence (% Freq = #samples with taxon/total # samples x 100) of toxic and noxious phytoplankton obsrved during cruises. A ? by Problem indicates that there is evidence implicating this species in causing this problem, but the link is not conclusive.

Taxon	April 1992	Oct 1992	April 1993	July 1993	April 1994	July 1994	Problem[1]
Pseudo-nitzschia spp.							
Max	2.47 x 106	8.37 x 105	4.40 x 106	8.89 x 104	1.01 x 108	2.19 x 105	ASP
% Freq	94.9	88.6	96.8	47.7	93.3	44.0	
Prorocentrum compressum							
Max	7.73 x 104	5.64 x 104	8.18 x 104	2.47 x 104	4.06 x 105	3.48 x 104	DSP?
% Freq	79.7	39.2	79.6	53.9	45.8	14.4	
Prorocentrum micans							
Max	6.90 x 104	7.74 x 104	3.25 x 104	7.55 x 103	3.00 x 103	2.77 x 104	DSP?
% Freq	40.5	38.0	54.8	32.3	0.83	4.00	
Prorocentrum minimum							
Max	1.48 x 103	0	0	0	8 x 102	0	DSP?
% Freq	2.53	0	0	0	4.2	0	VP Discolored Water
Dinophysis caudata							
Max	6.21 x 104	1.10 x 103	6.67 x 102	5.41 x 103	1.00 x 103	1.86 x 103	DSP?
% Freq	10.1	19.0	8.6	27.7	0.8	6.4	
Dinophysis ovum							
Max	7.63 x 103	6.63 x 103	4.00 x 102	2.4 x 101	0	0	DSP?
% Freq	1.3	1.3	4.3	0.8	0	0	
Gymnodinium sanguineum							
Max	0	0	1.66 x 103	2.99 x 103	0	5.32 x 102	Ichthyotoxic
% Freq	0	0	9.7	14.6	0	3.0	Oyster mortality Hypoxia
Ceratium spp.							
Max	3.39 x 103	6.63 x 102	3.25 x 103	9.44 x 103	6.76 x 103	9.55 x 103	DSP
% Freq	36.7	16.4	39.8	37.7	2.5	37.6	Hypoxia
Oscillatoria sp.							
Max	5.52 x 105	2.80 x 103	0	1.73 x 106	0	0	Ichthyotoxic
% Freq	16.7	0.8	0	16.9	0	0	Discolored Water

[1]ASP=Amnesic Shellfish Poisoning; DSP=Diahretic Shellfish Poisoning, VP=Villirupin Poisonin. See Hallegraeff (1993) for descriptions and Rabalais et al. (1995) for evidence of problems.

VIII. Zooplankton and Ichthyoplankton

Richard F. Shaw, Joseph S. Cope, James G. Ditty, and Talat Farooqi

A. Introduction

Historically, the Gulf of Mexico (GOM) has supported large shellfish and finfish fisheries in both the commercial and recreational sectors. Estimates of commercial catch from U.S. Department of Commerce (1992a) reveal the GOM accounted for 17% of the total U.S. shellfish and finfish catch in pounds and 72% of the total U.S. shrimp catch in pounds. About 40% of the nation's saltwater anglers and 50% of the recreational catch are concentrated in the southeastern U.S. (Schmied and Burgess, 1987) and over 35% of this regional total recreational catch is attributable to the GOM (U.S. Department of Commerce, 1992a). Considering the magnitude of these fisheries and their corresponding economical importance, it is unsettling to note that of the 80 species considered by the U.S. Department of Commerce (1992b) as important marine resources in GOM, 33% are overfished, while the utilization status of 54% is unknown.

Information on distributional and temporal patterns of holoplankton and the planktonic stages of shellfish and finfish is important for a better understanding of ecological/trophic dynamics and for the future management of these valuable fisheries. Zooplankton research in the shelf-waters of GOM has been reviewed by Hopkins (1973) and Iverson and Hopkins (1981). However, current knowledge of how these biological resources relate to dominant physical/chemical parameters at a large spatial (> 500 km) and temporal scale (i.e., years), is limited. With the notable exception of Arnold (1958), most studies have been site-specific or conducted within state waters (Davis, 1950; King, 1950; Angelovic et al., 1976; Park et al., 1976; Park, 1977, 1979; Park and Minello, 1980; Steen and Gunter, 1980; Vecchione et al., 1982; Vecchione et al., 1983; Wolff et al., 1984; Dagg et al., 1988; Rogers et al., 1993). A similar argument can be made for most ichthyoplankton studies (Finucane, 1976; Finucane et al., 1977, 1979a, 1979b; McGowan, 1985; Shaw et al., 1985a, 1985b, 1988; Cowan and Shaw, 1988, 1991; Govoni et al., 1989; Shaw and Drullinger, 1990a; Grimes and Finucane, 1991; Lang et al., 1994), with the exception being Sogard et al., 1987; Al-Yamani, 1988; and Ditty et al., 1988, and those analyses utilizing NOAA/NMFS Southeast Monitoring and Assessment Program (SEAMAP) data (Richards et al., 1984; Kelley et al., 1986; Shaw and Drullinger, 1990b; Ditty and Shaw, 1992, 1993, 1995; Ditty et al., 1994a, 1994b, 1994c). This report investigates zooplankton and ichthyoplankton species assemblages and pertinent biological and environmental variables collected from the Louisiana and Texas mid- to inner-shelf waters during six cruises over a three-year period (1992-1994).

B Materials And Methods

1. Field

Oblique plankton tows were made with a 60-cm bongo frame with 153- and 335-μm mesh nets. Each bongo net was fitted with a torpedo-type (General Oceanics) flowmeter for volume-filtered estimates. The 153-μm samples were initially fixed in 4% formaldehyde and later transferred to 70% ethanol. The 335-μm samples were preserved in 70% ethanol and transferred to fresh ethanol 24 hour later.

2. Laboratory

In the following procedures, samples were split with a Folsom plankton splitter (McEwen et al., 1954) and the identified and enumerated split was randomly selected. Dry weights (mg) were determined for all samples by oven-drying half samples at 60° C to constant weight (Lovegrove, 1966). Plankton biomass estimates ($\mu g/m^3$) were calculated as:

$$\text{Plankton Biomass} = 2 \times \text{Dry Weight} / \text{Volume Filtered.}$$

Zooplankton composition was determined at every other station from the 153-μm samples. Commercially important decapods (i.e., penaeids and portunids) were identified from half samples. Subsequent enumeration of the remaining zooplankton was conducted on samples that were split repeatedly until a subsample contained at least 200 organisms. Identification was made to the lowest taxonomic level possible. Squid and larval fish were removed from half samples of all 335-μm collections and were identified to the lowest taxonomic level possible. If a 335-μm mesh sample was not available at a particular station, the 153-μm sample was sorted. For each station, ichthyoplankton ($\#/100\ m^3$) and/or zooplankton density ($\#/m^3$) was calculated for each taxon as:

$$\text{Species Density} = \text{Constant} \times 2^A \times \#\ \text{Species}_x / \text{Volume Filtered,}$$

where Constant = 100 for ichthyoplankton or 1 for zooplankton; $\#\ \text{Species}_x$ = the number of individuals of the x^{th} species counted at that station; and A = number of splits.

3. Analytical

Canonical correlation analysis was used to determine interrelationships between species densities and environmental variables (Gittins, 1985). Environmental variables included chlorophyll *a* concentration (μg/L), water depth (m), heterotroph density (cells/mL), longitude (degree N), salinity (‰), and temperature (° C). Chlorophyll *a* concentration and heterotroph density were determined at surface, mid-water, and near-bottom depths and were averaged for each station. Filtered extracts were measured for chlorophyll *a* on a Turner Model 10 fluorometer (Rabalais). Heterotrophs were counted from aliquots under a microscope (Dortch) and consisted of single celled, non-photosynthetic organisms (mostly flagellates and ciliates). Water column-averaged salinity and temperature values were obtained from CTD data; however, graphics used to illustrate water density, salinity, and temperature contours made use of surface values obtained from a flow-through system (MIDAS). Two analyses, April 1992-93 and July 1993-94, included year as a variable. Plankton biomass estimates, as determined from dry weight of the 153-μm samples, were included in the larval fish canonical analyses. Separate analyses were conducted on zooplankton and larval fish densities. Selection of zooplankton species was made by inspection of overall density and frequency of occurrence; however, special consideration was given to Penaeidae and Portunidae taxa. All fish species present at more than 25% of the stations were considered in the larval fish analyses. In order to help normalize distributions and to lessen the influence of extreme values, species densities were transformed by ln(X+1), where X=species density (Jongman et al., 1987). Independence and dimensionality was evaluated by Wilks' likelihood ratio (L) with p environmental variables, q species variables, and n observations (i.e., stations). A canonical root was considered significant at a=0.05 by way of an F*-approximation (SAS Institute, Inc., 1989), where P[F>F*] is the probability of a value greater than the calculated (F*) value. Since the likelihood ratio test is conservative (Gittins, 1985), all significant roots and the first non-significant root were interpreted. An environmental variate was interpreted by the canonical weights of its standardized coefficient vector and by its intraset structure

correlations. The importance of an environmental variable was based on the absolute value of its weight relative to the weights of the other environmental variables, and on the magnitude of its correlation with the environmental variate, with the sign of the correlation indicating if the variable was directly (positive) or inversely (negative) related with the variate. The canonical variate scores of each environmental variate were plotted at the position of each station to verify the interpretation of that variate. Interset structure correlations were used to determine how each species was related to environmental variate. A species was considered to be related to the variate if the absolute value of the interset correlation was greater than 0.387 (i.e., the variate predicted 15% or more of the species variation within the model).

C. Results And Discussion

1. April

One hundred and seventeen stations were sampled during three April cruises (1992-94), a time period normally associated with high Mississippi/Atchafalaya discharge. Copepoda was the most abundant organism in the 57 samples analyzed for zooplankton, comprising 72% of the mean catch. Of this percent, Calanoida made up 55%, Cyclopoida 13%, and both Harpacticoida and copepod nauplii 4%. Other dominant forms included Appendicularia (*Oikopleura*; 6%), Sagittoidea (Sagittidae; 3%), Thaliacea (mostly Doliolidae; 3%), Cirripedia nauplii and cyprids (3%), and Mollusca (Bivalvia and Gastropoda, 3%).

All stations were analyzed for larval fish. Engraulidae was the most abundant taxa, comprising 45% of the mean catch, followed by Sciaenidae (19%). High abundance of engraulids in April collections was also noted by Ditty (1986) off the Louisiana coast. Bothidae (5%), Gobiidae, Clupeidae, and Bregmacerotidae (all 4%) were also common.

The following text briefly describes results of the April 1992 and 1993 cruises. These cruises are then combined in the canonical analysis. The April 1994 cruise is analyzed separately as this cruise was conducted mainly off Southwest Pass (Mississippi River Delta) and did not cover the same geographic range as the other two cruises.

a. April 22-28, 1992

Thirty-four biological stations were sampled during the April 1992 cruise. This particular April was characterized by unusually low Mississippi/Atchafalaya discharge. In contrast, Texas experienced large amounts of precipitation and substantial local flooding, which was manifested by locally reduced salinities over the inner shelf. Samples were collected from Timbalier Bay, Louisiana, to Aransas Pass, Texas, nearly the southwestern-most portion of the Mississippi/Atchafalaya plume's range. Water column-averaged temperatures ranged from 21.3 to 24.5° C , with low values occurring off Galveston Bay, Texas. Salinity ranged from 14.7 to 35.7‰, with low values nearshore in the central portion of the cruise.

(1) Zooplankton For the 153-μm net, zooplankton biomass tended to be high between Galveston and Matagorda Bay, Texas and at nearshore stations off Atchafalaya Bay, ranging from 20 to 1122 $\mu g/m^3$. For the 335-μm samples, zooplankton biomass was high at most nearshore stations, ranging from 4 to 149 $\mu g/m^3$. Zooplankton composition was determined for 17 stations. *Acartia tonsa* ($3024/m^3$), *Oikopleura* spp. ($1247/m^3$), and *Paracalanus crassirostris* ($1000/m^3$) were the most abundant and were present at all zooplankton stations (Table 32).

Table 32. Mean density (#/m^3) of zooplankton species caught during LATEX B cruises. Numbers in parentheses represent standard error of density estimate and number of positive stations, respectively. Also given in the last three rows are number of stations, total volume filtered, and average volume filtered, respectively, for each cruise. Mean density was calculated over all stations for each cruise. Cephalopods listed near the end of the table were identified at all biological stations (see last three rows of Table 2 for cruise statistics).

Taxon	April 1992	October 1992	April 1993	July 1993	April 1994	July 1994
Dinoflagellida	80.2 (44.8 ;4)	-	-	-	5.2 (5.2 ;1)	-
Foraminiferida	6.5 (4.5 ;2)	-	4.3 (4.3 ;1)	-	-	-
CLASS HYDROZOA	-	-	-	0.3 (0.3 ;1)	-	7.4 (6.8 ;2)
ORDER HYDROIDA	61.4 (26.9 ;11)	-	99 (69 ;10)	-	4.7 (3.5 ;2)	-
ORDER SIPHONOPHORA	7.7 (4.7 ;4)	-	2.9 (2.2 ;2)	-	7.5 (4.2 ;4)	-
Muggiaea kochi	18.2 (10.7 ;3)	-	6.9 (5.8 ;2)	-	5.5 (2.6 ;4)	4.1 (2.6 ;3)
Abylidae	-	-	0.3 (0.3 ;1)	-	-	-
Enneagonum spp.	-	-	-	-	0.7 (0.7 ;1)	-
PHYLUM CTENOPHORA	5.4 (3.3 ;3)	-	47.6 (26 ;5)	-	-	-
PHYLUM NEMERTINEA (pilidium)	1.5 (1.5 ;1)	-	0.5 (0.5 ;1)	-	-	-
CLASS POLYCHAETA (trochophore)	24.9 (15 ;5)	118.8 (39.5 ;18)	144.5 (39.3 ;16)	296.5 (83.9 ;19)	122.9 (32 ;18)	59.6 (18.9 ;14)
POLYCHAETA sp.A (trochophore)	92.4 (40.6 ;10)	-	115.7 (56.3 ;8)	-	-	-
POLYCHAETA sp.C (trochophore)	1.2 (1.2 ;1)	-	-	-	-	-
Spionidae (trochophore)	0.5 (0.5 ;1)	-	0.3 (0.3 ;1)	-	-	-
Chaetopteridae sp.A (trochophore)	1.8 (1.8 ;1)	-	-	-	-	-
Tomopteris spp.	-	-	-	-	8.4 (4.1 ;5)	2.5 (1.9 ;2)
Nereidae (trochophore)	2.8 (2.8 ;1)	-	-	-	-	-
CLASS BIVALVIA (veliger)	428.6 (248.2 ;9)	191.3 (59.6 ;16)	239.4 (62.6 ;17)	2989.1 (2633.9 ;19)	43.7 (10 ;16)	72.2 (18.6 ;13)
CLASS GASTROPODA (veliger)	175.1 (72.5 ;14)	47.7 (13.4 ;12)	349.5 (102.8 ;21)	68.1 (22.8 ;13)	60.9 (13.6 ;17)	111.7 (36.4 ;15)
Creseis spp.	2 (2 ;1)	1.9 (1.2 ;3)	-	543.4 (299.2 ;18)	-	6.8 (5.1 ;3)
Creseis virgula	-	-	1.2 (1.2 ;1)	-	6.9 (4.2 ;3)	-
Penilia avirostris	417.2 (242.9 ;7)	11.1 (5.4 ;4)	49.3 (29 ;4)	42.1 (22.8 ;6)	14.5 (8.1 ;4)	400.7 (214.8 ;9)
Evadne spp.	40.8 (29.9 ;3)	-	2.7 (1.9 ;2)	-	-	-
Evadne tergestina	14.3 (8.3 ;3)	-	29.5 (12.8 ;5)	155 (148.1 ;4)	-	41 (20.7 ;7)
Podon spp.	9 (6.5 ;2)	-	33.4 (32.1 ;4)	-	-	-
CLASS COPEPODA	8.6 (5.2 ;3)	-	1 (1 ;1)	-	-	-
COPEPODA (nauplius)	368.3 (164.5 ;16)	348.7 (75.7 ;20)	379.1 (63.2 ;21)	221.7 (46.4 ;19)	509.1 (75.3 ;19)	160.6 (37.5 ;15)
COPEPODA sp.1	-	-	-	1.5 (1.5 ;1)	-	1.9 (1.2 ;3)
ORDER CALANOIDA	171.2 (93.7 ;9)	111.4 (32.5 ;18)	6 (3.6 ;4)	259.8 (71.2 ;21)	8.1 (3.4 ;5)	246.2 (91.8 ;16)
CALANOIDA sp.A	1.2 (1.2 ;1)	-	-	-	-	-
CALANOIDA sp.B	2.1 (2.1 ;1)	-	-	-	-	-
CALANOIDA sp.1	-	-	-	1.1 (1.1 ;1)	-	0.7 (0.7 ;1)
CALANOIDA sp.2	-	-	-	3.3 (3.3 ;1)	-	-
CALANOIDA sp.3	-	2.8 (2.8 ;1)	-	-	-	-
CALANOIDA sp.4	-	0.4 (0.4 ;1)	-	-	-	-
Calanidae	-	-	-	-	0.5 (0.5 ;1)	-

Table 32, cont'd.

Nannocalanus minor	-	-	-	1.6 (1.6 ;1)	3.1 (1.4 ;4)	0.5 (0.5 ;1)
Undinula vulgaris	-	7.5 (5.7 ;4)	-	-	1.2 (1.2 ;1)	3.2 (2.1 ;3)
Eucalanus spp.	7.1 (6 ;2)	24.7 (10.9 ;8)	2.8 (2.3 ;2)	2.3 (2.3 ;1)	3.7 (3.7 ;1)	19.8 (5.9 ;10)
Eucalanus crassus	-	9.2 (4.4 ;5)	-	-	5.2 (2.3 ;5)	-
Eucalanus pileatus	56.6 (28.9 ;5)	193.7 (55.7 ;17)	66 (26.7 ;8)	154.2 (46.1 ;14)	428.9 (64.9 ;18)	102.1 (34.9 ;12)
Rhincalanus cornutus	-	-	0.3 (0.3 ;1)	-	-	0.2 (0.2 ;1)
Acrocalanus longicornis	-	2.8 (2.8 ;1)	-	-	-	-
Paracalanus spp.	6.3 (6.3 ;1)	218.9 (74.8 ;17)	-	688.2 (163.5 ;22)	-	194.6 (56.2 ;13)
Paracalanus crassirostris	1000.1 (267.5 ;17)	2340.3 (765.7 ;20)	2288.4 (494.7 ;21)	5644.7 (1473 ;24)	639.6 (145.1 ;19)	757.6 (311.7 ;14)
Paracalanus parvus	314.5 (88.3 ;15)	696.2 (198.3 ;18)	2209.4 (479 ;19)	974.8 (369.6 ;20)	807.5 (106.2 ;18)	186.6 (57.7 ;12)
Calocalanus spp.	-	-	-	0.7 (0.7 ;1)	15.7 (5.7 ;9)	8 (4.8 ;4)
Calocalanus pavo	-	2.6 (2.6 ;1)	-	7.7 (6 ;3)	-	-
Calocalanus pavoninus	-	-	-	1.6 (1.6 ;1)	-	-
Clausocalanus spp.	2.1 (2.1 ;1)	-	6.2 (4.2 ;3)	-	49.3 (22.1 ;9)	-
Clausocalanus arcuicornis	-	-	-	1.7 (1.7 ;1)	-	-
Clausocalanus furcatus	-	22 (16.4 ;2)	-	-	-	-
Aetideidae	-	-	-	-	2.2 (1.5 ;2)	-
Euchirella spp.	-	-	-	-	1.4 (1.4 ;1)	-
Euchaeta spp.	-	-	-	1.7 (1.7 ;1)	-	-
Euchaeta marina	-	2.8 (2.8 ;1)	0.6 (0.6 ;1)	-	5.3 (3 ;3)	0.9 (0.9 ;1)
Temora spp.	6.6 (6.3 ;2)	178.7 (77.2 ;16)	5.3 (2.6 ;4)	134.8 (67.7 ;15)	-	33.2 (19.6 ;6)
Temora stylifera	9.6 (7.2 ;2)	22.8 (7.7 ;9)	573.8 (264.5 ;13)	4.3 (2.6 ;3)	17.5 (5.1 ;10)	36.4 (15.5 ;9)
Temora turbinata	270 (74.7 ;14)	389 (104.9 ;19)	1126 (351.6 ;18)	513.9 (175.2 ;17)	83.2 (22.6 ;15)	679.4 (351.8 ;13)
Centropages furcatus	15.1 (8.4 ;5)	309.2 (76.3 ;19)	150.1 (41.9 ;14)	520.1 (97.7 ;20)	240.5 (45.9 ;18)	545.8 (91.3 ;16)
Lucicutia flavicornis	-	1.1 (1.1 ;1)	-	-	3.1 (1.3 ;5)	4.4 (2.7 ;3)
Candacia spp.	-	-	-	-	1.7 (1.2 ;2)	-
Candacia curta	-	1.1 (1.1 ;1)	-	-	-	-
Candacia longimana	-	-	-	-	-	0.5 (0.5 ;1)
Candacia pachydactyla	-	-	-	-	-	0.2 (0.2 ;1)
Calanopia americana	-	42.2 (20.9 ;11)	0.5 (0.5 ;1)	86.8 (32.8 ;10)	-	3 (2.5 ;2)
Labidocera spp.	8.4 (4.5 ;4)	93.7 (30.9 ;13)	246.2 (57.7 ;18)	5.8 (5.8 ;1)	56.3 (19 ;14)	-
Labidocera acutifrons	1.5 (1 ;2)	-	5.9 (4.1 ;3)	-	2.9 (2.2 ;2)	-
Labidocera aestiva	48.9 (12.4 ;11)	96.1 (34.8 ;12)	93.2 (33 ;12)	67.5 (26 ;9)	5.5 (4 ;2)	111.5 (57.8 ;13)
Labidocera nerii	1.2 (1.2 ;1)	-	5.9 (3.7 ;3)	-	0.7 (0.7 ;1)	-
Labidocera scotti	13.2 (7.7 ;4)	-	15.5 (6.7 ;6)	-	1.9 (1.4 ;2)	-
Acartia spp.	21.7 (21.7 ;1)	2423.1 (1292.6 ;14)	-	3767.5 (1419.2 ;22)	-	2.3 (1.9 ;2)
Acartia lilljeborgi	-	21.1 (21.1 ;1)	-	255.8 (150.2 ;5)	-	-
Acartia tonsa	3023.5 (796.4 ;17)	2626.3 (1389.8 ;13)	7565.6 (1940.7 ;20)	3753.1 (1842.4 ;21)	1896.2 (599 ;19)	4496.6 (3143.1 ;11)
ORDER HARPACTICOIDA	0.7 (0.7 ;1)	-	4.4 (3.2 ;2)	-	3.3 (2.7 ;2)	-
HARPACTICOIDA sp.A	3.6 (3.6 ;1)	-	-	-	-	-
HARPACTICOIDA sp.1	-	-	-	3.3 (3.3 ;1)	-	-
HARPACTICOIDA sp.2	-	3.4 (2.8 ;2)	-	-	-	-
HARPACTICOIDA sp.3	-	0.6 (0.6 ;1)	-	-	-	-
Longipedia helgolandica	-	-	-	-	-	0.5 (0.5 ;1)
Microsetella spp.	-	-	-	-	3.3 (2.7 ;2)	-
Microsetella sp.1	-	-	-	4 (4 ;1)	-	-

Table 32, cont'd.

Microsetella norvegica	-	-	-	1 (1 ;1)	-	-
Microsetella rosea	-	3.7 (2.7 ;2)	-	2.3 (2 ;2)	-	-
Clytemnestra scutellata	-	24 (8.3 ;8)	-	-	0.7 (0.7 ;1)	-
Macrosetella gracilis	-	0.4 (0.4 ;1)	-	2 (2 ;1)	-	-
Euterpina acutifrons	187.8 (50.5 ;12)	259.3 (69.1 ;18)	188.7 (43.6 ;16)	186.3 (48.8 ;19)	804.5 (127 ;18)	233.7 (84.1 ;16)
ORDER CYCLOPOIDA	16.3 (12.6 ;4)	14.4 (4.8 ;7)	-	473.7 (203.5 ;15)	0.4 (0.4 ;1)	3.8 (1.7 ;5)
CYCLOPOIDA sp.1	-	-	-	0.7 (0.7 ;1)	-	2.9 (2.3 ;2)
CYCLOPOIDA sp.2	-	2.6 (1.5 ;3)	-	-	-	-
Oithona spp.	792 (389.6 ;15)	-	1358.5 (313.3 ;20)	1.6 (1.6 ;1)	417.3 (122.9 ;19)	0.9 (0.9 ;1)
Oithona brevicornis	-	1424.8 (437.2 ;19)	-	2904.5 (717 ;22)	-	562.8 (113.7 ;17)
Oithona nana	-	-	-	125.1 (125.1 ;1)	-	-
Oithona plumifera	2.1 (2.1 ;1)	80.5 (38.1 ;9)	18.7 (8.4 ;6)	80 (32.1 ;10)	101.6 (19 ;16)	57.3 (22.1 ;8)
Oithona simplex	-	9.6 (5 ;4)	-	-	-	-
Saphirella spp.	2.1 (2.1 ;1)	-	3.3 (2.4 ;2)	-	4.1 (3.4 ;2)	-
Saphirella sp.1	-	-	-	1 (1 ;1)	-	6.8 (6.8 ;1)
Saphirella sp.2	-	1.4 (0.8 ;3)	-	5.9 (3.8 ;3)	-	-
Saphirella tropica	-	-	-	6.2 (6.2 ;1)	-	-
Oncaea spp.	92.8 (48.2 ;10)	-	72.8 (19.8 ;11)	26.5 (16.6 ;3)	404.4 (68.1 ;18)	8.5 (8.5 ;1)
Oncaea sp.1	-	3.2 (1.8 ;3)	-	-	-	3.7 (3.7 ;1)
Oncaea venusta	-	468.3 (154.9 ;16)	80.7 (26.9 ;13)	262.8 (77.6 ;17)	24.6 (6.5 ;10)	292.7 (101.4 ;15)
Copilia mirabilis	-	-	-	-	5.2 (3.7 ;4)	1.1 (0.6 ;3)
Sapphirina spp.	0.8 (0.8 ;1)	-	0.6 (0.6 ;1)	-	2.5 (1.8 ;2)	-
Sapphirina angusta	-	-	-	5.7 (5.7 ;1)	-	0.3 (0.3 ;1)
Sapphirina nigromaculata	-	6.2 (3.6 ;4)	-	-	7.8 (4.7 ;4)	2.2 (1.9 ;2)
Corycaeiidae	-	49.5 (28.9 ;9)	-	122.4 (36.5 ;15)	-	60.7 (38.1 ;7)
Corycaeus spp.	164.1 (68.4 ;15)	-	428.1 (79.4 ;17)	-	696.8 (112.3 ;18)	-
Corycaeus sp.1	-	7.6 (3.5 ;5)	-	10.2 (8.2 ;2)	-	1.7 (1.7 ;1)
Corycaeus amazonicus	-	83.8 (27.1 ;12)	-	168.2 (38.3 ;17)	-	160.1 (39.7 ;14)
Corycaeus latus	-	-	-	0.7 (0.7 ;1)	-	-
Corycaeus lautus	-	1.3 (1.3 ;1)	-	-	-	-
Corycaeus limbatus	-	-	-	-	-	0.2 (0.2 ;2)
Corycaeus subulatus	-	24.2 (8.3 ;8)	-	29.4 (19.5 ;4)	-	16.7 (13.2 ;4)
Farranula gracilis	-	10.2 (4.9 ;4)	-	6.4 (5.2 ;2)	-	14 (13.6 ;2)
Caligus spp.	-	-	-	-	-	1.5 (0.9 ;3)
CLASS CIRRIPEDIA (nauplius)	75.9 (24.6 ;13)	54.2 (20.8 ;9)	571 (295.7 ;17)	12.5 (8.8 ;3)	122.5 (23.2 ;16)	19.2 (9 ;7)
CLASS CIRRIPEDIA (cypris)	93.9 (22.2 ;15)	3.8 (1.7 ;5)	135.2 (51.8 ;12)	449.3 (375 ;10)	21.5 (9.7 ;5)	121.8 (47.6 ;13)
CLASS OSTRACODA	10.3 (10.3 ;1)	35.2 (13.2 ;8)	5.9 (4.9 ;2)	11.2 (7.1 ;4)	4.5 (3.1 ;2)	28.1 (18.9 ;6)
Euconchoecia chierchiae	20.6 (20.6 ;1)	149.5 (48.1 ;15)	29.4 (16.6 ;4)	95.7 (57.9 ;7)	22.7 (7.5 ;11)	26.5 (13.1 ;6)
Squillidae (pseudozoea)	1.5 (1.5 ;1)	-	11.8 (11.8 ;1)	-	-	-
Squilla spp. (pseudozoea)	-	0.3 (0.3 ;1)	-	1.6 (1.6 ;1)	-	2.9 (2 ;2)
Mysidae	-	-	3.1 (3.1 ;1)	-	5.6 (4.1 ;2)	-
Americamysis stucki	-	0.8 (0.8 ;1)	4 (4 ;1)	12.7 (7.6 ;3)	-	-
Brasilomysis castori	-	0.3 (0.3 ;1)	-	-	-	-
Metamysidopsis swifti	-	-	-	1.3 (1.3 ;1)	-	-
Promysis atlantica	2.8 (2.8 ;1)	-	3.5 (2.1 ;3)	2.7 (2.7 ;1)	28.6 (10.6 ;8)	0.5 (0.5 ;1)
Cyclaspis spp.	-	0.6 (0.6 ;1)	-	-	-	-

Table 32, cont'd.

Diastylidae	-	-	1.7 (1.7 ;1)	-	-	-
Hyperiidea	2.4 (1.6 ;2)	-	0.4 (0.4 ;1)	-	-	-
Lestrigonus beganlensis	28 (14.8 ;6)	9.1 (4.2 ;6)	4.3 (2.2 ;4)	23.3 (9.5 ;7)	36.9 (8.6 ;14)	7.6 (4.3 ;4)
Simorhynchotus antennarius	-	-	-	-	-	0.3 (0.3 ;1)
Gammaridea	1.5 (1.5 ;1)	-	5.5 (4.5 ;2)	-	-	-
Sychelidium americanum	-	-	-	0.7 (0.7 ;1)	-	-
Photidae	-	-	7.2 (5.1 ;2)	-	-	-
Aegathoa oculata	-	-	-	-	-	<0.1(0 ;1)
Munna spp.	-	-	5.5 (5.5 ;1)	-	-	-
Euphausiidae (furcilia)	-	1.3 (1.3 ;1)	-	-	-	-
CLASS DECAPODA	3 (2.5 ;2)	-	-	-	1.3 (1.3 ;1)	-
Penaeidae (nauplius)	-	4.1 (3 ;2)	1 (1 ;1)	1 (1 ;1)	1.4 (1 ;2)	-
Penaeus spp. (protozoea)	-	-	-	-	-	3.8 (3.8 ;1)
Penaeus spp. (mysis)	2 (2 ;1)	-	-	-	-	-
Penaeus spp. (postlarva)	2 (2 ;1)	-	-	-	-	-
Penaeus aztecus (postlarva)	-	<0.1(0 ;2)	<0.1(0 ;3)	<0.1(0 ;5)	<0.1(0 ;1)	0.1 (0.1 ;7)
Trachypenaeus spp. (protozoea)	-	3.1 (2.8 ;2)	-	-	-	4 (2.8 ;2)
Trachypenaeus spp. (mysis)	-	1.4 (0.8 ;3)	-	9.8 (6 ;3)	-	4 (3.4 ;2)
Trachypenaeus spp. (postlarva)	<0.1(0 ;1)	<0.1(0 ;1)	-	<0.1(0 ;4)	<0.1(0 ;2)	<0.1(0 ;2)
Xiphopenaeus spp. (protozoea)	-	-	1 (1 ;1)	-	-	-
Sicyonia spp. (mysis)	-	0.3 (0.3 ;1)	-	-	-	0.2 (0.2 ;1)
Sicyonia spp. (postlarva)	-	<0.1(0 ;1)	-	<0.1(0 ;2)	-	<0.1(0 ;2)
Acetes americanus (zoea)	1.2 (1.2 ;1)	31.9 (20 ;6)	0.8 (0.6 ;2)	7.9 (5.3 ;3)	-	31.4 (26.3 ;5)
Acetes americanus	-	-	-	7.3 (3.5 ;4)	3.1 (1.5 ;4)	6.8 (6.8 ;1)
Lucifer faxoni (zoea)	22.3 (10.9 ;5)	25.4 (9.1 ;12)	5.6 (4.1 ;3)	34.3 (13.1 ;9)	74.9 (23 ;10)	23.8 (7.8 ;8)
Lucifer faxoni	6.9 (4.1 ;3)	10.1 (5.4 ;5)	4.6 (4 ;2)	49 (25.2 ;7)	50 (20.7 ;11)	12.5 (11.2 ;3)
ORDER CARIDEA (zoea)	6.3 (6.3 ;1)	0.3 (0.3 ;1)	0.6 (0.6 ;1)	-	-	-
Leptochela serratorbita (zoea)	-	-	-	-	0.5 (0.5 ;1)	-
Leptochela serratorbita (postlarva)	-	-	<0.1(0 ;1)	-	-	-
Alpheus spp. (zoea)	-	-	0.6 (0.6 ;1)	-	3.1 (1.9 ;3)	-
Alpheus sp.1 (zoea)	-	-	-	-	-	1.7 (1.7 ;1)
Alpheus sp.2 (zoea)	-	0.3 (0.3 ;1)	-	0.7 (0.7 ;1)	-	0.2 (0.2 ;1)
Alpheus sp.3 (zoea)	-	1.7 (1.7 ;1)	-	-	-	-
Hyppolytidae sp.A (mysis)	6.3 (4.6 ;3)	-	8 (8 ;1)	-	-	-
Crangonidae sp.A (zoea)	1.5 (1.5 ;1)	-	0.7 (0.7 ;1)	-	-	-
ORDER THALLASSINIDEA (zoea)	0.5 (0.5 ;1)	-	-	-	-	-
THALLASSINIDEA sp.A (zoea)	2.8 (2.8 ;1)	-	0.7 (0.7 ;1)	-	-	-
THALLASSINIDEA sp.1 (zoea)	-	0.6 (0.6 ;1)	-	-	-	-
Axiidae/Callianassidae (zoea)	1.5 (1.2 ;2)	-	-	-	-	-
Axiidae/Callianassidae sp.A (zoea)	0.3 (0.3 ;1)	-	-	-	0.7 (0.7 ;1)	-
Axiidae/Callianassidae sp.B (zoea)	1.8 (1.8 ;1)	-	-	-	-	-
Axiidae/Callianassidae sp.C (zoea)	0.3 (0.3 ;1)	-	-	-	-	-
Axiidae/Callianassidae sp.1 (zoea)	-	0.3 (0.3 ;1)	-	-	-	-
Callianassa major (zoea)	-	-	-	-	-	0.5 (0.5 ;1)
Upogebia spp. (zoea)	13.6 (9.2 ;3)	0.3 (0.3 ;1)	0.7 (0.7 ;1)	4.2 (4.2 ;1)	1.8 (1.8 ;1)	0.2 (0.2 ;1)
Palinurus spp. (phyllosoma)	-	-	-	-	-	<0.1(0 ;1)

Table 32, cont'd.

ORDER ANOMURA (zoea)	1.2 (1.2 ;1)	-	-	-	-	-
Clibanarius vittatus (zoea)	-	-	-	-	-	0.8 (0.8 ;1)
Pagurus spp. (zoea)	10 (7.9 ;3)	0.9 (0.7 ;2)	1.1 (0.8 ;2)	9.5 (5.3 ;4)	-	-
Porcellanidae (zoea)	2 (2 ;1)	-	-	-	-	-
Euceramus praelongus (zoea)	2.8 (2.8 ;1)	-	-	-	-	-
Polyonyx gibbesi (zoea)	-	1.7 (1.7 ;1)	5.3 (5.3 ;1)	-	-	-
Porcellana sayana (zoea)	-	3.5 (3.5 ;1)	-	-	-	-
Albunea spp. (zoea)	2 (2 ;1)	-	-	-	-	2.2 (1.7 ;2)
ORDER BRACHYURA (zoea)	3.4 (2.5 ;2)	-	0.4 (0.4 ;1)	-	-	-
BRACHYURA sp.A (megalopa)	1.2 (1.2 ;1)	-	-	-	-	-
BRACHYURA sp.1 (megalopa)	-	-	-	-	-	-
BRACHYURA sp.2 (megalopa)	-	-	-	-	-	1.1 (1.1 ;1)
BRACHYURA sp.3 (megalopa)	-	-	-	-	-	-
Ebalia spp. (zoea)	-	1 (1 ;1)	-	12.4 (8.4 ;3)	-	-
Callinectes spp. (zoea)	7.9 (3.8 ;4)	4.2 (2.2 ;4)	0.5 (0.5 ;1)	6.9 (3.4 ;5)	1.4 (0.9 ;2)	9.5 (3.6 ;8)
Callinectes sapidus (megalopa)	<0.1(0 ;3)	0.5 (0.1 ;18)	-	2.6 (2 ;14)	-	0.4 (0.2 ;12)
Callinectes similis (megalopa)	0.1 (0 ;4)	0.1 (0 ;5)	0.2 (0.1 ;10)	0.3 (0.1 ;12)	<0.1(0 ;7)	0.2 (0.1 ;11)
Callinectes similis (juvenile)	<0.1(0 ;1)	<0.1(0 ;3)	0.1 (0 ;3)	<0.1(0 ;4)	-	<0.1(0 ;4)
Portunus spp. (zoea)	0.8 (0.8 ;1)	1.7 (1.7 ;1)	3.5 (2 ;3)	2.4 (2.4 ;1)	3.8 (3.5 ;2)	2.1 (1.7 ;2)
Portunus spp. (megalopa)	0.3 (0.1 ;7)	<0.1(0 ;5)	0.1 (0 ;6)	0.1 (0 ;7)	0.6 (0.2 ;14)	0.1 (0 ;7)
Portunus spp. (juvenile)	<0.1(0 ;4)	<0.1(0 ;2)	<0.1(0 ;6)	<0.1(0 ;4)	<0.1(0 ;5)	<0.1(0 ;1)
Xanthidae (zoea)	2.3 (2.3 ;1)	-	-	-	-	-
Xanthidae sp.A (zoea)	1.5 (1.5 ;1)	-	-	-	-	-
Hexapanopeus angustifrons (zoea)	14.6 (10.1 ;4)	-	2.5 (2 ;2)	-	3.9 (2.6 ;3)	0.3 (0.3 ;1)
Hexapanopeus angustifrons (megalopa)	2 (2 ;1)	-	-	-	-	-
Menippe adina (zoea)	-	-	-	2.3 (2.3 ;1)	-	-
Neopanope sayi (zoea)	-	-	-	1.3 (1.3 ;1)	-	-
Pilumninae spp. (zoea)	-	0.3 (0.3 ;1)	-	-	-	-
Pinnixa spp. (zoea)	89.5 (39.3 ;8)	-	12.5 (11.9 ;2)	-	-	-
Pinnixa sp.1 (zoea)	-	16.3 (14.2 ;4)	-	2.9 (2.5 ;2)	-	1.9 (1.9 ;1)
Pinnixa sp.2 (zoea)	-	-	-	5.3 (5.3 ;1)	-	-
Pinnixa sp.3 (zoea)	-	30.2 (18.9 ;6)	-	9.2 (8.5 ;2)	-	-
Uca (megalopa)	3.4 (2.4 ;2)	-	-	0.7 (0.7 ;1)	-	-
INVERTEBRATA (egg)	55.8 (15.3 ;11)	-	142.1 (51.5 ;15)	-	295.2 (70.6 ;19)	-
Actinotrocha spp.	0.8 (0.8 ;1)	-	6.6 (3.5 ;4)	-	-	-
PHYLUM BRYOZOA (cyphonautes)	3 (3 ;1)	3.6 (1.7 ;5)	4.8 (3.5 ;3)	6 (2.7 ;5)	-	7.9 (5.2 ;4)
PHYLUM BRACHIOPODA (lingulid)	-	-	-	-	1.5 (1.5 ;1)	-
Sagittidae	185.6 (69 ;14)	380 (91.3 ;18)	111.5 (38.7 ;13)	358.7 (85.3 ;20)	408.4 (59.1 ;19)	227.5 (40.1 ;16)
Ferosagitta hispida	2 (2 ;1)	2 (1.4 ;2)	5.4 (2.6 ;4)	11.3 (5.5 ;4)	23.9 (7.8 ;9)	-
Flaccisagitta enflata	-	32.3 (12.5 ;9)	1.5 (1.1 ;2)	18.1 (8.1 ;6)	18.8 (5.8 ;9)	10.9 (6.8 ;6)
Sagitta spp.	62.1 (17.9 ;11)	-	58.6 (22.5 ;12)	-	100 (17 ;17)	-
Sagitta friderici	-	13.6 (11.7 ;2)	-	29.2 (15.6 ;4)	-	30.4 (27.2 ;2)
Sagitta tenuis	-	61.3 (32.8 ;9)	-	29.2 (19.7 ;4)	-	3 (1.6 ;3)
ORDER ASTEROIDEA (bipinnaria)	8.2 (6.2 ;2)	-	32 (22.9 ;4)	-	-	0.7 (0.7 ;1)
ORDER OPHIUROIDEA (ophiopluteus)	2.1 (2.1 ;1)	23.6 (12.8 ;4)	5.2 (4.1 ;2)	41.1 (27 ;4)	-	9.7 (7 ;3)
CLASS ENTEROPNEUSTA (tornaria)	62.7 (53.9 ;4)	-	7.9 (5.2 ;3)	-	-	-

Table 32, cont'd.

CLASS ASCIDIACEA (tadpole larva)	-	-	5.7 (5.7 ;1)	-	-	-
Oikopleura spp.	1246.5 (469.5 ;17)	264.8 (101 ;19)	1141.8 (369.1 ;19)	925.1 (182.1 ;23)	454.1 (144.5 ;18)	286.9 (78.5 ;16)
CLASS THALIACEA	171.8 (70.6 ;9)	-	23.6 (20.1 ;2)	-	-	-
Dolioletta gegenbauri	30.1 (16 ;4)	1.3 (1.3 ;1)	4.4 (3.2 ;2)	-	-	9.1 (7.6 ;3)
Doliolum spp.	501.4 (190.8 ;12)	2.3 (1.8 ;2)	134.4 (107.3 ;7)	8.5 (5 ;3)	70 (12.9 ;17)	49.8 (28.5 ;6)
Salpa spp.	19 (12 ;3)	-	2.5 (1.7 ;2)	0.3 (0.3 ;1)	1.1 (0.8 ;2)	13.3 (6.9 ;5)
Amphioxi spp.	2.4 (2.4 ;1)	-	4.6 (3.2 ;2)	34.8 (9.9 ;11)	-	20.4 (10.6 ;6)
CLASS OSTEICHTHYES (egg)	8.1 (3.9 ;4)	-	23.6 (8.8 ;8)	-	4.9 (2.1 ;5)	-
CLASS OSTEICHTHYES	3 (2.3 ;2)	-	1.2 (1.2 ;1)	-	5 (3.9 ;2)	-
ORDER ANGUILLIFORMES	-	-	-	-	1.5 (1.5 ;1)	-
ORDER CLUPEIFORMES	4.2 (2 ;4)	-	4.6 (4 ;2)	-	2.4 (1.7 ;2)	-
Engraulidae	1.5 (1.2 ;2)	-	-	-	-	-
ORDER PERCIFORMES	-	-	-	-	0.7 (0.7 ;1)	-
Sciaenidae	-	-	-	-	1.5 (1.5 ;1)	-
Symphurus spp.	3 (3 ;1)	-	-	-	-	-
CEPHALOPODA						
LOLIGINIDAE)	-	-	-	-	0.6 (0.4 ;3)	0.8 (0.6 ;2)
Loligo spp.	0.2 (0.2 ;1)	-	2.2 (0.9 ;7)	-	1.1 (0.4 ;8)	0.3 (0.2 ;2)
Lolliguneula brevis	0.9 (0.5 ;3)	0.4 (0.2 ;3)	1 (0.6 ;3)	0.1 (0.1 ;1)	0.2 (0.1 ;2)	0.2 (0.2 ;1)
NUMBER OF STATIONS	17	20	21	24	19	17
TOTAL VOLUME FILTERED (m^3)	438.44	429.52	481.84	436.30	809.39	417.13
AVERAGE VOLUME FILTERED (m^3)	25.79	21.48	22.94	18.18	42.60	24.54

Oithona spp., *Doliolum* spp., bivalve veligers, *Penilia avirostris*, copepod nauplii, and *Paracalanus parvus* were also abundant.

(2) Fish Larvae Larval fish densities were highest between Atchafalaya Bay and Calcasieu Lake, Louisiana, and ranged from 15 to 6942 larvae/100 m^3. April samples were dominated by *Anchoa* spp. (347/100 m^3; identifiable specimens $\geq$ 10 μm standard length [SL], but $\leq$ 15 μm SL), *A. hepsetus* (134/100 m^3; specimens $\geq$ 14 μm SL), and unidentified engraulids (126/100 m^3; specimens < 8 μm SL; Table 33). The next most abundant taxon after anchovies was *Cynoscion arenarius* (126/100 m^3). *Anchoa mitchilli* (specimens $\geq$ 8 μm SL), *Etropus crossotus*, and *Symphurus* spp. were also abundant. Including all taxa, the family Engraulidae made up 74% of the total catch.

b. April 13-19, 1993

Samples were analyzed from 44 stations during the April 1993 cruise, a near-normal, high-river discharge period. Samples were collected between Timbalier and Corpus Christi Bays, the southwestern-most portion of the plume's range. Water column-averaged temperatures ranged from 18.7 to 21.3° C, and salinity ranged from 7.6 to 34.1‰. Low temperature values were found between Calcasieu Lake and Galveston Bay. Low salinity was noted off the Atchafalaya basin.

(1) Zooplankton Zooplankton biomass tended to be high from Atchafalaya Bay to slightly west of Sabine Lake, for both the 153- and 335-μm samples, with higher concentrations located at nearshore stations for the 335-μm samples. Plankton biomass estimates for the 153-μm samples ranged from 17 to 368 μg/m^3, while the 335-μm samples ranged from 7 to 157 μg/m^3. At the 21 zooplankton stations, *Acartia tonsa* (7566/m^3) was by far the most abundant zooplankton species. *Paracalanus crassirostris* (2288/m^3), *P. parvus* (2209/m^3), *Oithona* spp. (1359/m^3), *Oikopleura* spp. (1142/m^3), and *Temora turbinata* (1126/m^3) were also abundant, and *T. stylifera*, cirriped nauplii, *Corycaeus* spp., copepod nauplii, and gastropod veligers were less so.

(2) Fish Larvae Ichthyoplankton densities ranged from 3 to 936 larvae/100 m^3. Densities were highest off the Atchafalaya basin and along the coast between Galveston and Matagorda Bays. Samples were dominated by the unidentified engraulids (83 larvae/100 m^3) although *Anchoa* spp. (27/100 m^3), *Cynoscion arenarius* (26/100 m^3), and *Brevoortia patronus* (10/100 m^3) were also abundant. Gobiidae, and *Bregmaceros cantori* were also common. These results are similar to April 1992 results, where engraulids and *Cynoscion arenarius* dominated the catch; however, *Brevoortia patronus* was not abundant in April of 1992.

c. April 1992-1993

(1) Zooplankton Canonical analysis extracted a significant portion of the variance between the zooplankton and environmental variables (Table 34; $L=6.4x10^{-5}$, p=7, q=18, n=37, P[F>F*]=0.0001). Thus, species density varies linearly with the environmental variables. The first canonical root accounted for 74.5% of the predicted variation. The second root significantly accounted for an additional 15.7% ($\Lambda=2.7x10^{-3}$, P[F>F*]=0.0439), while the third root was not significant ($\Lambda=0.027$, P[F>F*]=0.5075), accounting for 3.5%. Thus, based on our criteria, the dimensionality of the linear association between the two sets of variables is three, and these three pairs of canonical variates will be further scrutinized.

Table 33. Mean density (#/100m^3) of larval fish species caught during LATEX B cruises. Numbers in parentheses represent standard error of density estimate and number of positive stations, respectively. Also given in the last three rows are number of stations, total volume filtered, and average volume filtered, respectively, for each cruise. Mean density was calculated over all stations for each cruise. Asterisk (*) indicates one station was excluded from the estimates due to insufficient volume filtered data.

Taxon	April 1992	October 1992	April 1993	July 1993	April 1994	July 1994
OSTEICHTHYES unk. (bony fishes)	-	-	-	2.1 (1 ;5)	6.4 (2.1 ;11)	0.1 (0.1 ;1)
ANGUILLIFORMES unk. (eels and morays)	-	-	-	0.4 (0.3 ;2)	0.6 (0.3 ;5)	1.5 (1 ;6)
MURAENIDAE unk. (morays)	-	-	-	-	0.1 (0.1 ;1)	-
OPHICHTHIDAE unk. (snake eels)	0.1 (0.1 ;1)	0.7 (0.3 ;4)	0.1 (0.1 ;1)	0.2 (0.2 ;2)	0.5 (0.2 ;5)	0.4 (0.2 ;3)
Aplatophis chauliodus (tusky eel)	-	-	-	0.1 (0.1 ;1)	-	-
Myrophis punctatus (speckled worm eel)	-	-	0.7 (0.6 ;2)	-	-	-
Ophichthus spp. (snake eels)	-	-	0.2 (0.2 ;1)	-	0.1 (0.1 ;1)	-
CONGRIDAE unk. (conger eels)	-	-	-	0.1 (0.1 ;1)	-	-
CLUPEIFORMES unk. (herrings and anchovies)	-	3.9 (2.4 ;4)	4.5 (2.3 ;6)	1.2 (1 ;2)	2.1 (1.8 ;3)	78.8 (70.2 ;13)
CLUPEIDAE unk. (herrings)	-	-	-	0.8 (0.8 ;1)	0.2 (0.2 ;1)	-
Brevoortia patronus (gulf menhaden)	-	0.2 (0.2 ;1)	10.1 (8.4 ;4)	-	7.4 (4.5 ;9)	-
Etrumeus teres (round herring)	-	-	-	-	14 (3.6 ;24)	0.3 (0.2 ;2)
Harengula jaguana (scaled sardine)	3.4 (1.4 ;7)	-	0.1 (0.1 ;1)	6 (3 ;8)	0.2 (0.2 ;2)	2.2 (1.4 ;5)
Opisthonema oglinum (Atlantic thread herring)	3.7 (1.6 ;7)	-	0.1 (0.1 ;1)	14.6 (5.6 ;10)	1.9 (0.9 ;5)	130.6 (84.8 ;12)
Sardinella aurita (Spanish sardine)	0.6 (0.6 ;1)	-	-	-	-	-
ENGRAULIDAE unk. (anchovies)	125.9 (60.4 ;10)	0.2 (0.2 ;1)	83.2 (26.3 ;26)	154.8 (38.3 ;39)	112.3 (25.1 ;31)	224.2 (58.6 ;31)
Anchoa spp. (anchovies)	347.3 (196.8 ;15)	5.9 (2.1 ;12)	27.5 (11.1 ;8)	3.9 (2.8 ;2)	1 (0.8 ;2)	188.8 (184.9 ;5)
Anchoa sp. A (anchovy sp. A)	0.2 (0.2 ;1)	-	-	-	-	-
Anchoa hepsetus (striped anchovy)	134.5 (61 ;8)	24.1 (7.6 ;16)	0.1 (0.1 ;1)	7.4 (6.9 ;3)	0.2 (0.2 ;1)	0.5 (0.5 ;1)
Anchoa mitchilli (bay anchovy)	115.6 (82.1 ;4)	5.6 (3.3 ;6)	-	-	-	-
Anchoa nasuta (longnose anchovy)	-	-	-	1.5 (1.1 ;2)	-	-
Anchoviella perfasciata (flat anchovy)	0.5 (0.5 ;1)	-	0.8 (0.7 ;2)	7.9 (7.3 ;3)	-	0.3 (0.3 ;1)
Engraulis spp. (anchovies)	-	0.4 (0.4 ;1)	-	-	-	2.6 (1.8 ;2)
Engraulis eurystole (silver anchovy)	-	-	-	-	-	0.2 (0.2 ;1)
STOMIIFORMES						
GONOSTOMATIDAE unk. (lightfishes)	-	-	-	-	0.3 (0.2 ;3)	0.2 (0.2 ;1)
Cyclothone braueri (lightfish)	-	-	-	-	0.1 (0.1 ;1)	-
Vinciguerria spp. (lightfishes)	-	-	-	-	0.2 (0.2 ;1)	-
AULOPIFORMES						
SYNODONTIDAE unk. (lizardfishes)	-	-	-	0.9 (0.8 ;2)	10.6 (2.6 ;20)	1.8 (1.2 ;4)
Saurida brasiliensis (largescale lizardfish)	-	-	-	-	-	0.1 (0.1 ;1)
Synodus spp. (lizardfishes)	-	0.2 (0.2 ;2)	0.3 (0.2 ;2)	0.4 (0.4 ;1)	1.8 (0.6 ;9)	0.4 (0.3 ;2)
Synodus foetens (inshore lizardfish)	0.4 (0.3 ;2)	-	0.4 (0.4 ;1)	-	-	0.1 (0.1 ;1)
PARALEPIDAE unk. (barracudinas)	-	-	-	-	-	0.1 (0.1 ;1)
Lestrolepis intermedia (barracudina)	-	-	-	-	0.3 (0.3 ;1)	-
MYCTOPHIFORMES						
MYCTOPHIDAE unk. (lanternfishes)	-	0.3 (0.3 ;1)	-	-	27.2 (7 ;25)	-

Table 33, cont'd.

GADIFORMES unk. (cods)	-	-	-	-	0.2 (0.1 ;2)	-
BREGMACEROTIDAE						
Bregmaceros spp. (codlets)	-	-	-	0.5 (0.3 ;3)	0.6 (0.5 ;2)	-
Bregmaceros cantori (codlet (Houde))	5.3 (2.9 ;6)	0.9 (0.6 ;3)	4.4 (2.1 ;7)	-	18 (5.5 ;24)	1.8 (1.4 ;3)
Bregmaceros houdei (stellate codlet)	0.7 (0.7 ;1)	-	-	-	-	-
MACROURIDAE unk. (grenadiers)	-	-	-	-	0.1 (0.1 ;1)	-
OPHIDIIDAE unk. (cusk-eels)	-	-	-	0.3 (0.3 ;1)	0.9 (0.4 ;5)	-
Lepophidium spp. (cusk-eels)	-	-	-	1 (0.4 ;5)	0.3 (0.2 ;2)	0.4 (0.3 ;2)
Lepophidium jeannae (mottled cusk-eel)	-	-	-	-	0.1 (0.1 ;1)	-
Lepophidium profundorum (fawn cusk-eel)	-	-	-	-	-	0.2 (0.2 ;1)
Lepophidium staurophor (cusk-eel (Gordon))	-	0.2 (0.2 ;1)	-	-	0.1 (0.1 ;1)	0.1 (0.1 ;1)
Ophidion spp. (cusk-eels)	-	2 (0.9 ;6)	1.2 (0.7 ;4)	-	0.6 (0.3 ;6)	0.1 (0.1 ;1)
Ophidion sp. I (cusk-eel sp. I (Gordon))	-	-	-	-	-	-
Ophidion sp. II (cusk-eel sp. II (Gordon))	-	3.2 (1.8 ;6)	-	-	-	-
Ophidion selenops (mooneye cusk-eel)	-	-	-	0.1 (0.1 ;1)	-	-
LOPHIIFORMES						
OGCOCEPHALIDAE unk. (batfishes)	-	-	-	0.1 (0.1 ;1)	0.1 (0.1 ;1)	-
Dibranchus atlanticus (Atlantic batfish)	-	0.1 (0.1 ;1)	-	-	-	-
CAULOPHRYNIDAE						
Caulophryne spp.	-	-	-	-	-	0.1 (0.1 ;1)
GOBIESOCIFORMES						
GOBIESOCIDAE						
Gobiesox strumosus (skilletfish)	0.4 (0.4 ;1)	-	0.5 (0.3 ;2)	-	0.3 (0.2 ;2)	-
ATHERINIFORMES						
EXOCOETIDAE						
Hyporhamphus unifasciatus (silverstripe halfbeak)	-	0.4 (0.4 ;1)	-	-	-	-
ATHERINIDAE unk. (silversides)	0.4 (0.4 ;1)	-	0.1 (0.1 ;1)	-	-	0.7 (0.7 ;1)
BERYCIFORMES						
MELAMPHAIDAE						
Melamphaes spp.	-	-	-	-	0.1 (0.1 ;1)	-
GASTEROSTEIFORMES						
SYNGNATHIDAE						
Syngnathus spp. (pipefishes)	-	-	0.1 (0.1 ;1)	-	0.2 (0.2 ;1)	-
Syngnathus louisianae (chain pipefish)	0.2 (0.2 ;1)	-	-	-	<0.1 (0 ;1)	-
DACTYLOPTERIFORMES						
DACTYLOPTERIDAE						
Dactylopterus spp. (flying gurnards)	-	0.1 (0.1 ;1)	-	-	-	-
SCORPAENIFORMES unk.	-	-	-	-	0.2 (0.2 ;1)	-
SCORPAENIDAE unk. (scorpionfishes)	1 (0.5 ;4)	-	-	-	0.1 (0.1 ;1)	-
Scorpaena spp. (scorpionfishes)	0.5 (0.4 ;2)	-	-	0.1 (0.1 ;1)	0.6 (0.6 ;1)	-
Scorpaena brasiliensis (barbfish)	-	-	-	-	-	0.6 (0.6 ;1)
TRIGLIDAE unk. (searobins)	0.8 (0.6 ;2)	-	-	-	0.2 (0.2 ;1)	0.2 (0.2 ;1)
Bellator militaris (horned sea robin)	-	0.2 (0.2 ;1)	-	-	-	-
Prionotus spp. (searobins)	0.5 (0.4 ;2)	0.1 (0.1 ;1)	0.1 (0.1 ;1)	-	6 (2 ;19)	0.3 (0.3 ;1)
Prionotus evolans (striped searobin)	0.2 (0.2 ;1)	-	-	-	-	-
PERCIFORMES unk. (perciform fishes)	6 (1.6 ;13)	4.7 (3.3 ;7)	4.2 (1.3 ;13)	0.7 (0.7 ;1)	14.2 (5.7 ;19)	24.7 (10.1 ;17)

Table 33, cont'd.

PERCIFORMES sp. A (perciform sp. A)	-	-	-	-	1.6 (0.7 ;7)	-
SERRANIDAE unk. (sea basses)	-	-	0.4 (0.3 ;2)	2.9 (1.4 ;6)	0.6 (0.4 ;3)	1.2 (0.7 ;4)
Anthias spp. (sea basses)	-	-	-	-	-	-
Centropristis spp. (sea basses)	0.7 (0.7 ;1)	-	-	-	0.2 (0.2 ;3)	-
Diplectrum spp. (sand perches)	-	-	-	-	0.1 (0.1 ;1)	-
Hemanthias vivanus (red barbier)	-	-	-	-	0.1 (0.1 ;1)	-
Serraniculus pumilio (pygmy sea bass)	-	-	-	0.1 (0.1 ;1)	-	1.1 (1.1 ;1)
Serranus spp. (sea basses)	0.8 (0.8 ;1)	-	-	-	-	-
PRIACANTHIDAE unk. (bigeyes)	-	-	-	-	-	0.2 (0.2 ;1)
MALACANTHIDAE						
Caulolatilus spp. (tilefishes)	-	-	-	-	0.7 (0.6 ;2)	-
RACHYCENTRIDAE unk. (cobias)	-	-	-	-	-	0.2 (0.2 ;1)
CARANGIDAE unk. (jacks)	-	-	-	0.2 (0.2 ;1)	0.2 (0.1 ;2)	-
Caranx crysos (blue runner)	-	-	-	-	-	0.2 (0.2 ;1)
Chloroscombrus chrysurus (Atlantic bumper)	-	0.9 (0.8 ;3)	-	14 (4 ;19)	0.1 (0.1 ;1)	60.1 (20.9 ;19)
Decapterus punctatus (round scad)	-	-	-	-	-	0.4 (0.3 ;2)
Oligoplites saurus (leatherjack)	-	-	-	-	-	0.4 (0.4 ;1)
Seriola spp. (amberjacks)	-	-	-	-	0.1 (0.1 ;1)	1.5 (1 ;2)
Trachurus lathami (rough scad)	-	-	-	-	0.5 (0.3 ;4)	-
LUTJANIDAE unk. (snappers)	-	-	-	0.3 (0.3 ;2)	0.3 (0.3 ;1)	-
Lutjanus spp. (snappers)	-	-	-	0.5 (0.3 ;3)	0.4 (0.2 ;3)	0.3 (0.3 ;1)
Lutjanus campechanus (red snapper)	-	-	-	-	-	0.4 (0.4 ;1)
SPARIDAE unk. (porgies)	0.8 (0.5 ;3)	-	0.2 (0.2 ;2)	-	0.7 (0.3 ;6)	-
Archosargus probatocephalus (sheepshead)	-	-	-	-	-	-
Lagodon rhomboides (pinfish)	0.2 (0.2 ;1)	-	-	-	0.1 (0.1 ;1)	-
Stenotomus caprinus (longspine porgy)	-	-	-	-	0.7 (0.4 ;4)	-
SCIAENIDAE unk. (drums)	0.1 (0.1 ;1)	0.1 (0.1;1)	2.9 (1.4 ;5)	0.5 (0.4 ;2)	-	4.5 (2.0 ;8)
Bairdiella chrysoura (silver perch)	-	-	-	0.1 (0.1 ;1)	-	11 (8.8 ;4)
Cynoscion spp. (seatrouts)	-	3.9 (2.8 ;3)	0.3 (0.3 ;1)	0.1 (0.1 ;1)	-	-
Cynoscion arenarius (sand seatrout)	125.8 (26.5 ;32)	4.1 (1.4 ;11)	25.8 (6 ;24)	14.4 (7.2 ;16)	21 (5.1 ;29)	44.8 (28 ;14)
Cynoscion nebulosus (spotted seatrout)	-	-	-	1.3 (0.8 ;3)	0.1 (0.1 ;1)	1.2 (1.2 ;1)
Cynoscion nothus (silver seatrout)	-	1.2 (0.6 ;5)	-	0.7 (0.5 ;3)	-	-
Larimus fasciatus (banded drum)	0.4 (0.3 ;2)	-	-	0.1 (0.1 ;1)	-	-
Menticirrhus spp. (kingfishes)	6.2 (2 ;12)	0.5 (0.3 ;4)	1 (0.5 ;5)	0.8 (0.4 ;4)	0.1 (0.1 ;1)	3 (1.6 ;4)
Menticirrhus americanus (southern kingfish)	-	-	-	-	0.2 (0.2 ;1)	-
Menticirrhus saxatilis (northern kingfish)	-	-	-	-	0.2 (0.2 ;1)	-
Micropogonias undulatus (Atlantic croaker)	0.6 (0.6 ;1)	86.2 (23.3 ;26)	1 (0.9 ;2)	-	0.3 (0.3 ;1)	-
Pogonias cromis (black drum)	0.5 (0.5 ;1)	-	2.9 (2.3 ;2)	-	0.2 (0.2 ;1)	-
Sciaenops ocellatus (red drum)	-	4.3 (1.4 ;14)	-	-	-	0.2 (0.2 ;1)
Stellifer lanceolatus (star drum)	-	-	-	8.5 (3.4 ;11)	-	2.7 (2.3 ;2)
EPHIPPIDAE unk. (spadefishes)	-	-	-	-	-	0.7 (0.7 ;1)
MUGILIDAE						
Mugil curema (white mullet)	-	-	0.2 (0.2 ;1)	-	0.2 (0.2 ;1)	-
SPHYRAENDIAE						
Sphyraena spp. (barracudas)	-	-	-	-	0.1 (0.1 ;1)	0.4 (0.3 ;2)
BLENNIDAE unk. (blennies)	0.3 (0.2 ;2)	-	0.6 (0.4 ;2)	1.1 (0.6 ;4)	2 (0.8 ;8)	0.7 (0.4 ;3)

Table 33, cont'd.

BLENNIDAE sp. F (blenny sp. F)	-	-	-	-	0.6 (0.6 ;2)	-
Ophioblennius atlanticus (redlip blenny)	-	-	1 (1 ;1)	-	0.1 (0.1 ;1)	-
Scartella cristata (molly miller)	1.1 (0.5 ;5)	0.3 (0.2 ;3)	-	0.2 (0.2 ;1)	0.1 (0.1 ;1)	-
CALLIONYMIDAE unk. (dragonets)	-	-	-	-	0.1 (0.1 ;1)	-
ELEOTRIDAE						
Dormitator maculatus (fat sleeper)	-	-	0.2 (0.2 ;1)	-	-	-
GOBIIDAE unk. (gobies)	10.8 (5 ;6)	5.1 (2 ;9)	4.8 (1.7 ;11)	2.4 (0.9 ;10)	10.1 (3.1 ;21)	6.1 (3 ;10)
GOBIIDAE sp. A (goby sp. A)	-	-	-	-	0.2 (0.2 ;2)	-
GOBIIDAE sp. B (goby sp. B)	-	-	-	-	0.9 (0.4 ;5)	-
GOBIIDAE sp. C (goby sp. C)	-	-	-	-	1 (0.7 ;2)	-
GOBIIDAE sp. D (goby sp. D)	-	-	-	-	6.7 (2.4 ;12)	-
Gobionellus boleosoma (darter goby)	0.2 (0.2 ;1)	-	-	-	-	-
Gobionellus oceanicus (highfin goby)	-	-	-	-	0.2 (0.2 ;1)	-
Gobiosoma bosc (naked goby)	1.5 (1.2 ;2)	0.9 (0.6 ;3)	-	0.1 (0.1 ;1)	-	-
MICRODESMIDAE unk. (wormfishes)	0.1 (0.1 ;1)	-	-	-	-	-
Microdesmus spp. (wormfishes)	-	-	-	-	0.1 (0.1 ;1)	0.1 (0.1 ;1)
Microdesmus lanceolatus (lancetail wormfish)	-	-	-	0.8 (0.5 ;3)	-	0.2 (0.1 ;2)
TRICHIURIDAE						
Trichiurus lepturus (Atlantic cutlassfish)	-	0.7 (0.4 ;3)	0.1 (0.1 ;1)	-	6.9 (1.5 ;22)	0.1 (0.1 ;1)
SCOMBRIDAE unk. (mackerels)	-	-	-	-	0.1 (0.1 ;2)	0.2 (0.2 ;1)
Auxis spp. (mackerels)	-	0.1 (0.1 ;1)	-	1.1 (0.8 ;3)	-	-
Euthynnus spp. (mackerels)	-	-	-	-	-	0.1 (0.1 ;1)
Euthynnus alletteratus (little tunny)	-	-	-	0.3 (0.2 ;2)	-	1 (0.7 ;3)
Scomber japonicus (chub mackerel)	-	0.1 (0.1 ;1)	-	-	-	-
Scomberomorus cavalla (king mackerel)	-	-	-	0.1 (0.1 ;1)	-	-
Scomberomorus maculatus (Spanish mackerel)	3 (1.1 ;7)	-	0.1 (0.1 ;1)	2.2 (1.1 ;6)	-	5.3 (2.1 ;8)
STROMATEIDAE unk. (butterfishes)	-	-	-	-	0.1 (0.1 ;1)	-
Ariomma spp. (butterfishes)	-	-	-	-	0.1 (0.1 ;2)	-
Peprilus alepidotus (harvestfish)	0.3 (0.3 ;1)	0.1 (0.1 ;1)	-	-	-	0.5 (0.5 ;1)
Peprilus burti (gulf butterfish)	0.3 (0.3 ;2)	1.5 (1 ;3)	0.3 (0.3 ;2)	-	1.6 (0.7 ;6)	0.5 (0.4 ;2)
PLEURONECTIFORMES unk. (flatfishes)	0.7 (0.7 ;1)	-	-	-	-	-
BOTHIDAE unk. (lefteye flounders)	0.8 (0.6 ;2)	-	2.3 (1.1 ;7)	0.2 (0.2 ;1)	0.9 (0.5 ;6)	1 (0.6 ;4)
Citharichthys spp. (whiffs)	0.2 (0.2 ;1)	0.6 (0.4 ;2)	1.6 (1.1 ;2)	0.3 (0.3 ;1)	0.5 (0.3 ;4)	0.9 (0.5 ;5)
Citharichthys cornutus (horned whiff)	0.4 (0.4 ;1)	-	-	-	-	-
Citharichthys spilopterus (bay whiff)	-	-	-	0.2 (0.2 ;1)	0.5 (0.3 ;3)	-
Cyclopsetta spp. (lefteye flounders)	-	0.1 (0.1 ;1)	-	-	-	0.6 (0.6 ;1)
Cyclopsetta fimbriata (spotfin flounder)	-	-	-	-	-	0.1 (0.1 ;1)
Engyophrys senta (spiny flounder)	-	-	-	0.1 (0.1 ;1)	-	-
Etropus spp. (lefteye flounders)	-	-	-	-	-	3.2 (1.5 ;6)
Etropus crossotus (fringed flounder)	18.1 (8 ;12)	8.7 (3.8 ;12)	1.1 (0.5 ;5)	3.7 (1.4 ;10)	15.3 (3.2 ;26)	3 (1.6 ;4)
Paralichthys spp. (lefteye flounders)	-	0.1 (0.1 ;1)	-	-	-	-
Syacium spp. (lefteye flounders)	-	1.4 (0.7 ;5)	1 (0.9 ;2)	1.8 (1.1 ;4)	-	3.7 (2.2 ;5)
Syacium gunteri (shoal flounder)	-	-	-	3 (2.8 ;3)	-	0.2 (0.2 ;1)
Syacium papillosum (dusky flounder)	0.1 (0.1 ;1)	-	-	-	-	8.9 (4.4 ;7)
Trichosetta ventralis (sash flounder)	-	-	-	0.3 (0.3 ;1)	-	-
SOLEIDAE unk. (soles)	-	-	-	-	-	3.4 (3.4 ;1)

Table 33, cont'd.

Achirus lineatus (lined sole)	-	-	-	0.1 (0.1 ;1)	-	-
Symphurus spp. (tonguefishes)	15.4 (4.9 ;12)	5.3 (3 ;6)	0.7 (0.4 ;4)	15.5 (4.6 ;24)	5 (1.9 ;18)	2.7 (1.3 ;5)
Symphurus sp. A (tonguefish sp. A)	3.6 (2.7 ;2)	-	-	-	-	-
Symphurus sp. B (tonguefish sp. B)	0.6 (0.6 ;1)	-	-	-	-	-
Symphurus civitatus (offshore tonguefish)	-	-	-	-	0.8 (0.5 ;4)	-
Symphurus diomedianus (spottedfin tonguefish)	0.2 (0.2 ;1)	-	-	-	-	-
Symphurus plagiusa (blackcheek tonguefish)	13.4 (7 ;6)	8 (5.7 ;7)	-	3.1 (2.1 ;4)	0.3 (0.2 ;2)	22.1 (6.5 ;19)
TETRAODONTIFORMES						
TETRAODONTIDAE						
Sphoeroides spp. (puffers)	-	-	0.2 (0.2 ;1)	0.1 (0.1 ;1)	0.1 (0.1 ;2)	-
NUMBER OF STATIONS	34	41*	44	52	39	38
TOTAL VOLUME FILTERED (m^3)	850.85	902.16	1067.38	999.82	2054.79	940.81
AVERAGE VOLUME FILTERED (m^3)	25.02	22.00	24.26	19.23	52.69	24.76

Depth had a large weight (0.85) in the first environmental coefficient vector and had a positive intraset correlation (0.94). Therefore, depth contributed substantially to the first linear combination of environmental variables and also correlated highly and positively with it. Chlorophyll (-0.76; Figures 184a and 184b) and salinity (0.77; Figures 185a and 185b) also had large intraset correlations and thus are linearly related to the first environmental variate, although in opposite directions. This variate was associated with deep-water, high-salinity stations with low chlorophyll values, which occurred at outer stations, and contrasted nearshore stations. *Eucalanus pileatus* (0.73; Figures 185a and 185b), *Paracalanus parvus* (0.67; Figures 186a and 186b), *Centropages furcatus* (0.65), *Euterpina acutifrons* (0.63), *Doliolum* spp. (0.59), *Oikopleura* spp. (0.53), and *Temora turbinata* (0.52) exhibited positive interset correlations and, thus, were positively correlated with the first environmental variate. These species tended to have greater abundance at the outermost stations over the two years. In contrast, *Acartia tonsa* (-0.52; Figures 187a and 187b) and *Labidocera aestiva* (-0.42) had negative interset correlations, and both had greater densities in nearshore waters. These results are consistent with those obtained considering each year separately.

The second environmental coefficient vector produced large weights on temperature (0.99) and salinity (0.81), and a moderate weight on depth (-0.61). Of these variables, only temperature had a large intraset correlation (0.71). Year had a large negative intraset correlation (-0.78). Inspection of temperature contours reveals temperatures were, in general, cooler in 1993 than in 1992. Furthermore, the range of low temperatures occurred over a larger area in 1993 (from Calcasieu Lake to midway between Galveston and Matagorda Bays) versus 1992 (coolest water extended west of Sabine Lake to Galveston Bay). Positive interset correlations were noted for *Penilia avirostris* (0.56; Figures 188a and 188b, *Doliolum* spp. (0.49), *Lucifer faxoni* (0.46), *Lestrigonus beganlensis* (0.45), and *Portunus* megalopae (0.45). These species were more abundant in 1992 and were typified by high densities in warmer waters. Copepod nauplii (-0.52), however, were found in cooler waters and were more abundant in 1993 (Figures 189a and 189b).

The third environmental coefficient vector produced large weights on temperature (1.53) and year (1.17); however, only longitude (-0.58) and temperature (0.44) had large intraset correlations. This variate distinguishes between the high temperature region in the eastern portion of the cruises and the cooler region in the central/western portion. Only *Paracalanus crassirostris* had a large interset correlation (-0.52). This species was common in the central cooler waters (Figures 190a and 190b).

(2) Fish Larvae *Cynoscion arenarius* was the only fish species present at more than 25% of the stations over the two years. Canonical analysis (which becomes a special case of multiple regression with one species) indicated that *C. arenarius* density was linearly related to the environmental variables (Table 35; Λ=0.573, p=8, n=72, P[F>F*]=0.0001). Year (0.66), chlorophyll (0.56), and longitude (0.45) received large weights in the environmental coefficient vector. However, only year (0.78) and temperature (-0.64) correlated with the variate. As mentioned before, temperatures were cooler in 1993. *C. arenarius* correlated negatively (-0.65) with this variate and was less abundant in 1992 (Figure 191a) than in 1993 (Figure 191b). Larvae of *C. arenarius* typically have a spring peak occurrence in March and April (Ditty, 1986). However, because of higher temperatures, spawning may have taken place earlier in 1992, and, thus, the April sampling would have missed the spring larval abundance peak.

Table 34. Results of the April 1992/93 canonical analysis for zooplankton (n=37).

Canonical Correlation	1		2		3	
	p	%	p	%	p	%
	0.0001	74.48	0.0439	15.72	0.5075	3.50
	Coeff.	Corr.	Coeff.	Corr.	Coeff.	Corr.
SPECIES						
Polychaeta sp. A	0.06	0.30	-0.01	0.29	-0.55	0.36
Penilia avirostris	0.02	0.26	-0.05	0.56	-0.73	-0.07
Copepoda nauplius	0.09	0.31	-0.66	-0.52	-0.03	-0.25
Eucalanus pileatus	0.16	0.73	-0.03	>-0.01	-0.31	0.21
Paracalanus crassirostris	0.07	0.31	-0.12	-0.30	-0.36	-0.52
Paracalanus parvus	0.13	0.67	-0.06	-0.15	-0.37	-0.31
Temora turbinata	0.03	0.52	0.14	0.02	0.44	-0.38
Centropages furcatus	0.32	0.65	-0.29	-0.30	-0.05	-0.13
Labidocera aestiva	-0.29	-0.42	0.21	-0.15	-0.40	-0.04
Labidocera scotti	0.27	>-0.01	-0.46	-0.21	0.33	0.22
Acartia tonsa	-0.23	-0.52	-0.02	-0.33	-0.29	-0.32
Euterpina acutifrons	0.10	0.63	0.04	0.24	0.28	-0.18
Lestrigonus beganlensis	0.04	0.36	0.10	0.45	-0.43	-0.15
Lucifer faxoni	-0.10	-0.11	-0.22	0.46	0.05	0.06
Callinectes similis	0.11	0.02	-0.35	-0.36	0.14	0.29
Portunus spp.	0.05	0.24	0.20	0.45	0.11	0.12
Oikopleura spp.	0.12	0.53	0.28	0.22	-0.26	-0.31
Doliolum spp.	0.15	0.59	0.41	0.49	0.90	0.17
ENVIRONMENTAL						
Year	0.12	0.22	-0.03	-0.78	1.17	-0.15
Longitude	0.28	0.41	0.20	0.12	-0.33	-0.58
Depth	0.85	0.94	-0.61	-0.10	0.74	0.15
Temperature	0.16	-0.35	0.99	0.71	1.53	0.44
Salinity	0.07	0.77	0.81	0.16	-0.02	-0.19
Chlorophyll	0.02	-0.76	-0.23	-0.22	0.68	0.33
Heterotrophs	-0.18	-0.42	-0.10	-0.16	-0.57	0.06
Redundancy	$U_{y\|u_1}$	$V_{x\|v_1}$	$U_{y\|u_2}$	$V_{x\|v_2}$	$U_{y\|u_3}$	$V_{x\|v_3}$
	0.3595	0.2057	0.1577	0.1186	0.0683	0.0674

"p" is the probability, based on an F approximation of the Wilks' L statistic, that the canonical correlations between the i^{th} pair of variates and between subsequent pairs equal zero. "%" is the proportion of the i^{th} eigenvalue to the sum of the eigenvalues. "Coeff." are the standardized canonical coefficients (weights) of the i^{th} canonical variate for each variable. "Corr." represents the interset correlations for the SPECIES variables and intraset correlations for the ENVIRONMENTAL variables. "Redundancy" is the result of the redundancy analysis, where $U_{y|u_i}$ is the proportion of variance explained by the i^{th} SPECIES canonical variate with respect to the observed ENVIRONMENTAL variables. Similarly, $V_{x|v_i}$ is defined as the proportion of variance explained by the i^{th} ENVIRONMENTAL canonical variate with respect to the observed SPECIES densities.

A

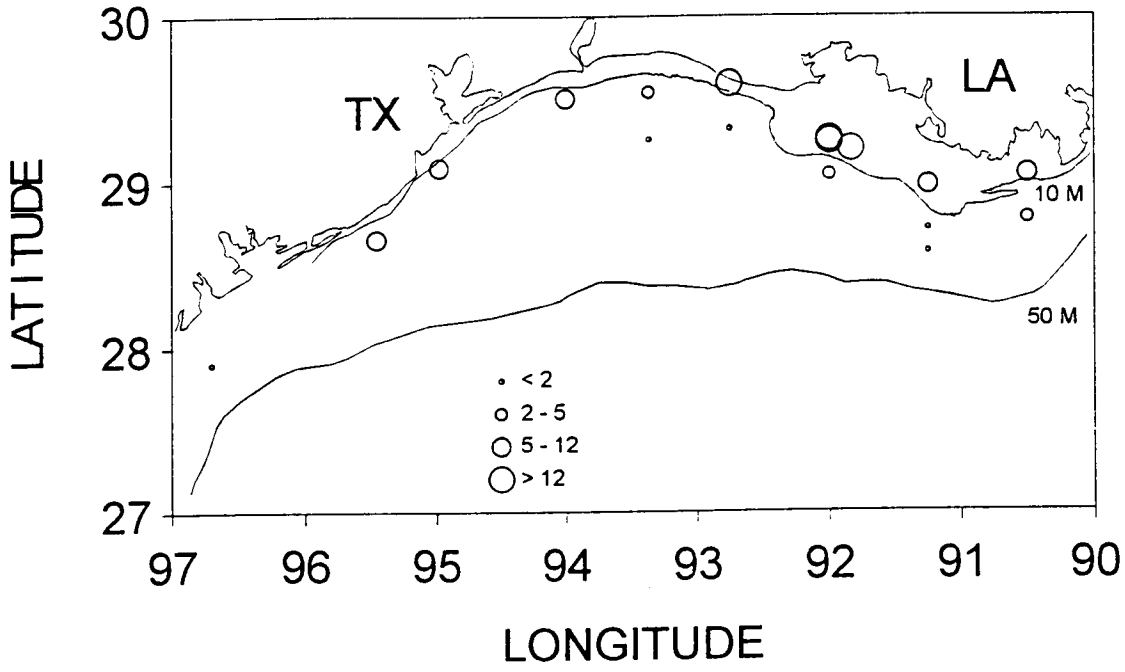

B

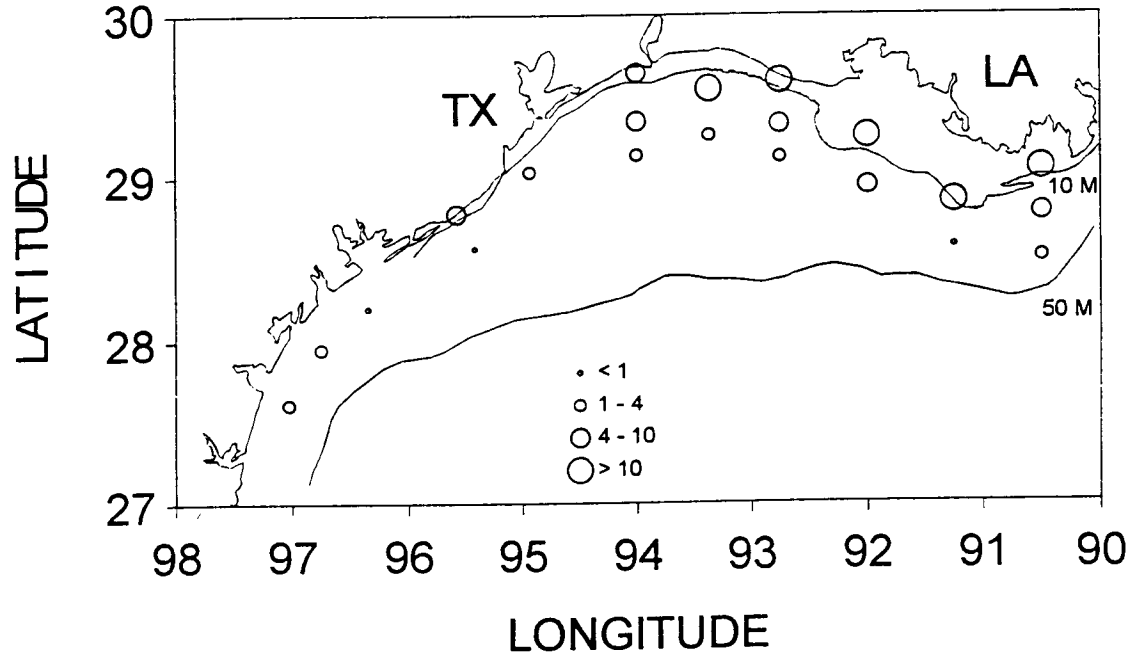

Figure 184. (a) April 1992 chlorophyll *a* concentration (mg/L); contour lines represent isobaths (m). (b) April 1993 chlorophyll *a* concentration (mg/L); contour lines represent isobaths (m).

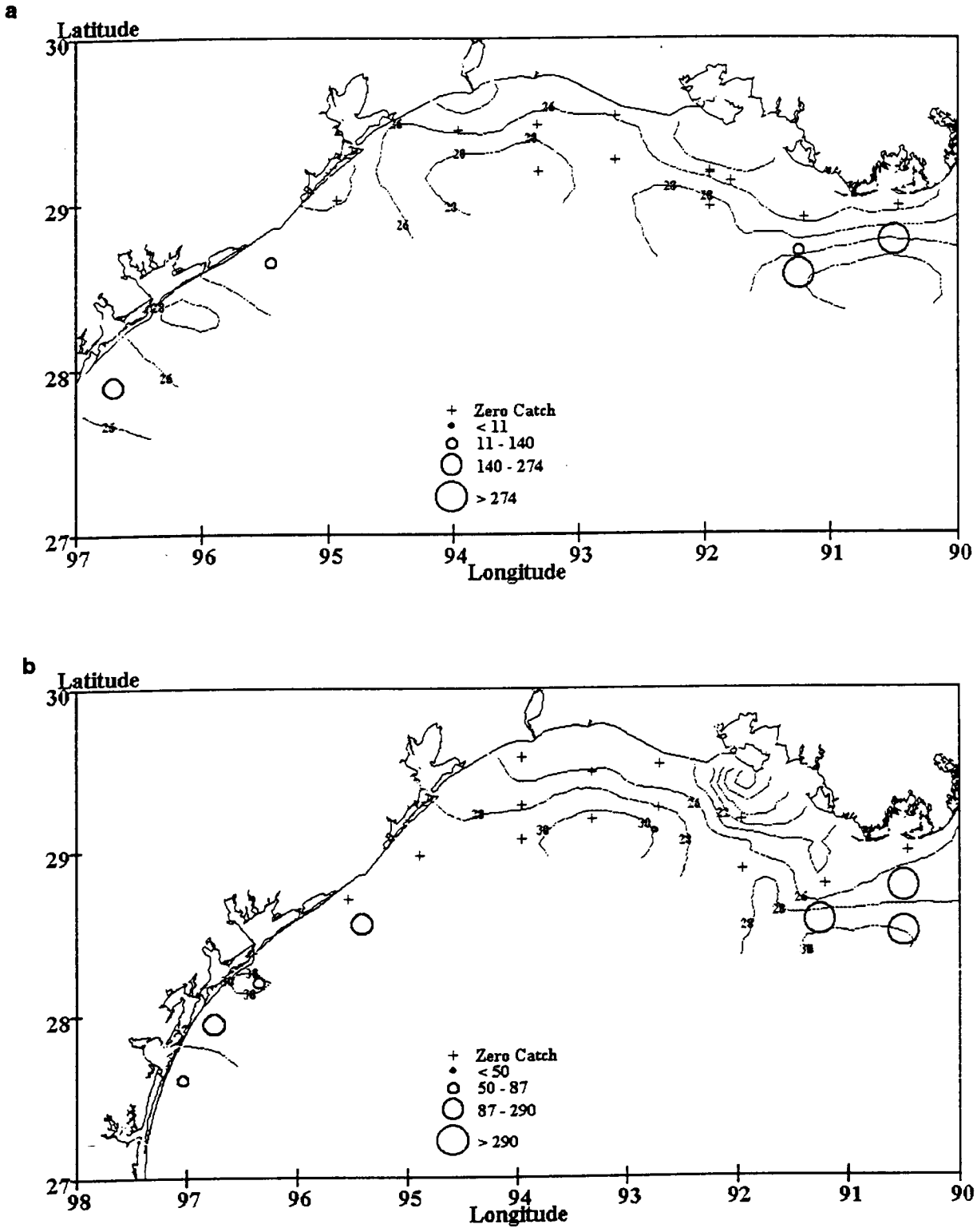

Figure 185. (a) April 1992 *Eucalanus pileatus* density (#/m^3); contour lines represent surface isohalines (‰). (b) April 1993 *Eucalanus pileatus* density (#/m^3); contour lines represent surface isohalines (‰).

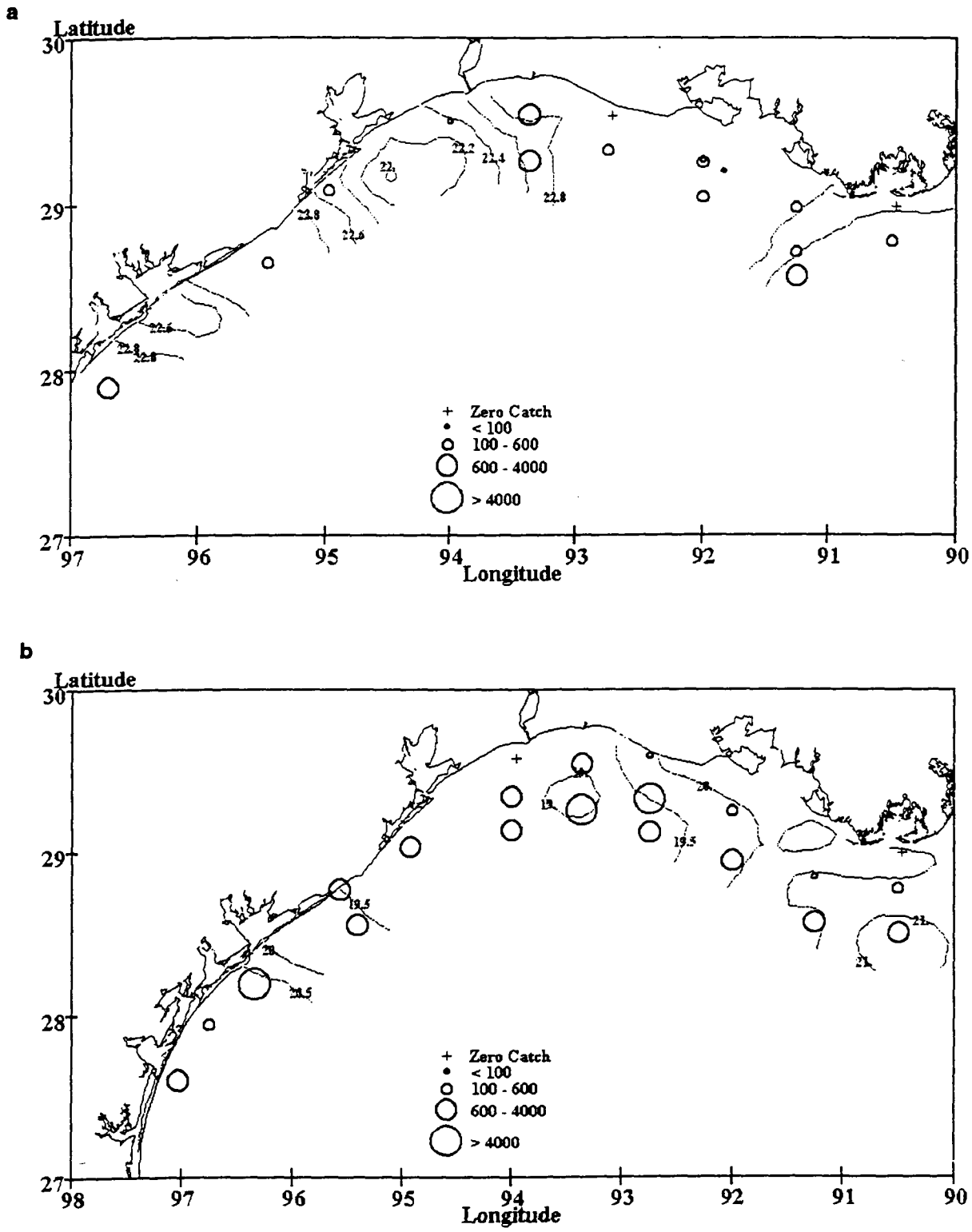

Figure 186. (a) April 1992 *Paracalanus parvus* density (#/m^3); contour lines represent surface isotherms (° C). (b) April 1993 *Paracalanus parvus* density (#/m^3); contour lines represent surface isotherms (° C).

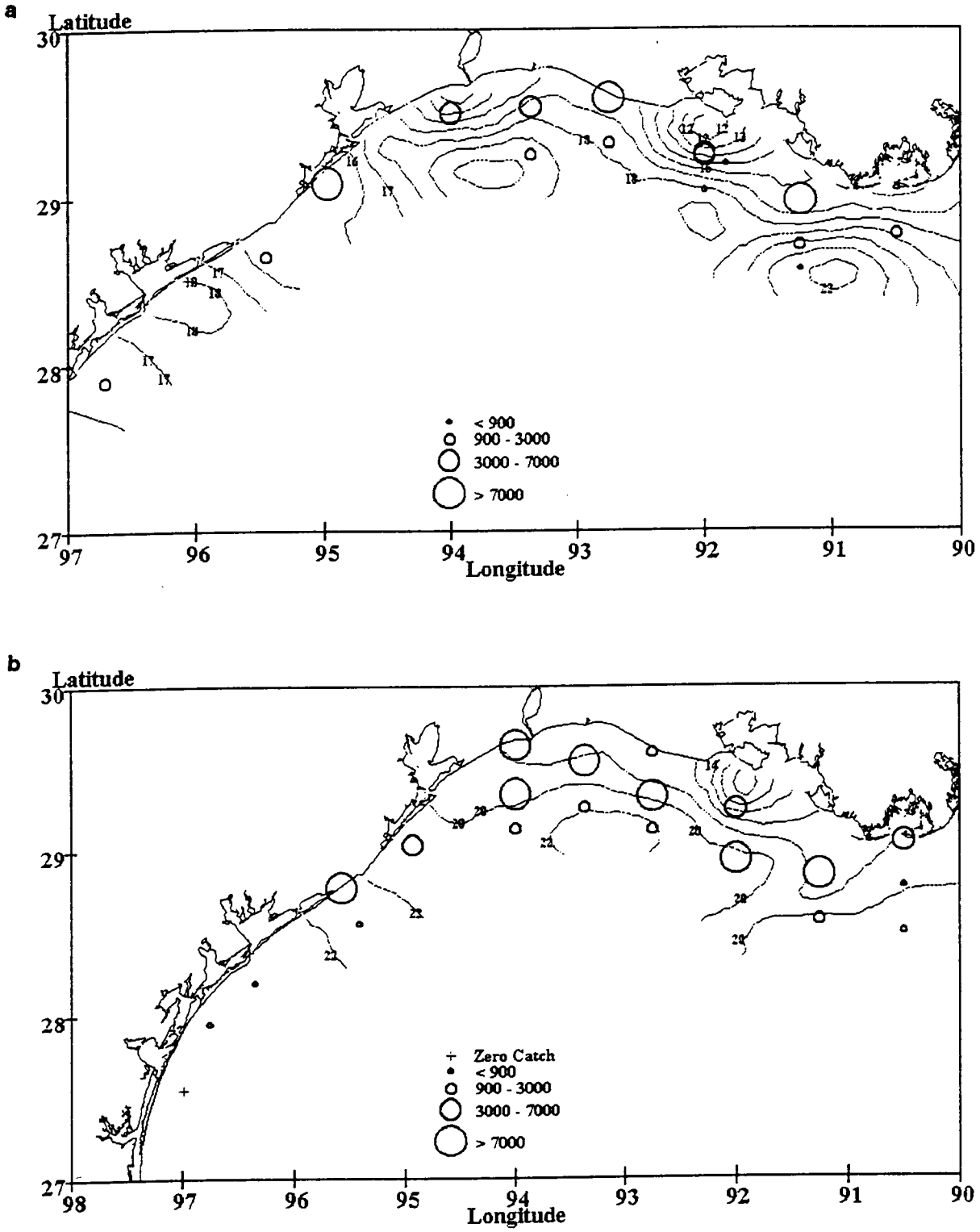

Figure 187. (a) April 1992 *Acartia tonsa* density (#/m^3); contour lines represent surface isopycnals (kg/m^3). (b) April 1993 *Acartia tonsa* density (#/m^3) contour lines represent surface isopycnals (kg/m^3).

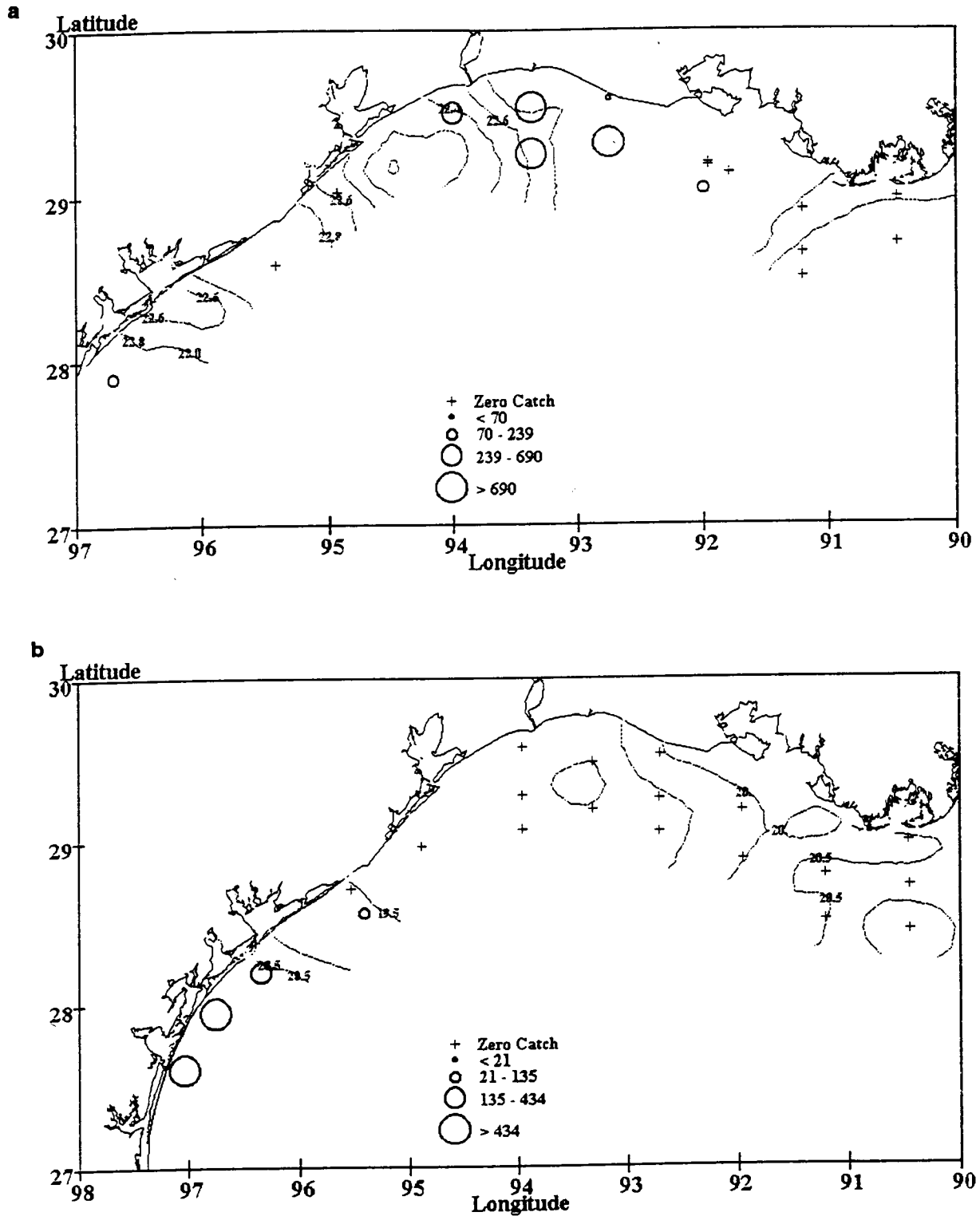

Figure 188. (a) April 1992 *Penilia avirostris* density (#/m^3); contour lines represent surface isotherms (° C). (b) April 1993 *Penilia avirostris* density (#/m^3); contour lines represent surface isotherms (° C).

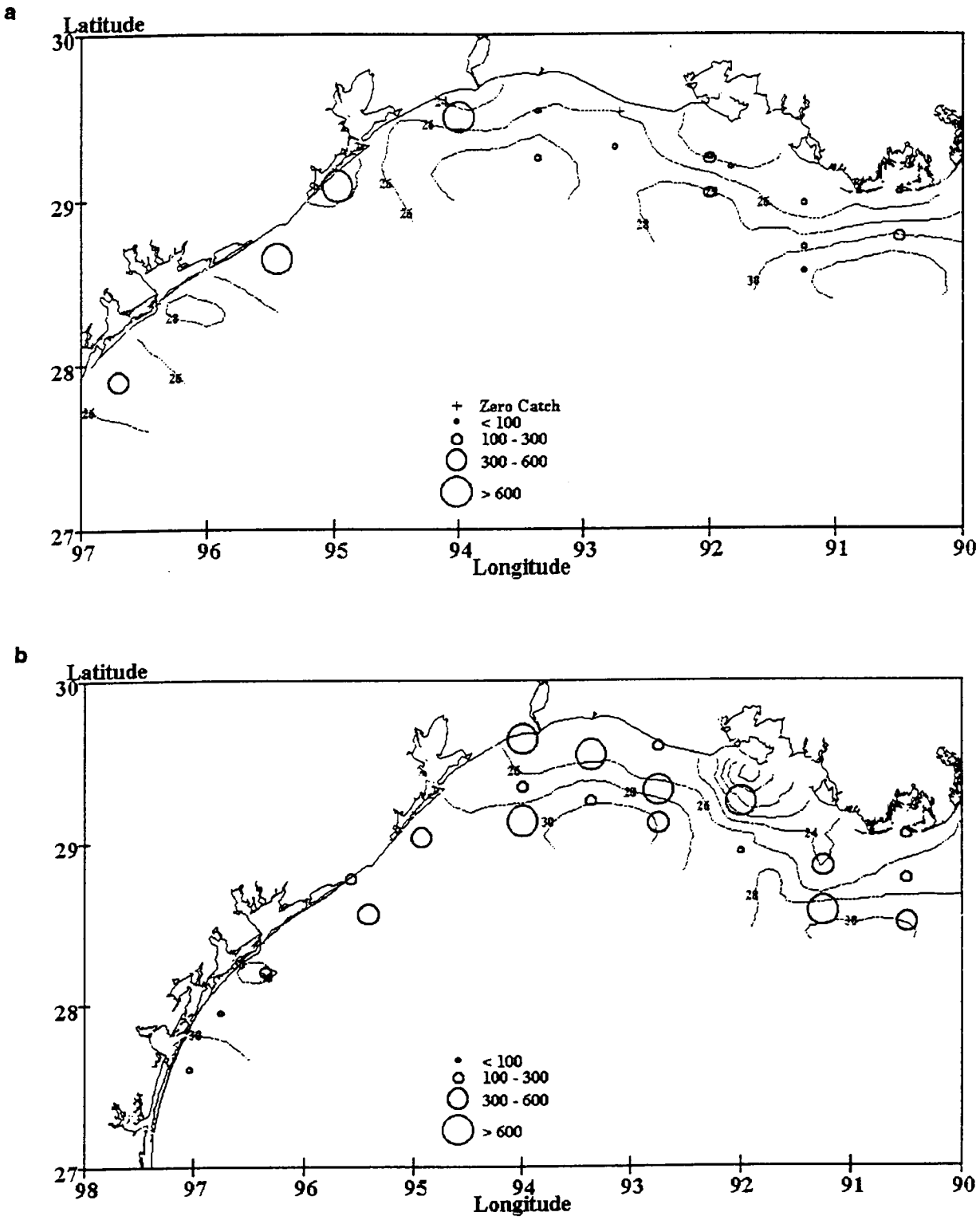

Figure 189. (a) April 1992 Copepoda nauplius density (#/m^3); contour lines represent surface isohalines (‰). (b) April 1993 Copepoda nauplius density (#/m^3); contour lines represent surface isohalines (‰).

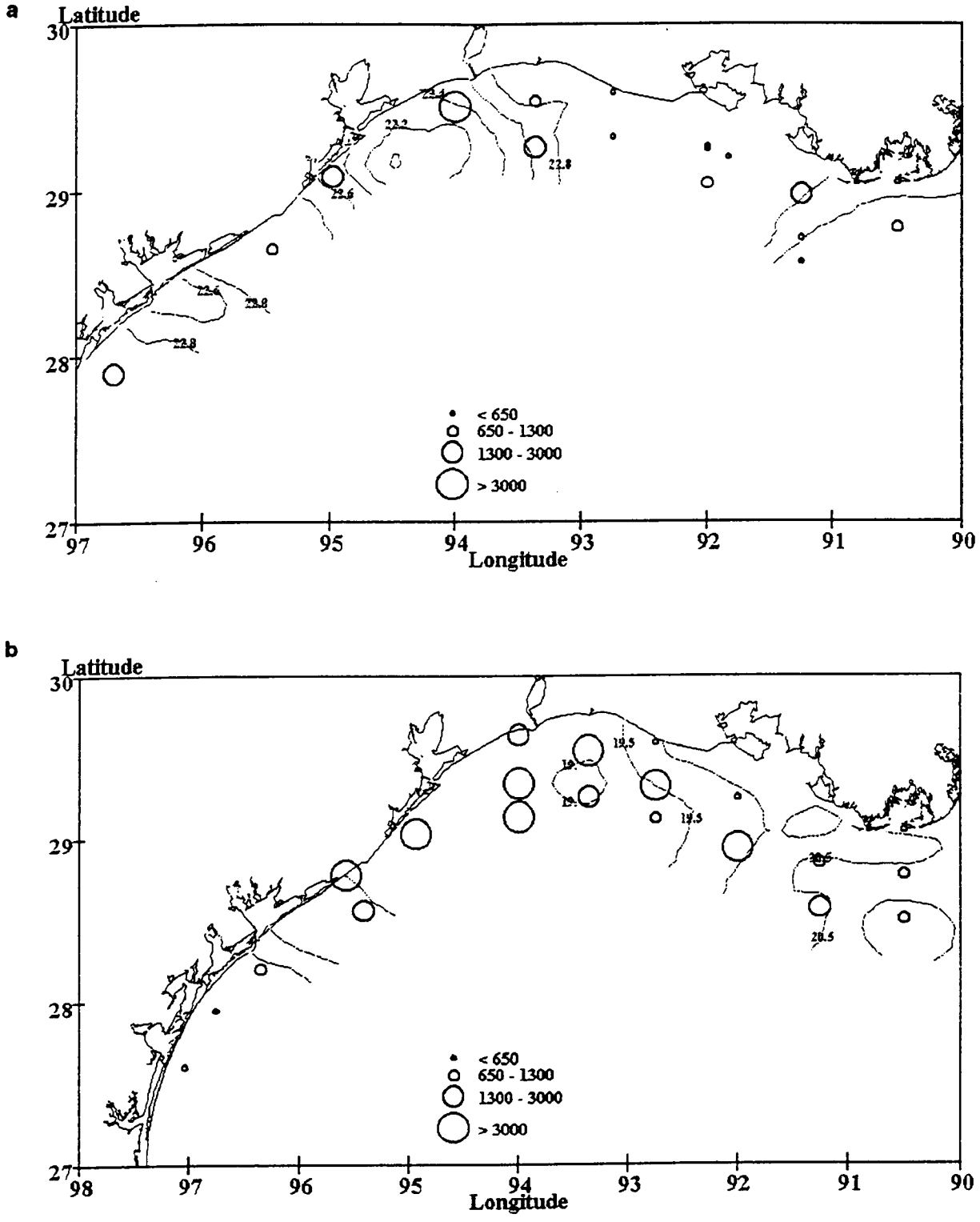

Figure 190. (a) April 1992 *Paracalanus crassirostris* density (#/m^3); contour lines represent surface isotherms (° C). (b) April 1993 *Paracalanus crassirostris* density (#/m^3); contour lines represent surface isotherms (° C).

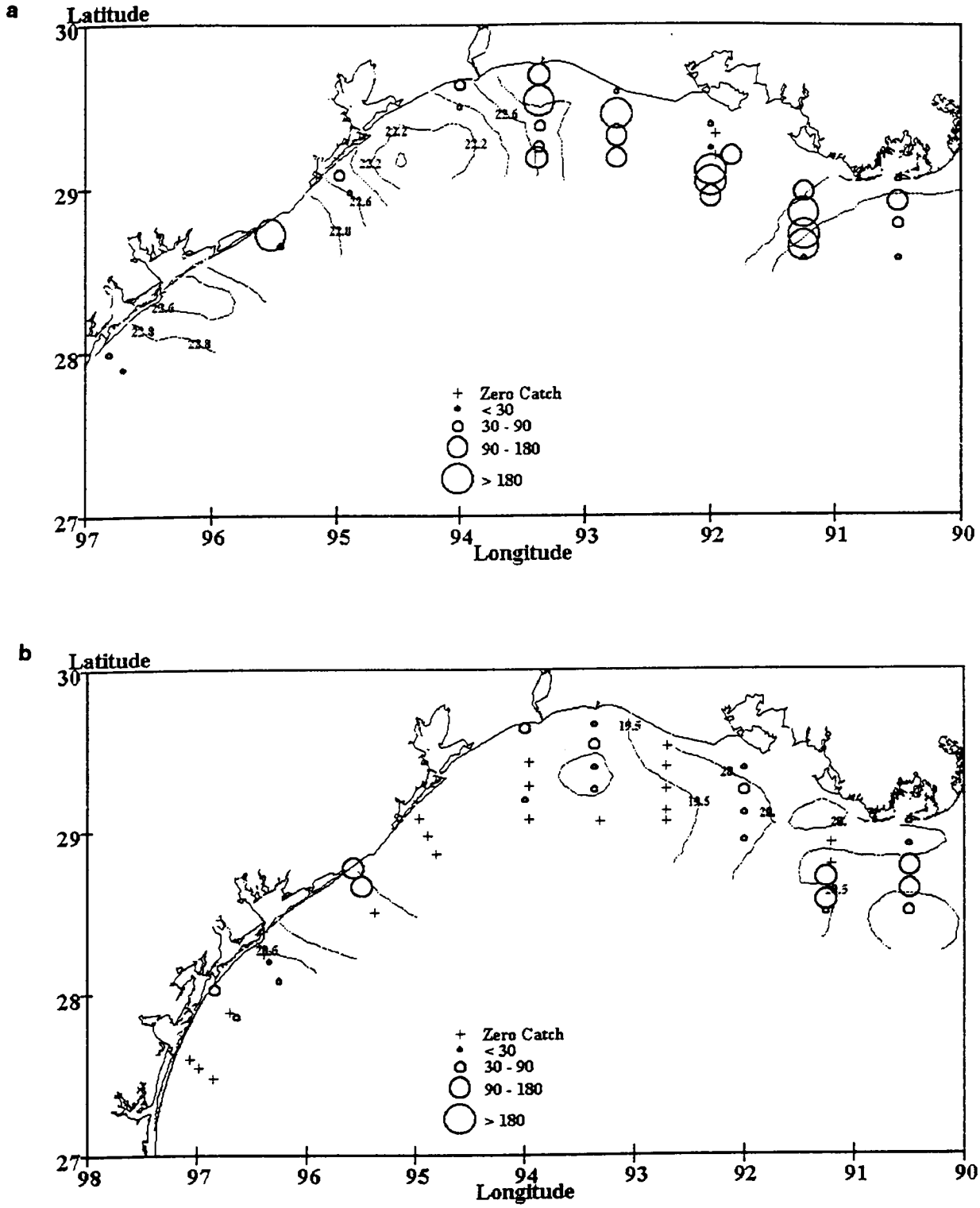

Figure 191. April 1992 and 1993 larval fish stations. (a) April 1992 *Cynoscion arenarius* density (#/100 m^3); contour lines represent surface isotherms (° C). (b) April 1993 *Cynoscion arenarius* density (#/100 m^3); contour lines represent surface isotherms (° C).

Table 35. Results of the April 1992/93 canonical analysis for fish larvae (n=72). Only one species met criteria for entry into analysis. Thus, only one canonical correlation was extracted. See Table 3 for table description.

	p	%
	0.0001	100
SPECIES	Coeff.	Corr.
Cynoscion arenarius	-1.00	-0.65
ENVIRONMENTAL		
Year	0.66	0.78
Longitude	0.45	0.47
Depth	-0.25	-0.12
Temperature	-0.11	-0.64
Salinity	0.25	0.02
Chlorophyll	0.56	0.28
Heterotrophs	<0.01	-0.03
Biomass Density	-0.14	-0.10
Redundancy	$U_{V\|U_1}$	$V_{X\|V_1}$
	0.0720	0.4270

d. April 12-21, 1994

Thirty-nine biological stations were sampled during the April 1994 cruise, which targeted dynamics off the Mississippi River Delta. The coverage of the cruise was limited to the area between Timbalier Bay and Southwest Pass, with the bulk of the sampling conducted off Southwest Pass. Column-averaged water temperature ranged from 19.5 to 21.7° C, and salinity ranged from 18.6 to 36.0‰. Low values for both variables were adjacent to Southwest Pass.

(1) Zooplankton High zooplankton biomass was noted at nearshore stations off Timbalier Bay and stations adjacent to Southwest Pass for both 153- and 335-µm mesh sizes. Biomass for the 153-µm samples ranged from 14 to 295 mg/m^3, while 335-µm samples ranged from 10 to 54 µg/m^3.

The most dominate zooplankton taxon was *Acartia tonsa* (1896/m^3) at the 19 stations surveyed. Also abundant were *Paracalanus parvus* (808/m^3) and *Euterpina acutifrons* (804/m^3). *Corycaeus* spp., *P. crassirostris*, copepod nauplii, *Oikopleura* spp., *Eucalanus pileatus*, *Oithona* spp., Sagittidae, and *Oncaea* spp. were common.

Canonical analysis accounted for a significant portion of the variance structure between the zooplankton and environmental variables (Table 36; $\Lambda=3.3\times10^{-7}$, p=6, q=10, n=17, P[F>F*]=0.0385). The first canonical root accounted for 56.8% of the predicted variation. The second root accounted for an additional 32.4%, which was nearly significant ($\Lambda=3.5\times10^{-5}$, P[F>F*]=0.0518).

Table 36. Results of the April 1994 canonical analysis for zooplankton (n=17). See Table 34 for table description.

Canonical Correlation	1		2	
	p	%	p	%
	0.0385	56.81	0.0518	32.44
SPECIES	Coeff.	Corr.	Coeff.	Corr.
Copepoda nauplius	0.29	0.12	-0.04	-0.11
Eucalanus pileatus	0.32	0.27	0.84	0.88
Paracalanus crassirostris	0.14	-0.10	-0.03	-0.27
Paracalanus parvus	-1.07	0.26	0.96	0.86
Centropages furcatus	-0.47	0.11	0.24	0.73
Acartia tonsa	-0.40	-0.23	-0.23	-0.50
Euterpina acutifrons	0.86	0.29	-1.14	0.78
Oithona plumifera	0.69	0.43	-0.05	0.60
Oikopleura spp.	-0.25	-0.44	0.12	-0.50
Doliolum spp.	-0.81	-0.57	0.25	0.45
ENVIRONMENTAL				
Longitude	-0.10	0.02	-0.30	-0.69
Depth	1.48	0.50	-1.12	0.32
Temperature	0.54	0.22	-0.21	-0.05
Salinity	-0.55	0.46	1.00	0.67
Chlorophyll	-0.09	-0.49	-0.52	-0.79
Heterotrophs	0.68	0.53	-0.20	-0.32
Redundancy	$U_{V1}u_1$	$V_{X1}v_1$	$U_{V1}u_2$	$V_{X1}v_2$
	0.1684	0.1020	0.2873	0.3797

The first environmental coefficient vector produced a large weight on depth (1.48) and moderate weights on heterotroph density (0.68), salinity (-0.55), and temperature (0.54). Intraset correlations were positive for heterotrophs (0.53), depth (0.50; Figure 192), and salinity (0.46; Figure 193). Chlorophyll had a negative correlation (-0.49; Figure 194). This variate was associated with outer, deep-water stations off Southwest Pass and contrasts with nearshore stations in the eastern portion of the cruise. *Oithona plumifera* was common in deep-water stations off Southwest Pass (Figure 193), and thus had a positive interset correlation (0.43). In contrast, *Doliolum* spp. (-0.57; Figure 195) and *Oikopleura* spp. (-0.44; Figure 196), which correlated negatively, were rare at these sites.

The second environmental coefficient vector produced large weights on depth (1.12) and salinity (1.00) and a moderate weight on chlorophyll (-0.52). Intraset correlations were positive for salinity (0.67) and negative for chlorophyll (-0.79) and longitude (-0.69). This variate was associated with seaward stations in the western portion of the cruise and near Southwest Pass. *Eucalanus pileatus* (0.88; Figure 197), *Paracalanus parvus* (0.86; Figure 198), *Euterpina acutifrons* (0.78), *Centropages furcatus* (0.73), *Oithona plumifera* (0.60), and *Doliolum* spp. (0.45) had positive interset correlations and tended to be more abundant at outer stations in the western portion of the

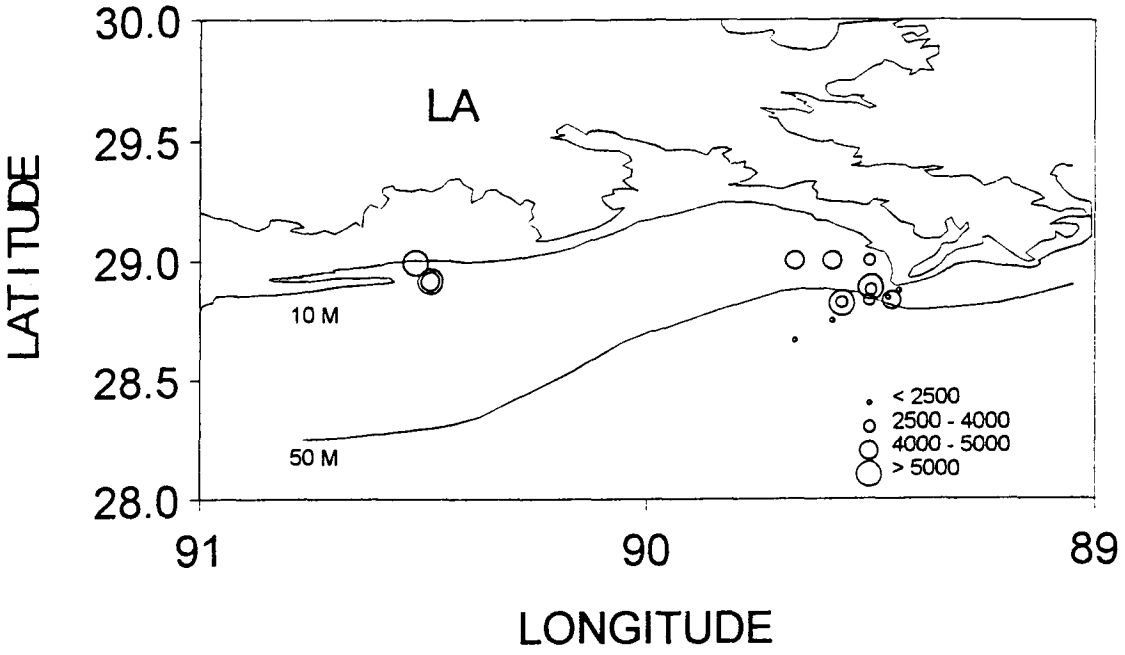

Figure 192. April 1994 heterotroph density (cells/mL). Contour lines represent isobaths (m).

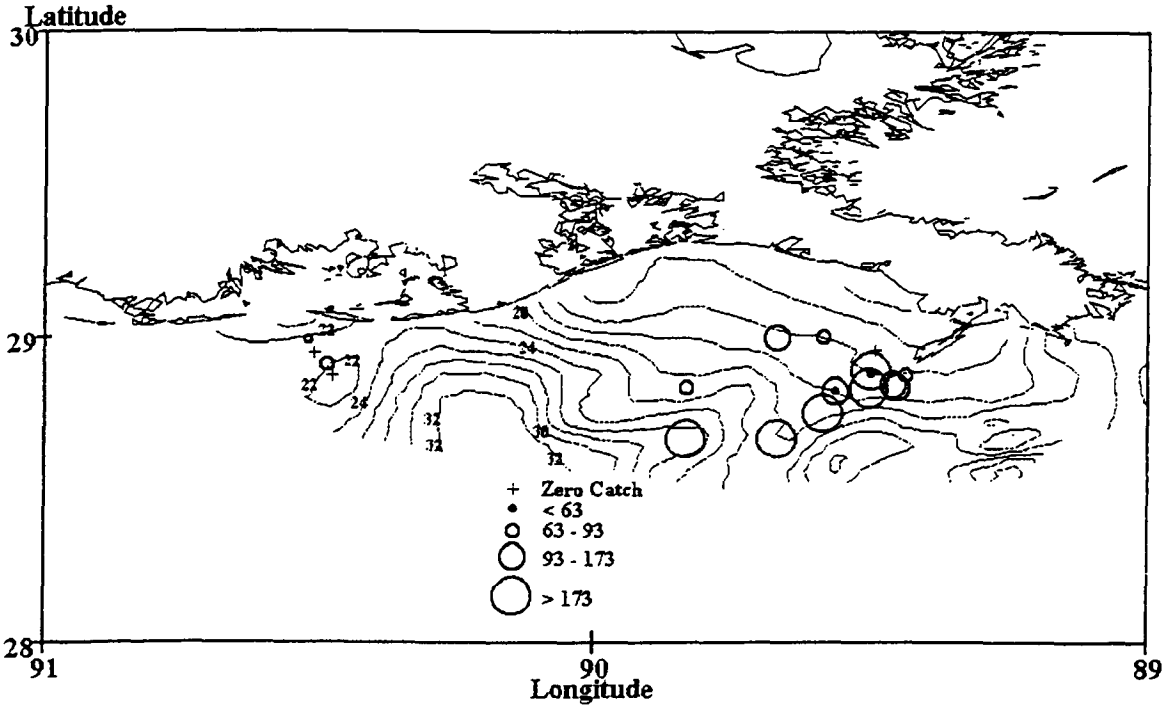

Figure 193. April 1994 *Oithona plumifera* density (#/m^3). Contour lines represent surface isohalines (‰).

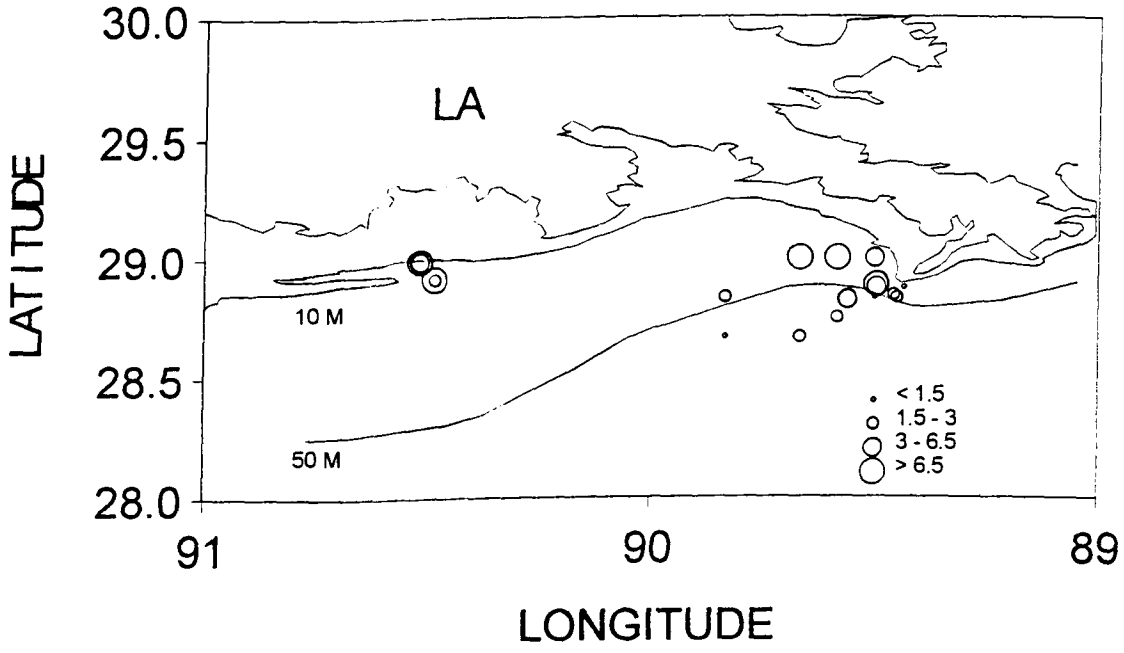

Figure 194. April 1994 Chlorophyll *a* concentration (mg/L). Contour lines represent isobaths (m).

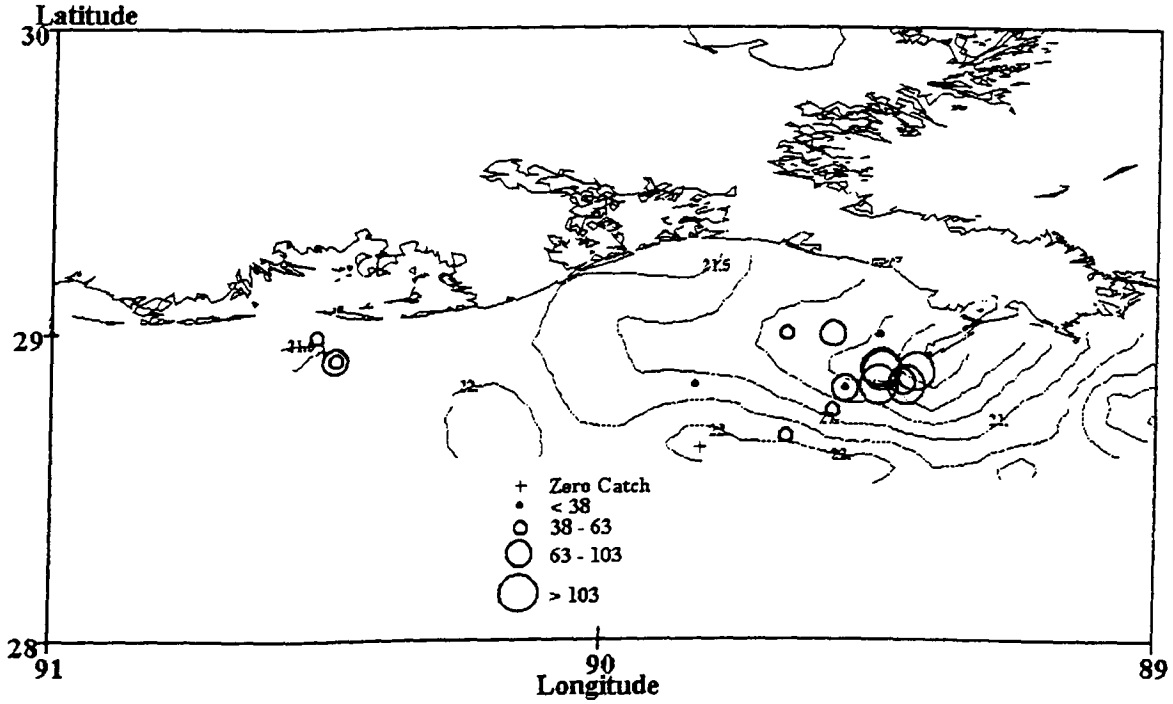

Figure 195. April 1994 *Doliolum* spp. density (#/m^3). Contour lines represent surface isotherms (°C).

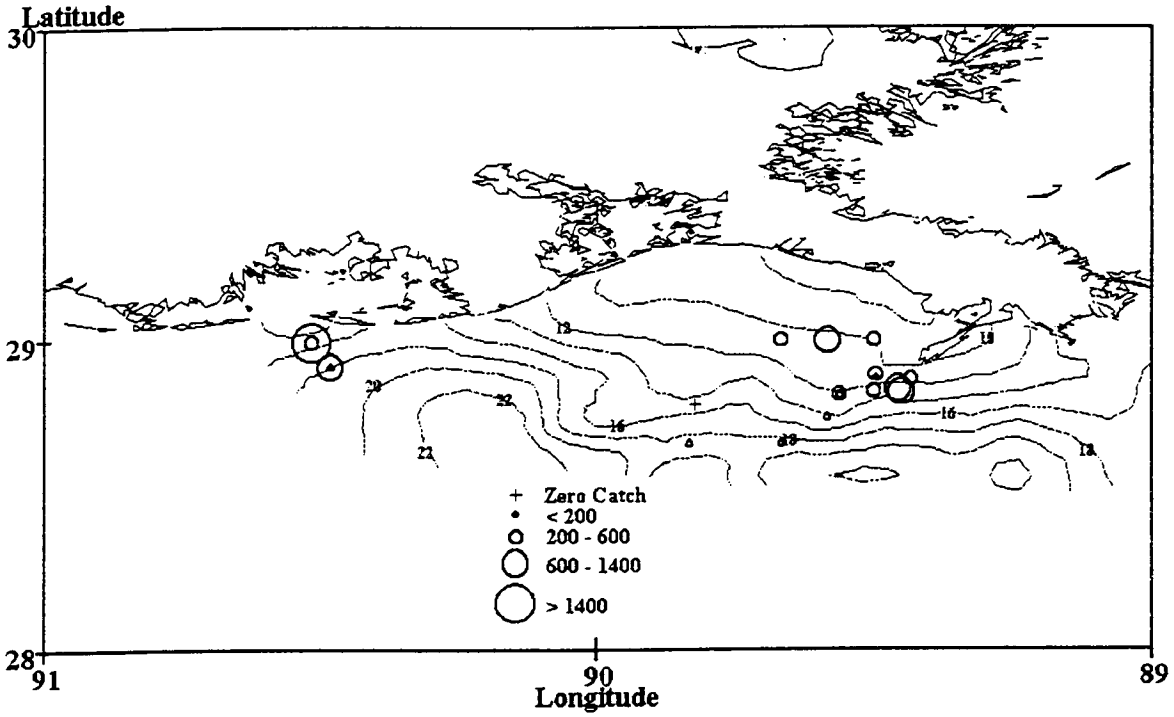

Figure 196. April 1994 *Oikopleura* spp. density (#/m^3). Contour lines represent surface isopycnals (kg/m^3).

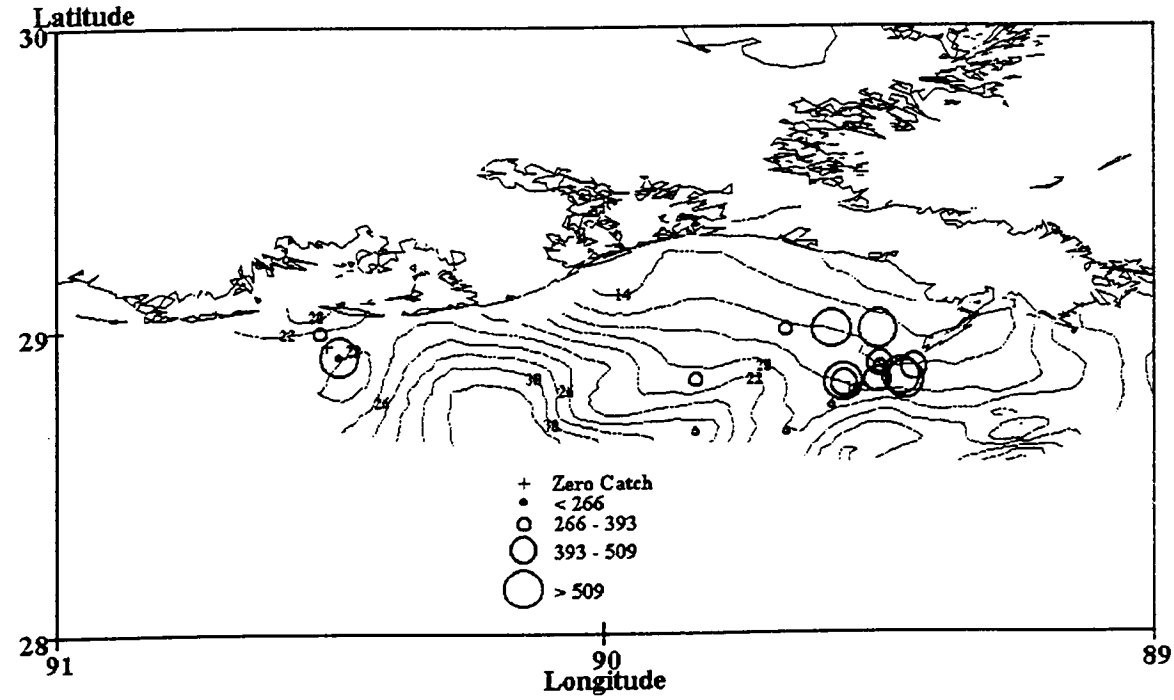

Figure 197. April 1994 *Eucalanus pileatus* density (#/m^3). Contour lines represent surface isohalines (‰).

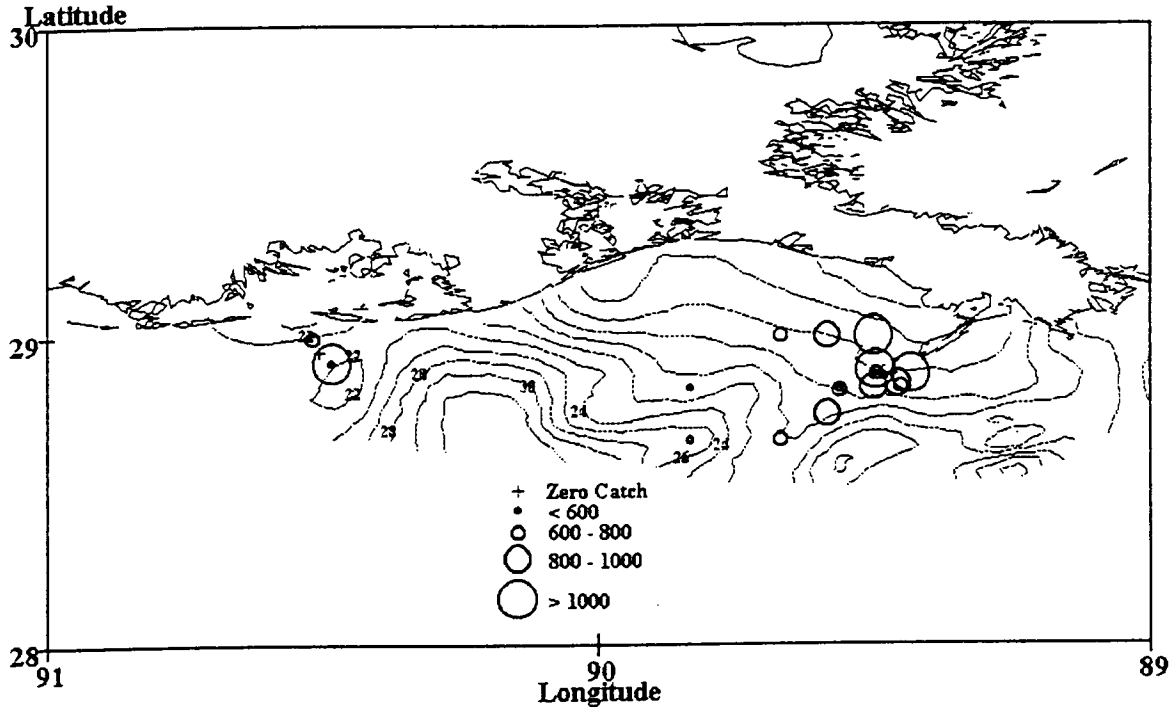

Figure 198. April 1994 *Paracalanus parvus* density (#/m^3). Contour lines represent surface isohalines (‰).

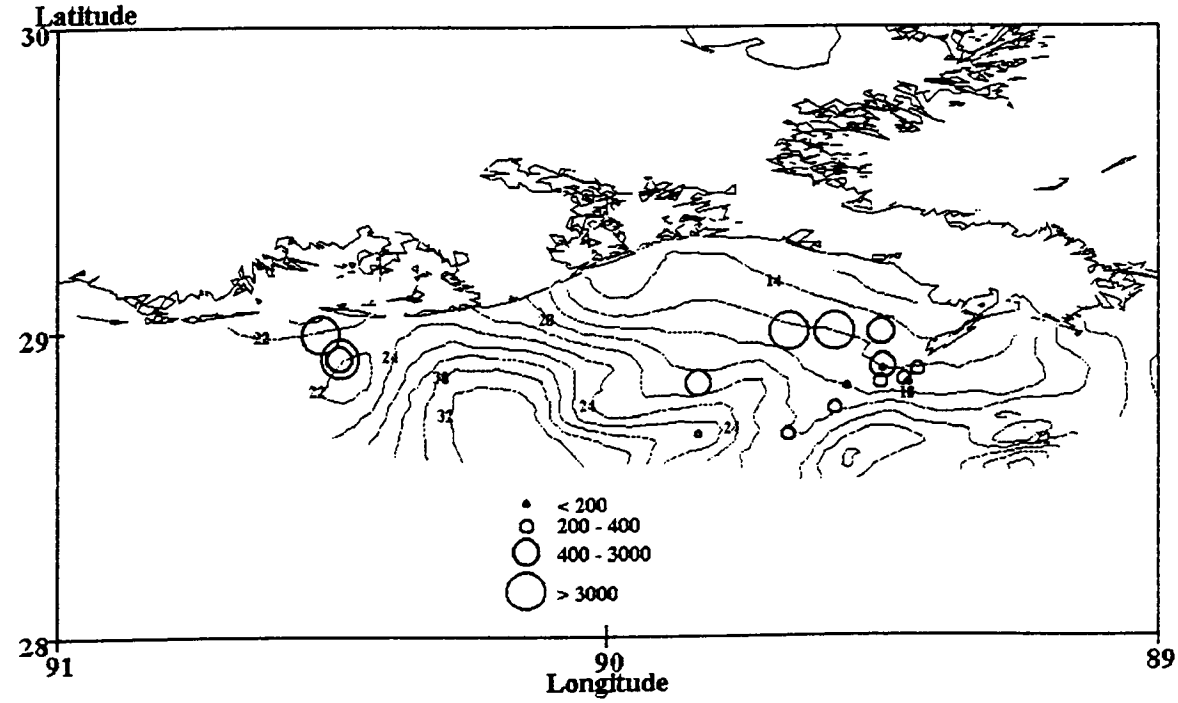

Figure 199. April 1994 *Acartia tonsa* density (#/m^3). Contour lines represent surface isohalines (‰).

cruise and adjacent to Southwest Pass. *Acartia tonsa* (Figure 199) and *Oikopleura* spp. (-0.50) had greater abundance at nearshore stations in the west and off Southwest Pass.

(2) Fish Larvae Ichthyoplankton densities were also highest at nearshore stations off Timbalier Bay and stations adjacent to Southwest Pass, ranging from 46 to 1151 larvae/100 m^3. Unidentified engraulids (112 larvae/100 m^3) were the most abundant taxa. Also abundant were Myctophidae (27/100 m^3), *Cynoscion arenarius* (21/100 m^3), *Bregmaceros cantori* (18/100 m^3), and *Etropus crossotus* (15/100 m^3). *Etrumeus teres*, Synodontidae, and Gobiidae were common.

Canonical analysis indicated that the fish and environmental variables were linearly related (Table 37; Λ=0.073, p=7, q=6, n=36, P[F>F*]=0.0024). The first canonical root accounted for 80.5% of the predictable variance. The second root was not significant (Λ=0.405, P[F>F*]=0.7174) and accounted for an additional 11.9%.

Table 37. Results of the April 1994 canonical analysis for fish larvae (n=36). See Table 34 for table description.

Canonical Correlation	1		2	
	p	%	p	%
	0.0024	80.45	0.7174	11.88
SPECIES	Coeff.	Corr.	Coeff.	Corr.
Etrumeus teres	0.24	0.74	-0.44	-0.17
Bregmaceros cantori	0.19	0.76	0.46	0.11
Cynoscion arenarius	-0.34	-0.29	-0.32	-0.29
Gobiidae sp. D	0.05	0.51	0.69	0.34
Trichiurus lepturus	0.26	0.61	0.06	0.42
Etropus crossotus	0.39	0.77	-0.66	-0.28
ENVIRONMENTAL				
Longitude	-0.53	-0.93	1.25	0.28
Depth	0.38	0.88	2.07	0.36
Temperature	-0.02	-0.61	0.62	0.07
Salinity	0.03	0.72	-1.20	0.03
Chlorophyll	0.01	-0.59	-0.38	0.09
Heterotrophs	-0.05	-0.46	-0.47	0.20
Biomass Density	-0.19	-0.65	-0.21	-0.11
Redundancy	U_{v1u_1}	V_{x1v_1}	U_{v1u_2}	V_{x1v_2}
	0.4122	0.4063	0.0158	0.0527

The first environmental coefficient vector produced large weights on longitude (-0.53) and depth (0.38). These variables also had large intraset correlations, although in opposite directions (-0.93 and 0.88, respectively). Since station depth tended to increase with decreasing longitude (Figure 192), this variate represents a longitudinal gradient. *Etropus crossotus* (0.77; Figure 200), *Bregmaceros cantori* (0.76; Figure 201), *Etrumeus teres* (0.74; Figure 202), *Trichiurus lepturus* (0.61; Figure 203), and an unidentified Gobiidae species (designated species D; 0.51) had large positive interset correlations.

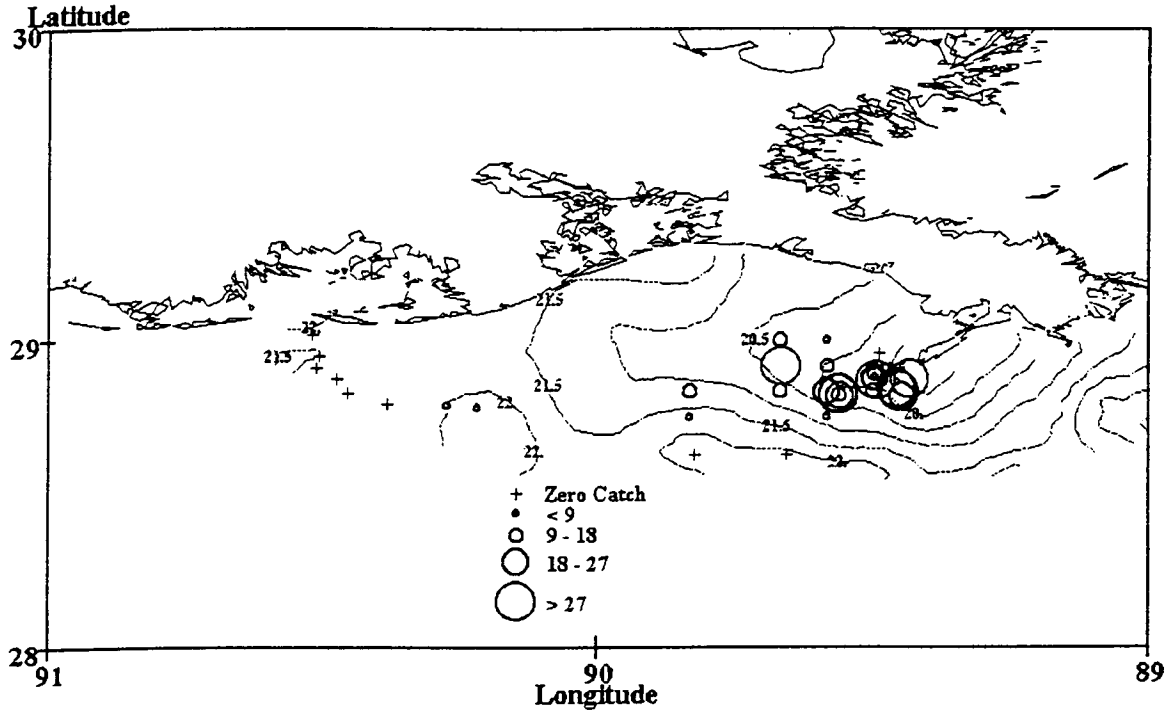

Figure 200. April 1994 *Etropus crossotus* density (#/100 m^3). Contour lines represent surface isotherms (° C).

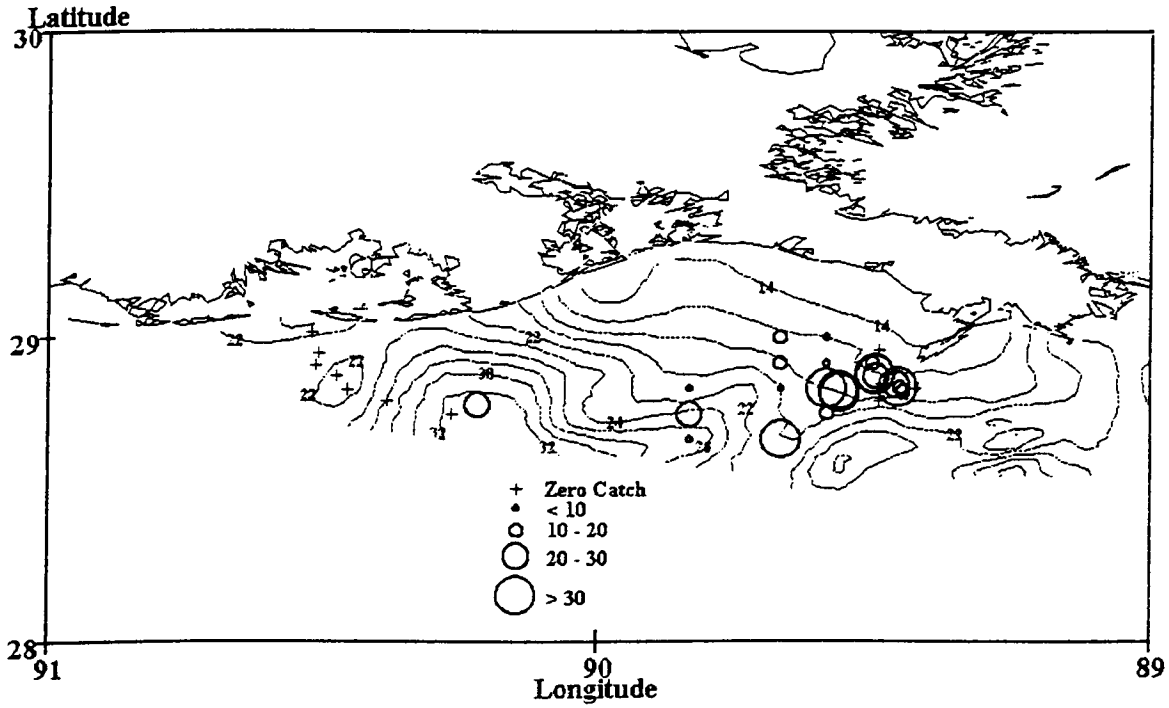

Figure 201. April 1994 *Bregmaceros cantori* density (#/100 m^3). Contour lines represent surface salinity (‰).

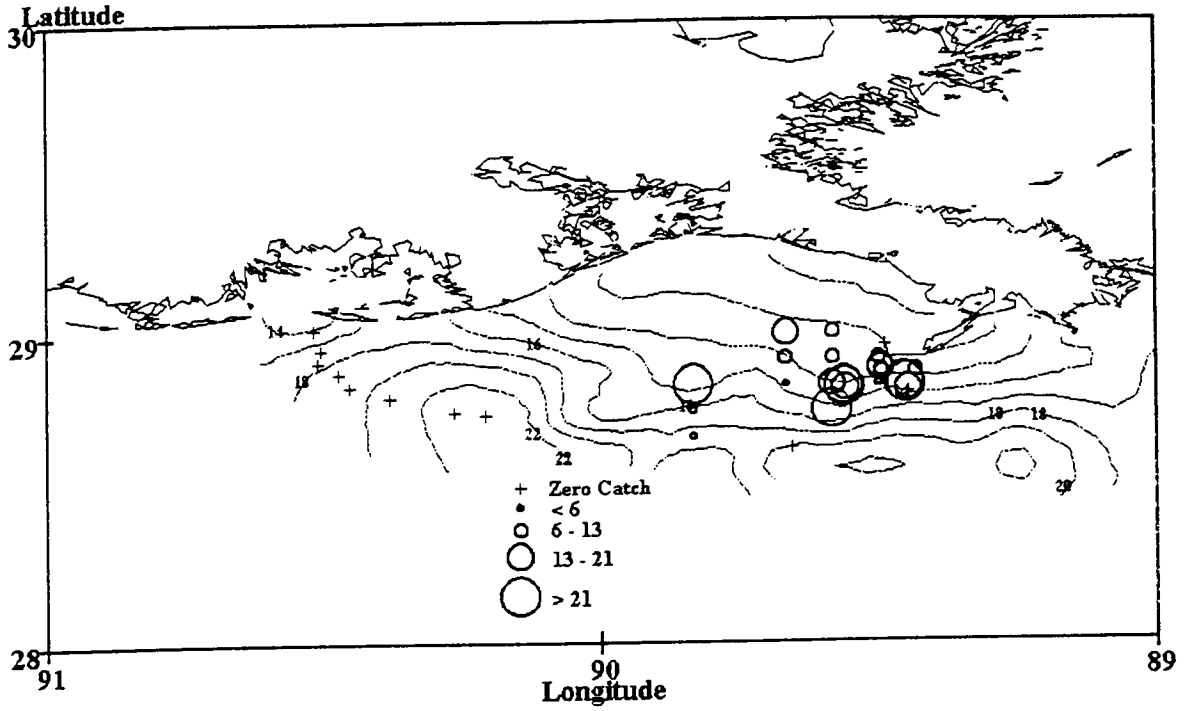

Figure 202. April 1994 *Etrumeus teres* density (#/100 m^3). Contour lines represent surface isopycnals (kg/m^3).

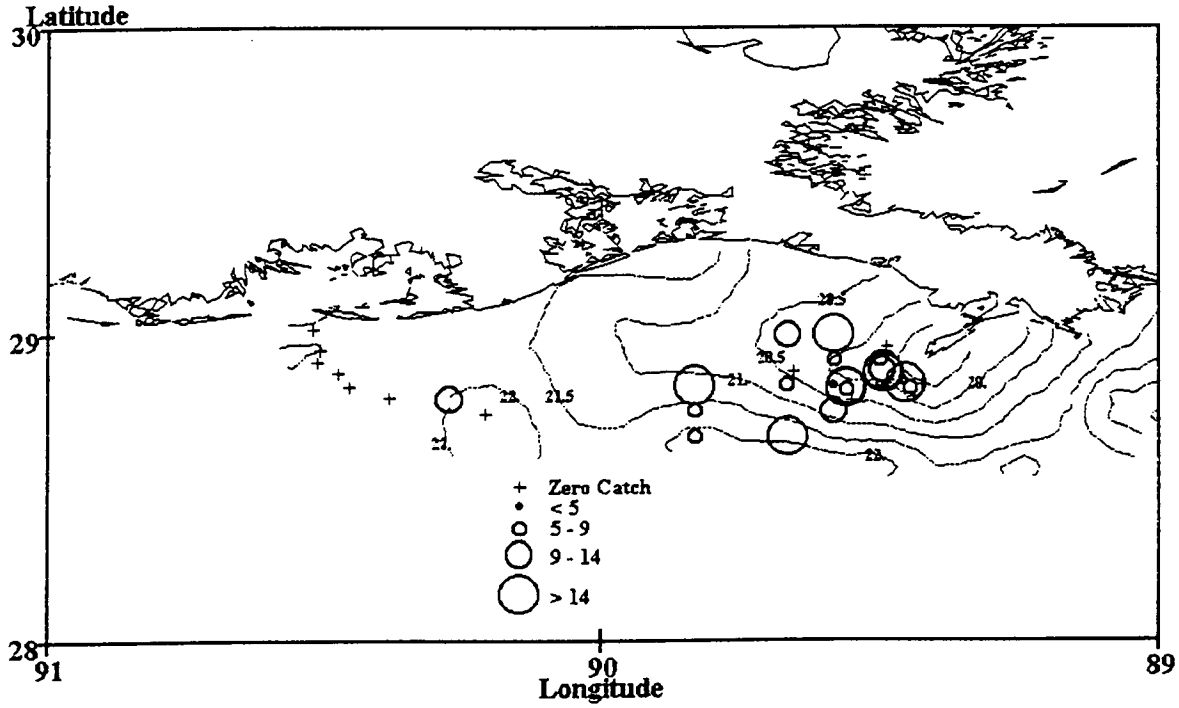

Figure 203. April 1994 *Trichiurus lepturus* density (#/100 m^3). Contour lines represent surface isotherms (° C).

These species were practically absent at stations off Timbalier Islands, the western portion of the cruise.

Depth also received a large weight (2.07) on the second environmental coefficient vector, although longitude (1.25) and salinity (-1.20) received medium weights. Depth (0.36) and longitude (0.28) had weak intraset correlations. This variate may differentiate stations off Southwest Pass. However, no species met our interset correlation requirements with this variate (i.e., all correlations were less than 37.8%).

2. July

Ninety stations were sampled during two July cruises (1993 and 1994). July is a period of high biological productivity and low river flow. The west/northwesterly coastal flow off east/central Louisiana typically converges with the well-developed north/northeasterly Texas coastal flow, which extends as far east as just downstream and offshore of Atchafalaya Bay, resulting in mid-shelf mixing at the area of convergence. Copepoda was again the most abundant organism in the 41 stations analyzed for zooplankton, comprising over 78% of the total mean catch. This catch was mainly Calanoida (55%), followed by Cyclopoida (19%), Harpactoida, and copepod nauplii (both at 2%). Other dominant forms included Appendicularia (*Oikopleura*; 5%), Mollusca (Bivalvia and Gastropoda; 5%), and Sagittidae (3%). For larval fish, Engraulidae was the dominant family, comprising 48% of the total mean catch. Other common families included Sciaenidae (10%), Soleidae (9%), Carangidae (8%), Clupeidae (7%), and Bothidae (5%).

a. July 13-21, 1993

Samples from 52 stations were collected during July 1993. The west/northwesterly coastal flow off east/central Louisiana was enhanced this particular year by very high Mississippi/Atchafalaya River discharge. Samples were collected from Timbalier Bay to west Matagorda Bay, with special emphasis on the Galveston Bay plume and in an area of convergence with the Louisiana westward flowing coastal current and the northeastward flowing Mexico/Texas coastal current. Column-averaged water temperature ranged from 25.2 to 31.0 ° C, while salinity ranged from 5.9 to 35.1 ‰. Low values for both variables were off the Atchafalaya basin.

(1) Zooplankton High zooplankton biomass estimates for both the 153- and 335-µm mesh samples were found west of Atchafalaya Bay to Sabine Lake and at nearshore stations between Timbalier and Atchafalaya Bays. High values were also noted within the Galveston Bay plume. Biomass for the 153-µm samples ranged from 16 to 261 mg/m^3 and 335-µm samples ranged from 0 to 108 mg/m^3.

Zooplankton composition was determined at 24 stations. *Paracalanus crassirostris* (5645/m^3) was the dominate zooplankton taxon, although *Acartia* spp. immature and *A. tonsa* (3768 and 3753/m^3, respectively), if considered together, would have dominated (*A. lilljeborgi* was common at several stations off Texas). Bivalve veligers (2989/m^3) and *Oithona brevicornis* (2905/m^3) were abundant also. *P. parvus*, *Oikopleura* spp., *Paracalanus* spp. immature, *Creseis* spp., *Centropages furcatus*, and *Temora turbinata* were common.

(2) Fish Larvae Ichthyoplankton fish densities were highest west of Calcasieu Lake, ranging from 0 to 1685 larvae/100 m^3. Again, unidentified engraulids made up the bulk of the catch (155 larvae/100 m^3). *Symphurus* spp. (15/100 m^3), *Opisthonema oglinum* (15/100 m^3), *Cynoscion arenarius* (14/100 m^3), and *Chloroscombrus chrysurus*

(14/100 m^3) were also abundant in July. *Stellifer lanceolatus*, *Anchoviella perfasciata* (specimens ≥ 16 mm SL), *Anchoa hepsetus*, and *Harengula jaguana* were common. *Symphurus* spp. represents *S. plagiusa* and, most likely, *S. civitatus* in the *S. plagusia* (Bloch and Schneider 1801) complex (Munroe 1991).

b. July 12-17, 1994

Samples were collected from 38 stations during July 1994. Sample coverage included the area between Timbalier and Matagorda Bays. Column-averaged water temperature ranged from 24.6 to 30.1 °C, and salinity ranged from 13.5 to 36.0 ‰. Again, low values for both variables were off the Atchafalaya basin.

(1) Zooplankton High zooplankton biomass values for the 153-μm samples were limited to nearshore waters between Timbalier Bay and Calcasieu Lake, while high values for the 335-μm samples were seen at nearshore waters throughout the survey. Biomass for the 153-μm samples ranged from 8 to 174 mg/m^3, while 335-μm samples ranged from 4 to 90 mg/m^3.

Zooplankton composition was determined at 17 stations. *Acartia tonsa* (4497/m^3) was the most abundant taxon, followed by *Paracalanus crassirostris* (758/m^3) and *Temora turbinata* (679/m^3). Common taxa included *Oithona brevicornis*, *Centropages furcatus*, and *Penilia avirostris*.

(2) Fish Larvae Larval fish densities were highest at stations west of Sabine Lake and at nearshore stations between Timbalier Bay and Calcasieu Lake and ranged from 24 to 8495 larvae/100 m^3. Unidentified engraulids (224 larvae/100 m^3) and *Anchoa* spp. (189/100 m^3) were the most abundant taxa. The next most abundant taxon after anchovies was *Opisthonema oglinum* (131/100 m^3), followed by *Chloroscombrus chrysurus* (60/100 m^3) and *Cynoscion arenarius* (45/100 m^3). *Symphurus plagiusa*, *Bairdiella chrysoura*, and *Syacium papillosum* were also common.

c. July 1993-1994

(1) Zooplankton Canonical analysis explained a significant portion of the variance between the zooplankton and environmental variables (Table 38; $\Lambda=2.9\times10^{-5}$, p=7, q=23, n=41, P[F>F*]=0.0003). The first canonical root accounted for 76.3% of the predicted variation. The second root accounted for an additional 8.3%, which was not significant ($\Lambda=1.3\times10^{-3}$, P[F>F*]=0.1467).

Salinity received a large weight on the first environmental coefficient vector (1.54), while temperature (0.78) and chlorophyll (0.64) received moderate weights. Chlorophyll (-0.64; Figures 204a and 204b) and salinity (0.89; Figures 188c and 188d) were correlated with this variate, although in opposite directions. This variate was associated with high salinities and low chlorophyll concentrations and contrasts with stations affected by the Atchafalaya plume. *Centropages furcatus* (0.66; Figures 205a and 205b), *Corycaeus amazonicus*(0.62), *Oithona plumifera* (0.55), *Euterpina acutifrons* (0.46), *Oncaea venusta* (0.46), *Temora turbinata* (0.45), *Eucalanus pileatus* (0.43), and *Penilia avirostris* (0.41) had positive interset correlations and tended to be associated with saline waters. In contrast, *Acartia tonsa* (-0.75; Figures 206a and 206b) and *Paracalanus crassirostris* (-0.49; Figures 207a and 207b) were associated with the Atchafalaya plume. These results are consistent with those obtained considering each year separately.

Table 38. Results of the July 1993/94 canonical analysis for zooplankton (n=41). See Table 34 for table description.

Canonical Correlation	1		2	
	p	%	p	%
	0.0003	76.32	0.1467	8.32
SPECIES	Coeff.	Corr.	Coeff.	Corr.
Penilia avirostris	0.03	0.41	-0.11	-0.02
Copepoda nauplius	0.07	0.19	0.14	0.27
Eucalanus pileatus	0.13	0.43	-0.19	0.17
Paracalanus crassirostris	-0.70	-0.49	0.90	0.50
Paracalanus parvus	0.49	0.29	-0.58	0.51
Temora turbinata	-0.03	0.45	0.49	0.20
Centropages furcatus	0.27	0.66	0.46	0.31
Labidocera aestiva	0.16	-0.22	-0.47	-0.29
Acartia tonsa	-0.20	-0.75	0.20	-0.07
Euterpina acutifrons	0.17	0.46	-0.04	0.22
Oithona brevicornis	0.12	-0.09	0.22	0.36
Oithona plumifera	0.27	0.55	0.14	0.21
Oncaea venusta	-0.30	0.46	0.28	0.28
Corycaeus amazonicus	-0.09	0.62	0.05	0.27
Euconchoecia chierchiae	-0.02	0.24	0.17	0.08
Penaeus aztecus	0.08	0.27	0.02	-0.01
Lucifer faxoni	-0.03	0.18	0.06	0.26
Callinectes sapidus	0.15	0.06	-0.27	0.28
Callinectes similis	0.02	0.05	0.55	0.23
Portunus spp.	-0.03	0.17	0.13	0.09
Flaccisagitta enflata	0.23	0.34	0.03	0.08
Oikopleura spp.	-0.11	-0.26	0.23	0.39
Amphioxi spp.	-0.13	0.01	0.06	0.15
ENVIRONMENTAL				
Year	0.30	0.46	-0.90	-0.77
Depth	0.46	0.54	-0.80	-0.01
Longitude	-0.44	0.27	-0.11	0.23
Temperature	0.78	-0.32	-0.49	0.13
Salinity	1.54	0.89	0.60	0.35
Chlorophyll	0.64	-0.64	-0.20	-0.55
Heterotrophs	-0.09	-0.36	-0.15	-0.47
Redundancy	$U_{V|U_1}$	$V_{X|V_1}$	$U_{V|U_2}$	$V_{X|V_2}$
	0.2808	0.1505	0.1551	0.0703

The second environmental coefficient vector produced large weights on year (-0.90), depth (-0.80), and salinity (0.60). Of these variables, only year was correlated with this variate (-0.77). Thus, this variate was associated with yearly differences in

a

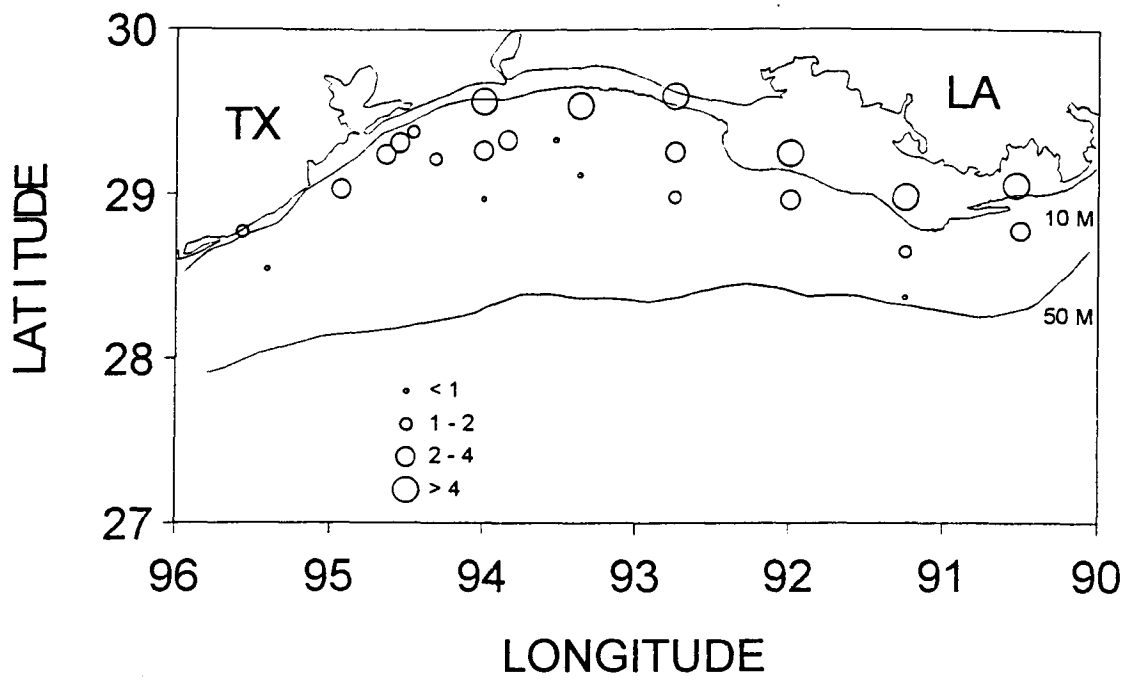

b

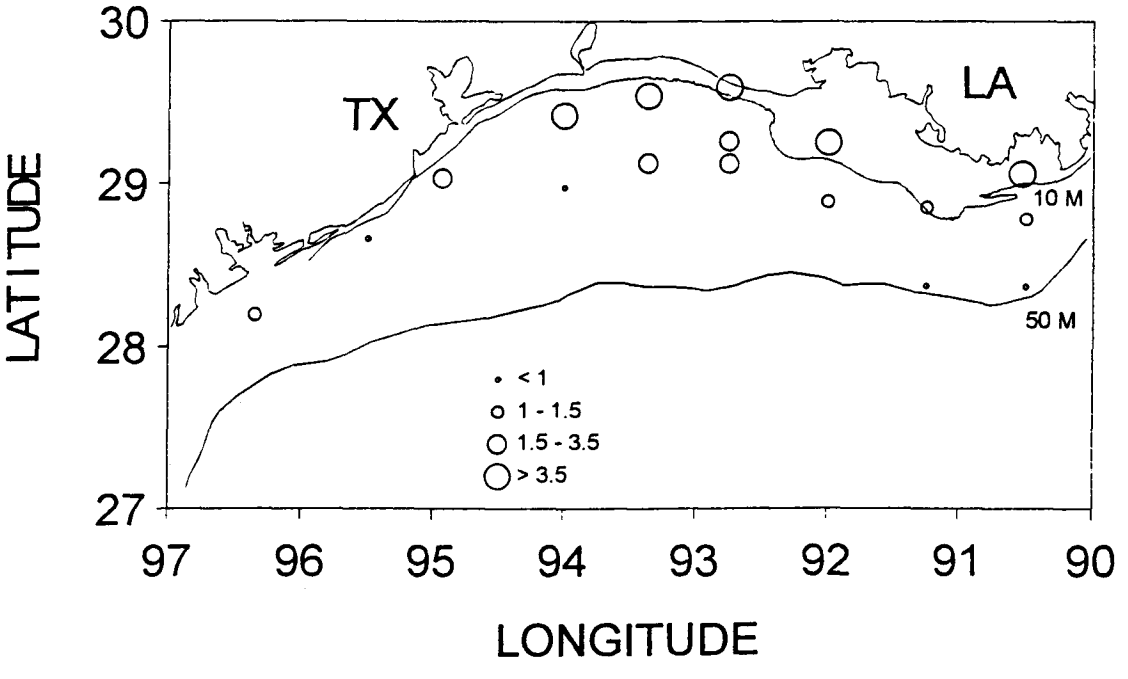

Figure 204. (a) July 1993 chlorophyll *a* concentration (mg/L); contour lines represent isobaths (m). (b) July 1994 chlorophyll *a* concentration (mg/L); contour lines represent isobaths (m).

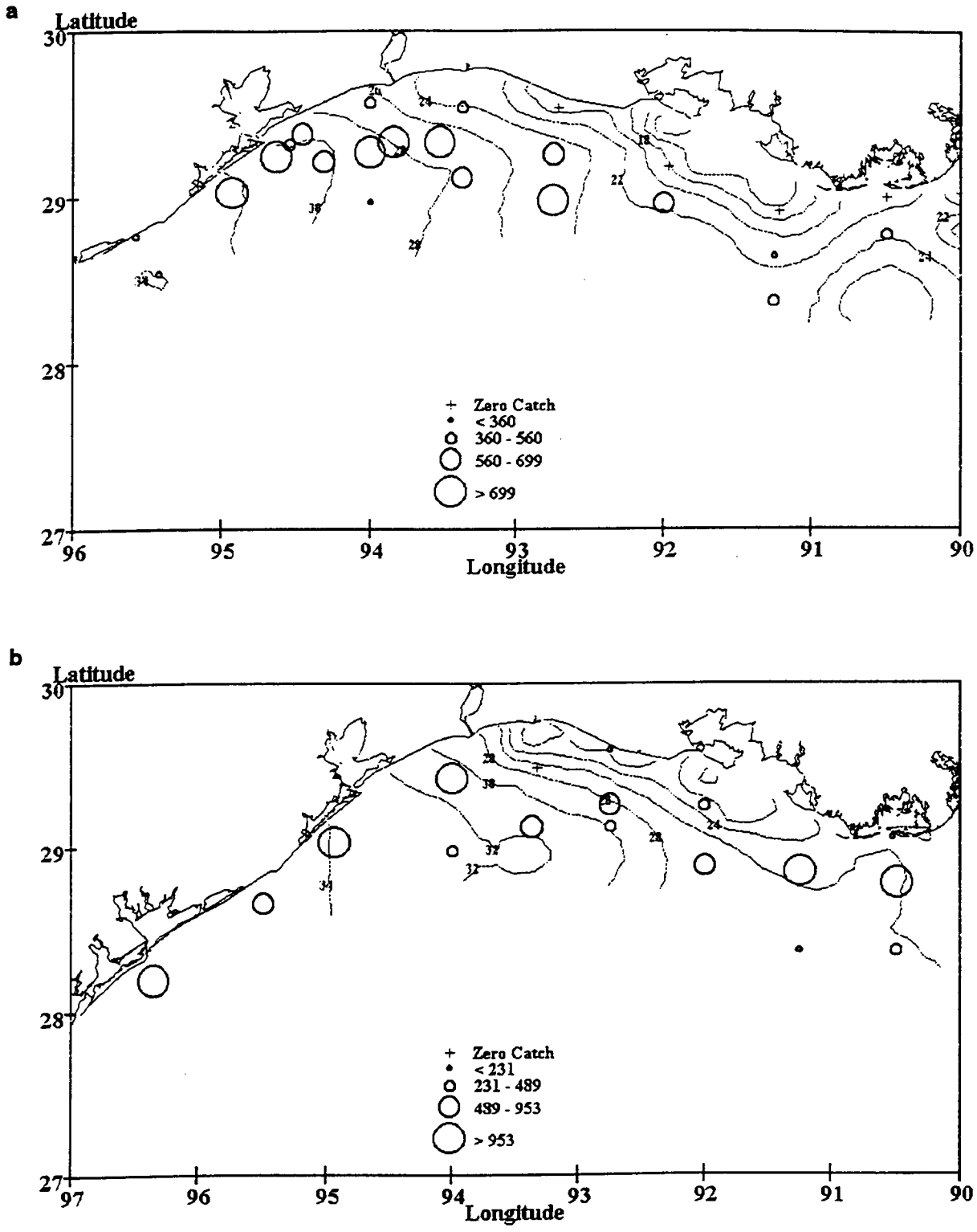

Figure 205. (a) July 1993 *Centropages furcatus* density (#/m^3); contour lines represent surface isohalines (‰). (b) July 1994 *Centropages furcatus* density (#/m^3); contour lines represent surface isohalines (‰).

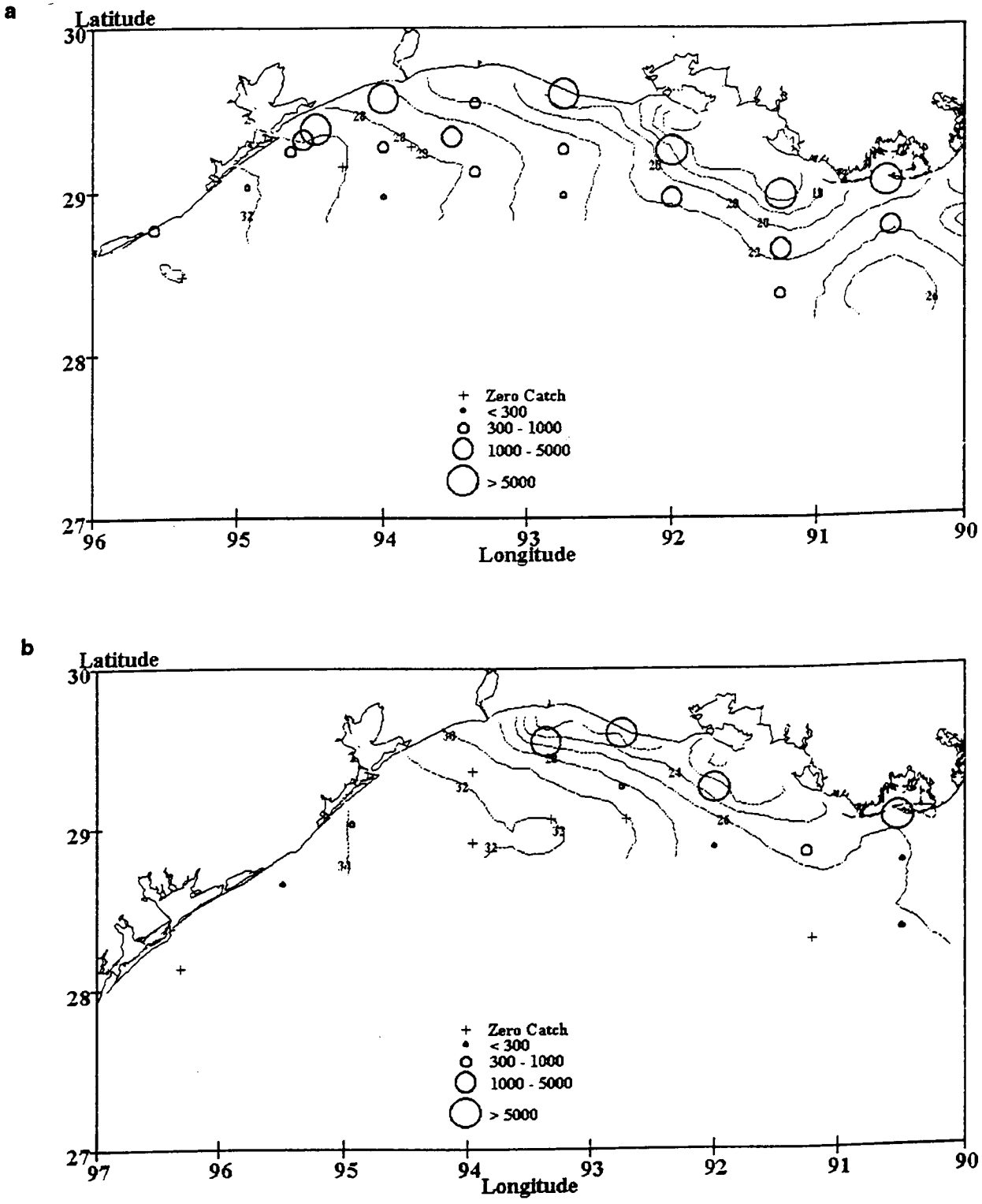

Figure 206. (a) July 1993 *Acartia tonsa* density (#/m^3); contour lines represent surface isohalines (‰). (b) July 1994 *Acartia tonsa* density (#/m^3); contour lines represent surface isohalines (‰).

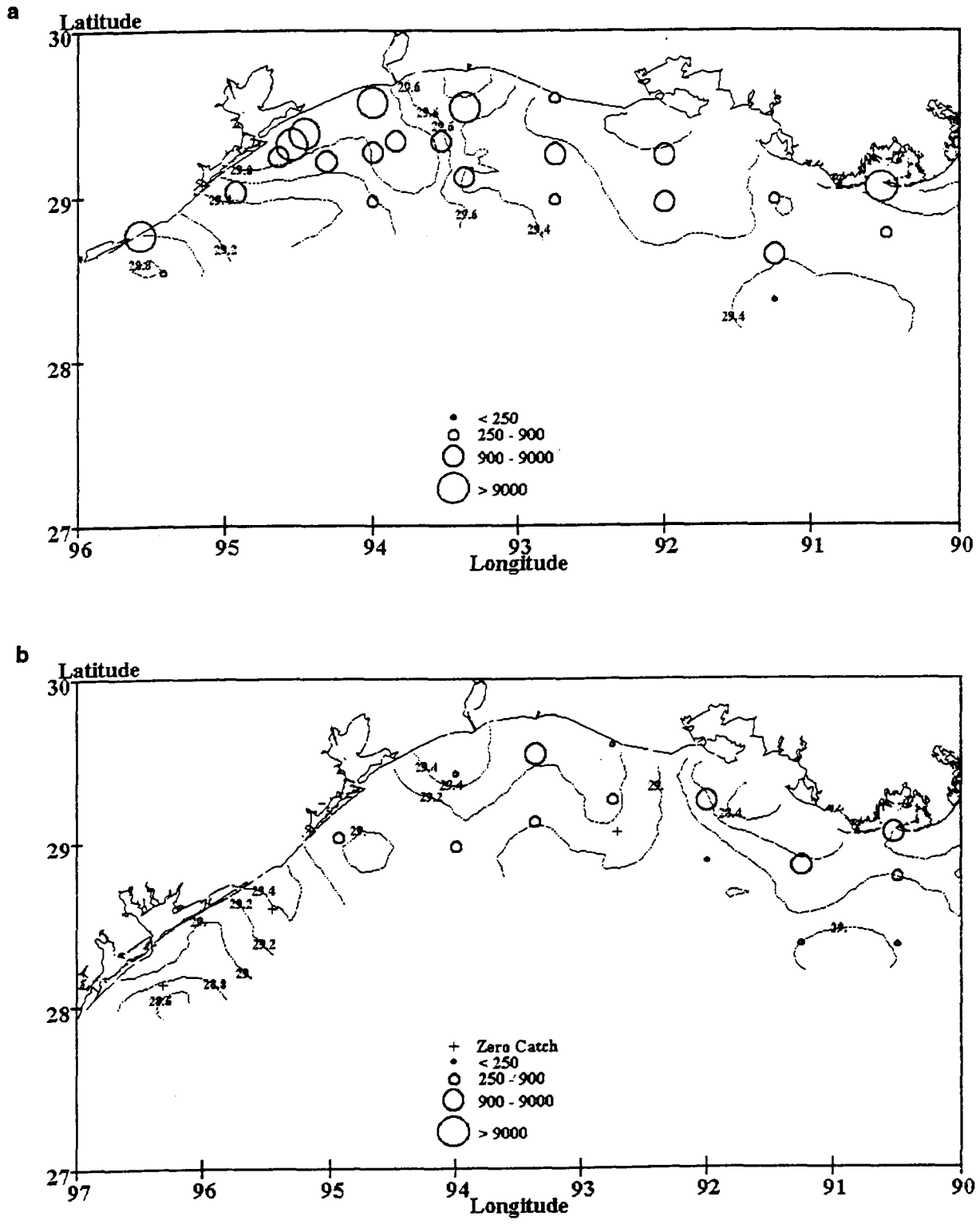

Figure 207. (a) July 1993 *Paracalanus crassirostris* density (#/m^3); contour lines represent surface isotherms (° C). (b) July 1994 *Paracalanus crassirostris* density (#/m^3); contour lines represent surface isotherms (° C).

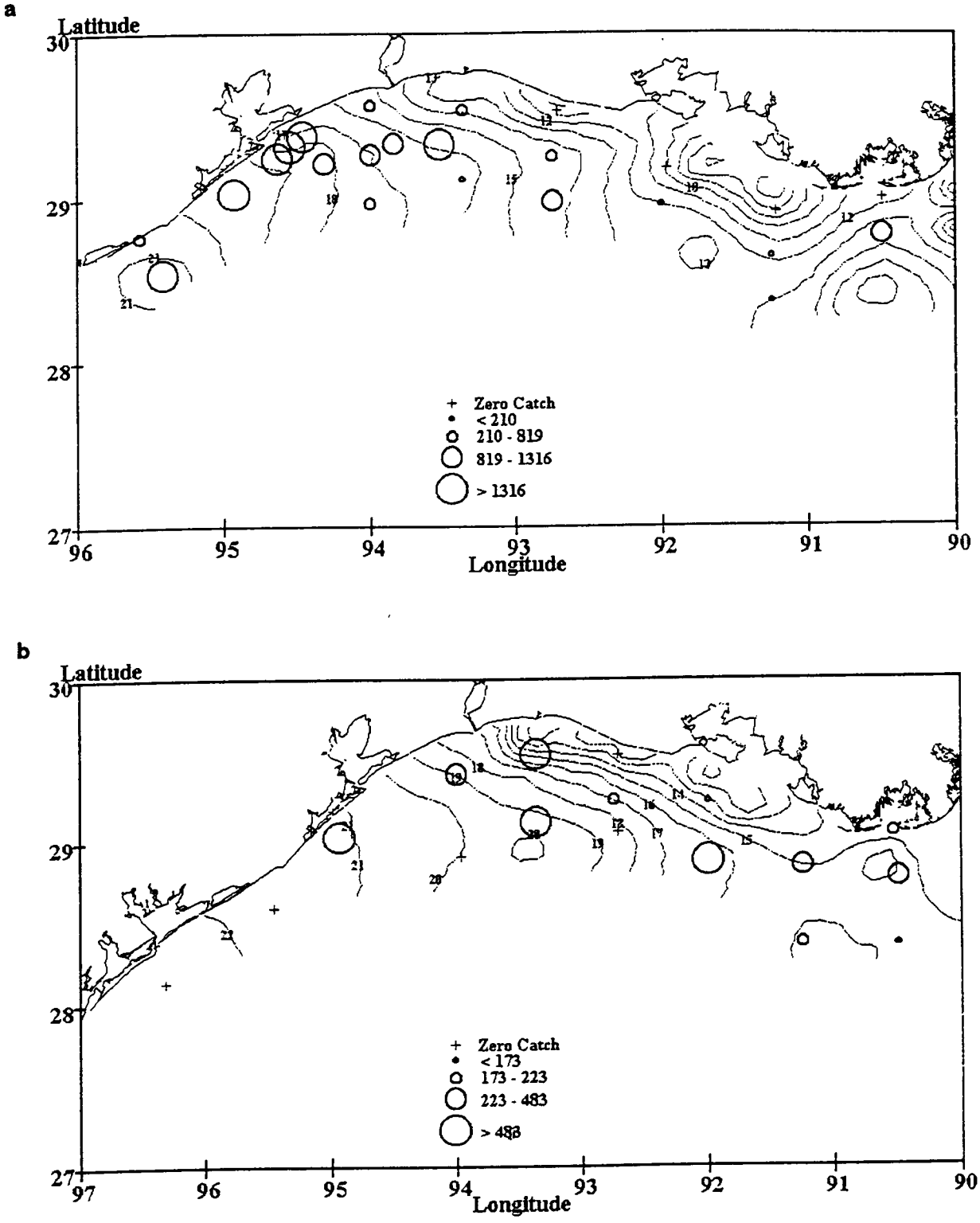

Figure 208. (a) July 1993 *Paracalanus parvus* density (#/m^3); contour lines represent surface isopycnals (kg/m^3). (b) July 1994 *Paracalanus parvus* density (#/m^3); contour lines represent surface isopycnals (kg/m^3).

abundance. *Paracalanus parvus* (0.51; Figures 208a and 208b) and *P. crassirostris* (0.50) had positive interset correlations and had greater abundance in 1993, the year of the July flood.

(2) Fish Larvae Canonical analysis indicated the fish and environmental variables were linearly related (Table 39, Λ=0.395, p=8, q=4, n=87, P[F>F*]=0.0001). The first canonical root accounted for 63.5% of the predictable variance. The second root accounted for an additional 22.6%, but was not significant (Λ=0.683, P[F>F*]=0.0859).

Table 39. Results of the July 1993/94 canonical analysis for fish larvae (n=87). See Table 34 for table description.

Canonical Correlation	1		2	
	p	%	p	%
	0.0001	63.51	0.0859	22.63
SPECIES	Coeff.	Corr.	Coeff.	Corr.
Opisthonema oglinum	0.16	0.20	0.24	0.27
Chloroscombrus chrysurus	0.11	0.29	0.32	0.25
Cynoscion arenarius	0.12	0.09	0.67	0.39
Symphurus spp.	0.93	0.62	-0.33	-0.13
ENVIRONMENTAL				
Year	0.96	0.82	0.36	0.07
Longitude	0.21	0.20	-0.19	0.13
Depth	0.37	0.29	-0.33	-0.80
Temperature	0.15	-0.23	0.61	0.77
Salinity	0.08	0.51	-0.12	-0.31
Chlorophyll	-0.19	-0.38	-0.48	0.15
Heterotrophs	-0.19	-0.27	0.28	0.35
Biomass Density	0.38	-0.18	0.40	0.52
Redundancy	U_{v1u_1}	V_{x1v_1}	U_{v1u_2}	V_{x1v_2}
	0.0714	0.1288	0.0454	0.0773

The first environmental coefficient vector produced a large weight on year (0.96), which correlated positively with this variate (0.82). Salinity also had a positive intraset correlation (0.51). Salinity was, on average, lower in 1993 (Figure 209a) than in 1994 (Figure 209b). This variate was associated with high salinity areas and contrasts waters associated with the Atchafalaya plume. *Symphurus* spp. had a positive interset correlation (0.62) and was absent at stations influenced by the plume.

Temperature (0.61) and chlorophyll (-0.48) received large weights in the second environmental coefficient vector, while depth (-0.80) and temperature (0.77) had large intraset correlations. This variate was associated with shallow, warm waters. This area extended from Calcasieu Lake to Galveston Bay in 1993 (Figure 210a) and from Atchafalaya Bay to Galveston Bay in 1994 (Figure 210b). *Cynoscion arenarius* had a positive interset correlation (0.39) and was common at stations in the areas described above.

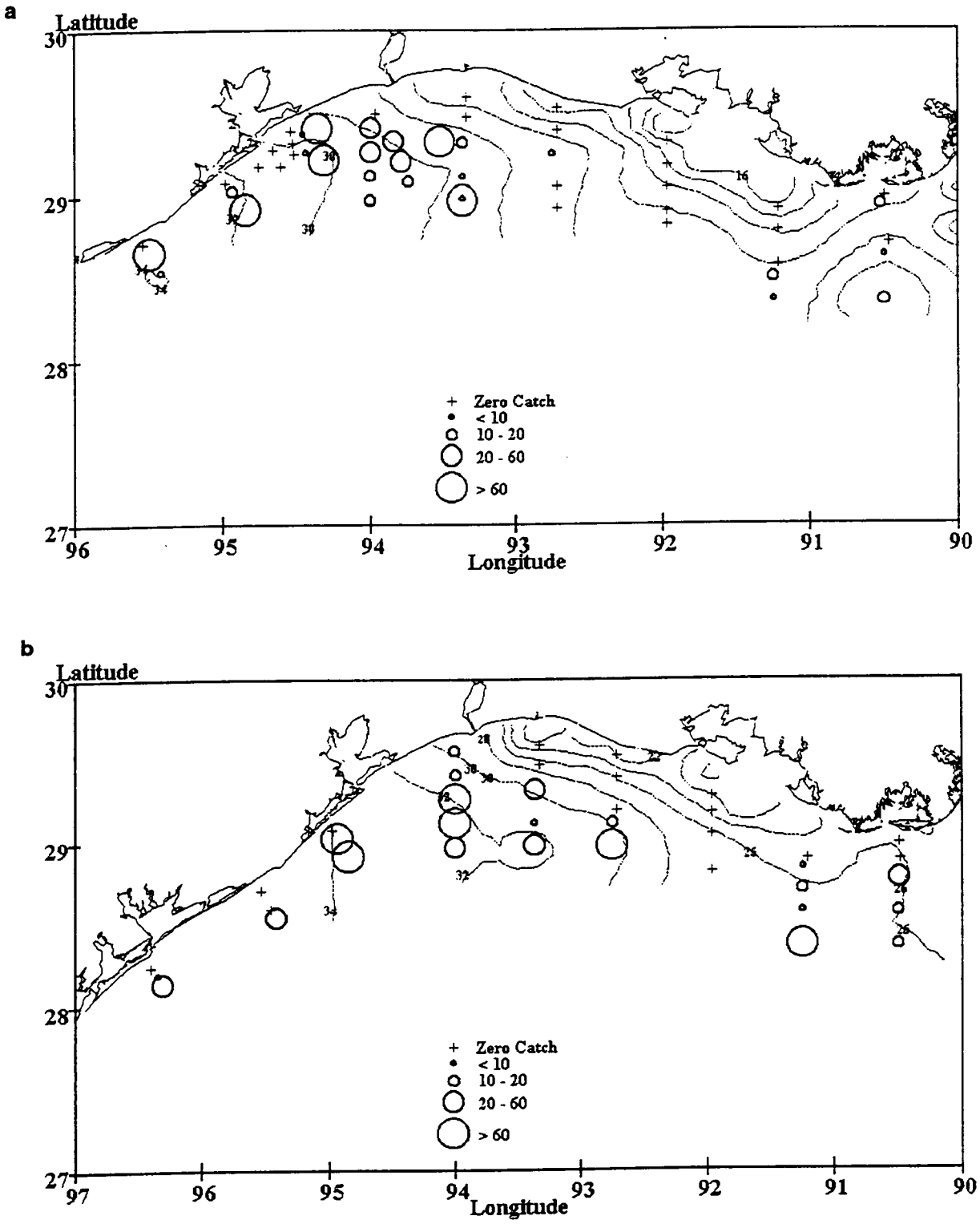

Figure 209. (a) July 1993 *Symphurus* spp. density (#/100 m^3); contour lines represent surface isohalines (‰). (b) July 1994 *Symphurus* spp. density (#/100 m^3) contour lines represent surface isohalines (‰).

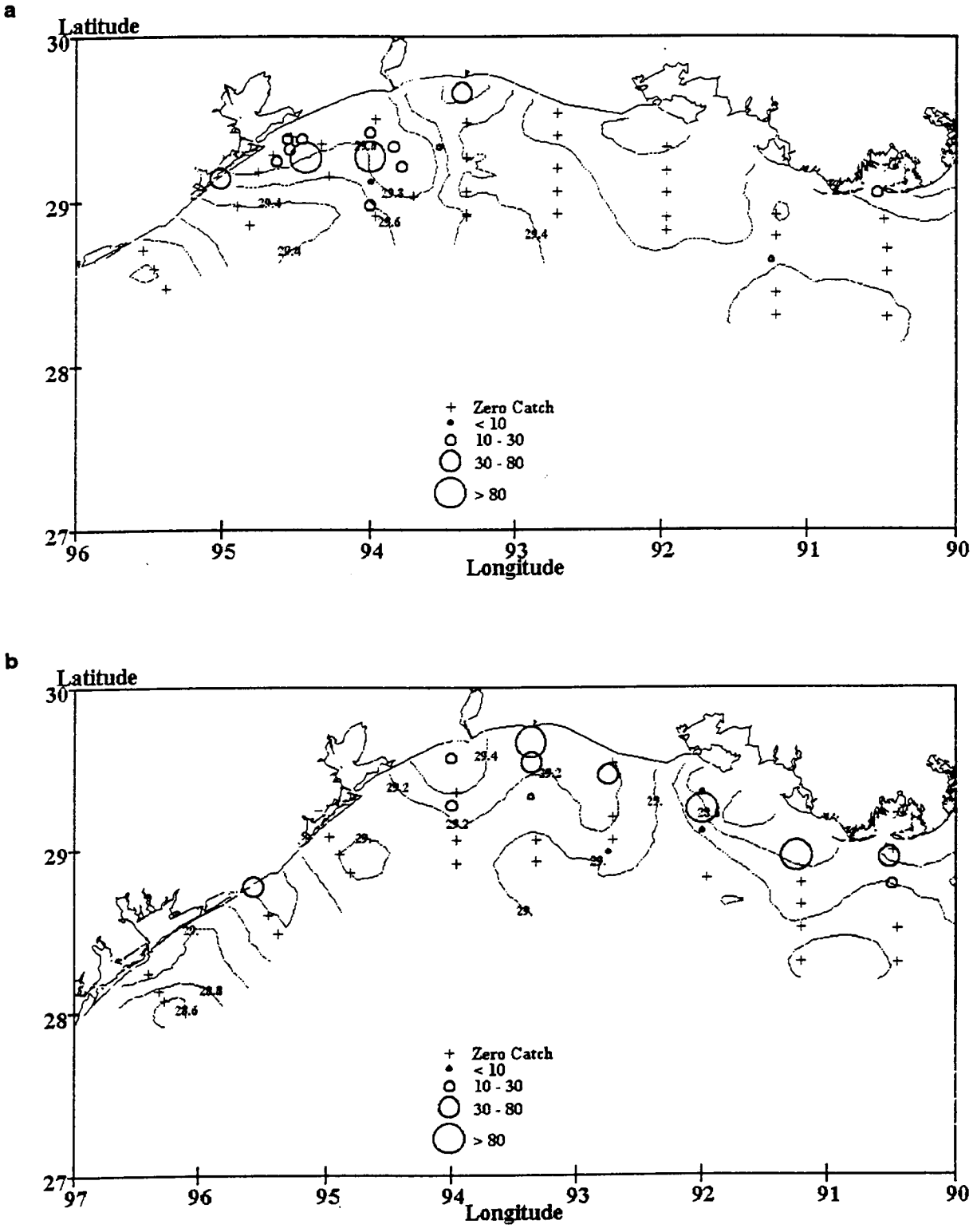

Figure 210. (a) July 1993 *Cynoscion arenarius* density (#/100 m^3); contour lines represent surface isotherms (° C). (b) July 1994 *Cynoscion arenarius* density (#/100 m^3); contour lines represent surface isotherms (° C).

d. October 6-14, 1992

Samples were collected from 42 stations in October 1992, a normal low-river discharge month. Samples were collected from Timbalier to Matagorda Bay. Column-averaged water temperature ranged from 23.2 to 25.9 °C, with low values occurring between western Atchafalaya Bay and Sabine Lake. Salinity ranged from 20.2 to 33.6 ‰, with low values off the Atchafalaya basin.

(1) Zooplankton Zooplankton biomass for the 153-mm mesh tended to be high at nearshore stations west of Atchafalaya Bay to Sabine Lake for both the 153- and 335-µm. Biomass for the 153-µm samples ranged from 15 to 741 mg/m^3, while 335-µm samples ranged from 4 to 84 mg/m^3.

Zooplankton composition was determined for 20 stations. At broad taxonomic resolution, Copepoda comprised over 81% of the total mean catch. Calanoida made up the bulk of this catch (57%), followed by Cyclopoida (17%), copepod nauplii (4%), and Harpactoida (3%). Other abundant taxa included Sagittidae (5%), Mollusca (Bivalvia and Gastropoda; 4%), Ostracoda (mainly *Euconchoecia chierchiae*; 3%), and Appendicularia (*Oikopleura*; 2%). At finer taxonomic resolution, *Acartia tonsa* (2626/m^3) was the most abundant zooplankton taxon, followed by *Acartia* spp. immature (2423/m^3), *Paracalanus crassirostris* (2340/m^3), and *Oithona brevicornis* (1425/m^3). Also common were *P. parvus*, *Oncaea venusta*, *Temora turbinata*, Sagittidae, copepod nauplii, and *Centropages furcatus*.

Canonical analysis explained a significant portion of the variance between the zooplankton and environmental variables (Table 40; $\Lambda=2.0\times10^{-8}$, p=6, q=13, n=20, P[F>F*]=0.0082). The first canonical root accounted for 97.9% of the predicted variation. The second root, which was not significant ($\Lambda=4.9\times10^{-5}$, P[F>F*]=0.1746), accounted for an additional 1.5%.

Depth (1.43), salinity (-0.89) and heterotroph density (-0.79) received large weights in the first environmental coefficient vector. Depth (0.61) and heterotrophs (-0.51) had large intraset correlations. This variate was associated with stations west of Sabine Lake and outer stations in general (Figure 211). *Temora turbinata* (0.52; Figure 212), *Oikopleura* spp. (0.47), *Eucalanus pileatus* (0.44), and *Paracalanus parvus* (0.42; Figure 213) had positive interset correlations. High abundance for these species was associated with outer stations. In contrast, *Callinectes sapidus* (-0.48) tended to be most abundant at nearshore stations (Figure 214).

Heterotroph density (-1.19) and chlorophyll (0.79) received large weights in the second environmental coefficient vector, although longitude (-0.62) and temperature (0.58) also received moderate weights. Longitude had a large negative intraset correlation (-0.73), while temperature (0.59; Figure 215) and heterotrophs (-0.43) had moderate correlations. This variate appears to be associated with an offshore component east of Sabine Lake. Many species had positive interset correlations: *Oncaea venusta* (0.66; Figure 190e), *Euterpina acutifrons* (0.64; Figure 216), copepod nauplii (0.57; Figure 217), *Euconchoecia chierchiae* (0.57), *E. pileatus* (0.50), *Oikopleura* spp. (0.46), and *Paracalanus parvus* (0.40). All were most abundant at offshore stations east of Sabine Lake, especially at offshore stations east of Terrebonne Bay.

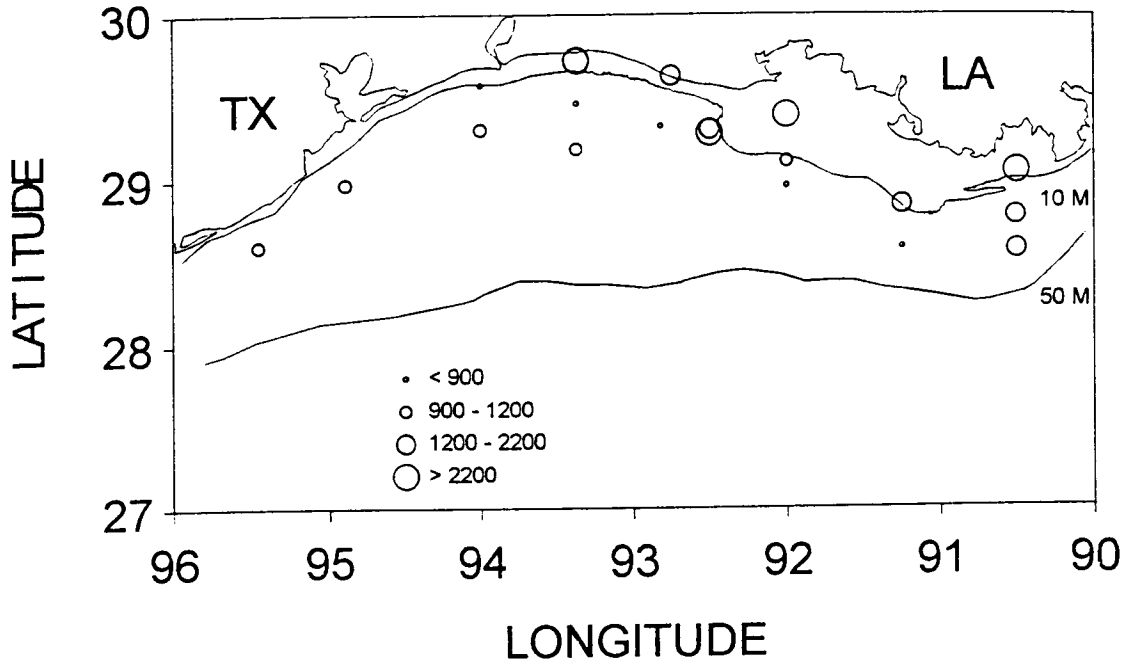

Figure 211. October 1992 heterotroph density (cells/mL). Contour lines represent isobaths (m).

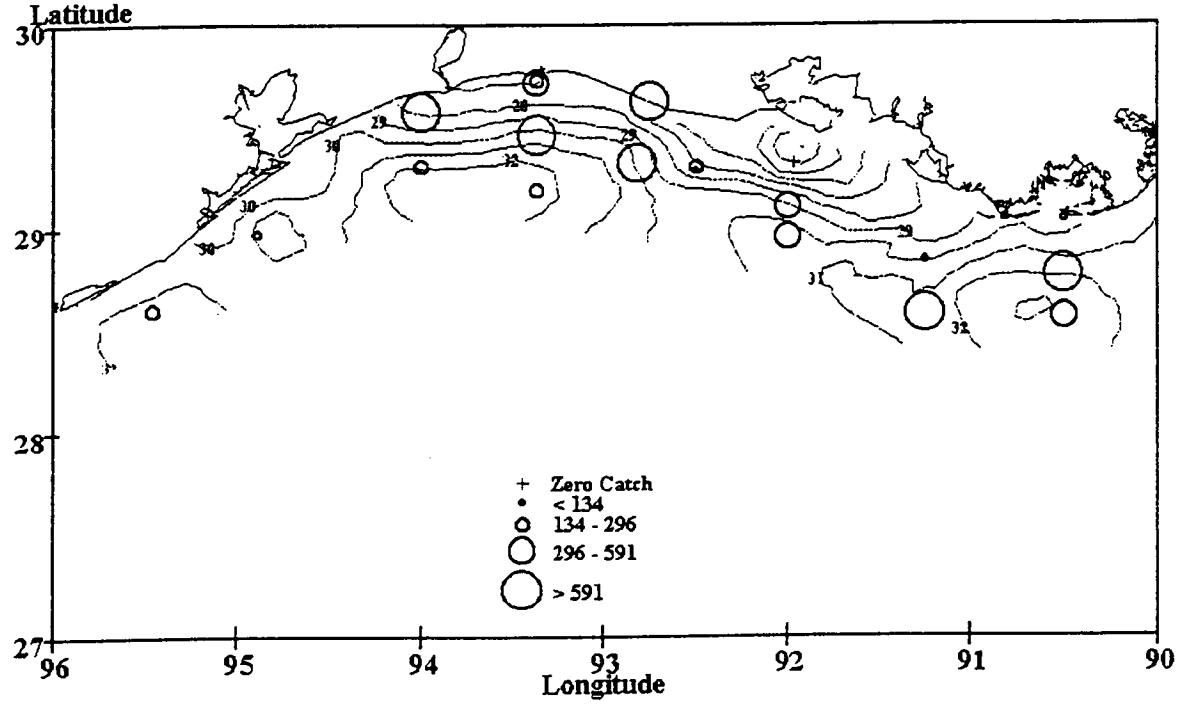

Figure 212. October 1992 *Temora turbinata* density (#/m^3). Contour lines represent surface isohalines (‰).

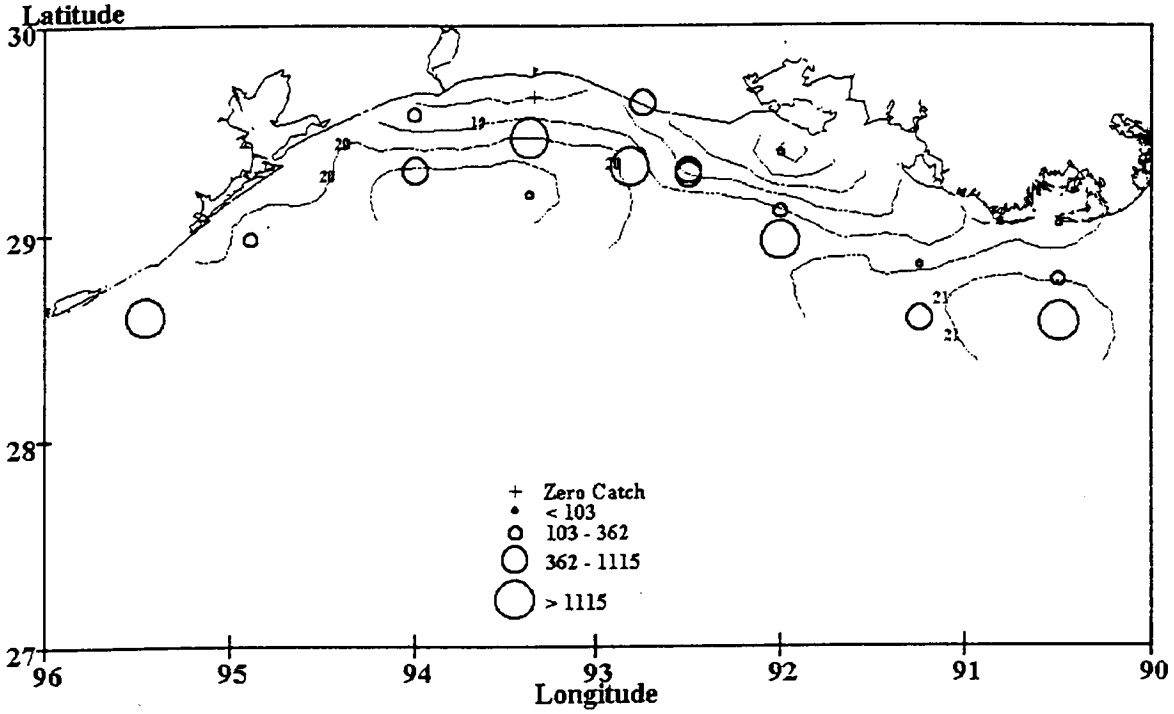

Figure 213. October 1992 *Paracalanus parvus* density (#/m^3). Contour lines represent surface isopycnals (kg/m^3).

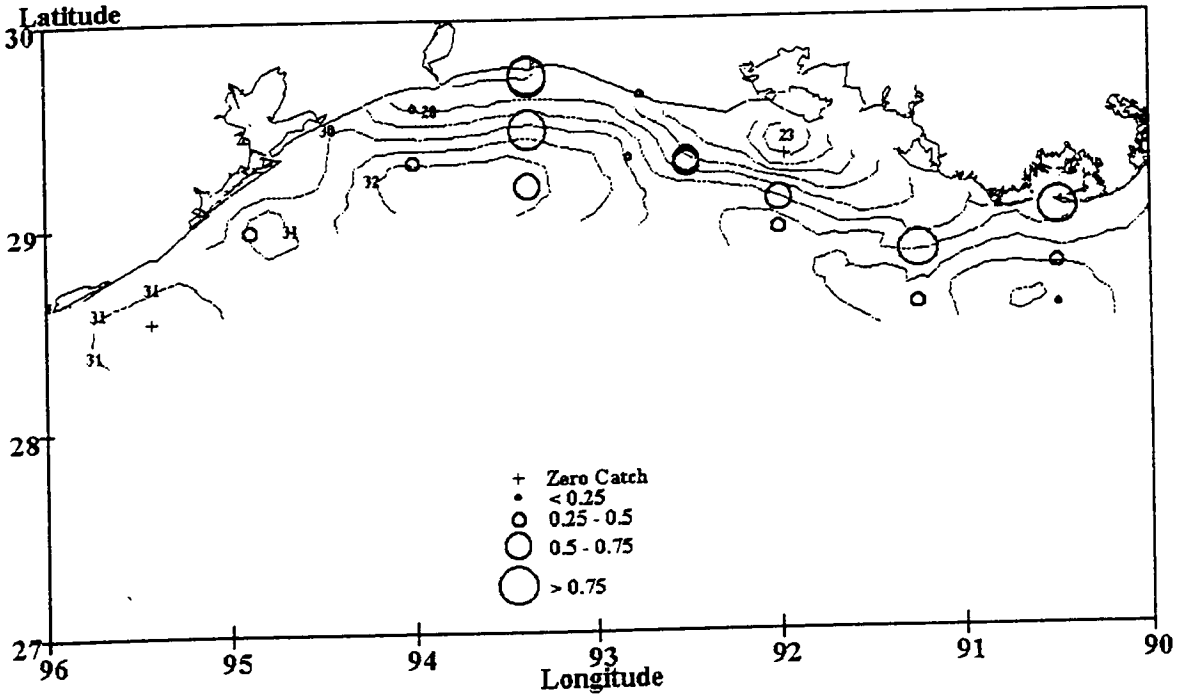

Figure 214. October 1992 *Callinectes sapidus* megalopa density (#/m^3). Contour lines represent surface isohalines (‰).

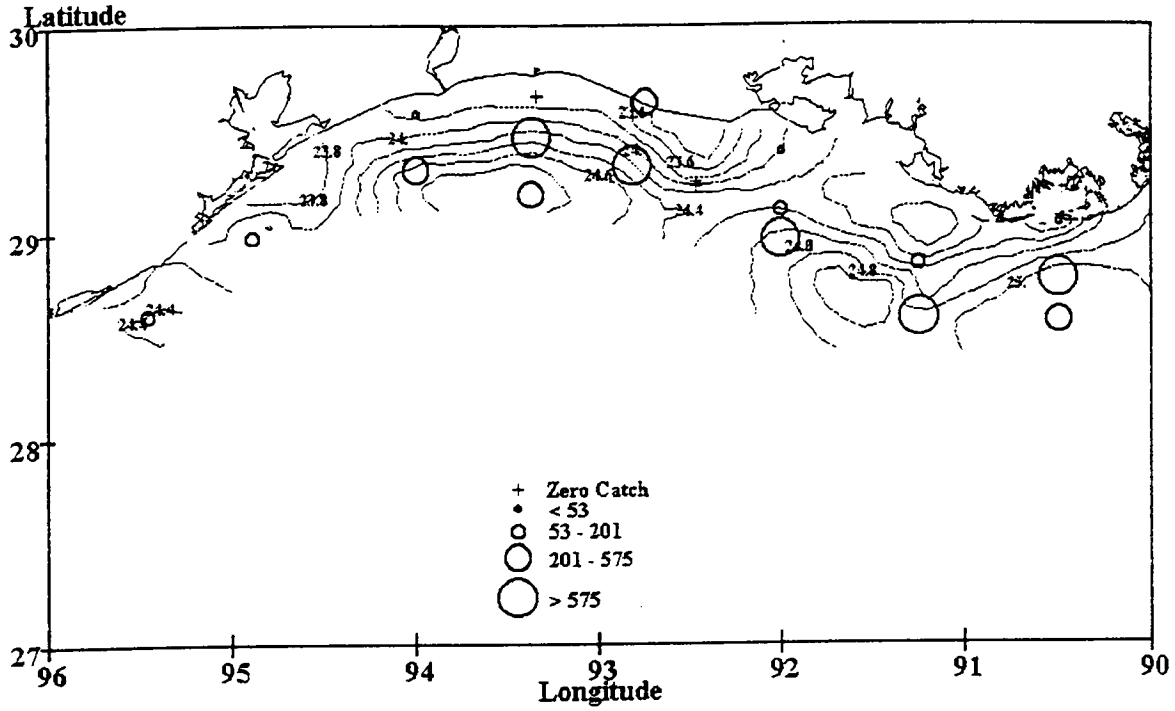

Figure 215. October 1992 *Oncaea venusta* density (#/m^3). Contour lines represent surface isotherms (° C).

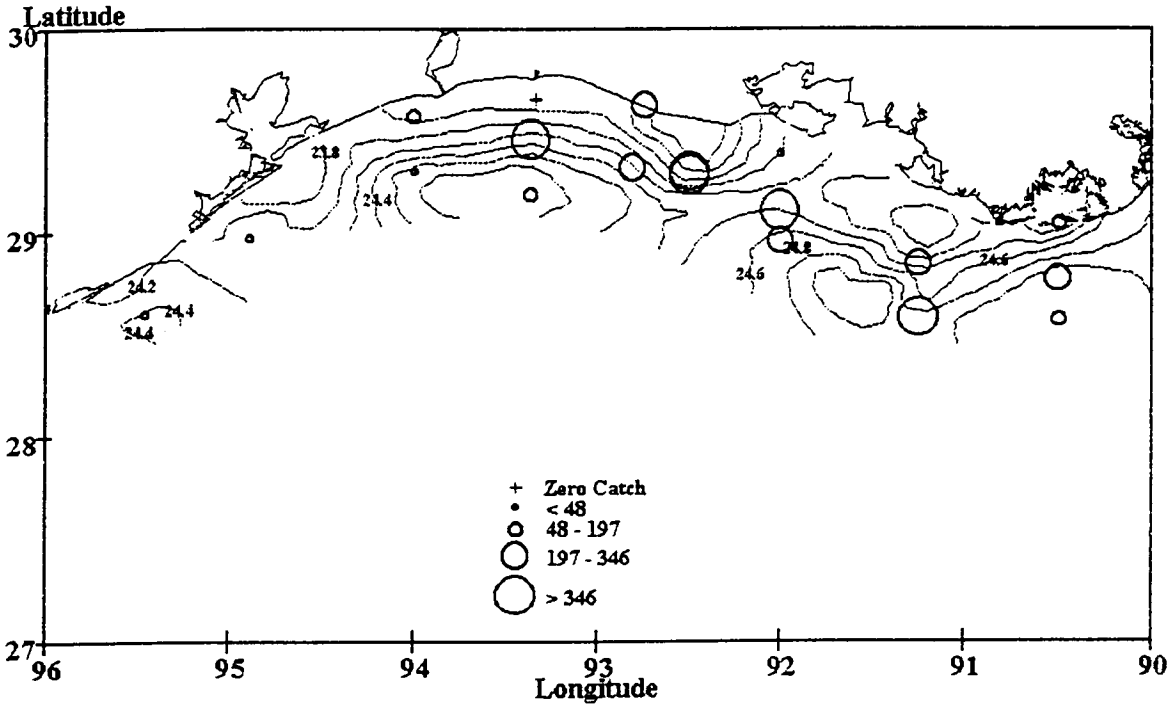

Figure 216. October 1992 *Euterpina acutifrons* density (#/m^3). Contour lines represent surface isotherms (° C).

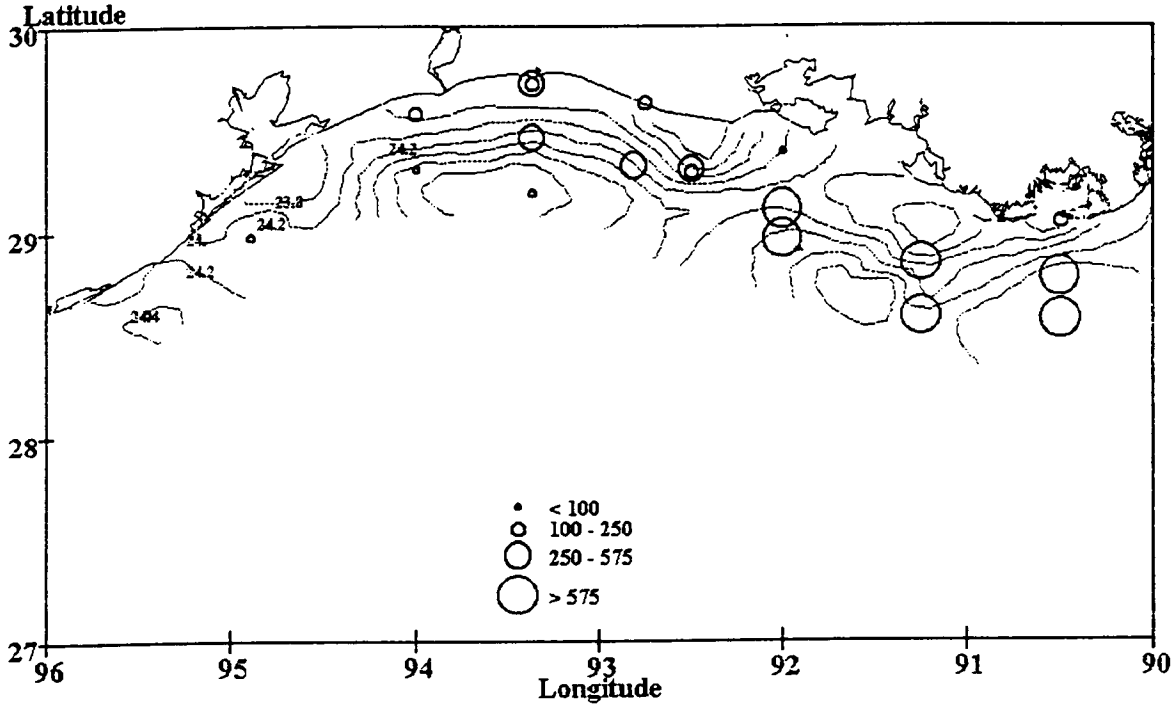

Figure 217. October 1992 Copepoda nauplius density (#/m^3). Contour lines represent surface isotherms (°C).

Table 40. Results of the October 1992 canonical analysis for zooplankton (n=20). See Table 34 for table description.

Canonical Correlation	1		2	
	p	%	p	%
	0.0082	97.93	0.1746	1.46
SPECIES	Coeff.	Corr.	Coeff.	Corr.
Copepoda nauplius	-0.06	0.08	0.54	0.57
Eucalanus pileatus	0.78	0.44	-0.04	0.50
Paracalanus crassirostris	0.54	0.21	-0.04	-0.04
Paracalanus parvus	0.06	0.42	-0.63	0.40
Temora turbinata	0.21	0.52	-0.15	0.16
Centropages furcatus	-0.04	0.27	-0.28	0.19
Acartia tonsa	0.16	-0.12	-0.15	-0.31
Euterpina acutifrons	-0.33	0.22	0.78	0.64
Oithona brevicornis	0.51	0.11	-0.16	-0.27
Oncaea venusta	-0.22	0.19	0.36	0.66
Euconchoecia chierchiae	0.63	0.28	0.23	0.57
Callinectes sapidus	-1.25	-0.48	-0.05	-0.06
Oikopleura spp.	-0.58	0.47	0.15	0.46
ENVIRONMENTAL				
Longitude	0.25	0.30	-0.62	-0.73
Depth	1.43	0.61	-0.38	0.41
Temperature	-0.54	0.25	0.58	0.59
Salinity	-0.89	0.15	-0.03	0.44
Chlorophyll	0.20	-0.42	0.79	-0.17
Heterotrophs	-0.79	-0.51	-1.19	-0.43
Redundancy	$U_{V\|U_1}$	$V_{X\|V_1}$	$U_{V\|U_2}$	$V_{X\|V_2}$
	0.1636	0.1073	0.2391	0.1815

(2) Fish Larvae Larval fish densities tended to be concentrated between Sabine and Calcasieu Lakes, ranging from 0 to 1293 larvae/100 m^3. At the family level, Sciaenidae was the most abundant taxon, comprising 48% of the total mean catch, followed by Engraulidae (27%). Other common families included Soleidae (4%), Bothidae (4%), and Gobiidae (3%). *Micropogonias undulatus* was the dominate species (86 larvae/100 m^3) collected, followed by *Anchoa hepsetus* (24/100 m^3). *Etropus crossotus, Symphurus plagiusa* and *Symphurus* spp., *Anchoa mitchilli* and *Anchoa* spp., and unidentified gobiids were also common in October samples.

Canonical analysis accounted for a significant portion of the variance between the fish species and environmental variables (Table 41; Λ=0.218, p=7, q=5, n=41, P[F>F*]=0.0414). The first canonical root accounted for 50.8% of the variation explained. The second root accounted for an additional 25.1%, but was not significant (Λ=0.437, P[F>F*]=0.2769).

Table 41. Results of the October 1992 canonical analysis for fish larvae (n=41). See Table 34 for table description.

Canonical Correlation	1		2	
	p	%	p	%
	0.0414	50.80	0.2769	25.06
SPECIES	Coeff.	Corr.	Coeff.	Corr.
Anchoa hepsetus	0.80	0.60	-0.27	0.12
Cynoscion arenarius	0.13	0.15	-0.22	>-0.01
Micropogonias undulatus	0.30	0.33	0.62	0.45
Sciaenops ocellatus	-0.58	0.06	0.74	0.47
Etropus crossotus	0.30	0.50	-0.12	0.15
ENVIRONMENTAL				
Longitude	0.28	0.58	0.30	0.09
Depth	-1.11	-0.08	1.11	0.93
Temperature	0.54	0.11	-0.22	0.71
Salinity	0.39	0.35	0.03	0.66
Chlorophyll	-0.79	-0.73	0.28	-0.59
Heterotrophs	0.08	-0.43	-0.32	-0.62
Biomass Density	0.19	0.06	-0.14	-0.30
Redundancy	$U_{V|U_1}$	$V_{X|V_1}$	$U_{V|U_2}$	$V_{X|V_2}$
	0.0852	0.1484	0.1248	0.0918

Depth (-1.11) and chlorophyll (-0.79) loaded heavily in the first environmental coefficient vector and temperature (0.54) to a lesser extent. However, only chlorophyll correlated highly (-0.73) with the first environmental variate. Thus, this variate is correlated with low chlorophyll concentrations, which occurred mainly at offshore stations west of Vermilion Bay (Figure 218). *Anchoa hepsetus* (0.59) and *Etropus crossotus* (0.50) had positive interset correlations and both species exhibited greater densities west of Vermilion (Figures 219 and 220, respectively).

Depth also received a large weight (1.11) in the second environmental coefficient vector. All other environmental variables had small weights. The intraset correlation for depth was positive (0.93), indicating the variate was associated with outer stations. This conclusion is strengthened by negative intraset correlations of heterotroph (-0.62; Figure 221) and chlorophyll density (-0.59), which both tended to decrease as distance from shore increased. The opposite was true for temperature (0.71; Figure 222) and salinity (0.66; Figure 223). *Sciaenops ocellatus* (0.47; Figure 222) and *Micropogonias undulatus* (0.45; Figure 223) had positive interset correlations and both species tended to have greater densities at outer stations.

3. Zooplankton

The biomass estimates from the 153 m mesh, 60-cm net were in general consistently high off Timbalier Bay and the Mississippi River Delta (if sampled), offshore, and to the west (downstream) of Atchafalaya Bay. High biomass estimates often extended

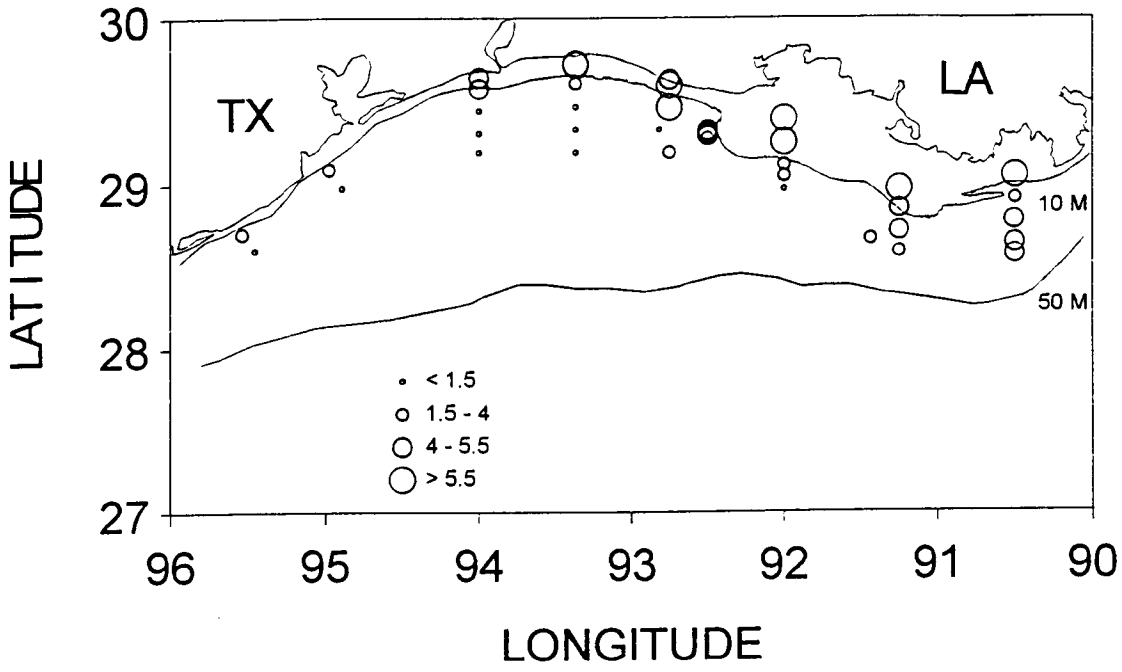

Figure 218. October 1992 chlorophyll *a* concentration (mg/L). Contour lines represent isobaths (m).

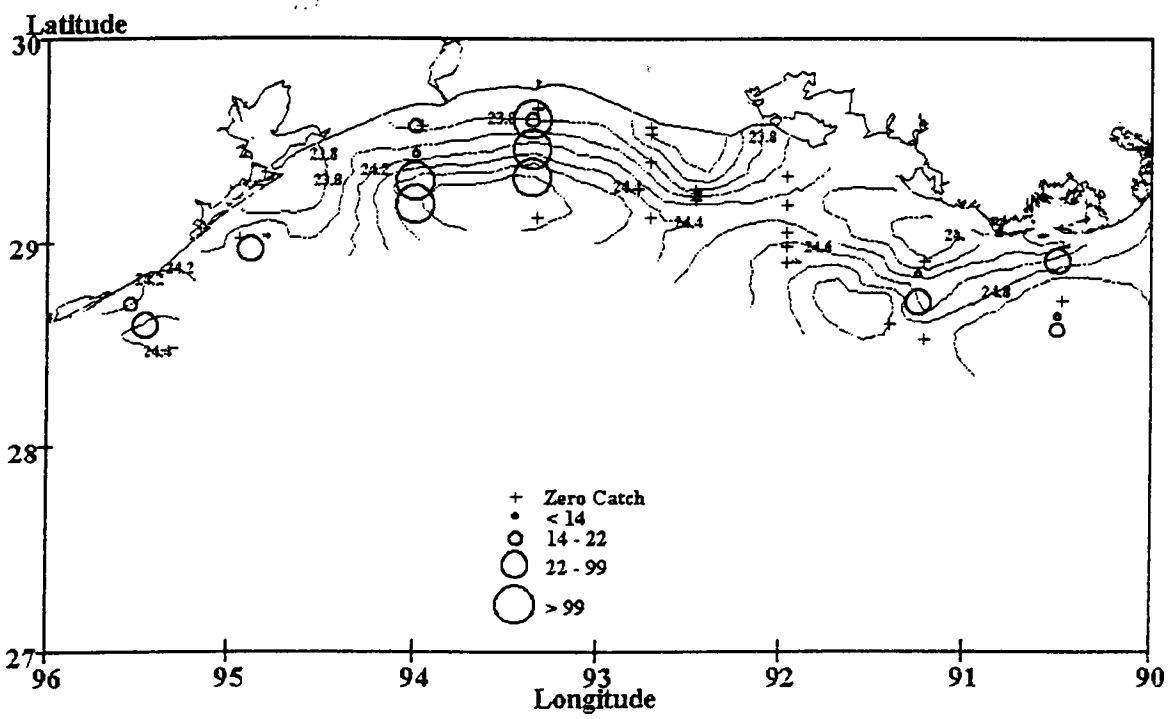

Figure 219. October 1992 *Anchoa hepsetus* density (#/100 m^3). Contour lines represent surface isotherms (°C).

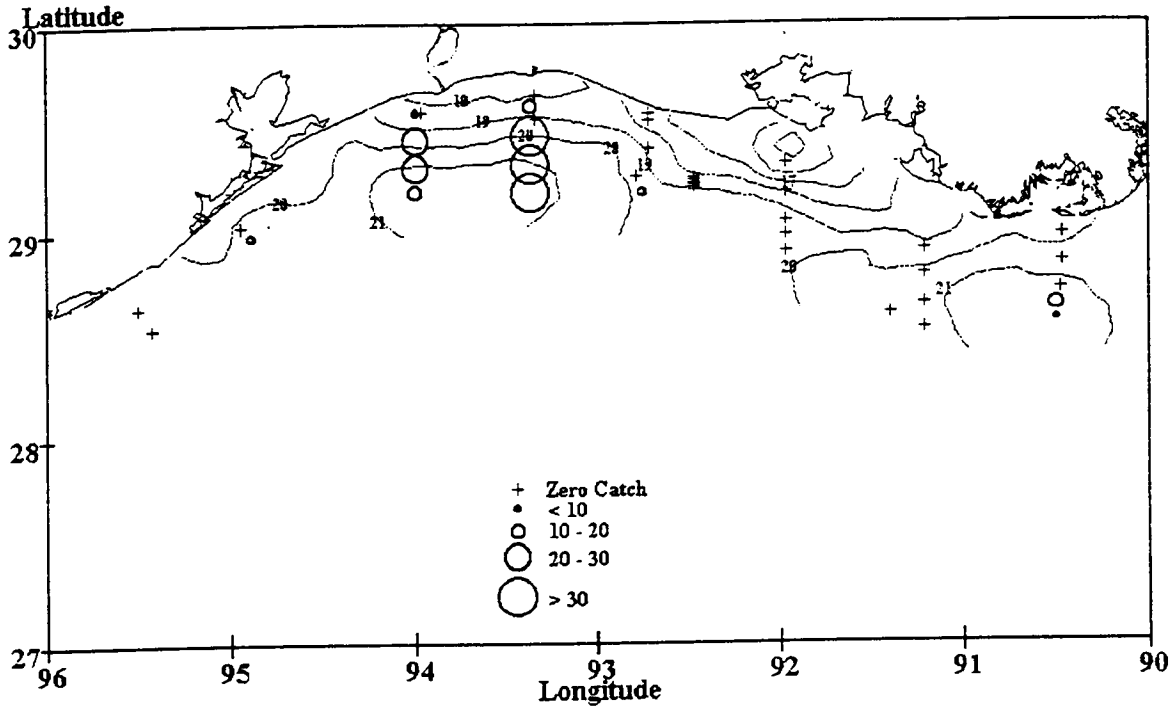

Figure 220. October 1992 *Etropus crossotus* density (#/100 m^3). Contour lines represent surface isopycnals (kg/m^3).

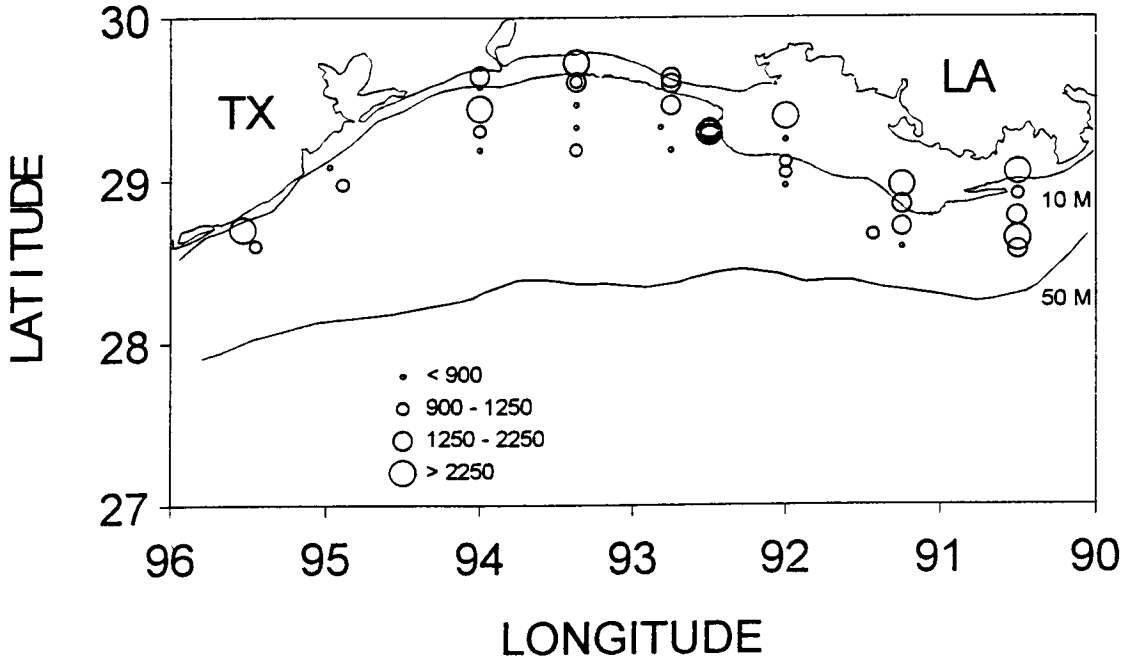

Figure 221. October 1992 Heterotroph density (cells/mL). Contour lines represent isobaths (m).

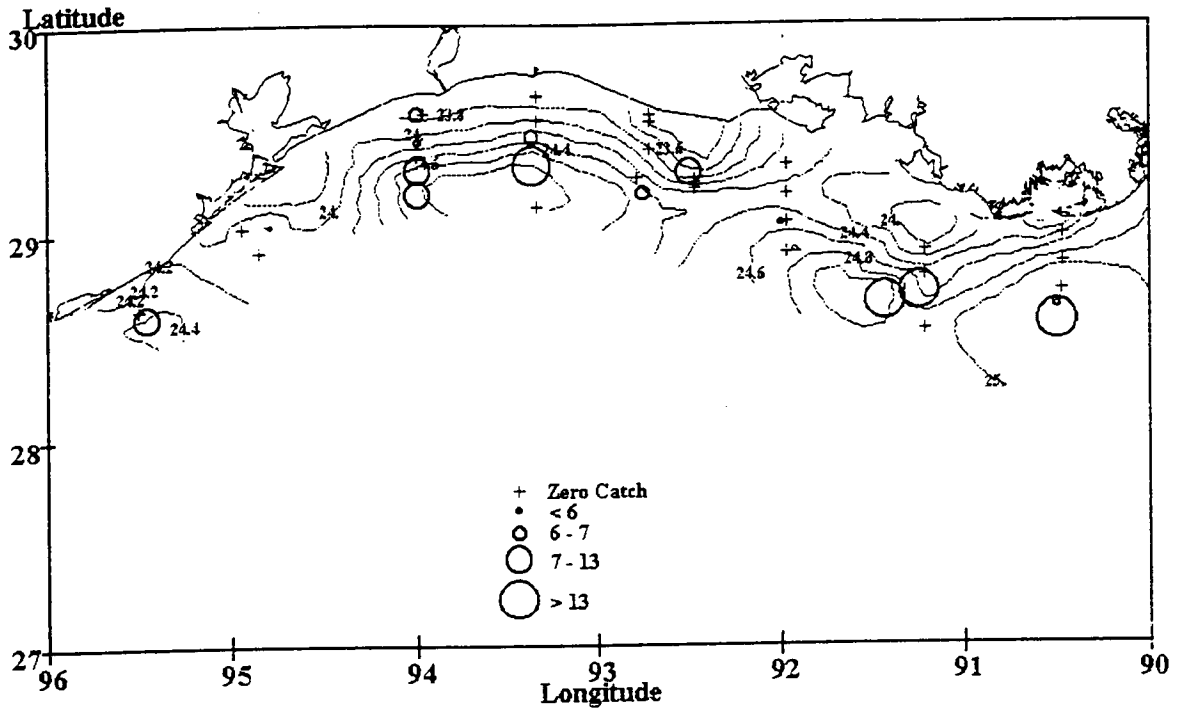

Figure 222. October 1992 *Sciaenops ocellatus* density (#/100 m^3). Contour lines represent surface isotherms (° C).

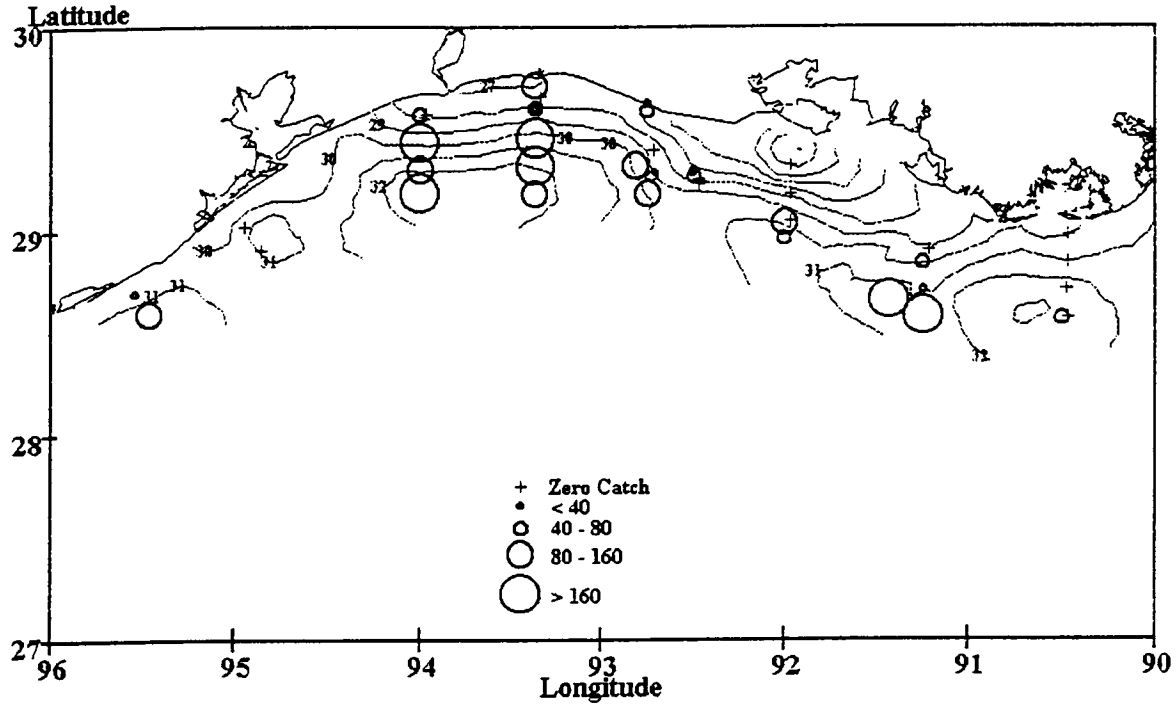

Figure 223. October 1992 *Micropogonias undulatus* density (#/100 m^3). Contour lines represent surface isohalines (‰).

as far west as Calcasieu and Sabine Lakes, and quite often displayed peaks off Galveston Bay occasionally extending southwestward as far as Matagorda Bay, TX (when sampled). The 333 m biomass estimates were generally abundant nearshore everywhere but often especially associated with the Atchafalaya Bay to Sabine Lake shoreline.

Our zooplankton taxonomic, distribution, and abundance results are in general agreement with the dominant taxa previously reported from three transects of the inner to outer shelf off south Texas (Park, 1979). In addition, our results are similar to the findings of Al-Yamani (1988) given that study's zooplankton sampling regime was based upon 5-liter Niskin bottles and 63 m mesh MOCNESS collections taken across the shelf off the Mississippi River Delta and the Louisiana-Texas border during February (1980-82).

In general, the canonical analyses were strongest in identifying the zooplankton community that characterizes mid-to-outer shelf (vs. inshore), high salinity, low chlorophyll *a* stations both in April and October. Those species which met our abundance and frequency of occurrence criteria that make up this more offshore community in April and October were: *Eucalanus pileatus, Oikopleura* spp., *Temora turbinata, Paracalanus parvus*, and *Centropages furcatus*. The coastal, low salinity zooplankton community was characterized by *Acartia tonsa, Labidocera aestiva*, and *Callinectes sapidus* (Oct.). *Centropages furcatus* and *Paracalanus parvus* were also identified with high salinity, low chlorophyll *a* stations in contrast with nearshore Atchafalaya or Mississippi plume stations in the July analysis as well. Both of these species were found in high abundances in high salinity waters, especially those associated with the Mexican-Texas coastal current and with the resultant convergence zone in mid-shelf waters between Galveston Bay and Sabine Lake.

4. Fish Larvae

The ichthyoplankton distributional abundances consistently showed highest April densities off Atchafalaya Bay and then again off the Louisiana-Texas border or even further west off Galveston to Matagorda Bays. The area off Sabine and Calcasieu Lakes was a high density region in July and the October cruises, with high densities extending eastward nearshore towards Timbalier Bay during July 1994. The larval fish canonical analysis in April was limited by the high year to year variability in species densities and frequency of occurrences. Only *Cynoscion arenarius* had consistent high shelf densities in the waters downstream of the Mississippi and Atchafalaya River plumes, with a consistent secondary density peak between Galveston and Matagorda Bays. In the July (1993 & 1994) analysis only *Symphurus* spp. could be deemed a characteristic species group having high density in high salinity waters mostly associated with the Mexican-Texas coastal current, especially during the July 1993 flood season. Even *C. arenarius*, which had a more eastern distribution of high densities in both April cruises, seems to have been displaced to the west during the July 1993 flood season. During October, two larval fish species appear to characterize the waters west of Vermilion Bay: *Etropus crossotus* and *Anchoa hepsetus*. Of interest also in October was the high densities encountered in more offshore waters for both *Sciaenops ocellatus* and *Micropogonias undulatus*. Both of these species would normally be considered coastal spawners and the high densities in more offshore areas probably reflect an offshore transport or mixing event prior to our 6-14 October 1992 cruise.

IX. Hypoxia

A. Hypoxia Distribution

by Nancy N. Rabalais

1. Introduction

Oxygen-depleted bottom waters are seasonally dominant features of the Louisiana-Texas continental shelf adjacent to the deltas of the Mississippi and Atchafalaya Rivers (Rabalais et al., 1991; 1994; 1996; 1998). The areal extent of bottom-water hypoxia ($\leq$ 2 mg O_2 l^{-1}) in mid-summer may cover up to 17,000 km^2 (Rabalais et al., 1998). Prior to the 1993 Mississippi River summer flood, the average areal extent of bottom-water hypoxia in mid-summer averaged 8,000 to 9,000 km^2 (Rabalais et al, 1991; 1998). Data from biweekly to monthly sampling off Terrebonne Bay on the southeastern Louisiana shelf and continuous time series data from a station in 20-m water depth within the core of the hypoxic area document hypoxic bottom waters as early as February and as late as October, with widespread, persistent and severe hypoxia/anoxia from mid-May through mid-September. Spatial and temporal variability in the distribution of hypoxia exists and is, at least partially, related to the amplitude and phasing of the Mississippi and Atchafalaya River discharges and, consequently, to nutrient fluxes to the coastal waters and subsequent flux of carbon from surface waters to the lower water column and seabed. Physical features of the system, e.g., large-scale circulation patterns, strong and persistent density stratification, and destratification caused by wind-mixing events from local winds, tropical storm activity and cold fronts, also control the dynamics of hypoxia.

The seasonal dynamics of net productivity on the inner Louisiana continental shelf (as exemplified by station C6B off Terrebonne Bay) are coherent with the dynamics of Mississippi River freshwater discharge (Justic et al., 1993). The surface water layer, above the prevalent pycnocline at 10 m, shows an oxygen surplus during February-July with the maximum in April and May that coincides with peak long-term Mississippi River flow. The bottom layer, below the pycnocline to 20 m, exhibits an oxygen deficit throughout the year, but reaches its highest value in July that is also the period of greatest surface-to-bottom density differences. Cross correlation analyses show that the correlation between Mississippi River flow and surface oxygen surplus peaks at a time-lag of one month and that the highest correlation for bottom oxygen deficit is for a time-lag of two months (Justic et al., 1993). Similar relationships were seen for the southwestern Louisiana shelf downfield of the effluent of the Atchafalaya River (Pokryfki and Randall, 1987). An oxygen surplus means that there is an excess of organic matter derived from primary production that can be redistributed within the system (Justic et al., 1993), much of which will eventually reach the lower water column and sediments (Qureshi, 1995; see also Section VI, this report).

The size of the hypoxia zone on the Louisiana-Texas shelf is one of the largest hypoxic areas in the world's coastal waters, exceeded only by the Baltic Sea and the northwestern shelf of the Black Sea. The linkage of hypoxia to discharges of the Mississippi and Atchafalaya Rivers is significant, because nitrate and phosphorus concentrations and loadings have doubled and silicate has decreased by 50% since the turn of the century with an acceleration since the 1950s (Turner and Rabalais, 1991). The biological responses on the adjacent continental shelf (reviewed in Rabalais et al., 1996a) follow these changes in nutrient delivery as demonstrated by (1) equal or greater net silicate-based phytoplankton community uptake of silica in the mixing zone; (2) greater accumulation rates of BSi (a surrogate for diatom production); (3) potential shifts in

phytoplankton community composition; (4) increased rates of accumulation of marine-origin carbon in the sediments; and, (5) a decrease in oxygen concentration. The biological effects on the Louisiana shelf are comparable to indicators of increased eutrophication observed worldwide, especially in areas receiving increased and/or altered nutrient fluxes. Documented and potential impacts exist for both commercial and recreational fisheries and the resources that support them as has been demonstrated in other areas experiencing increased severity of hypoxia (Diaz and Rosenberg, 1995).

2. Objectives

Long-term and ongoing studies of the distribution and dynamics of hypoxia on the Louisiana-Texas continental shelf (Rabalais et al., 1991; 1994; 1996a, 1998) generated data of three types: (1) biweekly to monthly surveys on the southeastern Louisiana shelf off Terrebonne and Timbalier Bays; (2) more frequent sampling at stations C6A, C6B or C6 on the southeastern shelf transect during maintenance of a moored instrument array; and, (3) shelfwide synoptic surveys during the expected maximal extent and severity of hypoxia, usually from mid-July through early August. Data from this long-term data set (obtained in 1992-1994 with funding from the NOAA NECOP program) overlap spatially and temporally with the hydrographic and biological surveys of the LATEX Mississippi River Plume Hydrography study. Individually, each data set allows for the examination of the spatial and temporal distribution of hypoxia, the relationship of physical oceanographic conditions to the variability in hypoxia, and comparison of the hypoxia zone to important biological factors, such as nutrient and phytoplankton pigment concentrations. Combination of the NECOP data with those generated from the LATEX program provides comparable spatial coverage within a two-week time frame. Therefore, the objectives of the hypoxia studies were to:

- describe the distribution of hypoxia and related physical and biological conditions during each of the LATEX B cruises,
- describe the seasonal and interannual variability of hypoxia, and
- compare the configuration the hypoxic zone and hypoxic water masses over short time intervals.

3. Data Collection

Hydrographic data collection methods varied somewhat between cruises and/or programs but were consistent in results and were cross-calibrated. Electronic hydrographic data were collected with either a SeaBird or Hydrolab CTD. The SeaBird CTD was factory-calibrated for salinity and temperature. Oxygen concentration determinations, at the high and low end, were made prior to each cruise and entered into the SeaSoft configuration file. Winkler titrations of discrete-depth water samples on board ship (Mettler DL21 titrator; methods of Parsons et al., 1984) were used to develop a regression against the CTD data, which were corrected, as necessary. The Hydrolab CTD was pre- and post-cruise laboratory-calibrated for salinity and pH with chemical standards and for dissolved oxygen by air-saturated water. Results from the Hydrolab CTD oxygen measurements were consistent with Winkler titrations. Because the SeaBird CTD comes to within 1-1.5 m of the seabed at most, characteristics of the lower 2 to 3 m of the water column were also recorded with the Hydrolab CTD during July cruises.

Water samples for chlorophyll *a* and phaeopigments, nutrients and salinity were collected from the surface by bucket, and from mid-water in 5-l Niskin bottles on a CTD /rosette system or a cable. Water samples from the bottom were collected in a 5-l bottom-tripping, horizontally-mounted Niskin bottle secured in a frame with the Hydrolab CTD, or a 5-l Niskin on the CTD/rosette or a cable. Salinity determinations

were made for surface water samples. Water for chlorophyll *a* and phaeopigment analysis (40-100 ml) was filtered through GF/F filters on board ship. The filters were fixed in 5 ml of DMSO/90% acetone (40/50) solution and allowed to extract for at least 1 hour in the dark. The extracts were measured pre- and post-acidification with 10% HCl on a Turner Model 10 fluorometer (Parsons et al., 1984). The fluorometer was calibrated for chlorophyll *a* against a chemical supply house chlorophyll *a* standard measured on a spectrophotometer. Water samples for nutrients, unfiltered, were frozen on board ship for later analysis in the laboratory. Nitrogen and phosphorus were analyzed according to methods in USEPA (1979) method 350.1 for ammonia-N, method 353.2 for nitrate/nitrite-N, and method 365.1 for phosphate-P. Silicate was analyzed according to method 186-72W/B (Technicon 1977).

Station design differences existed between the NECOP and LATEX cruises. NECOP shelfwide surveys of hypoxia were conducted during the expected maximal extent and severity of hypoxia, usually late July. The quasi-synoptic (within a five-day period) sampling grid for the NECOP cruises was similar from year to year, with variations dictated by modifications during sampling and/or availability of funds or time to complete the entire grid. On any single cross-shelf transect of the NECOP shelfwide grid, sampling was usually completed when the 2 mg O_2 l^{-1} isopleth was clearly defined. Thus, the same general area from the Mississippi River delta to the upper Texas coast was surveyed. LATEX station grids were determined by the overall purpose of the program to define the coastal plumes of the Mississippi and Atchafalaya Rivers. Closure of oxygen isopleths to 2 mg O_2 l^{-1} isopleth was not feasible during the LATEX cruises. Additional "hypoxia" stations were added on the eastern end of the LATEX sample grid during July cruises to coincide with NECOP transects C and B (Figure 131 in Murray and Donley, 1994). Portions of transect C (NECOP) and line S1 (LATEX) overlapped, and the two cross-shelf transects were used for comparisons. Other cross-shelf transects from the LATEX and NECOP cruises were also comparable.

In addition to shelfwide surveys during the maximal development of hypoxia, shelfwide cruises (both LATEX and NECOP) were conducted in April and October. Results from these surveys provided information on hypoxia during the periods when it is likely to be developing and to be dissipating, respectively.

4. Results and Discussion

a. Oxygen Conditions in April 1992 and April 1993

Near-bottom oxygen concentration were slightly below 2 mg O_2 l^{-1} l at only one station off Terrebonne Bay during the LATEX April 1992 cruise (Figure 224). There was, however, an area of oxygen concentration approaching hypoxia in a band along the mid- to outer stations of the S1 and S2 lines, respectively, from Terrebonne Bay to Point au Fer Island. Isolated areas of near-bottom waters low in oxygen but not hypoxic ($2 \leq x \leq 4$ mg O_2 l^{-1}), were located off the Sabine and Galveston estuaries. The low oxygen concentrations were confined to the lower two m of the measured water column, compared to a much thicker layer of oxygen deficiency in mid-summer. Comparable shelfwide NECOP data were not available for 1992, but a cross-shelf comparison between S1 line (4/22/92) and transect C (4/10-11/92) indicated the persistence of a mid-transect oxygen depletion feature on both dates and a similar density structure (Figures 134 and A-162 in Murray and Donley, 1996).

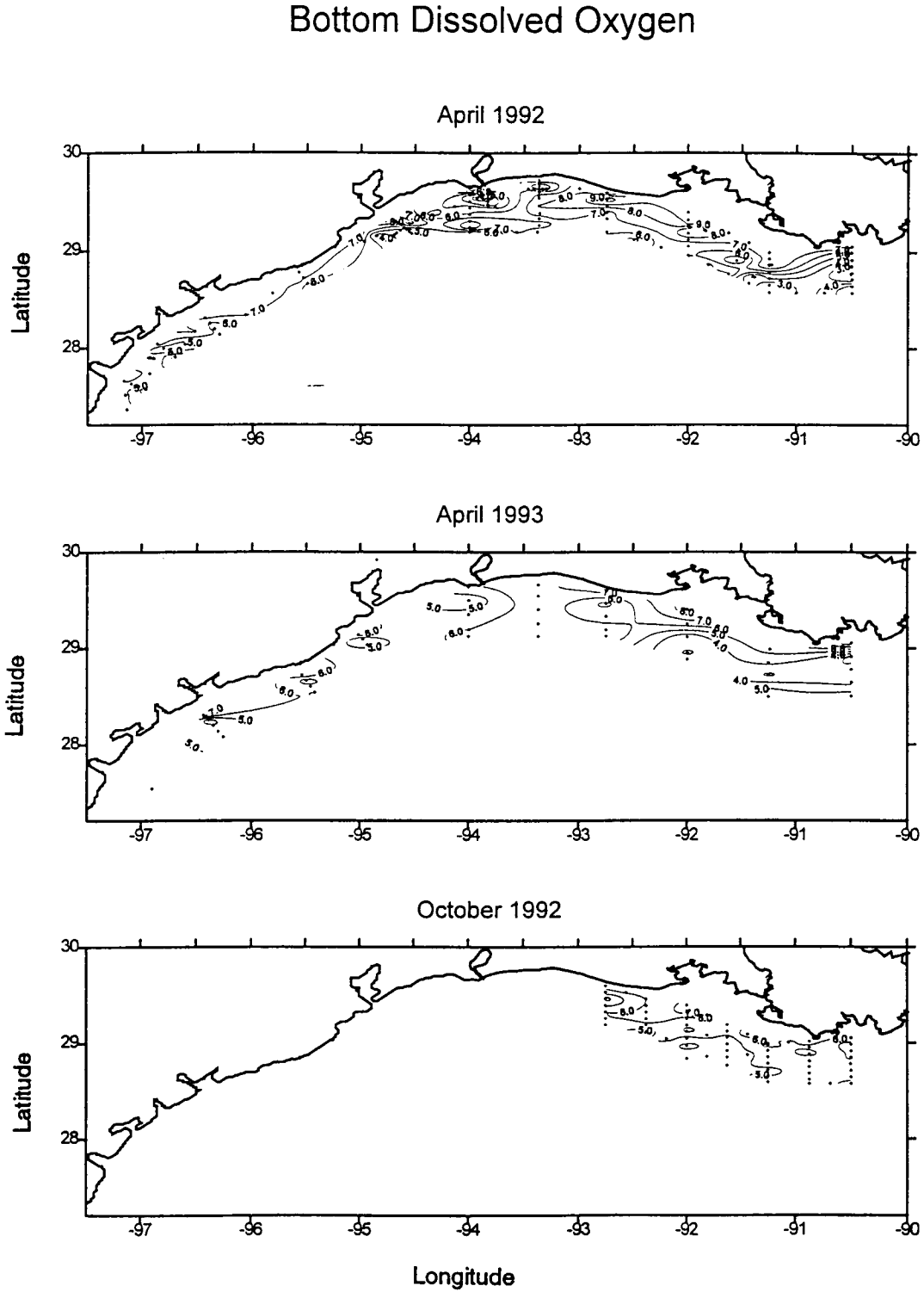

Figure 224. Bottom water dissolved oxygen for April and October LATEX cruises as indicated (data from SeaBird CTD).

Hypoxic near-bottom waters were not documented on the LATEX Cruise IV (April 13-22, 1993) (Figure NR1). Oxygen deficient ($2 \leq x \leq 4$ mg O_2 l^{-1}), but not hypoxic, waters were located along the S1, S2 and S3 lines, from offshore Terrebonne Bay to offshore Atchafalaya Bay. Lower oxygen concentrations were present along most of the length of the S1 line in the lowest two to three meters of the measured water column (Figure 225). The remainder of the LATEX study area was generally well-aerated. In contrast, several distinct patches of hypoxic bottom waters were observed during the NECOP cruise (April 26-30, 1993) (Figure 226) that were not evident during the LATEX cruise the previous week. The distribution of the low oxygen area off Terrebonne Bay (NECOP cruise, April 27) (Figure 226) was consistent with the lower concentrations of dissolved oxygen along the S1 line in mid-April (LATEX, Cruise IV, April 13). Reduced winds and calm seas were conducive to the further development of hypoxia off Terrebonne Bay during the interim. Respiration rates (see Chapter VI, Bottom Water Respiration Rates, Turner and Rabalais) could easily have led to depletion of the remaining oxygen in the lower water column between these two cruises.

The minimal distribution of oxygen-depleted bottom waters during April of 1992 and 1993 is consistent with the long-term database for transect C off Terrebonne Bay (Rabalais et al., unpublished data). Hypoxia is likely to develop there because of density stratification caused by springtime high riverine freshwater outflows, the likelihood of high rates of organic matter flux to the seabed from productive surface waters, and high respiration rates. If the density structure is maintained, hypoxia will continue to persist. If strong winds during frontal passages mix the water column, hypoxia will dissipate until stratification is re-established and oxygen-consuming processes deplete the oxygen levels in the lower water column.

Mississippi River discharge was unusually low in April 1992 (approx. 15,000 m^3 s^{-1}) compared to normal high spring discharge for spring in April 1993 (30,000 m^3 s^{-1}). The surface salinity field was fresher in the region of the S1 and S2 lines in April 1993 than 1992, and the density stratification was stronger. Less oxygen deficiency in 1992 may be related to reduced flow, less stratification, nutrient flux and surface net production, but it may also result from the passage of two cold fronts during that cruise compared to moderate southeasterly winds off Louisiana during April 1993 (i.e., less likely to disrupt the density structure). Continuous oxygen measurements (station C6B) from 1992 vs. 1993 (Rabalais et al., unpublished data) indicate that development of hypoxia in 1992 was frequently disrupted by mixing events every 7 to 10 days. In 1993 there was a gradual decline in hypoxia throughout the whole month of April, which indicates the lack of mixing events.

b. Oxygen Conditions in October 1992

Strong winds and rough sea conditions prior to and during the Cruise II (October 1992) resulted in a well-mixed water column and well-oxygenated waters throughout the water column (Figure 224). These results are consistent with the long-term database for transect C off Terrebonne Bay (Rabalais et al., unpubl. data). Hypoxia has not been recorded historically later than the first week in October and is not likely once strong cold fronts move across the study area and/or thermal cooling destabilizes the density structure.

c. Oxygen Conditions in July 1993 and July 1994

There were extensive areas of near-bottom and bottom water hypoxia during both Cruise IV (July 13-22, 1993) and Cruise VI (July 11-21, 1994). In mid-July 1993, the

NECOP Transect C
4/12/93
Dissolved Oxygen (mg/L)

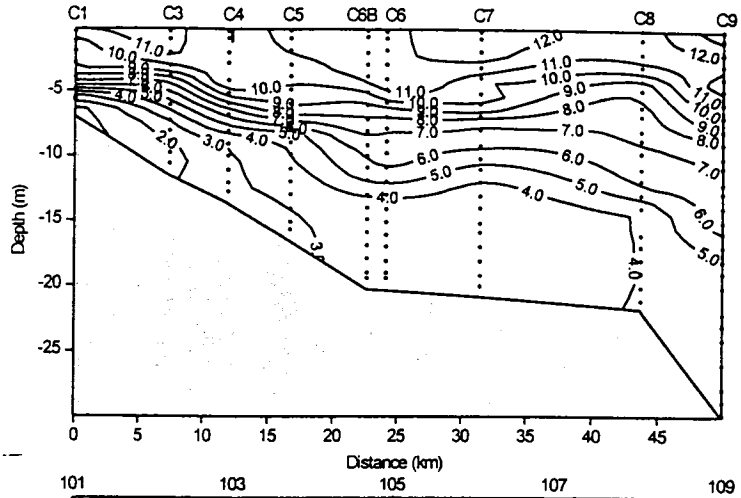

LATEX S1
4/13/93
Dissolved Oxygen (mg/L)

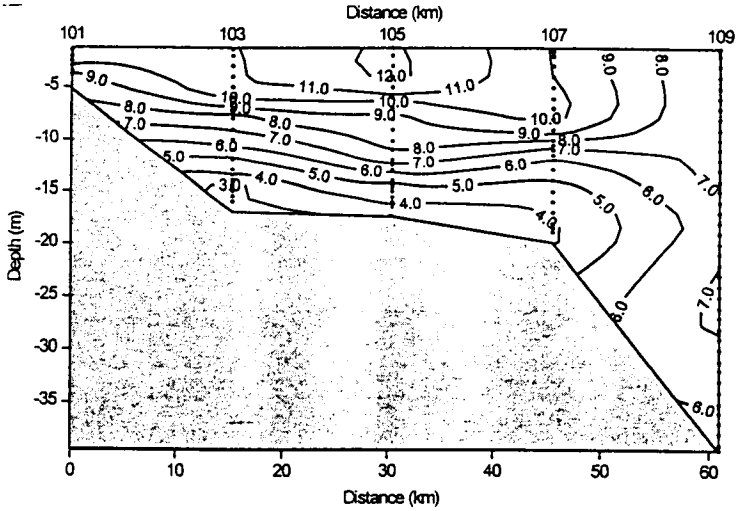

NECOP Transect C
4/27/93
Dissolved Oxygen (mg/L)

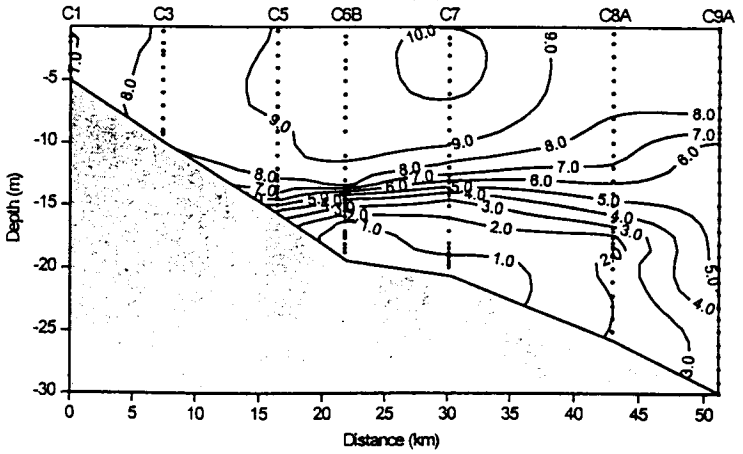

Figure 225. Cross-shelf contours for dissolved oxygen for April 1993 LATEX and NECOP cruises as indicated (data from SeaBird and Hydrolab CTDs, respectively).

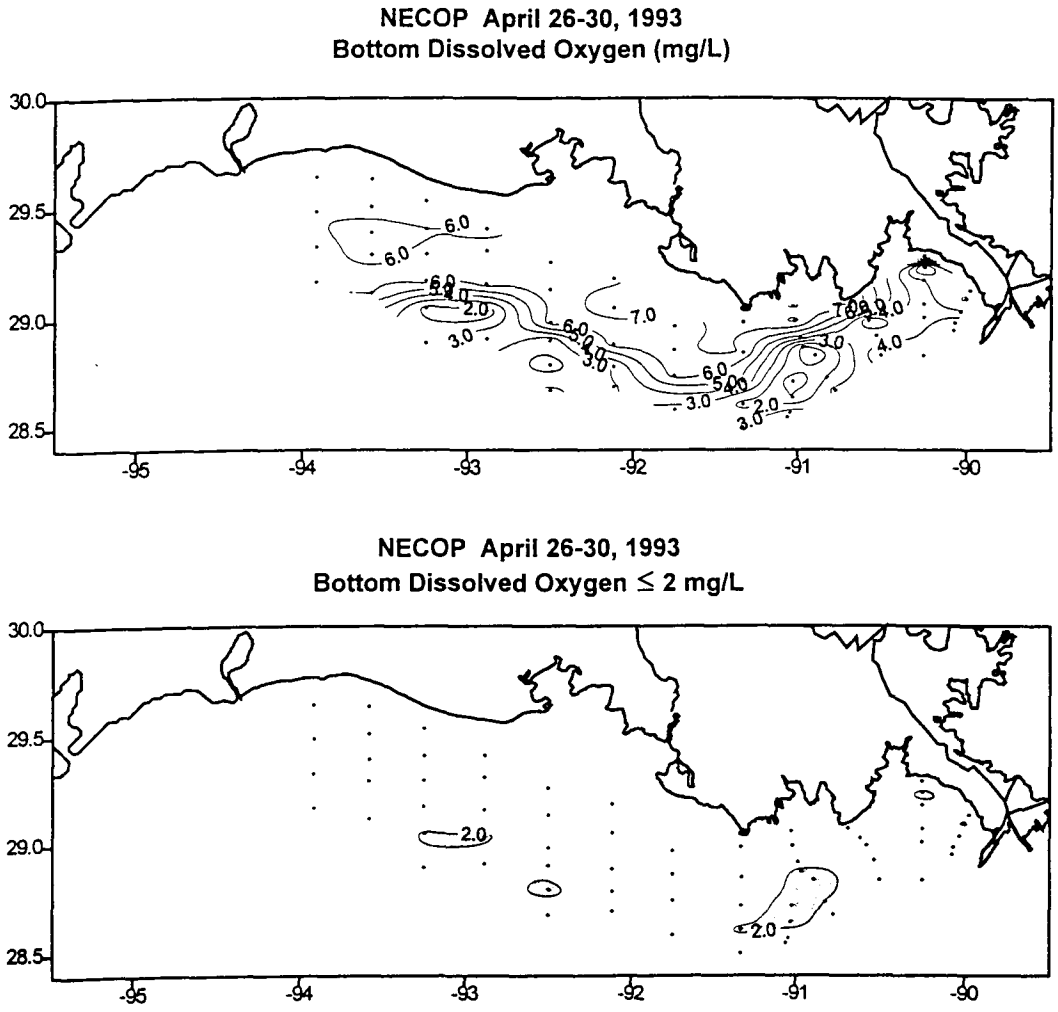

Figure 226. Bottom water dissolved oxygen for April 1993 NECOP shelfwide cruise (upper panel) and areal extent of hypoxia ($\leq$ mg O_2 l^{-1}) stippled (lower panel) (data from SeaBird CTD).

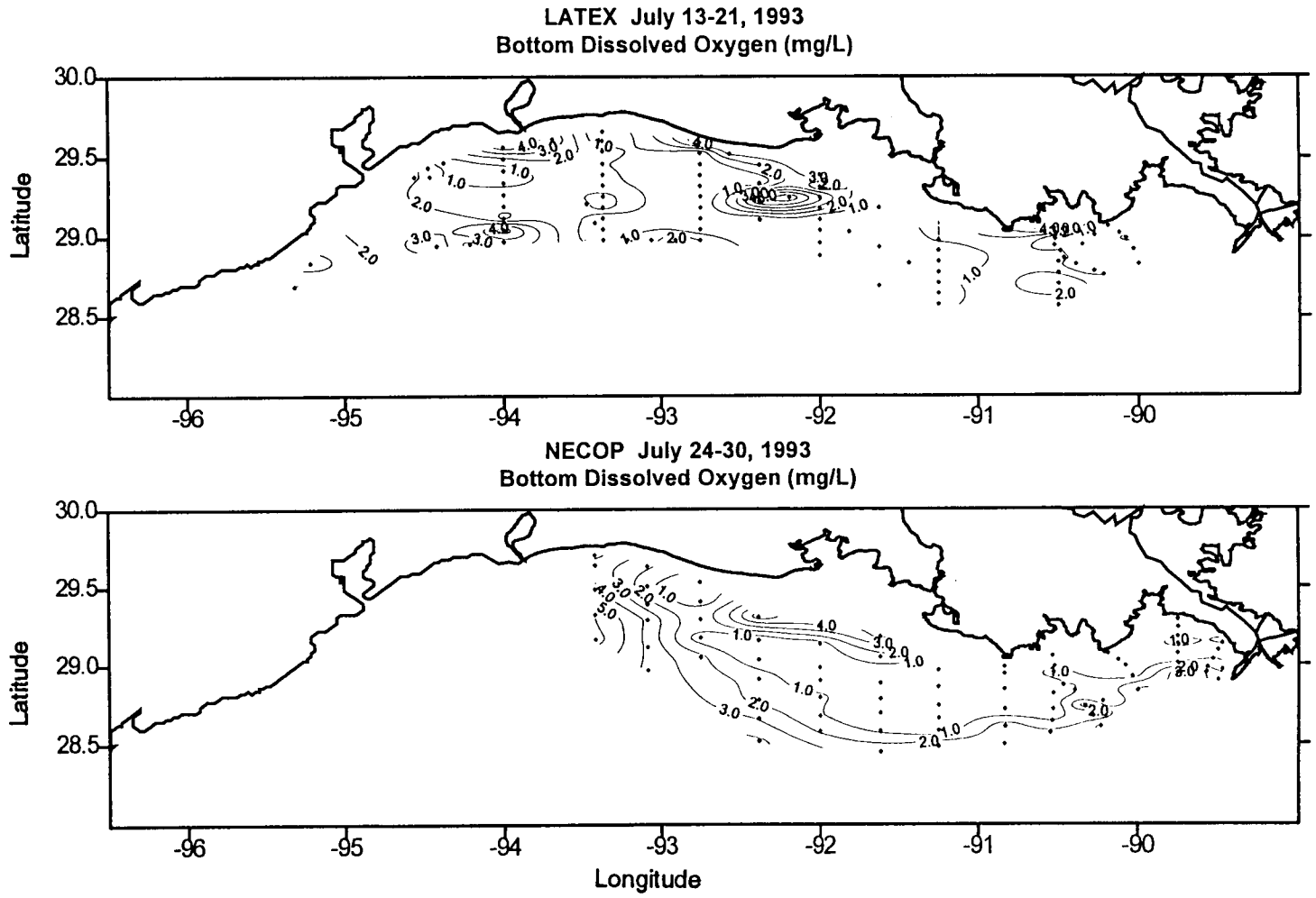

Figure 227. Bottom water dissolved oxygen for July 1993 LATEX B and NECOP cruises (data from SeaBird and Hydrolab CTDs, respectively).

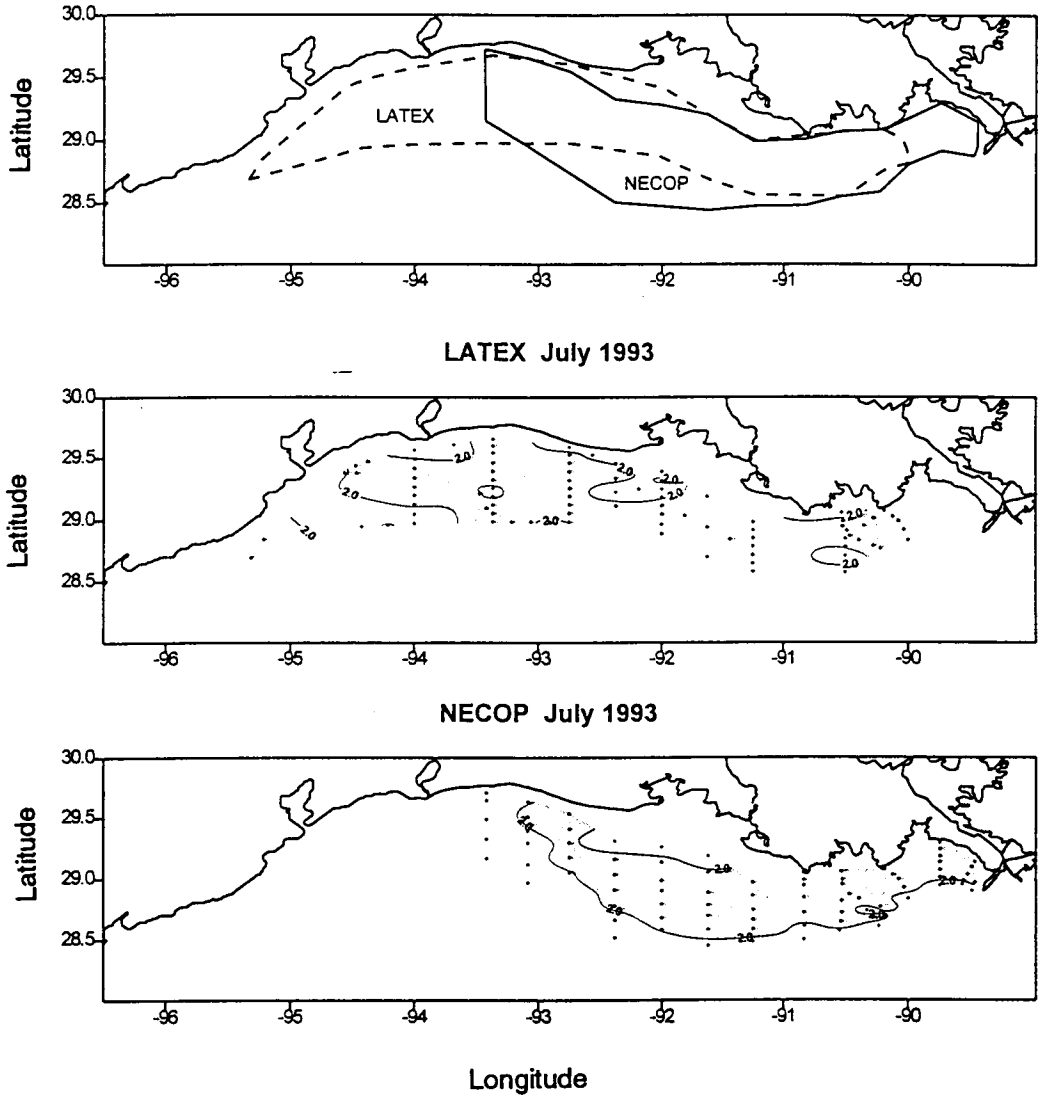

Figure 228. Areal extent of hypoxia ($\leq$ 2 mg O_2 l^{-1}) stippled for July 1993 LATEX B and NECOP cruises (data from SeaBird and Hydrolab CTDs, respectively). Upper panel outlines the two study areas.

hypoxic area extended from the transects off Terrebonne and Timbalier Bays on the east to the western end of the study area off Freeport, Texas (95.5° W) (Figures 227 and 228). The areal extent of hypoxia documented during late July 1993 (NECOP cruise) was twice the size documented over the same station design for the previous eight years . (Rabalais et al., 1998) (Figures 227 and 228). The increased size and severity followed record high and sustained flow of the Mississippi River in late spring and summer when flow is usually reduced. During the NECOP cruise (July 24-28, 1993), the hypoxic water mass did not extend as far to the west as during the LATEX Cruise IV (Figure 228). Persistent winds from a southerly and southwesterly direction displaced much of the surface waters to the east (along with lower salinities and higher nutrients) (Rabalais et al., 1998), as well as possibly some of the bottom water hypoxia (see below for cross-shelf comparisons). While hypoxia was extensive during the LATEX Cruise IV, it was located near the seabed and was somewhat patchy in distribution. One week later during the NECOP cruise, hypoxia had become well-developed and was present in much of the lower water column, was severe (well below 0.5 mg O_2 l^{-1}) at many stations, and was a continuous water mass (see discussion of comparative cross-shelf contours below).

Equally extensive and severely depleted oxygen zones were documented in mid- and late July 1994 (Figures 229 and 230). Hypoxic bottom waters extended farther to the west off the Calcasieu and Sabine estuaries in mid-July and also at isolated stations off Galveston in 1994 compared to 1993. The late July NECOP survey documented low oxygen conditions as far west as the Calcasieu estuary in 1994, which was similar to the results from the 1993 NECOP survey. Hypoxia was somewhat displaced farther offshore during late July 1994, compared to the previous week. Extensive zones of hypoxia occurred in 1994 even though river flow in July 1994 was much lower than in July 1993 (6,000 m^3 s^{-1} cf. 17,000 m^3 s^{-1}), and the surface salinity field in July 1994 indicated much less freshwater content in the surface layer (see Chapter VI, Pigment and Nutrient Distributions, Rabalais and Turner). The persistence of an enlarged hypoxia zone in 1994, similar to that seen during summer Mississippi River flooding in 1993, suggests the existence of residual effects of the 1993 flood into 1994 resulting from processes involving unrespired carbon and/or regenerated nutrients from the sediments.

d. Temporal Comparisons: Cross-shelf and C6B, Mid-summer

Comparisons of geographically similar cross-shelf transects from mid-July LATEX and late July NECOP cruises in 1993 and 1994 are provided below. Extensive areas of hypoxia were present during all cruises. These results point to the persistence of hypoxia over large areas for extended periods in mid-summer.

Differences in 1993 from the LATEX Cruise IV July 13-22) to the NECOP cruise (July 24-28) were evident as (1) more severely depleted oxygen concentrations; (2) a hypoxic zone encompassing more of the lower water column; (3) an eastward shift of the lower salinity surface waters from off Atchafalaya Bay to off Terrebonne Bay; and, (4) a shift eastward of the bottom water hypoxia on the southwestern Louisiana shelf. Strong winds and high waves were present in the LATEX/NECOP study area in mid-June because of the passage of a tropical storm across the Bay of Campeche. These wind-mixing events resulted in a reaeration of the water column that persisted into early July. During the progression of LATEX and NECOP cruises, high flow of the Mississippi River persisted, winds calmed, stratification became re-established and oxygen-consuming processes in the lower water column led to progressively lower oxygen concentrations in more of the lower water column.

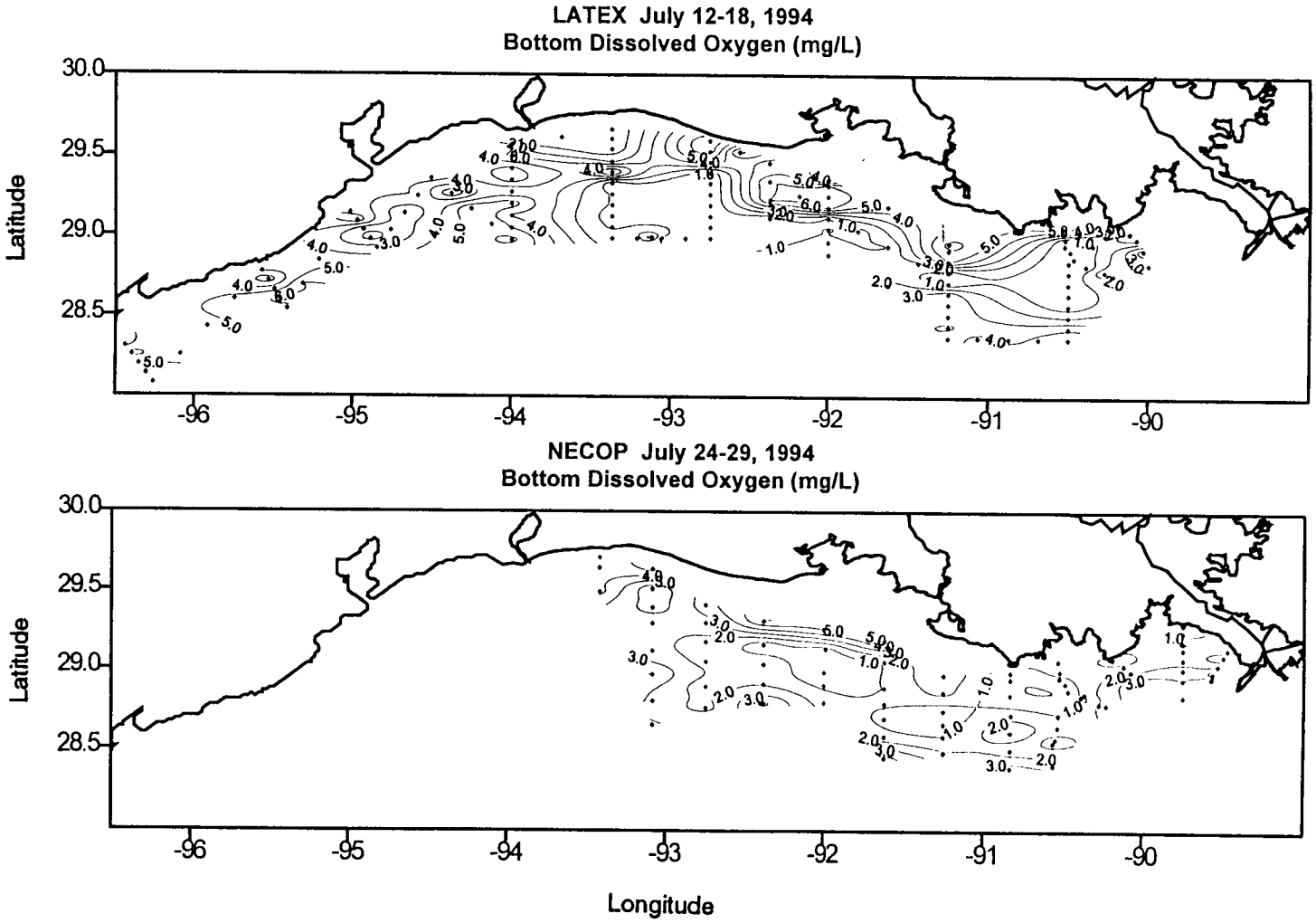

Figure 229. Bottom water dissolved oxygen for July 1994 LATEX B and NECOP cruises (data from SeaBird and Hydrolab CTDs, respectively).

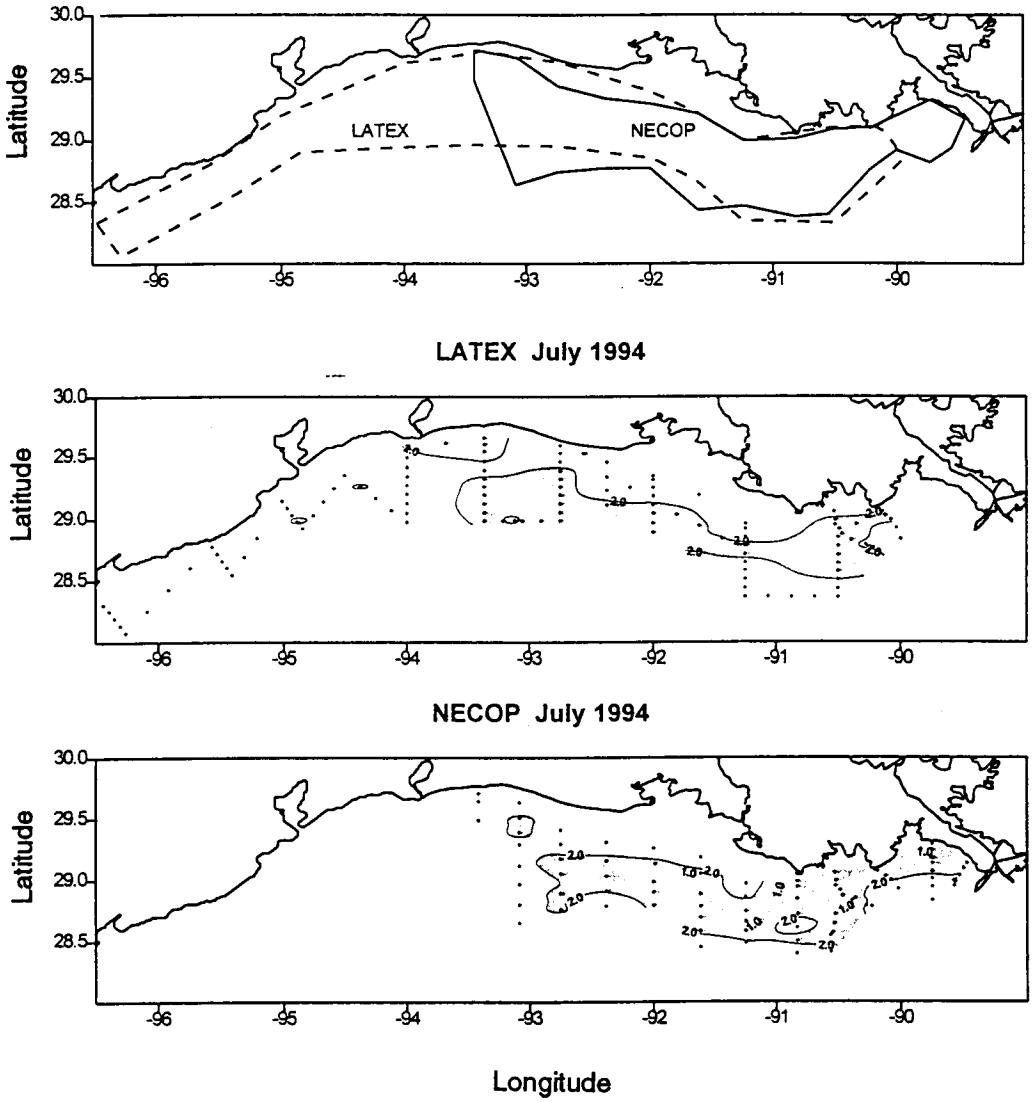

Figure 230. Areal extent of hypoxia ($\leq$ 2 mg O_2 l^{-1}) stippled for July 1994 LATEX B and NECOP cruises (data from SeaBird and Hydrolab CTDs, respectively). Upper panel outlines the two study areas.

ADCP data from LATEX Cruise IV (see Chapter II, Murray) and the late July NECOP cruise (Wiseman et al., unpublished data) indicate a typical summertime return flow regime that accounts for differences in the surface layer freshwater signature and bottom layer hypoxia distribution. South-southeasterly winds off Texas pushed the return flow upcoast and towards the Atchafalaya in the summer months. Winds and currents were lined up to push the high freshwater flow to the east, while low flow in the lower water column resulted in a stagnant bottom layer. NECOP ADCP data also showed strong west to east flow in the upper layer (6.7 m). Flow at 14.7 m was also to the east, slower at some stations, but similar to the 6.7 m average at others. Specific examples that illustrate the above scenarios are provided in Table 42 (Figures 231 through 235).

The progression of changes related to hypoxia at a single station over half a month in July 1993 are illustrated in Figure 236. During the LATEX cruise salinity in the surface layer was about 29 ppt and the pycnocline was located near 10 m (19-m station depth). Dissolved oxygen concentration in the lower 5 m of the water column was 2.5 mg O_2 l^{-1}. By 25 July, surface salinity was 27 ppt, the pycnocline was higher in the water column, at approximately 7-8 m, and dissolved oxygen in the lower 6 m of the water column was less than 1 mg O_2 l^{-1}. By July 30, the surface water salinity was 26 ppt, the pycnocline was gradual between 5 and 9 m, and hypoxia was present in the lower 12 m of the water column.

Comparisons for 1994 between 12-18 July LATEX and 24-28 July NECOP revealed fairly consistent distributions of hypoxic waters and water column structure through time. Mississippi River flow was typically low for the summer period, in contrast to 1993. ACDP data (see section II, Murray) indicated typical summertime return flow with a displacement of the Atchafalaya outflow to the east and sluggish bottom currents. Specific examples that illustrate the above are provided with figures are given in Table 43 (Figures 237 through 240).

e. Relationships of Low Oxygen Bottom Waters with Pigments and Nutrients

The LATEX data provide some insight into the relationships of hypoxia with pigment and nutrient distributions. The data, however, are limited when compared to more extensive data sets compiled over the course of hypoxia monitoring studies on the Louisiana shelf (1985-1996, Rabalais et al., unpublished data). A few relationships are apparent in the LATEX data set, but are much better demonstrated in the larger data set not presented here. Lack of strong relationships in the LATEX data usually seen in NECOP cruises might be caused by (1) the method of collection of "near-bottom" water in LATEX (Niskin on rosette, approximately 2-3 m above seabed) versus a bottom-tripping horizontally mounted Niskin for the NECOP studies and/or (2) differences in study design and sampling areas.

The distribution of low dissolved oxygen concentrations in bottom waters is related to high surface net production, but this relationship is lagged in time and space (Justic et al., 1993; Rabalais et al., 1994). Phytoplankton in surface waters falls into the bottom layers quickly, perhaps in a few days or less, but surface and bottom water currents are not traveling in the same direction or at the same speed. Most of the organic matter reaching the bottom is not consumed over hours but many days (and probably weeks). The depletion of oxygen is cumulative and depends also on the reaeration rate. No consistent patterns should therefore be expected between surface phytoplankton pigments in surface waters and low oxygen in bottom waters for one specific location in time. This is contrary to the pattern reported in Leming and Stuntz (1984), who suggested that satellite imagery of surface waters could describe the distribution of

Table 42. Specific examples taken from the 1993 LATEX B (MMS) and NECOP (NMFS) projects, which illustrate possible scenarios for hypoxic occurrences.

Location	Condition	Figure
- off Pass Fourchon	oxygen concentrations much lower over a greater distance and higher into the water column for NECOP stations B1-B9 on 7/25/93 compared to prior LATEX stations 509-513 on 7/13/93 .	231
- off Terrebonne Bay	oxygen concentrations much lower over a greater distance and higher into the water column for NECOP stations C1-C6B and D'1-D'4 on 7/25/93 compared to prior LATEX stations 501-111 on 7/13/93. Also, much fresher surface water layer on 7/25/93 NECOP than during prior LATEX cruise .	232
- off Point au Fer Island	oxygen concentrations much lower over a greater distance and higher into the water column for NECOP stations E1-E5 on 7/26/93 compared to prior LATEX stations on S2 line (115-124) on 7/15/93 . Density structure was similar between the two transects for the two cruises.	233
- off Marsh Island	LATEX S3 line is closer to shore and NECOP transect is farther offshore, but there were similar distributions of hypoxia on each of the cruises (7/16/93, cf. 7/27/93). Differences were apparent in the surface layer, however, where the low salinity surface layer present on S3 in mid-July was no longer present in late July on transect G. The surface waters were also much cooler on line S3 than on transect G, indicating a signature of Atchafalaya River water that had moved to the east before the NECOP transect G was occupied	234
S4 line	- oxygen, salinity, temperature, and density contours were very similar on the LATEX S4 line (stations 144-153) on 7/16/93 compared to the NECOP transect I on 7/28/93 . Hypoxia was confined to a thin lens near the seabed; the pycnocline was near the bottom.	235
- off Calcasieu estuary	hypoxia was very patchy in a thin lens near the seabed on the LATEX S5 ine on 7/17/93 . By 7/29/93 when transect K was occupied, oxygen had either dissipated or been pushed eastward by bottom currents.	236

Table 42 cont'd.

Location	Condition	Figure
- off Pass Fourchon	oxygen concentrations were very similar for LATEX stations 509-513 on 7/12/94 compared to NECOP stations B1-B9 on 7/25/94.	237
- off Terrebonne Bay	oxygen concentrations were very similar for LATEX stations 501-508 on 7/12/94 compared to NECOP stations C1-C9 on 7/25/94, and for LATEX stations 101-111 on 7/12/94 compared to NECOP stations C1-C6B and D'2-D'5 on 7/25/94 .	238
- off Point au Fer Island	LATEX S2 line is closer to shore and NECOP transect E is farther offshore, but there were similar distributions of hypoxia at 10-20 m water depth on each of the cruises (7/13/94 cf. 7/26/94). Surface salinities, however, were much fresher on transect E than on the S2 line, indicating a movement of Atchafalaya River outflow to the east during the interim (not illustrated).	239
- off Marsh Island	LATEX S3 line is closer to shore and NECOP transect G is farther offshore, but there were similar distributions of hypoxia on each of the cruises (7/14/94 cf. 7/27/94) with hypoxia extending a bit higher in the water column on transect G . Salinity and density structures were very similar (not illustrated).	240
- the LATEX S4 line	this line is closer to shore than NECOP transect I, but for the overlapping areas, there were similar oxygen, density, salinity and temperature contours for the two cruises (7/15/94 cf. 7/28/94) .	241
- off Calcasieu estuary	hypoxia was very patchy in a thin lens near the seabed on the LATEX S5 line on 7/15/94 . By 7/29/94 when transect K was occupied, oxygen had either dissipated or been pushed eastward by bottom currents.	242

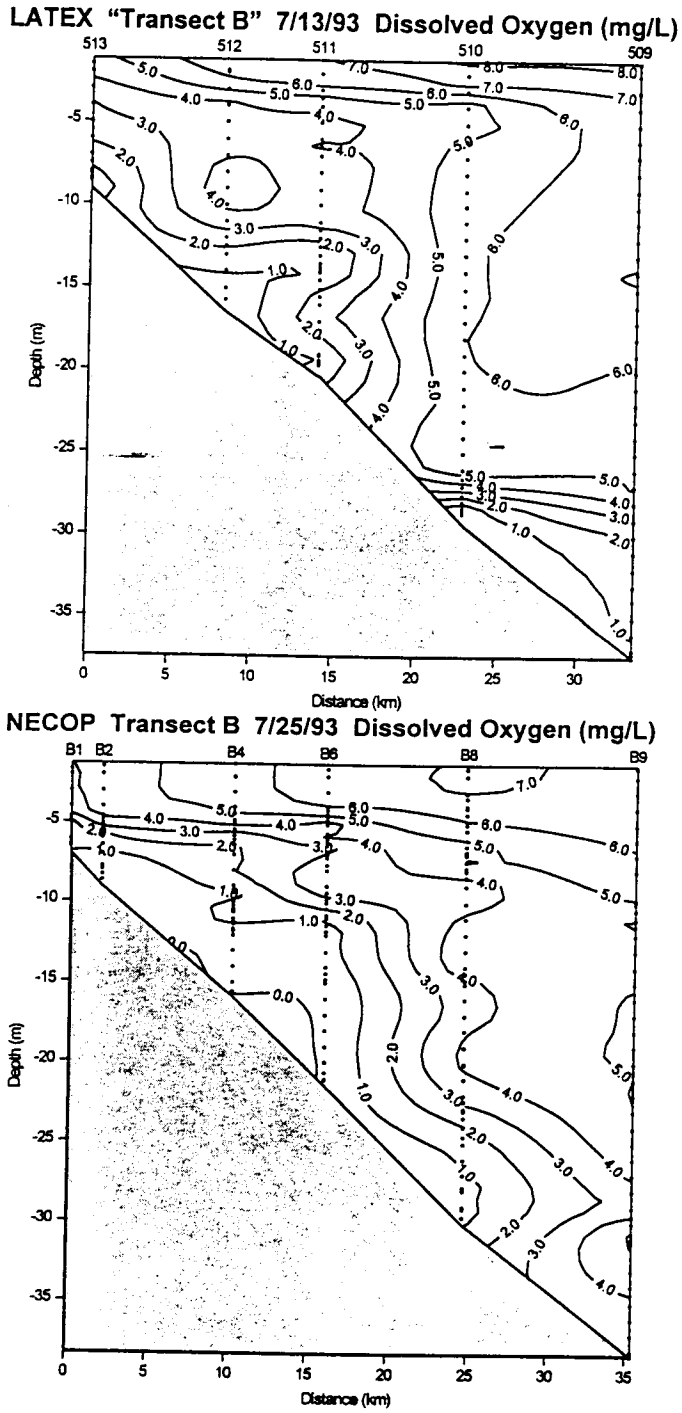

Figure 231. Cross-shelf contours (transect B) for dissolved oxygen for July 1993 LATEX and NECOP cruises as indicated (data from SeaBird CTD).

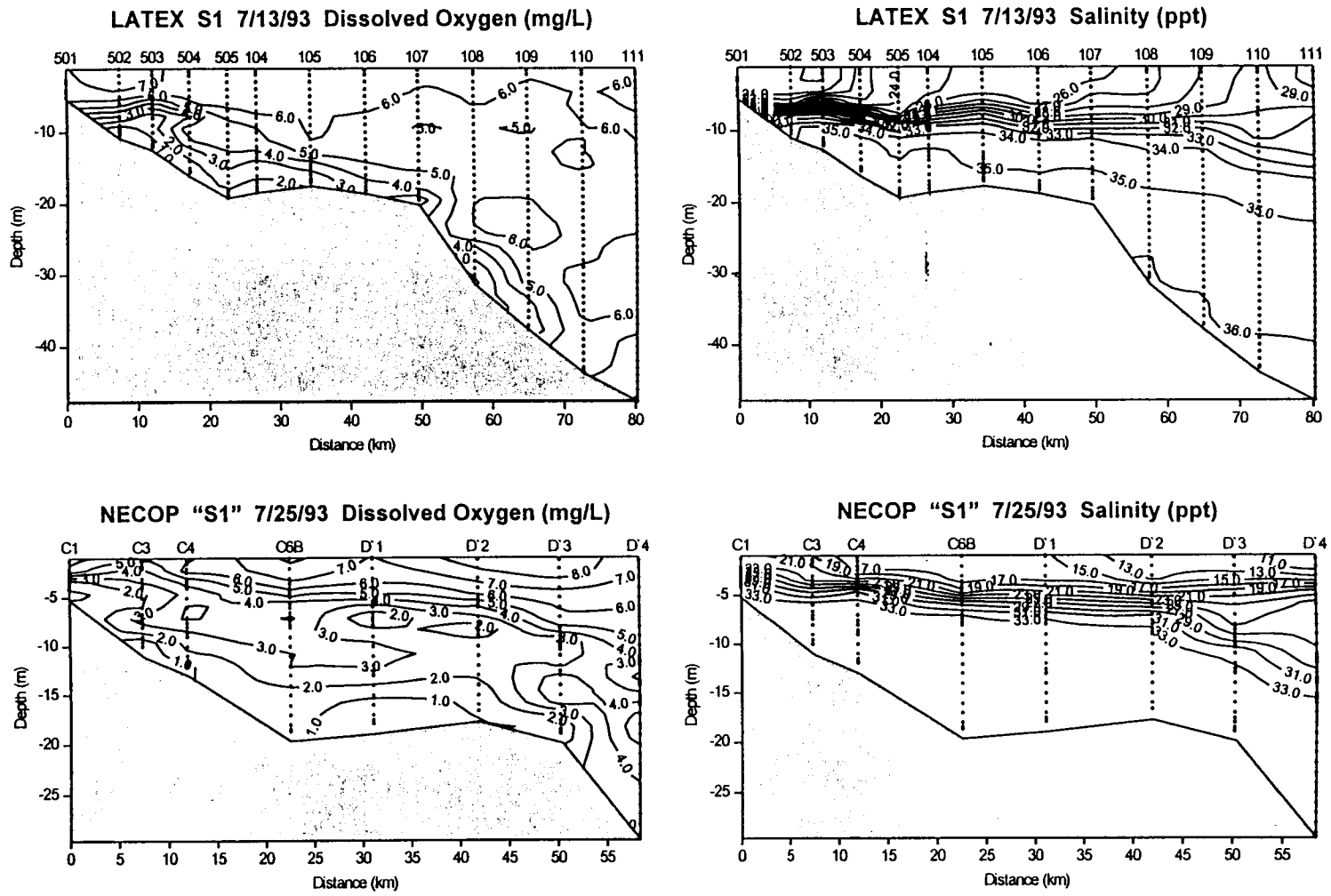

Figure 232. Cross-shelf contours (S1 line) for dissolved oxygen and salinity for July 1993 LATEX and NECOP cruises as indicated (data from SeaBird CTD).

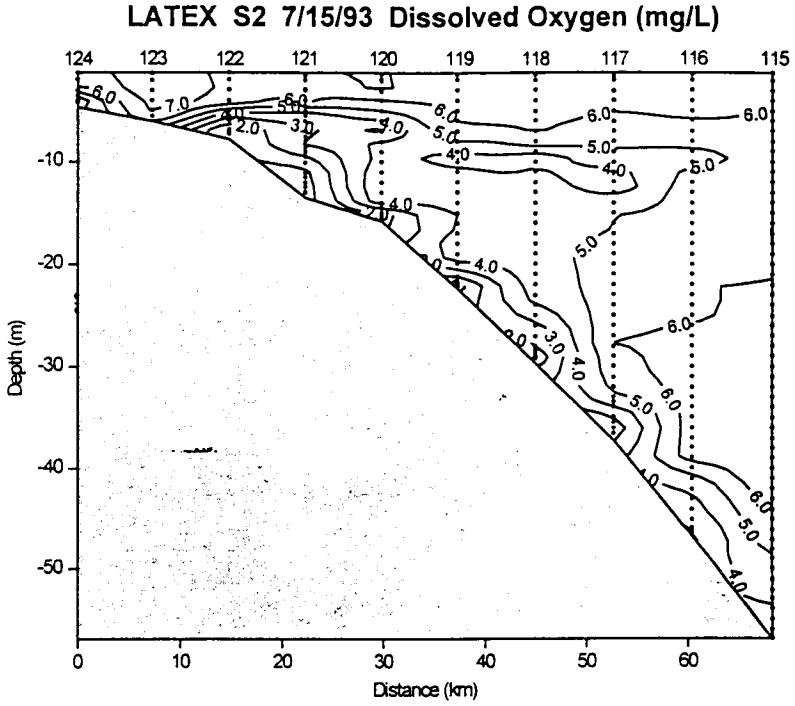

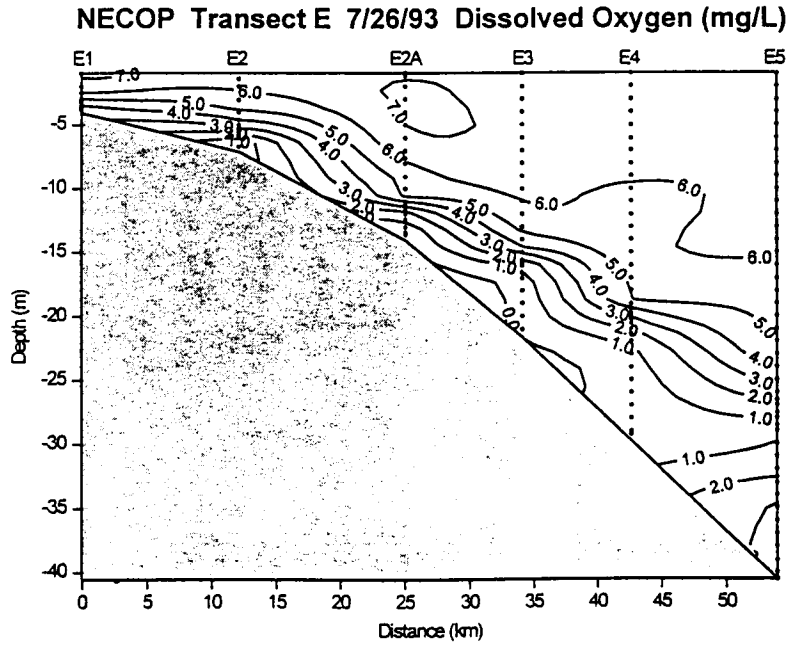

Figure 233. Cross-shelf contours (S2 line and transect E) for dissolved oxygen for July 1993 LATEX B and NECOP cruises as indicated (data from SeaBird CTD).

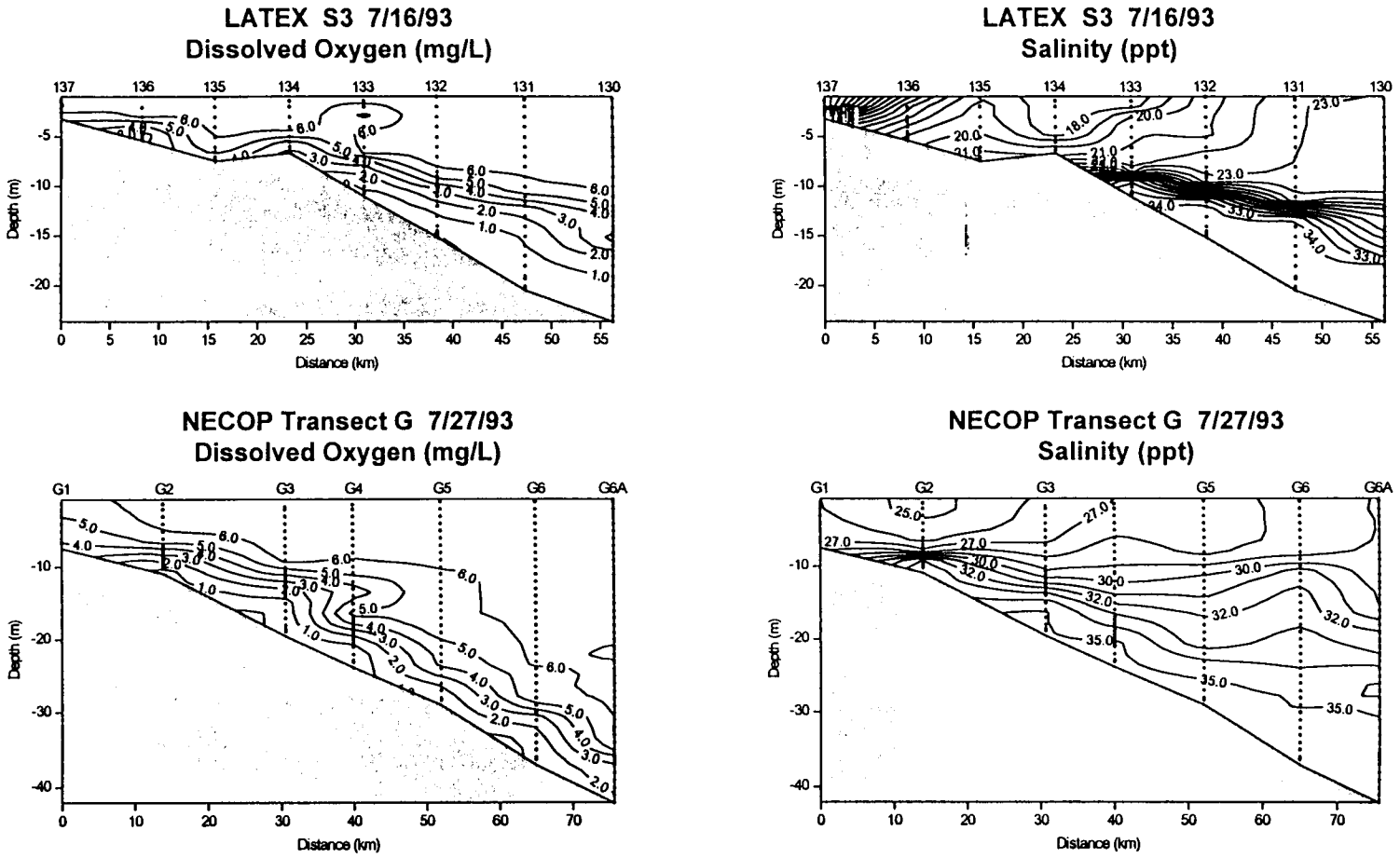

Figure 234. Cross-shelf contours (S3 line and transect G) for dissolved oxygen and salinity for July 1993 LATEX B and NECOP cruises as indicated (data from SeaBird CTD).

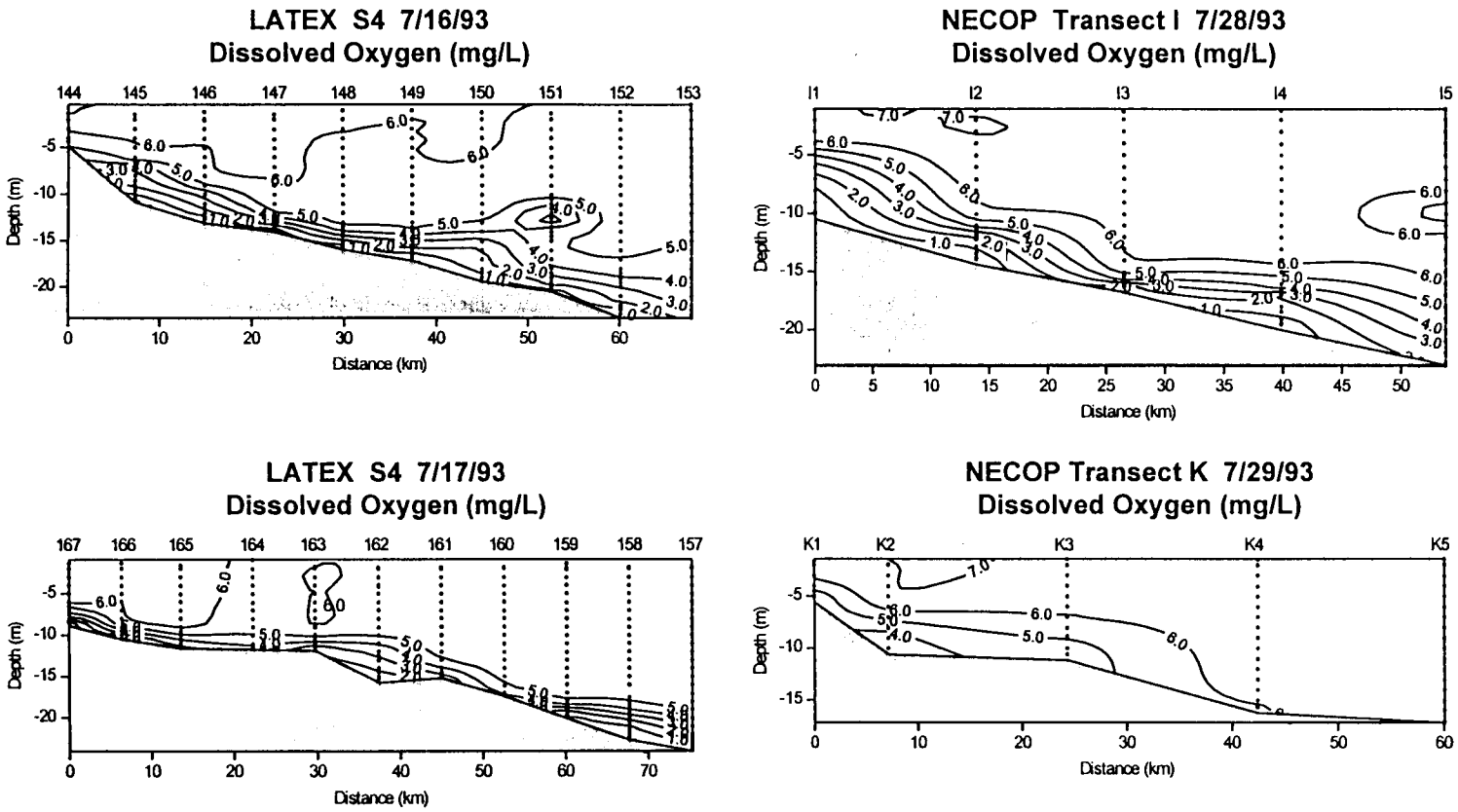

Figure 235. Cross-shelf contours (S4 line and transect I; S5 line and transect K) for dissolved oxygen for July 1993 LATEX B and NECOP cruises as indicated (data from SeaBird CTD).

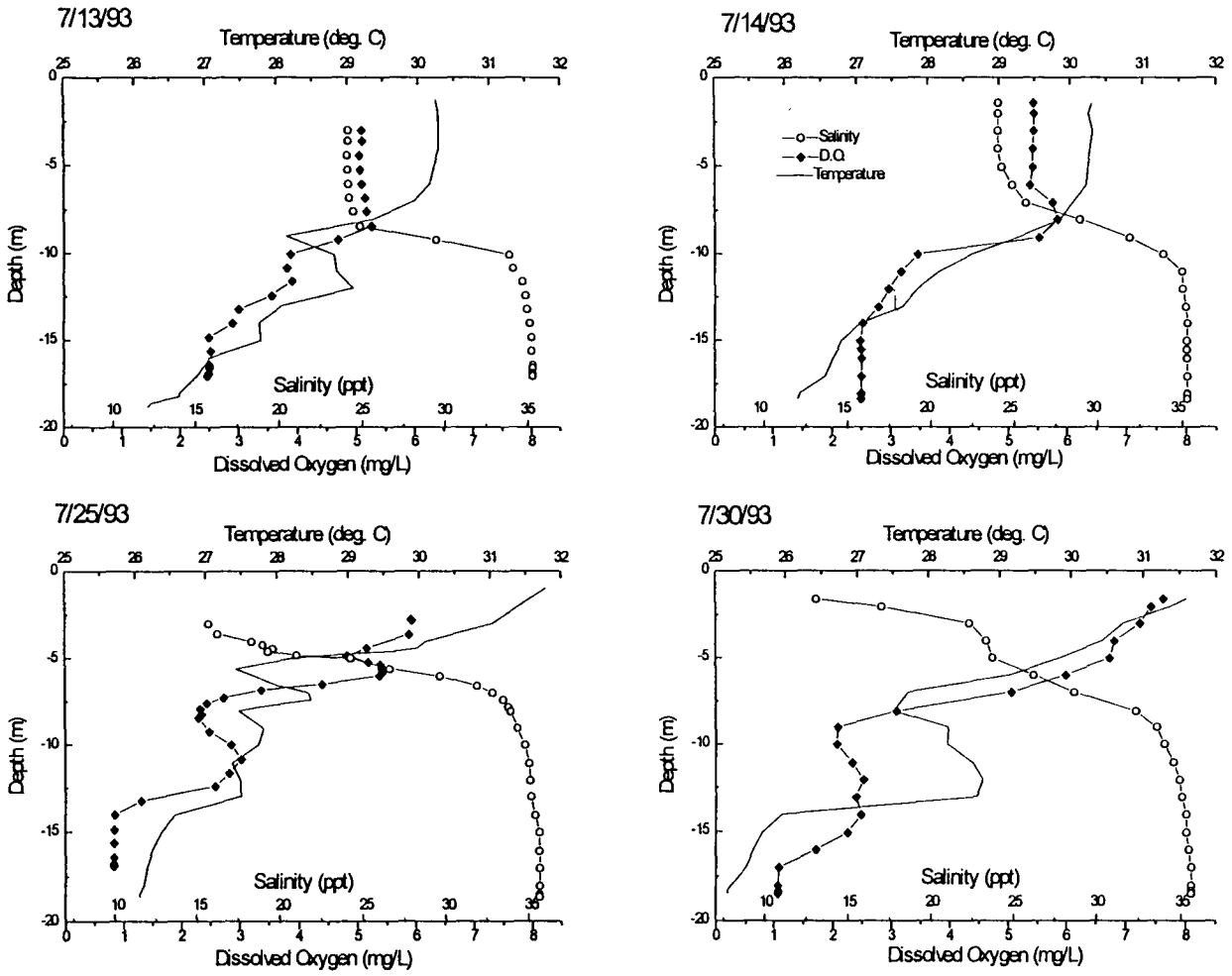

Figure 236. Vertical profiles for station C6B in July 1993 (data from SeaBird CTD for July 13-14 and from Hydrolab CTD for July 25 and 30).

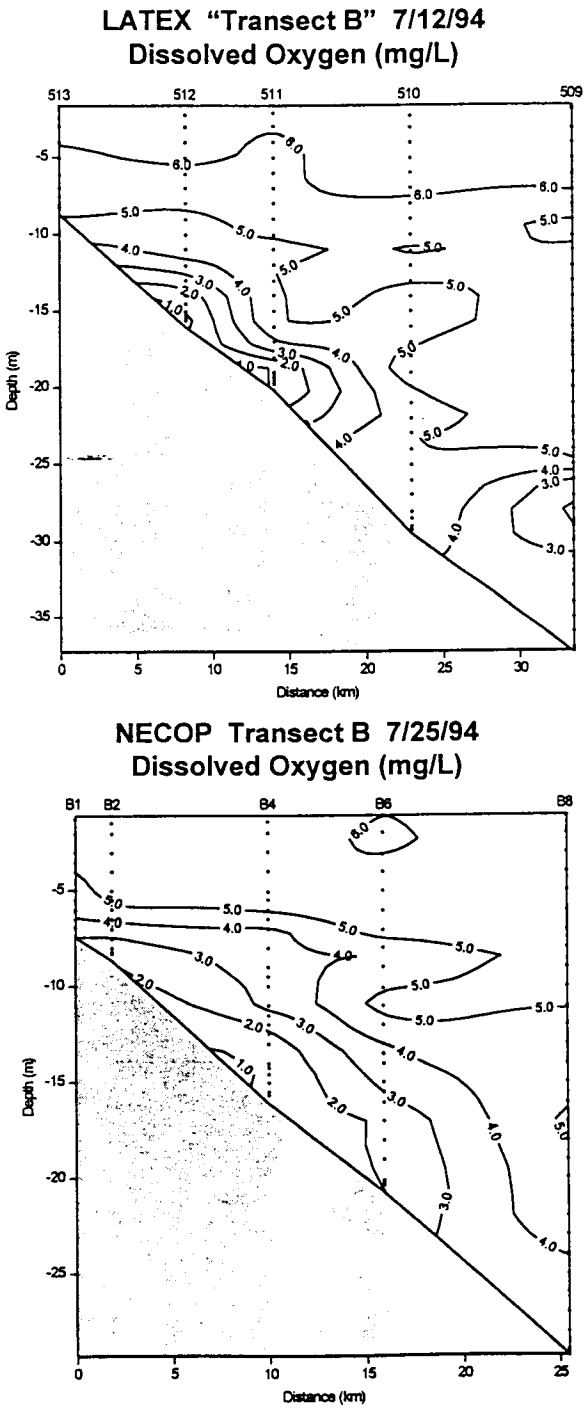

Figure 237. Cross-shelf contours (transect B) for dissolved oxygen for July 1994 LATEX B and NECOP cruises as indicated (data from SeaBird CTD).

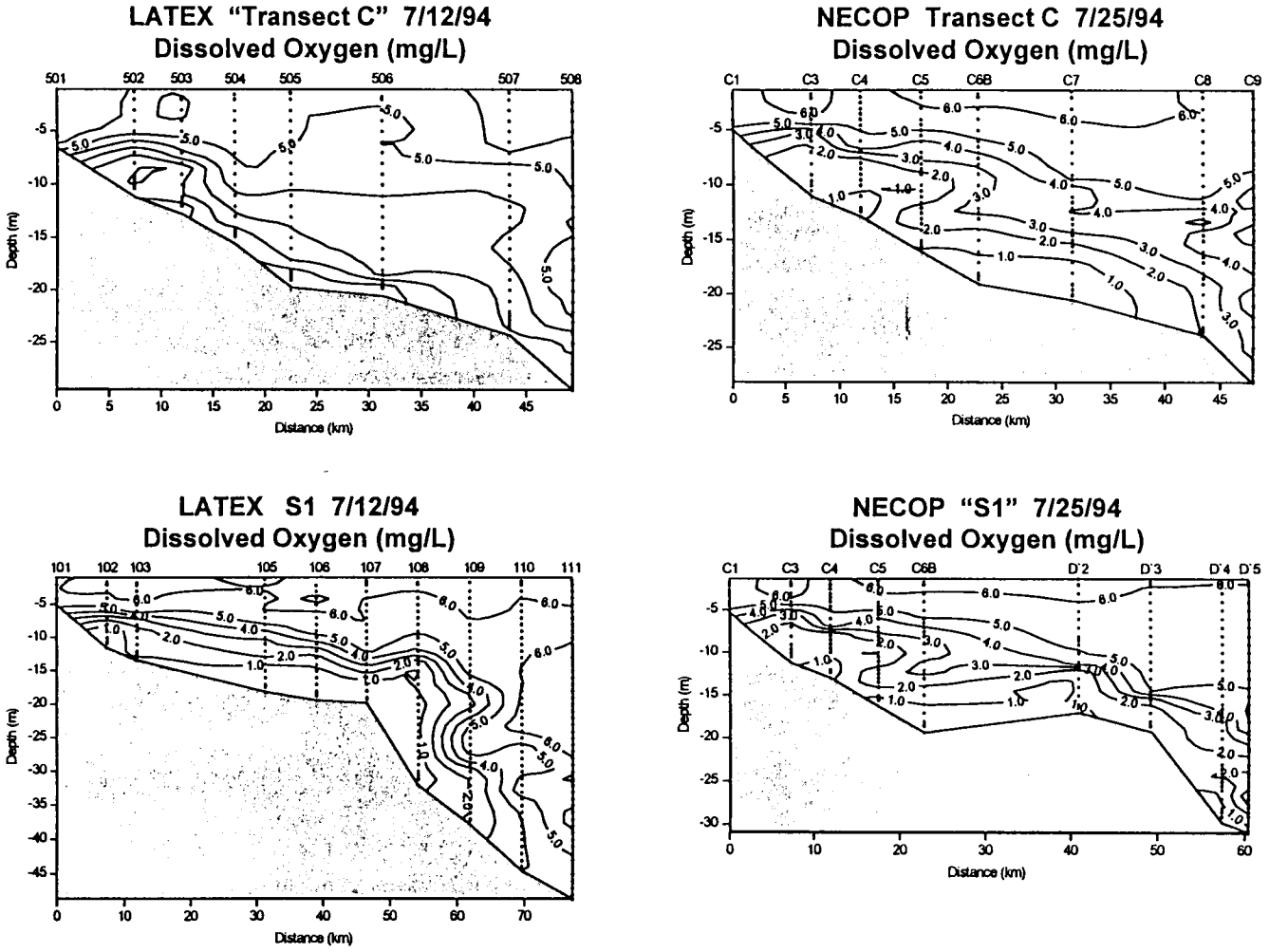

Figure 238. Cross-shelf contours (transect C and S1 line) for dissolved oxygen for July 1994 LATEX B and NECOP cruises as indicated (data from SeaBird CTD).

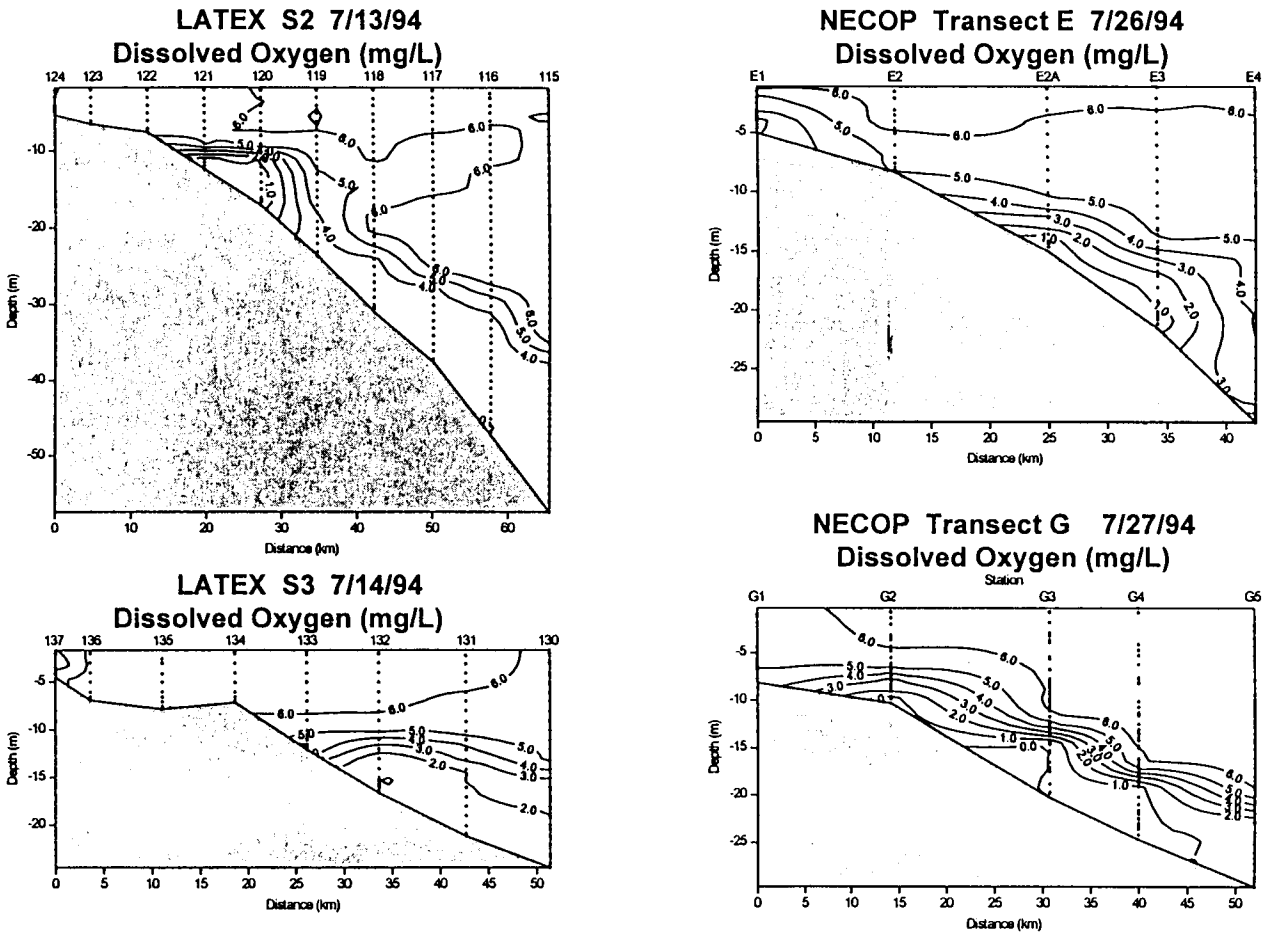

Figure 239. Cross-shelf contours (S2 line and transect E; S3 line and transect G) for dissolved oxygen for July 1994 LATEX B and NECOP cruises as indicated (data from SeaBird CTD).

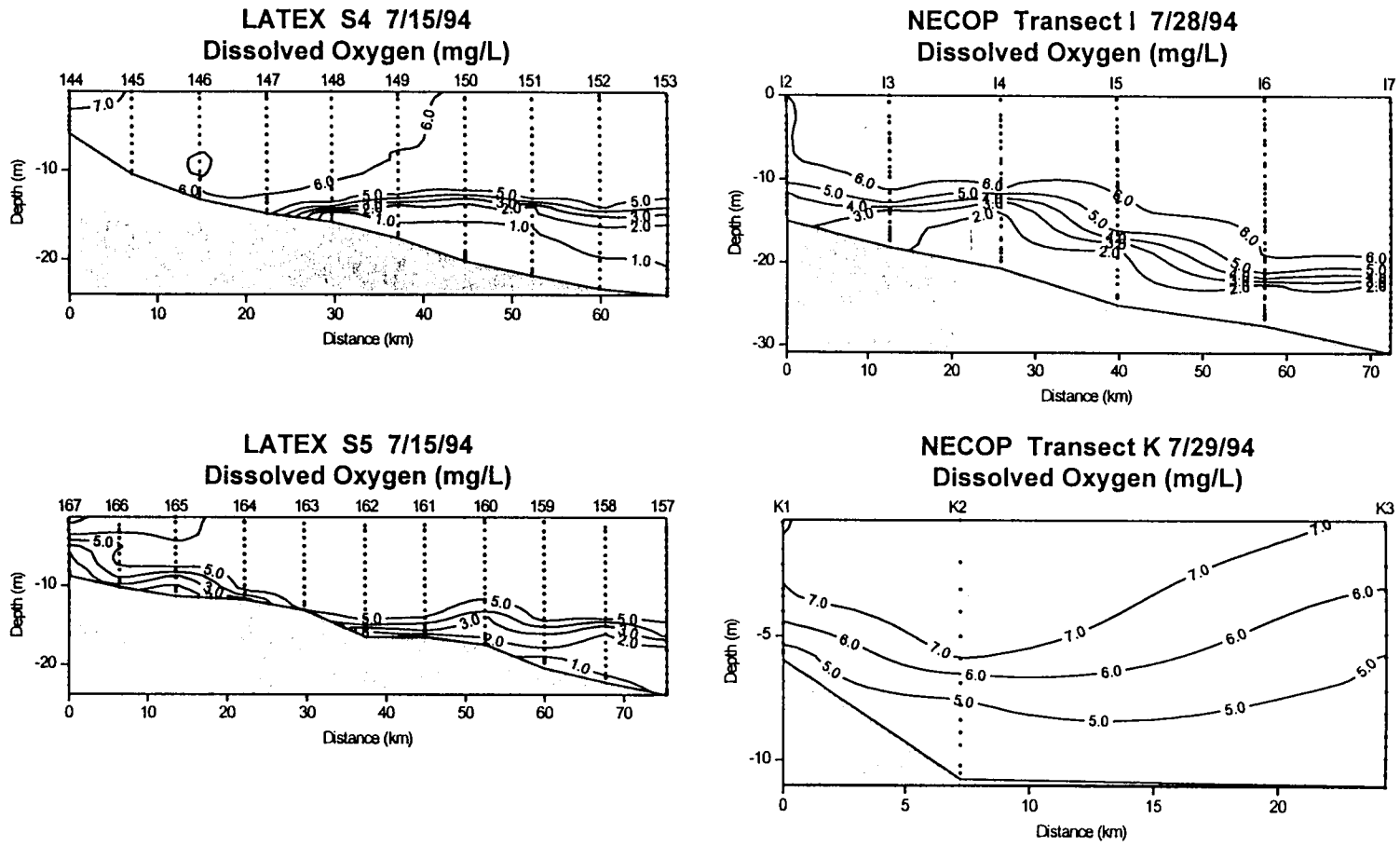

Figure 240. Cross-shelf contours (S4 line and transect I; S5 line and transect K) for dissolved oxygen for July 1994 LATEX B and NECOP cruises as indicated (data from SeaBird CTD).

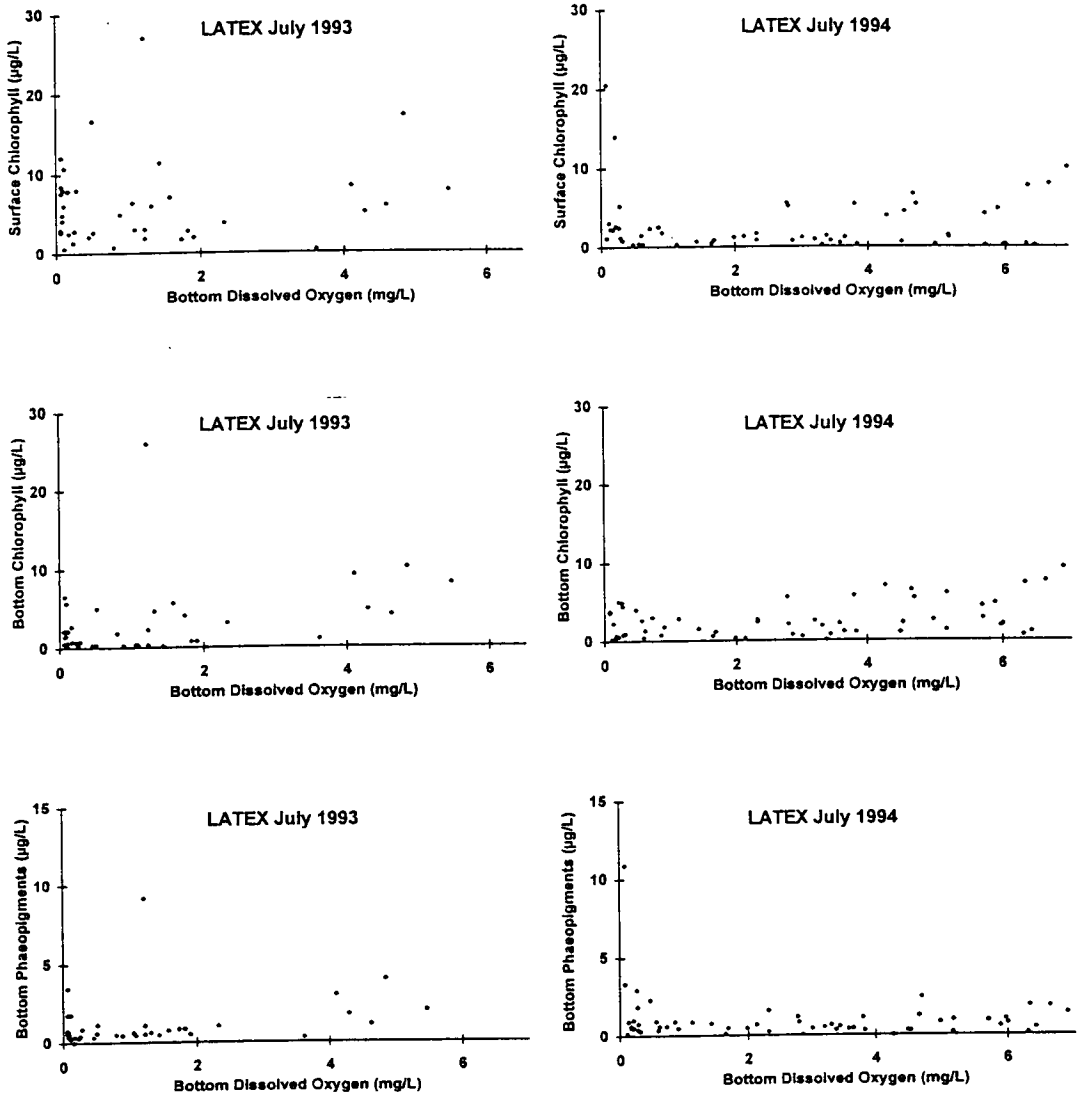

Figure 241. Comparisons of bottom water dissolved oxygen with surface water chlorophyll *a*, bottom water chlorophyll *a* and bottom water phaeopigments for LATEX B July 1993 and July 1994.

hypoxia. The lack of such a pattern (also suggested by Rabalais et al., 1991) was verified by data from LATEX Cruises IV and VI in mid-July (Figure 241). One might also predict that bottom waters with higher chlorophyll *a* concentrations are unlikely to be hypoxic or anoxic because of photosynthetic generation of oxygen (Dortch et al., 1994). This pattern, however, was not demonstrated with the mid-July data (Figure 241). Many hypoxic and anoxic stations had negligible chlorophyll *a* in the bottom waters, but there were also hypoxic and anoxic bottom waters with 2 to 5 or 7 $\mu g\ l^{-1}$ chlorophyll *a*. The amount of phytoplankton biomass in the bottom waters across the Louisiana inner and middle shelf is high, often exceeding 10 $\mu g\ l^{-1}$ total pigments, and a high percentage is composed of phaeopigments (i.e., degradation products of chlorophyll; Rabalais et al., 1991). In many of the data sets from NECOP shelfwide and transect C monitoring cruises, elevated phaeopigments in hypoxic or anoxic bottom waters are usually associated with very low oxygen concentrations (< 0.5 mg $O_2\ l^{-1}$). This pattern was not demonstrated with the LATEX mid-July data, with the exception of a single station in July 1994 (Figure 241).

The relationships between the oxygen and nutrient concentration in bottom water during periods of hypoxia or anoxia reveals information about decomposition and sediment-water interactions. In general, the relationship between oxygen concentration and the concentration of dissolved inorganic nitrogen, phosphate and silicate is an inverse relationship. At the lowest oxygen concentration, the nutrient concentrations rose even higher. Because oxygen consumption is dependent on recently derived organic matter (from the surface), nutrients are released upon decomposition. Benthic decomposition is under more reducing conditions than in the more oxygenated overlying waters, so ammonia and nitrite may accumulate in hypoxic waters (until transformation into nitrate). For July 1993, there were elevated concentrations of NH_4^+, NO_3^-, NO_2^- and PO_4^{3-} in hypoxic bottom waters especially where oxygen levels were less than 0.5 mg $O_2\ l^{-1}$ (Figure 242 and 243). Hypoxia was not as widespread and severe in July 1994 as in 1993, but there were elevated levels of NH_4^+, NO_2^-, PO_4^{3-} in water less than 0.5-1 mg $O_2\ l^{-1}$. Most of the inorganic nitrogen is present as nitrate, but there were significant amounts of NH_4^+ and NO_2^- at the lowest oxygen concentrations, indicating organic decomposition in sediments and nutrient release (similar to hypoxic/anoxic environments in the mid-reaches of Chesapeake Bay (Cowan and Boynton 1996) (Figures 242 and 243). It is possible that some of the NH_4^+ was converted to NO_3^- through nitrification. Higher dissolved silicate fluxes out of the sediments in hypoxic bottom waters in mid-Chesapeake Bay were related to the flux of organic matter from surface waters, but only after a temporal lag of one month was added between deposition events (shown as elevated sediment chlorophyll *a* concentrations) and sediment nutrient releases. One could predict, then, that those stations with higher SiO_4^+ concentrations where the oxygen concentration is low (Figure 243) received a greater flux of organic material in prior months.

5. Summary and Conclusions

Hypoxia was patchy and ephemeral in April 1992 and 1993 (several NECOP cruises and LATEX Cruises I and III), but was not present in October (LATEX Cruise II). A higher frequency of occurrence of hypoxia in April 1993 compared to April 1992 may be the result of either the higher river flow and/or fewer wind mixing events in 1993. Hypoxia was widespread in July of both 1993 and 1994. Persistence of hypoxic water masses over half a month (mid- to late July) is evidence that mid-summer hypoxia on a shelfwide basis is not an ephemeral event but that the severely reduced oxygen occurs over large areas of the Louisiana-Texas coast for extended periods.

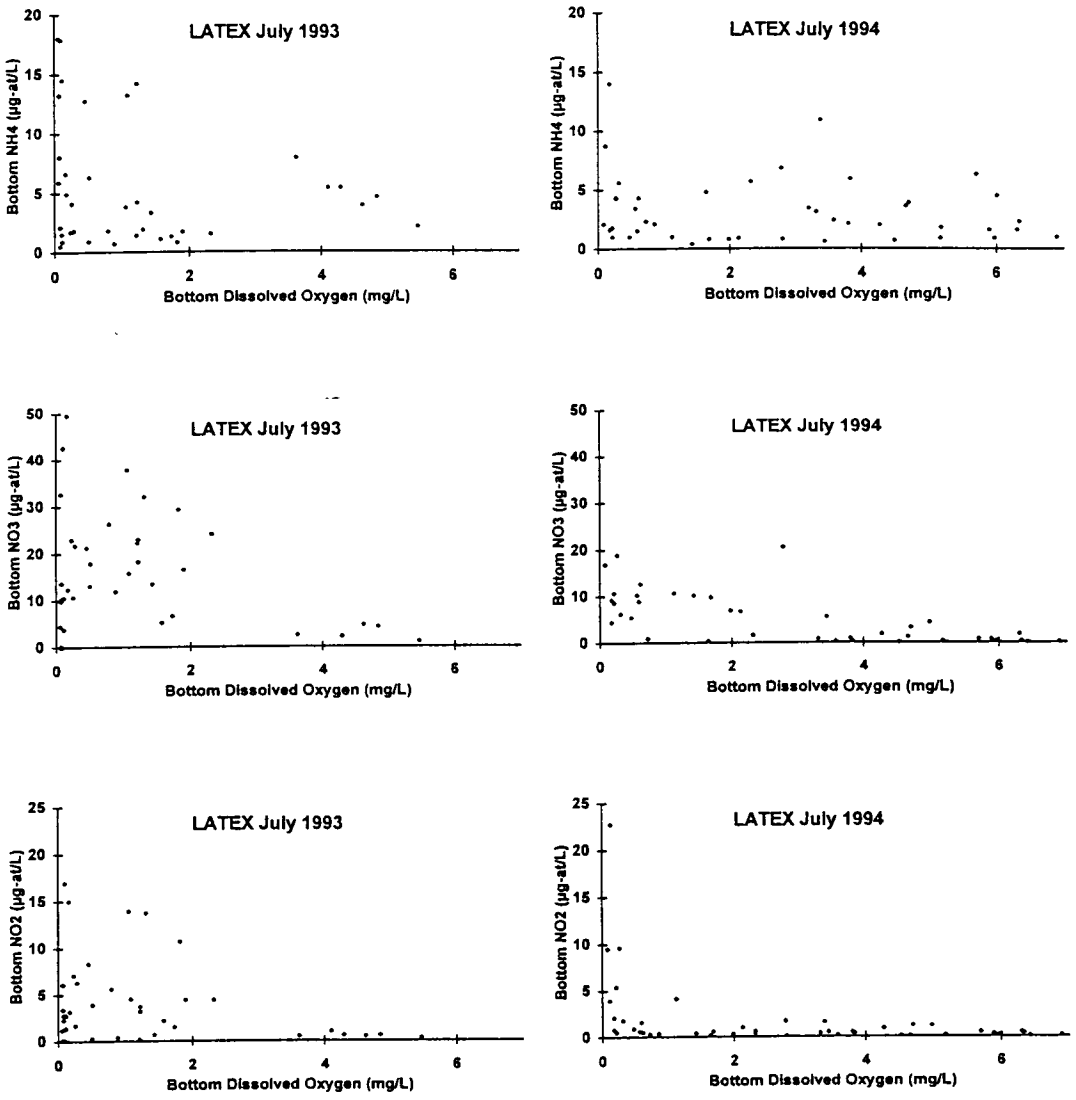

Figure 242. Comparisons of bottom water dissolved oxygen with bottom water NH_4^+, NO_3^- and NO_2^- for LATEX B July 1993 and July 1994.

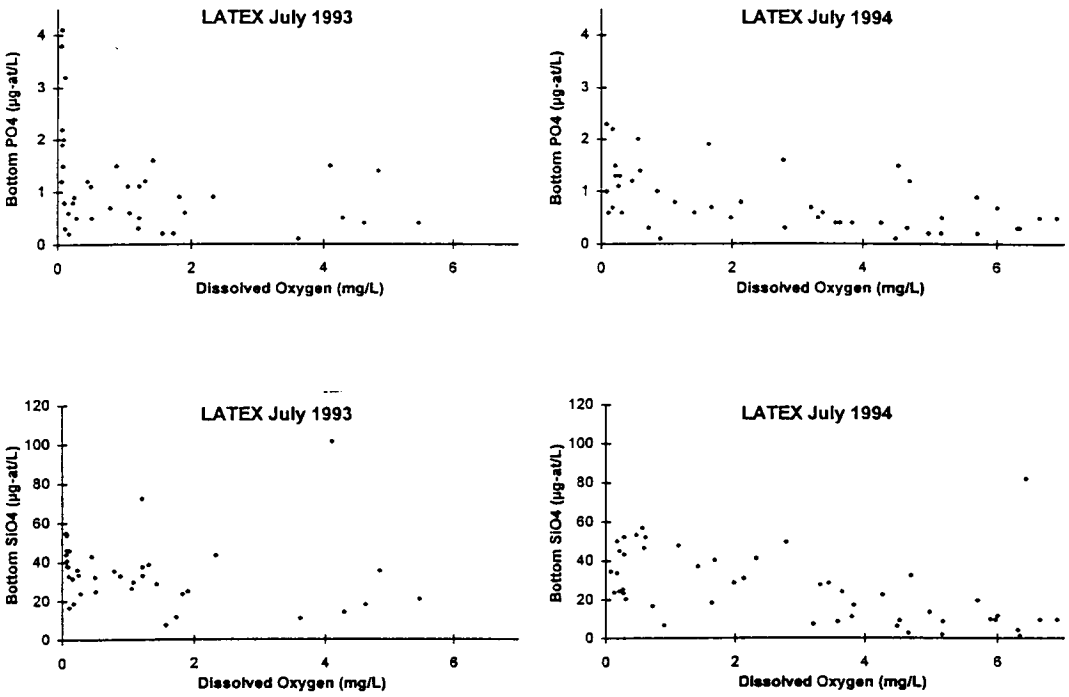

Figure 243. Comparisons of bottom water dissolved oxygen with bottom water PO_4^{3-} and SiO_4^{+} for LATEX B July 1993 and July 1994.

During maximal extent of mid-summer hypoxia, the severity, areal extent and distance up into the water column differs on the southeastern Louisiana coast versus the southwestern coast. Much of the lower half of the water column is hypoxic on the southeastern coast compared to a few meters above the seabed on the southwestern coast. Reasons for the differences include: less freshwater flux and subsequent differences in physical structure and biological processes (e.g., less freshwater content on the southwestern coast and less stratification); less nutrient flux, surface net production, and carbon flux on the southwestern coast; and better light conditions (see Section VI on Light Conditions) which allow for photosynthetic generation of oxygen in the lower water column.

The mid-summer cruises were affected by the 1993 record summer flood of the Mississippi River compared to a more normal low summer flow in July 1994. Extensive areas of hypoxia occurred in July 1993 (twice the areal extent of the previous eight years of monitoring by Rabalais et al.) and were also present in 1994. During July 1993, there was a buildup of hypoxia on the S1 line between the period of mid-July (LATEX Cruise IV) and late July (NECOP cruise). High seas in June resulting from a tropical storm passage across the Gulf of Campeche reaerated the water column along the S1 line/transect C. In the interim period of the two July 1993 cruises, there was evidence of movement of surface lower salinity waters from the west to the east and intensification of hypoxia. The effects of currents moving water masses from west to east were also seen in the displacement of low oxygen water in the lower water column in mid-July farther to the east by late July. Water column structure and distribution of hypoxia were fairly consistent between the mid-July and late July LATEX (Cruise VI) and NECOP cruises of 1994.

Oxygen deficient bottom waters are not associated with high chlorophyll *a* concentrations in surface waters (at least not at a specific location for a point in time), but lag temporally and spatially with high surface net production. Very low dissolved oxygen concentrations in bottom waters (less than 0.5 mg O_2 l^{-1}) are sometimes associated with high phaeopigment, NH_4^+, NO_3^-, NO_2 and PO_4^{3-} concentrations.

B. Bottom Water Respiration Rates in the Hypoxia Zone Within the Louisiana Coastal Current

by R. Eugene Turner and Nancy N. Rabalais

1. Introduction

The flux of organic material from the sea surface down through the water column in the open ocean typically declines with depth through aerobic biological decomposition occurring continuously enroute. Suess (1980) showed this, for example, using a synthesized data base from sediment trap deployments at various depths (>50m) and in various oceans. He also elegantly demonstrated a logarithmic reduction of water column respiration rate with depth as less and less organic material was transported into the water below. Smith (1978a) and Smith and Hinga (1983) showed a similar logarithmic reduction with depth for sediment community respiration rates and also the effect of temperature changes and sediment C/N ratio on these rates.

Water column respiration rates on continental shelves are thought to involve additional constraints that obscure the expression of these depth vs. respiration rate relationships. These additional factors include horizontal mixing, a spatially heterogeneous source of organic material in surface waters, and sufficient light for photosynthesis that may even occur in the benthos. Improving our knowledge of the

variability and influences on water column respiration rates is of particular concern for several reasons, including understanding coastal pollutant transformations, global carbon budgets, and, especially, hypoxic water (less than 2 mg/l) mass formation, maintenance and breakup.

Areas of oxygen-deficient bottom waters in the northern Gulf of Mexico share features with similar areas throughout the world (Rabalais et al., 1991; 1996a). The zones of hypoxic bottom water in the northern Gulf of Mexico may cover up to 18,000 km^2 during mid-summer on the inner continental shelf, from the Mississippi River delta onto the northeastern Texas coast (Rabalais et al., 1991 and 1996b). Oxygen depleted bottom waters occur as early as February and last until October but are most widespread, severe, and persistent from June through August. The intensity of oxygen depletion is tied to the strength of the density stratification during spring and summer. Density stratification is a function of surface water salinities that reflect the freshwater input of the Mississippi and Atchafalaya Rivers. The organic matter is found in sediment traps in the 20 m isobath, which originates from surface phytoplankton biomass (Qureshi, unpublished). Water column and benthic respiration rates are not completely known, but a preliminary analysis from a fall sampling cruise (Turner and Allen, 1982) demonstrated that bottom water respiration rates then were proportional to phytoplankton pigment concentrations. Bottom water phytoplankton pigment concentrations on the inner shelf of Louisiana are high (>1 μg/l). Reaeration rates are not constant and are not known, but the strong pycnocline coincident with hypoxic bottom waters inhibits exchange with the surface waters. The extent to which oxygen depletion is influenced by riverine and coastal nutrient inputs worldwide is of concern and is also a matter for concern in the northern Gulf of Mexico where the nutrient inputs of the two major rivers, the Mississippi and Atchafalaya, have changed dramatically over the last several decades (Turner and Rabalais, 1991). These changes have resulted in more biological material stored in sediments (Turner and Rabalais, 1994) and probable increased severity of hypoxia (Sen Gupta et al., 1996; reviewed in Rabalais et al., 1996a).

We describe here the results of field-based direct measurements of near-bottom water column respiration rates in the region of seasonally deficient oxygen near the Mississippi River delta. We used these data to test the following hypotheses:

- H1 respiration rates decrease with depth in a log:log pattern, per the arguments of Suess (1980) and others;
- H2 respiration rates are directly related to organic loading, and therefore directly related to indices of organic production, such as phytoplankton pigment concentration;
- H3 respiration rates vary among year and between seasons;

2. General Description of the Study Area

a. Physical Influences on Hypoxia

Critically depressed dissolved oxygen conditions (less than 2 mg/l) may occur in near-bottom waters quasi-continuously from April through October on the inner shelf off southeastern and southwestern Louisiana (Rabalais et al., 1991; Pokryfki and Randall, 1987). The zones of hypoxia are continuous, widespread, and persistent, and may envelop up to 40% of the water column in 10 to 30 m water depth. These oxygen-deficient bottom waters are maintained by an intense and persistent pycnocline resulting from large coastal freshwater inputs and weak wind mixing and strong solar heating during the summer months.

The flow of the Mississippi River system discharges through two major deltas— the bird's foot delta of the Mississippi River and the Atchafalaya River delta. Presently, the flow through the Atchafalaya delta is between 35 and 40% of the flow of the total system (Dinnel and Wiseman, 1986). Roughly 50% of the water emanating from the bird's foot delta flows westward. The riverine discharge forms a larger scale flow of low salinity water that moves westward (Wiseman et al., 1982). The winds are from the southeast at the beginning of the flood season in late winter and early spring. Wind reversals in late spring and summer drive nearshore waters back to the north and east, and large volumes of less saline waters are retained on the continental shelf off Louisiana.

The low salinity coastal waters are separated from the mid-shelf waters by an intense salinity front— separating the Louisiana Coastal Current (LCC) from the continental shelf. During low wind conditions, such as occur during the summer months, the frontal boundary assumes a nearly horizontal position, and a strong halocline separates upper layer waters that are in direct contact with the atmosphere from lower layer waters and that are isolated from direct air-sea interaction. One of the most perplexing problems in this region is identification of the processes that control dispersion across the frontal boundaries and halocline and the effect on hypoxic water formation. Wind mixing is clearly important during major storms and is suspected to be important during the more energetic winter months. The role of advection is less clear. The shallow nature of the LCC means that it responds rapidly to wind forcing. It appears that much of the onshore-offshore temporal variability can be attributed to wind-induced cross-shelf advection.

As a result of the seasonal shifting wind patterns, a convergence region develops along the southern Texas coast in spring. This region moves progressively northward and eastward during the summer season. Mean flow actually reverses and flows against the mean wind at some locations along the Louisiana coast (Cochrane and Kelly. 1986). This reversal has been documented as far eastward as Cameron, Louisiana, and inferred to occasionally occur as far eastward as the Isles Dernieres (Kimsey and Temple, 1964). Stratification confines this flow to a near-surface layer isolated from the bottom by a strong halocline. The deeper waters are often nearly stagnant with current speeds approaching 0 cm/s (Crout 1983). At other times these bottom waters flow at similar speeds to surface waters but in the opposite direction. In mid- to late July, the mean flow reversal begins to weaken and the convergence zone returns westward. These general patterns are, of course, modulated by wind-driven flows associated with localized weather patterns.

The characteristics of the hypoxic water masses appear, therefore, to be complex and linked to offshore stratification phenomena and these three-dimensional circulation patterns associated with the nearshore frontal zone. Clarification of any of these processes and their importance would greatly improve our understanding of the physics of the region and the formation, movements, and dissipation of hypoxic water masses.

b. Biological Processes Leading to Hypoxia

Significant oxygen consumption rates may occur in the water column or at the seabed, or both, and reaeration rates are not sufficient to maintain oxygen levels above 2 mg/l. The principal source of the organic matter respired in the bottom waters is from phytoplankton production in surface waters. The precise origin of the phytoplankton is not known. Possible sources are the plumes of the Mississippi and Atchafalaya rivers, the LCC, *in situ* production, or a combination of these. The percentage of this organic material reaching the bottom waters is high (e.g., Suess 1980; Qureshi, unpublished). In addition, the respiration rate in these waters is proportional to phytoplankton pigment

concentration (Turner and Allen, 1982). We have found very high levels of decomposition products (phaeopigments, dissolved nitrogen, silicate, and phosphate) in hypoxic bottom waters on occasion, but not consistently.

We have limited data on the respiration rates of the water column (Turner and Allen, 1982; Dortch et al., 1994) and benthic respiration rates have been determined for some areas of the Louisiana continental shelf (Rowe et al., 1975; Canfield, 1989). However, there is inadequate spatial or temporal resolution of estimates of respiration rates in the water column and benthos to compute an accurate oxygen budget for the continental shelf in the areas where hypoxia occurs. The relative contribution of water column and benthic respiration rates to oxygen depletion are also unknown. The water column and benthic respiration rates may have changed as a result of riverine nutrient loadings and subsequent phytoplankton community transformations.

There are enough measurements of the benthic and water column community to know that respiration by both are potentially important. For example, community plankton respiration rates in the bottom water were as high as 7 mg oxygen/m^3/h in November and July 1976 (Turner and Allen, 1982). Oxygen in a parcel of water 100% saturation could be depleted to hypoxic concentrations in 4 weeks at these rates. The depletion time is likely less, however, since much of the bottom water on the Louisiana shelf is continually undersaturated with oxygen. Published rates of benthic oxygen consumption on this shelf are a maximum of about 2 mg oxygen/m^2/h (near the delta; Canfield 1989). Studies in other areas indicate that both water column and benthic respiration may contribute substantially to the oxygen consuming processes (Falkowski et al., 1980; Kemp and Boynton, 1981). In general, however, benthic oxygen demand will be highest in organic rich sediments with high deposition rates (Canfield, 1989) and in shallow zones with high primary production because phytoplankton loading is highest there (e.g., Suess, 1980). The highest benthic respiration rates will be near the delta in shallow water and the lowest will be in deeper water away from the delta. In contrast, water column respiration rates were observed to be highest in shallow water but not near the delta (Turner and Allen, 1982). Both benthic and community plankton respiration rates appear to be fueled by primary production and not riverine sources, but the couplings are barely understood, with the exception of the relationship between phytoplankton pigments and respiration rates (Turner and Allen, 1982).

3. Materials and Methods

Water samples were collected between the Mississippi and Atchafalaya River deltas in July/August 1992, July 1993 and July 1994, and April 1994. Water column respiration rates were made with replicate subsamples of water collected within 3 meters of the sea bottom using a Rosette sampler. Vertical profiles were obtained with a continuous sampling factory-calibrated CTD profiler (SeaBird Instruments) or hand-held instrumentation (HydroLab Surveyor). The oxygen meters were calibrated using Winkler titrations on board the vessel.

We used an automatic titrating system to determine oxygen concentration in enclosed samples incubated over 24 hours. This approach is similar to that used by Pomeroy and Deibel (1986), Williams (1981), Chin-Leo and Benner (1992), but the basic approach was in place several decades ago and for similar purposes (e.g., Riley, 1941; Barnes and Collias, 1958). Replicate water samples were carefully put into acid-washed 300 ml BOD bottles in a manner to avoid introducing air bubbles and to flush the contents at least three times. These bottles were subsequently stored in the dark within 2° C of the *in situ* water temperature. Three or four samples were withdrawn from one bottle on four separate occasions over 24 hours for oxygen determination. We used a

Mettler Metrohm Titrator for sample processing, an instrument that is capable of determining the potentiometric titration end point with a precision of 0.0005 ml (delivery volume). The oxygen concentration was averaged for each bottle, and a linear regression of oxygen concentration versus time made to determine oxygen respiration (mg/l/hr) after correcting for bottle size and titrant strength. About 15% of the experiments were considered unacceptable because of a poor statistical fit. These were mostly for samples with low respiration rates. The rate of respiration rates observed was from 0.0008 to 0.29 mg oxygen/l/hr.

Chlorophyll *a* pigment determinations were conducted on the same samples using a fluorometric method and GF/F filters, which were then fixed in 5 ml DMSO/90% acetone (40/60) solution, allowed to extract for at least one hour in the dark, then measured pre- and post-acidification on a Turner Model 10 fluorometer. The fluorometer was calibrated for chlorophyll *a* against a chemical supply house chlorophyll *a* standard measured on a spectrophotometer.

Respiration rates were normalized per unit phytoplankton pigment for one analysis. The *in situ* oxygen concentration was divided by the estimated oxygen consumption rate to develop a turnover rate (days to depletion) for water mass. Data were analyzed using a PC-based statistical analysis software. All analyses reported are significant at the 95% level of confidence.

4. Results and Discussion

The first hypothesis, H1, concerns the relationship between respiration rates and depth. There is a clear inverse relationship between these two variables for each cruise data and for all data combined (Figure 244). For example, respiration rates on the Louisiana continental shelf decrease an order of magnitude going from 5 m to 100 m water depth. Clearly the highest respiration rates are in the shallow waters within, or near, the LCC. The slopes of the X-Y coordinates are the same for July/August 1992 and July 1993, and higher than in July 1994. The slope for the spring 1994 data set is lower than for the data for the other three cruises, and the average value is also higher. H1 is therefore not rejected.

The slope of this log:log regression of respiration rate and depth (-0.62) is lower than that calculated by Suess (1980) for carbon flux (-1.09) and respiration rates (-1.89) and depth in the open ocean, and by Smith and Hinga (1983) for benthic respiration and depth (-1.35) in deep water sites (Figure 245). The water column respiration rate on this continental shelf declines less with increasing depth than these other measures of community function. This result may be a consequence of greater vertical mixing on the shelf that keeps the material in suspension or because the organic material consumed is more labile in surface waters than in deeper waters. The Suess (1980) data analysis assumed a sinking rate for organic particles of 100 m/day. All other factors being equal, then if the quality of organic production is equivalent in both open ocean (the Suess 1980 data set) and this data set, then the sinking rate within the LCC is about 59 m/day. The implication of this more tentative speculation is that bloom conditions, with the potential of rapid losses, could result in equally rapid rises in water column respiration rates, and quick re-establishment of hypoxic conditions.

The second hypothesis, H2, concerns the relationship between the respiration rates and indices of organic production. Figure 246 illustrates the direct relationship between respiration rate and total phytoplankton pigment concentration. This relationship changed between years and season. The highest rates (normalized per

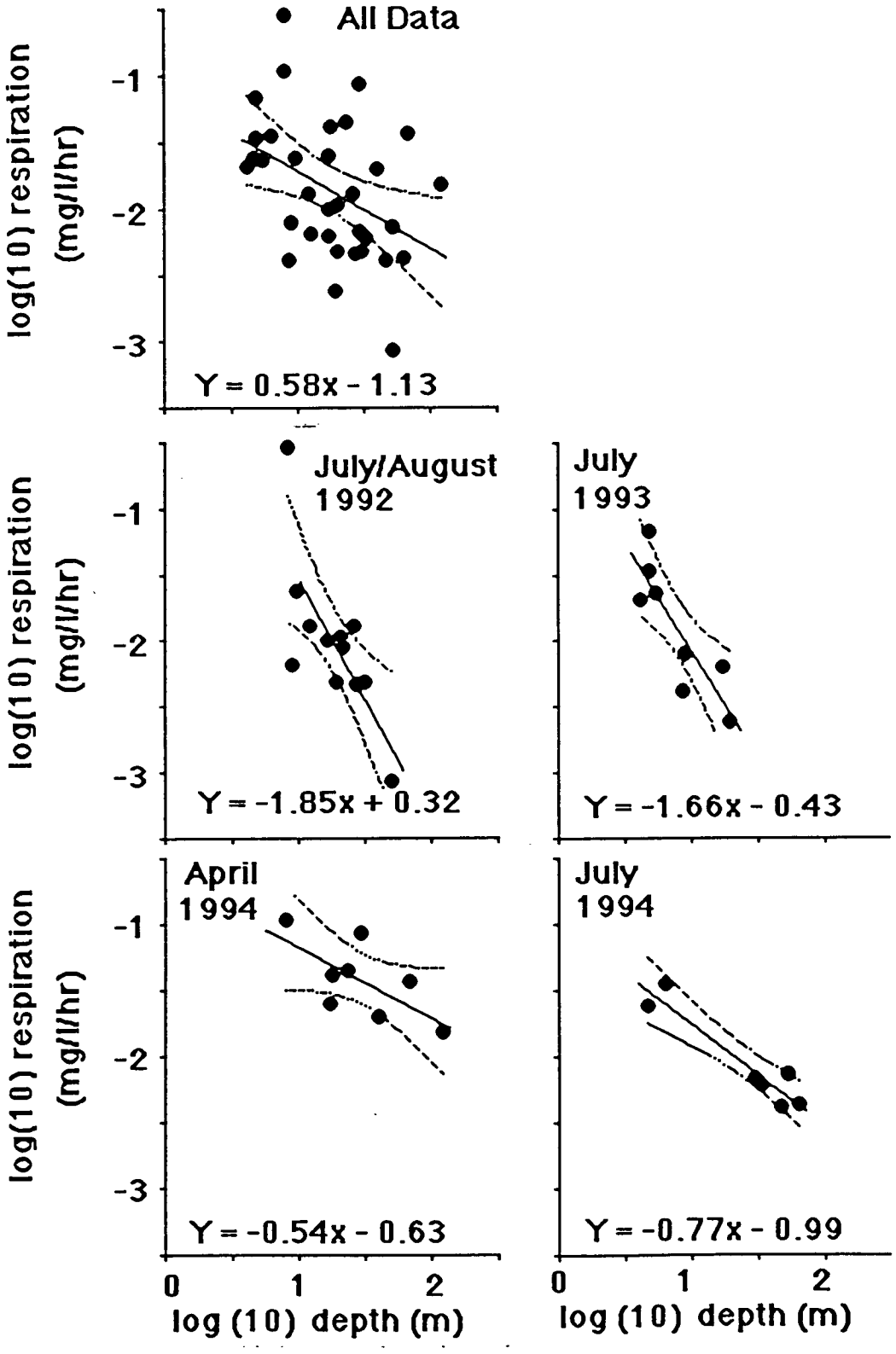

Figure 244. The relationship between the estimated water column respiration (mg oxygen/l/hr; near bottom) and sample depth. A 95% confidence interval for the Y value is shown with dotted lines.

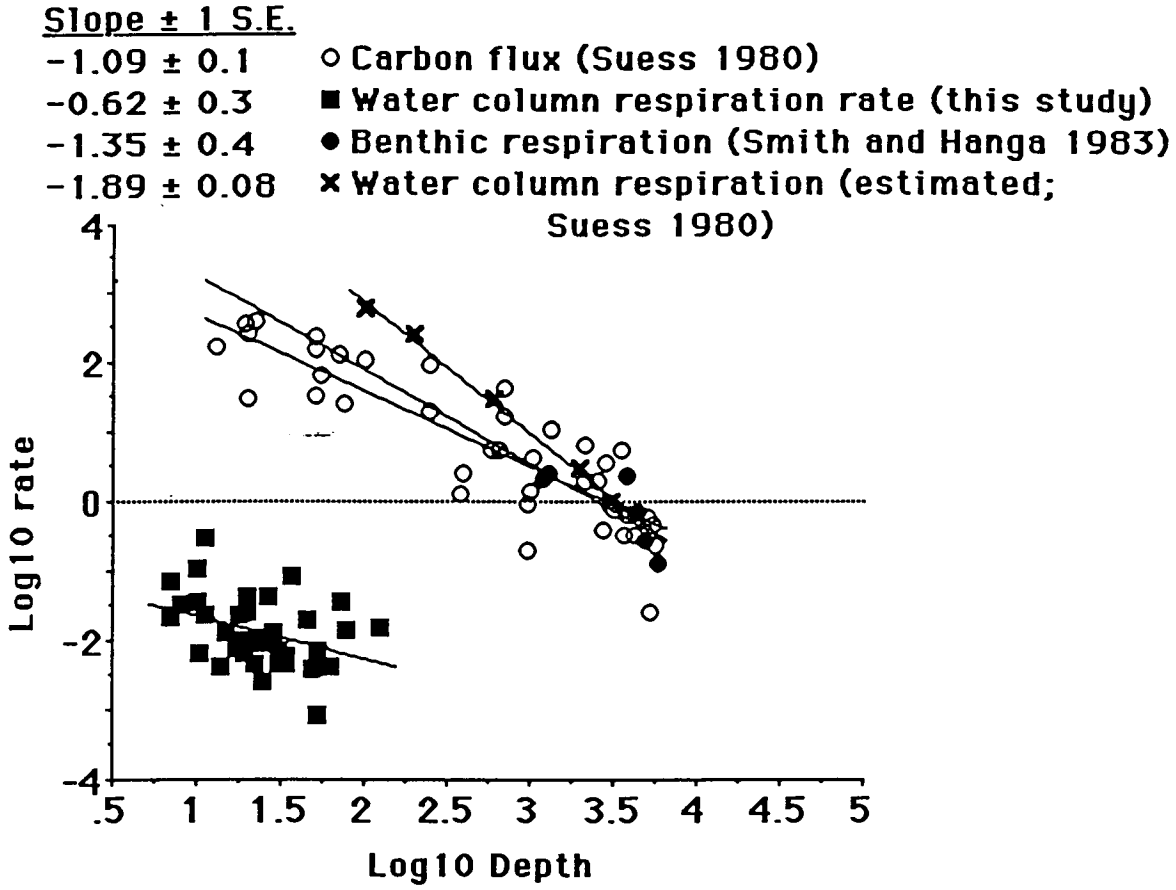

Figure 245. The relationship between the water column respiration rates for open ocean (synthetic) and from this study (direct measure), carbon flux (from sediment traps), and benthic respiration (*in situ*) versus depth. The slope of the regression and ±1 Standard Error is shown. The data are from Suess (1980), this study and Smith and Hinga (1983).

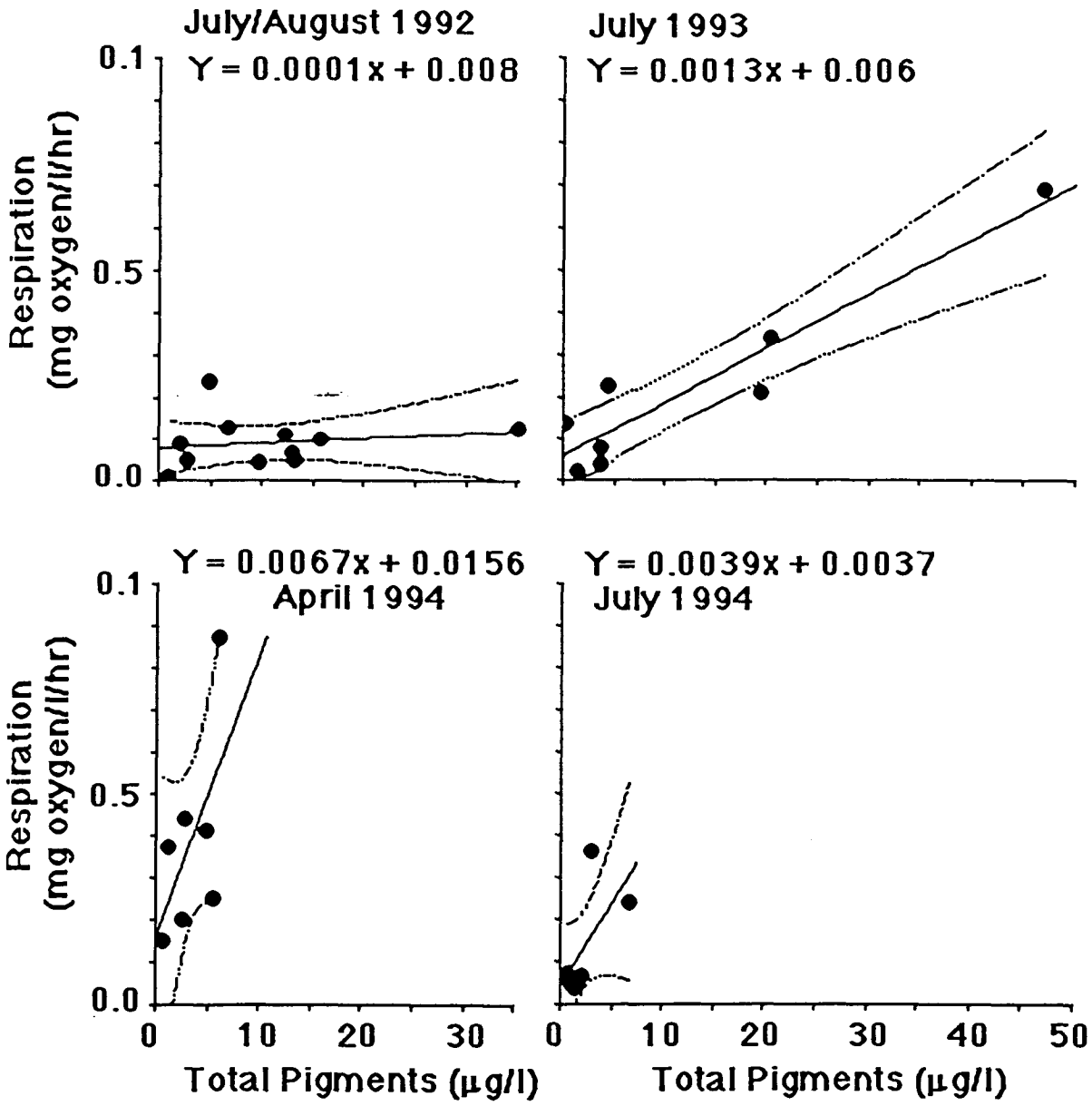

Figure 246. The relationship between the estimated water column respiration (mg oxygen/l/hr; near bottom) and total pigment concentration (µg/l pigments+pheopigments). A 95% confidence interval for the Y value is shown with dotted lines.

phytoplankton pigment) occurred in the spring (Figure 247). The ratio for June 1992, derived from a paper by Dortch et al. (1994) is noticeably lower than the others. These authors used an ETS method (Packard, 1985) to measure respiration rates. This enzymatic assay of filtered samples requires an empirical calibration factor to convert the color reaction to a respiration rate. Dortch et al. (1994) made this empirical conversion using five samples taken in July, and applied the resulting conversion factor to all other samples. It appears that seasonal conversion factors may be necessary to apply ETS methodologies in these waters.

Figure 245 also shows that there is seasonal variability in the absolute and relative rates of respiration. These results clearly demonstrate that the H3 should not be rejected.

The ratio of respiration rate:pigment concentration was highest near the river mouth, and declined heading westward along the coast (Figure 248). This result is consistent with H2 and provides an explanation for variability among seasons and years (H3). These results also support the idea that phytoplankton that are ultimately transported to the bottom waters are growing at optimal conditions in the eastern section of the study area and are growing at less than optimum conditions as water travels westward. Phytoplankton growing under higher physiological stress (e.g., nutrient limitation) are, presumably, of lesser nutritional value to the consuming organisms. A lower respiration rate is the result.

Figure 249 shows the time for oxygen depletion (days) for these samples arranged by water depth. The depletion rate (turnover time in days) ranged from around one day to over four weeks. The shortest turnover rate was in shallow waters, and, in particular, in the spring.

Three hypotheses were thus tested and not rejected. H1 (respiration rates decrease with depth in a log:log pattern) may not hold for other continental shelves, but certainly does appear true here. This result is not trivial. It means that the effects of horizontal diffusion and mixing are a less significant source of organic loading, at least in the region sampled, than vertical mixing. It implies a homogeneity in the organic loading of the surface water. If the surface water loading sources were spatially heterogeneous, then the relationship would not be so clear. These surface loading sources are not constant seasonally, however. It is thus consistent that H2 (respiration rates are directly related to organic loading) and H3 (respiration rates vary among year and between seasons) are also accepted, demonstrating the strength of the organic loading source in producing the observed respiration rates.

Respiration in sediments is an additional oxygen sink for these waters. Rowe (in Dortch et al., 1994) suggested that this oxygen sink may sometimes equal respiration in the overlying waters. Dortch et al. (1994) implied that photosynthesis might also occur in the lowest water layer. The low oxygen concentration observed in these samples (average 3.4 mg/l; n=40) suggests that benthic oxygen production is relatively low. However, light conditions could be an influential factor determining where hypoxic water masses were not located. That is, the extinction coefficients might be improved sufficiently at the edge of the hypoxic water masses to affect oxygen concentration. The light absorbing effect of phytoplankton pigments also results in additional oxygen and organic matter. Light conditions in the LCC, however, are dominated by the concentration of inorganic suspended matter. The "steering" effect of light conditions, if it is significant, is therefore expressed in the region of the offshore boundary of the hypoxic zone.

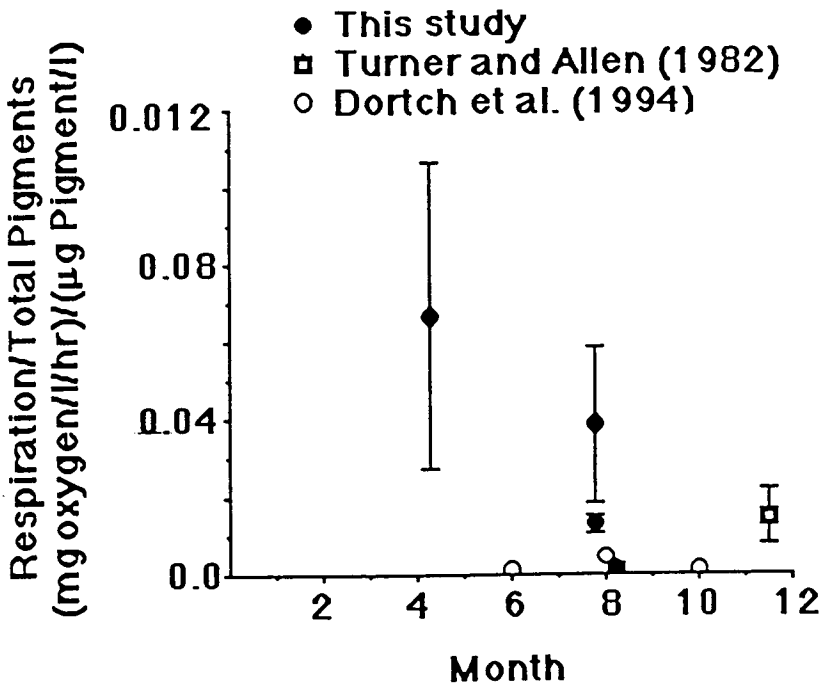

Figure 247. The respiration rate per total pigment ((mg oxygen/l/hr)/µg pigment/l) for three different studies plotted by sampling month (+/- 1 Std. Error). The ratio for Dortch et al. (1994) is an average from their Table 2.

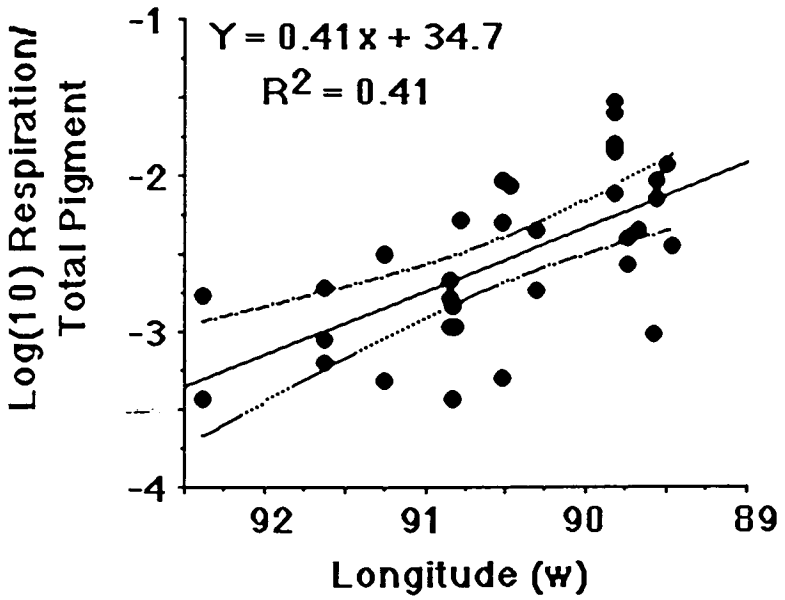

Figure 248. The relationship between the ratio of the estimated water column respiration (mg oxygen/l/hr; near bottom):total pigment concentration (µg/l (pigments+pheopigments)) along the coast from east (right) to west (left). The area covered includes from the Mississippi River to just east of the Atchafalaya River delta.

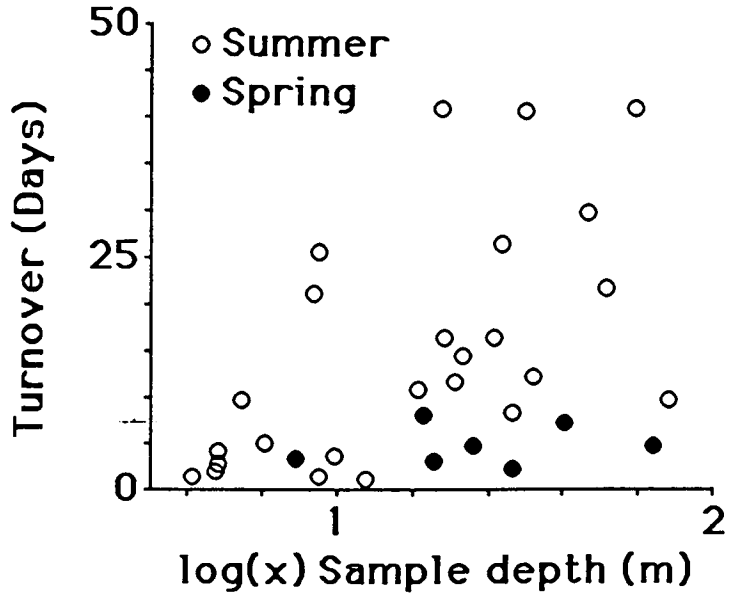

Figure 249. The relationship between the estimated turnover of oxygen in the water column (near bottom) and sample depth.

X. Pollutant Chemistry

by Jay C. Means and Debra J. McMillin

A. Introduction

The Minerals Management Service is charged with the responsibility to determine and evaluate environmental impacts of the development and production of oil and gas in the Outer Continental Shelf (OCS) regions of the nations coasts. Historically, the Gulf of Mexico has been an area of intensive exploration and production of oil and gas and is therefore a region where impacts might be expected to be the greatest if they occur. Impacts of production may result from chronic discharges of drilling muds, surfactants, produced waters and other chemicals used in the production process or they may result from accidental or catastrophic releases of oil as the consequence of spills, blowouts, fires or breaks in transportation lines.

In order to investigate the potential fate of chemicals discharges into Gulf of Mexico waters, a fairly complex set of physical and chemical oceanographic processes must be elucidated and understood. Among these are the bulk transport or advective processes of the water masses themselves (Figure 250). This includes mixing of fresh and saline waters, current direction and velocities, and temperature and salinity gradients and stratification. All of these forcing functions drive the dilution of chemical species in discharges. Along with these bulk phase physical processes, pollutant chemicals may undergo partitioning processes with suspended particulates (Means et al., 1980), which may have their origins in either allocthonous (riverine) or autochthonous (resuspension/biological production) sources.

The partitioning of both metals and organic compounds that occurs in this dynamic hydrologic environment is a function of compound/metal solubility and changes in salinity, temperature and redox potential. Sedimentation of particulates to the sediment bed is the major removal process of chemicals that may be introduced in discharges. Resuspension and bed load transport of materials may also occur in tidally energetic areas or as the result of strong weather events. Photolysis and hydrolysis reactions resulting in the decomposition of the chemical may be important for some chemical classes.

In recent years, a competing partitioning process with colloidal-sized, organic-rich micro-particulates has been recognized as a potential factor in the facilitation of transport processes in aquatic systems (Sigleo and Means, 1990). Because these colloidal solids can bind both metals and organic compounds and because they are relatively stable in the water column, they result in increasing the apparent "dissolved phase" transport of bound substances. The present study represents the first large geographic scale evaluation of the three-phase partitioning model that was developed in the laboratory.

Attempts to study such a complex array of transport processes using the low level chronic discharges from single sources in the Gulf of Mexico have been only partially successful in determining the fate of chemicals. At most the range of reliable information has extended only a few hundred meters from the discharge source (Rabalais et al., 1991) (Figure 251).

In the present study, the large and relatively intense chemical signatures of the Mississippi River and Atchafalaya River plumes, as well as other smaller riverine inputs to the Gulf of Mexico from the Calcasieu, Sabine and Galveston estuaries, have been

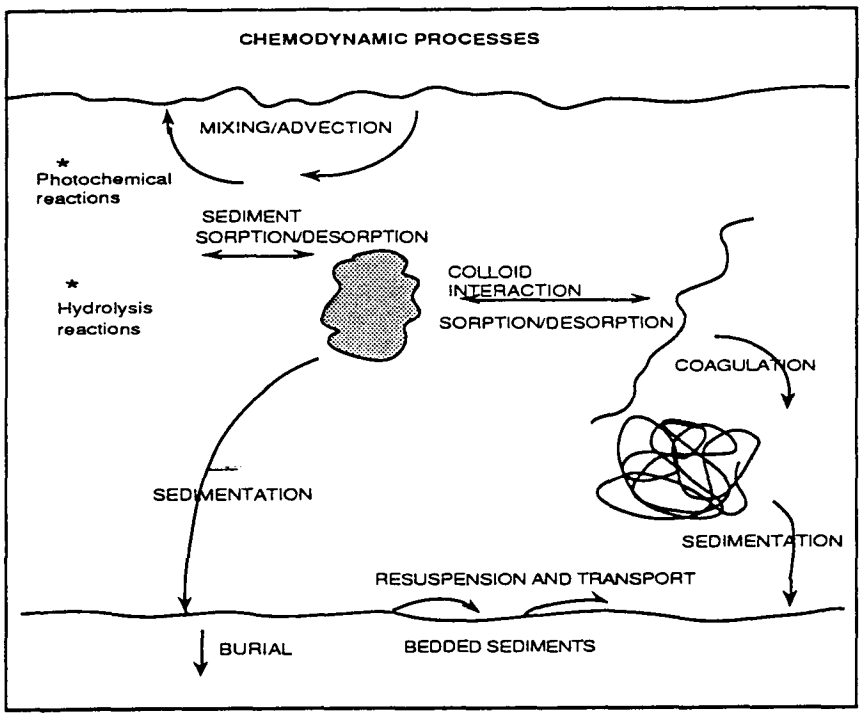

Figure 250. Fate and transport processes.

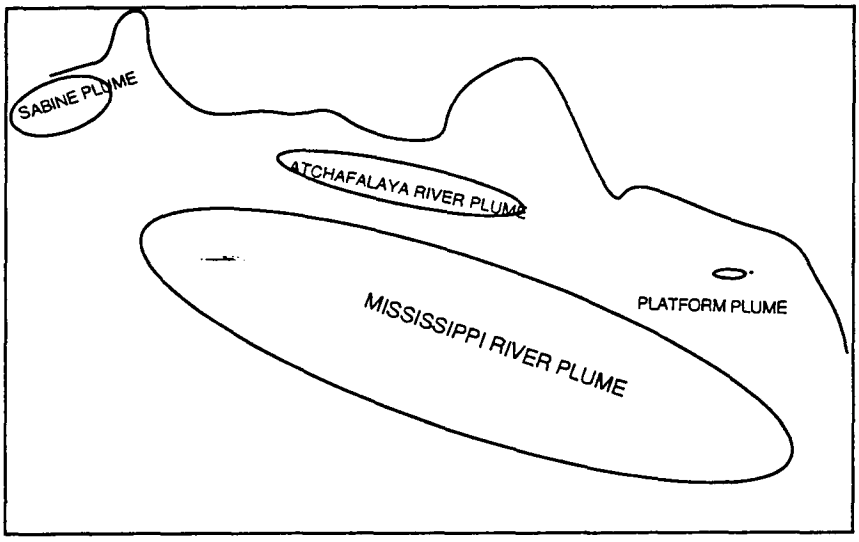

Figure 251. Schematic representation of relative sizes of contaminant plumes.

used to investigate transport processes over much greater distances and may provide the necessary information to develop long-range fate and transport models for the Gulf of Mexico that can be used by MMS in fulfilling their mandate to assess real and potential environmental impacts of chronic and catastrophic chemical releases during oil and gas production.

B. Objectives

The objectives of pollutant chemistry/pollutant transport subtask are:

(1) To make pollutant chemical measurements on samples collected on the hydrographic cruises whose geographic focus is the Mississippi-Atchafalaya plume (M-A plume), referred to as the Louisiana/Texas Coastal Current, from the Mississippi River to the south Texas coast, with special attention given to the area from the Atchafalaya River to the north Texas coast. The pollutant samples for measurements were acquired at 34 selected stations and two depths.

(2) To use these measurements to characterize the pollutant plume in the study area.

(3) To trace the movement and mixing of pollutants in particular water masses within the plume in conjunction with the data from the other parts of the study, particularly the remote sensing and current data.

(4) To assist in the interpretation of the importance of changes in water mass characteristics within the plume and offshore to pollutant and sediment transport.

(5) To identify and trace specific chemical pollutants as they enter into and mix and advect through the plume.

Based on our knowledge of the hydrography of the LATEX shelf, we designed and undertook a hydrographic sampling plan to meet the above objectives. We have begun to characterize—chemically, physically, and biologically—the hydrographic conditions of the plume and to determine the pollutants present in the plume and their speciation between the dissolved, colloidal and particulate phases in the plume. In addition, we collected and analyzed 52 sediment samples from coastal areas adjacent to estuaries between the mouth of the Mississippi River and the Galveston Bay estuary. The goal of sediment analyses was to characterize the scope of pollutants being deposited in surficial sediments in the coastal current region.

C. Data Collection

1. Sample Collection and Preparation on Ship

Water samples (20 L) were collected in 20-L cubitainers and transferred to a stainless steel, compressed nitrogen, pressurized vessel to facilitate filtration through a 149 mm, 0.4 μm Nucleopore membrane filter with glass fiber prefilter. This concentrated the particulate phase on the membrane filters, which were stored in small glass jars held at 5° C. The filtrate was ultrafiltered using an Amicon Model DC10 equipped with a spiral-wound cartridge (MW cutoff 3000 daltons) to separate dissolved and enriched colloidal phases. The colloidal fraction was concentrated to <240 ml and stored in amber glass jars at 5° C. Prior to SPE extraction 20 μl of the deuterated surrogate standard at 40 ppm in methanol was added to 4 L of the ultrafiltrate (dissolved phase). A two-liter aliquot was pumped through an SPE disk (Empore™, C18) housed in a Teflon filter holder attached in line with a MasterFlex pump set for a flow rate of ~25 ml/min. Extraction volume was determined by pumping time. The SPE disk was removed from the filter holder and stored in a small glass vial covered with 10 ml of methanol at -20° C.

Bedded surficial sediments were collected during the first cruise along crossing transects adjacent to the Calcasieu, Sabine, and Galveston estuaries and in a "box" design near the Atchafalaya outflow area. Sediments (0 to 10 cm) were collected using an Eckman dredge and placed in pre-cleaned specimen jars, sealed with tape in the field and packed on ice for transport to the laboratory. Once in the laboratory, the samples were stored at -20° C.

D. Organics

Detailed descriptions of laboratory extraction and instrumental analysis for organic pollutants can be found in McMillin and Means (1996), for herbicides, pesticides and PCBs, and McMillin and Means (in preparation) for PAH.

1. Sample Extraction (on-shore laboratory)

a. Sediments

The extraction method was a modification of that described by MacLeod et al. (1985). Excess water was decanted from sample jars prior to thorough mixing of the sediment sample, and 35 g were weighed into an amber bottle with a Teflon-lined cap. The sediment was covered with 125 ml of dichloromethane (DCM) and 65 g sodium sulfate incorporated until the sediment mixture was free-flowing. A suite of 6 deuterated PAH (800 ng each in hexane) was added, with the first solvent aliquot as a surrogate standard to monitor extraction efficiency. The jars were sealed and placed on a roller for 16, 6, and 16 hours, for a total of three extractions using the modified rock tumbler and rolling times specified by MacLeod et al. (1985). The DCM from each jar was decanted into an amber jar and refrigerated until 3 extracts were collected. The decanted DCM was filtered through sodium sulfate, and concentrated by rotoevaporation and a nitrogen stream to a final volume of 200 µl, with solvent exchange to hexane. Activated fine granular copper was added to reduce sulfur interferences.

b. Particulate Phase

The membrane and glass fiber prefilters were placed together in tared Teflon digestion bombs. The first extraction solvent was 45 ml of 2:1 hexane:acetone. A surrogate standard was added (120 ng in methanol of 6 deuterated PAH and dibromooctafluorobiphenyl) at the same time as the first extraction solvent, and the bombs placed in an ice-cooled sonicating bath for 6 minutes. After decanting, two more extractions were performed using 45 ml of hexane only. The extracts were combined and acetone removed by adding >75 ml of purified water. The top layer of hexane was removed by pipette and filtered through clean sodium sulfate. Subsequent concentration steps were the same as for sediment extracts, excluding the addition of copper. In order to obtain the particulate fraction weight, the Teflon bombs containing the filter sets were dried at 60° C overnight in an oven modified to exchange the atmosphere with charcoal-filtered air. The weight of the filters and bombs was recorded and the samples sent to the inorganics sample preparation laboratory for acid digestion.

c. Colloidal Phase

Samples were transferred to separatory funnels, surrogate standard added (400 ng in methanol of 6 deuterated PAH and dibromooctafluorobi-phenyl-DBOFBP) and extracted with DCM in triplicate, first at ambient (neutral) pH, then at acidic pH (2). The

extracts from both pH levels were combined and the extract concentrated as for sediment samples, without the addition of copper.

d. Dissolved Phase

An additional laboratory surrogate standard (120 ng each of DBOFBP, 1,3-dimethyl-2-nitrobenzene, and triphenylphosphate in methanol) was added to the vials containing SPE disks to monitor laboratory performance. The disks were extracted three times with 20 mL, 10 mL, and 10 mL of added DCM and using a sonicating bath for 1 minute per extraction. The extracts were combined in a separatory funnel and the DCM separated from methanol (storage solvent) and residual water by adding excess water (>25 mL) and decanting the DCM layer over clean sodium sulfate. Concentration steps were similar to colloidal samples.

2. Instrumental Analysis

A Hewlett-Packard 5890 Gas Chromatograph equipped with a 30 m by 25 mm ID, 0.25μ film DB-5 capillary column (J&W Scientific, Inc.) was directly interfaced to a Hewlett-Packard 5970B Mass Selective Detector. The GC was temperature programmed from 50° to 300° C using a series of linear temperature ramps to optimally separate the isomers of alkylated PAH's, while keeping analysis time to 60 min. The Mass Spectrometer was operated in Selected Ion Mode, using a dwell time of 30 ns/mass. The mass spectrometer was tuned daily prior to calibration using Perfluorotributylamine (PFTBA) and normalization to EPA criteria.

Alkylated PAH standards were purchased from Chiron Laboratories A.S. (Norway). The standards represent the 2 isomers of methylnaphthalene, all 10 of the dimethylnaphthalene isomers, isopropylnaphthalene and 1,6,7-trimethylnaphthalene for the class "C3" (3 substituted carbon groups) naphthalenes, all 4 isomers of methyldibenzothiophene, 1,2-dimethyldibenzothiophene, 5 of 5 possible methylphenanthrenes, 16 of 25 isomers of dimethylphenanthrenes, and 1,2,8-trimethylphenanthrene. Retention order of the alkylated PAH isomers has been determined by analysis of individual components. In addition to the individual alkylated isomers, concentrations of C3 and C4-naphthalenes, C2-dibenzothiophenes, and C3-phenanthrenes were estimated using response factors generated from similar analytes represented by the standard mixture. For example, total C3- and C4-naphthalenes were estimated using the response factor for 1,6,7-trimethylnaphthalene.

The quantitative standard, containing all target compounds and deuterated surrogate standards was used for daily calibration of the instrument prior to and following samples. An internal standard, 2-fluorobiphenyl, was added to each sample aliquot just prior to analysis to monitor performance of the instrument, but is not used in the calculations of analyte final concentrations.

A reagent blank, duplicate, and spiked sample were prepared for every set of samples (up to 10 samples per set) where sufficient sample was available or using clean filters or purified water for blanks and spikes. The spike standard was a dilution of the quantitation standard, containing all analytes, in methanol. Samples were spiked to a concentration averaging 0.5 ng/μl in the final extract volume.

Recovery was calculated for the surrogate and spiked standards using the equation: Recovery = 100*(Amt. detected/Amt. expected) using ng values calculated using the External Standard method. The mean response of reagent blanks for an analysis set (i.e., one phase from one cruise set) was subtracted from data for each

analyte, where necessary, prior to correction for surrogate recovery and dilution factors. The sample detection limit (DL) (Table 44) was estimated for each target analyte using the x-intercept (in ng) from a 5-point standard curve and correcting for sample size and extract concentration. The average DL for organics in the three phases was 0.16 and 5.3 ng/g (0.27 ng/g/L), respectively, for sediments and the particulate phase, and 1.4 and 10 pg/ml, respectively, the dissolved and colloidal phases. The data were not corrected for DL. Initial datasets contain the notation "tr" for trace-level detection; this indicates a confirmed response which was not automatically integrated.

3. Modification to Methodology during Project

The methodology used for extraction and analysis of samples was essentially the same for all cruises. The following changes were made to improve recovery or detection limits: The volume of the ultrafiltration-concentrated colloidal sample was increased to 480 ml for cruise P922 samples, and further increased to ~1000 ml for subsequent cruises to avoid heating of the sample which could lead to analyte losses due to volatilization. The amount of surrogate standard added to colloidal sample prior to extraction was reduced to 120 ng to put it in the same detection range as for the other phases and the calibration standard. The final volume of the particulates extract was reduced to 100 µl to improve detection limits. Finally, some analytes that were never detected in sediments or Cruise P92-1 water samples were eliminated from the analysis to improve detection limits, widen the mass spectrometer ion windows and economize through paper and data reduction time savings. The eliminated analytes were the BHCs (including lindane), heptachlor, heptachlor epoxide, aldrin, endosulfan I, II and -sulfate, mirex, and octachlorobiphenyls. A switch to an improved (more automated and interactive) data processing system after cruise P922 resulted in the elimination of the use of "tr" (trace) in the datasets.

4. Results

a. Bedded Sediments

Sediment samples were obtained from selected stations within Cruise Track I, taken as a box pattern adjacent to the Atchafalaya Bay, and in cruciform patterns of along- and across plume transects in front of the Calcasieu, Sabine, and Galveston estuaries. A summary of the data is given in Table 45, showing statistics for the four estuaries, and including two transects at the eastern and western edges of the Atchfalaya Bay discharge area. In general, concentrations of most analytes were similar between locations. One sample, P921100, from the nearshore side of the crossing transects off Galveston Bay, showed concentrations an order of magnitude higher than that found at other stations for most parent PAH. The PAH showing higher concentrations at this site tended to be those associated with petroleum sources, such as phenanthrene, benzanthracene, and chrysene, while anthracene, fluoranthene, and pyrene, PAH associated with combustion sources, did not show elevated values. Methyl-, and to a lessor extent dimethyl-phenanthrenes, also showed highest concentrations at P921100, while no trend was apparent for alkylated naphthalenes or dibenzothiophenes.

DDT metabolites and hexachlorobenzene (HCB) were detected at all locations except the S2 transect (Figure 252). Figure 253 shows that HCB concentrations were highest in the Atchafalaya box and at locations nearest to shore. Dieldrin was detected twice (3 ppb), both within the Atchafalaya box. PCBs were found at all locations except the Galveston Bay site (Figure 252). The S2 transect of the Atchafalaya box showed only CL2 (i.e., dichloro) PCBs, while the S3 transect had the most complete array of PCBs, lacking only in the detection of CL4 and CL7 PCBs. CL5 PCBs were most frequently

Table 44. Listing of organic analytes, abbreviations used in data tables, and sample detection limits for four sample matrices.

		Minimum Detection Limits (MDL)			
		Sediments	Water Samples, Three Phases:		
		(dry wt.)	Particulate	Colloidal	Dissolved
ANALYTE	Abbreviation	ng/g	ng/g*	pg/ml	pg/ml
d8 Naphthalene (SS)	d8 NAPH	0.012	0.40	0.77	0.11
Naphthalene		0.008	0.27	0.51	0.072
Hexachlorobutadiene		0.011	0.37	0.70	0.099
2-Methylnaphthalene	2-MN	0.045	1.5	2.8	0.40
1-Methylnaphthalene	1-MN	0.015	0.49	0.94	0.13
2-Ethylnaphthalene	2-EN	0.036	1.2	2.2	0.31
1-Ethylnaphthalene	1-EN	0.034	1.1	2.1	0.30
2,6/2,7-Dimethylnaphthalene	2,6/2,7-DMN	0.069	2.2	4.2	0.60
1,3/1,7-Dimethylnaphthalene	1,3/1,7-DMN	0.075	2.4	4.7	0.66
1,6-Dimethylnaphthalene	1,6-DMN	0.034	1.1	2.1	0.30
1,4/2,3-Dimethylnaphthalene	1,4/2,3-DMN	0.061	2.0	3.8	0.53
1,5-Dimethylnaphthalene	1,5-DMN	0.024	0.78	1.5	0.21
Acenaphthylene		0.080	2.6	4.9	0.70
1,2-Dimethylnaphthalene	1,2-DMN	0.036	1.2	2.2	0.31
2-Isopropylnapthalene	2-IPN	0.032	1.0	1.9	0.28
1,8-Dimethylnaphthalene	1,8-DMN	0.066	2.1	4.1	0.58
d10 Acenaphthene (SS)	d10 ACE	0.048	1.6	3.0	0.42
Acenaphthene		0.052	1.7	3.2	0.45
1,6,7-Trimthylnaphthalene	1,6,7-TMN	0.034	1.1	2.1	0.30
Fluorene		0.083	2.7	5.1	0.73
Dibromooctachlorobiphenyl (SS)	DBOFBP	0.086	2.8	5.3	0.75
Trifluralin		0.083	2.7	5.1	0.73
α-Benzene hexachloride	a-BHC	0.12	4.0	7.6	1.1
Dichlorobiphenyls	CL2-PCB	0.029	0.92	1.8	0.25
Hexachlorobenzene		0.034	1.1	2.1	0.30
Simazine		0.91	30	56	8.0
Dibenzothiophene		0.054	1.7	3.3	0.47
β-Benzene hexachloride	b-BHC	0.23	7.6	14	2.0
Atrazine		0.71	23	44	6.2
Lindane (γ-BHC)	(g-BHC)	0.12	3.9	7.4	1.1
d10 Phenanthrene (SS)	d10 PHEN	0.11	3.5	6.6	0.94
Phenanthrene		0.12	3.9	7.5	1.1
Anthracene		0.13	4.3	8.2	1.2
δ-Benzene hexachloride	d-BHC	0.27	8.8	17	2.4
Trichlorobiphenyls-PCB	CL3-PCB	0.009	0.30	0.58	0.082
4-Methyldibenzothiophene	4-MDBT	0.035	1.1	2.2	0.31
2/3-Methyldibenzothiophene	2/3-MDBT	0.10	3.3	6.3	0.89
Tetrachlorobiphenyls	CL4-PCB	0.037	1.2	2.3	0.33
3-Methylphenanthrene	3-MP	0.14	4.4	8.5	1.2
1-Methyldibenzothiophene	1-MDBT	0.059	1.9	3.7	0.52
2-Methylphenanthrene	2-MP	0.20	6.3	12	1.7
Heptachlor		0.29	9.3	18	2.5
Alachlor		0.12	3.9	7.4	1.0
4/9-Methylphenanthrene	4/9-MP	0.17	5.6	11	1.5
1-Methylphenanthrene	1-MP	0.11	3.7	7.0	1.0
Aldrin		0.29	9.3	18	2.5
Metolachlor		0.25	8.1	15	2.2
Cyanazine		1.6	52	98	14
3,6-Dimethylphenanthrene	3,6-DMP	0.070	2.3	4.3	0.61

Table 44 cont'd.

		Minimum Detection Limits (MDL)			
		Sediments	Water Samples, Three Phases:		
		(dry wt.)	Particulate	Colloidal	Dissolved
ANALYTE	Abbreviation	ng/g	ng/g*	pg/ml	pg/ml
3,5-Dimethylphenanthrene	3,5-DMP	0.067	2.2	4.1	0.59
2,6-Dimethylphenanthrene	2,6-DMP	0.070	2.3	4.3	0.61
2,7-Dimethylphenanthrene	2,7-DMP	0.022	0.72	1.4	0.19
3,9-Dimethylphenanthrene	3,9-DMP	0.063	2.0	3.9	0.55
1,6/2,5/2,9-Dimethylphenanthrene	1,6/2,5/2,9-DMP	0.16	5.3	10	1.4
1,7-Dimethylphenanthrene	1,7-DMP	0.068	2.2	4.2	0.59
1,9/4,9-Dimethylphenanthrene	1,9/4,9-DMP	0.086	2.8	5.3	0.75
1,2-Dimethyldibenzothiophene	1,2-DMDBT	0.089	2.9	5.5	0.78
Fluoranthene		0.13	4.1	7.8	1.1
1,5-Dimethylphenanthrene	1,5-DMP	0.035	1.1	2.2	0.31
Heptachlor Epoxide		0.29	9.3	18	2.5
1,8-Dimethylphenanthrene	1,8-DMP	0.048	1.6	3.0	0.42
1,2-Dimethylphenanthrene	1,2-DMP	0.064	2.1	4.0	0.56
9,10-Dimethylphenanthrene	9,10-DMP	0.057	1.8	3.5	0.50
Pyrene		0.14	4.5	8.5	1.2
o,p'-DDE		0.10	3.2	6.2	0.88
Endosulfan I		0.22	7.1	14	1.9
Chlordane		0.12	3.9	7.5	1.1
trans-Nonachlor		0.089	2.9	5.5	0.77
Pentachlorobiphenyls	CL5-PCB	0.069	2.2	4.3	0.60
Dieldrin		0.053	1.7	3.2	0.46
p,p'-DDE	p,p'-DDE	0.12	4.0	7.6	1.1
o,p'-DDD	o,p'-DDD	0.18	5.9	11	1.6
Hexachlorobiphenyls	CL6-PCB	0.058	1.9	3.6	0.51
Endrin		0.42	14	26	3.7
1,2,8-Trimethylphenanthrene	1,2,8-TMP	0.18	5.8	11	1.6
Endosulfan II		0.29	9.3	18	2.5
p,p'-DDD/o,p'-DDT		0.19	6.2	12	1.7
Heptachlorobiphenyls	CL7-PCB	0.056	1.8	3.5	0.49
Endosulfan sulfate		0.18	5.7	11	1.6
p,p'-DDT		0.21	6.8	13	1.8
Benzo(a)anthracene	Benzanthracene	0.25	8.2	16	2.2
d12 Chrysene (SS)	d12 CHRYS	0.23	7.4	14	2.0
Chrysene		0.21	6.9	13	1.9
Octachlorobiphenyls	CL8-PCB	0.051	1.7	3.2	0.45
Mirex		0.13	4.3	8.1	1.1
Benzo(b)fluoranthene	Benzo(b)fluor	0.15	5.0	10	1.4
Benzo(k)fluoranthene	Benzo(k)fluor	0.66	21	41	5.7
Benzo(a)pyrene		0.58	19	36	5.1
d12 Perylene (SS)	d12 PERYL	0.17	5.5	10	1.5
Indeno(1,2,3-cd)pyrene		0.77	25	47	6.7
Dibenz(a,h)anthracene		0.41	13	25	3.6
Benzo(g,h,i)perylene		0.27	8.6	16	2.3
MEANS		0.16	5.3	10	1.4
Sample size used in calculation, ave. all samples		35g	0.54g	567ml	4000ml

*based on 100µl final volume

Table 45. Mean sediment organic pollutant concentrations (ng/g dry wt.) for four estuarine areas, sampled April 1992.

	Atchafalaya Bay								Calcasieu R.				Sabine R.				Galveston Bay			
	Transect S2, 5 stations				Transect S3, 5 stations				11 stations				10 stations				10 stations			
ANALYTE	Mean	Min	Max	Freq.	Mean	Min	Max	Freq.	Mean	Min	Max	Freq.	Mean	Min	Max	Freq.	Mean	Min	Max	Freq.
Naphthalene	1.4	0.4	2.2	100%	2.2	0.3	6.5	100%	1.2	0.8	2.3	100%	1.5	0.5	2.8	100%	1.8	0.2	6.3	100%
2-MN	1.5	0.2	2.5	100%	3.0	0.2	10.0	100%	1.3	0.8	2.5	100%	1.9	0.6	3.9	100%	2.7	0.1	15.0	100%
1-MN	1.3	0.1	2.2	100%	2.7	0.1	8.7	100%	1.2	0.8	2.2	100%	1.7	0.5	3.3	100%	2.3	0.8	10.0	90%
2-/1-EN	0.7	0.1	1.1	100%	1.1	0.1	3.7	100%	0.5	0.3	1.2	100%	0.8	0.2	1.6	100%	1.3	0.4	4.8	90%
2,6-DMN	1.9	1.2	3.2	60%	1.3	1.0	1.5	40%	1.1	0.5	3.7	55%	15.3	4.6	26.0	20%	2.2	0.1	7.0	70%
2,7-DMN	nd	nd	nd	0%	1.7	0.6	4.4	80%	0.6	0.4	1.0	36%	0.7	0.5	1.5	50%	1.9	0.1	6.3	50%
1,3/1,7-DMN	1.3	0.1	2.2	100%	2.7	0.2	8.2	100%	1.1	0.6	2.5	100%	1.5	0.5	2.9	100%	2.2	0.1	11.0	100%
1,6-DMN	1.1	0.1	1.8	100%	2.0	0.2	6.3	100%	0.9	0.5	2.0	100%	1.2	0.4	2.3	100%	1.6	0.1	8.0	100%
1,4/2,3-DMN	1.3	0.1	2.3	100%	2.5	0.1	7.8	100%	1.1	0.6	2.5	100%	1.5	0.5	3.0	100%	1.8	0.1	7.0	100%
1,5-DMN	nd	nd	nd	0%	nd	nd	nd	0%	nd	nd	nd	0%	nd	nd	nd	0%	nd	nd	nd	0%
Acenaphthylene	0.3	0.1	0.6	100%	0.3	0.0	0.9	100%	0.2	0.1	0.4	100%	0.4	0.1	0.9	100%	0.4	0.2	0.9	80%
1,2-DMN	0.3	0.0	0.5	100%	0.5	0.0	1.6	100%	0.3	0.1	0.7	100%	0.4	0.2	1.1	100%	0.5	0.2	1.8	90%
Acenaphthene	0.3	0.1	0.5	80%	0.3	0.0	0.8	100%	0.2	0.1	0.5	100%	0.2	0.1	0.4	100%	5.5	0.1	48.0	90%
1,6,7-TMN	0.6	0.1	1.0	100%	1.1	0.1	3.2	100%	0.5	0.3	1.1	91%	0.7	0.2	2.0	100%	0.9	0.1	2.7	100%
Fluorene	0.4	0.1	0.7	80%	0.7	0.1	2.3	100%	0.5	0.3	1.7	91%	0.6	0.2	1.4	100%	8.1	0.4	68.0	90%
a-BHC	nd	nd	nd	0%	nd	nd	nd	0%	nd	nd	nd	0%	nd	nd	nd	0%	nd	nd	nd	0%
Hexachlorobenzene	nd	nd	nd	0%	0.2	0.1	0.4	80%	0.1	0.0	0.2	55%	0.1	0.0	0.1	70%	0.1	0.1	0.2	50%
CL2-PCB	1.3	1.3	1.3	20%	0.2	0.2	0.2	20%	nd	nd	nd	0%	nd	nd	nd	0%	nd	nd	nd	0%
b-BHC	nd	nd	nd	0%	nd	nd	nd	0%	nd	nd	nd	0%	nd	nd	nd	0%	nd	nd	nd	0%
Dibenzothiophene	0.4	0.1	0.7	100%	0.5	0.1	1.2	100%	0.3	0.1	1.1	100%	0.4	0.1	0.8	100%	2.3	0.2	18.0	90%
Lindane (g-BHC)	nd	nd	nd	0%	nd	nd	nd	0%	nd	nd	nd	0%	nd	nd	nd	0%	nd	nd	nd	0%
Phenanthrene	2.9	0.5	5.6	100%	4.0	0.4	13.0	100%	2.5	1.4	8.1	100%	2.9	0.8	6.7	100%	39.9	0.3	380.0	100%
Anthracene	0.8	0.7	0.9	60%	0.7	0.0	2.3	100%	0.6	0.3	2.4	100%	0.7	0.2	1.4	100%	12.7	0.3	110.0	90%
d-BHC	nd	nd	nd	0%	nd	nd	nd	0%	nd	nd	nd	0%	nd	nd	nd	0%	nd	nd	nd	0%
CL3-PCB	nd	nd	nd	0%	0.7	0.7	0.7	20%	nd	nd	nd	0%	nd	nd	nd	0%	nd	nd	nd	0%
4-MDBT	1.1	0.3	1.7	80%	1.0	0.2	2.2	100%	0.6	0.3	1.5	91%	0.9	0.4	2.0	100%	1.1	0.2	4.5	100%
CL4-PCB	nd	nd	nd	0%	nd	nd	nd	0%	nd	nd	nd	0%	nd	nd	nd	0%	nd	nd	nd	0%
2/3-MDBT	0.8	0.2	1.6	60%	0.5	0.2	1.0	100%	0.3	0.2	1.0	91%	0.4	0.1	0.9	100%	0.9	0.2	4.9	100%
3-MP	1.4	0.2	2.1	100%	1.7	0.2	5.1	100%	1.0	0.6	2.4	100%	1.2	0.4	2.4	100%	4.3	0.9	29.0	90%
Heptachlor	nd	nd	nd	0%	nd	nd	nd	0%	nd	nd	nd	0%	nd	nd	nd	0%	nd	nd	nd	0%
2-MP	1.1	0.2	1.8	100%	1.6	0.2	4.9	100%	0.9	0.5	2.0	100%	1.1	0.4	1.9	100%	4.2	0.8	29.0	90%
4/9-MP	1.3	0.2	2.1	100%	1.8	0.2	5.2	100%	1.0	0.6	2.4	100%	1.2	0.4	2.3	100%	2.9	0.8	17.0	90%
1-MP	0.8	0.2	1.4	100%	1.3	0.1	3.8	100%	0.7	0.4	1.7	100%	0.8	0.3	1.7	100%	3.3	0.6	24.0	90%
Aldrin	nd	nd	nd	0%	nd	nd	nd	0%	nd	nd	nd	0%	nd	nd	nd	0%	nd	nd	nd	0%
3,6-/3,5-DMP	0.7	0.1	1.1	100%	0.8	0.1	2.0	100%	0.4	0.3	0.8	100%	0.5	0.2	0.9	100%	1.0	0.3	4.1	90%
2,6-DMP	0.4	0.1	0.8	100%	0.6	0.1	1.8	100%	0.3	0.2	0.6	100%	0.4	0.1	0.7	100%	1.0	0.3	5.4	90%
2,7-DMP	0.5	0.1	0.8	100%	0.6	0.1	1.7	100%	0.3	0.2	0.6	100%	0.4	0.1	0.7	100%	0.9	0.3	4.4	90%
1,2-DMDBT	nd	nd	nd	0%	0.6	0.6	0.6	40%	nd	nd	nd	0%	nd	nd	nd	0%	0.3	0.3	0.3	10%
3,9-DMP	1.8	0.3	2.8	100%	2.2	0.3	5.9	100%	1.1	0.6	2.1	100%	1.3	0.5	2.4	100%	2.8	0.2	16.0	100%
1,6/2,5/2,9-DMP	1.0	0.2	1.7	100%	1.3	0.2	3.6	100%	0.6	0.4	1.2	100%	0.9	0.3	1.6	100%	1.8	0.1	10.0	100%

Table 45 cont'd.

ANALYTE	Atchafalaya Bay Transect S2, 5 stations Mean	Min	Max	Freq.	Transect S3, 5 stations Mean	Min	Max	Freq.	Calcasieu R. 11 stations Mean	Min	Max	Freq.	Sabine R. 10 stations Mean	Min	Max	Freq.	Galveston Bay 10 stations Mean	Min	Max	Freq.
1,7-DMP	**1.3**	0.2	2.4	100%	**2.2**	0.5	3.9	100%	**0.5**	0.2	0.8	100%	**0.6**	0.3	0.9	100%	**1.5**	0.1	9.4	100%
1,9/4,9-DMP	**1.0**	0.2	1.6	100%	**1.1**	0.2	3.1	100%	**0.6**	0.3	1.1	100%	**0.7**	0.3	1.3	100%	**1.5**	0.5	7.8	90%
Heptachlor Epoxide	**nd**	nd	nd	0%	**nd**	nd	nd	0%	**nd**	nd	nd	0%	**nd**	nd	nd	0%	**nd**	nd	nd	0%
1,5-DMP	**nd**	nd	nd	0%	**0.2**	0.2	0.2	20%	**0.1**	0.1	0.1	9%	**0.2**	0.2	0.2	10%	**0.3**	0.3	0.3	10%
Fluoranthene	**2.6**	0.3	4.9	100%	**4.5**	0.2	16.0	100%	**1.9**	1.2	4.0	100%	**2.3**	0.8	5.4	100%	**2.3**	0.1	4.3	90%
1,8-DMP	**0.3**	0.1	0.6	80%	**0.4**	0.1	0.9	80%	**0.1**	0.1	0.2	100%	**0.2**	0.1	0.3	100%	**0.5**	0.1	2.3	60%
1,2-DMP	**0.6**	0.5	0.8	40%	**0.5**	0.2	1.2	80%	**0.2**	0.1	0.3	100%	**0.2**	0.1	0.3	100%	**0.8**	0.1	3.1	50%
9,10-DMP	**nd**	nd	nd	0%	**0.2**	0.1	0.3	40%	**0.0**	0.0	0.0	9%	**0.1**	0.1	0.1	20%	**nd**	nd	nd	0%
Pyrene	**3.3**	0.5	6.6	100%	**6.6**	0.3	18.0	80%	**2.2**	1.3	4.0	100%	**2.9**	0.9	7.6	100%	**2.8**	0.1	4.7	90%
Endosulfan I	**nd**	nd	nd	0%	**nd**	nd	nd	0%	**nd**	nd	nd	0%	**nd**	nd	nd	0%	**nd**	nd	nd	0%
Chlordane	**nd**	nd	nd	0%	**0.1**	0.1	0.1	20%	**nd**	nd	nd	0%	**nd**	nd	nd	0%	**nd**	nd	nd	0%
trans-Nonachlor	**nd**	nd	nd	0%	**nd**	nd	nd	0%	**nd**	nd	nd	0%	**nd**	nd	nd	0%	**nd**	nd	nd	0%
CL5-PCB	**nd**	nd	nd	0%	**1.3**	1.3	1.3	20%	**0.9**	0.4	1.8	55%	**6.3**	6.3	6.3	10%	**nd**	nd	nd	0%
p,p'-DDE	**nd**	nd	nd	0%	**0.6**	0.1	1.8	100%	**0.6**	0.2	1.6	100%	**0.6**	0.4	1.0	70%	**0.3**	0.1	0.6	60%
Dieldrin	**nd**	nd	nd	0%	**3.0**	3.0	3.0	20%	**nd**	nd	nd	0%	**nd**	nd	nd	0%	**nd**	nd	nd	0%
CL6-PCB	**nd**	nd	nd	0%	**1.5**	1.5	1.5	20%	**0.5**	0.2	0.7	27%	**3.7**	3.7	3.7	10%	**nd**	nd	nd	0%
o,p'-DDD	**nd**	nd	nd	0%	**1.0**	0.6	1.6	80%	**0.4**	0.3	0.4	18%	**nd**	nd	nd	0%	**nd**	nd	nd	0%
Endrin	**nd**	nd	nd	0%	**nd**	nd	nd	0%	**nd**	nd	nd	0%	**nd**	nd	nd	0%	**nd**	nd	nd	0%
1,2,8-TMP	**nd**	nd	nd	0%	**0.3**	0.0	0.9	100%	**0.3**	0.0	0.9	82%	**0.3**	0.2	0.6	70%	**0.8**	0.4	1.1	20%
Endosulfan II	**nd**	nd	nd	0%	**nd**	nd	nd	0%	**nd**	nd	nd	0%	**nd**	nd	nd	0%	**nd**	nd	nd	0%
p,p'-DDD	**nd**	nd	nd	0%	**2.5**	2.5	2.5	20%	**0.1**	0.1	0.2	18%	**nd**	nd	nd	0%	**nd**	nd	nd	0%
CL7-PCB	**nd**	nd	nd	0%	**nd**	nd	nd	0%	**nd**	nd	nd	0%	**0.5**	0.5	0.5	10%	**nd**	nd	nd	0%
Endosulfan sulfate	**nd**	nd	nd	0%	**nd**	nd	nd	0%	**nd**	nd	nd	0%	**nd**	nd	nd	0%	**nd**	nd	nd	0%
p,p'-DDT	**nd**	nd	nd	0%	**nd**	nd	nd	0%	**nd**	nd	nd	0%	**nd**	nd	nd	0%	**nd**	nd	nd	0%
Benzanthracene	**2.0**	0.6	3.4	100%	**2.9**	0.2	9.9	100%	**1.6**	0.9	4.6	100%	**1.9**	0.5	3.7	100%	**31.3**	0.1	300.0	100%
Chrysene	**2.2**	0.2	4.3	100%	**3.9**	0.2	13.0	100%	**3.7**	1.3	21.0	100%	**3.1**	0.8	5.9	100%	**31.9**	0.1	300.0	100%
CL8-PCB	**nd**	nd	nd	0%	**nd**	nd	nd	0%	**nd**	nd	nd	0%	**nd**	nd	nd	0%	**nd**	nd	nd	0%
Benzo(b)fluor	**4.8**	0.5	9.6	100%	**8.0**	0.4	28.0	100%	**2.7**	1.5	4.5	100%	**3.9**	0.9	9.6	100%	**49.9**	0.1	470.0	100%
Benzo(k)fluor	**nd**	nd	nd	0%	**nd**	nd	nd	0%	**1.3**	1.3	1.3	9%	**0.7**	0.7	0.7	10%	**0.0**	0.0	0.0	10%
Benzo(a)pyrene	**1.7**	0.1	3.7	100%	**2.7**	0.1	8.5	100%	**1.6**	1.1	3.1	100%	**2.4**	0.7	4.6	100%	**31.8**	1.0	270.0	90%
Indenopyrene	**2.2**	0.3	4.7	100%	**2.4**	0.2	5.1	100%	**3.3**	1.2	8.1	100%	**3.6**	1.7	6.8	100%	**22.2**	1.8	180.0	90%
Dibenzanthracene	**0.6**	0.5	0.7	60%	**0.7**	0.1	1.6	100%	**0.8**	0.3	2.2	100%	**0.9**	0.5	1.6	100%	**4.4**	0.4	35.0	90%
Benzoperylene	**2.2**	0.2	4.9	100%	**2.3**	0.2	5.6	100%	**5.1**	1.3	14.0	100%	**4.8**	2.1	9.8	100%	**19.2**	1.9	150.0	90%
Estimated Totals																				
C1-Naphthalenes	**2.8**	0.3	4.7	100%	**5.7**	0.3	18.7	100%	**2.5**	1.6	4.7	100%	**3.6**	1.1	7.2	100%	**4.8**	0.1	25.0	100%
C2-Naphthalenes	**5.4**	0.5	10.9	100%	**10.7**	0.5	32.0	100%	**4.6**	2.4	12.6	100%	**8.9**	1.8	35.8	100%	**9.8**	0.4	45.9	100%
C1-Dibenzothiophenes	**1.7**	0.5	3.3	80%	**1.5**	0.4	3.2	100%	**1.0**	0.6	2.5	91%	**1.3**	0.5	2.9	100%	**2.1**	0.4	9.4	100%
C1-Phenanthrenes	**4.6**	0.7	7.2	100%	**6.4**	0.7	19.0	100%	**3.6**	2.1	8.5	100%	**4.4**	1.6	8.3	100%	**14.7**	3.2	99.0	90%
C2-Phenanthrenes	**7.2**	1.2	12.3	100%	**9.9**	1.3	24.5	100%	**4.0**	2.3	7.7	100%	**5.1**	1.9	9.1	100%	**10.8**	0.4	62.5	100%

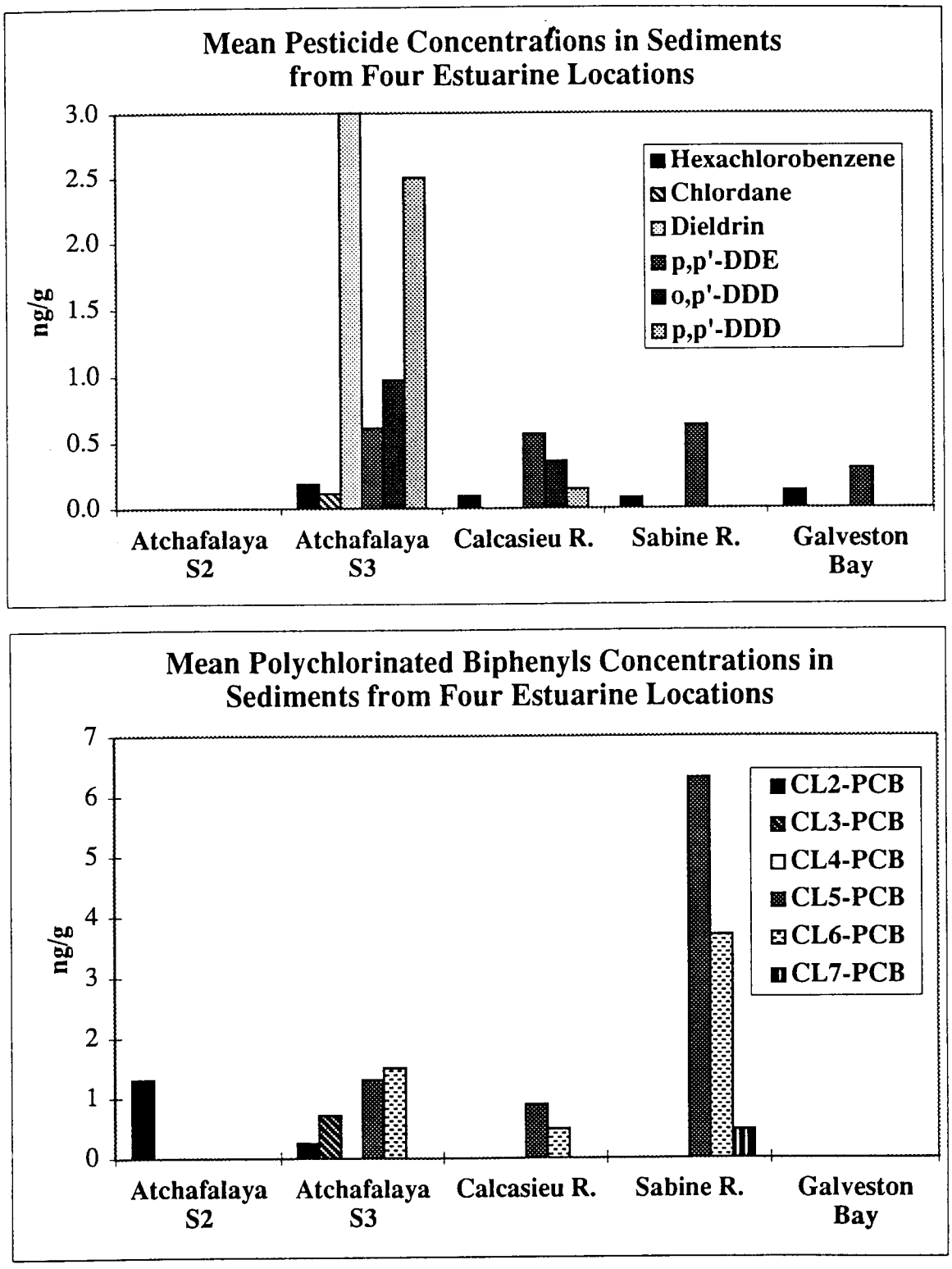

Figure 252. Mean organic pollutant concentrations (ng/g) in bedded coastal sediments sampled adjacent to major estuaries.

detected in Calcasieu estuary samples, however, highest concentrations were found near the Sabine estuary. CL6 PCBs were also at highest concentrations offshore of the Sabine estuary, and CL7 PCBs were detected only at this location.

In general, transect S3, on the west side of the Atchafalaya box, showed higher concentrations of pollutants than transect S2, on the east side, indicating substantial pollutant transport and deposition occurring as a result of the Atchafalaya Bay discharge. These observations are not surprising in light of this Bay's discharge volume, and data from water samples shows similar patterns. However, when the distance between the transects is considered, the contrast between these two transects would indicate that a more dense sediment sampling scheme should be applied in the eastern region near the Mississippi River discharge area if river-borne pollutant loadings to the sediments are to be quantified and distinguished from other sources.

b. Coastal Current Sampling

Tables 46 and 47 show summary statistics for water sample data from the five coastal current sampling cruises. Examination of the frequency of detection of the various analytes shows that alkylated and parent PAH (Table 46) are nearly ubiquitous in all phases of water samples. Herbicides (Table 47) were detected in the dissolved and colloidal phases in almost every sample. Chlorinated pesticides and PCBs (Table 47) were more frequently detected in the colloidal and suspended particulate phases. Note that the particulate phase data is presented in these tables in units of ng/g/L. If the data is expressed on a per gram basis, without correcting for the 20L volume from which the particulate material was obtained, then the concentrations for pollutants are approximately one order of magnitude higher compared to dissolved and colloidal phases. (The complete data tables for the particulates phase show units of ng/g.)

Tables 48-50 show summary data for each cruise for the three phases of water samples: dissolved, colloidal, and particulate, respectively. The herbicides, and especially Atrazine, formed a relatively complete dataset, with detection in two phases (dissolved and colloidal), at all stations, all cruises, and all depths. Therefore, this class was chosen for detailed examination of spatial, temporal, and mass transport trends.

(1) Dissolved Phase Alkylated naphthalenes were detected in nearly all dissolved phase samples, and showed the highest concentrations of all pollutants detected (Table 46). Naphthalene was the most abundant of the parent PAH followed by phenanthrene. Other alkylated and parent PAH were present with decreasing frequency and mean concentration as molecular weight increased. For the herbicides and pesticides (Table 47), Atrazine showed the highest concentrations, averaging 230 pg/ml for all hydrography cruises, was detected in 98% of samples, and ranged up to 1700 pg/ml (observed in October 1992). Cyanazine had the next highest mean concentration, 110 pg/ml, and was detected in 39% of samples, while Metolachlor was detected in 94% of samples, averaging 25 pg/ml. Note that averages are obtained from samples where a value was reported; zero values were not substituted for "not detected" for organics data analysis.

Temporal Distribution Regardless of pollutant class, highest mean concentrations were observed in samples collected in October, 1992 (Table 48). Figure 254 shows mean concentrations by cruise date for herbicides in the dissolved phase. Concentrations of herbicides tended to be highest during the low discharge volume periods (summer and fall cruises), with the exception of Alachlor, which was detected only in samples taken during April cruises. Figure 255 shows concentrations for Atrazine in surface samples collected along transect S1, adjacent to Timbalier Bay for each of the five seasonal basic

cruises. Again it can be seen that summer concentration profiles were much higher than in samples from the spring collections, with the fall, 1992 cruise profile yielding intermediate concentrations at this transect. This figure also shows the trend of decreasing concentrations away from shore (decreasing North latitude), with predominant gradients seen in April samples (see discussion of spatial distribution, below). The

Table 46. Summary of PAH data for water samples from core survey cruises.

	Dissolved Phase				Colloidal Phase				Particulate Phase			
	Mean	Range:		Freq.	Mean	Range:		Freq.	Mean	Range:		Freq.
ANALYTE	ng/L	min.	max.	n=261	ng/L	min.	max.	n=240	ng/g/L	min.	max.	n=234
Sample Dry Wt.									0.58g	0.01g	16g	
PARENT PAH												
Naphthalene	**142**	0.0094	1673	92%	**178**	0.28	1346	48%	**21**	0.12	401	80%
Acenaphthylene	**2.6**	0.38	23	71%	**4.1**	0.028	38	29%	**0.094**	0.001	0.62	42%
Acenaphthene	**15**	0.93	82	99%	**144**	1.72	3603	48%	**0.56**	0.004	17	54%
Fluorene	**22**	1.4	138	100%	**68**	0.55	2412	46%	**1.9**	0.009	52	70%
Dibenzothiophene	**11**	0.018	108	97%	**15**	0.19	169	36%	**0.55**	0.011	4.4	15%
Phenanthrene	**26**	0.062	221	98%	**63**	0.64	669	37%	**4.9**	0.49	107	13%
Anthracene	**4.1**	0.00074	55	62%	**7.3**	0.58	74	28%	**0.063**	0.001	0.32	8%
Fluoranthene	**2.8**	0.024	14	79%	**9.4**	0.036	194	61%	**0.97**	0.014	6.4	3%
Pyrene	**2.5**	0.048	20	85%	**8.4**	0.025	657	72%	**0.99**	0.028	5.7	8%
Benzanthracene	**1.2**	0.024	8.2	13%	**3.5**	0.039	38	17%	**0.37**	0.002	3.9	22%
Chrysene	**1.0**	0.016	6.8	36%	**6.6**	0.028	49	34%	**0.38**	0.004	8.6	37%
Benzo(b)fluor	**1.7**	0.87	3.1	3%	**12**	0.22	53	13%	**1.9**	0.001	65	27%
Benzo(k)fluor	**0.8**	0.40	1.5	2%	**4.9**	0.22	13	2%	**0.66**	0.030	4.8	4%
Benzo(a)pyrene	**6.5**	2.7	10	4%	**16**	1.9	61	5%	**1.4**	0.003	19	18%
Indenopyrene	**3.2**	1.4	7.1	3%	**25**	4.5	71	3%	**5.1**	0.002	21	8%
Dibenzanthracene	**12**	3.2	33	3%	**12**	12	12	0%	**6.2**	6.2	6.2	0%
Benzoperylene	**11**	0.46	19	3%	**32**	3.4	339	7%	**2.2**	0.005	8.5	14%
TOTALS & ESTIMATES OF ALKYLATED PAH												
C1-Naphthalenes	**313**	0.14	2362	98%	**169**	0.16	2587	55%	**16**	0.19	291	96%
C2-Naphthalenes	**361**	1.2	3095	100%	**203**	0.41	4126	55%	**34**	0.008	1312	99%
C3-Naphthalenes	**213**	3.0	1836	98%	**266**	0.98	3432	36%	**19**	0.079	716	85%
C4-Naphthalenes	**55**	2.1	398	77%	**231**	7.7	1794	27%	**6.8**	0.017	219	68%
C1-Dibenzothiophenes	**9.1**	0.36	141	82%	**15**	0.25	139	34%	**0.52**	0.004	3.1	22%
C2-Dibenzothiophenes	**23**	0.16	295	59%	**38**	1.9	236	33%	**2.6**	0.13	9.6	6%
C1-Phenanthrenes	**17**	0.39	306	93%	**28**	0.53	396	42%	**1.1**	0.018	7.1	7%
C2-Phenanthrenes	**13**	0.45	510	69%	**14**	0.51	250	45%	**2.6**	0.020	38	38%
C3-Phenanthrenes	**7.9**	0.43	88	28%	**29**	0.59	90	25%	**4.0**	0.047	28	17%

Table 47. Summary of pesticides and PCBs data for water samples from core survey cruises.

	Dissolved Phase				Colloidal Phase				Particulate Phase			
	Mean	Range:		Freq.	Mean	Range:		Freq.	Mean	Range:		Freq.
ANALYTE	ng/L	min.	max.	n=261	ng/L	min.	max.	n=240	ng/g/L	min.	max.	n=234
Sample Dry Wt.									**0.58g**	0.01g	15.71g	
HERBICIDES												
Trifluralin	**1.8**	0.96	2.8	2%	**2.0**	0.84	3.4	2%	**0.28**	0.004	1.1	3%
Simazine	**22**	2.5	160	44%	**15**	1.1	50	28%	**0.89**	0.83	1.0	1%
Atrazine	**232**	6.9	1682	98%	**115**	4.0	822	88%	**nd**	na	na	0%
Alachlor	**31**	11	68	3%	**nd**	na	na	0%	**nd**	na	na	0%
Metolachlor	**25**	1.6	147	94%	**20**	2.0	84	72%	**0.28**	0.18	0.48	3%
Cyanazine	**110**	0.60	523	39%	**77**	5.6	460	20%	**6.5**	4.0	9.0	1%
PESTICIDES												
Hexachlorobutadiene	**nd**	na	na	0%	**nd**	na	na	0%	**0.28**	0.032	1.1	2%
Hexachlorobenzene	**nd**	na	na	0%	**3.1**	0.81	6.0	2%	**0.18**	0.012	0.35	4%
Chlordane	**9.4**	2.6	17	2%	**2.3**	1.1	5.7	4%	**0.057**	0.033	0.13	3%
trans-Nonachlor	**0.50**	0.50	0.50	0%	**1.7**	0.74	4.3	2%	**0.033**	0.016	0.047	1%
Dieldrin	**11**	11	11	0%	**19**	2.3	62	4%	**nd**	na	na	0%
o,p'-DDE	**2.1**	0.33	5.4	1%	**nd**	na	na	0%	**0.30**	0.30	0.30	0%
p,p'-DDE	**3.5**	2.0	8.3	3%	**8.1**	1.9	13	2%	**nd**	na	na	0%
o,p'-DDD	**nd**	na	na	0%	**nd**	na	na	0%	**0.10**	0.10	0.10	0%
p,p'-DDD/o,p'-DDT	**nd**	na	na	0%	**nd**	na	na	0%	**nd**	na	na	0%
p,p'-DDT	**nd**	na	na	0%	**3.8**	3.8	3.8	0%	**nd**	na	na	0%
PCBS												
CL2-PCB	**6.5**	2.4	22	2%	**17**	0.64	70	11%	**0.42**	0.11	5.5	11%
CL3-PCB	**33**	0.45	209	8%	**33**	3.6	196	14%	**4.8**	0.018	47	16%
CL4-PCB	**78**	1.8	324	8%	**51**	8.7	313	13%	**3.4**	0.005	26	14%
CL5-PCB	**nd**	na	na	0%	**22**	3.6	130	14%	**1.9**	0.071	7.5	7%
CL6-PCB	**nd**	na	na	0%	**6.4**	1.0	22	5%	**0.33**	0.044	2.7	15%
CL7-PCB	**nd**	na	na	0%	**nd**	na	na	0%	**0.43**	0.37	0.49	1%

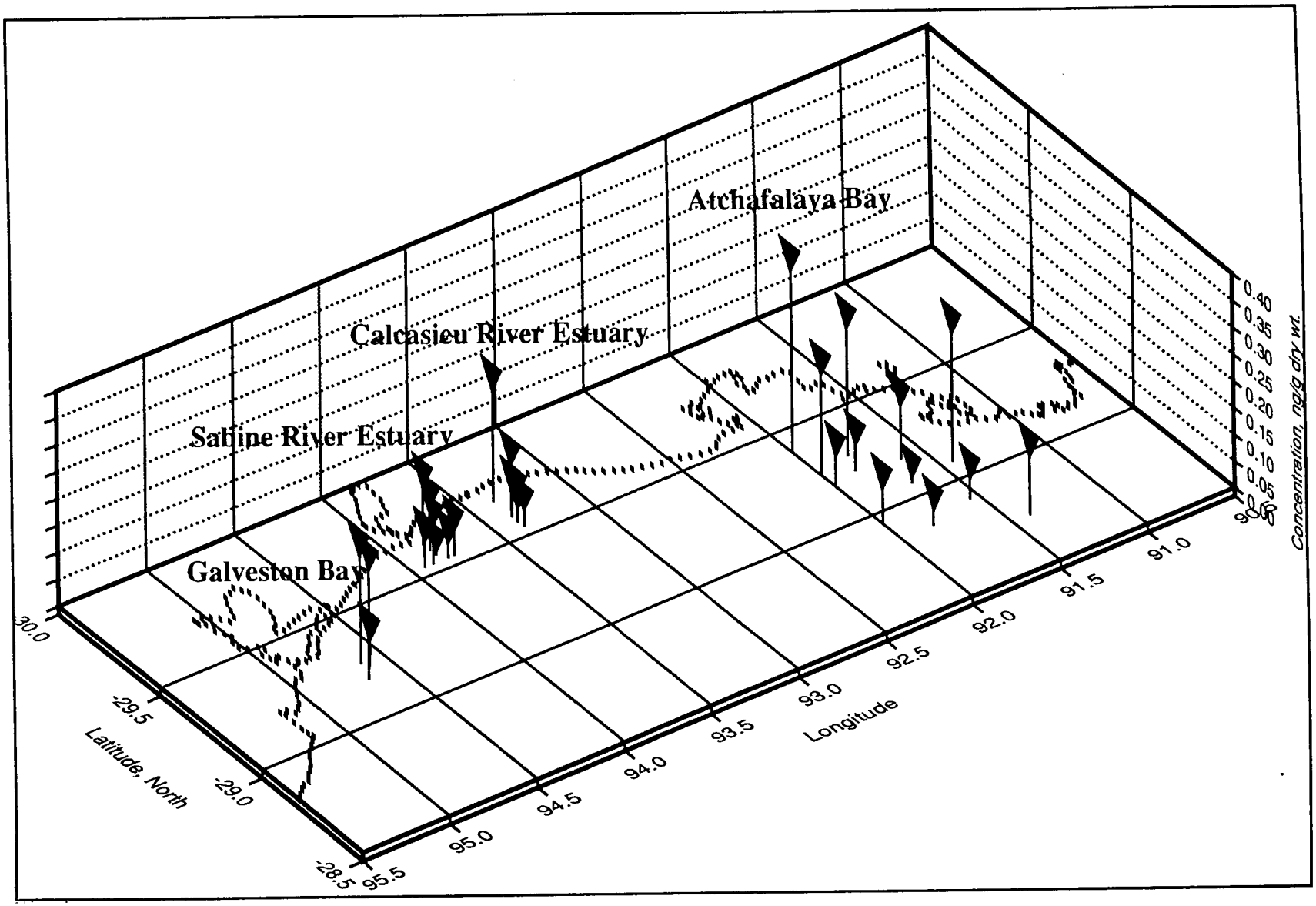

Figure 253. Spatial distribution of Hexachlorobenzene (ng/g) in bedded coastal sediments collected April 1992.

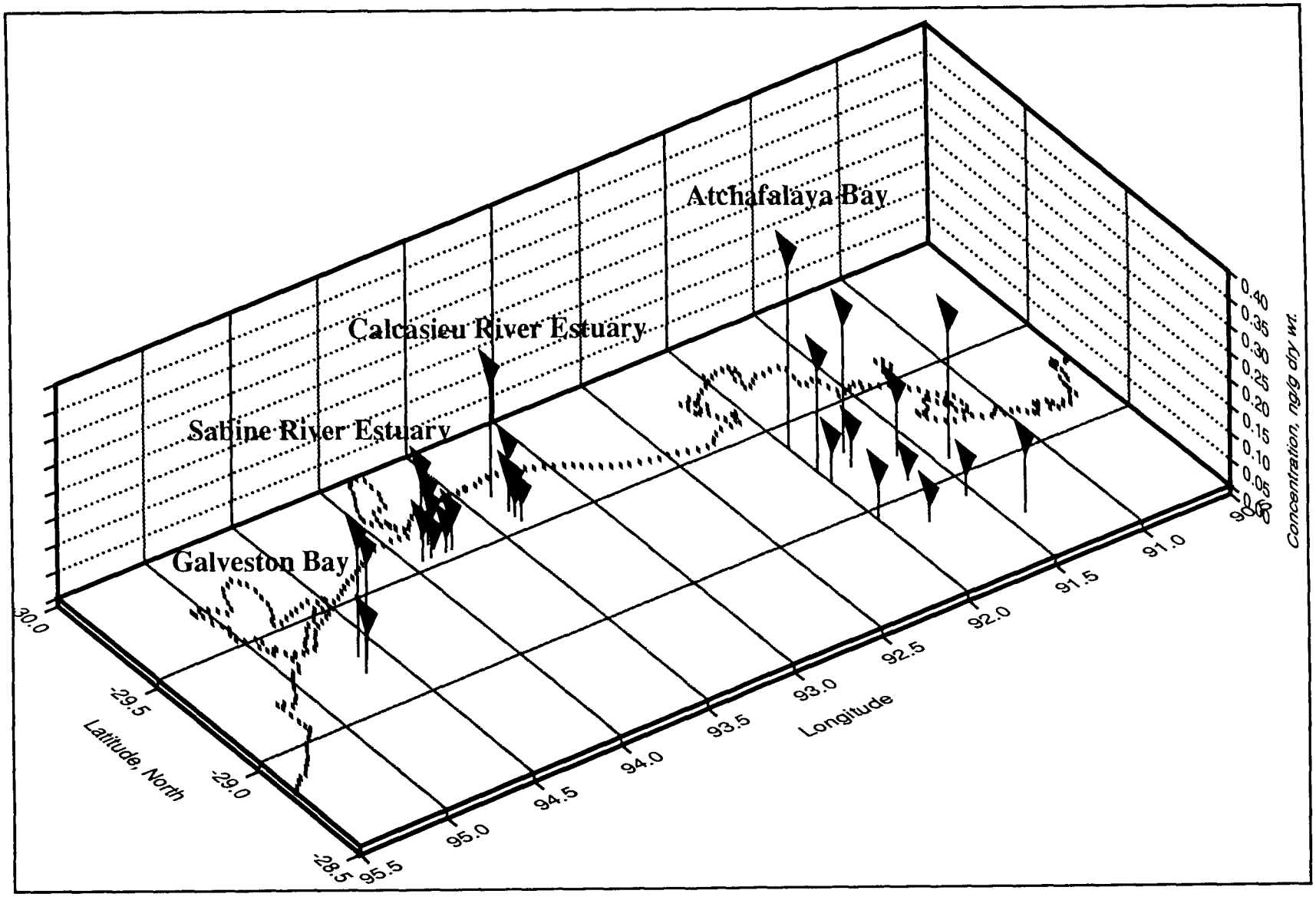

Figure 253 cont'd.

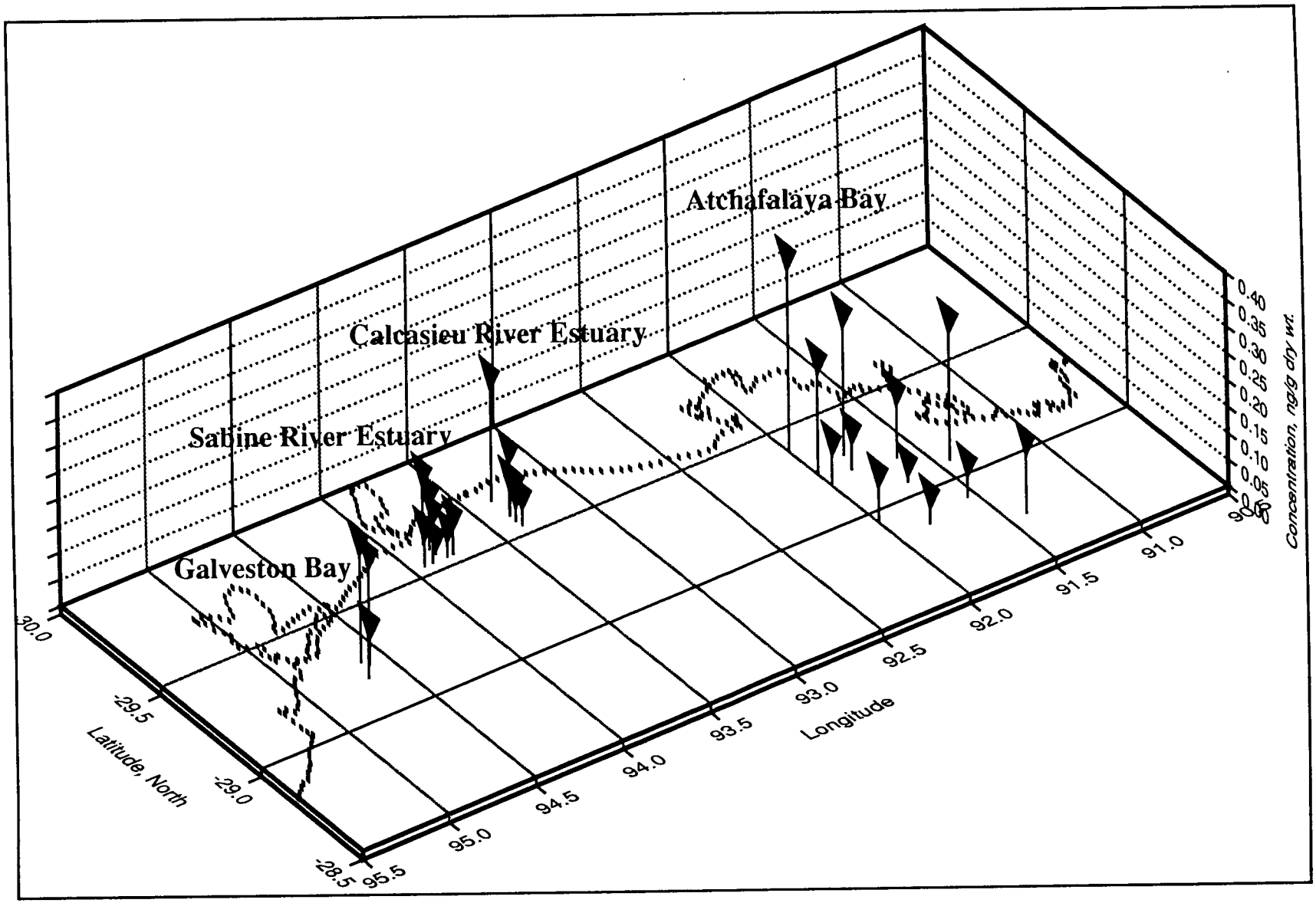

Figure 253 cont'd.

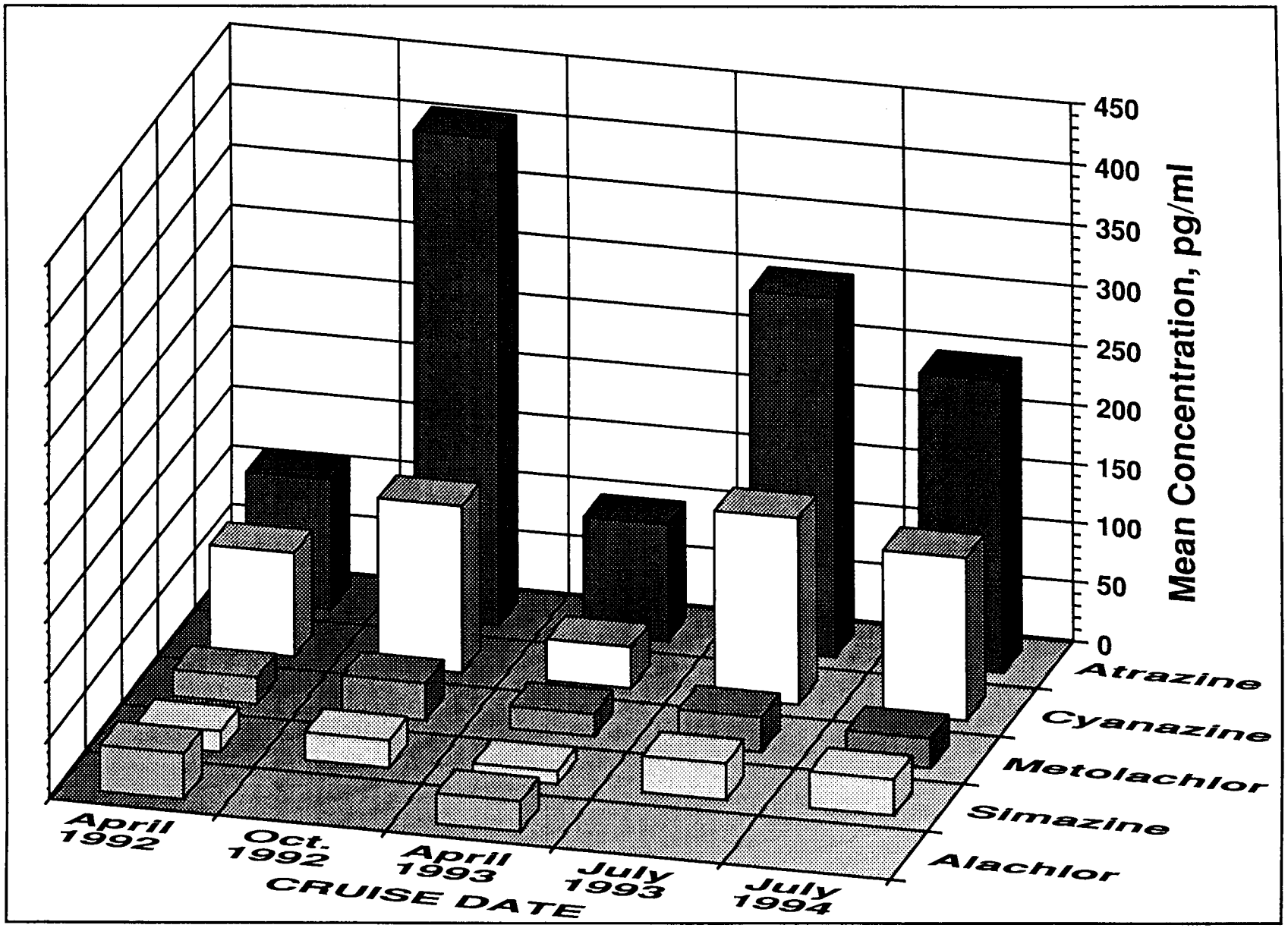

Figure 254. Mean concentrations of dissolved phase herbicides in water samples from core survey cruises.

Table 48. Summary of dissolved phase organic pollutant data from core survey cruises.

	CRUISE 1: April 1992				CRUISE 2: Oct. 1992				CRUISE 3: April 1993				CRUISE 4: July 1993				CRUISE 6: July 1994			
	MEAN	RANGE		FREQ	MEAN	RANGE		FREQ	MEAN	RANGE		FREQ	MEAN	RANGE		FREQ	MEAN	RANGE		FREQ
ANALYTE	pg/ml	MIN	MAX	(of 68)	pg/ml	MIN	MAX	(of 59)	pg/ml	MIN	MAX	(of 70)	pg/ml	MIN	MAX	(of 34)	pg/ml	MIN	MAX	(of 30)
Naphthalene	95	3.5	212	64	184	29	503	56	297	0.091	1673	63	68	11	133	29	65	0.0094	293	28
Hexachlorobutadiene	nd	na	na	0	nd	na	na	0	nd	na	na	0	nd	na	na	0	nd	na	na	0
2-MN	180	77	348	64	460	9.1	1468	59	149	11	332	66	130	12	294	32	43	1.4	155	28
1-MN	113	62	205	67	298	9.8	939	59	98	11	210	66	82	0.14	186	34	29	0.67	106	29
2-EN	28	2.7	100	68	72	3.7	303	59	31	1.1	69	70	37	2.7	94	34	11	0.54	37	27
1-EN	5.2	0.52	12	53	24	2.0	94	59	9.5	0.31	21	70	11	0.97	24	34	3.9	0.34	13	27
2,6/2,7-DMN	90	2.2	366	68	215	15	934	59	83	4.0	201	70	101	8.1	242	34	27	2.0	104	29
1,3/1,7-DMN	69	1.8	243	68	165	11	696	59	68	4.2	163	70	81	8.4	188	34	23	0.79	90	30
1,6-DMN	46	10	168	68	118	11	513	59	49	na	113	65	53	5.8	122	34	17	0.45	77	30
1,4/2,3-DMN	27	9.3	97	67	68	2.1	278	59	31	2.4	76	70	37	5.0	85	34	13	0.53	45	28
1,5-DMN	20	8.1	117	68	49	5.2	164	59	23	2.1	276	70	22	2.5	64	34	5.6	0.36	22	28
Acenaphthylene	3.6	1.1	23	30	3.8	1.4	12	43	1.7	0.38	4.4	68	1.6	0.47	3.3	28	2.2	1.0	6.3	17
1,2-DMN	12	4.3	44	67	28	1.5	118	59	15	1.8	37	70	18	2.9	41	34	6.2	0.46	25	28
2-IPN	9.4	4.6	20	23	13	6.2	32	46	4.1	0.80	10	59	14	2.2	36	34	3.7	1.0	10	21
1,8-DMN	3.9	3.9	3.9	1	4.1	1.5	16	31	nd	na	na	0	1.6	0.88	2.5	5	1.8	0.23	6.6	10
Acenaphthene	12	1.5	30	67	22	1.1	82	58	12	2.2	34	70	14	1.6	30	34	14	0.93	25	29
1,6,7-TMN	16	0.61	98	65	38	4.3	155	59	27	2.6	90	70	35	9.4	85	34	11	1.0	44	30
Fluorene	14	2.9	29	68	32	1.8	138	59	20	3.8	60	70	23	2.0	72	34	20	1.4	49	30
Trifluralin	nd	na	na	0	nd	na	na	0	1.8	0.96	2.8	4	nd	na	na	0	nd	na	na	0
CL2-PCB	nd	na	na	0	nd	na	na	0	3.9	2.5	5.3	2	2.4	2.4	2.4	1	13	4.0	22	2
Hexachlorobenzene	nd	na	na	0	nd	na	na	0	nd	na	na	0	nd	na	na	0	nd	na	na	0
Simazine	17	11	26	20	23	2.5	91	34	11	4.5	32	34	30	7.0	84	17	30	6.2	160	11
Dibenzothiophene	9.8	3.4	26	63	17	3.3	108	58	8.1	1.7	20	70	9.8	0.018	26	34	8.1	1.1	14	29
Atrazine	110	21	283	68	407	79	1682	56	98	6.9	514	69	302	13	1570	34	246	8.4	1033	30
Phenanthrene	19	3.6	52	67	39	3.7	221	57	26	2.9	138	69	24	0.062	61	34	23	2.8	51	28
Anthracene	4.1	1.2	18	25	4.0	1.2	17	42	1.2	0.0007	7.3	63	1.6	0.0047	4.6	21	9.8	0.67	55	11
CL3-PCB	nd	na	na	0	55	4.5	209	14	6.3	0.45	16	4	4.0	1.6	6.5	2	65	65	65	1
4-MDBT	4.0	1.6	11	27	11	2.5	73	56	3.5	0.36	12	68	4.7	0.70	13	34	4.2	0.49	15	28
2/3-MDBT	2.8	1.3	5.7	15	8.2	1.6	55	45	1.7	0.18	6.0	63	2.8	0.47	6.6	34	2.2	0.37	4.1	25
CL4-PCB	nd	na	na	0	78	1.8	324	20	nd	na	na	0	nd	na	na	0	nd	na	na	0
3-MP	1.6	0.14	3.7	49	12	0.45	102	59	4.2	0.29	13	68	5.9	0.69	14	34	6.9	0.73	15	29
1-MDBT	2.3	0.94	6.0	7	2.8	0.70	14	37	0.60	0.0003	1.5	35	1.4	0.46	2.7	28	1.1	0.75	1.4	6
2-MP	1.3	0.10	3.0	48	11	0.78	99	58	2.9	0.12	8.9	66	4.7	0.73	11	33	4.0	0.34	14	28
Alachlor	38	11	68	6	nd	na	na	0	25	14	37	2	nd	na	na	0	nd	na	na	0
4/9-MP	2.4	1.3	5.0	34	8.5	0.78	62	59	2.1	0.037	5.6	67	2.8	0.016	6.7	34	3.5	0.69	10	26
1-MP	7.0	3.1	11	2	13	1.0	49	19	1.4	0.059	4.0	65	2.7	0.27	5.5	33	4.3	1.5	26	14
Metolachlor	22	7.1	117	58	30	4.0	120	58	18	1.6	123	67	29	2.8	147	34	24	3.7	73	29
Cyanazine	87	8.8	271	29	140	8.9	523	34	34	13	69	11	156	12	401	13	135	0.60	381	14
3,6-DMP	0.97	0.80	1.1	2	14	1.6	48	6	1.4	0.034	5.4	8	1.4	1.2	1.5	2	nd	na	na	0
3,5-DMP	nd	na	na	0	nd	na	na	0	nd	na	na	0	nd	na	na	0	nd	na	na	0
2,6-DMP	nd	na	na	0	32	32	32	1	0.33	0.18	0.59	3	nd	na	na	0	nd	na	na	0
2,7-DMP	nd	na	na	0	347	347	347	1	27	2.6	76	69	nd	na	na	0	20	20	20	1

Table 48 cont'd.

	CRUISE 1: April 1992				CRUISE 2: Oct. 1992				CRUISE 3: April 1993				CRUISE 4: July 1993				CRUISE 6: July 1994			
	MEAN	RANGE		FREQ	MEAN	RANGE		FREQ	MEAN	RANGE		FREQ	MEAN	RANGE		FREQ	MEAN	RANGE		FREQ
ANALYTE	pg/ml	MIN	MAX	(of 68)	pg/ml	MIN	MAX	(of 59)	pg/ml	MIN	MAX	(of 70)	pg/ml	MIN	MAX	(of 34)	pg/ml	MIN	MAX	(of 30)
3,9-DMP	1.5	0.78	2.6	17	6.2	0.41	66	51	1.2	0.024	4.4	62	3.0	0.74	6.8	34	2.4	0.45	10	23
1,6/2,5/2,9-DMP	1.2	0.94	1.6	3	3.9	0.72	27	40	0.61	0.019	2.3	52	1.6	0.21	3.6	32	2.0	0.79	5.8	7
1,7-DMP	0.83	0.39	1.2	3	5.7	0.80	31	23	0.30	0.022	0.75	36	0.77	0.22	2.2	24	1.5	0.39	3.2	3
1,9/4,9-DMP	0.77	0.73	0.80	2	4.2	0.65	17	12	0.37	0.036	1.3	12	1.3	0.50	2.9	4	1.6	0.34	2.8	2
1,2-DMDBT	0.63	0.63	0.63	1	nd	na	na	0	nd	na	na	0	nd	na	na	0	4.3	1.6	8.4	3
Fluoranthene	1.8	0.83	3.7	45	3.0	0.091	13	55	1.8	0.23	6.5	68	5.1	0.024	14	12	2.5	0.26	5.3	25
1,5-DMP	nd	na	na	0	2.7	2.7	2.7	1	nd	na	na	0	nd	na	na	0	nd	na	na	0
1,8-DMP	0.44	0.44	0.44	1	2.5	0.62	4.1	10	nd	na	na	0	nd	na	na	0	nd	na	na	0
1,2-DMP	nd	na	na	0	4.0	1.2	8.8	9	nd	na	na	0	nd	na	na	0	nd	na	na	0
9,10-DMP	nd	na	na	0	2.4	0.41	5.6	10	nd	na	na	0	nd	na	na	0	nd	na	na	0
Pyrene	0.99	0.048	5.0	49	4.0	0.57	20	59	2.2	0.29	7.8	69	1.3	0.096	4.3	19	3.8	0.70	16	25
o,p'-DDE	nd	na	na	0	nd	na	na	0	nd	na	na	0	1.3	1.3	1.3	1	2.9	0.33	5.4	2
Chlordane	nd	na	na	0	9.4	2.6	17	5	nd	na	na	0	nd	na	na	0	nd	na	na	0
trans-Nonachlor	nd	na	na	0	nd	na	na	0	0.50	0.50	0.50	1	nd	na	na	0	nd	na	na	0
CL5-PCB	nd	na	na	0	nd	na	na	0	nd	na	na	0	nd	na	na	0	nd	na	na	0
Dieldrin	nd	na	na	0	nd	na	na	0	nd	na	na	0	11	11	11	1	nd	na	na	0
p,p'-DDE	nd	na	na	0	nd	na	na	0	2.8	2.8	2.8	1	nd	na	na	0	4.2	2.0	8.3	8
o,p'-DDD	nd	na	na	0	nd	na	na	0	nd	na	na	0	nd	na	na	0	nd	na	na	0
CL6-PCB	nd	na	na	0	nd	na	na	0	nd	na	na	0	nd	na	na	0	nd	na	na	0
1,2,8-TMP	nd	na	na	0	nd	na	na	0	2.0	0.58	6.9	27	nd	na	na	0	1.4	0.063	4.5	13
p,p'-DDD/o,p'-DDT	nd	na	na	0	nd	na	na	0	nd	na	na	0	nd	na	na	0	nd	na	na	0
CL7-PCB	nd	na	na	0	nd	na	na	0	nd	na	na	0	nd	na	na	0	nd	na	na	0
p,p'-DDT	nd	na	na	0	nd	na	na	0	nd	na	na	0	nd	na	na	0	nd	na	na	0
Benzanthracene	2.5	0.64	8.2	8	1.3	0.25	3.5	5	0.23	0.024	1.1	11	0.90	0.19	2.1	10	nd	na	na	0
Chrysene	1.3	0.28	5.0	29	1.4	0.36	6.8	18	0.63	0.016	3.1	32	0.66	0.14	1.6	16	nd	na	na	0
Benzo(b)fluor	2.3	1.5	3.1	5	nd	na	na	0	1.2	0.87	1.6	2	nd	na	na	0	nd	na	na	0
Benzo(k)fluor	0.95	0.40	1.5	2	nd	na	na	0	0.68	0.47	0.89	2	nd	na	na	0	nd	na	na	0
Benzo(a)pyrene	6.5	2.7	10	10	nd	na	na	0	nd	na	na	0	nd	na	na	0	nd	na	na	0
Indenopyrene	5.0	2.7	7.1	8	1.4	1.4	1.4	1	nd	na	na	0	nd	na	na	0	nd	na	na	0
Dibenzanthracene	4.2	3.2	5.2	2	20	5.6	33	5	nd	na	na	0	nd	na	na	0	nd	na	na	0
Benzoperylene	11	0.46	19	9	nd	na	na	0	nd	na	na	0	nd	na	na	0	nd	na	na	0
Estimated Totals																				
C1-Naphthalenes	283	35	553	67	758	19	2362	59	248	24	527	66	205	0.14	480	34	71	0.67	261	29
C2-Naphthalenes	294	20	1115	68	742	52	3095	59	305	20	729	70	362	40	847	34	104	1.2	396	30
C3-Naphthalenes	100	6.5	553	67	303	22	1836	59	312	49	819	70	252	60	661	34	98	3.0	393	27
C4-Naphthalenes	16	2.1	79	27	62	2.9	398	50	69	7.4	237	69	89	16	229	34	38	3.0	180	22
C1-Dibenzothiophenes	5.9	1.5	20	28	19	2.5	141	56	5.3	0.36	16	68	8.7	1.2	22	34	6.4	0.49	15	28
C2-Dibenzothiophenes	8.8	1.5	19	20	60	7.6	295	19	13	0.16	60	60	10	1.0	29	30	22	2.9	128	26
C1-Phenanthrenes	4.5	0.52	14	52	36	2.5	306	59	10	0.39	30	68	16	0.97	37	34	16	1.1	50	29
C2-Phenanthrenes	1.6	1.4	1.8	3.0	23	0.68	510	51	29	0.45	79	70	5.3	0.74	12	34	4.2	0.45	22	23
C3-Phenanthrenes	6.0	1.5	12	13	12	0.52	88	24	8.4	0.43	19	7	2.3	0.70	5.7	16	11	0.74	31	13

Table 49. Summary of colloidal phase organic pollutant data from core survey cruises.

	CRUISE 1: April 1992				CRUISE 2: Oct. 1992				CRUISE 3: April 1993				CRUISE 4: July 1993				CRUISE 6: July 1994			
	MEAN	RANGE		FREQ	MEAN	RANGE		FREQ	MEAN	RANGE		FREQ	MEAN	RANGE		FREQ	MEAN	RANGE		FREQ
ANALYTE	pg/ml	MIN	MAX	(of 68)	pg/ml	MIN	MAX	(of 58)	pg/ml	MIN	MAX	(of 48)	pg/ml	MIN	MAX	(of 34)	pg/ml	MIN	MAX	(of 32)
Sample Vol., ml	239	150	390	68	451	290	480	58	816	280	1000	48	864	505	1000	34	586	265	940	32
Naphthalene	5.3	2.0	11	11	9.6	0.28	19	2	129	1.5	226	42	451	21	1346	33	295	12	683	28
Hexachlorobutadiene	nd	na	na	0	nd	na	na	0	nd	na	na	0	nd	na	na	0	nd	na	na	0
2-MN	9.8	5.7	17	16	1.2	0.16	3.3	10	40	1.2	84	41	323	17	1490	33	129	11	430	30
1-MN	10	4.2	21	13	4.2	1.2	7.0	3	31	1.5	65	42	236	9.2	1097	33	81	9.0	283	30
2-EN	12	12	12	1	nd	na	na	0	5.8	1.1	30	39	53	5.5	309	33	29	6.9	106	30
1-EN	9.0	9.0	9.0	1	nd	na	na	0	0.75	0.14	1.9	25	13	2.1	62	30	8.5	2.4	34	26
2,6-/2,7-DMN	nd	na	na	0	0.17	0.11	0.22	2	10	1.3	32	41	187	16	1208	33	79	2.8	339	30
1,3/1,7-DMN	4.3	2.2	9.1	9	3.2	0.41	8.3	13	21	0.96	78	44	147	16	970	33	67	5.6	273	31
1,6-DMN	5.0	3.2	6.5	5	2.8	0.46	5.7	13	5.6	0.017	17	39	105	9.0	653	33	50	3.8	230	31
1,4/2,3-DMN	4.6	4.6	4.6	1	4.6	3.5	5.4	3	4.5	0.18	12	40	73	8.7	507	33	37	4.2	175	31
1,5-DMN	8.1	6.5	9.7	2	12	8.1	16	2	16	0.51	110	32	34	4.1	216	33	16	2.0	63	29
Acenaphthylene	nd	na	na	0	nd	na	na	0	0.66	0.028	1.6	12	7.5	1.8	38	29	4.3	1.6	12	29
1,2-DMN	nd	na	na	0	nd	na	na	0	2.8	0.028	13	39	29	4.4	188	33	15	2.0	62	31
2-IPN	nd	na	na	0	nd	na	na	0	2.4	2.4	2.4	1	9.8	2.8	28	14	9.2	1.6	32	24
1,8-DMN	nd	na	na	0	nd	na	na	0	nd	na	na	0	7.1	2.9	14	6	13	4.7	59	23
Acenaphthene	nd	na	na	0	3.5	2.2	5.3	6	62	1.7	128	44	459	2.0	3603	34	52	11	120	30
1,6,7-TMN	nd	na	na	0	8.9	1.4	16	2	2.5	0.42	4.7	15	78	3.5	541	33	62	10	276	31
Fluorene	7.4	7.4	7.4	1	1.5	1.4	1.5	2	35	0.55	95	43	249	8.3	2412	33	46	9.7	171	31
Trifluralin	nd	na	na	0	3.4	3.4	3.4	1	0.84	0.84	0.84	1	nd	na	na	0	1.8	1.5	2.0	3
CL2-PCB	nd	na	na	0	nd	na	na	0	nd	na	na	0	21	3.0	51	3	14	0.64	70	24
Hexachlorobenzene	nd	na	na	0	nd	na	na	0	nd	na	na	0	3.6	3.6	3.6	1	2.6	0.81	6.0	3
Simazine	nd	na	na	0	9.9	1.1	20	21	7.4	4.5	14	20	22	8.0	50	15	22	7.1	37	10
Dibenzothiophene	nd	na	na	0	1.2	0.33	2.0	3	3.7	0.19	13	22	25	0.23	169	32	31	2.3	120	30
Atrazine	82	17	190	46	124	23	413	58	54	4.0	162	42	176	17	822	34	138	17	351	31
Phenanthrene	12	2.0	45	7	34	34	34	1	12	0.64	48	22	114	4.4	647	27	143	14	669	31
Anthracene	7.4	5.9	8.8	2	1.8	0.58	3.0	2	3.6	1.1	8.4	16	13	1.7	74	29	11	2.9	35	18
CL3-PCB	nd	na	na	0	nd	na	na	0	nd	na	na	0	31	11	52	2	36	3.6	196	31
4-MDBT	nd	na	na	0	0.95	0.25	2.7	5	1.4	0.028	4.2	13	15	1.2	78	32	14	3.2	51	32
2/3-MDBT	nd	na	na	0	1.2	1.2	1.2	1	1.1	0.086	2.8	10	10	1.5	42	29	9.0	1.8	32	32
CL4-PCB	nd	na	na	0	nd	na	na	0	31	31	31	1	nd	na	na	0	71	8.7	313	31
3-MP	7.6	4.9	10	2	1.4	0.35	6.4	14	3.1	1.0	9.1	6	15	0.29	76	32	25	5.5	116	32
1-MDBT	nd	na	na	0	nd	na	na	0	2.2	1.7	2.8	2	5.3	2.0	19	24	4.1	1.1	13	29
2-MP	5.0	4.4	5.5	3	1.2	0.22	6.3	10	3.2	0.58	8.8	5	14	0.17	67	31	26	5.4	137	32
Alachlor	nd	na	na	0	nd	na	na	0	nd	na	na	0	nd	na	na	0	nd	na	na	0
4/9-MP	5.6	5.6	5.6	1	2.4	0.76	4.8	13	4.1	0.097	10	4	11	0.72	56	32	17	3.0	86	32
1-MP	14	9.6	18	5	5.8	3.2	15	12	4.4	3.1	5.7	2	6.5	0.089	29	28	11	2.5	57	25
Metolachlor	23	8.8	42	9	10	2.0	35	56	10	3.4	30	43	22	6.1	74	33	33	7.9	84	31
Cyanazine	nd	na	na	0	52	5.6	144	32	11	7.9	15	2	186	57	460	9	57	33	86	6
3,6-DMP	nd	na	na	0	nd	na	na	0	2.1	2.1	2.1	1	5.9	1.6	11	23	5.6	0.94	17	9
3,5-DMP	nd	na	na	0	nd	na	na	0	nd	na	na	0	nd	na	na	0	12	5.3	16	3
2,6-DMP	nd	na	na	0	nd	na	na	0	nd	na	na	0	3.8	0.022	18	17	83	83	83	1
2,7-DMP	nd	na	na	0	nd	na	na	0	12	0.51	35	22	5.5	0.84	17	19	17	17	17	1

Table 49 cont'd.

	CRUISE 1: April 1992				CRUISE 2: Oct. 1992				CRUISE 3: April 1993				CRUISE 4: July 1993				CRUISE 6: July 1994			
	MEAN	RANGE		FREQ	MEAN	RANGE		FREQ	MEAN	RANGE		FREQ	MEAN	RANGE		FREQ	MEAN	RANGE		FREQ
ANALYTE	pg/ml	MIN	MAX	(of 68)	pg/ml	MIN	MAX	(of 58)	pg/ml	MIN	MAX	(of 48)	pg/ml	MIN	MAX	(of 34)	pg/ml	MIN	MAX	(of 32)
3,9-DMP	8.1	8.1	8.1	1	2.0	1.0	4.4	15	4.1	0.27	16	8	9.2	1.6	36	30	11	1.9	62	32
1,6/2,5/2,9-DMP	nd	na	na	0	1.2	0.48	2.4	6	5.0	0.71	10	4	6.1	1.4	22	26	8.5	1.7	40	19
1,7-DMP	nd	na	na	0	0.63	0.63	0.63	1	3.2	0.41	6.6	4	3.1	1.1	10	26	5.0	1.1	21	19
1,9/4,9-DMP	nd	na	na	0	0.61	0.61	0.61	1	3.6	3.4	3.8	2	2.3	0.40	5.6	10	3.0	0.63	9.5	10
1,2-DMDBT	nd	na	na	0	nd	na	na	0	nd	na	na	0	nd	na	na	0	nd	na	na	0
Fluoranthene	6.8	1.2	47	46	8.0	0.048	194	30	5.2	0.036	20	16	7.4	0.50	20	23	20	3.7	81	32
1,5-DMP	nd	na	na	0	nd	na	na	0	nd	na	na	0	5.9	5.9	5.9	1	nd	na	na	0
1,8-DMP	nd	na	na	0	nd	na	na	0	1.3	0.97	1.6	2	1.8	1.8	1.8	1	2.4	0.82	4.2	6
1,2-DMP	nd	na	na	0	nd	na	na	0	2.2	1.7	2.8	2	2.3	2.3	2.3	1	4.2	3.7	4.7	2
9,10-DMP	nd	na	na	0	nd	na	na	0	nd	na	na	0	nd	na	na	0	2.3	2.2	2.4	2
Pyrene	7.2	1.5	46	47	13	0.13	657	57	5.7	0.025	35	22	7.9	0.6	23	26	8.2	1.7	17	21
o,p'-DDE	nd	na	na	0	nd	na	na	0	nd	na	na	0	nd	na	na	0	nd	na	na	0
Chlordane	nd	na	na	0	nd	na	na	0	nd	na	na	0	2.4	2.4	2.4	1	2.2	1.1	5.7	8
trans-Nonachlor	nd	na	na	0	nd	na	na	0	nd	na	na	0	1.7	1.7	1.7	1	1.7	0.74	4.3	4
CL5-PCB	nd	na	na	0	nd	na	na	0	25	25	25	1	9.2	9.2	9.2	1	33	3.6	130	32
Dieldrin	nd	na	na	0	nd	na	na	0	19	2.3	62	9	nd	na	na	0	nd	na	na	0
p,p'-DDE	nd	na	na	0	nd	na	na	0	3.3	1.9	5.3	3	nd	na	na	0	13	13	13	2
o,p'-DDD	nd	na	na	0	nd	na	na	0	nd	na	na	0	nd	na	na	0	nd	na	na	0
CL6-PCB	nd	na	na	0	nd	na	na	0	2.9	2.9	2.9	1	nd	na	na	0	9.9	1.0	22	10
1,2,8-TMP	4.4	1.5	6.4	3	1.2	0.59	3.8	16	7.0	2.1	12	2	2.2	1.3	3.2	3	1.9	0.41	3.4	13
p,p'-DDD/o,p'-DDT	nd	na	na	0	nd	na	na	0	nd	na	na	0	nd	na	na	0	nd	na	na	0
CL7-PCB	nd	na	na	0	nd	na	na	0	nd	na	na	0	nd	na	na	0	nd	na	na	0
p,p'-DDT	nd	na	na	0	nd	na	na	0	nd	na	na	0	nd	na	na	0	3.8	3.8	3.8	1
Benzanthracene	8.8	1.7	38	21	0.99	0.039	3.2	10	5.7	3.4	8.1	3	1.2	0.26	2.9	5	0.89	0.67	1.1	2
Chrysene	7.8	1.4	49	31	2.1	0.028	7.8	21	17	14	20	2	1.8	0.31	5.1	11	4.6	0.54	41	16
Benzo(b)fluor	27	7.9	53	8	5.7	0.22	36	20	19	15	24	2	4.7	4.7	4.7	1	0.72	0.72	0.72	1
Benzo(k)fluor	nd	na	na	0	0.22	0.22	0.22	1	11	8.3	13	2	3.9	3.9	3.9	2	nd	na	na	0
Benzo(a)pyrene	14	6.7	31	7	22	1.9	61	3	13	8.0	17	2	nd	na	na	0	nd	na	na	0
Indenopyrene	nd	na	na	0	45	18	71	2	24	18	29	3	5.3	4.5	6.1	2	nd	na	na	0
Dibenzanthracene	nd	na	na	0	nd	na	na	0	12	12	12	1	nd	na	na	0	nd	na	na	0
Benzoperylene	53	na	53	1	38	3.4	339	11	29	16	38	3	9.2	9.2	9.2	1	nd	na	na	0
Estimated Totals																				
C1-Naphthalenes	4.3	5.7	34	16	2.5	0.16	10	10	69	2.8	149	42	560	27	2587	33	210	20	681	30
C2-Naphthalenes	1.6	2.2	29	9	7.8	0.41	33	15	59	0.96	243	44	641	70	4126	33	306	22	1308	31
C3-Naphthalenes	nd	na	na	0	27	18	45	3	9.5	0.98	28	20	440	2.2	3432	33	588	23	2140	31
C4-Naphthalenes	nd	na	na	0	36	36	36	1	nd	na	na	0	227	7.7	1500	33	430	108	1794	30
C1-Dibenzothiophen	nd	na	na	0	1.2	0.25	3.9	5	2.6	0.26	9.8	13	28	1.2	139	32	27	5.0	96	32
C2-Dibenzothiophen	nd	na	na	0	nd	na	na	0	8.8	1.9	44	14	59	8.2	236	32	46	8.0	177	32
C1-Phenanthrenes	1.6	4.4	32	6	5.5	0.53	32	24	9.9	1.8	34	6	45	1.1	228	32	77	15	396	32
C2-Phenanthrenes	0.12	8.1	8.1	1	2.4	0.61	6.8	16	13	0.51	39	27	28	1.6	116	31	27	3.1	250	32
C3-Phenanthrenes	32	6.9	55	3	51	11	90	2	26	0.59	77	5	16	0.89	47	27	21	5.6	90	23

Table 50. Summary of particulate phase organic pollutant data from core survey cruises.

	CRUISE 1: April 1992				CRUISE 2: Oct. 1992				CRUISE 3: April 1993				CRUISE 4: July 1993				CRUISE 6: July 1994			
	MEAN	RANGE		FREQ	MEAN	RANGE		FREQ	MEAN	RANGE		FREQ	MEAN	RANGE		FREQ	MEAN	RANGE		FREQ
ANALYTE	ng/g	MIN	MAX	(of 68)	ng/g	MIN	MAX	(of 58)	ng/g	MIN	MAX	(of 38)	ng/g	MIN	MAX	(of 34)	ng/g	MIN	MAX	(of 36)
Sample Dry Wt.	1.1	0.17	16	68	0.78	0.43	4.14	58	0.28	0.010	1.54	38	0.40	0.21	1.3	34	0.38	0.14	1.1	36
Naphthalene	931	2.4	3776	67	139	19	1033	56	678	35	8022	23	73	24	162	11	251	7.6	1829	31
Hexachlorobutadiene	nd	na	na	0	2.9	2.1	3.7	2	8.4	0.64	23	3	nd	na	na	0	nd	na	na	0
2-MN	99	2.5	234	68	97	32	300	58	590	14	4466	34	164	1.1	534	31	142	21	647	34
1-MN	45	1.3	98	68	51	17	182	58	237	1.5	1357	33	90	1.1	253	31	68	2.3	348	32
2-EN	24	0.56	58	55	22	6.7	102	58	272	1.5	3392	36	56	1.9	196	32	48	4.1	186	36
1-EN	7.0	3.1	9.8	5	5.2	1.6	22	57	48	2.4	589	35	12	0.20	41	33	8.0	0.14	34	26
2,6/2,7-DMN	62	1.3	199	68	74	20	305	58	775	3.0	9641	36	168	5.4	549	33	160	26	497	36
1,3/1,7-DMN	43	1.1	143	68	37	10	174	58	356	0.15	4717	37	101	3.4	346	33	85	12	334	36
1,6-DMN	35	0.90	132	68	31	8.6	135	58	304	1.3	3802	36	81	2.3	288	33	72	11	300	36
1,4/2,3-DMN	22	0.59	83	63	17	5.2	79	58	180	1.0	2373	36	44	0.15	161	33	39	3.2	165	36
1,5-DMN	10	0.22	21	34	6.5	1.8	30	57	53	1.9	684	35	15	0.18	55	30	14	1.0	60	35
Acenaphthylene	2.3	0.77	4.6	4	0.36	0.019	1.3	42	3.4	0.044	12	20	0.23	0	0.50	5	3.1	0.83	10	28
1,2-DMN	11	0.23	22	46	5.8	0.88	24	56	79	0.009	1044	37	24	1.4	81	33	19	1.2	72	36
2-IPN	nd	na	na	0	2.8	0.11	7.9	12	35	2.6	302	12	16	0.80	82	20	15	0.43	48	20
1,8-DMN	nd	na	na	0	2.0	0.43	5.7	7	nd	na	na	0	nd	na	na	0	nd	na	na	0
Acenaphthene	9.7	0.77	20	32	3.9	0.074	56.4	36	32	0.23	336	37	3.8	0.11	13	9	7.5	0.32	27	13
1,6,7-TMN	22	0.51	54	45	8.0	0.34	38.0	51	190	15	2372	35	49	6.5	208	24	57	4.2	240	35
Fluorene	7.7	0.18	23	60	3.2	0.34	8.4	46	130	7.6	1045	36	20	6.6	59	6	28	1.1	75	16
Trifluralin	nd	na	na	0	nd	na	na	0	11.1	0.57	22	2	1.9	0.088	5.2	5	3.8	3.8	3.8	1
CL2-PCB	nd	na	na	0	nd	na	na	0	15	3.2	111	25	nd	na	na	0	2.1	2.1	2.1	1
Hexachlorobenzene	nd	na	na	0	nd	na	na	0	7.1	7.1	7.1	1	0.63	0.23	1.1	5	3.1	2.0	4.1	3
Simazine	nd	na	na	0	nd	na	na	0	nd	na	na	0	nd	na	na	0	18	17	19	2
Dibenzothiophene	2.1	0.23	7.6	4	1.2	0.48	1.8	4	35	8.1	89	24	7.7	4.9	11	2	9.0	9.0	9.0	1
Atrazine	nd	na	na	0	nd	na	na	0	nd	na	na	0	nd	na	na	0	nd	na	na	0
Phenanthrene	18	10	38	7	nd	na	na	0	180	9.7	2132	23	nd	na	na	0	nd	na	na	0
Anthracene	1.0	0.12	2.3	5	1.1	0.40	1.8	2	1.7	0.017	6.4	11	nd	na	na	0	nd	na	na	0
CL3-PCB	nd	na	na	0	nd	na	na	0	54	1.6	222	26	6.5	0.37	18	4	227	11	946	7
4-MDBT	15	15	15	1	2.6	2.5	2.7	2	4.3	2.2	10	8	8.4	0.68	20	8	nd	na	na	0
2/3-MDBT	6.0	6.0	6.0	1	nd	na	na	0	3.4	0.65	7.7	4	5.3	1.0	14	8	2.5	2.5	2.5	1
CL4-PCB	nd	na	na	0	nd	na	na	0	67	13	353	23	2.1	0.38	4.3	3	133	0.11	523	6
3-MP	13	13	13	1	nd	na	na	0	nd	na	na	0	8.4	0.91	30	7	nd	na	na	0
1-MDBT	0.12	0.12	0.12	1	nd	na	na	0	12	2.0	61	37	2.5	0.090	9.8	9	nd	na	na	0
2-MP	17	17	17	1	nd	na	na	0	9.2	9.2	9.2	1	11	1.1	29	4	nd	na	na	0
Alachlor	nd	na	na	0	nd	na	na	0	nd	na	na	0	nd	na	na	0	nd	na	na	0
4/9-MP	nd	na	na	0	nd	na	na	0	nd	na	na	0	13	0.37	51	14	nd	na	na	0
1-MP	3.4	3.4	3.4	1	nd	na	na	0	nd	na	na	0	6.2	1.1	32	12	nd	na	na	0
Metolachlor	5.6	5.4	5.9	2	5.7	3.6	9.6	6	nd	na	na	0	nd	na	na	0	nd	na	na	0
Cyanazine	130	80	181	2	nd	na	na	0	nd	na	na	0	nd	na	na	0	nd	na	na	0
3,6-DMP	6.3	6.3	6.3	1	nd	na	na	0	14	2.8	117	34	5.6	0.034	15	11	0.97	0.97	0.97	1
3,5-DMP	nd	na	na	0	4.4	4.4	4.4	1	nd	na	na	0	9.7	4.0	15	2	nd	na	na	0
2,6-DMP	3.2	0.074	7.3	4	nd	na	na	0	nd	na	na	0	9.1	1.3	22	24	1.0	1.0	1.0	1
2,7-DMP	20	20	20	1	1.8	1.8	1.8	1	12	12	12	2	11	1.0	27	29	4.8	1.4	11	4

Table 50 cont'd.

	CRUISE 1: April 1992				CRUISE 2: Oct. 1992				CRUISE 3: April 1993				CRUISE 4: July 1993				CRUISE 6: July 1994			
	MEAN	RANGE		FREQ	MEAN	RANGE		FREQ	MEAN	RANGE		FREQ	MEAN	RANGE		FREQ	MEAN	RANGE		FREQ
ANALYTE	ng/g	MIN	MAX	(of 68)	ng/g	MIN	MAX	(of 58)	ng/g	MIN	MAX	(of 38)	ng/g	MIN	MAX	(of 34)	ng/g	MIN	MAX	(of 36)
3,9-DMP	2.9	2.9	2.9	1	nd	na	na	0	43	7.2	244	38	43	4.5	111	27	nd	na	na	0
1,6/2,5/2,9-DMP	2.1	2.1	2.1	1	nd	na	na	0	26	5.6	167	38	22	0.20	63	30	nd	na	na	0
1,7-DMP	1.9	1.9	1.9	1	0.37	0.37	0.37	1	16	3.9	115	38	14	0.74	37	25	nd	na	na	0
1,9/4,9-DMP	0.20	0.20	0.20	1	3.8	2.6	5.0	2	7.5	1.4	28	32	8.5	1.3	24	28	nd	na	na	0
1,2-DMDBT	nd	na	na	0	6.4	2.5	12	4	6.3	5.8	6.8	2	1.2	0.052	3.3	13	7.6	7.6	7.6	1
Fluoranthene	66	15	128	3	11	11	11	1	0.27	0.27	0.27	1	0.84	0.84	0.84	1	nd	na	na	0
1,5-DMP	nd	na	na	0	4.2	0.53	11	7	15	5.1	29	6	9.2	9.2	9.2	1	nd	na	na	0
1,8-DMP	2.4	2.4	2.4	1	2.0	0.44	3.6	2	5.2	0.82	23	11	2.6	0.27	6.8	17	5.2	5.2	5.2	1
1,2-DMP	nd	na	na	0	nd	na	na	0	3.3	0.80	5.8	4	2.8	0.35	6.2	15	nd	na	na	0
9,10-DMP	nd	na	na	0	nd	na	na	0	18	0.77	46	3	2.2	0.040	6.2	14	1.5	0.40	3.1	5
Pyrene	42	0.73	115	5	9.1	1.6	18	4	nd	na	na	0	8.8	0.57	30	9	nd	na	na	0
o,p'-DDE	6.0	6.0	6.0	1	nd	na	na	0	nd	na	na	0	nd	na	na	0	nd	na	na	0
Chlordane	nd	na	na	0	nd	na	na	0	1.1	0.66	2.6	6	nd	na	na	0	nd	na	na	0
trans-Nonachlor	nd	na	na	0	nd	na	na	0	0.65	0.31	0.93	3	nd	na	na	0	nd	na	na	0
CL5-PCB	nd	na	na	0	nd	na	na	0	15	1.6	66	11	52	1.4	149	3	45	9.1	75	3
Dieldrin	nd	na	na	0	nd	na	na	0	nd	na	na	0	nd	na	na	0	nd	na	na	0
p,p'-DDE	nd	na	na	0	nd	na	na	0	nd	na	na	0	nd	na	na	0	nd	na	na	0
o,p'-DDD	nd	na	na	0	2.0	2.0	2.0	1	nd	na	na	0	nd	na	na	0	nd	na	na	0
CL6-PCB	nd	na	na	0	nd	na	na	0	11	1.8	54	32	1.9	0.88	3.4	3	nd	na	na	0
1,2,8-TMP	9.4	0.048	27	33	5.1	1.7	9.6	4	54	25	102	3	11	1.5	43	26	nd	na	na	0
p,p'-DDD/o,p'-DDT	nd	na	na	0	nd	na	na	0	nd	na	na	0	nd	na	na	0	nd	na	na	0
CL7-PCB	nd	na	na	0	nd	na	na	0	8.6	7.4	9.9	2	nd	na	na	0	nd	na	na	0
p,p'-DDT	nd	na	na	0	nd	na	na	0	nd	na	na	0	nd	na	na	0	nd	na	na	0
Benzanthracene	9.4	0.057	77	24	5.6	0.039	69	19	4.0	1.3	7.2	3	13	0.68	24	4	5.4	5.4	5.4	1
Chrysene	12	0.23	118	18	3.8	0.13	27	33	16	2.5	172	23	2.5	0.084	8.1	10	3.5	0.25	6.8	2
Benzo(b)fluor	125	0.17	1297	14	20	0.030	91	44	1.9	1.9	1.9	1	1.4	1.4	1.4	1	46	0.93	137	3
Benzo(k)fluor	15	0.84	29	2	1.5	1.4	1.5	3	0.86	0.86	0.86	1	0.73	0.73	0.73	1	49	0.60	97	2
Benzo(a)pyrene	47	0.061	381	17	21	3.6	53	20	9.1	9.1	9.1	1	0.46	0.46	0.46	1	66	0.43	132	2
Indenopyrene	255	93	418	2	50	4.1	124	11	nd	na	na	0	0.29	0.041	0.71	5	nd	na	na	0
Dibenzanthracene	124	124	124	1	nd	na	na	0	nd	na	na	0	nd	na	na	0	nd	na	na	0
Benzoperylene	49	0.11	163	24	74	0.47	170	3	49	45	54	2	2.9	2.1	3.7	4	nd	na	na	0
Estimated Totals																				
C1-Naphthalenes	144	3.8	331	68	148	49	482	58	820	16	5823	34	254	6.0	786	31	205	21	995	34
C2-Naphthalenes	193	4.9	557	68	198	57	872	58	2021	0.16	26242	37	497	13	1678	33	443	57	1641	36
C3-Naphthalenes	130	1.9	727	67	101	14	532	57	1190	92	14320	35	295	11	1090	22	159	1.6	774	17
C4-Naphthalenes	28	0.35	98	49	39	0.52	268	45	415	13	4382	32	104	4.0	413	7	99	2.5	409	26
C1-Dibenzothiophene	21	21	21	1	2.6	2.5	2.7	2	13	2.0	61	37	13	0.090	43	10	2.5	2.5	2.5	1
C2-Dibenzothiophene	64	64	64	1	nd	na	na	0	15	2.6	25	5	71	16	193	8	58	58	58	1
C1-Phenanthrenes	32	32	32	1	nd	na	na	0	9.2	9.2	9.2	1	25	0.37	143	14	nd	na	na	0
C2-Phenanthrenes	43	43	43	1	4.8	0.44	13	10	109	22	769	38	101	5.2	310	31	4.3	0.40	13	8
C3-Phenanthrenes	67	7.9	216	14	nd	na	na	0	nd	na	na	0	146	0.95	566	24	28	28	28	1

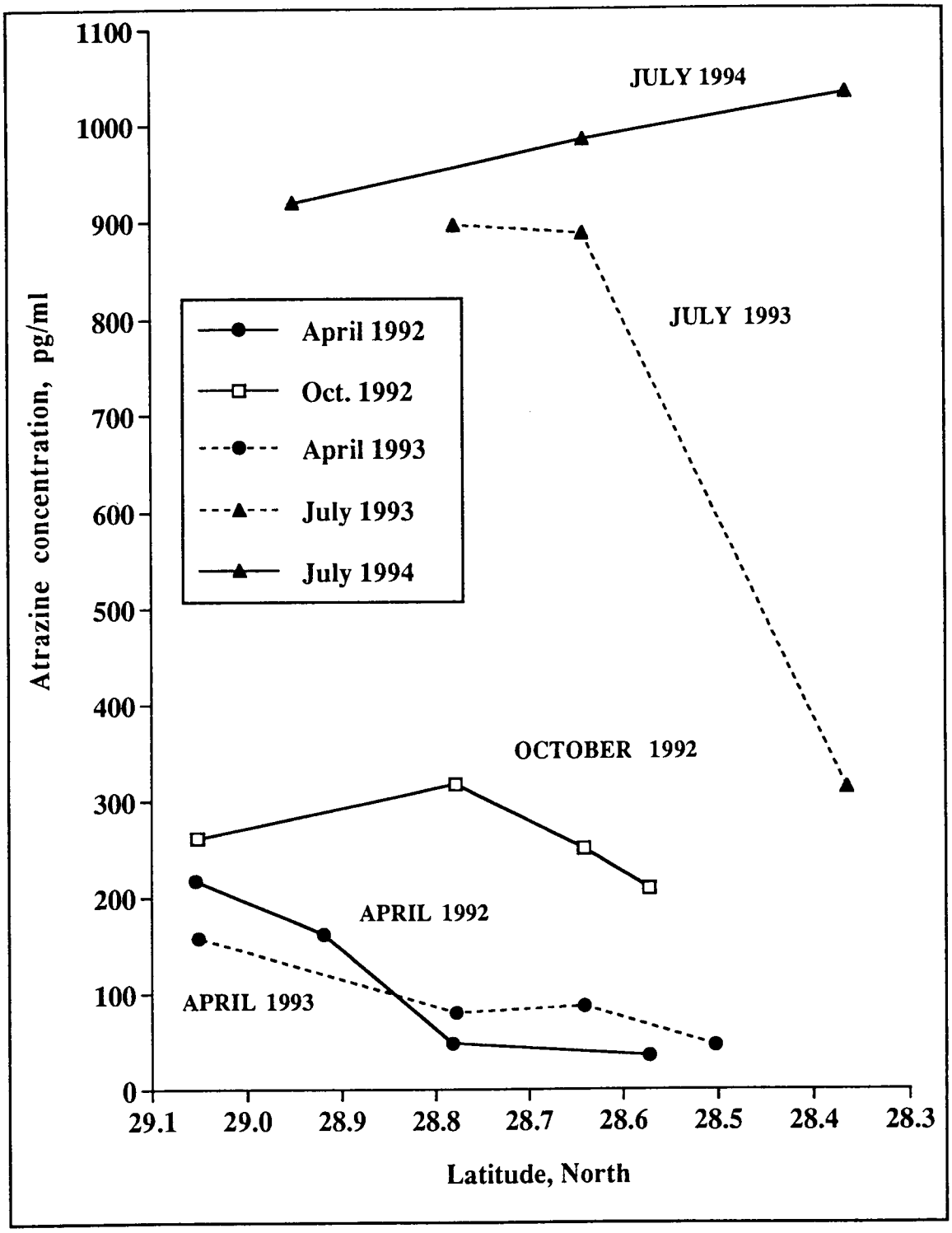

Figure 255. Atrazine concentrations in dissolved phase of water samples from transect S1 for core survey cruises.

exception was the pattern observed in July, 1994, where higher Atrazine concentrations were observed at stations further from shore. Correlation of salinity data to herbicide concentration profiles yields information on the nature of such trends. High discharge volumes during spring flooding lead to more intense salinity gradients, while in early summer, southerly and southeasterly winds push low salinity water easterly and offshore [15]. This appears to allow herbicide concentrations to remain relatively undiluted at further distances from shore as was observed in July, 1994 (Figure 255). Atrazine concentration profiles for the other transects are similar to what is seen in the first transect, especially for April collections. Temporal trends for other herbicides are less clear due to their lower concentrations, but generally show the same trends as noted for Atrazine; highest concentrations in summer samples and at near shore sampling stations.

Spatial Distribution Concentrations of analytes were generally highest near shore along the transects and were inversely correlated with salinity gradients. Contour plots of the data for dissolved phase Atrazine can be found in the appendix. For April data, concentration gradients were seen in surface and bottom samples with maximal concentrations nearshore at ~200 pg/ml in 1992 (Sabine) and ~400 pg/ml (Atchafalaya and Matagorda) in 1993. In contrast, high concentrations, 1500 pg/ml, were observed near the Atchafalaya outlet in summer data with the western area of the Gulf still showing concentrations in the 200 pg/ml range. Figure 256 shows contour plots for surface (a) and bottom (b) samples. Atrazine spatial contour plots for the October data appear similar to surface contours of July data, especially 1993, but with steeper gradients with distance from shore and a westward shift in peak concentrations (at S4) in the contour plot of bottom samples. Generally, the highest concentrations were found at the surface. This is consistent with the observation that more buoyant fresh waters entering the Gulf override more dense saline Gulf waters in the shelf zone. However, this pattern was reversed in the nearshore samples collected in October. Figure 257 shows data for transect S1 for the three seasons examined, while Figure 258 shows the October data for transects S1 through S6. Higher concentrations in bottom compared to surface samples were observed in transects S1, S4, and S6, while for transects S2 and S3, the surface samples showed highest concentrations, and these were at the highest levels found for this sampling period.

Metolachlor spatial contour plots showed highest concentrations for both surface and bottom samples near East Matagorda Bay in Spring data, and in transect S1 in April 1992. Summer contours showed highest pollutants loads near the Atchafalaya, at S3 for 1993 and S1 (surface) and S2 (bottom) for 1994. In October, highest concentrations were at S3 (surface) and S4 (bottom), similar to observations for Atrazine. Maximal bottom concentrations were often observed to the West of the highest surface concentrations. Again, as noted for Atrazine, October bottom concentrations were generally higher than surface samples, and when this trend was reversed, it generally occurred in samples taken nearer to the shore (transects S2 and S3).

Cyanazine contours show highest concentrations (surface and bottom) between S1 and S2 at station 11 in April 1992, and at S4 in 1993. In July, samples, surface concentrations were notably higher compared to the bottom samples and to samples from April collections, and were highest at S1 and S2 in the surface and at S3 in bottom samples. In October, 1992, Cyanazine was detected over a wider spatial range at 58% of sites at concentrations averaging 140 pg/ml, and ranging up to 520 pg/ml. Plots of the October Cyanazine data for transects S1 through S6 differ from the other herbicides (and PAH as well) in that there were only two detections in transects S1 and S2, and highest concentrations were always in surface samples. As with other herbicides, Cyanazine concentrations were highest nearshore in S3. Typical spatial plots for Cyanazine show contours emanating out from the Atchafalaya Bay area.

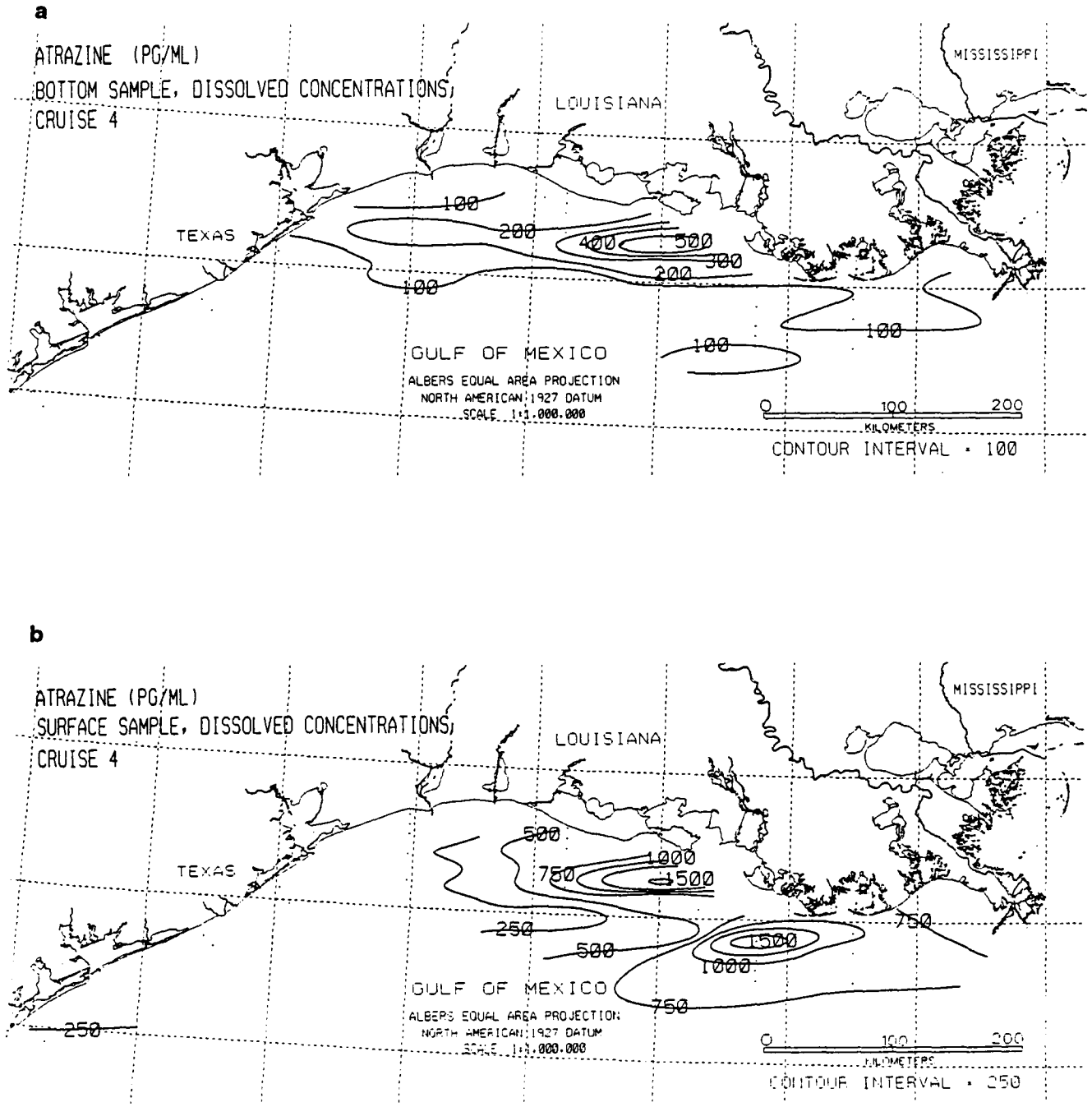

Figure 256. Spatial contours of dissolved phase Atrazine for July 1993 surface (a) and bottom (b) water samples.

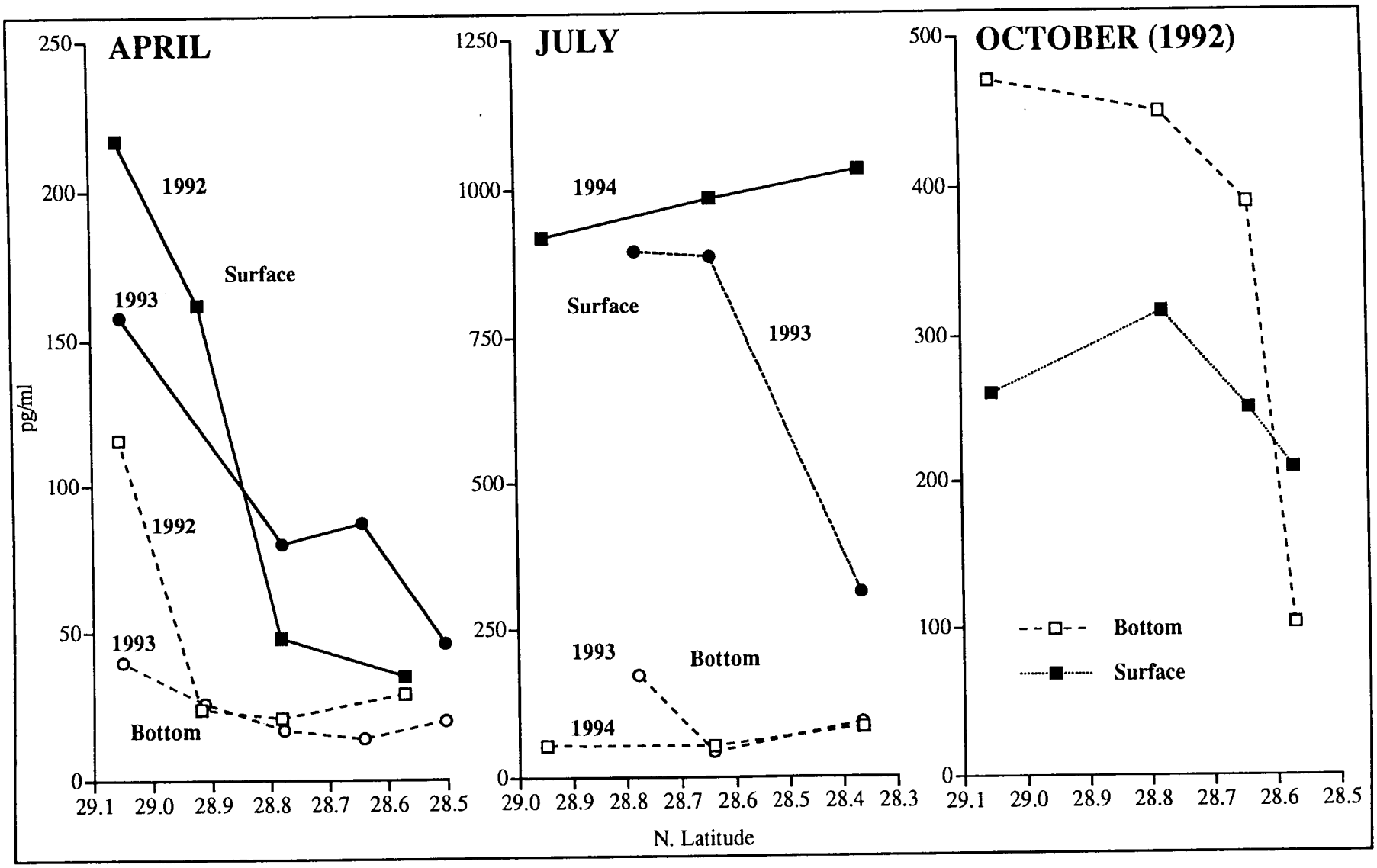

Figure 257. Variation in dissolved phase Atrazine with sample depth for three seasons at transect S1.

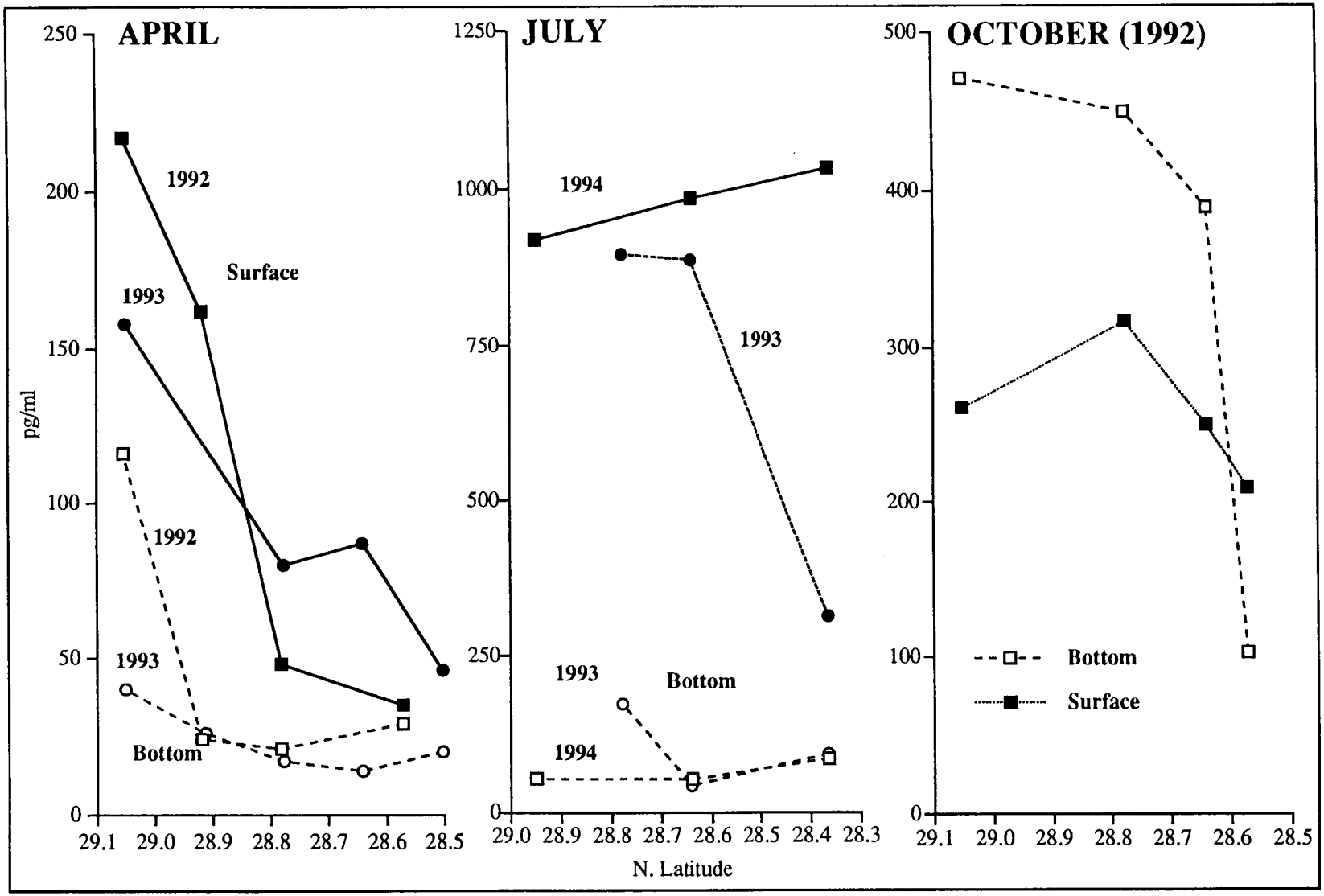

Figure 257 cont'd.

Simazine also tended to be highest near the Atchafalaya estuary (transects S3 and S4) regardless of sampling season, and was detected only at low concentrations in samples west of Sabine Pass. The Timbalier transect (S1) also had low concentrations or no detection of Simazine, except in July samples. These observations lead to the conclusion that the Simazine source is primarily through the Atchafalaya Bay. As a general conclusion, contour plots for the herbicide data show inputs (concentrations gradients and higher concentrations near estuaries) from each estuary in the spring, while during the other seasons the highest pollutant concentrations appear as a broad pool off the Atchafalaya.

From these observations, it appears that the high concentrations in bottom samples may represent older pollution (say July water) with fresh inputs from the Mississippi River discharge plume showing lower pollutant loads (S1 surface), and with additional fresh inputs (higher pollutant loads) coming in at the Atchafalaya Bay area (S2 and S3 surface). Atrazine inputs originating from the Mississippi River enter both through the river outlet and through the Atchafalaya Bay outlet. The latter also drains agricultural areas of western Louisiana and eastern Texas which contribute Atrazine runoff as well. Mass transport of herbicides in the lower Mississippi River was shown to at least quadruple between March-April and May-June samplings in 1989 (Pereira and Rostad, 1990). In the summer, water movement in the Gulf begins to reverse the transport, carrying dissolved components and suspended particulates eastward. As the fresh water is diluted with saline water the dissolved pollutants are carried to greater depths. In the fall, fresh water inputs from the Mississippi River outlet contain low concentrations of herbicide, as this outlet's drainage area is primarily Northern agricultural areas. It appears from our data, although it cannot be determined directly, that the Atchafalaya may contribute high inputs of herbicide pollution due to fall agricultural activities occurring in this southern drainage basin. Herbicide concentrations have not been monitored in the Atchfalaya Basin other than at the Old River diversion site. As a part of this project, samples were collected from the five major Gulf input sources along the LATEX coastline prior to cruise P922 (Table 51). Comparison of the data for dissolved or colloidal Atrazine shows the Atchafalaya River concentration (650 pg/ml) is the second highest of the five sources, second only to the Mississippi River sample (900 pg/ml) taken at Belle Chase. Complicating factors in the interpretation of this data include the observations of variable winds during collection of transects S2 through S4, with steady east-west winds at the remaining transects, as well as the time sequence of sample collection.

While true end-member salinity correlation analysis for the herbicides cannot be performed since samples were not collected in the fresh (zero salinity) portions of each estuary (see Chapter VIII), local dilution trend analysis against salinity can yield information on the conservative or non-conservative behavior of compounds entering and being transported through the coastal shelf current. In general, removal of Atrazine and other herbicides and chlorinated organics show non-conservative trends with respect to simple dilution (estimated from salinity). This suggests that removal processes such as sorption to particulates and subsequent removal by sedimentation and/or microbial degradation are active in the coastal shelf current. Estimates of the depositional flux rates to bedded sediments in the shallow shelf region for refractory compounds such as DDT and its metabolites or PCB congeners may be possible using average sedimentation rates measured during this study corrected for resuspension. For less refractory compounds, such as herbicides, such estimates are not possible since deposition appears to be in the form of metabolites rather parent compounds.

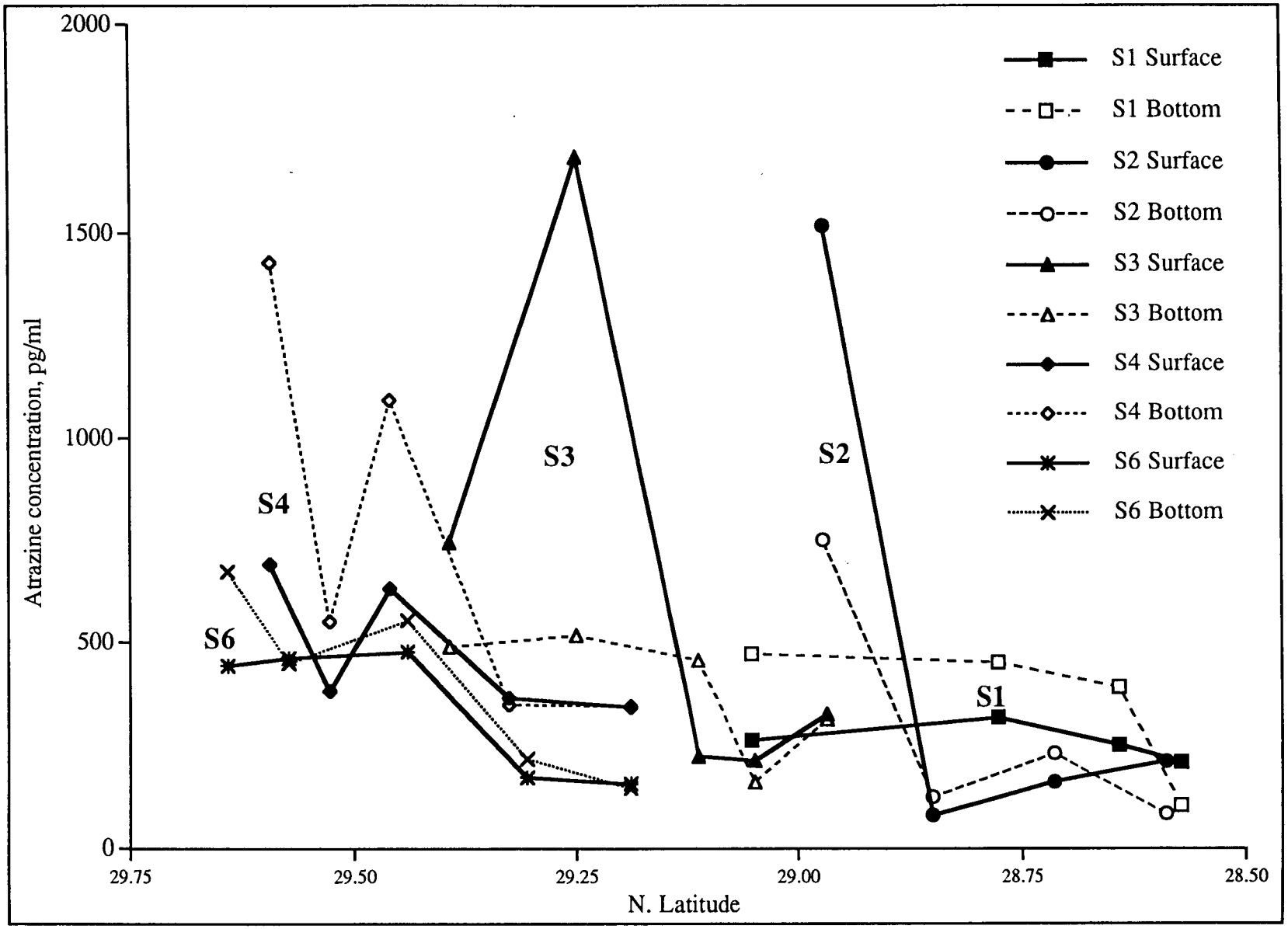

Figure 258. Variation of dissolved phase Atrazine with depth for transects S1-S6 sampled in October 1992.

Spatial contour plots were examined for several of the PAH found in the dissolved phase. Fluorene distributions were relatively uniform, averaging 22 pg/ml for the core survey cruises. Maximal concentrations were observed off the Atchafalaya Bay in mid-transect stations of S3 in October, both surface and bottom (~100 pg/ml), and in surface samples (~60 pg/ml) from July, 1993. Contour plots for 3,9-dimethylphenanthrene, an alkylated PAH associated with uncombusted petroleum products, also showed uniform concentrations, averaging 2.9 pg/ml for the core survey cruises. Samples taken in October show somewhat increased concentrations, averaging 6.2 pg/ml for this cruise, and maximum concentrations were again observed in transect S3 (39 pg/ml) at the surface (station 143) and also in a bottom nearshore sample at transect S6, 66 pg/ml.

Depth Distribution As discussed above, surface concentrations tended to be higher than bottom sample concentrations, and a notable reversal of this trend was observed in the October samples. Cyanazine was almost always found only in the surface samples.

(2) Colloidal Phase Data for the colloidal phase are reported as "pg/ml," reflecting the concentration of the sample containing the colloidal phase. The colloidal phase is actually suspended in an aliquot of the dissolved phase, and total organic carbon analysis is necessary to correct for the actual mass of colloids (along with subtraction of the dissolved phase contribution). The true pollutant concentrations would likely increase dramatically with such correction. For example the current factors for determining final concentration of analytes contain the value 240 (ml volume of sample) in the divisor. This value will be replaced by a much smaller number, the mass of colloids in g, which will most likely be <1g/L, and is expected to vary between samples and with salinity.

Herbicides concentrations tended to be slightly lower in the colloidal compared to the dissolved phase, while PAH were generally higher (Tables 46 and 47). The ratio of colloidal:dissolved concentration was examined for April data, and results shows that herbicides tended to have higher ratios in bottom compared to surface samples. As salinity increases with depth, the more water soluble herbicides may be moving preferentially into the colloidal phase. In contrast, for PAH, surface samples had larger ratios compared to bottom samples, but showed more variability.

Herbicide temporal patterns were similar to that observed for the dissolved phase, except that Alachlor was never detected. The July cruises showed highest mean concentrations (Table 49) for all pollutants, especially alkylated naphthalenes. PCBs were primarily detected during the July cruises, and Hexachlorobenzene, Chlordane, and Nonachlor were only detected in July. Dieldrin was only detected in April 1993.

Colloidal phase Atrazine data shows similar spatial distributions compared to the dissolved phase, however, the trends are less distinct due to higher detection limits. Highest concentrations are consistently observed in transects S3 and S4, similar to that shown in Figure 256. Cyanazine was found in April samples only twice, both at the surface. In July 1993 and 1994, Cyanazine was detected in transects S1 through S3 only, and only in surface samples. October data showed more variability, but highest concentrations again usually occurred in surface samples. For this collection, and in contrast to the other seasons, Cyanazine was detected at the surface beginning in transect S3 and with concentrations decreasing, but still present in all transects to the west. These observations are consistnet with those of the dissolved phase.

July 1993 spatial contours of several PAH, naphthalene, 2-methylnaphthalene and 1,3/1,7-dimethylnaphthalene, show highest concentrations at the south end of transect S6, indicating an offshore oil drilling platform as a likely source. All indicators of petroleum contamination peaked in the bottom sample at this location and were elevated at the surface and also in the sample at the end of transect S7, directly west of this sample. In July 1994 data, high concentrations of alkylated PAH were seen at the southern end of transect S4, with highest concentrations observed at the surface. PCBs were widespread in July 1994, with peak values in transects S3 and S4, and detection in all transects. The pentachlorobiphenyls were most abundant, averaging 71 pg/ml in 31 of 32 samples analyzed. Highest concentrations generally occurred at the surface, with the exception of the nearshore samples at S3 and S4. All classes of pollutants except herbicides showed peak concentrations in S4, notably in the offshore samples (surface and bottom).

(3) Particulate Phase In the first annual report, it was stated that high Naphthalenes concentrations seen in early samples taken on cruise 1 were assumed to be an artifact of sample processing. However, the data for April 1993 also show high concentrations, up to 8000 pg/ml, though the distribution shown for this cruise was more variable. With the exception of October, when high concentrations were noted southwest of Galveston Bay, naphthalene was always highest in transects S1 through S3. Cruise-means for alkylated naphthalenes were approximately one order of magnitude higher in April 1993 compared to April 1992. Concentrations increased offshore beginning in transect S4 in April 1993 and were highest in western transects, while concentrations increased nearshore in 1992 with a more even distribution overall. July data showed alkylated naphthalenes approximately twice the mean values for April 1992, while the October, 1992, data was roughly equivalent. Other alkylated PAH did not show any consistent trends for similar seasons.

Parent PAH were found at lower concentrations and less frequently than the alkylated PAH. Chlorinated pesticides were detected infrequently. Hexachlorobenzene was detected in July samples at nearshore stations of S7 and S8, only in the bottom samples in 1994, and at both depths in 1993. Metolachlor and Cyanazine were detected in 1992 only (April and October), while Trifluralin was detected seven time in 1993 and once in 1994. PCBs were detected in most samples in April 1993, and several times, at highest mean concentrations in July samples. Spatial plots of PCBs for the April 1993 cruise show highest concentrations detected in transect S7, at the station furthest from shore, and with lower concentrations in transects to the east or west. At transect S3 concentrations appear to decrease with distance from shore, while at the other transects (S1, S2, S4, and S6) concentrations appear to increase with distance from shore. As always, concentrations were usually highest in surface samples, and this was true regardless of chlorination level. High mean values for PCBs (CL3-5) were calculated from July 1994 data, although detection frequency was lower than seen in April 1993 and similar to July 1993 (Table 50). High values were found in isolated samples with the exception of surface and bottom detections of CL3 PCBs at two stations in S1.

Data for the particulate phase is more variable and less useful due to higher detection limits arising from the small sample size. Examination of the sample weight, or weight of particulate material collected from 20L of water, shows good agreement with contours produced from reflectance data for the October 1992 cruise. Data for the October cruise show profiles of decreasing particulate concentration with distance from shore. Particulate weights for both April and October 1992 were higher overall than for other cruises, with high particulate loads measured in nearshore samples, especially at S3. Both April cruises showed high values in a single sample near Corpus Christi Bay. July

1993 particulate weights were highest in S2, followed by S1, while July 1994 weights were high nearshore in S7, followed by S3, and S6.

(4) Mass Transport Estimates Mass transport (pollutant flux) was calculated using 10-day smoothed water volume transport values obtained from LATEX A current meters. In estimating pollutant flux, we chose to use the water flux value 5 days prior to the transect chemistry sampling date, to adjust for the approximate time span of the plume. The LATEX A G4 transect was used to estimate pollutant flux for transects S1 and S2, U4 for transects S3 and S4, U3 for transect S6, and U2 for transects S7 and S8. The formula used was:

$$\text{Pollutant Mass transport} = \text{water flux} * \text{pollutant concentration} * 8.64 \times 10^{-5},$$

where mass transport is kg/day, water flux (volume transport) is cu.m/s, and concentration is ng/L [3]. The value 8.64×10^{-5} is a combination of conversion factors for time (seconds to day), mass (ng to kg) and volume (cu.m to L) between water volume transport and pollutant concentration values. This formula was applied to mean concentrations for an entire transect, including both surface and bottom depth samples, and thus represents total transport across a plane defined by the transect, water surface and bottom depth. Particulate data were corrected for the 20 L water sample size, and the calculated mass transport values have units of kg/g/day.

Table 52 shows mean values by cruise date of calculated pollutant mass transport for the dissolved, colloidal, and particulate phases, for herbicides and alkylated PAH totals. For all cruises, the naphthalenes (C0-C4) showed highest pollutant flux values, followed by the herbicides. The particulate phase played a minute role in transport of pollutants compared to the dissolved and colloidal phases. This is primarily a result of the difference in absolute mass between the phases, i.e., the particulate phase represented an average of 0.54g for every 20L of dissolved phase.

For samples taken in April (P921 and P931) or October (P922), the dissolved phase transport was predominant, and transport was to the West (negative values), while for samples taken in July (P932 and P942) transport was higher in the colloidal phase, and transport was to the East. These relationships existed in spite of the fact that the actual transport values varied considerably between years. For example, in 1992, April dissolved phase transport values for the naphthalenes ranged up to around -1000 kg/day, while in April, 1993, the values ranged only up to -180 kg/day (Table 52). The same was true for July, with 1993 colloidal phase transport for naphthalenes ranging up to 4900 kg/day, while 1994 values ranged only up to 230 kg/day. The differences between years for the same seasons are primarily a function of variation in water flux values; the actual concentrations measured in the samples were more consistent between years as was shown previously.

The highest transport values for all pollutants were observed in the October dissolved phase data. For the herbicides, dissolved phase transport was consistently the greatest, regardless of collection date. Herbicide transport peaked in October 1992, with Atrazine at ~8000 kg/day, and Cyanazine, -6000 kg/day. The USGS reported Atrazine mass transport at 2000 kg/day for April, 1992 in the Mississippi River at Belle Chase, LA [3]. Figure 259 shows plots of water flux values used in pollutant mass transport calculations (a), and Atrazine mass transport (b) for all transects. The influence of water flux value can be seen from the similarity of the plots. These plots show that both the greatest movement of water and pollutants occurs in the first two transects. Plots of the other analytes were similar to these two. Differences that were noted between the water

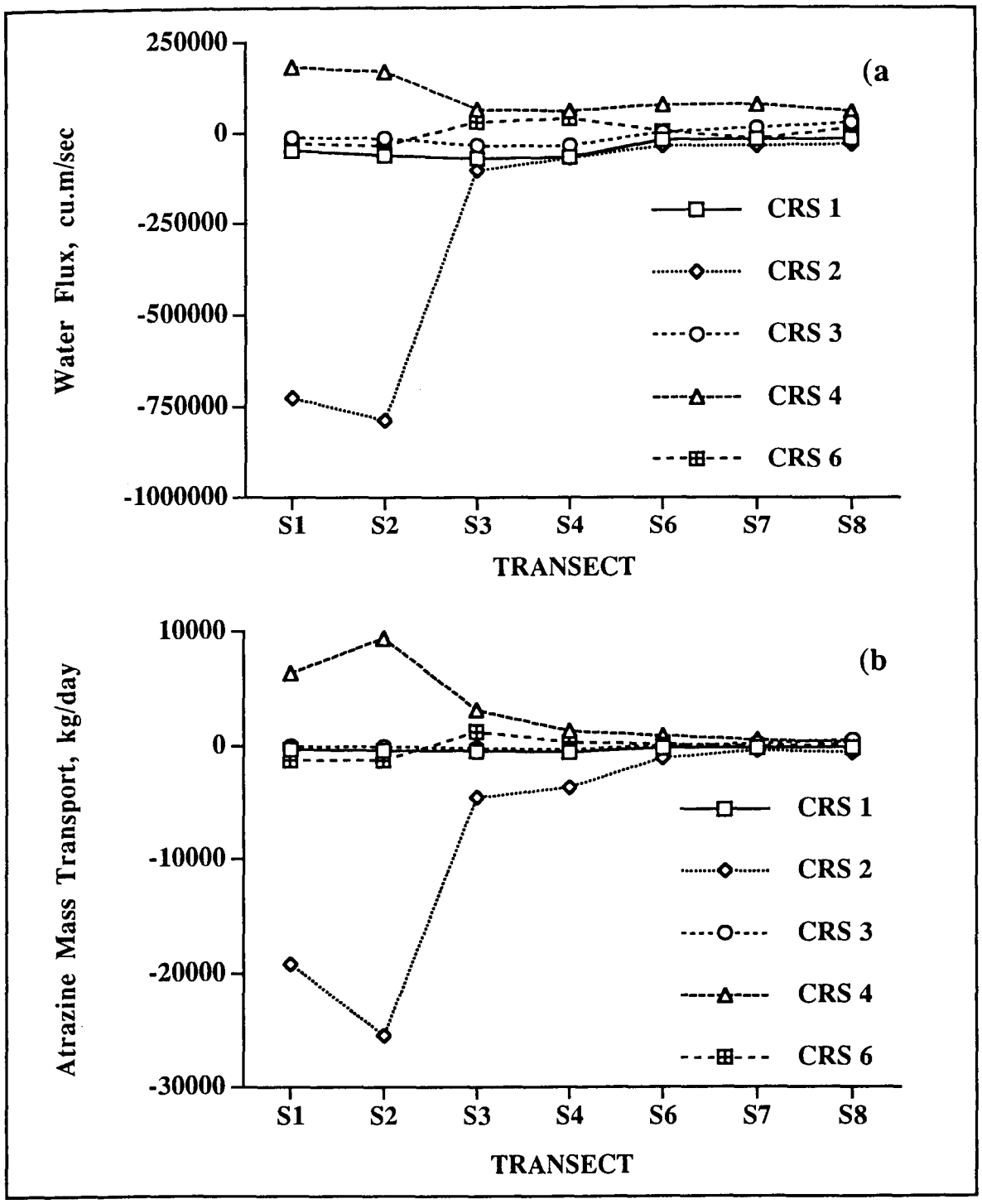

Figure 259. Water flux (a) and dissolved phase Atrazine mass transport (b) for core survey cruises by transect (-values indicate westerly transport).

Table 51. Summary of organic pollutant data for dissolved (pg/ml), colliodal (pg/ml), and particulate (ng/g) phases of river samples, Sept. 29-30, 1992.

	DISSOLVED PHASE							COLLOIDAL PHASE							PARTICULATE PHASE						
ANALYTE	MR BC	MR BR	AMR BR	BATCH	CALC	SAB	GALV	MR BC	MR BR	AMR BR	BATCH	CALC	SAB	GALV	MR BC	MR BR	AMR BR	BATCH	CALC	SAB	GALV
Naphthalene	nd	65	20	nd	nd	nd	nd	nd	nd	nd	nd	4.1	nd	nd	7.7	75	1681	7.8	40	1.2	nd
Hexachlorobutadiene	nd	nd	nd	nd	nd	nd	nd	nd	nd	nd	nd	nd	nd	nd	nd	TR	11	nd	nd	nd	nd
2-MN	nd	230	125	nd	10	nd	15	nd	nd	nd	nd	7.9	nd	3.8	39	79	233	7.8	54	1.0	14
1-MN	3.5	156	81	2.5	3.0	nd	16	nd	nd	nd	nd	7.3	nd	4.0	12	58	143	5.1	30	0.49	9.4
2-EN	nd	66	23	0.50	nd	nd	1.0	nd	nd	nd	nd	3.9	nd	nd	nd	14	32	nd	nd	nd	nd
1-EN	nd	22	7.8	nd	nd	TR	nd	nd	nd	nd	nd	nd	nd	nd	nd	3.9	14	nd	nd	nd	nd
2,6/2,7-DMN	nd	218	73	3.5	2.5	nd	0.50	nd	nd	nd	nd	nd	nd	nd	17	47	120	2.5	29	0.37	1.2
1,3/1,7-DMN	nd	183	73	5.5	0.50	nd	3.0	nd	nd	nd	nd	5.9	nd	2.1	12	29	97	1.9	18	0.28	TR
1,6-DMN	nd	123	48	4.5	1.0	nd	3.0	nd	nd	TR	nd	5.1	nd	0.58	TR	18	70	2.1	16	0.26	TR
1,4/2,3-DMN	nd	79	35	2.0	nd	nd	0.50	nd	nd	nd	nd	nd	nd	TR	nd	15	50	TR	nd	TR	nd
1,5-DMN	nd	72	72	nd	nd	1.5	nd	nd	nd	nd	nd	nd	nd	TR	nd	7.0	36	nd	nd	TR	nd
Acenaphthylene	4.5	3.5	3.5	6.0	4.4	1.4	4.5	nd	nd	nd	nd	nd	nd	nd	nd	4.4	9.0	nd	nd	nd	nd
1,2-DMN	1.8	34	16	3.3	1.8	nd	2.8	nd	nd	nd	nd	nd	nd	nd	nd	5.2	17	nd	nd	nd	nd
2-IPN	10	20	14	7.0	11	nd	nd	nd	nd	nd	nd	53	38	nd	nd	1.2	5.3	nd	nd	nd	nd
1,8-DMN	9.0	nd	nd	7.0	nd	nd	4.8	nd	nd	nd	nd	nd	2.2	nd	nd	nd	2.6	nd	nd	nd	nd
Acenaphthene	3.0	24	14	8.0	3.5	nd	5.0	nd	nd	nd	nd	2.7	nd	nd	nd	6.0	20	nd	nd	nd	nd
1,6,7-TMN	3.0	90	50	12	2.5	nd	3.5	nd	nd	nd	nd	nd	nd	nd	33	9.2	89	nd	nd	nd	nd
Fluorene	7.0	41	30	19	7.0	0.80	9.5	nd	nd	nd	nd	0.43	nd	nd	TR	14	29	TR	nd	TR	TR
Trifluralin	nd	TR	nd	nd	nd	nd	nd	nd	nd	nd	nd	nd	nd	nd	nd	nd	nd	nd	nd	nd	nd
a-BHC	nd	nd	nd	nd	nd	nd	nd	NA	NA	NA	NA	NA	NA	NA	nd	NA	NA	nd	nd	nd	nd
CL2-PCB	nd	nd	nd	nd	nd	nd	nd	nd	nd	nd	nd	nd	nd	nd	nd	nd	nd	nd	nd	nd	nd
Hexachlorobenzene	nd	nd	nd	nd	nd	nd	nd	nd	nd	nd	nd	nd	nd	nd	nd	TR	1.8	nd	nd	nd	nd
Simazine	60	80	60	43	nd	nd	nd	21	33	36	22	11	nd	13	nd	nd	nd	nd	nd	nd	nd
Dibenzothiophene	5.5	25	30	13	7.5	1.9	8.0	nd	nd	TR	TR	nd	nd	nd	TR	3.2	19	nd	TR	nd	nd
b-BHC	nd	nd	nd	nd	nd	nd	nd	NA	NA	NA	NA	NA	NA	NA	nd	NA	NA	nd	nd	nd	nd
Atrazine	900	550	500	650	360	6.0	360	298	220	223	240	142	89	150	nd	nd	nd	TR	nd	nd	nd
Lindane (g-BHC)	nd	nd	nd	nd	nd	nd	nd	NA	NA	NA	NA	NA	NA	NA	nd	NA	NA	nd	nd	nd	nd
Phenanthrene	11	55	60	65	11	nd	26	TR	nd	nd	nd	nd	nd	nd	nd	9.3	62	nd	nd	nd	nd
Anthracene	2.9	4.1	3.9	6.5	7.0	nd	3.9	nd	nd	nd	nd	nd	nd	nd	TR	6.4	7.6	nd	nd	nd	nd
d-BHC	nd	nd	nd	nd	nd	nd	nd	NA	NA	NA	NA	NA	NA	NA	nd	NA	NA	nd	nd	nd	nd
CL3-PCB	nd	nd	nd	nd	nd	nd	nd	nd	nd	nd	nd	nd	nd	nd	nd	nd	nd	nd	nd	nd	nd
4-MDBT	0.45	9.6	8.6	2.6	4.6	0.55	1.4	nd	nd	nd	nd	nd	nd	nd	TR	nd	5.1	TR	TR	nd	nd
2/3-MDBT	2.6	7.5	6.0	3.2	3.3	nd	2.4	nd	nd	nd	nd	nd	nd	nd	nd	0.29	1.7	nd	nd	nd	nd
CL4-PCB	nd	nd	nd	nd	nd	nd	nd	nd	nd	nd	nd	nd	nd	nd	nd	nd	nd	nd	nd	nd	nd
3-MP	0.30	10	9.5	3.0	0.10	nd	0.75	nd	nd	nd	4.4	0.53	nd	nd	nd	nd	nd	TR	nd	nd	nd
1-MDBT	0.95	2.2	2.1	3.1	1.0	nd	0.70	nd	nd	nd	nd	nd	nd	nd	nd	nd	nd	nd	nd	nd	nd
2-MP	nd	9.3	7.8	2.3	nd	nd	0.40	nd	nd	nd	nd	0.076	nd	nd	nd	nd	0.89	TR	nd	nd	nd
Heptachlor	nd	nd	nd	nd	nd	nd	nd	NA	NA	NA	NA	NA	NA	NA	nd	NA	NA	nd	nd	nd	nd
Alachlor	nd	22	22	nd	nd	nd	nd	5.2	9.0	nd	nd	nd	nd	nd	nd	11	8.8	nd	nd	nd	nd
4/9-MP	0.35	6.2	5.7	2.8	nd	nd	nd	nd	nd	nd	nd	1.9	nd	nd	TR	nd	nd	nd	TR	nd	nd
1-MP	nd	nd	4.0	1.4	nd	nd	nd	nd	nd	nd	nd	nd	nd	nd	TR	nd	0.30	nd	TR	nd	nd
Aldrin	nd	nd	nd	nd	nd	nd	nd	NA	NA	NA	NA	NA	NA	NA	nd	NA	NA	nd	nd	nd	nd
Metolachlor	165	215	205	115	18	nd	19	57	79	78	45	8.5	7.0	8.4	nd	8.3	23	TR	nd	nd	nd
Cyanazine	nd	nd	nd	nd	nd	nd	nd	101	nd	nd	13	TR	nd	8.4	nd	nd	181	nd	nd	nd	nd
3,6-DMP	nd	nd	nd	nd	nd	nd	nd	nd	nd	nd	nd	nd	nd	nd	nd	0.71	nd	nd	nd	nd	nd
3,5-DMP	nd	nd	nd	nd	nd	nd	nd	nd	nd	nd	nd	nd	nd	nd	nd	nd	nd	nd	nd	nd	nd
2,6-DMP	nd	nd	nd	nd	nd	nd	nd	nd	nd	nd	nd	nd	nd	nd	nd	2.3	nd	nd	nd	0.054	nd
2,7-DMP	nd	nd	nd	nd	nd	nd	nd	nd	nd	nd	nd	nd	nd	nd	nd	60	58	nd	nd	nd	nd
3,9-DMP	0.60	2.5	2.1	1.2	0.20	nd	0.20	nd	nd	nd	3.2	nd	nd	nd	TR	nd	nd	nd	nd	nd	nd
1,6/2,5/2,9-DMP	nd	1.3	1.1	0.65	0.15	nd	0.30	nd	nd	nd	nd	nd	nd	nd	TR	nd	nd	nd	TR	nd	nd
1,7-DMP	0.70	1.4	1.3	1.2	0.55	nd	0.85	nd	nd	nd	nd	nd	nd	nd	TR	nd	nd	nd	TR	nd	nd

Table 51 cont'd.

	DISSOLVED PHASE							COLLOIDAL PHASE							PARTICULATE PHASE						
ANALYTE	MR BC	MR BRA	MR BRB	ATCH	CALC	SAB	GALV	MR BC	MR BRA	MR BRB	ATCH	CALC	SAB	GALV	MR BC	MR BRA	MR BRB	ATCH	CALC	SAB	GALV
1,9/4,9-DMP	2.6	1.7	2.9	0.60	2.1	nd	0.39	nd	nd	nd	nd	nd	nd	nd	nd	nd	nd	nd	nd	nd	nd
1,2-DMDBT	1.5	0.37	nd	0.90	1.5	nd	1.6	nd	nd	nd	nd	nd	nd	nd	nd	nd	nd	nd	nd	nd	nd
Fluoranthene	0.65	1.8	3.5	2.6	0.60	nd	1.0	TR	1.7	3.8	nd	0.14	nd	nd	57	49	45	nd	108	nd	nd
1,5-DMP	nd	nd	nd	nd	nd	nd	nd	nd	nd	nd	nd	nd	nd	nd	nd	nd	nd	nd	nd	nd	nd
Heptachlor Epoxide	nd	nd	nd	nd	nd	nd	nd	NA	NA	NA	NA	NA	NA	NA	nd	NA	NA	nd	nd	nd	nd
1,8-DMP	nd	nd	nd	nd	nd	nd	nd	nd	nd	nd	nd	nd	nd	nd	nd	nd	nd	nd	nd	nd	nd
1,2-DMP	nd	nd	nd	nd	nd	nd	nd	nd	nd	nd	nd	nd	nd	nd	nd	nd	nd	nd	nd	nd	nd
9,10-DMP	nd	nd	nd	nd	nd	nd	nd	nd	nd	nd	nd	nd	nd	nd	nd	nd	nd	nd	nd	nd	nd
Pyrene	0.65	2.3	2.3	1.9	0.95	0.15	1.0	1.5	3.0	4.2	1.5	0.88	1.1	0.26	nd	39	32	nd	61	nd	nd
o,p'-DDE	nd	nd	nd	nd	nd	nd	nd	nd	nd	nd	nd	nd	nd	nd	nd	nd	nd	nd	nd	nd	nd
Endosulfan I	nd	nd	nd	nd	nd	nd	nd	NA	NA	NA	NA	NA	NA	NA	nd	NA	NA	nd	nd	nd	nd
Chlordane	nd	nd	nd	nd	nd	nd	nd	nd	nd	nd	nd	nd	nd	nd	nd	TR	TR	nd	nd	nd	nd
trans-Nonachlor	nd	nd	nd	nd	nd	nd	nd	nd	nd	nd	nd	nd	nd	nd	nd	TR	TR	nd	nd	nd	nd
CL5-PCB	nd	nd	nd	nd	nd	nd	nd	nd	nd	nd	nd	nd	nd	nd	nd	nd	nd	nd	nd	nd	nd
Dieldrin	nd	nd	nd	nd	nd	nd	nd	nd	nd	nd	nd	nd	nd	nd	nd	nd	nd	nd	nd	nd	nd
p,p'-DDE	nd	nd	nd	nd	nd	nd	nd	nd	nd	nd	nd	nd	nd	nd	nd	nd	nd	nd	nd	nd	nd
o,p'-DDD	nd	nd	nd	nd	nd	nd	nd	nd	nd	nd	nd	nd	nd	nd	nd	nd	nd	nd	nd	nd	nd
CL6-PCB	nd	nd	nd	nd	nd	nd	nd	nd	nd	nd	nd	nd	nd	nd	nd	nd	2.1	nd	nd	nd	nd
Endrin	nd	nd	nd	nd	nd	nd	nd	NA	NA	NA	NA	NA	NA	NA	nd	NA	NA	nd	nd	nd	nd
1,2,8-TMP	0.90	1.0	0.85	1.7	2.4	1.7	1.2	nd	2.5	1.6	1.5	0.59	0.76	1.1	13	9.1	nd	nd	16	0.18	5.9
Endosulfan II	nd	nd	nd	nd	nd	nd	nd	NA	NA	NA	NA	NA	NA	NA	nd	NA	NA	nd	nd	nd	nd
p,p'-DDD/o,p'-DDT	nd	nd	nd	nd	nd	nd	nd	nd	nd	nd	nd	nd	nd	nd	nd	nd	nd	nd	nd	nd	nd
CL7-PCB	nd	nd	nd	nd	nd	nd	nd	nd	nd	nd	nd	nd	nd	nd	nd	nd	nd	nd	nd	nd	nd
Endosulfan sulfate	nd	nd	nd	nd	nd	nd	nd	NA	NA	NA	NA	NA	NA	NA	nd	NA	NA	nd	nd	nd	nd
p,p'-DDT	nd	nd	nd	nd	nd	nd	nd	nd	nd	nd	nd	nd	nd	nd	24	nd	nd	nd	nd	nd	nd
Benzanthracene	nd	nd	nd	nd	nd	0.0050	nd	0.080	1.2	4.4	nd	nd	0.20	nd	36	31	29	nd	26	nd	4.9
Chrysene	4.2	nd	nd	1.2	1.1	0.60	1.1	4.6	3.6	6.9	1.4	0.53	5.8	0.81	50	49	45	nd	43	0.0042	6.5
CL8-PCB	nd	nd	nd	nd	nd	nd	nd	NA	NA	NA	NA	NA	NA	NA	nd	NA	NA	nd	nd	nd	nd
Mirex	nd	nd	nd	nd	nd	nd	nd	NA	NA	NA	NA	NA	NA	NA	nd	NA	NA	nd	nd	nd	nd
Benzo(b)fluor	nd	0.55	1.0	0.19	nd	nd	0.23	TR	9.2	13	nd	nd	TR	nd	299	461	580	0.15	383	nd	31
Benzo(k)fluor	nd	0.37	nd	0.22	nd	nd	nd	TR	nd	nd	nd	nd	nd	nd	nd	nd	nd	nd	nd	nd	nd
Benzo(a)pyrene	nd	nd	nd	nd	nd	0.17	nd	nd	nd	nd	nd	nd	nd	nd	109	188	288	nd	105	nd	8.6
Indenopyrene	nd	nd	nd	nd	nd	nd	nd	nd	nd	TR	nd	nd	nd	nd	TR	207	400	nd	TR	nd	nd
Dibenzanthracene	nd	nd	nd	nd	0.50	0.70	nd	nd	nd	nd	nd	nd	nd	nd	nd	41	148	nd	nd	nd	nd
Benzoperylene	nd	4.0	4.3	nd	nd	nd	nd	nd	nd	TR	nd	nd	nd	nd	nd	2.5	nd	TR	TR	TR	TR
Estimated Totals																					
C1-Naphthalenes	3.5	386	206	2.5	13	nd	31	nd	nd	nd	nd	15	nd	7.7	51	137	375	13	84	1.5	23
C2-Naphthalenes	11	795	346	26	5.8	1.5	16	nd	nd	TR	nd	15	2.2	2.7	30	139	439	6.5	62	0.90	1.2
C3-Naphthalenes	44	737	380	209	87	nd	144	nd	nd	nd	nd	nd	nd	nd	25	107	527	TR	TR	TR	TR
C4-Naphthalenes	5.0	261	175	49	37	nd	nd	nd	nd	nd	nd	nd	nd	nd	nd	71	408	nd	nd	nd	nd
C1-Dibenzothiophenes	4.0	19	17	8.9	8.8	0.55	4.5	nd	nd	nd	nd	nd	nd	nd	TR	0.29	6.7	TR	TR	nd	nd
C2-Dibenzothiophenes	35	23	18	47	37	nd	36	nd	nd	nd	nd	nd	nd	nd	nd	nd	nd	TR	TR	TR	nd
C1-Phenanthrenes	0.65	25	27	9.4	0.10	nd	1.2	nd	nd	nd	4.4	2.5	nd	nd	nd	nd	1.2	TR	nd	nd	nd
C2-Phenanthrenes	3.9	6.7	7.3	3.6	3.0	nd	1.7	nd	nd	nd	3.2	nd	nd	nd	TR	63	58	nd	TR	nd	nd
C3-Phenanthrenes	12	1.0	0.85	8.5	23	1.7	10	nd	nd	nd	nd	nd	nd	nd	nd	nd	5.3	nd	nd	nd	nd

*MR BC-Miss. R.@ Belle Chase; MR BRA, B-Miss. R.@ Baton Rouge; ATCH-Atchafalaya R.@ Morgan City; CALC-Calcasieu R.@ Cameron; SAB-Sabine R.@ Port Athur; GALV-Galveston

Table 52. Total mass transport (kg/day, -=West) averaged over 5 transects for herbicides and alkylated PAH in three phases of water.

CRUISE	P921 April			P931 April			P932 July			P942 July			P922 October		
PHASE	DISS	COLL	PART	DISS	COLL	PART	DISS	COLL	PART	DISS	COLL	PART	DISS	COLL	PART
Analyte	kg/day	kg/day	kg/g/day	kg/day	kg/day	kg/g/day	kg/day	kg/day	kg/g/day	kg/day	kg/day	kg/g/day	kg/day	kg/day	kg/g/day
Herbicides															
Trifluralin	nd	nd	nd	0.4	0.2	0.1	nd	nd	1	nd	-3	-0.5	nd	-30	nd
Simazine	-76	nd	nd	-7	-7	nd	357	212	nd	-13	-7	2	-454	-311	nd
Atrazine	-360	-295	nd	-21	-37	nd	3080	1620	nd	-151	3	nd	-7896	-1967	nd
Alachlor	-127	nd	nd	-5	nd	nd	nd	nd	nd	nd	nd	nd	nd	nd	nd
Metolachlor	-81	-101	-2	-2	-6	nd	225	167	nd	-14	11	nd	-641	-188	-0.8
Cyanazine	-356	nd	-52	-36	-45	nd	1801	2227	nd	-141	-74	nd	-6007	-1014	nd
Alkylated PAH															
C1-Naphthalenes	-986	-97	-26	-181	-37	15	1903	4303	104	28	97	1	-14956	-157	-139
C2-Naphthalenes	-1047	-30	-34	-106	-31	24	3349	4935	204	42	83	5	-13596	-343	-177
C3-Naphthalenes	-359	nd	-24	-67	-8	-7	2334	3414	113	62	127	-4	-5401	-1092	-83
C4-Naphthalenes	-67	nd	-6	-2	nd	-12	805	1818	42	83	228	1	-1003	-109	-27
C1-Dibenzothiophenes	-20	nd	-4	-1	-5	-1	72	224	3	-1	16	-0.3	-325	-15	-5
C2-Dibenzothiophenes	-43	nd	-13	-6	-7	-1	82	465	22	6	25	-7	nd	nd	nd
C1-Phenanthrenes	-14	-100	-7	-5	-33	-1	136	357	9	2	60	nd	-449	-112	nd
C2-Phenanthrenes	-8	nd	-9	-12	-13	-3	48	239	45	7	37	0.1	-259	-31	-10
C3-Phenanthrenes	-30	-119	-11	9	-39	nd	19	130	64	8	15	-3	nd	-289	nd
MEAN WATER FLUX	-42852			-6983			100005			1792			-255640		

flux and pollutant transport plots were 1) for the herbicides, the S2 transect showed the greatest value for July 1993 (Crs 4) and October (Crs 2), 2) C2- and C3-phenanthrenes and C2-Dibenzothiophenes showed increases in transport values at S4 for the October data. This may be an indication of non-river source inputs in this area during this time period.

E. Inorganics

1. Sample Preparation on Ship

The preparation of water and sediment samples was performed as described in section 3a1.

2. Sample Digestion in the Laboratory (on shore)

Sediments: The top 5 cm of sediment from each core was stored at -20°C until sub-sampled for analysis. At the time of sub-sampling, the sediments were thawed, excess water was decanted and the sediments mixed to homogeneity. A 1 g sample of sediment was placed in an acid cleaned teflon digestion bomb and 10 ml of concentrated, high purity nitric acid was added. After sealing, the bombs (10 samples, one reagent blank and one standard reference material [NIST SRM 1645]) were inserted into a rotating, pressure-regulating on curve was prepared with each set of samples analyzed. All sample analyses were performed in triplicate and were reported with means, standard deviations and standard errors. All samples which required dilutions prior to analysis were diluted with ultrapure water containing 3% high purity nitric acid and calculated results were corrected for dilution factors. Typically sediment and particulate samples required dilutions of 20-fold, while dissolved and colloidal samples required dilutions of 10-fold.

a. Particulate Phase

The organic extracted filter membranes, prepared as described above, had 10 ml of concentrated, high purity nitric acid was added to them and were inserted into a rotating, pressure-regulation cassette and placed in a CEM Model 2000 microwave digestion oven for two successive 1 hr digestions. Temperature and pressure within the bombs was regulated automatically by the system to prevent the loss of volatile metals. The resulting digest for each sample was decanted into 50 ml volumetric flask, taken up to volume with ultrapure water and transferred to acid-washed polyethylene bottles until analyzed.

b. Colloidal Phase

A fifteen milliliter aliquot of each enriched colloidal phase sample was acidified to pH <2 and stored at 4°C until analyzed.

c. Dissolved Phase

Acidified ultrafiltrate samples prepared on shipboard were stored in the laboratory at 4°C until analyzed.

3. Instrumental Analysis

All elemental analyses on acidified aqueous samples or acid digests of solid samples were performed on a Fisons Plasmaquad II+ inductively coupled plasma/mass spectrometer system operated in the scanning mode. Element menus were prepared which included one to three stable isotopic forms of the elements selected. All samples were spiked with 50 ppb of Yttrium as an internal standard. Samples were introduced into the ICP/MS after solubilization at a flow rate of 1.0 ml/min. using a Gilson multi-channel peristaltic pump. The samples wre nebulized with a V-groove nebulizer at a flow of 0.91 L/min. of 0.9999% pure argon. Auxiliary gas and cooling gas flow rates of 1.3 and 15 L/min., respectively, were used. The argon plasma was operated at 1350 W. The mass spectrometer was operated under standard conditions: -200 V extraction lens, -2.5 V collector, and the electron multiplier was held at 3000 V in the pulse counting mode and 650 V in the analog mode. The instrument was operated in the dual scanning mode to increase the dynamic range of the system. A mass range of 4 to 240 AMU was scanned at a rate of 47 scans/min.

A five-point, blank corrected and internal standard normalized calibration curve was prepared with each set of samples analyzed. All sample analyses were performed in triplicate and were means, standard deviations and standard errors. All samples which required dilutions prior to analysis were diluted with ultrapure water containing 3% high purity nitric acid and calculated results were corrected for dilution factors. Typically sediment and particulate samples required dilutions of 20-fold, while dissolved and colloidal samples required dilutions of 10-fold.

4. Bedded Sediments

a. Results

Table 53 summarized the results of the determinations of trace elements in sediment samples collected in the regions of the Atachafalaya River, the Calcasieu River, the Sabine River and the Galveston Bay estuaries during Cruise 92-1 in April, 1992. The table presents the means, and ranges of each element measured in these bedded sediment samples. Figures 260 through 265 show the spatial distribution of selected elements in these samples. The metals selected are potential contaminants of concern except for Uranium 238 which is a marker of geochemical erosion processes occurring in the drainage basins of all riverine systems. These data were initially utilized to identify elements being deposited by the individual estuaries.

b. Discussion and Conclusions

Chromium 52 concentrations in bedded sediments show a clear pattern of increasing concentrations at stations nearest the mouths of the estuaries sampled. Peak concentrations were observed off the mouths of the Atchafalaya, the Sabine and Galveston estuaries. Lessor amounts were seen off of the Calcasieu estuary. High concentrations at the southeastern corner of the Atchafalaya box may indicate inputs from the Mississippi River plume. Cu 65 concentrations also showed a pattern consistent with riverine sources with the Sabine river showing the most prominent source pattern. High concentrations were also observed in the northwestern and southeastern portions of the Atchafalaya box (AT box). Cd 111 concentrations were very high off of the Sabine and Calcasieu estuaries and in the northwestern portion of the Atachafalaya box only. The Galveston estuary does not appear to be a source of this metal while the other rivers do. The lack of detectable Cd in the southeastern AT box may mean that Cd entering from the Mississippi River is not reaching these regions of the Gulf. Cd 111 concentrations were 10-20 times the expected geochemical background for this element suggesting long

Table 53. Trace element data for bedded sediments collected during Cruise P921.

Sediment sample #:	12	14	16	17	19	20	21	22	23	25	26	28	30	31	32	33	35	36
Element & isotope	ng/g*	ng/g	ng/g	ng/g	ng/g	ng/g	ng/g	ng/g	ng/g	ng/g	ng/g	ng/g	ng/g	ng/g	ng/g	ng/g	ng/g	ng/g
LITHIUM 7	36,114	24,453	28,451	8,066	7,667	12,171	10,731	43,606	19,302	16,283	9,921	9,852	11,038	13,924	14,673	15,978	15,796	15,437
BERYLLIUM 9	1,408	906	1,019	259	307	538	471	1,908	973	705	497	472	541	722	731	855	766	668
BORON 10	72,613	41,644	48,213	13,203	14,438	25,931	21,137	65,017		30,923	22,673	16,164	16,637		23,495		21,978	18,761
BORON 11	83,068	45,564	53,737	15,302	16,785	29,490	23,899	73,836		35,042	26,063	13,327	14,447		20,092		18,530	17,679
TITANIUM 48	226,204	124,936	175,547	186,485	160,818	152,887	166,876	202,265	62,959	181,474	155,294	63,531	62,926	60,825	73,721	76,696	59,372	64,323
TITANIUM 49	241,343	127,808	183,624	216,707	173,456	180,702	165,887	208,983	51,923	200,500	198,572	36,928	29,884	29,833	37,892	52,712	32,999	34,930
VANADIUM 51	81,147	51,001	60,350	23,343	20,722	28,124	23,907	79,091	16,283	33,510	22,283	11,154	10,801	12,192	15,888	15,119	16,766	15,542
CHROMIUM 52	31,981	20,715	24,047	8,292	7,868	11,769	9,546	33,904	15,987	14,560	9,843	8,275	9,278	12,898	12,054	15,678	12,892	12,204
MANGANESE 55	725,272	513,056	610,422	223,209	342,999	390,075	341,301	1,078,649	389,000	440,107	329,446	219,433	271,897	221,192	333,007	243,035	368,206	351,546
NICKEL 58	166,764	116,082	185,129	71,389	85,047	108,824	97,651	202,322	138,115	139,760	103,372	67,410	76,328	104,877	91,439	115,595	96,197	103,611
COBALT 59	13,543	8,836	10,590	6,369	7,520	8,633	8,613	16,199	8,491	11,638	10,170	5,592	6,390	7,089	6,675	7,119	6,263	6,856
NICKEL 60	34,586	23,010	28,321	13,062	14,666	17,080	17,519	44,498	19,496	22,680	17,406	10,850	12,461	14,630	14,040	15,965	14,699	14,943
ZINC 64	91,480	61,153	72,482	28,615	35,008	40,754	42,378	106,100	55,407	59,261	45,363	34,576	40,652	45,116	47,128	48,758	49,455	49,644
COPPER 65	18,435	13,846	17,541	3,081	2,530	5,368	5,437	28,925	13,528	7,996	3,230	6,335	6,860	8,255	8,053	9,703	9,991	10,234
ZINC 66	99,237	65,060	78,869	30,638	37,991	44,095	45,751	114,856	58,045	63,878	48,964	37,532	43,666	47,403	51,236	49,878	53,237	52,932
ARSENIC 75	5,982	4,694	6,030	3,513	2,896	3,668	3,051	6,717	2,606	3,945	3,131	2,057	2,524	2,404	2,560	2,410	2,342	2,933
SELENIUM 82	1,896	1,272	1,532	562	503	964	855	2,272	633	882	1,063	645	728	395	900	866	847	670
STRONTIUM 88	108,071	67,929	89,117	31,039	46,442	47,950	97,545	105,319	35,214	82,297	37,916	27,638	35,126	44,595	47,759	44,046	37,919	36,186
MOLYBDENUM 95	231	188	225	50	29	67	78	317	tr	139	33	178	172	tr	199	22	181	204
PALLADIUM 106	335	157	141	tr	tr	73	59	304	306	134	105	93	91	330	132	187	137	124
PALLADIUM 108	56	tr	tr	tr	tr	tr	tr	tr	158	tr	tr	51	56	156	54	48	54	71
CADMIUM 111	tr	tr	tr	tr	tr	tr	tr	tr	100	tr	tr	36	48	51	59	20	43	53
CADMIUM 114	tr	tr	tr	tr	tr	tr	tr	29	136	32	tr	28	28	68	33	52	33	37
TIN 118	766	450	565	331	883	248	220	838	445	324	215	261	225	128	415	494	299	342
TIN 120	822	506	600	367	710	283	238	870	445	358	213	257	242	120	361	474	321	324
ANTIMONY 121	tr	tr	tr	tr	tr	tr	tr	tr	tr	tr	tr	14	20	tr	23	tr	13	12
BARIUM 137	1,243,267	867,038	653,835	184,516	148,398	321,096	200,902	485,526	334,003	525,711	102,104	268,423	242,762	488,610	661,264	508,374	454,707	334,355
BARIUM 138	1,287,469	1,023,005	783,824	222,370	180,017	387,322	242,455	581,739	354,118	501,573	121,823	264,427	242,441	510,751	582,712	529,275	498,829	336,059
CERIUM 140	77,835	51,921	68,278	42,985	43,588	51,738	44,530	90,498	40,652	50,862	50,000	23,650	24,926	36,069	28,353	38,267	28,914	29,384
IRIDIUM 191	36	14	14	10	5	8	9	21	5	30	8	10	13	tr	4	tr	14	17
IRIDIUM 193	37	7	8	9	tr	20	1	44	3	9	28	6	7	1	6	tr	5	14
PLATINUM 194	7	tr	tr	tr	tr	tr	tr	tr	tr	10	37	tr	tr	tr	tr	tr	tr	tr
PLATINUM 195	tr	tr	tr	tr	tr	tr	tr	tr	tr	7	tr	tr	tr	tr	tr	tr	tr	tr
GOLD 197	433	27	55	93	43	18	17	37	43	13	7	3	22	21	13	tr	33	50
MERCURY 200	66	11	25	37	17	7	9	30	16	8	4	8	18	11	16	2	25	35
MERCURY 202	68	12	25	37	20	9	9	32	15	5	6	4	15	10	14	5	21	32
THALLIUM 203	563	362	364	40	4	244	216	783	269	299	272	191	181	226	202	250	216	202
THALLIUM 205	405	278	303	24	23	181	168	609	288	263	238	160	172	248	202	252	204	213
LEAD 206	37,782	23,778	28,588	9,794	10,043	15,117	11,510	42,087	20,812	18,310	13,281	10,297	12,719	17,657	15,237	19,998	15,637	14,762
LEAD 208	25,584	15,974	19,434	6,800	6,731	10,181	8,028	28,448	19,200	12,388	9,159	9,286	11,782	16,636	14,298	18,638	14,104	13,565
BISMUTH 209	445	313	390	52	55	153	135	588	263	213	112	120	142	224	167	231	191	192
THORIUM 232	15,939	10,620	13,100	6,347	6,387	8,859	6,452	19,147	7,457	9,693	7,669	4,240	4,582	6,396	5,114	6,478	5,455	5,347
URANIUM 238	2,974	1,861	2,209	851	1,129	1,501	1,387	3,262	797	1,852	1,589	650	875	1,269	842	1,098	707	825

*dry wt. basis

Table 53 cont'd.

Sediment sample #:	37	38	52	53	54	55	56	57	58	59	60	61	62	80	81	82	83	84
Element & Isotope	ng/g	ng/g	ng/g	ng/g	ng/g	ng/g	ng/g	ng/g	ng/g	ng/g	ng/g	ng/g	ng/g	ng/g	ng/g	ng/g	ng/g	ng/g
LITHIUM 7	3,482	6,065	8,883	14,601	11,625	12,447	8,923	6,759	13,484	11,366	6,520	10,401	9,082	24,796	21,992	14,023	9,478	4,515
BERYLLIUM 9	178	302	488	619	622	685	530	427	913	708	417	510	462	1,158	1,175	736	498	290
BORON 10	7,333	10,100	13,333	15,962			26,643	10,544	25,214	26,486	14,422	13,914		26,061				9,250
BORON 11	6,349	8,568	11,235	14,536			43,709	18,789	45,127	46,718	24,949	11,946		23,877				15,646
TITANIUM 48	54,195	63,233	51,689	51,625	55,315	110,559	39,008	31,616	74,252	43,318	58,778	60,508	113,037	67,636	59,417	66,606	59,010	39,412
TITANIUM 49	41,497	44,109	29,444	29,752	44,203	40,403	27,718	20,098	29,301	27,639	41,392	36,719	47,460	46,672	50,960	43,087	31,102	22,760
VANADIUM 51	4,887	7,173	9,464	14,189	10,725	10,372	6,975	5,727	10,715	8,975	5,909	10,806	8,165	26,763	18,382	12,311	8,193	3,908
CHROMIUM 52	3,318	5,032	8,321	14,652	10,888	11,218	8,767	6,441	13,028	10,853	6,958	7,887	8,587	26,098	19,973	12,551	8,508	4,266
MANGANESE 55	177,278	257,330	194,136	273,745	183,124	229,169	256,485	291,313	498,050	415,751	199,940	240,669	147,304	647,783	408,588	222,354	155,120	138,605
NICKEL 58	36,617	58,825	65,508	88,202	91,295	100,446	67,023	54,963	102,479	85,402	56,753	75,118	79,810	147,976	154,841	105,640	77,946	34,805
COBALT 59	4,099	6,001	5,640	6,202	6,248	7,282	4,639	3,634	5,947	5,099	4,206	6,566	6,367	9,845	9,160	7,196	6,203	3,157
NICKEL 60	6,607	9,202	10,275	13,306	12,498	13,932	10,014	7,858	15,063	12,568	8,213	11,433	11,089	20,721	20,945	14,302	10,532	5,589
ZINC 64	19,580	32,462	33,643	43,154	36,821	41,625	40,527	29,726	51,724	44,465	29,985	37,949	32,899	71,255	61,665	44,430	32,567	22,441
COPPER 65	1,213	2,673	5,583	8,488	7,227	8,137	5,329	4,608	9,389	7,351	3,739	5,596	5,185	14,388	14,197	8,483	5,674	2,457
ZINC 66	21,087	34,627	36,017	46,556	37,543	43,715	41,117	29,421	51,299	43,518	28,923	40,596	34,063	77,702	64,743	46,031	34,205	22,050
ARSENIC 75	1,258	1,693	1,931	2,407	1,830	2,317	1,934	1,822	2,474	2,081	1,519	2,393	1,921	4,568	3,119	2,137	1,661	1,187
SELENIUM 82	431	360	598	717	627	872	684	727	1,233	1,162	800	735	528	1,121	951	760	606	571
STRONTIUM 88	22,139	34,998	30,504	34,641	28,789	62,257	21,616	25,135	75,639	31,597	25,329	25,174	99,757	47,268	38,842	45,913	45,599	16,254
MOLYBDENUM 95	65	95	125	140	tr	tr	165	101	178	137	106	139	tr	263	tr	tr	tr	73
PALLADIUM 106	44	69	84	92			115	79	129	105	80	156	212	142	200	235	192	67
PALLADIUM 108	18	35	35	45			48	32	53	41	34	123	105	71	58	120	96	29
CADMIUM 111	6	2	30	43	45	60	68	67	82	53	66	34	46	65	74	52	26	19
CADMIUM 114	8	11	33	40	63	65	76	64	88	67	80	33	58	66	91	71	51	31
TIN 118	86	154	224	332	358	367	366	283	497	448	307	283	251	622	641	408	296	175
TIN 120	98	137	218	358	357	350	375	295	516	471	305	278	252	647	668	415	283	176
ANTIMONY 121	4	18	15	19	tr	tr	26	14	7	9	11	13	tr	36	tr	tr	tr	6
BARIUM 137	53,067	105,462	422,386	386,864	489,253	499,465	260,614	286,550	294,302	262,397	273,683	235,595	202,649	387,193	398,729	429,257	279,492	86,831
BARIUM 138	51,924	103,255	461,859	382,630	508,679	523,609	366,567	461,932	416,971	374,574	387,659	234,623	213,015	383,514	414,236	448,584	293,187	123,051
CERIUM 140	18,530	21,575	23,322	25,243	30,948	33,773	25,289	22,340	34,563	29,265	24,090	25,102	30,307	42,323	45,996	34,775	27,712	16,993
IRIDIUM 191	8	7	7	10	3	tr	23	8	0	2	3	56	1	11	tr	tr	tr	16
IRIDIUM 193	3	2	7	3	8	1	21	6	2	1	1	54	tr	11	tr	tr	tr	16
PLATINUM 194	tr	tr	tr	tr	tr	tr	tr	tr	tr	tr	tr	tr	tr	tr	tr	tr	tr	tr
PLATINUM 195	tr	tr	tr	tr	tr	tr	tr	tr	tr	tr	tr	tr	tr	tr	tr	tr	tr	tr
GOLD 197	3	tr	3	tr	52	32	86	65	8	43	18	28	8	4	tr	1	11	111
MERCURY 200	6	9	8	6	16	11	29	43	17	23	13	7	4	31	2	5	5	59
MERCURY 202	6	6	6	6	20	9	35	44	11	26	11	7	3	38	1	4	5	68
THALLIUM 203	60	88	161	204	204	219	176	114	198	187	136	170	153	287	322	196	153	106
THALLIUM 205	64	89	152	169	212	241	182	123	216	200	152	159	180	273	328	232	180	102
LEAD 206	5,234	7,135	10,036	13,197	13,486	15,503	12,464	10,981	20,666	16,029	9,963	10,877	11,541	24,879	25,176	15,687	11,116	6,234
LEAD 208	4,896	6,480	9,369	12,115	12,373	14,127	10,710	9,468	17,617	13,812	8,433	9,733	10,605	22,771	22,832	14,307	10,337	5,398
BISMUTH 209	33	63	109	153	151	169	152	126	258	207	99	114	117	292	309	185	127	79
THORIUM 232	2,653	3,080	4,057	4,666	5,345	5,706	4,312	4,344	6,621	5,456	3,950	4,248	4,205	7,760	8,164	5,797	4,323	2,584
URANIUM 238	341	424	639	578	683	855	622	407	652	562	503	706	779	900	898	794	636	412

Table 53 cont'd.

Sediment sample #:	85	87	88	89	90	93	94	95	96	97	98	99	100	101	102
Element & Isotope	ng/g	ng/g	ng/g	ng/g	ng/g	ng/g	ng/g	ng/g	ng/g	ng/g	ng/g	ng/g	ng/g	ng/g	ng/g
LITHIUM 7	4,165	6,068	6,858	6,991	7,594	7,190	5,603	9,448	8,939	11,805	542	7,626	11,498	7,800	7,761
BERYLLIUM 9	258	401	407	417	322	299	254	395	356	482	34	451	479	310	305
BORON 10	8,413	10,374	12,408	14,652	9,854	8,670	8,820	13,376	11,981	18,401	2,917		15,541	11,007	11,896
BORON 11	15,736	18,735	20,651	25,643	11,789	10,238	10,609	15,386	14,112	21,581	3,906		18,083	13,083	13,943
TITANIUM 48	37,175	34,973	34,261	75,354	43,405	28,860	38,984	41,516	38,800	55,131	64,205	53,510	46,183	37,151	47,882
TITANIUM 49	20,529	22,596	23,690	24,094	19,604	18,074	20,188	29,121	24,706	40,158	6,678	27,457	29,261	24,753	32,876
VANADIUM 51	3,477	4,676	5,862	5,849	5,256	5,234	4,116	6,913	6,028	9,279	670	6,871	8,543	5,546	5,964
CHROMIUM 52	4,621	5,984	6,896	6,916	11,387	15,266	9,123	14,408	13,294	18,826	1,059	7,082	17,482	11,988	12,184
MANGANESE 55	133,829	181,998	198,618	185,704	143,257	125,949	105,121	151,641	141,251	215,435	92,901	178,900	239,857	119,344	116,368
NICKEL 58	37,210	49,208	59,366	54,887	50,898	48,653	40,820	59,790	58,165	73,198	7,769	60,899	71,759	51,449	50,619
COBALT 59	3,230	3,766	4,012	3,957	5,971	5,890	5,380	6,678	6,815	7,450	1,515	4,502	7,210	6,451	6,223
NICKEL 60	5,583	7,798	8,084	7,962	7,630	7,159	5,952	8,722	8,562	10,514	1,197	7,663	10,126	7,557	7,434
ZINC 64	19,300	25,648	31,056	29,492	21,758	27,982	17,506	24,592	24,252	28,670	3,325	24,195	28,096	21,906	21,063
COPPER 65	2,339	3,881	4,142	4,067	5,457	4,759	3,989	6,017	5,758	7,309	327	4,593	7,299	4,780	4,551
ZINC 66	18,713	25,021	30,185	29,160	22,308	29,055	18,027	25,232	24,780	29,530	3,396	24,958	29,213	22,376	21,805
ARSENIC 75	1,036	1,411	1,598	1,481	1,815	2,274	1,672	2,313	2,226	2,612	569	1,159	2,662	1,757	1,865
SELENIUM 82	539	591	813	699	791	532	687	945	964	1,206	352	451	888	813	902
STRONTIUM 88	22,395	16,620	19,608	72,731	27,719	14,894	20,779	18,745	18,883	24,372	57,282	40,114	25,195	16,376	17,714
MOLYBDENUM 95	69	101	119	150	139	101	74	134	121	109	15	tr	163	70	77
PALLADIUM 106	50	65	79	79	2	tr	tr	82	tr	76	tr	102	51	tr	tr
PALLADIUM 108	19	26	33	33	tr	tr	tr	tr	tr	tr	tr	33	tr	tr	tr
CADMIUM 111	16	43	44	37	tr	tr	tr	tr	tr	tr	tr	12	tr	tr	tr
CADMIUM 114	24	45	48	47	tr	tr	tr	tr	tr	tr	tr	34	tr	tr	tr
TIN 118	156	232	274	279	158	148	133	209	189	284	4	634	271	168	169
TIN 120	149	225	269	277	253	232	218	365	315	488	4	619	436	296	284
ANTIMONY 121	8	6	6	6	tr	tr	tr	tr	tr	tr	tr	tr	tr	tr	tr
BARIUM 137	153,287	115,224	212,984	136,763	212,355	157,663	123,978	172,058	197,682	240,296	17,957	143,737	224,281	171,023	208,186
BARIUM 138	218,637	164,329	302,307	192,929	269,004	198,787	158,102	218,712	253,114	306,668	22,129	149,945	284,486	219,159	265,440
CERIUM 140	17,290	20,542	24,875	22,477	30,135	30,012	27,101	35,226	36,288	43,064	13,029	23,598	41,982	34,017	31,947
IRIDIUM 191	2	tr	4	2	tr	92	tr	tr	tr	tr	tr	tr	19	tr	tr
IRIDIUM 193	tr	tr	1	1	tr	80	tr	tr	tr	tr	tr	tr	tr	tr	tr
PLATINUM 194	tr	tr	tr	tr	tr	tr	tr	tr	tr	tr	tr	tr	tr	tr	tr
PLATINUM 195	tr	tr	tr	tr	tr	tr	tr	tr	tr	tr	tr	tr	tr	tr	tr
GOLD 197	tr	tr	7	16	20	56	4	14	11	10	7	1	38	7	12
MERCURY 200	5	8	13	8	tr	375	tr	tr	tr	tr	tr	6	tr	tr	tr
MERCURY 202	6	10	10	14	tr	304	tr	tr	tr	tr	tr	4	tr	tr	tr
THALLIUM 203	80	114	113	119	tr	tr	tr	tr	tr	tr	tr	118	tr	tr	tr
THALLIUM 205	93	122	126	133	tr	tr	tr	tr	tr	10	tr	145	tr	tr	1
LEAD 206	6,391	9,042	9,985	9,520	7,137	25,744	5,635	8,186	8,407	9,968	1,632	10,180	10,090	7,068	6,654
LEAD 208	5,459	7,809	8,601	8,155	6,710	24,065	5,041	7,619	7,641	9,206	1,343	9,327	9,106	6,622	6,227
BISMUTH 209	66	108	113	112	59	67	32	62	54	101	tr	121	89	54	50
THORIUM 232	2,542	3,411	3,529	3,526	3,405	3,486	2,871	3,976	4,281	5,222	632	3,391	4,849	3,707	3,573
URANIUM 238	387	501	514	505	427	456	422	476	544	527	90	439	443	412	443

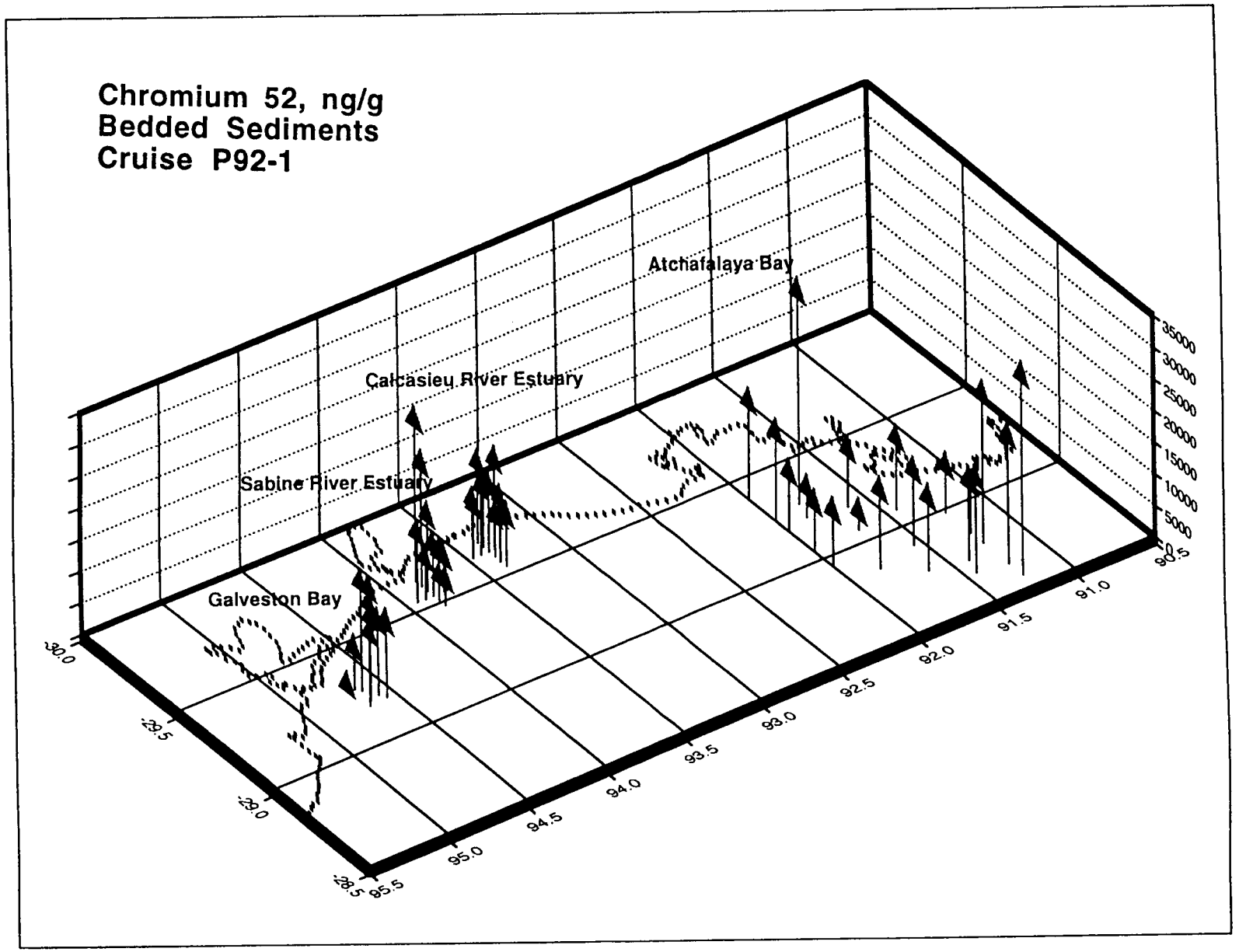

Figure 260. Spatial distribution of Chromium 52 (ng/g) in bedded coastal sediments in the northwestern Gulf of Mexico.

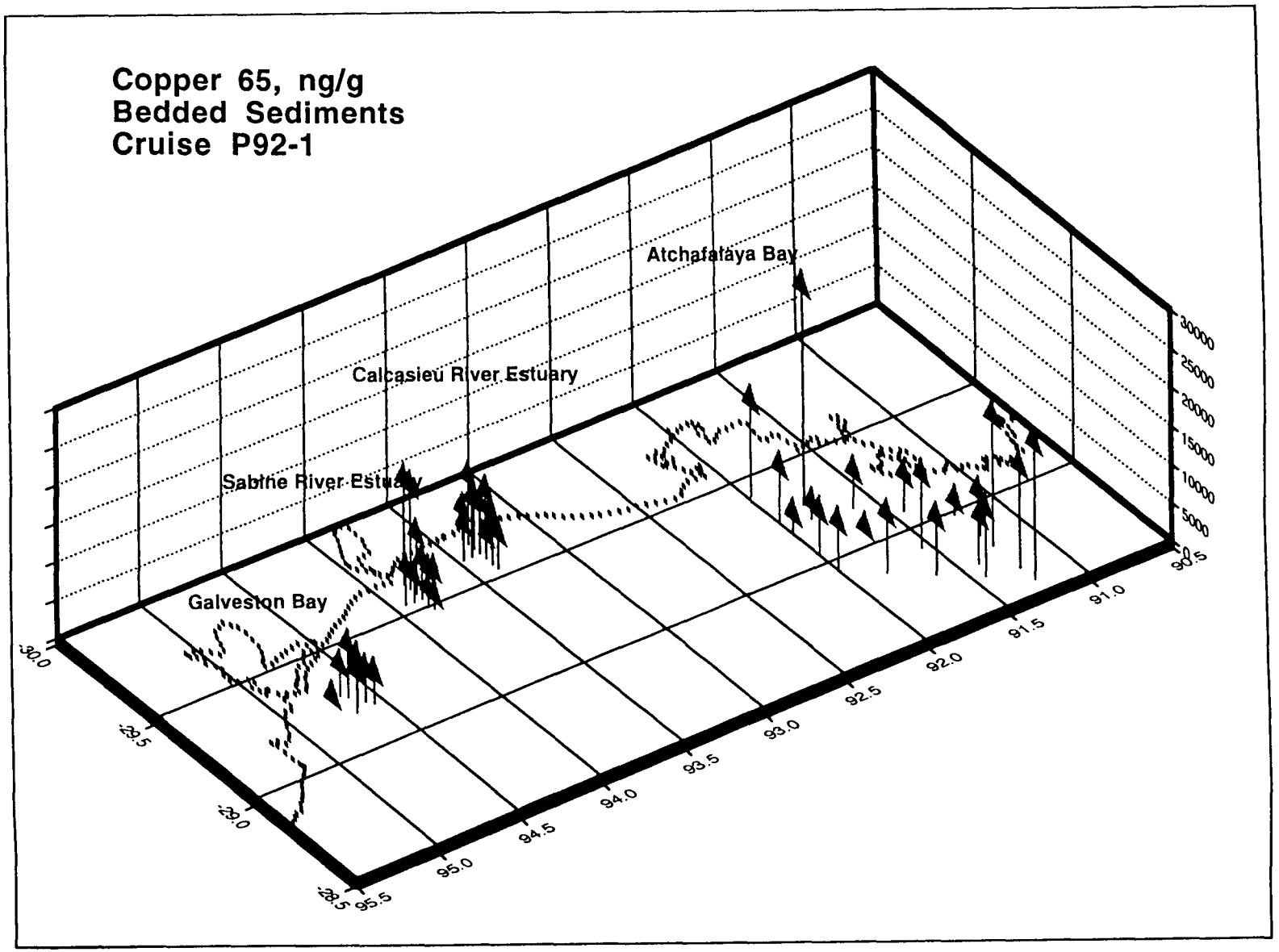

Figure 261. Spatial distribution of Copper 65 (ng/g) in bedded coastal sediments in the northwestern Gulf of Mexico.

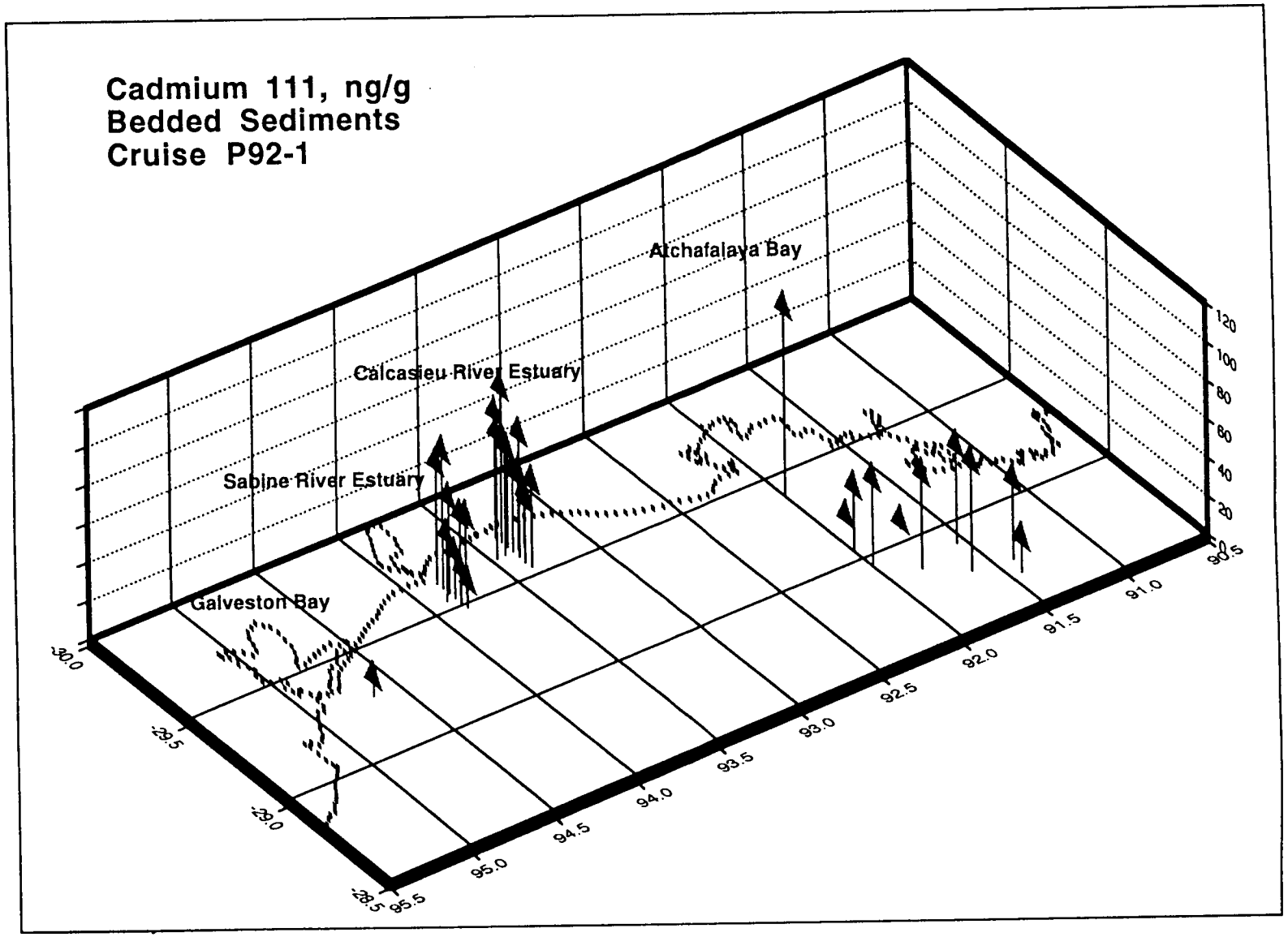

Figure 262. Spatial distribution of Cadmium 111 (ng/g) in bedded coastal sediments in the northwestern Gulf of Mexico.

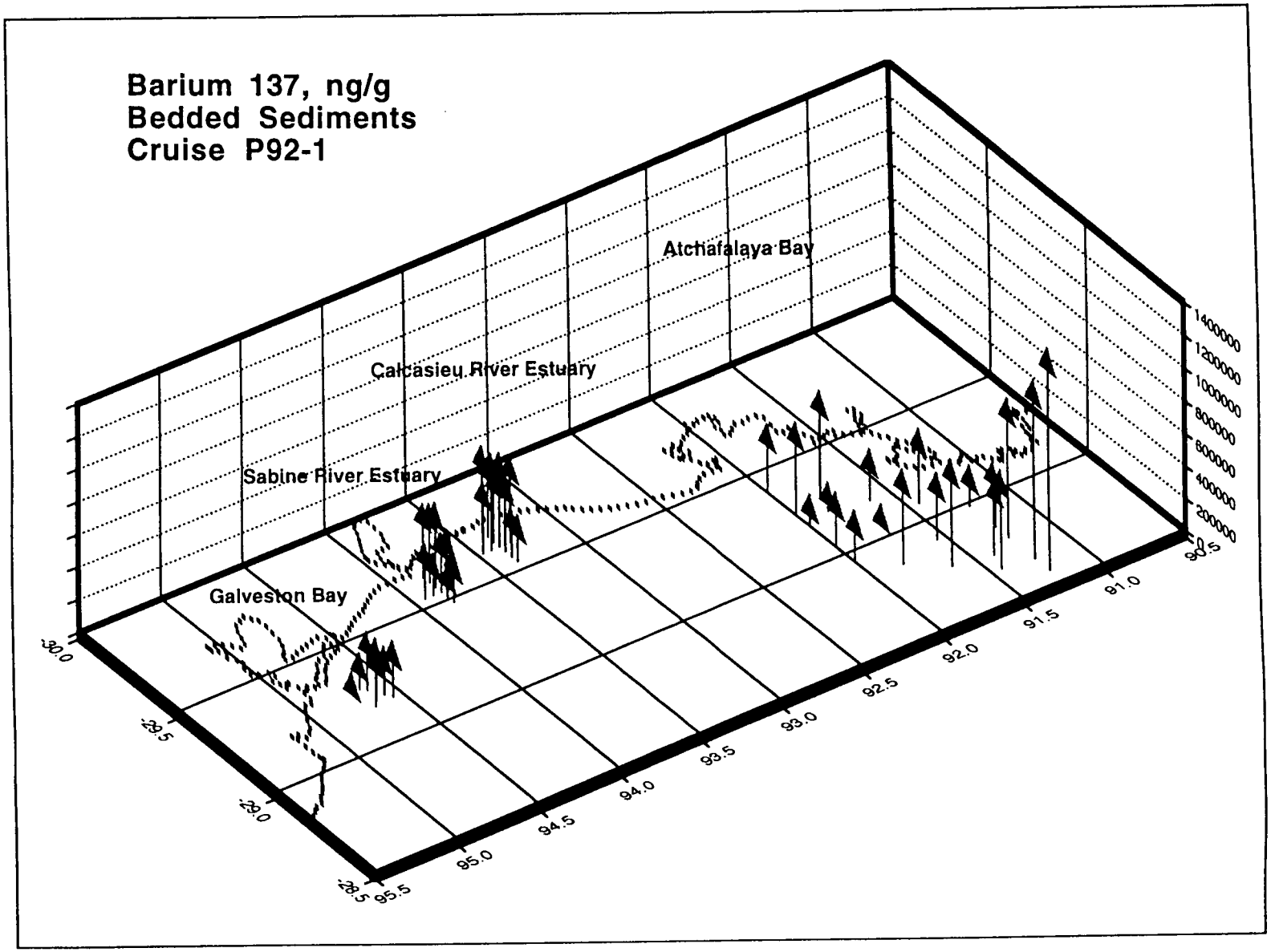

Figure 263. Spatial distribution of Barium 137 (ng/g) in bedded coastal sediments in the northwestern Gulf of Mexico.

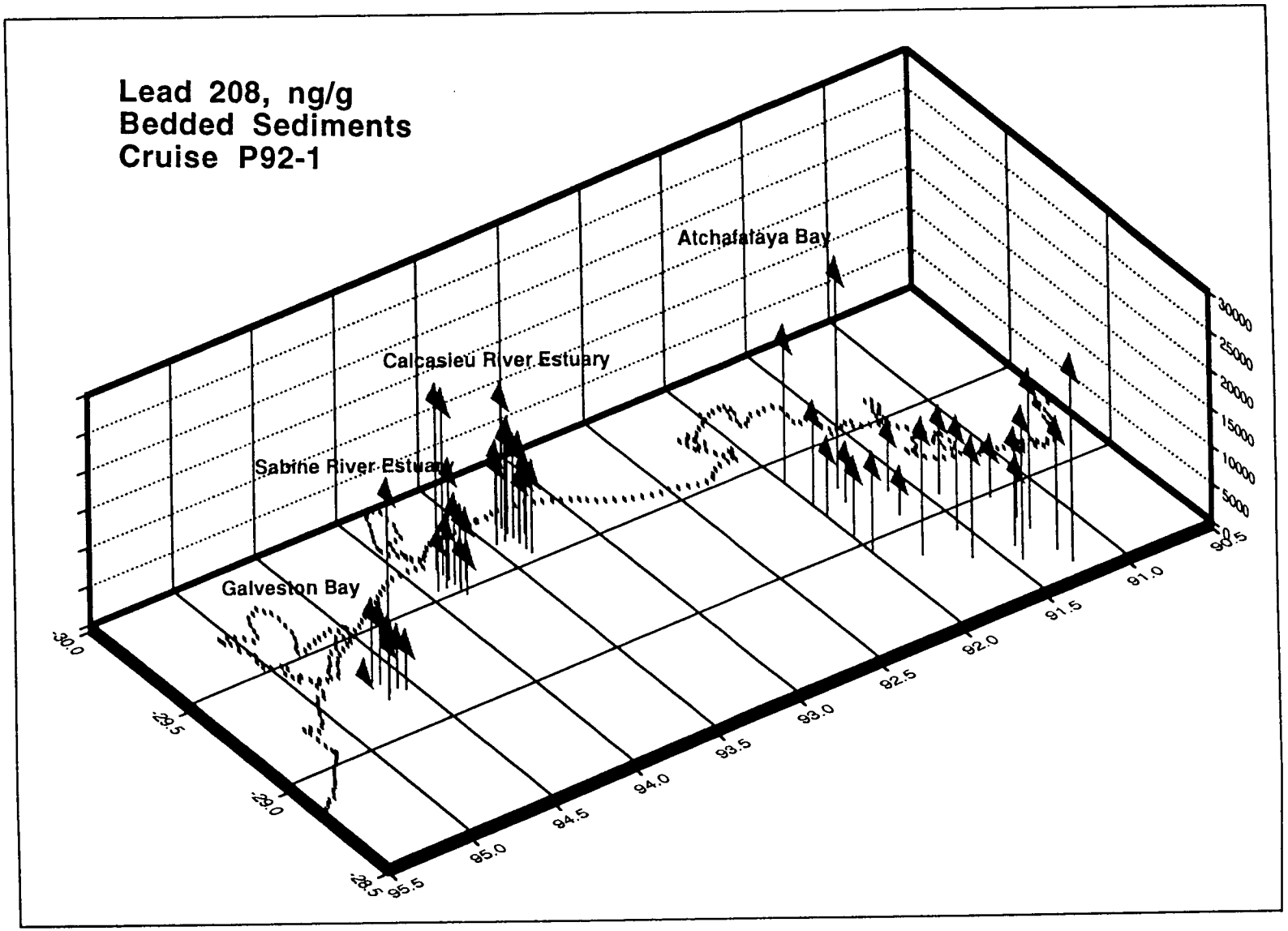

Figure 264. Spatial distribution of Lead 208 (ng/g) in bedded coastal sediments in the northwestern Gulf of Mexico.

term contamination in some regions. Barium 137 levels in the sediments showed the highest values near the southeastern portion of the AT box, suggesting a source to the east, probably the Mississippi River. All other estuaries showed some weak sources component but concentrations were not out of the range of normal marine sediments. Lead 208 concentrations were highest off the mouths of all of the estuaries sampled. There is a clear source pattern associated with the Sabine, Calcasieu and AT box. The Galveston site shows a very high value off the estuary at a site were based upon data from organic measurements and other metals, we concluded that this area had been a dredge spoil depository. High Lead 208 values at the northwestern and southeastern corners of the AT box suggest that lead is entering this region both from the Atchafalaya River and the Mississippi River plume. U 238 concentrations in sediments were very high in the northwestern and southeastern AT box relative to all other estuaries. These data reflect the inputs from upstream erosional processes in an estuary and thus are consistent with the size of the discharge and the area in the drainage basin. The pattern of concentrations observed in the AT box suggest that inputs of particulates from the Atachafalaya and the Mississippi River are dominant in this region of the coastal Gulf of Mexico.

From the data obtained on these samples, we can conclude that there are measurable and traceable inputs of particulate materials from each of the estuaries sampled, and that our analytical methodology is capable of resolving such input patterns. Significant input of contaminant trace elements such as lead, cadmium and mercury are entering the Gulf of Mexico from riverine sources.

5. Dissolved Phase

Trace elements were determined in the truly dissolved phase of waters at two depths in the Northwestern Gulf of Mexico. The samples analyzed had had the suspended particulates removed as well as the microparticulate (>1 nm) colloidal material removed. This allowed for determination of true solution concentrations and modeling of transport processes in that phase independent from interfering particulates which were analyzed and modeled separately.

a. Results

Table 54 presents a summary of mean concentrations, ranges and frequencies of detection for each element in the dissolved phase for each cruise in the study. Figures 266-271 show selected spatial distribution plots of trace elements of concern in the Gulf of Mexico.

b. Discussion and Conclusions

Dissolved trace elements were found at detectable levels in most samples in waters of the Gulf of Mexico. Concentrations ranged from a few ppb (ng/ml) for elements like Cd and Pd to ppm concentrations for Ba and Sr. Spatial distribution plots demonstrate that most elements are distributed throughout the coastal current region. Elements such as Cu, Cd, Pb and Ba show a consistent tendency to exhibit higher concentrations near shore than at off-shore stations, while Sr concentrations in the dissolved phase appear to be fairly consistent over large areas of the NW Gulf. Ba and Cd in particular shows the highest levels just of the mouths of the Atchafalaya, Sabine and Calcasieu estuaries. This is somewhat different than the patterns of dissolved concentrations observed in the near-field Mississippi River plume (discussed later in this report) where dissolved trace element concentrations were lowest in fresher water and higher in more saline sites. This difference may reflect different chemistries of the

Table 54. Dissolved phase trace element summary.

	Cruise 1: April 1992			Cruise 2: October 1992			Cruise 3: April 1993		
	Mean	Min	Max	Mean	Min	Max	Mean	Min	Max
Isotope	µg/L	µg/L	µg/L	µg/L	µg/L	µg/L	µg/L	µg/L	µg/L
Li 7	243.91	50.52	681.71	118.90	44.75	210.98	161.58	76.73	230.04
Be 9	2.21	0.00	129.17	0.61	0.00	3.74	0.80	0.00	1.59
B 10	6810.10	1246.50	27645.25	1180.38	0.00	3304.51	1989.81	1055.40	3877.64
B 11	7842.96	1546.80	32161.77	1223.48	0.00	3378.17	2046.49	1039.80	4293.99
Al 27	51.14	0.00	843.54	10.70	0.00	95.98			
Si 28	1317.71	0.00	9488.99	0.00	0.00	0.00			
Ti 48	2450.17	537.23	6186.69	1223.83	586.98	3483.23	1525.58	697.63	2300.94
Ti 49	184.38	22.12	835.59	73.50	25.13	137.10	111.14	44.40	163.00
V 51	386.04	9.67	2370.96	11.49	0.00	48.03	1.55	0.00	9.02
Cr 52	23.52	1.23	128.96	11.49	0.00	27.54	9.50	0.00	31.57
Mn 55	9.91	0.00	91.69	3.17	0.29	10.93	2.68	0.00	32.92
Ni 58	8.67	0.00	343.32	4.83	0.00	24.37	11.01	0.00	59.20
Co 59	2.58	0.00	45.57	1.04	0.22	2.35	1.49	0.60	2.41
Ni 60	14.40	0.00	326.78	5.26	0.00	22.09	12.87	0.00	65.20
Zn 64	59.24	0.00	2473.48	176.92	0.00	467.38	259.97	14.33	1248.57
Cu 65	14.79	0.00	378.36	13.84	0.00	38.84	18.02	3.40	50.84
Zn 66	10.67	0.00	357.05	148.91	0.00	435.95	22.67	0.00	107.60
As 75	215.69	1.29	6952.64	138.52	77.56	214.75	98.58	8.48	215.88
Se 82	3681.12	340.63	24928.40	534.87	283.47	838.02	387.85	138.98	623.76
Sr 88	12465.68	16.87	35699.62	9100.08	3237.13	14095.67	6388.99	2863.27	8421.04
Mo 95	45.01	2.03	171.37	11.76	5.19	16.42	11.65	5.80	14.80
Pd 106	0.40	0.00	4.74	0.46	0.00	6.29	0.89	0.00	2.78
Pd 108	1.39	0.00	6.05	1.26	0.00	7.84	2.27	0.80	6.28
Cd 111	3.40	0.00	173.59	0.68	0.00	2.19	0.76	0.12	1.86
Cd 114	1.44	0.00	49.86	0.48	0.00	5.00			
Sn 118	1.15	0.00	42.31	2.84	0.00	157.96	0.64	0.00	3.46
Sn 120	1.06	0.00	34.55	2.73	0.00	151.66	0.58	0.00	3.15
Sb 121	1.86	0.00	39.16	0.42	0.07	1.10	0.74	0.00	2.82
Ba 137	93.02	7.25	431.46	36.23	7.90	77.37	21.59	6.60	49.69
Ba 138	90.95	2.90	442.11	36.47	7.88	74.93	21.39	6.80	48.61
Ce 140	0.18	0.00	5.09	0.12	0.00	0.45	0.07	0.00	0.40
Ir 191	1.69	0.00	46.51	0.09	0.00	0.58	0.23	0.00	0.63
Ir 193	1.20	0.00	18.59	0.07	0.00	0.49	0.15	0.00	0.42
Pt 194	0.25	0.00	7.31	0.17	0.00	1.92	0.14	0.00	0.46
Pt 195	0.31	0.00	7.80	0.27	0.00	0.99	0.14	0.00	0.49
Au 197	17.28	0.00	432.20	2.77	0.00	98.34	2.20	0.40	20.93
Hg 200	3.71	0.00	150.05	0.71	0.00	5.71	1.46	0.00	8.67
Hg 202	2.41	0.00	73.64	0.48	0.00	3.26	1.63	0.00	6.82
Tl 203	0.31	0.00	4.67	0.39	0.05	1.19	0.30	0.00	0.85
Tl 205	0.37	0.00	10.98	0.18	0.00	1.16	0.15	0.00	0.35
Pb 206	3.12	0.00	56.63	11.62	0.00	507.14	1.41	0.00	44.80
Pb 208	2.61	0.00	30.69	10.12	0.00	437.14	1.30	0.00	41.20
Bi 209	0.53	0.00	15.19	0.17	0.00	0.68	0.10	0.00	0.32
Ra 226	0.59	0.00	39.92	0.00	0.00	0.00			
Th 232	0.24	0.00	5.25	0.22	0.00	0.86	0.11	0.00	0.35
U 238	2.20	0.00	10.18	4.07	0.97	9.60	1.87	0.31	3.28

Table 54 cont'd.

	Cruise 4: July 1993			Cruise 6: July 1994			Summary of All Cruises		
	Mean	Min	Max	Mean	Min	Max	Mean	Min	Max
Isotope	µg/L	µg/L	µg/L	µg/L	µg/L	µg/L	µg/L	µg/L	µg/L
Li 7	127.18	0.00	232.31	103.44	46.11	163.90	151.00	0.00	681.71
Be 9	0.26	0.00	1.01	0.16	0.00	0.40	0.81	0.00	129.17
B 10	1766.24	0.00	3003.57	1798.15	879.13	2709.63	2708.94	0.00	27645.25
B 11	1808.75	0.00	3048.73	1921.56	915.41	3022.15	2968.65	0.00	32161.77
Al 27	1336.79	0.00	1952.92				466.21	0.00	1952.92
Si 28	81.51	0.00	135.34				466.41	0.00	9488.99
Ti 48	2.86	0.00	9.19	1475.76	661.41	1926.81	1335.64	0.00	6186.69
Ti 49	9.49	0.00	19.64	54.91	26.39	98.64	86.68	0.00	835.59
V 51	17.73	0.00	379.52	3.77	0.95	7.28	84.12	0.00	2370.96
Cr 52	26.09	0.00	141.27	6.11	0.00	12.66	15.34	0.00	141.27
Mn 55	1.25	0.00	2.14	6.62	1.49	80.58	4.73	0.00	91.69
Ni 58	25.04	0.00	135.15	35.34	0.00	76.17	16.98	0.00	343.32
Co 59	823.60	0.00	12337.84	1.15	0.56	1.68	165.97	0.00	12337.84
Ni 60	22.01	0.00	64.37	31.29	1.83	66.25	17.17	0.00	326.78
Zn 64	23.36	0.00	91.20	597.09	0.00	3441.99	223.32	0.00	3441.99
Cu 65	87.54	0.00	417.73	17.29	0.00	72.07	30.30	0.00	417.73
Zn 66	325.41	0.00	661.87	219.24	0.00	2242.84	145.38	0.00	2242.84
As 75	5604.29	0.00	7922.97	66.73	27.19	108.01	1224.76	0.00	7922.97
Se 82	10.67	0.00	19.19	267.09	128.83	419.39	976.32	0.00	24928.40
Sr 88	0.39	0.00	2.47	5304.80	2892.89	7942.62	6651.99	0.00	35699.62
Mo 95	465.29	0.00	23476.63	11.00	6.16	13.85	108.94	0.00	23476.63
Pd 106	1.97	0.00	5.09	0.20	0.00	0.84	0.78	0.00	6.29
Pd 108	577.22	0.00	24304.03	1.04	0.26	1.87	116.64	0.00	24304.03
Cd 111	0.40	0.00	2.04	0.58	0.00	4.27	1.16	0.00	173.59
Cd 114	0.09	0.00	0.51	0.38	0.00	3.38	0.60	0.00	49.86
Sn 118	0.26	0.00	1.98	0.37	0.02	1.98	1.05	0.00	157.96
Sn 120	0.22	0.00	1.45	0.40	0.05	2.47	1.00	0.00	151.66
Sb 121	0.66	0.00	1.62	0.85	0.24	1.39	0.91	0.00	39.16
Ba 137	28.06	0.00	102.21	31.55	14.91	114.91	42.09	0.00	431.46
Ba 138	27.83	0.00	110.27	32.38	15.97	115.58	41.80	0.00	442.11
Ce 140	0.04	0.00	0.39	0.05	0.00	0.19	0.09	0.00	5.09
Ir 191	0.13	0.00	0.69	0.05	0.00	0.27	0.44	0.00	46.51
Ir 193	0.11	0.00	0.86	0.04	0.00	0.29	0.31	0.00	18.59
Pt 194	0.14	0.00	0.93	0.05	0.00	0.69	0.15	0.00	7.31
Pt 195	0.21	0.00	0.99	0.07	0.00	0.40	0.20	0.00	7.80
Au 197	1.57	0.00	14.32	1.00	0.00	4.53	4.96	0.00	432.20
Hg 200	0.90	0.00	11.60	9.20	0.00	30.44	3.20	0.00	150.05
Hg 202	1.41	0.00	8.53	9.96	0.00	38.20	3.18	0.00	73.64
Tl 203	0.16	0.00	0.81	0.06	0.00	0.20	0.24	0.00	4.67
Tl 205	0.06	0.00	0.54	0.05	0.00	0.19	0.16	0.00	10.98
Pb 206	0.49	0.00	12.57	0.43	0.00	3.54	3.41	0.00	507.14
Pb 208	0.40	0.00	11.68	0.39	0.00	3.33	2.96	0.00	437.14
Bi 209	0.05	0.00	0.34	0.03	0.00	0.21	0.18	0.00	15.19
Ra 226							0.29	0.00	39.92
Th 232	0.10	0.00	0.40	0.04	0.00	0.33	0.14	0.00	5.25
U 238	1.85	0.00	3.60	2.23	0.15	3.95	2.44	0.00	10.18

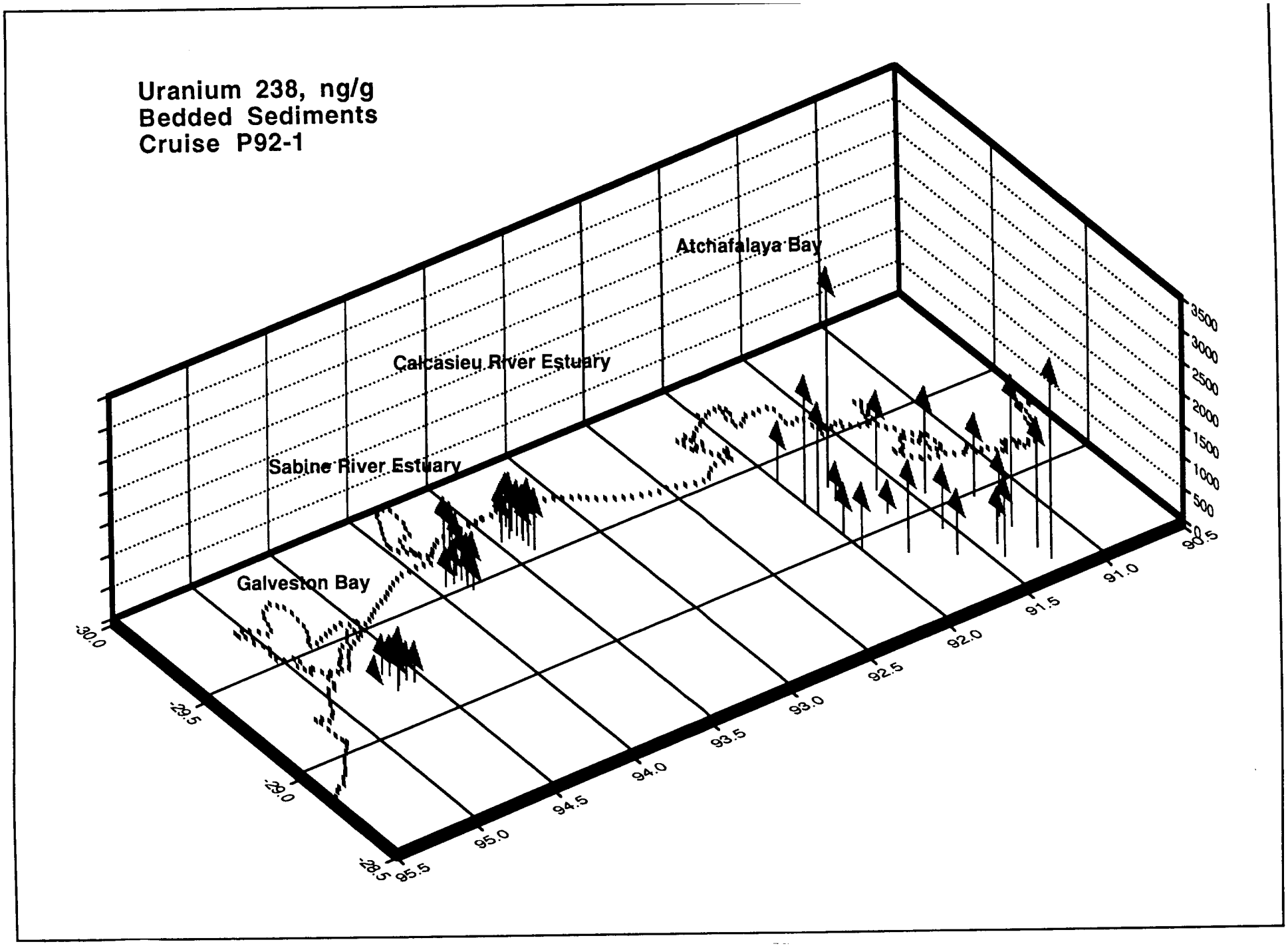

Figure 265. Spatial distribution of Uranium 238 (ng/g) in bedded coastal sediments in the northwestern Gulf of Mexico.

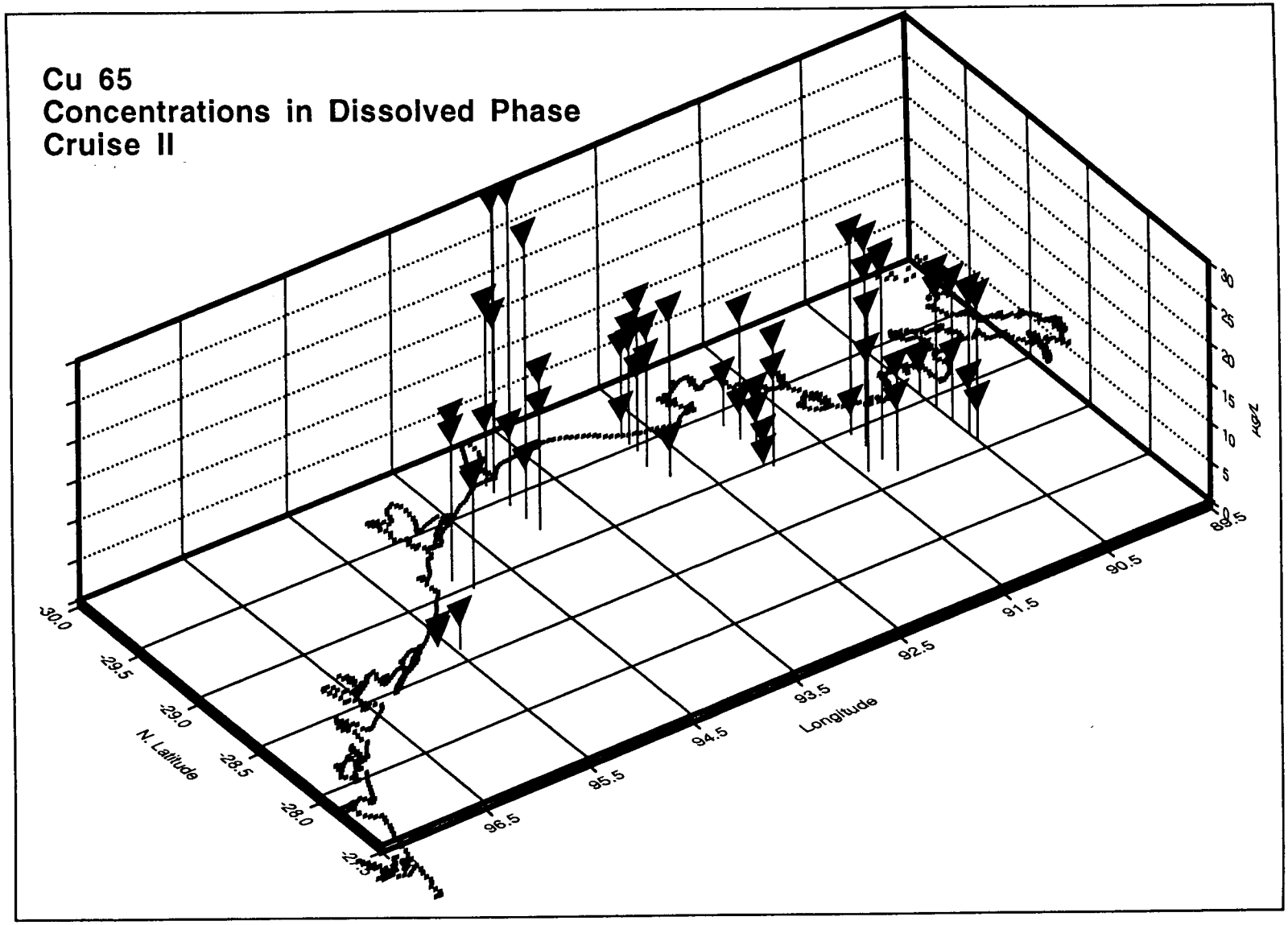

Figure 266. Spatial distribution of Cu 65 (ug/L) in the dissolved phase of water samples collected during cruise P922.

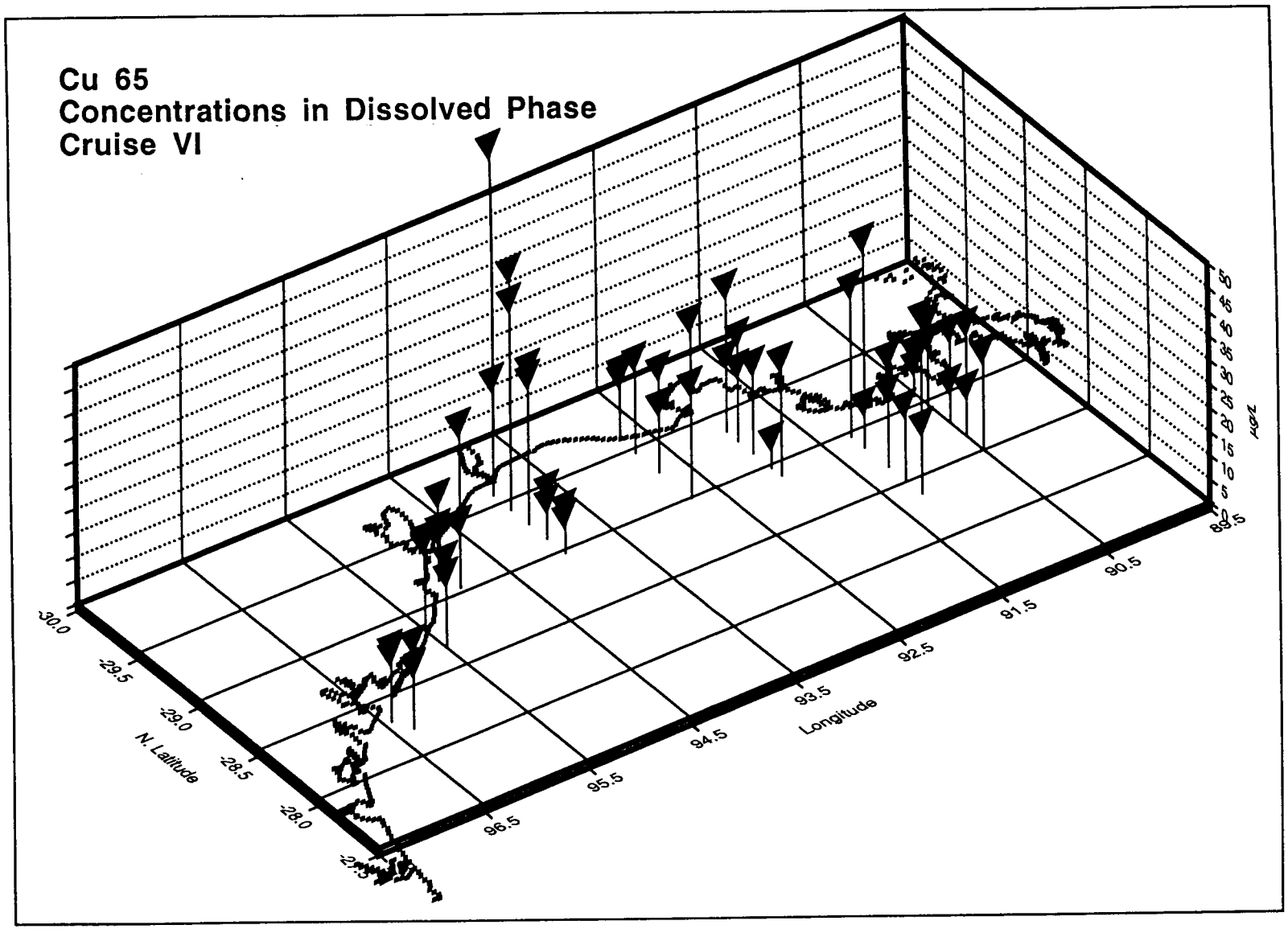

Figure 267. Spatial distribution of Cu 65 (ug/L) in the dissolved phase of water samples collected during cruise P942.

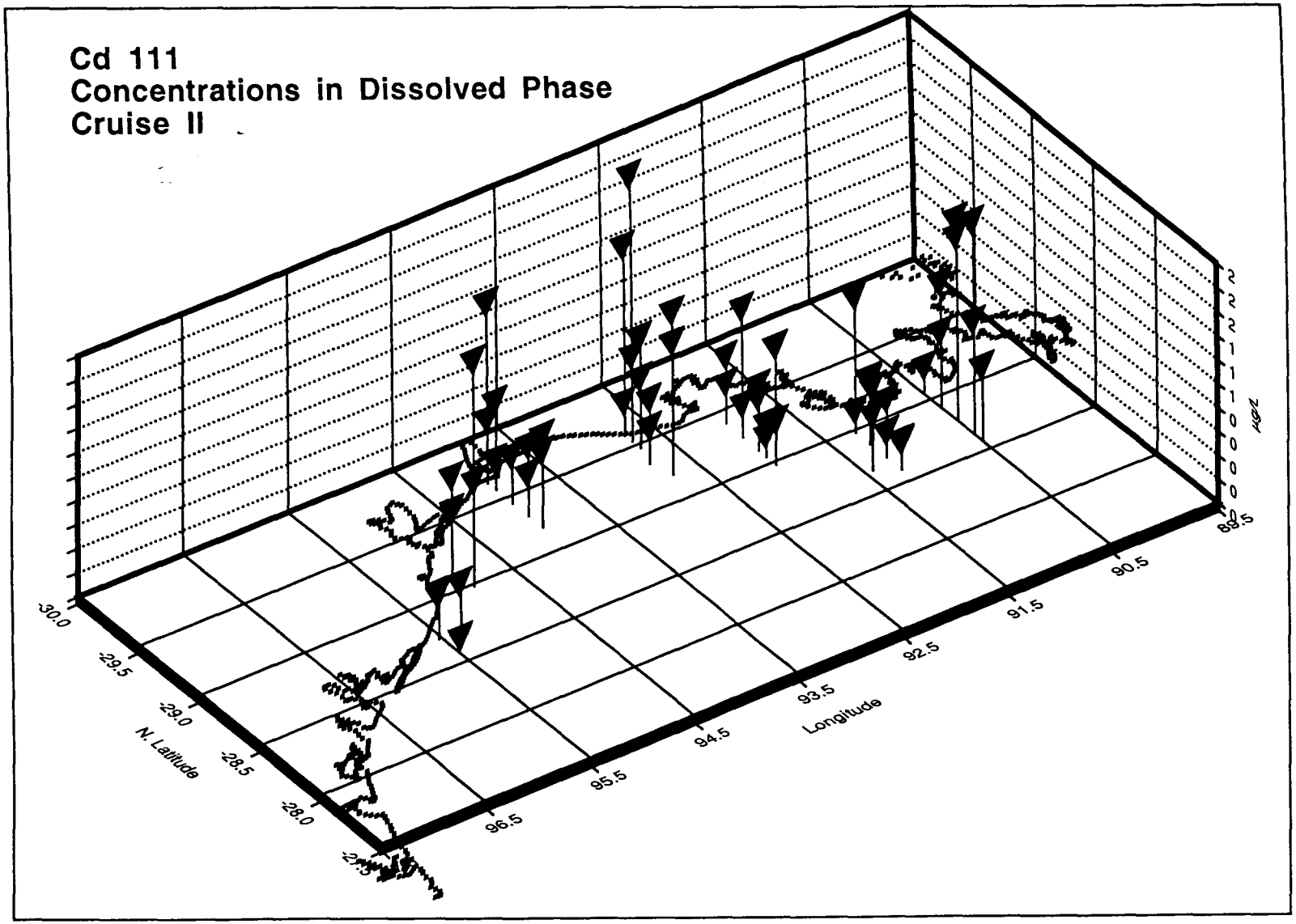

Figure 268. Spatial distribution of Cd 111 (ug/L) in the dissolved phase of water samples collected during cruise P922.

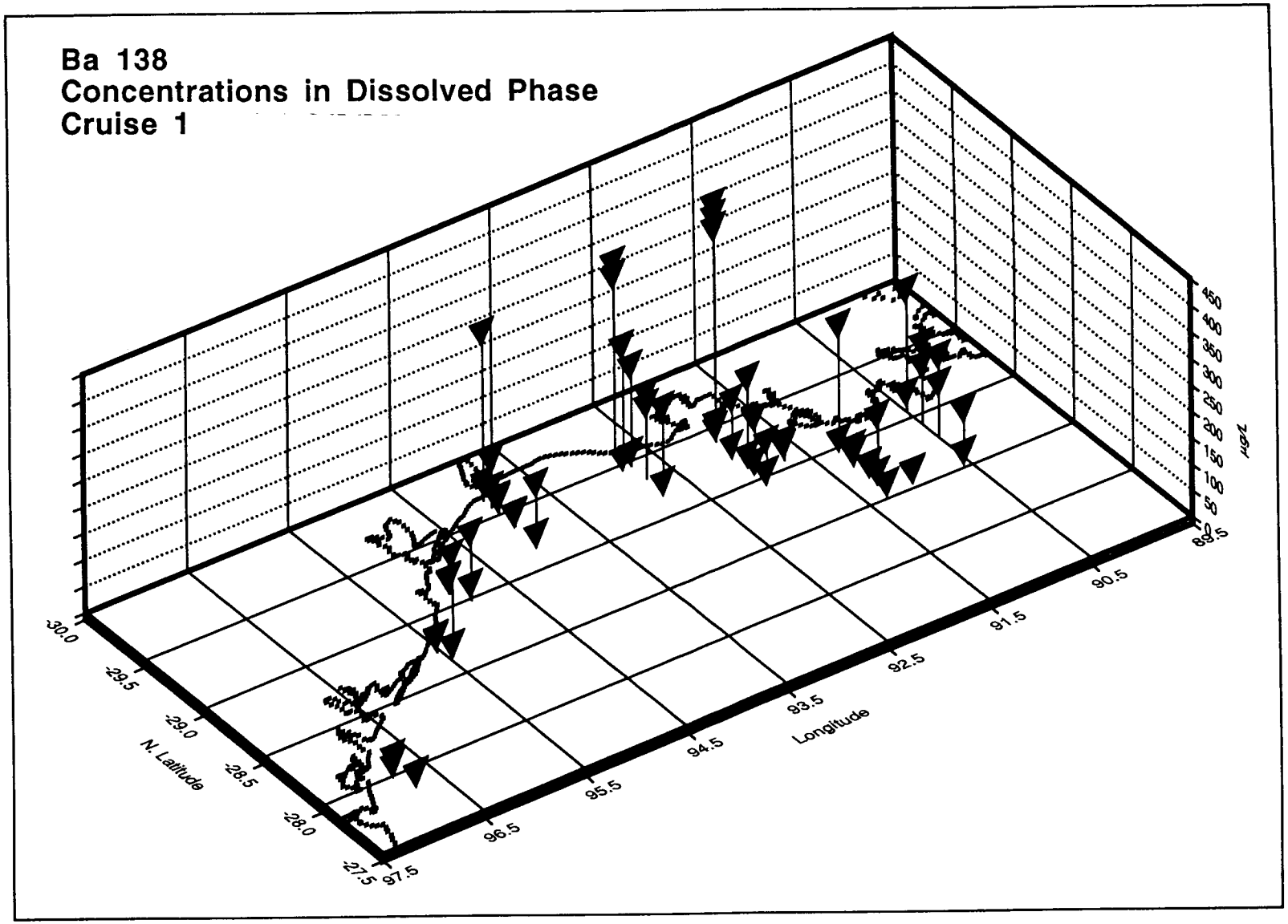

Figure 269. Spatial distribution of Ba 138 (ug/L) in the dissolved phase of water samples collected during cruise P921.

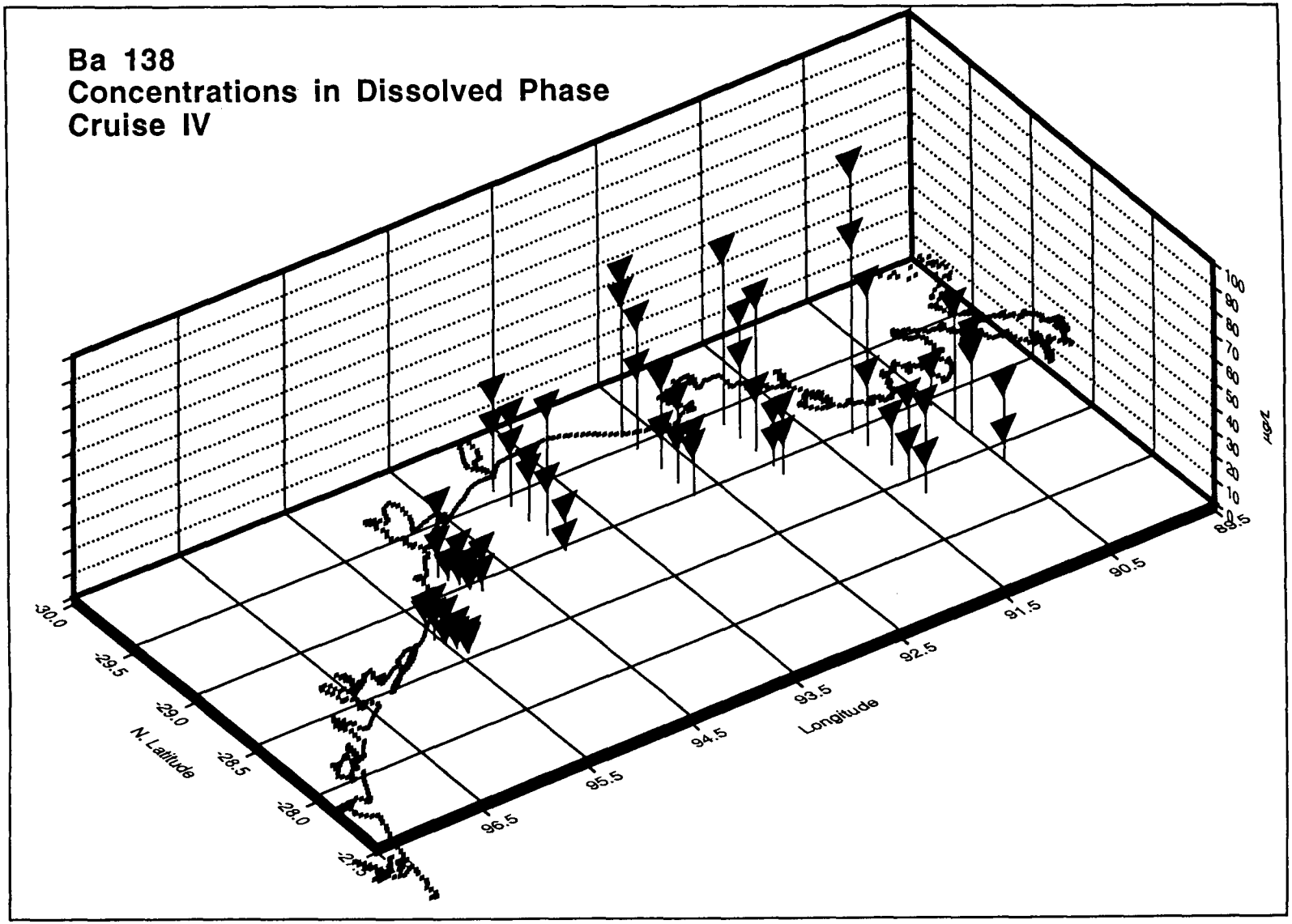

Figure 270. Spatial distribution of Ba 138 (ug/L) in the dissolved phase of water samples collected during cruise P932.

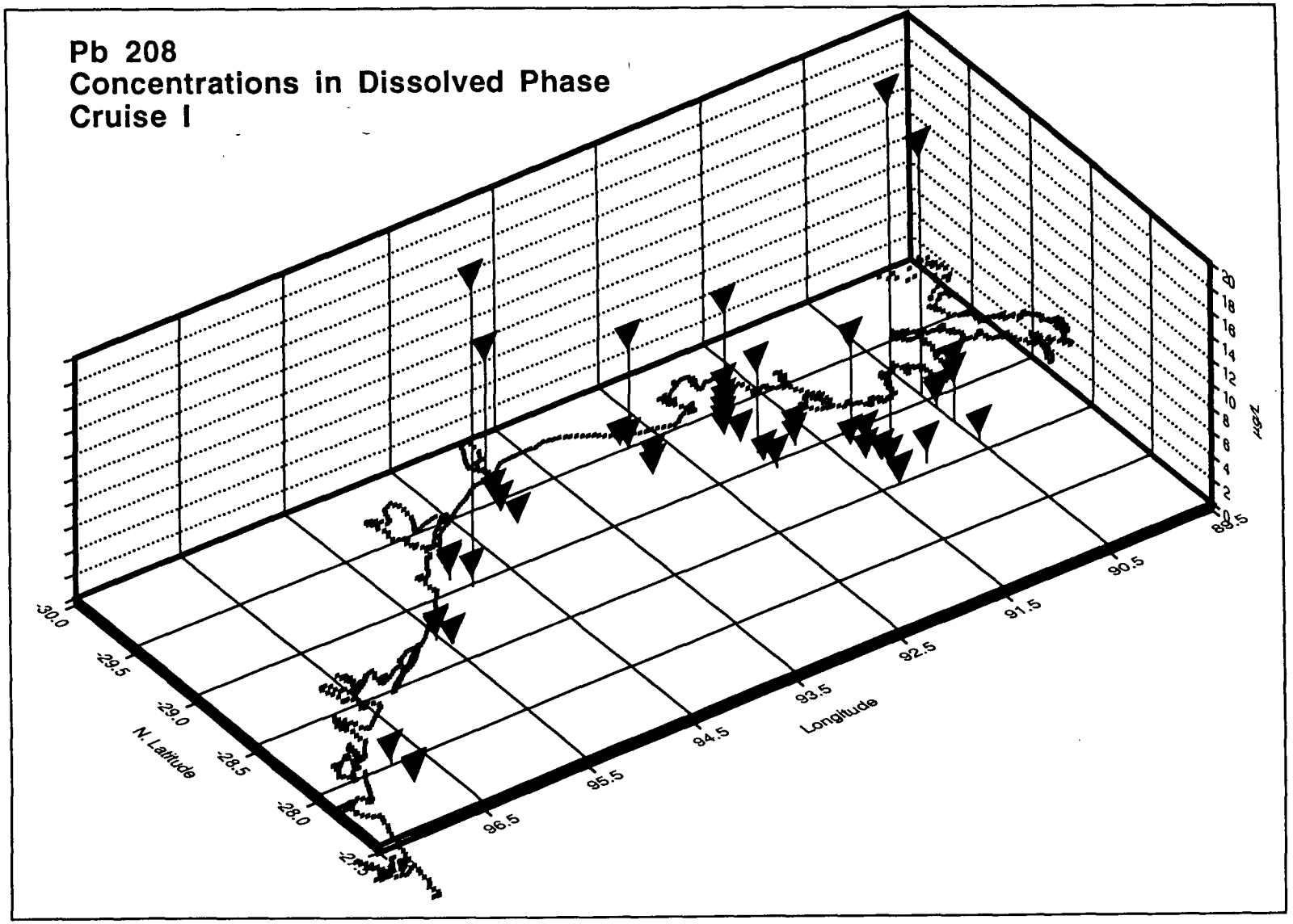

Figure 271. Spatial distribution of Pb 208 (ug/L) in the dissolved phase of water samples collected during cruise P921.

effluents of some of the smaller estuaries as compared to the Mississippi or it may mean that there are near shore sources of some of these elements.

A conversion of trace element concentration data to dissolved flux data (kg/d transported) show that the dissolved phase is very important, if not dominant in the mass transport of trace elements in the NW Gulf of Mexico. These data are paralleled to a large extent by information developed for the colloidal-enriched phase discussed next. Due to limitation on space, plots of these fluxes are not provided but the trends observed are very similar to those discussed next with respect to the colloidal phase.

6. Colloidal Phase

The isolation and analysis of a microparticulate phase as performed in this study represents the first large scale evaluation of this fraction as it impacts contaminant transport processes in the field. The potential role of colloidal material in facilitating transport processes for certain elements is examined. These data along with that obtained on organics and combined with physical oceanographic information provide strong evidence that colloidal materials are important in coastal ocean transport processes.

a. Results

Table 55 presents a summary of mean concentrations, ranges and frequencies of detection for each element in the colloidal-enriched phase for each cruise in the study. Figures 272-277 show selected spatial distribution plots of trace elements of concern in the Gulf of Mexico. Figures 278-281 show the calculated fluxes of selected elements (Cu, Cd, Ba and Pb) in the NW Gulf of Mexico over the three-year period of the investigation.

b. Discussion and Conclusions

Most trace elements were detected in all colloidal phase samples collected in the NW Gulf of Mexico. The presence of detectable quantities of some elements and higher concentrations of others than measured in the dissolved phase give the first indication of this fractions potential role in transport processes. Critical limitations in the present data sets are, first, the lack of complete separation of the colloidal material from the dissolved phase (These colloid materials were enriched ~200 fold but not completely isolated in the samples. Funding and equipment were not made available for complete isolation and characterization of the colloids on this grant.) Second, there was no mass based estiamtor of colloid concentration available in the enriched isolates so the concentrations are reported on a volumentric basis. Nevertheless, general trends in trace metal behavior in thsi phase can be made.

Figures 272-277 show the distribution of selected trace elements in the colloidal phase accross othe caostal current region of the NW Gulf of Mexico. Copper concentrations were similar to or slightly higher than concentrations in the dissolved phase and showed the same input sources. Cadmium distributions showed inputs at Sabine for Cruise P922 data, and uniform spatial patterns in July. Colloidal barium distributions show input sources at the AT, Calcasieu and Sabine estuaries, with these inputs apparent in April and October data, while July distributions were more uniform. Lead concentrations were generally lower than for dissolved phase data and uniformly distributed among sample locations.

Figure 278-281 show the calculated fluxes of copper, cadmium, barium and lead, respectively, in the colloidal phase samples. The relative magnitude of the patterns of the fluxes are controlled by the movement of water masses rather than by element

Table 55. Colloidal phase trace elements summary.

	Cruise 1: April 1992			Cruise 2: October 1992			Cruise 3: April 1993		
	Mean	Min	Max	Mean	Min	Max	Mean	Min	Max
Isotope	µg/L	µg/L	µg/L	µg/L	µg/L	µg/L	µg/L	µg/L	µg/L
Li 7	111.80	46.77	194.99	169.57	0.00	290.16	201.77	23.00	1527.35
Be 9	0.04	0.00	1.34	1.61	0.00	7.96	0.59	0.00	3.85
B 10	2601.98	1055.77	5239.29	4903.13	0.00	16508.24	2134.01	242.85	14749.46
B 11	3057.16	1322.83	6261.70	5809.76	0.00	17405.83	2161.14	219.77	15231.04
Ti 48	1176.63	515.01	1916.88	2681.57	0.00	7987.97	1783.28	507.70	15598.55
Ti 49	50.69	20.68	166.58	207.11	0.00	1001.45	125.48	32.90	1281.61
V 51	122.24	14.63	422.21	31.35	0.00	135.85	6.30	0.00	119.13
Cr 52	8.15	0.00	89.87	31.27	0.00	148.83	38.50	0.00	574.78
Mn 55	2.33	0.00	16.96	11.58	0.00	91.79	14.18	0.00	679.21
Ni 58	6.07	0.00	47.43	53.30	0.00	1017.61	57.72	0.00	330.44
Co 59	0.92	0.00	2.70	3.46	0.00	19.50	2.16	0.50	14.41
Ni 60	9.86	0.00	47.89	55.46	0.00	898.62	54.99	2.40	339.07
Zn 64	80.40	0.00	286.94	337.57	0.00	2054.65	602.14	0.00	6428.62
Cu 65	16.68	3.18	52.60	39.42	0.00	398.28	29.63	5.30	198.33
Zn 66	43.99	0.00	210.59	86.10	0.00	274.45	51.52	0.00	279.63
As 75	41.96	4.95	122.45	165.27	0.00	752.50	122.58	13.34	1218.58
Se 82	971.22	154.21	2061.21	673.58	0.00	3660.10	415.00	97.10	3850.44
Sr 88	4295.05	1433.71	14126.13	12744.84	0.00	33369.35	6861.13	1406.16	69394.38
Mo 95	16.22	6.88	35.11	22.45	0.00	73.43	15.79	3.20	128.37
Pd 106	0.26	0.00	5.65	1.80	0.00	5.37	0.66	0.00	4.84
Pd 108	0.20	0.00	5.03	0.90	0.00	3.30	4.38	0.65	20.57
Cd 111	0.31	0.00	6.97	2.39	0.00	13.08	0.57	0.00	5.28
Cd 114	0.23	0.00	6.08	0.78	0.00	3.64			
Sn 118	0.07	0.00	2.30	1.71	0.00	17.00	0.43	0.00	3.74
Sn 120	0.07	0.00	2.27	1.73	0.00	16.82	0.35	0.00	2.64
Sb 121	0.33	0.00	2.28	1.63	0.00	14.87	1.53	0.00	16.94
Ba 137	26.70	7.98	87.72	47.09	0.00	128.22	24.34	4.70	214.17
Ba 138	26.83	7.85	87.72	45.96	0.00	131.06	24.70	5.30	222.53
Ce 140	0.38	0.00	12.60	0.16	0.00	0.96	0.04	0.00	0.88
Ir 191	0.12	0.00	1.16	1.01	0.00	5.60	0.15	0.00	1.54
Ir 193	0.16	0.00	1.43	0.34	0.00	2.60	0.09	0.00	0.88
Pt 194	0.41	0.00	11.11	1.16	0.00	9.48	0.03	0.00	0.36
Pt 195	0.39	0.00	11.44	0.64	0.00	6.87	0.02	0.00	0.55
Au 197	6.10	0.00	342.91	2.75	0.00	26.23	1.23	0.00	12.32
Hg 200	0.17	0.00	3.98	3.06	0.00	17.24	1.03	0.00	10.01
Hg 202	0.17	0.00	4.29	2.54	0.00	20.12	0.80	0.00	4.50
Tl 203	0.59	0.00	13.39	1.76	0.00	9.50	0.26	0.00	2.20
Tl 205	0.57	0.00	14.41	0.97	0.00	9.60	0.17	0.00	2.64
Pb 206	2.00	0.00	16.90	0.75	0.00	19.47	0.84	0.00	17.34
Pb 208	1.96	0.00	17.20	0.50	0.00	14.43	0.72	0.00	14.61
Bi 209	0.09	0.00	2.63	0.79	0.00	8.70	0.10	0.00	1.54
Ra 226	0.00	0.00	0.00	0.00	0.00	0.00			
Th 232	0.46	0.00	9.22	1.98	0.00	19.04	0.09	0.00	1.32
U 238	3.06	0.00	24.18	4.38	0.00	17.13	2.19	0.40	24.53

Table 55 cont'd.

	Cruise 4: July 1993			Cruise 6: July 1994			Summary of All Cruises		
	Mean	Min	Max	Mean	Min	Max	Mean	Min	Max
Isotope	µg/L	µg/L	µg/L	µg/L	µg/L	µg/L	µg/L	µg/L	µg/L
Li 7	155.77	82.10	232.63	150.41	86.49	211.94	157.86	0.00	1527.35
Be 9	1.64	0.24	5.08	0.46	0.09	1.73	0.87	0.00	7.96
B 10	1648.58	877.17	4250.73	1960.72	1430.52	2485.68	2649.68	0.00	16508.24
B 11	1653.34	717.57	4693.58	2103.32	1387.22	2959.26	2956.94	0.00	17405.83
Ti 48	1589.53	1040.24	2442.96	1538.17	1095.00	1934.90	1753.84	0.00	15598.55
Ti 49	123.90	79.37	296.11	261.70	66.73	926.02	153.78	0.00	1281.61
V 51	6.06	0.79	18.07	5.67	0.00	43.61	34.32	0.00	422.21
Cr 52	16.83	5.55	104.76	19.71	2.76	86.37	22.89	0.00	574.78
Mn 55	8.95	0.00	188.01	6.38	1.26	57.98	8.69	0.00	679.21
Ni 58	57.93	0.00	261.23	16.24	0.10	51.69	38.25	0.00	1017.61
Co 59	1.68	1.01	2.92	2.14	1.03	3.94	2.07	0.00	19.50
Ni 60	50.58	1.24	211.93	20.17	6.93	45.79	38.21	0.00	898.62
Zn 64	555.38	98.27	2979.61	193.07	36.13	431.96	353.71	0.00	6428.62
Cu 65	32.83	11.89	106.92	18.11	3.80	51.12	27.33	0.00	398.28
Zn 66	11.39	0.00	205.42	33.95	8.93	138.00	45.39	0.00	279.63
As 75	122.64	25.91	385.85	75.68	10.33	148.54	105.63	0.00	1218.58
Se 82	420.40	255.80	910.88	377.06	212.38	603.28	571.45	0.00	3850.44
Sr 88	7167.77	3827.52	10250.11	6804.94	5003.68	8752.12	7574.74	0.00	69394.38
Mo 95	12.40	7.44	16.74	14.78	9.48	21.39	16.33	0.00	128.37
Pd 106	0.17	0.00	0.76	1.25	0.00	6.21	0.83	0.00	6.21
Pd 108	2.05	1.06	5.76	2.36	0.48	7.39	1.98	0.00	20.57
Cd 111	0.41	0.00	2.65	1.38	0.12	3.88	1.01	0.00	13.08
Cd 114	0.18	0.00	2.57	0.43	0.00	2.80	0.41	0.00	6.08
Sn 118	0.12	0.00	0.65	0.47	0.00	2.68	0.56	0.00	17.00
Sn 120	0.17	0.00	0.59	0.42	0.09	1.46	0.55	0.00	16.82
Sb 121	1.11	0.37	2.18	2047.84	0.24	65478.86	410.49	0.00	65478.86
Ba 137	4115.43	2633.79	6547.32	23.85	15.48	43.34	847.48	0.00	6547.32
Ba 138	25.27	6.43	60.86	24.18	15.12	43.57	29.39	0.00	222.53
Ce 140	25.35	6.25	62.36	0.12	0.00	0.61	5.21	0.00	62.36
Ir 191	0.08	0.00	1.30	0.25	0.00	1.44	0.32	0.00	5.60
Ir 193	0.13	0.00	0.36	0.15	0.00	2.18	0.17	0.00	2.60
Pt 194	0.05	0.00	0.14	0.27	0.00	2.04	0.38	0.00	11.11
Pt 195	0.03	0.00	0.20	0.35	0.00	2.39	0.29	0.00	11.44
Au 197	0.05	0.00	0.29	2.05	0.10	27.58	2.43	0.00	342.91
Hg 200	0.76	0.00	3.68	1.22	0.00	8.31	1.25	0.00	17.24
Hg 202	0.47	0.00	2.90	1.31	0.00	9.76	1.06	0.00	20.12
Tl 203	0.72	0.00	2.32	0.21	0.00	1.12	0.71	0.00	13.39
Tl 205	0.22	0.04	0.46	0.14	0.00	0.74	0.41	0.00	14.41
Pb 206	0.09	0.00	0.22	0.36	0.00	5.78	0.81	0.00	19.47
Pb 208	0.86	0.00	10.80	0.47	0.00	5.07	0.90	0.00	17.20
Bi 209	0.77	0.00	9.38	0.09	0.00	0.71	0.37	0.00	9.38
Ra 226	0.11	0.04	0.26				0.04	0.00	0.26
Th 232	0.07	0.00	0.16	0.15	0.00	2.05	0.55	0.00	19.04
U 238	1.81	1.03	2.83	2.96	0.74	6.76	2.88	0.00	24.53

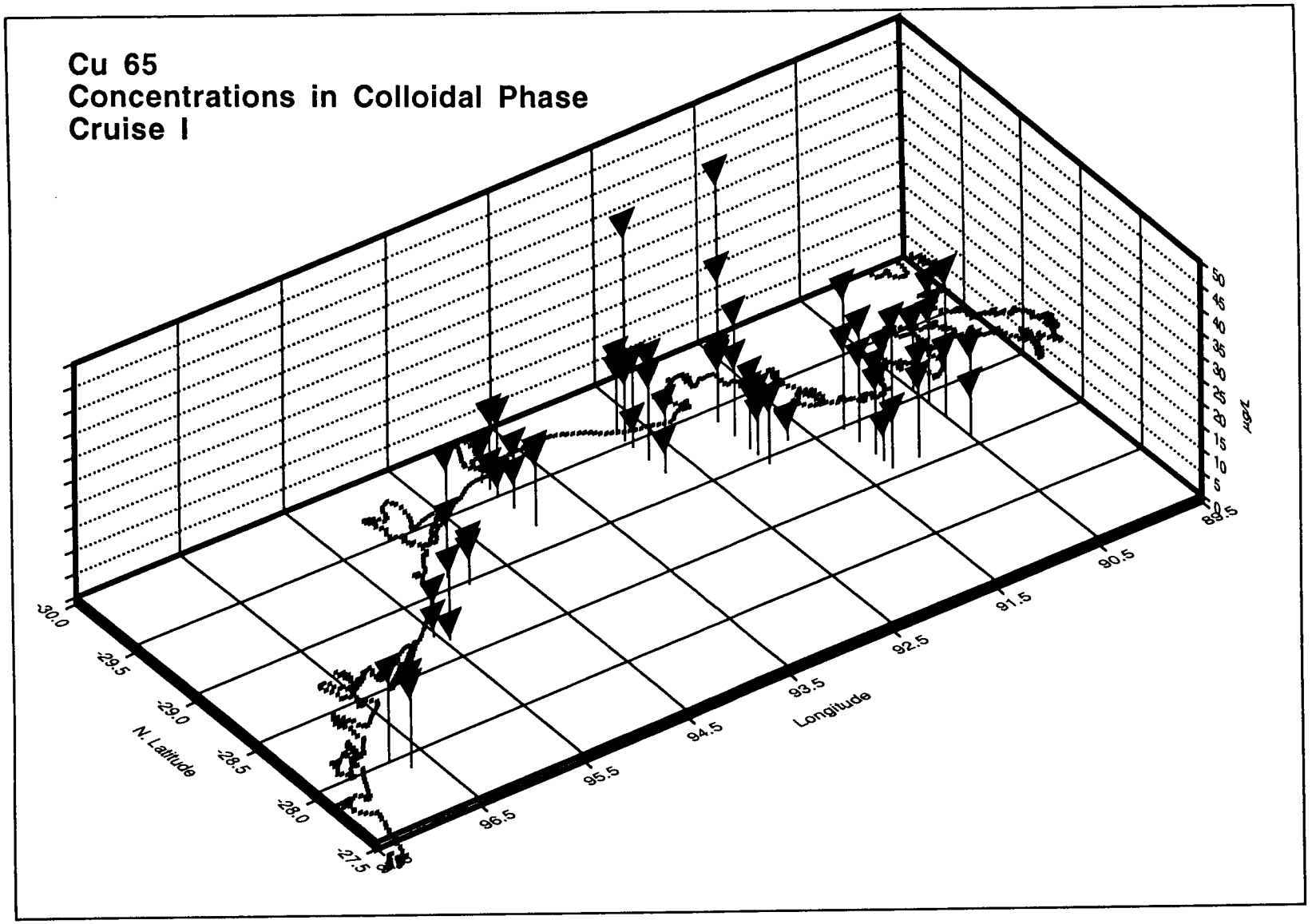

Figure 272. Spatial distribution of Cu 65 (ug/L) in the colloidal phase of water samples collected during cruise P921.

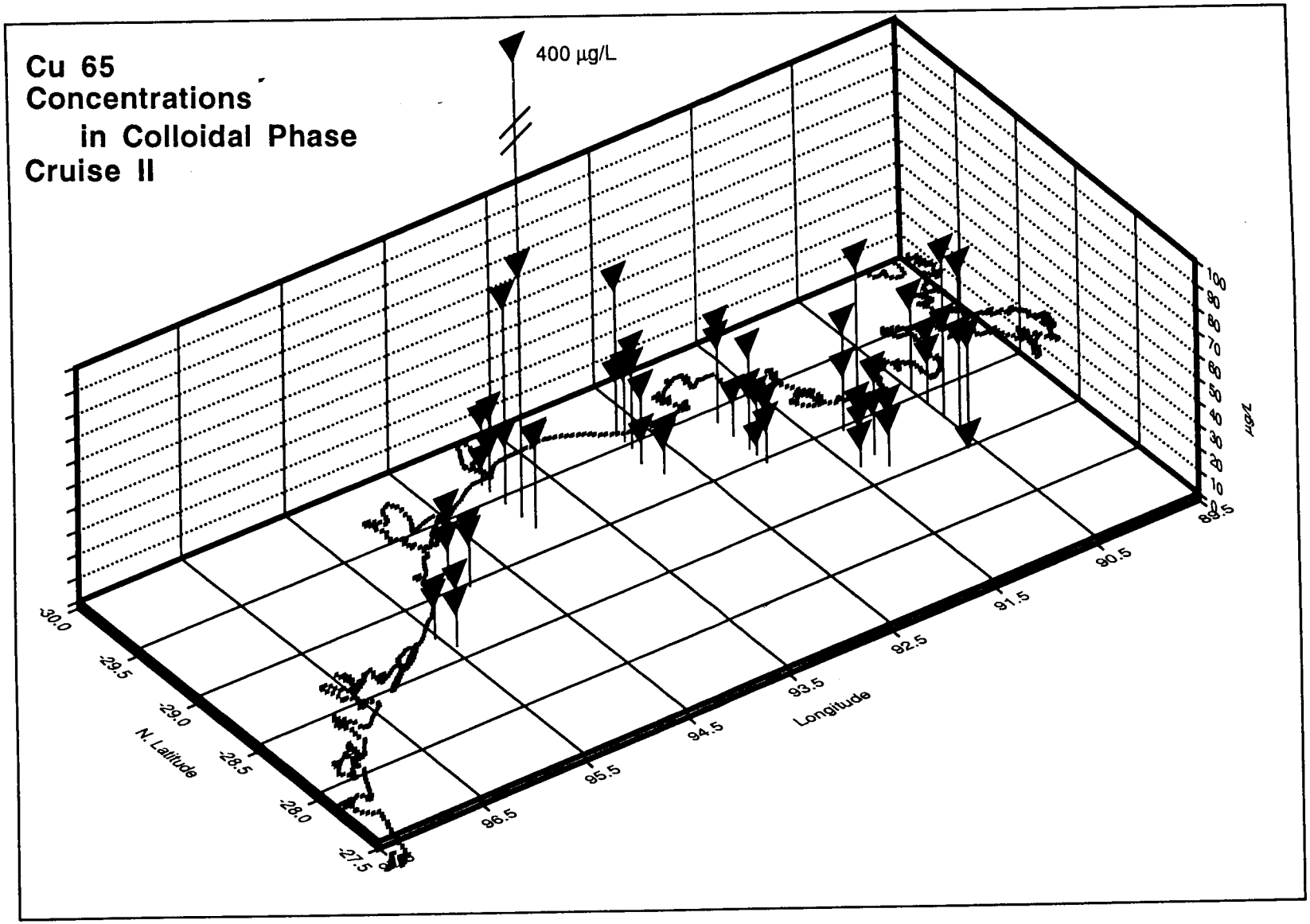

Figure 273. Spatial distribution of Cu 65 (ng/ml) in the colloidal phase of water samples collected during Cruise P922.

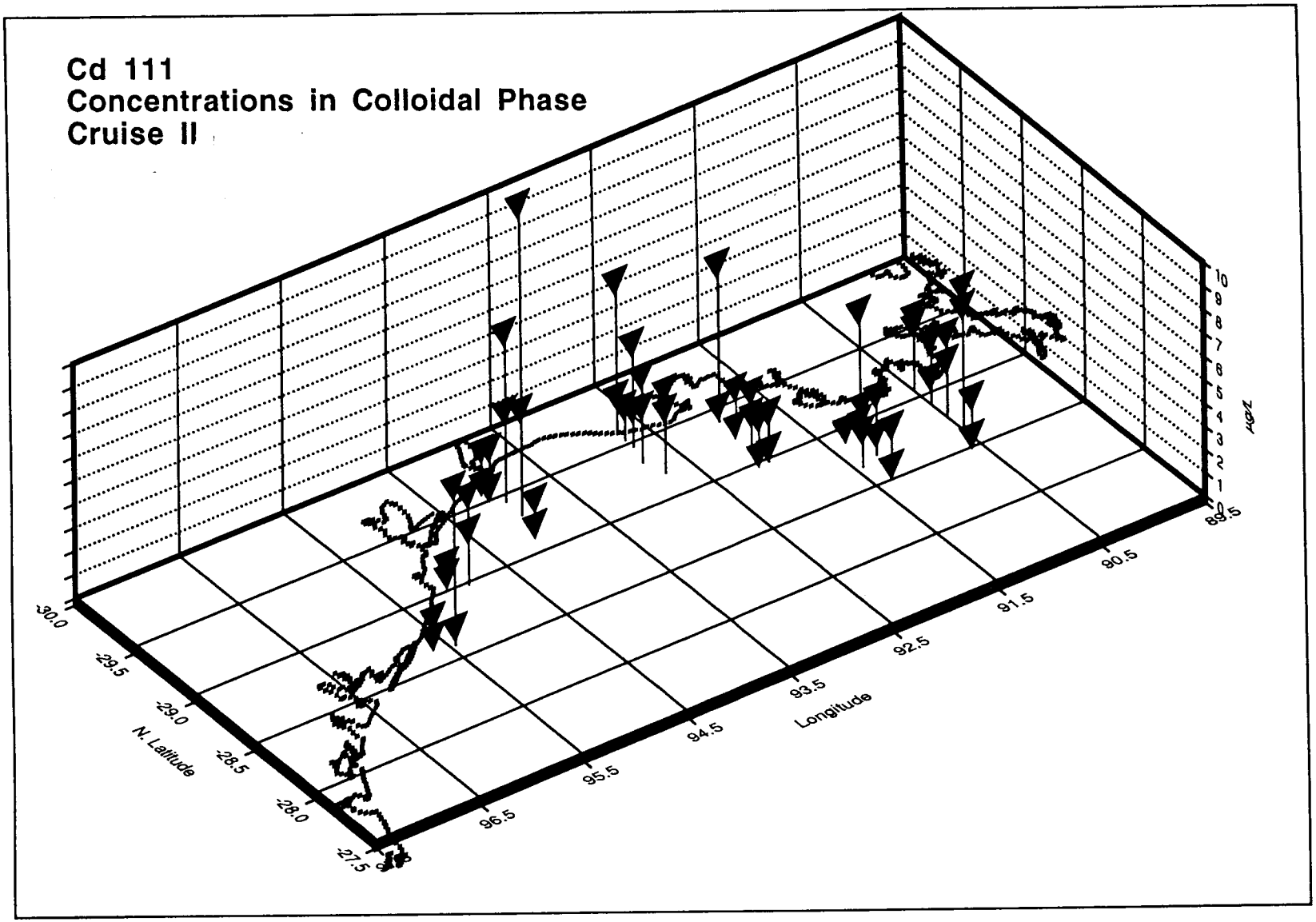

Figure 274. Spatial distribution of Cd 111 (ug/L) in the colloidal phase of water samples collected during Cruise P922.

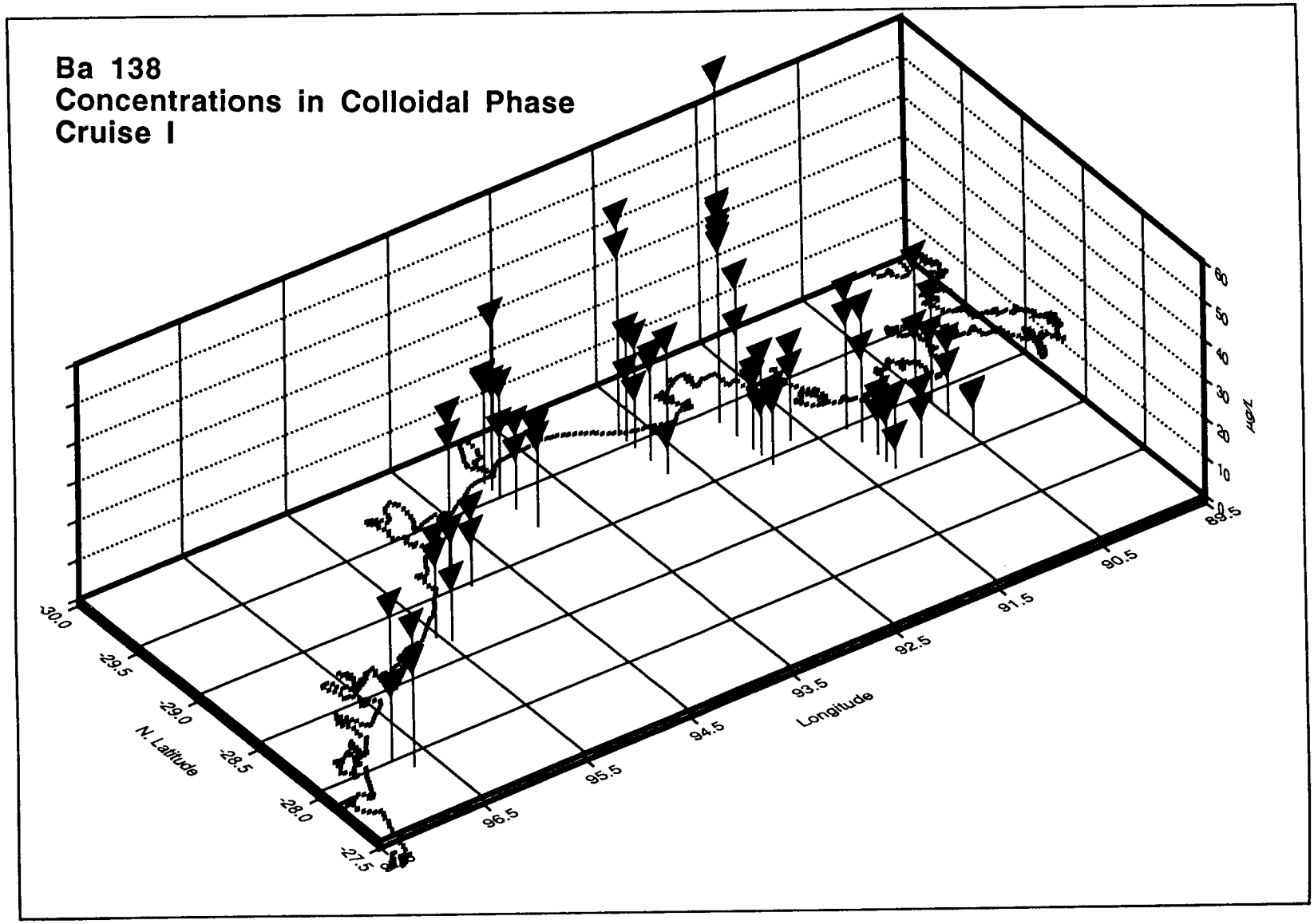

Figure 275. Spatial distribution of Ba 138 (ug/L) in the colloidal phase of water samples collectedduring Cruise P921.

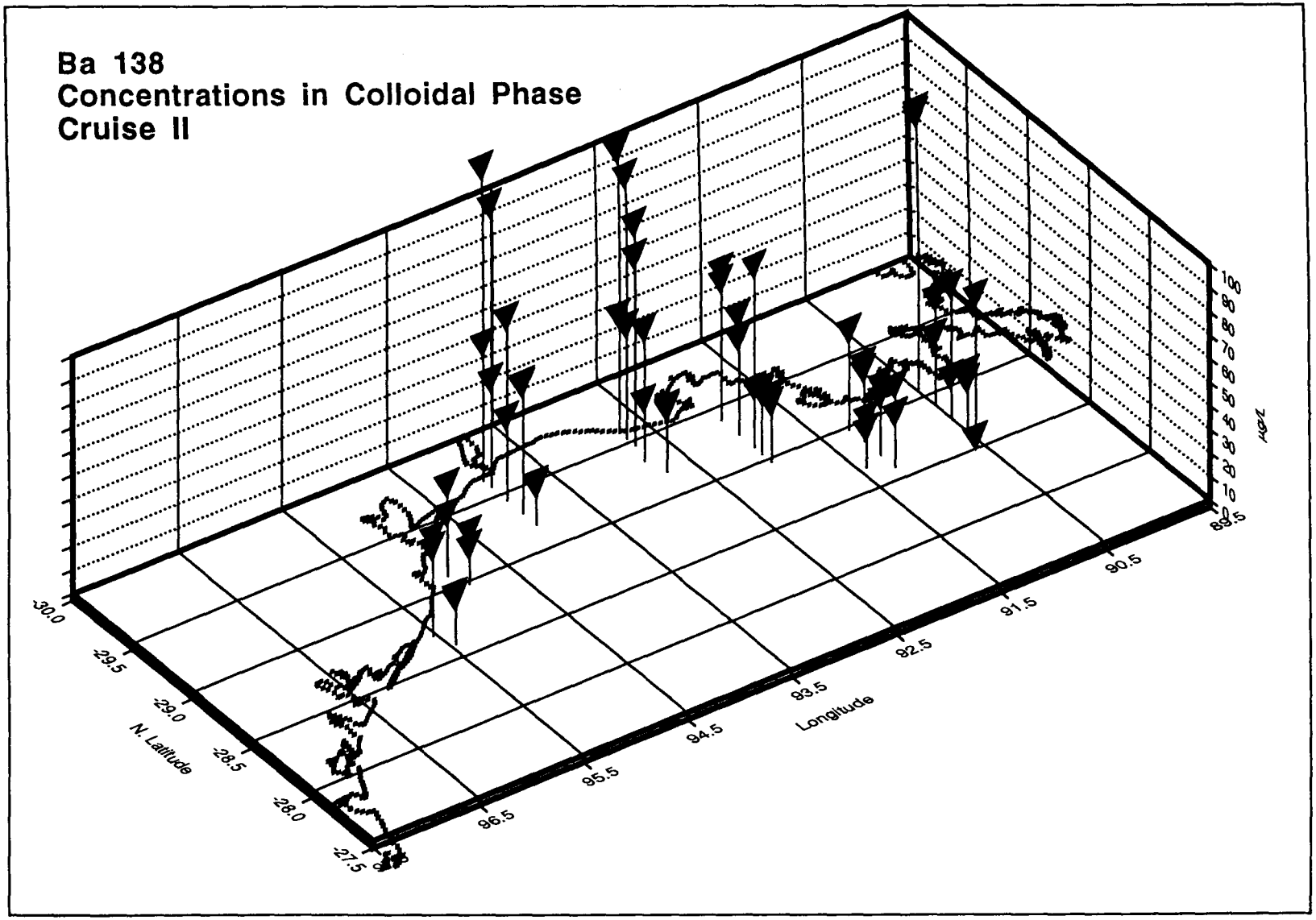

Figure 276. Spatial distribution of Ba 138 (ug/L) in the colloidal phase of water samples collected during Cruise P922.

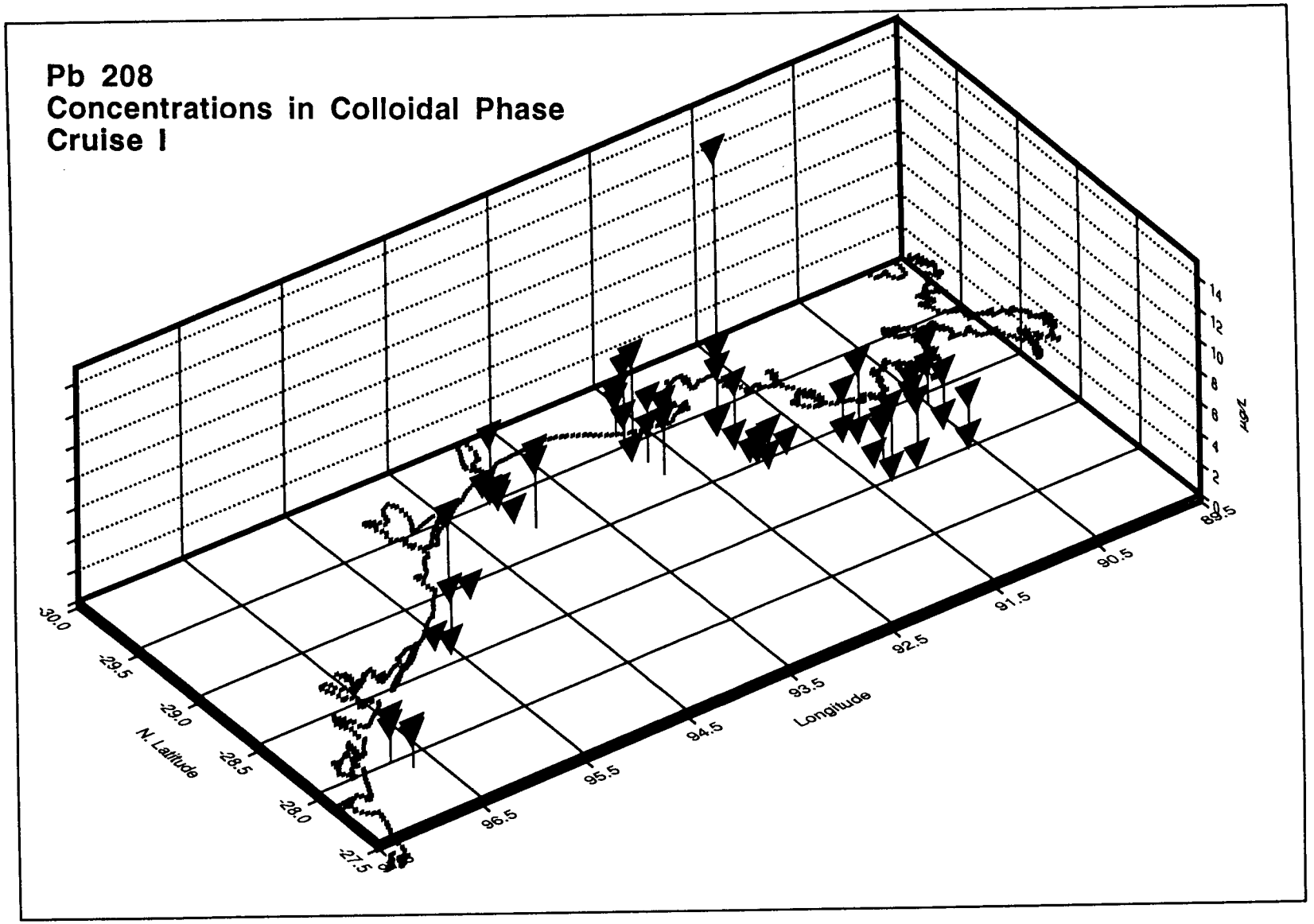

Figure 277. Spatial distribution of Pb 208 (ug/L) in the colloidal phase of water samples collected during Cruise P921.

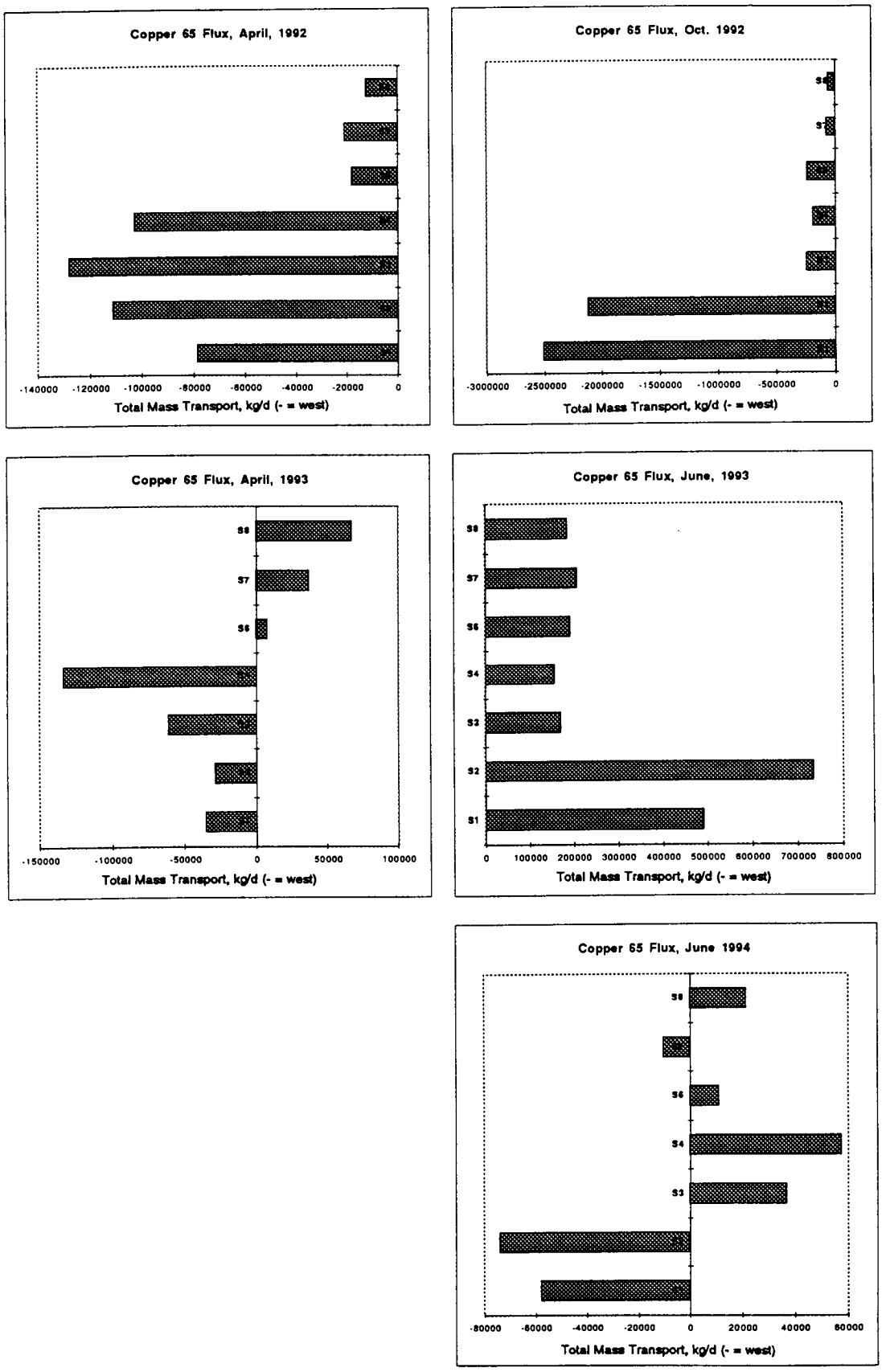

Figure 278. Calculated total mass transport (kg/d) of Copper 65 in the colloidal phase in the northwestern Gulf of Mexico coastal shelf.

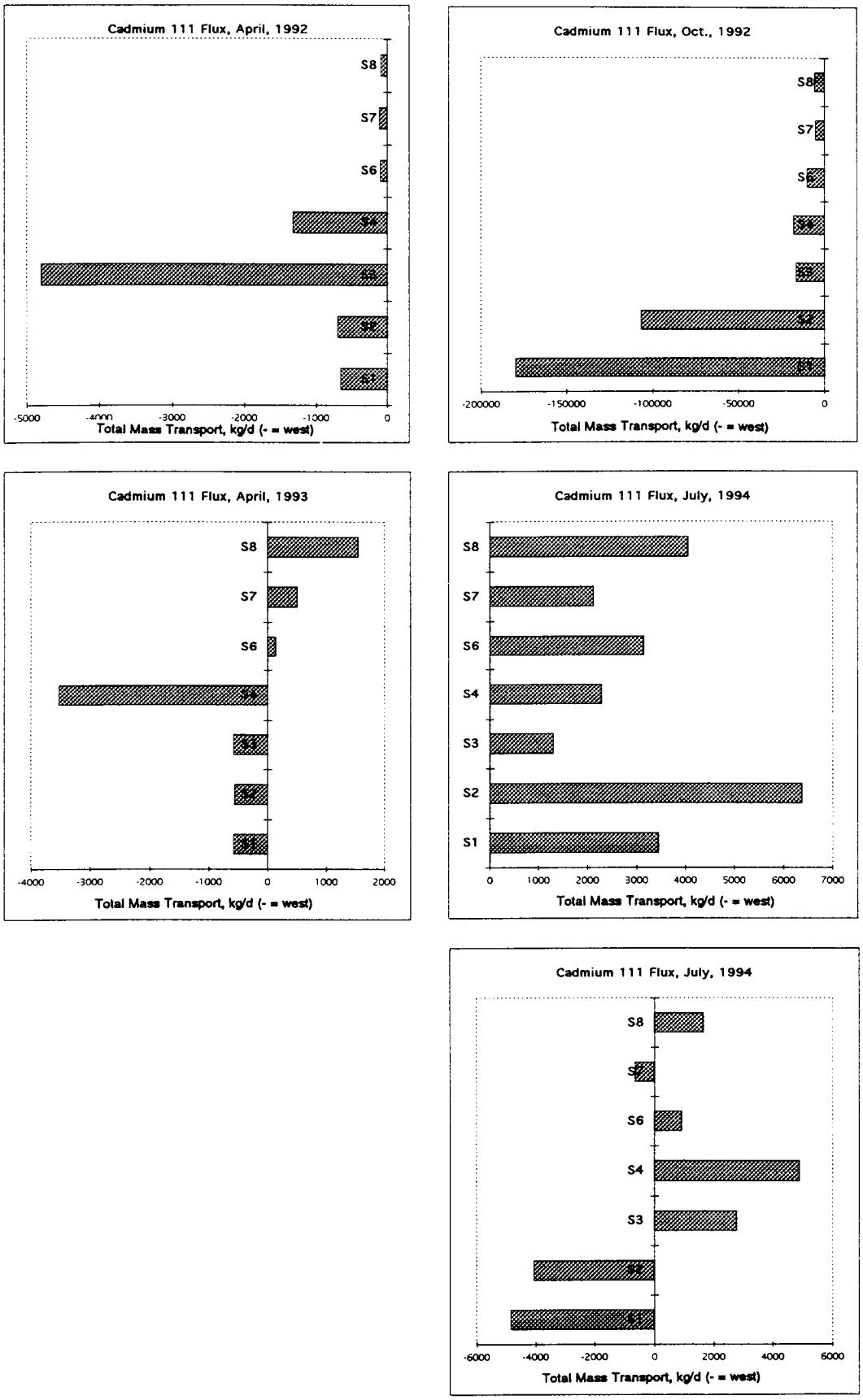

Figure 279. Calculated total mass transport (kg/d) of Cadmium 111 in the colloidal phase in the northwestern Gulf of Mexico coastal shelf.

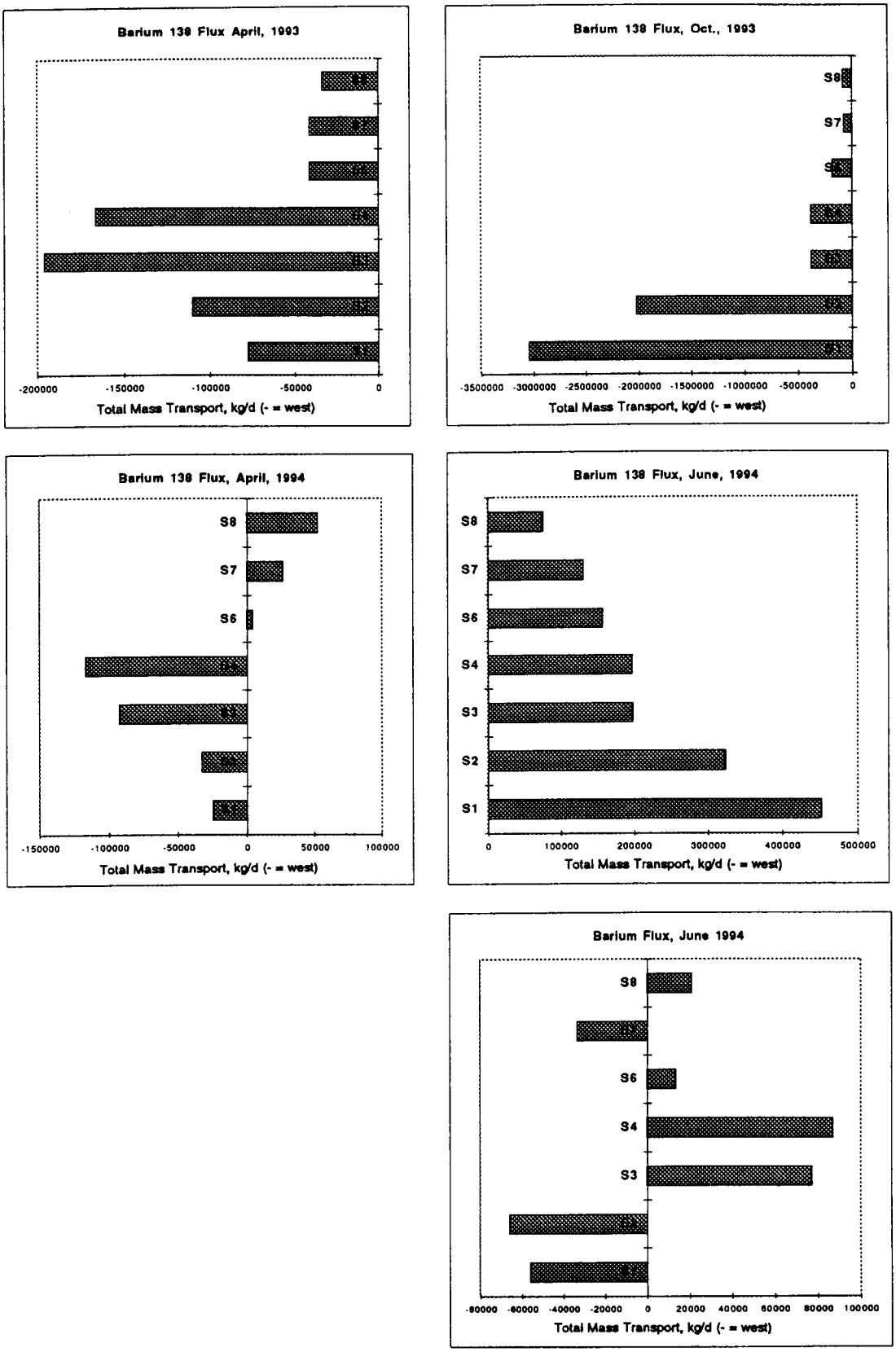

Figure 280. Calculated total mass transport (kg/d) of Barium 138 in the colloidal phase in the northwestern Gulf of Mexico coastal shelf.

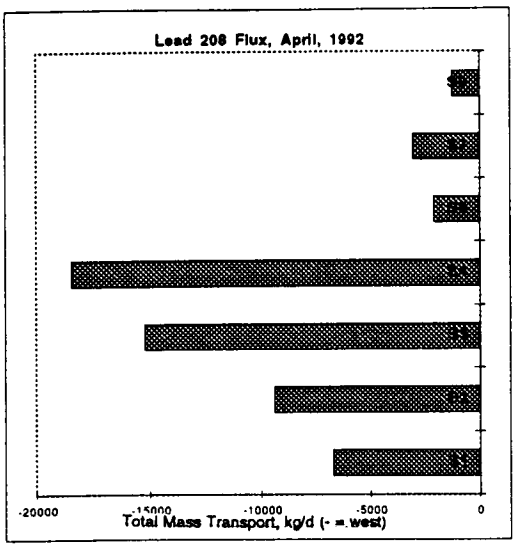

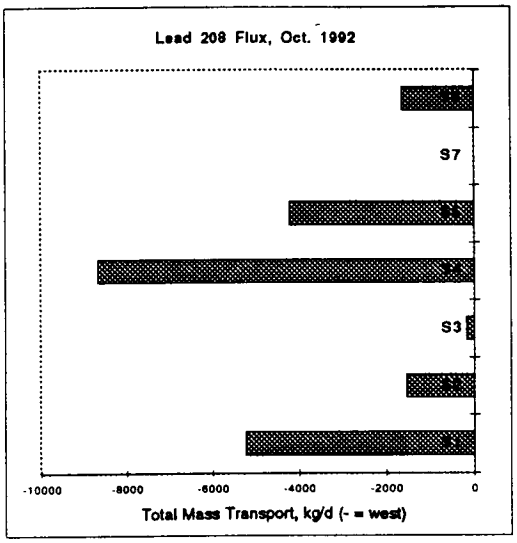

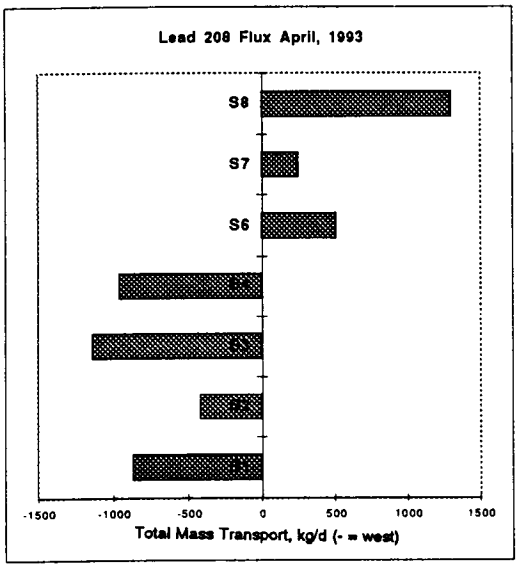

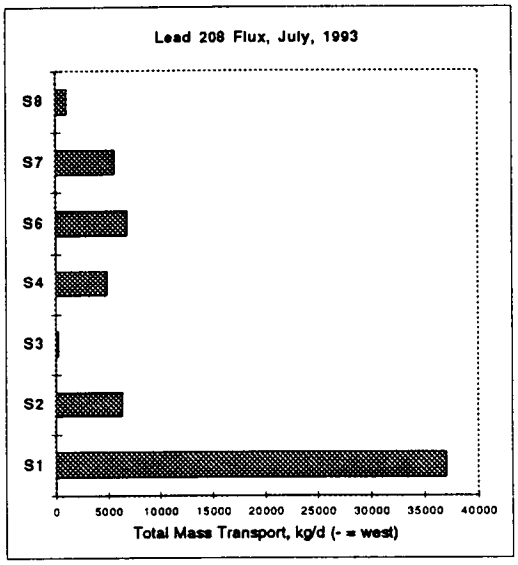

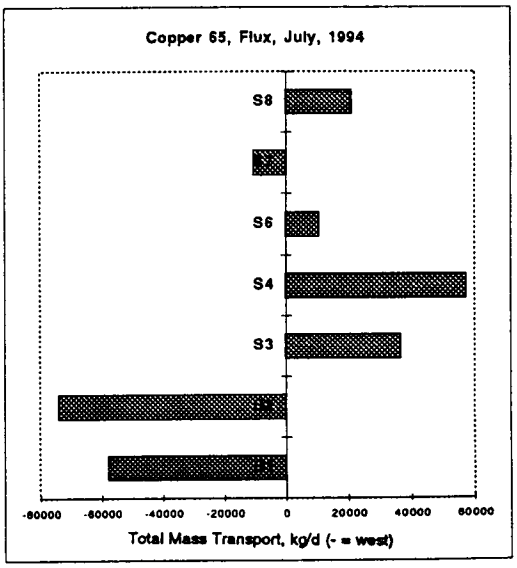

Figure 281. Calculated total mass tTransport (kg/d) of Lead 208 in the colloidal phase in the northwestern Gulf of Mexico coastal shelf.

concentrations so all of the patterns appear similar. The absolute values reported, however, reflect the mass of element being moved though the system in this phase relative to other phases collected, analyzed and measured. For all elements, certain spatial and temporal trends are very apparent. For example, in April, 1992 all element fluxes calculated were much lower at the western transects (S-6,S-7 and S-8) relative to the eastern transects (S-1, S-2, S-3 and S-4). The April, 1993 data consistently show a convergence of transported materials with elements detected along S-1 to S-4 movingwestward while elements detected in S-6 to S-8 are moving eastward. In all cases, there is a strong movement of elements in the colloidal phase observed in June, 1993 and a mixed easterly and westerly transport of materials. Some differences which appear to be concentration dependent are observable in these data. For example, Cd appears to be relatively depleted along transects S-1 to S-3 relative to other elements detected such as
Cu, Ba, etc. Another example is the apparent enhancement of lead fluxes along transects S-4 and S-6 relative to other elements detected. These patterns of fluxes may suggest that there are inputs of colloidal lead in this region of the NW Gulf, while Cd appears to have fewer sources in the eastern portion of the study area.

7. Suspended Particulate Phase

Concentrations of trace elements are reported on suspended particulate samples collected at all station in this investigation. While we report the concentrations of trace elements detected in this phase on a mass basis, we have reported the mass transport data on a volumetric corrected basis to facilitate comparisons with other phases and to provide a realistic view of the relative contribution of particles in the overall mass transport scheme in the NW Gulf of Mexico.

a. Results

Table 56 presents a summary of mean concentrations, ranges and frequencies of detection for each element in the suspended particulate phase for each cruise in the study. Figures 282-287 show selected spatial distribution plots of trace elements of concern in the Gulf of Mexico. Figures 288-291 show the calculated fluxes of selected elements (Cu, Cd, Ba and Pb) in the NW Gulf of Mexico over the three-year period of the investigation.

b. Discussion and Conclusions

The spatial distribution patterns of selected trace elements in the particulate phase show distribution patterns similar to that observed for the dissoved and colloidal phases. This phase shows more variability in Copper concentrations between seasons, with highest concentrations observed in April data, followed by July data. Concentration gradients (showing decreasing values with distance from shore) appear more frequently in transect S1, indicating inputs from the Mississippi river outlet. Cadmium was clearly elevated aroung the AT outlet during cruises P931 and somewhat in cruise P932. Barium distributions showed greater spread between bottom and surface samples, with highest concentrations at the surface; this was most notable in the cruise P932 (July) data.

The relative importance of the suspended particulate phase in mass transport of trace elements in the NW Gulf of Mexico yielded general trends of transport which were similar to those observed in the other phases due top the controlling nature of the movements of water masses as discussed earlier. The most striking observation, is that in spite of the much higher absolute concentrations of trace elements in the particulate phase relative to the dissolved or colloidal phases, the role of particles in total mass transport is less than the combined dissolved and colloidal phases. A comparison the magnitude of

Table 56. Particulate phase trace element summary.

	Cruise 1: April 1992			Cruise 2: October 1992			Cruise 3: April 1993		
	Mean	Min	Max	Mean	Min	Max	Mean	Min	Max
Isotope	ng/g/L	ng/g/L	ng/g/L	ng/g/L	ng/g/L	ng/g/L	ng/g/L	ng/g/L	ng/g/L
Li 7	1745	0	5036	27	10	74	1617	0	5293
Be 9	318	0	959	4	1	11	204	1	594
B 10	402611	0	1505192	6381	0	28561	784184	338	2691841
B 11	278619	0	1444475	4914	0	26408	579944	332	2932734
Ti 48	6435	0	23705	120	47	307	20546	407	62839
Ti 49	3100	0	11468	58	12	253	13676	260	46766
V 51	388	0	1899	11	1	39	2770	41	16745
Cr 52	581	0	2035	11	3	31	4111	115	19588
Mn 55	5956	0	30794	103	8	389	18573	357	69898
Ni 58	742	0	4754	19	1	86	5236	112	20346
Co 59	77	0	389	1	0	4	315	4	1005
Ni 60	220	0	915	4	0	15	1156	0	8009
Zn 64	211125	0	1199629	10122	539	29880	812140	870	3340273
Cu 65	6164	0	19623	16	3	53	9403	349	86093
Zn 66	228623	0	1301551	10904	799	29635	889551	921	3573383
As 75	165	0	630	4	0	33	2783	0	15324
Se 82	444	0	1731	5	1	9	824	0	8966
Sr 88	12610	0	47342	325	112	633	30103	610	84874
Mo 95	53	0	144	1	0	5	162	0	704
Pd 106	11	0	35	0	0	0	132	0	422
Pd 108	9	0	30	0	0	0	38	1	110
Cd 111	31	0	93	0	0	1	112	0	336
Cd 114	30	0	80	0	0	2			
Sn 118	55	0	257	1	0	1	142	5	846
Sn 120	54	0	269	1	0	1	140	5	1039
Sb 121	4	0	20	0	0	0	25	0	266
Ba 137	202508	0	1140998	7422	203	17109	602689	304	2978510
Ba 138	199613	0	1283745	6592	196	16889	529021	312	2393294
Ce 140				5	1	17	1329	21	4740
Ir 191	1	0	3	0	0	0	8	0	110
Ir 193	1	0	4	0	0	0	3	0	40
Pt 194	1	0	15	0	0	0	17	0	276
Pt 195	1	0	15	0	0	0	36	0	452
Au 197	2	0	10	1	0	7	35	0	391
Hg 200	5	0	52	0	0	2	180	0	2146
Hg 202	2	0	24	0	0	1	193	0	1535
Tl 203	17	0	50	1	0	3	33	0	117
Tl 205	18	0	58	2	0	11	32	0	98
Pb 206	665	0	2889	11	3	23	1590	35	7432
Pb 208	614	0	2678	9	2	21	1497	32	7532
Bi 209	3	0	11	0	0	2	13	0	66
Ra 226	0	0	0	0	0	2			
Th 232	28	0	216	1	0	3	174	3	630
U 238	19	0	69	0	0	2	54	0	202

Table 56 cont'd.

	Cruise 4: July 1993			Cruise 6: July 1994			Summary of All Cruises		
	Mean	Min	Max	Mean	Min	Max	Mean	Min	Max
Isotope	ng/g/L	ng/g/L	ng/g/L	ng/g/L	ng/g/L	ng/g/L	ng/g/L	ng/g/L	ng/g/L
Li 7	453	141	1002	92	0	216	787	0	5293
Be 9	25	10	40	4	0	10	111	0	959
B 10	661542	166759	1388135	94576	12157	197373	389859	0	2691841
B 11	679951	181641	1656110	93247	12127	282220	327335	0	2932734
Ti 48	13181	5214	25926	2066	114	4332	8470	0	62839
Ti 49	6076	2248	12157	1117	31	2857	4805	0	46766
V 51	777	204	1126	141	6	420	817	0	16745
Cr 52	1086	350	1919	164	20	343	1191	0	19588
Mn 55	7435	16	30719	1344	184	4227	6682	0	69898
Ni 58	1112	176	3420	293	19	949	1480	0	20346
Co 59	70	13	182	14	1	43	96	0	1005
Ni 60	248	48	649	68	2	256	339	0	8009
Zn 64	1085435	0	3433253	114771	8089	267310	446719	0	3433253
Cu 65	3245	1060	7141	230	39	667	3812	0	86093
Zn 66	1171638	213323	3591266	128500	8548	271839	485843	0	3591266
As 75	160	0	498	27	0	97	628	0	15324
Se 82	317	82	643	41	2	86	326	0	8966
Sr 88	23016	8933	62682	3379	175	7527	13887	0	84874
Mo 95	42	12	135	3	1	4	52	0	704
Pd 106	24	5	72	1	0	3	34	0	422
Pd 108	10	3	26	1	0	2	11	0	110
Cd 111	34	0	89	3	0	7	36	0	336
Cd 114	29	12	66	3	0	9	16	0	80
Sn 118	94	28	145	12	1	20	61	0	846
Sn 120	91	25	140	11	1	19	59	0	1039
Sb 121	14	3	26	1	0	5	9	0	266
Ba 137	517423	2718	1292422	56910	2618	115631	277390	0	2978510
Ba 138	469735	2741	1038975	45119	2559	111020	250016	0	2393294
Ce 140	476	142	856	69	4	173	470	1	4740
Ir 191	1	0	9	0	0	0	2	0	110
Ir 193	2	0	11	0	0	0	1	0	40
Pt 194	7	1	23	1	0	1	5	0	276
Pt 195	7	0	25	1	0	1	9	0	452
Au 197	12	0	60	1	0	4	10	0	391
Hg 200	225	22	839	17	0	52	85	0	2146
Hg 202	192	0	817	17	4	64	81	0	1535
Tl 203	6	0	14	1	0	2	12	0	117
Tl 205	6	1	21	1	0	2	12	0	98
Pb 206	535	51	1266	69	2	138	574	0	7432
Pb 208	510	33	1214	65	2	131	539	0	7532
Bi 209	7	2	13	1	0	1	5	0	66
Ra 226							0	0	2
Th 232	62	14	139	9	0	23	55	0	630
U 238	26	8	47	4	0	18	21	0	202

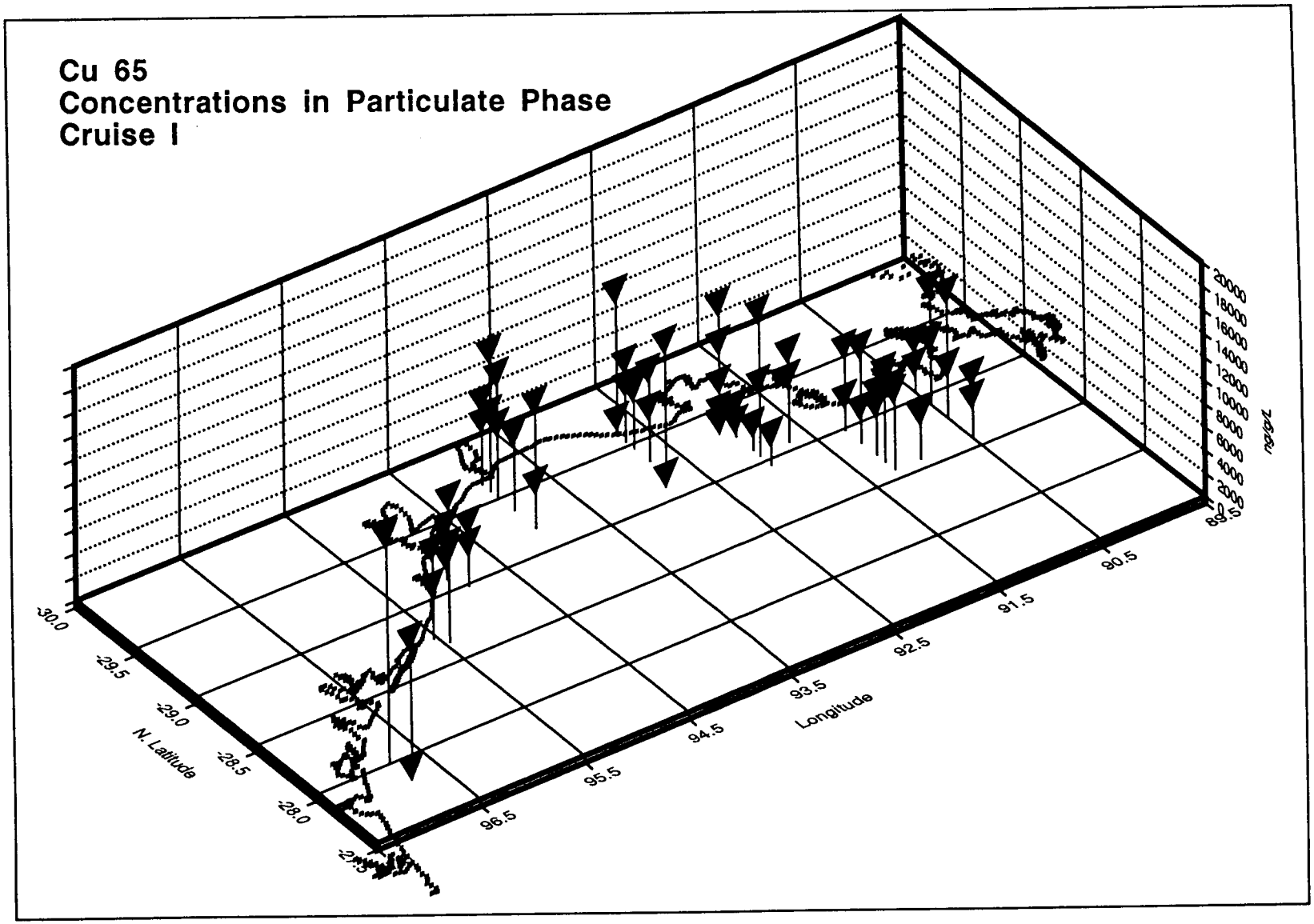

Figure 282. Spatial distribution of Cu 65 (ng/g/L) in the suspended particulate phase of water samples collected during Cruise P921.

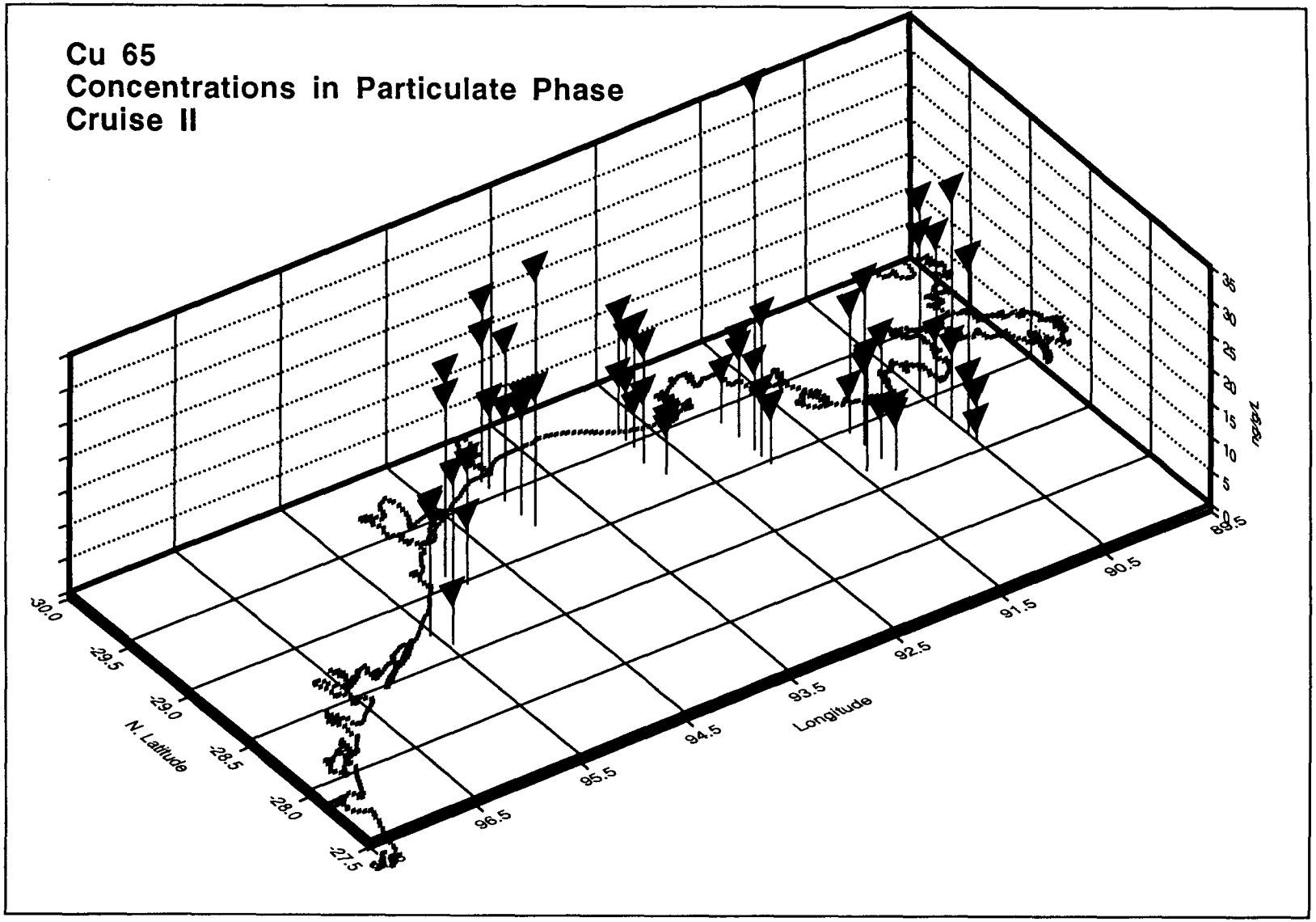

Figure 283. Spatial distribution of Cu 65 (ng/g/L) in the suspended particulate phase of water samples collected during Cruise P922.

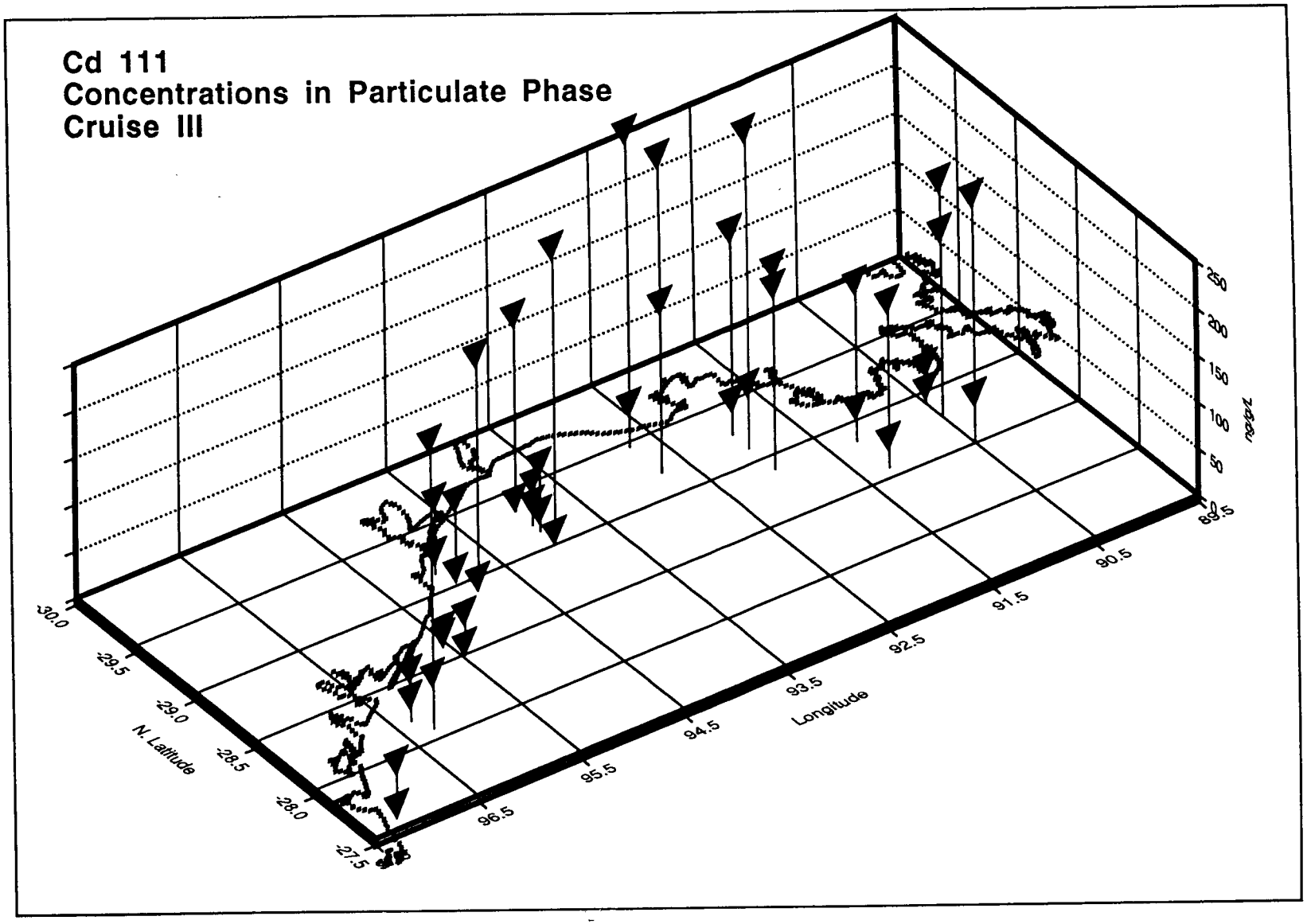

Figure 284. Spatial distribution of Cd 111 (ng/g/L) in the suspended particulate phase of water samples collected during Cruise P931.

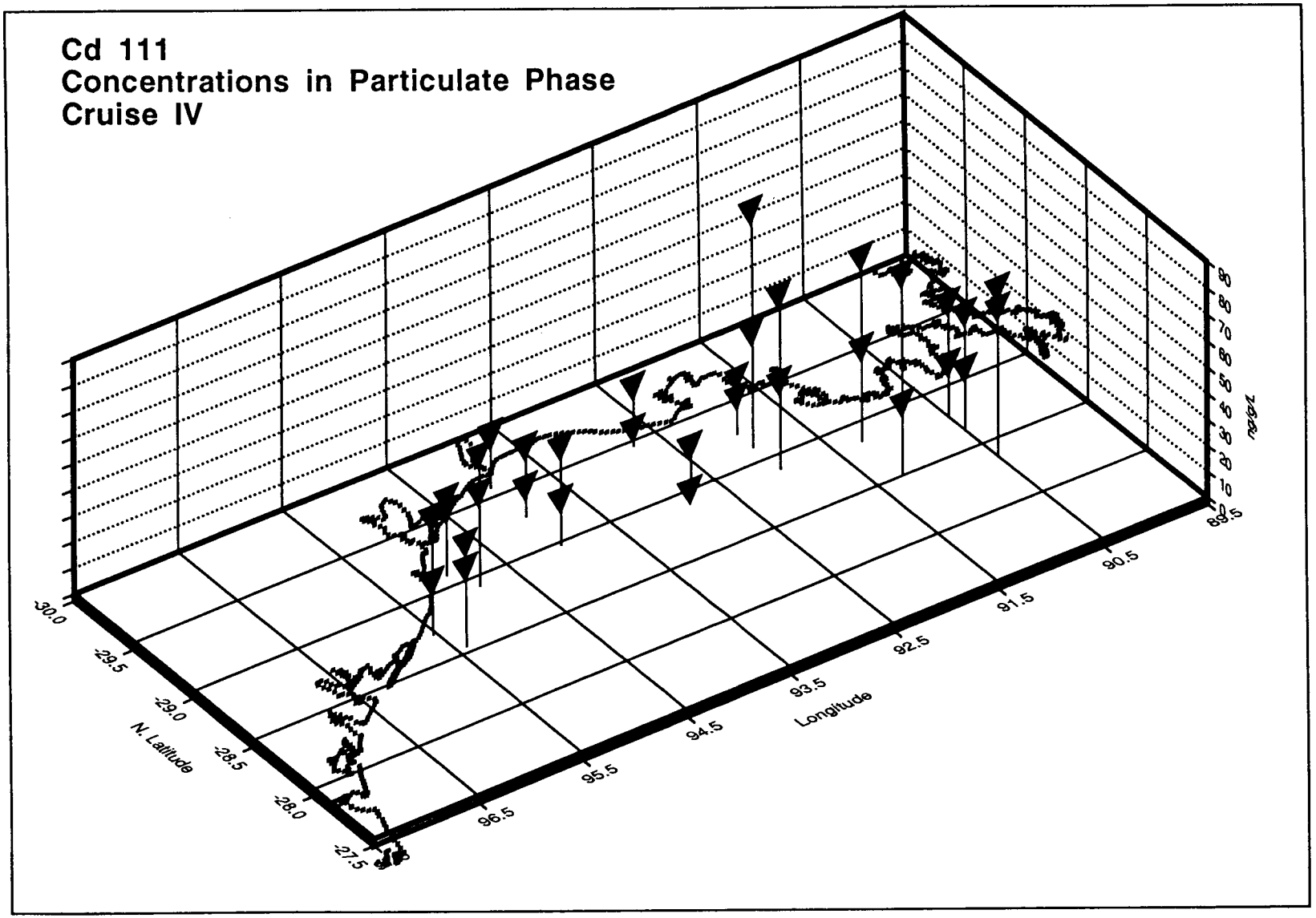

Figure 285. Spatial distribution of Cd 111 (ng/g/L) in the suspended particulate phase of water samples collected during Cruise P932.

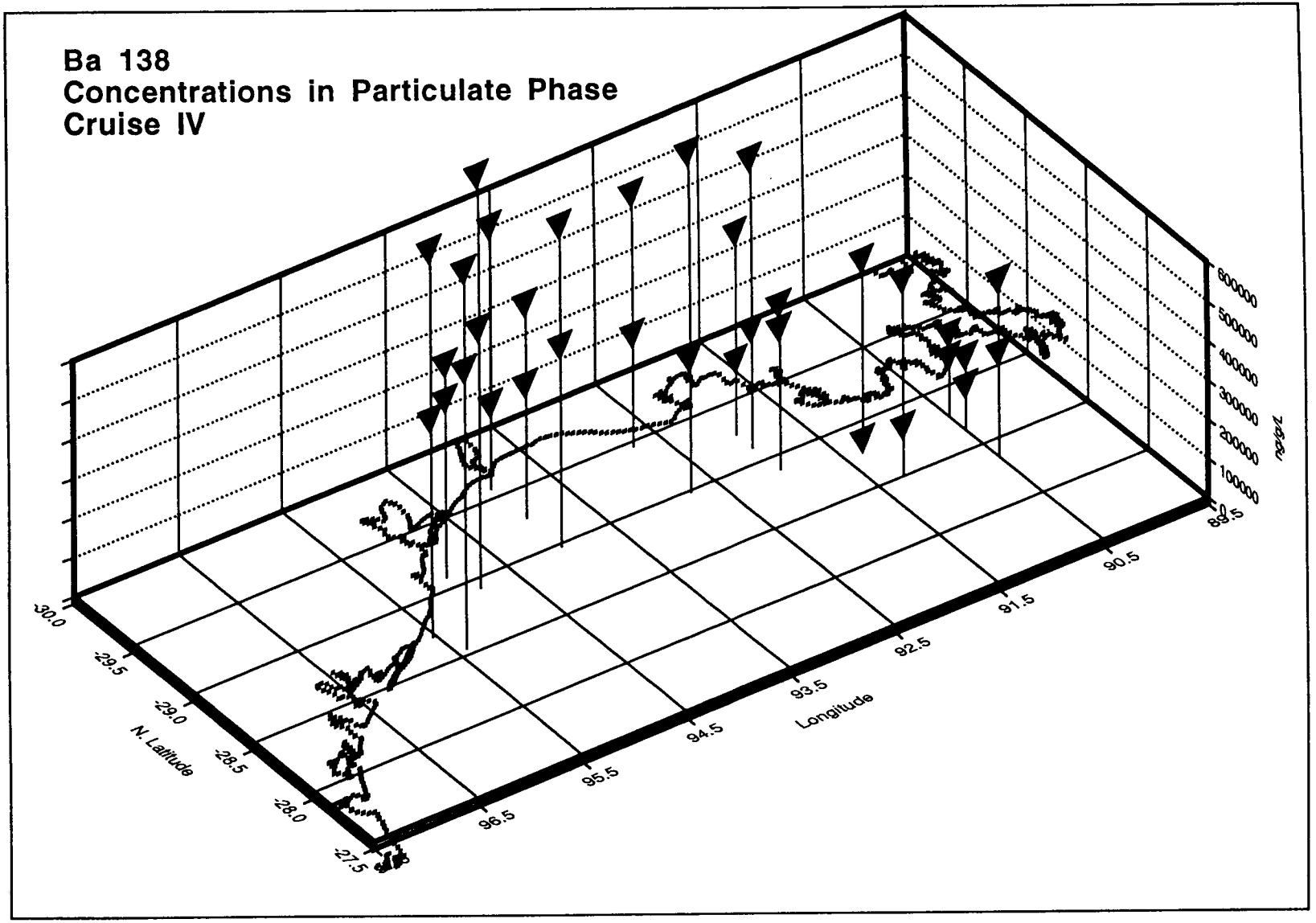

Figure 286. Spatial distribution of Ba 138 (ng/g/L) in the suspended particulate phase of water samples collected during Cruise P932

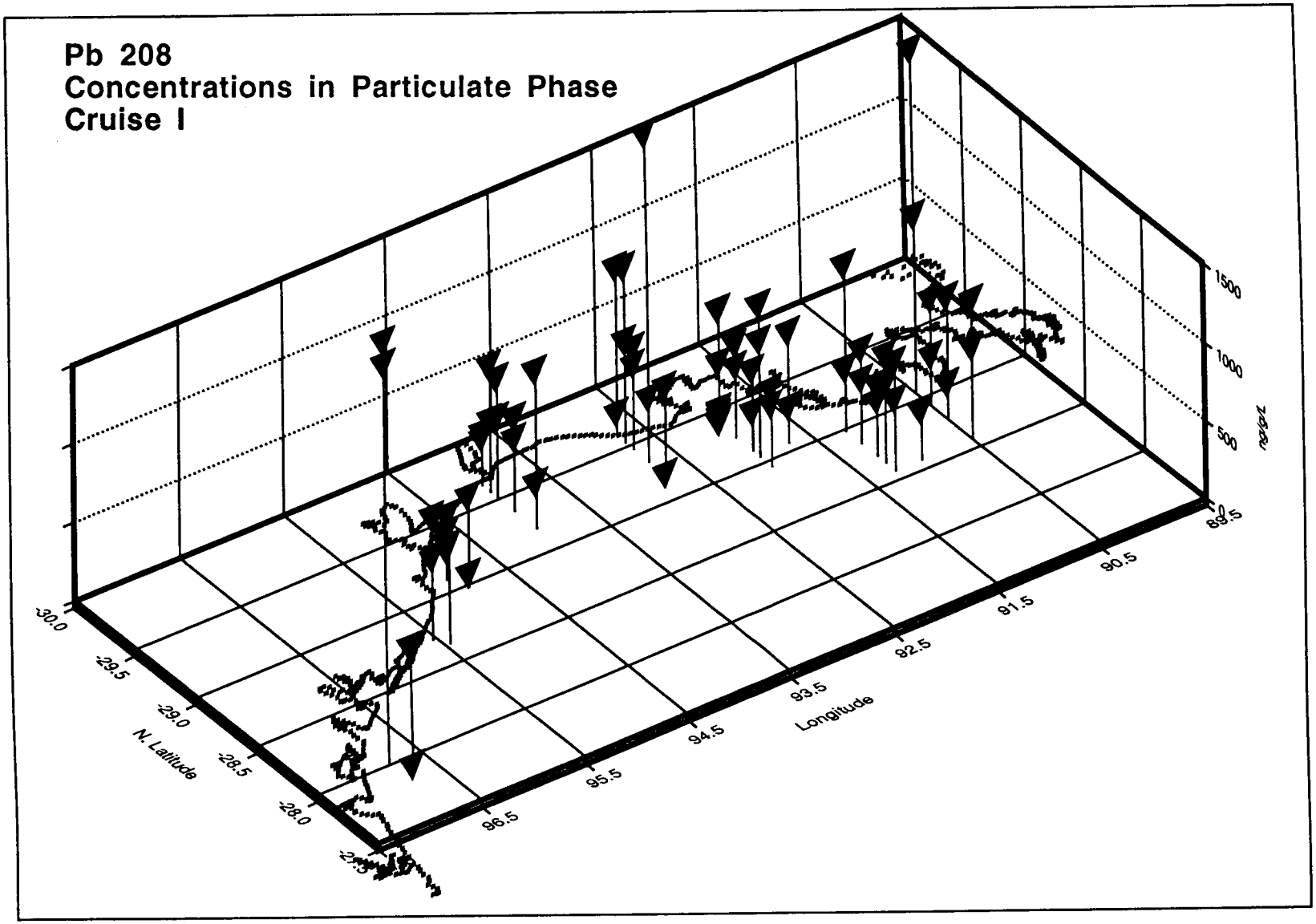

Figure 287. Spatial distribution of Pb 208 (ng/g/L) in the suspended particulate phase of water samples collected during Cruise P921.

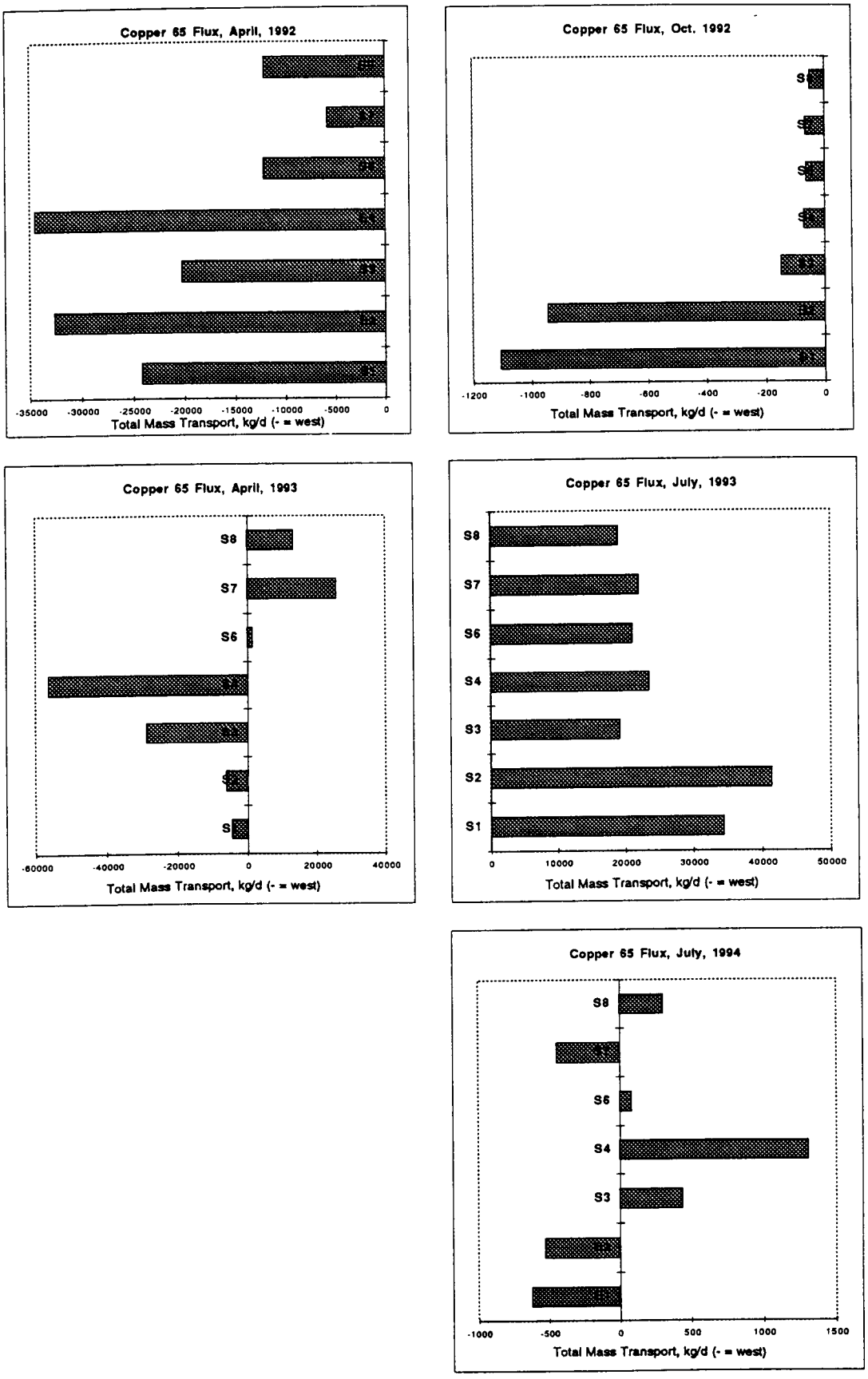

Figure 288. Calculated total mass transport (kg/d) of Copper 65 in the suspended particulate phase in the nNorthwestern Gulf of Mexico coastal shelf.

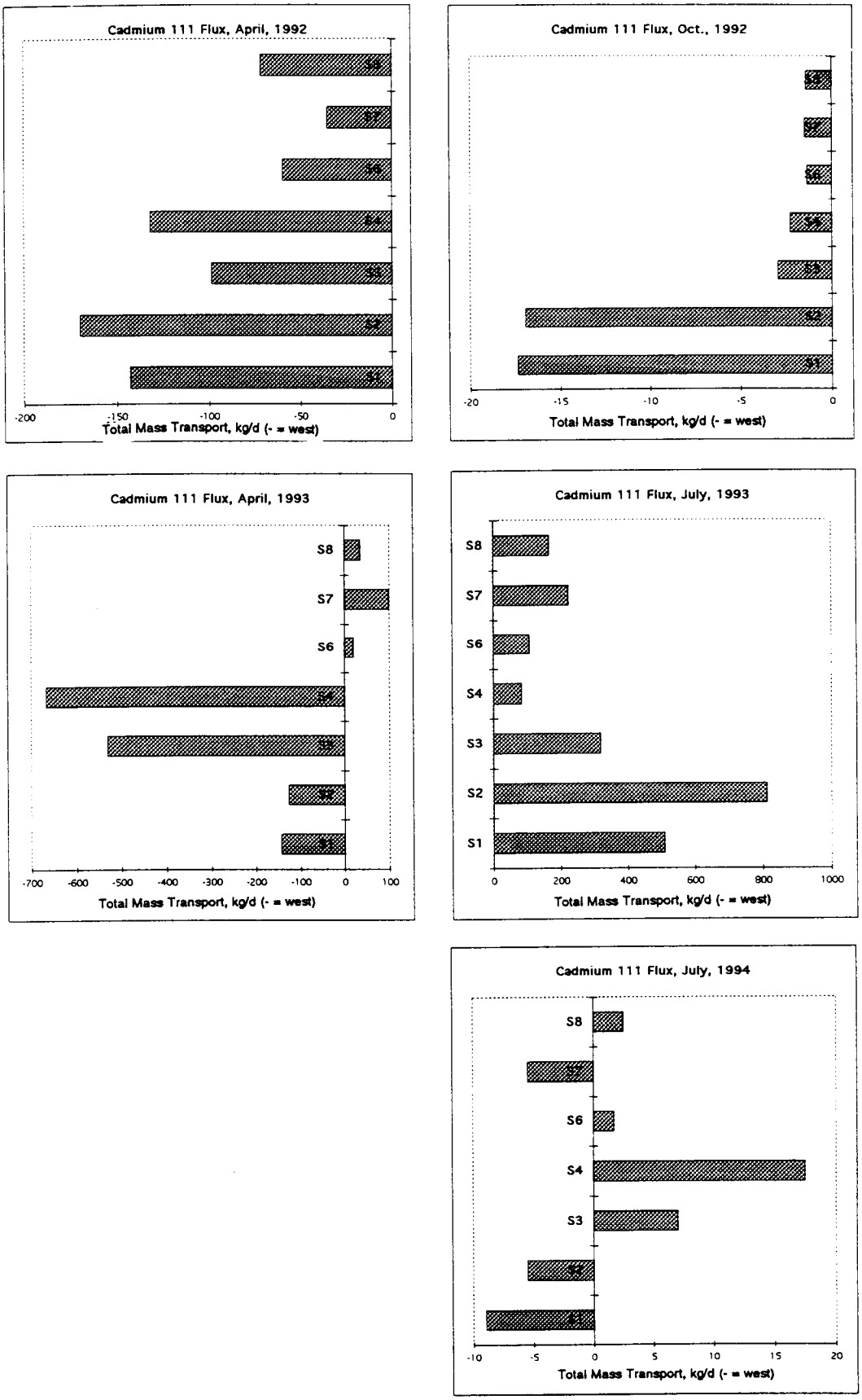

Figure 289. Calculated total mass transport (kg/d) of Cadmium 111 in the suspended particulate phase in the northwestern Gulf of Mexico coastal shelf.

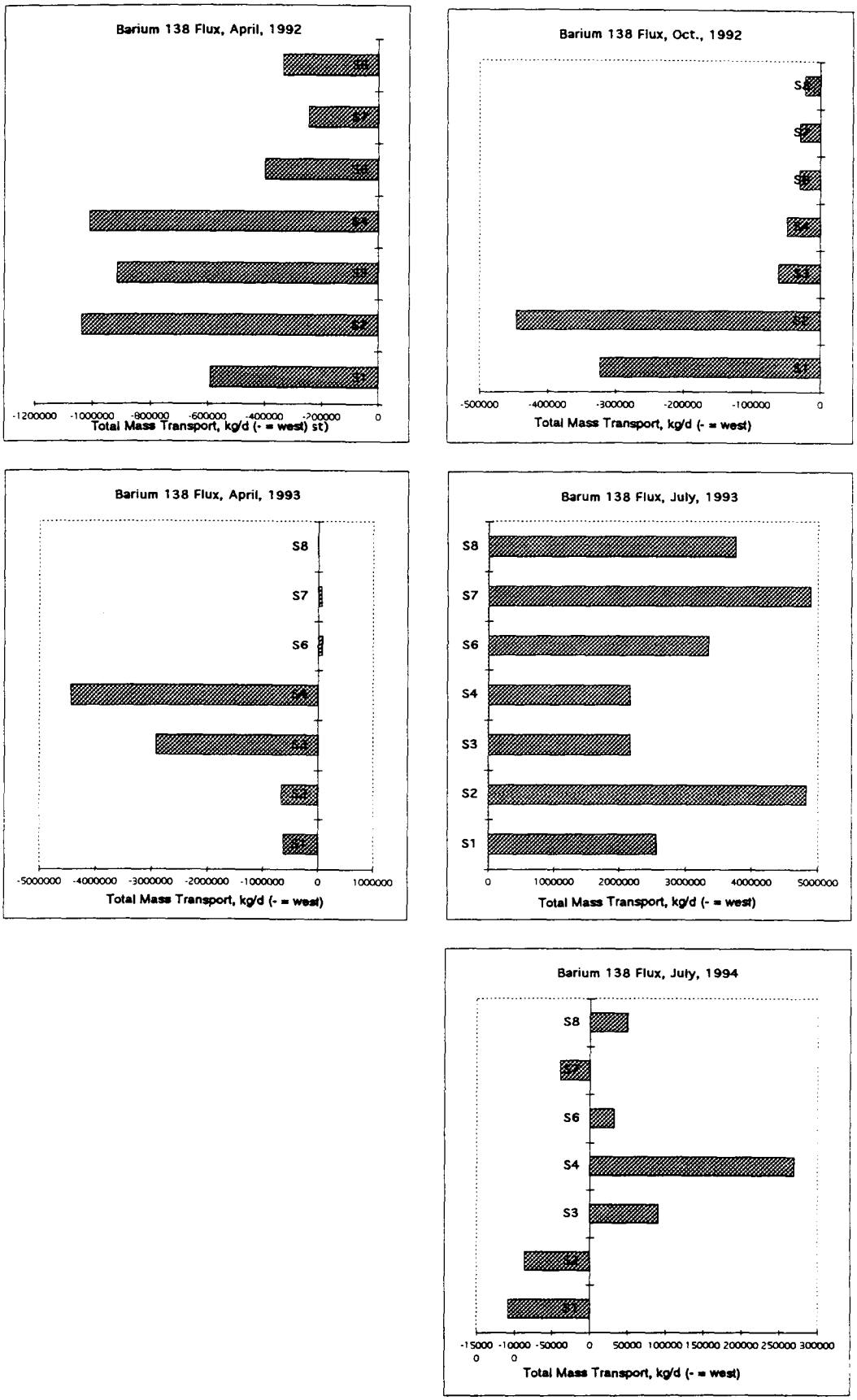

Figure 290. Calculated total mass transport (kg/d) of Barium 138 in the suspended particulate phase in the northwestern Gulf of Mexico coastal shelf.

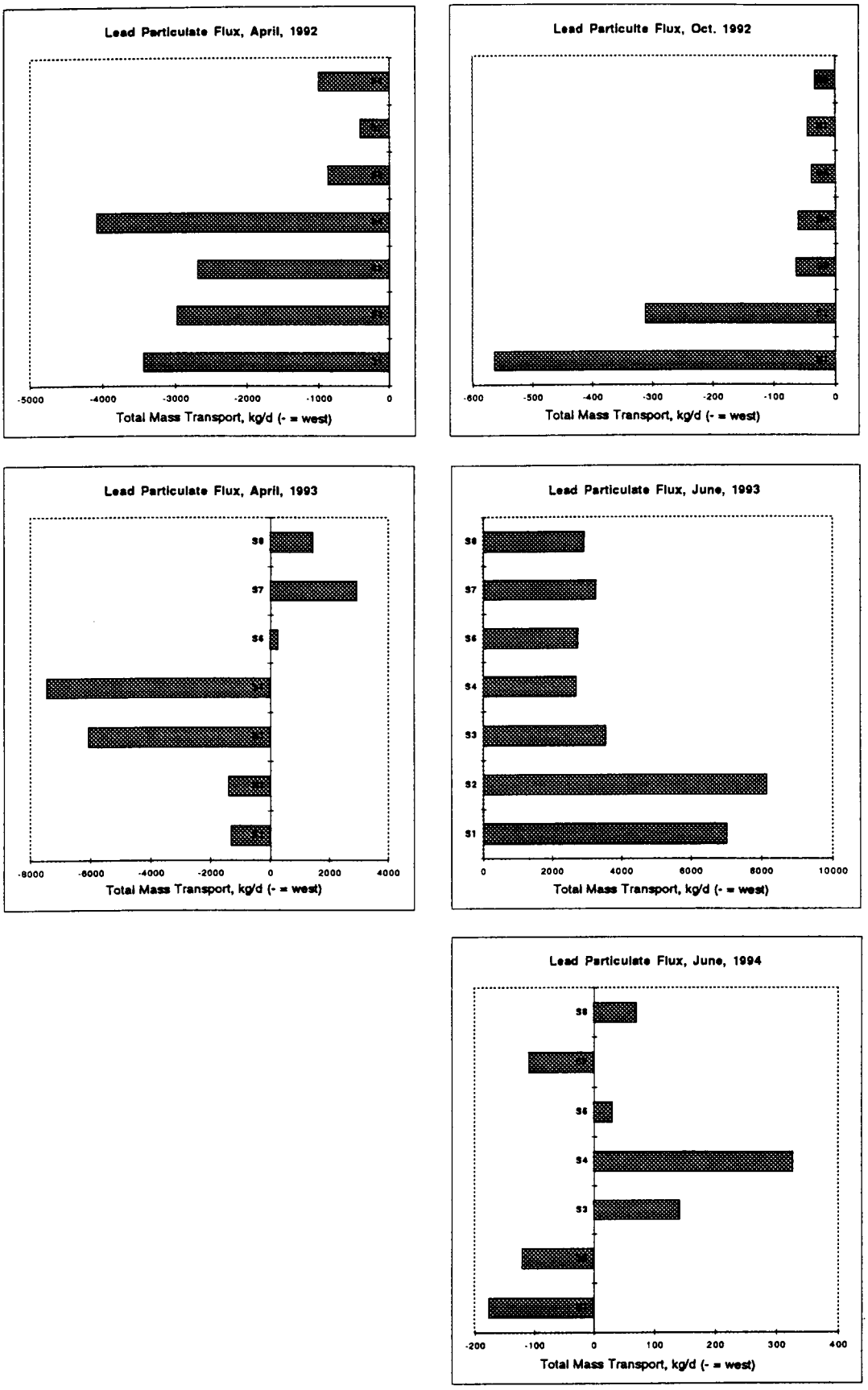

Figure 291. Calculated total mass transport (kg/d) of Lead 208 in the suspended particulate phase in the northwestern Gulf of Mexico coastal shelf.

the total mass transport fluxes in Figures 288-291 clearly show that particulates move far less material. For example, in April, 1992 the total mass transport of Cu measured along Transect S-1 in the particulate phase was ~3,500 kg/d, while at the same stations the total mass transport in the colloidal phase was nearly 80,000 kg/d or more than 20 times the particulate flux. In general, temporal and spatial trend in mass transport fluxes were similar among the elements. Ratios of some elements were shifted relative to one another suggesting possible inputs of particulate elements at certain regions or a slightly greater or lessor role of this phase in transport processes along some transects as was discussed with the colloidal data.

F. Sediment Trap Samples

Samples of particulates collected as part of the Texas A&M sediment trap flux experiments (Section V) were analyzed for trace elements only due to the small sample sizes typically collected. This precluded the analysis of trace organics in these samples. Sediment traps 14 through 19 were analyzed. Figure 292 shows the locations of the sediment trap mooring relative to our normal sampling cruise transects. Trap stations 15 and 16 correspond to Transect S-1 in our data sets, while Traps 17 and 18 correspond to our Transect S-3. Because sufficient material for analysis was only obtained in traps moored near the bottom, we have utilized some of our average surficial suspended sediment data to estimate vertical fluxes in the upper water column which may reflect new deposition, while the concentrations and fluxes calculated from the actual sediment trap materials probably reflect resuspension processes.

1. Results

Trace element concentrations were determined in all sediment trap samples provided and the data obtained is presented in Table 57. Means and standard deviations of trace element concentrations in sediments collected in traps that were sampled more than once are provided in Table 57. Data for Mooring 18 are the most complete and cover a three year period. Table 58 contained the estimated vertical fluxes of trace elements in samples from all traps, using the flux values provided by Texas A&M. Table 59 presents the estimated vertical fluxes in surface waters using average concentrations determined in our samples and the vertical flux data from surface water traps as reported by Texas A&M. Figure 292 shows the locations of the sediment traps relative to the basic cruise track used in our investigations. Figures 293-298 show the vertical flux values for six selected elements at Mooring 18 over the entire three year study period. Figures 299-304 show the vertical fluxes of selected trace elements in the upper water column estimated from suspended particulate concentrations and flux data from Texas A&M.

2. Discussion and Conclusions

Absolute trace element concentrations measured in the sediment traps were similar in those observed in the bedded sediment samples collected in April, 1992 during Cruise 92-1 in the so-called Atchafalaya box region of the Northwestern Gulf of Mexico. Where multiple collections of sediments occurred at Moorings 14, 15, 16 and 18 were available for analysis, comparisons of trace element concentrations were made. There was little difference between trace element concentrations (ng/g) collected at different times. Most % relative standard deviation (%RSD) values calculated for these data sets were less than 20% or less. This type of evaluation was not possible for samples collected at Moorings 17 and 19. No statistical significant differences between trace element concentrations (ug/g) as a function of depth were observed at any of the Moorings where sufficient data were available for such analysis. Certain elements such

Table 57. Mean trace element concentrations in sediment trap samples

Mean Trace Element Concentrations in Sediment Trap Samples																	
Ave./S.D. of MEAN PART.CONC.																	
Mooring /depth		M14/47m			M15/26m			M15/23m			M16/19m			M17/6.6m	M18/21 m		
														(single sample)			
Concentration units :	ppb (ng/g)	mean	STD DEV	%RSD	mean	STD DEV	%RSD	mean	STD DEV	%RSD	mean	STD DEV	%RSD	Mean	mean	STD DEV	%RSD
Element	Isotope																
Lithium	Li 7	23909	1531	6	19001	989	5	22168	432	2	24059	703	3	18900	18521	1713	9
Beryllium	Be 9	1187	62	5	929	81	9	1110	156	14	1147	27	2	951	948	146	15
Boron	B 10	38560	63	0	25517	1532	6	35198	4856	14	41463	18725	45	22200	25233	4072	16
Boron	B 11	42255	670	2	24892	1849	7	37458	9022	24	44427	23860	54	21200	25577	5058	20
Titanium	Ti 48	174504	14677	8	134726	10927	8	153086	44163	29	169973	18895	11	106000	128723	18155	14
Titanium	Ti 49	119201	17296	15	95600	6223	7	106494	31025	29	140491	15019	11	79200	91917	14489	16
Vanadium	V 51	56627	3352	6	42263	1466	3	51856	4705	9	58735	5281	9	36100	35311	4666	13
Chromium	Cr 52	33413	10	0	21577	1163	5	27751	6525	24	33080	1213	4	45900	26741	6602	25
Manganese	Mn 55	712332	173872	24	609651	44334	7	564214	122701	22	533950	93582	18	506000	538807	112764	21
Nickel	Ni 58	199652	12936	6	137009	5644	4	173904	50443	29	177875	25279	14	133000	128381	20386	16
Cobalt	Co 59	11716	391	3	9221	380	4	10284	3465	34	9437	696	7	8370	8332	1014	12
Nickel	Ni 60	27534	205	1	9749	621	6	18531	13700	74	18537	13597	73	6340	8919	4978	56
Zinc	Zn 64	216479	3289	2	101085	5537	5	135266	45714	34	309855	254353	82	127000	149193	123097	83
Copper	Cu 65	28364	3278	12	21883	1862	9	42933	8031	19	42843	19892	46	14700	23942	9721	41
Zinc	Zn 66	223618	4434	2	106887	4403	4	145864	52384	36	339892	274833	81	141000	161666	139942	87
Arsenic	As 75	11763	920	8	10089	2276	23	9601	795	8	11811	832	7	10300	9044	1156	13
Selenium	Se 82	7024	512	7	19645	1633	8	10078	1554	15	17964	1834	10	13000	17804	5485	31
Strontium	Sr 88	110022	8946	8	61798	2260	4	94970	874	1	90505	46755	52	52200	64655	8831	14
Molybdenum	Mo 95	1175	93	8	318	69	22	2910	1412	49	1694	1643	97	653	1213	2102	173
Palladium	Pd 106	1103	42	4	1724	23	1	1847	1173	64	1762	934	53	1370	1757	403	23
Palladium	Pd 108	503	22	4	730	143	20	902	624	69	617	266	43	685	840	394	47
Cadmium	Cd 111	394	25	6	311	119	38	271	11	4	686	350	51	240	394	162	41
Cadmium	Cd 114	266	102	38	162	65	40	246	76	31	530	364	69	319	251	197	79
Tin	Sn 118	1326	278	21	729	86	12	1266	601	47	1354	600	44	2440	928	277	30
Tin	Sn 120	1315	516	39	688	9	1	1203	510	42	1426	319	22	2440	939	264	28
Antimony	Sb 121	62	62	100	124	12	10	127	33	26	190	178	94	132	91	44	48
Barium	Ba 137	1610757	880901	55	333085	90630	27	428639	152806	36	455023	271090	60	432000	384629	69064	18
Barium	Ba 138	1700649	991718	58	337745	100049	30	442783	167264	38	463565	269028	58	462000	380524	65322	17
Cerium	Ce 140	48524	1755	4	61446	490	1	50617	8833	17	54955	21277	39	56900	56368	7863	14
Iridium	Ir 191	49	12	25	69	12	18	76	24	32	46	47	104	38	74	45	61
Iridium	Ir 193	51	4	7	28	3	12	55	1	1	49	4	9	56	55	38	70
Platinum	Pt 194	71	0	0	65	19	29	127	35	27	118	110	93	196	146	60	41
Platinum	Pt 195	55	23	41	165	1	0	145	83	58	150	45	30	164	180	51	28
Gold	Au 197	518	121	23	338	95	28	1243	1389	112	440	210	48	346	840	1175	140
Mercury	Hg 200	333	416	125	916	1	0	608	970	160	132	352	267	915	1108	395	36
Mercury	Hg 202	357	211	59	605	25	4	643	824	128	138	153	111	756	684	474	69
Thallium	Tl 203	300	29	10	468	142	30	345	13	4	407	123	30	413	408	93	23
Thallium	Tl 205	274	10	4	389	21	5	345	63	18	372	205	55	332	339	54	16
Lead	Pb 206	17400	1806	10	21672	1030	5	18500	41	0	22471	7191	32	34300	21229	5014	24
Lead	Pb 208	16977	816	5	20673	2019	10	17197	750	4	21343	5957	28	32800	20507	4633	23
Bismuth	Bi 209	317	27	8	408	49	12	333	1	0	391	132	34	367	364	67	18
Thorium	Th 232	8009	665	8	15306	699	5	9311	2083	22	12143	7498	62	14500	12526	2252	18
Uranium	U 238	1318	31	2	2023	433	21	1506	172	11	1618	493	30	1990	1836	387	21

Table 57 cont'd.

Mean Trace Element Co										
Ave./S.D. of MEAN PART.CONC.										
Mooring /depth		M18/17 m			M18/13m			M19/45m	M19/41m	M19/13
								(single sample)	(single sample)	(single sample)
Concentration units :	ppb (ng/g)	mean	STD DEV	%RSD	mean	STD DEV	%RSD	MEAN	MEAN	MEAN
Element	Isotope							98	100	119
Lithium	Li 7	19871	6889	35	18140	2003	11	26373	24900	7381
Beryllium	Be 9	968	340	35	933	82	9	2059	1400	1190
Boron	B 10	36999	22202	60	61158	26537	43	179706	286000	640701
Boron	B 11	40248	28917	72	66079	28406	43	188627	277600	677214
Titanium	Ti 48	168174	92170	55	272256	233447	86	193725	217600	121190
Titanium	Ti 49	98276	16937	17	107107	46006	43	102549	117000	66905
Vanadium	V 51	48030	17579	37	49279	2306	5	51667	52600	14762
Chromium	Cr 52	25809	13023	50	28890	1218	4	45686	64100	36071
Manganese	Mn 55	532467	331586	62	573063	160399	28	351765	361400	128571
Nickel	Ni 58	140979	76620	54	147010	4754	3	165784	154900	57500
Cobalt	Co 59	9206	4109	45	10163	3335	33	9314	8500	3690
Nickel	Ni 60	17261	20804	121	29967	9935	33	21373	20200	8810
Zinc	Zn 64	167661	17906	11	183912	75700	41	230490	232500	379405
Copper	Cu 65	68036	55912	82	104553	79159	76	97549	82100	238095
Zinc	Zn 66	183327	16019	9	197493	85272	43	232549	240500	387262
Arsenic	As 75	11295	4590	41	13189	7994	61	7353	10400	7262
Selenium	Se 82	19830	2164	11	23168	14536	63	8235	10500	10714
Strontium	Sr 88	158364	153816	97	347808	324196	93	287745	376900	284643
Molybdenum	Mo 95	3804	2013	53	4460	3170	71	1078	1300	1310
Palladium	Pd 106	1067	287	27	967	284	29	784	800	833
Palladium	Pd 108	492	176	36	628	232	37	490	500	952
Cadmium	Cd 111	486	70	14	1363	1155	85	490	700	952
Cadmium	Cd 114	364	307	84	1289	1330	103	490	700	952
Tin	Sn 118	973	439	45	1168	29	3	1275	1100	1786
Tin	Sn 120	1007	430	43	1182	19	2	1275	1200	1786
Antimony	Sb 121	52	29	55	222	211	95	294	300	1071
Barium	Ba 137	400520	41748	10	754721	171028	23	13637255	17941100	15039286
Barium	Ba 138	412640	54645	13	774530	180245	23	13628922	18928300	15530833
Cerium	Ce 140	40450	5162	13	31353	9580	31	38627	37400	18095
Iridium	Ir 191	12	6	51	76	11	15	294	100	595
Iridium	Ir 193	28	7	24	48	46	96	294	100	595
Platinum	Pt 194	79	10	12	158	56	35	294	200	595
Platinum	Pt 195	131	46	35	129	16	12	392	300	714
Gold	Au 197	311	44	14	1946	2062	106	686	1200	3452
Mercury	Hg 200	376	116	31	723	362	50	882	1300	3333
Mercury	Hg 202	533	124	23	728	528	73	980	1100	3333
Thallium	Tl 203	235	43	18	195	71	36	490	400	595
Thallium	Tl 205	250	55	22	201	76	38	490	400	595
Lead	Pb 206	18389	157	1	21338	1757	8	34412	59000	52143
Lead	Pb 208	17838	337	2	19176	1905	10	36373	62900	57143
Bismuth	Bi 209	281	10	3	257	45	18	490	400	595
Thorium	Th 232	8031	3916	49	5086	2374	47	6569	6900	3333
Uranium	U 238	1733	448	26	1752	707	40	1176	1600	1190

Table 58. Estimated vertical flux in trace elements from all sediment traps.

Mooring Fluxes		depth-47m	depth-47m	depth-43	depth-39	depth-13	depth-26	depth-23	depth-21	depth-26	depth-23	depth-19m	depth-19m
VERT ICAL FLUX,NG/ M²/D		M14	M14	M14	M14	M14	M15	M15	M15	M15	M15	M16	M16
Deployment/[end date]		D10[9/93]	D13[3/94]	D13[3/94]	D13[3/94]	D13[3/94]	D10[9/93]	D10[9/93]	D10[9/93]	D12+D13[3/94]	D12+D13[3/94]	D10	D13
Lithium	Li 7	1844341	3021412	972300	491078	144800	4129120	226977	212758	13806943	1427637	716285	37272878
Beryllium	Be 9	99465	138189	56250	24436	7488	206666	12322	10551	657609	65300	34291	1770883
Boron	B 10	3112012	4667224	1634775	950852	370495	5575360	390183	430646	18432981	2074235	1663002	42838511
Boron	B 11	3375905	5165936	1699950	1072601	394319	5491520	442754	463751	17792453	2029422	1863459	41826578
Titanium	Ti 48	13261381	22352234	6028913	3461528	744584	26619200	1230766	1496317	107466415	12035686	4761005	278281667
Titanium	Ti 49	8643257	15890008	3789450	2496306	687286	19115520	854016	947206	75440000	8386569	3948078	229371556
Vanadium	V 51	4383966	7132737	2370000	1246831	573863	9075680	557348	615604	31101208	3168971	1899058	83484500
Chromium	Cr 52	2700336	4038785	1372875	693228	214151	4695040	326887	349826	15657358	1510863	1031685	48910111
Manganese	Mn 55	67490462	71256767	19461188	10007793	2781726	134353600	6574868	8620762	436270943	31177549	18243739	710039889
Nickel	Ni 58	15392804	25243799	7503413	3818597	1239268	29553600	2116677	1841506	100349434	9026765	5950800	242864000
Cobalt	Co 59	968954	1382975	444900	239338	75909	1989104	128613	115878	6754015	511517	301842	13576772
Nickel	Ni 60	2236463	3311330	1054538	570290	189437	1951376	285002	296454	7686340	577457	855790	13543041
Zinc	Zn 64	17679363	25891098	6568650	4610778	8314368	22008000	1692659	2167537	73304906	6722059	14887154	197327000
Copper	Cu 65	2479106	3148961	1510425	924161	461210	4862720	490981	804962	15515019	2432745	1730034	43681789
Zinc	Zn 66	17815026	27414438	6907238	4890849	8954070	23056000	1847341	2237805	78286792	7106176	16240531	220938778
Arsenic	As 75	897850	1500732	278775	144689	74387	1777408	102646	101922	8825057	590261	376930	17034211
Selenium	Se 82	596789	805436	162938	133599	87922	4359680	90688	140184	13949283	729824	585534	25298333
Strontium	Sr 88	8378637	14066352	4616400	2381137	645798	12617920	952955	1376126	47826113	6241912	3756406	87194922
Molybdenum	Mo 95	89607	150037	32475	20603	49664	76923	39481	29401	203546	124838	86822	807860
Palladium	Pd 106	86698	136980	42788	18491	7334	364704	10272	9618	1288174	174774	33470	3676691
Palladium	Pd 108	39350	62626	16388	7606	3627	131838	4646	5306	627006	87707	13042	1222753
Cadmium	Cd 111	30381	49811	17738	4982	9617	82792	2818	4699	170808	17157	28394	666189
Cadmium	Cd 114	27310	23455	13725	15683	39205	43597	3020	5509	87539	12548	23925	413206
Tin	Sn 118	122978	136496	182138	287841	906505	165584	17079	14846	504594	54929	54051	1411647
Tin	Sn 120	135744	114855	178350	272753	913483	142947	15786	14089	523810	54993	50190	1821480
Antimony	Sb 121	8484	2176	2738	1415	963	27667	1525	1496	86827	6786	9606	97820
Barium	Ba 137	79819573	270048043	43437975	14819635	4034011	56382400	5420559	6834494	299624906	20934412	19660045	399713667
Barium	Ba 138	80751358	290389589	49466138	15450625	4074414	55963200	5666676	6856309	308165283	21190490	19875429	414892667
Cerium	Ce 140	3820466	6016589	1864500	916904	292003	12806560	448147	377634	46616226	3713137	1213264	106253000
Iridium	Ir 191	4606	4836	2138	984	502	12576	939	625	58359	3841	2402	18552
Iridium	Ir 193	4282	5803	1238	615	243	6288	566	466	19216	3585	1398	79268
Platinum	Pt 194	5737	8584	2363	1784	1222	10899	1040	625	59071	9923	1216	296834
Platinum	Pt 195	3151	8584	4988	2091	761	34374	869	211	124547	13316	3587	276595
Gold	Au 197	34906	72903	18450	4428	4339	56802	2636	5764	306030	145325	17875	441878
Mercury	Hg 200	3151	75804	24975	7216	4436	191784	-788	3098	691771	84506	-3557	578489
Mercury	Hg 202	16806	61175	16763	615	3133	130581	606	4453	443388	80025	912	374415
Thallium	Tl 203	22543	38688	10200	4879	1708	119262	3575	2693	277562	21959	9728	748831
Thallium	Tl 205	21574	33973	8213	5474	1570	84678	3030	2666	282544	25416	6901	784248
Lead	Pb 206	1302738	2258049	684150	390013	840261	4695040	186557	146318	15799698	1209971	528534	41826578
Lead	Pb 208	1325120	2122279	668588	377385	877168	4632160	179053	138996	14518642	1088333	520782	38790778
Bismuth	Bi 209	27149	36028	10088	5515	2348	92853	3373	1980	281832	21703	9059	735338
Thorium	Th 232	609151	1025111	307275	143418	52676	3311680	79164	64979	11173660	704216	207966	26478922
Uranium	U 238	108272	156686	44663	23780	8508	488368	13978	12408	1295291	106273	38608	2985203

Table 58 cont'd.

Mooring Fluxes		depth-13m	depth-6.6m	depth-21m	depth-21m	depth-21m	depth-21m	depth-21m	depth-21m	depth-21m	depth-21m	depth-13m	depth-17m
VERT ICAL FLUX,NG/ M²/D		M16	M17	M18	M18	M18	M18	M18	M18	M18	M18	M18	M18
Deployment/[end date]		D13	D[3/94]	D1[5/92]	D2[7/92]	D3[8/92]	D4[10/92]	D5[12/92]	D6[1/93]	D7+D8[5/93]	D9[7/93]	D10[9/93]	D10[9/93]
Lithium	Li 7	1039350	27599670	3145350	2760320	7531765	8054090	8684327	6195130	6407619	7023709	71912	153404
Beryllium	Be 9	56277	1388745	172591	130570	378262	381170	497588	276453	330793	406058	3763	7492
Boron	B 10	1414530	32418660	4387360	3613840	9707608	9647680	10608962	7233620	8970667	11596436	343667	326730
Boron	B 11	1450020	30958360	4516400	3668320	9707608	9475400	10092596	6982950	8610238	11779345	370512	376309
Titanium	Ti 48	5779800	154791800	23065900	18704800	60672549	46946300	49758846	41539600	47656667	53043636	1880513	1446760
Titanium	Ti 49	4507230	115655760	16291300	13057040	42261569	33379250	31779942	28970290	33760143	40240000	600444	683566
Vanadium	V 51	2925390	52716830	5790670	5012160	15063529	13437840	15725673	9704510	12014286	14596145	218911	374852
Chromium	Cr 52	1358760	67027770	4193800	3977040	8201255	9260050	9670115	14037520	6607857	9694182	127930	217109
Manganese	Mn 55	20229300	738911800	62100500	71187200	317589412	213196500	301639038	145746700	205043810	197541818	2951873	4754987
Nickel	Ni 58	7757100	194219900	21936800	17778640	51885490	52545400	64310962	35666760	39046429	51946182	646597	1209977
Cobalt	Co 59	423852	12222711	1304917	1144080	3569220	3510205	4351552	2624873	2735252	3171644	53842	75092
Nickel	Ni 60	598260	9258302	1398471	592016	3293055	3161338	3872740	1779757	2142548	3541120	159069	198224
Zinc	Zn 64	5779800	185458100	15662230	96792800	38537529	43931400	54453077	40465300	29915571	39142545	1020989	1118000
Copper	Cu 65	1034280	21466410	7516580	3886240	6150941	5986730	9764000	6087700	9251000	10462400	690268	666944
Zinc	Zn 66	6438900	205902300	16613900	108960000	41173647	48238400	58677885	44046300	32358476	40605818	1108494	1206856
Arsenic	As 75	562770	15041090	1569449	1441904	3385110	3820309	4182560	2753789	3428076	3731345	81019	90153
Selenium	Se 82	1389180	18983900	3564730	3868080	5314078	8097160	5633077	6051890	6327524	7938255	143820	132437
Strontium	Sr 88	3183960	76227660	12823350	9225280	26110118	26444980	28165385	19122540	22186381	29960509	2481310	1656196
Molybdenum	Mo 95	114582	953576	1300078	115134	143104	128349	160543	160429	129354	457273	28815	32411
Palladium	Pd 106	98865	2000611	403250	274216	799204	671892	751077	572960	600714	782851	3297	5358
Palladium	Pd 108	35845	1000306	316148	101151	278675	246791	362395	219515	266717	391425	1996	2279
Cadmium	Cd 111	32904	350472	68230	64105	135572	170127	92946	196955	84901	149620	9373	3322
Cadmium	Cd 114	22055	465836	30647	42313	48956	68481	77924	76992	49259	80846	9588	3606
Tin	Sn 118	147537	3563132	150009	124214	316334	349298	450646	418977	272324	344967	4935	7957
Tin	Sn 120	135369	3563132	166139	138561	305455	355758	382110	348431	220262	327407	5140	8127
Antimony	Sb 121	2129	192760	10162	11441	61928	31872	15022	35810	38045	46459	1597	450
Barium	Ba 137	13638300	630849600	64197400	48305600	169046275	174002800	181666731	124260700	122545714	154375273	2725279	2666248
Barium	Ba 138	12827100	674658600	66939500	47034400	164025098	170557200	176033654	128916000	117339524	143400727	2782433	2797931
Cerium	Ce 140	2981160	83091070	8339210	8626000	27783843	25928140	32437135	15469920	21745857	22314909	105688	228160
Iridium	Ir 191	2738	55491	22743	19794	22595	6891	30513	11817	28434	45727	292	47
Iridium	Ir 193	2180	81777	19840	12712	17993	12921	23471	13250	10813	31460	67	145
Platinum	Pt 194	7859	286219	28389	28148	47701	44362	53514	51925	78493	75724	850	532
Platinum	Pt 195	11103	239489	26453	37773	41006	65897	122989	85944	70083	76090	604	610
Gold	Au 197	15616	505264	745206	67918	261938	124903	140358	80214	198236	435324	2099	2118
Mercury	Hg 200	104442	1336175	258080	239712	335164	615901	779242	266068	297554	293020	2007	1819
Mercury	Hg 202	36098	1103987	287114	48487	335164	516840	292451	143240	18021	406058	1525	3849
Thallium	Tl 203	21345	603104	62907	49577	176160	164527	292920	150760	146574	222417	625	1266
Thallium	Tl 205	24843	484820	45487	53209	140593	136963	171339	116383	105726	164618	635	1307
Lead	Pb 206	3422250	50088290	2822750	3341440	8201255	9518470	9951769	6911330	6768048	8267491	97098	113321
Lead	Pb 208	3194100	47897840	2451760	3123520	8410471	9260050	10562019	6696470	6367571	8157745	88247	112075
Bismuth	Bi 209	19722	535930	49358	56841	130969	215781	184483	103133	116939	163521	1244	1783
Thorium	Th 232	866970	21174350	1561384	2233680	5063020	6934270	7323000	4762730	4044810	4719055	14651	32628
Uranium	U 238	139932	2905997	233885	332328	912180	1042294	915375	540731	540643	797484	9685	8778

Table 58 cont'd.

Mooring Fluxes		depth-21m	depth-21m	depth-21m	depth-13m	depth-17m	depth-21m	depth-21m	depth- 45M	depth-41M	depth-13M
VERT ICAL FLUX,NG/ M^2/D		M18	M18	M18	M18	M18	M18	M18	M19	M19	M19
Deployment/[end date]		D10[9/93]	D11[12/93]	D12[2/94]	D13[3/94]	D13[3/94]	D13[3/94]	D14+D15[7/94]	D[5/93]	D[5/93]	D[5/93]
Lithium	Li 7	1823200	13686790	15125784	240551	754500	7689489	7186833	585470.588	251490	31738.0952
Beryllium	Be 9	78864	750214	855898	12189	36618	364556	362413	45705.8824	14140	5119.04762
Boron	B 10	2363800	21785936	20216902	521446	1071390	10700433	10135278	3989470.59	2888600	2755015.12
Boron	B 11	2438000	24486311	20216902	565714	995940	10839400	10473120	4187529.41	2803760	2912021.43
Titanium	Ti 48	11872000	91198598	114365686	1318363	5180900	63461444	43305278	4300705.88	2197760	521119.048
Titanium	Ti 49	8999400	65219783	81900588	917285	4340890	46785444	31327222	2276588.24	1181700	287690.476
Vanadium	V 51	3953800	25944474	28775882	586070	1790680	17741411	13390852	1147000	531260	63476.1905
Chromium	Cr 52	3784200	20073518	21028529	344744	834980	11626878	11394509	1014235.29	647410	155107.143
Manganese	Mn 55	70384000	374418403	396959608	5653609	14989400	193626889	212226574	7809176.47	3650140	552857.143
Nickel	Ni 58	12932000	117711677	106987255	1766870	4366040	54197000	47297963	3680411.76	1564490	247250
Cobalt	Co 59	841640	6920992	7186592	96002	316890	3469534	2942302	206764.706	85850	15869.0476
Nickel	Ni 60	765320	15741955	7747353	282187	128265	3163808	3961972	474470.588	204020	37880.9524
Zinc	Zn 64	15688000	165817855	78211373	1603723	7796500	39234922	36241296	5116882.35	2348250	1631440.48
Copper	Cu 65	2904400	22943617	23832333	597522	1433550	5743956	5589759	2165588.24	829210	1023809.52
Zinc	Zn 66	16218000	180972714	83376275	1687523	8651600	42477478	36548426	5162588.24	2429050	1665226.19
Arsenic	As 75	974140	5785764	7208727	92693	404915	4956478	2641315	163235.294	105040	31226.1905
Selenium	Se 82	2395600	6790233	10772510	158535	920490	12368033	4299815	182823.529	106050	46071.4286
Strontium	Sr 88	6052600	49498961	51427667	1458374	2494880	29924156	21222657	6387941.18	3806690	1223964.29
Molybdenum	Mo 95	128260	233782	206596	27281	119714	690201	215605	23941.1765	13130	5630.95238
Palladium	Pd 106	177020	619455	1837229	14366	63881	680937	614259	17411.7647	8080	3583.33333
Palladium	Pd 108	75896	270764	900169	9742	30985	328888	313272	10882.3529	5050	4095.2381
Cadmium	Cd 111	86708	200101	332767	6716	21981	195943	78011	10882.3529	7070	4095.2381
Cadmium	Cd 114	94234	197460	163063	4293	7394	93571	69718	10882.3529	7070	4095.2381
Tin	Sn 118	89994	451053	680291	14625	33349	727259	319415	28294.1176	11110	7678.57143
Tin	Sn 120	104092	581812	819006	14366	35361	708730	328629	28294.1176	12120	7678.57143
Antimony	Sb 121	9010	11887	132812	898	1610	49102	26106	6529.41176	3030	4607.14286
Barium	Ba 137	37842000	249323454	279642549	10770569	18661300	243191667	125923148	302747059	181205110	64668928.6
Barium	Ba 138	39008000	254859587	276691176	11094391	18812200	233464000	127765926	302562059	191175830	66782583.3
Cerium	Ce 140	5395400	30105655	46484118	468962	2218230	24597100	20331981	857529.412	377740	77809.5238
Iridium	Ir 191	3498	20472	120268	1033	805	25014	21806	6529.41176	1010	2559.52381
Iridium	Ir 193	2438	13208	102560	996	1660	24551	3993	6529.41176	1010	2559.52381
Platinum	Pt 194	25228	31699	144617	1464	3622	24088	44534	6529.41176	2020	2559.52381
Platinum	Pt 195	10388	87833	177082	1451	8249	81064	57126	8705.88235	3030	3071.42857
Gold	Au 197	31694	255575	863276	41869	14084	121364	235261	15235.2941	12120	14845.2381
Mercury	Hg 200	109180	206705	929682	12042	23037	611453	420768	19588.2353	13130	14333.3333
Mercury	Hg 202	66038	58776	426473	13555	22384	391423	191342	21764.7059	11110	14333.3333
Thallium	Tl 203	40492	184252	304729	3014	13330	187605	107803	10882.3529	4040	2559.52381
Thallium	Tl 205	40916	148590	295137	3137	14537	167223	125002	10882.3529	4040	2559.52381
Lead	Pb 206	2745400	9190787	15125784	247181	930550	14545178	7831806	763941.176	595900	224214.286
Lead	Pb 208	2766600	8521141	15052000	219297	885280	12970222	7739667	807470.588	635290	245714.286
Bismuth	Bi 209	39326	179629	303254	2768	13782	188531	128380	10882.3529	4040	2559.52381
Thorium	Th 232	1420400	4840732	9296824	83210	543240	5975567	4453380	145823.529	69690	14333.3333
Uranium	U 238	215180	612851	1394524	15400	103115	861593	721755	26117.6471	16160	5119.04762

Table 59. Estimated vertical flux in surface waters.

MOORING		15	16	18	18	18	18	18
CRUISE		4	4	1	2	3	4	6
Sample ID		107S	105S	030S	139S	126S	130S	130S
Element	Isotope	ng/m²/day	ng/m²/day	ng/m²/day	ng/m²/day	ng/m²/day	ng/m²/day	ng/m²/day
FLUX		8.8	3.4	9.0	22.3	25.3	18.4	25.2
Sediment Trap Deployment Date		9/25/93	9/26/93	5/31/92	10/20/92	5/24/93	7/16/93	7/24/94
Lithium	Li 7	316.70	101.87	521.80	14.89	4124.25	129.37	75.96
Beryllium	Be 9	11.52	4.70	104.56	2.79	577.10	29.39	2.40
Boron	B 10	321133.56	118935.71	108317.41	15273.46	2960499.18	344311.73	142868.87
Boron	B 11	342650.97	117434.19	115107.36	13617.05	956480.79	342753.47	105544.83
Aluminium	Al 27	NA	NA	51901.54	8720.31	NA	NA	NA
Silicon	Si 28	NA	NA	16217.48	1556.78	NA	NA	NA
Titanium	Ti 48	5983.01	2074.33	2623.99	94.24	42121.04	12229.64	2694.07
Titanium	Ti 49	2163.75	890.55	1484.10	31.73	22937.62	5404.08	1415.79
Vanadium	V 51	250.28	64.56	114.10	4.73	3289.23	746.33	94.76
Chromium	Cr 52	414.20	156.16	151.05	3.37	5929.57	1272.88	167.71
Manganese	Mn 55	1192.08	435.24	373.08	15.81	14476.52	4626.08	458.04
Nickel	Ni 58	167.23	149.44	57.87	1.54	4763.66	360.79	83.24
Cobalt	Co 59	17.28	6.34	14.15	0.42	418.86	45.79	5.61
Nickel	Ni 60	89.32	110.32	29.42	0.50	1443.27	69.71	37.52
Zinc	Zn 64	903024.73	325091.18	149380.08	6915.90	1880055.30	597315.87	142127.38
Copper	Cu 65	796.08	346.55	1234.39	9.19	8039.43	2966.04	190.49
Zinc	Zn 66	1005304.26	371248.28	166295.41	7925.10	2229017.38	647351.40	198186.77
Arsenic	As 75	48.15	9.31	60.65	36.63	4905.51	0.00	31.50
Selenium	Se 82	80.61	29.87	67.86	5.75	1084.39	96.15	73.37
Strontium	Sr 88	16130.29	6136.50	4596.14	264.48	71949.45	16278.91	3734.38
Molybdenum	Mo 95	13.29	3.19	11.05	5.63	547.70	25.61	2.73
Palladium	Pd 106	7.94	6.18	8.03	0.20	210.83	53.66	0.87
Palladium	Pd 108	4.88	1.24	6.41	0.24	65.71	16.74	0.64
Cadmium	Cd 111	19.26	7.27	12.20	0.26	247.14	60.69	3.50
Cadmium	Cd 114	19.80	7.73	11.07	0.00	NA	19.77	3.37
Tin	Sn 118	32.64	12.22	16.10	0.57	226.65	83.66	16.25
Tin	Sn 120	30.21	10.16	17.55	0.57	199.71	67.09	16.89
Antimony	Sb 121	2.93	2.54	1.70	0.07	23.66	19.08	1.21
Barium	Ba 137	49945.01	45133.34	11972.27	10325.56	824989.12	387672.80	94423.35
Barium	Ba 138	49254.10	25398.77	12362.78	9746.96	742233.95	383500.74	54136.06
Cerium	Ce 140	166.07	49.92	NA	1.87	1654.34	442.64	52.31
Iridium	Ir 191	0.95	0.60	0.69	0.00	8.67	8.23	0.40
Iridium	Ir 193	1.26	0.25	0.74	0.02	0.35	10.33	0.13
Platinum	Pt 194	2.43	0.87	0.04	0.00	1.76	12.79	0.57
Platinum	Pt 195	2.12	1.05	1.78	0.00	8.20	15.19	0.35
Gold	Au 197	4.08	3.05	1.80	0.08	7.26	42.04	0.74
Mercury	Hg 200	111.33	19.94	0.00	0.38	331.24	631.01	18.74
Mercury	Hg 202	98.27	12.66	0.00	0.26	645.50	272.33	19.42
Thallium	Tl 203	2.82	1.86	7.67	0.93	95.11	11.84	0.93
Thallium	Tl 205	4.91	1.94	7.22	5.13	67.94	6.03	0.59
Lead	Pb 206	278.42	118.15	179.26	6.47	2271.61	402.45	67.36
Lead	Pb 208	270.99	105.06	171.20	2.97	2155.54	375.13	60.59
Bismuth	Bi 209	2.85	0.83	0.63	0.00	3.40	4.13	0.45
Radium	Ra 226	NA	NA	0.00	0.00	NA	NA	NA
Thorium	Th 232	21.01	6.75	1.31	0.00	155.90	45.02	6.97
Uranium	U 238	13.17	3.00	8.50	0.00	88.55	22.10	6.73

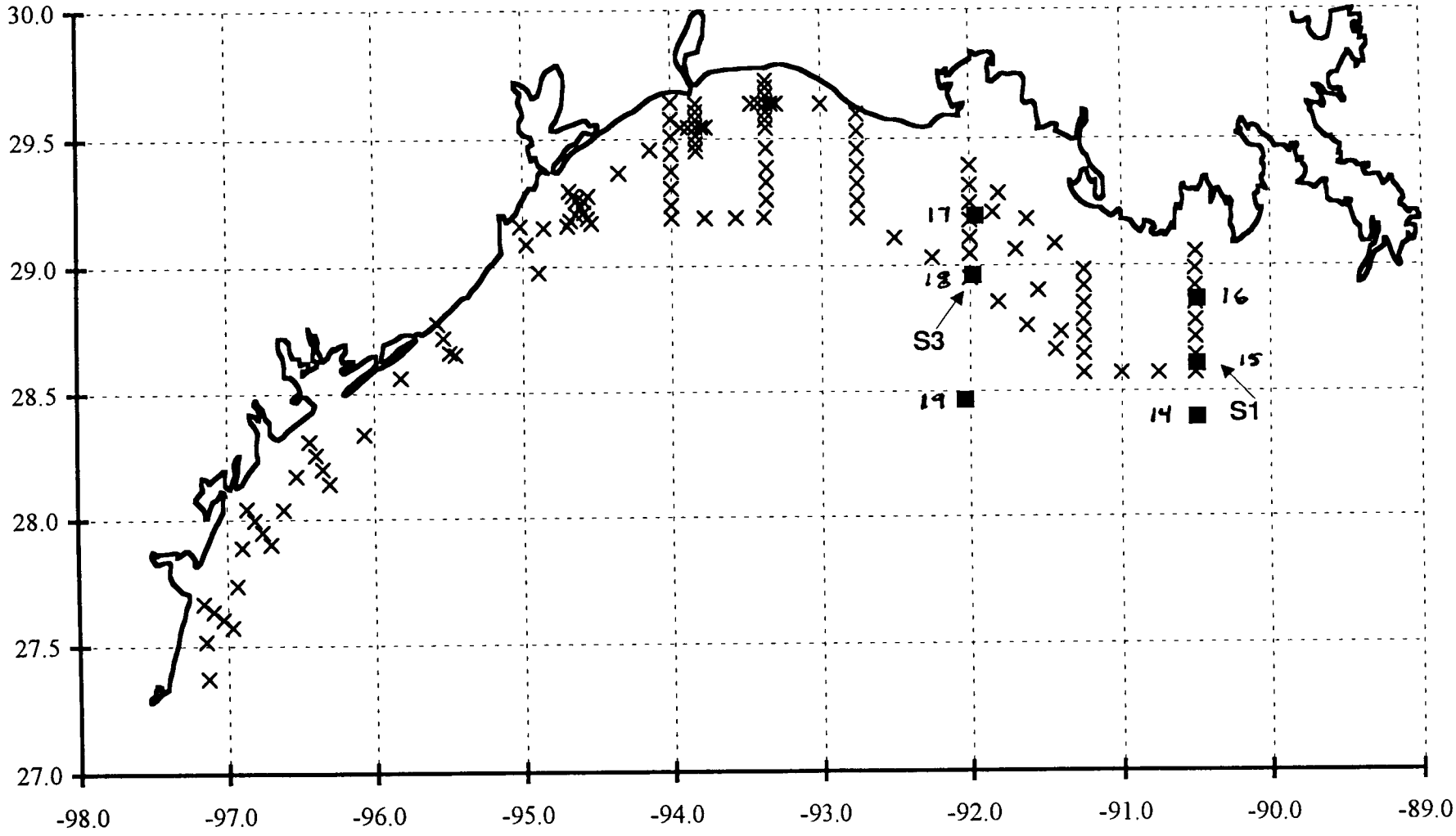

Figure 292. Locations of sediment trap moorings relative to core survey cruise tracks.

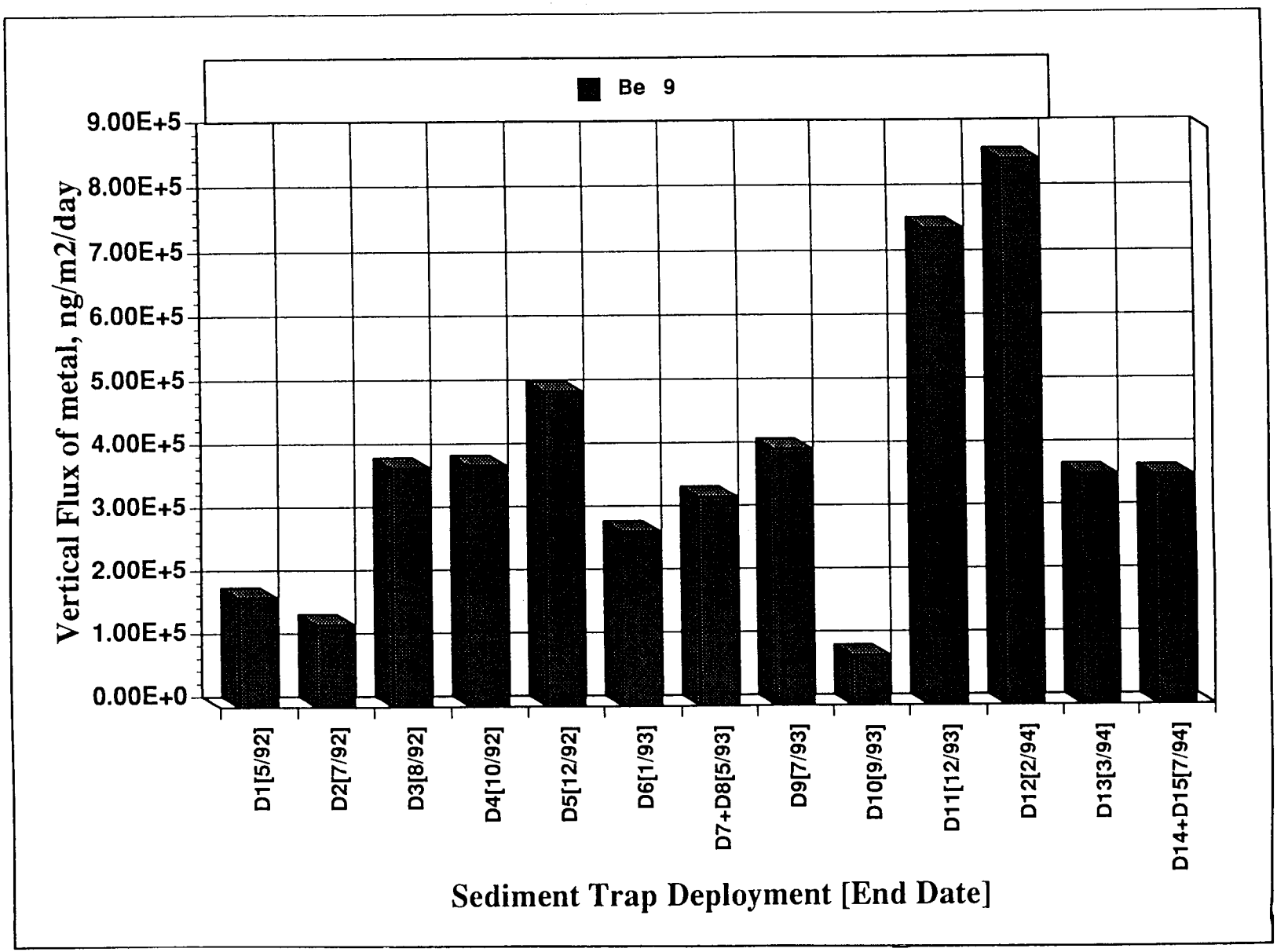

Figure 293. Vertical fluxes (ng/m^2/d) of Be 9 measured in mooring 18 sediment traps over a three-year period.

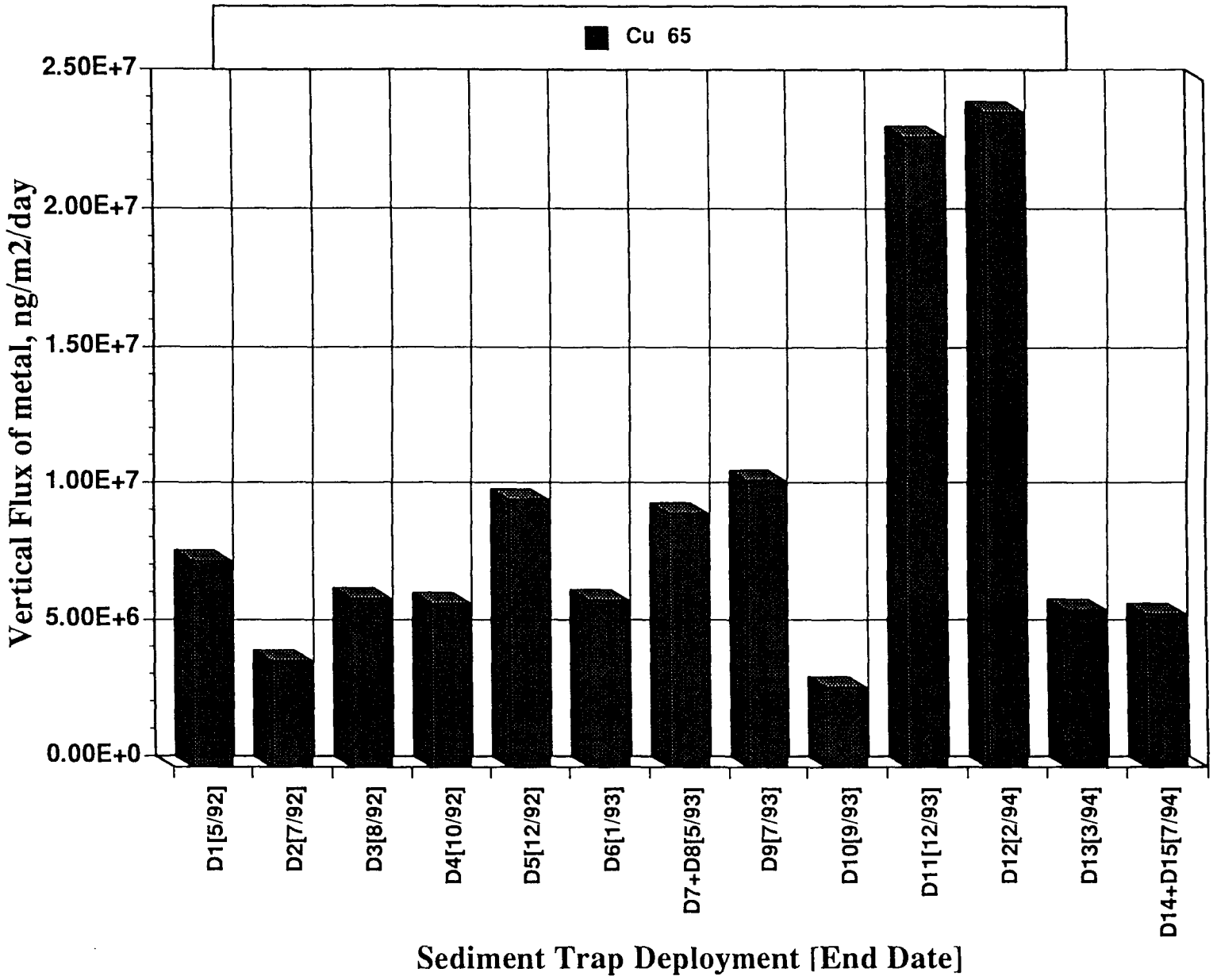

Figure 294. Vertical fluxes (ng/m^2/d) of Cu 65 measured in mooring 18 sediment traps over a three-year period.

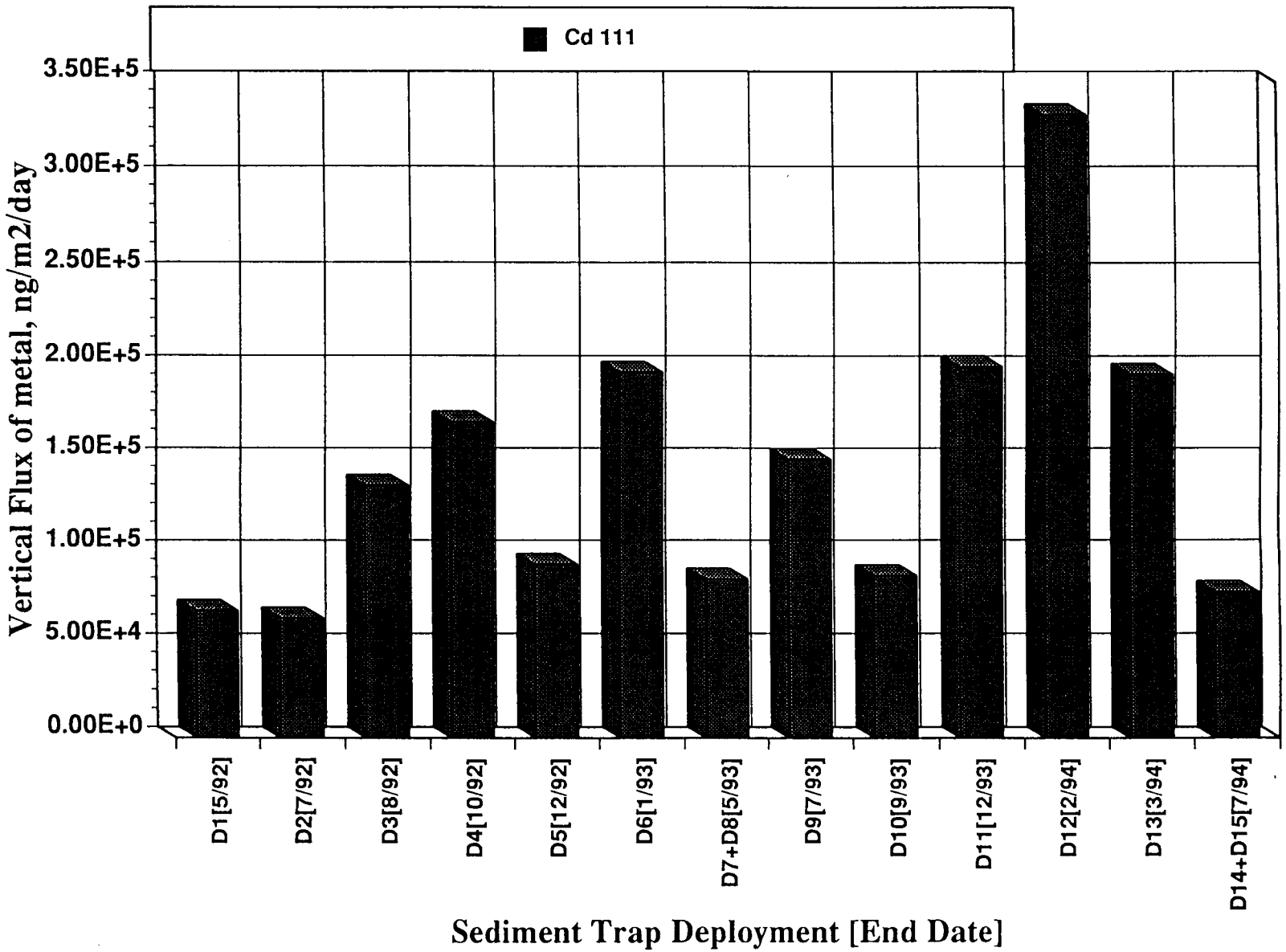

Figure 295. Vertical fluxes (ng/m^2/d) of Cd 111 measured in mooring 18 sediment traps over a three-year period.

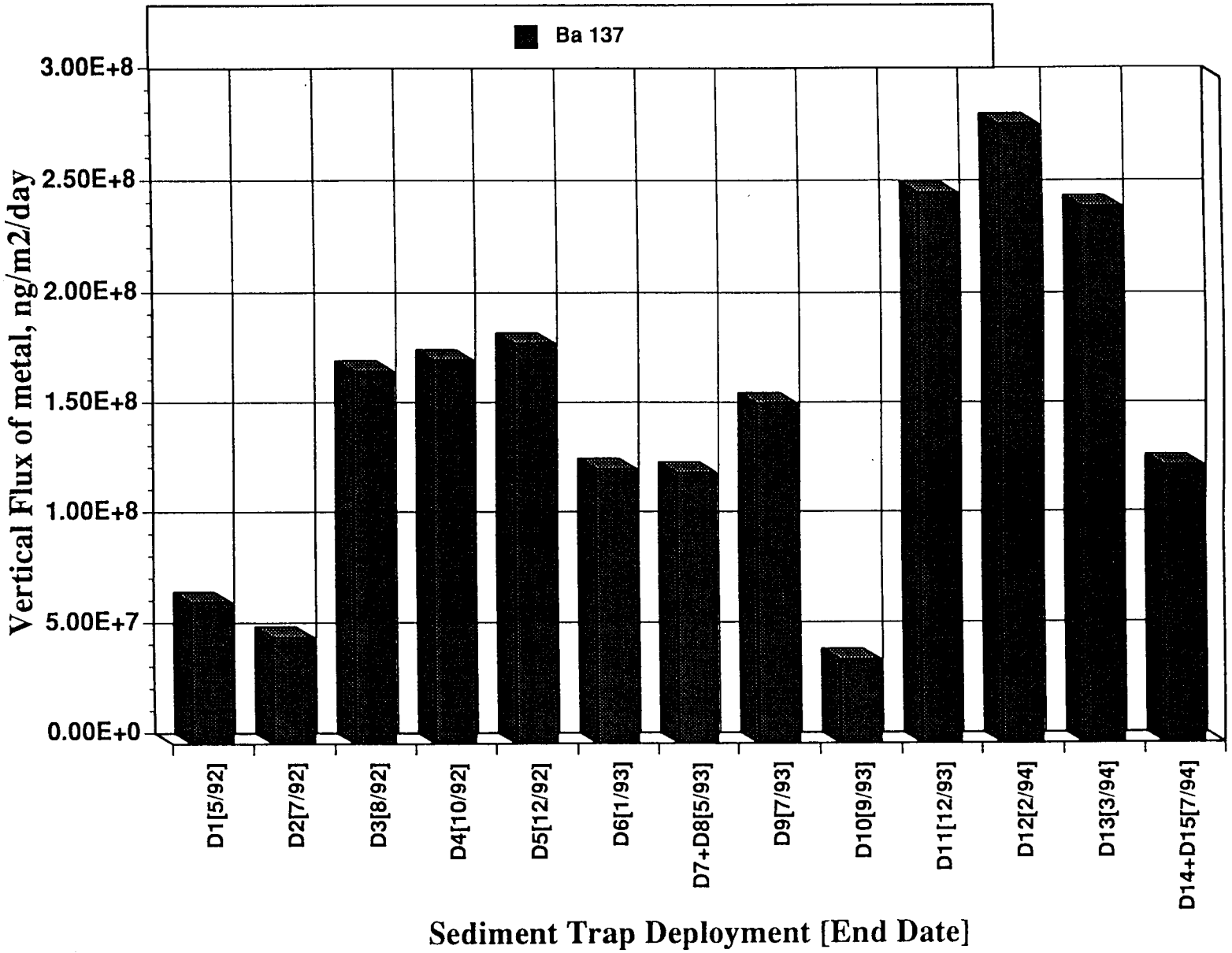

Figure 296. Vertical fluxes (ng/m^2/d) of Ba 138 measured in mooring 18 sediment traps over a three-year period.

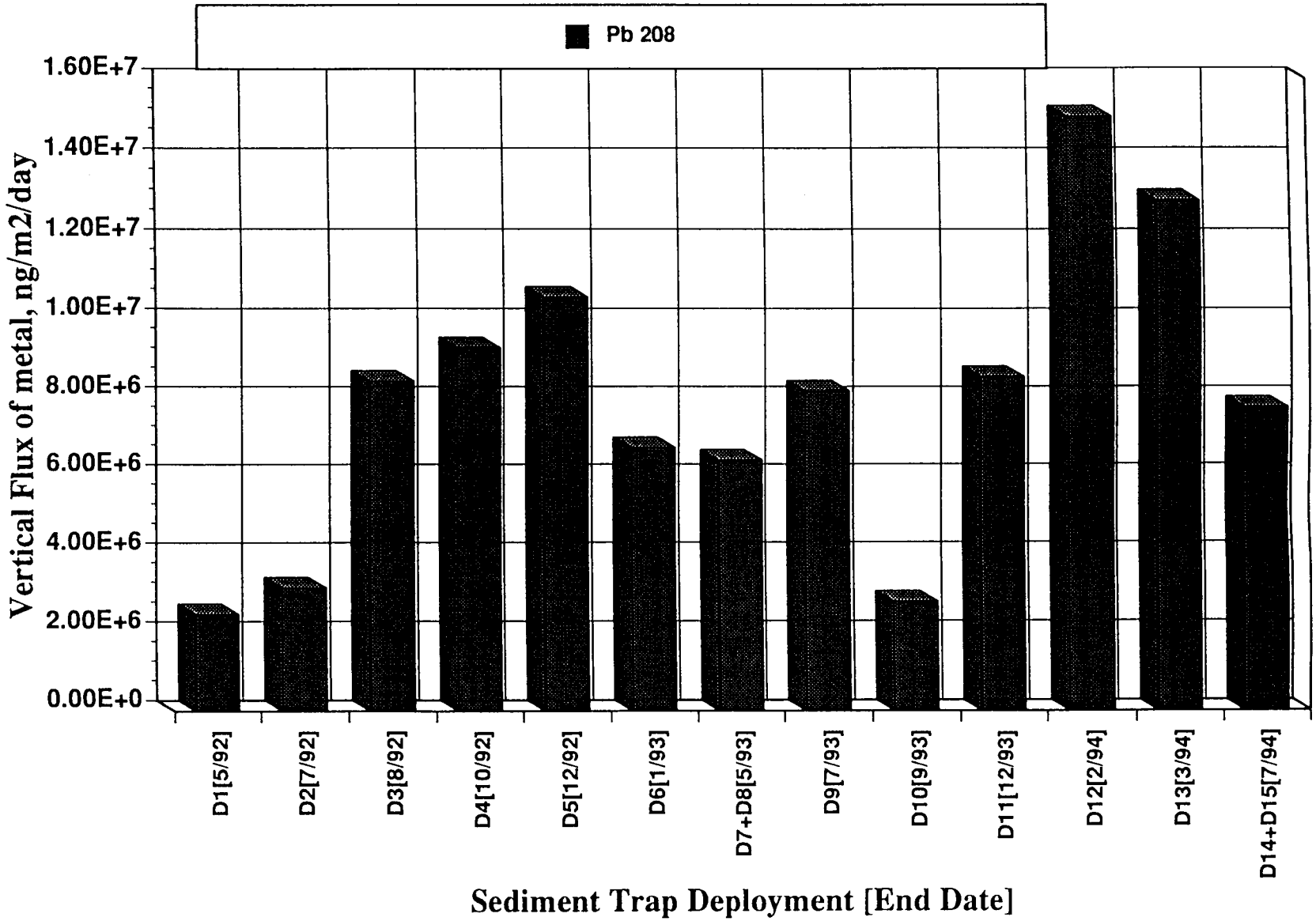

Figure 297. Vertical fluxes (ng/m^2/d) of Pb 208 measured in mooring 18 sediment traps over a three-year period.

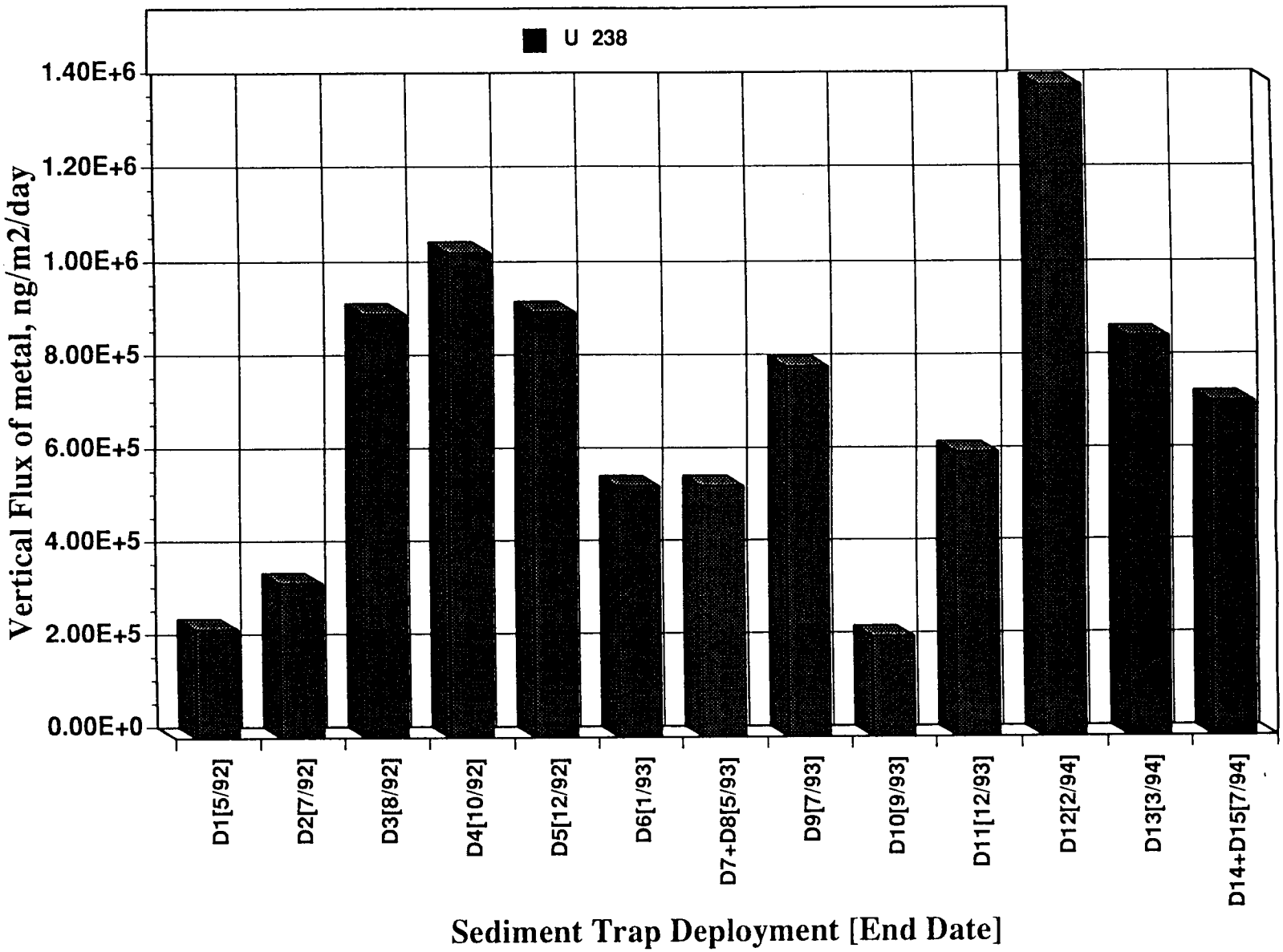

Figure 298. Vertical fluxes (ng/m^2/d) Of U 238 measured in mooring 18 sediment traps over a three-year period.

as Barium and Strontium were found in exceptionally high concentrations in the sediments collected at Mooring 19. The origin of these very high values is unknown but may be associated with drilling muds.

While trace element concentrations in sediment trap particulates were relative consistent over time and showed few spatial differences, the fluxes of trace elements, reported as ng/m2/day deposited in a sediment trap varied widely over time (and spatially). Figures 293-298 show the temporal variations in selected trace element fluxes observed at Mooring 18 over the three years of the study. It is clear from these data that the transport behavior of trace elements is controlled by particulate processes rather than concentration gradients. Since most of the sediment trap samples received for analysis were from fairly deep deployments, we concluded that sediment re-suspension processes were the dominant trace metal transport mechanism. In an attempt to confirm this conclusion, we selected suspended sediment data from our normal cruise track data sets which corresponded in time and approximate location to the Moorings at stations 15, 16 and 18 along our Transects S-1 and S-3. We then applied the particulate fluxes reported in the near-surface traps to our trace element concentration data. Figures 299-304 show the comparable fluxes of selected trace elements derived from this synthesis. In all cases, the flux of trace elements determined in the upper water column are orders of magnitude below those observed near the bottom. This suggests that new deposition rates of trace elements are relatively small when compared to fluxes of previously deposited materials.

From these data, we can conclude that near-bottom fluxes of trace elements and other particle associated contaminants will be driven by and dominated by resuspension and re-deposition of be Additional material will constantly be added to this mix from the upper water column as fresh particulate material enters the system from estuaries and coastal erosion processes. However, for some elements for which the major route of transport in the upper water column is the suspended particulate phase, These inputs must be considered as significant.

G. Mississippi River Near-field Plume Study- Cruise Five

Chemistry samples were collected during Phase III of the plume cruise, with samples taken at several points near the middle of each transect, as shown in Figure 305. Samples were processed into three phases and analyzed as described in Chapter VI. Results for organic pollutants are summarized in Table 60. A sample processing error on ship resulted in low recovery of field surrogates for the dissolved phase sample, and concentration calculations for this phase were performed without recovery correction. Even so, the concentrations for the dissolved phase are suspected to be low, although trends are still apparent. Because of this problem, the discussion below focuses primarily on the colloidal and particulate phases.

1. Organics

a. Characterization of Pollutants

Overall, the pollutant composition of the three phases of water was similar to that of April samples from the core survey cruises. Colloidal phase Simazine and Metolachlor mean concentrations were three to five times higher than mean concentrations for 1993 core survey samples, while Atrazine was only slightly higher, and equal to the mean cruise concentration for April 1992. The ratio of phenanthrene:anthracene ratio was somewhat lower than what was seen in core survey April data. Concentrations of parent PAH generally were about the same or lower

Table 60. Summary of organic pollutants data for three phases of water samples from Cruise P941, April 1993.

	Dissolved Phase				Colloidal Phase				Particulate Phase			
	MEAN	RANGE		FREQ	MEAN	RANGE		FREQ	MEAN	RANGE		FREQ
ANALYTE	pg/ml	MIN	MAX	(of 32)	pg/ml	MIN	MAX	(of 32)	ng/g	MIN	MAX	(of 32)
Particulate Sample Wt.									**0.35**	0.16	3.2	32
Naphthalene	**27**	6.2	72	32	**11**	0.28	27	12	**430**	1.7	2343	28
Hexachlorobutadiene	**nd**	na	na	0	**nd**	na	na	0	**0.56**	0.56	0.56	1
2-MN	**19**	2.6	34	32	**12**	0.43	21	16	**273**	19	1381	32
1-MN	**13**	2.4	25	32	**11**	1.3	17	17	**141**	9.8	652	32
2-EN	**4.2**	0.53	8.7	32	**2.0**	0.31	3.2	13	**65**	3.3	267	32
1-EN	**1.4**	0.54	2.9	31	**1.4**	1.3	1.7	4	**14**	0.84	54	32
2,6/2,7-DMN	**11**	0.64	27	32	**7.3**	6.3	8.3	2	**192**	8.3	803	32
1,3/1,7-DMN	**10**	1.6	22	32	**5.3**	0.46	12	18	**112**	5.2	410	32
1,6-DMN	**7.2**	0.96	15	32	**3.1**	1.0	6.1	15	**95**	4.3	392	32
1,4/2,3-DMN	**4.5**	0.56	9.6	32	**4.3**	1.9	6.4	13	**57**	0.54	183	32
1,5-DMN	**10**	1.2	51	31	**7.9**	7.0	9.2	5	**26**	0.98	89	32
Acenaphthylene	**0.98**	0.11	2.4	30	**nd**	na	na	0	**4.9**	0.94	16	14
1,2-DMN	**2.3**	0.33	4.5	32	**2.3**	1.4	3.6	5	**24**	0.95	80	32
2-IPN	**1.5**	0.84	2.5	16	**nd**	na	na	0	**9.4**	0.10	43	24
1,8-DMN	**3.9**	0.0012	7.7	10	**nd**	na	na	0	**nd**	na	na	0
Acenaphthene	**4.9**	0.69	25	30	**0.94**	0.13	4.4	12	**11**	0.42	55	27
1,6,7-TMN	**5.4**	1.9	11	31	**6.0**	6.0	6.0	1	**72**	0.41	299	28
Fluorene	**6.2**	0.25	23	31	**1.9**	0.49	4.3	10	**29**	0.50	152	30
Trifluralin	**nd**	na	na	0	**nd**	na	na	0	**0.79**	0.20	1.7	5
CL2-PCB	**nd**	na	na	0	**nd**	na	na	0	**0.65**	0.58	0.71	2
Hexachlorobenzene	**nd**	na	na	0	**nd**	na	na	0	**2.5**	0.74	3.8	5
Simazine	**5.3**	0.010	11	12	**23**	12	36	9	**nd**	na	na	0
Dibenzothiophene	**3.6**	0.82	9.0	32	**1.1**	0.24	3.1	14	**27**	0.27	120	27
Atrazine	**33**	1.1	148	32	**82**	8.3	279	32	**16**	16	16	1
Phenanthrene	**14**	0.054	59	31	**6.1**	0.020	32	14	**107**	12	221	14
Anthracene	**1.8**	0.0064	11	28	**4.3**	1.4	12	4	**8.0**	0.51	30	22
CL3-PCB	**nd**	na	na	0	**nd**	na	na	0	**3.4**	0.41	9.9	4
4-MDBT	**1.5**	0.62	2.9	29	**1.3**	1.3	1.3	1	**19**	2.9	66	15
2/3-MDBT	**1.0**	0.55	1.6	22	**nd**	na	na	0	**13**	0.068	53	17
CL4-PCB	**nd**	na	na	0	**nd**	na	na	0	**10**	2.9	15	6
3-MP	**2.5**	0.88	4.9	30	**1.2**	0.052	3.0	17	**35**	6.0	121	17
1-MDBT	**0.61**	0.43	0.72	5	**nd**	na	na	0	**4.8**	0.034	12	14
2-MP	**1.6**	0.41	3.8	29	**0.75**	0.11	3.9	18	**36**	1.0	169	24
Alachlor	**5.4**	4.6	6.3	3	**nd**	na	na	0	**1.4**	1.4	1.4	1
4/9-MP	**1.7**	0.89	2.8	18	**2.0**	1.1	2.7	11	**24**	1.6	51	9
1-MP	**0.87**	0.53	1.5	14	**1.6**	0.96	2.2	4	**17**	0.25	76	24
Metolachlor	**18**	3.0	79	30	**55**	10	155	27	**14**	4.5	33	3
Cyanazine	**8.6**	8.6	8.6	1	**nd**	na	na	0	**45**	45	45	1
3,6-DMP	**0.98**	0.98	1.0	1	**nd**	na	na	0	**25**	0.50	120	24
3,5-DMP	**nd**	na	na	0	**nd**	na	na	0	**0.28**	0.19	0.38	2
2,6-DMP	**0.0041**	0.0030	0.0051	2	**11**	11	11	1	**14**	0.071	65	18
2,7-DMP	**14**	2.0	40	31	**12**	2.0	32	18	**17**	0.70	54	22
3,9-DMP	**1.0**	0.49	1.3	5	**1.9**	1.4	2.5	4	**53**	9.6	164	14
1,6/2,5/2,9-DMP	**nd**	na	na	0	**nd**	na	na	0	**33**	0.19	114	15
1,7-DMP	**nd**	na	na	0	**nd**	na	na	0	**19**	3.0	68	14
1,9/4,9-DMP	**nd**	na	na	0	**nd**	na	na	0	**9.3**	1.5	28	14
1,2-DMDBT	**nd**	na	na	0	**nd**	na	na	0	**1.4**	0.98	2	4
Fluoranthene	**2.0**	0.048	7.2	28	**9.0**	0.23	54	14	**35**	0.94	156	16
1,5-DMP	**nd**	na	na	0	**nd**	na	na	0	**nd**	na	na	0
1,8-DMP	**nd**	na	na	0	**nd**	na	na	0	**2.8**	0.058	5.8	7
1,2-DMP	**nd**	na	na	0	**nd**	na	na	0	**3.2**	0.42	7.9	7
9,10-DMP	**nd**	na	na	0	**nd**	na	na	0	**0.55**	0.55	0.6	1
Pyrene	**1.2**	0.14	3.7	30	**6.9**	0.25	45	16	**34**	3.6	204	21
o,p'-DDE	**nd**	na	na	0	**nd**	na	na	0	**nd**	na	na	0
Chlordane	**nd**	na	na	0	**nd**	na	na	0	**0.47**	0.26	0.68	2
trans-Nonachlor	**nd**	na	na	0	**nd**	na	na	0	**0.27**	0.27	0.27	1

Table 60 cont'd.

	Dissolved Phase				Colloidal Phase				Particulate Phase			
	MEAN	RANGE		FREQ	MEAN	RANGE		FREQ	MEAN	RANGE		FREQ
ANALYTE	pg/ml	MIN	MAX	(of 32)	pg/ml	MIN	MAX	(of 32)	ng/g	MIN	MAX	(of 32)
CL5-PCB	**nd**	na	na	0	**nd**	na	na	0	**6.6**	0.059	22	11
Dieldrin	**nd**	na	na	0	**nd**	na	na	0	**nd**	na	na	0
p,p'-DDE	**nd**	na	na	0	**nd**	na	na	0	**nd**	na	na	0
o,p'-DDD	**nd**	na	na	0	**nd**	na	na	0	**1.3**	0.011	2.7	2
CL6-PCB	**nd**	na	na	0	**nd**	na	na	0	**1.4**	0.13	3.4	8
1,2,8-TMP	**nd**	na	na	0	**nd**	na	na	0	**13**	0.74	35	14
p,p'-DDD/o,p'-DDT	**nd**	na	na	0	**nd**	na	na	0	**nd**	na	na	0
CL7-PCB	**nd**	na	na	0	**nd**	na	na	0	**0.90**	0.90	0.90	1
p,p'-DDT	**nd**	na	na	0	**nd**	na	na	0	**10**	10	10	1
Benzanthracene	**0.21**	0.010	0.53	24	**4.3**	0.18	16	9	**13**	1.0	51	15
Chrysene	**0.22**	0.031	0.77	29	**2.8**	0.00095	21	27	**13**	0.18	43	19
Benzo(b)fluor	**nd**	na	na	0	**6.4**	1.0	19	13	**7.3**	0.81	52	14
Benzo(k)fluor	**nd**	na	na	0	**5.5**	0.54	16	12	**4.3**	0.20	33	13
Benzo(a)pyrene	**nd**	na	na	0	**4.3**	1.1	13	11	**7.6**	0.70	48	12
Indenopyrene	**nd**	na	na	0	**nd**	na	na	0	**30**	6.5	97	4
Dibenzanthracene	**nd**	na	na	0	**nd**	na	na	0	**16**	14	19	2
Benzoperylene	**nd**	na	na	0	**nd**	na	na	0	**46**	2.5	90	2
Estimated Totals												
C1-Naphthalenes	**33**	5.0	59	32	**22**	1.7	39	17	**414**	29	2033	32
C2-Naphthalenes	**52**	4.6	119	32	**15**	0.46	32	19	**585**	24	2263	32
C3-Naphthalenes	**53**	5.1	140	32	**22**	16	32	5	**403**	6.5	1719	31
C4-Naphthalenes	**25**	7.1	170	28	**nd**	na	na	0	**183**	21	408	13
C1-Dibenzothiophenes	**2.4**	0.79	4.4	29	**1.3**	1.3	1.3	1	**34**	0.068	128	17
C2-Dibenzothiophenes	**9.0**	5.3	13	13	**nd**	na	na	0	**284**	59	876	27
C1-Phenanthrenes	**5.5**	1.3	12	30	**3.1**	0.43	11	20	**84**	0.25	398	25
C2-Phenanthrenes	**14**	2.0	40	31	**12**	1.7	32	19	**111**	0.38	553	26
C3-Phenanthrenes	**3.7**	3.5	3.9	2	**nd**	na	na	0	**120**	1.2	378	25

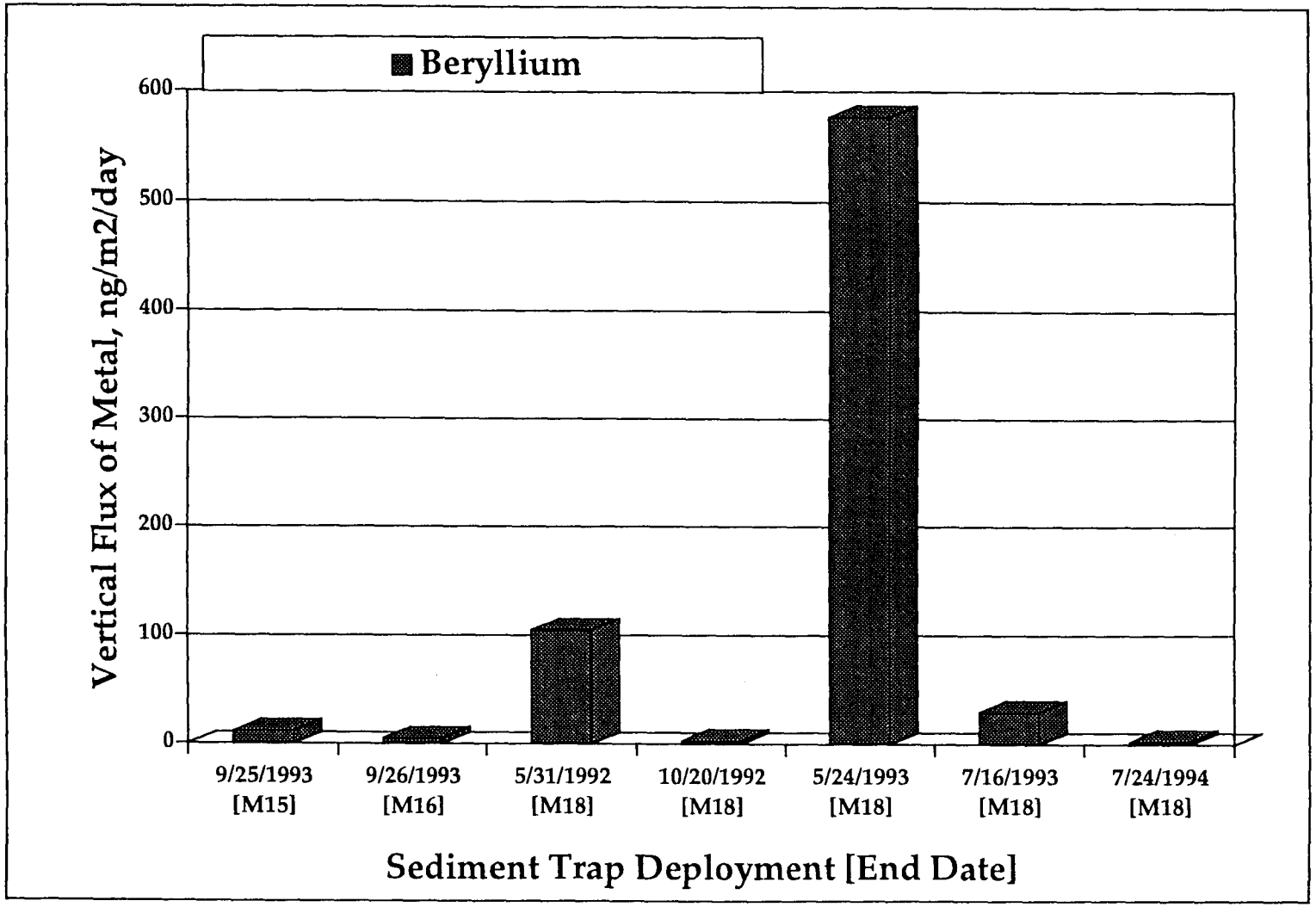

Figure 299. Vertical fluxes (ng/m^2/d) of Be 9 estimated from suspended sediment measurements and calculated from near surface sediment fluxes in mMoorings 15, 16 and 18 sediment traps.

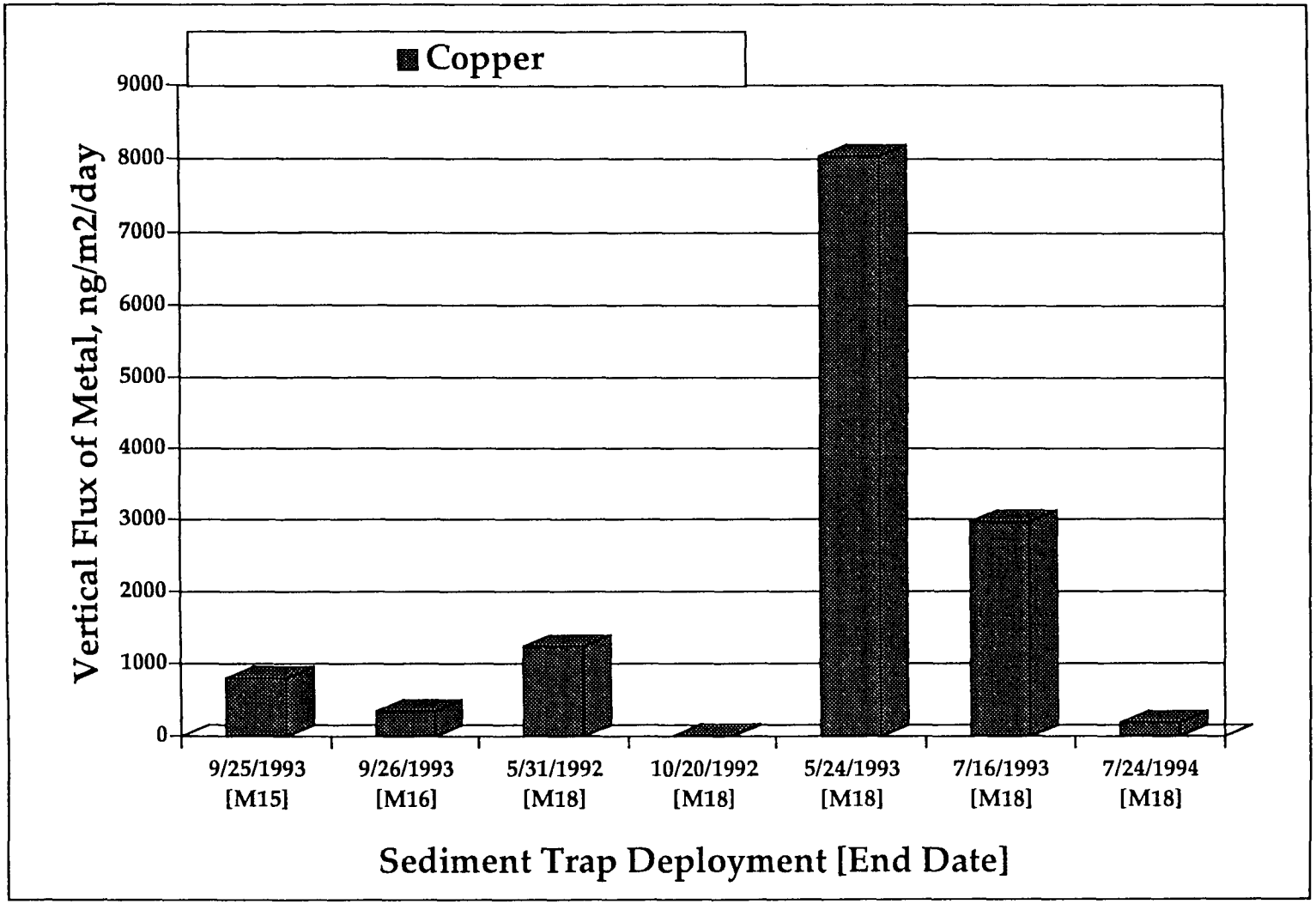

Figure 300. Vertical fluxes (ng/m^2/d) of Cu 65 estimated from suspended sediment measurements and calculated from near surface sediment fluxes in moorings 15, 16 And 18 sediment traps.

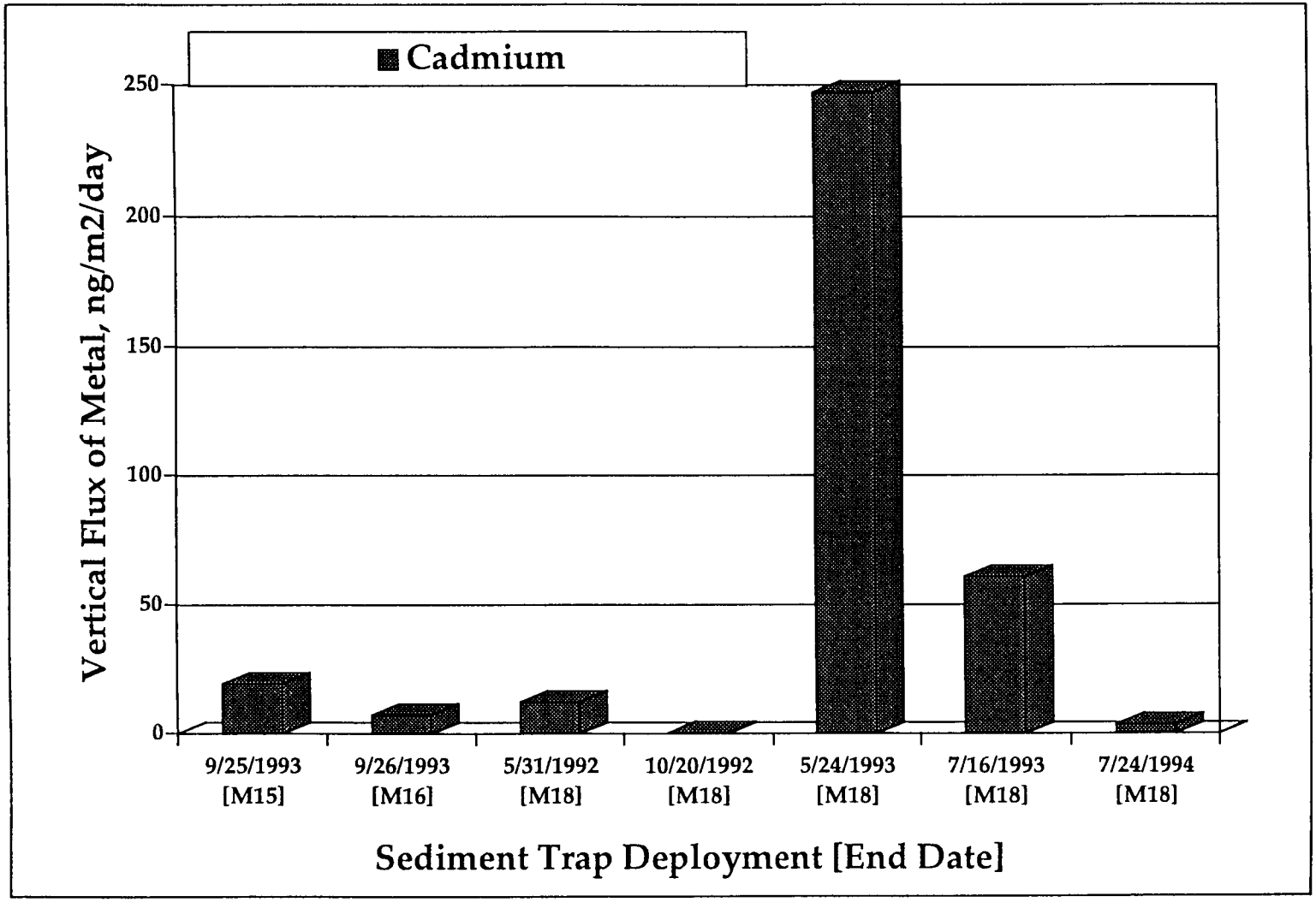

Figure 301. Vertical fluxes (ng/m^2/d) of Cd 111 estimated from suspended sediment measurements and calculated from near surface sediment fluxes in moorings 15, 16 and 18 sediment traps.

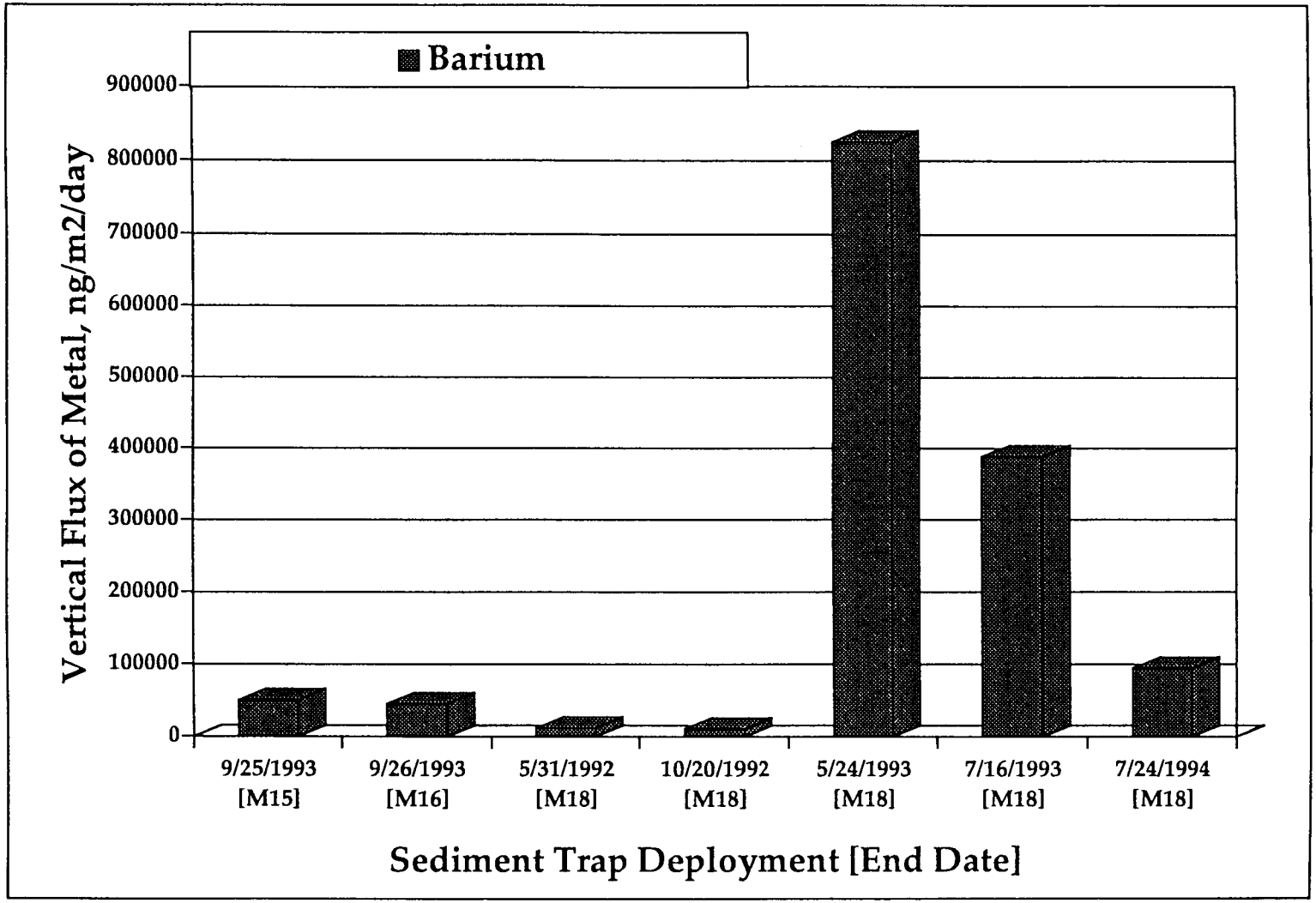

Figure 302. Vertical fluxes (ng/m^2/d) of Ba 138 estimated from suspended sediment measurements and calculated from near surface sediment fluxes in moorings 15, 16 and 18 sediment traps.

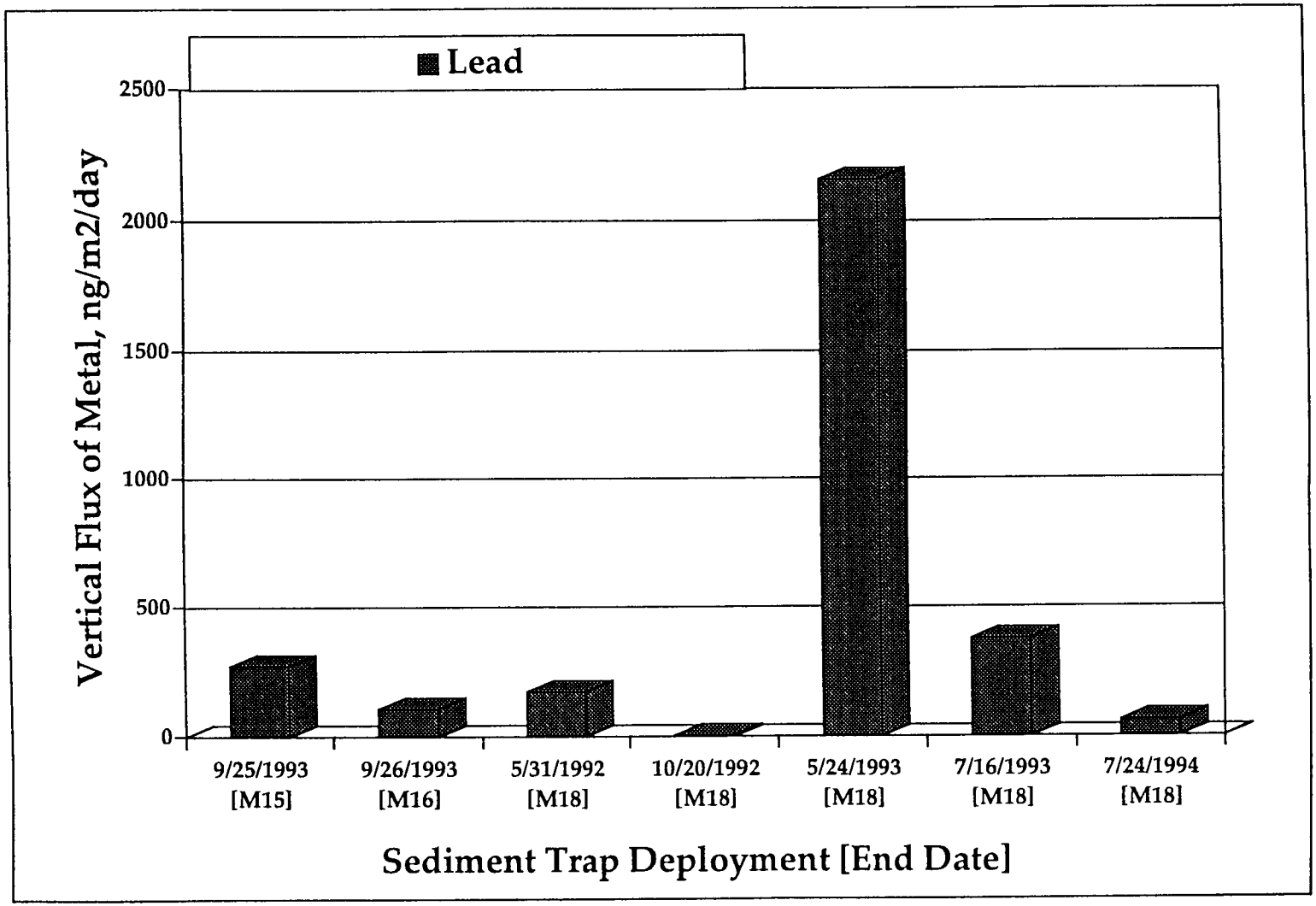

Figure 303. Vertical fluxes (ng/m^2/d) of Pb 208 estimated from suspended sediment measurements and calculated from near surface sediment fluxes in moorings 15, 16 And 18 sediment traps.

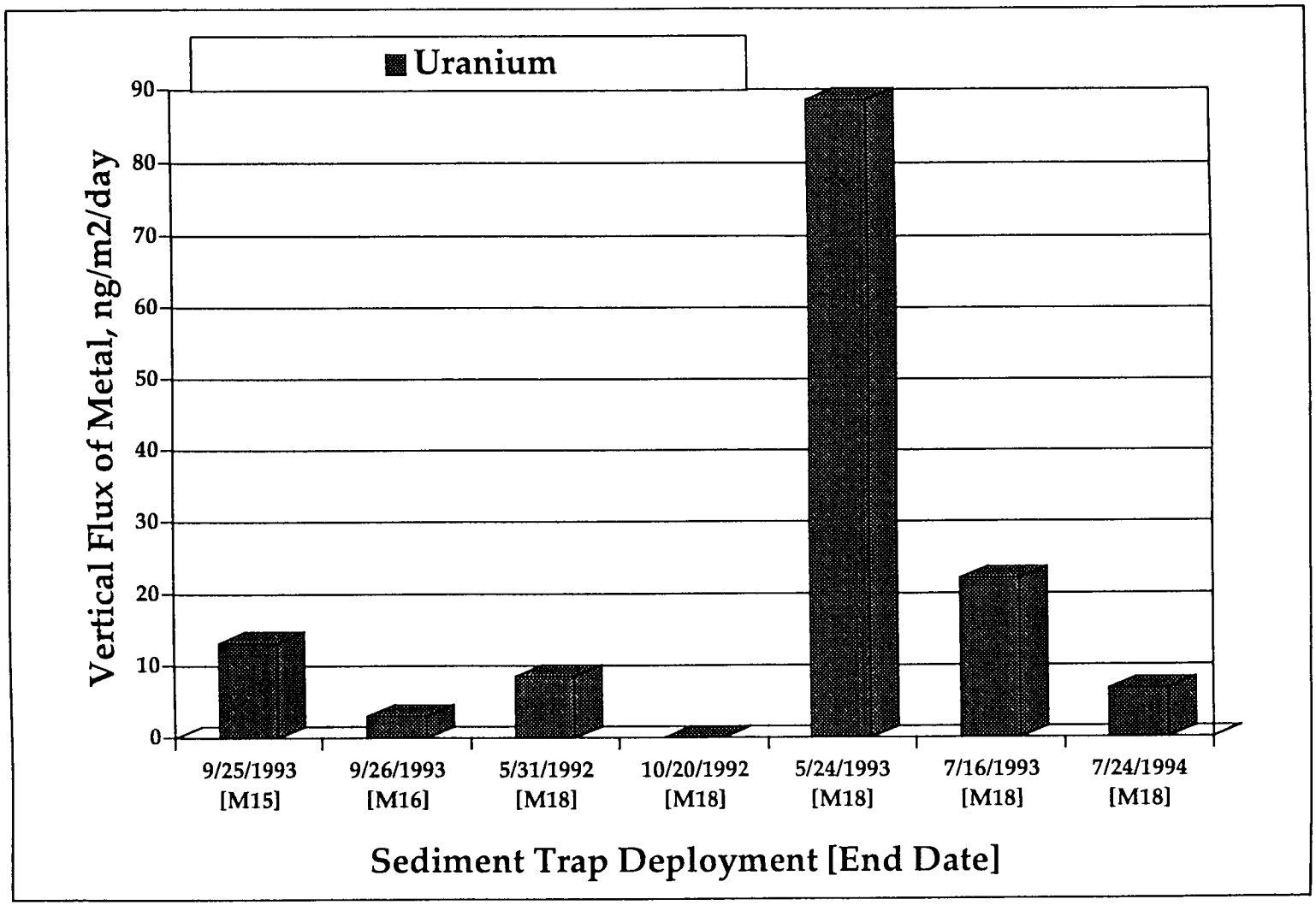

Figure 304. Vertical fluxes (ng/m^2/d) of U 238 estimated from suspended sediment measurements and calculated from near surface sediment fluxes in moorings 15, 16 and 18 sediment traps.

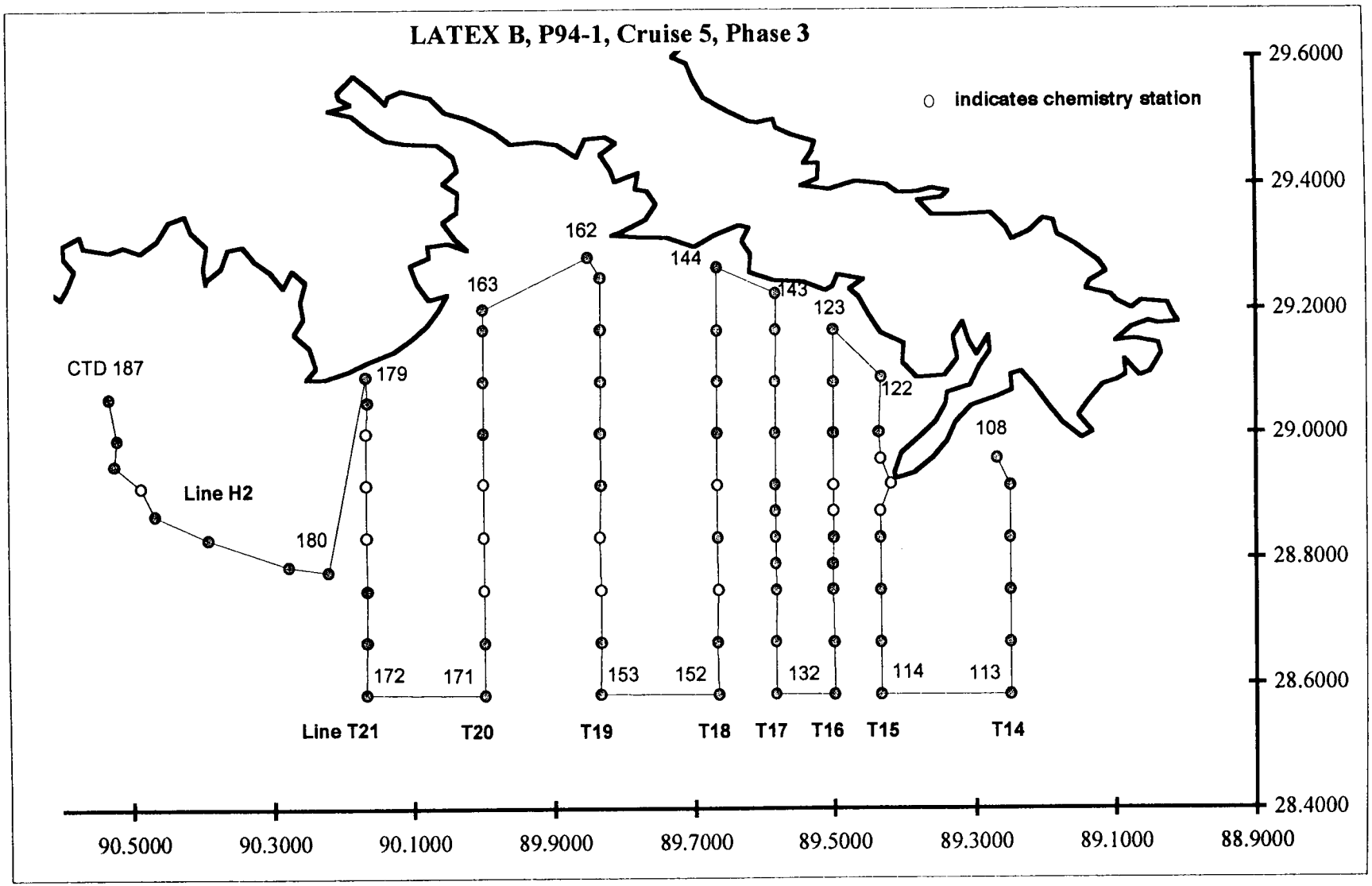

Figure 305. Cruise track for Cruise P941, showing location of chemistry samples.

compared to April core surveys. In the particulate phase, herbicides were detected more often than in core survey cruise, with Trifluralin detected most frequently (n=5). Methyl phenanthrenes were detected in a majority of samples at higher concentrations than for core survey cruises, with highest values closest to the mouth of the river and along line T21, south of Bay Champagne. DDT was also detected in a surface sample taken nearest to shore along this line.

Spatial distributions of colloidal phase Atrazine, Simazine, and Metolachlor show decreasing concentrations with distance (west) away from the river outlet. Highest concentrations of all three were found at station 119, and the bottom sample here showed the highest concentration of Atrazine (280 pg/ml). Elsewhere, concentrations of all three were significantly higher in surface samples. Simazine was only detected at the surface, and was detected only once beyond Line 18, indicating that this herbicides was being rapidly removed from the water column.

For alkylated PAH in the colloidal phase, C1-naphthalenes were highest at the mouth of the river, and were fairly evenly distributed elsewhere. C1-phenanthrenes also were highest at the first station, showed low concentrations in the middle lines, and increased again along line T21. In contrast, the C2-phenanthrenes showed higher concentrations in the lines beginning T19 and west, suggesting that the river was not the source, which agrees with the observation of high C1-phenanthrenes in the particulate phase along T21.

b. Salinity Correlations

Because the salinity showed a complete range of values in this area, correlation analysis was performed on data for all three phases of water. In the dissolved and colloidal phases, good inverse correlations (R2>-0.70) were found for the three detected herbicides-Atrazine, Simazine, Metolachlor. Correlations for the colloidal phase herbicides were all greater than R2=-0.960. Significant regressions lines with negative slopes were found for Atrazine (R2=0.96) and Metolachlor (R2=0.92). (Regression analysis calculated "nd" values at zeroes and thus provided a more stringent test.) Both regression lines predicted an x-intercept (0 concentration) at a salinity of 38 ppt. Alachlor was detected only three times in the dissolved phase, at salinities ranging from 0 to 15 ppt, showing an R2 of -0.987. These inverse correlation show that the river discharge is the source of the herbicides, and that, in this small region of the Gulf the herbicides exhibit conservative behavior. In contrast to the herbicides, PAH and alkylated PAH tended to show positive correlations (all non-significant) with salinity (Figure 306), suggesting that these compounds have their origin in the offshore environment (e.g., oil and gas exploration, oil seeps).

For the particulate phase, Fluorene was inversely correlated (R2=-0.632) with salinity, with most observations occurring at salinities greater than 26 ppt. Fluoranthene, pyrene, benzanthracene, and chrysene showed correlations, with the latter two showing an even spread of points over the salinity range and R2 values of -0.773 and -0.896, respectively. For alkylated PAH, only colloidal phase C3-naphthalenes showed correlation, R2=-0.659. This lack of correlations indicates that the source of alkylated PAH can not be attributed to the fresh water input. In addition, regression lines (all non-significant) of alkylated phenanthrenes in the dissolved and colloidal phases showed positive slopes, indicating increasing concentrations in more saline waters.

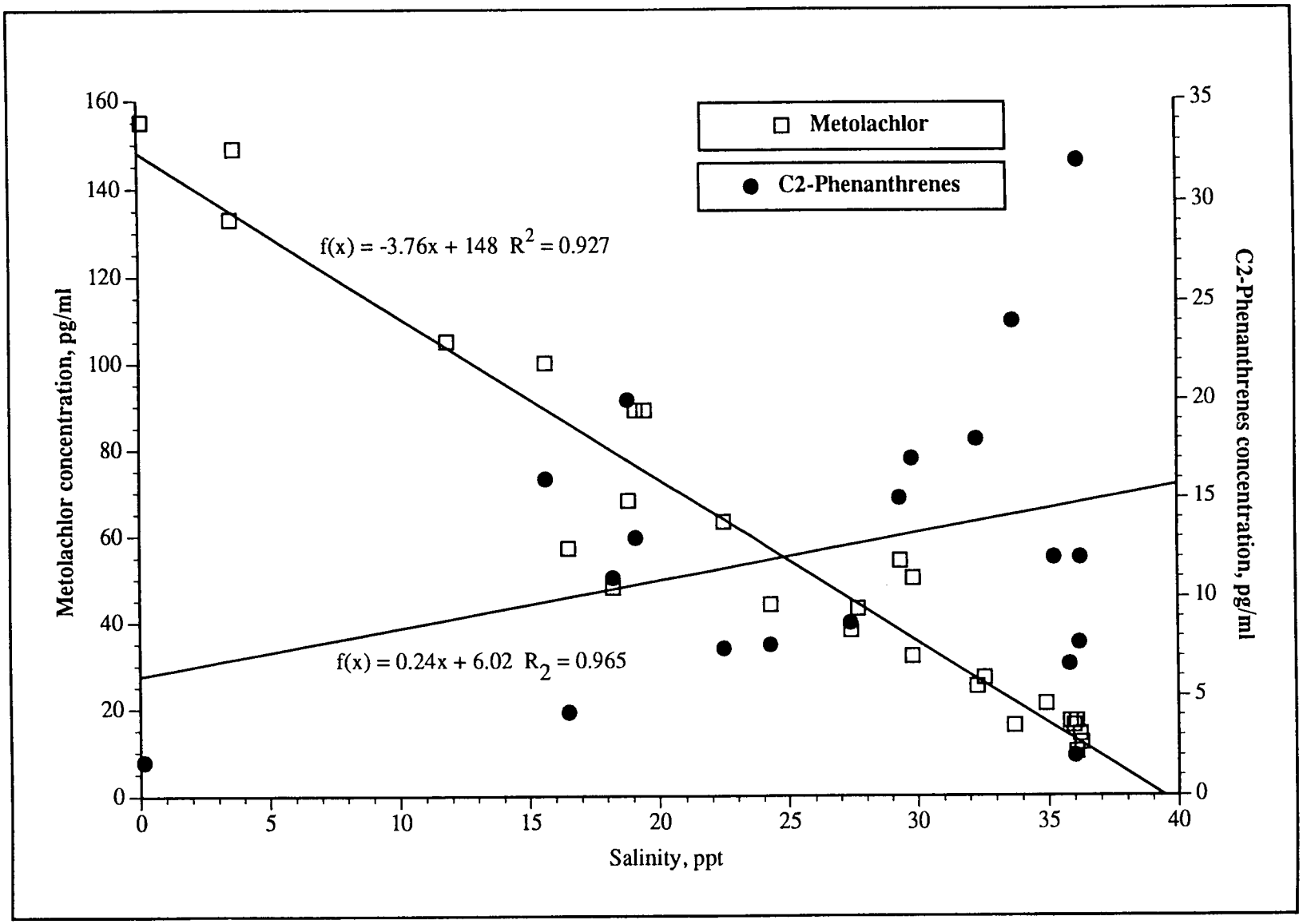

Figure 306. Relationship of two colloidal phase pollutants with salinity.

c. Mass Transport

Figure 307 shows the relationship between water phases and various pollutants with respect to mass tranport averaged over sampling lines. As with April core survey cruises, transport was to the West, and the dissolved phase was predominant, with highest transport values for naphthalenes and herbicides. The colloidal phase was the next in importance for magnitude of transport, similar to the other data, however the particulate phase appears to play an increased role in this region compared to the core survey area. Overall, the transport of herbicides was greater in this area, keeping in mind the low dissolved phase values as discussed above.

Figure 308(a) shows water flux values (LATEX A current meter data, line G4, from 5 days prior to collection-April 13-16, 1994) used in transport calculation (see Chapter VI) and colloidal phase tranport of herbicides for the various lines sampled on this cruise. (Note that the scale for water flux(a) is in negative values and reversed compared to Figure 257) The bottom graph shows that pollutant transport is highest near the discharge, decreases rapidly in the second line (T16) and begins to increase to T19 and then decline slightly again further to the west. The increase in the middle of the lines may be related to the gyre circulation observed in this area. Transport in this region differs from the core survey estimates in that the water flux values (a) show an inverse trend with pollutant transport values (b), i.e., as the magnitude of the water flux increased to the west, the pollutant transport values fell. Thus, water velocity in this region plays less a role in herbicide transport than other factors, such pollutant concentration in the discharge and dilution with saline waters. Table 61 shows a summary of mean concentrations and calculated mass transport values for the various sampling lines. This table shows an interesting trend in the relationship of dissolved and colloidal transport to particulate phase transport. In sampling lines close to the river discharge (T15, low salinity) the particulate phase shows dominant transport, while along sampling lines to the west (H2), the dissolved and colloidal phases become increasingly important. Finally, the table shows average particulate weights for each line, and mass transport values corrected for the particulate weights. These values illustrate that the particulate phase as a means of bound pollutant transport may not be as significant compared to dissolved and colloidal transport regardless of salinity. These relationships held for the range of alkylated PAH studied.

2. Inorganics

The near field plume investigation (Section III) was intended to examine the sources of potential contaminants entering the coastal shelf region of the Northwestern Gulf of Mexico and sampled in more detail in Cruises 1-4 and 6 to understand the movement patterns of chemicals in the far field. In the near field study, focus was placed upon : 1) understanding which chemicals of trace elements have their origins in the Mississippi Rivers; 2) to understand near-field processes which may influence the fate and transport of these substances once they enter the Gulf of Mexico and 3) to establish a baseline level of contaminants being transported further to the west in an attempt to assess the contribution of more western estuaries to coastal shelf levels of contaminants in the water column.

a. Results

All trace elements were detected in most samples above the average detection limit of 0.1 ng/g or ng/ml. Tables 62, 63 and 64 presents the means, ranges and simple correlation coefficients with salinity of trace elements detected in all Cruise 5 samples in the dissolved, colloidal and particulate fractions of the samples at all depths and stations.

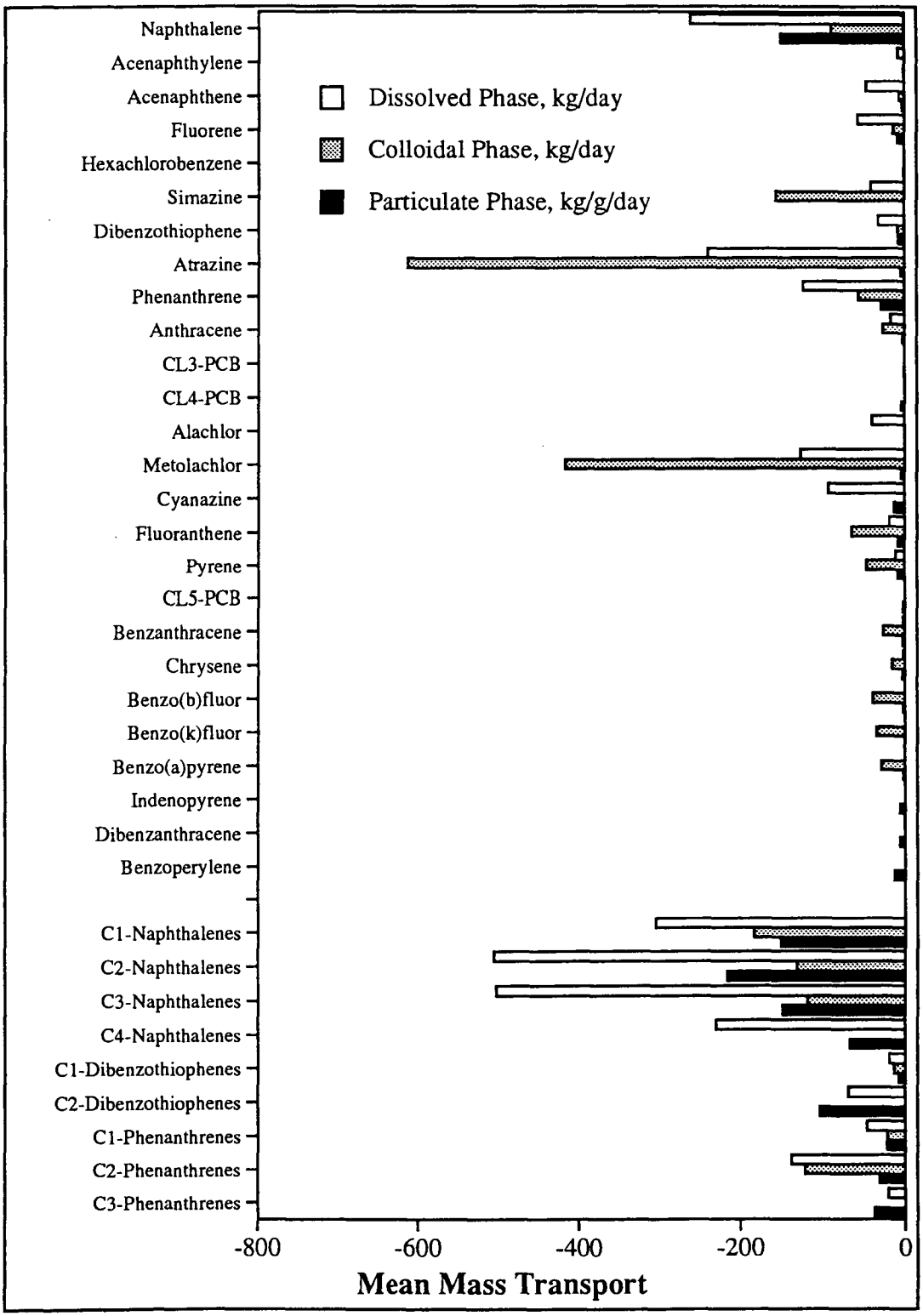

Figure 307. Mass transport of organic pollutants in three phases of water, showing mean values for all samples from Cruise P941, April 1994.

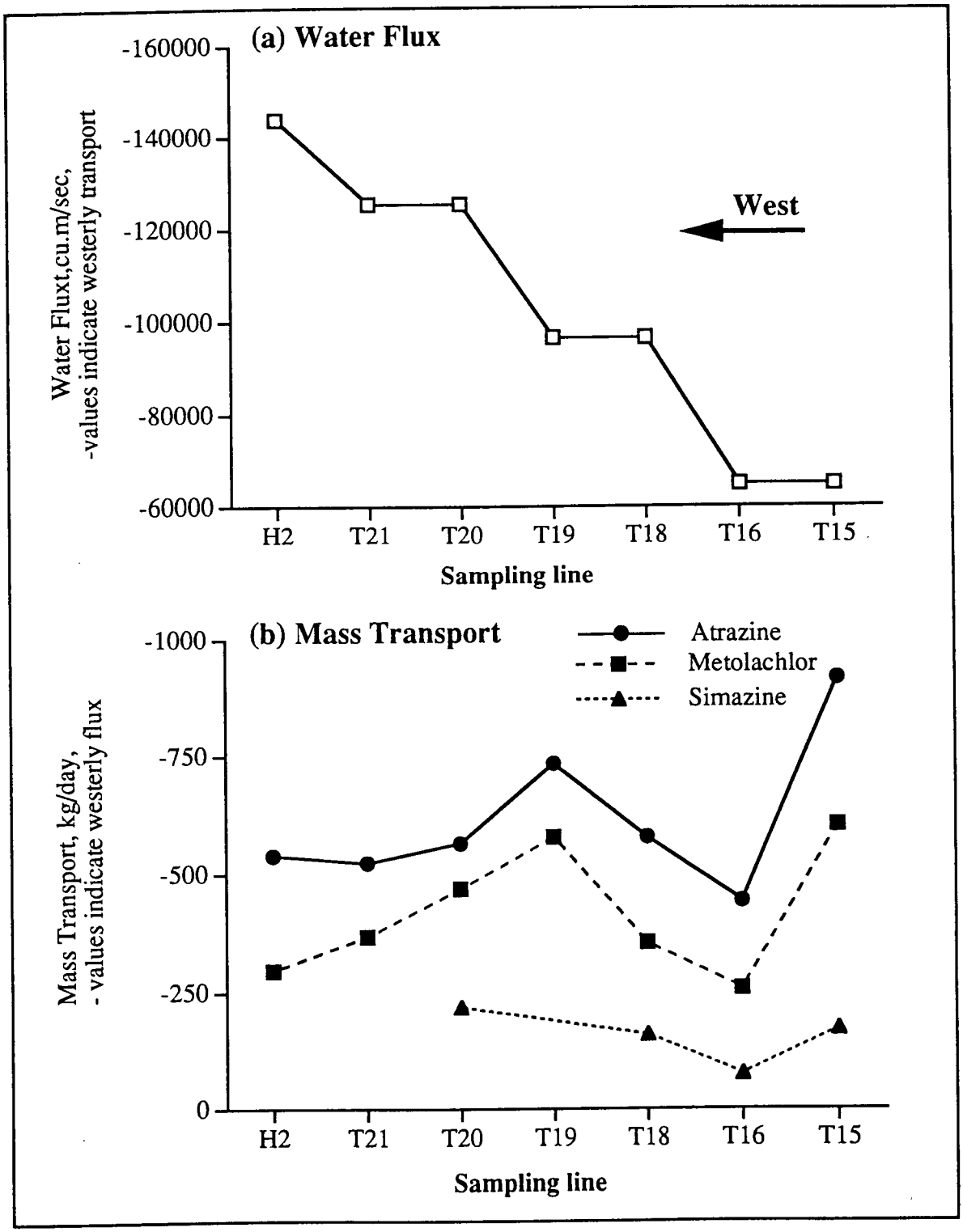

Figure 308. Water flux (a) and colloidal phase herbicides mass transport (b) for plume cruise (P941) data by sampling line (-values indicate westerly transport).

Table 61. Summary of mean concentrations and mass transport values for 2-Methylnaphthalene for sampling lines from Cruise P941.

	Sampling Line						
	T15	**T16**	**T18**	**T19**	**T20**	**T21**	**H2**
Mean Concentration							
Dissolved, ng/L	20	14	20	23	17	20	25
Colloidal, ng/L	15	3	8	16	14	10	nd
Particulate, ng/g/L	28	15	12	17	8	7	5
Mass Transport							
Dissolved, kg/day	-114	-81	-168	-189	-182	-216	-306
Colloidal, kg/day	-84	-19	-64	-130	-150	-112	nd
Particulate, kg/g/day	-154	-84	-100	-138	-86	-72	-64
Particulate weight, g. ave.	0.34	0.29	0.27	0.21	0.73	0.22	0.27
Particulate Mass transport, kg/day*	-53	-24	-27	-28	-62	-16	-17

*corrected for particulate weight

Table 62. Means and ranges of trace element concentrations in dissolved phase samples collected in the near-field Mississippi River Plume

Sample ID		Mean	Min	Max	Freq	Corr. w/ Salinity
Element	Isotope	µg/L	µg/L	µg/L		
Lithium	Li 7	126.08	1.72	196.34	32	0.926
Beryllium	Be 9	0.11	0.02	0.31	31	0.027
Boron	B 10	1676.03	41.19	2629.51	32	0.956
Boron	B 11	1722.83	44.51	2681.93	32	0.952
Titanium	Ti 48	1412.40	213.19	2146.70	32	0.968
Titanium	Ti 49	68.19	16.30	98.17	32	0.831
Vanadium	V 51	4.36	1.09	8.47	32	0.074
Chromium	Cr 52	9.39	1.67	16.38	32	0.170
Manganese	Mn 55	15.67	1.74	165.39	32	0.163
Nickel	Ni 58	54.00	1.35	119.31	28	0.020
Cobalt	Co 59	1.40	0.20	2.19	32	0.821
Nickel	Ni 60	42.91	0.88	98.59	30	-0.013
Zinc	Zn 64	398.94	10.53	1085.73	22	-0.064
Copper	Cu 65	30.64	6.90	47.72	23	-0.100
Zinc	Zn 66	13.21	6.83	19.59	2	1.000
Arsenic	As 75	68.53	11.71	110.13	32	0.866
Selenium	Se 82	293.10	47.68	447.71	32	0.912
Strontium	Sr 88	5265.21	142.65	7895.27	32	0.902
Molybdenum	Mo 95	9.93	1.71	13.85	32	0.972
Palladium	Pd 106	0.25	0.01	0.63	30	0.090
Palladium	Pd 108	0.88	0.02	1.73	32	0.787
Cadmium	Cd 111	0.44	0.14	0.73	32	0.183
Cadmium	Cd 114	0.14	0.00	0.37	27	-0.246
Tin	Sn 118	0.33	0.02	0.76	32	0.086
Tin	Sn 120	0.39	0.10	0.66	32	0.171
Antimony	Sb 121	0.82	0.19	1.47	32	0.638
Barium	Ba 137	25.78	11.48	65.91	32	-0.943
Barium	Ba 138	25.98	11.70	66.93	32	-0.945
Cerium	Ce 140	0.03	0.00	0.13	23	-0.378
Iridium	Ir 191	0.07	0.00	0.30	28	-0.077
Iridium	Ir 193	0.06	0.00	0.26	30	-0.332
Platinum	Pt 194	0.10	0.03	0.25	23	-0.228
Platinum	Pt 195	0.08	0.00	0.32	17	-0.321
Gold	Au 197	0.97	0.20	4.50	32	0.075
Mercury	Hg 200	7.72	0.14	22.23	30	0.599
Mercury	Hg 202	7.23	0.79	20.17	32	0.593
Thallium	Tl 203	0.06	0.00	0.13	21	0.353
Thallium	Tl 205	0.04	0.00	0.07	29	0.043
Lead	Pb 206	0.22	0.01	0.81	11	-0.023
Lead	Pb 208	0.18	0.02	0.37	4	0.655
Bismuth	Bi 209	0.04	0.00	0.11	22	-0.364
Thorium	Th 232	0.04	0.01	0.11	32	-0.118
Uranium	U 238	1.66	0.25	2.82	32	0.814

Table 63. Means and ranges of concentrations of trace elements in the colloidal phase collected in the near-field Mississippi River Plume

Sample ID		Mean	Min	Max	Freq	Corr. w/ Salinity
Element	Isotope	µg/L	µg/L	µg/L		
Lithium	Li 7	103.27	14.89	165.19	30	0.859
Beryllium	Be 9	0.36	0.09	0.67	32	-0.202
Boron	B 10	1710.57	49.30	2606.44	32	0.896
Boron	B 11	1978.87	64.43	3115.38	32	0.883
Titanium	Ti 48	1572.33	394.14	2545.82	32	0.859
Titanium	Ti 49	102.48	62.79	169.04	32	0.596
Vanadium	V 51	7.88	4.00	11.51	32	0.276
Chromium	Cr 52	20.02	3.95	28.80	32	-0.038
Manganese	Mn 55	16.83	1.47	164.06	32	0.150
Nickel	Ni 58	35.29	0.72	67.15	29	-0.306
Cobalt	Co 59	1.47	0.52	2.19	32	0.746
Nickel	Ni 60	28.55	1.99	57.40	32	-0.137
Zinc	Zn 64	799.78	35.40	3321.11	21	-0.016
Copper	Cu 65	31.61	4.72	64.73	31	-0.446
Zinc	Zn 66	96.61	14.76	223.96	13	-0.669
Arsenic	As 75	94.89	52.88	171.89	32	0.517
Selenium	Se 82	436.39	231.46	767.63	32	0.542
Strontium	Sr 88	5459.26	151.66	8188.70	32	0.862
Molybdenum	Mo 95	10.55	2.28	14.86	32	0.873
Palladium	Pd 106	1.35	0.71	1.99	32	0.068
Palladium	Pd 108	1.21	0.36	2.18	31	0.827
Cadmium	Cd 111	0.56	0.00	1.88	29	0.410
Cadmium	Cd114	0.28	0.04	1.04	29	0.129
Tin	Sn 118	0.49	0.01	1.64	31	0.231
Tin	Sn 120	0.24	0.01	0.86	26	-0.063
Antimony	Sb 121	0.74	0.16	1.58	32	-0.035
Barium	Ba 137	24.38	4.66	56.83	32	-0.858
Barium	Ba 138	24.13	5.95	61.68	32	-0.867
Cerium	Ce 140	0.07	0.00	0.24	23	-0.192
Iridium	Ir 191	0.26	0.09	0.61	32	0.380
Iridium	Ir 193	0.18	0.01	0.49	31	0.080
Platinum	Pt 194	0.33	0.02	0.82	31	-0.182
Platinum	Pt 195	0.24	0.05	0.48	26	0.161
Gold	Au 197	1.46	0.37	8.68	32	0.285
Mercury	Hg 200	8.43	0.37	40.31	31	0.102
Mercury	Hg 202	8.58	0.25	35.07	26	0.231
Thallium	Tl 203	0.21	0.01	0.63	31	-0.031
Thallium	Tl 205	0.14	0.01	0.56	29	-0.393
Lead	Pb 206	1.83	0.05	4.58	4	0.781
Lead	Pb 208	1.48	0.44	3.62	4	0.664
Bismuth	Bi 209	0.08	0.01	0.16	27	-0.135
Thorium	Th 232	0.13	0.01	0.47	32	0.039
Uranium	U 238	1.78	0.30	3.19	32	0.849

Table 64. Means and ranges of trace element concentrations in suspended particulates collected in the near-field Mississippi River Plume

Sample ID		Mean	Min	Max	Freq	Corr. w/ Salinity
Element	Isotope	ng/g/L	ng/g/L	ng/g/L		
Beryllium	Be 9	981.63	31.02	3414.22	32	-0.703
Boron	B 10	18232446.17	331395.50	48483641.13	32	-0.127
Boron	B 11	13956409.94	322707.54	32731232.46	32	-0.160
Titanium	Ti 48	442926.07	504.87	1348705.54	32	-0.547
Titanium	Ti 49	260216.72	123.92	1086802.02	32	-0.648
Vanadium	V 51	38085.16	235.86	153362.90	32	-0.710
Chromium	Cr 52	36084.44	1680.77	128559.80	32	-0.610
Manganese	Mn 55	429975.38	160.93	1420123.14	32	-0.585
Nickel	Ni 58	80523.50	583.13	339304.76	32	-0.730
Cobalt	Co 59	4139.91	9.94	15475.73	32	-0.722
Nickel	Ni 60	14076.79	550.52	44025.86	32	-0.725
Zinc	Zn 64	25709093.01	29661.40	62919504.39	32	0.074
Copper	Cu 65	62957.88	427.53	184319.42	32	0.013
Zinc	Zn 66	29179739.75	27736.92	67992800.44	32	0.111
Arsenic	As 75	8063.36	256.75	17157.96	32	-0.355
Selenium	Se 82	9141.27	536.93	20651.70	32	0.290
Strontium	Sr 88	670522.29	330.74	1707721.18	32	-0.036
Molybdenum	Mo 95	817.52	54.14	1658.06	32	-0.034
Palladium	Pd 106	427.50	14.00	1033.96	32	-0.239
Palladium	Pd 108	227.96	11.07	398.61	32	-0.015
Cadmium	Cd 111	741.33	24.73	1673.29	32	-0.139
Cadmium	Cd 114	817.73	29.57	1646.04	32	-0.259
Tin	Sn 118	2955.05	162.33	5456.56	32	0.034
Tin	Sn 120	2954.28	76.27	5817.84	32	-0.004
Antimony	Sb 121	278.40	15.49	703.66	32	0.108
Barium	Ba 137	13884917.01	11184.42	34384831.40	32	0.027
Barium	Ba 138	9797272.07	11574.27	27608592.11	32	-0.070
Cerium	Ce 140	20394.43	8.77	59335.16	32	-0.637
Iridium	Ir 191	24.74	0.68	79.23	27	0.239
Iridium	Ir 193	21.66	1.76	100.79	30	0.097
Platinum	Pt 194	54.38	1.16	232.67	25	0.035
Platinum	Pt 195	98.93	3.91	364.57	27	0.132
Gold	Au 197	229.53	5.62	1188.78	31	0.103
Mercury	Hg 200	4042.88	67.92	9534.14	26	-0.093
Mercury	Hg 202	3277.13	29.41	8460.53	30	-0.009
Thallium	Tl 203	208.80	7.76	718.81	31	-0.653
Thallium	Tl 205	217.66	6.84	766.69	32	-0.621
Lead	Pb 206	17419.54	256.80	35987.69	32	-0.356
Lead	Pb 208	16364.95	183.81	33677.42	32	-0.338
Bismuth	Bi 209	199.79	14.19	461.75	31	-0.595
Thorium	Th 232	2719.60	145.28	8212.87	31	-0.698
Uranium	U 238	706.90	36.06	1487.30	31	-0.570

Figures 309 and 310 show selected plots of the regression coefficients of each element concentration in the dissolved phase against the conservative measurement of salinity as the effluent of the river is diluted into Gulf of Mexico water. Figures 311 and 312 show selected plots of similar regressions of trace elements in the colloidal phase and Figure 313 and 314 show similar regressions for the suspended particulate phase. Figures 315 through 320 show the spatial distribution of selected toxic trace elements in the near-field Mississippi River plume.

b. Discussion and Conclusions

A large number of the trace elements tested in the dissolved phase showed significant positive correlations between element concentrations and salinity (Table 62 and Figures 309 and 310), suggesting that, at least in the short term, these elements do not have their origins in the fresh waters of the river plume but rather are dissolved in seawater at concentrations in excess of the riverine source and are diluted out by fresher water coming in from the river. A few elements such as barium, were negatively correlated with salinity suggesting a strong riverine source. Several elements such as copper, cadmium, vanadium, tin and uranium show weak positive or negative correlations with salinity suggesting that multiple processes are controlling the distribution of these elements beyond simple dilution. Only Barium showed a significant negative correlation with salinity.

An examination of the salinity correlations with trace element concentrations in the colloidal phase show some similarities and some differences with the dissolved fraction data (Table 63 and Figure 311 and 312). These include increased concentrations for elements such as cadmium, and strontium, suggesting that there may be enrichment due to partitioning processes of these elements on colloidal solids and significantly improved correlations with salinity for elements such as cadmium and uranium suggesting that colloidally-bound forms of these elements are more predictably associated with seawater or freshwater sources. Only Barium showed a highly negative correlation with salinity in this phase.

Examination of the suspended particulate phase for trace element concentration trends with salinity (Table 64 and Figures 313 and 314) yielded results which showed a significant negative correlation between element concentrations on suspended particulates on a mass-volumetric basis (ug/g/L) suggesting that riverine particulates were the main source of trace elements entering the Gulf of Mexico. Elements which conformed to this relationship included: Be, Ti, V, Cr, Ni, Co, Cu, Cd, Ba, Pb, and U. The contrast between these results and those observed in the dissolved phase and colloidal phase suggest that there may be rapid changes in the distribution of metals entering the saline waters of the Gulf of Mexico, transferring increasing amounts of trace elements from the particulate phase to the dissolved and colloidal phases.

Spatial distributions of trace element concentrations showed different trends at the sampling locations relative to the mouth of the Mississippi River depending upon the phase analyzed. Lead 208 (Figure 315) concentrations in particulates entering the Gulf show a clear declining trend as the river water mixes with the saline Gulf waters. This pattern is consistent with most trace elements detected in this phase. In contract, Be 9 (Figure 316), Cu 65 (Figure 317), Cd 111 (Figure 318), and U 238 (Figure 319) measured in the colloidal phase show increasing concentrations of these elements as the river plume moves into the Gulf. This is reflective of the trends seen in the salinity plots and suggests that some trace elements are being mobilized from particulates into colloidally-bound and/or the dissolved phase during mixing. Ba 138 (Figure 320) measured in the colloidal phase showed a general dilution trend from the mouth of the river to the west.

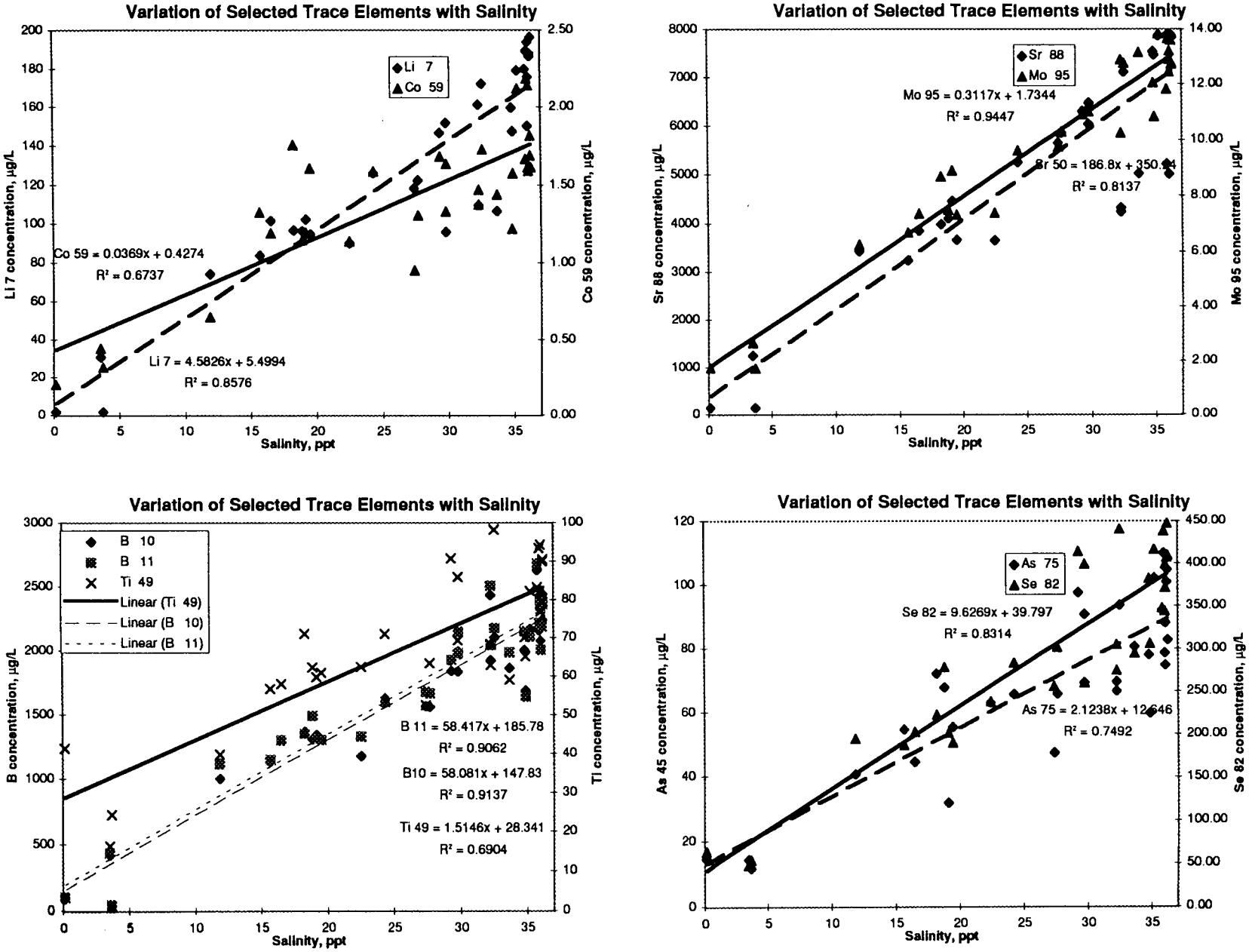

Figure 309. Regression plots of selected trace elements (lithium, cobalt, strontium, molybdenum, boron, titanium, arsenic, and selenium) concentration against salinity in the dissolved phase of water samples collected in the near-field Mississippi River plume.

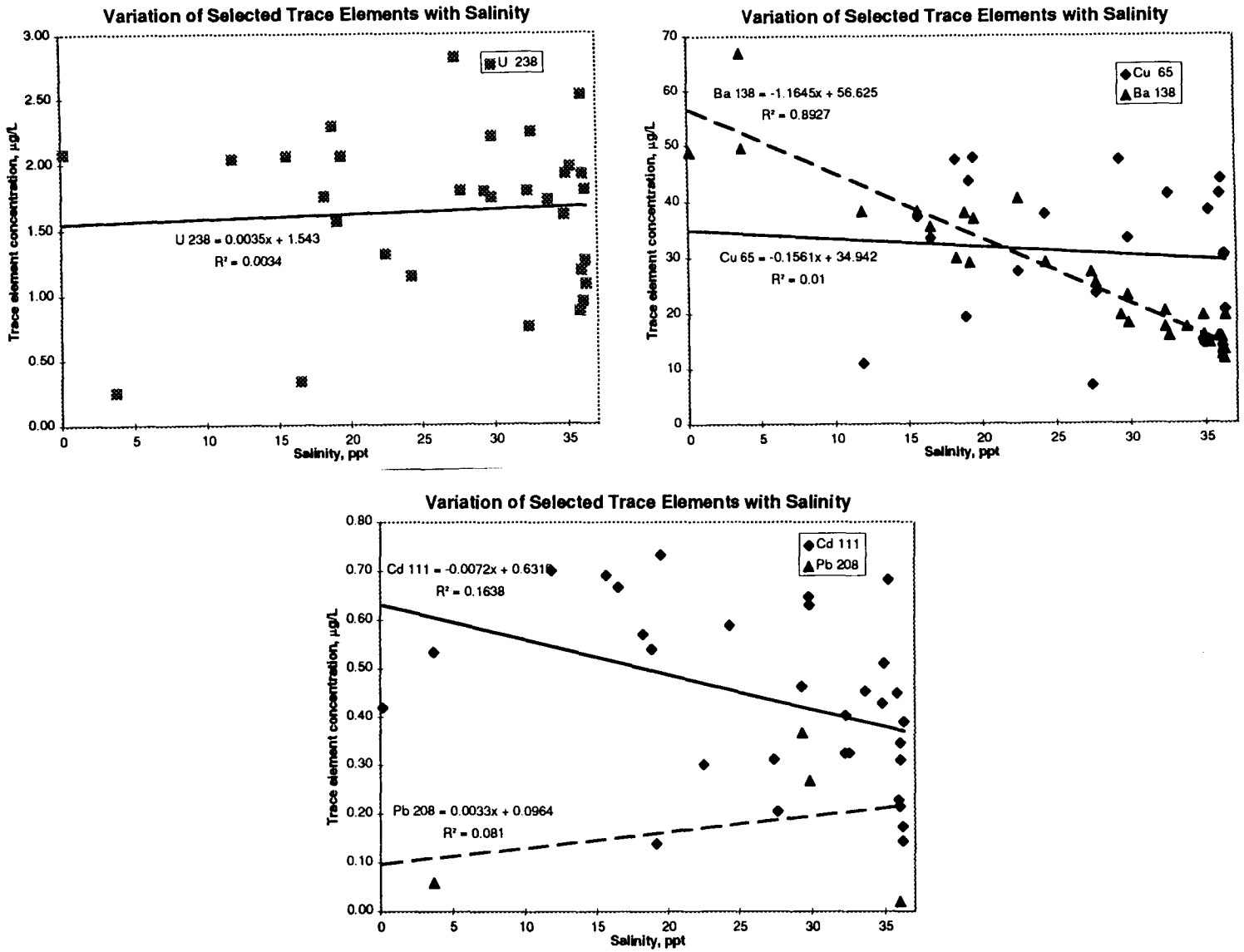

Figure 310. Regression plots of selected trace elements (copper, barium, cadmium, lead, and uranium) concentrations against salinity in the dissolved phase of water samples collected in the near-field Mississippi River plume.

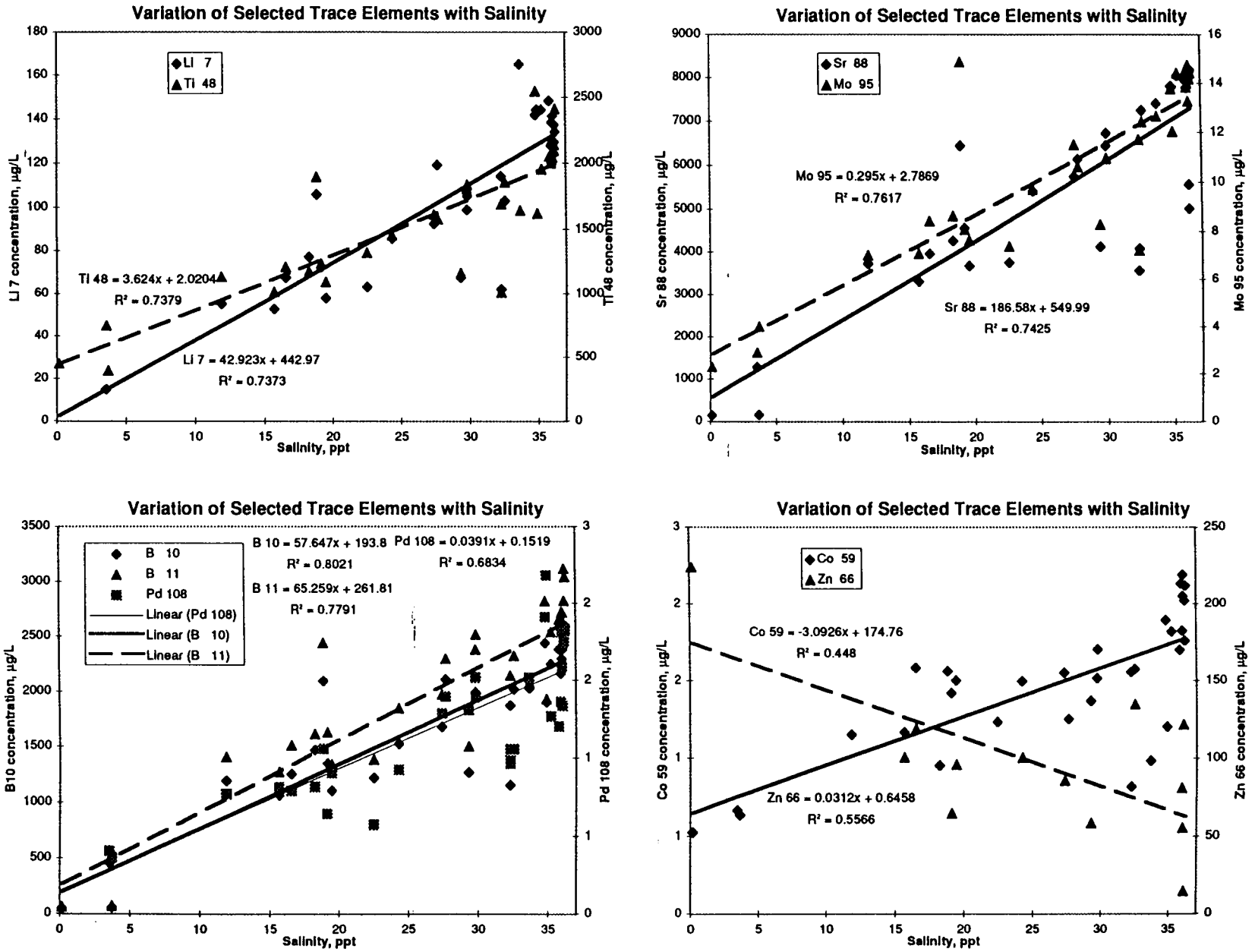

Figure 311. Regression plots of selected trace elements (lithium, titanium, strontium, molybdenum, boron, palladium, cobalt and zinc) concentrations against salinity in the colloidal phase of water samples collected in the near-field Mississippi River plume.

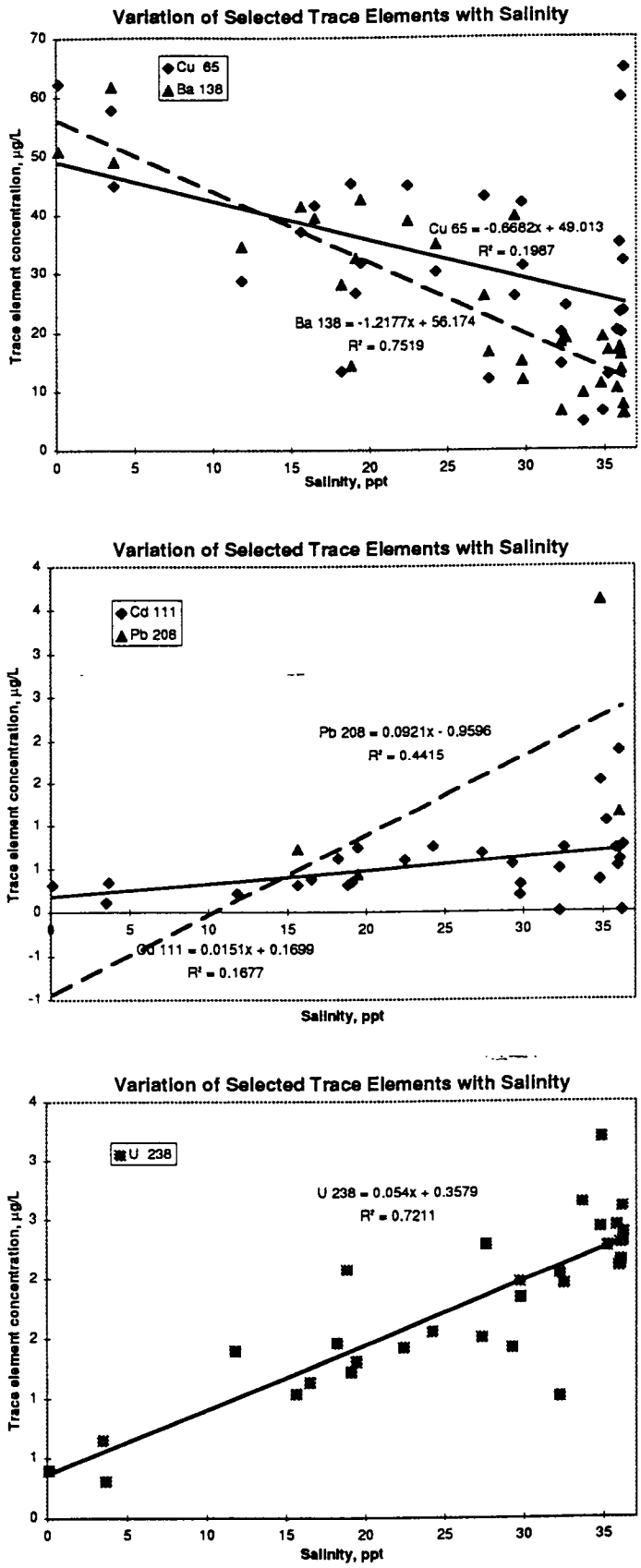

Figure 312. Regression plots of selected trace elements (copper, barium, cadmium, lead, and uranium) concentrations against salinity in the colloidal phase of water samples collected in the near-field Mississippi River plume.

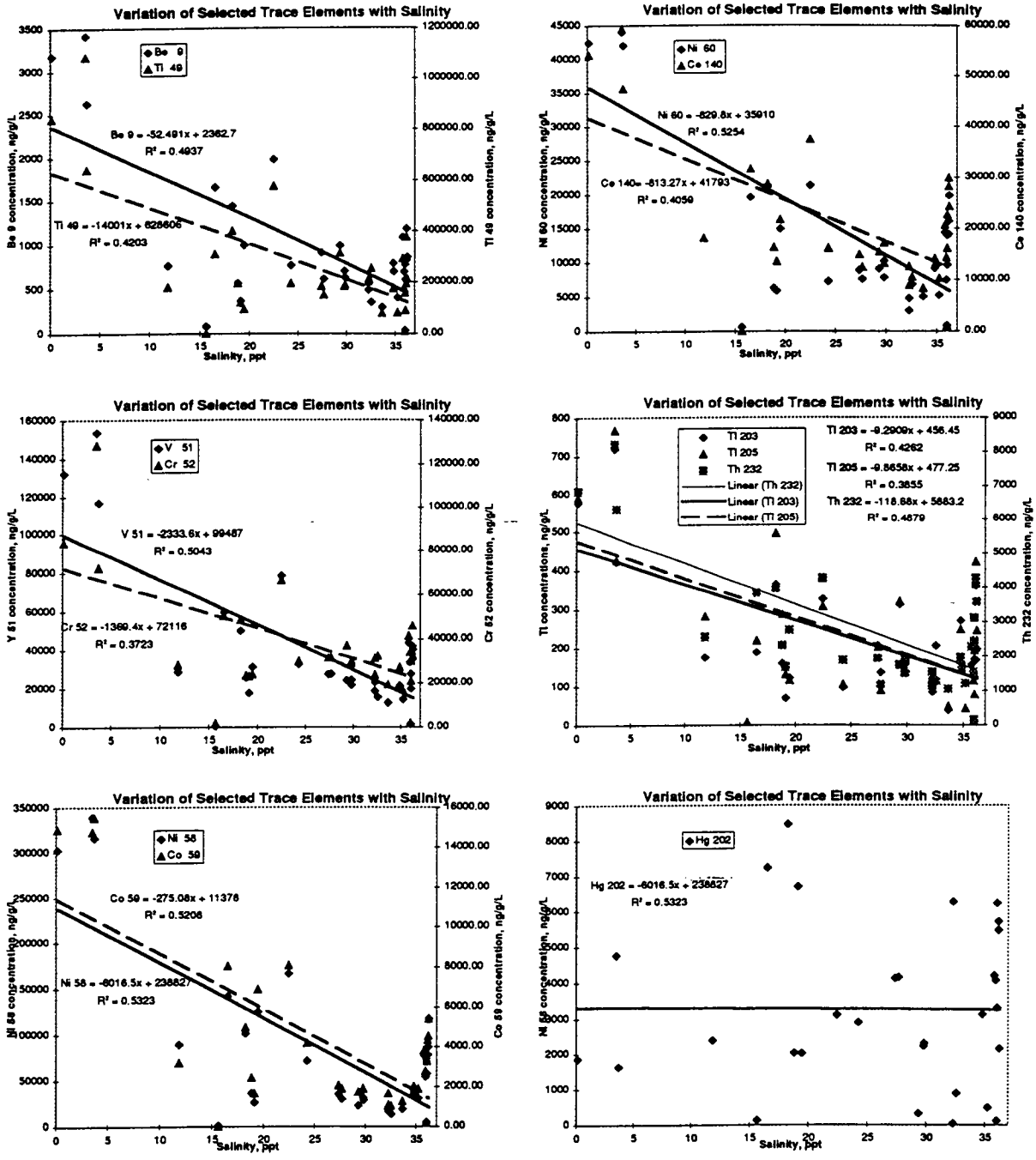

Figure 313. Regression plots of selected trace elements (beryllium, titanium, nickel, cerium, vanadium, chromium, thallium, thorium, nickel, cobalt, and mercury) concentrations against salinity in the suspended particulate phase of water samples collected in the near-field Mississippi River plume.

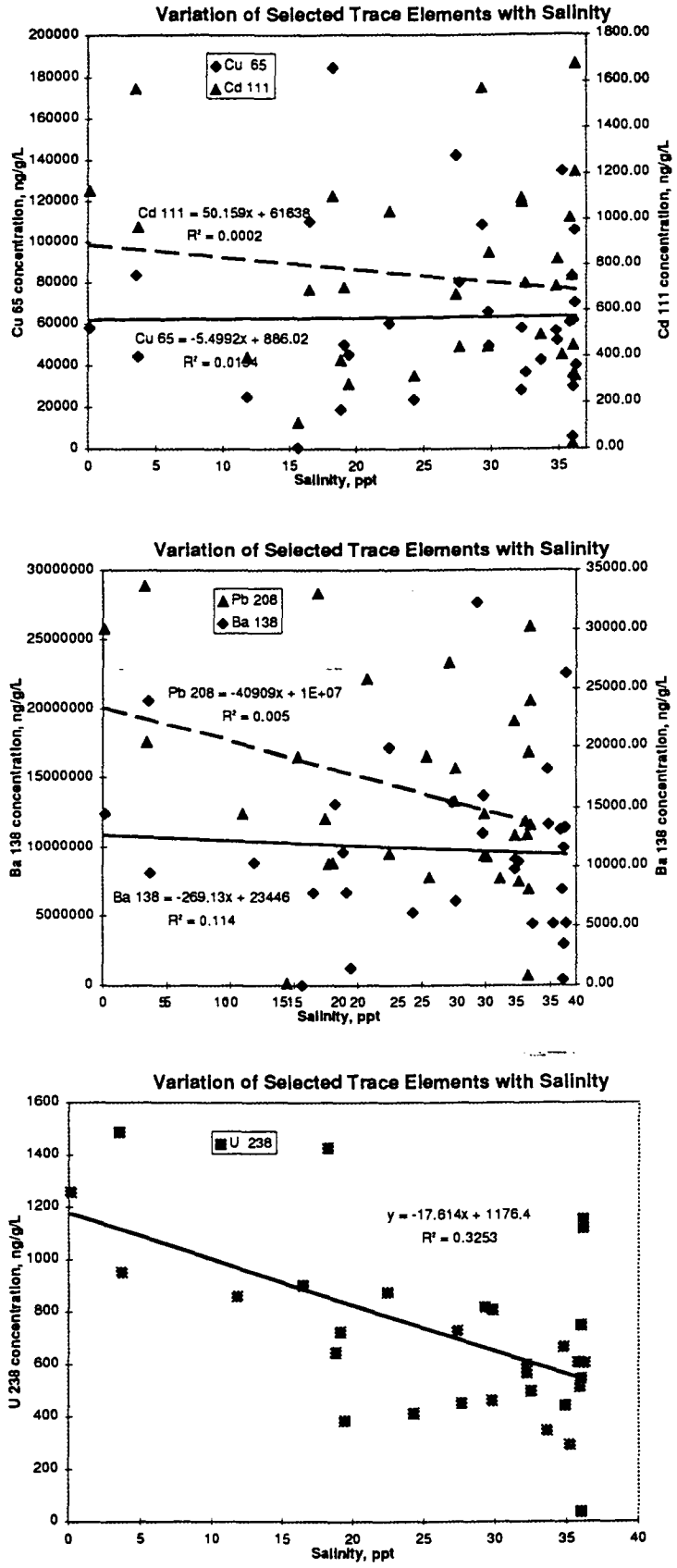

Figure 314. Regression plots of selected trace elements (copper, cadmium, lead, barium, and uranium) concentrations against salinity in the suspended particulate phase of water samples collected in the near-field Mississippi River plume.

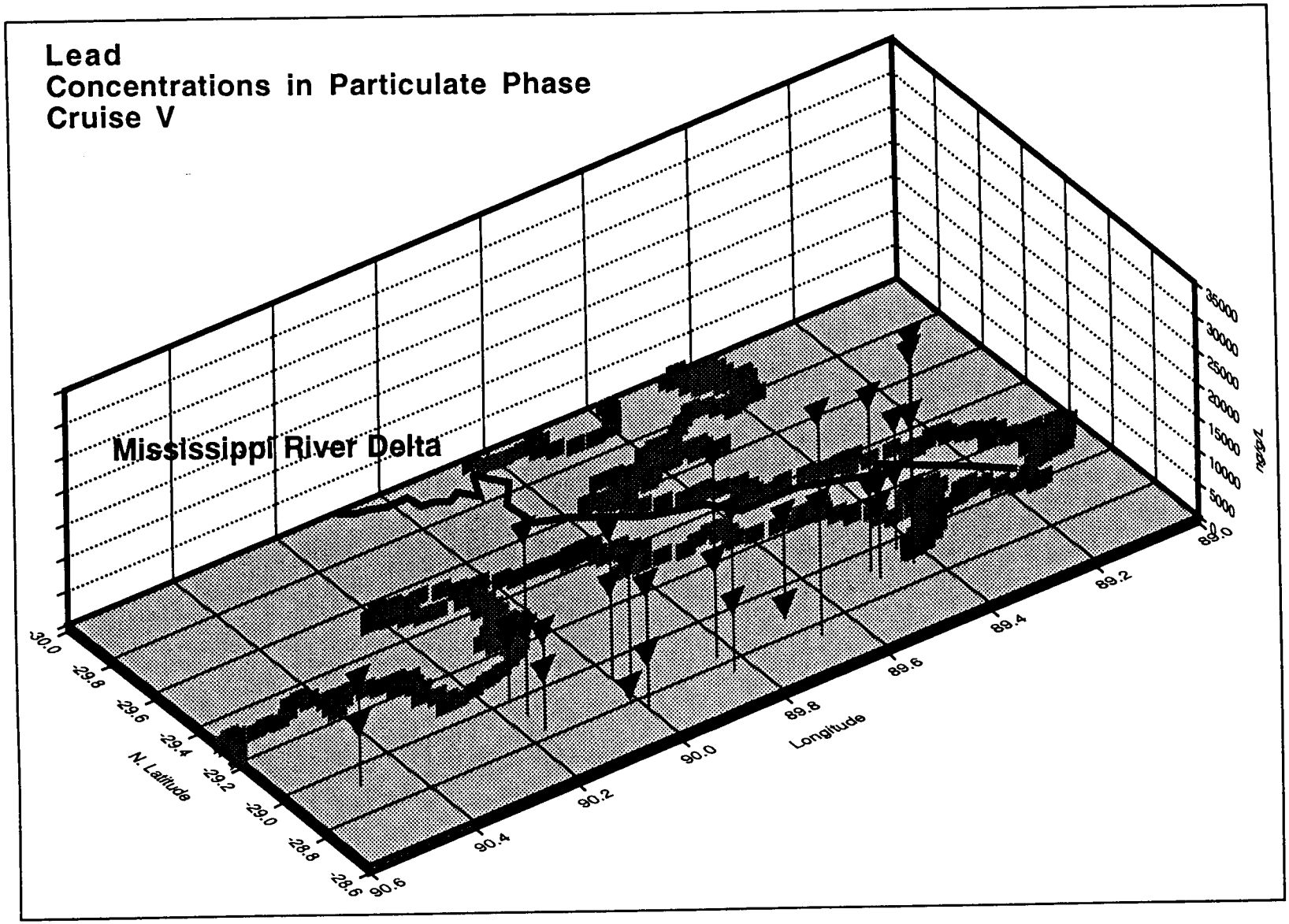

Figure 315. Spatial distribution of pb 208 (ng/g) in particulate phase samples collected in the near-field Mississippi River plume.

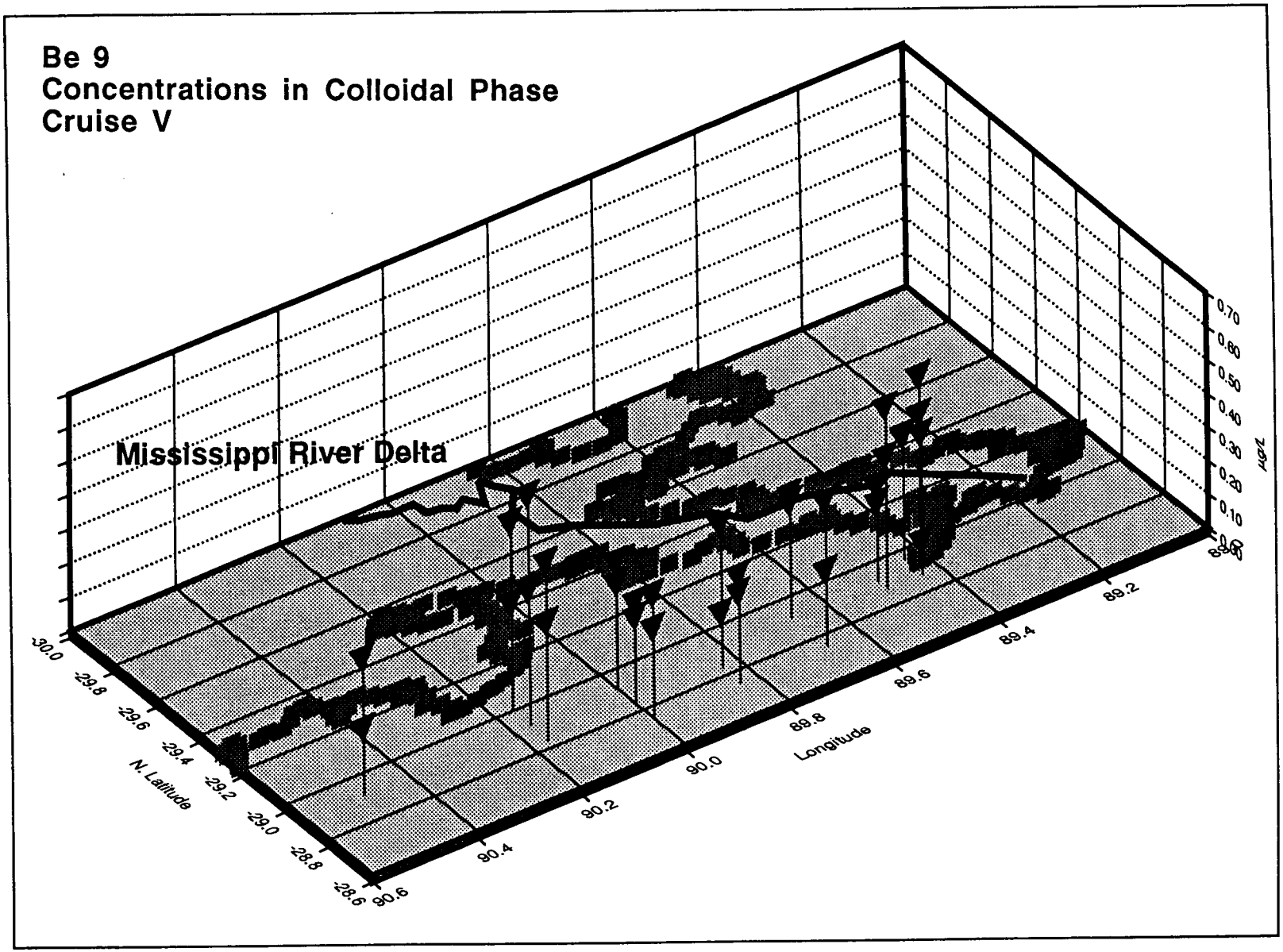

Figure 316. Spatial distribution of Be 9 (ng/g) in colloidal phase samples collected in the near-field Mississippi River plume.

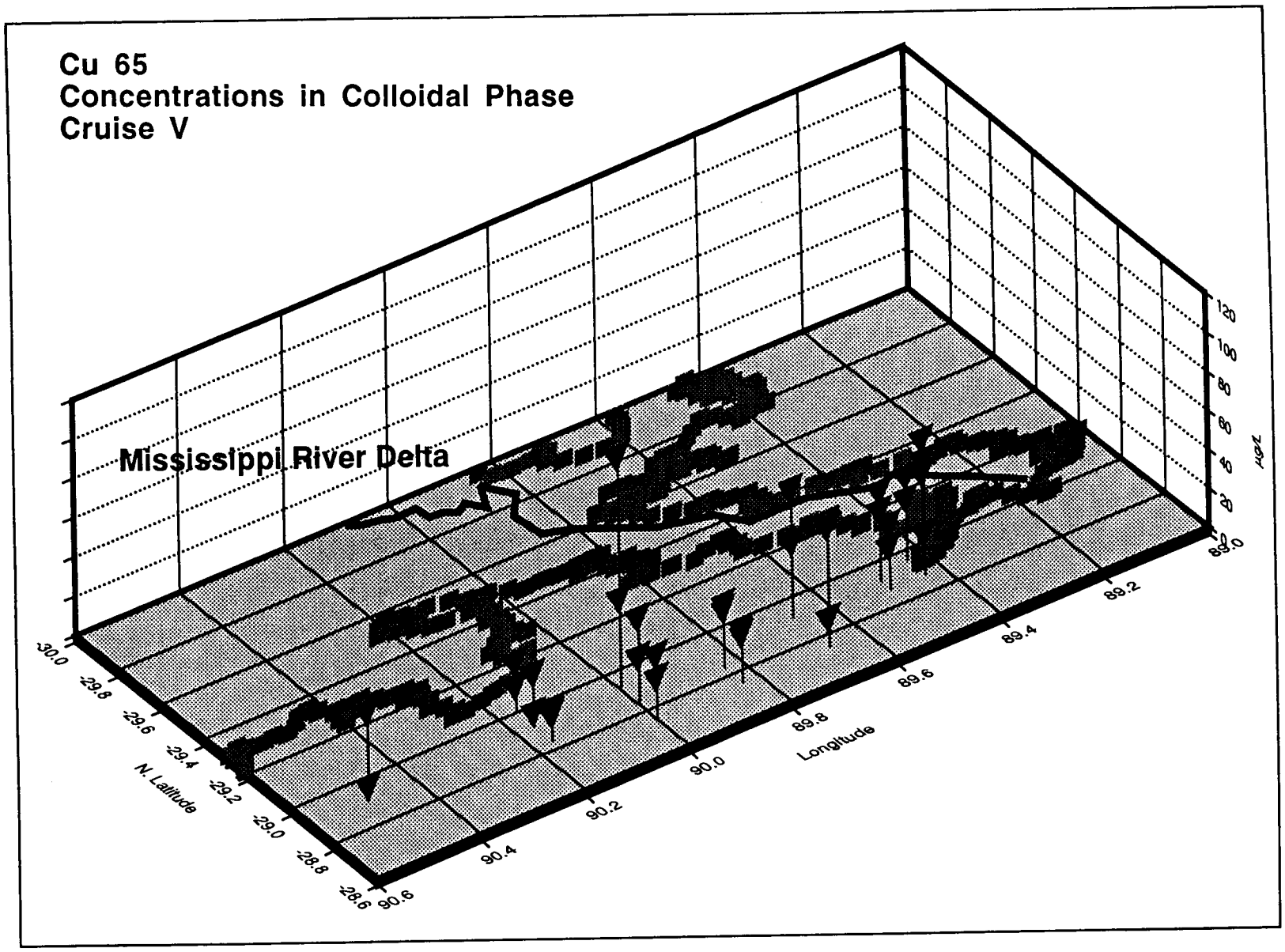

Figure 317. Spatial distribution of Cu 65 (ng/g) in colloidal phase samples collected in the near-field Mississippi River plume.

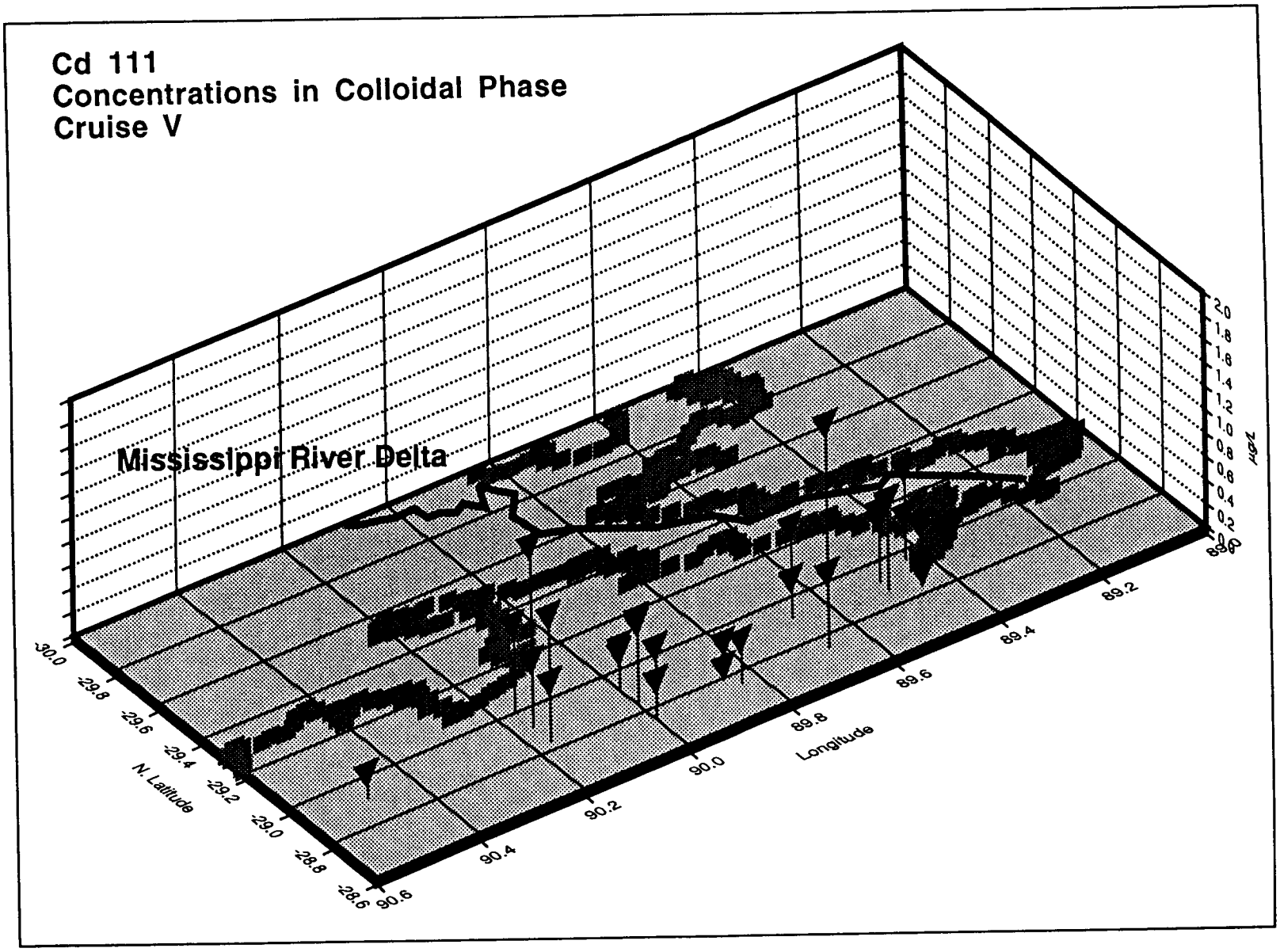

Figure 318. Spatial distribution of Cd 111 (ng/g) in colloidal phase samples collected in the near-field Mississippi River plume.

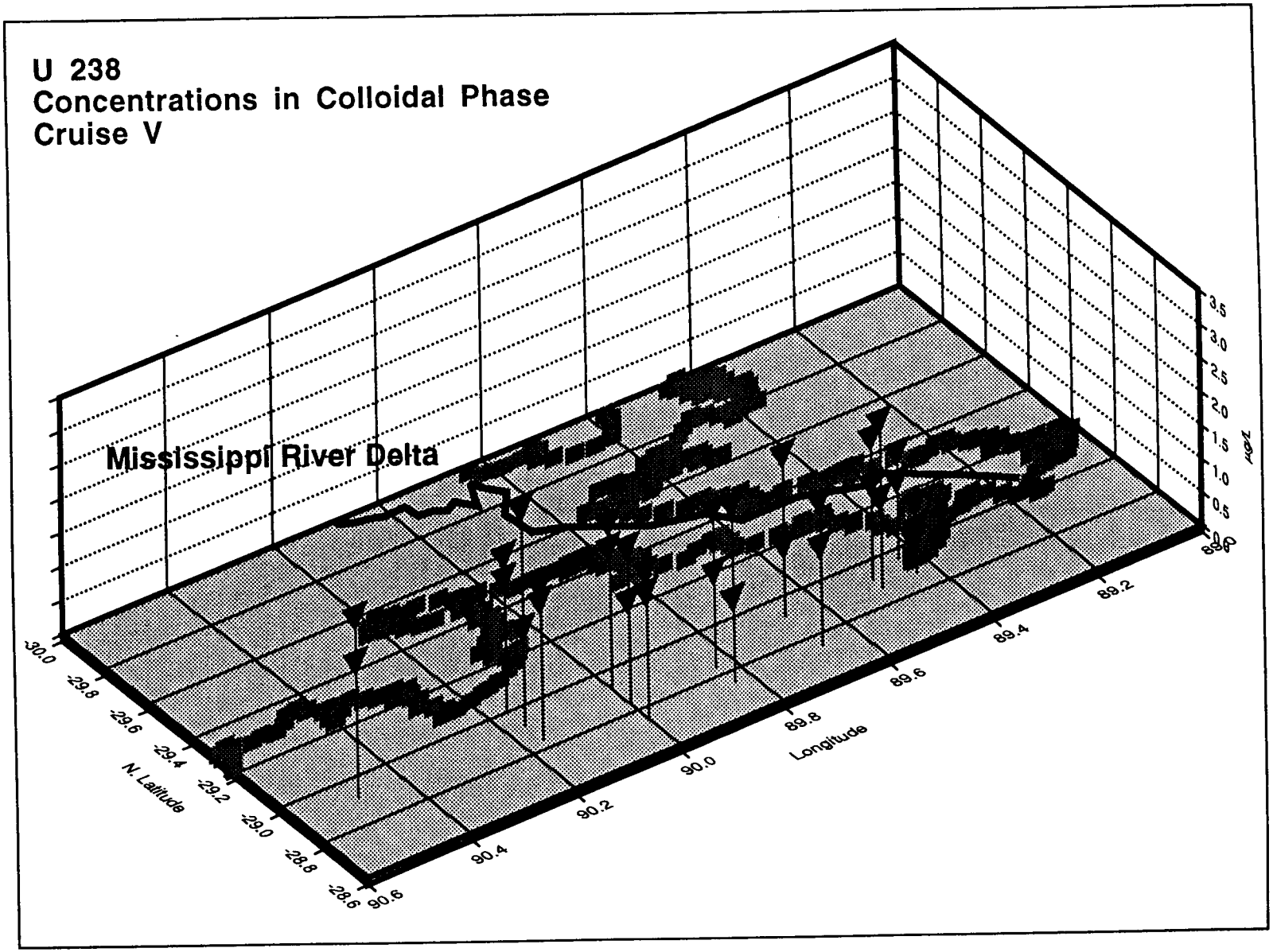

Figure 319. Spatial distribution of U 238 (ng/g) in colloidal phase samples collected in the near-field Mississippi River plume.

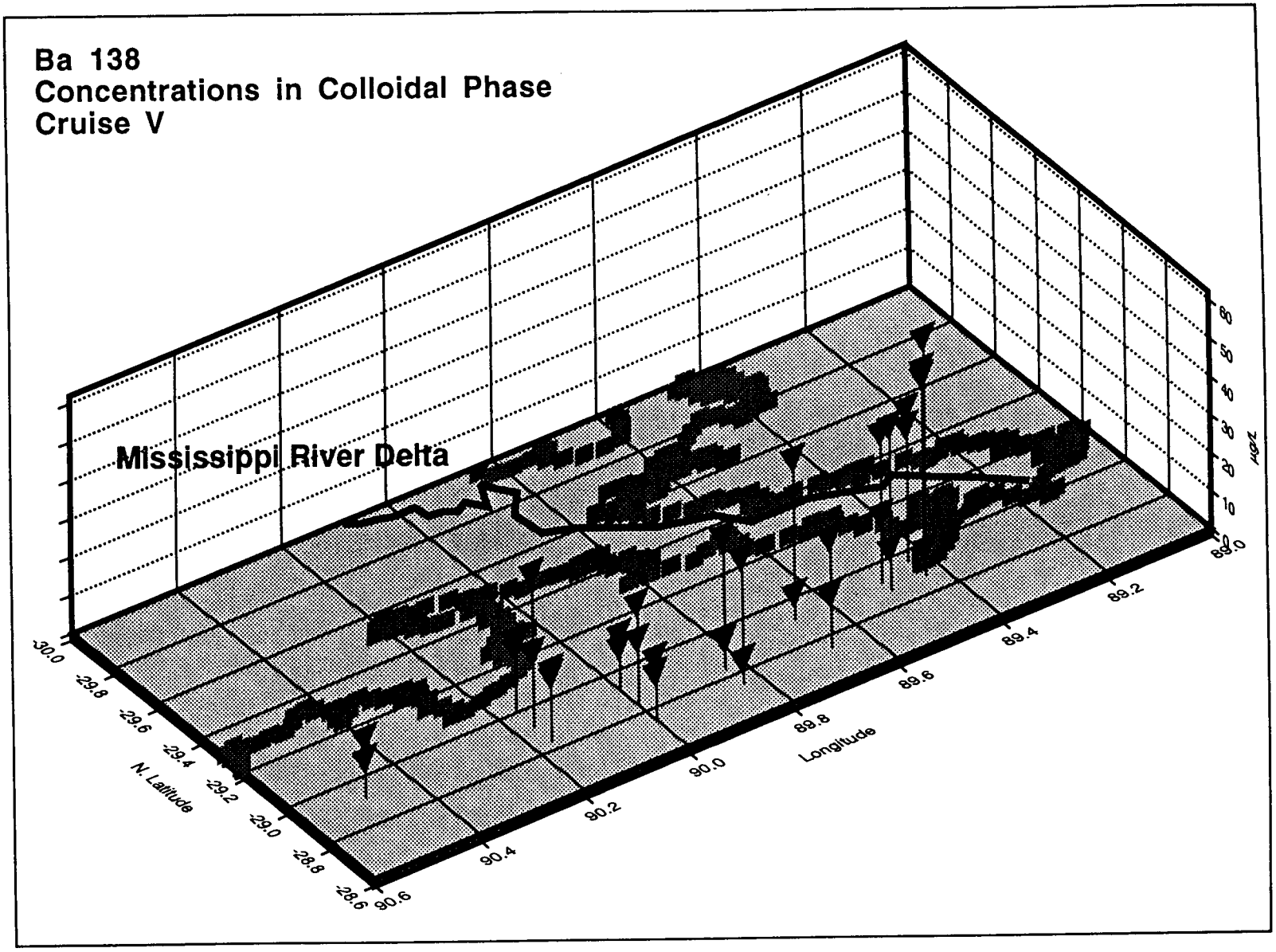

Figure 320. Spatial distribution of Ba 138 (ng/g) in colloidal phase samples collected in the near-field Mississippi River plume.

The area immediately adjacent to the mouth of an estuary is a dynamic region in which many processes are occurring simultaneously. From the data obtained in this investigation of trace elements, it is clear that this region is one in which there are major changes occuring in the distribution of elements between the particulate phase and the colloidally-bound phase and truly dissolved phase. Substances which have been transported in riverine systems on particles are entering the Gulf of Mexico and in some cases rapidly desorbing into the dissolved phase. Thus modeling of transport processes without consideration of phase changes may lead to errors in contaminant transport estimates. These changes are important because they determine to a large extent the ultimate fate of the element as well as its impacts upon the coastal environment.

H. Summary and Conclusions

The data reported here represent the first detailed examination of pollutant identification, and distribution in the northern Gulf of Mexico. The magnitude of this study provides a database for modeling of transport phenomenon and phase distribution as well as establishing temporal patterns that will be useful in future studies monitoring the health of this important ecosystem.

Spatial distributions of pollutants showed that the Atchafalaya Bay area is the most impacted by pollutants entering the system. Colloids acted in transport of parent PAH to a greater extent than for other pollutants, and acted least in the transport of herbicides.

Mass transport of pollutants was primarily in the dissolved phase due to the relative mass of dissolved phase compared to the mass of colloidal or particulate matter. In spite of this, particulate matter and bedded sediments in the Gulf remain a repository for persistent pollutants such as chlorinated pesticides and PCBs. The detection of persistent pollutants in the particulate phase of water samples indicates continued transport from riverine sources into the Gulf. Mass transport was largely influenced simply by the rate of water movement.

An important discovery was that herbicides, and especially Atrazine, are a major pollutant at all times and locations. Concentrations approached federal drinking water action levels off the Atchafalaya Bay in July. The ubiquitous nature of these pollutants may present both long-term impacts on aquatic life (Atrazine has been reported to be a carcinogen), as well as short-term impacts during the critical summer months when high temperatures and hypoxic conditions work to increase the toxicity of pollutants. Since the inception of this project, the EPA has acted to reduce the application of Atrazine, and many new herbicides have been introduced. Future studies are recommended to characterize both temporal trends as well as to identify new pollutant inputs.

I. Overall Conclusions of Coastal Current Studies

Several important conclusions can be drawn from the analysis of the trace element data collected as part of this study. First, it is apparent that the NW Gulf of Mexico is a dynamic environment both chemically and physically with respect to processes controlling trace elements distributions. Very large quantities of trace elements are entering the Gulf for both major and minor riverine sources. Upon entering the Gulf system, many trace elements are redistributed between the particulate and dissolved phases. The presence of a third or colloidal microparticulate phase may also be an important contributor to the dynamics of the system by competing with particles for

bound trace elements, thus facilitating transport rather than deposition of trace elements. Large inter-annual and intra-annual trends are observed in the fate and transport of trace elements. Key to the overall understanding of these processes is an appreciation of bulk solution (plus colloid-bound) transport relative to particulate transport of materials. This behavior may have profound implications for the health and nutrition of Gulf of Mexico biological communities.

XI. REFERENCES

Adams, C.E., J.T. Wells, and J.M. Coleman, 1982. Sediment trqansport on the central Louisiana continental sheld: Implications for the developing Atchafalaya River delta. Contributions in Marine Science 25:133-148.

Al-Yamani, F.Y. 1988. Distributional ecology of zooplankton and fish larvae (spot, croaker, and menhaden) in the northern Gulf of Mexico. Ph.D Dissertation. Univ. of Miami. Coral Gables, FL. 421 pp.

Allen, R.L., and R.E. Turner. 1977. Mississippi delta bight studies, Hydrographic data. 7 volumes. Center for Wetland Resources, Louisiana State University, Baton Rouge, LA.

Angelovic, J.W., C.R. Arnold, C.W. Caillouet, Jr., M.E. Chittenden, J.H. Finucane, R.Juhl, J.A. Martin, J.D. McEachran, E.L. Nakamura, E.T. Park, R.F. Temple, and W.L. Trent. 1976. Plankton and fisheries. In: W.B. Jackson (ed.). Environmental Studies of the South Texas Outer Continental Shelf, 1975. Volume I. NOAA Final Report to Bureau of Land Management. U.S. Department of Commerce.

Arnold, E.L., Jr. 1958. Gulf of Mexico plankton investigations, 1951-1953. Spec. Scient. Rep., U.S. Fish Widl. Ser. Fisheries No. 269.

Baker, E.T., H.B. Milburn and D.A. Tennant. 1988. Field assessment of sediment trap efficiency under varying flow conditions. J. Mar. Res. 46:573-592.

Barnes, C. A. and E. E. Collias. 1958. Some consideration of oxygen utilization rates in Puget Sound. J. Mar. Res. 17:69-80.

Barron, C.N., Jr. and A. C. Vastano. 1994. Satellite observations of surface circulation in the northwestern Gulf of Mexico during March and April 1989. Cont. Shelf Res., 14(6):607-628.

Biggs, D. C. , Nutrients, plankton, and productivity in a warm-core ring in the western Gulf of Mexico, Journal of Geophysical Research, 97, 2143-2154, 1992.

Bode, A., and Q. Dortch. 1996. Uptake and regeneration of inorganic nitrogen in coastal waters influenced by the Mississippi River: spatial and seasonal variations. J. Plankton Res. In press.

Bontempi, P.S. 1995. Phytoplankton distributions and species composition across the Texas-Louisiana continental shelf during two flow regimes of the Mississippi River. M.S. Thesis, Texas A&M University, 261 pp.

Bontempi, P.S., and C.A.N. Lyons. 1996. An assessment of oxygen, salinity, and phytoplankton distributions near an area off Sabine Pass, Texas, characterized by demersal fish and marine mammal mortalities. Fish. Bull. In press.

Candela, J., R. C. Beardsley, and R. Limeburner. 1992. Separation of tidal and subtidal currents in ship-mounted acoustic doppler current profiler, observations. J. of Geophysical Res., Jan. 15, 1992, pp. 769-788.

Canfield, D. E. 1989. Sulfate reduction and oxic respiration in marine sediments: Implications for organic carbon preservation in euxinic environments. Deep-Sea Res. 36:121-138.

Carpenter, E.J., and S. Dunham. 1985. Nitrogenous nutrient uptake, primary production, and species composition of phytoplankton in the Carmans River estuary, Long Island, New York. Limnol. Oceanogr. 30: 513-526.

Chen, C., R. O. Reid, and W. D. Nowlin, Jr. 1996. Near-inertial oscillations over the Texas-Louisiana shelf. J. Geophys. Res., 101(C2):3509-3524.

Chin-Leo, G. and R. Benner. 1992. Enhanced bacterioplankton, production and respiration at intermediate salinities in the Mississippi River plume. Mar. Ecol. Progr. Ser. 87:87-103.

Chloern, J.E., C. Grenz, L. Vidergar-Lucas. 1995. An empirical model of the phytoplankton chlorophyll:carbon ratios—the conversion factor between productivity and growth rate. Limnol. Oceanogr. 40: 1313-1321.

Chao, S-Y. 1987. Wind-driven motion near inner shelf fronts. J. Geophys. Res., 92(C4)3849-3860.

Chuang, W.S. and W. J. Wiseman, Jr. 1983. Coastal sea-level response to frontal passage on the Louisiana-Texas shelf. J. Geophys. Res., 88:2615-2620.

Cochrane, J. D. and F. J. Kelly. 1986. Low-frequency circulation on the Texas-Louisiana shelf. J. Geophysical Res. 91(C9):10645-10659.

Cooper, C., G.Z. Forristall, and T.M. Joyce, Velocity and hydrographic structure of two Gulf of Mexico warm-core rings, Journal of Geophysical Research, 95, 1663-1679, 1990.

Cowan, J.H., Jr., and R.F. Shaw. 1988. Distribution, abundance, and transport of larval sciaenids collected during winter and spring from the continental shelf waters off west Louisiana. Fish. Bull. 86(1): 129-142.

Cowan, J.H., Jr., and R.F. Shaw. 1991. Ichthyoplankton off west Louisiana and its relationship to zooplankton biomass. Contrib. Mar. Sci. 32: 103-121.

Crout, R. L. 1983. Wind-driven, near-bottom currents over the west Louisiana inner continental shelf. Ph.D. Dissertation, Department of Marine Science, Louisiana State University, Baton Rouge, Louisiana, 117 p.

Crout, R.L., W.J. Wiseman, Jr., and W.-S. Chuang. 1984. Variability of wind-driven currents, west Louisiana inner continental shelf: 1978-1979. Contrib. Mar. Sci. 27:1-11.

Csanady, G.T.. 1982. Circulation in the Coastal Ocean, D. Reidel, Hingham, Mass., 279 pp.

Daddio, E., W. J. Wiseman, Jr., and S.P. Murray. 1978. Inertial currents over the inner shelf near 30° N, J. Phys. Oceanogr., 8:728.

Dagg, M.J. 1988. Physical and biological responses to the passage of a winter storm in the coastal and inner shelf waters of the northern Gulf of Mexico. Cont. Shelf Res. 8: 167-178.

Dagg, M., Q. Dortsch, B. McKee, N. Rabalais, C. Adams, J. Fleeger, L. Rouse, R. Shaw, R.Turner, R. Twilley, J Govoni, S. Lorenz, and T. Whitledge. 1988. Oceanographic processes on continental shelves influenced by large rivers. Ninth Annual Minerals Management Service, Gulf of Mexico OCS Region, Information Transfer Meeting, New Orleans.

Davis, C.C. 1950. Observations of plankton taken in marine waters of Florida in 1947 and 1948. Q. J. Fla. Acad. Sci. 12(2): 67-103.

Diaz, R. J. and R. Rosenberg. 1995. Marine benthic hypoxia: a review of its ecological effects and the behavioural responses of benthic macroinfauna. Oceanogr. Mar. Biol. Annual Rev. 33: 245-303.

Dinnel, S.P., and W.J. Wiseman, Jr. 1986. Freshwater on the Louisians shelf. Continental Shelf Research 6: 709-718.

Ditty, J.G. 1986. Ichthyoplankton in neritic waters of the northern Gulf of Mexico off Louisiana: Composition, relative abundance, and seasonality. Fish. Bull. 84(4): 935-946.

Ditty, J.G., E.D. Houde, and R.F. Shaw. 1994a. Egg and larval development of Spanish sardine, *Sardinella aurita* (Family Clupeidae), with a synopsis of characters to identify clupeid larvae from the northern Gulf of Mexico. Bull. Mar. Sci. 54(2): 367-380.

Ditty, J.G., and R.F. Shaw. 1992. Larval development, distribution, and ecology of cobia *Rachycentron canadum* (Family: Rachycentridae), in the northern Gulf of Mexico. Fish. Bull. 90(4): 668-677.

Ditty, J.G., and R.F. Shaw. 1993. Larval development of tripletail, *Lobotes surinamensis* (Pisces: Lobotidae), and their spatial and temporal distribution in the northern Gulf of Mexico. Fish Bull. 92(1): 33-45.

Ditty, J.G., and R.F. Shaw. 1995. Seasonal occurrence, distribution, and abundance of larval bluefish, *Pomatomus saltatrix* (Family: Pomatomidae), in the northern Gulf of Mexico. Bull. Mar. Sci. 56(2): 564-573.

Ditty, J.G., R.F. Shaw, and J.S. Cope. 1994b. A re-description of Atlantic spadefish larvae (*Chaetodipterus faber*, Family: Ephippididae) and their distribution, abundance, and seasonal occurrence in the northern Gulf of Mexico. Fish. Bull. 92(2): 262-274.

Ditty, J.G., R.F. Shaw, C.B. Grimes, and J.S. Cope. 1994c. Larval development, distribution, and ecology of common dolphin, *Coryphaena hippurus*, and pompano dolphin, *C. equiselis* (Family: Coryphaenidae), in the northern Gulf of Mexico. Fish. Bull. 92(2): 275-291.

Ditty, J.G., G.G. Zieske, and R.F. Shaw. 1988. Seasonality and depth distribution of larval fishes in the northern Gulf of Mexico above latitude 26° N. Fish Bull. 86(4): 811-823.

Dortch, Q. 1994. Phytoplankton Survey. In: S.P. Murray and J. Donley (eds.), Mississippi River plume hydrography: annual report. OCS Study/MMS 94-0028. U.S. Dept. of the Interior, Minerals Management Service, Gulf of Mexico OCS Regional Office, New Orleans, LA, p. 124-142.

Dortch, Q. 1996. Phytoplankton Survey. In: S.P. Murray and J. Donley (eds.), Mississippi River plume hydrography: second annual report. OCS Study/MMS 96-0022. U.S. Dept. of the Interior, Minerals Management Service, Gulf of Mexico OCS Regional Office, New Orleans, LA, p. 74-90.

Dortch, Q., D. Milsted, N.N. Rabalais, S.E. Lohrenz, D.G. Redalje, M.J. Dagg, R.E. Turner, and T.E. Whitledge. 1992. Role of silicate availability in phytoplankton species composition and the fate of carbon. In Nutrient Enhanced Coastal Ocean Productivity Workshop Proceedings, TAMU-SG-92-109 Technical Report, pp. 76-83.

Dortch, Q., R.J. Robichaux, S. Pool, D. Milsted, G. Mire, N.N. Rabalais, T.M. Soniat, G. A. Fryxell, R.E. Turner, and M.L. Parsons. Submitted. Abundance and vertical flux of *Pseudo-nitzschia* in the northern Gulf of Mexico. Mar. Ecol. Prog. Ser.

Dortch, Q., N. N. Rabalais, R. E. Turner and G. T. Rowe. 1994. Respiration rates and hypoxia on the Louisiana shelf. Estuaries 17(4): 862-872.

Dowgiallo, M.J. (ed.) 1994. Coastal Oceanographic Effects of 1993 Mississippi River Flooding. NOAA Coastal Ocean Office/National Weather Service, Silver Spring, MD, pp. 46-49.

Etter, Paul C. 1996. Heat and freshwater budgets of the Texas-Louisiana shelf, April 1992 through November 94. LATEX Shelf Data Report, TAMU Oceanography Technical Report No. 96-1-T, College Station, TX, 123 pp.

Fahnenstiel, G.L., M.J. McCormick, G.A. Lang, D.G. Redalje, S.E. Lohrenz, M.Markowitz, B. Wagoner, H.J. Carrick. 1995. Taxon-specific growth and loss rates for dominant phytoplankton populations from the northern Gulf of Mexico. Mar. Ecol. Prog. Ser. 117: 229-239.

Falkowski, P., G. T. S. Hopkins, and J. J. Walsh. 1980. An analysis of factors affecting oxygen depletion in the New York Bight. J. Mar. Res. 38:479-506.

Finucane, J.H. 1976. Baseline survey of ichthyoplankton. pp. 20-42 and 163-305. In: W.B. Jackson (ed.). Environmental studies of the south Texas outer continental shelf 1975. Vol. 1: Plankton and fisheries. NOAA Final Report to BLM. Contract No. 08550-1A5-19. 425 pp.

Finucane, J.H., L.A. Collins, and L.E. Barger. 1979a. Determine the effects of discharges on seasonal abundance, distribution, and composition of ichthyoplankton in the oil field. pp. 2.3.6-1 through 2.3.6-157. In: W.B. Jackson (ed.). Environmental assessment of an active oil field in the northwestern Gulf of Mexico, 1977-1978. Vol. 2: Data management and biological investigation. NOAA Final Report to EPA. Contract No. EPA-IAG-D5-E693-EO.

Finucane, J.H., L.A. Collins, L.E. Barger, and J.B. McEachran. 1979b. Ichthyoplankton/mackerel eggs and larvae. In: W.B. Jackson (ed.). Environmental studies of the south Texas outer continental shelf 1977 NOAA Final Report to BLM. Contract No. AA550-1A7-21. 504 pp.

Finucane, J.H., L.A. Collins, L.E., and J.B. McEachran. 1977. Ichthyoplankton/mackerel eggs and larvae. In: W.B. Jackson (ed.). Environmental studies of the south Texas outer continental shelf 1976 NOAA Final Report to BLM. Contract No. AA550-TA7-3. 484 pp.

Fisher, T.R., E.R. Peele, J.W. Ammerman, and L.W. Harding. 1992. Nutrient limitation of phytoplankton in Chesapeake Bay. Mar. Ecol. Prog. Ser. 82: 51-63.

Forristall, G.Z., K.J. Schaudt, C.K. Cooper, Evolution and kinematics of a Loop Current eddy in the Gulf of Mexico during 1985, Journal of Geophysical Research, 97, 2173-2184, 1992.

Fryxell, G.A., M.E. Reap, D.L. Valencic. 1990. *Nitzschia pungens* Grunow f. *multiseries* Hasle: Observations of a known neurotoxic diatom. Nova Hedwigia 100: 171-188.

Fucik, K.W., and S.Z. El-Sayed. 1973. Effect of oil production and drilling operations on the ecology of phytoplankton in the OEI study area: In: Ward, C.H., Bender, M.E., Reisch, D.J. (eds), The Offshore Ecology Investigation, Effects of Oil Drilling and Production in a Coastal Environment, Rice University Studies 65: 325-353.

Gardner, W. D. and M.J. Richardson, 1992. Particle export and resuspension fluxes in the western North Atlantic. In: Rowe, G. T. and V. Pariente, (eds.). Deep-Sea Food Chains and the Global Carbon Cycle. Netherlands: Kluwer Academic Publishers; 1992: pp. 339-364. 400 pp.

Garvine, R.W. 1995. A dynamical system for classifying buoyant coastal discharges. Cont. Shelf Res., 15(13:1585-1596.

Gittins, R. 1985. Canonical Analysis: A Review with Applications in Ecology. Springer-Verlag. New York. 351 pp.

Glover, H.E. 1985. The physiology and ecology of the marine cyanobacterial genus *Synechococcus*. Advances in Microbiology 3: 49-107.

Govoni, J.J., D.E. Hoss, and D.R. Colby. 1989. Spatial distribution of larval fish about the Mississippi River plume. Limnol. Oceanogr. 34(1): 178-187.

Grimes, C.B., and J.H. Finucane. 1991. Spatial distribution and abundance of larval and juvenile fish, chlorophyll, and macrozooplankton around the Mississippi River discharge plume, and the role of the plume in fish recruitment. Mar. Ecol. Prog. Ser. 75(2-3): 109-119.

Hamilton, P., Lower continental slope cyclonic eddies in the central Gulf of Mexico, Journal of Geophysical Research, 97, 2185-2200, 1992.

Harris, G. P. 1986. Phytoplankton Ecology: Structure, Function and Fluctuations. Chapman and Hall, New York.

Hauschild, C.A., H.J.G., McMurter, F.r. Pick. 1991. Effect of spectral quality on growth and pigmentation of picocyanobacteria. J. Phycol. 27: 699-702.

Hitchcock, G.L., W.J. Wiseman, Jr., W.C. Boicourt, A.J. Mariano, N. Walker, T.A. Nelsen, and E. Ryan. 1997. Property fields in an effluent plume of the Mississippi River. J. M. Sys. 12:109-125.

Hopkins, T.L. 1973. Zooplankton. pp. IIIF1-11. In: A Summary of Knowledge of the Eastern Gulf of Mexico. Report to the Committee on Exploration. American Petroleum Institute.

Huh, O.K., Wiseman, W.J., Jr., and Rouse, L.J., Jr., Winter cycle of sea surface thermal patterns: Northeastern Gulf of Mexico, Journal of Geophysical Research, 83, 523-4529, 1978.

Huh, O.K. and Schaudt, K.J., Satellite imagery tracks currents in Gulf of Mexico. Oil and Gas Journal, 88, 70-76, 1990.

Ikeda, M. and W.J. Emery, Satellite ovservations and modeling of meanders in the California Current system off Oregon and northern California, J. Phys. Oceanogr. 14, 1434-1450, 1984.

Iverson, R.L., and T.L. Hopkins. 1981. A summary of knowledge of plankton production in the Gulf of Mexico: Recent phytoplankton and zooplankton research. pp. 147-211. In: D.K. Atwood (ed.). Proceedings of a Symposium on Environmental Research Needs in the Gulf of Mexico (GOMEX). Key Biscayne, Florida, 30 September -5 October 1979. U.S. Department of Commerce. National Oceanic and Atmospheric Administration.

Johnson, W.R and P.P. Niiler, SCULP drifter study in the Northwest Gulf of Mexico, American Geophysical Union, Fall Meeting, San Francisco, O52C-8, 1994.

Jongman, R.H., C.J.F. ter Braak, and O.F.R. van Tongeren. 1987. Data Analysis in Community and Landscape Ecology. Pudoc. Wageningen, Netherlands. 299 pp.

Joyce, T.M. 1989. On in situ "calibration" of shipboard ADCPS. J. Atmos. oceanic Technol., 6:169-172.

Justic', D., N. N. Rabalais, R. E. Turner and Q. Dortch. 1995a. Changes in nutrient structure of river-dominated coastal waters: stoichiometric nutrient balance and its consequences. Estuarine and Coastal Shelf Science 40:339-356.

Justic', D., N. N. Rabalais, and R. E. Turner. 1995b. Stoichiometric nutrient balance and origin of coastal eutrophication. Marine Pollution Bulletin 30:41-66.

Justic, D., N. N. Rabalais, R. E. Turner and W. J. Wiseman, Jr. 1993. Seasonal coupling between riverborne nutrients, net productivity and hypoxia. Mar. Pollut. Bull. 26: 184-189.

Kelley, S., T. Potthoff, W.J. Richards, L. Ejsymont, and J.V. Gartner. 1986. SEAMAP 1983 - Ichthyoplankton: Larval distribution and abundance of Engraulidae, Carangidae, Clupeidae, Lutjanidae, Serranidae, Sciaenidae, Coryphaenidae, Istiophoridae, Xiphiidae, and Scombridae in the Gulf of Mexico. U.S. Dept. Commer. NOAA Tech. Memo. NMFS-SEFC-167.

Kelly, F.J., J.D. Cochrane, R.E. Randall, and J.E. Schmitz. 1983. Physical oceanography, in evaluation of brine disposal from the west Hackberry site of the Strategic Petroleum Reserve Program. Texas A&M University/Texas A&M Research Foundation, College Station, TX. Vol. II, pp. 10180.

Kemp, W. M. and W. R. Boynton. 1981. External and internal factors regulating metabolic rates of an estuarine benthic community. Oecologia 51:19-27.

Ketchum, B.H., and D.J. Keen. 1944. The accumulation of river water over the continental shelf between Cape Cod and Chesapeake Bay. Papers in Marine Biology and Oceanography, Supplement to Deep Sea Research 3, 346-357.

Kimsey, J. B. and R. F. Temple. 1964. Currents on the continental shelf of the northwestern Gulf of Mexico. U. S. Bureau of Commercial Fisheries Circular 183:25-27.

King, J.E. 1950. Preliminary report on the plankton of the west coast of Florida. Q. J. Fla. Acad. Sci. 12(2): 109-137.

Kosro, P.M. and A. Huyer CTD and velocity surveys of seaward jets off northern California, July 1981 and 1982, J. Geophys. Res. 91, 11,727-11,740, 1986.

Kourafalou, V.H., L-Y. Oey, J.D. Wang and T.N. Lee. 1996a. The fate of river discharge on the continental shelf, 1. Modeling the river plume and inner shelf coastal current. J. Geophys. Res., 101(C2):3415-3434.

Kourafalou, V.H., T. N. Lee, L.-Y. Oey and J.D. Wang. 1996b. The fate of river discharge on the continental shelf, 2. Transport of coastal low-salinity waters under realistic wind and tidal forcing. J. Geophys. Res., 101(C2):3454-3455.

Kuparinen, J., and H. Kuosa. 1991. Autotrophic and heterotrophic picoplankton in the Baltic Sea. Advances in Mar. Biol. 29: 73-128.

Lang, K.L., C.B. Grimes, and R.F. Shaw. 1994. Age, growth, and mortality of larval yellowfin tuna, *Thunnus albacares*, collected about the Mississippi River plume. Environ. Biol. Fish. 39: 259-270.

Laws, E.A., and J.W. Archie. 1981. Appropriate use of regression analysis in marine biology. Mar. Biol. 65:13-16.

Leben, R.R., G.H. Born, D.C. Biggs, D.R. Johnson, N.D. Walker, Verification of TOPEX altimetry in the Gulf of Mexico, TOPEX/POSEIDON Research News, vol. 1, 3-8, 1993.

Leming, T. D. and W. E. Stuntz. 1984. Zones of coastal hypoxia revealed by satellite scanning have implications for strategic fishing. Nature 310: 136-138.

Lentz, S. J. 1995. The Amazone River plume during AMASSEDS: Subtidal current variability and the importance of wind forcing. J. Geophys. Res., 100(C2):2377-2390.

Lewis, J.K. and A.D. Kirwan, Some observations of ring topography and ring-ring interactions in the Gulf of Mexico, Journal of Geophysical Research, 90, 9017-9028, 1985.

Lohrenz, S.E., G.L. Fahnenstiel, and D.G. Redalje. 1994. Spatial and temporal variations in photosynthesis parameters in relation to environmental conditions in coastal waters of the northern Gulf of Mexico. Estuaries 17: 779-795.

Lohrenz, S.E., M.J. Dagg, and T.E. Whitledge. 1990. Enhanced primary production at the plume/oceanic interface of the Mississippi River. Continental Shelf Research 10: 639-664.

Lovegrove, T. 1966. The determination of the dry weight of plankton and the effect of various factors on the values obtained. pp. 429-467. In: H. Barnes (ed.). Some Contemporary Studies in Marine Science. George Allen and Unwin Ltd. London.

MacLeod, W.D., D.W. Brown, A.J. Friedman, D.G. Burrows, O. Maynes, R.W. Pearce, C.A. Wigren, and R.G. Bogar. 1985. Standard analytical procedures of the NOAA, National Analytical Facility. Extractable Toxic Organic Compounds, Second Edition. NOAA/NMFS, Seattle, WA, 121 pp.

Malone, T.C., D.J. Conley, T.R. Fisher, P.M. Glibert, L.W. Harding, and K. Sellner. 1996. Scales of nutrient-limited phytoplankton productivity in Chesapeake Bay. Estuaries 19: 371-385.

Malone, T.C., H.W. Ducklow, E.R. Peele, and S.E. Pike. 1991. Picoplankton carbon flux in Chesapeake Bay. Mar. Ecol. Prog. Ser. 78: 11-22.

Maples, R., R. Donahoe, and G.J. Fister. 1981. Seasonal variability of chlorophyll *a* in the nearshore marine waters of southwestern Louisiana. Louisiana Academy of Sciences 46: 53-55.

Maul, F.A. and F.M. Vukovich, The relationship between variations in the Gulf of Mexico Loop Current and Straits of Florida volume transport, Journal of Physical Oceanography, 23, 785-7, 1993.

McClain, E.P., W.G. Pichel, and C.C. Walton, Comparative performance of AVHRR-based multi-channel sea surface temperatures, Journal of Geophysical Research, 90, 11,587-11,601, 1985.

McEwen, G.F., M.W. Johnson, and Th.R. Folsom. 1954. A statistical analysis of the performance of the Folsom plankton sample splitter, based upon test observations. Arch. Met. Geophys. Bioklim, Series A. 7: 502-527.

McGowan, M.F. 1985. Ichthyoplankton of the Flower Garden Banks, northwest Gulf of Mexico. Ph.D. Dissertation. Univ. of Miami. Coral Gables, FL. 376 pp.

Meade, R.H. and R.S. Parker. 1985. Sediment in rivers of the United States. National Water Supply-Summary 1984. U.S. Geological Survey Water-Supply Paper No. 2275, U.S. Department of the Interior, Geological Survey, Washington, DC.

Means, J.C., S.G. Wood, J.J. Hassett, and W.E. Banwart. 1980. Sorption properties of polynuclear aromatic hydrocarbons by sediment and soils. Environ. Sci. Technol. 14:1525-1528.

Merrell, W.J., Jr. and J. Morrison, On the circulation of the western Gulf of Mexico with observations from April 1978, Journal of Geophysical Research, 86, 4181-4185, 1981.

Methot, Jr., R.D., and D. Kramer. 1979. Growth of northern anchovy, Engraulis mordax, larvae in the sea. Fish. Bull. 77(2): 413-423.

Milliman, J.D. and R.H. Mead. 1983. World-wide delivery of river sediment to the ocean. J. Geol. 91:1-21.

Mossa, J. and H.H. Roberts. 1990. Synergism of riverine and winter storm-related sediment trsnport processes in Louisiana's coastal wetlands. Gulf Coastal Association of Geological Societies 40:635-642.

Munchow, A., C. S. Coughran, M. C. Hendershott, and C. D. Winant. 1995. Performance and calibration of an acoustic Doppler current profiler towed below the surface. J. Atmos. Oceanic Technolog., 12(2).

Munchow, A.C. and R.W. Garvine. 1993a. Buoyancy and wind forcing of a coastal current. J. Mar. Res., 51:293-322.

Munchow, A.C. and R.W. Garvine. 1993b. Dynamical properties of buoyancy-driven coastal current. J. Geophys. Res., 98(C11):20,063-20,077.

Munchow, A. C and R.W. Garvine. 1992. Subtidal currents from a shipboard acoustic doppler current profiler in tidally dominated waters. Cont. Shelf Res. 12(4):

Munroe, T.A. 1991. Western Atlantic tonguefishes of the Symphurus plagusia complex (Cynoglossidae: Pleuronectiformes), with descriptions of two new species. Fish. Bull. 89:247-287.

Murphy, L.S., and E.M. Haugen. 1985. The distribution and abundance of phototrophic ultraplankton in the North Atlantic. Limnol. Oceanogr. 30: 47-58.

Murray, S. P. and J. Donley (eds.). 1994. Mississippi River Plume Hydrography: Annual Report. OCS Study/MMS 94-0028. U.S. Dept. of the Interior, Minerals Management Service, Gulf of Mexico OCS Regional Office, New Orleans, Louisiana, 229 pp.

Murray, S.P. and J. Donley (eds.). 1996. Mississippi River plume hudrography: Second annual report. OCS Study MMS 96-0022. U.S. Department of the Interior, Minerals Mgmt. Service, Gulf of Mexico OCS Region, New Orleans, La. 175 pp.

Murray, S.P. 1982. The effects of weather systems, currents, and coastal processes on major oil spills at sea. In: Kullenberg, G. (ed.). Pollutant Transfer and Transport in the Sea, Vol., II, CRC Press, Boca Raton, Fla., 169-228.

Nelson, D. M. and Q. Dortch 1996. Silicic acid depletion and silicon limitation in the plume of the Mississippi River: evidence from kinetic studies in spring and summer. Mar. Ecol. Progr. Ser. 136:163-178.

Niiler, P. 1995. SCULP Drifting Buoy Data, October 1993-January 195, Interim Data Report to the U.S. Minerals Management Service.

Nowlin, W.D. and C.A. 1974. Parker, Effects of a cold-air outbreak on shelf waters of the Gulf of Mexico, Journal of Physical Oceanography, Vol. 4, 467-486.

Nowlin, W. D., A.E. Jochens, R.O. Reid, S.F. DiMarco, L.C. bender, III, W. Wang, M.K. Howard, Y. Li, L.E. Sahl, C.A.N. Lyons, S.A. Hsu, M.R. Reap, D.A. Wiesenburg, D.A. DeFreitas, and C.L. Current. 1998. Texas-Louisiana Shelf Circulation and Transport Processes Study: Synthesis Report, Volume I. OCS Study/MMS 98-00nn. U.S. Department of the Interior, Minerals Mgmt. Service, Gulf of mexico OCS Region, New Orleans, La., 492 pp.

Oey, L.-Y., Eddy and wind-forced shelf circulation, Journal of Geophysical Research, 100, 8621-8637, 1995.

Officer, C. B. and J. H. Ryther. 1980. The possible importance of silicon in marine eutrophication. Mar. Ecol. Progr. Ser. 3: 83-91.

Olson, R.J., S.W. Chisholm, E.R. Zettler, and E. V. Armbrust. 1990. Pigments, size, and distribution of *Synechococcus* in the North Atlantic and Pacific Oceans. Limnol. Oceanogr. 35: 45-58.

Olson, R.J., S.W. chisholm, E.R. Zettler, and E.V. Armbrust. 1988. Analysis of *Synechococcus* pigment types in the sea using single and dual beam flow cytometry. Deep-Sea Res. 35: 425-440.

Packard, T. T. 1985. The estimation of oxygen utilization rate in seawater from the activity of the respiratory electron transport system in plankton. Ph.D. Dissertation, University of Washington, Seattle, Washington.

Park, E.T. 1977. Mesoplankton. pp. 180-190. In: H.L.Berryhill, Jr. (ed.). Environmental Studies of the South Texas Continental Shelf, 1975: An Atlas and Integrated Summary. U.S. Department of Commerce.

Park, E.T. 1979. Historical zooplankton. 61 pp. In: W.B. Jackson (ed.). Environmental Studies of the South Texas Continental Shelf, 1976-1977. NOAA Final Report to Bureau of Land Management*f*. U.S. Department of Commerce.

Park, E.T., S. Hamaoka, P. Turk, P. Jones, M. Valentine, and J. Haney. 1976. Zooplankton project. pp. 154-193. In: Environmental Studies, South Texas Outer Continental Shelf, 1975, Biology and Chemistry. U.S. Department of Commerce.

Park, E.T., and T.J. Minello. 1980. Chapter 6. Zooplankton. 64 pp. In: R.W. Hann and R.E. Randall (eds.). Evaluation of Brine Disposal from the Bryan Mound Site of the Strategic Petroleum Reserve Program. Final Report of Predisposal Studies. Volume 1. U.S. Department of Energy.

Parsons, T. R., Y. Maita and M. Lalli. 1984. A Manual of Chemical and Biological Methods for Seawater Analysis. Pergamon Press, New York, 173 pp.

Pennock, J.R. 1987. Temporal and spatial variability in phytoplankton ammonium and nitrate uptake in the Delaware Estuary. Est. Coast. Shelf Sci. 24: 841-857.

Pereira, W.E. and C.E. Rostad. 1990. Occurrence, distribution, and transport of herbicides and their degradation products in the lower Mississippi river and its tributaries. Environmental Science and Technology 24: 1400-1406.

Pettigrew, N. and S. P. Murray. 1986. The coastal boundary layer and inner shelf In: Mooers, C. (ed.), Baroclinic Proccesses on Continental Shelves, Coastal and Estuarine Sciences No. 3, AGU, Washington, D.C., 95-108

Pick, F.R. 1991. The abundance and composition of freshwater picocyanobacteria in relation to light penetration. Limnol. Oceanogr. 36: 1457-1451.

Pokryfki, L. and R. E. Randall. 1987. Nearshore hypoxia in the bottom water of the northwestern Gulf of Mexico from 1981 to 1984. Mar. Environ. Res. 22:75-90.

Pollard, R.T. and J.F. Read. 1989. A method of calibrating ship-mounted acoustic Doppler current profilers and the limitations of gyro compasses. J. Atmos. Oceanic Technol., 6:859-865.

Pomeroy, L. R. and D. Deibel. 1986. Temperature regulation of bacterial activity during the spring bloom in Newfoundland coastal waters. Sci. 233:359-361.

Qureshi, N. A. 1995. The role of fecal pellets in the flux of carbon to the sea floor on a river-influenced continental shelf subject to hypoxia. Ph.D. Dissertation, Department of Oceanography and Coastal Sciences, Louisiana State University, Baton Rouge, LA. 255 pp.

Rabalais, N .N. 1995. In Murray, S.P. and J. Donley (eds.). 1995. Mississippi River plume hudrography: Second annual report. OCS Study MMS 96-0022. U.S. Department of the Interior, Minerals Mgmt. Service, Gulf of Mexico OCS Region, New Orleans, La. 175 pp.

Rabalais, N. N., R. E. Turner, W. J. Wiseman, Jr. and D. F. Boesch. 1991. A brief summary of hypoxia on the northern Gulf of Mexico continental shelf: 1985--1988. Pp. 35-45 in R. V. Tyson and T. H. Pearson (eds.), Modern and Ancient Continental Shelf Anoxia. Geological Society Special Publ. No. 58, The Geological Society, London.

Rabalais, N.N., R.E. Turner, and W.J. Wiseman, Jr. 1992. A brief summary of hypoxia on the northern Gulf of Mexico continental shelf: 1985-1988. In: Modern and Ancient Continental Shelf Anoxia, ed by R.V. Tyson and T.H. Pearson, Geological Society Special Publ. No. 58, The Geological Society, London, pp. 35-46.

Rabalais, N.N., R.E. Turner, and W.J. Wiseman, Jr. 1994a. Hypoxic conditions in bottom waters on the Louisiana-Texas shelf. In: Coastal oceanographic effects of 1993 Mississippi River flooding. Special NOAA Report. NOAA Coastal Ocean Office/National Weather Service, Silver Springs, MD, pp 50-54.

Rabalais, N.N., W.J. Wiseman, Jr., and R.E. Turner. 1994b. Comparison of continuous records of near-bottom dissolved oxygen from the hypoxic zone along the Louisiana coast. Estuaries 17(4): 850-861.

Rabalais, N.N., Q. Dortch, D. Justic', M.B. Kilgen, P.L. Klerks, P.H. Templet, R.E. Turner, B. Cole, D. Duet, M. Beacham, S. Lentz, M. Parsons, S. Rabalais, and R. Robichaux. 1995. Status and Trends of Eutrophication, Pathogen Contamination, and Toxic Substances in the Barataria and Terrebonne Estuarine System. BTNEP Publ. No. 22, Barataria-Terrebonne National Estuary Program, Thibodaux, LA, 265 pp., plus Appendices.

Rabalais, N. N., R. E. Turner, D. Justic', Q. Dortch, W. J. Wiseman, Jr., and B. K. Sen Gupta. 1996. Nutrient changes in the Mississippi River and system responses on the adjacent continental shelf. Estuaries 19 (2b):386-407.

Rabalais, N. N., R. E. Turner, W. J. Wiseman, Jr. and Q. Dortch. 1998. Consequences of the 1993 Mississippi River flood in the Gulf of Mexico. Regulated Rivers 14:161-177.

Ray, R.T., L.W. Haas, M.E. Sieracki. 1989. Autotrophic picoplankton dynamics in a Chesapeake Bay sub-estuary. Mar. Ecol. Prog. Ser. 52: 273-285.

Redfield, A. C. 1958. The biological control of chemical factors in the environment. Am. Sci. 46:205-222.

Renaud, M.L. 1986. Hypoxia in Louisiana coastal wataers during 1983: implications for fisheries. Fish. Bull. 84(1):19-26.

Rhodes, R.C., A.J. Wallcraft, and J.D. Thompson, Navy-corrected geostrophic wind set for the Gulf of Mexico, NORDA Tech. Note 310, 103 pp. Naval Oceanogr. and Atmos. Res. Lab., Stennis Space Center, Mississippi, 1985.

Richards, W.J., T. Potthoff, S. Kelley, M.F. McGowan, L. Ejsymont, J.H. Power, and R.M. Olvera L. 1984. SEAMAP 1982 - Ichthyoplankton: Larval distribution and abundance of Engraulidae, Carangidae, Clupeidae, Lutjanidae, Serranidae, Coryphaenidae, Istiophoridae, Xiphiidae, and Scombridae in the Gulf of Mexico. U.S. Dept. Commer. NOAA Tech. Memo. MNFS-SEFC-144. 4 pp.

Richardson, L.L. 1996. Remote sensing of algal bloom dynamics. BioScience 46: 492-501.

Riley, G. A. 1941. Plankton Studies III. Long Island Sound. Bull. Bingham Oceanographic Collection 7:1-93.

Robert, H.H., O.K. Hud, S.A. Hsu, L.J. Rouse Jr., and D.A. Rickman. 1987. Impact of cold-front passages on geomorphic evolution and sediment dynamics of the complex Louisiana coast. Coastal Seidments "87, WW Div.?ASCE, New Orleans, La., May 12-14.

Robichaux, R.J., Q. Dortch, and J.H. Wrenn. 1996. *Occurrence of Gymnodinium sanguineum* in Louisiana and Texas coastal waters 1989-1994. Fish. Bull. In press.

Rogers, B.D., R.F. Shaw, W.H. Herke, and R.H. Banchet. 1993. Recruitment of postlarval and juvenile brown shrimp (*Penaeus aztecus* Ives) from offshore to estuarine waters of the northwestern Gulf of Mexico. Estuar. Coast. Shelf Sci. 36: 377-394.

Rosenberg, R. 1985. Eutrophication - the future marine coastal nuisance? Marine Pollution Bull. 16: 227-231.

Rouse, L.J., and J.M. Coleman. 1976. Circulation observations in the Louisiana Bight using Landsat imagery. Remote Sensing of Environment. 5:55-66.

Rouse, L.J. and Coleman, J.M., Circulation observations in the Louisiana Bight using LANDSAT imagery, Remote Sensing of Environment, XL, 635-642, 1976.

Rowe, G. T., C. H. Clifford, K. L. Smith and P. L. Hamilton. 1975. Benthic nutrient regeneration and its coupling to primary production in coastal waters. Nature 255:215-217.

SAS Institute Inc. 1989. SAS/STAT User's Guide, Version 6, Fourth Edition, Volume 1. SAS Institute Inc. Cary, NC. 943 pp.

Schmied, R.L., and E.E. Burgess. 1987. Marine recreational fisheries in the southeastern United States: An overview. Mar. Fish. Rev. 49(2): 3-7.

Scott, J.T. and Csanady, G.T. 1976. Nearshore currents off Long Island. J. Geophys. Res., 81(30):5401.

Sen Gupta, B. K., R. E. Turner and N. N. Rabalais. 1996. Seasonal oxygen depletion in continental-shelf waters of Louisiana: Historical record of benthic foraminifers. Geology 24:227-230.

Shapiro, L.P., and E.M. Haugen. 1988. Seasonal distribution and temperature tolerance of Synechococcus in Boothbay Harbor, ME. Est.Coast. Shelf Sci. 26: 517-525.

Shapiro, S.P., E.M. Haugen, and E.J. Carpenter. 1989. Occurrence and abundance of green-fluorescing dinoflagellates in the surface waters of the Northwest Atlantic and Northeast Pacific Oceans. J. Phycol. 25: 189-191.

Shaw, R.F., J.H. Cowan, Jr., and T.L. Tillman. 1985a. Distribution and abundance of *Brevoortia patronus* (gulf menhaden) eggs and larvae in the continental shelf waters of western Louisiana. Bull. Mar. Sci. 36(1): 96-103.

Shaw, R.F., and D.L. Drullinger. 1990a. Early life history profiles, seasonal abundance and distribution of four species of carangid larvae off Louisiana, 1982 and 1983. NOAA Tech. Rep. NMFS 89. 37 pp.

Shaw, R.F., and D.L. Drullinger. 1990b. Early life history profiles, seasonal abundance and distribution of four species of clupeid larvae from the northern Gulf of Mexico, 1982 and 1983. NOAA Tech. Rep. NMFS 88. 60 pp.

Shaw, R.F., B.D. Rogers, J.H. Cowan, Jr., and W.H. Herke. 1988. Ocean-estuary coupling of ichthyoplankton and nekton in the northern Gulf of Mexico. Am. Fish. Soc., Symposium. 3: 77-89

Shaw, R.F., W.J. Wiseman, Jr., R.E. Turner, L.J. Rouse, Jr., R.E. Condrey, and F.J. Kelly, Jr. 1985b. Transport of larval gulf menhaden *Brevoortia patronus* in continental shelf waters of western Louisiana: A hypothesis. Trans. Am. Fish. Soc. 114(4): 452-460.

Sigleo, A.C. and J.C. Means. 1990. Organic and inorganic components in estuarine colloids: Implications for sorption and transport of pollutants. Reviews of Environmental Contamination and Toxicology 12:123-147.

Simmons, E.G., and W.H. Thomas. 1962. Phytoplankton of the eastern Mississippi delta. Publications of the Institute of Marine Science, University of Texas 8: 269-298.

Sklar, F.H., and R.E. Turner. 1981. Characteristics of phytoplankton production off Barataria Bay in an area influenced by the Mississippi River. Contributions to Mar. Sci. 24: 93-106.

Smith, K. L., Jr. 1978a. Benthic community respiration in the N.W. Atlantic Ocean: *in situ* measurements from 40 to 5200 m. Marine Biology 47:337-347.

Smith, K. L., Jr. and K. R. Hinga. 1983. Sediment community respiration in the deep sea. pp. 331-370 In: G. T. Rowe (ed.) Deep-Sea Biology, Vol. 8. Wiley Interscience Publ., New York.

Smith, N.P. 1978b. Low-frequency reversals of nearshore currents in the north-western Gulf of Mexico, Contributions to Marine Science, 21:103-115.

Smith, N.P. 1980. Temporal and spatial variability in longshore motion along the Texas Gulf Coast. J. Geophys. Res, 85:1531-1536.

Smith, R.A., R.B. Alexander and M.G. Wolman. 1987. Water-quality trends in the nation's rivers. Science 235:1607-1615

Sogard, S.M., D.E. Hoss, and J.J. Govoni. 1987. Density and depth distribution of larval gulf menhaden *Brevoortia patronus*, Atlantic croaker *Micropogonias undulatus*, and spot *Leiostomus xanthurus*, in the northern Gulf of Mexico. Fish. Bull. 85: 601-609.

Steen, J.P., Jr., and G. Gunter. 1980. Zooplankton study at the Mobile OTEC site in the northern Gulf of Mexico. U.S. Department of Energy. 27 pp.

Strub, P.T., P.M. Kosro, and A. Huyer, The nature of cold filaments in the California Current system, J. Geophys. Res., 96, 14,743-14,768, 1991.

Sturges, W., The frequency of ring separations from the Loop Current, Journal of Physical Oceanography, 24, 1647-1651, 1994.

Stumpf, R.P. 1992. Remote sensing of water clarity and suspended sediments in coastsal waters. In: Proceedings of the First Thermatic Conference on Remote Sensing for Marine and Coastal Environments. 13 pp.

Suess, E. 1980. Particulate oxygen flux in the oceans--surface productivity and oxygen utilization. Nature 288:260-263.

Tamigneaux, E., E. Vazquez, M. Mingelbier, B. Klein, and L. Legendre. 1995. Environmental control of phytoplankton assemblages in nearshore marine waters, with special emphasis on phototrophic ultraplankton. J. Plankton Res. 17: 1421-1447.

Technicon. 1977. Silicates in Water and Seawater. Technicon AutoAnalyzer II Industrial Method No. 186-72W/B, Technicon Industrial Systems, Tarrytown, New York.

Tennant, D. A., and E. T. Baker. 1992. A fast, high-precision splitter for particle suspensions. Mar. Geol. 107: 247-252.

Turner, R.E., R. Kaswadji, N.N. Rabalais, and D.F. Boesch. 1987. Long-term changes in the Mississippi River water quality and its relationship to hypoxic continental shelf waters. In: Estuarine and Coastal Management—Tools of the Trade. Proceedings, Tenth National Conference, the Coastal Scoeity, October 12-15, 1986, New Orleans, Louisiana, pp 261-266.

Turner, R. E. and N. N. Rabalais. 1994. Evidence for coastal eutrophication near the Mississippi River plume. Nature 368:619-621.

Turner, R.E. and N.N. Rabalais. 1991. Changes in Mississippi River water quality this centruy. Implications for coastal food webs. BioScience 41(3): 140-147.

Turner, R. E., N. N. Rabalais and Z.-N. Zhang. 1990. Phytoplankton biomass, production and growth limitations on the Huanghe (Yellow River) continental shelf. Cont. Shelf Res. 10:545-571.

Turner, R. E. and R. L. Allen. 1982. Plankton respiration rates in the bottom waters of the Mississippi River Delta Bight. Contr. Mar. Sci. 25:173-179.

U.S. Department of Commerce. 1992a. Fisheries of the United States, 1991. U.S. Department of Commerce. National Oceanic and Atmospheric Administration. National Marine Fisheries Service. Current Fisheries Statistics No. 9100. 113 pp.

U.S. Department of Commerce. 1992b. Our Living Oceans: Report on the Status of U.S. Living Marine Resources, 1992 U.S. Department of Commerce. National Oceanic and Atmospheric Administration. National Marine Fisheries Service. NOAA Tech. Memo. NMFS-F/SPO-2. 148 pp.

USEPA. 1979. Methods for Chemical Analysis of Water and Wastes. Publ. No. EPA-600/4-79-020, U.S. Environmental Protection Agency, Environmental Monitoring and Support Laboratory, Office of Research and Development, Cincinnati, Ohio.

Valiela, I. 1984. Marine Ecological Processes. Springer Verlag, New York.

Vastano, A.C., C.N. Barron, Jr., and E.W. Shaar, Jr. 1995. Satellite observations of the Texas current. Cont. Shelf Res., 15(6):729-754.

Vaulot, D., and N. Xiuren. 1988. Abundance and cellular characteristics of marine *Synechococcus* spp. in the dilution zone of the Changjiang (Yangtze) River, China. Cont. Shelf Res. 8: 1171-1186.

Vecchione, M., C.M. Lascara, C.L. Stubblefield, and W.O. James. 1983. Chapter 9: The relationship between brine-diffuser operation and zooplankton distribution. In: L.R. DeRouen, R.W. Hann, D.M. Casserly, C. Giammona, and V.J. Lascara (eds.). West Hackberry Brine Disposal Monitoring. Year 1 Report. Final Report. U.S. Department of Energy.

Vecchione, M., C.E. Meyer, and C.L. Stubblefield. 1982. Chapter 8. Zooplankton. 69 pp. In: L.R. DeRouen, R.W. Hann, D.M. Casserly, and C. Giammona (eds.). West Hackberry Brine Disposal Project. Pre-Discharge Characterization. Final Report, January 1982. U.S. Department of Energy.

Walker, N.D. 1994. Satellite-based asessment of the Mississippi River discharge plume's spatial structure and temporal variability. OS Study MMS 94-0053. U.S. Dept. of the Interior, Minerals Manageament Service, Gulf of Mexico OCS Region, New Orleans, La., 56 pp.

Walker, N.D. 1996a. Satellite assessment of Mississippi River plume variability: causes and predictability, Remote Sensing of Environment, 58 (1):21-35.

Walker, N.D. 1996b. Remote Sensing and Imaging, In Murray, S.P. and J. Donley, Mississippi River Plume Hydrography, 2nd Annual Report, OCS Study/MMS 96-0022, U.S. Dept of the Interior, Minerals Management Service, Gulf of Mexico OCS Region, New Orleans, LA, pp. 127-147.

Walker, N.D., Huh, O.K., Rouse, L.J. Jr., Murray, S.P. 1996. Evolution and structure of a coastal squirt off the Mississippi River Delta: Northern Gulf of Mexico, Journal of Geophysical Research, 101(C9):20,643-20,655.

Walker, N.D. and L.J. Rouse, Jr. 1993. Satellite assessment of Mississippi River discharge plume variability. OCS Study MMS 93-0044. U.S. Dept. of the Interior. Minerals Mgmt. Service, Gulf of Mexico OCS Region, New Orleans, LA, 50 pp.

Walker, N.D., L.J. Rouse, Jr., and O.K. Huh. 1994. Remote sensing and imaging. In: Murray, S.P., Mississippi River Plume Hydrography: Annual Report, OCS Study/MMS 94-0028, U.S. Depart. of the Interior, Minerals Mgmt. Service, Gulf of Mexico OCS Regional Office, New Orleans, La., pp. 191-209.

Waterbury, J.B., S.W. Watson, F.W. Valois, and D.G. Franks. 1986. Biological and ecological characterizationof the marine unicellular cyanobacteria *Synechococcus*. Can. Bull. Fish. Aquat. Sci. 214: 71-120.

Williams, P. J. LeB. 1981. Microbial contributions to overall marine plankton metabolism: direct measurements of respiration. Oceanologica Acta 4:359-364.

Wiseman, W.J., Jr. and S.P. Dinnel. 1988. Shelf currents near the mouth of the Mississippi River. J. Phys. Oceanogr. 18:9.

Wiseman, W.J., Jr., S.P. Murray, J.M. Bane, and M.W. Tubman. 1976. Offshore physical oceanography. In J.G. Gosselink, R.R. Miller, M. Hood, and L.M. Bahr, Jr., (eds.) *Louisiana Offshore Oil Port: Environmental Baseline Study*. LOOP, Inc., New Orleans, LA.

Wiseman, Jr., W. J., S. P. Murray, J. M. Bane, and M. W. Tubman. 1982. Temperature and salinity variability within the Louisiana Bight. Contr. Mar. Sci. 25:109-120.

Wiseman, Jr., W.J. and R.W. Garvine. 1995. Plumes and coastal currents near large river mouths. Estuaries 18(3):509-517.

Wolff, G.A., B.L. Andryszak, J.H. Wormuth, and S.P. Berkowitz. 1984. Chapter 8: Zooplankton. 106 pp. In: R.W. Hann, C.P. Giammona, and R.E. Randall (eds.). Offshore Oceanographic and Environmental Monitoring Services for the Strategic Petroleum Reserve. Eighteen-month Report for the West Hackberry Site from May 1982 through November 1983. Volume I. U.S. Department of Energy.

Wood, A.M., P.K. Horan, K. Muirhead, D.A. Phinney, C.M. Yentsch, and J.B. Waterbury. 1985. Discrimination between types of pigments in marine *Synechococcus* spp. by scanning spectroscopy, epifluorescence microscopy, and flow cytometry. Limnol. Oceanogr. 30: 1303-1315.

Wright, L.D. and J. M. Coleman. 1971. Effluent expansion and interfacial mixing in the presence of a salt wedge, Mississippi River delta. J. Geophys. Res., 76:8649.

Wulff, F. and L. Rahm. 1988. Long-term, seasonal and spatial variations of nitrogen, phosphorus and silicate in the Baltic: An overview. Mar. Environmental Res. 26: 19-37.

The Department of the Interior Mission

As the Nation's principal conservation agency, the Department of the Interior has responsibility for most of our nationally owned public lands and natural resources. This includes fostering sound use of our land and water resources; protecting our fish, wildlife, and biological diversity; preserving the environmental and cultural values of our national parks and historical places; and providing for the enjoyment of life through outdoor recreation. The Department assesses our energy and mineral resources and works to ensure that their development is in the best interests of all our people by encouraging stewardship and citizen participation in their care. The Department also has a major responsibility for American Indian reservation communities and for people who live in island territories under U.S. administration.

The Minerals Management Service Mission

As a bureau of the Department of the Interior, the Minerals Management Service's (MMS) primary responsibilities are to manage the mineral resources located on the Nation's Outer Continental Shelf (OCS), collect revenue from the Federal OCS and onshore Federal and Indian lands, and distribute those revenues.

Moreover, in working to meet its responsibilities, the **Offshore Minerals Management Program** administers the OCS competitive leasing program and oversees the safe and environmentally sound exploration and production of our Nation's offshore natural gas, oil and other mineral resources. The MMS **Royalty Management Program** meets its responsibilities by ensuring the efficient, timely and accurate collection and disbursement of revenue from mineral leasing and production due to Indian tribes and allottees, States and the U.S. Treasury.

The MMS strives to fulfill its responsibilities through the general guiding principles of: (1) being responsive to the public's concerns and interests by maintaining a dialogue with all potentially affected parties and (2) carrying out its programs with an emphasis on working to enhance the quality of life for all Americans by lending MMS assistance and expertise to economic development and environmental protection.